

Olena Fesenko  
Leonid Yatsenko *Editors*

# Nanophysics, Nanomaterials, Interface Studies, and Applications

Selected Proceedings of the  
4th International Conference  
Nanotechnology and Nanomaterials  
(NANO2016), August 24-27, 2016, Lviv,  
Ukraine

# **Springer Proceedings in Physics**

Volume 195

The series Springer Proceedings in Physics, founded in 1984, is devoted to timely reports of state-of-the-art developments in physics and related sciences. Typically based on material presented at conferences, workshops and similar scientific meetings, volumes published in this series will constitute a comprehensive up-to-date source of reference on a field or subfield of relevance in contemporary physics. Proposals must include the following:

- name, place and date of the scientific meeting
- a link to the committees (local organization, international advisors etc.)
- scientific description of the meeting
- list of invited/plenary speakers
- an estimate of the planned proceedings book parameters (number of pages/articles, requested number of bulk copies, submission deadline).

More information about this series at <http://www.springer.com/series/361>

Olena Fesenko • Leonid Yatsenko  
Editors

# Nanophysics, Nanomaterials, Interface Studies, and Applications

Selected Proceedings of the 4th International  
Conference Nanotechnology and  
Nanomaterials (NANO2016), August 24-27,  
2016, Lviv, Ukraine

 Springer



*Editors*

Olena Fesenko  
National Academy of Sciences of Ukraine  
Institute of Physics  
Kiev, Ukraine

Leonid Yatsenko  
National Academy of Sciences of Ukraine  
Institute of Physics  
Kiev, Ukraine

ISSN 0930-8989

Springer Proceedings in Physics

ISBN 978-3-319-56244-5

DOI 10.1007/978-3-319-56422-7

ISSN 1867-4941 (electronic)

ISBN 978-3-319-56422-7 (eBook)

Library of Congress Control Number: 2017948243

© Springer International Publishing AG 2017

Chapter 34 was created within the capacity of an US governmental employment. US copyright protection does not apply.

This work is subject to copyright. All rights are reserved by the Publisher, whether the whole or part of the material is concerned, specifically the rights of translation, reprinting, reuse of illustrations, recitation, broadcasting, reproduction on microfilms or in any other physical way, and transmission or information storage and retrieval, electronic adaptation, computer software, or by similar or dissimilar methodology now known or hereafter developed.

The use of general descriptive names, registered names, trademarks, service marks, etc. in this publication does not imply, even in the absence of a specific statement, that such names are exempt from the relevant protective laws and regulations and therefore free for general use.

The publisher, the authors and the editors are safe to assume that the advice and information in this book are believed to be true and accurate at the date of publication. Neither the publisher nor the authors or the editors give a warranty, express or implied, with respect to the material contained herein or for any errors or omissions that may have been made. The publisher remains neutral with regard to jurisdictional claims in published maps and institutional affiliations.

Printed on acid-free paper

This Springer imprint is published by Springer Nature

The registered company is Springer International Publishing AG

The registered company address is: Gewerbestrasse 11, 6330 Cham, Switzerland

# Preface

This book highlights the most recent advances in nanoscience from leading researchers in Ukraine, Europe, and beyond. It features contributions from participants of the 4th International Research and Practice Conference “Nanotechnology and Nanomaterials” (NANO-2016), held in Lviv, Ukraine, on August 24–27, 2016. This event was organized jointly by the Institute of Physics of the National Academy of Sciences of Ukraine, Ivan Franko National University of Lviv (Ukraine), University of Tartu (Estonia), University of Turin (Italy), and Pierre and Marie Curie University (France). Internationally recognized experts from a wide range of universities and research institutes shared their knowledge and key results in the areas of nanocomposites and nanomaterials, nanostructured surfaces, microscopy of nano-objects, nano-optics, nanophotonics, nanoplasmonics, nanochemistry, nanobiotechnology, and surface-enhanced spectroscopy.

Today, nanotechnology has become one of the most actively developing and promising fields of science. Nanotechnology research has already resulted in numerous productive results that can be applied in various areas of human activity from science and electronics to medicine and pharmacology. The aim of this book is to highlight the latest developments from different areas of nanotechnology and to excite new interest in this field. The book chapters cover such important topics as nanocomposites, nanostructured interfaces and surfaces, nanochemistry, nano-optics, nanoplasmonics, and enhanced vibrational spectroscopy.

The book is divided into five sections: Part I, *Nanoscale Physics*; Part II, *Nano-optics and Photonics*; Part III, *Nanostructured Interfaces and Surfaces*; Part IV, *Nanochemistry and Biotechnology*; and Part V, *Nanocomposites and Nanomaterials*.

## Part I: Nanoscale Physics

In Chap. 1 (Fitio), the possibilities of a new method for solving the one-dimensional stationary Schrödinger equation in the frequency domain for different functions of potential energy have been analyzed. In Chap. 2 (Frolova), the effects of

ultrasonic synthesis on the basic properties of  $\text{CoFe}_2\text{O}_4$  nanoparticles are studied. In Chap. 3 (Dawid and Gburski), the structural and dynamical properties of an argon-krypton binary mixture confined between graphite slabs have been investigated and a molecular dynamics simulation has been made. In Chap. 4 (Gburski), three cholesterol-fullerene binary clusters varying in the number of fullerenes have been investigated. Chapter 5 (Grinevich) presents thermogravimetric studies of two different precursor complexes of tin dioxide. In Chap. 6 (Gudyma), modeling problems of spin crossover nanocrystals have been investigated. In Chap. 7 (Kaniukov), PET track membrane parameters have been comprehensively studied at the various formation stages. Chapter 8 (Korostil) investigates features of the current spin-orbit-induced magnetic dynamics in multilayer nanostructures with nonmagnetic heavy metal layers possessing a strong spin-orbit interaction. Chapter 9 (Luzanov) reviews the old and new tools for the interpretation of orbitals and excited states of nanodiamonds with defects. In Chap. 10 (Pokutnyi), the theory of excitonic quasimolecules (formed of spatially separated electrons and holes) in a nanosystem that consists of semiconductor quantum dots synthesized in a borosilicate glass matrix is presented. In Chap. 11 (Savka), the authors carried out molecular dynamics simulations to investigate the process of formation of ZnO nanoclusters from the gas phase. Chapter 12 (Sulymenko) presents an investigation of global coupling of microwave phase-locking of weakly coupled spin-torque nanoscillators. Chapter 13 (Suprun) presents the calculation of the current density in the complete absence of violations of electrostatic equilibrium at a nonzero temperature. In Chap. 14 (Vasylyuk), the authors investigate the mechanisms of nanoconductivity in polyene polymers. Chapter 15 (Kizilova) focuses on complex flows of immiscible microfluids and nanofluids with velocity slip boundary conditions.

## Part II: Nano-optics and Photonics

Chapter 16 (Bulavinets) reviews modern methods for improving the quality of digital interferograms, including methods for eliminating zero order and filtering the resulting hologram phase map. In Chap. 17 (Dawid) the interaction-induced absorption spectrum of confined Ar-Xe mixture has been observed. Chapter 18 (Glushko) focuses on electromagnetic modes inside the island-kind 2D photonic crystal resonator. In Chap. 19 (Shopa), dynamic light scattering with nanoparticles has been studied. The effect of soft X-rays with photon energy  $W = 8$  keV on the kinetics of decay photovoltage in solar silicon crystals is studied in Chap. 20 (Steblenko). In Chap. 21 (Hryn), two-dimensional photonic crystals formed by ordering of nanoparticles of different nature in the polymeric matrix are studied. The authors of Chap. 22 (Tatarchuk) present an overview of the preparation, crystal structure, and applications of SFs used in technology for the design of new materials and devices. In Chap. 23 (Kaladkevich), MAX phase-based compacts obtained by shock wave are studied. The authors of Chap. 24 (Wisz) present standard silicon photovoltaic devices improved by ZnO film obtained by pulsed laser deposition at

different temperatures of silicon and ITO/glass substrates using second harmonic of YAG:Nd<sup>3+</sup> laser. In Chap. 25 (Potera), the results of research on the effect of the transmission spectrum of copper oxide films on glass substrate versus conditions of growth and heating in air are presented.

### **Part III: Nanostructured Interfaces and Surfaces**

In Chap. 26 (Honcharov), the structural, catalytic, and thermal properties of stainless steel with a nanoscale metal surface layer are studied. The authors of Chap. 27 (Kharchenko) present studies on the formation of nano-sized patterns in surface layers based on local changes in the surface layer temperature. The effect of the Fermi velocity on the conductivity of the graphene-superconductive graphene junction is investigated in Chap. 28 (Korol). In Chap. 29 (Nedolya), the possibility of carbon atoms' drift to the surface of an FCC iron nanocluster through tetrahedral interstice is investigated. Chapter 30 (Savkina) presents the results of the formation of nanoscale patterns on the surface of a ternary compound. In Chap. 31 (Tarasov), a detailed theory of the scattering of plasmon-polariton waves by a segment of the metal-dielectric (vacuum) interface with randomly distributed surface impedance is developed. In Chap. 32 (Wiśniewska), the authors investigate the influence of solution pH on the nanostructure of the adsorption layer of selected ionic polyamino acids and their copolymers at the solid-liquid interface. The authors of Chap. 33 (Bazela) investigate the poly- and nanocrystalline TbMnO<sub>3</sub> samples crystallized in the orthorhombically distorted perovskite structure. In Chap. 34 (Gab), the dispersion kinetics of palladium and platinum nanofilms of 100 nm thickness deposited onto oxide substrate (quartz glass, leucosapphire, ZrO<sub>2</sub> ceramic) and annealed in a vacuum at 1000–1600 °C are studied. In Chap. 35 (Chrzanowska), the properties of the twist bend phase of liquid crystals obtained on the basis of the Landau de Gennes theory are presented. The authors of Chap. 36 (Klym) investigate the influence of inner free-volume structure on the functional properties of chalcogenide GeSe<sub>2</sub>-Ga<sub>2</sub>Se<sub>3</sub> and GeS<sub>2</sub>-Ga<sub>2</sub>S<sub>3</sub>-CsCl glasses as well as oxide Cu<sub>0.4</sub>Co<sub>0.4</sub>Ni<sub>0.4</sub>Mn<sub>1.8</sub>O<sub>4</sub> and MgO-Al<sub>2</sub>O<sub>3</sub> ceramics.

### **Part IV: Nanochemistry and Biotechnology**

In Chap. 37 (Barbash), the possibility of obtaining nanocellulose from organosolv straw pulp is studied. The authors of Chap. 38 (Sakhnenko) investigate the nanoscale oxide PEO coatings forming from diphosphate electrolytes. The authors of Chap. 39 (Kucherenko) have developed an amperometric biosensor based on a bienzyme system (GOx/HEX) for ATP determination and investigate three different methods of GOx/HEX immobilization on the surface of working electrodes. The authors of Chap. 40 (Kushevskaya) have synthesized nanodispersed iron powders by

means of thermal decomposition of iron citrate salt  $\text{Fe}_3\{\text{C}_3\text{H}_5(\text{O})(\text{COO})_3\}_2$  in a protective hydrocarbon mixture atmosphere in temperatures of 250–500 °C. The authors of Chap. 41 (Maizelis) propose electrochemical methods of Cu/(Ni-Cu) and nickel-copper oxide multilayer coating formation in pyrophosphate-ammonium electrolyte. Chapter 42 (Marchenko) presents the development of a creatinine-sensitive biosensor consisting of pH-sensitive field-effect transistor (pH FET) and creatinine deiminase (CD) immobilized with various types of zeolites, in particular, silicalite, zeolites beta (BEA) and nanobeta, and BEA zeolites, modified with gold nanoparticles and ions. The authors of Chap. 43 (Kutsevol) synthesize and characterize branched nanostructured copolymers dextran-g-polyacrylamide (D-g-PAA) in uncharged and anionic form and test them in flocculation in comparison with linear PAA. The authors of Chap. 44 (Raczyński) present the results of molecular dynamics simulations of the dynamics of small cholesterol systems. A quantum chemical study of water molecule adsorption on nitrogen-doped titania thin films is presented in Chap. 45 (Smirnova). In Chap. 46 (Stetsko), the authors present research on the effects of chemical vapor deposition of elements on the structure of nanocomposite layers. In Chap. 47 (Vasylyv), the authors investigate the effect of the quantity of water vapor in hydrogenous atmospheres on reducing ability of the YSZ-NiO fuel cell anode material. Chapter 48 (Borysova) focuses on sol-gel synthesis and conductivity of  $\text{NaLn}_9(\text{SiO}_4)_6\text{O}_2$ .

## Part V: Nanocomposites and Nanomaterials

Chapter 49 (Demchenko) is devoted to the structure, morphology, and properties of copper-containing polymer nanocomposites. In Chap. 50 (Derhachov), the possibility of opal infiltration with high-temperature melted  $\text{Bi}_{12}\text{SiO}_{20}$ ,  $\text{Bi}_2\text{TeO}_5$ , and  $\text{NaBi}(\text{MO}_4)_2$  is examined and the obtained composite is characterized. Chapter 51 (Dzyazko) focuses on improvement of antifouling stability of polymer membranes. Chapter 52 (Gab) presents a chemicompetallurgical method for obtaining of tungsten-based nanopowders. Chapter 53 (Guglya) covers the methods of production, the structure formation mechanism, and the properties of nano-porous thin film  $\text{VN}_x$  hydrogen absorbents. The authors of Chap. 54 (Makarchuk) have created and studied magnetic nanocomposite sorbents on bases of saponite, palygorskite, and spondyle clay. Chapter 55 (Nawrocki) is devoted to measurements of electrical conductance in nanostructures and their use in nanotechnology. The authors of Chap. 56 (Nosach) present a study of nano-particulate structures with glucose-derived char and compacted fumed silica in gaseous and aqueous media. In Chap. 57 (Panko), nano- and microdisperse structures are investigated in processes of metamorphism, reduction sintering, and component separation of iron-oxide-silicate materials. Chapter 58 (Pinchuk-Rugal) focuses on the electron radiation effect on polyvinylchloride (PVC) nanocomposites with multi-walled carbon nanotubes. Chapter 59 (Prokopov) presents the results of studies of resistivity, thermopower, and Hall phenomenon in fine crystalline pyrolytic anisotropic graphite intercalated

compounds with bromine and iodine chloride in the temperature range of phase transformation in intercalate layers. In Chap. 60 (Raczyński), the authors study the system of cholesterol molecules placed between two parallel graphene sheets using molecular dynamics (MD). Chapter 61 (Revo) presents the structural features, strength, and microhardness of nanocomposites obtained from Fe, Cu, and carbon nanotubes. In Chap. 62 (Shevchenko), the authors investigate the influence of radio-frequency electromagnetic radiation on the magnetic properties of a magneto-mechano-chemically synthesized antitumor nanocomplex. Chapter 63 (Tchervinka) is focused on continuum modeling of nanoelements. In Chap. 64 (Vyshnevskaya), a range of methods for obtaining poly(diphenylamine)-Ag NP nanocomposites are studied and the resulting hybrid materials characterized using SEM, TEM, AFM, and IR spectroscopy. The semiconducting and optical properties of compact graphene-like nanoparticles of molybdenum disulfide are investigated in Chap. 65 (Len). The electromagnetic and microwave absorbing properties of nanocarbon-epoxy Laritte 285 composites filled with GNPs and MWCNTs, as well as ternary CMs filled with GNPs and MWCNTs simultaneously, are studied as a function of frequency and filler weight content in Chap. 66 (Melnichenko).

Summing up, in this volume you can see many surveys of the latest advances in the field of nanotechnology that point the way to exciting future investigations and applications. The book demonstrates some of the latest research in nano-optics, nanoplasmonics, nanochemistry, and nanophotonics and their applications that concern a very interesting and exciting area of modern science that has already attracted the attention of thousands of scientists, engineers, and young researchers.

Kiev, Ukraine

Olena Fesenko  
Leonid Yatsenko

# Contents

## Part I Nanoscale Physics

<b>1</b>	<b>Numerical Solution of One-Dimensional Stationary Schrödinger Equation in the Frequency Domain</b> .....	<b>3</b>
	V.M. Fitio, I.Ya. Yaremchuk, V.V. Romakh, and Ya.V. Bobitski	
<b>2</b>	<b>Effects of Ultrasonic Synthesis Variable on Basic Properties of CoFe<sub>2</sub>O<sub>4</sub> Nanoparticles</b> .....	<b>19</b>
	L.A. Frolova, O.I. Kushnerov, and Y.D. Galivets	
<b>3</b>	<b>Structural and Dynamical Properties of Argon-Krypton Binary Mixture Confined Between Graphite Slabs: Molecular Dynamics Simulation</b> .....	<b>29</b>
	A. Dawid and Z. Gburski	
<b>4</b>	<b>Properties of Cholesterol-Fullerene Binary Cluster: MD Simulations</b> .....	<b>45</b>
	Z. Gburski, Violetta Raczyńska, and Przemysław Raczyński	
<b>5</b>	<b>Thermogravimetric Study of Nano-SnO<sub>2</sub> Precursors</b> .....	<b>53</b>
	Viktor S. Grinevych, Liudmila M. Filevska, Sergij M. Savin, Valentyn A. Smyntyna, and Bulent Ulug	
<b>6</b>	<b>Modeling Problems of Spin Crossover Nanocrystals</b> .....	<b>63</b>
	Iurii Gudyma, Artur Maksymov, and Andrej Bobák	
<b>7</b>	<b>Characterization of Pet Track Membrane Parameters</b> .....	<b>79</b>
	Egor Kaniukov, Alena Shumskaya, Dzmitry Yakimchuk, Artem Kozlovskiy, Anel Ibrayeva, and Maksim Zdorovets	
<b>8</b>	<b>Current Spin-Orbit-Induced Microwave Magnetic Dynamics in Layered Nanostructures</b> .....	<b>93</b>
	A.M. Korostil and M.M. Krupa	

<b>9</b>	<b>Localization of Orbitals and Electronic Properties in Nanodiamonds with Color Centers: Semiempirical Models</b> .....	115
	Anatoliy V. Luzanov	
<b>10</b>	<b>Excitonic Quasimolecules in Nanoheterosystems Containing Semiconductor and Dielectric Quantum Dots</b> .....	131
	Sergey I. Pokutnyi	
<b>11</b>	<b>Molecular Dynamics Simulations of the Formation Processes of Zinc Oxide Nanoclusters in Oxygen Environment</b> .....	145
	S.S. Savka, D.I. Popovych, and A.S. Serednytskyi	
<b>12</b>	<b>Microwave Phase-Locking of Weakly Coupled Spin-Torque Nano-Oscillators: The Case of Global Coupling</b> .....	157
	O.R. Sulymenko and O.V. Prokopenko	
<b>13</b>	<b>Temperature Effect on the Basis States for Charge Transfer Through a Polypeptide Fragments of Proteins and on the Nanocurrent in It</b> .....	175
	A.D. Suprun and L.V. Shmeleva	
<b>14</b>	<b>About Possible Mechanisms of Nanoconductivity in Polyenes Polymers: The Charge Solitons at Extremely Weak External Fields</b> .....	187
	S.V. Vasylyuk, A.D. Suprun, and V.N. Yashchuk	
<b>15</b>	<b>Complex Flows of Immiscible Microfluids and Nanofluids with Velocity Slip Boundary Conditions</b> .....	207
	Vitalina Cherevko and Natalya Kizilova	
<b>Part II Nanooptics and Photonics</b>		
<b>16</b>	<b>Optimization of the Parameters of Digital Holographic Microscope</b> .....	231
	Yu. Kotsiuba, H. Petrovska, V.M. Fitio, T. Bulavinets, and Ya. V. Bobitski	
<b>17</b>	<b>Computer Simulation of Collision-Induced Absorption Spectra of Confined Argon-Xenon Mixture</b> .....	249
	A. Dawid and Z. Gburski	
<b>18</b>	<b>Electromagnetic Modes Inside the Island Kind 2D Photonic Crystal Resonator</b> .....	263
	E.Ya. Glushko and A.N. Stepanyuk	
<b>19</b>	<b>Dynamic Light Scattering with Nanoparticles: Setup and Preliminary Results</b> .....	275
	G. Derkachov, D. Jakubczyk, K. Kolwas, Y. Shopa, and M. Woźniak	



<b>20</b>	<b>Application of Nanofilled Polymer Coatings for Increasing Radiation Resistance of Solar Cells</b> .....	283
	L.P. Steblenko, A.A. Podolyan, L.N. Yashchenko, D.V. Kalinichenko, A.N. Kuryliuk, Yu. L. Kobzar, L.A. Voronzova, V.N. Kravchenko, S.N. Naumenko, and A.N. Krit	
<b>21</b>	<b>Two-Dimensional Periodic Structures Recorded in Nanocomposites by Holographic Method: Features of Formation, Applications</b> .....	293
	V.O. Hryn, P.V. Yezhov, and T.N. Smirnova	
<b>22</b>	<b>Spinel Ferrite Nanoparticles: Synthesis, Crystal Structure, Properties, and Perspective Applications</b> .....	305
	Tetiana Tatarchuk, Mohamed Bououdina, J. Judith Vijaya, and L. John Kennedy	
<b>23</b>	<b>Study of MAX Phase-Based Compacts Obtained by Shock-Wave Loading Method</b> .....	327
	Larysa Sudnik, Aleksey Luchenok, Yuliya Kaladkevich, Victor Tkachuk, Tatiana Prikhna, and Artem Kozyrev	
<b>24</b>	<b>Standard Si Photovoltaic Devices Improved by ZnO Film Obtained by Pulsed Laser Deposition</b> .....	335
	G. Wisz, I. Virt, P. Sagan, I. Hatala, Ł. Głowa, M. Kaczor, and R. Yavorskyi	
<b>25</b>	<b>Influence of Growth Condition and Thermal Treatment of Thin Copper Oxide Films Obtained by Magnetron Sputtering on Their Transmission Spectra</b> .....	347
	G. Wisz, P. Potera, Ł. Głowa, and M. Kaczor	
<b>Part III Nanostructured Interfaces and Surfaces</b>		
<b>26</b>	<b>Structural, Catalytic, and Thermal Properties of Stainless Steel with Nanoscale Metal Surface Layer</b> .....	355
	V. Honcharov, V. Zazhigalov, Z. Sawlowicz, R. Socha, and J. Gurgol	
<b>27</b>	<b>Thermal Effects at Nano-sized Pattern Formation in Surface Layers</b> .....	365
	Dmitrii O. Kharchenko and Vasyl O. Kharchenko	
<b>28</b>	<b>The Effect of the Fermi Velocity on the Conductivity of the Graphene-Superconductive Graphene Junction</b> .....	383
	A.M. Korol, S.I. Litvynchuk, N.V. Medvid, and V.M. Isai	
<b>29</b>	<b>On the Possibility of Carbon Atoms' Drift to the Surface of a FCC Iron Nanocluster Through Tetrahedral Interstice</b> .....	395
	A.V. Nedolya and N.V. Bondarenko	

<b>30</b>	<b>Nanostructuring Surfaces of HgCdTe by Ion Bombardment</b> .....	405
	A.B. Smirnov and R.K. Savkina	
<b>31</b>	<b>The Plasmon-Polariton Mirroring Due to Strong Fluctuations of the Surface Impedance</b> .....	417
	Yu. V. Tarasov, O.V. Usatenko, and D.A. Iakushev	
<b>32</b>	<b>Influence of Solution pH on the Nanostructure of Adsorption Layer of Selected Ionic Polyamino Acids and Their Copolymers at the Solid-Liquid Interface</b> .....	431
	Małgorzata Wiśniewska, Iwona Ostolska, and Agnieszka Nosal-Wiercińska	
<b>33</b>	<b>Grain Size Effect on Crystal Microstructure of the Nanoparticle TbMnO<sub>3</sub> Manganite</b> .....	445
	Wiesława Bażela, Marcin Dul, Andrzej Szytuła, and Volodymyr Dyakonov	
<b>34</b>	<b>Influence of Annealing in Vacuum on Dispersion Kinetics of Palladium and Platinum Nanofilms Deposited onto Oxide Materials</b> .....	457
	Y.V. Naidich, I.I. Gab, T.V. Stetsyuk, B.D. Kostyuk, and V.V. Kavelin	
<b>35</b>	<b>Nematic Twist-Bend Phases of Liquid Crystals</b> .....	469
	Agnieszka Chrzanowska	
<b>36</b>	<b>Influence of Free Volumes on Functional Properties of Modified Chalcogenide Glasses and Oxide Ceramics</b> .....	479
	H. Klym, O. Shpotyuk, A. Ingram, L. Calvez, I. Hadzaman, Yu. Kostiv, A. Ivanusa, and D. Chalyy	
<b>Part IV Nanochemistry and Biotechnology</b>		
<b>37</b>	<b>Preparation of Nanocellulose from Organosolv Straw Pulp Using Acid Hydrolysis and Ultrasound</b> .....	497
	V.A. Barbash, O.V. Yaschenko, O.M. Shniruk, and V.O. Kovalchuk	
<b>38</b>	<b>Nanoscale Oxide PEO Coatings Forming from Diphosphate Electrolytes</b> .....	507
	Nikolay D. Sakhnenko, Maryna V. Ved, and Ann V. Karakurkchi	
<b>39</b>	<b>Gold Nanoparticle/Polymer/Enzyme Nanocomposite for the Development of Adenosine Triphosphate Biosensor</b> .....	533
	Ivan S. Kucherenko, Carole Farre, Gaetan Raimondi, Carole Chaix, Nicole Jaffrezic-Renault, Oleksandr O. Soldatkin, Alexei P. Soldatkin, and Florence Lagarde	

<b>40</b>	<b>Novel Ferromagnetic Iron-Based Nanocomposite Powders with High Magnetic Characteristics</b> .....	547
	N.F. Kuschevskaya, V.V. Malyshev, D.B. Shakhnin, and E.A. Paprotskaya	
<b>41</b>	<b>Electrochemical Formation of Multilayer Metal and Metal Oxide Coatings in Complex Electrolytes</b> .....	557
	Antonina Maizelis and Boris Bairachniy	
<b>42</b>	<b>Development of a New Biosensor by Adsorption of Creatinine Deiminase on Monolayers of Micro- and Nanoscale Zeolites</b> .....	573
	Svitlana V. Marchenko, Ihor I. Piliponskiy, Olha O. Mamchur, Oleksandr O. Soldatkin, Ivan S. Kucherenko, Berna Ozansoy Kasap, Burcu Akata Kurç, Sergei V. Dzyadevych, and Alexei P. Soldatkin	
<b>43</b>	<b>Nanostructured Dextran-Graft-Polyacrylamide Flocculants: Effect of Internal Molecular Structure on Flocculative Efficiency</b> ....	585
	N.V. Kutsevol, V.A. Chumachenko, A.V. Balega, O.M. Nadtocka, and A.P. Naumenko	
<b>44</b>	<b>Molecular Dynamics Simulations of the Dynamics of Small Cholesterol Systems</b> .....	595
	Przemysław Raczyński and Z. Gburski	
<b>45</b>	<b>Quantum Chemical Study of Water Molecule Adsorption on the Nitrogen-Doped Titania Thin Films</b> .....	603
	O. Smirnova, A. Grebenyuk, O. Linnik, and V. Lobanov	
<b>46</b>	<b>Effect of Chemical Vapor Deposition on the Morphology of the Nanocomposite Layer in the Complex Method</b> .....	611
	Andrew E. Stetsko	
<b>47</b>	<b>Effect of Water Vapor Amount in Hydrogenous Atmospheres on Reducing Ability of the YSZ –NiO Fuel Cell Anode Material</b> .....	623
	B.D. Vasyliv, V.Ya. Podhurska, and O.P. Ostash	
<b>48</b>	<b>Sol-gel Synthesis and Conductivity <math>\text{NaLn}_9(\text{SiO}_4)_6\text{O}_2</math></b> .....	631
	K.V. Borysova and E.I. Getman	
<b>Part V Nanocomposites and Nanomaterials</b>		
<b>49</b>	<b>Structure, Morphology, and Properties of Copper-Containing Polymer Nanocomposites</b> .....	641
	V. Demchenko, S. Riabov, N. Rybalchenko, and V. Shtompel'	
<b>50</b>	<b>Nanocomposites on the Base of Synthetic Opals and Nanocrystalline Phases of Bi-containing Active Dielectrics</b> .....	661
	V. Moiseienko, M. Derhachov, B. Abu Sal, R. Holze, and M. Brynza	

<b>51</b>	<b>Organic-Inorganic Materials for Baromembrane Separation</b> .....	675
	Yurii Zmievskii, Ludmila Rozhdestvenska, Yuliya Dzyazko, Ludmila Kornienko, Valerii Myronchuk, Alexander Bildukevich, and Anatolii Ukrainetz	
<b>52</b>	<b>Chemico-metallurgical Method for Obtaining Tungsten-Based Nanopowders</b> .....	687
	N.F. Kuschevskaya, A.I. Gab, E.A. Paprotskaya, and V.V. Malyshev	
<b>53</b>	<b>Nanoporous Thin Film VN<sub>x</sub> Hydrogen Absorbents: Method of Production, Structure Formation Mechanism, and Properties</b> .....	693
	Alexey Guglya, Alexander Kalchenko, Yury Marchenko, Elena Solopikhina, Viktor Vlasov, and Elena Lyubchenko	
<b>54</b>	<b>Magnetic Nanocomposite Sorbents on Mineral Base</b> .....	705
	Oksana Makarchuk, Tetiana Dontsova, and Anatolii Perekos	
<b>55</b>	<b>Measurements of Electrical Conductance in Nanostructures and Their Use in Nanotechnology</b> .....	721
	Waldemar Nawrocki	
<b>56</b>	<b>Nano-particulate Structures with Glucose-Derived Char and Compacted Fumed Silica in Gaseous and Aqueous Media</b> .....	729
	L.V. Nosach, E.F. Voronin, E.M. Pakhlov, B. Charnas, J. Skubiszewska-Zięba, E. Skwarek, W. Janusz, and V.M. Gun'ko	
<b>57</b>	<b>Nano- and Microdisperse Structures in Processes of Metamorphism, Reduction Sintering, and Component Separation of Iron-Oxide-Silicate Materials</b> .....	743
	A.V. Panko, I.G. Kovzun, V.A. Prokopenko, O.A. Tsyganovich, V.O. Oliinyk, and O.M. Nikipelova	
<b>58</b>	<b>The Electron Radiation Effect on Polyvinylchloride (PVC) Nanocomposites with Multiwalled Carbon Nanotubes</b> .....	757
	T.M. Pinchuk-Rugal, O.P. Dmytrenko, M.P. Kulish, Yu. I. Prylutsyy, O.S. Nychyporenko, M.I. Shut, V.M. Tkach, and V.V. Shlapatska	
<b>59</b>	<b>Peculiarities of Charge Transfer in Graphite Intercalation Compounds with Bromine and Iodine Chloride</b> .....	771
	Oleksandr I. Prokopov, Irina V. Ovsiienko, Lyudmila Yu. Matzui, Oleksandra S. Zloi, Nikolai A. Borovoy, Tatiana A. Len, and Dina D. Naumova	
<b>60</b>	<b>Computer Simulations of the Dynamics of Cholesterol Molecules Located Between Graphene Sheets</b> .....	789
	Przemysław Raczyński, Violetta Raczyńska, and Z. Gburski	

<b>61</b>	<b>Structure Features, Strength, and Microhardness of Nanocomposites Obtained from Fe, Cu, and Carbon Nanotubes ..</b>	<b>799</b>
	S.L. Revo, M.M. Melnichenko, M.M. Dashevskiy, N.N. Belyavina, O.I. Nakonechna, K.O. Ivanenko, O.I. Boshko, and T.G. Avramenko	
<b>62</b>	<b>Influence of Radiofrequency Electromagnetic Radiation on Magnetic Properties of Magneto-Mechanochemically Synthesized Antitumor Nanocomplex .....</b>	<b>813</b>
	V. Orel, A. Shevchenko, O. Rykhalskyi, A. Romanov, A. Burlaka, and S. Lukin	
<b>63</b>	<b>Continuum Modeling of Nanoelements .....</b>	<b>827</b>
	T.S. Nahirnyj and K.A. Tchervinka	
<b>64</b>	<b>The Electrochromic Feedback Methods for Obtaining Nanoparticles, Nanoalloys and Core-Shell Objects in Quasi-reversible Redox Systems .....</b>	<b>837</b>
	Yu. P. Vyshnevska and I.V. Brazhnyk	
<b>65</b>	<b>Semiconducting and Optical Properties of Compact Graphene-Like Nanoparticles of Molybdenum Disulfide .....</b>	<b>845</b>
	Leonid M. Kulikov, N.B. Konig-Ettel, Lyudmila Yu. Matzui, Antonina P. Naumenko, Tetyana A. Len, Iryna V. Ovsienko, and Vladimir I. Matzui	
<b>66</b>	<b>Dielectric Properties of Nanocarbon Polymer Composites with Binary Filler .....</b>	<b>855</b>
	M.S. Melnychenko, Yu. S. Perets, L.L. Aleksandrovych, L.L. Vovchenko, O.A. Lazarenko, and Lyudmila Yu. Matzui	
	<b>Index .....</b>	<b>873</b>

# Contributors

**L. L. Aleksandrovykh** Physics Faculty of Taras Shevchenko National University of Kyiv, Kyiv, Ukraine

**T. G. Avramenko** Taras Shevchenko National University of Kyiv, Kyiv, Ukraine

**B. I. Bairachniy** National Technical University, “Kharkov Polytechnic Institute”, Kharkov, Ukraine

**A. V. Balega** Institute of Biology, Taras Shevchenko National University of Kyiv, Kyiv, Ukraine

**V. A. Barbash** National Technical University of Ukraine “Igor Sikorsky Kyiv Polytechnic Institute”, Kyiv, Ukraine

**Wiesława Bażela** Institute of Physics, Cracow University of Technology, Cracow, Poland

**N. N. Belyavina** Taras Shevchenko National University of Kyiv, Kyiv, Ukraine

**Alexander Bildukevich** Institute of Physical Organic Chemistry, National Academy of Sciences of Belarus, Minsk, Belarus

**Andrej Bobák** Department of Theoretical Physics and Astrophysics, Faculty of Science, P.J. Šafárik University, Košice, Slovak Republic

**Ya. V. Bobitski** Department of Photonics, Lviv Polytechnic National University, Lviv, Ukraine

Faculty of Mathematics and Natural Sciences, University of Rzeszow, Rzeszow, Poland

**N. V. Bondarenko** Applied Physics Department, Zaporizhzhya National University, Zaporizhzhya, Ukraine

**Nikolai A. Borovoy** Departments of Physics and Chemistry, Taras Shevchenko National University of Kyiv, Kyiv, Ukraine

- K. V. Borysova** Donetsk National University, Vinnytsia, Ukraine
- O. I. Boshko** Taras Shevchenko National University of Kyiv, Kyiv, Ukraine
- Mohamed Bououdina** Department of Physics, College of Science, University of Bahrain, Southern Governorate, Bahrain
- I. V. Brazhnyk** Gimasi SA Ukraine R&D Centre, Mendrisio, Switzerland
- M. Brynza** Oles Honchar Dnipro National University, Dnipro, Ukraine
- T. Bulavinets** Department of Photonics, Lviv Polytechnic National University, Lviv, Ukraine
- A. Burlaka** R. E. Kavetsky Institute of Experimental Pathology, Oncology and Radiobiology, Kyiv, Ukraine
- L. Calvez** Equipe Verres et et Céramiques, UMR-CNRS 6226, Institute des Sciences chimiques de Rennes, Université de Rennes, Rennes Cedex, France
- Carole Chaix** Univ Lyon, CNRS, Université Claude Bernard Lyon1, ENS de Lyon, Institut des Sciences Analytiques, Villeurbanne, France
- D. Chalyy** Lviv State University of Life Safety, Lviv, Ukraine
- B. Charmas** Maria Curie-Skłodowska University, Lublin, Poland
- Vitalina Cherevko** Kharkov National University, Kharkov, Ukraine
- Agnieszka Chrzanowska** Institute of Physics, Kraków University of Technology, Kraków, Poland
- V. A. Chumachenko** Faculty of Chemistry, Taras Shevchenko National University of Kyiv, Kyiv, Ukraine
- M. M. Dashevskiy** Taras Shevchenko National University of Kyiv, Kyiv, Ukraine
- A. Dawid** Department of Computer Science, The University of Dąbrowa Górnicza, Dąbrowa Górnicza, Poland
- V. Demchenko** Institute of Macromolecular Chemistry, The National Academy of Sciences of Ukraine, Kiev, Ukraine
- M. Derhachov** Oles Honchar Dnipro National University, Dnipro, Ukraine
- G. Derkachov** Institute of Physics, Polish Academy of Sciences, Warsaw, Poland
- O. P. Dmytrenko** Taras Shevchenko National University of Kyiv, Kyiv, Ukraine
- Tetiana Dontsova** National Technical University of Ukraine “Kyiv Polytechnic Institute”, Kyiv, Ukraine
- Marcin Dul** Institute of Physics, Cracow University of Technology, Cracow, Poland

**Volodymyr Dyakonov** Institute of Physics, Polish Academy of Science, Warsaw, Poland

**Sergei V. Dzyadevych** Laboratory of Biomolecular Electronics, Institute of Molecular Biology and Genetics, National Academy of Sciences of Ukraine, Kyiv, Ukraine

Institute of High Technologies, Taras Shevchenko National University of Kyiv, Kyiv, Ukraine

**Yuliya Dzyazko** V. I. Vernadskii Institute of General and Inorganic Chemistry of the National Academy of Science of Ukraine, Kyiv, Ukraine

**Carole Farre** Univ Lyon, CNRS, Université Claude Bernard Lyon1, ENS de Lyon, Institut des Sciences Analytiques, Villeurbanne, France

**Liudmila M. Filevska** Odessa I. I. Mechnikov National University, Odessa, Ukraine

**V. M. Fitio** Department of Photonics, Lviv Polytechnic National University, Lviv, Ukraine

**L. A. Frolova** Ukrainian State University of Chemical Technology, Dnipropetrovsk, Ukraine

**A. I. Gab** Open International University of Human Development “Ukraine”, Kyiv, Ukraine

**I. I. Gab** Frantsevich Institute for Problems of Materials Science, National Academy of Sciences of Ukraine, Kyiv, Ukraine

**Y. D. Galivets** Ukrainian State University of Chemical Technology, Dnipropetrovsk, Ukraine

**Z. Gburski** Institute of Physics, University of Silesia, Katowice, Poland

**E. I. Getman** Donetsk National University, Vinnytsia, Ukraine

**Ł. Głowa** Faculty of Mathematics and Natural Sciences, University of Rzeszow, Rzeszow, Poland

**E. Ya. Glushko** Institute of Semiconductor Physics, National Academy of Sciences of Ukraine, Kyiv, Ukraine

**A. Grebenyuk** Chuiko Institute of Surface Chemistry, National Academy of Sciences of Ukraine, Kyiv, Ukraine

**Viktor S. Grinevych** Odessa I. I. Mechnikov National University, Odessa, Ukraine

**Iurii Gudyma** Department of General Physics, Institute of Physical, Technical and Computer Sciences, Yuriy Fedkovych Chernivtsi National University, Chernivtsi, Ukraine



**Alexey Guglya** National Science Center, “Kharkov Institute of Physics and Technology”, Kharkov, Ukraine

**V. M. Gun’ko** Chuiko Institute of Surface Chemistry, National Academy of Sciences of Ukraine, Kyiv, Ukraine

**J. Gurgol** J. Haber Institute of Catalysis and Surface Chemistry, Krakow, Poland

**I. Hadzaman** Drohobych State Pedagogical University, Drohobych, Ukraine

**I. Hatala** Faculty of Mathematics and Natural Sciences, University of Rzeszow, Rzeszow, Poland

**R. Holze** Technische Universität Chemnitz, Institute of Chemistry, Chemnitz, Germany

**V. Honcharov** Institute of Chemical Technology, V. Dal’ East-Ukrainian National University, Rubizhne, Ukraine

**V. O. Hryn** Institute of Physics, National Academy of Sciences of Ukraine, Kiev, Ukraine

**D. A. Iakushev** A.Ya.Usikov Institute for Radiophysics and Electronics of the NAS of Ukraine, Kharkov, Ukraine

**Anel Ibrayeva** Astana Branch of the Institute of Nuclear Physics, Astana, The Republic of Kazakhstan

L. N. Gumilyov Eurasian National University, Astana, The Republic of Kazakhstan

**A. Ingram** Opole University of Technology, Opole, Poland

**V. M. Isai** National University of Food Technologies, Kyiv, Ukraine

**K. O. Ivanenko** Taras Shevchenko National University of Kyiv, Kyiv, Ukraine

**A. Ivanusa** Lviv State University of Life Safety, Lviv, Ukraine

**Nicole Jaffrezic-Renault** Univ Lyon, CNRS, Université Claude Bernard Lyon1, ENS de Lyon, Institut des Sciences Analytiques, Villeurbanne, France

**D. Jakubczyk** Institute of Physics, Polish Academy of Sciences, Warsaw, Poland

**W. Janusz** Maria Curie-Skłodowska University, Lublin, Poland

**L. John Kennedy** Materials Division, School of Advanced Sciences, Vellore Institute of Technology (VIT) University, Chennai, India

**J. Judith Vijaya** Catalysis and Nanomaterials Research Laboratory, Department of Chemistry, Loyola College, Chennai, India

**M. Kaczor** Faculty of Mathematics and Natural Sciences, University of Rzeszow, Rzeszow, Poland

**Yuliya Kaladkevich** Research Institut of Pulse Processes with Pilot Plant, Minsk, Belarus

**Alexander Kalchenko** National Science Center, “Kharkov Institute of Physics and Technology”, Kharkov, Ukraine

**D. V. Kalinichenko** Faculty of Physics, Taras Shevchenko National University of Kyiv, Kyiv, Ukraine

**Egor Kaniukov** Scientific-Practical Materials Research Centre, Minsk, Belarus

**Ann V. Karakurkchi** National Technical University “Kharkiv Polytechnic Institute”, Kharkiv, Ukraine

**Berna Ozansoy Kasap** Central Laboratory, Middle East Technical University, Ankara, Turkey

**V. V. Kavelin** Institute of Physics, National Academy of Sciences of Ukraine, Kyiv, Ukraine

**Dmitrii O. Kharchenko** Institute of Applied Physics, National Academy of Sciences of Ukraine, Sumy, Ukraine

**Vasyl O. Kharchenko** Institute of Applied Physics, National Academy of Sciences of Ukraine, Sumy, Ukraine

**Natalya Kizilova** Warsaw University of Technology, Warsaw, Poland  
Vilnius Gediminas Technical University, Vilnius, Lithuania

**H. Klym** Lviv Polytechnic National University, Lviv, Ukraine

**Yu. L. Kobzar** Faculty of Physics, Taras Shevchenko National University of Kyiv, Kyiv, Ukraine

**K. Kolwas** Institute of Physics, Polish Academy of Sciences, Warsaw, Poland

**N. B. Konig-Ettel** Frantsevich Institute for Problems of Materials Science, National Academy of Sciences of Ukraine, Kyiv, Ukraine

**A. M. Korol** Laboratory on Quantum Theory in Linkoping, Linkoping, Sweden  
National University for Food Technologies, Kyiv, Ukraine

**A. M. Korostil** Department of Physics of Magnetic Materials and Nanocrystalline Structures, Institute of Magnetism, National Academy of Sciences and Ministry of Education of Ukraine, Kyiv, Ukraine

**Yu. Kostiv** Lviv Polytechnic National University, Lviv, Ukraine

**B. D. Kostyuk** Frantsevich Institute for Problems of Materials Science, National Academy of Sciences of Ukraine, Kyiv, Ukraine

**Yu. Kotsiuba** Department of Photonics, Lviv Polytechnic National University, Lviv, Ukraine

**Ludmila Kornienko** National University of Food Technologies of the Ministry of Education and Science of Ukraine, Kyiv, Ukraine

**V. O. Kovalchuk** National Technical University of Ukraine “Igor Sikorsky Kyiv Polytechnic Institute”, Kyiv, Ukraine

**I. G. Kovzun** F.D. Ovcharenko Institute of Biocolloid Chemistry of NAS of Ukraine, Kyiv, Ukraine

**Artem Kozlovskiy** Astana Branch of the Institute of Nuclear Physics, Astana, The Republic of Kazakhstan

L. N. Gumilyov Eurasian National University, Astana, The Republic of Kazakhstan

**Artem Kozyrev** Institut for Superhard Materials NAS of Ukraine, Kyiv, Ukraine

**V. N. Kravchenko** Faculty of Physics, Taras Shevchenko National University of Kyiv, Kyiv, Ukraine

**A. N. Krit** Faculty of Physics, Taras Shevchenko National University of Kyiv, Kyiv, Ukraine

**M. M. Krupa** Department of Physics of Magnetic Materials and Nanocrystalline Structures, Institute of Magnetism, National Academy of Sciences and Ministry of Education of Ukraine, Kyiv, Ukraine

**Ivan S. Kucherenko** Laboratory of Biomolecular Electronics, Institute of Molecular Biology and Genetics, National Academy of Sciences of Ukraine, Kyiv, Ukraine

**Leonid M. Kulikov** Frantsevich Institute for Problems of Materials Science, National Academy of Sciences of Ukraine, Kyiv, Ukraine

**M. P. Kulish** Taras Shevchenko National University of Kyiv, Kyiv, Ukraine

**Burcu Akata Kurç** Central Laboratory, Middle East Technical University, Ankara, Turkey

**A. N. Kuryliuk** Faculty of Physics, Taras Shevchenko National University of Kyiv, Kyiv, Ukraine

**N. F. Kuschevskaya** University “Ukraine”, Kyiv, Ukraine

**O. I. Kushnerov** Oles Honchar Dnipropetrovsk National University, Dnipropetrovsk, Ukraine

**N. V. Kutsevol** Faculty of Chemistry, Taras Shevchenko National University of Kyiv, Kyiv, Ukraine

**Florence Lagarde** Univ Lyon, CNRS, Université Claude Bernard Lyon1, ENS de Lyon, Institut des Sciences Analytiques, Villeurbanne, France

**O. A. Lazarenko** Physics Faculty of Taras Shevchenko National University of Kyiv, Kyiv, Ukraine

**Tatiana A. Len** Departments of Physics and Chemistry, Taras Shevchenko National University of Kyiv, Kyiv, Ukraine

**Tetyana A. Len** Departments of Physics, Taras Shevchenko National University of Kyiv, Kyiv, Ukraine

**O. Linnik** Chuiko Institute of Surface Chemistry, National Academy of Sciences of Ukraine, Kyiv, Ukraine

**S. I. Litvynchuk** National University of Food Technologies, Kyiv, Ukraine

**V. Lobanov** Chuiko Institute of Surface Chemistry, National Academy of Sciences of Ukraine, Kyiv, Ukraine

**Aleksey Luchenok** Research Institut of Pulse Processes with Pilot Plant, Minsk, Belarus

**S. N. Lukin** R. E. Kavetsky Institute of Experimental Pathology, Oncology and Radiobiology, Kyiv, Ukraine

**Anatoliy V. Luzanov** SSI “Institute of Single Crystals”, NAS of Ukraine, Kharkiv, Ukraine

**Elena Lyubchenko** National Technical University, “Kharkov Polytechnic Institute”, Kharkov, Ukraine

**Antonina Maizelis** National Technical University, “Kharkov Polytechnic Institute”, Kharkov, Ukraine

**Oksana Makarchuk** National Technical University of Ukraine “Kyiv Polytechnic Institute”, Kyiv, Ukraine

**Artur Maksymov** Department of General Physics, Institute of Physical, Technical and Computer Sciences, Yuriy Fedkovych Chernivtsi National University, Chernivtsi, Ukraine

**V. V. Malyshev** University “Ukraine”, Kyiv, Ukraine

**Olha O. Mamchur** Faculty of Biotechnology and Environmental Control, National University of Food Technologies, Kyiv, Ukraine

**Svitlana V. Marchenko** Laboratory of Biomolecular Electronics, Institute of Molecular Biology and Genetics, National Academy of Sciences of Ukraine, Kyiv, Ukraine

**Yury Marchenko** National Science Center, “Kharkov Institute of Physics and Technology”, Kharkov, Ukraine

**Lyudmila Yu. Matzui** Departments of Physics and Chemistry, Taras Shevchenko National University of Kyiv, Kyiv, Ukraine

**Vladimir I. Matzui** G. V. Kurdyumov Institute for Metal Physics, National Academy of Science of Ukraine, Kyiv, Ukraine

- N. V. Medvid** National University of Food Technologies, Kyiv, Ukraine
- M. M. Melnichenko** Taras Shevchenko National University of Kyiv, Kyiv, Ukraine
- M. S. Melnychenko** Physics Faculty of Taras Shevchenko National University of Kyiv, Kyiv, Ukraine
- V. Moiseienko** Oles Honchar Dnipro National University, Dnipro, Ukraine
- Valerii Myronchuk** National University of Food Technologies of the Ministry of Education and Science of Ukraine, Kyiv, Ukraine
- O. M. Nadtoka** Faculty of Chemistry, Taras Shevchenko National University of Kyiv, Kyiv, Ukraine
- T. S. Nahirnyj** Centre of Mathematical Modeling, Pidstryhach Institute of Applied Problems of Mechanics and Mathematics of Ukrainian NAS, Lviv, Ukraine
- Faculty of Mechanical Engineering, University of Zielona Góra, Zielona Góra, Poland
- Y. V. Naidich** Frantsevich Institute for Problems of Materials Science, National Academy of Sciences of Ukraine, Kyiv, Ukraine
- O. I. Nakonechna** Taras Shevchenko National University of Kyiv, Kyiv, Ukraine
- Antonina P. Naumenko** Department of Physics, Taras Shevchenko National University of Kyiv, Kyiv, Ukraine
- S. N. Naumenko** Faculty of Physics, Taras Shevchenko National University of Kyiv, Kyiv, Ukraine
- Dina D. Naumova** Departments of Physics and Chemistry, Taras Shevchenko National University of Kyiv, Kyiv, Ukraine
- Waldemar Nawrocki** Faculty of Electronics and Telecommunications, Poznan University of Technology, Poznan, Poland
- A. V. Nedolya** Applied Physics Department, Zaporizhzhya National University, Zaporizhzhya, Ukraine
- O. M. Nikipelova** State Agency “Ukrainian Research Institute of Medical Rehabilitation and Balneology, Ministry of Health of Ukraine”, Odessa, Ukraine
- L. V. Nosach** Chuiko Institute of Surface Chemistry, National Academy of Sciences of Ukraine, Kyiv, Ukraine
- Agnieszka Nosal-Wiercińska** Department of Analytical Chemistry and Instrumental Analysis, Faculty of Chemistry, Maria Curie-Skłodowska University, Lublin, Poland

**O. S. Nychyporenko** Taras Shevchenko National University of Kyiv, Kyiv, Ukraine

**V. O. Oliinyk** F.D. Ovcharenko Institute of Biocolloid Chemistry of NAS of Ukraine, Kyiv, Ukraine

**V. Orel** National Cancer Institute, Kyiv, Ukraine

**O. P. Ostash** Karpenko Physico-Mechanical Institute of the NAS of Ukraine, Lviv, Ukraine

**Iwona Ostolska** Department of Radiochemistry and Colloids Chemistry, Faculty of Chemistry, Maria Curie-Sklodowska University, Lublin, Poland

**Irina V. Ovsiienko** Departments of Physics and Chemistry, Taras Shevchenko National University of Kyiv, Kyiv, Ukraine

**Iryna V. Ovsiienko** Departments of Physics, Taras Shevchenko National University of Kyiv, Kyiv, Ukraine

**E. M. Pakhlov** Chuiko Institute of Surface Chemistry, National Academy of Sciences of Ukraine, Kyiv, Ukraine

**A. V. Panko** F.D. Ovcharenko Institute of Biocolloid Chemistry of NAS of Ukraine, Kyiv, Ukraine

**E. A. Paprotskaya** University “Ukraine”, Kyiv, Ukraine

**Anatolii Perekos** Institute of Magnetism of the NAS of Ukraine and Ministry for Education and Science of Ukraine, Kyiv, Ukraine

**Yu. S. Perets** Physics Faculty of Taras Shevchenko National University of Kyiv, Kyiv, Ukraine

**H. Petrovska** Department of Photonics, Lviv Polytechnic National University, Lviv, Ukraine

**Ihor I. Piliponskiy** Faculty of Biotechnology and Environmental Control, National University of Food Technologies, Kyiv, Ukraine

**T. M. Pinchuk-Rugal** Taras Shevchenko National University of Kyiv, Kyiv, Ukraine

**V. Ya. Podhurska** Karpenko Physico-Mechanical Institute of the NAS of Ukraine, Lviv, Ukraine

**A. A. Podolyan** Faculty of Physics, Taras Shevchenko National University of Kyiv, Kyiv, Ukraine

**Sergey I. Pokutnyi** Chuiko Institute of Surface Chemistry, National Academy of Sciences of Ukraine, Kyiv, Ukraine

**D. I. Popovych** Pidstryhach Institute for Applied Problems of Mechanics and Mathematics, NASU, Lviv, Ukraine

National University Lvivska Polytechnika, Lviv, Ukraine

**P. Potera** Faculty of Mathematics and Natural Sciences, University of Rzeszow, Rzeszow, Poland

**Tatiana Prikhna** Institut for Superhard Materials NAS of Ukraine, Kyiv, Ukraine

**O. V. Prokopenko** Faculty of Radio Physics, Electronics and Computer Systems, Taras Shevchenko National University of Kyiv, Kyiv, Ukraine

**V. A. Prokopenko** F.D. Ovcharenko Institute of Biocolloid Chemistry of NAS of Ukraine, Kyiv, Ukraine

National Technical University of Ukraine “KPI”, Kyiv, Ukraine

**Oleksandr I. Prokopov** Departments of Physics and Chemistry, Taras Shevchenko National University of Kyiv, Kyiv, Ukraine

**Yu. I. Prylutsky** Taras Shevchenko National University of Kyiv, Kyiv, Ukraine

**Violetta Raczyńska** Institute of Physics, University of Silesia, Katowice, Poland

**Przemysław Raczyński** Institute of Physics, University of Silesia, Katowice, Poland

**Gaetan Raimondi** Univ Lyon, CNRS, Université Claude Bernard Lyon1, ENS de Lyon, Institut des Sciences Analytiques, Villeurbanne, France

**S. L. Revo** Taras Shevchenko National University of Kyiv, Kyiv, Ukraine

**S. Riabov** Institute of Macromolecular Chemistry, The National Academy of Sciences of Ukraine, Kiev, Ukraine

**V. V. Romakh** Department of Photonics, Lviv Polytechnic National University, Lviv, Ukraine

**A. Romanov** National Cancer Institute, Kyiv, Ukraine

**Ludmila Rozhdestvenska** V. I. Vernadskii Institute of General and Inorganic Chemistry of the National Academy of Science of Ukraine, Kyiv, Ukraine

**N. Rybalchenko** Zabolotny Institute of Microbiology and Virology, The National Academy of Sciences of Ukraine, Kiev, Ukraine

**O. Rykhalskyi** National Cancer Institute, Kyiv, Ukraine

**P. Sagan** Faculty of Mathematics and Natural Sciences, University of Rzeszow, Rzeszow, Poland

**B. Abu Sal** Applied Physics Department, Tafila Technical University, Tafila, Jordan

- Nikolay D. Sakhnenko** National Technical University “Kharkiv Polytechnic Institute”, Kharkiv, Ukraine
- Sergij M. Savin** Odessa I.I. Mechnikov National University, Odessa, Ukraine
- S. S. Savka** Pidstryhach Institute for Applied Problems of Mechanics and Mathematics, NASU, Lviv, Ukraine
- R. K. Savkina** V. Lashkaryov Institute of Semiconductor Physics, NAS of Ukraine, Kyiv, Ukraine
- Z. Sawlowicz** Jagellonian University, Krakow, Poland
- A. S. Serednytski** Pidstryhach Institute for Applied Problems of Mechanics and Mathematics, NASU, Lviv, Ukraine
- D. B. Shakhnin** University “Ukraine”, Kyiv, Ukraine
- A. Shevchenko** G.V. Kurdyumov Institute for Metal Physics, Kyiv, Ukraine
- V. V. Shlapatska** Pisarghevskiy Institute of Physical Chemistry of NAS of Ukraine, Kyiv, Ukraine
- L. V. Shmeleva** Departments of Theoretical Physics, Faculty of Physics, Taras Shevchenko National University of Kyiv, Kyiv, Ukraine
- O. M. Shniruk** National Technical University of Ukraine “Igor Sikorsky Kyiv Polytechnic Institute”, Kyiv, Ukraine
- Y. Shopa** Cardinal Stefan Wyszyński University in Warsaw, Warsaw, Poland
- O. Shpotyuk** Vlokh Institute of Physical Optics, Lviv, Ukraine  
Jan Dlugosz University in Czestochowa, Czestochowa, Poland
- V. Shtompel’** Institute of Macromolecular Chemistry, The National Academy of Sciences of Ukraine, Kiev, Ukraine
- Alena Shumskaya** Scientific-Practical Materials Research Centre, Minsk, Belarus
- M. I. Shut** National Pedagogical Dragomanov University, Kyiv, Ukraine
- J. Skubiszewska-Zięba** Maria Curie-Skłodowska University, Lublin, Poland
- E. Skwarek** Maria Curie-Skłodowska University, Lublin, Poland
- A. B. Smirnov** V. Lashkaryov Institute of Semiconductor Physics, NAS of Ukraine, Kyiv, Ukraine
- O. Smirnova** Chuiko Institute of Surface Chemistry, National Academy of Sciences of Ukraine, Kyiv, Ukraine
- T. N. Smirnova** Institute of Physics, National Academy of Sciences of Ukraine, Kiev, Ukraine



**Valentyn A. Smyntyna** Odessa I.I. Mechnikov National University, Odessa, Ukraine

**R. Socha** J. Haber Institute of Catalysis and Surface Chemistry, Krakow, Poland

**Alexei P. Soldatkin** Laboratory of Biomolecular Electronics, Institute of Molecular Biology and Genetics, National Academy of Sciences of Ukraine, Kyiv, Ukraine

Institute of High Technologies, Taras Shevchenko National University of Kyiv, Kyiv, Ukraine

**Oleksandr O. Soldatkin** Laboratory of Biomolecular Electronics, Institute of Molecular Biology and Genetics, National Academy of Sciences of Ukraine, Kyiv, Ukraine

Institute of High Technologies, Taras Shevchenko National University of Kyiv, Kyiv, Ukraine

**Elena Solopikhina** National Science Center, “Kharkov Institute of Physics and Technology”, Kharkov, Ukraine

**L. P. Steblenko** Faculty of Physics, Taras Shevchenko National University of Kyiv, Kyiv, Ukraine

**A. N. Stepanyuk** Kryvyi Rih State Pedagogical University, Kryvyi Rih, Ukraine

**Andrew E. Stetsko** Ukraine Academy of Printing, Lviv, Ukraine

**T. V. Stetsyuk** Frantsevich Institute for Problems of Materials Science, National Academy of Sciences of Ukraine, Kyiv, Ukraine

**Larysa Sudnik** Research Institut of Pulse Processes with Pilot Plant, Minsk, Belarus

**O. R. Sulymenko** Faculty of Radio Physics, Electronics and Computer Systems, Taras Shevchenko National University of Kyiv, Kyiv, Ukraine

**A. D. Suprun** Departments of Theoretical Physics, Faculty of Physics, Taras Shevchenko National University of Kyiv, Kyiv, Ukraine

**Andrzej Szytuła** M. Smoluchowski Institute of Physics, Jagiellonian University, Cracow, Poland

**Yu. V. Tarasov** A.Ya.Usikov Institute for Radiophysics and Electronics of the NAS of Ukraine, Kharkov, Ukraine

**Tetiana Tatarchuk** Department of Inorganic and Physical Chemistry, Faculty of Natural Science, Vasyl Stefanyk Precarpathian National University, Ivano-Frankivsk, Ukraine

**K. A. Tchervinka** Department of Mathematical Modeling, Ivan Franko National University of Lviv, Lviv, Ukraine

**V. M. Tkach** Bakul Institute for Superhard Materials of NAS of Ukraine, Kyiv, Ukraine

**Victor Tkachuk** Research Institut of Pulse Processes with Pilot Plant, Minsk, Belarus

**O. A. Tsyganovich** F.D. Ovcharenko Institute of Biocolloid Chemistry of NAS of Ukraine, Kyiv, Ukraine

**Anatolii Ukrainetz** Institute of Physico-Organic Chemistry, National Academy of Sciences of Belarus, Minsk, Belarus

**Bulent Ulug** Department of Physics, Faculty of Science, Akdeniz University, Antalya, Turkey

**O. V. Usatenko** A.Ya.Usikov Institute for Radiophysics and Electronics of the NAS of Ukraine, Kharkov, Ukraine

**B. D. Vasyliv** Karpenko Physico-Mechanical Institute of the NAS of Ukraine, Lviv, Ukraine

**S. V. Vasylyuk** Physics Faculty of Kyiv National Taras Shevchenko University, Kiev, Ukraine

**Maryna V. Ved** National Technical University “Kharkiv Polytechnic Institute”, Kharkiv, Ukraine

**I. Virt** Faculty of Mathematics and Natural Sciences, University of Rzeszow, Rzeszow, Poland

Drohobych State University, Drohobych, Ukraine

**Viktor Vlasov** National Science Center, “Kharkov Institute of Physics and Technology”, Kharkov, Ukraine

**E. F. Voronin** Chuiko Institute of Surface Chemistry, National Academy of Sciences of Ukraine, Kyiv, Ukraine

**L. A. Voronzova** Institute of Macromolecular Chemistry, National Academy of Sciences of Ukraine, Kyiv, Ukraine

**L. L. Vovchenko** Physics Faculty of Taras Shevchenko National University of Kyiv, Kyiv, Ukraine

**Yu. P. Vyshnevska** National Technical University of Ukraine “Igor Sikorsky Kyiv Polytechnic Institute”, Kyiv, Ukraine

Institute for Renewable Energy, Kyiv, Ukraine

**Małgorzata Wiśniewska** Department of Radiochemistry and Colloids Chemistry, Faculty of Chemistry, Maria Curie-Sklodowska University, Lublin, Poland

**G. Wisz** Faculty of Mathematics and Natural Sciences, University of Rzeszow, Rzeszow, Poland

**M. Woźniak** Institute of Physics, Polish Academy of Sciences, Warsaw, Poland

**Dzmitry Yakimchuk** Scientific-Practical Materials Research Centre, Minsk, Belarus

**I. Ya. Yaremchuk** Department of Photonics, Lviv Polytechnic National University, Lviv, Ukraine

**O. V. Yaschenko** National Technical University of Ukraine “Igor Sikorsky Kyiv Polytechnic Institute”, Kyiv, Ukraine

**L. N. Yashchenko** Institute of Macromolecular Chemistry, National Academy of Sciences of Ukraine, Kyiv, Ukraine

**V. N. Yashchuk** Physics Faculty of Kyiv National Taras Shevchenko University, Kiev, Ukraine

**R. Yavorskyi** Faculty of Mathematics and Natural Sciences, University of Rzeszow, Rzeszow, Poland

Vasyl Stefanyk PreCarpathian National University, Ivano-Frankivsk, Ukraine

**P. V. Yezhov** Institute of Physics, National Academy of Sciences of Ukraine, Kiev, Ukraine

**V. Zazhigalov** Institute for Sorption and Problems of Endoecology, National Academy of Sciences of Ukraine, Kyiv, Ukraine

**Maksim Zdorovets** Astana Branch of the Institute of Nuclear Physics, Astana, The Republic of Kazakhstan

L. N. Gumilyov Eurasian National University, Astana, The Republic of Kazakhstan

Ural Federal University Named After the First President of Russia B.N. Yeltsin, Ekaterinburg, The Russian Federation

**Oleksandra S. Zloi** Departments of Physics and Chemistry, Taras Shevchenko National University of Kyiv, Kyiv, Ukraine

**Yurii Zmievskii** National University of Food Technologies of the Ministry of Education and Science of Ukraine, Kyiv, Ukraine

**Part I**  
**Nanoscale Physics**

# Chapter 1

## Numerical Solution of One-Dimensional Stationary Schrödinger Equation in the Frequency Domain

V. M. Fitio, I. Ya. Yaremchuk, V. V. Romakh, and Ya. V. Bobitski

### 1.1 Introduction

Recently, quantum wells on base of semiconductor heterostructures are most widely studied [1] since their physical effects can be seen at room temperature [2] and can be applied in actual devices, for example, as some components of optoelectronic devices such as photodetectors in infrared spectral range [3], quantum cascade lasers [4], and other optoelectronic devices [5]. A detailed theory of optoelectronic devices based on quantum wells can be found in the book by G. Bastard in [6].

An analysis of devices based on quantum wells requires a solution of the stationary Schrödinger equation. Solution is reduced to the transcendental equation if a potential well has a rectangular form. In case of two or more rectangular wells, the obtained transcendental equation becomes much more complicated. Potential energy of multi-quantum structures (quantum cascade laser) is a set of potential wells and barriers with specific width and height [4]. Design of quantum cascade lasers requires determination of the discrete energy levels and corresponding wave functions of such structure. Determination of discrete energy levels and corresponding wave functions of multi-quantum structures by the traditional method reduces

---

V.M. Fitio (✉) • I.Y. Yaremchuk • V.V. Romakh  
Department of Photonics, Lviv Polytechnic National University, S. Bandery Str.,  
12, 79013, Lviv, Ukraine  
e-mail: [v.m.fitio@gmail.com](mailto:v.m.fitio@gmail.com)

Y.V. Bobitski  
Department of Photonics, Lviv Polytechnic National University, S. Bandery Str.,  
12, 79013, Lviv, Ukraine

Faculty of Mathematics and Natural Sciences, University of Rzeszow, Pigoia Str.1, 35959,  
Rzeszow, Poland

to solution of the transcendental equation and is quite complicated. Moreover, computational complexity nonlinearly increases when the number of potential wells and barriers increases.

In addition, the solution becomes more complicated if the potential well has no rectangular barrier. Precise solutions of one-dimensional stationary Schrödinger equation [7] have been obtained only for a small number of functional dependencies of the potential well. Therefore, search of solutions of one-dimensional Schrödinger stationary equation continues, and there are attempts to form potential energy in such way to obtain a precise analytical solution of the corresponding equation [8–10].

There is a similar problem in finding propagation constants of waveguide modes in the gradient planar waveguides [11–17]. The methods presented in [12–17] can be used for solving the Schrödinger equation since structure of the wave equation is equal to the one-dimensional stationary Schrödinger equation for planar waveguides. On the other hand, the approaches developed in quantum mechanics, for instance, the WKB approximation technique [11, 18], can be used to search propagation constants of gradient planar waveguides. Prediction of resonance phenomena in gratings [19, 20] and explanation of the physical processes into waveguide distributed feedback microlasers [21, 22] require determination of propagating constants.

It should be noted that the current state of computer technologies and the sophistication of software allow applied numerical methods to solve equations of the various types (differential, integral, nonlinear algebraic equations).

It is expected that the numerical method in the frequency domain is also suitable for the solution of one-dimensional Schrödinger equation since wave equations differ only in the sign before the second derivative of the unknown function. Such method of the solution of the stationary Schrödinger equation is presented in [23], where the potential well has a nonrectangular shape. Previous studies have shown that the analysis of structures (planar waveguides and multilayer quantum structures) significantly is simplified in the frequency domain with high efficiency and numerical stability. In this method, the wave function using Fourier transform can be transformed into integral equation and solved by numerical methods. Thus, a main problem is transformed in the eigenvalue/eigenvector problem which corresponds to discrete energy levels as well as the Fourier transform of wave functions. All discrete energy levels or all propagation constants of waveguide modes and corresponding wave functions can be defined using one calculation cycle.

Moreover, it should be noted that the known methods of searching of the propagation constants of waveguide modes are based on replacing the second derivative in the wave equation by the different operator in a coordinate domain [16]. Solution of this method also is transformed in the eigenvalue/eigenvector problem. Moreover, described method can be used to search discrete energy levels of the stationary Schrödinger equation. However, it doesn't offer high accuracy. In addition, the evidence of numerical differentiation is found as a source of noise due to approximation in the numerical process [17].

Solution of the Schrödinger stationary equation proposed method is based on that the relevant wave functions and the primary derivatives of coordinate  $x$  at  $\pm\infty$  are zero for discrete levels of energy. Therefore, there is the Fourier transform [24] of the wave function, and the appropriate wave equation can be transformed into a frequency domain by the Fourier transform. At the same time, integral equation will be obtained and also can be solved by numerical methods [23].

The aim of this study is development of a new numerical method to solve the one-dimensional stationary Schrödinger equation using the Fourier transform for certain functional dependencies of the potential energy.

The second section of this paper is devoted to numerical implementation of the proposed method. The third section presents results of the numerical analysis of the stationary Schrödinger equation for certain functional dependencies of the potential energy. The fourth section presents the results of the solution of the one-dimensional stationary Schrödinger equation in accordance with the proposed method for the one-dimensional crystal which has several periods. The fifth section presents the results of the solution of the one-dimensional stationary Schrödinger equation for multilayer structure where potential energy consists of a few rectangular potential well separated by potential rectangular barriers.

## 1.2 Numerical Method for Solving of One-Dimensional Stationary Schrödinger Equation in the Frequency Domain

The one-dimensional stationary Schrödinger equation is:

$$-\frac{\hbar^2}{2m} \frac{d^2\psi(x)}{dx^2} + U(x)\psi(x) = E\psi(x), \quad (1.1)$$

where  $U(x)$  is a potential energy of particle which can have only discrete values and  $\psi(x)$  is a wave function.

Dimensionless equation [7, 25] is used frequently in quantum mechanics where coordinate  $x$  is the dimensionless value and which is obtained by replacing the variables. The dimensionless equation (1.1) can be presented as:

$$-\frac{d^2\psi(x)}{dx^2} + U(x)\psi(x) = E\psi(x). \quad (1.2)$$

Function  $\psi(x)$  is absolutely integrated as the solution of the stationary Schrödinger equation, which corresponds to discrete levels of energy, and their primary derivatives tend to be zero at  $x \rightarrow \pm\infty$ . Therefore, the Fourier transform for these functions as well as for their primary and secondary derivatives exists. Let's write the appropriate proportions for  $\psi(x)$ . Thus, the Fourier transform of

$\psi(x)$  and its primary and secondary derivatives are zero [24], and it can be written as follows:

$$\psi(u) = \int_{-\infty}^{\infty} \psi(x) \exp(-i2\pi ux) dx, \quad (1.3)$$

$$i2\pi u\psi(u) = \int_{-\infty}^{\infty} \frac{d\psi(x)}{dx} \exp(-i2\pi ux) dx, \quad (1.4)$$

$$-(2\pi u)^2\psi(u) = \int_{-\infty}^{\infty} \frac{d^2\psi(x)}{dx^2} \exp(-i2ux) dx. \quad (1.5)$$

In addition, for functions for which a Fourier transform exists ( $F\{g(x)\} = G(u)$ ,  $F\{h(x)\} = H(u)$ ), the next conditions are satisfied [24]:

$$F\{g(x)h(x)\} = \int_{-\infty}^{\infty} G(u-v)H(v)dv, \quad (1.6)$$

where  $F\{\dots\}$  is the Fourier transform. Expression (1.6) describes the content of the convolution theorem.

Let's execute the Fourier transform of left and right parts of Eq. (1.2) by using Eqs. (1.3), (1.5), and (1.6). As a result we obtain:

$$4\pi^2 u^2 \psi(u) + \int_{-\infty}^{\infty} U(u-v) \psi(v) dv = E\psi(u). \quad (1.7)$$

Therefore, we have moved from the differential equation (1.2) for eigenfunctions and eigenvalues to the integral one equation (1.7). In the last equation, we can replace integral by sum, so the continuous values  $u$  and  $v$  can be replaced by discrete ones:

$$4\pi^2 (s\Delta)^2 \psi(s\Delta) + \sum_{p=-(N-1)/2}^{(N-1)/2} U(s\Delta - p\Delta) \psi(p\Delta) \Delta = E\psi(s\Delta), \quad (1.8)$$

where  $\Delta = u_{\max}/N$ ,  $u_s = s\Delta$ ,  $v_p = p\Delta$ ,  $-(N-1)/2 \leq s, p \leq (N-1)/2$ , and  $s$  and  $p$  are integers;  $|u| \geq u_{\max}/2$ ; values of  $\psi(x)$  are almost equal to zero. Value of  $N$  must



be large and preferably unpaired. Obviously, sum in equation (1.8) should have  $N$  elements.

Let's write the last equation for all discrete spatial frequencies  $u_s = s\Delta$ , where  $s$  changes between  $-(N-1)/2$  and  $(N-1)/2$ . Then a set of equations in the amount of  $N$  can be written in a matrix form, where  $E$  is common for all values of  $s$ :

$$(\mathbf{P} + \mathbf{U}) \boldsymbol{\psi} = E\boldsymbol{\psi}, \quad (1.9)$$

where  $\mathbf{P}$  is a diagonal matrix with elements  $4(\pi s\Delta)^2$ ,  $\mathbf{U}$  is a square symmetric matrix with elements  $U(s\Delta - p\Delta)$ , and  $\boldsymbol{\psi}$  is a vector column with elements  $\psi(s\Delta)$ .

Therefore, in the last case, the problem is reduced to the problem of eigenvalues (energy) and eigenvectors (the discrete Fourier transform of  $\psi(x)$ ) which corresponds to the given value of energy. We can have many eigenvalues and its corresponding eigenvectors. By carrying out the inverse discrete Fourier transform of eigenvector, we obtain the eigenfunction  $\psi(x)$ . All eigenvalues (discrete levels of energy) are determined inside the potential well for quantum-mechanical problems. If the potential well has finite depth, then the precision is determined by  $N$  and  $\Delta$ . If the potential energy varies from zero to infinity (e.g.,  $U = x^2$ ), then the potential energy is limited in this method, i.e., it serves up to the certain value as  $U(x)$  and further acquires a constant value. Obviously, in this case, the lowest levels of energy can be determined with the highest accuracy. In our numerical calculations whose results are presented below, we used the simplest way to replace integral by sum.

### 1.3 Examples of Numerical Solution of the Schrödinger Equation with One Potential Well

**Example 1** Schrödinger equation according to Eq. (1.2), for which potential energy is  $U = \begin{cases} x^2, & |x| \leq a, \\ a^2, & |x| > a = 7. \end{cases}$

Numerical process parameters are sampling number  $N = 1001$  and maximum frequency  $u_{\max} = 10.01$ . The 25 eigenvalues of energy are obtained by numerical calculations and which have next values:  $E_0 = 1.0000000000$ , ...,  $E_9 = 18.9999999999$ , ...,  $E_{13} = 26.9999999999$ , ...,  $E_{24} = 48.640$ , and they accurately fit the data of [23], where  $E_j = 2j + 1$ . Obviously  $a$  should be increased in (1.12) to improve the accuracy. Moreover, at the same time,  $N$  and  $u_{\max}$  should be increased also. Figure 1.1a shows normalized wave functions for the three lowest values of energy. Continuous curves  $\psi_{j,theor}$  correspond to the exact value of the wave functions, and points correspond to results calculated by developed method  $\psi_{j,num}$ . You can see good fitting between points and continuous curves; however, it is difficult to evaluate the accuracy of calculation by the proposed

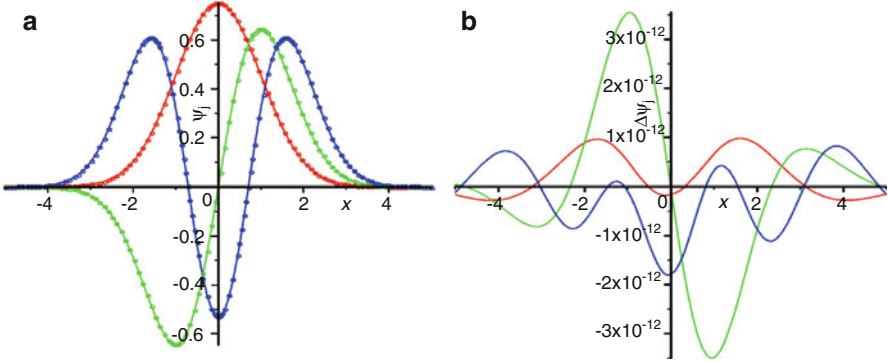


**Fig. 1.1** The waveguide functions (where  $\psi_0$  is defined by red color,  $\psi_1$  by green color,  $\psi_2$  by blue color) of harmonic oscillator which correspond to three lowest energies values (a); the difference between accuracy and numerical solutions  $\Delta\psi_j = \psi_{j,num} - \psi_{j,theor}$  (b)

method. Figure 1.1b shows the difference  $\Delta\psi_j$  between the wave functions  $\psi_{j,theor}$  for the three lowest states which are analytical solutions of the quantum harmonic oscillator, and  $\psi_{j,num}$  obtained numerical method. Analytical solutions (functions  $\psi_{j,theor}$  renormalized) according to [25] are given as:

$$\psi_{0,theor} = \frac{\exp\left(-\frac{x^2}{2}\right)}{\sqrt[4]{\pi}}, \quad \psi_{1,theor} = \frac{2x \exp\left(-\frac{x^2}{2}\right)}{\sqrt[4]{4\pi}}, \quad \psi_{2,theor} = \frac{(4x^2 - 2) \exp\left(-\frac{x^2}{2}\right)}{\sqrt[4]{64\pi}}.$$

The difference between the accurate analytical solutions and the solutions obtained by numerical method, in the range  $[-5, 5]$  for all three wave functions, is in the range from  $-3.5 \times 10^{-12}$  to  $3.5 \times 10^{-12}$  (see Fig. 1.1b). Thus, proposed numerical method provides high accuracy of solution of the stationary Schrödinger equation. These results are confirmed by work [18], where research of accuracy of the waveguide equation solution is carried out by the same method.

**Example 2** Schrödinger equation according to Eq. (1.2), for which potential energy is  $U = \begin{cases} |x|, & \text{if } |x| \leq a, \\ a, & \text{if } |x| > a = 16. \end{cases}$

Numerical process parameters are sampling number  $N = 501$  and maximum frequency  $u_{max} = 5.01$ . The 11 lowest eigenvalues of energy are obtained by numerical calculations and which have next values:  $E_0 = 1.01879311, \dots, E_5 = 5.52055983, \dots, E_{10} = 8.48848676$ . This problem can be solved analytically [7], and corresponding accurate values are equal:  $E_0 = 1.01879297, \dots, E_5 = 5.52055983, \dots, E_{10} = 8.48848673$ . We can see accurately fit between data obtained, proposed method, and well-known methods.

**Example 3** Schrödinger equation according to Eq. (1.2), for which potential energy is  $U = \begin{cases} x^4, & \text{if } |x| \leq a, \\ a^4, & \text{if } |x| > a = 3. \end{cases}$

Numerical process parameters are sampling number  $N = 509$  and maximum frequency  $u_{\max} = 5.09$ . The 11 lowest eigenvalues of energy are obtained by numerical calculations and which have next values:  $E_0 = 1.060357758, \dots, E_5 = 21.2383517, \dots, E_{10} = 50.24459206$ . This problem cannot be solved precisely by analytical methods. Thus, value of the lowest level of energy is found by approximate approach at which  $E_0 = 1.060357758$  [7]. In other words, the approximate value is found with a large error.

**Example 4** Schrödinger equation according to Eq. (1.2), for which potential energy can be described by the following analytical function:

$$U(x) = a - a \exp(-\pi x^2) \quad (1.10)$$

where  $a$  is the certain positive number determining the depth of the potential well.

Schrödinger equation has not been the precisely analytical expression for such potential energy. Thereby, it needs to find the discrete energy levels by proposed method at different  $N$  and  $u_{\max}$ . If calculated discrete energy levels will be constant in some range of  $N$  and  $u_{\max}$ , then we can suppose that these calculated values are accurate. The Fourier transform of this function is:

$$F\{U(x)\} = a\delta(x) - a \exp(-\pi x^2). \quad (1.11)$$

The five energy levels were obtained for potential energy according to (1.11) using numerical process parameters  $N = 1001, u_{\max} = 10 \div 20, a = 100$ :  $E_0 = 16.539595, E_1 = 47.036248, E_2 = 72.011285, E_3, E_2$ . A more detailed dependence of the calculated energy levels as function on  $u_{\max}$  is presented in Table 1.1. Table 1.2 shows the dependence of the calculated energy levels on  $N$  at  $u_{\max} = 15$ . Analysis of Table 1.1 indicates that there is a frequency range at sufficiently large  $N$  in which values of energy are constant (these values of energy in the tables are shown in bold).

It is too easy to see from Table 1.2 that calculated energy is toward to a specific value at increasing  $N$  for a certain frequency.

Analyzing the tables, we can conclude that the values of energy are constant within eight decimal places after the point for  $N \geq 801$  at  $u_{\max} = 15$ ; the calculated energy levels are constant at range  $u_{\max} = 10 \div 20$  for  $N = 1001$ .

Thereby, accuracy of the proposed method is defined by  $N$  and  $u_{\max}$ , which are defining value  $\Delta = \frac{u_{\max}}{N}$  in compliance with theorem of residues [24]. Values  $\frac{1}{\Delta}$  define interval in coordinate space ( $x_{\max}$ ) on the edges of which calculated value  $\psi_j(\pm \frac{0.5}{\Delta})$  with the lowest index must be almost the same. It can be predicted that the interval  $\frac{1}{\Delta}$  should be several times greater than the maximum width of the potential well. Minimal values of  $u_{\max}$  are defined by functional dependence of Fourier transform of potential energy function. It is clear that Fourier transform

**Table 1.1** The dependence of the calculated energy levels on  $u_{\max}$  at  $N = 1001$ 

$u_{\max}$	4	6	10	14	20	24	28
$E_0$	16.5460735	16.53959718	16.53959510	<b>16.53959509</b>	<b>16.53959509</b>	<b>16.53959509</b>	16.53959510
$E_1$	47.0821923	47.03626733	<b>47.03624767</b>	<b>47.03624767</b>	<b>47.03624767</b>	<b>47.03624767</b>	47.03624768
$E_2$	72.1504457	72.01136385	<b>72.01128540</b>	<b>72.01128540</b>	<b>72.01128540</b>	<b>72.01128540</b>	72.01128541
$E_3$	90.6602579	90.44709161	<b>90.44693968</b>	<b>90.44693968</b>	<b>90.44693968</b>	<b>90.44693968</b>	90.44693969
$E_4$	99.8844591	99.83277513	<b>99.83272955</b>	<b>99.83272955</b>	<b>99.83272955</b>	99.83272950	99.832729002

**Table 1.2** The dependence of the calculated energy levels on  $N$  at  $u_{\max} = 15$ 

$N$	101	201	401	601	801	1001	1501
$E_0$	16.53959512	16.53959510	16.53959511	<b>16.53959509</b>	<b>16.53959509</b>	<b>16.53959509</b>	<b>16.53959509</b>
$E_1$	47.03624768	47.03624766	47.03624768	<b>47.03624767</b>	<b>47.03624767</b>	<b>47.03624767</b>	<b>47.03624767</b>
$E_2$	72.01128540	72.01128539	72.01128542	<b>72.01128540</b>	<b>72.01128540</b>	<b>72.01128540</b>	<b>72.01128540</b>
$E_3$	90.44694122	90.44693968	90.44693970	<b>90.44693968</b>	<b>90.44693968</b>	<b>90.44693968</b>	<b>90.44693968</b>
$E_4$	99.76898968	99.82787662	99.83270759	99.83272945	<b>99.83272955</b>	<b>99.83272955</b>	<b>99.83272955</b>

should be near zero at  $u = \pm \frac{u_{\max}}{2}$ . You can find detailed description of  $u_{\max}$  selection in work [18].  $N$  can be obtained from  $N = \frac{u_{\max}}{\Delta}$  at given  $u_{\max}$  and  $\Delta$ .

## 1.4 Numerical Simulation of the One-Dimensional Crystal

One-dimensional crystal consists of periodic placement of unit cells. The unit cell has potential energy which is described by the analytical function (1.10). If we have  $M$  number of periodically placed ( $M$  is unpaired) potential wells on a distance  $\Lambda$  from each other, we will receive one-dimensional crystal, whose potential energy will be described as follows:

$$U(x)_{kr} = a - a \sum_{m=(M-1)/2}^{(M-1)/2} \exp \left[ -\pi(x - m\Lambda)^2 \right]. \quad (1.12)$$

After simple mathematical transformations, we obtain the Fourier transform of Eq. (1.12):

$$F \{U(x)_{kr}\} = a\delta(u) - a \exp(-\pi u^2) \frac{\sin[\pi M \Lambda u]}{\sin(\pi \Lambda u)}. \quad (1.13)$$

Figure 1.2 shows the potential energy of one-dimensional crystal with 11 unit cells according to Eq. (1.12), where period is  $\sqrt{3}$  at  $a = 50$ . Irrational number is chosen for  $\Lambda$  to avoid division by zero in expression (1.13) at  $u \neq 0$ . Figure 1.2b presents second-term Fourier transform potential energy of the crystal according to Eq. (1.13). As you can see, Fourier transform contains narrow peaks whose width is determined according to Eq. (1.13) by the number of unit cells in the crystal. Moreover, the maximum of the central peak is proportional to the number of cells and is equal to  $Ma = 11 \times 50 = 550$ . Half period of oscillation of the Fourier transform can be defined using condition that the numerator of the second term of (1.13) is equal to zero, i.e.,  $\pi M \Lambda u = \pi$ .

We can find  $\Delta < 1/2M\Lambda$  from  $2M\Lambda\Delta < 1$  if supposed that at least two residues should be on half period in compliance with theorem of residues [24]. Therefore, we can write  $x_{\max} = \frac{1}{\Delta} > 1M\Lambda$ . The maximal frequency range  $u_{\max}$  can be evaluated using Fig. 1.2b. Fourier transform of potential energy should be practically equal to zero at frequencies  $\pm \frac{u_{\max}}{2}$ . Range  $-\left[\frac{u_{\max}}{2}, \frac{u_{\max}}{2}\right]$  does not depend on number of unit cell in the crystal as follows from Eq. (1.13). We can choose that  $u_{\max} > 3$  in compliance with Fig. 1.2b. Total number of residues  $N$  must satisfy to condition  $N > x_{\max} u_{\max}$  [24].

Let's analyze one-dimensional crystal that consists of 33 unit cells, and their potential energy is described by (1.12) at  $a = 50$ ,  $\Lambda = \sqrt{3}$ . At first, we can find the energy levels of one potential well in accordance with the Eq. (1.10). Numerical calculations performed for such numerical parameters of the process as  $N = 2001$ ,

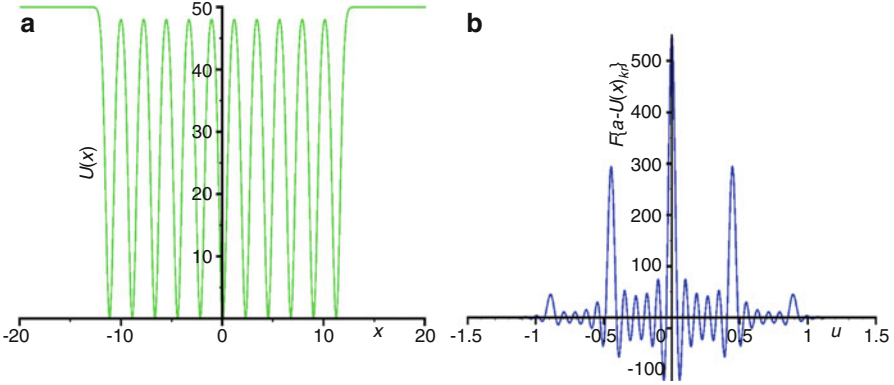


**Fig. 1.2** Dependence of the potential energy of the one-dimensional crystal which consists of 11 unit cells with period  $\Lambda = \sqrt{3}$  according to Eq. (1.12) (a); the second term of Fourier transform of potential energy of the crystal according to Eq. (1.13) (b)

$u_{\max} = 5 \div 20$ . The three discrete energy levels are obtained for the potential well as follows:

$$E_0 = 11.34694069, \quad E_1 = 31.34026975, \quad E_2 = 45.22214696. \quad (1.14)$$

The first two levels split into 33 sublevels and form allowed bands if there is one-dimensional crystal which consists of 33 potential wells in accordance with the Eq. (1.13). However, level  $E_2$  is split only on 29 sublevels; four sublevels have energies greater than the depth of the potential well and get into continuous spectrum of energies. Figure 1.3 shows the band structure of the one-dimensional crystal. Widths of allowed bands increase when energy increases. The width of the band with the lowest energy levels is within 11.202565...11.344461. The width of the band, formed by split of  $E_1$ , is within 29.707432...32.175102. The width of the band, formed by split of  $E_2$ , is within 41.137983...49.982381. The analysis dimensional crystal is fitted with the data presented in work [26].

## 1.5 Numerical Simulation of the Quantum Multilayer Structure

The multilayer structure presented in Fig. 1.4 has been analyzed by the proposed method. The width of the central potential barrier and widths of the two potential wells adjacent to this barrier are 1 nm. The remaining potential wells and barriers have a width of 0.25 nm. The height of the barrier is  $U_0 = 0.3$  eV. The depth of the potential wells is zero.

Potential energy within ranges  $(-\infty, -3]$ ,  $[3, \infty)$  is  $U_0 = 0.3$  eV.

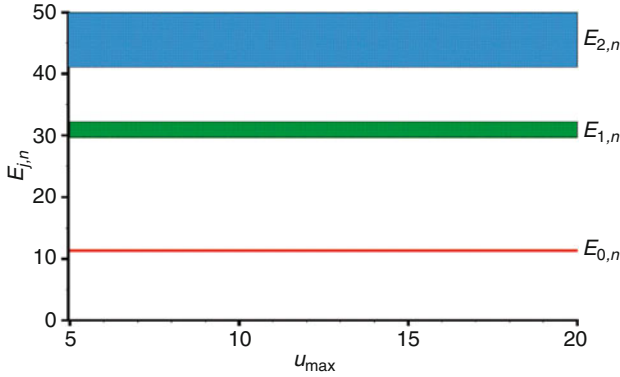


**Fig. 1.3** Band structure of one-dimensional crystal which consists of 33 unit cells. Numerical calculation carried out for such numerical parameters of the process as  $N = 2001$ ,  $u_{\max} = 5 \div 20$

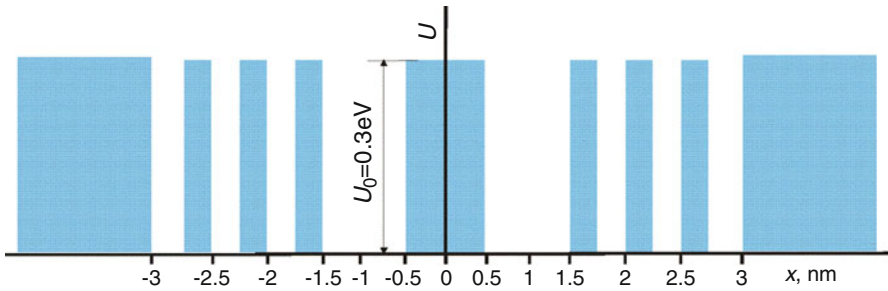


**Fig. 1.4** Potential energy of the multilayer quantum structure

Schrödinger equation in form (1.1) is selected for this structure where mass  $m$  is equal to electron mass. The numerical parameters of the process are  $N = 2001$ ,  $u_{\max} = 12 \times 10^{10} \text{ m}^{-1} = 120 \text{ nm}^{-1}$ . There are obtained values of energy levels as follows:  $E_0 = 0.101034 \text{ eV}$ ,  $E_1 = 0.112622 \text{ eV}$ ,  $E_2 = 0.213972 \text{ eV}$ ,  $E_3 = 0.221988 \text{ eV}$ . It should be noted that discrete levels on energy scale group by pairwise as  $E_0, E_1$  and  $E_3, E_4$ .

Figure 1.5 shows dependence of the calculated values of energy levels on  $u_{\max}$ . Calculated energy levels are practically constant in the range  $u_{\max} = 20 \div 200 \text{ nm}^{-1}$ . The value  $x_{\max} = \frac{N}{u_{\max}} \cong 16.7 \text{ nm}$  can be obtained at  $N = 2001$ ,  $u_{\max} = 120 \text{ nm}^{-1}$ . Waveguide functions should be equal to zero on edges of the range  $[-\frac{x_{\max}}{2}, \frac{x_{\max}}{2}]$  (see Fig. 1.5b). Since the potential energy of multilayer quantum structure according to Fig. 1.4 is symmetrical, the wave functions with an even number are symmetrical and with the odd number are antisymmetrical that can be seen in Fig. 1.5b. Such behavior of the wave functions is corresponding to the quantum theory [7].



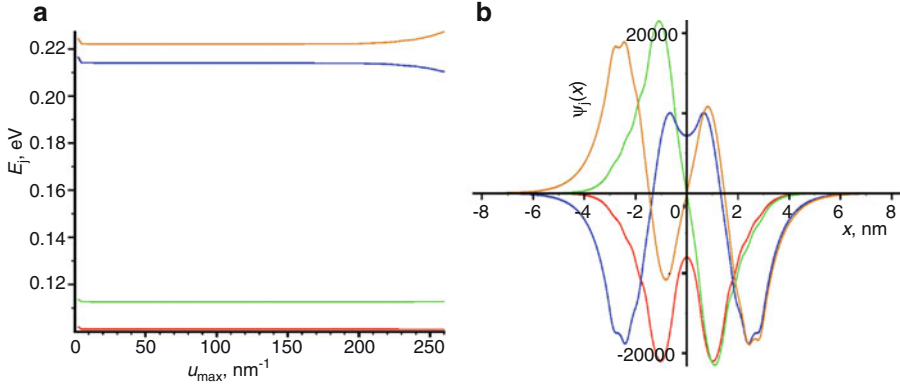


**Fig. 1.5** Dependence of the calculated energy levels on frequency (a); dependence of the corresponding waveguide functions calculated at  $u_{\max} = 120 \text{ nm}^{-1}$ ,  $N = 2001$  where  $E_0 = 0.101034 \text{ eV}$  is labeled by *red color*,  $E_1 = 0.112622 \text{ eV}$  by *green color*,  $E_2 = 0.213972 \text{ eV}$  by *blue color*, and  $E_3 = 0.221988 \text{ eV}$  by *red-brown color* (b)

## 1.6 Conclusions

The possibilities of the new method for solving one-dimensional stationary Schrödinger equation in the frequency domain for different functions of potential energy have been analyzed. The method is tested in many examples; some of them have accurate analytical solutions, and it allows to compare the analytical solutions and the solutions obtained by numerical method. The comparison showed high accuracy of determination, discrete energy levels, and corresponding wave functions. If a potential energy in  $\pm\infty$  tends to be infinite, then the lowest discrete energy levels and corresponding wave functions can be found with great accuracy by the proposed method. The discrete energy levels and corresponding wave functions are defined with great precision if the depth of potential well is finite. Moreover, there are found solutions to stationary Schrödinger equation of one-dimensional crystal, which consists of 33 unit cells arranged periodically.

It demonstrates that discrete levels are split and form bandgap and allowed band during the formation of one-dimensional crystal. Allowed bands contain a number of sublevels equal to the number of unit cells in the crystal. Width of bands increases when energy increases. Multilayer structure which consists of the set potential wells and barriers has been analyzed. It should be noted that the quantum cascade laser has such structure. Discrete energy levels and corresponding wave functions were obtained. The accuracy of numerical solutions is determined by the parameters of the process  $N$  and  $u_{\max}$ . The accuracy increases when  $N$  increases. The  $u_{\max}$  should be selected such that  $\frac{N}{u_{\max}}$  is several times larger than the width of the potential well or width of the one-dimensional crystal. At the same time, the wave function with the highest range should be equal to about zero on the edges of the range

$\left[-\frac{0.5N}{\mu_{\max}}, \frac{0.5N}{\mu_{\max}}\right]$ . It should be noted that all discrete energy levels for a finite potential well depth and corresponding wave functions can be obtained using one series of computer calculations. The method is characterized by high numerical stability.

## References

1. West LC, Eglash SJ (1985) First observation of an extremely large-dipole infrared transition within the conduction band of a GaAs quantum well. *Appl Phys Lett* 46(12):1156–1158
2. Faist J, Capasso F, Hutchnson AL, Pfeiffer L, West KW (1993) Suppression of optical absorption by electric-field induced quantum interference in coupled potential wells. *Phys Rev Lett* 71(1):3573–3576
3. Levine BF (1993) Quantum well infrared photodetectors. *J Appl Phys* 74:R1–R81
4. Faist J, Capasso P, Sivco DL, Sirtori C, Hutchnson AL, Cho AY (1994) Quantum cascade lasers. *Science* 264:553–556
5. Noda S, Yamashita T, Ohya M, Muromoto Y, Sasaki A (1993) All-optical modulation for semiconductor lasers by using three energy levels in n-doped quantum wells. *IEEE J Quantum Electron* 29(6):1640–1647
6. Bastard G (1988) *Wave mechanics applied to semiconductor heterostructures*. Les editions de physique, Les Ulis
7. Vakarchuk IO (2004) *Quantum mechanics*. Ivan Franko National University of Lviv, Lviv, (in Ukrainian)
8. Caticha A (1995) Construction of exactly soluble double-well potentials. *Phys Rev A* 51(5):4264–4267
9. Dutra AS (1993) Conditionally exactly soluble class quantum potentials. *Phys Rev A* 47(4):R2435–R2437
10. Tkachuk VM, Fityo TV (2003) Multidimensional quasi-exactly solvable potentials with two known eigenstates. *Phys Lett A* 309(5–6):351–356
11. Gedeon A (1974) Comparison between rigorous theory and WKB-analysis of modes in graded-index waveguides. *Opt Commun* 12(3):329–332
12. Smith RE, Houde-Walter SN, Forbes GW (1990) Mode determination for planar waveguide using the four-sheeted dispersion relation. *J. Quantum Electron* 26(4):627–630
13. Anemogiannis E, Glytsis EN (1992) Multilayer waveguides: efficient numerical analysis of general structures. *J Lightwave Technol* 10(10):1344–1351
14. Chatak AK, Thyagarajan K, Shenoy MR (1987) Numerical analysis of planar optical waveguides using matrix approach. *J Lightwave Technol* 5(5):660–667
15. Baba T, Kokubun Y (1992) Dispersion radiation loss characteristics of antiresonant reflecting optical waveguides-numerical results and analytical expressions. *J Quantum Electron* 28(7):1689–1700
16. Rganov AG, Grigas SE (2010) Numerical algorithm for waveguide and leaky modes determination in multilayer optical waveguides. *Tech Phys* 55(11):1614–1618
17. Fitio VM, Romakh VV, Bobitski YV (2014) Numerical method for analysis of waveguide modes in planar gradient waveguides. *Material Science (Medžiagotyra)* 20(3):256–261
18. Fitio VM, Romakh VV, Bartkiv LV, Bobitski YV (2016) The accuracy of computation of mode propagation constants for planar gradient waveguides in the frequency domain. *Mater Sci Eng Technol (Materialwissenschaft und Werkstofftechnik)* 47(2–3):237–245
19. Meškiniš Š, Čiegis A, Vasiliauskas A, Šlapikas K, Gudaitis R, Yaremchuk I, Fitio V, Bobitski Y, Tamulevičius S (2016) Annealing effects on structure and optical properties of diamond-like carbon films containing silver. *Nanoscale Res Lett* 11:146. doi:[10.1186/s11671-016-1362-4](https://doi.org/10.1186/s11671-016-1362-4)
20. Yaremchuk I, Tamulevičius T, Fitio V, Grazulevičute I, Bobitski Y, Tamulevičius S (2013) Guide-mode resonance characteristics of periodic structure on base of diamond-like carbon film. *Opt Commun* 301:1–6

21. Smirnova N, Sakhno O, Fitio V, Gritsai Y, Stumpe J (2014) Simple and high performance DFB laser based on dye-doped nanocomposite volume gratings. *Laser Phys Lett* 11(5):125814–1 – 8
22. Smirnova TN, Sakhno OV, Stumpe J, Fitio VM (2016) Polymer distributed feedback dye laser with an external volume Bragg grating inscribed in a nanocomposite by holographic technique. *JOSA B* 33(2):202–210
23. Fitio VM, Yaremchuk IY, Romakh VV, Bobitski YV (2015) A solution of one-dimensional stationary Schrödinger equation by the Fourier transform. *Appl Comput Electromagn Soc* 30(5):534–539
24. Goodman JW (1968) *Introduction to fourier optics*. McGraw-Hill Book Company, San Francisco
25. Yariv A (1975) *Quantum electronics*. John Wiley and Sons, New York
26. Kittel C (1978) *Introduction to solid state physics*, 4th edn. John Wiley and Sons, Inc., New York

# Chapter 2

## Effects of Ultrasonic Synthesis Variable on Basic Properties of $\text{CoFe}_2\text{O}_4$ Nanoparticles

L. A. Frolova, O. I. Kushnerov, and Y. D. Galivets

### 2.1 Introduction

Recently, the interest in the development of new methods for the production of ferrite dispersed particles is increasing. This is due to their unique magnetic and electrical properties. Cobalt ferrite is a promising material because of its high crystallographic anisotropy, high coercivity, moderate saturation magnetization, chemical resistance, thermal stability and wear resistance [1–4]. Cobalt ferrite is used in magnetic recording, ferrofluid technology, biotechnology, medicine, biology, etc. [5–8].

Technological properties of cobalt ferrite are largely determined by the way it was received. Ceramic methods require large energy inputs and high-temperature synthesis. Thus, obtained ferrites are coarse. They have unstable composition and corresponding anion impurities. Therefore hydrophase synthesis methods are developing nowadays. The most modern are co-precipitation [9, 10], hydrothermal method [11, 12], method of reverse micelles [13], sol–gel [14], mechanochemistry [15] and high-energy technologies [16–19]. Hydrophase methods allow to adjust the composition, crystallinity and morphology of the particles.

All of these methods have been studied by many researchers and successfully applied for the synthesis of cobalt ferrite. Precipitation methods usually comprise several stages. The first is precipitation, while the second is direct synthesis of

---

L.A. Frolova (✉) • Y.D. Galivets  
Ukrainian State University of Chemical Technology, Gagarin ave., 8, Dnipropetrovsk, 49005,  
Ukraine  
e-mail: [frolova\\_l.a@mail.ru](mailto:frolova_l.a@mail.ru)

O.I. Kushnerov  
Oles Honchar Dnipropetrovsk National University, Gagarin ave., 72, Dnipropetrovsk, 49010,  
Ukraine

ferrite, carried out by oxidation, ageing, etc. Recently scientists started to initiate the second main step of ferrite production, for example, using such oxidizing agents as  $\text{KNO}_3$  or  $\text{H}_2\text{O}_2$ . During ultrasound treatment, the solution flows through a set of complex chemical reactions involving radical particles and free electrons.

The major ultimate products of these interactions are oxygen, hydrogen peroxide and hydrogen. Oxidative activity of “activated” solutions can be used in the synthesis of complex oxide compounds.

The unique properties of ultrasound were used for the synthesis of complex inorganic compounds [20–23], for example, the sonochemical decomposition of volatile metal organic precursors for the preparation of cobalt ferrite. Sonochemical synthesis of ferrites is considered in the article [21]. Such materials have a wide range of biomedical applications, including their use as echo contrast agents for ultrasonic diagnosis, magnetic resonance imaging as well as oxygen or drug delivery. The impact of acoustic cavitation creates unique conditions of high energy to chemical reactions in the preservation of low-temperature liquid. Sonochemistry possibilities have been studied in the synthesis of unusual inorganic and biomedical materials. The authors of [22] have carried out a study on the magnetic properties of cobalt ferrite nanofluids under the influence of ultrasonic vibrations. In [23] the effects of pH and the composition of precursor intensity ultrasound treatment on the properties of cobalt ferrite derived from citrate solution were studied. Cobalt ferrites were prepared by combining the sol–gel method and ultrasonic irradiation. The pH values ranged from 5 to 9. In the present work, we studied the phase formation in the system  $\text{Fe}^{2+}$ – $\text{Co}^{2+}$ – $\text{SO}_4^{2-}$ – $\text{OH}^-$  under the influence of ultrasonic vibrations. The variety of possible reaction products require additional study of the impact of frequency, pH and the intensity of exposure.

Our research of solution ultrasonic processing showed that the composition of the synthesized compounds is dependent on a wide range of factors [20, 24]. Using US processing provides a high degree of homogeneity in the distribution of components in the initial solution and in the ferrite formed during the oxidation. This contributes to effective interaction between them to form a homogeneous structure and composition of the compounds. We studied the process of nanoscale cobalt ferrite production at various pH.

## 2.2 Methodology of the Experiment

Production of co-precipitated compounds was carried out by pouring under continuous stirring the appropriate mixture of sulphate solutions with the required ratio of cations as in the ferrite. We used 0.5 M solutions of iron and cobalt salts. Polyhydrocomplex sol obtained at different pH was treated with ultrasound in a laboratory setup (Fig. 2.1). pH range is 7–12, period – 1.

It consisted of a ceramic reaction vessel, in which the ultrasonic dispersant transmitter USDN–2T was immersed and connected to the generator of ultrasonic vibrations. We investigated the influence of ultrasound at a frequency of 22 kHz and

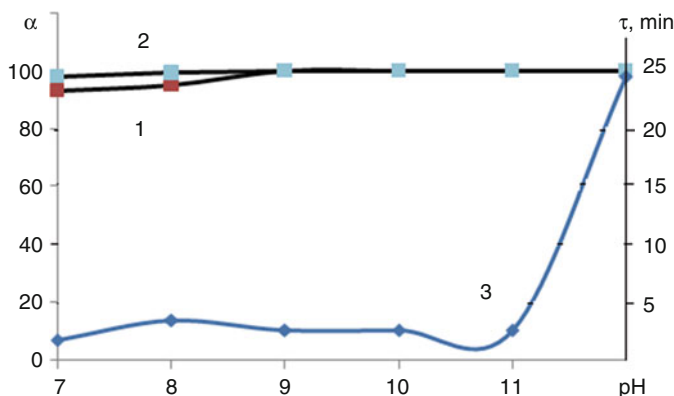


**Fig. 2.1** Dependence of the degree precipitation of cobalt cation (1) and iron cations (2) and complete oxidation time (3) on the pH

the ultrasonic intensity at the load within  $1 \text{ MW/m}^2$ . The optimal treatment time was selected in accordance to a plan drawn up previously.

The study of the phase composition of the samples was carried out using X-ray diffractometer DRON – 2.0 in  $\text{Cu-K}\alpha$  monochromatic radiation. Scanning was performed at room temperature in the angle range of  $5\text{--}85^\circ$ , period =  $0,04^\circ$ .

The microstructure of the nanoparticles obtained was investigated by scanning microscopy with a help of Remme-102 microscope. The study of the magnetic properties of cobalt ferrite nanopowders was performed by vibrating magnetometry.

### 2.3 Results and Discussion

Possible mechanisms including the most probable processes that occur in the cavitation bubble were described by many researchers [20, 25, 26]. The basic idea of the ultrasonic treatment is based on cavitation effect.

As a result of passing through powerful acoustic wave cavitation, bubbles arise in the liquid, in which pressure and temperature are growing strongly. Thus electric discharges and explosions are generated, which lead to various physical and chemical processes that are not observed in other conditions [24].

During the processing of dispersion, medium crystalline precipitate is formed. Its disperse and phase composition is heavily dependent on the mode of the oxidation process: the nature of the oxidant, the oxidation rate, temperature, pH, oxidation start, the concentration of the precipitating agent and initial salt solution.

Kinetic curves showed that, under the influence of ultrasound, the pH of the sol will decrease due primarily to the oxidation of  $\text{Fe}^{2+}$  cations to  $\text{Fe}^{3+}$  (Fig. 2.1). The study of pH change differential curve made US possible to set the time of complete

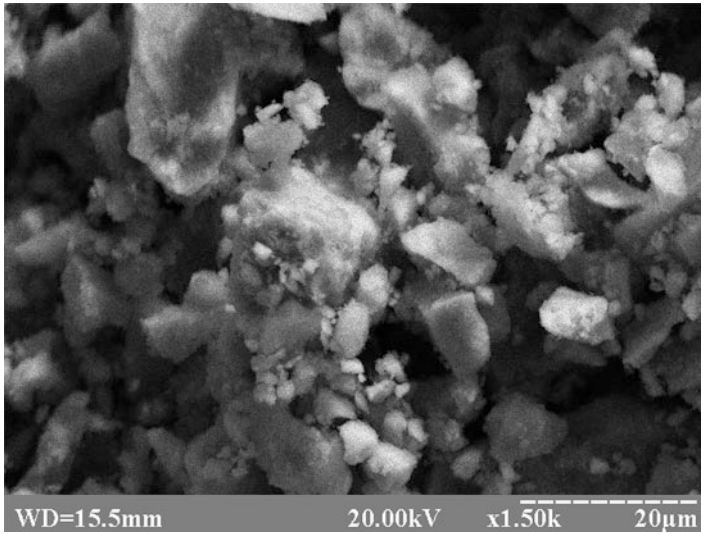


**Fig. 2.2** CoFe<sub>2</sub>O<sub>4</sub> powder microphotograph

oxidation. Decreasing pH causes partial dissolution of the precipitate, which affects the degree of precipitation (Fig. 2.2).

The extent of cobalt cation precipitation for pH 7 and 8 amounted 98.14 and 99.2, respectively; iron ions are present in the filtrate for pH 7 and 8 (the degree of precipitation was 93.23 and 95.2, respectively). In pH range of 9–12, almost complete precipitation of cobalt and iron cations takes place. Optimum pH can be considered as the value at which the relationship makes a straight line parallel to x axis.

It is known that the phase composition formed during the ultrasonic processing of products can be diverse.

Variable valency of the starting materials used in the synthesis and the oxidizing medium yield suggest the possibility of formation of undesirable phases of mixed oxyhydroxide, solid solutions of maghemite, lepidocrocite, goethite, hydrated oxides, etc. To assess the influence of ultrasound, it is necessary to define composition and properties of the resulting products during the ultrasonic treatment. According to experimental data, the oxidation process time with pH increasing in the range of 7–11 remains constant and then abruptly increases.

Figure 2.3 shows a typical microphotograph of cobalt ferrite sample prepared at pH = 12. The powder represents separate particles and irregular-shaped and different-sized faceted composites of agglomerated particles. Particle size analysis of the powder showed a great variation of particles sizes. Agglomerate size ranges within 1–20 mm. Thus there is particle shape anisotropy.

X-ray diffractions are shown in Figs. 2.3 and 2.4.

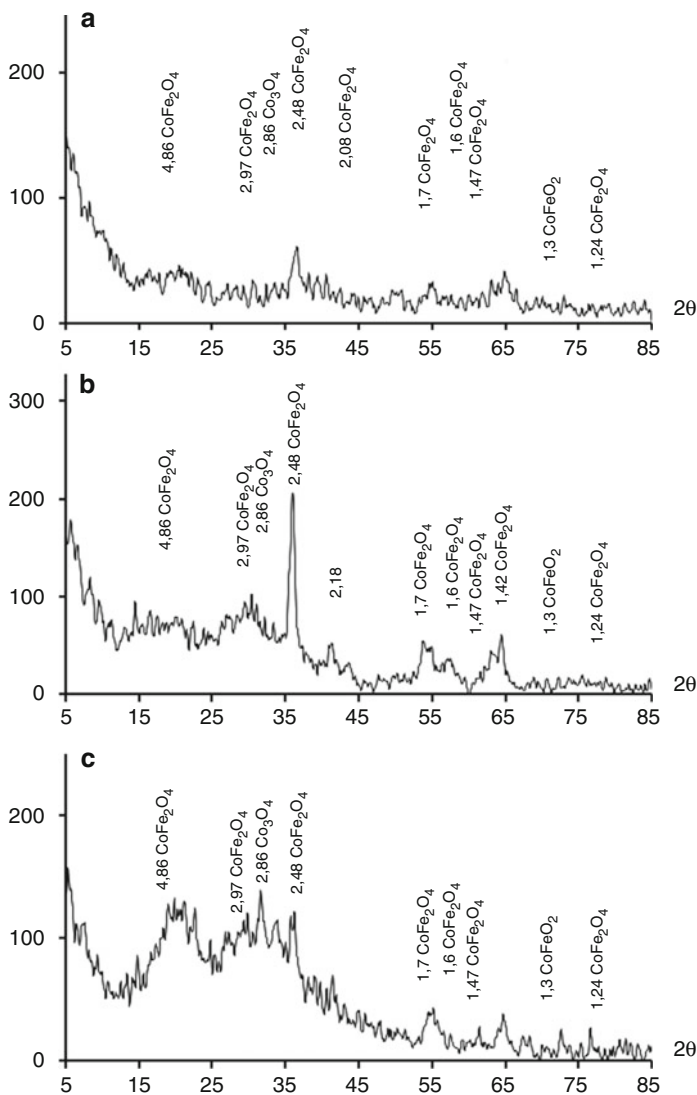


**Fig. 2.3** X-ray diffraction pattern of samples obtained at different pH. **a-7, b-8, c-9**

The above-mentioned X-ray diffractions show only reflections corresponding to the spinel crystal lattice of cubic symmetry, which corresponds to JCPUS-22-1086 (Fig. 2.4c) and  $\gamma\text{-(CoFe)}_2\text{O}_3$  and  $(\text{CoFe})_3\text{O}_4$ . The values of the lattice parameter calculated from the XRD spectra were  $0.83941 \pm 0.00011$  (Fig. 2.4c).

At low pH, amorphous phase is observed which is explained by the non-completion of the crystallization process. With increasing pH, the degree of crystallinity also increases. However, abnormally low values pH of coercive force



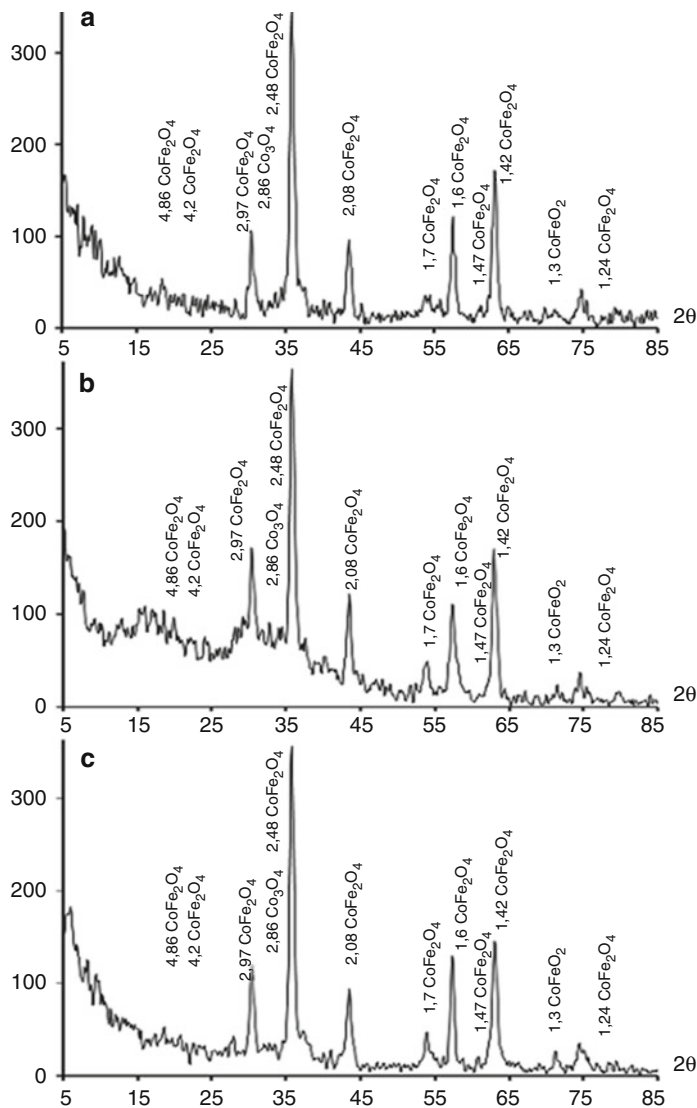


**Fig. 2.4** X-ray diffraction pattern of samples obtained at different pH. **a**-10, **b**-11, **c**-12

at pH = 9 – 10 can be associated with the formation of maghemite crystal structure with integrated cobalt cations.

At pH = 12, cobalt ferrite is formed, which is confirmed by the magnetic measurements. Similar structure and similar reflections make it difficult to conduct quality identification with the help of X-ray analysis. Figure 2.5 shows magnetization measurement samples obtained at different pH. As follows from the figure, all

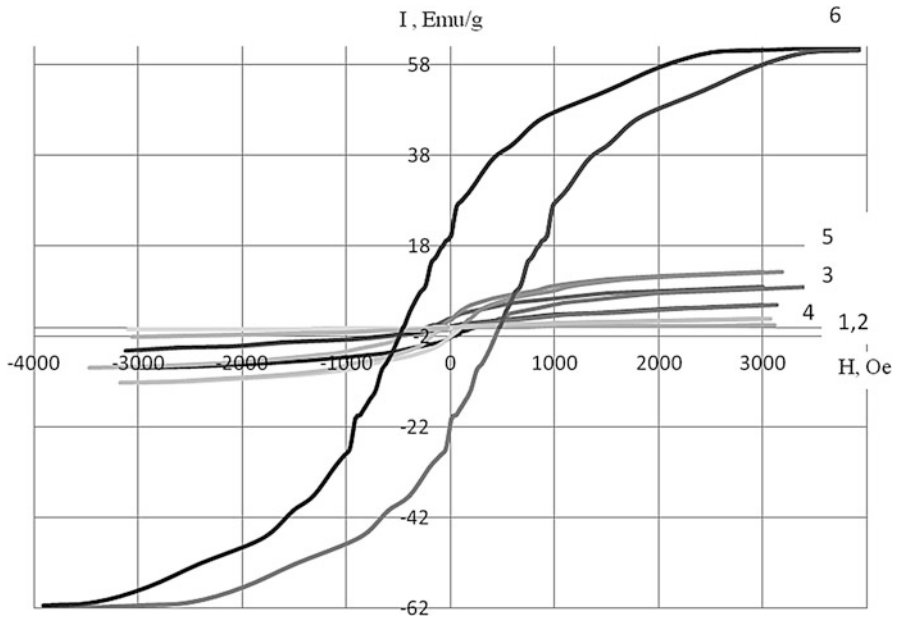


**Fig. 2.5** Magnetization curves at room temperature of the samples prepared at pH. 1-7, 2-8, 3-9, 4-10, 5-11, 6-12

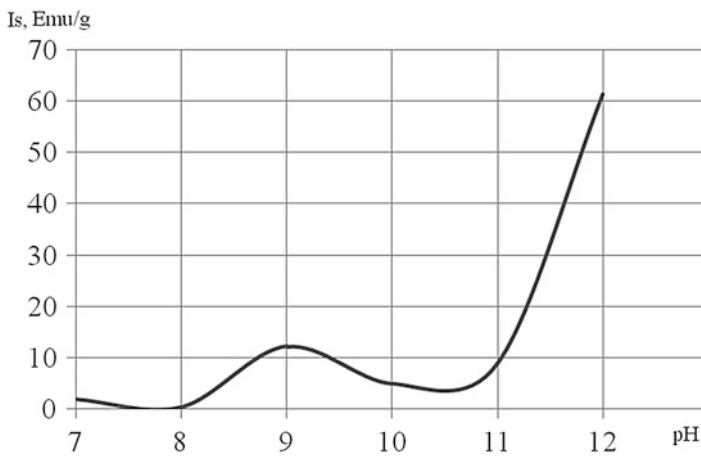


**Fig. 2.6** The dependence of the coercive force on the pH

the samples in a magnetic field have saturation magnetization and hysteresis loop (Figs. 2.6 and 2.7).

The magnetic properties of cobalt ferrite are largely determined by the presence of superparamagnetic relaxation, which is represented in nanostructured systems. However, the presence and expression of the specific properties of nanodispersed

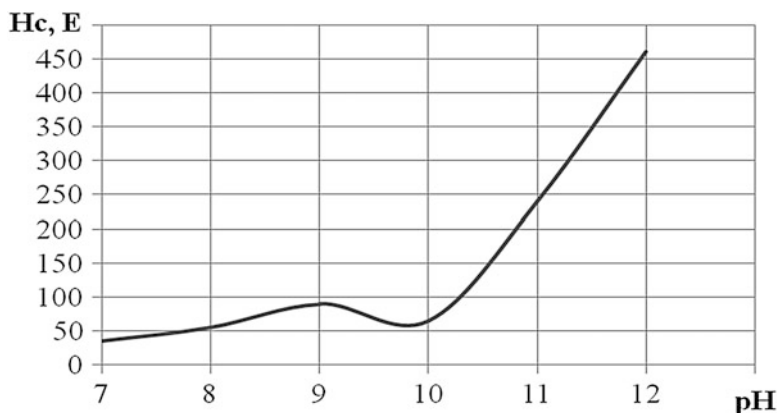


**Fig. 2.7** Dependence of the saturation magnetization on the pH

materials are associated with the appearance of the magnetic dipole interaction between nanodisperse particles and magnetic field.

Saturation magnetization of the samples ranges from 0.5 to 59 emu/g. Coercive force, respectively, accounted for 50–450 Oe, which is correlated with the numbers shown in [5, 27]. It is known that fine ferromagnets possess specific magnetic properties. In this case, particle sizes of 1–20 mcm commensurate with magnetic domain boundary thickness. In this case, the boundary of the magnetic domain is larger than the magnetostatic energy of a single-domain particle, i.e. particles without boundaries. In this case, particles of such sizes do have boundaries, and they are called single-domain particles. In ferromagnets, consisting of such single-domain particles, magnetization can only take place by rotation of the magnetization vectors of individual particles. The value of the coercive force increases and is close to the theoretical value.

Comparative analysis of the nature of magnetic saturation curves and coercive force has shown a correlation of graphs 1, 6 and 7. This is primarily due to the fact that the magnetic characteristics are determined by the composition of the compounds formed.

The sequence of phases of formation can be represented as follows:  $\gamma\text{-(CoFe)}_2\text{O}_3 \rightarrow (\text{CoFe})_3\text{O}_4 \rightarrow \text{CoFe}_2\text{O}_4$ .

## 2.4 Conclusion

The studies established the conditions for obtaining fine particles  $\text{CoFe}_2\text{O}_4$  under the influence of ultrasound. It is found that the particles have a faceted shape with an average size of agglomerates of 2–20  $\mu$  and a developed surface.

XR analysis showed that, depending on the pH synthesis, particles have different structures of crystal lattice of spinel cubic structure. The sequence of phases of formation can be represented as follows:  $\gamma(\text{CoFe})_2\text{O}_3 \rightarrow (\text{CoFe})_3\text{O}_4 \rightarrow \text{CoFe}_2\text{O}_4$ . Measurements of the magnetic properties of powders confirmed the stated assumption. Saturation magnetization ( $M_s$ ) of samples ranged from 1.5 to 58 emu/g; coercivity ( $H_c$ ) was 45–450 Oe depending on synthesis conditions.

## References

1. Zhou JP, He H, Shi Z, Nan CW (2006) Magnetoelectric  $\text{CoFe}_2\text{O}_4/\text{Pb}(\text{Zr}_{0.52}\text{Ti}_{0.48})\text{O}_3$  double-layer thin film prepared by pulsed-laser deposition. *Appl Phys Lett* 88(1):013111
2. Wang Y, Su D, Ung A, Ahn JH, Wang G (2012) Hollow  $\text{CoFe}_2\text{O}_4$  nanospheres as a high capacity anode material for lithium ion batteries. *Nanotechnology* 23(5):055402
3. George M, Nair SS, Malini KA, Joy PA, Anantharaman MR (2007) Finite size effects on the electrical properties of sol–gel synthesized  $\text{CoFe}_2\text{O}_4$  powders: deviation from Maxwell–Wagner theory and evidence of surface polarization effects. *J Phys D Appl Phys* 40(6):1593
4. Limaye MV, Singh SB, Date SK, Kothari D, Reddy VR, Gupta A et al (2009) High coercivity of oleic acid capped  $\text{CoFe}_2\text{O}_4$  nanoparticles at room temperature. *J Phys Chem B* 113(27):9070–9076
5. Sangmanee M, Maensiri S (2009) Nanostructures and magnetic properties of cobalt ferrite ( $\text{CoFe}_2\text{O}_4$ ) fabricated by electrospinning. *Appl Phys A* 97(1):167–177
6. Torres TE, Roca AG, Morales MP, Ibarra A, Marquina C, Ibarra MR, Goya GF (2010) Magnetic properties and energy absorption of  $\text{CoFe}_2\text{O}_4$  nanoparticles for magnetic hyperthermia. *J Phys Conf Ser* 200(7):072101
7. Liu B, Li Q, Zhang B, Cui Y, Chen H, Chen G, Tang D (2011) Synthesis of patterned nanogold and mesoporous  $\text{CoFe}_2\text{O}_4$  nanoparticle assemblies and their application in clinical immunoassays. *Nanoscale* 3(5):2220–2226
8. Rajendran M, Pullar RC, Bhattacharya AK, Das D (2001) Chintalapudi S.N. And Majumdar C. K., Magnetic properties of nanocrystalline  $\text{CoFe}_2\text{O}_4$  powders prepared at room temperature: variation with crystallite size. *J Magn Magn Mater* 232:71–83
9. Frolova L, Derimova A, Khlopyskyi A, Galivets Y, Savchenko M (2016) Investigation of phase formation in the system  $\text{Fe}^{2+}/\text{Co}^{2+}/\text{O}_2/\text{H}_2\text{O}$ . *East Eur J Enterpr Technol* 6 ( 83 ): 55 – 59
10. Hamad MA (2013) Calculations on nanocrystalline  $\text{CoFe}_2\text{O}_4$  prepared by polymeric precursor method. *J Supercond Nov Magn* 26(3):669–673
11. Adschiri T, Kanazawa K, Arai K (1992) Rapid and continuous hydrothermal crystallization of metal oxides particles in supercritical water. *J Am Ceram Soc* 75(4):1019–1022
12. Millot N, Xin B, Pighini C, Aymes D (2005) Hydrothermal synthesis of nanostructured inorganic powders by a continuous process under supercritical conditions. *J Eur Ceram Soc* 25:2013–2016
13. Pillai V, Shah DO (1996) Synthesis of high coercivity cobalt ferrite particles using water in oil microemulsions. *J Magn Magn Mater* 163:243–248
14. Lee JG, Lee HM, Kim CS, Oh YJ (1998) Magnetic properties of  $\text{CoFe}_2\text{O}_4$  powders and thin films grown by a sol–gel method. *J Magn Magn Mater* 177:900–902
15. Guigue-Millot N, Begin-Colin S, Champion Y, Hytch MJ, Le Caer G, Perriat P (2003) Control of grain size and morphologies of nanograined ferrites by adaptation of the synthesis route: mechanochemistry and soft chemistry. *J. Solid State Chem* 170:30–38
16. Frolova LA, Shapa NN (2011) Technology of extraction manganese compounds from the discharge water of metallurgical enterprises with the use of ultrasound. *Metall Min Ind* 3(6):65–69

17. Frolova L, Pivovarov A, Tsepich E (2016) Ultrasound ferritization in  $\text{Fe}^{2+}$ - $\text{Ni}^{2+}$ - $\text{SO}_4^{2-}$ - $\text{OH}^-$  system. *J Chem Technol Metall* 51(2):163–167
18. Obara G, Yamamoto H, Tani M, Tokita M (2002) Magnetic properties of spark plasma sintering magnets using fine powders prepared by mechanical compounding method. *J Magn Magn Mater* 239:464–467
19. Tokita M (1999) Development of large size ceramic/metal bulk FGM fabricated by SPS. *Mater Sci Forum* 308:83–88
20. Baranchikov A, Ivanov V, Tretyakov Y (2007) Kinetics and mechanism of nickel ferrite formation under high temperature ultrasonic treatment. *Ultrason Sonochem* 14:131–134
21. Vicentea de J, Bossis G, Lacisc S, Guyotd M (2002) Permeability measurements in cobalt ferrite and carbonyl iron powders and suspensions. *J Magn Magn Mater* 251:100–108
22. Rashin M, Nabeel HJ (2014) Magnetic and ultrasonic studies on stable cobalt ferrite magnetic nanofluid. *Ultrasonics* 54:834–840
23. Madani S, Mahmoudzadeh G, Khorrami S (2012) Ceramic processing research influence of pH on the characteristics of cobalt ferrite powder prepared by a combination of sol-gel auto-combustion and ultrasonic irradiation techniques. *J Ceram Process Res* 13(2):123–126
24. Frolova LA, Pivovarov AA (2015) Investigation of conditions for ultrasound-assisted preparation of nickel ferrite. *High Energy Chem* 49(1):10–15
25. Meskin PE, Gavrilov AI, Maksimov VD, Ivanov VK, Churagulov BP (2007) Hydrothermal/microwave and hydrothermal/ultrasonic synthesis of nanocrystalline titania, zirconia, and hafnia. *Russ J Inorg Chem* 52(11):1648–1656
26. Larichev MN, Shaitura NS, Laricheva OO (2008) The influence of ultrasonic field on the oxidation of al powders with water. *Russ J Phys Chem B* 2(5):757–758
27. Kovacheva D, Ruskov T, Krystev P, Asenov S, Tanev N, Monch I, Koseva R, Wolff U, Gemming T, Markova-Velichkova M, Nihtianova D (2012) Synthesis and characterization of magnetic nano-sized  $\text{Fe}_3\text{O}_4$  and  $\text{CoFe}_2\text{O}_4$ . In: *Bulgarian chemical communications, vol 44, Proceedings of the III rd National Crystallographic Symposium*, 90–97

# Chapter 3

## Structural and Dynamical Properties of Argon-Krypton Binary Mixture Confined Between Graphite Slabs: Molecular Dynamics Simulation

A. Dawid and Z. Gburski

### 3.1 Introduction

The noble gases like argon or krypton play an important role as the thermal isolators in double glazing windows [1, 2]. On the other hand, the thermal conductivity in nanometers slots is very important when it comes to designing new cooling systems for electronic devices [3]. The properties of noble gases in small, nanometer-confined space are very important due to its potential applications in nanoelectronic devices, nanoscale molecule sensors [4], and gas storage devices. The dynamical and structural properties of bulk argon-krypton mixture have been studied for many years both in the theoretical and experimental works [5–7]. In recent years the understanding of the atomics dynamics has been enhanced by the computer simulations. At the beginning of computer modeling era, the researchers concentrated on the small aggregates of atoms, called clusters [8–11]. The finite-size clusters are currently being intensively studied because their properties are significantly modified from those of bulk materials. By studying clusters, we can also better understand the origins of collective behavior in bulk systems [12–16]. For instance, in the small  $\text{Ar}_{13}$  clusters, the interaction-induced light scattering spectra proved to be a sensitive indicator of the phase transitions [8]. Further improvement of computer technology allows the simulation of molecular dynamics in bulk samples of noble gas atoms [17–25]. The dynamics of fluids inside small confinement of the size of a few atoms differs from that for a bulk matter. There

---

A. Dawid  
Department of Computer Science, The University of Dąbrowa Górnicza, ul. Ciepłaka 1c,  
Dąbrowa Górnicza, Poland

Z. Gburski (✉)  
Institute of Physics, University of Silesia, Uniwersytecka 4, 40-007 Katowice, Poland  
e-mail: [zygmunt.gburski@us.edu.pl](mailto:zygmunt.gburski@us.edu.pl)

are some works about the dynamics of a thin layer of noble gas atoms adsorbed on fullerene [26–31] and carbon nanotube [32–35]. In our previous research [18, 20, 22], the noble gases like argon, krypton, or xenon between graphite walls were simulated. Those simulations were performed for varying density inside the slot and showed the increasing mobility of the noble gas atoms, with the increasing distance between the graphite slabs.

In the case of double glazing windows, the slot between two panes of glass is of the order of centimeters. In this study our slot between graphite plates is about seven orders of magnitude smaller than in double glazing windows. In our work we have calculated dynamical and structural properties of argon and krypton atoms' binary mixture confined between graphite slabs.

### 3.2 Simulation Details

The system of noble gases mixture between two graphite walls was simulated using classical equations of motion. The interaction potential between noble gases and noble gases-carbon was taken to be Lennard-Jones (LJ) potential with the usual form:

$$V(r_{ij}) = 4\varepsilon_{ij} \left[ \left( \frac{\sigma_{ij}}{r_{ij}} \right)^{12} - \left( \frac{\sigma_{ij}}{r_{ij}} \right)^6 \right],$$

where  $r_{ij}$  is the distance between atoms and  $\varepsilon_{ij}$  and  $\sigma_{ij}$  are the LJ potential parameters listed in Table 3.1. The parameters between unlike atoms were calculated using Lorentz-Berthelot mixing rule [36]. The graphite walls are simulated as interacting sites without internal degrees of freedom. The walls did not move during the MD simulation; all atoms in graphite were fixed. It approximates bulk sample of graphite sheets. Simulations were performed with the three-dimensional orthogonal periodic boundary conditions (PBC) using minimum image convention algorithm. The simulation cell was of the edge size  $x = 28.31 \text{ \AA}$ ,  $y = 25.73 \text{ \AA}$ , and  $z = 60 \text{ \AA}$ . The size of the simulation box in  $z$ -direction was chosen so to switch off PBC in that direction. The Lennard-Jones interaction cutoff distance between all unlike atoms was set to  $20 \text{ \AA}$ , which fulfills that periodic interactions are only in  $x$ - and  $y$ -directions. The classical equations of motion were integrated up to 5 ns by the velocity Verlet algorithm [37]. The integration time step used in simulation is 5 fs which ensures total energy conservation within 0.01%. The average temperature

**Table 3.1** Lennard-Jones potential parameters

Atom	$\varepsilon$ [meV]	$\sigma$ [Å]
Carbon	2.413	3.40
Argon	10.341	3.40
Krypton	14.391	3.63

was adjusted as desired by a process of velocity scaling using Berendsen algorithm [37]. The system was equilibrated for  $5 * 10^6$  MD steps. We have used our own developed simulation software named RIGMD to perform all calculations [38].

### 3.3 General Relations

The mobility of argon or krypton atom can be expressed by the mean square displacement function  $MSD(t) = \langle |\Delta r_{ij}(t)|^2 \rangle$ , where  $r_{ij}$  is the distance between noble gas atoms. The linear slope of the function indicates diffusion in the system, according to Einstein relation:

$$D = \frac{1}{6} \frac{d\langle |\Delta r(t)|^2 \rangle}{dt}$$

When two dissimilar rare gas atoms interact, a dipole moment is generated, due to mutual distortion of the atomic charge clouds. The corresponding absorption spectrum lies in the far infrared, typically in the range  $0-250 \text{ cm}^{-1}$ . The interaction-induced absorption spectrum is related to the Fourier transform of the time correlation function  $G(t) = \sum \langle \mu_{ij}(t) \cdot \mu_{kl}(0) \rangle$ , where  $\mu_{ij}$  is the dipole moments induced in a pair of dissimilar atoms and the sum is over all pairs of unlike atoms in the mixture containing  $c_A$  and  $c_B$  concentrations of atoms type  $A$  and  $B$ ,  $c_A + c_B = c$ . The correlation function  $G(t)$  of the total dipole moment  $\mu = \sum_{i,j} \mu_{ij}$  can be decomposed into pair, triplet, and quadruplet contributions [39]:

$$G(t) = G_2(t) + G_{3a}(t) + G_{3b}(t) + G_4(t),$$

$$G_2(t) = \sum_{i \in c_A, i' \in c_B} \langle \mu_{ii'}(t) \cdot \mu_{ii'}(0) \rangle,$$

$$G_{3a}(t) = \sum_{i \in c_A, i' \neq j' \in c_B} \langle \mu_{ii'}(t) \cdot \mu_{ij'}(0) \rangle,$$

$$G_{3b}(t) = \sum_{i \neq j \in c_A, i' \in c_B} \langle \mu_{ii'}(t) \cdot \mu_{jj'}(0) \rangle,$$

$$G_4(t) = \sum_{i \neq j \in c_A, i' \neq j' \in c_B} \langle \mu_{ii'}(t) \cdot \mu_{jj'}(0) \rangle,$$

where eventual irreducible three-body dipole moments have been neglected. In the following, the two-body dipole moments  $\mu_{ij}$  are identified with dipole functions available in the literature [7, 40]:

$$\vec{\mu}_{ij} = \mu(r_{ij}) \hat{n}_{ij},$$

$$\mu(r) = \mu_0 e^{-\alpha r - \beta(r-r_0)^2} + D_7/r,$$



**Table 3.2** Parameters for the Ar-Kr-induced dipole

$\mu_0$ ( $10^{-31}$ cm)	$r_0$ ( $10^{-10}$ m)	$\alpha$ ( $10^{-10}$ m $^{-1}$ )	$\beta$ ( $10^{-10}$ m $^{-1}$ )	$D_7$ ( $10^{-31}$ cm)
0.741	3.468	2.961	0.984	-615.854

Taken from Dawid and Gburski [8]

where  $\mu_0$ ,  $\alpha$ ,  $\beta$ , and  $r_0$  are parameters evaluated for different rare gas pairs. The values of these parameters for the Ar-Kr induced dipole were taken from [7] and are given in Table 3.2.

### 3.4 Results

We started the simulations of interaction-induced absorption spectra by modeling the argon-krypton mixture places between graphite slabs. The graphite structure model was constructed, as two layers of sixfold carbon rings multiplied in  $x$ - and  $y$ -direction. The distance between near carbon atoms in the hexagonal rings was set to 1.42 Å and the angle between three near atoms to 120°. The interlayer distance was equal to 3.4 Å. We have assumed that the masses of graphite slabs are much bigger than argon or krypton atoms, so they will not move during simulation. In all our simulations, the distances between the slabs were set to  $d = 28.2$  Å. We have prepared two systems of Ar-Kr mixture between graphite. In the first one, we have used 208 argon atoms and 48 krypton atoms which give 19% concentration of krypton in argon. In the second system, we have reversed proportions of constituents, i.e., we have used 48 argon and 208 krypton atoms. These two systems have different total densities, the first  $\rho_I = 1.326$  g/cm $^2$  and the second  $\rho_{II} = 2.084$  g/cm $^2$ , respectively. The initial locations of argon and krypton atoms between graphite were distributed uniformly. The instantaneous configurations of two systems are shown in Fig. 3.1. The bulk systems of interacting argon and krypton atoms were prepared using constant total number of atoms ( $N = 256$ ). Then we have adjusted the volume of master cell reaching the desired density which equal to density of binary mixture inside the confined space between graphite walls, for two different concentrations of krypton.

We begin the study of the dynamics in the system by calculation of the interaction-induced light absorption. We have decomposed the  $G(t)$  correlation function into two-, three-, and four-body contributions. The quantum corrections to  $G(t)$  are expected to be small in case of Ar-Kr mixture [5] and have been neglected. The simulated components of  $G(t)$  function at  $T = 110$  K are presented in Fig. 3.2. In low concentration of krypton (19%), the positive  $G_2(t)$  function decays fast to  $3.4 \times 10^{-32}$  cm within 0.4 ps and then after small dip decays less rapidly to zero within 70 ps (Fig. 3.2a). The fast decay in short times can be connected with the ballistic region of argon-krypton dynamics. In high concentration of krypton atoms (81%),  $G_2(t)$  function decays even faster to  $2.2 \times 10^{-32}$  cm within 0.4 ps and to zero within 45 ps (Fig. 3.2b). In the low concentration of krypton, the negative three-body function  $G_{3a}(t)$  (two argons and one krypton) rises to zero within 12 ps.

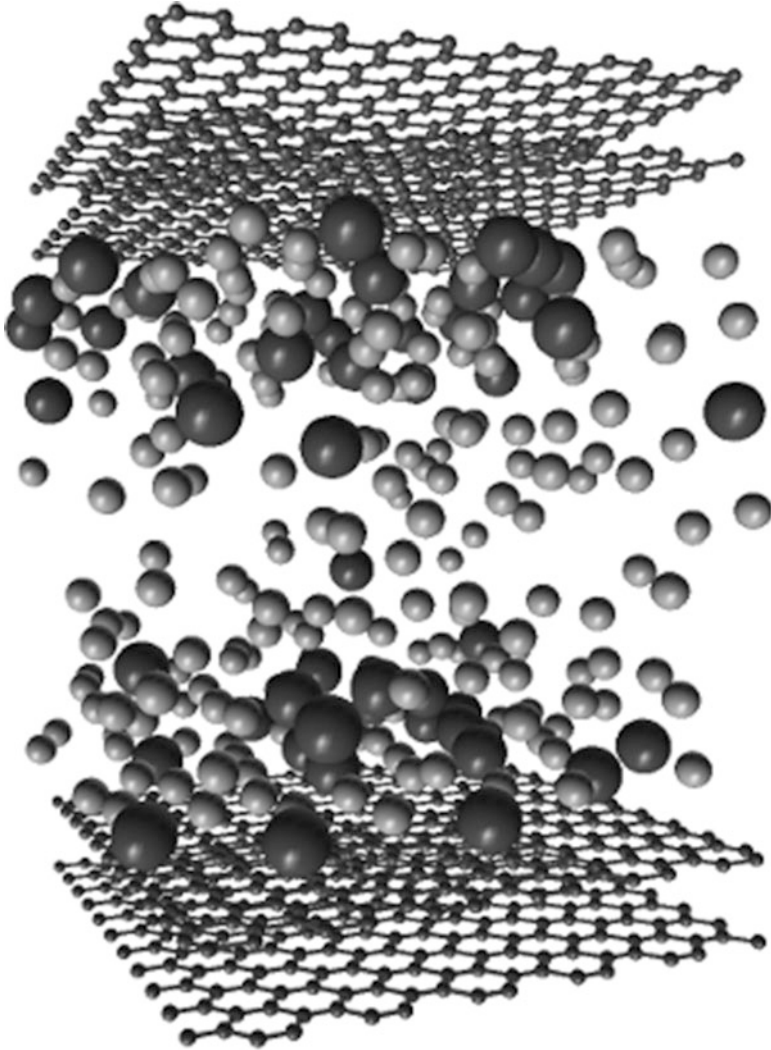


**Fig. 3.1** The instantaneous configuration of argon-krypton mixture between graphite walls at  $T = 110.0$  K

At  $t = 0.4$  ps, we can observe the small dip. When we look at the second three-body function  $G_{3b}(t)$  (one argon and two krypton atoms), the minimum of first dip is located at the same value as for  $G_{3a}(t)$ , but it becomes much deeper and equal to  $-2.5 \times 10^{-32}$  cm. The situation is reversed for high concentration of krypton (81%). The first dip is higher for  $G_{3a}(t)$  function and is equal to  $-2.1 \times 10^{-32}$  cm. The four-body functions  $G_4(t)$  (two argons and two kryptons) both in small and high concentration of krypton have mainly oscillatory character and rise to zero within 120 ps. Next we have calculated the Fourier transform of  $G_2(t)$  and  $G(t)$  and compared these two results with bulk argon-krypton mixture spectrum of the

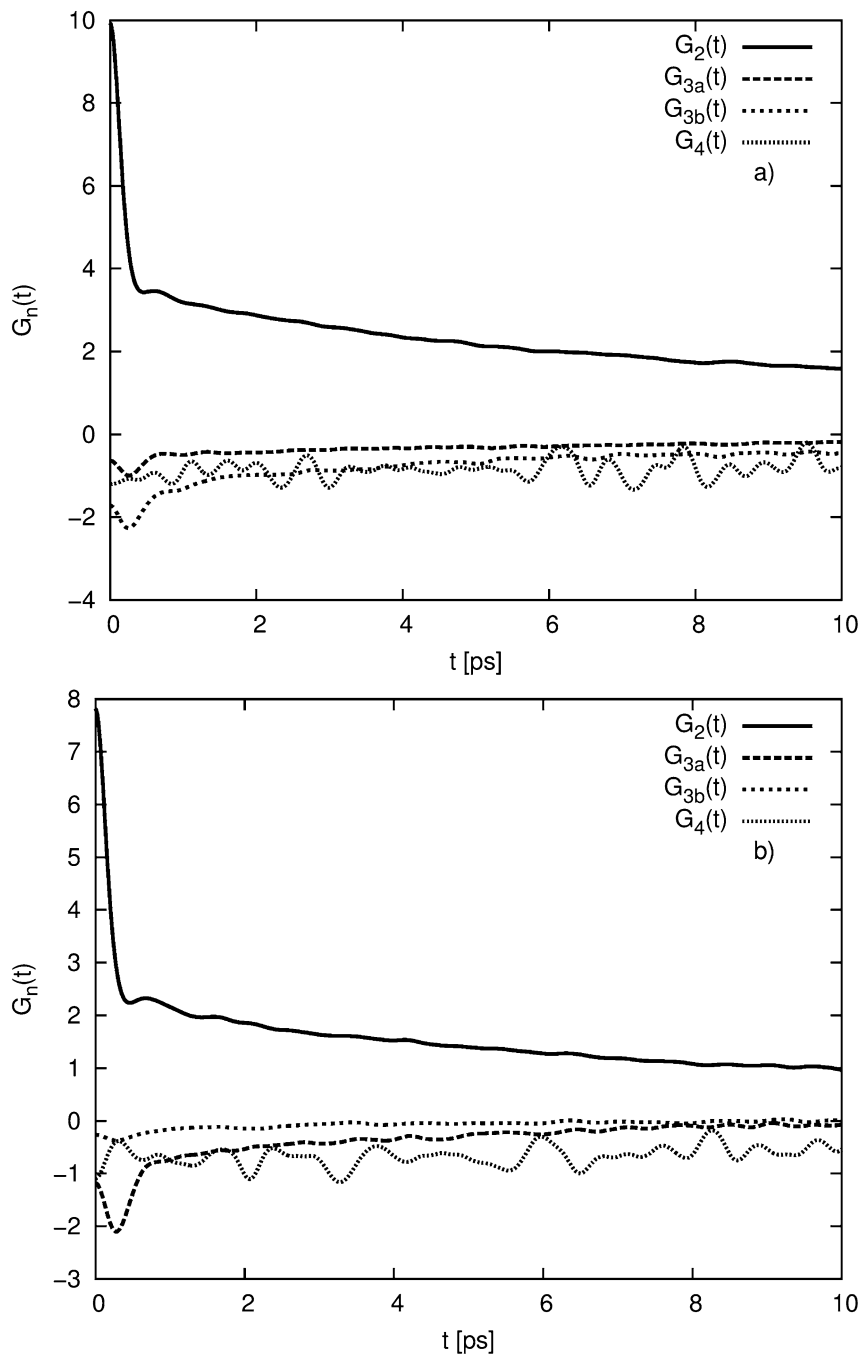


**Fig. 3.2** Interaction-induced dipole moment correlation functions at  $T = 110$  K and concentration of krypton (a) 19% and (b) 81%

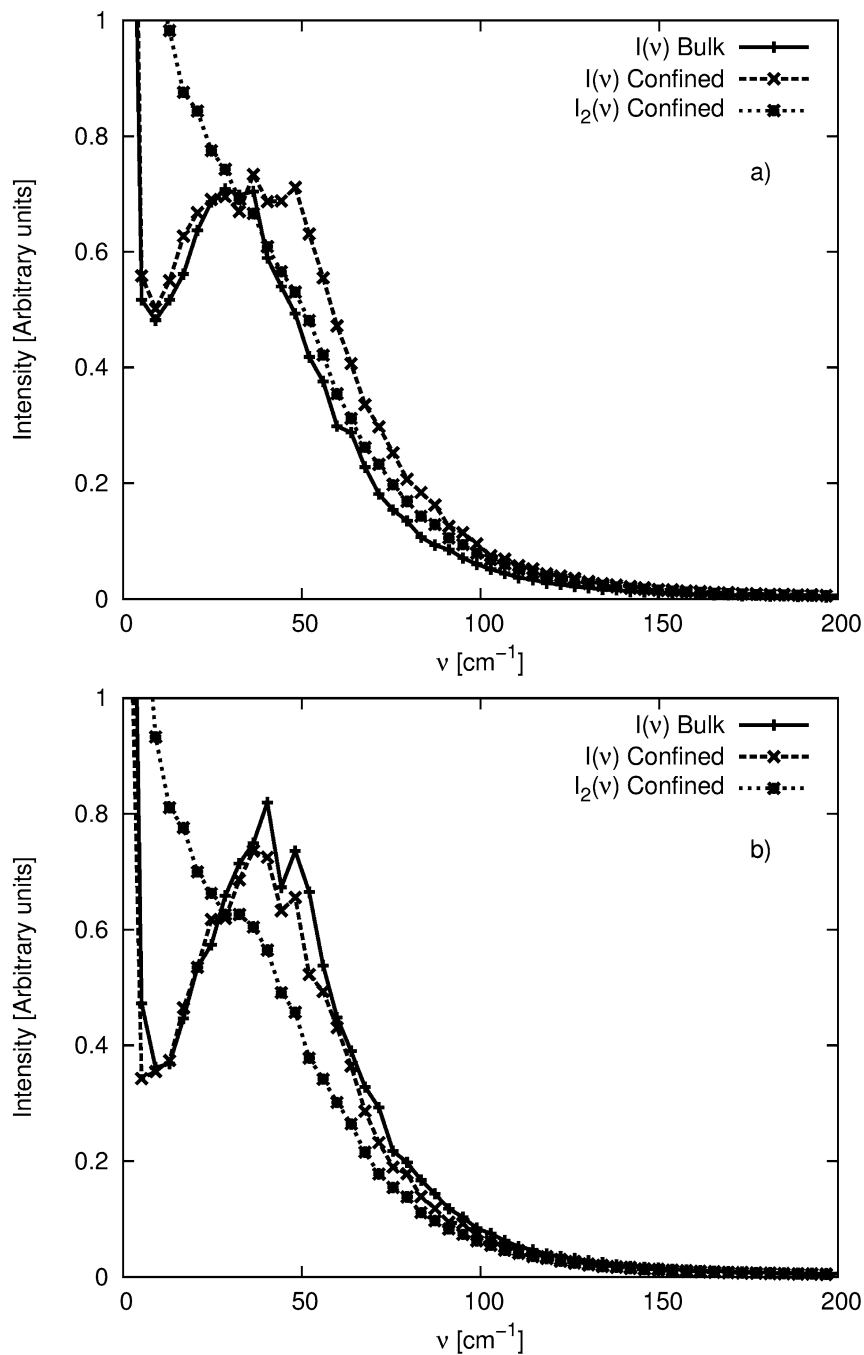


**Fig. 3.3** The total intensity  $I(\nu)$  and two-body  $I_2(\nu)$  of confined and bulk argon-krypton mixture at  $T = 110.0$  K and the concentration of krypton equal to (a) 19% and (b) 81%

same concentrations (Fig. 3.3). The resulting spectra consist of two peaks; the first peak is in zero frequency and is responsible for longtime dynamics and the second one is in the range of 12–200  $\text{cm}^{-1}$  with the maximum at 48  $\text{cm}^{-1}$ . The change of dynamics by confinement in Ar-Kr mixture can be observed in the case of low krypton concentration (Fig. 3.3a). The location of second maximum in confined spectrum is shifted toward higher frequencies. The shift is equal to 15  $\text{cm}^{-1}$ . The shift is not visible at high concentration of krypton. Comparing  $I_2(\nu)$  with  $I(\nu)$ , one can realize that three- and four-body contributions are responsible for formation of the second maximum. In Fig. 3.4, we can see the temperature dependence of interaction-induced spectra. The second maximum grows with the increase of the temperature from 0.6 at 50 K to 0.9 at 140 K. We can also observe the narrowing of the second band at high concentration of krypton (Fig. 3.4b). It can be connected with a reduced mobility of argon atoms in krypton solution. The dynamics of argon and krypton atoms can also be analyzed by observing the mean square displacement functions at  $T = 110$  K (Fig. 3.5). The mobility of argon at low concentration in confined argon-krypton mixture seems to be higher than in bulk argon-krypton of krypton, but the mobility of krypton is lower in confined space compared to the bulk system (Fig. 3.5a). At high concentration of krypton, the mobility of both argon and krypton is higher than in bulk system (Fig. 3.5b). The mean square displacement function is related with diffusion coefficient by the Einstein formula. In Fig. 3.6, we see the temperature dependence of diffusion coefficients. The diffusion coefficient increases with temperature. The increase is slower in the region between 50 and 90 K and faster in the region between 90 and 140 K. The values of diffusion coefficient are higher for argon atoms than for krypton atoms. The influence of concentration is visible; low concentration of krypton results in higher values of diffusion coefficients at temperature range between 50 and 150 K (Fig. 3.6a). This region of temperature is related to fluid phase of Ar-Kr mixture between graphite slabs. The structural property of the system was investigated by calculation of density profile  $\rho(z)$  (Figs. 3.7 and 3.8). We have looked at the probability of finding argon or krypton atom in the certain location along  $z$ -axis perpendicular to the graphite slabs. The results showed that argon and krypton atoms are not distributed uniformly in the graphite slot. They create the layered structure that fades in the inner most part of the slot. The increase of temperature melts the inner most layers. The layers closest to the graphite surface remain still visible at  $T = 140$  K. The low concentration of krypton in Ar-Kr mixture gives the most pronounced argon peaks (Fig. 3.7). The reverse situation is observed at high concentration of krypton atoms; it means that layers are mainly made of krypton (Fig. 3.8).

### 3.5 Conclusions

This study shows that the dynamics of argon and krypton atoms in confined system differs from those in bulk system. We have observed that the interaction-induced absorption spectrum of confined Ar-Kr mixture is shifted toward the higher

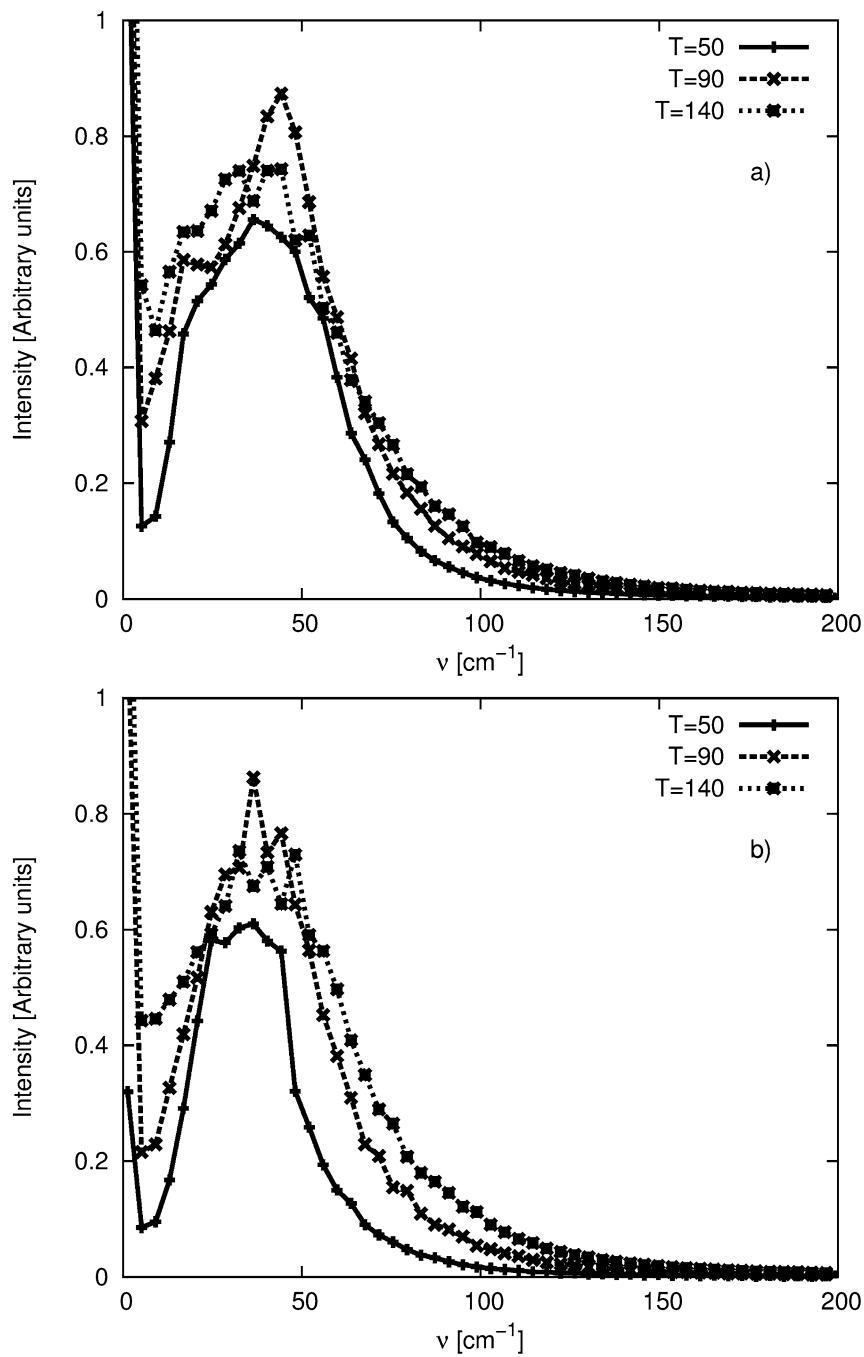


**Fig. 3.4** The total intensity  $I(\nu)$  of confined argon-krypton mixture at three temperatures and the concentration of krypton equal to (a) 19% and (b) 81%

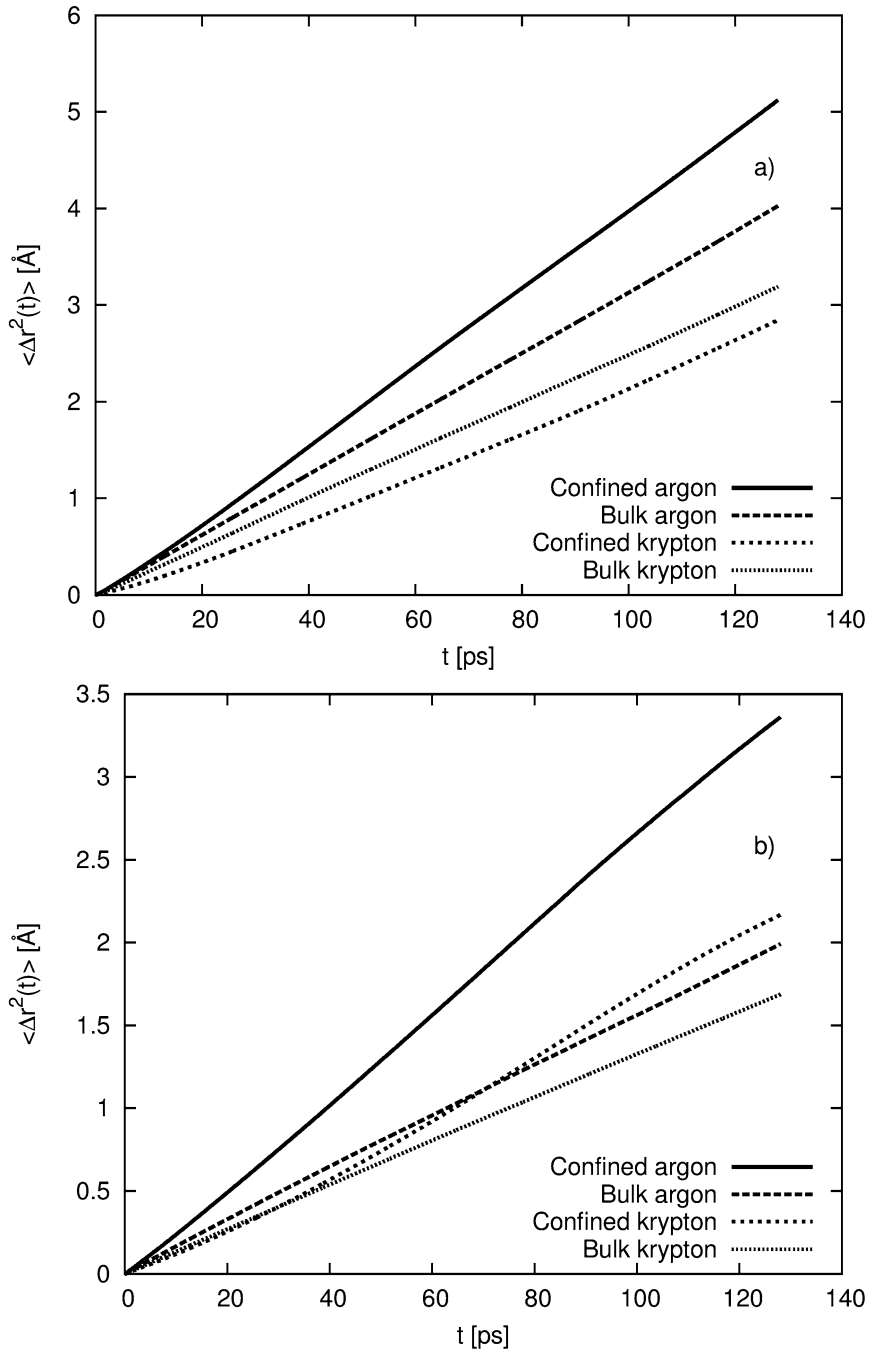


**Fig. 3.5** The mean square displacement functions of krypton concentration at (a) 19% and (b) 81%

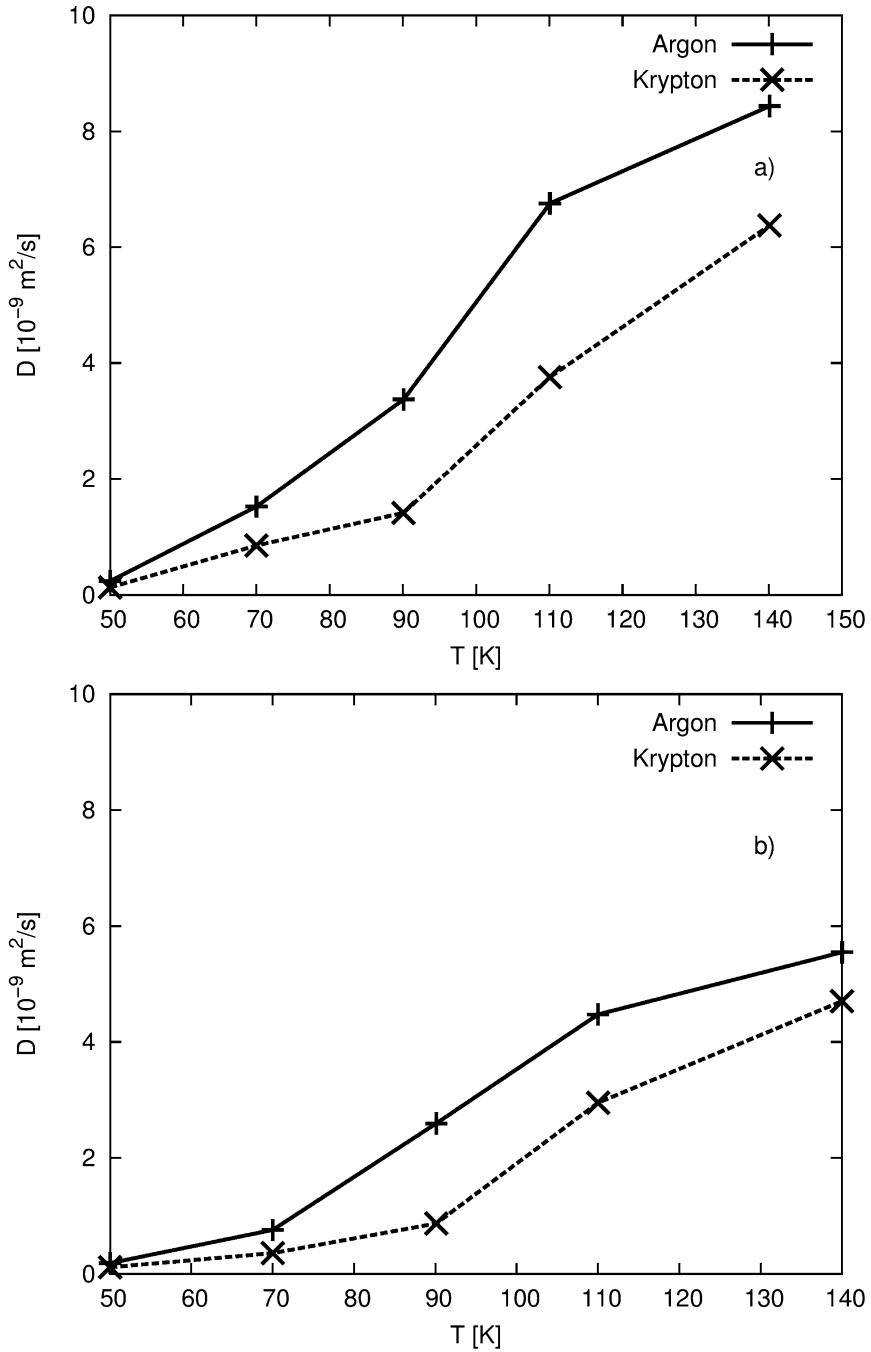
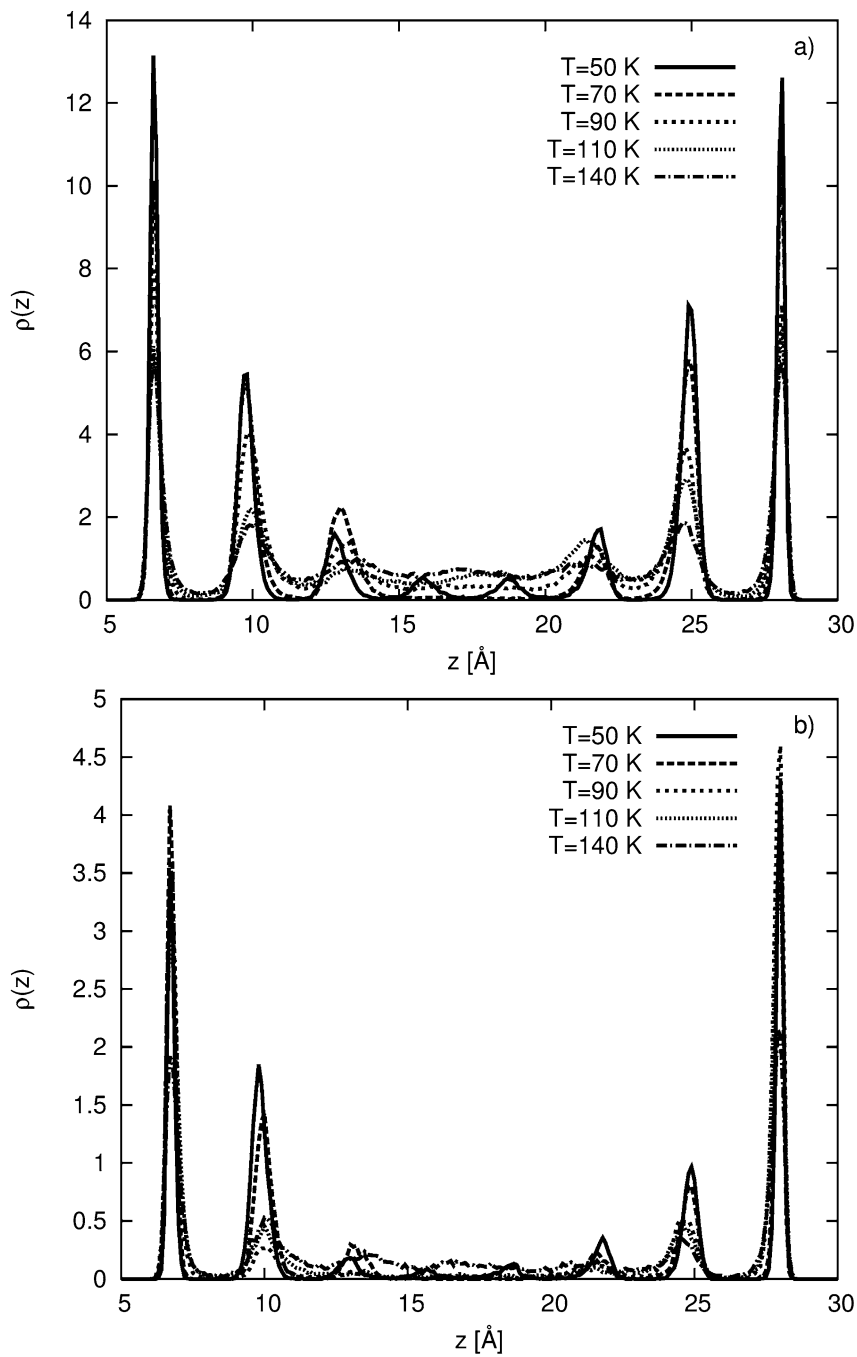
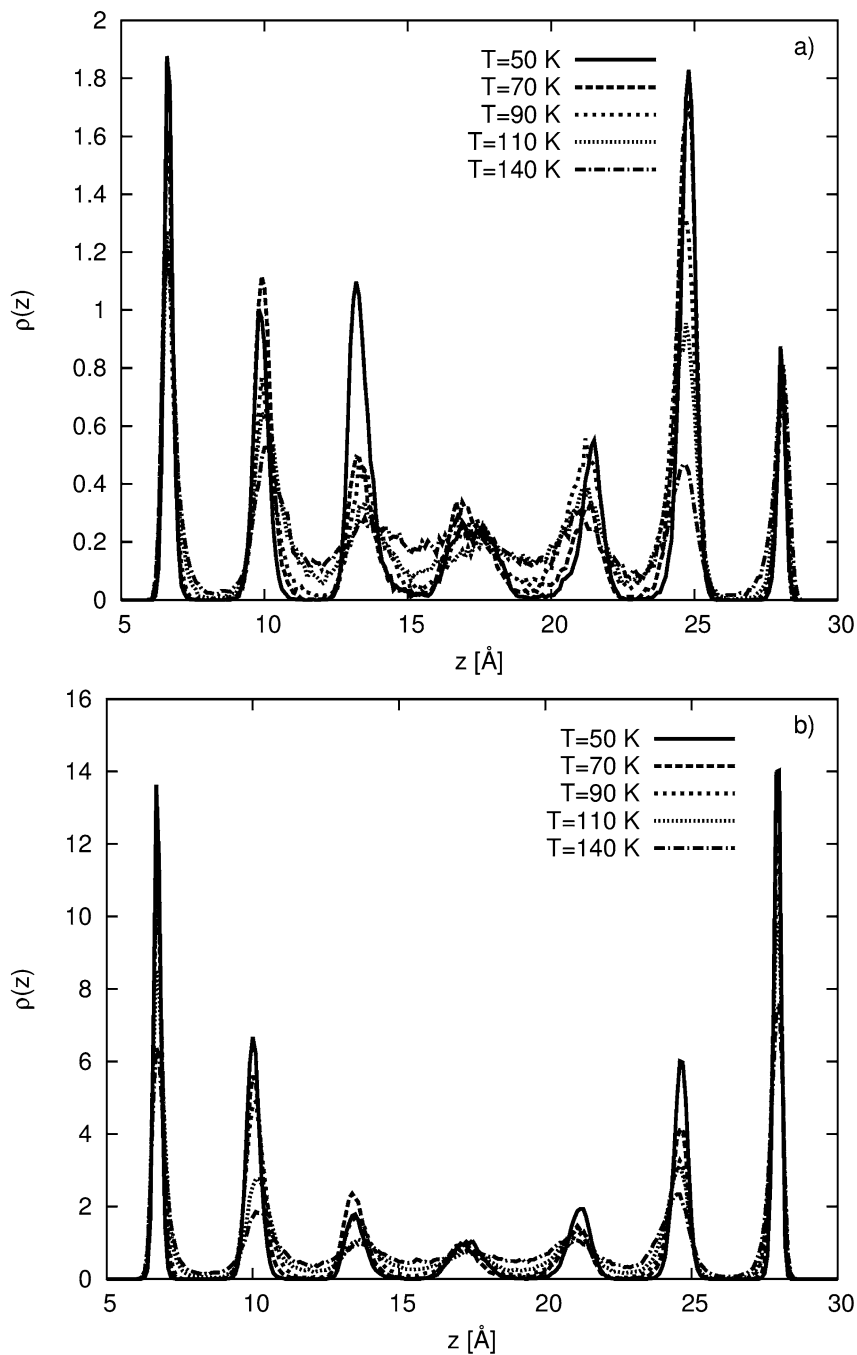


Fig. 3.6 The temperature dependence of diffusion coefficient (a) 19% Kr (b) 81% Kr





**Fig. 3.7** The  $z$ -profile distribution of (a) argon and (b) krypton with concentration of krypton equal to 19%



**Fig. 3.8** The  $z$ -profile distribution of (a) argon and (b) krypton with concentration of krypton equal to 81%

frequencies. It can be interpreted that in confined space, the collisions between atoms occur more often than in bulk system. The higher mobility of argon or krypton atoms in confined space is also visible in the mean square displacement function. We have also found that the shape of the spectra depends on many-body contributions to  $G(t)$  function. The structural study shows that in the slot between graphite slabs, Ar-Kr mixture forms layers parallel to the graphite surface. We have also observed that these layers are less visible in the inner most part of the slot. The simulations reported here might boost the future experimental research and theoretical modeling of the thin layer of noble gas binary mixture confined between graphite slabs.

**Acknowledgment** This research was supported in part by PL-Grid Infrastructure. Grant id molinter 2015 and fulinter 2016.

## References

1. Weir G, Muneer T (1998) Energy and environmental impact analysis of double-glazed windows. *Energy Convers Manag* 39:243–256. doi:[10.1016/S0196-8904\(96\)00191-4](https://doi.org/10.1016/S0196-8904(96)00191-4)
2. Clarke JA, Janak M, Ruyssevelt P (1998) Assessing the overall performance of advanced glazing systems. *Sol Energy* 63:231–241. doi:[10.1016/S0038-092X\(98\)00034-6](https://doi.org/10.1016/S0038-092X(98)00034-6)
3. Huang B, Li Z, Liu Z et al (2008) Adsorption of gas molecules on graphene nanoribbons and its implication for nanoscale molecule sensor. *J Phys Chem C* 112:13442–13446. doi:[10.1021/jp8021024](https://doi.org/10.1021/jp8021024)
4. Arash B, Wang Q, Duan WH (2011) Detection of gas atoms via vibration of graphenes. *Phys Lett A* 375:2411–2415. doi:[10.1016/j.physleta.2011.05.009](https://doi.org/10.1016/j.physleta.2011.05.009)
5. Guillot B (1989) Triplet dipoles in the absorption spectra of dense rare gas fluids. II. Long range interactions. *J Chem Phys* 91:3456–3462. doi:[10.1063/1.456874](https://doi.org/10.1063/1.456874)
6. Krauss M, Regan RM, Konowalow DD (1988) Rare-gas interaction energy curves. *J Phys Chem* 92:4329–4333. doi:[10.1021/j100326a018](https://doi.org/10.1021/j100326a018)
7. Guillot B (1987) Theoretical investigation of the dip in the far infrared absorption spectrum of dense rare gas mixtures. *J Chem Phys* 87:1952–1961. doi:[10.1063/1.453167](https://doi.org/10.1063/1.453167)
8. Dawid A, Gburski Z (1997) Interaction-induced light scattering in Lennard-Jones argon clusters: computer simulations. *Phys Rev A* 56:3294–3296. doi:[10.1103/PhysRevA.56.3294](https://doi.org/10.1103/PhysRevA.56.3294)
9. Bhattacharya A, Chen B, Mahanti SD (1996) Structural dynamics of clusters near melting. *Phys Rev E* 53:R33–R36. doi:[10.1103/PhysRevE.53.R33](https://doi.org/10.1103/PhysRevE.53.R33)
10. Dawid A, Gburski Z (1998) Interaction-induced absorption in argon-krypton mixture clusters: molecular-dynamics study. *Phys Rev A* 58:740–743. doi:[10.1103/PhysRevA.58.740](https://doi.org/10.1103/PhysRevA.58.740)
11. Dawid A, Gburski Z (1999) Interaction-induced light scattering in xenon clusters: molecular dynamics study. *J Mol Struct* 482–483:271–276. doi:[10.1016/S0022-2860\(98\)00668-1](https://doi.org/10.1016/S0022-2860(98)00668-1)
12. Dawid A, Gburski Z (2002) Interaction-induced absorption in liquid argon–xenon mixture cluster: MD simulation. *J Mol Struct* 614:177–182. doi:[10.1016/S0022-2860\(02\)00243-0](https://doi.org/10.1016/S0022-2860(02)00243-0)
13. Piatek A, Dawid A, Gburski Z (2006) The existence of a plastic phase and a solid–liquid dynamical bistability region in small fullerene cluster (C60)7: molecular dynamics simulation. *J Phys Condens Matter* 18:8471. doi:[10.1088/0953-8984/18/37/006](https://doi.org/10.1088/0953-8984/18/37/006)
14. Dawid A, Gburski Z (1997) Dynamical properties of the argon-krypton clusters: molecular dynamics calculations. *J Mol Struct* 410–411:507–511. doi:[10.1016/S0022-2860\(96\)09512-9](https://doi.org/10.1016/S0022-2860(96)09512-9)
15. Piatek A, Dawid A, Gburski Z (2011) The properties of small fullereneol cluster (C-60(OH)(24))(7): computer simulation. *Spectrochim Acta A Mol Biomol Spectrosc* 79:819–823. doi:[10.1016/j.saa.2010.08.059](https://doi.org/10.1016/j.saa.2010.08.059)

16. Raczyński P, Dawid A, Gburski Z (2005) Depolarized light scattering in small fullerene clusters—computer simulation. *J Mol Struct* 744–747:525–528. doi:[10.1016/j.molstruc.2004.12.064](https://doi.org/10.1016/j.molstruc.2004.12.064)
17. Bucaro JA, Litovitz TA (1971) Rayleigh scattering: collisional motions in liquids. *J Chem Phys* 54:3846–3853. doi:[10.1063/1.1675436](https://doi.org/10.1063/1.1675436)
18. Dawid A, Raczynski P, Gburski Z (2014) Depolarised Rayleigh light scattering in argon layer confined between graphite plains: MD simulation. *Mol Phys* 112:1645–1650. doi:[10.1080/00268976.2013.853111](https://doi.org/10.1080/00268976.2013.853111)
19. Bancewicz T, Glaz W, Godet J-L, Maroulis G (2008) Collision-induced hyper-Rayleigh spectrum of H(2)-Ar gas mixture. *J Chem Phys*. doi:[10.1063/1.2981042](https://doi.org/10.1063/1.2981042)
20. Dawid A, Gorny K, Wojcieszuk D et al (2014) Collision-induced light scattering in a thin xenon layer between graphite slabs – MD study. *Spectrochim Acta A Mol Biomol Spectrosc* 129:594–600. doi:[10.1016/j.saa.2014.03.101](https://doi.org/10.1016/j.saa.2014.03.101)
21. Gburski Z (1985) Convergence of memory functions for the vibrational dephasing process in liquids. *Chem Phys Lett* 115:236–240. doi:[10.1016/0009-2614\(85\)80687-4](https://doi.org/10.1016/0009-2614(85)80687-4)
22. Dawid A, Wojcieszuk D, Gburski Z (2016) Collision-induced light scattering spectra of krypton layer confined between graphite slabs – MD simulation. *J Mol Struct* 1126:103–109. doi:[10.1016/j.molstruc.2016.01.063](https://doi.org/10.1016/j.molstruc.2016.01.063)
23. Gburski Z, Gray CG, Sullivan DE (1984) Lineshape in collision-induced absorption. *Mori Theory Chem Phys Lett* 106:55–59. doi:[10.1016/0009-2614\(84\)87010-4](https://doi.org/10.1016/0009-2614(84)87010-4)
24. Stassen H, Gburski Z (1994) Instantaneous normal-mode analysis of binary-liquid Ar-Kr mixtures. *Chem Phys Lett* 217:325–332. doi:[10.1016/0009-2614\(93\)E1390-3](https://doi.org/10.1016/0009-2614(93)E1390-3)
25. Gburski Z, Zerda T (1980) Vibrational dephasing and intermolecular interactions in liquids. *Acta Phys Pol A* 57:447–454
26. Dawid A, Dendzik Z, Gburski Z (2004) Molecular dynamics study of ultrathin argon layer covering fullerene molecule. *J Mol Struct* 704:173–176. doi:[10.1016/j.molstruc.2004.01.065](https://doi.org/10.1016/j.molstruc.2004.01.065)
27. Kachel A, Gburski Z (1997) Chain formation in a model dipolar liquid: computer simulation study. *J Phys Condens Matter* 9:10095–10100. doi:[10.1088/0953-8984/9/46/007](https://doi.org/10.1088/0953-8984/9/46/007)
28. Dawid A, Gburski Z (2003) Rayleigh light scattering in fullerene covered by a spherical argon film – a molecular dynamics study. *J Phys Condens Matter* 15:2399–2405. doi:[10.1088/0953-8984/15/14/315](https://doi.org/10.1088/0953-8984/15/14/315)
29. Gruszka M, Gburski Z (1992) Interaction-induced light scattering in atomic fluids — a two-body contribution studied by MD simulations. *J Mol Struct* 275:129–133. doi:[10.1016/0022-2860\(92\)80188-N](https://doi.org/10.1016/0022-2860(92)80188-N)
30. Dawid A, Gburski Z (2003) Interaction-induced light scattering in a fullerene surrounded by an ultrathin argon “atmosphere”: molecular dynamics simulation. *Phys Rev A* 68:065202. doi:[10.1103/PhysRevA.68.065202](https://doi.org/10.1103/PhysRevA.68.065202)
31. Skrzypek M, Gburski Z (2002) Fullerene cluster between graphite walls – computer simulation. *Europhys Lett* 59:305–310. doi:[10.1209/epl/i2002-00242-8](https://doi.org/10.1209/epl/i2002-00242-8)
32. Dawid A, Gburski Z (2007) Dielectric relaxation of 4-cyano-4-n-pentylbiphenyl (5CB) thin layer adsorbed on carbon nanotube – MD simulation. *J Non-Cryst Solids* 353:4339–4343. doi:[10.1016/j.jnoncrsol.2007.02.072](https://doi.org/10.1016/j.jnoncrsol.2007.02.072)
33. Dendzik Z, Kosmider M, Dawid A, Gburski Z (2005) Interaction induced depolarized light scattering from ultrathin Ne film covering single-walled carbon nanotubes of different chiralities. *J Mol Struct* 744:577–580. doi:[10.1016/j.molstruc.2004.12.049](https://doi.org/10.1016/j.molstruc.2004.12.049)
34. Kośmider M, Dendzik Z, Pałucha S, Gburski Z (2004) Computer simulation of argon cluster inside a single-walled carbon nanotube. *J Mol Struct* 704:197–201. doi:[10.1016/j.molstruc.2004.02.050](https://doi.org/10.1016/j.molstruc.2004.02.050)
35. Dendzik Z, Kośmider M, Dawid A et al (2005) Interaction-induced depolarized light scattering spectra of exohedral complexes of Ne and Ar with fullerenes and nanotubes. *Mater Sci Pol* 23(2):s.475–s.481
36. Allen MP, Tildesley DJ (1989) *Computer simulation of liquids*. Oxford University Press, New York

37. Rapaport DC (2004) *The art of molecular dynamics simulation*. Cambridge University Press, Cambridge
38. Dawid A (2012) RIGid molecular dynamics (RIGMD) – simulation software. In: <http://prac.us.edu.pl/~dawid/RIGMD/rigmdUS.php>
39. Mountain RD, Birnbaum G (1987) Molecular dynamics study of intercollisional interference in collision-induced absorption in compressed fluids. *J Chem Soc Faraday Trans 2* 83:1791. doi:[10.1039/f29878301791](https://doi.org/10.1039/f29878301791)
40. Birnbaum G, Krauss M, Frommhold L (1984) Collision-induced dipoles of rare gas mixtures. *J Chem Phys* 80:2669–2674. doi:[10.1063/1.447062](https://doi.org/10.1063/1.447062)

# Chapter 4

## Properties of Cholesterol-Fullerene Binary Cluster: MD Simulations

Z. Gburski, Violetta Raczyńska, and Przemysław Raczyński

### 4.1 Introduction

Cholesterol is perceived as a source of cardiovascular diseases which are the main cause of death and morbidity throughout the world, representing 40% of the mortality rate in western societies [1]. In 2015, approximately 30% of the world mortality was attributed to cardiovascular diseases, with atherosclerosis being the main pathological cause. One of the main risks factors associated with atherosclerosis is the accumulation of the low-density lipoprotein (LDL) cholesterol in the intima-media layer of the artery. The endothelial dysfunction causes structural changes that allow the accumulation and retention of LDL in the arterial intima, thereby leading to the development of atheromatous plaques.

On the other hand, cholesterol is essential in human organism due to its function in regulation of the fluidity of the phospholipid bilayer – natural barrier created in the evolution process to protect the interior of the eukaryotic cell from the outside environment [2–6].

Nowadays, determination of cholesterol level in human blood is of great significance in clinical diagnostics [7]. Regular monitoring of the cholesterol level in human serum demands very fast, economic, and highly selective cholesterol biosensing for managing the various cardiovascular diseases [8]. Cholesterol may exhibit interesting properties in other applications. Here we study cholesterol mixed with one of the carbon nanostructures –  $C_{60}$  fullerene. We placed three, five, and seven fullerenes between 70 cholesterol molecules to assess the impact of fullerene on the behavior of cholesterol.

---

Z. Gburski (✉) • V. Raczyńska • P. Raczyński  
Institute of Physics, University of Silesia, Uniwersytecka 4, 40-007, Katowice, Poland  
e-mail: [zygmunt.gburski@us.edu.pl](mailto:zygmunt.gburski@us.edu.pl)

Unique photophysical and electrochemical properties of  $C_{60}$  fullerene lead to promising applications in many materials and even in biological sciences [6]. In nanotechnology and molecular electronics, fullerene derivatives mixed with different molecules are being examined for their thermal and electrical conductivities. Since the fullerene molecules and their derivatives have interesting properties with potential applications in wide range of areas, there is a general interest in the study of the interaction of fullerenes and its derivatives with other molecules [7–13].

## 4.2 Simulation Details

All full-atomistic molecular dynamics simulations [9, 14–17] were performed with NAMD 2.9.2 simulations code [18, 19], with the all-atom CHARMM force field. Simulated clusters were visualized in VMD 1.9.2 [20].

The studied systems consisted of 70 cholesterol molecules. Among them three, five, or seven  $C_{60}$  molecules were placed. Fullerenes were not located in one region of cluster but were dispersed. To better assess the impact of fullerenes on the cluster obtained, results were compared with the results acquired for pure cholesterol cluster.

All simulations were performed in NVT ensemble (constant volume and temperature). First, the systems were equilibrated for 2 ns, and after this initial simulation for the next 5 ns, the data was collected.

The binary clusters varying in number of fullerenes were studied, each at four temperatures ( $T = 290, 300, 310, \text{ and } 320 \text{ K}$ ). Between neighboring temperatures the system was slowly heated and again equilibrated. To ensure sufficient energy conservation, the integration time step was set to  $\Delta t = 0.5 \text{ fs}$  for all simulation runs. The standard NAMD integrator (Brünger–Brooks–Karplus algorithm) was used [21].

All interactions in the simulated systems were described with an adapted form of CHARMM potential. Atomic charges on cholesterol molecule were taken from [22].

## 4.3 Results

Firstly we would like to present snapshots of initial and final configuration of the cluster with seven fullerenes.

Figure 4.1a shows system before equilibration. It can be seen that fullerenes are distributed in this way and that they are not near neighbors to the other fullerene molecules. Figure 4.1b shows that during simulations some of  $C_{60}$  molecules can get together, being close to the other fullerenes. In the figure a group of five fullerenes is observed. The interactions between fullerenes are much stronger than fullerene – cholesterol, it is the reason for clusterization of  $C_{60}$  molecules.

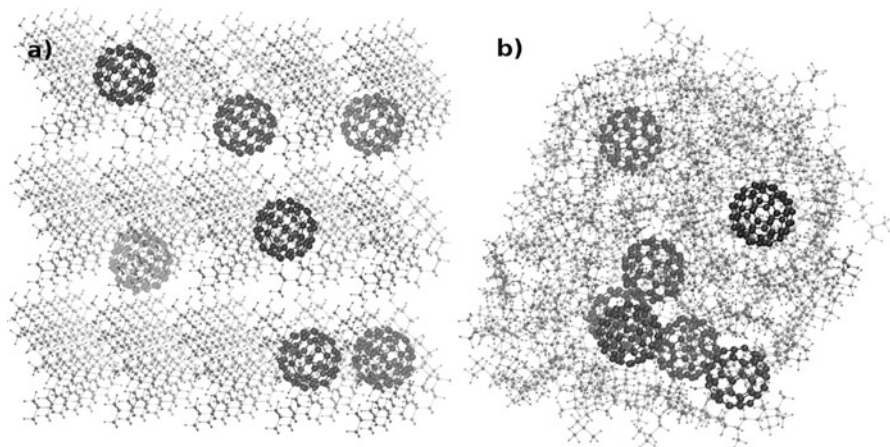


**Fig. 4.1** The configurations of the system with seven cholesterol before equilibration stage (a) and final, after all simulations (b)

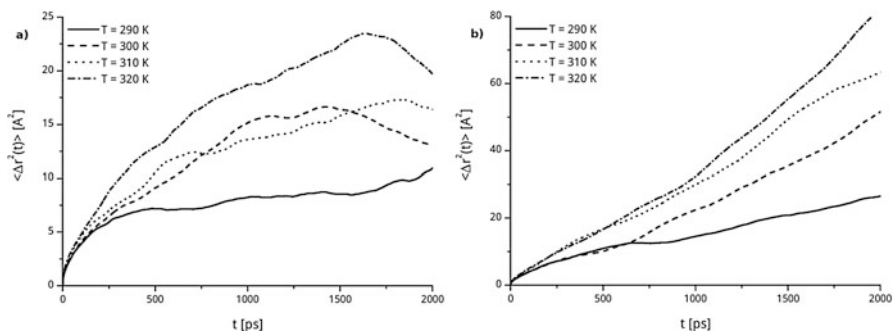


**Fig. 4.2** The comparison of the mean square displacement of the center of mass of cholesterol for the pure (no fullerenes) system (a) and for the system with  $n = 5$  fullerenes (b)

Figure 4.2 shows the comparison of the mean square displacement  $\langle |\Delta \vec{r}(t)|^2 \rangle$  of the center of mass of cholesterol between the pure cluster (Fig. 4.2a) and cluster with  $n = 5$  fullerenes (Fig. 4.2b).

First conclusion is that in both systems, the mobility of cholesterol grows with the heating of the systems. Furthermore, the values of  $\langle |\Delta \vec{r}(t)|^2 \rangle$  for both clusters show that in systems with fullerenes the mobility of cholesterol is higher.

The obtained values of translational diffusion coefficient  $D$ , defined via Einstein [14] relation as  $\langle |\Delta \vec{r}(t)|^2 \rangle \approx 6Dt$ , confirm previous observation.

The values of  $D$  for all systems and for all temperatures are shown in Fig. 4.3. It is clearly observed that in pure cholesterol cluster, the mobility of cholesterol is the lowest. In case of systems with fullerenes, the general tendency is that more fullerenes means higher mobility of cholesterol. The presence of  $C_{60}$  molecules



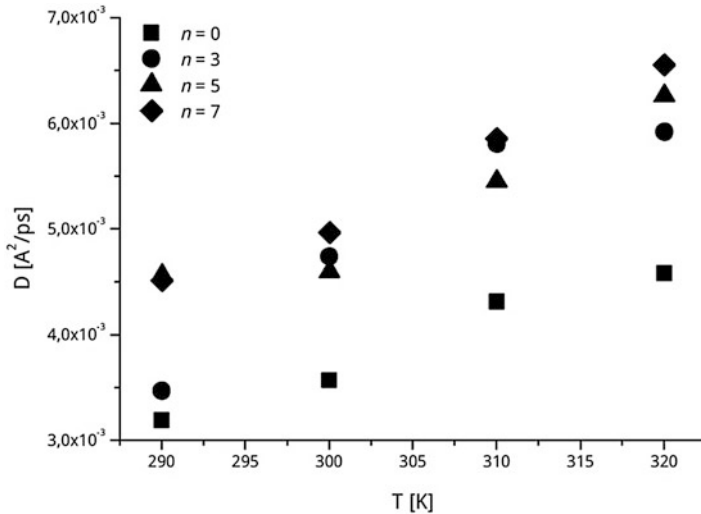


**Fig. 4.3** The temperature dependence of diffusion coefficient for all systems studied

causes the cholesterol molecules to surround them and they do not mesh with other cholesterols in the same way as in the pure system. In this system cholesterols overlap with others with hydrocarbon tails but the fullerene with its spherical shape diminishes this process. In consequence the mobility of cholesterols grows. The described process is magnified when the fullerenes group together because in this case cholesterols surround a very small fullerene cluster placed between them.

Presence of fullerene molecules has an impact not only on the dynamic of the cholesterols but also on the second rank order parameter  $S_2$  defined as the highest eigenvalue of order tensor [23]:

$$Q_{\alpha\beta} = \frac{1}{N} \sum_{j=1}^N \left( \frac{3}{2} \hat{e}_{j\alpha} \hat{e}_{j\beta} - \frac{1}{2} \delta_{\alpha\beta} \right), \alpha, \beta = x, y, z,$$

where  $Q$  is a second rank tensor,  $\hat{e}_j$  is a unit vector along the molecular long axis, and  $\delta_{\alpha\beta}$  is the Kronecker delta. Diagonalization of this tensor gives three eigenvalues and  $\hat{n}$  is the eigenvector associated with the largest eigenvalue. The  $\hat{n}$  vector is usually called the director of the sample. Value of  $S_2$  is usually calculated as:

$$S_2 = \langle P_2(n \cdot e) \rangle = \langle P_2(\cos \theta) \rangle = \left\langle \frac{3}{2} \cos^2 \theta - \frac{1}{2} \right\rangle,$$

where  $P_2$  is the second order Legendre polynomial,  $\theta$  is the angle between a molecular axes and the director  $n$ , and  $\langle \rangle$  denotes average over ensemble and time.

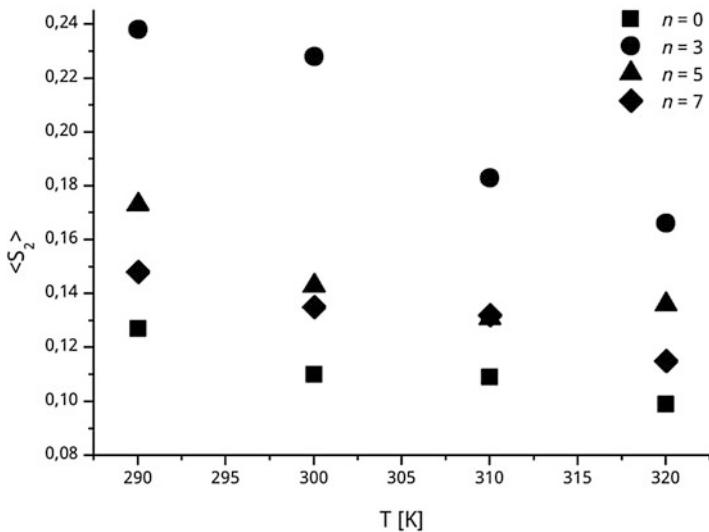


**Fig. 4.4** The temperature dependence of the second rank order parameter of the system

The obtained values of the second rank order parameter (averaged over time) are shown in Fig. 4.4. The impact of fullerenes on the values of  $S_2$  can be clearly observed. More  $C_{60}$  molecules in cluster means less order. Fullerenes impact on the arrangement of cholesterol in the same way as in the case of mobility. Cholesterols surround particular individual  $C_{60}$  molecules or the groups of these molecules, and this process diminishes order in the clusters with larger number of fullerenes.

We have also calculated the values of the Lindemann index to find whether the phase transition occurs at the studied temperature range.

Lindemann index  $\delta_L$  is defined as [24–28]:

$$\delta_L = \frac{2}{N(N-1)} \sum_{i < j}^N \frac{\left( \langle r_{ij}^2 \rangle - \langle r_{ij} \rangle^2 \right)^{\frac{1}{2}}}{\langle r_{ij} \rangle},$$

where  $r_{ij}$  is the distance between the center of mass of  $i$ th and  $j$ th molecules.

The obtained values of the  $\delta_L$  are shown in Fig. 4.5. The values of  $\delta_L$  grow with the heating of the clusters, but there is no any significant discontinuity, which could be an indicator of the phase transition. The conclusion is that no phase transition occurs in examined binary clusters at the studied temperature range.

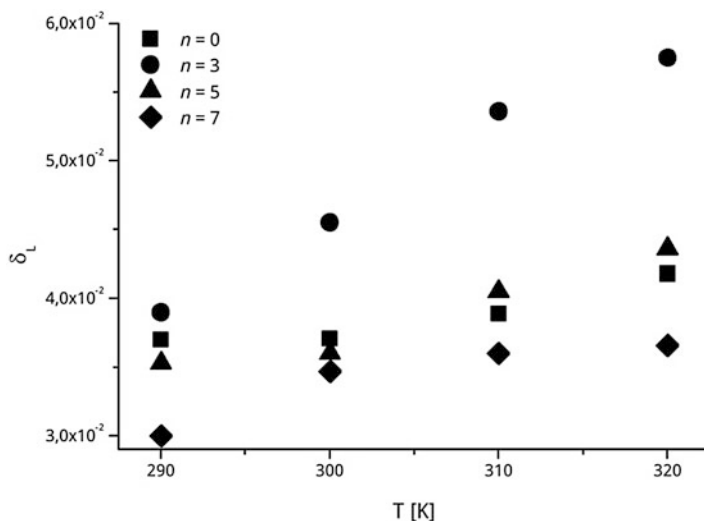


Fig. 4.5 The temperature dependence of Lindemann index for all systems studied

## 4.4 Conclusions

The properties of binary fullerene–cholesterol cluster have been studied using molecular dynamic technique. Fullerene molecules are able to get together with other fullerenes even if they were separated at the initial configuration. After that fullerenes keep together and cholesterol molecules are not able to separate them. Cholesterol molecules surround particular fullerenes or groups of fullerenes, and this behavior has strong impact on their dynamics and other parameters presented in this work, for example, the values of the second rank order parameter.

## References

1. Klafke JZ, Pereira RLD, Hirsch GE, Parisi MM, Porto FG, de Almeida AS, Rubin FH, Schmidt A, Beutler H, Nascimento S, Trevisan G, Brusco I, de Oliveira SM, Duarte MMMF, Duarte T, Viecili PRN (2016) Study of oxidative and inflammatory parameters in LDLR-KO mice treated with a hypercholesterolemic diet: comparison between the use of Campomanesia xanthocarpa and acetylsalicylic acid. *Phytomedicine* 23:1227–1234. doi:[10.1016/j.phymed.2015.11.010](https://doi.org/10.1016/j.phymed.2015.11.010)
2. Alberts B (2008) *Molecular biology of the cell*. Garland Science, New York [etc.]
3. Lusis AJ (2000) Atherosclerosis. *Nature* 407:233–241. doi:[10.1038/35025203](https://doi.org/10.1038/35025203)
4. Kachel A, Gburski Z (1997) Chain formation in a model dipolar liquid: computer simulation study. *J Phys Condens Matter* 9:10095–10100. doi:[10.1088/0953-8984/9/46/007](https://doi.org/10.1088/0953-8984/9/46/007)
5. Gburski Z (1985) Convergence of memory functions for the vibrational dephasing process in liquids. *Chem Phys Lett* 115:236–240. doi:[10.1016/0009-2614\(85\)80687-4](https://doi.org/10.1016/0009-2614(85)80687-4)
6. Stassen H, Gburski Z (1994) Instantaneous normal-mode analysis of binary-liquid Ar-Kr mixtures. *Chem Phys Lett* 217:325–332. doi:[10.1016/0009-2614\(93\)E1390-3](https://doi.org/10.1016/0009-2614(93)E1390-3)

7. Komathi S, Muthuchamy N, Lee K-P, Gopalan A-I (2016) Fabrication of a novel dual mode cholesterol biosensor using titanium dioxide nanowire bridged 3D graphene nanostacks. *Biosens Bioelectron* 84:64–71. doi:[10.1016/j.bios.2015.11.042](https://doi.org/10.1016/j.bios.2015.11.042)
8. Umar A, Ahmad R, Kumar R, Ibrahim AA, Baskoutas S (2016) Bi<sub>2</sub>O<sub>2</sub>CO<sub>3</sub> nanoplates: fabrication and characterization of highly sensitive and selective cholesterol biosensor. *J Alloys Compd* 683:433–438. doi:[10.1016/j.jallcom.2016.05.063](https://doi.org/10.1016/j.jallcom.2016.05.063)
9. Gburski Z, Gray CG, Sullivan DE (1984) Lineshape in collision-induced absorption. Mori theory. *Chem Phys Lett* 106:55–59. doi:[10.1016/0009-2614\(84\)87010-4](https://doi.org/10.1016/0009-2614(84)87010-4)
10. Gburski Z, Zerda T (1980) Vibrational dephasing and intermolecular interactions in liquids. *Acta Phys Pol A* 57:447–454
11. Ghanbari B, Gholamnezhad P (2016) Spectroscopic evidence on improvement in complex formation of O<sub>2</sub>N<sub>2</sub> aza-crown macrocyclic ligands with Cu(II) acetate upon incorporation with [60]Fullerene. *Spectrochim Acta A Mol Biomol Spectrosc* 169:202–207. doi:[10.1016/j.saa.2016.06.047](https://doi.org/10.1016/j.saa.2016.06.047)
12. Lundgren MP, Khan S, Baytak AK, Khan A (2016) Fullerene-Benzene purple and yellow clusters: theoretical and experimental studies. *J Mol Struct* 1123:75–79. doi:[10.1016/j.molstruc.2016.06.007](https://doi.org/10.1016/j.molstruc.2016.06.007)
13. Raczynski P, Dawid A, Gburski Z (2005) Depolarized light scattering in small fullerene clusters – computer simulation. *J Mol Struct* 744:525–528. doi:[10.1016/j.molstruc.2004.12.064](https://doi.org/10.1016/j.molstruc.2004.12.064)
14. Allen MP, Tildesley DJ (1989) *Computer simulation of liquids*. Clarendon Press/Oxford University Press, Oxford/New York
15. Frenkel D, Smit B (2001) *Understanding molecular simulation, second edition: from algorithms to applications*, 2nd edn. Academic Press, San Francisco
16. Rapaport DC (2004) *The art of molecular dynamics simulation*. Cambridge University Press, New York
17. Dawid A, Gburski Z (2003) Interaction-induced light scattering in a fullerene surrounded by an ultrathin argon “atmosphere”: molecular dynamics simulation. *Phys Rev A* 68:065202. doi:[10.1103/PhysRevA.68.065202](https://doi.org/10.1103/PhysRevA.68.065202)
18. Kale L, Skeel R, Bhandarkar M, Brunner R, Gursoy A, Krawetz N, Phillips J, Shinozaki A, Varadarajan K, Schulten K (1999) NAMD2: greater scalability for parallel molecular dynamics. *J Comput Phys* 151:283–312. doi:[10.1006/jcph.1999.6201](https://doi.org/10.1006/jcph.1999.6201)
19. Phillips JC, Braun R, Wang W, Gumbart J, Tajkhorshid E, Villa E, Chipot C, Skeel RD, Kalé L, Schulten K (2005) Scalable molecular dynamics with NAMD. *J Comput Chem* 26:1781–1802. doi:[10.1002/jcc.20289](https://doi.org/10.1002/jcc.20289)
20. Humphrey W, Dalke A, Schulten K (1996) VMD: visual molecular dynamics. *J Mol Graph Model* 14:33–38. doi:[10.1016/0263-7855\(96\)00018-5](https://doi.org/10.1016/0263-7855(96)00018-5)
21. Brunger A, Kuriyan J, Karplus M (1987) Crystallographic R-factor refinement by molecular-dynamics. *Science* 235:458–460. doi:[10.1126/science.235.4787.458](https://doi.org/10.1126/science.235.4787.458)
22. Henin J, Chipot C (2006) Hydrogen-bonding patterns of cholesterol in lipid membranes. *Chem Phys Lett* 425:329–335. doi:[10.1016/j.cplett.2006.04.115](https://doi.org/10.1016/j.cplett.2006.04.115)
23. Pasini P, Zannoni C (2013) *Advances in the computer simulations of liquid crystals*. Springer Science & Business Media
24. Jena P, Rao BK, Khanna SN (1987) *Physics and chemistry of small clusters*. Plenum Press, New York
25. Gburski Z, Górny K, Raczynski P (2010) The impact of a carbon nanotube on the cholesterol domain localized on a protein surface. *Solid State Commun* 150:415–418. doi:[10.1016/j.ssc.2009.12.005](https://doi.org/10.1016/j.ssc.2009.12.005)
26. Skrzypiek M, Gburski Z (2002) Fullerene cluster between graphite walls – computer simulation. *Europhys Lett* 59:305–310. doi:[10.1209/epl/i2002-00242-8](https://doi.org/10.1209/epl/i2002-00242-8)
27. Piątek A, Dawid A, Gburski Z (2006) The existence of a plastic phase and a solid-liquid dynamical bistability region in small fullerene cluster (C-60)(7): molecular dynamics simulation. *J Phys Cond Matter* 18:8471–8480. doi:[10.1088/0953-8984/18/37/006](https://doi.org/10.1088/0953-8984/18/37/006)
28. Dawid A, Gburski Z (1997) Dynamical properties of the argon-krypton clusters: molecular dynamics calculations. *J Molec Struct* 410:507–511. doi:[10.1016/S0022-2860\(96\)09512-9](https://doi.org/10.1016/S0022-2860(96)09512-9)

# Chapter 5

## Thermogravimetric Study of Nano-SnO<sub>2</sub> Precursors

Viktor S. Grinevych, Liudmila M. Filevska, Sergij M. Savin,  
Valentyn A. Smyntyna, and Bulent Ulug

### 5.1 Introduction

Adsorption-sensitive thin film elements on the basis of nanoscale oxide materials, especially nanoscale tin dioxide, are widely used in the modern gas analyzers. Well-known production methods of nanoscale metal oxide like tin dioxide are liquid phase chemical methods: sol-gel method, chemical solution deposition, chemical vapor deposition, etc. [1–3]. One of the main stages in such technologies is the decomposition of one, thermally unstable, compound to produce tin dioxide as the final product. The production of such compounds is limited enough. The limited and contradictory literature data on their physical and chemical properties determined the necessity to find a suitable precursor for nanosized tin dioxide production. Previously, authors [4] by means of the method of chemical precipitation from solution proposed the preparation technique for SnO<sub>2</sub> film production with polyvinyl acetate (PVA) as a structuring additive. The complex bis(acetylacetonato)dichlorotin (BADCT) was used as a precursor of tin dioxide. In [5], it was firstly mentioned the fact of obtaining of BADCT (Sn(C<sub>5</sub>H<sub>7</sub>O<sub>2</sub>)<sub>2</sub>Cl<sub>2</sub>) in 1903. Earlier in the literature [5–8], it was reported the BADCT production using chloroform [5] or dry toluene [8] as solvents. A special feature of our method is using of water as a solvent.

In [9], it was reported the thin films' ZrO<sub>2</sub> preparation with similar compounds, namely, zirconium acetylacetonate. Using of BADCT-based complex, prepared by

---

V.S. Grinevych (✉) • L.M. Filevska • S.M. Savin • V.A. Smyntyna  
Odessa I.I. Mechnikov National University, Odessa, Ukraine  
e-mail: [grinevich@onu.edu.ua](mailto:grinevich@onu.edu.ua)

B. Ulug  
Department of Physics, Faculty of Science, Akdeniz University, Antalya, Turkey  
e-mail: [bulug@akdeniz.edu.tr](mailto:bulug@akdeniz.edu.tr)

the authors by the different from the prior method, makes it possible to obtain transparent thin film of tin dioxide with nanoscale grains [4].

The precursor complexes for comparative studies were prepared by two methods differing only in the last stage: the drying process. In the Odessa I. I. Mechnikov National University (ONU), Odessa, Ukraine, the drying was performed in an air and, in Akdeniz University, Antalya, Turkey, in a vacuum. Presumably, the difference in the drying process is determined by the preservation of water molecules in the precursor complex, which, on our opinion, has an impact on the resulting film structure.

In the presented paper, the precursor complexes were investigated by thermographic methods (thermogravimetry, TG; derivatography, DTG; differential thermal analysis, DTA), allowing to investigate in a programmable heating the nature and thermal parameters of physical and chemical processes in the material. The relevance of these studies is determined by the specifics of the processes at the precursor decomposition. This contributes to the creation of a reproducible technology for nanoscale films of it. The aim of the work was a comparative thermographic study of complexes, obtained by the two abovementioned methods thus establishing which one provides a tin dioxide layer of a nanoscale structure.

## 5.2 Precursor Preparation and Research Methods

Preparation of precursor complexes was carried out in several stages. The first stage is production of the working solution N 1: 50 ml (0.5 mol) of acetylacetone was mixed with 250 ml of distilled water and left for 24 h until complete dissolution. Then N 2 working solution was prepared: 14 ml (0.12 mol) of tin tetrachloride was added to 100-ml-volume conical flask with the subsequent addition of 50-ml-cooled (2–5 °C) distilled water. The heating of the resulting mixture is observed. In the second stage, the working solutions N 1 and N 2 were mixed in 1.0 l flask with further addition of 5 ml of 20% aqueous  $\text{NH}_3$  solution. The resulting mixture was stirred for 2 h at 40 °C using a magnetic stirrer. As a result, a dense white precipitate fell out. Then 600 ml of distilled water was added to this same flask. After standing for 10–15 min, the supernatant was decanted. The precipitate was separated by vacuum filtration on a sinter (residual pressure of  $P = 500$  mm Hg), washed with 100 ml of distilled water, and dried at 20–25 °C for 3 days. Then it was washed with benzene and dried for 5–6 h at 60 °C complex N 1, in air, and complex N 2, in vacuum.

The resulting product is a fluffy white powder which melts at 200–220 °C and ignites spontaneously in air at a temperature 250–270 °C. Preliminary chemical analysis (for chlorine and tin) revealed that the resulting compound contains 1.9 of chlorine atoms and 2.2 water molecules for one tin atom.

Simultaneous thermogravimetric and differential thermal analysis was performed for the precursor complexes by means of derivatographs (Q-1500 Hungary D production) for complex N 1 and (Perkin-Elmer 6000) for complex N 2 in air

and nitrogen at a heating rate of 10 °C/min. The powder mass loss resulted during thermogravimetric studies is shown below.

### 5.3 Experimental Results and Discussion

As soon as tin tetrachloride (SnCl<sub>4</sub>) and acetylacetonate (C<sub>5</sub>H<sub>8</sub>O<sub>2</sub>) were used for obtaining precursor, this gives the possibility to suppose the presence of bis(acetylacetonato)dichlorotin and tin tetra acetylacetonate in the precursor. The presence of chlorine in complex N 1 was determined analytically and was 17.5%. In [10], it was also confirmed the presence of chlorine in complex number 2 in the amount of  $16.50 \pm 0.60\%$ . Such an amount of chlorine in both complexes indicates a predominant content of BADCT in both of them. The thermal decomposition of the precursor complex has to include the stages of decomposition specific for its components.

Figures 5.1 and 5.2 show the results of TG, DTG, and DTA studies of complexes number 1 and number 2, respectively.

The DTG curve for complex number 1 (Fig. 5.1) clearly shows a peak at 100 °C, and the loss of mass on TG curve was 8%. If it is considered that the basic substance is a precursor complex crystalline BADCT (Sn(C<sub>5</sub>H<sub>7</sub>O<sub>2</sub>)<sub>2</sub>Cl<sub>2</sub>•2H<sub>2</sub>O), then the calculated percentage of the coordinated water in its structure is of 8.5% order. As it is shown, the resulting TG value is close to the mass loss calculated for the coordinated water content, thus indicating the presence of water in complex N 1. In addition to the evaporation of coordinated water, the evaporation of adsorbed water may also occur, amount of which is smaller compared with the coordinated one.

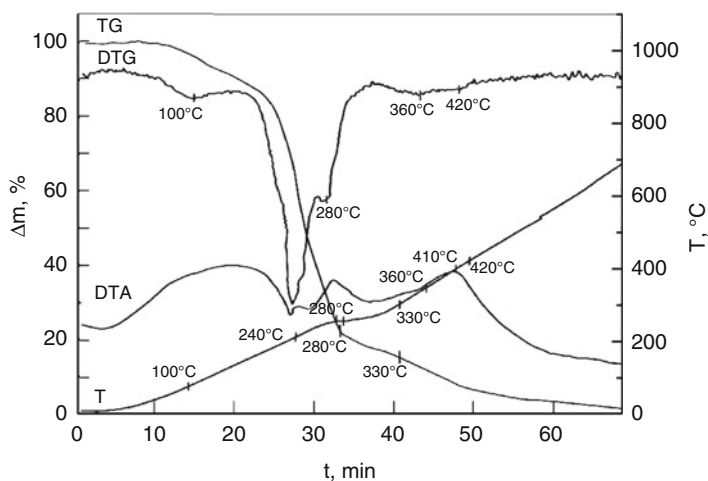
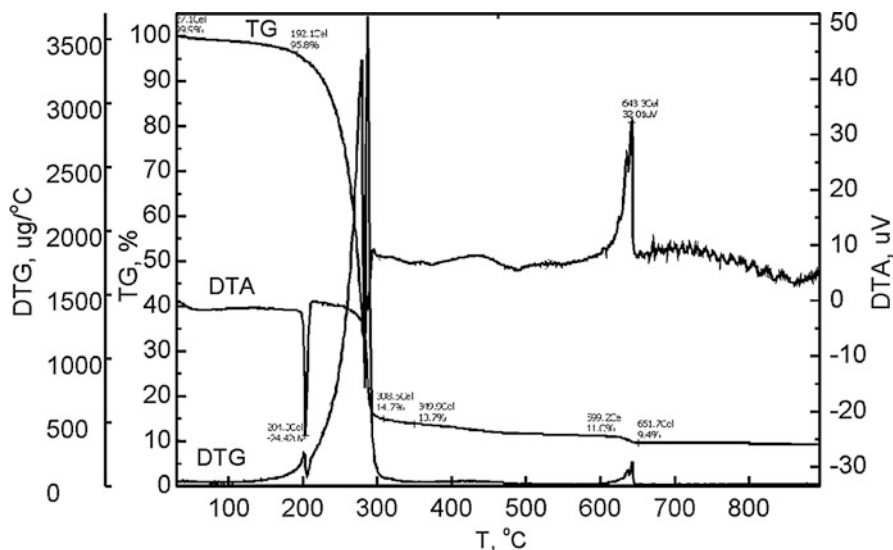


Fig. 5.1 TG, DTG, and DTA results of complex N 1



**Fig. 5.2** TG, DTG, and DTA results of complex N 2

At heating up to 190 °C on the DTG curve of complex N 2, the change in mass is less than 4%, thus indicating the much less water molecule presence in complex N 2. In [10], the quantitative content of hydrogen (3.41%) in complex number 2 corresponds to the anhydrous BADCT. According to other authors [11], water after 200 °C is almost not detectable in tin compounds, i.e., except for dehydration, other changes in the phase composition of the material at a temperature below 190 °C are unlikely. Consequently, the mass change in complex N 2 up to this temperature is supposed to be connected with evaporation of adsorbed water.

The DTA curve for complex N 1 (Fig. 5.1) contains the endothermic process peak at about 240 °C. According to TG and DTG curves, the process beginning corresponds to 200 °C. The absorption but not the release of energy is attributed to the substance phase transformation (i.e., melting or evaporation of the material). In the processes of thermal decomposition of the complexes, the flammable release of energy, not absorption, is observed. The coincidence of DTA and DTG that peaks at 240 °C shows that there has been not only the melting but the intensive evaporation of the complex. This assumption is confirmed by the loss of mass, visible on the TG curve for complex number 1 in the range of 200–240 °C. For complex N 2 (Fig. 5.2), the DTA peak at 200–210 °C is of endothermic type, but significant mass loss is not observed in this case, i.e., in the specified temperature range, this complex just melted. The gradual evaporation of complex number 2 occurs at higher temperatures up to 280 °C, which is evident due to its mass loss on the TG and DTG curves and to energy absorption in the DTA curve.

For complex N 1 at 280 °C and for complex N 2 at a higher temperature (286 °C), the exothermal distinct peaks on the DTA curve are accompanied by the



intensive mass loss, thus indicating that the complexes burned away in the oxygen of air. Subsequently (280–310 °C), the DTA curve for complex N 1 exhibits an endothermic process with a mass loss, which is reflected in the TG and DTG curves and is associated with intense final reaction product evaporation at the complex decomposition.

The further study shows another strong exothermic effect: for complex N 1 at 410 °C and for complex N 2 at 640 °C. Obviously, the residue of SnO is oxidized up to SnO<sub>2</sub>. This is confirmed by the data of [12], where it was shown that the oxidation of the SnO up to SnO<sub>2</sub> takes place before 650 °C. For complex N 1, this process occurs at a temperature of 230 °C lower than for complex N 2. This difference is explained by the influence of the oxidized SnO particles' sizes. Complex N 1 is a hydrated BADCT. Upon separation of water, it is loosened, which promotes the formation of small mass particles. The further decomposition up to oxide occurs simultaneously with the evaporation of the gas phase (confirmed by corresponding changes in the above-described curves: TG, DTA, and DTG). Upon decomposition of anhydrous N 2, apparently, complex oxide is formed with larger particles' size and mass. Therefore, for complex N 1, no residue remains after thermogravimetry, and for complex N 2, about 10% of the material remains (by the experience of decomposition studies of acetylacetonates of other metals of group IV [13], the residue is a tin dioxide). As it can be seen from the TG, DTG, and DTA results of the study of complex N 1 (Fig. 5.1) at 700 °C, the weight loss was 100%, i.e., it is completely evaporated.

The thermogravimetric study results for both complexes are summarized in Tables 5.1 and 5.2.

Comparative thermogravimetric studies of complex N 2 in air and in nitrogen were also conducted in the Akdeniz University (Antalya, Turkey). Figure 5.3 shows the TG, DTG, and DTA results of the thermal decomposition of the product.

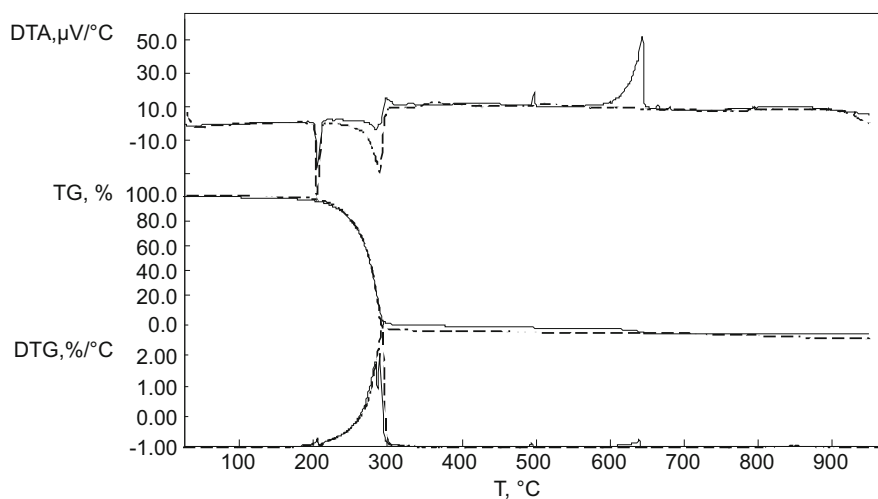
The mass loss observed between room temperature and 192 °C was about 4% and occurred, as mentioned above, due to the evaporation of adsorbed water. Well-seen endothermic peak at 204 °C is associated with the melting point. TG and DTA data (Fig. 5.3) show the complex structuring connected with oxygen in the temperature

**Table 5.1** The thermogravimetry results of complex 1

T, °C	TG	DTA	Possible process
100 °C	Mass loss 8%		Coordinated water evaporation
240	Mass loss	Endothermic peak	Melting and intensive evaporation of the complex fragments
280	Intensive mass loss	Exothermic peak	The complex fragments' reaction with oxygen
280–310	Mass loss	Endothermic process	Intensive evaporation of decomposition products of the complex fragments
410	Mass loss	Exothermic peak effect	Oxidation of the complex fragments (SnO oxidized to SnO <sub>2</sub> )

**Table 5.2** The thermogravimetry results of complex 2

T, °C	TG	DTA	Possible process
Under 192	Mass loss 4%		Adsorbed water evaporation
204		Endothermic peak	Melting of complex N 2
Over 210	Gradual mass loss	Endothermic peak	Fragment of the complex evaporation
277	Intensive mass loss	Endothermic peak	The complex intensive evaporation fragment
286	Mass loss	Exothermic peak	The complex reaction with oxygen fragments
500	Small mass loss (1.5–2%)	Exothermic peak	Fragments of the complex oxidation
620–650	Small mass loss (1.5–2%)	Exothermic peak	Fragments of the complex oxidation (SnO oxidized to SnO <sub>2</sub> )

**Fig. 5.3** The results of DTA (1), DTG (2), and DTG (3) studies of complex N 2. The solid and dotted curves represent data obtained in nitrogen and in air, respectively

range 192.0–308.5 °C, one at 277.4 °C and the other at 286.6 °C. Comparison of thermogravimetric curves obtained in oxygen and in air shows the presence of two competing processes at a temperature of about 277.4 °C – evaporation and oxidation of the complex fragments. Evaporation is confirmed by a large value of the absorbed energy in the DTA curve, registered at this temperature in nitrogen and a large mass loss (TG curve) also in nitrogen. On the contrary, in air at 277.4 °C, both the endothermic DTA peak value and the mass loss are less. Besides that, the exothermic peak appears in DTA curve at 286.6 °C in the air indicating the complex fragments' reaction with oxygen, before they leave the complex. Thus, the

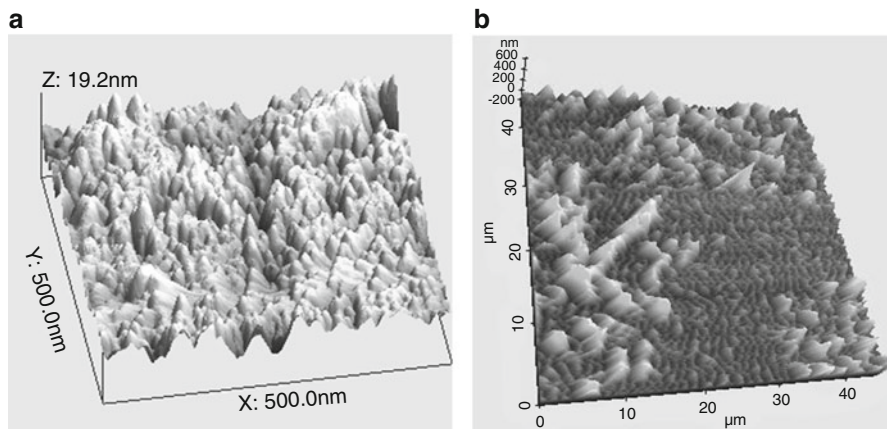


**Fig. 5.4** AFM images of the surfaces for films obtained from the precursor complexes N 1 (a) and N 2 (b)

residual mass of fragments studied in the air in the considered temperature interval is more of the fragments' residual mass studied in the nitrogen. These witnesses to the nonvolatility of the reaction products formed in the air due to their comparatively considerable size.

The residual mass at 308.5 °C, Fig. 5.3 (in the air), is approximately 14.7%, which is apparently due to the tin compounds' presence in the product. A small exothermic peak at 500 °C and a strong exothermic peak between 620 and 650 °C for the DTA curve measured in air are not observed on the curve measured in nitrogen. These exothermic peaks observed in the air correspond to a small loss of mass of the complex (about 1.5–2%) and may occur due to combustion of organic residues formed during BADCT decomposition. The further temperature increase does not lead to greater loss of mass.

Due to the method proposed by the authors [4], tin dioxide films were obtained from two precursor complexes. The surface morphology of SnO<sub>2</sub> films prepared from precursor complexes N 1 (a) and N 2 (b) is shown at Fig. 5.4 using an atomic force microscope. The image comparison shows that in case of using of a hydrated precursor (complex N 1), the film with a grain size of 10–20 nm was obtained. At the same time, the size of films' grains obtained from complex N 2 (anhydrous BADCT) is more than 500 nm.

These studies support the preference of using the hydrated precursor complex to obtain tin dioxide film with a smaller grain size of a nanoscale.

## 5.4 Conclusions

TG, DTG, and DTA studies of two sets of precursors allowed to establish and to compare the main stages of their decomposition: water evaporation, melting, evaporation of materials, and combustion of the material remnants in oxygen. The complexes' decomposition differences are caused by differences in their structure, namely, in the presence (in complex N 1) or absence (in complex N 2) of coordinated water molecules. The formation of a crystalline complex in the case of N 1 happened at the last stage of preparation – the drying step. Air drying facilitated to preserve the crystalline hydrate complex which is important for the further obtaining of nanoscale tin dioxide. In the thermal decomposition of the complex, the water in its structure acts for loosening and subsequent formation of smaller (nanosized) particles. Therefore, the use of precursor complex containing crystalline hydrate (N 1) should be preferred in the preparation of nanosized tin dioxide with a well-developed surface which provides a high sensitivity of its physical parameters to a changing environment and hence the widespread use as sensitive elements of the sensors.

## References

1. Gong J, Chen Q (2004) Sol-gel prepared single wall carbon nanotube SnO<sub>2</sub> thin film for micromachined Gas Sensor. *Nanotech* 3:232–235
2. Ivanov VV, Sidorak IA, Shubin AA, Denisova LT (2010) *Poluchenie poroshkov SnO<sub>2</sub> razlozheniem termicheski nestabil'nykh soedineniy* (obtaining of SnO<sub>2</sub> powders by means of decomposition of thermally unstable compounds). *J Sib Fed Univ Eng Technol* 2(3):189–213
3. Popov VS (2012) Theses of the candidate of sciences dissertation. Institute of General and Inorganic Chemistry, Russian Academy of Sciences, Moscow
4. Filevskaya LN, Smytyna VA, Grinevich VS (2006) Morphology of nanostructured SnO<sub>2</sub> films prepared with polymers employment. *Photoelectronics* 15:11–14
5. Stepanov AG (1989) A new general method for the preparation of bis(acetylacetonato)dihalogenotin(IV) by action of molecular oxygen on tin(II) halides in acetylacetone. *J Organomet Chem* 361(2):157–159; Diltthey W (1903) *Ber Deut Chem Ges* 36:923–930
6. Ueeda R, Kawasaki Y, Tanaka T, Okawara R (1966) Organometal complexes: II. Organotin and organolead bis(acetylacetonates). *J Organomet Chem* 5(2):194–197
7. Morgan GT, Drew HDK (1924) Researches on residual affinity and co-ordination. Part XVII. Stannic derivatives of β-diketones. *J Chem Soc Trans* 125:372–381
8. Shahzadi SA, Jin G-X (2006) Synthesis, characterization and crystal structure of Bis(acetylacetonato)dichlorotin(IV). *J Iranian Chem Soc* 3(4):323–326
9. Borillo LP (2003) Thesis's of the doctor of chemical sciences dissertation. Russian Federation, Tomsk
10. Ulug B, Türkdemir HM, Ulug A, Büyükgüngör O, Yücel MB, Smytyna VA, Grinevich VS, Filevskaya LN (2010) Structure, spectroscopic and thermal characterization of bis(acetylacetonato)dichlorotin(IV) synthesized in aqueous solution. *Ukrainian Chem J* 76(7):12–17

11. Fetisova TN (2008) Theses of the candidate of sciences dissertation. Russian Federation, Samara
12. Domashevskaya EP, Ryabtsev SV, Turischev SY, Kashkarov VM, Yurakov YA, Chuvenkova OA, Schukarev AV (2008) *XPS i XANES issledovaniya nanoslojev SnO<sub>x</sub>* (XPS and XANES investigations of SnO<sub>x</sub> nanolayers) *Kondensirovannye sredy I megfasnye granitsy*. *Condensed Matter Interphase Boundaries* 10(2):98–108
13. Tsyganova EI, Dyagileva LM (1996) *Reaktionnaya sposobnost' β-diketonatov metallov v reakzii termoraspada* (the reaction ability of metals β-diketonats in the reaction of thermal disintegration), *Uspekchi Khimii* (successes in chemistry). *Russ Chem Rev* 65(4):334–350

# Chapter 6

## Modeling Problems of Spin Crossover Nanocrystals

Iurii Gudyma, Artur Maksymov, and Andrej Bobák

### 6.1 Introduction

The application of spin-based phenomena is very promising due to their features like high switching rate, high quantum yield, memory effects that are very useful for high-performance data processing, recording, and storage systems. The potential of spin-based phenomena that could be observed in nowadays' nanomaterials directly depends on the possibility of relatively easy control of system properties together with the low energy consumption of final devices. Following the ongoing process of miniaturization, the development of nanotechnology tends to realize the very important principle "one molecule – one bit of information". Obviously this is the emergence problem of contemporaneous researches of molecular magnetic materials with the focus on multifunctional properties and low energy consumption. One of the most perspective molecular magnets, able to satisfy the current needs in the field of information technology, is spin-crossover compounds. They are the vivid representatives of molecular magnets in which the molecular bistability is visible probably in the most spectacular way, especially for iron(II) spin-crossover systems.

---

Iu. Gudyma (✉) • A. Maksymov  
Department of General Physics, Institute of Physical, Technical and Computer Sciences,  
Yuriy Fedkovych Chernivtsi National University, 2 Kotsjubynskyi Str., 58012, Chernivtsi,  
Ukraine  
e-mail: [yugudyma@gmail.com](mailto:yugudyma@gmail.com)

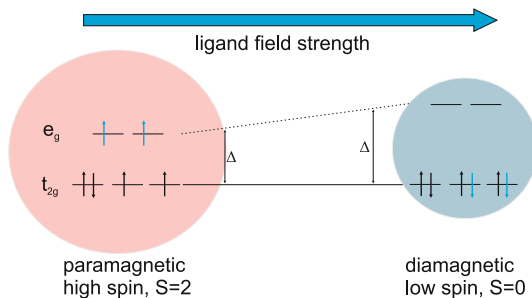
A. Bobák  
Department of Theoretical Physics and Astrophysics, Faculty of Science, P.J. Šafárik University,  
Park Angelinum 9, 041 54, Košice, Slovak Republic  
e-mail: [andrej.bobak@upjs.sk](mailto:andrej.bobak@upjs.sk)

Before describing the fundamental physical processes that define the behavior of spin-crossover coordination complexes, it is worth to make a brief review of the history of spin-crossover phenomenon that helps us to understand better how the contemporary concepts about spin transition materials were established. The interconversion of two spin states as a result of variation in temperature was observed for the first time in the works of Cambi and coworkers in the 1930s by studying the unusual magnetism of iron(III) derivatives of various dithiocarbamates [1, 2]. Their works focused on the study of magnetism of various derivatives of iron(II) and iron(III), and it was found that in these naturally existing systems, the spin states were very sensitive to the character of the axial ligands. Later, in the 1960s, Busch and coworkers reported for the first time the spin-crossover phenomenon in the synthetic six-coordinated Co(II) complexes [3]. In few years later, in 1967 König and Madeja [4] realized extensive magnetic and Mössbauer spectroscopic studies on spin-crossover complexes and gave the explanation of the nature of spin transition in some of the first iron(II) compounds. The possibility of spin transition in artificial systems plays a pivotal role for synthesizing the spin-crossover compounds with necessary properties. The turning point took place in 1984 when Decurtins et al. [5] have discovered that, at cryogenic temperatures, solid iron (II) spin-crossover systems can be quantitatively trapped in the HS state by light monochromatic irradiation. This effect is known as light-induced excited spin-state trapping (LIESST). The considerable contribution in the explanation of spin-crossover phenomenon has been provided by Hauser in the 1990s. Hauser has described the fundamental consideration of the occurrence of spin crossover in terms of ligand field theory (in particular for iron(II) complexes) [6, 7]. The interpretation of spin-crossover complexes as nonequilibrium magnetic systems with noise has been done for the first time in 2004 in the paper [8].

The spin-crossover compounds are the class of inorganic coordination complexes of the chemical elements with  $d^4 - d^7$  electronic configuration of the outer orbital which form the ligand environment with first-row transition metal ion centered in octahedral ligand field. These coordination complexes belong to the bistable materials due to the existence of stable low-spin (LS) and high-spin (HS) states. Between the states of spin crossover that are defined by spin configuration of d-orbital, the transition perturbed by influence of external physical fields could occur. The transition between the states of spin-crossover compounds may be caused mainly by the action of external stimuli like temperature, light irradiation, pressure, (very strong) magnetic fields, and others [9–13]. It leads to the drastic change of spin-crossover material's properties which is determined by the electron distribution on the sublevels of d-orbital for LS and HS states. As already mentioned among the spin-crossover systems, especial attention deserves the iron(II) spin-crossover compounds where the changes between the spin configurations are very pronounced due to maximal difference of magnetic moment between LS and HS states. This is one of the main reasons why spin-crossover phenomenon is convenient to be studied with the focus on the ferrous-based compounds.

To understand the mechanism of interconversion between LS and HS configurations, the structural features of spin-crossover complexes and the way of populating

**Fig. 6.1** The illustration of electron distribution on d-orbital of iron(II) spin-crossover complexes



the high-energy levels have to be considered. This typical spin-crossover compound with sixfold  $Fe^{2+}$  ion is characterized by the total spin number  $S = 0$  for the low-spin state and  $S = 2$  for the high-spin state. For the free iron(II) ion, the five non-degenerated levels of its d-orbitals are filled up according to Hund's rule in such a way that four electrons are unpaired and only two of them form one pair. In perfectly octahedral coordination complexes, the action of crystal field, created by nonmetallic ligand environment, on metal ion, provokes the splitting of its d-orbital into a subset of three orbitals  $d_x, d_y,$  and  $d_z,$  which are basis of the irreducible representation  $t_{2g}$  sublevel, and a subset of two orbitals  $d_{x1}$  and  $d_{y1}$  which are the basis to the irreducible representation  $e_g$  sublevel (see Fig. 6.1). The LS configuration is characterized by a large energy difference between metastable  ${}^5T_{2g}$  and ground state  ${}^1A_{1g}$ ; thus the strength of electron-electron repulsion is not enough to populate  $e_g$  sublevel. In this case, according to Hund's rule, the d-electrons will nicely pair up in the  $t_{2g}$  sublevel, resulting in a diamagnetic low-spin ground state due to spin compensation. In the neighborhood of transition point, the energy difference between  ${}^5T_{2g}$  and  ${}^1A_{1g}$  states decreases, leading to the equilibrium between ligand field strength and electron-electron repulsion. In this case, according to the same Hund's rule, the d-electrons enter the  $t_{2g}$  and  $e_g$  orbitals, but the spins are not compensated, which leads to a resultant magnetic moment. For LS configuration, the metal-ligand bonds are stronger and shorter due to electron absence on  $e_g$  sublevels, whereas for HS, the situation is opposite. For this reason, on the macroscopic scale, the spin transition is accompanied by changes in the volume of spin-crossover materials.

There are several effective theoretical approaches for description of spin-crossover transition. The most popular are the thermodynamic approach and Ising-like cooperative two-level model or mixt of these treatments. Ising-type model allows intensive use of the Monte Carlo method for advanced numerical simulation. The spin transition and HS-LS state (principally the ground state) properties have been previously investigated by means of density functional theory (DFT), but power DFT calculations have yet to consistently reproduce experimental data in material science. Nevertheless, the DFT calculations are decisive for proper descriptions of the electronic structure [14]. One of the first attempts to study the properties of typical Fe(II) spin-crossover systems has been made, basing on the Becke three-parameter Lee-Yang-Parr hybrid functionals and taking into account



the crystal lattice periodicity and the effect of strong correlation on the electronic structure of the Fe(II) ion [15]. It opens the path for the study of cooperativity, which is mainly contributed by the magneto-elastic coupling effects. However the modeling by ab initio quantum chemistry provides complete description of electronic structure for which it is necessary to consider a set of one-electron states (basis functions), number of electrons in the system, and nuclear charges. For the light-induced spin-crossover transition, macroscopic phenomenological model gives good results. The issues discussed in this chapter are an attempt to review the theoretical studies of spin-crossover complexes and are mostly based on previous papers of the authors. The suggested illuminations of the problems represent the writers' subjective understanding and are not meant to be exhaustive.

## 6.2 Thermodynamic Consideration

In 1972, Slichter and Drickamer [16] assumed that the interacting centers have great influence on the behavior of spin transition. Following the conjecture of König and Madeja [4] who proposed the possible existence of cooperative phenomenon, they developed the thermodynamic (macroscopic) model which successfully describes the effect of an external applied pressure on the spin transition phenomena and represented the starting point for many macroscopic models attempting to describe the origin of the interactions (atom-phonon coupling, elastic energy, etc.). This thermodynamic model is based on Guggenheim theory of regular solutions which assumes a random distribution of molecules in the material. This comprehensive model was also able to reproduce hysteresis phenomena accompanying discontinuous spin transitions in spin-crossover materials. Slichter and Drickamer [16] characterized the spin-crossover material by its Gibbs free energy

$$G = U + pV - TS. \quad (6.1)$$

This is some function of the site fraction of converted material as well as the pressure  $p$  and the temperature  $T$  where the first two terms represent the enthalpy of the system. Only two states of transition metal ion and hence of the molecule are taken into account. If we denote by  $n_L$  and  $n_H$  the associated thermally populated mole fractions of the LS and HS states, respectively, the simple expansion of the Gibbs free energy of the interacting ions centers up to quadratic term can be then expressed as

$$G = N(n_L G_L + n_H G_H + \Gamma n_H n_L) - TS_{\text{mix}}, \quad (6.2)$$

where  $\Gamma$  is the term of intermolecular interaction and  $S_{\text{mix}}$  is the mixed entropy of an ideal mixing solution of LS and HS molecules;  $G_L$  and  $G_H$  refer to the Gibbs free energy per molecule in the LS state and the HS state, respectively.  $N$  is the number of magnetic molecules in the system. Following the developed thermodynamic

considerations, in 1974, Sorai and Seki [17] made the attempt to explain the first-order spin-state transitions in spin-crossover materials. Once again, we notice that this result is written similar to the regular solution theory from the considerations that the mixing entropy of both HS and LS molecules is presented in the lattice

$$S_{\text{mix}} = k_B N \{ \ln(N) - n_H \ln(Nn_H) - (1 - n_H) \ln[N(1 - n_H)] \}, \quad (6.3)$$

where  $k_B$  is Boltzmann's constant. We took into account that  $n_H + n_L = 1$ . The equilibrium mole fraction is determined by the requirement that  $\partial G / \partial n_H |_{T=0} = 0$ . This implies that

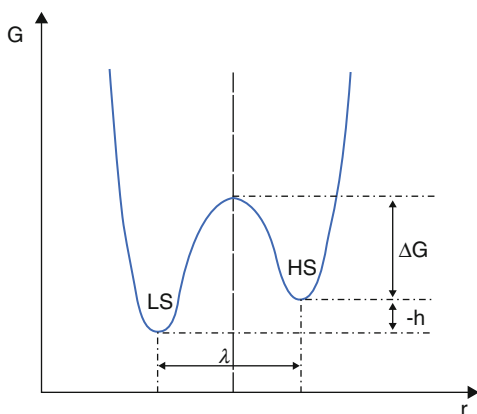
$$n_H = 1 / (1 + \exp(\Delta G / (RT))), \quad (6.4)$$

where  $\Delta G = G_H - G_L$ . The free energy change  $\Delta G$  determines the relative stability of the different spin states. Therefore it is easy to determine the spin transition temperature. The spin transition temperature is the temperature at which  $n_H = n_L = 1/2$ . In addition, Sorai and Seki [17] found that the vibrational part constitutes in general the largest contribution for the total entropy change. Slichter and Drickamer [16] have shown that the general Eqs. (6.2) and (6.4) may be used to render the different types of spin transition curves. Notice the cross section through the true Gibbs free energy surface (thermodynamic potential) is largely applied to experimental data; therefore this quantity is widely used in modern theoretical consideration of spin-crossover phenomenon. The example of this cross section is given in Fig. 6.2.

The theory suggests that the driving force of the spin transition is determined by intramolecular properties of the spin crossover complexes as well as intermolecular interactions communicated through the lattice. This is the basic assumption of any contemporary theory of spin crossover materials.

The effect of hydrostatic pressure on the transition temperature and the hysteresis widths of first-order spin crossover phase transitions has been studied successfully basing on the thermodynamic consideration [18]. Quite remarkable is the fact

**Fig. 6.2** The schematic representation of thermodynamic potential of spin-crossover complexes on phase interface



that the two-step spin crossover is qualitatively predicted by the Bragg-Williams approximation within the regular solution theory which is successfully developed in the work of Koudriavtsev [19]. A quantitative description of the two-step spin crossover was obtained on the basis of the Bragg and Williams approximation modified by taking into account the effects of the nature of two nearest neighbors along a normal coordinate.

It is obvious that wide thermodynamic studies are necessary to understand the mechanism of such an interesting phenomenon as spin crossover in complex compounds.

### 6.3 Microscopic Approach

The phase transition in spin-crossover materials within microscopic approach may be studied by Ising-like model where the magnetic molecules are regarded simply as two-level units [20, 21]. In the framework of Ising-like model, the characteristic of LS and HS states of spin-crossover compound is described by a fictitious variable (Ising spin)  $s$ , which takes the values  $-1$  for LS state and  $+1$  for HS one [22, 23]. The general form of the Ising-like Hamiltonian for spin-crossover system is described by the next equation

$$H = -J \sum_{\langle ij \rangle} s_i s_j - h \sum_i s_i. \quad (6.5)$$

Here  $h = \Delta - k_B T \ln(g_H/g_L)$  is the effective “magnetic field,” which represents the total effect from crystal field induced by ligand environment and external stimuli.  $J$  describes the intermolecular interaction of elastic origin through a phenomenological parameter accounting the ferromagnetic coupling ( $J > 0$ ) between neighboring spins  $i$  and  $j$  in Ising form,  $\Delta$  is the energy difference between HS and LS states for an individual spin-crossover molecule,  $g_H/g_L$  is degeneracy ratio of each state, and  $\langle s \rangle = m$  is fictitious magnetization. The ratio  $g_H/g_L$  may take large value (around some thousands) due to consideration of degeneracy and density of vibrational levels in each state. The intermolecular interaction  $J$  is given by some short-range potential, whose explicit form is not considered in the review.

The Hamiltonian (6.5) of spin-1/2 Ising model is a map of reduced spin-1 Ising model taking into account a single-ion magnetic anisotropy and a quadrupolar (or biquadratic) coupling of spins

$$H = -K \sum_{ij} \sigma_i^2 \sigma_j^2 - D \sum_i \sigma_i^2. \quad (6.6)$$

Here spin variable  $\sigma_i$  takes values  $\pm 1$  for HS state and 0 for LS state. The second term displays the simplest zero-field spin Hamiltonian of transition metal ion with single-ion anisotropy where  $D$  is the anisotropy constant that, for example, results from spin-orbit interaction which is considered with second-order correction of perturbation theory. First term corresponds to the cooperative behavior of magnetic molecular system but has no magnetic nature. This is evidenced by the absence of the bilinear exchange interaction. It has the form like the biquadratic interaction part with the coupling constant  $K$ . It is considered that it has elastic origin. The Hamiltonian (6.6) will be mapping into (6.5) up to a constant using the simple transformation  $s_i = 2\sigma_i^2 - 1$ . It is worth noting that there is no adequate simple theoretical model of the spin-crossover Prussian blue analogue [24], similar to that used for the molecular-based magnetic alloy with a structure of Prussian blue analogues [25].

The effective external field  $h$  given above is regarded as identical for all molecules in the sample and does not depend on time, i.e., it is considered in framework of zero-order mean field approximation, but instantaneous local thermal fluctuations provoke deviations from ligand field zero-order approximation. The instantaneous local random deviations can be treated through random field as a generalization of a stochastic process. It must be noticed that within the formalism of random fields it is possible to describe the deviations that differ from thermal nature (for example, caused by structural, pressure, light irradiation, or any other kind of physical stimuli that could perturb the so-called external effective magnetic field from Eq. (6.5)).

It is obvious that the effective field  $h$  in the present form describes the zero-order approximation of the mean-field theory. Therefore the model (6.5) must be improved for the case with “breathing” crystal field [26]. This means that the external site-dependent effective field  $h_i^{\text{eff}}(t)$  varies in time according to the relation

$$h_i^{\text{eff}}(t) = h + \xi_i(t), \quad (6.7)$$

which leads to the Hamiltonian of the next form:

$$H = -J \sum_{ij} s_i s_j - \sum_i [\Delta - kT \ln(g_H/g_L) + \xi_i(t)] s_i. \quad (6.8)$$

From the point of view of Ising model, the term with the stochastic process  $\xi_i(t)$  reflects the local random field. It is clear that the random field becomes significant especially when it is closer to critical temperature.

It is usually assumed that the stochastic process is a white Gaussian one, i.e., it is defined by two parameters, namely, zero mean and variance:

$$\langle \xi(t) \xi(t') \rangle = 2\varepsilon^2 \delta(t - t'). \quad (6.9)$$

Here,  $\varepsilon$  is the spectral density of stochastic variable  $\xi(t)$ , i.e., strength of fluctuations, and  $t$  and  $t'$  are distinct times.

If we are going beyond the simplest case, the more rigorous approach requires considering at least the correlated in time fluctuations. Following the widely used description of time-correlated fluctuations as Ornstein-Uhlenbeck (OU) process, the time autocorrelation function can be expressed in the form

$$\langle \xi(t)\xi(t') \rangle = \frac{\varepsilon^2}{\tau} \exp\left(-\frac{t-t'}{\tau}\right), \quad (6.10)$$

where  $\tau$  is the autocorrelation time of the stochastic process  $\xi(t)$ , i.e., a measure of its memory in time. The stochastic differential equation that governs the evolutions of OU process is written as

$$\frac{d\xi(t)}{dt} = -\frac{\xi(t)}{\tau} + \frac{\varepsilon}{\tau}\eta(t), \quad (6.11)$$

where  $\eta(t)$  is the independent white-noise source that satisfies the statistical conditions  $\langle \eta(t) \rangle = 0$  and  $\langle \eta(t)\eta(t') \rangle = 2\delta(t-t')$ . The stationary OU process is frequently used as model of real noisy signal for which the values of  $\xi(t)$  and  $\xi(t')$  are noticeably correlated at  $|t-t'| \sim \tau$ .

Below we provide the numerical analysis of behavior of temperature transition curves at various system's parameters for deterministic effective field and for the case with fluctuations based on Monte Carlo algorithm with Metropolis transition probabilities. For simulations we have chosen the crystal field  $\Delta = 1000$ , the degeneracy ratio between HS and LS states as  $g_H/g_L = 150$ , the lattice size  $L = 40$  (starting from this system size the further its increasing gives approximately the same transition curves for periodic and open boundary conditions [26]), and 5000 Monte Carlo steps. For the provided simulations, the periodic boundary conditions have been applied.

It is obvious that the hysteretic behavior of the system is directly dependent on the intermolecular interaction  $J$  which is one of the main parameters that defines the order of phase transition in spin-crossover Ising-like system. In Fig. 6.3 the behavior of temperature driven transition curves for cooling and heating regimes is shown, together with spin configurations at critical temperatures, for several intermolecular interaction values described in the caption.

The analysis of transition curves has been started from threshold value between non-hysteretic and hysteretic behaviors which corresponds to  $J = 80$ . The behavior of hysteresis width and domain size with increase of intermolecular interaction  $J$  in case of deterministic effective field  $h$  is similar to the one from classic Ising model.

In order to analyze the temperature-driven transition for external effective field with fluctuations, the threshold intermolecular interaction was chosen. At first, a more simple case with white fluctuations was analyzed. The results are shown in Fig. 6.4. From the figure, it is seen that the action of fluctuations is similar to the action of intermolecular interactions  $J$ . Besides the appearance and widening of

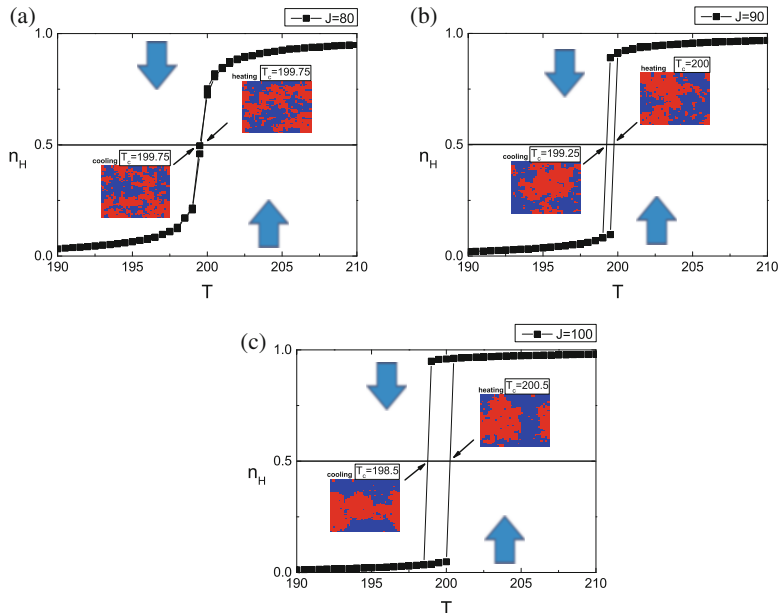
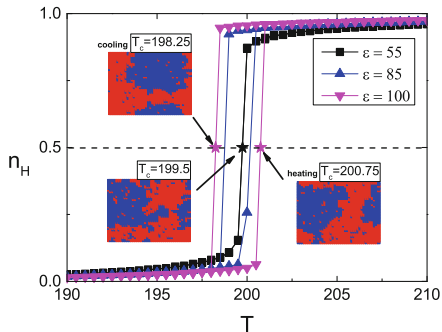


**Fig. 6.3** The behavior of temperature transition curves at the following values of interaction constant:  $J = 80$  (a),  $J = 90$  (b) and  $J = 100$  (c). The insets show the spin configurations of the system at critical temperatures

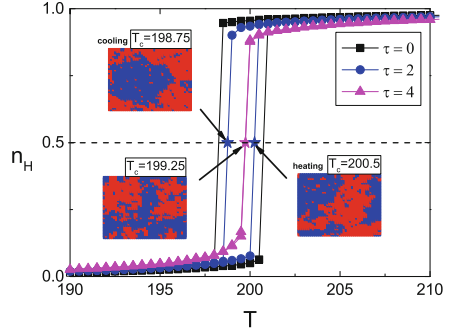
**Fig. 6.4** The widening of hysteresis loop of spin-crossover system with fluctuating external field. Here, the autocorrelation time is zero, i.e., the white fluctuations are considered



hysteresis loop, the increasing of the homogeneity of the domains that could be explained by the respective increasing of the correlation lengths in the lattice is also observed. However it must be noticed that the decreasing of cooling temperature and increasing of heating one, which contribute to the widening of hysteresis loop, are characterized by some asymmetry, and in result, the center of hysteresis is shifted toward lower temperatures in comparison to the same widening induced by intermolecular interaction constant, where the hysteresis center remains unchanged.

In real system, we deal with fluctuations of common nature with limited spectral range. Following the theoretical descriptions of colored fluctuations given above, we

**Fig. 6.5** The destructive impact of autocorrelation time  $\tau$  on hysteresis loop. Here, the noise intensity is  $\varepsilon = 100$



have considered that coupling between two consequent time moments is dependent on initial conditions, i.e., the autocorrelation time  $\tau$  is different from zero. The resulting temperature transition curves for several fixed values of autocorrelation time are shown in Fig. 6.5. As one can see, the narrowing of hysteresis loop with increase of autocorrelation time is observed. It is obvious that the domain sizes, which define the spatial correlation lengths of Ising lattice, are reduced.

Besides, a compressible model of spin-crossover solids was studied in the framework of the Ising-like model with two-order parameters, where the effect of elastic strain on interaction integral is considered [27]. These considerations led to examination of the relation between the order parameters during temperature changes.

## 6.4 The Specific Phenomenological Model

The discovering of LIESST effect by Decurtins et al. [5] has opened a new way for interpretations of spin-crossover phenomenon under light irradiation. The phenomenological model is based on competing processes between photoexcitation and relaxation of HS molecules and describes well the experimental data. In the simplest case, if we neglect the interaction of spin-crossover molecules, the general macroscopic master equation describing the system's evolution including the action of light intensity is given by [28]

$$\frac{dn_H}{d\hat{t}} = I_0\omega n_L(\hat{t}) - k_{HL}(T)n_H(\hat{t}) + k_{LH}(T)n_L(\hat{t}). \quad (6.12)$$

Here  $I_0$  is intensity of light irradiation,  $\omega$  is product of absorption cross-section with the quantum yield of the system, and  $k_{HL}$  and  $k_{LH}$  are the rates of spontaneous transition from HS to LS and LS to HS states, respectively, at constant temperature  $T$ . Equation (6.12) describes the evolution in time  $\hat{t}$  of HS fraction  $n_H$  which is considered as an order parameter.

The first term in Eq. (6.12)  $I_0\omega n_L(\hat{t})$  describes the induced photoexcitation of LS molecules due to absorption of light quanta, the second term  $k_{HL}(T)n_H(\hat{t})$  represents the spontaneous relaxation of HS molecules, and the third term  $k_{LH}(T)n_L(\hat{t})$  describes the spontaneous transition from LS to HS state. Because the probability of spontaneous transition is much less in comparison with photo-induced transition, i.e.,  $k_{LH}(T)n_L(\hat{t}) \ll k_{HL}(T)n_H(\hat{t})$ ; hereinafter the spontaneous LS  $\rightarrow$  HS transition described by  $k_{LH}(T)n_L(\hat{t})$  is not taken into account.

Therefore, the macroscopic master equation of light-induced system with dimensionless quantities, obtained by substitution  $t = k_{HL}^\infty \hat{t}$  and considering that  $n_L = (1 - n_H)$ , is written by

$$\frac{dn_H}{dt} = \beta(1 - n_H) - n_H \exp(-\alpha n_H) \equiv f_{\text{exc}} - f_{\text{rel}} \equiv f(n_H). \quad (6.13)$$

Here the control parameter is  $\beta = I_0\omega/k_{HL}^\infty$ , the photoexcitation term is  $f_{\text{exc}} = \beta(1 - n_H)$ , and the relaxation is  $f_{\text{rel}} = n_H \exp(-\alpha n_H)$ , where  $\alpha$  is self-acceleration factor of relaxation. The stationary solutions of Eq. (6.13) give the description of system steady states.

The system dynamics described by the rate Eq. (6.13) can be analyzed in the framework of dynamic potential based on Lyapunov functions [8]

$$\frac{dn_H}{dt} = -\frac{dU(n_H)}{dn_H}, \quad (6.14)$$

where  $U(n_H) = -\int_0^{n_H} f(x)dx$  is non-equilibrium (dynamic) potential.

The evolution of spin-crossover system perturbed by noise in simplest way can be described by a one-variable nonlinear Langevin equation, written in terms of transition rates [8, 29, 30]:

$$\frac{dn_H}{dt} = f(n_H) + \xi(t), \quad (6.15)$$

where  $\xi(t)$  indicates the noise induced by the environment and, generally, could obey the statistical conditions (6.9), (6.10) and (6.11). The Langevin Eq. (6.15) with additive noise term  $\xi(t)$  describes the dynamics of a system in the presence of an interaction with environment. This kinetic equation simulates the system dynamics as a motion of Brownian particle in the phase space. Several particular realizations of stochastic trajectory for various initial conditions which were chosen uniformly between interval  $[0; 1]$  with step 0.2 starting at  $n_H = 0$  are shown in Fig. 6.6. The intensity of light irradiation and self-acceleration factor were chosen as  $\beta = 0.0812$  and  $\alpha = 5.14$ , respectively. The stochastic process  $\xi(t)$  was described as white Gaussian noise with autocorrelation function (6.9). The value of  $\beta$  which is used for simulations provides the equal deep of potential wells for LS and HS states. The trajectories shown in Fig. 6.6 are evolving to the steady values of  $n_H$  which are the solutions of kinetic equation (6.15) and correspond to the minima of dynamic



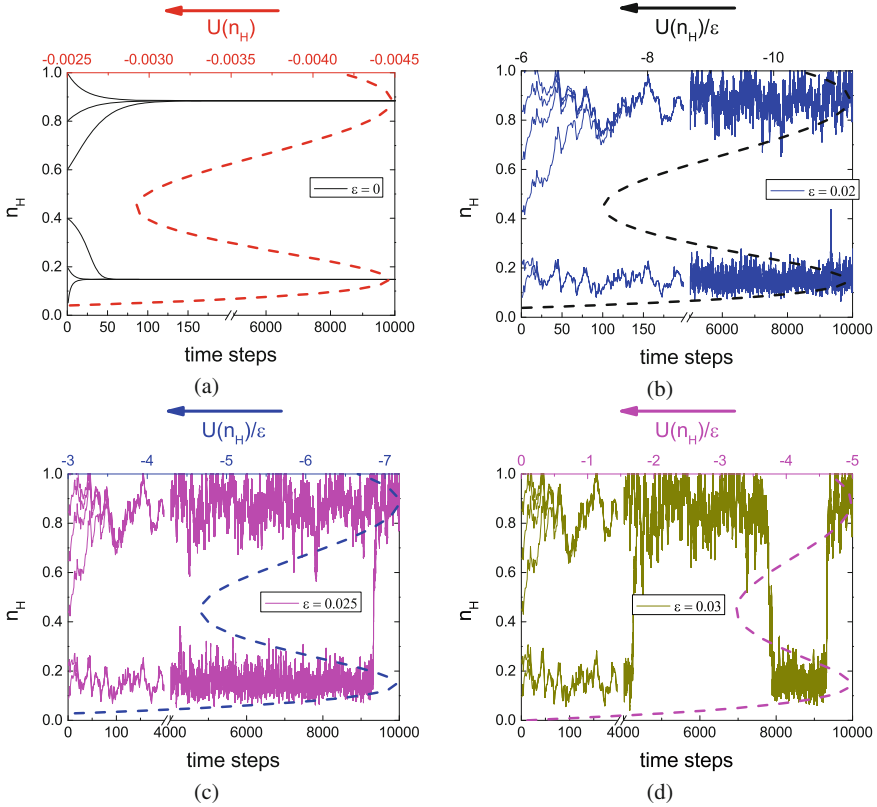


**Fig. 6.6** The behavior of particular realizations of stochastic trajectory with different initial conditions at noiseless case (a) and following fixed noise values:  $\epsilon = 0.02$  (b),  $\epsilon = 0.025$  (c) and  $\epsilon = 0.03$  (d)

potential (6.14). For convenience, the dynamic potential are shown in Fig. 6.6 too. If the noise is maintained quite low, the system is living in its stable states (HS and LS configurations) infinitely long. When the noise achieves some threshold value (here  $\epsilon = 0.025$ ), the spontaneous transitions between system's states arise. In this case, the system's potential is characterized as bistable one, but the energy which is brought into the system by external noise is enough to overcome the barrier height between LS and HS states. This is the main reason for the occurrence of interstate transitions.

In order to characterize the memory effects of the system under noise action, the light-induced hysteresis loop for several fixed noise values has been computed. In Fig. 6.7b, the light-induced hysteresis for noiseless case (black curves) and noise intensities  $\epsilon = 0.02$  (red curve),  $\epsilon = 0.025$  (blue curve), and  $\epsilon = 0.03$  (green curve) together with dynamic potential for the same fixed values are shown. The noiseless hysteresis obtained analytically (black dashed curve) coincides with the one obtained from numerical simulations (black solid curve).

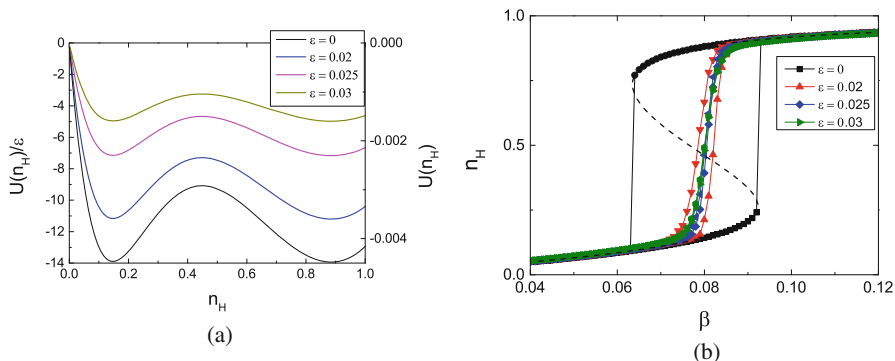
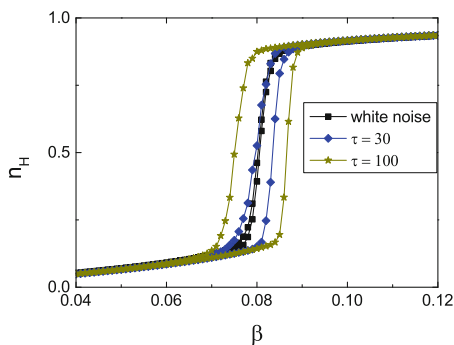


**Fig. 6.7** The behavior of dynamic potential (a) and light-induced hysteresis loop (b) for noiseless case and several fixed noise values indicated in the text

**Fig. 6.8** The widening of light-induced hysteresis loop with increase of autocorrelation time of additive noise



The increase of noise intensity decreases the barrier height of the potential and makes its overcoming favorable (see Fig. 6.7a). At the same time, the width of light-induced hysteresis is decreasing up to its vanishing which is observed at threshold noise intensity  $\epsilon = 0.025$ . The further increasing of noise leads to more gradual light-induced transition of the system in non-hysteretic regime.

Besides the analysis of hysteretic behavior of the system driven by white noise, we also have analyzed the action of colored noise. For this case, the stochastic process from Eq. (6.15) has been described by the conditions (6.10) and (6.11). The resulting transition curves for white noise and two fixed values of autocorrelation time  $\tau = 30$  and  $\tau = 100$  are shown in Fig. 6.8.

## 6.5 Conclusion

The interaction mechanism leading to the cooperative nature of the LS-HS transition is not fully examined. A more complete conception of the interactions in crystals, powders, and solutions is needed. In addition to considering the volume difference

of the two spin states at zero pressure, it is important to include the compressibility and the pressure dependence of the compressibility.

Assumption that the ligand field energy depends only on the distance between the metal ion and ligand donor atoms leads to an oversimplified picture since the effects of the mutual spatial orientation on the ligand field must be taken into account. The detailed molecular mechanism of spin-state conversion is still under discussion.

When measuring the properties of nanoparticles, additional studies are desirable to clarify the unavoidable influence of the surface, size, and environmental distribution upon the behaviors. The mechanisms of the spin transition at the nanoscale and in particular the size dependence of the collective behavior are still not completely understood. Challenges remain in the still-underdeveloped modeling of transition induced by perturbations other than temperature.

Questionless, a general, appropriate theory should recover not only the conversation curve but also the whole profile of heat capacity. Promising theories of qualitative and quantitative estimates on spin crossover materials should take under consideration the above features.

**Acknowledgements** One research of us (IuG) was supported by the National Scholarship Programme of the Slovak Republic. This work was also partially supported by the Grant VEGA No.1/0331/15 (AB). IuG thanks the theoretical group of the Institute of Physics for the hospitality at Faculty of Science, P. J. Šafárik University in Košice where this work was in progress.

## References

1. Cambi L, Szegö L (1931) Über die magnetische susceptibilität der komplexen verbindungen. Ber Deutsch Chem Ges 64:2591–2598
2. Cambi L, Malatesta L (1937) Magnetismus und polymorphie innerer kompleksalze: eisensalze der dithiocarbamidsäuren. Ber Deutsch Chem Ges 70:2067–2078
3. Robinson MA, Busch DH (1963) Complexes derived from strong field ligands. XVI. The transition metal complexes of 2-pyridinalhydrazones. Inorg Chem 2:1171–1177
4. König E, Madeja K (1966) Unusual magnetic behaviour of some iron(II)bis-(1,10-phenanthroline) complexes. Chem Commun 3:61–62
5. Decurtins S, Gütlich P, Köhler CP, Spiering H, Hauser A (1984) Light-induced excited spin state trapping in a transition-metal complex: the hexa-1-propyltetrazole-iron (II) tetrafluoroborate spin-crossover system. Chem Phys Lett 105:1–4
6. Hauser A, Vef A, Adler P (1991) Intersystem crossing dynamics in Fe(II) coordination compounds. J Chem Phys 95:8710–8717
7. Hauser A (1991) Intersystem crossing in the  $[Fe(ptz)_6](BF_4)_2$  spin crossover system (ptz = 1-propyltetrazole). J Chem Phys 94:2741–2748
8. Gudyma Yu, Semenko O (1991) Nonequilibrium kinetics in spin-crossover compounds. Phys Status Solidi B 241:370–376
9. Gütlich P, Goodwin HA (eds) (2004) Spin crossover in transition metal compounds I. Springer, Berlin
10. Gütlich P, Goodwin HA (eds) (2004) Spin crossover in transition metal compounds II. Springer, Berlin
11. Gütlich P, Goodwin HA (eds) (2004) Spin crossover in transition metal compounds III. Springer, Berlin

12. Halcrow MA (ed) (2013) Spin-crossover materials: properties and applications. John Wiley and Sons, Chichester
13. Gudyma Iu, Maksymov A, Ivashko V (2015) Spin-crossover nanocrystals and Ising model. In: Fesenko O, Yatsenko L (eds) Nanoplasmonics, nano-optics, nanocomposites, and surface studies. Springer, Cham, pp 165–192
14. Reiher M (2002) Theoretical study of the  $Fe(phen)_2(NCS)_2$  spin-crossover complex with reparametrized density functionals. *Inorg Chem* 41:6928–6935
15. Lebègue S, Pillet S, Ángyán JG (2008) Modeling spin-crossover compounds by periodic DFT+U approach. *Phys Rev B* 78:024433
16. Slichter CP, Drickamer HG (1972) Pressure-induced electronic changes in compounds of iron. *J Chem Phys* 56:2142–2160
17. Sorai M, Seki S (1974) Phonon coupled cooperative low-spin  $^1A_1$  high-spin  $^5T_2$  transition in  $[Fe(phen)_2(NCS)_2]$  and  $[Fe(phen)_2(NCSe)_2]$  crystals. *J Phys Chem Solids* 35:555–570
18. Ksenofontov V, Spiering H, Schreiner A, Levchenko G, Goodwin HA, Gütlisch P (1999) The influence of hydrostatic pressure on hysteresis phase transition in spin crossover compounds. *J Phys Chem Solids* 70:393–399
19. Koudriavtsev AB (1999) A modified Bragg and Williams approximation of the two-step spin crossover. *Chem Phys* 241:109–126
20. Wajnlasz J (1970) Etude de la transition “Low Spin”–“High Spin” dans les complexes octaédriques d’ion de transition. *Phys Status Solidi B* 40:537–545
21. Wajnlasz J, Pick R (1971) Transitions “Low Spin”–“High Spin” dans les complexes de  $Fe^{2+}$ . *J Phys Colloques* 32:C1-91–C1-92
22. Bousseksou A, Nasser J, Linares J, Boukheddaden K, Varret F (1992) Ising-like model for the two-step spin-crossover. *J Phys I* 2:1381–1403
23. Bousseksou A, Varret F, Nasser J (1993) Ising-like model for the two-step spin-crossover of binuclear molecules. *J Phys I* 3:1463–1473
24. Papanikolaou D, Kosaka W, Margadonna S, Kagi H, Ohkoshi S, Prassides K (2007) Piezomagnetic behavior of the spin crossover Prussian blue analogue  $CsFe[Cr(CN)_6]$ . *J Phys Chem C* 111:8086–8091
25. Dely J, Bobák A (2007) Magnetic properties of the ternary alloy with a structure of Prussian blue analogs. *Physica B* 388:49–58
26. Gudyma Iu, Maksymov A, Enachescu C (2014) Phase transition in spin-crossover compounds in the breathing crystal field model. *Phys Rev B* 89:224412
27. Gudyma Iu, Ivashko V, Linares J (2014) Diffusionless phase transition with two order parameters in spin-crossover solids. *J Appl Phys* 116:173509
28. Desaix A, Roubeau O, Jęfcić J, Haasnoot JG, Boukheddaden K, Codjovi E, Linares J, Noguès M, Varret F (1998) Light-induced bistability in spin transition solids leading to thermal and optical hysteresis. *Eur Phys J B* 6:183–193
29. Gudyma Iu, Maksymov A, Enachescu C (2010) Decay of a metastable high-spin state in spin-crossover compounds: mean first passage time analysis. *Eur Phys J B* 78:167–172
30. Gudyma Iu, Maksymov A (2012) Optically induced switching in spin-crossover compounds: microscopic and macroscopic models and their relationship. *Appl Opt* 51:C55–C61

# Chapter 7

## Characterization of Pet Track Membrane Parameters

Egor Kaniukov, Alena Shumskaya, Dzmitry Yakimchuk, Artem Kozlovskiy, Anel Ibrayeva, and Maksim Zdorovets

### 7.1 Introduction

In recent years, methods of formation and studying track membrane parameters attract a great attention due to the possibility to use a wide range of materials (polymers [1, 2], oxides [3, 4]) with different pore geometries (cylinders [5], cones [6, 7], “cigar-shaped” [8, 9], “bottle-shaped” [2, 5], and “tie-shaped” pores [8]). Polyethylene terephthalate (PET) is the most commonly used as a material for membrane, due to it refers to the large-tonnage industrial polymers widespread in electronics, food, and medical industries.

The range of nano-objects obtained by means of track membranes is intensively growing due to their advantages [10, 11] that is confirmed by a large number of works with a detailed research of the track formation mechanisms [12–18], the

---

E. Kaniukov (✉) • A. Shumskaya • D. Yakimchuk  
Scientific-Practical Materials Research Centre, NAS of Belarus, Minsk, 220072, Belarus  
e-mail: [ka.egor@mail.ru](mailto:ka.egor@mail.ru)

A. Kozlovskiy • A. Ibrayeva  
Astana Branch of the Institute of Nuclear Physics, 010008, 2/1, Ablay Khan Street, Astana,  
The Republic of Kazakhstan

L.N. Gumilyov Eurasian National University, 010008, 2, Satpayev Street, Astana, the Republic of  
Kazakhstan

M. Zdorovets  
Astana Branch of the Institute of Nuclear Physics, 010008, 2/1, Ablay Khan Street, Astana,  
The Republic of Kazakhstan

L.N. Gumilyov Eurasian National University, 010008, 2, Satpayev Street, Astana, the Republic of  
Kazakhstan

Ural Federal University Named After the First President of Russia B.N. Yeltsin, 620002, 19,  
Mira Street, Ekaterinburg, the Russian Federation

formation of pores with different forms [19–21] and geometry [22–24], as well as obtaining nanostructures based on them [25–28].

Despite the large number of investigations devoted to the pore formation mechanisms, there are problems related to obtaining pores with desired characteristics for specific industrial applications, as well as the least expensive method of controlling template parameters. In this regard, in the work templates based on PET with pore diameters in the range of 30–130 nm are considered, their parameters are studied in details by different methods. The advantages and disadvantages of these methods are analyzed.

## 7.2 Methods

Twelve micron thick polymeric films based on polyethylene terephthalate (PET) of the Hostaphan® type manufactured by “Mitsubishi Polyester Film” (Germany) were used as a material for template matrices. PET films were irradiated at the DC-60 accelerator [29] with krypton ions with 1.75 MeV/nucleon energy and  $10^9 \text{ cm}^{-2}$  fluence.

Irradiated films for photooxidation of surface polymer layer were exposed to UV sensitization (UV-C lamp with 253.7 nm wavelength) for 30 min on each side. Bilateral chemical etching was carried out in 2.2 M NaOH solution at  $85 \pm 0.1 \text{ }^\circ\text{C}$  during etching times up to 70 s. After etching, track membranes were washed in the neutralization solution (1.0% solution of acetic acid and deionized water) and the distilled water.

The surface and the side edges of track membranes formed by chemical etching were investigated using the JEOL-7500F scanning electron microscope (SEM). Side edges were obtained by cracking polymeric films prefrozen in liquid nitrogen. No less than 70 pores were measured for each sample to reduce the error associated with the inaccuracy of measuring of lateral dimensions during SEM research.

The hydrophilicity of track membranes was determined by measuring the contact angle ( $\theta$ ) by the sessile drop technique. For this purpose, the 15  $\mu\text{l}$  of working fluid drop was deposited by a micropipette onto the sample surfaces. The contact angle was measured by a goniometric method.

Calculation of membrane performance for water and air was carried out according to the data obtained using the manometric method of gas and water permeability on 1  $\text{cm}^2$  membranes. The bubble point determination was performed by a partial membrane immersion in the water so that the upper part of the membrane is contacted with liquid and the bottom one with the air supplied from the compressed air source through a pressure regulator.

Conductivity measurements were carried out in a two-chamber conductivity cell, in which chambers were separated by the track membrane. KCl water solutions with concentration in the range of 0.01–0.1 mol/l were used as the electrolyte to determine the specific conductivity.

The crystallinity degree determination of track membranes was carried out by X-ray analysis (XRD) at D8 ADVANCE diffractometer using Cu  $K_{\alpha}$  radiation and graphite monochromator. Diffraction patterns were recorded in the  $2\theta$  angular range of  $15^{\circ}$ – $150^{\circ}$  with  $0.02^{\circ}$  increments for 5 s at each point.

### 7.3 Results and Discussion

At different stages of the track membrane formation, the crystallinity degree of PET films has been monitored using X-ray diffraction (Fig. 7.1).

Two major peaks are observed at the XRD spectra: a wide peak at the range of  $15$ – $35^{\circ}$ , which is characterized by high intensity, and a small peak at  $54^{\circ}$ . Changes of the small peak intensity (inset in the Fig. 7.1) reflect the PET structure evolution under various external effects: the peak intensity decreases after irradiation with krypton ions. This fact indicates the growth of disorder degree of polymer structure. The track core etching leads the removal of the track high defective core, although the growth of the peak intensity does not occur due to the dangling bonds formation on the pore walls.

After pore etching, the morphology of the track membranes has been researched by SEM. Specific images of the surface and cross sections are shown in Fig. 7.2. The scan of template surface (Fig. 7.2a) shows that the pores are stochastically distributed over the surface, and the porosity corresponds to the fluence of irradiation. Analysis of cross sections (Fig. 7.2b) indicates that the pores have a cylindrical shape, and the aspect ratio is about 100 and a slight change in diameter along their length. A detailed analysis of the top (Fig. 7.2c) and the bottom film surface

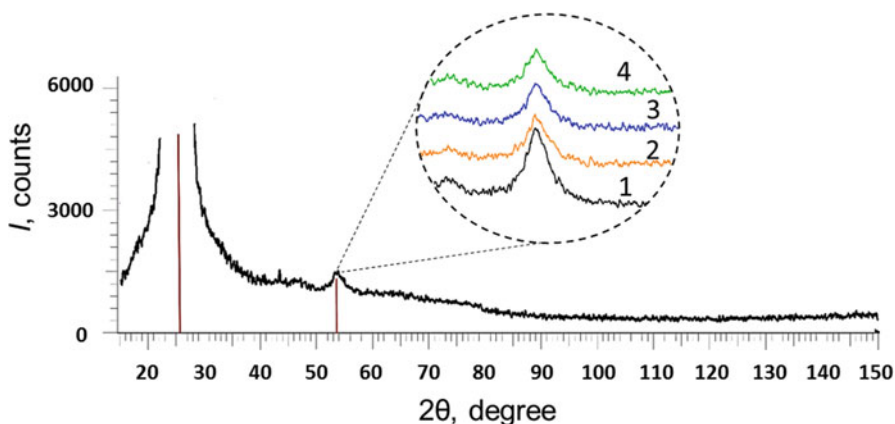


**Fig. 7.1** X-ray diffraction spectra of PET. The inset in the figure: XRD spectra of PET film is prior to irradiation (1), after irradiation of krypton ions (2), UV sensitizing (3), and etching (4)

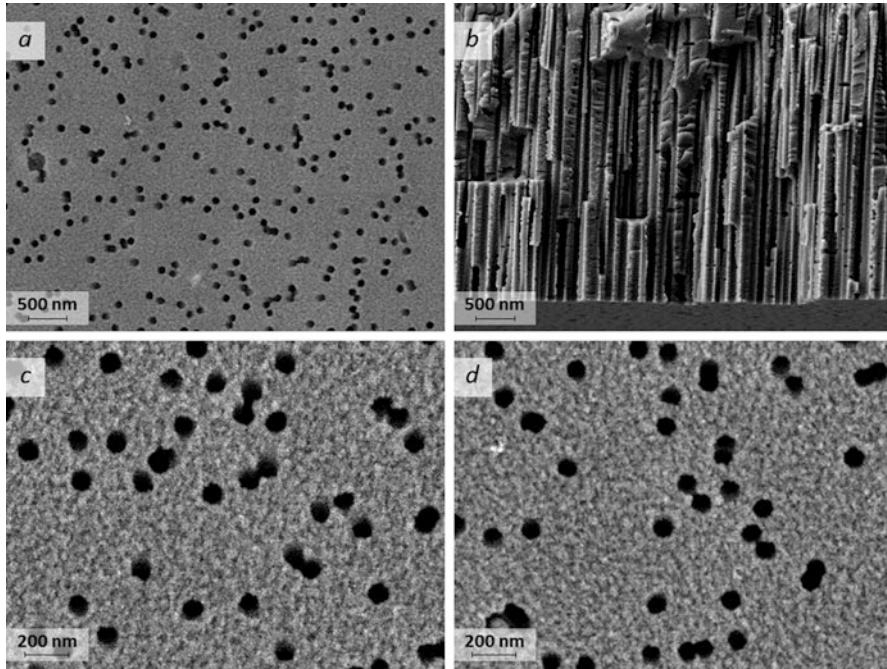


**Fig. 7.2** SEM images of PET template obtained by polymer film irradiation with krypton ions with 1.75 MeV/nucleon energy and  $10^9 \text{ cm}^{-2}$  fluence at the etching time (60 s) in the 2.2 M NaOH solution at 85 °C. PET template top (**a**, **c**) and bottom surface (**d**) and its cross section (**b**)

(Fig. 7.2d) indicates that the difference in pore diameters does not exceed 5–7% at different sides of the track membrane.

The study of the pore sizes and shapes' evolution during different etching times (Fig. 7.3a) has revealed that in the polymer film at small etching times (20 s), there are small pores with diameters  $\sim 20 \text{ nm}$ , located at a considerable distance from each other. In this case, a hole within the polymeric matrix is cylindrical even at such short times etching. Over time, pore diameter is increasing, while average distance between them is decreasing. Additionally, a pore form also remains cylindrical.

Accordingly, the following scheme-irradiated areas (latent tracks) in PET films have been modified under the influence of the etching agent. At placing the sample in an aqueous or aqueous-alcoholic-alkaline solution, there is a rapid bilateral etching of the track core (diameter  $\sim 10 \text{ nm}$ ) oriented at  $90^\circ$  angle to the surface and its halo (diameter  $\sim 100 \text{ nm}$ ) with a speed  $V_T$  and slow layering etching of the film surfaces with a speed  $V_B$  [2, 18]. Etching solution diffuses into the formed pore from where the reaction products are coming into the reaction vessel, mixing with the original etching solution. By continuing the etching process, the evolution of the pore form with etched tracks is mainly determined by the etching speed of the intact polymer  $V_B$ .



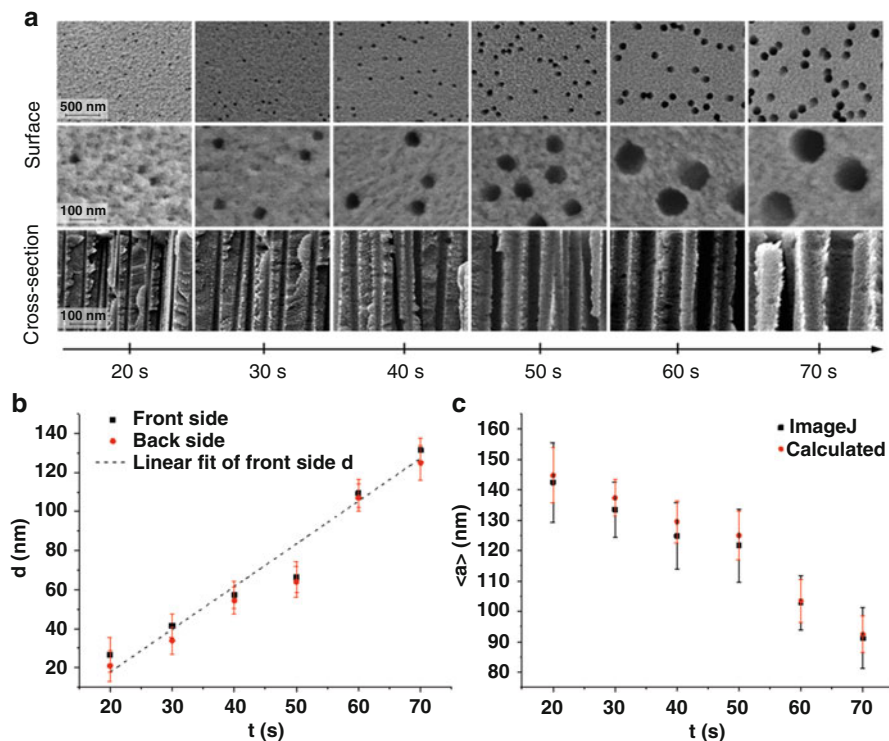


**Fig. 7.3** SEM images of the surface and cross section of the PET template at different etching times (a). The scale is the same for each row. The dependence of pore diameter (b) and the average distance between them (a) on the etching time

The pore diameters on the outside and the inside of the track membrane (Fig. 7.3b) and the average distance between them  $\langle a \rangle$  were determined for different etching times (Fig. 7.3c) by the analysis of SEM images using the “ImageJ” software package, as had been described in [30]. The research of pore sizes at different etching stages indicates that a character of the time dependence of the diameters is close to linear (Fig. 7.3b), and the difference of the diameter values is not more than 10 nm on the surface and the underside. The average distance between the pores is monotonically decreasing with the etching time growth, and the individual pores start overlapping at times about 70 s. The subsequent etching leads the increase of the events frequency, in which the walls separating the adjacent pores are etched through to form paired and multiple crossings. Taking into account that the mutual pore intersection has a significant impact on the membrane strength, chemical treatment of PET membranes has not been conducted at times over 70 s.

The dependence shown in Fig. 7.3c is well described by the formula  $\langle a \rangle = \frac{1}{2\sqrt{f}}$  [31], where  $f$  is a number of pores per  $\text{cm}^2$ . The simple dependence of values  $\langle a \rangle$ , which is easily determined on the basis of the pore diameter and the irradiation

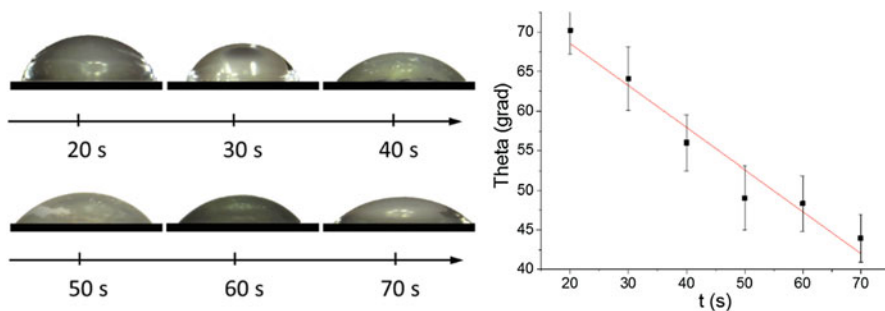


**Fig. 7.4** The micrographs illustrating change in contact angle at the different etching time and the dependence of the contact angle on the etching time

fluence, allows selecting the template parameters before the etching so as to obtain a matrix with the minimal number of intersecting pores.

The above analysis shows that the REM method allows not only determining the morphology of the track membranes at various etching stages but also measuring the pore sizes with a high accuracy. However, a method with the possibility to assess the qualitative and quantitative parameters of porous matrices in vitro is necessary for the express analysis of a large membrane area. The simplest method of qualitative analysis is a method for determining the hydrophilic degree of the track membranes by measuring the contact angle ( $\theta$ ) by the sessile drop technique. In this case, the contact angle is calculated according to the formula:

$$\operatorname{tg}\theta = \frac{2h \cdot r}{r^2 - h^2} \quad (7.1)$$

where,  $\theta$  is a contact angle,  $r$  is the radius of a contact area of the drop with the surface, and  $h$  is the drop height. Images of the drop, lying on the track membrane surface at different etching times, and the time dependence of  $\theta$  are presented in Fig. 7.4.

It can be seen that the hydrophilicity of PET track membranes is increasing with the etching time growth from 20 to 70 s, resulting in decreasing the contact angle. In this case, the almost linear dependence of  $\theta$  on time allows conducting a qualitative express analysis of track membrane parameters. Unfortunately, the accuracy of this method is not high.

Practical application of track membranes requires knowledge of the uniformity degree of pore distribution in size within a porous matrix. Determination of the maximal pore diameters and their deviation from the mean diameter is possible by using the bubble point technique. The bubble point technique is that the water column height is increasing due to the influence of surface tension forces when the capillary diameter is reducing. The previous liquid level can be returned by applying pressure equivalent to the water column height in the capillary, that is, the air bubble will permeate through the pore at a certain pressure under the equality condition of

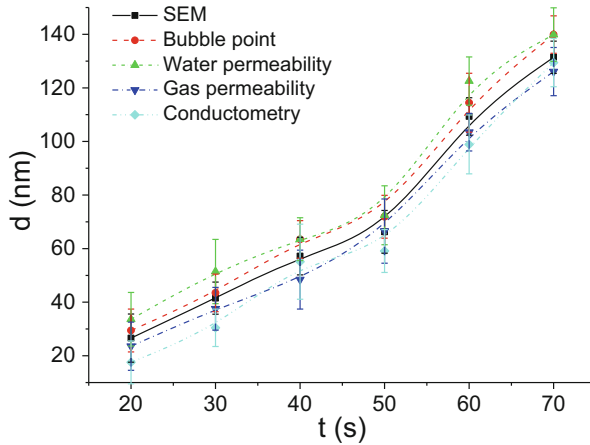


**Fig. 7.5** Changes in the pore diameter as etching time functions of the track membranes with  $10^9 \text{ cm}^{-2}$  pore density obtained by chemical etching of the irradiated PET films

the bubble diameter to the pore diameter, which in turn allows calculating the size of the largest pores in the template. At conducting measurements, the air pressure has gradually raised until occurrence of gas bulk flow (a condition in which the surface tension is overcome in the large pores due to the additional gas pressure with the liquid displacement that is accompanied by a sharp increase of the flow rate). This transitional pressure  $P$  called “bubble point” is due to the average value of the maximal diameter  $D$  with ratio which is valid for cylindrical pores (Laplace equation):

$$D = 4 \cdot \gamma \cdot (\cos \theta) / P, \quad (7.2)$$

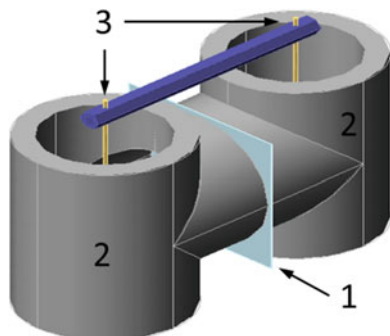
where  $D$  is a diameter of a capillary-shaped pore (microns);  $\gamma$  is a surface tension at the liquid-air border (for water 72 dyne/cm);  $\theta$  is a contact angle (moment of passing gas through a capillary means that the contact angle  $\theta$  is equal to zero ( $\cos \theta = 1$ ));  $P$  is a pressure value at moment of the bubble point formation. Pore diameters determined by the bubble point technique are shown in Fig. 7.5.

Taking into account that the bubble point corresponds to the greatest air flow through the template pores, the close values of the obtained information to the SEM results indicate a narrow distribution of pores by diameter.

The performance of track membranes by air has been studied by the manometric method of the gas permeability at a pressure differential up to 20 kPa. The effective pore diameter has been calculated according to the formula:

$$r^3 = \frac{Q \cdot 3l}{\sqrt{\frac{2\pi}{R \cdot T \cdot M}} \cdot \Delta p \cdot 4n}, \quad (7.3)$$

**Fig. 7.6** Cell scheme for measuring the current-voltage characteristics during the study of the pore diameter of track membranes by conductometric method. In the figure: (1) track membrane, (2) U-shaped tube, and (3) electrodes



where  $r$  is a pore radius,  $Q$  is an air capacity,  $l$  is the film thickness,  $\Delta p$  is a pressure applied,  $R$  is the universal gas constant,  $M$  is the air molar mass,  $n$  is a radiation density, and  $T$  is a temperature.

The membrane performance by water in  $\text{m}^3/\text{h} \cdot \text{m}^2$  has been determined by passing deionized water (18 Mohm) through a track membrane sample at a pressure difference of 15 kPa. Performance  $Q$  has been evaluated using the equation:

$$Q = \frac{n \cdot \pi \cdot r^4}{8\mu \cdot l} \cdot \Delta p, \quad (7.4)$$

where  $\mu$  is a dynamic viscosity of fluid. Pore diameters calculated during the determination of the track membrane performance by air and water are shown in Fig. 7.5.

Another method to determine the pore diameters, including an etching process, is the conductometric method. Figure 7.6 is a diagram of conductivity cell, used during the etching of the irradiated PET films.

The cell looks the U-shaped tube (2) which is filled with an electrolyte solution from both sides, wherein the track membrane (1) is placed between its two halves. The gold electrodes are used to create a potential difference between the chambers (3); the entire system impedance is determined by the voltage drop between them and the current value in the circuit. Since a track membrane is the insulating layer between the two chambers, the solution resistance in pores will determine the resistance of the whole system. The electric resistance of the  $R$  solution, filling the etched volume, is given by:

$$R = \int_0^l \frac{4}{\pi\sigma} \frac{dx}{d^2(x)} \quad (7.5)$$

where  $\sigma$  is a specific solution conductivity,  $l$  is a film thickness, and  $D(x)$  is a pore diameter at a distance  $x$  from the film surface. The diameter of cylindrical pores is associated with the electrical solution resistance in the membrane  $R$  by the expression [23]:

$$d^2 = \frac{4l}{\pi\sigma pR} \quad (7.6)$$

where  $p$  is a pore density (the irradiation fluence). The pore diameters obtained by conductometric method are shown in Fig. 7.5.

Comparison of pore diameter dependencies on etching time obtained by different methods (Fig. 7.5) indicates that the  $D$  values have slight differences which can be caused by the following reasons. The difference between results of SEM and other methods used in this study is associated with the fact a limited area has been examined at analyzing photomicrographs, while using the rest methods, the calculation has been carried out over the entire sample area. On the other hand, similar values of SEM, bubble point (maximal pore size in the sample), gas, and water permeability indicate a high quality of track membranes obtained under the selected etching conditions.

In Table 7.1 advantages and disadvantages of techniques used in this study are shown to facilitate comparison of different methods of determination of pore diameters in track membranes.

Having analyzed the data in the table, it can be seen that the methods have their own advantages and disadvantages despite all of them allow to determine the pore parameters. Thus, SEM studies provide the highly accurate measurements of sizes and shape and give direct information about the surface morphology, although the method is relatively labor-consuming and does not allow to conduct researches on large surface areas.

The hydrophilicity of the track membrane determination is the easiest method to conduct the express analysis in the laboratory, but it has low accuracy and does not provide direct information about the pore sizes and form, as well as the distribution character on the surface.

The calculation of the membrane performance for air and water (manometric method to determine the gas and water permeability) makes it possible to determine the effective diameter of the pores in the laboratory, as well as to evaluate important parameters for the practical use of track-etched membranes (performance for the air and different gases, performance for the water), but it does not provide any information about the surface morphology.

Determination of the bubble point makes it possible to get data about the maximal pore diameter, which provides comprehensive information about the quality of track membranes together with the SEM study, though the method is time-consuming, that is related to measuring the surface tension of the liquid.

Conductometry provides the possibility to determine the pore diameter by analyzing the current-voltage characteristics and is the only method that allows conducting researches during the etching process. At the same time, this process of determination of the pore parameters is quite time-consuming and gives only the average value of pore sizes.

**Table 7.1** Comparative analysis of methods to determine the track membrane parameters

Method	Advantages	Disadvantages
SEM	High accuracy; it gives a direct information about the surface morphology; allows determining the size, shape of pores (the study of chips), as well as their distribution over the surface	Requires a sample preparation and complicated equipment (SEM microscope); it is impossible to conduct researches on large surface areas
Determination of the hydrophilicity degree (measurement of a contact angle)	The possibility to conduct express analysis in the laboratory; no need to use complicated equipment; simplicity	Only a qualitative analysis; absence of the direct data about pore sizes; evaluation of pore shapes is impossible
The calculation of the membrane performance for air (manometric method of a gas permeability)	The possibility to determine the effective pore diameters in the laboratory and a membrane performance for air or various gases	The average value, complicated equipment
The calculation of the membrane performance for water (manometric method of a water permeability)	The possibility to determine the effective pore diameters in the laboratory and a membrane performance for water	The evaluation of pore shapes is impossible, the average value
Determination of the bubble point	The possibility to determine the maximal pore diameter	Time-consuming measurements related to determining the surface tension of the liquid used in the research
Conductometry	The possibility to determine the pore diameter by analyzing the voltage characteristics, as well as during the etching process [23]	Time-consuming process, sophisticated calculation. The average value for all pores

## 7.4 Conclusion

The formation of PET track membranes is comprehensively studied. Using XRD method, the evolution of polymer structures has been shown in various stages of the track membrane formation: under irradiation, UV sensitization, and etching.

Based on SEM studying the surface and the cross section of track membranes, the dynamics of changes in the pore shape and sizes has been demonstrated at different times of the etching. It is shown that pores have a cylindrical shape even at small pore diameters (small etching times). Etching time growth leads to the increase of the pore diameter with the simultaneous decrease of the average distance between them, at this case the pore shape is cylindrical. 110 nm pore diameters are critical at

$10^9 \text{ cm}^{-2}$  density, because the size growth leads to the overlap of large number of pores, which affects the mechanical strength of the track membrane.

The study of the track membranes by SEM methods, measuring the contact angle, determination of the bubble point, conductivity, as well as gas and water permeability, has found that all of these methods allow us to accurately determine the pore parameters and revealed to distinguish advantages and disadvantages of the methods use.

Similar values obtained by different methods indicate the narrow distribution of pores by diameter. Due to the unique ability to manage the parameters of porous templates, a high degree of controlling the etching process and narrow distribution of etching characteristics of individual pores, and also opportunity to obtain templates with relatively low cost and high quality, track membranes based on PET are indispensable material for applications such as porous matrices at template synthesis of various nanostructure types, as filters for fine purification of gases and liquids, for microfiltration processes to separate viruses and to fractionate colloidal solutions, and for hemofiltration and plasmapheresis procedures.

## References

1. Fleischer RL, Price PB, Walker RM (1975) Nuclear tracks in solids. University of California Press, Berkeley
2. Fink D (2004) Fundamentals of ion-irradiated polymers: fundamentals and applications, vol 1. Springer, Berlin/Heidelberg
3. Dallanora A, Marcondes TL, Bermudez GG, Fichtner PFP, Trautmann C, Toulemonde M, Papaléo RM (2008) Nanoporous SiO<sub>2</sub>/Si thin layers produced by ion track etching: dependence on the ion energy and criterion for etchability. *J Appl Phys* 104(2):24307–1–24307–8
4. Kaniukov EY, Ustarroz J, Yakimchuk DV, Petrova M, Terryn H, Sivakov V, Petrov AV (2016) Tunable nanoporous silicon oxide templates by swift heavy ion tracks technology. *Nanotechnology* 27(11):115305
5. Реутов ВФ, Дмитриев СН (2002) Ионно-трековая Нанотехнология. *Рос хим ж XLVI*(5):74–80
6. Fink D, Petrov AV, Hoppe K, Fahrner WR, Papaleo RM, Berdinsky AS, Chandra A, Chemseddine A, Zrineh A, Biswas A, Faupel F, Chadderton LT (2004) Etched ion tracks in silicon oxide and silicon oxynitride as charge injection or extraction channels for novel electronic structures. *Nucl Instrum Methods Phys Res Sect B Beam Interact With Mater Atoms* 218(1–4):355–361
7. Enculescu I, Sima M, Enculescu M, Matei E, Molares MET, Cornelius T (2008) Nickel nanotubes prepared by electroless deposition in ion track templates. *Optoelectron Adv Mater Rapid Commun* 2(3):133–136
8. Apel PY, Blonskaya IV, Dmitriev SN, Orelovitch OL, Presz A, Sartowska BA (2007) Fabrication of nanopores in polymer foils with surfactant-controlled longitudinal profiles. *Nanotechnology* 18(30):305302
9. Bercu B, Enculescu I, Spohr R (2004) Copper tubes prepared by electroless deposition in ion track templates. *Nucl Instrum Methods Phys Res Sect B Beam Interact With Mater Atoms* 225(4):497–502
10. Yamazaki IM, Paterson R, Geraldo LP (1996) A new generation of track etched membranes for microfiltration and ultrafiltration. Part I. Preparation and characterisation. *J Memb Sci* 118(2):239–245

11. Apel PY, Dmitriev SN (2011) Micro- and nanoporous materials produced using accelerated heavy ion beams. *Adv Nat Sci Nanosci Nanotechnol* 2(1):13002
12. Apel P, Spohr R, Trautmann C, Vutsadakis V (1999) Track structure in polyethylene terephthalate irradiated by heavy ions: let dependence of track diameter. *Radiat Meas* 31(1–6):51–56
13. Apel P, Schulz A, Spohr R, Trautmann C, Vutsadakis V (1998) Track size and track structure in polymer irradiated by heavy ions. *Nucl Instrum Methods Phys Res Sect B Beam Interact With Mater Atoms* 146(1–4):468–474
14. Apel PY, Blonskaya I, Oganessian V, Orellovitch O, Trautmann C (2001) Morphology of latent and etched heavy ion tracks in radiation resistant polymers polyimide and poly(ethylene naphthalate). *Nucl Instrum Methods Phys Res Sect B Beam Interact With Mater Atoms* 185(1–4):216–221
15. Vilensky AI, Zagorski DL, Apel PY, Pervov NV, Mchedlishvili BV, Popok VN, Mel'nik NN (2004) Thermal regression of latent tracks in the polymer irradiated by high energy heavy ions. *Nucl Instrum Methods Phys Res Sect B Beam Interact With Mater Atoms* 218:294–299
16. Zhu Z, Maekawa Y, Liu Q, Yoshida M (2005) Influence of UV light illumination on latent track structure in PET. *Nucl Instrum Methods Phys Res Sect B Beam Interact With Mater Atoms* 236(1–4):61–67
17. Mo D, Liu JD, Duan JL, Yao HJ, Latif H, Cao DL, Chen YH, Zhang SX, Zhai PF, Liu J (2014) Fabrication of different pore shapes by multi-step etching technique in ion-irradiated PET membranes. *Nucl Instrum Methods Phys Res Sect B Beam Interact With Mater Atoms* 333:58–63
18. Apel P (2001) Track etching technique in membrane technology. *Radiat Meas* 34(1–6):559–566
19. Apel PY, Blonskaya I, Didyk AY, Dmitriev S, Orellovitch O, Root D, Samoiloa L, Vutsadakis V (2001) Surfactant-enhanced control of track-etch pore morphology. *Nucl Instrum Methods Phys Res Sect B Beam Interact With Mater Atoms* 179(1):55–62
20. Flerov GN, Apel PY, Didyk AY, Kuznetsov VI, Oganessian RT (1989) Use of heavy-ion accelerators to produce nuclear membranes. *Sov At Energy* 67(4):763–770
21. Apel PY, Blonskaya IV, Orellovitch OL, Root D, Vutsadakis V, Dmitriev SN (2003) Effect of nanosized surfactant molecules on the etching of ion tracks: new degrees of freedom in design of pore shape. *Nucl Instrum Methods Phys Res Sect B Beam Interact With Mater Atoms* 209:329–334
22. Buford Price P (2005) Science and technology with nuclear tracks in solids. *Radiat Meas* 40(2–6):146–159
23. Oganessian VR, Trofimov VV, Vetter J, Danziger M, Dörschel B, Hermsdorf D (2003) Conductometric determination of single pores in polyethylene terephthalate irradiated by heavy ions. *Radiat Meas* 37(6):609–612
24. Apel PY, Korchev Y, Siwy Z, Spohr R, Yoshida M (2001) Diode-like single-ion track membrane prepared by electro-stopping. *Nucl Instrum Methods Phys Res Sect B Beam Interact With Mater Atoms* 184(3):337–346
25. Kozlovskiy A, Zhanbotin A, Zdorovets M, Manakova I, Ozernoy A, Kiseleva T, Kadyrzhanov K, Rusakov V, Kanyukov E (2016) Mossbauer research of Fe/Co nanotubes based on track membranes. *Nucl Instrum Methods Phys Res Sect B Beam Interact With Mater Atoms* 381:103–109
26. Kaniukov E, Kozlovsky A, Shlimas D, Yakimchuk D, Zdorovets M, Kadyrzhanov K (2016) Tunable synthesis of copper nanotubes. *IOP Conf Ser Mater Sci Eng* 110:12013
27. Kozlovskiy A, Meirimova T, Mashentseva A, Zdorovets M, Kanyukov E, Yakimchuk D, Petrov A, Kadyrzhanov K (2015) Electrochemical synthesis and crystal structure of ordered arrays of Co – nanotubes. *Chem Bull Kazakh Natl Univ* 3:72–80
28. Kozlovskiy A, Zdorovets M, Kanukov E, Shumskaya E, Kadyrzhanov K, Rusakov V (2016) Fe nanotubes: synthesis, structural and magnetic properties. *Chem Bull Kazakh Natl Univ* 2:4–11



29. Zdorovets M, Ivanov I, Koloberdin M, Kozin S, Alexandrenko V, Sambaev E, Kurakhmedov A, Ryskulov A, Physics N (2014) Accelerator complex based on DC-60 cyclotron. In: Proceedings of RuPAC2014. pp 287–289
30. Haeri M, Haeri M (2015) ImageJ plugin for analysis of porous scaffolds used in tissue engineering. *J Open Res Softw* 3(1):2–5 Ubiquity Press, London, United Kingdom
31. Clark PJ, Evans FC (1954) Distance to nearest neighbor as a measure of spatial relationships in populations. *Ecology* 35(4):445–453

# Chapter 8

## Current Spin-Orbit-Induced Microwave Magnetic Dynamics in Layered Nanostructures

A. M. Korostil and M. M. Krupa

### 8.1 Introduction

There is much current interest in dynamical processes in magnetically ordered systems both from scientific and technological viewpoints. The special interest is related to the problem of the intercoupling between a spin-polarized electron current and the magnetic dynamics in multilayer magnetic nanostructures that can be exhibited in such phenomena, as magnetic switching and a sustained precession of magnetic order vectors.

The interrelation between the spin-polarized current and magnetic order vectors in magnetic multilayer nanostructures [1–3], permitting their mutual control [4], constitutes the basis of the operation of novel nano-devices [5], some of them with properties of a magnetic random-access memory (MRAM) [6], magnetic logic, and coherent microwave radiation sources that present considerable fundamental and application interest [7, 8]. The operation of these devices can be based on both the spin-polarized current-induced and the current spin-orbit-induced magnetic dynamics including magnetic switching and precession [9–11]. Such phenomena have real potential for application in systems of high-speed magnetic processing information and high-frequency fine-tuned GHz and THz electromagnetic radiation.

The intercoupling between a spin current and magnetic state in magnetic nanostructures constitutes the basis of the current-induced manipulation by magnetic dynamics and vice versa, i.e., the magnetic state-induced manipulation by the spin current [12–15]. The spin current can be converted from an incoming

---

A.M. Korostil (✉) • M.M. Krupa  
Department of Physics of Magnetic Materials and Nanocrystalline Structures, Institute of Magnetism, National Academy of Sciences and Ministry of Education of Ukraine, Prospect Vernadsky, 36-b, Kyiv, 03142, Ukraine  
e-mail: [amand@rambler.ru](mailto:amand@rambler.ru)

charge current under internal effective magnetic fields of interactions of a different origin (including  $s$ - $d$  exchange and spin-orbit interactions) with corresponding features of the action of a spin torque on the magnetic states and their dynamics. Inducing magnetic dynamics such as the spin torque can cause switching and precession of the magnetic order vectors (including ferro- and antiferromagnetic orders) in magnetic nanolayers with ferromagnetic (FM) and antiferromagnetic (AF) interactions. The frequency of the magnetic dynamics is determined by the magnitude of magnetic exchange interaction, which is the largest for antiferromagnetic materials. The prospect of obtaining the technological magnetic nanostructures with low-threshold incoming currents, low power consumption, and controlled high-frequency operation is related to utilization of the spin-orbit effects of the spin polarization and magnetic nanostructures with AF exchange interactions.

Generally, the spin-orbit interaction includes the bulk spin Hall effect (SHE) [12, 13] of the transverse (relatively to an incoming current) deflection of electrons with opposite spins in opposite sides and the inverse spin Hall effect (ISHE) of conversion of a charge current into the transverse spin current. In two-dimensional structures (instance, interfaces), the spin-orbit interaction can be manifested via the Rashba spin-orbit effect [14, 15] of the spin splitting of an electron disperse along an electron wave vector. The impact of the spin current on the magnetic states realizes via the spin torque  $\mathbf{T}$  [16–18] consisting of so-called field-like and dumping-like parts  $T_{\parallel}$  and  $T_{\perp}$ , respectively, which are related to the effects of magnetic order switching and precession dumping or antidumping. The field-like torque  $T_{\parallel}$  originates predominantly by the spin-orbit coupling at the interface in combination with the perturbation of the electron distribution function. The torque  $T_{\perp}$  originates predominantly by the perturbation of electronic states by the applied electric field.

The current spin-orbit-controlled microwave magnetic dynamics is realized for nanostructures composed of a heavy metal nanolayer (for instance, Pt, Ta) possessing the strong enough spin-orbit interaction and the adjacent active magnetic nanolayer with a strong exchange interaction attaining maximum values of the order of tens THz in the AF cases. For multisublattice magnetic structures (for instance, for AF), a general magnetic dynamics is a combined effect of dynamics of each of the magnetic sublattices coupled by the strong exchange interaction.

The interconnection between the incoming charge current and magnetic dynamics occurs in the mentioned case via the spin current and the spin transfer effect for each sublattice. In such magnetic systems, the simultaneous action of SHE and the inverse SHE (of the transverse to spin current charge current) results in the feedback between the incoming charge current and the magnetic dynamics. This provides sustained steady-state spin torque magnetic oscillations, convertible via a magnetoresistance effect into an AC voltage and the current-driven high-frequency radiation.

The paper is organized as follows. In Sect. 8.2, features of the scattering of spin currents at the interfaces are studied in multilayer magnetic nanostructures with heavy metal sublayers. Section 8.3 is devoted to the dynamic feedback between a magnetization and controlling incoming charge current in ferromagnetic-layered nanostructures with heavy metal sublayers. The strong spin-orbit interaction, SHE,

and ISHE can provide the robustness of the magnetization precession converting via magnetoresistance effects into microwave radiation. In Sect. 8.4, features of spin pumping and spin transfer torques as two reciprocal phenomena are considered in AF-based nanostructures. Section 8.5 is devoted to the dynamic feedback between the controlling charge current and the magnetic dynamics in AF-layered magnetic nanostructures with heavy metal sublayers. In Sect. 8.6, spin Hall magnetoresistance effect (SME) of the impact of the magnetization dynamics on the resistance of the incoming charge current is considered in the bilayer AF nanostructures with insulating AF layers and adjusted heavy metal sublayers as the result of simultaneous action of SHE and ISHE.

## 8.2 Spin and Charge Currents in Magnetic Nanostructures with Normal Heavy Metal Sublayers

Features of the electron transport in the mentioned magnetic nanostructures are related to the spin-dependent scattering on interfaces. The electron scattering on the normal metal (NM)/magnetic metal (M) interface represents the special interest for magnetic heterostructures with the strong spin-orbital interaction and SHE. In the ferromagnetic case, by scattering theory [19], the spin current  $j_s^{(N|F)}$  through an N|F interface (on the N side, flowing into F) can be expressed in terms of the F magnetization  $\mathbf{M}$  and the (vector) spin accumulation  $\boldsymbol{\mu}_{sN}$  in N:

$$\mathbf{j}_{sN}(\mathbf{m}) = (j_{\uparrow} - j_{\downarrow}) \mathbf{m} - \frac{1}{e} (G_r \mathbf{m} \times (\mathbf{m} \times \boldsymbol{\mu}_{sN}) + G_i (\mathbf{m} \times \boldsymbol{\mu}_{sN})) \quad (8.1)$$

where  $\mathbf{m} = \mathbf{M}/|\mathbf{M}|$ ,  $e = -|e|$  is the electron charge, and

$$j_{\uparrow(\downarrow)} = \frac{G_{\uparrow(\downarrow)}}{e} [(\mu_{cN} - \mu_{cF}) \pm (\mathbf{m} \cdot \boldsymbol{\mu}_{sN} - \mu_{sF})] \quad (8.2)$$

is the flow of electrons with spin-up and spin-down along  $\mathbf{m}$  driven by the difference between effective charge chemical potentials in N and F ( $\mu_{cN} - \mu_{cF}$ ) and the difference between spin accumulations at both sides of the interface ( $\mathbf{m} \cdot \boldsymbol{\mu}_{sN} - \mu_{sF}$ ).

The spin-dependent conductance at the interface

$$G_{\uparrow(\downarrow)} = G_0 \sum_{nm} \left[ \delta_{nm} - |r_{nm}^{\uparrow(\downarrow)}|^2 \right] \quad (8.3)$$

where  $G_0 = e^2/\hbar$  is the conductance quantum, related to the spin-dependent reflection coefficient  $r_{nm}^{\uparrow(\downarrow)}$  corresponding to the electron transition between quantum states  $n$  and  $m$  in with spin projections  $\uparrow$  and  $\downarrow$ , respectively, in N. Conductance  $G_r$  and  $G_i$  in (8.1) are determined as real and imaginary parts of the spin-mixing conductance

$$G_{\uparrow\downarrow} = G_0 \sum_{nm} \left[ \delta_{nm} - \left( r_{nm}^{\uparrow} \right) \left( r_{nm}^{\downarrow} \right)^* \right] \quad (8.4)$$

i.e.,  $G_{r(i)} = \text{Re}(\text{Im})G_{\uparrow\downarrow}$  is related to spin-flip electron scattering at the interface.

Due to (8.1), the longitudinal (with respect to the magnetization in F) component of the spin current  $(j_{\uparrow} - j_{\downarrow})\mathbf{m}$  can flow in a metallic F. At the same time, its transverse components are absorbed at the interface on the atomic length scale and act as a torque on the magnetization. The corresponding spin transfer torque (STT) at the interface is described by the expression

$$\mathbf{T}_{\text{STT}} = \frac{\hbar}{2e} \mathbf{m} \times \left( \mathbf{m} \times \mathbf{j}_s^{(N|F)} \right) \quad (8.5)$$

Specially, large STT is realized in the current-in-plane (CIP) configuration with the spin current generated by the SHE [20–22] in the N layer and converted to a magnetization torque by the exchange interaction at the interface. This contributes a so-called “damping-like” torque proportional to  $G_r$  with symmetry identical to the exchange-mediated term. On the other hand, the Rashba spin-orbit effect at the interface may generate a spin accumulation that acts on the magnetization exerting a “field-like” torque corresponding to  $G_i$ .

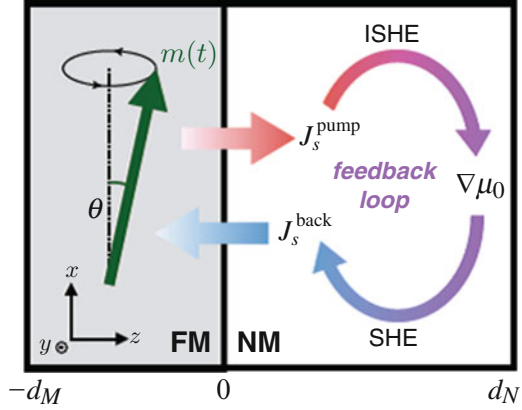
### 8.3 Robustness of Ferromagnetic Dynamics

In ferromagnetic/normal metal heterostructures, the spin pumping and the spin transfer torque are two reciprocal processes that occur concomitantly. Their interplay introduces a dynamic feedback effect interconnecting energy dissipation channels of both magnetization and current. The solution of the spin diffusion process in the presence of the SHE in the NM shows that the dynamic feedback gives rise to a nonlinear magnetic damping that is crucial to sustain uniform steady-state oscillations of a spin Hall oscillator [23–25].

In ferromagnetic (FM)/normal metal (NM) heterostructures, nonlocal effects arise because conduction electrons and magnetization reside in different materials and couple only at the interface. In this regime, spin pumping plays the role of spin electromotive force, which refers to the generation of spin current from a precession FM into the NM [25]. The pumped spin current is accompanied by a backflow of spin current [24, 25], which reacts on the FM through the spin transfer torque (STT). The combined effect of spin pumping and backflow-induced STT renormalizes the spin-mixing conductance at the interface [17, 23]. However, in the presence of the SHE, spin pumping and spin backflow are also connected by the combined effect of the SHE and its inverse process ISHE, which forms a feedback loop as illustrated in Fig. 8.1.

This additional feedback mechanism, proportional to the SH angle squared,  $\theta_s^2$ , is essential to the electron transport in FM/NM heterostructures. Consequently, this

**Fig. 8.1** A FM/NMS bilayer, spin pumping, and backflow are connected by the SHE and its inverse process (ISHE)



feedback effect is important to the magnetization dynamics. In a reciprocal sense, if we apply an AC current density to the NM, the SHE will drive the magnetization precession via the STT, which in turn can pump spin current back into the NM and renormalize the resistivity by means of the ISHE.

The feedback effect qualitatively modifies the dynamical behavior of an FM/NM heterostructure. The feedback manifests as a novel nonlinear damping effect in the magnetization dynamics. It enables uniform auto-oscillations of a spin Hall oscillator and prevents magnetic switching. The feedback effect gives rise to a spin Hall magnetoimpedance in the electron transport, which reduces to the observed SMR in the DC limit.

Consider a FM/NM bilayer structure represented in Fig. 8.1 with the layer thicknesses are  $d_M$  and  $d_N$ , respectively. The coordinate system is chosen such that the magnetization direction at rest is along  $x$ , and the interface normal is along  $z$ . It is assumed that the FM is insulating (e.g., YIG), but the essential physics remains valid for a conducting FM since the feedback process takes place only on the NM side. In terms of the electrochemical potential  $\mu_0/2$  and the vector of spin accumulation  $\boldsymbol{\mu}$  in the NM, the charge and spin current densities  $J_i^c$  and  $J_{(ij)}^s$ , respectively, are described by the expression  $J_{i(j)}^{c(s)} = -\frac{\sigma}{2e}(\partial_i\mu_{0(j)} \pm \theta_s\varepsilon_{ijk}\partial_{j(k)}\mu_k(0))$  with the transport direction  $i$ , the spin polarization direction  $j$ , the conductivity  $\sigma$ , and the electron charge  $e$ . In a given device geometry, only the spin current flowing along  $z$ -direction is relevant, and so  $\boldsymbol{\mu} = \boldsymbol{\mu}(z, t)$ . Correspondingly, the spin (charge) current density reduces to a vector  $\boldsymbol{J}_{z(c)}$ . The electron and spin dynamics in the NM are described by equations

$$\frac{\partial \boldsymbol{\mu}}{\partial t} = D \frac{\partial^2 \boldsymbol{\mu}}{\partial z^2} - \frac{1}{\tau_{sf}} \boldsymbol{\mu} \quad (8.6)$$

$$\boldsymbol{J}_c = -\frac{\sigma}{2e} \left[ \nabla \mu_0 + \theta_s \boldsymbol{z} \times \frac{\partial \boldsymbol{\mu}}{\partial z} \right] \quad (8.7)$$

$$\mathbf{J}_s = -\frac{\sigma}{2e} \left[ \frac{\partial \boldsymbol{\mu}}{\partial z} + \theta_s \mathbf{z} \times \nabla \mu_0 \right] \quad (8.8)$$

where  $D$  is the diffusion constant and  $\tau_{sf}$  is the spin-flip relaxation time.

To solve the spin accumulation  $\boldsymbol{\mu}$ , we assume that the charge current density  $\mathbf{J}_c$  is fixed by external circuit and is uniform in space. Besides that, we have two boundary conditions  $\mathbf{J}_s(d_N) = 0$  and

$$\mathbf{J}_{s0} = \frac{G_r}{e} \left[ \mathbf{m} \times (\mathbf{m} \times \boldsymbol{\mu}_{s0}) + \hbar \mathbf{m} \times \dot{\mathbf{m}} \right] \quad (8.9)$$

where  $\boldsymbol{\mu}_{s0} = \boldsymbol{\mu}(0)$  and  $G_r$  is the real part of the areal density of the spin-mixing conductance and the imaginary part is the real part of the areal density of the spin-mixing conductance (the imaginary part  $G_i$  is neglected since  $G_r \gg G_i$ ). In the right-hand side of (8.9), the first term is the STT and the second term is the spin pumping. They are two fundamental ingredients bridging the electron (spin) transport in the NM with the magnetization dynamics of the FM. Due to the conservation of spin angular momentum, the spin current density  $\mathbf{J}_{s0}$  is absorbed by the FM, which is reflected by the Landau-Lifshitz-Gilbert (LLG) equation

$$\frac{d\mathbf{m}}{dt} = \gamma \mathbf{H}_{eff} \times \mathbf{m} + \alpha_0 \mathbf{m} \times \frac{d\mathbf{m}}{dt} + \frac{\hbar \gamma_{ex}}{2eM_s d_M} \mathbf{J}_{s0} \quad (8.10)$$

$M_s$  is the saturation magnetization,  $\alpha_0$  is the Gilbert damping constant, and  $\mathbf{H}_{eff}$  is the effective magnetic field.

For typical FMs, the magnetization dynamics is much slower than the spin relaxation rate in the NM so that  $\omega r_{sf} \ll 1$ . In this limit, the spin accumulation  $\boldsymbol{\mu}(z, t)$  adapts to the instantaneous magnetization orientation and is kept quasi-equilibrium. As a result, the spin dynamics described by (8.6) reduces to a stationary spin diffusion process at any specified time. Retaining to second order in  $\theta_s^2$  in (8.6) gives

$$\boldsymbol{\mu}(z) = \frac{2e\lambda}{\sigma} \left\{ \theta_s \Lambda_1(z) \mathbf{z} \times \mathbf{J}_c - \Lambda_2(z) \left[ \mathbf{J}_{s0} + \theta_s^2 \mathbf{z} \times (\mathbf{z} \times \mathbf{J}_{s0}) \right] \right\} \quad (8.11)$$

where  $\lambda = \sqrt{D\tau_{sf}}$  is the spin diffusion length,  $\Lambda_1(z) = \sinh A(z)/\cosh A(0)$ , and  $\Lambda_2(z) = \cosh B(z)/\sinh B(0)$  with  $A(z) = (2z - d_N)/2\lambda$  and  $B(z) = (z - d_N)/\lambda$ . Here, the  $t$  variable in  $\boldsymbol{\mu}(z)$  is suppressed since its time dependence simply originates from  $\mathbf{J}_c$  and  $\mathbf{J}_{s0}$ . The dynamic feedback mechanisms are realized via an effective magnetization dynamics and an effective electron magneto-transport which are described by the system (8.6, 8.7, 8.8, 8.9, 8.10, and 8.11) after elimination electron degrees of freedom ( $\mathbf{J}_c$  and  $\mathbf{J}_{s0}$ ) and the time derivative of the magnetization, respectively.

The DC charge current ( $\mathbf{J}_c$ ) applied to normal metal nanolayer (Fig. 8.1), due to the SHE, induces the total spin current density  $\mathbf{J}_{s0}$  flowing across the interface. The feedback effect is expressed in the intercoupling between the spin current

density  $\mathbf{J}_{s0}$  and the magnetization  $\mathbf{m}(t)$  without any electron degree of freedom, by which the LLG (8.10) will no longer involve any electron degrees of freedom. The combination of (8.9) and (8.11) results in two convoluted relations of  $\mathbf{J}_{s0}$  and  $\boldsymbol{\mu}_{s0}$ , from which the solution for  $\mathbf{J}_{s0}$  as a function of  $\mathbf{J}_c$ ,  $\mathbf{m}(t)$  and its time derivative can be obtained. Substituting this solution into (8.10) yields the effective magnetization dynamics

$$\frac{d\mathbf{m}}{dt} = \gamma \mathbf{H}_{eff} \times \mathbf{m} + \omega_s \mathbf{m} \times [(\mathbf{z} \times \mathbf{j}_c) \times \mathbf{m}] + (\alpha_0 + \alpha_{sp}) \mathbf{m} \times \frac{d\mathbf{m}}{dt} \quad (8.12)$$

where  $\mathbf{j}_c$  is the unite vector of  $\mathbf{J}_c$  and

$$\omega_s = \theta_s J_c \frac{\hbar \gamma}{e M_s d_M} \frac{\lambda G_r \tanh \frac{d_N}{2\lambda}}{\sigma + 2\lambda G_r \coth \frac{d_N}{\lambda}} \quad (8.13)$$

is the strength of the STT (driven by  $\mathbf{J}_c$ ) scaled in the frequency dimension. The two damping coefficients are described by the expression

$$a_{sp(fb)} = \frac{(\lambda \theta_s^2 \beta)^{0(1)} \hbar^2 \gamma}{2e^2 M_s d_M} \frac{\sigma G_r}{(\sigma + 2\lambda G_r \beta)^{1(2)}} \quad (8.14)$$

where  $\beta = \coth(d_N/\lambda)$ . Here,  $\alpha_{sp}$  describes the conventional enhanced damping from spin pumping with the spin backflow effects taken into account [25]; it is independent of the SHE. By contrast, the  $a_{fb}$  term reflects the dynamic feedback realized by virtue of the combined effect of the SHE and its inverse process as schematically shown in Fig. 8.1. By virtue of (8.10), this damping term is nonlinear in  $\mathbf{m}_\perp$  – the component of  $\mathbf{M}$  transverse to the effective field  $\mathbf{H}_{eff}$  – whereas the Gilbert damping term is linear in  $\mathbf{m}_\perp$ .

The feedback-induced nonlinear damping effect can be explained in the following way. If the magnetization precession is getting larger, it will trigger a chain reaction: first, the pumped spin current  $\mathbf{J}_{s0}$  increases, and then the spin diffusion becomes stronger (i.e.,  $|\partial_z \boldsymbol{\mu}|$  gets larger). This will necessarily lead to a larger  $\nabla \mu_0$  in the NM according to (8). Finally, the change of the emf will feed back into  $\mathbf{J}_{s0}$  according to (8.9), preventing its further increase. Therefore, the growing magnetization precession is inhibited. The entire process realizes a negative feedback.

## 8.4 Spin Currents in Antiferromagnetic Nanostructures

The spin pumping and spin transfer torque in antiferromagnetic (AF)-based nanostructures represent the combined effect of their action in each of magnetic sublattices coupled by a strong AF exchange interaction. Magnetization dynamics of these



coupled sublattices leads to an AF order ( $\mathbf{l}$ ) dynamics manifesting as precession and switching. Similarly to the magnetization in the ferromagnetic case, the AF order precession generates the spin pumping current, which via the ISHE in adjacent nonmagnetic nanolayers can convert into the transverse charge current. Thereby, in AF nanostructures the influence of the AF dynamics on the charge current occurs in AF nanostructures [26]. The inverse impact of the charge current on the AF precession is realized via the SHE effect of the conversion of the charge current into the transverse spin current, which owing to the exchange interaction exerts the spin transfer torque on the AF order precession.

Characteristic features of the AF dynamics and its interconnection with the spin currents in the form of the precession-induced spin pumping and spin transfer torque are manifested in the AF two-sublattice model with an easy axis directed along the axis  $z$  and magnetization unit vectors  $\mathbf{m}_1$  and  $\mathbf{m}_2$ . These vectors are driven by the exchange interaction, the anisotropy, and a magnetic field in the  $z$  direction. In units of frequency, they are represented by  $\omega_E$ ,  $\omega_A$ , and  $\omega_H = \gamma H_0$ , respectively. The equations of motion in a free precession approximation are

$$\begin{aligned}\dot{\mathbf{m}}_1 &= \mathbf{m}_1 \times [\omega_E \mathbf{m}_2 - (\omega_E + \omega_H) \mathbf{z}], \\ \dot{\mathbf{m}}_2 &= \mathbf{m}_2 \times [\omega_E \mathbf{m}_1 - (\omega_E - \omega_H) \mathbf{z}],\end{aligned}\quad (8.15)$$

where the effective field causing the magnetization precession in a magnetic sublattice contains the contribution from the exchange interaction with an adjacent magnetic sublattice. In linear response, when  $\mathbf{m}_{1(2)} = \pm \mathbf{z} - \mathbf{m}_{1(2),\perp} \exp i\omega t$  at  $|\mathbf{m}_{\perp}| \ll 1$ , the resonance frequencies are then

$$\omega = \omega_H \pm \omega_R = \omega_H \pm \sqrt{\omega_A (\omega_A \pm 2\omega_E)} \quad (8.16)$$

where the two corresponding eigenmodes are characterized by different chiralities. In the left-handed (right-handed) mode, both  $\mathbf{m}_1$  and  $\mathbf{m}_2$  undergo a circular clockwise (counterclockwise) precession with  $\pi$  phase difference. In the absence of magnetic field, viz.,  $\omega_H = 0$ , the two modes are degenerate.

Since without the AF interaction spin current pumped from each of two magnetic sublattices is proportional to  $\mathbf{m}_{1(2)} \times \partial_t \mathbf{m}_{1(2)}$ , the total pumped spin current is roughly proportional to  $\mathbf{l} \times \partial_t \mathbf{l}$ , where  $\mathbf{l} = (\mathbf{m}_1 - \mathbf{m}_2)/2$  denotes the staggered field. The different cone angles  $\theta_1$  and  $\theta_2$  of  $\mathbf{m}_1$  and  $\mathbf{m}_2$ , respectively, result in an induced small magnetization  $\mathbf{m} = (\mathbf{m}_1 + \mathbf{m}_2)/2$ . These cone angles obey the relation  $\theta_2/\theta_1 = \eta$ , where  $\eta \approx \left(1 + \sqrt{\omega_A/\omega_E}\right)^2$ .

The spin currents in AF nanostructure determined by mixed scattering channels associated with different sublattices on a N|AF interface. Typical AF materials are insulators, and incident electrons from the normal metal cannot penetrate far. Only a single atomic layer of AF directly connected to N suffices to describe the dominant contribution to interface scattering. Therefore, the essential physics is captured by modeling the N|AF interface as being semi-infinite in the transport direction and infinite in the transverse direction.

Features of kinetics of the polarized electrons in the considered AF nanostructures are described by their scattering matrix ( $S$ ) near interfaces. In the nearest-neighbor tight-binding model on a cubic lattice, this matrix in a linear in the small magnetization approximation is described by the general expression

$$S = S_0 + S_\omega \tau_1 \sigma_0 + \Delta S [\tau_3 (\mathbf{l} \cdot \boldsymbol{\sigma}) + \tau_0 (\mathbf{m} \cdot \boldsymbol{\sigma})] \quad (8.17)$$

where  $\tau_{1,2,3}$  are pseudospin Pauli matrices for sublattice degree of freedom,  $\boldsymbol{\sigma}$  are the vector of spin Pauli matrices, and  $\tau_0$  and  $\sigma_0$  are identity matrices. The last two terms of (8.17) with a common coefficient  $\Delta S$  are spin dependent and represent umklapp and normal scatterings, respectively. Pumping currents are related to the coefficients in (8.17) through the spin-mixing conductance  $G_{\uparrow\downarrow} = G_r + iG_i$ , where

$$G_j = (e^2 A / \hbar \pi^2) \iint dk_y dk_z (\delta_{j,r} |\Delta S|^2 + \delta_{j,i} \text{Im} [S_0^* \Delta S]), \quad j = (r, i),$$

where  $A$  is the interface cross section and  $k_y$  and  $k_z$  are the transverse momenta.

Although the AF resonance frequency reaches the THz region ( $1 \sim 10$  meV), the motion of the staggered field remains adiabatic. The spin eigenstates and the scattering matrix (8.17) adiabatically adapt to the instantaneous configuration of AFs. Regarding the staggered field  $\mathbf{l}$  and the magnetization  $\mathbf{m}$  as two independent adiabatic parameters [24, 27, 28], the pumped spin current  $\mathbf{I}_s$  with the scattering matrix can be obtained in the form

$$\mathbf{I}_s = \frac{e}{\hbar} \left[ G_r (\mathbf{l} \times \dot{\mathbf{l}} + \mathbf{m} \times \dot{\mathbf{m}}) - G_i \dot{\mathbf{m}} \right] \quad (8.18)$$

This expression arises from a coherent sum of two independent spin pumping contributions by  $\mathbf{m}_1$  and  $\mathbf{m}_2$ . Due to the mixing of scattering channels from different magnetic sublattices, the spin-mixing conductance  $G_r$  and  $G_i$  are different from those of F. Moreover, AF dynamics is much faster than F that corresponds to a stronger spin pumping.

By taking a time average of (8.18) over one period of oscillation, only the first two terms survive and contribute to the DC component of spin current  $I_s^{dc}$ . Despite that  $|\dot{\mathbf{m}}| \ll |\dot{\mathbf{l}}|$ , the contribution of  $\mathbf{m} \times \partial_t \mathbf{m}$  to  $I_s^{dc}$  can be comparable to that of  $\mathbf{l} \times \partial_t \mathbf{l}$ . This is because  $I_s^{dc}$  is proportional to the precession cone angle  $\theta^2$  and the cone angle associated with the staggered field is much smaller than the one associated with the magnetization,  $\theta_l \approx 0$  but  $\theta_m \approx \pi/2$ .

From the sublattice degree of freedom involved in the AF dynamics, it follows a staggered spin pumping. A staggered spin current represents the imbalance between the spin current carried by the two sublattices. It has three components  $\mathbf{I}_{ss}^{(i)}$  ( $i = 1, 2, 3$ ) associated with three pseudo-spin Pauli matrices, from which after the time average only the component

$$\mathbf{I}_{ss}^{(3)} = \frac{\hbar}{e} G_r \left( \mathbf{l} \times \dot{\mathbf{m}} + \mathbf{m} \times \dot{\mathbf{l}} \right) - G_i \dot{\mathbf{l}} \quad (8.19)$$

survives. Elastic scattering in the normal metal will destroy any staggered spin accumulation, which decays on the time scale of  $\hbar/t$ . Therefore, the staggered spin current is defined within a distance of the mean free path away from the interface.

The reciprocal effect of spin pumping is STT, which describes the back action that a spin current exerts on the AF. In linear response, an AF is driven by two thermodynamic forces  $\mathbf{f}_l = -\delta F/\delta \mathbf{l}$  and  $\mathbf{f}_m = -\delta F/\delta \mathbf{m}$  (energy dimension), where

$$F = \frac{\hbar}{2} \int dv \left[ \frac{\omega_0}{a^2} \mathbf{m}^2 + \frac{\omega_l}{a\omega_H} \sum_i (\partial_i \mathbf{l})^2 - \omega_H \mathbf{H} \cdot \mathbf{m} \right] \quad (8.20)$$

is the free energy. Here  $\omega_0 = \omega_A + 2\omega_E$  and  $\omega_l$  are the homogeneous and inhomogeneous exchange frequencies, respectively. Enforced by  $\mathbf{m} \cdot \mathbf{l} = 0$  and  $(\mathbf{l})^2 \approx 1$ , the symmetry allowed dynamics described by the system [25, 26]

$$\hbar \dot{\mathbf{l}} = (a^3/v) \mathbf{f}_m \times \mathbf{l} \quad (8.21a)$$

$$\hbar \dot{\mathbf{m}} = (a^3/v) \mathbf{f}_l \times \mathbf{l} + \mathbf{f}_m \times \mathbf{m} \quad (8.21b)$$

where  $v$  is the system volume. Inserting them into (8.18) gives the response of the spin current to  $\mathbf{f}_m$  and  $\mathbf{f}_l$ . Invoking the Onsager reciprocity relation, we derive the response of  $\mathbf{l}$  and  $\mathbf{m}$  to a given spin voltage  $\mathbf{V}_s$  in the normal metal, which are identified as two STT terms  $\mathbf{T}_l$  and  $\mathbf{T}_m$ . To linear order in  $\mathbf{m}$

$$\begin{aligned} \mathbf{T}_l &= -\frac{\alpha^3}{ev} [G_r \mathbf{l} \times (\mathbf{m} \times \mathbf{V}_s) - G_i \mathbf{l} \times \mathbf{V}_s], \\ \mathbf{T}_m &= -\frac{\alpha^3}{ev} G_r \mathbf{n} \times (\mathbf{m} \times \mathbf{V}_s), \end{aligned} \quad (8.22)$$

that treats STTs on the two sublattices as completely independent.

In solving the AF dynamics, it is instructive to eliminate magnetization and derive a closed equation of motion in terms of  $\mathbf{l}$  alone [27–30]. In the linear approximation in  $\mathbf{V}_s$ ,  $\mathbf{m}$ , and  $\partial_i \mathbf{l}$ , the effective dynamics is described by the equation

$$\mathbf{l} \times \left( \ddot{\mathbf{l}} + \alpha \omega_0 \dot{\mathbf{l}} + \omega_R^2 \mathbf{l}_\perp \right) = \frac{\omega_0 a^3 G_r}{ev} \mathbf{l} \times \mathbf{l} \times \mathbf{V}_s \quad (8.23)$$

where  $\alpha$  is the Gilbert damping constant and  $\mathbf{l}_\perp$  are perpendicular components of  $\mathbf{l}$  with respect to the easy axis. Since the STT only acts on the interface for a thin AF film, a possible nonuniform motion of  $\mathbf{l}$  is disregarded.

At small enough  $\mathbf{V}_s$  collinear with the easy axis, the solution for a spectrum of (8.23) characterizes by a negative imaginary part of the frequency  $\omega$  so that any perturbed motion will decay exponentially in time and the system is stable. However, a sufficiently large  $\mathbf{V}_s$  flips the sign of  $\text{Im}[\omega]$ , which makes the system

unstable and marks the onset of uniform AF excitation. The condition  $\text{Im}[\omega] = 0$  determines the threshold spin voltage  $V_s^{th} = \pm (ev \alpha \omega_l) / (a^3 G_r)$ , where  $+(-)$  corresponds to the excitation of the right-handed (left-handed) mode.

## 8.5 Dynamic Feedback in Antiferromagnetic/Spin Hall Structures

In the framework the current-induced dynamics of insulating antiferromagnets in a spin Hall geometry and sufficiently large in-plane currents perpendicular to the Néel AF order can trigger spontaneous oscillations at frequencies between the acoustic and the optical eigenmodes [17, 23, 26]. The direction of the driving current determines the chirality of the excitation. When the current exceeds a threshold, the combined effect of current-induced torques and spin pumping introduces a dynamic feedback that sustains steady-state oscillations with amplitudes controllable via the applied current. This permits to obtain the SH nano-oscillator with operating frequencies in THz range.

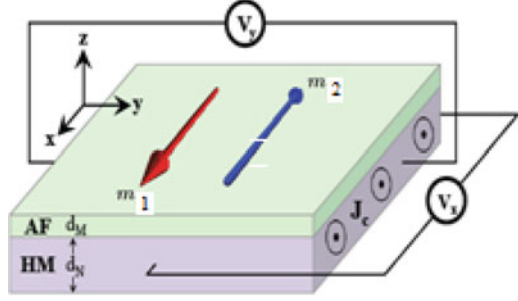
When an applied STT compensates the magnetic damping, the magnetization becomes unstable: it either switches to another direction or evolves into a steady-state oscillation. While the former improves writing operations in magnetic memory devices, the latter enables sustainable AC signal generation from DC inputs, giving rise to spin torque oscillators (STOs) [31, 32]. In ferromagnets, currents or magnetic fields can tune the STO output frequency from the MHz to the GHz regime.

STOs can potentially be operated at much higher THz frequencies when antiferromagnets (AFs) replace ferromagnets. It is possibly owing to the THz range of the eigenfrequencies of typical AFs and possibility of spontaneous excitations of an AF by anti-damping STTs. While most AFs are insulators where STTs cannot be operated by passing through a current, the SHE can produce STTs even when electrons do not flow through the magnet [31]. Therefore, integrating STOs with the SHE paves the way toward low-dissipation spin Hall nano-oscillators (SHNOs) [6].

However, to realize AF-based SHNOs, current-induced excitations should not grow indefinitely, but instead should evolve into steady-state oscillations and generate a substantial AC output. Although an AF under the action of an anti-damping STT does not suffer magnetic switching, its Néel AF vector experiences either no dynamics or a right-angle precession around the direction of the spin accumulation [18]. Since the oscillation amplitude is not continuously tunable via the applied current, the device does not meet the requirements of an SHNO.

Steady-state oscillations are realizable in ferromagnetic STOs for the following reasons. In a spin valve device, the angle dependence of the Gilbert damping and that of the anti-damping STT differs. As a result, when the driving current is above the threshold, there exists a unique angle where the two competing effects compensate.

**Fig. 8.2** An insulating AF/HM heterostructure. The applied DC current density  $J_c$  drives the AF via the SHE. The dynamics of the AF pumps spin current back into N, and converts into electric field via the ISHE, which is monitored by two voltmeters



Then, a steady-state oscillation is stabilized at that angle. However, this features no longer active where the SHE creates the anti-damping STT. Therefore, one needs to introduce alternative mechanisms to prevent a spontaneous excitation from growing into magnetic switching.

Solution of the mentioned problem is based on the use of a feedback mechanism [17] that is realizable in an AF/heavy metal heterostructure. The feedback effect originates from the combined effect of the SHE and its reverse process that connects the spin pumping with the spin backflow [33, 34], which is independent of the dipolar interaction. The threshold of spontaneous excitations is determined via solving the AF order dynamics in the linear response regime. The correlation between the threshold and a current density is related to the SHE in the heavy metal. The feedback is indispensable to sustain uniform auto-oscillation properties of magnetic dynamics of the AF in device geometry in Fig. 8.2 and can be described in the framework of two-sublattice crystal structure with the magnetizations vectors  $m_1$  and  $m_2$ .

The magnetic dynamics is characterized by the AF vector  $l = (m_1 - m_2)/2$  and the small magnetization  $m = (m_1 + m_2)/2$  and angular frequencies  $\omega_{\perp}$ ,  $\omega_{\parallel}$ , and  $\omega_E$  corresponding to the hard axis, easy plane anisotropy, and the Heisenberg exchange interaction, respectively. In the macrospin description, the free energy is

$$F = -\hbar\omega_3 l^2 - \hbar \sum_{i=1,2} \frac{\omega_i}{2} \left( (r_i l)^2 + (r_i m)^2 \right) \quad (8.24)$$

where  $\omega_3 = \omega_E + \omega_{\perp}$ ,  $\omega_{1(2)} = \omega_E + \omega_{\parallel(\perp)}$ , and  $r_{1(2)} = x(z)$ , which defines thermodynamic forces,  $\hbar f_{l(m)} = -\partial F/\partial l(m)$ . The coupled equations of motion are

$$\dot{l} = f_2 \cdot (m, l) + \alpha (m \times \dot{l} + l \times \dot{m}) + T_l \quad (8.25)$$

$$\dot{m} = f_1 \cdot (m, l) + \alpha (m \times \dot{m} + l \times \dot{l}) + T_m \quad (8.26)$$

where  $\mathbf{f}_{1(2)} = (\mathbf{f}_{m(l)} \times, \mathbf{f}_{l(m)} \times)$ , (here the sign “ $\times$ ” denotes the vector multiplication),  $\alpha$  is the Gilbert damping constant, and the STTs given (see [13, 21]) by

$$\begin{aligned} \mathbf{T}_m &= \mathbf{l} \times (\boldsymbol{\omega}_s \times \mathbf{l}) + \mathbf{m} \times (\boldsymbol{\omega}_s \times \mathbf{m}), \\ \mathbf{T}_l &= \mathbf{l} \times (\boldsymbol{\omega}_s \times \mathbf{m}) + \mathbf{m} \times (\boldsymbol{\omega}_s \times \mathbf{l}). \end{aligned} \quad (8.27)$$

Here the STT strength is determined via the vector of spin accumulation  $\boldsymbol{\omega}_s$ . The vector decomposition  $\mathbf{l} = \mathbf{x} + \mathbf{l}_\perp \exp i\omega t$  in (8.26) results in the eigenfrequency expression

$$\omega_\pm = i\omega_E\alpha + \left[ \omega_E^2\omega' \pm \omega_E \sqrt{\omega_\perp^2 - 4\omega_s^2} \right]^{1/2} \quad (8.28)$$

where  $\omega' = \omega_\perp + 2\omega_\parallel - \alpha^2$ ,  $+$  ( $-$ ) denotes the optical (acoustic) mode. As  $\omega_s$  increase, the real parts  $\text{Re}[\omega_+]$  and  $\text{Re}[\omega_-]$  approach each other until they become degenerate at  $\omega_s = \omega_\perp/2$ . The imaginary parts  $\text{Im}[\omega_+]$  and  $\text{Im}[\omega_-]$  remain degenerate and unaffected for  $\omega_s < \omega_\perp/2$ . When  $\omega_s > \omega_\perp/2$ ,  $\text{Im}[\omega_+]$  ( $\text{Im}[\omega_-]$ ) reduces (grows) rapidly, indicating that the damping is diminished (enhanced) by the STT.

At the threshold [18],

$$\omega_s^{th} = \sqrt{\frac{\omega_\perp^2}{4} + \alpha^2 (2\omega_\parallel + \omega_\perp) \omega_E} \quad (8.29)$$

$\text{Im}[\omega_+]$  vanishes, which marks the onset of spontaneous excitation of the optical mode and the breakdown of the linear response approximation. The uniaxial symmetry enforces that  $\text{Im}[\omega_+]$  also vanishes for the threshold so that the auto-oscillation can be triggered by a reversed current as well.

In the absence of the hard axis anisotropy, the threshold (8.29) is linear in  $\alpha$ , so the anti-damping effect occurs when the STT is turned on. However, in the general case where  $\omega_\perp > 0$ , the anti-damping effect appears only when  $\omega_s > \omega_\perp/2$ . Vectors  $\mathbf{m}_1$  and  $\mathbf{m}_2$  always exhibit opposite chiralities, i.e., they rotate counterclockwise (clockwise). However, at the degenerate point  $\omega_s = \omega_\perp/2$ , the chirality of  $\mathbf{m}_1(\mathbf{m}_2)$  in the optical (acoustic) mode reverses. At  $\omega_s > \omega_\perp/2$ , both  $\mathbf{m}_1$  and  $\mathbf{m}_2$ , hence the Néel vector  $\mathbf{l}$ , all acquire the same chirality. At the threshold  $\omega_s^{th}$ , the excited optical mode is right handed. If  $\omega_s$  changes sign, the optical mode is still excited, but its chirality becomes left handed. These suggest that the direction of the current determines the chirality of the excitation.

In the considered two-layered nanostructure, insulating AF/heavy normal metal (HM) with strong spin-orbit coupling (Fig. 8.2), a current density  $\mathbf{J}_c$  is applied along the direction perpendicularly to the AF vector  $\mathbf{l}$ . The SHE in the HM generates anti-damping STTs to drive the AF vector dynamics, which in turn pumps spin current back into the HM. The pumped spin current converts into a charge voltage due to the inverse SHE. The spin diffusion equation in the presence of the SHE under boundary conditions involving both spin pumping and STT results in the expression

$$J_c^{th} = \omega_c^{th} \frac{d_M (\hbar\sigma + 2\lambda e^2 G_r \coth \frac{d_N}{\lambda})}{2\theta_s \alpha^3 \lambda e G_r \tanh \frac{d_N}{\lambda}} \quad (8.30)$$

describing the dependence of the a critical current density on the threshold STT (8.29), the spin Hall angle  $\theta_s$ , and the areal density of transverse mixing conductance  $G_r'$ . From (8.30) it is follows that the critical current density  $J_c^{th}$  can be lowered by reducing (increasing) the thickness of the AF  $d_M$  (HM  $d_N$ ).

The sustained steady-state oscillation of the AF vector in the mentioned nanostructure can be realized via the dynamic feedback effect. The pumped spin current from a precessing AF vector into the HM experiences a backflow [33, 34]. In HMs, however, the spin pumping and the spin backflow are also connected via the combined effect of the SHE and its inverse process, which feeds the Néel vector dynamics back into itself. In ferromagnets, such a feedback mechanism manifests as a nonlinear damping effect in the magnetization dynamics. Similar feedback-induced damping effect can occur for AFs. In this case, the pumped spin current into the HM converts into an electric field  $\mathbf{E}$  due to ISHE. According to Ohm's law,

$$\mathbf{J}_c = \sigma \mathbf{E} - \theta_s (\sigma/2e) \mathbf{z} \times \partial_z \boldsymbol{\mu}_s \quad (8.31)$$

where  $\boldsymbol{\mu}_s$  is the spin accumulation in the HM. At the fixed current density  $\mathbf{J}_c$  through external circuits, a change of the electric field  $\mathbf{E}$  necessarily leads to a change of the spin accumulation. Subsequently, the change of  $\boldsymbol{\mu}_s$  diffuses and generates an additional spin current, which will finally deliver the influence of spin pumping back into the AF vector through STTs. Closing such a feedback loop results in a feedback torque that should be added to (8.27) as

$$\mathbf{T}_{FB} = \alpha_{NL} \left[ l_z^2 \mathbf{l} \times \dot{\mathbf{l}} - \dot{l}_z (\mathbf{z} \times \mathbf{l}) \right] \quad (8.32)$$

where the feedback coefficient is

$$a_{NL} = \frac{\theta_s^2 \alpha^3}{d_M} \frac{2\hbar - e^2 G_r^2 \coth \frac{d_N}{\lambda}}{(\hbar\sigma + 2\lambda e^2 G_r \coth \frac{d_N}{\lambda})} \quad (8.33)$$

While the feedback effect seems to be a higher-order effect as  $a_{NL}$  is proportional to  $\theta_s^2$ , it can be significantly enhanced by searching for materials with large  $\theta_s$ . The feedback-induced nonlinear damping is a critical ingredient because it dramatically modifies the dynamical behavior of an SHNO using AF.

A salient feature of the considered stable oscillation phase is that the applied DC current density  $\mathbf{J}_c$  controls the output power and that the output power is substantial that is indispensable for an SHNO. In the stable oscillation phase, the actual frequency output lies between the acoustic and the optical modes. The AC voltage output is determined by ISHE and the spin pumping. For a fixed  $\mathbf{J}_c$  the total electric field  $\mathbf{E} = \mathbf{J}_c/\sigma + \Delta\mathbf{E}$  includes a time-varying part

$$\Delta E = \frac{\theta_s \hbar}{d_N} \frac{\lambda e G_r \tanh \frac{d_N}{2\lambda}}{h\sigma - 2\lambda e^2 G_r \coth \frac{d_N}{\lambda}} (\mathbf{l} \times \mathbf{l}) \times \mathbf{z} \quad (8.34)$$

A time average of (8.34) results in the effective value of the components  $\overline{E_x}$  and  $\overline{E_y}$  which are appreciably large in the stable oscillation phase.

## 8.6 Spin Hall Magnetoresistance in Magnetic Nanostructures

Interconnection between the magnetic dynamics in magnetic layers and the charge current in the adjacent nonmagnetic heavy metal (HM) nanolayers with the strong spin-orbit interaction can exhibit via the so-called spin Hall magnetoresistance effect (SME) [35, 36] of the magnetic-induced change of the charge current. The impact of the magnetic dynamics on the charge current in nonmagnetic layers is related to a nonequilibrium proximity effect caused by the simultaneous action of the SHE and ISHE [37, 38]. The impact of the magnetization on the charge current occurs via the magnetic-induced variation of the nonequilibrium spin diffusion in the normal metal layers at the interface, converting by the ISHE into the charge current. Herewith, the spin diffusion occurs from the dynamic state of the spin accumulation caused by the interface reflection of the SHE-induced spin current. The spin diffusion current is in direct dependence on the exchange interaction between the magnetization and the spin current nearby the interface.

Especially clearly, SME is exhibited in the case of insulating magnetic (IM) nanolayer (specifically, yttrium iron garnet (YIG)) adjusting to the HM nanolayer (specifically, Pt) possessing the strong enough spin-orbit interaction. When a charge current  $\mathbf{J}_c$  is sent through a Pt nanolayer, a transverse spin current  $\mathbf{J}_s$  is generated by the SHE following  $\mathbf{J}_c \propto \sigma \times \mathbf{J}_s$ , where  $\sigma$  is the polarization direction of the spin current. Part of this spin current is directed toward the interface as is shown in Fig. 8.3.

At the interface, the electrons in the Pt will interact with the localized moments in the YIG. Depending on the magnetization ( $\mathbf{M}$ ) direction of the YIG, electron spins will be absorbed ( $\mathbf{M} \perp \sigma$ ) or reflected ( $\mathbf{M} \parallel \sigma$ ). By changing the direction of the magnetization of the YIG, the polarization direction of the reflected spins and thus the direction of the additional created charge current can be controlled. A charge current with a component in the direction perpendicular to  $\mathbf{J}_e$  can also be created, which generates a transverse voltage.

In a diffusion approximation for both magnetic and HM nanolayers, the spin and charge currents are expressed in terms of gradients of charge and spin accumulations (or spin-dependent electrochemical potentials and densities). The charge current density is the expectation value of the current operator  $\mathbf{j} = e(n\mathbf{v} + \mathbf{v}n)/2$ , where  $e$  is the electron charge,  $n$  is the electron density, and  $\mathbf{v}$  is the velocity operator. For a normal metal with constant density  $n_N$  and drift velocity  $\mathbf{v}_N$ ,  $\mathbf{j}_{eN} = en_N \mathbf{v}_N$ . The spin current in the nonrelativistic limit is the second-order tensor



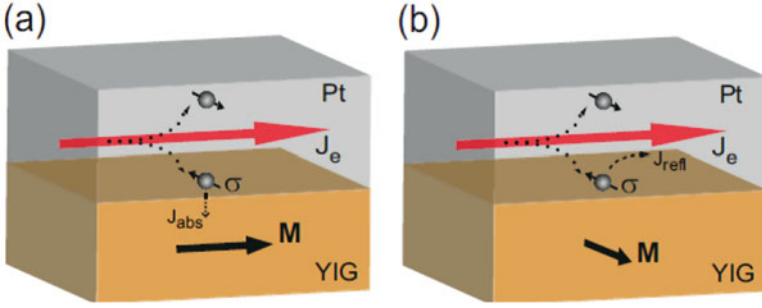


**Fig. 8.3** Schematic of the passage of spin and charge currents at the SME in a YIG/Pt nanostructure. (a) When the magnetization  $M$  YIG is perpendicular to the spin polarization  $\sigma$  of the spin accumulation created in the Pt by the SHE, the spin accumulation will be absorbed ( $J_{abs}$ ) by the localized moments in the YIG. (b) For  $M$  parallel to  $\sigma$ , the spin accumulation cannot be absorbed, which results in a reflected spin current back into the Pt, where an additional charge current  $J_{refl}$  will be created by the ISHE

$$\overleftrightarrow{\mathbf{j}}_{sN} = \frac{e}{2} \langle \mathbf{j} \otimes \sigma + \sigma \otimes \mathbf{j} \rangle = (j_{sx}, j_{sy}, j_{sz})^T \quad (8.35)$$

where  $\sigma$  is the vector of Pauli spin matrices,  $\otimes$  denotes the tensor product, and  $\langle \dots \rangle$  denotes an expectation value. The row vectors  $\mathbf{j}_{si} = en(v\sigma_i + \sigma_i v)/2$  are the spin current densities polarized in the  $i$ -direction. In metallic ferromagnets with homogenous texture, the average spin current is projected along the unit vector of the magnetization direction  $\mathbf{m}$ , so the charge current and spin current tensor have the form

$$\begin{aligned} \mathbf{j}_{cF} &= e(n_{\uparrow F} \mathbf{v}_{\uparrow F} + n_{\downarrow F} \mathbf{v}_{\downarrow F}), \\ \overleftrightarrow{\mathbf{j}}_{sF} &= \mathbf{j}_{sF} \otimes \mathbf{m} = (\mathbf{j}_{\uparrow F} - \mathbf{j}_{\downarrow F}) \otimes \mathbf{m}, \end{aligned} \quad (8.36)$$

where  $\mathbf{j}_{cF}$  is the spin current density direction vector.

In the diffusion approach and the two-channel model, currents close to the interface of the heterostructure are determined via gradients of the spin-dependent chemical potentials  $\mu_{\zeta F}$ ,  $\mathbf{j}_{\zeta F} = -(\sigma_{\zeta F}/e)\nabla\mu_{\zeta F}$ , where  $\zeta = (\uparrow, \downarrow)$  represents the spin direction along of the magnetization and  $\sigma_{\zeta F}$  is the spin-dependent conductivity. The charge current  $\mathbf{j}_{cF} = \mathbf{j}_{\uparrow F} + \mathbf{j}_{\downarrow F}$  and the spin current  $\mathbf{j}_{sF} = \mathbf{j}_{\uparrow F} - \mathbf{j}_{\downarrow F}$  are expressed via charge and spin chemical potentials  $\mu_{cF} = (\mu_{\uparrow F} + \mu_{\downarrow F})/2$  and  $\mu_{sF} = (\mu_{\uparrow F} - \mu_{\downarrow F})/2$ , respectively. These currents are described by the general expression [37]

$$\mathbf{j}_i = -\frac{\sigma_F}{e} \left[ \delta_{i,cF} \left( \nabla\mu_{cF} + \frac{1}{2}P\nabla\mu_{sF} \right) + \delta_{i,sF} \left( P\nabla\mu_{cF} + \frac{1}{2}\nabla\mu_{sF} \right) \right], \quad i = (cF, sF) \quad (8.37)$$

where  $P = (\sigma_{\uparrow F} - \sigma_{\downarrow F})/(\sigma_{\uparrow F} + \sigma_{\downarrow F})$ . The abovementioned potentials are determined by the diffusion equations

$$\nabla^2 \mu_{sF} = \frac{\mu_{sF}}{\lambda_F^2}, \quad \nabla^2 (\mu_{cF} + P\mu_{sF}/2) = 0 \quad (8.38)$$

where the spin-flip diffusion length  $\lambda_F = \left( \lambda_{\uparrow F}^{-2} + \lambda_{\downarrow F}^{-2} \right)^{-1/2}$  is expressed in terms of the spin diffusion lengths  $\lambda_{sF} = \sqrt{D_{sF} \tau_{sf,sF}}$  for each spin ( $\tau_{sf,sF}$  is the spin-dependent spin-flip time). The spin-dependent charge diffusion constant  $D_{sF} = \tau_{sF} v_{sF}^2 / 3$  depends on the spin-dependent relaxation time  $\tau_{sF}$  and Fermi velocity  $v_{sF}$ . Solutions of (8.38), corresponding to boundary conditions at interface, due to (8.37) determine the charge and spin currents.

In normal metals, the induced spin accumulations are represented by the (position-dependent) vector  $\boldsymbol{\mu}_{sN} = (\mu_{sx}, \mu_{sy}, \mu_{sz})^T - \mu_{cN} \mathbf{1}$ , components of which together with the charge chemical potential obey the diffusion equation system

$$\nabla^2 \mu_{si} = \frac{\mu_{si}}{\lambda^2}, \quad \nabla^2 \mu_{cN} = 0 \quad (8.39)$$

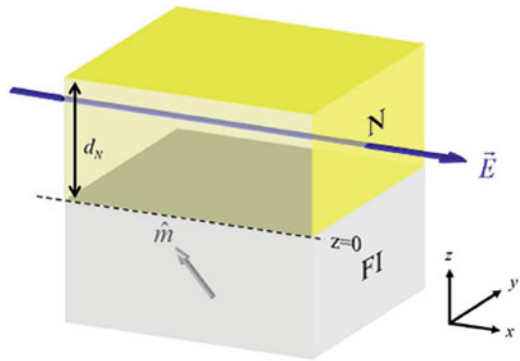
Without the SHE, charge and spin currents are expressed by the system

$$\mathbf{j}_{cN} = -\frac{\sigma_{cN}}{e} \nabla \mu_{cN}, \quad \mathbf{j}_{si} = -\frac{\sigma_{si}}{e} \nabla \mu_{si} \quad (8.40)$$

The spin polarization in the case of the NM layers has arbitrary direction in contrast to the case of the magnetic layers.

In the considered case of the bilayer nanostructure HM/FI (FI denotes insulating magnetic) represented in Fig. 8.4, the charge current flow in the metal parallel to the applied electric field  $\mathbf{E}$  and the SHE generate a spin accumulation. The generalized Ohm's law in this can be represented by the system [19]

**Fig. 8.4** The N|FI bilayer structure with the charge flow along an electric field  $\mathbf{E}$



$$\mathbf{j}_{si} = \frac{\sigma_N}{e} \left( \theta_S \mathbf{x}_i \times \nabla \mu_{cN} + \frac{1}{2} \nabla \mu_{sx_i} \right) \quad (8.41)$$

$$\mathbf{j}_{cN} = \frac{\sigma_N}{e} \left( \nabla \mu_{cN} + \frac{\theta_S}{2} \sum_i \mathbf{x}_i \times \nabla \mu_{sx_i} \right) \quad (8.42)$$

where  $\boldsymbol{\mu}_{sN} = (\mu_{sx}, \mu_{sy}, \mu_{sz})^T - \mu_{cN} \mathbf{1}$  is the spin accumulation, i.e., the spin-dependent chemical potential relative to the charge chemical potential  $\mu_{cN} = e\phi$ ,  $\sigma_N$  is the electric conductivity, and “ $\times$ ” denotes the vector product operating on the gradients of the spin-dependent chemical potentials. The SHE is governed by the first term in (8.41) that generates the spin currents parallel to the applied electric field  $\mathbf{E} = E_x \mathbf{x}$  (Fig. 8.4). The ISHE is governed by the second term in (8.42) that connects the gradients of the spin accumulations to the charge current density.

According to (8.41) and (8.42), the spin current in N consists of conventional diffusion and spin Hall drift contributions. The spin current density flowing in the  $z$ -direction is described by the expression

$$\mathbf{j}_{sz} = -\frac{\sigma_N}{2e} \nabla_z \boldsymbol{\mu}_{sN} - j_{s0}^{SH} \mathbf{y} \quad (8.43)$$

where  $j_{s0}^{SH} = \theta_S \sigma_N E_x$  is the bare spin Hall current, i.e., the spin current generated directly by the SHE. Due to the boundary conditions,  $\mathbf{j}_{sz}(z)$  is continuous at the interfaces ( $z = d_N, 0$ ). The spin current density at a vacuum interface ( $z = d_N$ ) vanishes, while at the magnetic interface ( $z = 0$ ), it is governed by the spin accumulation and spin-mixing conductance according to (8.1),  $\mathbf{j}_{sz}(0) = -\mathbf{j}_s^{(N|F)}$ . With these boundary conditions, solution of (8.39) for the spin accumulation is described by the expression

$$\frac{\boldsymbol{\mu}_{sN}(z)}{\mu_s^0} = -\mathbf{y} \frac{\sinh A(z)}{\sinh A(0)} - \frac{2\lambda \cosh B(z)}{\sinh B(0)} [\mathbf{m} \times (\mathbf{m} \times \mathbf{y}) \operatorname{Re} + (\mathbf{m} \times \mathbf{y}) \operatorname{Im}] \varphi(G_{\uparrow\downarrow}) \quad (8.44)$$

where  $A(z)$  and  $B(z)$  were defined in (8.11),  $\varphi(z) = z(\sigma_N + 2\lambda z \coth B(2d_N))^{-1}$ , and  $\mu_s^0$  is the spin accumulation at the interface in the absence of spin transfer. By virtue of (8.44), the spin current in N is described by the expression

$$\frac{\mathbf{j}_s^z(z)}{j_{s0}^{SH}} = \mathbf{y} (\Delta_1(z) - 1) - \Delta_2(z) \mathbf{R} \varphi(G_{\uparrow\downarrow}) \quad (8.45)$$

where

$$\Delta_1(z) = \frac{\cosh A(z)}{\cosh A(0)}, \quad \Delta_2(z) = \frac{2\lambda \tanh A(0) \sinh B(z)}{\sinh B(0)}$$

$\mathbf{R}$  denotes the expression emphasized by squared brackets in (8.44). The spin current at the interface N|F vanishes when the magnetization is along  $\mathbf{y}$ . The spin current at the interface and the torque on the magnetization are activated, while the spin accumulation is dissipated by rotation of the magnetization from  $\mathbf{y}$  to  $\mathbf{x}$ . The  $\mathbf{x}$ -components of both spin accumulation and spin current vanish when the magnetization is along  $\mathbf{x}$  and  $\mathbf{y}$  and are largest at  $(\mathbf{x} + \mathbf{y})/2$ .

The ISHE drives a change current in the  $x$  -  $y$  plane by the diffusion spin current component flowing along  $y$ -direction. The total longitudinal (along  $\mathbf{x}$ ) and transverse (along  $\mathbf{y}$ ) charge currents [37]

$$\frac{j_{cx}(z)}{\sigma_N E_x} = 1 + \theta_S^2 [\Lambda_1(z) + (1 - m_y^2) \Lambda_2(z) \operatorname{Re} \varphi (G_{\uparrow\downarrow})] \quad (8.46)$$

$$\frac{j_{cy}(z)}{\sigma_N E_x} = \theta_S^2 \Lambda_2 (1 - m_y^2) [m_x m_y \operatorname{Re} - m_z \operatorname{Im}] \varphi (G_{\uparrow\downarrow}) \quad (8.47)$$

describe the magnetization dependence of the charge current.

Averaging (8.46) and (8.47) over the thickness  $z$  results in the corresponding electrical resistances, which in the first-order approximation in  $\theta_S^2$  are described by the expressions

$$\rho_x = \rho - \frac{\theta_{SH}^2 \tanh A(0)}{A(0)} \left( 1 - \frac{\lambda (1 - m_y^2) \tanh A(0)}{2} \operatorname{Re} \varphi (G_{\uparrow\downarrow}) \right) \quad (8.48)$$

$$\rho_y = - \frac{\theta_S^2 \lambda \tanh^2 A(0)}{A(0)} (m_x m_y \operatorname{Re} - m_z \operatorname{Im}) \varphi (G_{\uparrow\downarrow}) \quad (8.49)$$

Here, when the N layer thickness increases relatively to the spin-flip diffusion length ( $\lambda/d_N \rightarrow 0$ ),  $A(0) \rightarrow 0$  and SME vanishes. Its magnitude is proportional to the second power of the spin Hall angle and is related to the spin-mixing conductance at the interface.

## References

1. Zutic L, Fabian J, Das Sarma S (2004) Spintronics: fundamentals and applications. Rev Mod Phys 76:323
2. Manchon A, Koo HC, Nitta J, Frolov SM, Duine RA (2015) New perspective for Rashba spin-orbit coupling. Nat Mater 36:871
3. Hoffmann A (2013) Spin Hall effects in metals. IEEE 49:5172
4. Tserkovnyak Y, Brataas A, Bauer GE, Halperin BI (2005) Nonlocal magnetization dynamics in ferromagnetic heterostructures. Rev Mod Phys 77:1375
5. Edwards ERJ, Ultrichs H, Demidov VE, Demokritov SO, Urazhdin S (2012) Parametric excitation of magnetization oscillations controlled by pure spin current. Phys Rev B 86:134220
6. Liu L, Pai C-F, Li Y, Ralph DC, Buhram RA (2012) Spin-torque switching with the Giant spin-Hall effect. Science 336:555

7. Liu RH, Lim WL, Urazhdin S (2013) Spectral characteristics of the microwave emission by the spin Hall Nano-oscillator. *Phys Rev Lett* 110:147601
8. Baither D, Schmitz G, Demokritov SO (2012) Magnetic nanooscillators driven by pure spin current. *Nat Mater* 11:1028
9. Yang T, Kimura T, Otani Y (2008) Giant spin accumulation signal and pure spin-current-induced reversible magnetization at switching. *Nature Phys* 4:851
10. Ebrahim-Zaden E, Urazhdin S (2013) Optimization of Pt-based spin-Hall effect spintronic devices. *Appl Phys Lett* 102:13402
11. Volkov NV (2012) Spintronics: manganite-based magnetic tunnel structures. *PHYS-USP* 55:250
12. Hirsch JE (1999) Spin Hall effect. *Phys Rev Lett* 83:1834
13. Chudnovsky EM (2007) Theory of spin Hall effect. *Phys Rev Lett* 99:206601
14. Miron IM, Gaudin G, Auffere S, Rodmacq B, Schuhl A, Pizzini S, Vogel J, Gambardella P (2010) Current-driven spin torque induced by the Rashba effect in ferromagnetic metal layer. *Nat Mater* 9:230
15. Manchon A, Zhang S (2009) Theory of spin torque due to spin-orbit coupling. *Phys Rev B* 79:094422
16. Wang X, Manchon A (2012) Diffusive spin dynamics in ferromagnetic thin films with a Rashba interaction. *Phys Rev Lett* 108:117201
17. Cheng R, Zhu J-G, Xiao D (2016) Dynamic feedback in Ferromagnet/spin-Hall Heterostructures. *Phys Rev Lett* 117:097202
18. Gomonay HV, Loktev VM (2010) Spin transfer and current-induced switching in antiferromagnets. *Phys Rev B* 81:144427
19. Brataas A, Bauer GEW, Kelly PJ (2006) Non-collinear magnetoelectronics. *Phys Rep* 427:157
20. Gambardella P, Miron IM (2011) Current-induced spin-orbit torque. *Phil Trans R Soc A* 369:3175
21. Ou Y, Ralph DC, Buhram RA (2012) Strong spin Hall effect in the antiferromagnetic PtMo. *Phys Rev B* 93:220405
22. Ando K, Takahashi S, Harii K, Sasage K, Ieda J, Maekawa S, Saitosh E (2008) Electric manipulation of spin relaxation in a film using spin-Hall effect. *Phys Rev Lett* 101:036601
23. Cheng R, Xiao D, Brataas A (2015) Terahertz Antiferromagnetic Spin Hall Nano-Oscillator. *Phys Rev Lett* 116:207603
24. Tserkovnyak YA, Bender SA (2014) Spin Hall phenomenology of magnetic dynamics. *Phys Rev B* 90:014428
25. Tserkovnyak YA, Brataas A, Bauer EW (2002) Spin pumping and magnetic dynamics in metallic multilayers. *Phys Rev B* 66:224403
26. Cheng R, Xiao D, Niu Q, Brataas A (2014) Spin pumping and spin-transfer torques in Antiferromagnets. *Phys Rev Lett* 113:057601
27. Mosendz O, Vlaminc V, Pearson JE, Fradin FY, Bauer GEW, Bader SD, Hoffmann A (2010) Detection and quantification of the inverse spin Hall effect from spin pumping in permalloy/normal metal bilayers. *Phys Rev B* 82:214403
28. Brouwer PW (1998) Scattering approach to parametric pumping. *Phys Rev B* 58:R10135
29. Demidov VE, Urazhdin S, Ulrichs H, Tiberkevich V, Slavin A, Baither D, Schmitz G, Demokritov SO (2012) Magnetic nano-oscillator driven by pure spin current. *Nat Mater* 11:1028
30. Pai C-F, Liu L, Tseng HW, Ralph DC, Buchram BA (2012) Spin transfer torque devices utilizing the giant spin Hall effect of tungsten. *Appl Phys Lett* 101:082407
31. Kim K-W, Moon J-H, Lee K-J, Lee H-W (2012) Prediction of Giant spin motive force due to Rashba spin-orbit coupling. *Phys Rev Lett* 108:21722
32. Wong CH, Tserkovnyak YA (2009) Hydrodynamic theory of coupled current and magnetization dynamics in spin-textured ferromagnets. *Phys Rev B* 80:184411
33. Wang HL, Due CH, Pu Y, Adur R, Hammel PC, Yang FV (2014) Scaling of spin Hall angle in 3d, 4d and 5d metals from  $Y_3Fe_5O_{12}$ /metals spin pumping. *Phys Rev Lett* 112:197201

34. Brataas A, Tserkovnyak YA, Bauer EW, Halperin PC (2014) Spin battery operated by ferromagnetic resonance. *Phys Rev B* 66:060404
35. Vietstra N, Shan J, Castel V, Wees V-T, Yousset JB (2013) Spin-Hall magnetoresistance in platinum yttrium iron garnet: dependence on platinum thickness and in-plane/out-of-plane magnetization. *Phys Rev B* 87:184421
36. Nakayama H, Althammer M, Chen Y-T, Uchida K, Kajiwara Y, Kikuchi D, Ohtani T, Geprags S, Opel M, Takahashi S, Gross R, Bauer GEW, Goennenwein STB, Saitosh E (2013) Spin Hall Magnetoresistance induced by a Nonequilibrium proximity effect. *Phys Rev Lett* 110:206601
37. Chen YT, Takahashi S, Nakayama N, Althammer M, Goennenwein STB, Saitosh E, Bauer GEW (2013) Theory of spin Hall magnetoresistance. *Phys Rev B* 87:14411
38. Jungfleisch MB, Lauer V, Neb R, Chumak AK, Hillebrands B (2013) Improvement of the yttrium iron garnet/platinum interface for spin-pumping application. *Appl Phys Lett* 103:022411

# Chapter 9

## Localization of Orbitals and Electronic Properties in Nanodiamonds with Color Centers: Semiempirical Models

Anatoliy V. Luzanov

### 9.1 Introduction

Nanodiamonds (ND) and their functionalized analogs have attracted wide interest during the recent years because of a versatile array of applications of ND particles – from biomedicine to quantum computing [1–8]. This is especially true for ND containing color centers, such as nitrogen-vacancy (NV) centers. For instance, the photostable color centers are considered as promising candidates for qubit (quantum bit) in future quantum information processing [6–11]. Our own interest in these objects was stimulated by one earlier paper [12] where the spin properties of the small clusters with NV color centers were modeled; for further development, see many other quantum chemical works [13–19]. Particularly, excited states play the significant role in nanophysics of the paramagnetic nanodiamond color centers [20–22], and a thorough analysis of these states is an interesting and useful field to study.

The main aim of this chapter is to present, in a wide context, the description of orbital nature and other important aspects of the excited states in nanodiamonds with NV defects. For these purposes we employ the previously developed interpretation tools [23–27] which provide a visual analysis of molecular excited states. We generalize our recent results on the nanocluster excited states [28–31] and add supplementary quantification measures which help us to see what happens at the electronic level when the color center is excited.

The plan of the paper is as follows. In the next section, we describe the quantum chemical models and computational details used in this work. In Sect 9.3, the quantification of electron localization is proposed based on the generalized partition ratio indices. These indices are exploited in studying the orbital localization in Sect.

---

A.V. Luzanov (✉)

SSI “Institute of Single Crystals”, NAS of Ukraine, 60 Nauky Ave, 61078, Kharkiv, Ukraine  
e-mail: [luzanov@xray.isc.kharkov.com](mailto:luzanov@xray.isc.kharkov.com); [avluzanov@gmail.com](mailto:avluzanov@gmail.com)

9.4. In Sect. 9.5 an effective interpretative scheme for the electronically excited color centers is provided. Section 9.6 deals with interesting points concerning a compact description of hole-particle amplitudes related to the lowest transitions. The peculiarities of modeling triplet-singlet excitations are considered in Sect. 9.7. The results of computing color center spin properties are displayed in Sect. 9.8, and the last section summarizes this chapter.

## 9.2 Models and Computational Details

We will study the ground and excited states of nanoclusters with hundreds of atoms by using the semiempirical model of CNDO type, namely, the CNDOL2 (or simply, CNDOL) approximation which is well elaborated in refs. [32–34]. It should be stressed that the practically used TDDFT (time-dependent density functional theory) has its known limitations and inaccuracies (recall Burke’s ironic and witty remark about DFT: “The good, the bad and the ugly” [35]). It seems that in practice, the semiempirical approaches, such as CNDOL, are not too inferior to that of TDDFT. Due to the simplicity of CNDOL, we could program and do most numerical computations within a mathematica 5.2 environment [36] on a modest laptop. Specifically, we employed the unrestricted Hartree-Fock (UHF) method for the ground state and the configurational interaction singles (CIS) model (more exactly, CIS/UHF) for the lowest excited states. For finding the latter, we have taken advantage of the conventional Lanczos diagonalization method which is particularly suitable for dealing with the CIS/UHF matrix algorithm given previously in ref. [37]; details and modifications will be published elsewhere.

We shall now briefly describe the systems under study. The main molecular model we study here is the  $C_{3v}$  symmetry nanostructure with NV color center of composition  $C_{273}H_{176}N^-$ . It was generated from the idealized tetrahedral ND structure  $C_{275}H_{176}$ . The latter was optimized at the semiempirical AM1 method, and then NV center was made in a usual way (by forming a vacancy in the cluster center and substituting an adjacent atom with the negative nitrogen ion). By using UHF/CNDOL for this NV center, we predict the spin-triplet ground state with symmetry  $^3A_2$ , as it should be in accordance with experiment and nonempirical calculations of typical NV centers [10–12].

In a similar way, we constructed two smaller systems  $C_{85}H_{76}N^-$  and  $C_{173}H_{112}N^-$  which served us for comparison with the main nanostructure. In particular, we obtained the following calculated values of the lowest triplet-triplet  $^3A_2 \rightarrow ^3E$  transition energy (in eV): 2.06, 1.96, and 1.94 for  $C_{85}H_{76}N^-$ ,  $C_{173}H_{112}N^-$ , and  $C_{273}H_{176}N^-$ , respectively. We see that in the case of the last (main) system, we get almost a limiting value of the transition energy (with accuracy allowed by the method employed). Seemingly, the study of diamondoids with nearly 300 carbon atoms is quite sufficient for simulating optical properties of a single-color center in large nanodiamonds. The basic cause of this is the well-known localized nature of defect states. We give a detailed description of it in subsequent sections.



### 9.3 Main Localization Indices

Before specifying the problems, we provide definitions of the main localization measures which are used throughout the paper. As usual in quantum mechanics, the squared expansion coefficients define appropriate probabilities. For instance, in most one-electron theories, conventional LCAO (linear combination of atomic orbitals) of all atoms in molecule  $1, 2, \dots, A, \dots, M$ , represents molecular orbital (MO). Then, corresponding sum of squares of LCAO coefficients generates probability  $w_A$  of finding the electron (associated with the given MO) at a respective molecular region  $A$ . In what follows, we will use set  $\{w_A\}$  which will be assigned only to the individual atoms of the studied systems. Generally, when considering electrons in atomic clusters or molecules, we will compute probability sets  $\{w_A\}$  representing other quantum process in the cluster considered (e.g.,  $w_A$  as local excitation probability). Note for further use that atomic distributions  $\{w_A\}$  will be displayed by colored circles of size proportional to the corresponding  $w_A$  magnitude.

Given the probability set, it is easy to compute global localization indices which were designed long ago in [38] for analyzing vibrational modes. This is the so-called partition relation (PR) index

$$\text{PR} = 1 / \sum_A w_A^2 \quad (9.1)$$

and the related inverse partition relation (IPR) index

$$\text{IPR} = \sum_A w_A^2 \quad (9.2)$$

It is not difficult to understand that PR shows how many significant members appear in  $\{w_A\}$ . In passing, note that the similar quantities, termed the collectivity numbers, were independently proposed in [23, 39] for hole-particle amplitudes of the abovementioned CIS model.

There are also high-order PR indices which were considered recently in [40]. We will use the second-order index of the form

$$\text{PR2} = \left( \sum_A w_A^2 \right)^2 / \left( \sum_A w_A^4 \right) \quad (9.3)$$

that was applied in our works as well [31, 41]. The index provides a more suitable estimation of the number of the active centers of localization. In the present paper, we additionally employ a new index  $\sigma_{\text{IPR}}$  which we identify, up to a factor, with a standard deviation of IPR itself (for more detail, see [31]). By definition,  $\sigma_{\text{IPR}}$  as IPR fluctuation index is of the form

$$\sigma_{\text{IPR}} = \text{dim} \left[ \sum_A w_A^3 - \left( \sum_A w_A^2 \right)^2 \right]^{1/2} \quad (9.4)$$

with  $\text{dim}$  being a size of  $\{w_A\}$ . The quantity turns out to be very sensitive to an inhomogeneity in the probability set and serves us as a suitable measure of localization without inspecting the whole probability array and corresponding visual images (see the next section). This is a good merit that is especially helpful for nanoclusters where a great set of large-size state vectors should be inevitably investigated.

## 9.4 Orbital Localization

We start with the orbital localization measures. First of all, they are necessary for analyzing the ground electronic states of molecules or atomic clusters in question. By working with the triplet (open-shell) ground state at the UHF level, we make the conventional distinction between  $\alpha$ -orbitals (spin-up orbitals) and  $\beta$ -orbitals (spin-down orbitals). For our analysis, it means that we must compute indices (9.1), (9.2), (9.3), and (9.4) for each sort of orbitals. In Figs. 9.1 and 9.2, we display  $\sigma_{\text{IPR}}$  vs orbital number  $j$  and give the spatial images of HOMO and LUMO localizations for spin-up and spin-down orbitals. All the images represent here only the most important NV region including the nitrogen atom and 142 carbon atoms. In the plots the maximum value of  $\sigma_{\text{IPR}}$  is marked on the ordinate.

The presented  $\sigma_{\text{IPR}}$  plots provide a very clear indication that HOMO and LUMO, i.e., frontier orbitals, are most localized (somewhere). Additionally, from the given spatial localization images, we simply detect the region where our frontier MOs are really localized. We observe that  $\alpha$ -HOMO and both  $\beta$ -frontier MOs are strongly localized in the vacancy vicinity, whereas  $\alpha$ -LUMO is not. These peculiarities are essential for understanding low-lying excited states we consider later. The

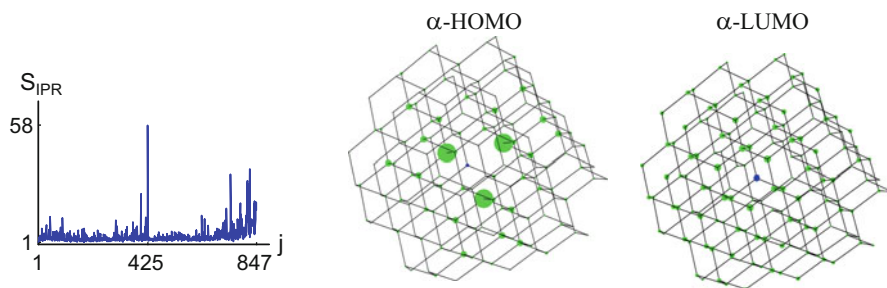


**Fig. 9.1** Fluctuation index  $\sigma_{\text{IPR}}$ , for all  $\alpha$ -MOs (the first panel), and the atomic localization diagrams for the frontier  $\alpha$ -MOs (the rest panels) in  $\text{C}_{273}\text{H}_{176}\text{N}^-$

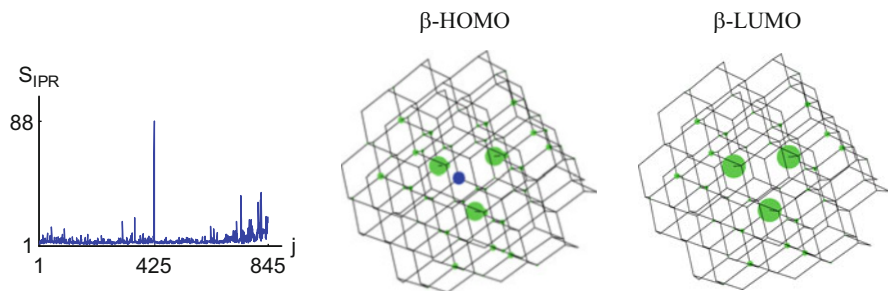


**Fig. 9.2** Fluctuation index  $\sigma_{IPR}$ , for all  $\beta$ -MOs (the first panel), and the atomic localization diagrams for the frontier  $\beta$ -MOs (the rest panels) in  $C_{273}H_{176}N^-$

**Table 9.1** Generalized partition ratio index PR2; fluctuation index  $\sigma_{IPR}$ , and NV center localization  $L_{[NV]}$  for frontier orbitals

	$\alpha$ -HOMO	$\alpha$ -LUMO	$\beta$ -HOMO	$\beta$ -LUMO
PR2	3.5	68.8	3.8	3.1
$\sigma_{IPR}$	57.8	3.3	58.0	88.4
$L_{[NV]}$ (in %)	44	2	52	75

supplementary information is given in Table 9.1. The corresponding data describe quantitatively the abovementioned differences in  $\alpha$ - and  $\beta$ -MOs. In the table the index  $L_{[NV]}$  gives a direct measure of the orbital localization on four atoms nearest to the vacancy. Thus, we fully characterize the  $\alpha$ -LUMO as significantly delocalized, unlike the rest frontier MOs.

The above analysis enables us to understand what can be expected, at least qualitatively, for the localization of various physical properties, e.g., optical transitions. Really, in a simplistic purely orbital model, the lowest excitations are identified with HOMO  $\rightarrow$  LUMO transitions. Within such a model the conservation of spin projection is valid, and we obtain two independent triplet-triplet (TT) transitions, namely,  $\alpha$ -HOMO  $\rightarrow$   $\alpha$ -LUMO (or  $[\alpha]$ -type) and  $\beta$ -HOMO  $\rightarrow$   $\beta$ -LUMO (or  $[\beta]$ -type). Then, excitation energies are equal to differences of the corresponding orbital energies (Fock matrix eigenvalues for  $\alpha$ - and  $\beta$ -shells). We will denote these differences by  $\Delta_\alpha$  and  $\Delta_\beta$  for  $[\alpha]$ -type and  $[\beta]$ -type, respectively. Specific computations give the following values (in eV):  $\Delta_\alpha = 9.51$ , and  $\Delta_\beta = 6.67$ . We see that  $\Delta_\beta$  is markedly lesser than  $\Delta_\alpha$ , so that the lowest transition is of  $[\beta]$ -type. In such a case, we can suppose that the lowest TT transition is strongly localized in the vacancy vicinity site because of the localization properties of the  $\beta$ -frontier MOs (see Fig. 9.2). Now take into account that  $\beta$ -HOMO has  $a_1$  symmetry and  $\beta$ -LUMO has symmetry  $e$ . Thus, in agreement with more rigorous theories, the lowest  $[\beta]$ -excitation should be of symmetry species  $E$ .

## 9.5 Localization of Excited States

In a more consistent CIS/UHF theory, all  $[\alpha]$ - and  $[\beta]$ -transitions are intermixed. However, owing to their different spatial localization, the mixing is insignificant, and the final lowest TT excitation retains its  $[\beta]$ -character and symmetry. This consideration is confirmed by a direct CIS/UHF calculation involving all possible one-electron  $[\alpha]$ - and  $[\beta]$ -transitions (806,448 ones for our main nanocluster). Indeed, we find that the sum of squares of all (403224) hole-particle  $\beta$ -amplitudes is equal to 0.981; hole-particle  $\alpha$ -amplitudes make up the remainder (0.019). Practically the same values are obtained for other, smaller, nanoclusters mentioned in Sect. 9.2.

Now we examine in more detail the nature of the lowest TT transition  ${}^3A_2 \rightarrow {}^3E$  in  $C_{273}H_{176}N^-$ . We will use interpretation technique [23, 24] based on a special set of indices. These are the atomic excitation indices  $L_A^*$  and charge transfer (CT) numbers  $l_{A \rightarrow B}$  where  $A$  and  $B$  are individual atoms. The number  $l_{A \rightarrow B}$  can be viewed as probability of occurrence of the individual CT state  $\dots A^+ \dots B^- \dots$  due to the excitation. The total excitation index  $L_A^*$  captures all possible CT processes connected with the given atom  $A$ :

$$L_A^* = l_{A \rightarrow A} + \sum_{B \neq A} (l_{A \rightarrow B} + l_{A \leftarrow B})/2$$

In Fig. 9.3 we show the computed atomic distribution  $\{L_A^*\}$  along with the diagram of electronic charge differences  $\{\Delta P_A\}$  where for the given  $A$ ,  $\Delta P_A$  is the difference between the net charge in the excited state and that in the ground state. We

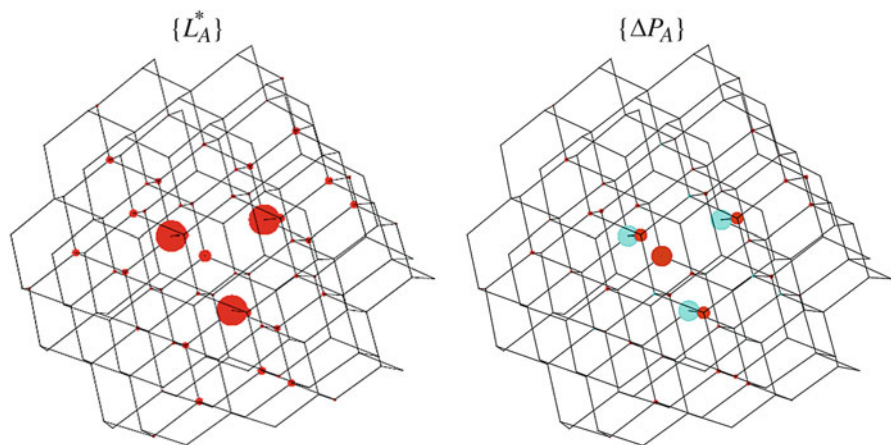


**Fig. 9.3** Atomic distribution,  $\{L_A^*\}$ , of the lowest TT excitation and the corresponding charge difference diagram  $\{\Delta P_A\}$

see that indeed the excitation is preferably localized on four atoms at the vacancy site, where just the  $\beta$ -frontier MOs are concentrated. Recall that these four atoms are the substitutional nitrogen atom and three dangling carbon atoms.

We will also give several quantitative results characterizing the excitation:

$$\text{PR2}^* = 3.15, \quad \sigma_{\text{IPR}}^* = 44.7, \quad L_{[\text{NV}]}^* = 71\% \quad (9.5)$$

where  $\text{PR2}^*$  and  $\sigma_{\text{IPR}}^*$  are computed by (9.3) and (9.4). The so-called excitation radius,  $R_{\text{exc}}$ , serves as the additional physical characteristics of spreading excitation. Following [26] we define  $R_{\text{exc}}$  by averaging interatomic distances  $r_{AB}$  over probability set  $\{l_{A \rightarrow B}\}$ :

$$R_{\text{exc}} = \sum_{A,B} r_{AB} l_{A \rightarrow B}$$

Our computations give  $R_{\text{exc}} = 2.67 \text{ \AA}$  that can be compared with the distance between the dangling carbon atoms  $r_{AA} = 2.53 \text{ \AA}$  and with the corresponding distance  $r_{AA} = 1.54\sqrt{8/3} = 2.515 \text{ \AA}$  in the ideal diamondoid. Notice that for the smaller nanocluster  $\text{C}_{173}\text{H}_{112}\text{N}^-$ , we obtained a somewhat smaller value  $R_{\text{exc}} = 2.65 \text{ \AA}$ . This reflects the expected effect of reducing delocalization due to decreasing cluster size. Furthermore, individual CT numbers for atoms around the vacancy provide more information on the character of the excitation. For atoms in interest (N and three equivalent dangling C atoms), we have the following block of the CT matrix:

$$\|l_{A \rightarrow B}\| = \left\| \begin{array}{cccc} 0. & 0.017 & 0.017 & 0.017 \\ 0. & 0.053 & 0.050 & 0.050 \\ 0. & 0.050 & 0.053 & 0.050 \\ 0. & 0.050 & 0.050 & 0.053 \end{array} \right\| \quad (9.6)$$

We see that the lowest transition has a significant CT character caused by the interatomic CT processes around the vacancy. The CT processes of the rest of the atoms are also important. The sum of all  $l_{A \rightarrow B}$  ( $A \neq B$ ) can be identified with a total measure of CT character  $\text{CT}_{\text{tot}}$  [27]. In the case considered, we obtain (in %)  $\text{CT}_{\text{tot}} = 83\%$ .

## 9.6 Natural Hole and Particle Orbitals

For completeness, we briefly discuss a hole-particle structure of our excited states treated within the CIS approximation. Recall that wave functions  $|\Psi^*\rangle$  of CIS-excited states are superpositions of all hole-particle excitations  $|i \rightarrow a\rangle$ :

$$|\Psi^*\rangle = \sum_{i;a} \tau_{ai} |i \rightarrow a\rangle \quad (9.7)$$

Here  $\tau_{ai}$  are hole-particle amplitudes, and  $|i \rightarrow a\rangle$  is the Slater determinant produced from the initial Hartree-Fock determinant by substituting a “hole” orbital  $|i\rangle$  with a “particle” orbital  $|a\rangle$ . In turn, hole and particle orbitals can be taken as certain superpositions of occupied and virtual MOs, respectively. In earlier work [23], we constructed the most concise representation of (9.7) by using a special diagonalizing procedure of non-Hermitian hole-particle matrix

$$\tau = || \tau_{ai} || \quad (9.8)$$

In modern terminology it corresponds to the so-called singular value decomposition of  $\tau$ . Now this representation of CIS and related amplitudes became very popular after its rediscovery [42] within the TDDFT approach. By SVD technique we transform (9.7) to the following form

$$|\Psi^*\rangle = \sum_u \tau_u |u \rightarrow u^*\rangle \quad (9.9)$$

where  $\tau_u$  are new hole-particle amplitudes (in fact, singular values of  $\tau$ ) and  $\{|u\rangle\}$  and  $\{|u^*\rangle\}$  comprise new suitable sets of hole and particle orbitals, respectively. As shown in refs. [23, 39], these sets are but natural orbitals of the CIS-excited state. It means that the respective one-electron density matrix is diagonal in this representation. A measure of conciseness of representation (9.9) is just collectivity number  $\kappa$ , that is, a PR index of the form

$$\kappa = 1 / \sum_u (\tau_u)^4 \quad (9.10)$$

proposed in [39] for probability set  $\{(\tau_u)^2\}$ . In other words,  $\kappa$  provides the localization measure in a hole-particle space. Notice that computation on (9.10) can avoid a direct SVD if using a simple explicit formula in terms of matrix (9.8) [27]:  $\kappa = 1/\text{Tr}(\tau^+ \tau)^2$ .

Now turn to our problem of  ${}^3E$  excitation. We first give its collectivity measure:  $\kappa = 1.09$ . Practically the same value is obtained for other systems. It means that, in fact, each of two sublevels of  ${}^3E$  term is mainly formed by single hole-particle excitation. If needed, the respective singular value spectrum can be obtained in a usual way. For instance, we have the following main part of singular value spectrum:  $\{0.979, 0.0612, 0.045, 0.044 \dots\}$  for one of  $\tau$ -matrices for  ${}^3E$ , and practically the same spectrum for the second  $\tau$ -matrix.

We can also find the overlap between respective natural orbitals of the lowest excitation and the HOMO and LUMO of the UHF ground state. Let us recall that  $[\beta]$ -transitions constitute a major contribution to the total excitation. Thus, it is sufficient to analyze the corresponding natural orbitals of  $\beta$ -type. The computations

indicate a very high overlap integral of the leading natural hole  $\beta$ -orbital (with maximal  $\tau_u$ ) and  $\beta$ -HOMO, namely, the overlap integral is 0.972. The particle natural orbital (with the same  $\tau_u$ ) exhibits even greater overlap integral 0.995.

Of course, in a general case, such overlaps can be not so close to unity. But judging from our experience, the main conclusion that  $\kappa$  is only a little more than 1 is typical for lowest excitations in color NV centers and related problems. In other words, the lowest excitations can be treated as an effective single hole-particle transition – only one term in Eq. (9.5). This is an important inference from which a certain simplified technique can be derived. Particularly, we might turn to the earlier Hartree-Fock-like theories of excited states [43]. They can be easily reformulated for problems of our type, thus avoiding CIS computations, too complicated for large nanoclusters. Another, more general approach is to use a multiconfigurational self-consistent (MCSCF) theory in the CIS/UHF context. A suitable MCSCF matrix representation from [44] can be used for this purpose. The study in this line is now in progress.

## 9.7 Triplet-Singlet Excitations

Usually, spin-triplet states of the ND color centers are of the most interest for applications. Nevertheless, low-lying spin-singlet states attract attention in its own right, and many new researches appeared in this field [45–47]. We preliminarily studied the color center singlet states [28] wherein a special technique which is known as the spin-flip approach was exploited. The core idea of using spin flips was conceived by Bethe in his classical model of a 1D antiferromagnetic chain [48]. In quantum chemistry, the simplified semiempirical studies based on spin-flip transformations were first given in [49]. The most advanced are the ab initio approaches proposed in [50]. Here, for our main cluster  $C_{273}H_{176}N^-$ , we reconsider the problem of singlet states by using CNDOL approach.

For the singlet states, we will employ the following wave function of CIS-type (9.7):

$$|\Psi^*\rangle = \sum_{i;a} \tau_{ai} |i_\uparrow \rightarrow a_\downarrow\rangle \quad (9.11)$$

where  $i_\uparrow$  denotes a spin-up occupied (hole) orbital, and  $a_\downarrow$  is a spin-down vacant (particle) orbital in the reference UHF determinant of the ground triplet state. Such type of CIS is termed the SF-CIS model [50]. Clearly, elementary hole-particle transitions  $|i_\uparrow \rightarrow a_\downarrow\rangle$  decrease a spin projection of the initial ground state. It produces a possible superposition of determinants with zero spin projection. Thus, among variational solutions of the SF-CIS problem, almost spin-pure singlet states must appear.

For our system with the triplet ground state, the corresponding computational algorithm [51] gives the lowest transition to  $^1E$  symmetry singlet state with

excitation energy  $\lambda = 0.85$  eV. This value provides only a crude estimate of the unknown experimental quantity of  ${}^3A_2 \rightarrow {}^1E$  transition energy. Existing estimates of  ${}^3E$  are ranging from 0.42 eV to 0.9 eV (see Table 9.1 in [17]), but the value near 0.5 eV can be treated as a more reliable. Even though we can hope that the main physical features of the transition are well captured by the used semiempirical model. It follows from the results we discuss later.

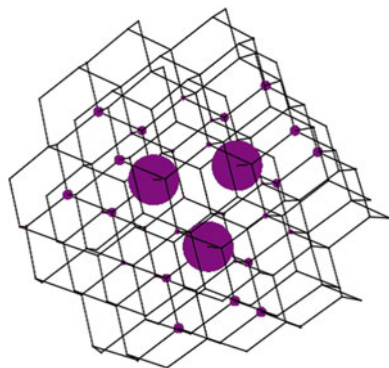
There is one point that we would like touch upon now and that is a specificity of singlet states in comparison with triplet states. Indeed, singlet states have no spin density and no other direct spin properties at all. However, in quantum chemistry there is a way to consider a counterpart of spin or quasispin effects for singlet states too. This is the effectively unpaired electron (EUE) theory which appeared in [52]; the state of the art in this field is given in review [41]. Simply speaking, we can construct the needed counterpart of the spin density by defining a deviation density matrix,  $D_{\text{odd}}$ , by the expression proposed in [52]:

$$D_{\text{odd}} = 2D - D^2$$

where  $D$  is a full one-electron density matrix summed up over spin variables. For the one-electron models,  $D_{\text{odd}} = 0$  for any singlet state, so (9.10) describes a deviation from the maximal closed-shell picture and thereby can serve as the density matrix of the effectively unpaired electrons occurring due to electron correlation. In particular, matrix trace,  $\text{Tr } D_{\text{odd}}$ , is treated a number of EUE. Somewhat more appropriate is the modified variant given in [53], where the EUE density matrix is redefined. This matrix is denoted as  $D_U$ , and it can be shown that  $D_U = (D_{\text{odd}})^2$ , and the total measure of EUE is identified with  $N_U = \text{Tr } D_U$ . These  $D_U$  and  $N_U$  quantities will be used below.

Now we describe the obtained results. For singlet state  ${}^1E$ , we found that  $N_U = 2.07$ , and such  $N_U \cong 2$  is a typical value for the low-lying spin-singlet excitations [41]. It means that this state is the so-called open-shell singlet in which we have in average two unpaired electron spins. These electrons are distributed inhomogeneously over the nanocluster, and it can be read off by merely glancing at Fig.9.4 where the corresponding diagram of atomic contributions  $\{L_A^U\}$  is presented

**Fig. 9.4** Unpaired electron distribution  $\{L_A^U\}$  in the lowest singlet state





(unpaired electron densities are colored by magenta). We see that the distribution is of the same type as the  $\{L_A^*\}$  distribution of the lowest TT transition given in Fig. 9.3. Localization measures are also close to indices in Eq. (9.5):  $\text{PR2} = 3.04$ ,  $\sigma_{\text{IPR}} = 46.0$ , and  $L_{[\text{NV}]}^{\text{U}} = 77\%$ .

## 9.8 Spin Properties

As a final topic, we briefly address the spin densities and related properties of the lowest energy states. Studying such properties is an important part of the current investigations of paramagnetic color centers, particularly for designing quantum computers based on the nanodiamond NV centers (see, e.g., [54]). The localization of electronic spins is one of the themes which is discussed frequently. Interestingly, it was established in past ESR studies [55] that the unpaired electrons are highly localized around the NV defect. The same picture was reported in the computations given in [12, 18, 56] and many other works. Even a rather simplified semiempirical model which was used in [28] produces a similar picture. It is no wonder that the present computations at a more sophisticated (CNDOL) level also provide a reasonable description of the spin density distribution. In particular, we obtained that in the ground triplet state, the spin density  $Q_A^0$  on atom  $A$  is practically the same for all three ND clusters we are studying here:  $Q_{\text{dangl}}^0 = 0.550$  for any of three dangling carbon atoms (in the vacancy vicinity), and  $Q_{\text{N}}^0 = 0$  (i.e., no spin density on the nitrogen atom in agreement with [57]). In the excited state, we have  $Q_{\text{dangl}}^* = 0.486$ , and a small  $Q_{\text{N}}^* = 0.063$  now occurs. It means that near the vacancy, almost 83% of total spin density is concentrated in case of the  ${}^3A_2$  ground state, and a bit smaller (76%) in case of  ${}^3E$  state. Independently, the spin localization is characterized by the PR indices (PR2 is equal to 3.05 for  ${}^3A_2$ , and  $\text{PR2} = 3.11$  for  ${}^3E$ ). We see that spin localization characteristics are in fact identical to those given in (9.5).

At this stage it is pertinent to consider again the lowest triplet-singlet excitation which is also strongly localized in the vacancy vicinity. We would like to clarify the fine difference between the singlet and triplet excitations which look, however, very similar in respect to their spatial localization. This clarification can be done by analyzing the spin correlators. Within the molecular electronic structure theory, they were introduced long ago by Penney [58], and recently became an important tool of quantum chemistry machinery [41, 59]. We follow the general consideration given in [60]. Let  $K_{AB}$  be the spin correlator of atoms (sites)  $A$  and  $B$ , that is,

$$K_{AB} = \langle \mathbf{S}_A \cdot \mathbf{S}_B \rangle \quad (9.12)$$

where  $\mathbf{S}_A$  is a local spin operator corresponding to the given atom  $A$ , and average  $\langle \rangle$  in (9.12) is over the state vector in question (CIS/UHF and SF-CIS/UHF wave functions here). Evidently,  $K_{AB} = 3/4$  for one-electron spins  $A$  and  $B$  ( $A \neq B$ ) which are exactly aligned parallel to one another, and  $K_{AB} = -3/4$  for the antiparallel spin

**Table 9.2** Spin correlator matrix  $\|K_{AB}\|$  for atoms near the vacancy (N-atom and three equivalent dangling C atoms) in the lower-energy states

${}^3A_2$	${}^3E$	${}^1E$
$\begin{pmatrix} 1.131 & -.001 & -.001 & -.001 \\ -.001 & 1.531 & .054 & .054 \\ -.001 & .054 & 1.531 & .054 \\ -.001 & .054 & .054 & 1.531 \end{pmatrix}$	$\begin{pmatrix} 1.178 & .003 & .003 & .003 \\ .003 & 1.479 & .041 & .041 \\ .003 & .041 & 1.479 & .041 \\ .003 & .041 & .041 & 1.479 \end{pmatrix}$	$\begin{pmatrix} 1.178 & .003 & -.002 & -.002 \\ -.002 & 1.489 & -.133 & -.133 \\ -.002 & -.133 & 1.489 & -.133 \\ -.002 & -.133 & -.133 & 1.489 \end{pmatrix}$

pair ( $A$ ,  $B$ ). In molecules, the correlators behave in a more complicated manner. For the chemically bonded atoms, usually  $K_{AB} \approx -1$ . Autocorrelator  $K_{AA} \approx 1$  and small  $K_{AB} \approx 0$  are typical of non-neighboring atoms  $A$  and  $B$  at large distances of separation. In Table 9.2 we give the corresponding values for the main four atoms of the vacancy vicinity (their ordering is the same as in [9.6]). We see that in all states, the nitrogen atom takes no part in spin coupling with the dangling carbon atoms. In turn, the latter show spin coupling with each other. But this coupling effect is most significant in the  ${}^1E$  singlet state, and the negative sign of the corresponding correlators indicates an antiferromagnetic character of spin interactions in this state.

## 9.9 Conclusion

In this chapter we presented a brief overview and add new results and appropriate means for a refined theoretical study of the excited states of color centers. We focused first of all on the localization measures for individual one-electron orbitals (PR and  $\sigma_{\text{IPR}}$  indices from Sect. 9.2). It allows us to understand a general orbital background to a strong localization of the NV color center in the vacancy vicinity. A more detailed description of excitation is achieved here by invoking the excited state structural analysis (ESSA) previously proposed for  $\pi\pi^*$  excitations and afterward extended to more complex problems [27].

By using the ESSA technique, namely, excitation and charge transfer indices, we provide a rather comprehensive analysis of the lowest TT excitation and show its essential charge transfer character. At the same time, it was fairly surprising to find no significant difference between the triplet-triplet and triplet-singlet excitations treated by ESSA. For this reason we brought into play the atomic spin correlator technique which was able to reveal a clear antiferromagnetic-type coupling of dangling carbon atoms in the singlet-excited NV center. At the same time, only a slight ferromagnetic-type coupling of the same atoms was detected in the triplet-excited NV center.

Here we were dealing with the nanodiamond NV color centers. However the same technique of the electronic-excitation visual analysis can be applied to many other related problems. For instance, the carborundum nanoclusters, including the

clusters with divacancy, can be considered as new prospective materials for quantum electronics [61], and in the future we will study them as well.

**Acknowledgments** This work is supported in part through the joint grant from the National Academy of Sciences of Ukraine and the National Academy of Sciences of Belarus (Grant No. 09-06-15). The author much benefited from useful discussions with A. P. Nizovtsev.

## References

1. Holt KB (2007) Diamond at the nanoscale: applications of diamond nanoparticles from cellular biomarkers to quantum computing. *Phil Trans R Soc A* 365:2845
2. Schrand AM, Cifta N, Hens SA, Shenderova OA (2009) Nanodiamond particles: properties and perspectives for bioapplications. *Crit Rev Solid State Mater Sci* 34:18; Shenderova OA, McGuire GE (2015) Science and engineering of nanodiamond particle surfaces for biological applications. *Biointerphases* 10:030802
3. Schirhagl R, Chang K, Loretz M, Degen CL (2014) *Annu Rev Phys Chem* 65:83
4. Nebel C, Nesladek M (eds) (2008) *Physics and applications of CVD diamond*. Wiley-VCH, Weinheim
5. Mildren CRP, Rabeau JR (eds) (2013) *Optical engineering of diamond*. Wiley-VCH, Berlin
6. Childress L, Walsworth R, Lukin M (2014) Atom-like crystal defects: from quantum computers to biological sensors. *Phys Today* 67:38
7. Praver S, Aharonovich I (eds) (2014) *Quantum information processing with Diamond*. Elsevier LTD, Oxford
8. Wrachtrup J, Kilin SY, Nizovtsev AP (2001) Quantum computation using the  $^{13}\text{C}$  nuclear spins near the single NV defect center in diamond. *Opt Spectrosc* 91:429
9. Awschalom DD, Epstein R, Hanson R (2007) The Diamond Age of Spintronics. *Sci Am* 297:84
10. Jelezko F, Wrachtrup J (2006) Single defect centres in diamond: A review. *Phys Stat Sol (A)* 203:3207
11. Doherty MW, Manson NB, Delaney P, Jelezko F, Wrachtrup J, Hollenberg CL (2013) The nitrogen-vacancy colour centre in diamond. *Phys Reports* 528:1
12. Pushkarchuk VA, Kilin SY, Nizovtsev AP, Pushkarchuk AL, Borisenko VE, von Borczyskowski C, Filonov AB (2005) Ab initio modeling of the electronic and spin properties of the [NV]— centers in diamond nanocrystals. *Opt Spectrosc* 99:245
13. Pushkarchuk VA, SYa K, Nizovtsev AP, Pushkarchuk AL, Filonov AB, Borisenko VE (2007) Modeling the atomic and electronic structure of diamond nanocrystals containing [NV]— centers by the density functional method. *J Appl Spectrosc* 74:95
14. Zyubin AS, Mebel AM, Hayash M (2009) Quantum chemical modeling of photoadsorption properties of the nitrogen-vacancy point defect in diamond. *J Comput Chem* 30:119
15. Gali A, Janzén E, Deák P, Kresse G, Kaxiras E (2009) Theory of Spin-Conserving Excitation of the N—V— Center in Diamond. *Phys Rev Lett* 103:186404
16. Kratochvílová I, Kovalenko A, Taylor A, Fendrych F, Řezáčová V, Vlček J, Zálíš S, Šebera J, Cígler P, Ledvina M, Nesládek M (2010) The fluorescence of variously terminated nanodiamond particles: Quantum chemical calculations. *Phys Status Sol (A)* 207:2045
17. Delaney P, Greer JC, Larsson JA (2010) Spin-polarization mechanisms of the nitrogen-vacancy center in diamond. *Nano Lett* 10:610
18. Ranjbar A, Babamoradi M, Saani MH, Vesaghi MA, Esfarjani K, Kawazoe Y (2011) Many-electron states of nitrogen-vacancy centers in diamond and spin density calculations. *Phys Rev B* 84:245315

19. Nizovtsev AP, Kilin SYA, Pushkarchuk AL, Pushkarchuk VA, Jelezko F (2014) Theoretical study of hyperfine interactions and optically detected magnetic resonance spectra by simulation of the C291[NV]-H172 diamond cluster hosting nitrogen-vacancy center. *New J Phys* 16:083014
20. Fuchs GD, Dobrovitski VV, Hanson R, Batra A, Weis CD, Schenkel T, Awschalom D (2008) Excited-State Spectroscopy Using Single Spin Manipulation in Diamond. *Phys Rev Lett* 101:117601
21. Rogers LJ, Doherty MW, Barson MSJ, Onoda S, Ohshima T, Manson NB (2014) Singlet levels of the NV— centre in diamond. *New J Phys* 17:013048
22. Neumann P, Kolesov R, Jacques V BJ, Tisler J, Batalov A, Rogers L, Manson NB, Balasubramanian G, Jelezko F, Wrachtrup J (2009) Excited-state spectroscopy of single NV defects in diamond using optically detected magnetic resonance. *New J Phys* 11:013017
23. Luzanov AV, Sukhorukov AA, Umanski VE (1974) Application of transition density matrix for analysis of excited states. *Theor Experim Chem* 10:354
24. Luzanov AV (1980) The Structure of the Electronic Excitation of Molecules in Quantum-chemical Models. *Russ Chem Rev* 49:1033
25. Luzanov AV, Prezhdo OV (2005) Irreducible charge density matrices for analysis of many-electron wave functions. *Int J Quant Chem* 102:582
26. Luzanov AV, Zhikol OA (2010) Electron invariants and excited state structural analysis for electronic transitions within CIS, RPA, and TDDFT models. *Int J Quant Chem* 110:902
27. Luzanov AV, Zhikol OA (2012) In: Leszczynski J, Shukla MK (eds) *Practical aspects of computational chemistry I: an overview of the last two decades and current trends*. Springer, New York, p 415
28. Luzanov AV (2015) Simplified computations of spin excitations in high-spin carbon nanoclusters and related systems. *Funct Mater* 22:514
29. Luzanov AV, Zhikol OA (2016) Excited state structural analysis (ESSA) for correlated states of spin-flip type: application to electronic excitations in nanodiamonds with defects. *Funct Mater* 23:63
30. Luzanov AV, Zhikol OA, Omelchenko IV, Nizovtsev AP, SYA K, Puchkarchuk AL, Puchkarchuk VA (2016) A semiempirical description of functionalized nanodiamonds with NV color centers. *Funct Mater* 23:268
31. Luzanov AV (2016) Modified participation ratio approach: application to edge-localized states in carbon nanoclusters. *Funct Mater* 23:599
32. Montero LA, Alfonso L, Alvarez JR, Perez E (1990) From PPP-MO theory to all-valence electron calculations of ionic and excited states in organic molecules. *Int J Quantum Chem* 37:465
33. Montero LA, Díaz LA, Castillo N (2002) UV–Vis spectrum of simple hydrocarbons in a zeolite cavity. A supramolecular charge transfer. *Chem Phys Lett* 364:176
34. Montero-Alejo AL, Fuentes ME, Menéndez-Proupin E, Orellana W, Bunge CF, Montero LA, García de la Vega JM (2010) Approximate quantum mechanical method for describing excitations and related properties of finite single-walled carbon nanotubes. *Phys Rev B* 81:235409
35. Jacobsen H, Cavallo L (2011) In: Leszczynski J (ed) *Handbook of computational chemistry*. Springer, Berlin/Heidelberg, p 95
36. Wolfram Research Inc. (2005) *Mathematica*, Version 5.2, Champaign, IL
37. Luzanov AV (1987) Configuration interaction in a nonorthogonal determinant basis. *Theor Experim Chem* 22:489
38. Bell RJ, Dean P, Hibbins-Butler DC (1970) Localization of normal modes in vitreous silica, germania and beryllium fluoride. *J Phys C* 3:2111
39. Luzanov AV, Umanski VE (1977) On the determination of the degree of collectivity of electronic excitations in molecules. *Theor Experim Chem* 13:162
40. Murphy NC, Wortis R, Atkinson WA (2011) Generalized inverse participation ratio as a possible measure of localization for interacting systems. *Phys Rev B* 83:184206

41. Luzanov AV (2016) In: Leszczynski J, Shukla MK (eds) Practical aspects of computational chemistry IV. Springer, New York, p 151
42. Martin RL (2003) Natural transition orbitals. *J Chem Phys* 118:4775
43. Morokuma K, Iwata K (1972) Extended Hartree-Fock theory for excited states. *Chem Phys Lett* 16:192; Caldwell JW, Gordon MS (1976) *Chem Phys Lett* 43:493
44. Luzanov AV, Klimko GT, Vul'fov AL (1987) The multiconfiguration SCF method and large-scale configuration interaction in calculations for the A1 and B1 states of the water molecule. *Theor Experim Chem* 23:1
45. Toyli DM, Christle DJ, Alkauskas A, Buckley BB, Van de Walle CG, Awschalom DD (2012) Measurement and Control of Single Nitrogen-Vacancy Center Spins above 600 K. *Phys Rev X* 2:031001
46. Kehayias P, Doherty MW, English D, Fischer R, Jarmola A, Jensen K, Leefer N, Hemmer P, Manson NB, Budker D (2013) Infrared absorption band and vibronic structure of the nitrogen-vacancy center in diamond. *Phys Rev B* 88:165202
47. Goldman ML, Doherty MW, Sipahigil A, Yao NV, Bennett SD, Manson NV, Kubanek A, Lukin MD (2015) State-selective intersystem crossing in nitrogen-vacancy centers. *Phys Rev B* 91:165201
48. Bethe HZ (1931) *Zur Theorie der Metalle*. *Physik* 71:205; Mattis DC (1965) *The theory of magnetism*. Harper and Row, New York
49. Luzanov AV (1981) One-particle approximation in valence-scheme superposition. *Theor Experim Chem* 17:228; Luzanov AV (1991) Operator methods in full configuration interaction theory for molecular systems. *Theor Experim Chem* 27:413
50. Krylov AI (2001) Size-consistent wave functions for bond-breaking: the quation-of-motion spin-flip model. *Chem Phys Lett* 338:375
51. Luzanov AV (2004) Spin Flip Models in the Spin Coupling Method of Many-Particle Amplitudes. *J Struct Chem* 45:729
52. Takatsuka K, Fueno T, Yamaguchi K (1978) Distribution of odd electrons in ground-state molecules. *Theor Chim Acta* 48:175
53. Head-Gordon M (2003) Characterizing unpaired electrons from the one-particle density matrix. *Chem Phys Lett* 372:508
54. Morton JLL, Elzerman J (2014) Quantum computing: Three of diamonds. *Nat Nanotechnol* 9:167
55. Loubser JHN, van Wyk JA (1978) Electron spin resonance in the study of diamond. *Rep Prog Phys* 41:1201; He F, Manson NB, Fisk PTH (1993) Paramagnetic resonance of photoexcited N-V defects in diamond. *Phys Rev B* 47:8816
56. Gali A, Fyta M, Kaxiras E (2008) Ab initio supercell calculations on nitrogen-vacancy center in diamond: Electronic structure and hyperfine tensor. *Phys Rev B* 77:155206
57. Goss JP, Jones R, Breuer SJ, Briddon PR, Öberg S (1996) The twelve-line 1.682 eV luminescence center in diamond and the vacancy-silicon complex. *Phys Rev Lett* 77:3041
58. Penney WG (1937) The electronic structure of some polyenes and aromatic molecules. III. Bonds of fractional order by the pair method. *Proc Roy Soc A* 158:306
59. Clark AE, Davidson ER (2001) Local spin. *J Chem Phys* 115:7382; Clark AE, Davidson ER (2002) Local spin II. *Mol Phys* 100:373
60. Luzanov AV, Prezhdo OV (2007) High-order entropy measures and spin-free quantum entanglement for molecular problems. *Mol Phys* 105:2879; Luzanov AV (2012) Some spin and spin-free aspects of coulomb correlation in molecules. *Int J Quant Chem* 112:2915
61. Morello A (2015) Quantum spintronics: Single spins in silicon carbide. *Nat Mater* 14:135

# Chapter 10

## Excitonic Quasimolecules in Nanoheterosystems Containing Semiconductor and Dielectric Quantum Dots

Sergey I. Pokutnyi

### 10.1 Introduction

The idea of superatom was fruitful for the development of nanophysics [1–3]. A superatom (quasiatomic nanoheterostructures) consists of a spherical quantum dot (QD) with radius  $a$ , the volume of which contains the semiconductor (or dielectric) material. QD is surrounded by dielectric (semiconductor) matrix [2, 3]. A hole is localized in the volume of QD, and the electron is localized over a spherical interface (QD-matrix). In this nanosystem, the lowest electronic level is in matrix, and the lowest hole level is within volume of QD. A large shift of the valence band (700 meV) generates the localization of holes in the volume of QD. A significant shift of the conduction band (about 400 meV) is a potential barrier for electrons [4] (see Fig. 10.1). The electrons move in the matrix and do not penetrate in the volume of QD [2–4]. The energy of the Coulomb interaction of electron with hole and the energy of the polarization interaction of electron with interface (QD-matrix) form a potential well, in which the electron is localized over the surface of quantum dot. Certain orbitals, localized to the surrounding quantum dot, correspond to electrons in superatom [2, 3].

During investigation of the optical characteristics of nanosystems with CdS, ZnSe, Al<sub>2</sub>O<sub>3</sub>, and Ge quantum dots in experimental papers [4–8], it was found that the electron can be localized above the surface of the QD while the hole here moves in the volume of the QD. In [4–8], the appearance of superatoms located in dielectric matrices as cores containing CdS, ZnSe, Al<sub>2</sub>O<sub>3</sub>, and Ge quantum dots was apparently established experimentally for the first time. A substantial increase in the

---

S.I. Pokutnyi (✉)

Chuiko Institute of Surface Chemistry, National Academy of Sciences of Ukraine, 17 General Naumov Str, Kyiv, UA 03164, Ukraine  
e-mail: [pokutnyi.serg@gmail.com](mailto:pokutnyi.serg@gmail.com)

© Springer International Publishing AG 2017

O. Fesenko, L. Yatsenko (eds.), *Nanophysics, Nanomaterials, Interface Studies, and Applications*, Springer Proceedings in Physics 195,  
DOI 10.1007/978-3-319-56422-7\_10

131

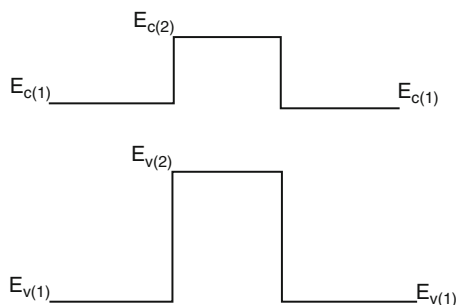


**Fig. 10.1** Band diagram of the QD-matrix nanoheterostructure. In the nanoheterostructure, the QD is a potential well for a hole and a barrier for an electron. The energies  $E_{c(1)}$ ,  $E_{v(1)}$ ,  $E_{c(2)}$ , and  $E_{v(2)}$  correspond to the positions of the bottom of the conduction band and the top of the valence band of the matrix and QD, respectively

binding energy of the ground state of an electron in a superatom in comparison with the binding energy of an exciton in CdS, ZnSe, and  $\text{Al}_2\text{O}_3$ , and single crystals was detected in [2, 3, 9, 10].

In [5–8], the optical characteristics of samples of borosilicate glasses doped with CdS, ZnSe, and  $\text{Al}_2\text{O}_3$  at concentrations between  $x \approx 0.003\%$  and 1% were investigated. The average radii  $\bar{a}$  of CdS and ZnSe QDs were in the range of  $\bar{a} \approx 2.0$ –20 nm. When there were large concentrations of CdS quantum dots in the samples (from  $x \approx 0.6\%$  to  $x \approx 1\%$ ), a maximum, interpreted on the basis of the appearance of bonded QD states, was detected in the low-temperature absorption spectra. In order to explain the optical characteristics of such nanosystems, we proposed a model of a quasimolecule representing two ZnSe and CdS QDs that form an exciton quasimolecule as a result of the interaction of electrons and holes [3, 11–14].

It was noted [4, 6] that, at such levels of QD content in the samples, one must take into account the interaction between charge carriers localized above the QD surfaces. Therefore, in [11–14], we develop the theory of an exciton quasimolecule (or biexciton) (formed from spatially separated electrons and holes) in a nanosystem that consists of ZnSe and CdS QDs synthesized in a borosilicate glassy matrix. Using the variational method, we obtain the total energy and the binding energy of the exciton quasimolecule (or biexciton) singlet ground state in such system as functions of the spacing between the QD surfaces and of the QD radius. We show that the biexciton formation is of the threshold character and possible in a nanosystem, in which the spacing between the QD surfaces exceeds a certain critical spacing. It is established that the spectral shift of the low-temperature luminescence peak [6] in such a nanosystem is due to quantum confinement of the energy of the biexciton ground state.

The convergence of two (or more) QDs up to a certain critical value  $D_c$  between surfaces of QD leads to overlapping of electron orbitals of superatoms and the emergence of exchange interactions [3, 11–14]. In this case, the overlap integral of the electron wave functions takes a significant value. As a result, the conditions for

the formation of quasimolecules from QDs can be created [3, 11–14]. One can also assume that the above conditions of formation of quasimolecules can be provided by external physical fields. This assumption is evidenced by results of [15, 16], in which the occurrence of the effective interaction between QDs at considerable distances under conditions of electromagnetic field was observed experimentally. In [17], energies of the ground state of “vertical” and “horizontal” located pair of interacting QDs (“molecules” from two QDs) were determined as a function of the steepness of the confining potential and the magnetic field strength. The quantum part of nanocomputer, which was implemented on a pair of QDs (“molecules” from two QDs) with charge states, is  $n$  qubits [18]. The first smoothly working quantum computer has been on QDs with two electron orbital states as qubits, described by a pseudospin ( $1/2$ ). A single cell was taken as a couple of asymmetric pair QDs with different sizes and significantly different energies. The electron is injected into the heterostructure from the channel which occupied the lower level. That is, it was located in a QD with larger size.

The theory of excitonic quasimolecules (formed of spatially separated electrons and holes) in nanosystems that consist of semiconductor quantum dots synthesized in a borosilicate glass matrix is presented. It is shown that exciton quasimolecule formation is of the threshold character and possible in nanosystem, if the spacing between the quantum dots surfaces is larger than a certain critical spacing. It was found that the binding energy of singlet ground state of exciton quasimolecule, consisting of two semiconductor quantum dots is a significant large value, larger than the binding energy of the biexciton in a semiconductor single crystal almost two orders of magnitude. Such quasimolecule exciton is promising to create new elements of silicon in infrared optoelectronics, including new infrared sensors.

## 10.2 Binding Energy of Singlet Ground State of Excitonic Quasimolecule

Consider the model of nanosystems [3, 11–14], containing two superatoms. In this model, superatoms consist of spherical semiconductor QDs,  $A$  and  $B$ , synthesized in a matrix of borosilicate glass with dielectric constant  $\varepsilon_1$ . Let the QD radii be  $a$ , the spacing between the spherical QD centers be  $L$ , and the spacing between the spherical QD surfaces be  $D$ . Each QD is formed from a semiconductor material with dielectric constant  $\varepsilon_2$ . For simplicity and without loss of generality, we assume that holes  $h(A)$  and  $h(B)$  with effective masses  $m_h$  are localized in centers of QD( $A$ ) and QD( $B$ ) and electrons  $e(1)$  and  $e(2)$  with effective masses  $m_e^{(1)}$  are localized near the spherical surfaces of QD( $A$ ) and QD( $B$ ), respectively.  $r_{A(1)}$  is the distance of the electron  $e(1)$  from the QD( $A$ ) center;  $r_{B(2)}$  is the distance of the electron  $e(2)$  from the QD( $B$ ) center;  $r_{A(2)}$  is the distance of the electron  $e(2)$  from the QD( $A$ ) center;  $r_{B(1)}$  is the distance of the electron  $e(1)$  from the QD( $B$ ) center;  $r_{12}$  is the distance between the electron  $e(1)$  and  $e(2)$ ; (see Fig. 10.2). The above assumption is reasonable, since the ratio between the effective masses of electron and hole in



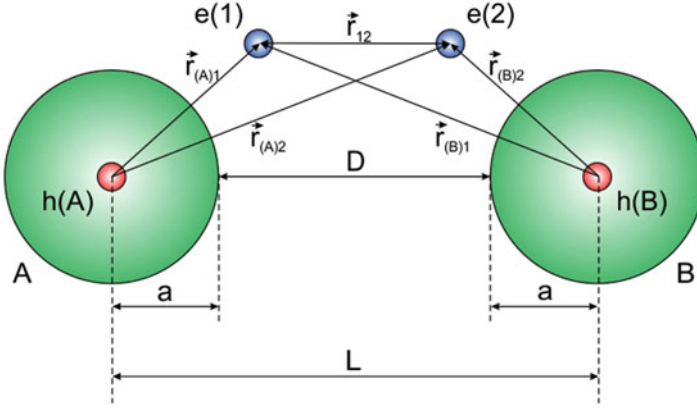


**Fig. 10.2** Schematic representation of a nanosystem consisting of two spherical QDs, QD(A) and QD(B), of radii  $a$ . The holes  $h(A)$  and  $h(B)$  are located in the QD(A) and QD(B) centers, and the electrons  $e(1)$  and  $e(2)$  are localized near the QD(A) and QD(B) surfaces ( $r_{A(1)}$  is the distance of the electron  $e(1)$  from the QD(A) center;  $r_{B(2)}$  is the distance of the electron  $e(2)$  from the QD(B) center;  $r_{A(2)}$  is the distance of the electron  $e(2)$  from the QD(A) center;  $r_{B(1)}$  is the distance of the electron  $e(1)$  from the QD(B) center;  $r_{12}$  is the spacing between the electrons  $e(1)$  and  $e(2)$ ;  $L$  is the spacing between the QD centers;  $D$  is the spacing between the QD surfaces;  $e'(1)$ ,  $e'(2)$  and  $h'(A)$ ,  $h'(B)$  are the image charges of the electrons and holes)

the nanosystem is much smaller than unity ( $(m_e^{(1)}/m_h) \ll 1$ ). Let us assume that there is an infinitely high potential barrier on the spherical QD-matrix interface. In the nanosystem, the holes do not therefore escape from the volume of the QD while the electrons do not enter the QD.

In such a model of the nanosystem, we will study the possible formation of an exciton quasimolecule from spatially confined electrons and holes. The holes are located at the centers of QD(A) and QD(B), while the electrons are localized close to the spherical surfaces of QD(A) and QD(B). In terms of the adiabatic approximation and also in the effective mass approximation, we write the Hamiltonian of such a quasimolecule in the following form [3, 11]:

$$\hat{H} = \hat{H}_{A(1)} + \hat{H}_{B(2)} + \hat{H}_{\text{int}} \quad (10.1)$$

Here  $\hat{H}_{A(1)}$  and  $\hat{H}_{B(2)}$  are the Hamiltonians of the superatoms. The hole  $h(A)$  is at the center of QD(A) while the electron  $e(1)$  is localized above the surface of QD(A); the hole  $h(B)$  is located at the center of QD(B) while the electron  $e(2)$  is localized above the surface of QD(B), respectively. The Hamiltonian of the superatom  $\hat{H}_{A(1)}$  will therefore take the following form [3, 11]:

$$\begin{aligned} \hat{H}_{A(1)} = & -\frac{\hbar^2}{2\mu} \Delta_{(1)} + V_{e(1)h(A)}(\mathbf{r}_{A(1)}, \mathbf{r}_{h(A)}) + U(\mathbf{r}_{A(1)}, \mathbf{r}_{h(A)}, a) \\ & + V_{e(1)}(r_{A(1)}) + V_{h(A)}(r_{h(A)}) + E_g, \end{aligned} \quad (10.2)$$

In (10.2), the first term is the kinetic energy operator of the exciton; the energy of Coulomb interaction  $V_{e(1)h(A)}$  between the electron  $e(1)$  and the hole  $h(A)$  is described by the formula [2]:

$$V_{e(1)h(A)} = -\frac{1}{2} \left( \frac{1}{\varepsilon_1} + \frac{1}{\varepsilon_2} \right) \frac{e^2}{|\mathbf{r}_{e(1)} - \mathbf{r}_{h(A)}|} \quad (10.3)$$

The potentials

$$V_{h(A)}(r_{h(A)}) = \begin{cases} 0, & r_{h(A)} \leq a \\ \infty, & r_{h(A)} > a \end{cases} \quad (10.4)$$

$$V_{e(1)}(r_{A(1)}) = \infty, \quad r_{e(1)} \leq a \quad (10.5)$$

describe the motion of quasiparticles in the nanosystem in the model of an infinitely deep potential well; and  $E_g$  is the band gap in the semiconductor with the permittivity  $\varepsilon_2$ .

In [2], in the context of the modified effective mass method [19], the theory of an exciton formed from an electron and a hole spatially separated from the electron was developed (the hole was in motion within the QD and the electron was localized on the outer side of the spherical QD-matrix interface). In [2], the energy of the polarization interaction of the electron and hole with the spherical interface with the relative permittivity ( $\varepsilon = (\varepsilon_2/\varepsilon_1) \gg 1$ ),  $U(\mathbf{r}_{A(1)}, \mathbf{r}_{h(A)}, a)$  is represented as the algebraic sum of the energies of interaction of the hole  $h(A)$  and the electron  $e(1)$  with their own ( $V_{h(A)h'(A)}$ ,  $V_{e(1)e'(1)}$ ) and foreign ( $V_{e(1)h'(A)}$ ,  $V_{h(A)e'(1)}$ ) images:

$$U(r_{A(1)}, r_{h(A)}, a) = V_{h(A)h'(A)}(r_{h(A)}, a) + V_{e(1)e'(1)}(r_{A(1)}, a) + V_{h(A)e'(1)}(r_{h(A)}, r_{A(1)}, a) + V_{e(1)h'(A)}(r_{A(1)}, r_{h(A)}, a) \quad (10.6)$$

$$V_{h(A)h'(A)} = \frac{e^2 \beta}{2\varepsilon_2 a} \cdot \left( \frac{a^2}{a^2 - r_{h(A)}^2} + \varepsilon \right), \quad (10.7)$$

$$V_{e(1)e'(1)} = -\frac{e^2 \beta}{2\varepsilon_1 a} \cdot \frac{a^4}{r_{A(1)}^2 (r_{A(1)}^2 - a^2)}, \quad (10.8)$$

$$V_{h(A)e'(1)} = \frac{e^2 \beta}{2\varepsilon_2 a} \cdot \frac{a^2}{r_{A(1)} |\mathbf{r}_{h(A)} - (\mathbf{a}/r_{A(1)})^2 \mathbf{r}_{A(1)}|}, \quad (10.9)$$

$$V_{e(1)h'(A)} = -\frac{e^2 \beta}{2\varepsilon_1 a} \cdot \frac{a^2}{r_{h(A)} |\mathbf{r}_{A(1)} - (\mathbf{a}/r_{h(A)})^2 \mathbf{r}_{h(A)}|}. \quad (10.10)$$

Here  $r_{h(A)}$  is the distance of the hole from the QD( $A$ ) center.

In the quasimolecule Hamiltonian (10.1),  $\widehat{H}_{B(2)}$  is the Hamiltonian of an exciton formed from an electron and a hole spaced from the electron (the hole  $h(B)$  is located in the  $QD(B)$  center and the electron  $e(2)$  is localized above the  $QD(B)$  surface). The Hamiltonian  $\widehat{H}_{B(2)}$  has a form similar to that of the Hamiltonian  $\widehat{H}_{A(1)}$  in (10.2):

$$\begin{aligned} \widehat{H}_{B(2)} = & -\frac{\hbar^2}{2\mu} \Delta_{(2)} + V_{e(2)h(B)} \left( (r_{B(2)}, r_{h(B)}) + U(r_{B(2)}, r_{h(B)}, a) \right) \\ & + V_{e(2)}(r_{B(2)}) + V_{h(B)}(r_{h(B)}) + E_g \end{aligned} \quad (10.11)$$

The terms entering into the Hamiltonian (10.11) are expressed by formulas similar to the corresponding formulas in the Hamiltonian (10.2). Let us write the expression for the Hamiltonian  $\widehat{H}_{\text{int}}$  [3, 11]:

$$\widehat{H}_{\text{int}} = V_{AB}(D, a) + V_{e(1)h(B)}(r_{B(1)}, r_{h(B)}) + V_{e(2)h(A)}(r_{A(2)}, r_{h(A)}) + V_{e(1)e(2)}(r_{12}), \quad (10.12)$$

Here,  $V_{AB}(D, a)$  is the energy of the interaction of charge carriers (the electrons  $e(1)$  and  $e(2)$  and the holes  $h(A)$  and  $h(B)$ ) with polarization fields induced by these charge carriers at the  $QD(A)$  and  $QD(B)$  surfaces:

$$\begin{aligned} V_{AB}(D, a) = & V_{h(A)h(B)}(D, a) + V_{h(A)h'(B)}(D, a) \\ & + V_{h(A)e'(2)}(r_{B(2)}, a) + V_{e(1)e'(2)}(r_{A(1)}, r_{B(2)}, a) \\ & + V_{e(1)h'(B)}(r_{B(1)}, a) + V_{h(B)h'(A)}(D, a) \\ & + V_{h(B)e'(1)}(r_{B(1)}, a) + V_{e(2)e'(1)}(r_{B(2)}, r_{A(1)}, a) + \\ & + V_{e(2)h'(A)}(r_{A(2)}, a), \end{aligned} \quad (10.13)$$

$V_{e(1)h(B)}$  is the energy of interaction of the electron  $e(1)$  with the hole  $h(B)$ ; and  $V_{e(2)h(A)}$  is the energy of interaction of the electron  $e(2)$  with the hole  $h(A)$ . The aforementioned energies are described by the expressions:

$$V_{e(1)h(B)}(\mathbf{r}_{B(1)}) = -\frac{e^2}{\boldsymbol{\varepsilon}_1 \mathbf{r}_{B(1)}}, \quad (10.14)$$

$$V_{e(2)h(A)}(\mathbf{r}_{A(2)}) = -\frac{e^2}{\boldsymbol{\varepsilon}_1 \mathbf{r}_{A(2)}}; \quad (10.15)$$

The energy of Coulomb interaction between the electrons  $e(1)$  and  $e(2)$ ,  $V_{e(1)e(2)}(r_{12})$ , is determined by the formula:

$$V_{e(1)e(2)}(r_{12}) = -\frac{e^2}{\boldsymbol{\varepsilon}_1 r_{12}}; \quad (10.16)$$

and the energy of interaction between the holes  $h(A)$  and  $h(B)$  is described by the expression:

$$V_{h(A)h(B)}(D, a) = -\frac{e^2}{\epsilon_1(D + 2a)} \quad (10.17)$$

According to [2], the major contribution to the energy of the ground state of the exciton (formed by an electron and a hole spatially separated from the electron) is made by the average energy of the Coulomb interaction between the electron and hole  $\langle R_0(r_{A(1)}, \tilde{a}) | V_{e(1)h(A)}(r_{A(1)}) | R_0(r_{A(1)}, \tilde{a}) \rangle$  (or  $\langle R_0(r_{B(2)}, \tilde{a}) | V_{e(2)h(B)}(r_{B(2)}) | R_0(r_{B(2)}, \tilde{a}) \rangle$ ) on the basis of the Coulomb-shaped variational wave functions  $R_0(r_{A(1)}, a)$ :

$$R_0(r_{A(1)}, \tilde{a}) = \tilde{A} \exp(-\tilde{\mu}(\tilde{a})(r_{A(1)}/a_{\text{ex}}^0)). \quad (10.18)$$

Here,  $\tilde{\mu}(\tilde{a}) = (\tilde{\mu}(\tilde{a})/m_0)$  is the variational parameter ( $\tilde{\mu}(a)$  is the reduced exciton effective mass,  $m_0$  is the electron mass in vacuum) and the normalization constant is

$$\tilde{A} = \pi^{-1/2} (a_{\text{ex}}^0)^{-3/2} \tilde{\mu}^{3/2} \exp(\tilde{\mu}\tilde{a}) \left[ 2(\tilde{\mu}\tilde{a})^2 + 2(\tilde{\mu}\tilde{a}) + 1 \right]^{-1/2} \quad (10.19)$$

where  $\tilde{a} = (a/a_{\text{ex}}^0)$  is the dimensionless QD radius,  $a_{\text{ex}}^0 = \frac{2\epsilon_1\epsilon_2}{(\epsilon_1 + \epsilon_2)} \cdot \frac{\hbar^2}{\mu_0 e^2}$  is the Bohr radius of a two-dimensional (2D) exciton localized above the planar interface between a semiconductor with the permittivity  $\epsilon_2$  and a matrix with the permittivity  $\epsilon_1$  (the hole is in motion within the semiconductor, whereas the electron is in the matrix),  $e$  is the electron charge, and  $\mu_0 = m_e^{(1)} m_h / (m_e^{(1)} + m_h)$  is the reduced 2D exciton effective mass.

The abovementioned feature allows us to retain only the energies of the Coulomb interaction between the electron and hole  $V_{e(1)h(A)}(r_{A(1)})$  [Eq. (10.3)] and  $V_{e(2)h(B)}(r_{B(2)})$  determined by a formula similar to [Eq. (10.3)], correspondingly, in the Hamiltonians  $\hat{H}_{A(1)}$  (2) and  $\hat{H}_{B(2)}$  [Eq. (10.14)], and to retain only the energy of the interaction between the holes  $h(A)$  and  $h(B)$   $V_{h(A)h(B)}(D, a)$  [Eq. (10.17)] in the interaction energy  $V_{AB}(D, a)$  [Eq. (10.13)]. At the same time, the energy  $V_{AB}(D, a)$  is determined by the formula [Eq. (10.17)]:

$$V_{AB}(D, a) = V_{h(A)h(B)}(D, a) = -\frac{e^2}{\epsilon_1(D + 2a)}. \quad (10.20)$$

With the above assumptions, the superatom Hamiltonians  $\hat{H}_{A(1)}$  (10.2) and  $\hat{H}_{B(2)}$  (10.11) take the form:

$$\hat{H}_{A(1)} = -\frac{\hbar^2}{2\mu} \Delta_{(1)} + V_{e(1)h(A)}(r_{A(1)}) + E_g, \quad (10.21)$$

$$\hat{H}_{B(2)} = -\frac{\hbar^2}{2\mu} \Delta_{(2)} + V_{e(2)h(B)}(r_{B(2)}) + E_g \quad (10.22)$$

In this case, the quasimolecule Hamiltonian  $\hat{H}$  (10.1) involves the superatom Hamiltonians  $\hat{H}_{A(1)}$  (10.21) and  $\hat{H}_{B(2)}$  (10.22) as well as the Hamiltonian  $\hat{H}_{\text{int}}$  (10.15), in which  $\hat{H}_{\text{int}}$  (10.12), in which the interaction energy  $V_{AB}(D, a)$  is determined by formula (10.20).

On the assumption that the spins of electrons e(1) and e(2) are antiparallel, we write the normalized wave function of the singlet ground state of the exciton quasimolecule in the form of a linear combination of wave functions  $\Psi_1(r_{A(1)}, r_{B(2)})$  and  $\Psi_2(r_{A(2)}, r_{B(1)})$  [11–14]:

$$\Psi_s(\mathbf{r}_{A(1)}, \mathbf{r}_{A(2)}, \mathbf{r}_{B(1)}, \mathbf{r}_{B(2)}) = [2(1 + S^2(\mathbf{D}, \mathbf{a}))]^{-1/2} [\Psi_1(r_{A(1)}, r_{B(2)}) + \Psi_2(r_{A(2)}, r_{B(1)})] \quad (10.23)$$

Considering that electrons e(1) and e(2) move independently of each other, we represent wave functions  $\Psi_1(r_{A(1)}, r_{B(2)})$  and  $\Psi_2(r_{A(2)}, r_{B(1)})$  [Eq. (10.23)] as the product of one-electron variational wave functions  $\varphi_{A(1)}(r_{A(1)})$  and  $\varphi_{B(2)}(r_{B(2)})$  and also  $\varphi_{A(2)}(r_{A(2)})$  and  $\varphi_{B(1)}(r_{B(1)})$ , respectively [3, 11–14]:

$$\Psi_1(\mathbf{r}_{A(1)}, \mathbf{r}_{B(2)}) = \varphi_{A(1)}(r_{A(1)}) \varphi_{B(2)}(r_{B(2)}), \quad (10.24)$$

$$\Psi_2(r_{A(2)}, r_{B(1)}) = \varphi_{A(2)}(r_{A(2)}) \varphi_{B(1)}(r_{B(1)}). \quad (10.25)$$

We represent the one-electron wave functions  $\varphi_{A(1)}(r_{A(1)})$  and  $\varphi_{B(2)}(r_{B(2)})$  that describe, correspondingly, the electron e(1) localized above the QD(A) surface and the electron e(2) localized above the QD(B) surface and the wave functions  $\varphi_{A(2)}(r_{A(2)})$  and  $\varphi_{B(1)}(r_{B(1)})$  that describe, correspondingly, the electron e(2) localized above the QD(A) surface and the electron e(1) localized above the QD(B) surface as variational Coulomb-shaped wave functions [11]:

$$\varphi_{A(1)}(r_{A(1)}) = \tilde{A} \exp(-\tilde{\mu}(\tilde{a})(r_{A(1)}/a_{ex}^0)), \quad (10.26)$$

$$\varphi_{B(2)}(r_{B(2)}) = \tilde{A} \exp(-\tilde{\mu}(\tilde{a})(r_{B(2)}/a_{ex}^0)), \quad (10.27)$$

$$\varphi_{A(2)}(r_{A(2)}) = \tilde{A} \exp(-\tilde{\mu}(\tilde{a})(r_{A(2)}/a_{ex}^0)), \quad (10.28)$$

$$\varphi_{B(1)}(r_{B(1)}) = \tilde{A} \exp(-\tilde{\mu}(\tilde{a})(r_{B(1)}/a_{ex}^0)). \quad (10.29)$$

Because of the identity of the electrons, the wave function  $\Psi_2(r_{A(2)}, r_{B(1)})$  (10.25) is equivalent to the wave function  $\Psi_1(r_{A(1)}, r_{B(2)})$  (10.24). In (10.23), the overlapping integral  $S(D, a)$  is determined by the formula

$$S(D, a) = \int d\tau_1 \varphi_{A(1)}(r_{A(1)}) \varphi_{B(1)}(r_{B(1)}) \quad (10.30)$$

where  $d\tau_1$  is the volume element of the electron e(1).

In the first approximation, the energy of the exciton quasimolecule singlet ground state is defined by the average value of the Hamiltonian  $\widehat{H}$  (10.1) on the basis of states described by the zero-approximation wave functions  $\Psi_s$  (10.23) [11]:

$$E(D, \bar{\mu}(a, D), a) = \left\langle \Psi_s(r_{A(1)}, r_{A(2)}, r_{B(1)}, r_{B(2)}) \left| \widehat{H} \right| \Psi_s(r_{A(1)}, r_{A(2)}, r_{B(1)}, r_{B(2)}) \right\rangle. \quad (10.31)$$

With the explicit form of the wave functions (10.23), (10.24), (10.25), (10.26), (10.27), (10.28), and (10.29), the energy functional of the exciton quasimolecule singlet ground state takes the form

$$E_0(\tilde{D}, \bar{\mu}(\tilde{a}, \tilde{D}), \tilde{a}) = 2E_{\text{ex}}(\tilde{a}, \bar{\mu}(\tilde{a})) + \frac{J(\tilde{D}, \bar{\mu}(\tilde{a}, \tilde{D}), \tilde{a}) + K(\tilde{D}, \bar{\mu}(\tilde{a}, \tilde{D}), \tilde{a})}{1 + S^2(\tilde{D}, \bar{\mu}(\tilde{a}, \tilde{D}), \tilde{a})}, \quad (10.32)$$

Here,  $E_{\text{ex}}(\tilde{a}, \bar{\mu}(\tilde{a}))$  is the energy functional of the exciton ground state (for the exciton formed from an electron and a hole spatially separated from the electron):

$$E_{\text{ex}}(\tilde{a}, \bar{\mu}(\tilde{a})) = \left\langle \varphi_{A(1)}(r_{A(1)}) \left| \widehat{H}_{A(1)} \right| \varphi_{A(1)}(r_{A(1)}) \right\rangle. \quad (10.33)$$

The second term in (10.32) is a functional  $E_b(D, a)$  representing the binding energy of singlet ground state of excitonic quasimolecule. In the functional determined by formula (10.32),  $J(\tilde{D}, \bar{\mu}(\tilde{a}, \tilde{D}), \tilde{a})$  is determined by the expression here ( $\tilde{D} = (D/a_{\text{ex}}^0)$ ).

$$J(\tilde{D}, \bar{\mu}(\tilde{a}, \tilde{D}), \tilde{a}) = \left\langle \varphi_{A(1)}(r_{A(1)}) \varphi_{B(2)}(r_{B(2)}) \left| H_{\text{int}} \right| \varphi_{A(1)}(r_{A(1)}) \varphi_{B(2)}(r_{B(2)}) \right\rangle. \quad (10.34)$$

The functional  $J(\tilde{D}, \bar{\mu}(\tilde{a}, \tilde{D}), \tilde{a})$  (10.34) can be represented as the algebraic sum of the functionals of the average energies of Coulomb interaction [11].

In the functional described by (10.32),  $K(\tilde{D}, \bar{\mu}(\tilde{a}, \tilde{D}), \tilde{a})$  is determined by the formula:

$$K(\tilde{D}, \bar{\mu}(\tilde{a}, \tilde{D}), \tilde{a}) = \left\langle \varphi_{B(1)}(r_{B(1)}) \varphi_{A(2)}(r_{A(2)}) \left| \widehat{H}_{\text{int}} \right| \varphi_{A(1)}(r_{A(1)}) \varphi_{B(2)}(r_{B(2)}) \right\rangle. \quad (10.35)$$

The functional  $K(\tilde{D}, \bar{\mu}(\tilde{a}, \tilde{D}), \tilde{a})$  (10.35) can be represented as the algebraic sum of the functionals of the average energies of the exchange interaction [11].

In the case it spins of e(1) and e(2) electrons are parallel than similarly to the theory of the chemical bond of hydrogen molecule [20] the excitonic quasimolecule, consisting of two QDs is not formed [14]. Therefore, we did not consider this case.

Within the framework of the variational method at a first approximation, the total energy of ground singlet state of excitonic quasimolecule is determined by average value of the Hamiltonian  $\hat{H}$  (1) for states, which are described by wave functions of the zero approximation  $\Psi_s(r_{A(1)}, r_{A(2)}, r_{B(1)}, r_{B(2)})$  (10.23) [14]:

$$E_0(D, a) = 2E_{\text{ex}}(a) + E(D, a), \quad (10.36)$$

where  $E_B(D, a)$  is the binding energy of singlet ground state of excitonic quasimolecule and the binding energy of  $E_{\text{ex}}(a)$  of ground state of electron in superatom, found in [2, 9]. The wave function  $\Psi_s(r_{A(1)}, r_{A(2)}, r_{B(1)}, r_{B(2)})$  (10.23) contains wave functions (10.24), (10.25), (10.26), (10.27), (10.28), and (10.29). The results of a numerical variational calculation of the binding energy  $E_0(D, a)$  of ground singlet state of excitonic quasimolecule, containing two CdS QDs with average radii of  $\bar{a}_1 = 4$  nm and  $\bar{a}_2 = 4.4$  nm ( $\varepsilon_2 = 9.3$ , effective hole mass in QD ( $m_h/m_0$ ) is 5)), grown in a matrix of borosilicate glass ( $\varepsilon_1 = 2$ , the electron effective mass in the matrix ( $m_e^{(1)}/m_0$ ) is 0.537)), which was investigated in experimental work [5, 6], are shown in Tables 10.1 and 10.2 [14].

In [5, 6], we studied the optical properties of the samples of borosilicate glass, doped with CdS with concentrations from  $x \approx 0,003\%$  to 1%. The average radius  $\bar{a}$  of CdS QDs ranged over  $\bar{a} \approx 2.0\text{--}20$  nm. At concentrations CdS QD in the order of  $x \approx 0.6\%$  to  $x \approx 1\%$ , the peak, which is  $(E - E_g) \approx -712$  meV, was found in the absorption spectra of the samples at a temperature of 4 K (where  $E_g$  is width band gap of CdS QD) [6].

The variational method, used for estimation of the binding energy  $E_B(D, a)$  of ground singlet state of excitonic quasimolecules will be valid if the binding energy  $E_B(D, a)$  of quasimolecule is small, compared with the binding energy  $E_{\text{ex}}(a)$  of the ground state of superatom [11, 14]:

$$(E_B(D, a)/E_{\text{ex}}(a)) \ll 1 \quad (10.37)$$

**Table 10.1** Dependence of the binding energy  $E_B(D, \bar{a}_1)$  and also the total energy  $E_0(D, \bar{a}_1)$  of the singlet ground state of the excitonic quasimolecule, consisting of two CdS QDs with average radii  $\bar{a}_1 = 4$  nm on the distance  $D$  between the surfaces of the QD

$\bar{a}_1$ nm	$E_{\text{ex}}(\bar{a}_1)$ meV	$D$ nm	$E_B(D, \bar{a}_1)$ meV	$E_0(D, \bar{a}_1)$ meV
4	-320	1.8	0	-640
4	-320	2.2	-27	-667
4	-320	2.6	-28.1	-668.1
4	-320	3	-27.8	-667.8
4	-320	4	-23.2	-663.2
4	-320	6	-9.5	-649.5
4	-320	8.4	0	-640

In this case, the binding energies of an electron in a superatoms are  $E_{\text{ex}}(\bar{a}_1) \cong -320$  meV

**Table 10.2** Dependence of the binding energy  $E_B(D, \bar{a}_2)$  and also the total energy  $E_0(D, \bar{a}_2)$  of the singlet ground state of the excitonic quasimolecule, consisting of two CdS QDs with average radii  $\bar{a}_2 = 4.4$  nm on the distance  $D$  between the surfaces of the QD

$\bar{a}_2$ nm	$E_{\text{ex}}(\bar{a}_2)$ meV	$D$ nm	$E_B(D, \bar{a}_2)$ meV	$E_0(D, \bar{a}_2)$ meV
4.4	-344	1.6	0	-688
4.4	-344	2.2	-29.4	-717.4
4.4	-344	2.48	-32.8	-720.8
4.4	-344	2.6	-31.9	-719.9
4.4	-344	3	-28.9	-716.9
4.4	-344	4	-24.4	-712.4
4.4	-344	6	-13.2	701.2
4.4	-344	8	-3.4	-691.4
4.4	-344	9.8	0	-688

In this case, the binding energies of an electron in a superatoms are  $E_{\text{ex}}(\bar{a}_2) \cong -344$  meV

Binding energies  $E_B(D, a)$  of ground singlet state of excitonic quasimolecule, containing two CdS QDs with average radii of  $\bar{a}_1 = 4$  nm and  $\bar{a}_2 = 4.4$  nm, have a minimum  $E_B^{(1)}(D_1, \bar{a}_1) \approx -28.1$  meV for a distance  $D_1 \cong 2.6$  nm and  $E_B^{(2)}(D_2, \bar{a}_2) \approx -32.8$  meV for a distance  $D_2 \cong 2.48$  nm  $E_B^{(1)}$  and  $E_B^{(2)}$  correspond to critical temperatures  $T_{c(1)} \approx 326$  K and  $T_{c(2)} \approx 380$  K (see Tables 10.1 and 10.2) [14]. Binding energies of the ground state of electron of superatoms are  $E_{\text{ex}}(\bar{a}_1) \cong -320$  meV and  $E_{\text{ex}}(\bar{a}_2) \cong -344$  meV [9]. In this case, energies of singlet ground state (10.4) of the excitonic quasimolecule are  $E_0(D_1, \bar{a}_1) \approx -668.1$  meV and  $E_0(D_2, \bar{a}_2) \approx -720.8$  meV (see Tables 10.1 and 10.2). From a comparison of the total energy  $E_0(D, \bar{a}_2)$  of quasimolecule with a maximum  $(E - E_g) \approx -712$  meV, we get the value of the distance  $D_3 \approx 4.0$  nm between QDs [14]. Criterion (10.11) of the applicability of variational estimation of the binding energy  $E_B(D, a)$  of the quasimolecule is implemented as  $\left( E_B^{(1)}(D_1, \bar{a}_1) / E_{\text{ex}}(\bar{a}_1) \right), \left( E_B^{(2)}(D_2, \bar{a}_2) / E_{\text{ex}}(\bar{a}_2) \cong 0.09 \right)$ .

With increasing of QD radius  $a$ , the binding energy  $E_{\text{ex}}(a)$  of the ground state of electron in a superatom increases [2, 9]. The average size of the state of electron in the superatom decreases. Therefore the distance, for which the square of the overlapping integral  $S(D, a)$  of the one-electron wave functions, takes on a maximum value. Also it decreases with increasing of QD radius  $a$ , and so the distance between surfaces of QD  $D_2$  is less than  $D_1$ ). As a result, with increasing of QD radius  $a$ , also the maximum value of the binding energy of singlet ground state of excitonic quasimolecule  $|E_B(D, a)|$  increases (i.e.,  $|E_B^{(2)}|$  more  $|E_B^{(1)}|$ ). In this case, criterion (10.11) of the applicability of variational estimation of the binding energy  $E_B(D, a)$  of the quasimolecule is implemented [14].

Thus, proposed model of excitonic quasimolecule [14] lets us explain the optical properties of nanosystems, consisting of CdS QDs, grown in a borosilicate glass matrix [5, 6] and, in particular, the appearance of a peak  $(E - E_g) \approx -712$  meV in the absorption spectra of the samples at 4 K.



It should be noted that the binding energy  $E_{\text{ex}}(a)$  of the ground state of an electron in superatom [2, 9] can be applicable only for values of binding energy  $E_{\text{ex}}(a)$ , for which the inequality

$$((E_{\text{ex}}(a) - E_g) \ll V) \quad (10.38)$$

is correct, where  $\Delta V$  is the depth of the potential well for electron and hole in a QD. In the experimental work [5], it was found that for CdS QDs with radii of  $a \leq 20$  nm that  $\Delta V = 2.5$  eV. This condition (10.38) makes it possible to consider the motion of electron and hole in the superatom, using QD model as an infinitely deep potential well [2, 9] (see Fig. 10.1).

In the Hamiltonian (10.1) of quasimolecule members, causes of fluctuations of QD in quasimolecule were not considered. The obtained quasimolecule binding energies (see Tables 10.1 and 10.2) are significantly higher than typical energy of QD fluctuations.

From Tables 10.1 and 10.2, it is seen that the excitonic quasimolecule, consisting of two QD, occurs, starting from the distance between surfaces of QDs  $D \geq D_c^{(1)} \cong 1.8$  nm for QD with a radius of  $\bar{a}_1 = 4$  nm and  $D \geq D_c^{(1)} \cong 1.6$  nm for QD with a radius of  $\bar{a}_2 = 4.4$  nm [14]. The formation of such quasimolecule is of threshold character. It is possible only for nanosystems, containing QD with average radii of  $\bar{a}_1$  and  $\bar{a}_2$ , in which the distance  $D$  between surfaces of QDs exceeds some critical distance  $D_c^{(1)}$ . The existence of such critical distance  $D_c^{(1)}$  is associated with dimensional quantum effect, for which a decreasing of distance  $D$  between surfaces of QDs led to decrease in the interaction energies of electrons and holes in the Hamiltonian (10.1) of quasimolecule which cannot compensate the increase in the kinetic energy of electrons. With the increase in the distance  $D$  between surfaces of QDs, starting from values  $D \geq D_c^{(2)} \cong 8.4$  nm for QD with a radius of  $\bar{a}_1 = 4$  nm and  $D_c^{(2)} \cong 9.8$  nm for QD with a radius of  $\bar{a}_2 = 4.4$  nm, the excitonic quasimolecule splits into two superatoms.

Thus, the excitonic quasimolecule of nanosystem may occur when the condition  $D_c^{(1)} \leq D \leq D_c^{(2)}$  is realized (see Tables 10.1 and 10.2) [14]. In addition, quasimolecule can exist only at temperatures below a certain critical temperature,  $T_{c(1)} \approx 326$  K and  $T_{c(2)} \approx 380$  K. Biexcitons arose in CdS single crystal with a binding energy  $E_b = 0.59$  meV [11].

The binding energies  $E_B^{(1)}$  and  $E_B^{(2)}$  of excitonic quasimolecule are significant, exceeding  $E_g$  by almost two orders of magnitude. This effect is a significant increase in the binding energy of the ground singlet state excitonic quasimolecule due to the fact that due to the presence in nanoscale interfaces (QD-matrix), the energy of the exchange interaction of the electrons with the holes (renormalized Coulomb interaction between electrons and holes) in the excitonic quasimolecule will be much greater than the energy exchange interaction between electrons and holes in a single crystal. Apparently the latter fact opens the possibility of observing such excitonic quasimolecules at room temperature. The energy of the exchange interaction between electrons and holes mainly contributes to the binding energy of excitonic quasimolecule, which is significantly greater than that for energy

of the Coulomb interaction between electrons and holes (i.e., their ratio  $\leq 0.11$ ). The estimations of the binding energy  $|E_B(D, a)|$  of the singlet ground state of quasimolecule are variational and may give low values of the binding energy  $|E_B(D, a)|$  and  $|E_B^{(1)}|$ .

### 10.3 Conclusion

The binding energies of the exciton quasimolecule consisting of two CdS QDs acquire an anomalously high value that exceeds the binding energy  $E_B$  of the biexciton in CdS by almost two orders of magnitude. This effect is a significant increase in the binding energy of the ground singlet state excitonic quasimolecule due to the fact that due to the presence in nanoscale interfaces (QD-matrix), the energy of the exchange interaction of the electrons with the holes (renormalized Coulomb interaction between electrons and holes) in the excitonic quasimolecule will be much greater than the energy exchange interaction between electrons and holes in a single crystal. Such an effect opens up the possibility of using the exciton quasimolecules as an active medium in nanolasers emitting in the infrared region and operating on exciton transitions at room temperatures [22–25] in the elementary base of quantum nanocomputers [17, 18, 21]. The results presented demonstrate the fundamental possibility of creating novel quasiatomic nanosystems in the form of exciton quasimolecules, including natural systems with new physical characteristics [3, 11–14, 21–25]. On their basis, it is possible to construct new nanosystems or quasicrystals in which control of the symmetry and lattice constant will make it possible to realize unique physical effects and phenomena and to create new principles in materials behavior.

Such quasimolecule exciton is promising to create new elements of silicon in infrared optoelectronics, including new infrared sensors [21–25].

### References

1. Ashoori RC (1996) Electrons in artificial atoms. *Nature* 379:413–415
2. Pokutnyi SI (2013) On an exciton with a spatially separated electron and hole in quasi-zero-dimensional semiconductor nanosystems. *Semiconductors* 47(6):791–798
3. Pokutnyi SI (2014) Theory of excitons and excitonic quasimolecules formed from spatially separated electrons and holes in quasi-zero-dimensional nanosystems. *Optics* 3(1):10–21
4. Yakimov AI, Dvurechensky AV et al (2001) Effects of electron-electron interaction in the optical properties of dense arrays of quantum dots Ge/Si. *JETP* 119:574–589
5. Grabovskis V, Dzenis Y, Ekimov A (1989) Photoionization of semiconductor microcrystals in glass. *Sov Phys Solid State* 31(1):272–275
6. Bondar N (2010) Photoluminescence quantum and surface states of excitons in ZnSe and CdS nanoclusters. *J Luminescence* 130(1):1–7
7. Ovchinnikov OV, Smirnov MS, Shatskikh TS (2014) Spectroscopic investigation of colloidal CdS quantum dots – methylene blue hybrid associates. *J Nanopart Res* 16:2286–2292

8. Dzyuba VP, Kulchin YN, Milichko VA (2013) Quantum size states of a particle inside the nanospheres. *Adv Mater Res A* 677:42–48
9. Pokutnyi SI (2013) Binding energy of the exciton with a spatially separated electron and hole in quasi-zero-dimensional semiconductor nanosystems. *Tech Phys Lett* 39(3):233–235
10. Pokutnyi SI, Kulchin YN, Dzyuba VP (2015) Binding energy of excitons formed from spatially separated electrons and holes in insulating quantum dots. *Semiconductors* 49(10):1311–1315
11. Pokutnyi SI (2013) Biexcitons formed from spatially separated electrons and holes in quasi-zero-dimensional semiconductor nanosystems. *Semiconductors* 47(12):1626–1635
12. Pokutnyi SI (2016) Biexciton in Nanosystem of quantum dots of cadmium Sulfide in a dielectric matrix. *Tech Phys* 61(11):1737–1739
13. Pokutnyi SI, Kulchin YN, Dzyuba VP, Amosov AV (2016) Biexciton in nanoheterostructures of dielectric quantum dots. *J Nanophotonics* 10(3):036008-1–036008-8
14. Pokutnyi SI (2016) Quantum – chemical analysis of system consisting of two CdS quantum dots. *Theor Exp Chem* 52(1):27–32
15. Lalumiure K, Sanders B, Van Loo F et al (2013) Input - output theory for waveguide QED with an ensemble of inhomogeneous atoms. *Phys Rev A* 88:43806–43811
16. Van Loo F, Fedorov A, Lalumiure K et al (2013) Photon-mediated interactions between distant artificial atoms. *Science* 342:1494–1496
17. Lozovik YE (2014) Electronic and collective properties of topological insulators. *Advanc. Phys. Scienc.* 57:653–658
18. Valiev K (2005) Quantum computers and quantum computing. *Advanc Phys Scienc* 48:1–22
19. Pokutnyi SI (2007) Exciton states in semiconductor quantum dots in the framework of the modified effective mass method. *Semiconductors* 41(11):1323–1328
20. Schiff L (1955) *Quantum mechanics*. McGraw-Hill Book Company, Inc. New York- Toronto-London
21. Pokutnyi SI, Ovchinnikov OV, Kondratenko TS (2016) Absorption of light by colloidal semiconductor quantum dots. *J Nanophotonics* 10(3):033506-1–033506-9
22. Pokutnyi SI (1992) Size quantization of excitons in quasi-zero-dimensional semiconductor structures. *Phys Lett A* 168(5–6):433–436
23. Pokutnyi SI (2005) Optical nanolaser on the heavy hole transition in semiconductor nanocrystals: theory. *Phys Lett A* 342:347–350
24. Pokutnyi SI et al (2004) Stark effect in semiconductor quantum dots. *J Appl Phys* 96(2):1115–1119
25. Pokutnyi SI, Kulchin YN (2016) Special section guest editorial: optics, spectroscopy, and Nanophotonics of quantum dots. *J. Nanophotonics* 10(3):033501-1–033501-8

**Sergey I. Pokutnyi** is a professor of theoretical physics (doctor of sciences in physics and mathematics) of the Chuiko Institute of Surface Chemistry, National Academy of Sciences of Ukraine, Kyiv. His current research interests are theoretical optics and spectroscopy nanosystems (electron, exciton, and biexciton states in nanosystems, nanophotonics nanosystems), theory of condensed matter (theory of excitons and biexcitons in nanosystems, theory of local electron states in nanosystems, theory of transfer energy electron excitation states in nanosystems), and magneto-electro-optics nanosystems. He has published more than 240 papers in ISI journals and ten books.

# Chapter 11

## Molecular Dynamics Simulations of the Formation Processes of Zinc Oxide Nanoclusters in Oxygen Environment

S.S. Savka, D.I. Popovych, and A.S. Serednytski

### 11.1 Introduction

The development of nanotechnology has attracted great interest to study the properties of nanoparticles and their synthesis. Investigation of the nanoparticle will allow to more fully understand the processes of phase transitions and self-organization in complex disperse systems. Currently, studying of individual nanoparticles is one of the most rapidly developing areas of research in physics, chemistry, and engineering. Huge scientific and practical interest in such research results from the uncommon properties of nanoparticles that are already or will be widely used in the future for the fabrication of miniature electronic devices, and production of new materials.

From all metal oxide nanomaterials, which are now widely used, zinc oxide takes a special place. ZnO is a quite interesting material with a wide range of technical applications. Zinc oxide is a wide-bandgap semiconductor with bandgap  $E_g = 3.37$  eV; it is suitable for applications in optoelectronic devices with short wavelengths, such as UV light-emitting diodes and transparent field-effect transistors. It has several favorable properties, including good transparency, high electron mobility, wide bandgap, and strong room temperature luminescence. Zinc oxide

---

S.S. Savka (✉) • A.S. Serednytski  
Pidstryhach Institute for Applied Problems of Mechanics and Mathematics, NASU,  
Naukova Street 3b, 79060, Lviv, Ukraine  
e-mail: [savka.stepan.92@gmail.com](mailto:savka.stepan.92@gmail.com)

D.I. Popovych  
Pidstryhach Institute for Applied Problems of Mechanics and Mathematics, NASU, Naukova  
Street 3b, 79060, Lviv, Ukraine

National University Lvivska Polytechnika, Bandera Street 12, 79013, Lviv, Ukraine  
e-mail: [popovych@iapmm.lviv.ua](mailto:popovych@iapmm.lviv.ua)

crystallizes in two main structures – hexagonal wurtzite and cubic zincblende, with lattice constants ( $a = 3.24992 \text{ \AA}$ ,  $c = 5.20658 \text{ \AA}$ ) [1]. Nanopowdered zinc oxide is promising material as a working environment in lasers. Thin films and other nanostructures based on zinc oxide can be used as sensors of gas and biological sensors [2].

The shape of nanoparticles depends on the method and conditions of synthesis. One of the easiest and most popular methods obtaining nanoparticles is gas-phase evaporation of the solid target material in an inert atmosphere, followed by condensation on the surface of the substrate. This method has a rather high efficiency and is widely used in industrial scale. The technology of this method is quite well designed for production of a large number of powdered nonferrous metals such as aluminum, copper, antimony, zinc, palladium, and silver. In this method, the evaporation of material occurs by pulsed laser ablation. In recent years, pulsed laser ablation (PLA) has become a promising nanocluster synthesis technique for photonics, electronics, and medicine. We proposed a method of synthesis of metal oxide nanopowder by pulsed laser ablation of a metal target (Zn, Sn, etc.) in chemically active environment [3]. Laser impulse heats material of metallic target to a high temperature, and atoms evaporate into the background gas. Inert gas contributes reducing of the kinetic energy of evaporated atoms and formation of nanoclusters. Carefully selecting laser radiation parameters and pressure of background gas, we can control structure and particle size. Understanding the physical and chemical processes, which influence on the evolution of nanoparticles in the presence of gas, is extremely important for the further development of this technology.

It is known that the properties of nanoparticles are determined by their structure, and the structure is determined by the process of the growth of nanoparticles. Depending on technological features of the synthesis of particles, processes of the formation can vary significantly. Experimental study of the formation mechanisms of nanoparticles is technically a challenging and time-consuming task because of the small size of these objects. In conditions of experimental synthesis, sometimes it is complicated to study in detail the impact of the basic parameters of synthesis on physical, chemical, and structural properties and outer shape of derived particles. However, computer modeling is an alternative and promising way to study the mechanisms of formation of nanoobjects. Using the methods of computer modeling, we can investigate in detail the processes of synthesis of nanoparticles upon condensation from the gas phase [4, 5]. In this article we considered processes of formation of zinc oxide nanoparticles upon condensation from the gas phase in the oxygen environment by molecular dynamics method. Molecular dynamics simulation has contributed significantly to enhance the fundamental understanding of physical and chemical mechanisms at nanoscale. It can be used to study many important unanswered questions relating to nanoparticles that cannot be directly addressed by continuum approaches.

## 11.2 Model and Method

Simulation of the formation processes of nanoparticles, which reproduces the synthesis technology process of thermal saturation and condensation with subsequent formation of nanoclusters, was carried out by molecular dynamics [6] method that is based on numerical solution of Newtonian differential equations of motion for each atom of the system with initial values of speed and coordinates.

$$m_i \frac{d^2 \mathbf{r}_i(t)}{dt^2} = - \frac{\partial U(\mathbf{r}(t))}{\partial \mathbf{r}(t)} \quad (11.1)$$

$$\mathbf{r}_i(t_0) = \mathbf{r}_{i0} \quad (11.2)$$

$$\frac{d\mathbf{r}_i(t_0)}{dt} = \mathbf{v}_i(t_0) = \mathbf{v}_{i0}, \quad (11.3)$$

where  $i = 0, \dots, N$ ,  $N$  is the number of atoms in system,  $m_i$  is mass of  $i$  atom,  $U(\mathbf{r}(t))$  is potential energy of the system, and  $\mathbf{r}_i(t)$  is coordinate of  $i$  atom.

In classical MD simulations, interactions between atoms are described by empirical force fields which are parameterized based upon spectroscopy measurements of small molecules and quantum mechanics calculations. So, central element of the molecular dynamics method is the empirical interatomic potential, through which is carried out calculation of the interaction forces between the particles. Most often, in classical molecular dynamics, particles are presented in the form of point masses. The choice of potential is determined by the character of the problem. Modeling of nanostructures is completely based on the detailed description of particles, which is included in their composition. Therefore, the modeling of the formation of zinc oxide nanoclusters from high-temperature gas phase was conducted using a reactive force field (ReaxFF) that was developed by David Raymond and Adri C.T. van Duin [7].

ReaxFF was designed for a wide range of chemical compounds including ZnO. Common expression for the total energy of the system includes the sum of all terms that describe individual chemical bonds in materials, thus providing accurate modeling of chemical processes:

$$\begin{aligned} E_{\text{system}} = & E_{\text{bond}} + E_{\text{over}} + E_{\text{under}} + \\ & + E_{\text{pen}} + E_{\text{conj}} + E_{\text{tors}} + \\ & + E_{\text{val}} + E_{\text{lp}} + E_{\text{vdWaals}} + E_{\text{Coulomb}} \end{aligned} \quad (11.4)$$

These partial contributions include bond energies ( $E_{\text{bond}}$ ), under-coordination penalty energies ( $E_{\text{under}}$ ), lone-pair energies ( $E_{\text{lp}}$ ), over-coordination penalty energies ( $E_{\text{over}}$ ), valence angle energies ( $E_{\text{val}}$ ), energy penalty for handling atoms with two double bonds ( $E_{\text{pen}}$ ), torsion angle energies ( $E_{\text{tors}}$ ), conjugated bond energies ( $E_{\text{conj}}$ ), and terms to handle nonbonded interactions, namely van der Waals ( $E_{\text{vdWaals}}$ )

and Coulomb ( $E_{\text{Coulomb}}$ ) interactions. All terms except the last two are bond order dependent, i.e., will contribute more or less depending on the local environment of each atom [7].

Essentially, the reactive force field is an empirical force field derived from a quantum mechanics parameterization [8]. The bond order is directly calculated from an interatomic distance and updated every iteration for all bonded interactions, including covalent bonds, valence, and torsion angles. In addition, the ReaxFF describes nonbonded van der Waals and Coulomb interactions. Such interactions are calculated for all pairs of atoms, and, by incorporating a shielding term, extremely close-range interactions can be modified. Polarization effects also are considered by using a geometry-dependent charge distribution derived from an electronegativity equalization method [9].

For modeling and analysis of the formation processes of ZnO nanoparticles, we have been used Large-scale Atomic/Molecular Massively Parallel Simulator, which was developed by a scientific group from Sandia National Laboratories (USA). Calculations were performed on a computing cluster of the Institute for Applied Problems of Mechanics and Mathematics, which is based on four Intel Xeon multi-core processors under operating system Linux ROCKS.

We carried out the research with two initial configurations. The first configuration composed of four hundred atoms of zinc and the same number of oxygen atoms, and the second one composed of four thousand atoms of zinc and four thousand oxygen atoms, which were uniformly distributed with periodic boundary conditions in a region of space with a volume of  $V = 8000 \text{ nm}^3$ . Cell size for these two configurations was the same ( $200 \times 200 \times 200 \text{ \AA}^3$ ); it was done in order to set two different initial concentrations of atoms ( $10^{19}$ ,  $10^{20} \text{ atoms/cm}^3$ ). In order to avoid premature unification of atoms at the very early stages of evolution, the average interatomic distance was set greater than the potential cutoff radius.

The direction of the initial velocities was selected randomly. Our system was cooled with certain fixed speed to the desired final temperature  $T = 300 \text{ K}$ . Important aspect of the simulation is coupling the system with a heat bath. Since significant amount of binding energy was being released, when clusters formed, such coupling is necessary in order to avoid unphysical temperature increases. In real experiments this coupling is provided by the inert gas atmosphere. In our computational simulation, the control of temperature was carried out using the Berendsen thermostat method. This method is widely used for molecular dynamics simulations of the large number degrees of freedom. To maintain the temperature system is coupled to an external heat bath with fixed temperature. The velocities are scaled at each step, such that the rate of change of temperature is proportional to the difference in temperature.

Throughout the simulation, system snapshots were saved every 0.5 ps. These images, except visual observation, also had been used to analyze the shape, size, structure, and number of newly formed nanoparticles. It was believed that atoms belong to one cluster, when the distance between them is less than  $3 \text{ \AA}$ . In this work

the CNA method was used to analyze the internal structure of clusters [10]. Analysis was carried out layer by layer on samples, which have the typical characteristics for all nanoobjects.

### 11.3 Results and Discussion

It is known that the properties of nanoparticles are determined by their structural features, which in its turn are the result of nanoparticle growth. Therefore, we have thoroughly analyzed the structure, shape, and sizes of the investigated nanoclusters.

It was established that grouping of atoms into nanoclusters was carried out rather actively in the first moments of time, and it was accompanied by the formation of a significant number of monomers. At the following moments of time, condensation of already formed nanoobjects was observed that was accompanied by gradual decrease of the number of nanoparticles and increase of their size (Figs. 11.1 and 11.2).

The processes of condensation of atoms from the high-temperature gas environment are divided into several stages: nucleation, surface growth, aggregation and coagulation, and coalescence and agglomeration. The first stage is the nucleation process. After termination of this process, the subsequent growth of clusters can proceed according to various mechanisms. The main mechanisms of this process are agglomeration and coalescence. During the nucleation process, there is an association of free atoms into small particles, into so-called dimers and trimers, that leads to a dramatic increase of particles in the system (Fig. 11.3). With further heat removal, small clustered fragments begin to form liquid drops with sizes of a few tens of atoms. This stage is shown in Fig. 11.2b, where a snapshot of trajectory of the system at time 0.3 ns is given. As a result of spontaneous collisions of these liquid drops, up to 0.5 ns, there are formed massive amorphous clustered aggregation.

The next stage after a high nucleation process was the stage of surface growth and coagulation process. At the stage of surface growth, single atoms, dimers, or trimers of the gas phase are joined to the cluster surface, causing its gradual growth. The reverse process is also possible – single atoms are evaporated from the surface of nanocluster. But, mostly, this process was observed in small quantities. It was caused by the intense heat removal, and at the same time decreasing of energy, that is required to overcome the potential barrier for breaking out from the surface of the cluster.

The last stage of the cluster formation was the processes of collision of already existing clusters on the scenario of agglomeration or coalescence. At agglomeration scenario, clusters were combined almost with no change of their original shape. In other words, the result of the agglomeration process was nanoobjects with different shapes that differ from spherical shape (Fig. 11.4). At coalescence scenario, nanoparticles merge together and form a single particle with shape that differ from shape that was before the collision of nanoclusters. Such mechanism is possible on



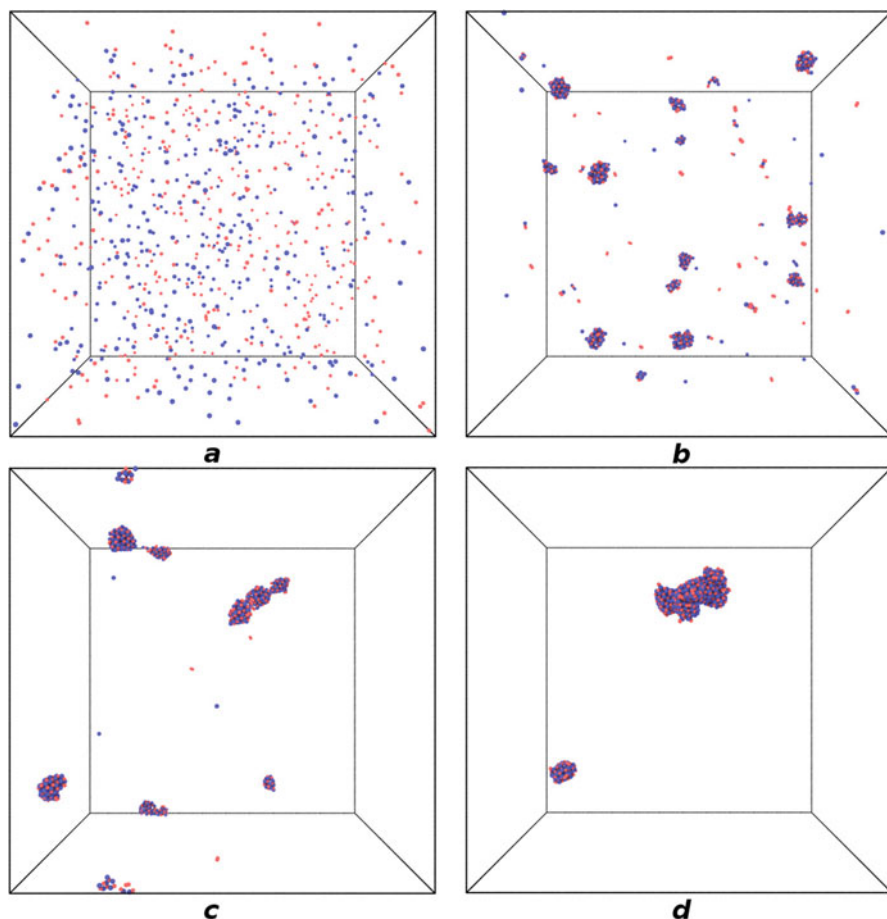


**Fig. 11.1** Evolution of a system of 400 O atoms and 400 Zn atoms from (a)  $t = 0$  ns,  $T = 1800$  K to (d)  $t = 5$  ns,  $T = 300$  K

the not very late stages of synthesis, when the temperature is still enough in order for nanoclusters to be in a liquid state. In other words, at low cooling rates, the main growth scenario is agglomeration, and the result was nonspherical shape of obtained nanoclusters, and at higher cooling rates the main scenario is coalescence, and clusters, mostly, had a spherical shape. Also, further, a slight change of the shape of nanoclusters due to changes in the position of individual atoms is possible. Therefore, a shape of newly created objects directly depends on the mechanism of the final stage of formation and, hence, on the cooling rate. So, depending on how quickly the system will be cooled, one or another mechanism will be more important.

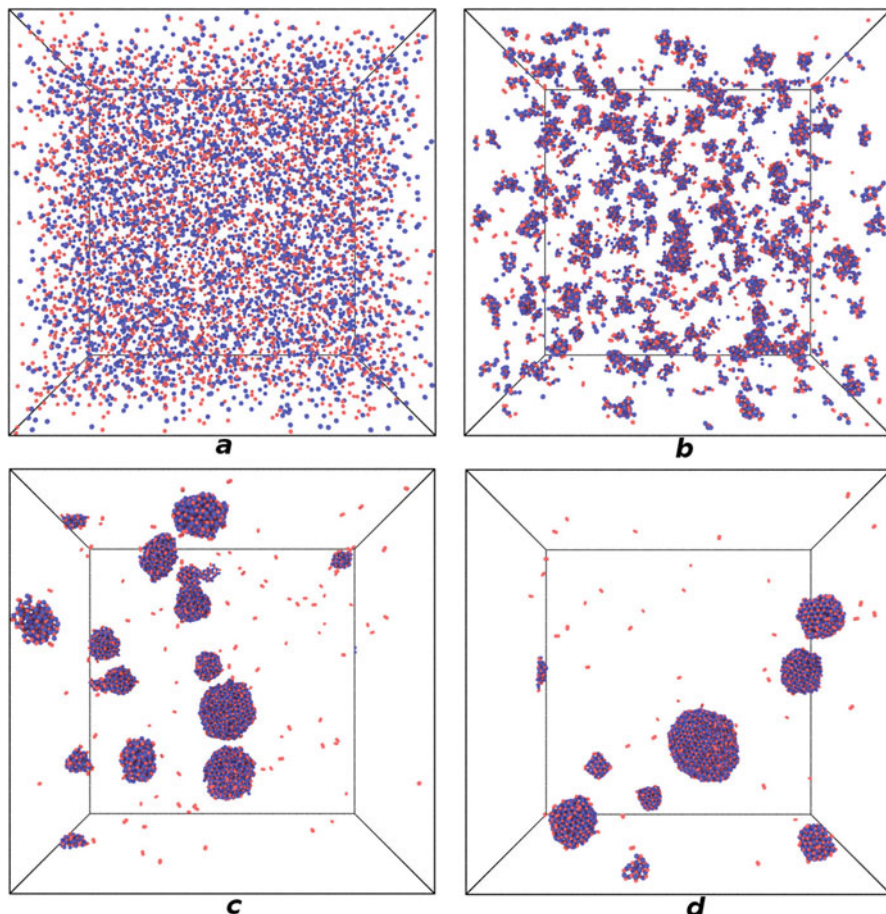


**Fig. 11.2** Evolution of a system of 4000 O atoms and 4000 Zn atoms from (a)  $t = 0$  ns,  $T = 1800$  K to (d)  $t = 5$  ns,  $T = 300$  K

We had been observed change of the main parameters of the system from condensation dynamics, setting different initial cooling rate. Depending on the concentration and cooling rate, it is possible different mechanisms of cluster growth. To study the influence of cooling rate and concentration of atoms on the physical parameters of nanoparticles, it was conducted six computer experiments with different initial cooling rates ( $0.0364$ ,  $0.0036$ ,  $0.0003$  ps<sup>-1</sup>) and initial concentrations of atoms ( $10^{19}$ ,  $10^{20}$  atoms/cm<sup>3</sup>). From the simulation results follows that the cooling rate directly affects the number of obtained particles. At reduction of cooling rate in 10 times, the number of obtained nanoparticles decreases approximately in 12 times (Fig. 11.5). Such dependence is quite logical, as, during slow cooling of the system,

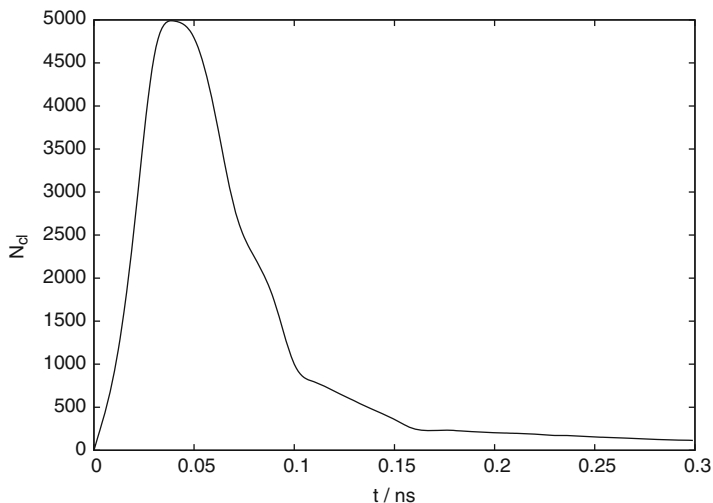
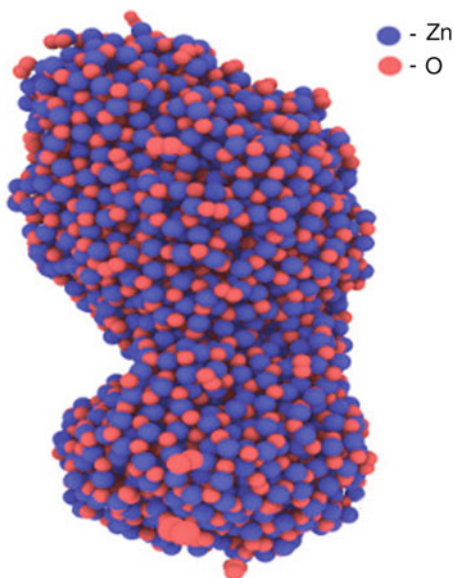


**Fig. 11.3** Changes in the number of monomers in system as a function of time

**Fig. 11.4** Snapshot of a non-spherical cluster



there is enough kinetic energy in order to chaotically move particles, at the same time, confronted among themselves, forming rather large clusters. These clusters are composed of hundreds of atoms, and they were created by the union between smaller clusters. Speaking about the number of obtained nanoparticles depending on the initial concentration, then obviously, the greater the concentration is, the greater the number of nanogranules will be.

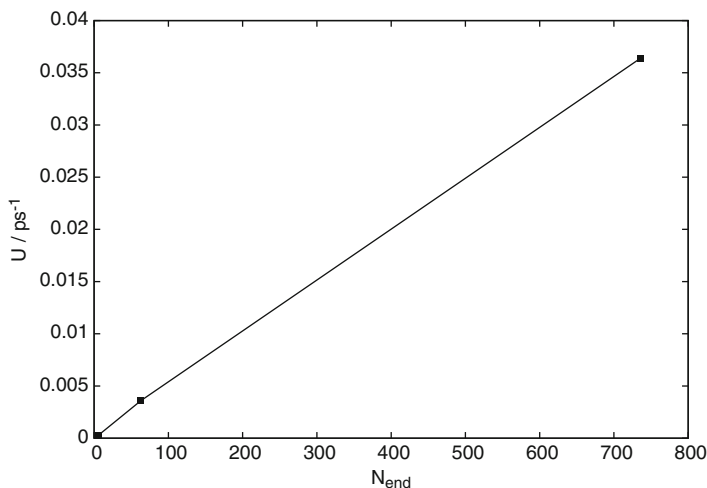


**Fig. 11.5** Changes in the cooling rate as a function of number of finite nanoclusters

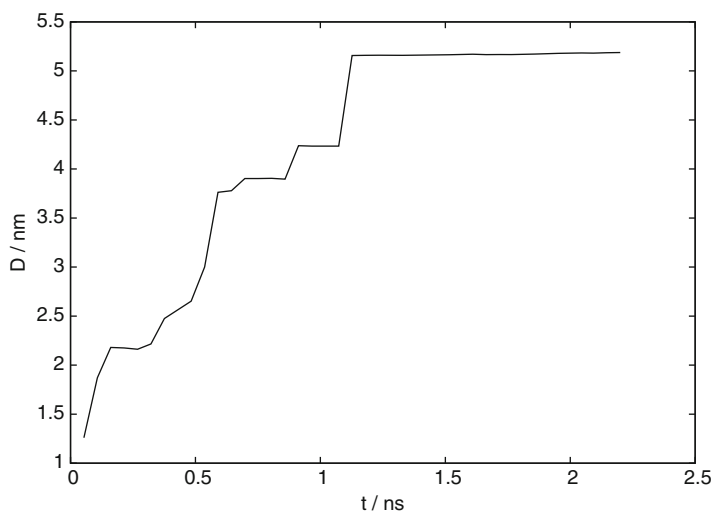


**Fig. 11.6** Size of the largest cluster as a function of time

Observation on resizing of clusters has shown that the formation of stable cluster occurs through the formation of metastable cluster with its subsequent stabilization. In order to analyze the size of the received nanoparticles, we have considered changing the size of the largest cluster from time (Fig. 11.6). From the figure we can see that the cluster size increases with time. This is due to the fact that the potential energy of any cluster is less than the energy in the gas state, and thus, transition of the system to statistically equilibrium state accompanied by a constant

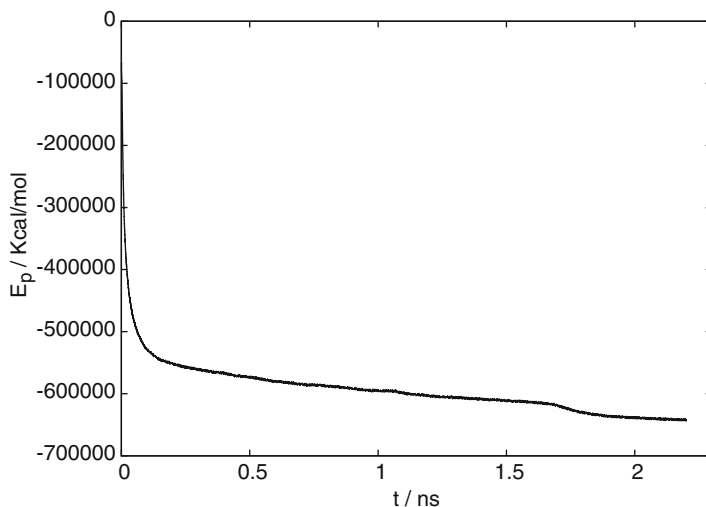


**Fig. 11.7** Changes in the potential energy of the system as a function of time

reduction of potential energy, and, hence, there is increasing number of bonds in the system, so that there is a gradual clustering. On the basis of curve of potential energy of the system from the time (Fig. 11.7), it can be concluded that there is a separation between nucleation of clusters and their growth. In the first case, the dependence of the potential energy from time describes exponential dependence, and in the second, it has a linear dependence. Analyzing the impact of the rate of condensation on particle size distribution, it can be concluded that by increasing the cooling rate, in system a quite large number of small particles are formed, the average size of which does not exceed a few tens of atoms. At lower rate in system, much less clusters are formed and their average size was several thousand atoms (Fig. 11.8). This is associated to the fact that at such speeds of heat removal, atoms are quickly absorbed by nanoclusters, and in case, even, if they evaporate from the surface of the cluster, they cannot move away from it and again fall in a zone of its attraction.

Using the CNA method, the internal morphology of obtained nanoclusters was thoroughly analyzed. During the analysis it was found that created clusters mainly are formed in three structural phases – amorphous, hexagonal wurtzite, and cubic zincblende. Based on results that are represented on Fig. 11.9, it can be said that the most appropriate cooling rate for getting nanoparticles with hexagonal structure is  $0.0003 \text{ ps}^{-1}$ . From the figure, we can see that at high cooling rates it mainly formed amorphous particles and with decreasing rate, it increases percentage of clusters with structure which differs from amorphous. Namely, with decreasing rate in 10 times, percentage not amorphous clusters is increasing in 14 times. This is because the cooling rate is directly related to a time of simulation, namely, longer time

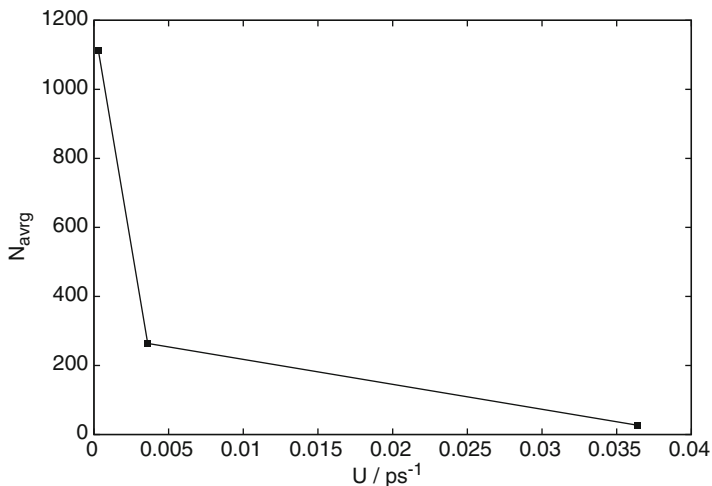


**Fig. 11.8** The average size of nanoclusters as a function of cooling rate

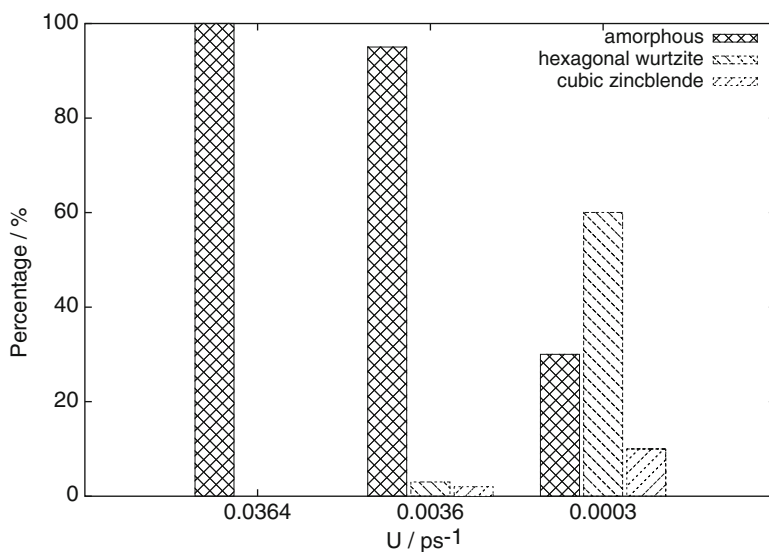


**Fig. 11.9** Changes in the structure of obtained nanoparticles as a function of cooling rate

corresponds lower rate of condensation, and, so, for such short time, atoms have not time to form energetically stable and with right internal structure nanoclusters. Therefore, the final structure of the particles directly depends on the cooling rate, and by the controlling of it, it is possible to control character of structure of obtained nanoclusters.

## 11.4 Conclusions

In this study, the gas-phase condensation of ZnO nanoclusters was simulated by method of molecular dynamics using reactive force field. In this simulation, the process of synthesis of zinc oxide nanoparticles was conducted with three different cooling rates and two initial concentrations of atoms. It was shown that the structure, shape, and size of the obtained particles depend on the cooling rate and the concentration of atoms. During the analysis it was found that the main scenario, during the transition to lower cooling rates, becomes coalescence of nanoparticles and that created clusters mainly are formed in three structural phases – amorphous, hexagonal wurtzite, and cubic zincblende. So, understanding of the features and growth of nanoparticles can help in the manufacture of nanopowders with fixed size, shape, and structure and accordingly with fixed physicochemical properties.

## References

1. Fierro JLG (2006) Metal oxides chemistry and applications, vol 182. CRC Press, Boca Raton
2. Zhyrovetsky V, Kovalyuk B, Mocharskyi V, Nikiforov Y, Onisimchuk V, Popovych D, Serednytski A (2013) Modification of structure and luminescence of ZnO nanopowder by the laser shock-wave treatment. *Phys Status Solidi* 10:1288–1291
3. Gafiychuk VV, Ostafiychuk BK, Popovych DI, Popovych ID, Serednytski AS (2011) ZnO nanoparticles produced by reactive laser ablation. *Appl Surf Sci* 257:8396–8401
4. Bovgyra OV, Bovgyra RV, Kovalenko MV et al (2013) The Density Functional Theory Study of Structural and Electronical Properties of ZnO Clusters. *J Nano- Electron Phys* 5(1):01027
5. Bovgyra OV, Bovgyra RV, Popovych DI, Serednytski AS (2015) The Density Functional Theory Study of Electronical Properties of (ZnO)<sub>12</sub> Clusters During Gas Adsorption. *J Nano-Electron Phys* 7(4):04090
6. Rapaport DC (2004) The art of molecular dynamics simulation. Cambridge University Press, Cambridge
7. Raymond D, van Duin ACT, Baudin M, Hermansson K (2008) A reactive force field (ReaxFF) for zinc oxide. *Surf Sci* 602:1020–1031
8. van Duin ACT, Veners O, Shin Y-K (2013) Reactive force fields: concepts of ReaxFF and applications to high energy materials. *Int J Energ Matter Chem Propul* 12:95–118
9. Mortier WJ, Ghosh SK, Shankar S (1986) Electronegativity-equalization method for the calculation of atomic charges in molecules. *J Am Chem Soc* 108:4315–4320
10. Honeycutt JD, Andersen HC (1987) Molecular dynamics study of melting and freezing of small Lennard-Jones clusters. *J Phys Chem* 91:4950–4963

# Chapter 12

## Microwave Phase-Locking of Weakly Coupled Spin-Torque Nano-Oscillators: The Case of Global Coupling

O.R. Sulymenko and O.V. Prokopenko

### 12.1 Introduction

The spin-transfer torque (STT) effect theoretically predicted by J.C. Slonczewski [1] and L. Berger [2] provides a new method of generation of microwave oscillations in nanoscale magnetic systems and can be used for the development of novel microwave signal sources based on spin-torque nano-oscillators (STNOs) [3–10]. There are several different types of STNOs including conventional STNOs thoroughly investigated in early works [3–7], vortex-based STNOs [11, 12], recently proposed spin orbit STNOs [13], etc.

The typical STNO is a multilayer magnetic structure consists of at least three layers (the real number of layers in manufactured structures including buffered layers and multilayers of a synthetic antiferromagnetic layer may be of several tens). One of these layers serves as a pinned magnetic (or polarizer) layer (PL); the other magnetic layer is a free magnetic (or analyzer) layer (FL). There is also a nonmagnetic spacer situated between the magnetic layers. According to the STT [1, 2], when an electric dc current passes through an STNO, it becomes spin-polarized in the PL and can transfer the acquired spin angular momentum to the FL. If the current density is sufficiently high, the spin-polarized current can destabilize the static equilibrium orientation of magnetization in the thinner (“free”) magnetic layer of the multilayered structure that gives rise to the magnetization precession in the FL. The frequency of this current-induced precession is close to the frequency of the most unstable spin wave mode of the FL, depends on the current magnitude, and, typically, lies in the microwave range [7].

---

O.R. Sulymenko (✉) • O.V. Prokopenko  
Faculty of Radio Physics, Electronics and Computer Systems, Taras Shevchenko National University of Kyiv, Volodymyrska Street 64/13, 01601, Kyiv, Ukraine  
e-mail: [olgasulymenko@gmail.com](mailto:olgasulymenko@gmail.com)



The spin-torque nano-oscillators are now considered as promising base elements for modern electronics; however, their output microwave powers, phase noises, linewidths, working frequency range, and frequency stability must be improved if they are to be used for practical applications [9, 13–15]. There are several approaches to improve work parameters of STNO-based devices: (i) the use of additional delay circuits, phase-locked loops, or other microwave circuits [8, 15–17]; (ii) the utilization of complex STNO structures having multiple FLs and/or PLs [18–22]; (iii) the variation of temperature and other experimental parameters, material and geometry parameters of STNO structures [23–28]; (iv) the synchronization of several oscillators one to each other and/or to an external microwave signal [29–35]. From all the approaches mentioned above, only the last is suitable for the substantial improvement of STNOs' working characteristics. It is well known that synchronizing  $N$  oscillators one can increase the output power of the  $N$ -oscillator array by  $N^2$  times in comparison to the power of a single oscillator, reduce the linewidth of the generated signal by  $N$  times, improve the stability of the generated signal frequency [36], etc. However, the synchronization of many STNOs faces several principal problems: (i) practical realization of STNOs' synchronization is quite complicated due to the strongly nonlinear and non-isochronous nature of the oscillators [7]; (ii) STNO manufacturing technology is not well developed yet and provide quite large spread of STNO's working parameters [23, 24]; (iii) the general theory of STNOs synchronization is not yet completed, only some partial cases of STNOs synchronization is analyzed [7, 31–34]. All these factors prevent the creation of effective microwave devices with many synchronized STNOs.

In this paper we report numerical simulation of several STNO synchronizations (two, three, and five oscillators) with an account of the spread of STNO's working parameters caused by the limitations of the STNO manufacturing technology. We believe that the obtained results might be important for the development and creation of practical microwave devices with many synchronized STNOs having optimal working characteristics.

The paper has the following structure. In Sect. 12.2 fundamentals of STNOs are introduced. In Sect. 12.3 we consider basic physics of STNO synchronization and introduce different models of STNO synchronization. In Sect. 12.4 we describe our numerical model of STNO synchronization, present, and discuss the results of our numerical simulations. Finally, a summary of the obtained results and conclusions are presented in Sect. 12.5.

## 12.2 Basic Physics of an STNO

The operation of an STNO is based on the STT [1, 2] effect. According to the effect a spin-polarized or pure spin dc current passing through a magnetized ferromagnetic layer can transfer spin angular momentum to this layer and, as a result, change the orientation of the magnetization vector in the layer. This phenomenon leads to the magnetization precession with the frequency close to

the frequency of the ferromagnetic resonance (FMR) in the magnetic layer at relatively low amplitudes of the current and, therefore, to the microwave oscillations of the multilayer resistance due to the giant magnetoresistance (GMR) [3, 5] or tunneling magnetoresistance (TMR) [4, 6] (type of the observed effect depends on the multilayer structure and properties).

The STNO could be realized in two possible geometries [7, 37]: magnetic nano-pillar or magnetic nano-contact. In the first case, the FL has finite lateral sizes in the plane of the layer, so the spin wave modes of the FL excited by the current have discrete frequencies determined by the finite in-plane sizes of the pillar [7]. In the case of a nano-contact the FL has the form of a magnetic film, and, therefore, the magnetic oscillations excited by the current have the form of propagating spin wave modes in the FL [7].

The typical STNO has the following geometrical parameters: radius of the structure  $R \sim 10\text{--}10^3$  nm (for circular nano-pillars only), thickness of the FL  $L \sim 1\text{--}10$  nm, thickness of the PL  $L_p \sim 10\text{--}100$  nm, and spacer thickness  $d \sim 1\text{--}10$  nm. The operation efficiency of the STNO strongly depends on the degree of spin polarization of the current, which is characterized by a dimensionless spin-polarization efficiency of the PL  $\eta$ . Typical values of  $\eta$  are about 0.2–0.5 for GMR STNOs and 0.5–0.7 for TMR junctions. The characteristic static resistance of an STNO  $R_{dc}$  can also vary in a wide range from  $R_{dc} \sim 1$  Ohm for GMR STNOs to  $R_{dc} \sim 1$  kOhm for TMR STNOs, respectively [10].

The dynamics of the magnetization vector  $\mathbf{M} = \mathbf{M}(t, \mathbf{r})$  in the FL of an STNO in the presence of spin-polarized current is described by the Landau–Lifshitz–Gilbert equation [7] with an additional Berger–Slonczewski STT term [1, 2]:

$$\begin{aligned} \frac{\partial \mathbf{M}}{\partial t} = & \gamma [\mathbf{B}_{\text{eff}} \times \mathbf{M}] + \frac{\alpha_G}{M_0} \left[ \mathbf{M} \times \frac{\partial \mathbf{M}}{\partial t} \right] \\ & + \frac{\sigma I_{dc}(\mathbf{r})}{M_0} [\mathbf{M} \times [\mathbf{M} \times \mathbf{p}]] . \end{aligned} \quad (12.1)$$

The first term in the right-hand side of this equation describes conservative precession of the magnetization vector  $\mathbf{M}$  about the direction of the effective magnetic field  $\mathbf{B}_{\text{eff}}$ . The second term is the dissipative torque which describes energy dissipation, and the third term is the Berger–Slonczewski STT, which characterizes interaction of the magnetization  $\mathbf{M}$  with the spin-polarized current traversing the FL [7]. The effective magnetic field  $\mathbf{B}_{\text{eff}}$  may have contributions from the Zeeman energy of magnetization interaction with the external magnetic field, energy of crystallographic anisotropy, magneto-dipolar energy, energy of inhomogeneous intra-layer exchange, energy of interaction with the Oersted magnetic field created by the current, etc. Consequently, the effective field can be written as a sum of these terms. In (12.1)  $\gamma = g\mu_B/\hbar \approx 2\pi \cdot 28$  GHz/T is the modulus of the gyromagnetic ratio,  $g$  is the spectroscopic Lande factor,  $\mu_B$  is the Bohr magneton,  $\hbar$  is the reduced Planck constant,  $M_0 = |\mathbf{M}|$  is the saturation magnetization of the FL,  $\alpha_G$  is the dimensionless Gilbert damping parameter,  $\sigma$  is the spin-torque coefficient, which

depends on the spin-polarization efficiency  $\eta$  [7, 37],  $I_{dc} = I_{dc}(\mathbf{r})$  is the spin-polarized current,  $\mathbf{r}$  is the radius-vector, and  $\mathbf{p}$  is the unit vector in the direction of the spin polarization of the current ( $\mathbf{p}$  coincides with the direction of magnetization of the PL).

There are several different theoretical approaches to the problem of the excitation of microwave magnetization oscillations in the FL by a spin-polarized or pure spin current (for details see [7, 38]). Here we briefly consider only a simple approximate analytic theory developed by A.N. Slavin and V.S. Tiberkevich [7]. This theory gives a clear and simple physical picture of the nonlinear dynamical processes taking place in current-driven STNOs and can give an adequate description of most of the salient characteristics of real STNOs.

The theory is based on the introduction of the dimensionless complex spin wave amplitude  $c \equiv c(t)$  in the form [7]:

$$c = \frac{M_x - iM_y}{\sqrt{2M_0(M_0 + M_z)}}, \quad (12.2)$$

where  $M_x$ ,  $M_y$ , and  $M_z$  are the components of the magnetization vector  $\mathbf{M}$ , respectively,  $i = \sqrt{-1}$ . The magnetization vector  $\mathbf{M}$  can be expressed through the complex amplitude  $c$  as [7]:

$$\mathbf{M} = M_0(1 - 2|c|^2)\mathbf{z} + M_0\sqrt{1 - |c|^2}[(\mathbf{x} + i\mathbf{y})c + (\mathbf{x} - i\mathbf{y})c^*], \quad (12.3)$$

where  $\mathbf{x}$ ,  $\mathbf{y}$ ,  $\mathbf{z}$  are the unit vectors of  $x$ ,  $y$ ,  $z$  axis, respectively, and  $c^*$  is the complex-conjugated value of  $c$ . Substituting (12.3) to Eq. (12.1) one can obtain the model equation for the dimensionless complex spin wave amplitude [7]:

$$\frac{dc}{dt} + i\omega(p, I_{dc})c + \Gamma_+(p, I_{dc})c - \Gamma_-(p, I_{dc})c = S(t), \quad (12.4)$$

where term  $i\omega(p, I_{dc})c$  describes a conservative magnetization precession in the FL, term  $\Gamma_+(p, I_{dc})c$  characterizes damping of magnetization oscillations in the FL, the last term gives the effect of “negative” damping caused by the STT, and  $S(t)$  is the “external force” function describing the action of an external signal on STNO. Here  $p = |c|^2$ ,  $\omega(p, I_{dc}) \approx \omega_0 + N_\omega p$  is the nonlinear angular frequency of magnetization precession,  $\omega_0$  is the FMR frequency,  $N_\omega$  is the nonlinear frequency shift ( $\sim \omega_M$ ),  $\omega_M = \gamma\mu_0 M_0$ ,  $\mu_0$  is the vacuum permeability,  $\Gamma_+(p, I_{dc}) \approx \Gamma(1 + Yp)$  is the nonlinear “positive” damping coefficient in the system with natural damping rate  $\Gamma = \alpha_G\omega_0$ ,  $Y$  is the nonlinear damping parameter, and  $\Gamma_-(p, I_{dc}) \approx \sigma I_{dc}(1 - p)$  is the “negative” damping rate caused by the dc current  $I_{dc}$  traversing the structure.

The developed theory [7] in the case when the model parameters are known can be used to predict the behavior of an individual STNO (or an oscillator array) of any nature under the influence of external signal (for instance, it can be used for describing the dynamics in vortex-based STNOs [39]).

## 12.3 Basic Physics of STNO Synchronization

The synchronization of STNOs raises several problems unusual for the spintronics but well known in the field of nonlinear dynamics [33, 40–43]. The main difficulty of synchronizing STNOs has been caused by their strongly nonlinear non-isochronous behavior that in contradiction to the linear and/or isochronous oscillators substantially complicates the theoretical and experimental investigations in this area of physics. The other important factor is the limitations of existing technology of STNO fabrication that does not allow to manufacture STNOs with almost identical parameters [23, 24, 40]. It was shown [40–43] that in some situation the spread of STNOs' working parameters less than 5% could cause the failure of STNOs synchronization, while the existing manufacturing technology provide the spread of the oscillators' parameters of about 5–10%. Regarding to this nowadays experimental advances toward synchronizing STNOs have been minimal. After the first observation of phase-locking of two STNOs [29, 30] and developing a simple theory of mutual phase-locking of STNOs [31, 32], a long enough delay in achievements was observed. Until 2016 the better achieved experimental result was the synchronization of four vortex-based STNOs [35]; however, the recent results obtained in the group of Prof. J. Åkerman have proved the possibility to phase-lock up to nine spin Hall STNOs [44].

### 12.3.1 Basic Equations

There can be several approaches to describe mutual phase-locking of STNOs [33, 34, 42, 43]. Below we use the approach based on the nonlinear auto-oscillator model (12.4) developed by A.N. Slavin and V.S. Tiberkevich [7]. For the closed system of  $N$  interacting STNOs, the model equation (12.4) transforms to a system of equations:

$$\begin{aligned} \frac{dc_1}{dt} + i\omega_1(p_1)c_1 + \Gamma_{\text{eff},1}(p_1)c_1 &= S_1(t), \\ \frac{dc_2}{dt} + i\omega_2(p_2)c_2 + \Gamma_{\text{eff},2}(p_2)c_2 &= S_2(t), \\ &\dots\dots\dots \\ \frac{dc_N}{dt} + i\omega_N(p_N)c_N + \Gamma_{\text{eff},N}(p_N)c_N &= S_N(t), \end{aligned} \quad (12.5)$$

which can be presented in a general form

$$\frac{dc_i}{dt} + i\omega_i(p_i)c_i + \Gamma_{\text{eff},i}(p_i)c_i = S_i(t). \quad (12.6)$$

Here index  $i = \overline{1, N}$  labels the parameters relating to  $i$ -th STNO. Functions  $S_i(t)$  in the right-hand side of these equations characterize “external influences” on the magnetization dynamics of  $i$ -th STNO. In Eqs. (12.5) and (12.6) we also introduce the effective damping rate  $\Gamma_{\text{eff},i} = \Gamma_{+,i} - \Gamma_{-,i}$  of  $i$ -th STNO.

Now we assume that “external forces”  $S_i(t)$  in (12.6) describe only the influence of all nano-oscillators except  $i$ -th STNO on  $i$ -th STNO (there is no self-influence for any STNOs). We also neglect other types of influence (noises, external microwave signals, etc.). With these limitations, model equation (12.6) can be written in the final form [7]:

$$\frac{dc_i}{dt} + i\omega_i(p_i)c_i + \Gamma_{\text{eff},i}(p_i)c_i = \sum_{\substack{j=1 \\ j \neq i}}^N \Omega_{i,j} e^{i\delta_{i,j}} c_j. \quad (12.7)$$

Here  $\Omega_{i,j}$  is the amplitude of the coupling between  $i$ -th and  $j$ -th oscillators, and  $\delta_{i,j}$  is the coupling phase; index  $j$  changes in the same range as the index  $i$ , moreover  $j \neq i$ .

The obtained model equations (12.7) have the closed form and can be used for the analysis of mutual phase-locking of  $N$  STNOs. In the case of uncoupled free-running STNOs, the solution of Eq. (12.7) can be given as

$$c_{0i}(t) = \sqrt{p_{0i}} e^{i\phi_{0i}(t)}, \quad (12.8)$$

where  $\phi_{0i}(t) = \omega_{0i}(p_{0i})t + \phi_{0i}$ ,  $p_{0i}$  and  $\omega_{0i}(p_{0i})$  are the dimensionless power of magnetization oscillations and angular frequency of free-running oscillations of  $i$ -th STNO, which correspond to the equilibrium state of the  $i$ -th STNO, respectively.

### 12.3.2 Power–Phase Model

In the case of small perturbations, the solution of Eq. (12.7) is similar to the solution (12.8). It can be written in the form for the first time introduced in [45] and then discussed in articles [7, 46]:

$$c_i(t) = \sqrt{p_{0i}} [1 + \rho_i(t)] e^{i\phi_i(t)}, \quad (12.9)$$

where  $\rho_i(t)$  is the small normalized fluctuation deviation of dimensionless magnetization power  $p_i(t)$  from its equilibrium value  $p_{0i}$ , and  $\phi_i(t)$  is the phase of the magnetization oscillation in  $i$ -th STNO. Substituting expression (12.9) in (12.7) and writing perturbed angular frequency  $\omega_i(p_i)$  and perturbed damping rate  $\Gamma_{\text{eff},i}(p_i)$  as [46]:

$$\omega_i(p_i) \approx \omega_i(p_{0i}) + 2p_{0i} \left( \frac{d\omega_i(p_i)}{dp_i} \right), \quad (12.10)$$

$$\Gamma_{\text{eff},i}(p_i) \approx \Gamma_{\text{eff},i}(p_{0i}) + 2p_{0i} \left( \frac{d\Gamma_{\text{eff},i}(p_i)}{dp_i} \right), \quad (12.11)$$

one can get the complex equations for variables  $\rho_{i,j}(t)$  and  $\phi_{i,j}(t)$ . These equations can be presented in the following form (here we use the linear approximation and take into account only the first order small values  $\sim \Omega_{ij}$  or  $\rho_{i,j}(t)$ ):

$$\begin{aligned} \frac{d\rho_i}{dt} + 2G_i p_{0i} \rho_i = \\ \text{Re} \left\{ \Omega_{ij} \frac{\sqrt{p_{0j}}}{\sqrt{p_{0i}}} e^{-i\phi_i} e^{i\phi_j} e^{i\beta_{ij}} \right\}, \end{aligned} \quad (12.12)$$

$$\begin{aligned} \frac{d\phi_i}{dt} + \omega_{0i} - 2N_i p_{0i} \rho_i = \\ \text{Im} \left\{ -\Omega_{ij} \frac{\sqrt{p_{0j}}}{\sqrt{p_{0i}}} e^{-i\phi_i} e^{i\phi_j} e^{i\beta_{ij}} \right\}, \end{aligned} \quad (12.13)$$

where

$$N_i = \frac{d\omega_i(p_{0i})}{dp_i}, \quad G_i = \frac{d\Gamma_{\text{eff},i}(p_{0i})}{dp_i}, \quad (12.14)$$

and  $\beta_{ij}$  is the phase shift of the spin wave (radiated by the  $j$ -th STNO) acquired during its propagation to the  $i$ -th STNO.

Introducing extinction coefficient of power fluctuations  $\Gamma_i = 2G_i p_{0i}$  and dimensionless nonlinear frequency shift of  $i$ -th STNO,  $\nu_i = N_i/G_i$ , we can obtain the system of equations [46]:

$$\begin{aligned} \frac{d\rho_i}{dt} + \Gamma_{0i} \rho_i = \Omega_{ij} \frac{\sqrt{p_{0j}}}{\sqrt{p_{0i}}} \cos(\beta_{ij} + \phi_j - \phi_i), \\ \frac{d\phi_i}{dt} + \omega_{0i} - \nu_i \Gamma_{0i} \rho_i = -\Omega_{ij} \frac{\sqrt{p_{0j}}}{\sqrt{p_{0i}}} \sin(\beta_{ij} + \phi_j - \phi_i). \end{aligned} \quad (12.15)$$

This model is the so-called power–phase model. It explicitly takes into account both the power fluctuations  $\rho_i(t)$  and the phase  $\phi_i(t)$  of the oscillator. The applicability condition of this model is  $|\rho_i(t)| \ll 1$ , i.e., relatively small level of power fluctuations. This condition is satisfied for typical experiments involving STNOs.

### 12.3.3 Phase Model

The power–phase model can be additionally simplified by introducing the “effective” magnetization oscillation phases  $\Phi_i \equiv \Phi_i(t)$  as [46]:

$$\Phi_i(t) = \phi_i(t) + v_i \rho_i(t). \quad (12.16)$$

Effective phase satisfies the equation

$$\frac{d\Phi_i}{dt} - \omega_{0i} = \sum_{\substack{j=1 \\ j \neq i}}^N \lambda_{ij} \sin(\Phi_j - \Phi_i + \beta_{ij}), \quad (12.17)$$

where  $\lambda_{ij}$  is the normalized amplitude of coupling coefficient of  $j$ -th STNO with  $i$ -th,

$$\lambda_{ij} = \Omega_{ij} \sqrt{\frac{p_{0j}}{p_{0i}}} \sqrt{1 + v_i^2},$$

$\beta_{ij} = \delta_{ij} - \arctan v_i$  is the normalized coupling phase. The phase model (12.17) is correct if  $|v_i \rho_i(t)| \ll 1$  for  $\forall i$ .

This phase model is very popular in the theory of auto-oscillators. When applied to the problem of phase-locking to an external signal, it becomes the Adler model [47]; for the case of mutual phase-locking of many oscillators, it is called the Kuramoto model [48].

## 12.4 Numerical Simulation of STNOs Synchronization

Our numerical simulations are based on the numerical phase model (12.17), where we use the global coupling approximation. According to this, we assume that each STNO interacts with some average microwave signal generated by all other nano-oscillators. Respectively, the amplitude and phase coefficients of the coupling are constant:

$$\lambda_{ij} = \frac{\Lambda}{N} \quad \beta_{ij} = \beta. \quad (12.18)$$

Taking this into account, the model equation (12.17) takes its final form:

$$\frac{d\Phi_i}{dt} - \omega_{0i} = \frac{\Lambda}{N} \sum_{\substack{j=1 \\ j \neq i}}^N \sin(\Phi_j - \Phi_i + \beta). \quad (12.19)$$

Approach of global coupling describes the systems of coupled oscillators when the interaction has symmetry [36, 48], such as system of two oscillators, three oscillators located at the vertices of an equilateral triangle, and for a large number of oscillators located at the same distance one from each other within the array. The behavior of oscillators located at the boundary of the oscillator array should be described a little differently, because in such a case the system is antisymmetric.

Our numerical analysis of mutual phase-locking of  $N$  globally coupled STNOs is based on the numerical solution of Eq. (12.19) for given amplitude  $\Lambda$  and phase  $\beta$  of the coupling signal, known STNO's natural frequencies  $f_{0i} = \omega_{0i}/2\pi$  and initial values of the "effective" phases  $\Phi_i(0)$  in the moment of time  $t = 0$ . Solving the system of Eqs. (12.19) on the time interval  $[0; T]$  allows us to obtain the time dependence of the phases  $\Phi_i(t)$ .

In experiments, frequencies  $f_{0i}$  of oscillators in an array differ due to uncertainties in technological process, presence of impurities, etc. Therefore, the free-running frequencies  $f_{0i}$  in Eq. (12.19) should be considered as random quantities having certain probability distribution  $P(f_{0i})$  (we assume that probability distribution is the same for each oscillator). In this paper we analyze the case of nano-oscillators with Gaussian frequency distribution

$$P_G(f_i) = \frac{1}{\Delta f \sqrt{2\pi}} e^{-\frac{1}{2} \left( \frac{f_i - f_0}{\Delta f} \right)^2}, \quad (12.20)$$

where  $f_0$  is the average value of frequency, and  $\Delta f$  is the standard frequency deviation.

To determine the state of the system (phase-locking is present or not) we estimate the complex order parameter  $r$  [36] using previously calculated generalized phases  $\Phi_i(t)$ :

$$r \equiv r(t) = R(t) e^{i\Psi(t)} = \frac{1}{N} \sum_{i=1}^N e^{i\Phi_i(t)}. \quad (12.21)$$

The amplitude  $R \equiv R(t) = |r|$  of the order parameter characterizes number of phase-locked oscillators, while the rate of change of the phase  $\Psi \equiv \Psi(t)$  gives the frequency of phase-locked oscillations  $d\Psi/dt$ .

When the system is not synchronized the difference of phase values is not constant and the amplitude  $R$  of the complex order parameter fluctuates. That is why it is necessary to check time-dependent fluctuations of  $R$  over some characteristic time to see whether the synchronization exists or not.

Characteristic deviation of the complex order parameter  $\Delta R$  depends not only on a number of non-synchronized oscillators  $N_{\text{nonSync}}$ , but it also depends on the total number of oscillators  $N_0$  in its array. As one can see in Fig. 12.1, the increases of  $N_{\text{nonSync}}$  causes the increase of  $\Delta R$ , however the increase of  $N_0$  causes decrease of  $\Delta R$ .



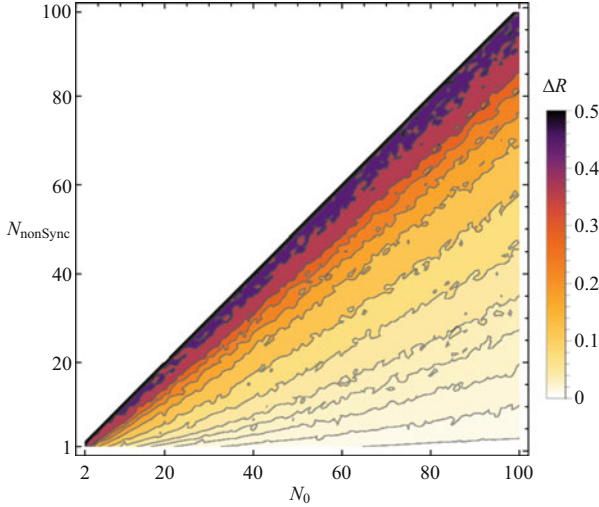


**Fig. 12.1** Dependence of the number of non-synchronized oscillators  $N_{\text{nonSync}}$  on its total number  $N_0$  for different relative deviations of the modulus of the order parameter  $\Delta R$  (the average values of  $\Delta R$  are color-coded and shown in the figure legend)

In addition with the increase of the number of oscillators in the array  $N_0$  the value of  $\Delta R$  decreases for a fixed number of non-synchronized STNOs  $N_{\text{nonSync}}$ . This effect can be explained by an increase of signal power, generated by the oscillators. During the calculations we also found that there was possible a cluster synchronization scenario, when there were several different groups of phase-locked nano-oscillators.

### 12.4.1 Two STNOs

With substitution of phase variables  $\Phi_i(t) \rightarrow \Phi_i(t) + 2\pi f_0 t$ ,  $\Phi_j(t) \rightarrow \Phi_j(t) + 2\pi f_0 t$  in (12.19), this equation can be written as:

$$\frac{d\Phi_i}{dt} - 2\pi \Delta f_i = \frac{\Lambda}{N} \sum_{\substack{j=1 \\ j \neq i}}^N \sin(\Phi_j - \Phi_i + \beta). \quad (12.22)$$

As one can see this phase transformation does not change the equation that allows one to replace absolute values of STNOs' natural frequencies  $f_{0i}$  with their deviations  $\Delta f_i = f_{0i} - f_0$  relative to some arbitrary frequency  $f_0$ . This frequency is convenient to choose as the average value of both natural frequencies of STNOs:  $f_0 = (f_{01} + f_{02})/2$ . Taking this into account and considering for definition  $f_{02} > f_{01}$ , the system of Eqs. (12.22) takes the form:

$$\frac{d\Phi_1}{dt} + 2\pi\Delta f = \frac{\Lambda}{2} \sin(\Phi_2 - \Phi_1 + \beta), \quad (12.23a)$$

$$\frac{d\Phi_2}{dt} - 2\pi\Delta f = \frac{\Lambda}{2} \sin(\Phi_1 - \Phi_2 + \beta), \quad (12.23b)$$

where  $\Delta f = (f_{02} - f_{01})/2$ .

We use numerical algorithm for the analysis of mutual phase-locking of two STNOs described as follows:

1. We solve the equations system (12.23) and determine  $\Phi_i(t)$  for given values of  $\Lambda$ ,  $\beta$ . We assume that  $\Lambda = 2\pi\xi f_0$ , where  $\xi$  varies from 0 to 1 with step 0.01;  $\beta$  varies from 0 to  $2\pi$  with step  $2\pi/100$ . We also use the following parameters:  $\Phi_1(0) = 0$ ,  $\Phi_2(0)$  is random value between 0 and  $2\pi$ ,  $f_0 = 10$  GHz,  $\Delta f$  varies from  $f_0/100$  to  $f_0/20$  with step  $f_0/100$ .
2. For each simulation we calculate  $R$  and  $\Delta R$  as time-averaged relative deviation value from the average value of  $R$  for a given  $\xi$ ,  $\beta$  (see [49] for details). Using this parameters we determine the state of the system (synchronization is present or not).
3. Then we construct the phase diagram in coordinates  $(\xi, \beta)$  and determine the conditions of qualitative change of the system's state.

The results of numerical simulations for two STNOs are presented in Fig. 12.2. The white areas correspond to the synchronized state of the system, while the other color-coded areas correspond to the different values of relative deviation of the complex order parameter  $\Delta R$ . The increase of color intensity for the areas in Fig. 12.2 indicates lesser probability of STNOs synchronization. The presented data were obtained for the case of STNOs' frequency distribution (12.20). In order to get statistically averaged results, we do 100 simulations for each pair of values  $\Lambda$  and  $\beta$  and then calculate the average value of  $\Delta R$  (for details see [49]). Although the analysis is performed for a large number of  $\Delta f$  values, we reveal that the phase diagram weakly depends on the exact  $\Delta f$  value. Thus, the contour plots in Fig. 12.2 presented only for four values of  $\Delta f$ : 100 MHz, 250 MHz, 350 MHz, and 500 MHz.

It can be seen from Fig. 12.2, that the synchronization of two STNOs is most effective when the coupling amplitude  $\Lambda$  is larger than the difference of nano-oscillator's own frequencies and the coupling phase  $\beta$  differs from  $(2k + 1)\pi/2$ , where  $k \in \mathbb{Z}$ .

### 12.4.2 Three STNOs

The system of three globally coupled nano-oscillators is described by the equations:

$$\frac{d\Phi_j}{dt} - \omega_j = \frac{\Lambda}{3} \sum_{j \neq i}^3 \sin(\Phi_j - \Phi_i + \beta), \quad (12.24)$$

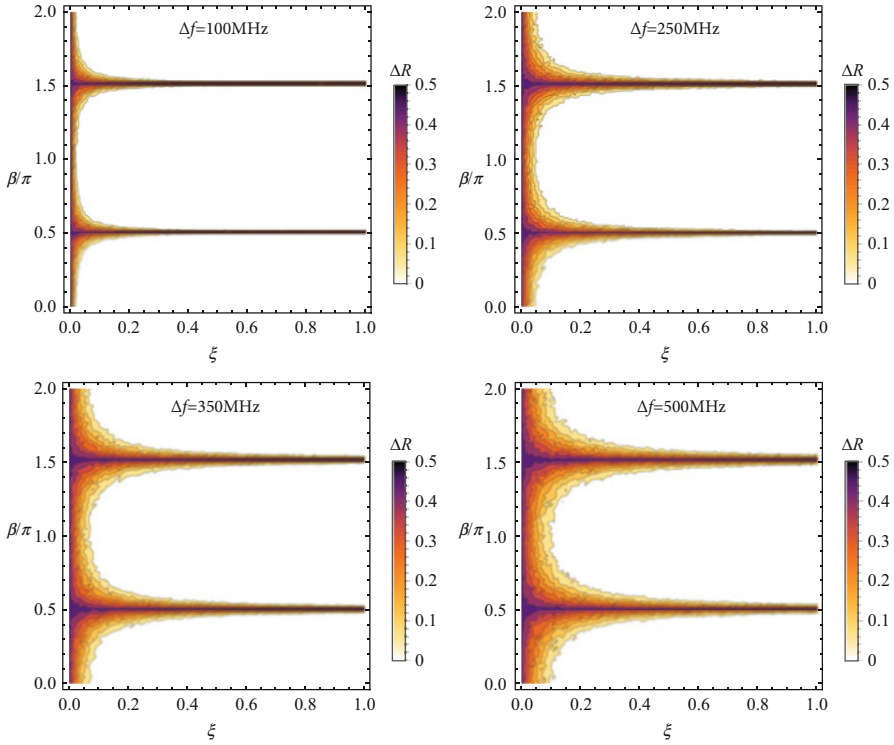


**Fig. 12.2** Contour plots of the relative deviation of the complex order parameter  $\Delta R$  for different phases of coupling  $\beta$  and amplitudes of coupling  $\Lambda = 2\pi\xi f_0$  for the system of 2 STNOs. The figures calculated for the different values of  $\Delta f$ : 100 MHz, 250 MHz, 350 MHz, 500 MHz. White regions correspond to the synchronized state of the system

where the phase transformations previously used in (12.22) have no effect. Like in the case of two coupled STNOs, the oscillator's frequencies are considered to be normally distributed by the expression (12.20). The average frequency of oscillations was chosen to be  $f_0 = 10$  GHz.

In the case of three coupled STNOs, our numerical algorithm can be described as follows:

1. We solve the equations system (12.24) and determine  $\Phi_i(t)$  for chosen values of  $\Lambda$ ,  $\beta$ , while eigenfrequencies of the oscillators calculated from (12.20), where  $f_0 = 10$  GHz,  $\Delta f$  is chosen as 100 MHz, 250 MHz, 350 MHz, 500 MHz.
2. For each simulation we calculate time-averaged values of  $R$  and  $\Delta R$  (see [49] for details). Using this parameters we determine the state of the system (synchronization is present or not).
3. Then we construct the phase diagram in coordinates  $(\xi, \beta)$  and determine the conditions of qualitative change of the system's state.

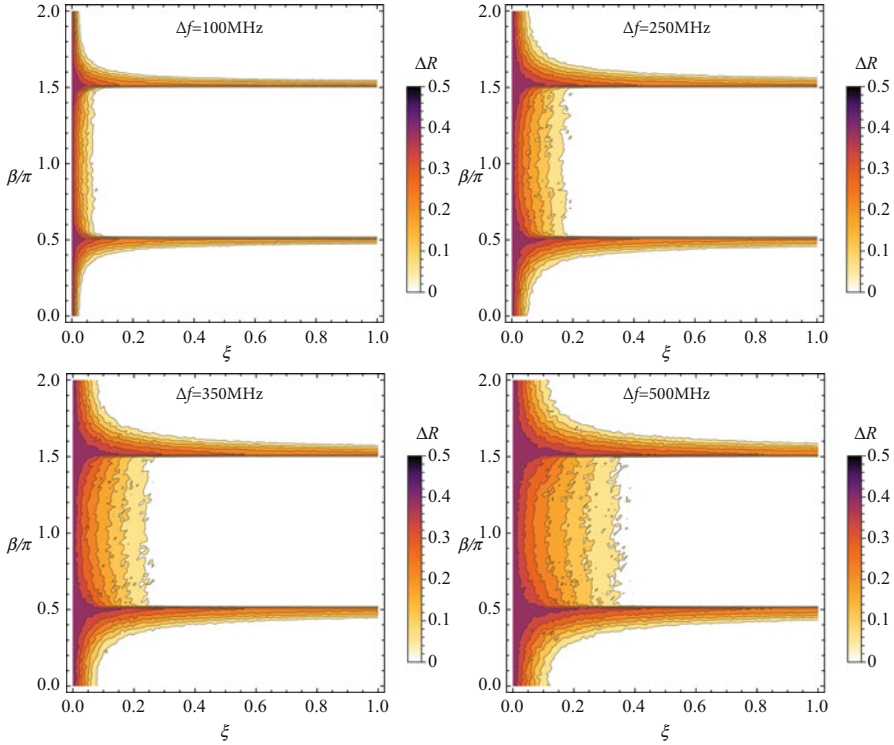


**Fig. 12.3** Contour plots of the relative deviation of the complex order parameter  $\Delta R$  for different phases of coupling  $\beta$  and amplitudes of coupling  $\Lambda = 2\pi\xi f_0$  for the system of 3 STNOs. The figures calculated for the different values of  $\Delta f$ : 100 MHz, 250 MHz, 350 MHz, 500 MHz. White regions correspond to the synchronized state of the system

The results shown in Fig. 12.3 indicate that the behavior of the system for the phase coupling coefficients  $\beta$  close to 0 and/or  $\pi$  is not the same. In the area  $\beta < \pi/2$  the synchronization is robust and can occur at the smaller values of  $\Lambda$ , while for the case  $\pi/2 < \beta < 3\pi/2$  the system could be in the frustrated state. Nevertheless, generally the synchronization scenario for three STNOs remains similar to the synchronization scenario for two STNOs.

### 12.4.3 Many STNOs

In this section of the paper, we consider mutual phase-locking of five globally coupled nano-oscillators. In this case the equation for each STNO has the form

$$\frac{d\Phi_j}{dt} - \omega_j = \frac{\Lambda}{5} \sum_{j \neq i}^5 \sin(\Phi_j - \Phi_i + \beta). \quad (12.25)$$

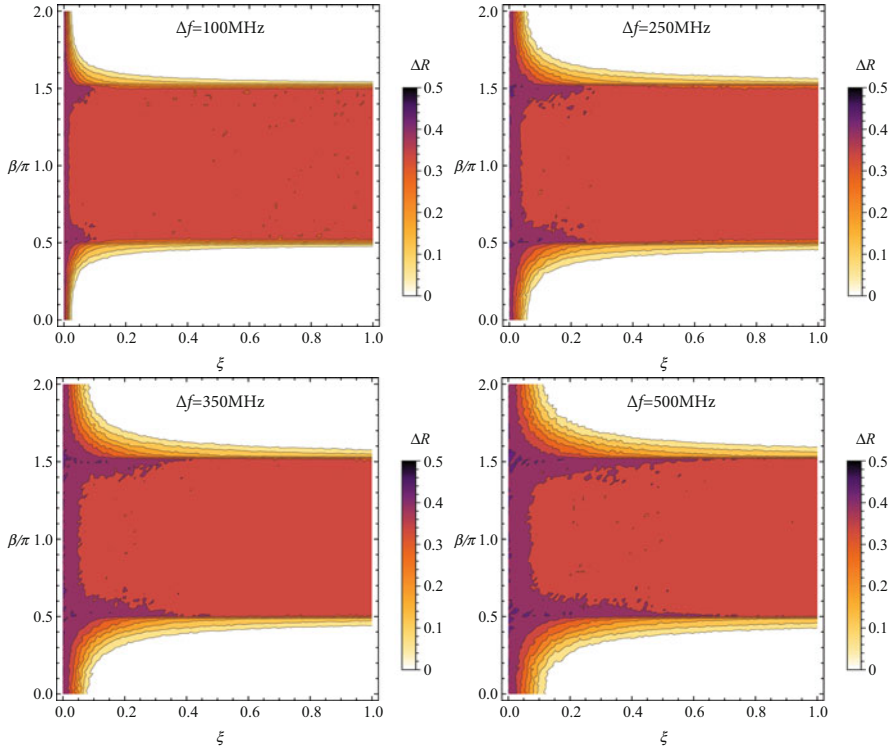


**Fig. 12.4** Contour plots of the relative deviation of the complex order parameter  $\Delta R$  for different phases of coupling  $\beta$  and amplitudes of coupling  $\Lambda = 2\pi\xi f_0$  for the system of 5 STNOs. The figures calculated for the different values of  $\Delta f$ : 100 MHz, 250 MHz, 350 MHz, 500 MHz. White regions correspond to the synchronized state of the system

Oscillators' eigenfrequencies are given by the distribution (12.20). We also use the numerical algorithm described above in the Sect. 12.4.2.

The simulation results are presented in Fig. 12.4. As one can see in the case of five STNOs, it appears remarkable reduction of the synchronization area for the coupling phase  $\beta$  lying in the range  $[\pi/2; 3\pi/2]$ . This effect could be explained by the frustration of the oscillators system's state.

## 12.5 Conclusions

Using numerical simulations we analyzed mutual phase-locking of two, three, and five globally coupled STNOs in the scope of the phase model. We have shown that STNOs synchronization is the most effective when the coupling amplitude  $\Lambda$  is larger than the characteristic frequency deviations of the oscillators and the

phase coupling  $\beta$  is close to 0 or  $2\pi$ . When  $\beta$  lies in range from  $\pi/2$  to  $3\pi/2$ , the state of the oscillators system could be frustrated. And in the case of three and more STNOs the formation of clusters of synchronized oscillators became possible. We believe that the obtained results might be important for the development and creation of practical microwave devices with many synchronized STNOs having optimal working characteristics. Calculated numerical data can also be used for the estimation of the phase-locking efficiency for the different numbers of STNOs.

**Acknowledgements** Publication is based on the research provided by the grant support of the State Fund for Fundamental Research of Ukraine, the Ministry of Education and Science of Ukraine (grant No. 16BF052-01) and by the grants from Taras Shevchenko National University of Kyiv and National Academy of Sciences of Ukraine.

## References

1. Slonczewski JC (1996) Current-driven excitation of magnetic multilayers. *J Magn Magn Mater* 159:L1
2. Berger L (1996) Emission of spin waves by a magnetic multilayer traversed by a current. *Phys Rev B* 54:9353
3. Kiselev SI, Sankey JC, Krivorotov IN et al (2003) Microwave oscillations of a nanomagnet driven by a spin-polarized current. *Nature* 425:380
4. Lee KJ, Deac A, Redon O et al (2004) Excitations of incoherent spin-waves due to spin-transfer torque. *Nat Mater* 3:877
5. Krivorotov IN, Emley NC, Sankey JC et al (2005) Time-domain measurements of nanomagnet dynamics driven by spintransfer torques. *Science* 307:228
6. Houssameddine D, Ebels U, Delaët B et al (2007) Spin-torque oscillator using a perpendicular polarizer and a planar free layer. *Nat Mater* 6:447
7. Slavin A, Tiberkevich V (2009) Nonlinear auto-oscillator theory of microwave generation by spin-polarized current. *IEEE Trans Magn* 45:1875
8. Prokopenko O, Bankowski E, Meitzler T et al (2011) Spin-torque nano-oscillator as a microwave signal source. *IEEE Magn Lett* 2:3000104
9. Locatelli N, Cros V, Grollier J (2014) Spin-torque building blocks. *Nat Mater* 13:11
10. Prokopenko O (2015) Microwave signal sources based on spin-torque nano-oscillators. *Ukr J Phys* 60:104
11. Pribiag VS, Krivorotov IN, Fuchs GD et al (2007) Magnetic vortex oscillator driven by d.c. spin-polarized current. *Nat Phys* 3:498
12. Dussaux A, Georges B, Grollier J et al (2010) Large microwave generation from dc driven magnetic vortex oscillators in magnetic tunnel junctions. *Nat Commun* 1:8
13. Yang L, Verba R, Tiberkevich V et al (2015) Reduction of phase noise in nanowire spin orbit torque oscillators. *Sci Rep* 5:16942
14. Choi HS, Kang SY, Cho SJ et al (2014) Spin nano-oscillator-based wireless communication. *Sci Rep* 4:5486
15. Tamaru S, Kubota H, Yakushiji K et al (2015) Extremely coherent microwave emission from spin torque oscillator stabilized by phase locked loop. *Sci Rep* 5:18134
16. Khalsa G, Stiles MD, Grollier J (2015) Stable oscillation in spin torque oscillator excited by a small in-plane magnetic field. *Appl Phys Lett* 106:242402
17. Tiberkevich VS, Khymyn RS, Tang HX, Slavin AN (2013) Sensitivity to external signals and synchronization properties of a non-isochronous auto-oscillator with delayed feedback. *Sci Rep* 4:3873

18. Fuchs GD, Krivorotov IN, Braganca PM et al (2005) Adjustable spin torque in magnetic tunnel junctions with two fixed layers. *Appl Phys Lett* 86:152509
19. Rowlands GE, Krivorotov IN (2012) Magnetization dynamics in a dual free-layer spin-torque nano-oscillator. *Phys Rev B* 86:094425
20. Moriyama T, Finocchio G, Carpentieri M et al (2012) Phase locking and frequency doubling in spin-transfer-torque oscillators with two coupled free layers. *Phys Rev B* 86:060411(R)
21. Sharad M, Yogendra K, Roy K (2013) Dual pillar spin torque nano-oscillator. *Appl Phys Lett* 103:152403
22. Prokopenko OV, Krivorotov IN, Bankowski EN et al (2013) Hysteresis regime in the operation of a dual-free-layer spintorque nano-oscillator with out-of-plane counter-precessing magnetic moments. *J Appl Phys* 114:173904
23. Katine JA, Fullerton EE (2008) Device implications of spin-transfer torques. *J Magn Magn Mater* 320:1217
24. Silva TJ, Rippard WH (2008) Developments in nano-oscillators based upon spin-transfer point contact devices. *J Magn Magn Mater* 320:1260
25. Tiberkevich VS, Slavin AN, Kim J-V (2008) Temperature dependence of nonlinear auto-oscillator linewidths: application to spin-torque nano-oscillators. *Phys Rev B* 78:092401
26. Schneider ML, Rippard WH, Pufall MR et al (2009) Temperature dependence of spin-torque-driven self-oscillations. *Phys Rev B* 80:144412
27. Prokopenko O, Melkov G, Bankowski E et al (2011) Noise properties of a resonance-type spin-torque microwave detector. *Appl Phys Lett* 99:032507
28. Prokopenko OV, Bankowski E, Meitzler T et al (2012) Influence of temperature on the performance of a spin-torque microwave detector. *IEEE Trans Magn* 48:3807
29. Kaka S, Pufall MR, Rippard WH et al (2005) Mutual phase-locking of microwave spin torque nano-oscillators. *Nature* 437:389
30. Mancoff FB, Rizzo ND, Engel BN, Tehrani S (2005) Phase-locking in double-point-contact spin-transfer devices. *Nature* 437:393
31. Slavin AN, Tiberkevich VS (2005) Nonlinear self-phase-locking effect in an array of current-driven magnetic nanocontacts. *Phys Rev B* 72:092407
32. Slavin AN, Tiberkevich VS (2006) Theory of mutual phase locking of spin-torque nanosized oscillators. *Phys Rev B* 74:104401
33. Grollier J, Cros V, Fert A (2006) Synchronization of spin-transfer oscillators driven by stimulated microwave currents. *Phys Rev B* 73:060409(R)
34. Georges B, Grollier J, Darques M et al (2008) Coupling efficiency for phase locking of a spin transfer nano-oscillator to a microwave current. *Phys Rev Lett* 101:017201
35. Ruotolo A, Cros V, Georges B et al (2009) Coupling efficiency for phase locking of a spin transfer nano-oscillator to a microwave current. *Nat Nanotechnol* 4:528
36. Pikovsky A, Rosenblum M, Kurths J (2007) Synchronization: a universal concept in nonlinear sciences. University Press, Cambridge
37. Ralph DC, Stiles MD (2008) Spin transfer torques. *J Magn Magn Mater* 320:1190
38. Tsymbal EY, Žutić I (eds) (2012) Handbook of spin transport and magnetism. CRC Press, New York
39. Sanches F, Tiberkevich V, Guslienko KY et al (2014) Current-driven gyrotropic mode of a magnetic vortex as a nonisochronous auto-oscillator. *Phys Rev B* 89:140410(R)
40. Rippard W, Pufall M, Russek S (2006) Comparison of frequency, linewidth, and output power in measurements of spintransfer nanocontact oscillators. *Phys Rev B* 74:224409
41. Persson J, Zhou Y, Akerman J (2007) Phase-locked spin torque oscillators: impact of device variability and time delay. *J Appl Phys* 101:09A503
42. Muruges S, Lakshmanan M (2009) Bifurcation and chaos in spin-valve pillars in a periodic applied magnetic field. *Chaos* 19:043111
43. Li D, Zhou Y, Zhou C, Hu B (2010) Global attractors and the difficulty of synchronizing serial spin-torque oscillators. *Phys Rev B* 82:140407
44. Awad AA, Dürrenfeld P, Houshang A et al (2017) Long-range mutual synchronization of spin Hall nano-oscillators. *Nat Phys* 13:292 (published online November 14, 2016)

45. Prokopenko O, Tyberkevych V, Slavin A (2008) Mutual phase-locking of two spin-torque oscillators: influence of time delay of a coupling signal. In: Proceedings of the Europe international magnetics conference (Intermag), 4–8 May, Madrid, DP-06, pp 682–683
46. Prokopenko O (2010) Mutual phase-locking of two nano-size magnetic structures considering an influence of signal delay. *Radio Electron Comput Sci Control* 2:11
47. Adler R (1946) A study of locking phenomena in oscillators. *Proc IRE* 34:351
48. Acebrón JA, Bonilla LL, Pérez Vicente CJ et al (2005) The Kuramoto model: a simple paradigm for synchronization phenomena. *Rev Mod Phys* 77:137
49. Swift J, Strogatz S, Wiesenfeld K (1992) Averaging of globally coupled oscillators. *Phys D* 55:239



# Chapter 13

## Temperature Effect on the Basis States for Charge Transfer Through a Polypeptide Fragments of Proteins and on the Nanocurrent in It

A. D. Suprun and L. V. Shmeleva

### 13.1 Introduction

Transfer of energy or charge transport in the polypeptide fragments of protein molecules is increasingly frequently analysed [1] taking into account the actual structure of these fragments, particularly, finite length of the  $\alpha$ -spiral section [2], and other factors, which are inherent in general to the physical objects containing carbon [3–5]. The processes, which occur in the course of the donor-acceptor electron transfer between organelles of those cells (polypeptide fragments of protein molecules), particularly, influence of temperature upon these processes, are already sufficiently investigated [6]. These polypeptide fragments can be used in the nonnative state in the perspective as nanowires of the semiconductor nature in the nanodevices, as, for example, in [7–9]. The problem concerning mechanisms of electron transfer over these organelles in the idealised conditions of zero temperature was analysed in detail in [10, 11]. Particularly, average-electron structure and average-nuclear structure of the protein molecule were analysed in detail in article [10]. On the basis of this analysis in article [11], a check calculation of current density was carried out at the zero temperature in the conditions of complete absence of the factors, which violate electrostatic equilibrium of the system and may be interpreted as external fields. As opposed to article [11], such calculation was carried out in the present article as well, but it was carried out on the condition that the influence of the nonzero temperature upon the electron subsystem of the polypeptide fragments of protein molecules was taken into account. It was shown that at  $T \neq 0$  various power-law dependences are realised in practice between the energetic positions of

---

A.D. Suprun • L.V. Shmeleva (✉)

Departments of Theoretical Physics, Faculty of Physics, Taras Shevchenko National University of Kyiv, Volodymyrska Street, 64/13, Kyiv, 01601, Ukraine  
e-mail: [LShmel@univ.kiev.ua](mailto:LShmel@univ.kiev.ua)

© Springer International Publishing AG 2017

O. Fesenko, L. Yatsenko (eds.), *Nanophysics, Nanomaterials, Interface Studies, and Applications*, Springer Proceedings in Physics 195,  
DOI 10.1007/978-3-319-56422-7\_13

175

each separate state in the conduction band and the temperature, but all of them are in proportion to factor  $227^\circ/T$ . In spite of this fact, all these states taken together ensure the absence of current in accordance with the abovestated conditions (complete absence of violation of the electrostatic equilibrium of the system). This proves compliance to the model adopted for the conductivity of the polypeptide fragment of the protein molecule in the real conditions  $T \neq 0$  also. Therefore, it is possible to use this model for a real protein system not only in respect to the factors, which may be interpreted as external fields, but in respect to the temperature also.

## 13.2 Materials and Methods

*Description of the electron injection to the conductance band, as the excited state of the protein molecule, on the condition that  $T \neq 0$ .* Functional for a work was found in article [11]:

$$E(\{a\}) = \sum_{\mathbf{n}\mathbf{m}}' w_{\mathbf{n}\mathbf{m}} + \sum_{\mathbf{n}} (\tilde{W}_{\mathbf{n}\mathbf{n}}^{cc} + D_{\mathbf{n}}^c) \cdot |a_{\mathbf{n}}|^2 + 2 \sum_{\mathbf{n}\mathbf{m}}' M_{\mathbf{n}\mathbf{m}}^c a_{\mathbf{n}}^* a_{\mathbf{m}} \quad (13.1)$$

in respect of the wave function  $a_{\mathbf{n}}$ , which describes the spatiotemporal distribution of the excitation and which occurs due to injecting of electron into the polypeptide fragments of protein molecules. The values  $w_{\mathbf{n}\mathbf{m}}$ ,  $D_{\mathbf{n}}^c$ ,  $M_{\mathbf{n}\mathbf{m}}^c$ , and  $\tilde{W}_{\mathbf{n}\mathbf{n}}^{cc}$ , which are included into (13.1), for the type of the system under examination are determined with the help of the following correlations.

Interatomic interaction energy:

$$w_{\mathbf{n}\mathbf{m}} \equiv K_{\mathbf{n}-\mathbf{m}}/2 - \sum_f N_{f0}^{(T)} \left[ Q_{0,\mathbf{m}-\mathbf{n},0}^f - \sum_g N_{g0}^{(T)} \gamma_{\mathbf{n}\mathbf{m}\mathbf{m}\mathbf{n}}^{fggf}/2 \right],$$

plays the key role in the process of integration of the isolated atoms into the single interconnected non-excited system.  $K_{\mathbf{n}-\mathbf{m}} = (ze)^2/|\mathbf{n}-\mathbf{m}|$  is the direct Coulomb interaction energy between nuclei of atoms.  $Q_{0,\mathbf{m}-\mathbf{n},0}^f \equiv \langle \varphi_f(\mathbf{r}) | ze^2/|\mathbf{r}-(\mathbf{m}-\mathbf{n})| | \varphi_f(\mathbf{r}) \rangle$  is the module of the averaged energy (in the quantum understanding of term “average” by the  $\mathbf{r}$  variable) for the Coulomb interaction of the electron in the state  $f$ , localised in the neighbourhood of the atomic position of the lattice  $\mathbf{n}$ , while the atomic nucleus is in the position  $\mathbf{m}$ . Factor  $\gamma_{\mathbf{n}\mathbf{m}\mathbf{m}\mathbf{n}}^{fggf}$  is determined by the ratio:  $\gamma_{\mathbf{n}\mathbf{m}\mathbf{m}\mathbf{n}}^{fggf} \equiv V_{\mathbf{n}\mathbf{m}\mathbf{m}\mathbf{n}}^{fggf} - V_{\mathbf{n}\mathbf{m}\mathbf{m}\mathbf{m}}^{fggf}$ . Here

$$V_{\mathbf{n}\mathbf{m}\mathbf{m}\mathbf{n}}^{fggf} \equiv \langle \varphi_{f\mathbf{n}}(\mathbf{r}_1) \varphi_{g\mathbf{m}}(\mathbf{r}_2) | e^2/|\mathbf{r}_1-\mathbf{r}_2| | \varphi_{g\mathbf{m}}(\mathbf{r}_2) \varphi_{f\mathbf{n}}(\mathbf{r}_1) \rangle$$

is the module of the averaged energy (in the quantum understanding of term “average” by the  $\mathbf{r}_1, \mathbf{r}_2$  variables) for the Coulomb interaction between the electrons, which are in the states  $f, g$  and which are localised in the neighbourhood of the atomic positions of the lattice  $\mathbf{n}, \mathbf{m}$ . Matrix element

$$V_{\mathbf{nm}\mathbf{m}\mathbf{n}}^{f g f g} \equiv \langle \varphi_{f\mathbf{n}}(\mathbf{r}_1) \varphi_{g\mathbf{m}}(\mathbf{r}_2) | e^2 / |\mathbf{r}_1 - \mathbf{r}_2| | \varphi_{f\mathbf{n}}(\mathbf{r}_2) \varphi_{g\mathbf{m}}(\mathbf{r}_1) \rangle$$

is the module of the averaged energy (with respect to  $\mathbf{r}_1, \mathbf{r}_2$  variables) for the exchange interaction between the electrons, which are in the states  $f, g$  and which are localised in the neighbourhood of the atomic positions of the lattice  $\mathbf{n}, \mathbf{m}$ . Factors of the type  $N_{f\mathbf{0}}^{(T)}$  are actually Fermi-Dirac distributions. They have the following form for the temperature  $T < 10^4 \text{K}$ :  $N_{f\mathbf{0}}^{(T)} = [1 + \exp \{(E_f - \mu) / kT\}]^{-1}$ , where  $\mu$  is the chemical potential. As it is known, when  $T$  tends to zero, factors  $N_{f\mathbf{0}}^{(T)}$  tend to the Heaviside step function:  $N_{f\mathbf{0}}^{(T \rightarrow 0)} \Rightarrow \theta(\mu - E_f)$ . This same situation ( $T \rightarrow 0$ ) was analysed in article [11]. As it was already stated, the goal of this article was as follows: on the one hand, to take into account the influence of temperature upon the conductance states, because it is an important factor for the regulatory influences upon the processes of metabolism. On the other hand, to carry out this operation in such a way that would be no any violations of main principle: "external fields are absent – current is absent". In considered conditions,  $\mu$  is determined by the following correlation:  $\mu = (E_c + E_v) / 2$ , where, subscript "c" is used in order to denote the lowest energy conductance band, while subscript "v" denotes the valence band, which is the closest to this conductance band. If to substitute this definition of  $\mu$  into  $N_{f\mathbf{0}}^{(T)} = [1 + \exp \{(E_f - \mu) / kT\}]^{-1}$  for the states  $f = c$  and  $f = v$ , it is possible to find (taking into account that  $E_c - E_v > 0$ ):

$$N_{c\mathbf{0}}^{(T)} = [1 + \exp \{(E_c - E_v) / 2kT\}]^{-1};$$

$$N_{v\mathbf{0}}^{(T)} = [1 + \exp \{-(E_c - E_v) / 2kT\}]^{-1}.$$

For all other states, there exist the following high-precision equalities:  $N_{f\mathbf{0}}^{(T)} = 1$ , if  $E_f - E_c < 0$ , and  $N_{f\mathbf{0}}^{(T)} = 0$ , if  $E_f - E_v > 0$ . Therefore, on the basis of the general definition of energy of a non-excited crystal:

$$E_0 \equiv N_a \sum_f N_{f\mathbf{0}}^{(T)} \left( \varepsilon_f + \sum_g N_{g\mathbf{0}}^{(T)} \gamma_{\mathbf{0}\mathbf{0}\mathbf{0}\mathbf{0}}^{f g g f} / 2 \right) \equiv N_a \sum_f N_{f\mathbf{0}}^{(T)} E_f,$$

where  $N_a$  is the number of atoms in a polypeptide fragment of the protein molecule; the energy of separate level (band) in recalculation per a single atom may be presented in the form as follows:  $E_f \equiv \varepsilon_f + \sum_g N_{g\mathbf{0}}^{(T)} \gamma_{\mathbf{0}\mathbf{0}\mathbf{0}\mathbf{0}}^{f g g f} / 2$ .

$D_{\mathbf{n}}^c \equiv -\sum_{\mathbf{m}(\neq \mathbf{n})} \left[ Q_{\mathbf{0}, \mathbf{m}-\mathbf{n}, \mathbf{0}}^c - \sum_f N_{f\mathbf{0}}^{(T)} \gamma_{\mathbf{n}\mathbf{m}\mathbf{m}\mathbf{n}}^{c f f c} \right]$  is additional to the interatomic interaction energy  $w_{\mathbf{n}\mathbf{m}}$ , which is essentially connected with the occurrence of excitation.

Influence of the external fields (both real and efficient ones) upon the injected electron is presented by the summand as follows:

$$\tilde{W}_{\mathbf{n}\mathbf{n}}^{cc} \equiv \langle \varphi_{c\mathbf{n}}(\mathbf{r}) | W(\mathbf{r}) - (1/13) \sum_{\mathbf{l}} (ze^2/|\mathbf{r}-\mathbf{l}|) | \varphi_{c\mathbf{n}}(\mathbf{r}) \rangle, \quad (13.2)$$

where  $W(\mathbf{r})$  is the external field (real), while  $(1/13) \sum_{\mathbf{l}} (ze^2/|\mathbf{r}-\mathbf{l}|)$  is the efficient external field (which is connected with the amino acid inhomogeneity of the polypeptide fragment of the protein molecule). If this summand is equal to zero, then this fact must ensure the absence of current at any temperature. In this case, the accepted model of the polypeptide fragments of protein molecules may be used for further forecast calculations in the actual conditions, which are characterised by availability of the nonzero temperature and external fields (both actual and efficient).

Lastly the matrix element  $M_{\mathbf{n}\mathbf{m}}^{cc}$ , which is included to the functional (13.1), is determined by the following equality:  $M_{\mathbf{n}\mathbf{m}}^{cc} \equiv - (1/2) \sum_{\mathbf{l}} \left[ Q_{0,\mathbf{l}-\mathbf{n},\mathbf{m}-\mathbf{n}}^c - \sum_f N_{f0}^{(T)} \gamma_{\mathbf{n}\mathbf{l}\mathbf{m}}^{cfff} \right]$ . As well as  $D_{\mathbf{n}}^c$  this is the additional summand to  $w_{\mathbf{n}\mathbf{m}}$  energy, and it describes the dynamic of excitation, if it is considered as the quasiparticle, that is, as the object of the classic type. The matrix element  $M_{\mathbf{n}\mathbf{m}}^{cc}$ , being a part of the system energy, is the real factor and satisfies the condition:  $M_{\mathbf{n}\mathbf{m}}^{cc} = M_{\mathbf{m}\mathbf{n}}^{cc}$ . Then it is possible to present functional (13.1) in the following final form:

$$E(\{a\}) = \sum_{\mathbf{n}\mathbf{m}} w_{\mathbf{n}\mathbf{m}} + \sum_{\mathbf{n}} (\tilde{W}_{\mathbf{n}\mathbf{n}}^{cc} + D_{\mathbf{n}}^c) \cdot |a_{\mathbf{n}}|^2 + \sum_{\mathbf{n}\mathbf{m}} M_{\mathbf{n}\mathbf{m}}^{cc} (a_{\mathbf{n}}^* a_{\mathbf{m}} + a_{\mathbf{m}}^* a_{\mathbf{n}}). \quad (13.3)$$

The above-presented detailing determinations of the values, which are included into functional (13.3), are necessary for further quantity analysis of the problems under examination, as well as in order to ensure possibilities for making forecast conclusions concerning utilisation of the external fields in the regulatory medical and diagnostic purposes in respect to the polypeptide fragments of protein molecules.

## 13.3 Results and Discussion

### 13.3.1 *The Effect of Temperature on the Energy Positions of the Conduction States of the Polypeptide Fragments of Protein Molecules*

As it was noticed [11], in the approximation of linear elongated polypeptide nanowires, the spatial variables  $\mathbf{n}$ ,  $\mathbf{m}$  of the functional (13.3) lose their vector nature, and the functional (13.3) takes the form

$$E(\{a\}) = \sum_{nm} w_{nm} + \sum_n \left( \tilde{W}_{nn}^{cc} + \sum_{m(\neq n)} D_{nm}^{cc} \right) |a_n|^2 + \sum_{nm} M_{nm}^{cc} (a_n^* a_m + a_m^* a_n), \quad (13.4)$$

where, in particular, the matrix element

$$D_n^c \equiv - \sum_{m(\neq n)} \left[ Q_{0,m-n,0}^c - \sum_f N_{f0}^{(T)} \gamma_{nmmn}^{c f f c} \right],$$

is detailed to the form  $D_{nm}^{cc} = - \left( Q_{0,m-n,0}^c - \sum_f N_{f0}^{(T)} \gamma_{nmmn}^{c f f c} \right)$ . If further taken into account the real structure of the unit cell (which is actually the average amino acid residue) and to ignore the effects of nonlinear response [12] of “crystal lattice” of polypeptide fragment of protein molecule to electron injection, then all matrix elements will have not just index  $n$  (which takes values from 1 to  $N_a$ , by the number of atoms in the polypeptide fragment) but will have double index  $n, \alpha$ , where  $\alpha = 0, 1, 2, 3, 4$ . That is, adopt 5 values according to average number of atoms in the amino acid residue; herewith  $n = 1, \dots, N_0$ , where  $N_0 = N_a/5$  is the number of amino acid residues. Then the functional (13.4) can be reduced to a working form:

$$E(\{a\}) = N_a w + \sum_{n=1}^{N_0} \left[ \sum_{\alpha=0}^4 (\tilde{W}_n^\alpha + P_\alpha) |a_{n\alpha}|^2 + M \left\{ \sum_{\alpha=0}^1 (a_{n\alpha}^* a_{n,\alpha+1} + a_{n,\alpha+1}^* a_{n\alpha}) + \sum_{\alpha=2}^3 (a_{n,\alpha-1}^* a_{n,\alpha+1} + a_{n,\alpha+1}^* a_{n,\alpha-1}) + (a_{n2}^* a_{n+1,0} + a_{n+1,0}^* a_{n2}) \right\} \right]. \quad (13.5)$$

Here, indices “ $c$ ”, which symbolise the conductance band, are discarded and designations  $w \equiv w(R_0)$  and  $M \equiv M(R_0)$ , where  $R_0$  is the average distance between neighbouring atoms, can be consistently obtained from the general definitions:

$$w_{nm} \equiv K_{n-m}/2 - \sum_f \left[ N_{f0}^{(T)} Q_{0,m-n,0}^{f f} - \sum_g N_{f0}^{(T)} N_{g0}^{(T)} \gamma_{nmmn}^{f g g f} / 2 \right]; \quad (13.6)$$

$$M_{nm}^{cc} \equiv - (1/2) \sum_1 \left[ Q_{0,1-n,m-n}^c - \sum_f N_{f0}^{(T)} \gamma_{n11m}^{c f f c} \right],$$

for the approximation of nearest neighbours and linear elongated polypeptide fragments of a protein molecule.

For the summand, which represents the field, it is possible to introduce such a redesignation sequentially from the definition (13.2):  $\tilde{W}_{n\alpha n\alpha}^c \equiv \tilde{W}_n^\alpha$ , and the coefficients  $P_\alpha$ , with account of the notation  $D \equiv D^{cc}(R_0)$  and of the general definition:

$$D_{nm}^{cc} = - \left( Q_{0,m-n,0}^c - \sum_f N_{f0}^{(T)} \gamma_{nmfn}^{cc} \right), \quad (13.7)$$

which are given by

$$P_0 \equiv D^{cc}(R_0) \equiv D; P_1 \equiv D^{cc}(R_0) + D^{cc}(R_0)/2 \equiv 3D/2; P_2 \equiv D^{cc}(R_0)/2 + D^{cc}(R_0) \equiv 3D/2; P_3 \equiv D^{cc}(R_0)/2 \equiv D/2; P_4 \equiv D^{cc}(R_0)/2 \equiv D/2.$$

Here we also use approximation of nearest neighbours and approximation linear extended polypeptide fragment of protein molecule.

As a result of the variation of the functional (13.5) under condition  $\tilde{W}_n^\alpha = 0$  and of the presentation  $a_{n\alpha} = A_\alpha \exp(i k R_0 n)$ , where  $k$ , one-dimensional wave vector, the system of 5 equations for determining of the coefficients  $A_\alpha$  and eigenvalues  $x \equiv \varepsilon/|D|$  was obtained. This system has a single parameter  $v \equiv |M/D|$  (except of wave vector  $k$ ). With the total absence of external fields, this system of 5 equations did not change formally, and, therefore, the formal condition of its compatibility remains unchanged:

$$\begin{aligned} 16x^5 + 80x^4 + 8(19 - 10v^2)x^3 + 8(17 - 26v^2 + 4v^3 \cos(kR_0))x^2 \\ + (57 - 164v^2 + 32v^3 \cos(kR_0) + 48v^4)x \\ + (9 - 40v^2 + 8v^3 \cos(kR_0) + 32v^4) = 0. \end{aligned} \quad (13.8)$$

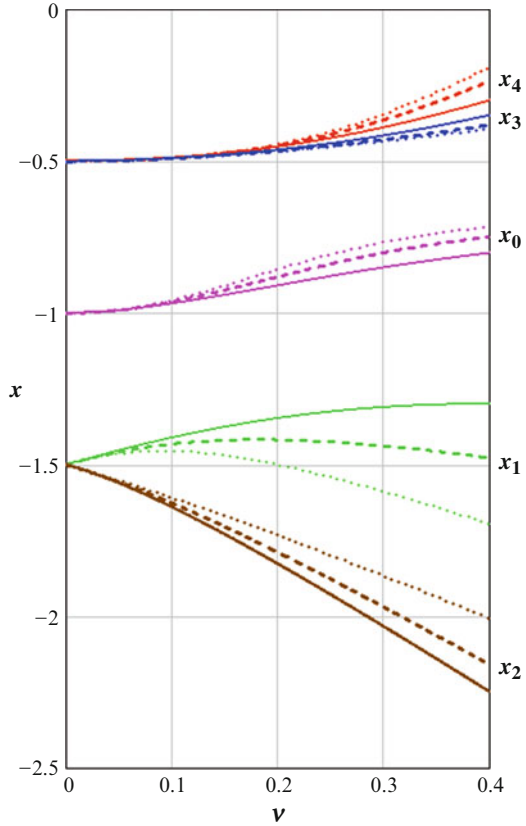
Detailed graphical and numerical analysis of the Eq. (13.8) is shown in Figs. 13.1 and 13.2, where the relative positions of roots  $x_s(v, k)$  ( $s = 0, 1, 2, 3, 4$ ) are presented. The dependencies, which are represented in Figs. 13.1 and 13.2, are quite accurate in quantitative meaning within the range  $0 < v < 1$ , especially near the default value  $v = 0.4$ . This analysis makes it possible to build quite satisfactory, even in a quantitative meaning, analytical solutions [11]. The results arising from the condition (13.8) do not formally change their form compared with those obtained for zero temperature. But now the parameter  $v \equiv |M/D|$  essentially depends on the temperature. This dependence is determined by the structure of the following type:

$$v(T) = \Gamma - \gamma 227.45^\circ / T. \quad (13.9)$$

Here the parameters  $\Gamma$  and  $\gamma$  are positive and close to unit in typical situations for matrix elements  $M$  and  $D$  in polypeptide fragments of protein molecules. They have the following general property within physiologically acceptable temperature range:

$$\Gamma > \gamma 227.45^\circ / T.$$

**Fig. 13.1** The dependence of the roots  $x_s(v, k)$  of Eq. (13.8) on the dimensionless energy of resonance exchange interaction  $v$  for the three key values of the wave vector:  $k = 0$  solid curves;  $|k|R_0 = \pi/2$  dashed curves;  $|k|R_0 = \pi$  curves made by a dotted line



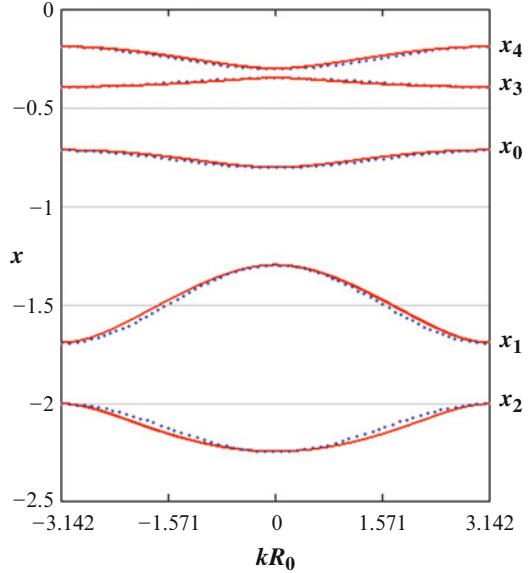
The numerical value  $227.45^\circ$  is originated from the structure  $\frac{(E_c - E_v)/k}{T}$  where the difference  $E_c - E_v$  for medium-oxygen model of the electronic subsystem is equal to 0.0196 eV [13], and Boltzmann constant  $k$  is equal to  $8.6173 \cdot 10^{-5}$  eV/K.

In analysing (13.9), it is not difficult to see that the factor  $v(T)$  has the same “behaviour” as the temperature. In other words, it increases or decreases along with the temperature. In this meaning, the dependencies shown in the Fig. 13.1 may be used for qualitative analysis of the temperature influence upon energy positions of states of conductivity. However, the analysis of direct quantitative dependencies of their positions on the temperature within physiologically acceptable range is definitely advisable from a practical point of view. For such dependency, formula (13.9) was used in an expression for the roots of Eq. (13.8), which were obtained in [11], for the most typical values  $\Gamma = 1$  and  $\gamma = 0.8$ . Herewith:

$$v(T) = 1 - 182^\circ/T, \tag{13.10}$$

and the dependencies of these roots with temperature is as follows

**Fig. 13.2** Dispersive dependencies of energies  $x_s(v, k)$  on the wave vector  $k$  (at  $v = 0.4$ ): *solid curves*, the exact solutions of the Eq. (13.8); *dashed lines*, solutions, constructed by a formula of [11] for  $x_s(v, k)$



$$x_s(T, k) = \begin{pmatrix} -1 + v(T)^2 + 3.15 v(T)^4 - 0.68v(T)^3 \cos(kR_0) \\ -3/2 + v(T) - 2.49v(T)^2 + 3.10v(T)^3 \cos(kR_0) \\ -3/2 - v(T) - 1.42v(T)^2 - 1.90v(T)^3 \cos(kR_0) \\ -1/2 + v(T)^2 - 1.23v(T)^4 + 0.35v(T)^3 \cos(kR_0) \\ -1/2 + v(T)^2 + 3.72v(T)^4 - 0.87v(T)^3 \cos(kR_0) \end{pmatrix} \quad (13.11)$$

These dependencies are shown in Fig. 13.3 for  $k=0$ . As it is seen in Fig. 13.3, all five states of conductivity depend on temperature differently. States  $x_0$  and  $x_1$  are almost independent of temperature, while the state  $x_2$  shows the strongest dependence.

Therefore, it is necessary to investigate the question of the properties of current: on the one side, under conditions of a nonzero temperature and, on the other side, under conditions of complete absence of external factors that violate electrostatic balance of the system. It is clear that under such conditions, the current should not occur at any temperature.

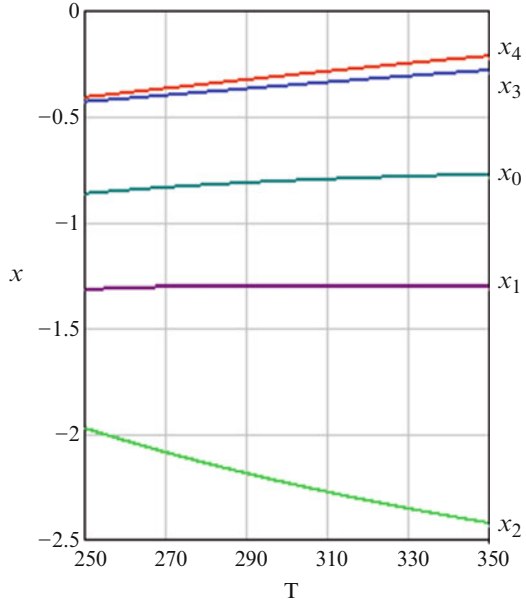
Due to the invariance of condition (13.8), it will not change the real (with dimension) eigenvalues in the form of energy:  $\varepsilon_s(T, k) = |D(T)| x_s(T, k)$ , as well as the total energy of protein nanowires, excited by injected electron:

$$E_s(T, k) = N_a w(T) + \varepsilon_s(T, k) \equiv N_a w(T) + |D(T)| x_s(T, k)$$

The energy  $E_s(T, k)$  can be extended to a complete predicted-estimated level by means of definitions (13.6) ÷ (13.7). In particular, such an extension is interesting from the point of view of the temperature influence upon the electronic subsystem



**Fig. 13.3** Dependencies of dimensionless energies  $x_s$  from temperature within physiologically acceptable range  $-23^\circ\text{C}$  to  $+77^\circ\text{C}$



and microcurrent of injected electron in complete absence of external fields. But to analyse the temperature influence upon studied conductance states, it is sufficient to analyse the difference:

$$E_s(T, k) - N_a w(T) = \varepsilon_s(T, k) = |D(T)| x_s(T, k),$$

as the temperature dependence  $w(T)$  is similar for all states, and specific temperature “behaviour” of conductance states is defined only by the factor:

$$\varepsilon_s(T, k) = |D(T)| x_s(T, k).$$

So now it is enough to consider only the factor  $|D(T)|$  in details, because this factor is general for all five states (13.11). The dependence  $|D(T)|$  is defined by the formula:

$$|D(T)| = |D_0| + \text{sign}(D_0) \text{sign}(D_1) |D_1| \frac{227.45^\circ}{T}, \quad (13.12)$$

where the parameters  $D_0$  and  $D_1$  satisfy the condition:  $|D_0| \gg |D_1|$ , and  $\text{sign}(x)$  is a sign function.

### 13.3.2 Current Absence in the Absence of External Fields at Any Temperature

The current is determined on the basis of the presentation for the injected electrons as free quasiparticles of classical type in the conduction band of primary structure of the protein molecules [14–16]. Thus, each of the eigenvalues  $E_s(T, k)$  takes the meaning of the classical Hamiltonian dependent on the wave momentum  $p = \hbar k$  [12, 16]. Therefore, a standard definition of velocity in spatially one-dimensional case for solids is used:

$$V_s(T, k) = \frac{1}{\hbar} \frac{d}{dk} [E_s(T, k)] = \frac{1}{\hbar} v(T)^3 |D(T)| R_0 \begin{pmatrix} 0.68 \\ -3.10 \\ 1.90 \\ -0.35 \\ 0.87 \end{pmatrix} \sin(kR_0),$$

where the dependencies  $v(T)$  and  $|D(T)|$  are determined in (13.10) and (13.12), respectively. Consequently to the definition of current density  $J = e nV$ , we will obtain the following:

$$J_s = \frac{ev(T)^3 |D(T)| R_0}{\hbar N_0 V_0} \begin{pmatrix} 0.68 \\ -3.10 \\ 1.90 \\ -0.35 \\ 0.87 \end{pmatrix} \sin(kR_0),$$

where it was taken into account that for one injecting electron, it must be:  $n \equiv 1/N_0 V_0$ . Here  $V_0$  is the effective average volume of amino acid residue, and  $N_0$ , as it was already noted, is the number of amino acid residues. As it is seen, each subband of conductivity (for each value  $s = 0, 1, 2, 3, 4$ ) has a strong enough temperature dependence, and this dependence is determined by the product:

$$v(T)^3 |D(T)| = \left(1 - \frac{182^\circ}{T}\right)^3 \left(|D_0| + \text{sign}(D_0) \text{sign}(D_1) |D_1| \frac{227.45^\circ}{T}\right).$$

But, as well as in [11], the total value of current density  $J = e nV$  for the whole conductance band, which is defined by the sum of the individual currents  $J_s$ , is equal to zero. This is due to the absence of temperature influence on the set of the following factors (0.68 –3.1 1.9 –0.35 0.87). The sum of these factors is equal to zero, and this set is determined by general symmetry of amino acid residues and interactions between atoms, which are formed by these residues.

So, if real external field and the effective field, conditioned by amino acid heterogeneity, does not influence on the polypeptide fragment of the protein

molecule, the current does not occur in this system. This result is more fundamental than that obtained in [11], as it proves that the proposed model provides an absence of current also at an arbitrary temperature in the complete absence of external fields (both real and effective).

## 13.4 Conclusions

The main aim of the study was the calculation of the current density in the complete absence of violations of electrostatic equilibrium (as in the previous study [11]). But, unlike [11], this calculation was performed for the temperature not equal to zero. It was shown that at  $T \neq 0$  and in the absence of any external electrostatic influence, the current does not occur in the system. That is, the temperature does not affect the current from an electron, injected during metabolism, if there are no external electrostatic factors for its occurrence, and just this must be from a physical point of view.

## References

1. Brizhik L, Eremko A, Piette B, Zakrzewski W (2006) Charge and energy transfer by solitons in low-dimensional nanosystems with helical structure. *Chem Phys* 324(1):259–266
2. Suprun AD, Shmeleva LV (2014) Alpha-helical regions of the protein molecule as organic nanotubes. *Nanoscale Res Lett* 9(1):200
3. Prylutskyi YI, Buchelnikov AS, Voronin DP, Kostjukov VV, Ritter U, Parkinson JA, Evstigneev MP (2013) C60 fullerene aggregation in aqueous solution. *Phys Chem Chem Phys* 15(23):9351–9360
4. Prylutska SV, Grynyuk II, Matyshevska OP, Prylutskyi YI, Ritter U, Scharff P (2008) Antioxidant properties of C60 fullerenes in vitro. *Fullerenes Nanotubes Carbon Nanostruct* 16(5–6):698–705
5. Prylutska SV, Matyshevska OP, Grynyuk II, Prylutskyi YI, Ritter U, Scharff P (2007) Biological effects of C60 fullerenes in vitro and in a model system. *Mol Cryst Liq Cryst* 468:265–274
6. Petrov EG, May V, Hänggi P (2002) Controlling electron transfer processes through short molecular wires. *Chem Phys* 281(2):211–224
7. Ievlev AV, Morozovska AN, Eliseev EA, Ya V, Shur SVK (2014) Ionic field effect and memristive phenomena in single-point ferroelectric domain switching. *Nat Commun* 5:4545
8. Morozovska AN, Eliseev EA, Ievlev AV, Varenyk OV, Pusenkova AS, Chu Y-H, Ya. shur V, Strikha MV, Kalinin SV (2014) Ferroelectric domain triggers the charge modulation in semiconductors. *J Appl Phys* 116:066817
9. Ievlev AV, Morozovska AN, Ya V, Shur SV (2015) Kalinin. Ferroelectric switching by the conductive scanning probe microscopy tip. *Phys Rev B* 91:214109
10. Suprun AD, Shmeleva LV (2015) Primary structure of proteins as a nanowire for metabolic electronic transport. *Nanoscale Res Lett* 10(1):121
11. Suprun AD, Shmeleva LV (2016) Current in the protein nanowires: quantum calculations of the base states. *Nanoscale Res Lett* 11(1):74

12. Suprun A, Shmeleva L (2014) The centrally-symmetric solutions of electronic excitations of semiconductors in the conditions of relativistic like degeneracy of dynamical properties. *Funct Mater* 21(1):69–79
13. Radcig AA, Smirnov BM (1980) *Spravochnik po Atomnoj i Molekularnoj Fizikie* (handbook of atomic and molecular physics), vol 240. Atomizdat, Moscow
14. Davydov AS (1979) *Biology and quantum mechanics*. Scientific thought, Kiev. (In Russian)
15. Ishizaki A, Calhoun TR, Schlau-Cohen GS, Fleming GR (2010) Quantum coherence and its interplay with protein environments in photosynthetic electronic energy transfer. *Phys Chem Chem Phys* 12:7319–7337
16. Suprun A, Shmeleva L (2012) Degeneracy effect of dynamical properties of quasi-particles of electronic origin in semiconductor materials. *Funct Mater* 19(4):508–519

# Chapter 14

## About Possible Mechanisms of Nanoconductivity in Polyenes Polymers: The Charge Solitons at Extremely Weak External Fields

S. V. Vasylyuk, A. D. Suprun, and V. N. Yashchuk

### 14.1 Introduction

Molecular compounds, that have alteration of simple and multiple bonds, are called linear conjugated systems, in such systems which will be considered in paper, can be presented by the following formula:  $[R_1 - (CH)_m - R_2]$ , where  $R_1$  and  $R_2$  are terminal groups, superimposed with polymethine chain. These systems are both electrically neutral and charged positively or negatively [1–2], depending on what is injected in them – electron or hole. Carbon atom of the methine group (CH) in the chain is in  $sp^2$ -hybridized state [1–2].

Linear conjugated systems are being widely investigated in their functions of single-photon and two-photon excited fluorescent probes, polarity indicators, materials for three-dimensional record of information, and other fields of organic chemistry and nonlinear optics [1–4].

We are able to explain such properties of a number of organic compounds as quasi-metallic conductivity and significant change of the spectral properties of ionic dyes [1–4], which adsorb and radiate light in the near IR spectral region in particular, due to the concept of solitons [5–7]. It has been established that injection of electrons/holes in the conduction band results in the appearance of the soliton level inside of the forbidden zone and is accompanied by noticeable shifts of the

---

S.V. Vasylyuk (✉) • V.N. Yashchuk  
Physics Faculty of Kyiv National Taras Shevchenko University, Volodymyrska, 64, Kiev, Ukraine  
e-mail: [bladewalker@ukr.net](mailto:bladewalker@ukr.net); [saddas.new@gmail.com](mailto:saddas.new@gmail.com)

A.D. Suprun  
Departments of Theoretical Physics, Faculty of Physics, Taras Shevchenko National University of Kyiv, Volodymyrska Street, 64/13, Kyiv, 01601, Ukraine

top of the valence zone and bottom of the conduction zone: in the case of electron injection, to the side of the energy attenuation and, in the case of the hole injection, to the side of its increase [8–13].

Construction of physical models, which describe charge transfer in one-dimensional condensed systems of the polymer type, was initiated in works of [6–17]. In particular, one of the models of such a type is a model of conductivity, based on the concept of the hopping [17–21] in donor-acceptor systems and zone theory [17–19] in the molecular crystals. However, other soliton models of conductivity also attract the scientists' attention: in these models the influence of the external actions on the solitons appears at autolocalization of excitations with regard to their dynamics in molecular one-dimensional chains [9–24].

In this paper the model of the charge transfer, based on the concept of solitons, which adds and develops other models [9–23], is considered. Similarly to [24], this paper considers (the “slowly changing coefficient” method) the slowing down of solitons under the action of the friction forces, which act from the side of the chain molecules. Appearance of charge in a chain results in the alteration of the lengths of neighboring CC-bonds by the value (as it is shown in investigations [7, 11–13]). According to A. S. Davydov [11–16], excitation, which consists of the electron (hole) and encircle deformation of the crystal lattice (or its analogue) and moves with a constant speed (if the external fields are absent), is accepted to call as electron (hole) soliton. Hereinafter the term charge soliton or soliton is used [9–27].

## 14.2 Description of the Geometry

To specify the model, polyene-like polymer chain with alteration of double and single carbon-carbon bonds, known as conjugate (bonded) pi-electron system, is considered (see Fig. 14.1). Abscise axis is directed along the chain, and ordinate axis is orthogonal to it. In such a case, the area of the chain and coordinate area ( $x, y$ ) coincide (see Fig. 14.1). Each of two carbon chains differs in the parameter (index)  $\alpha = \{0; 1\}$ . In such a case,  $x$  axe (abscise) is considered as it coincides with the lower chain and corresponds to the value  $\alpha = 0$ , and the upper chain is associated with the value  $\alpha = 1$  (see Fig. 14.1).

Triangles, shown in Fig. 14.1, are formed by three atoms of carbon. Here  $d$  is the length of the double bond and  $b$  is the length of the single bond. It is known [7, 25–27] that these values are approximately equal:  $d = 1,36\text{\AA}$ ,  $b = 1,44\text{\AA}$ , and  $d - b = 0,08\text{\AA}$ .

Such insignificant difference enables one to use further equilibrium model of the carbon-carbon chain, in which the lengths of bonds are considered as equal and are accepted equal to  $1,4\text{\AA}$  [27]. The accepted method of separation of the lattice cell is well seen in Fig. 14.1. Here three lattice cells are shown in detail:  $n - 1$ ,  $n$ , and

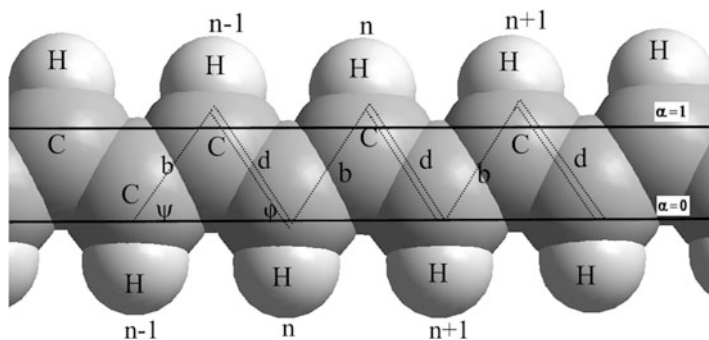


**Fig. 14.1** Illustration to description of the accepted model of the polyene chain

$n + 1$ . It is seen that each lattice cell contains a couple of carbon atoms or, to be more precise, a couple of CH-groups, which are referred to as single bond between carbon atoms. At such a choice of the coordinate system, radius vectors  $\mathbf{R}_{\alpha,n}$  for positions of CH-groups in each chains under conditions of equilibrium are determined by the formula

$$\mathbf{R}_{\alpha n} = \mathbf{e}_x (R_0 n + \alpha b \cos \psi) + \mathbf{e}_y \alpha d \sin \varphi; \quad \alpha = \{0; 1\}, \quad (14.1)$$

where

$$R_0 = d \cos \varphi + b \cos \psi; \quad (14.2)$$

As hereinafter the approximation of the nearest neighbors is used, it is necessary to define the following differences between the vectors:

$$\mathbf{R}_{1n} - \mathbf{R}_{0n} = \mathbf{e}_x b \cos \psi + \mathbf{e}_y d \sin \varphi; \quad (14.3)$$

$$\mathbf{R}_{0,n+1} - \mathbf{R}_{1n} = \mathbf{e}_x (R_0 - b \cos \psi) - \mathbf{e}_y d \sin \varphi; \quad (14.4)$$

$$\mathbf{R}_{1,n+1} - \mathbf{R}_{0n} = \mathbf{e}_x (R_0 + b \cos \psi) + \mathbf{e}_y d \sin \varphi; \quad (14.5)$$

$$\mathbf{R}_{0,n+1} - \mathbf{R}_{0n} = R_0 \mathbf{e}_x; \quad (14.6)$$

$$\mathbf{R}_{1,n+1} - \mathbf{R}_{1,n} = R_0 \mathbf{e}_x. \quad (14.7)$$

### 14.3 Work Statement

To describe the dynamics of the electron, which is injected into polyene chain, the Hamiltonian is used [28, p. 52], which, with regard to peculiarities of this object, has a form

$$\begin{aligned}
 E(\{a\}) = E_c + W^{(0)} + \frac{1}{2} \sum_{\alpha n} \sum_{\beta m} w_{\alpha n, \beta m} \\
 (\alpha n \neq \beta m) \\
 + \frac{1}{2} \sum_{\alpha n} (D_{\alpha n} + W_{\alpha n}^{(1)}) |a_{\alpha n}|^2 + \sum_{\alpha n} \sum_{\beta m} M_{\alpha n, \beta m} a_{\alpha n}^* a_{\beta m}. \\
 (\alpha n \neq \beta m)
 \end{aligned} \tag{14.8}$$

It is typical for condensates of the crystalline type with the semiconductor or dielectric zone structure. The first summand  $E_c$  in (14.8) corresponds to the electron energy of  $N$  isolated molecular groups (in the case of polyenes, it will be CH-groups), to which the energy of the injected electron, that interacts only with the electrons of such isolated molecular group, is added.  $W^{(0)}$  is the energy of interaction of the external field with the electrons of the valence zone. The energy  $w_{\alpha n, \beta m}$  in (14.8) plays the main role in the incorporation of the isolated molecular groups into the united bonded system and determines interaction between them under conditions of the absence of excitation. Energy  $D_{\alpha n}$  in the Hamiltonian (14.8) by its physical sense reflects the change in the interaction of the excited molecular group with non-excited surrounding in comparison with the similar interaction, when all molecular groups are not excited. The summand  $W_{\alpha n}^{(1)}$  represents the influence of the external field on the injected electron. Value  $a_{\alpha n}$  is, in fact, the wave function of the variables  $\alpha, n$ , which determines the distribution in the molecular chain of the electron, injected in the conduction zone, and  $|a_{\alpha n}|^2$  is usually interpreted as the probability of the localization of the electron on the knot with the number  $\alpha n$ . At last, the energy  $M_{\alpha n, \beta m}$ , which is included into the Hamiltonian (14.8), is called as the energy of the resonance exchange interaction. By its physical sense, it determines not so much additional interaction among molecular groups, as the dynamics of the considered charge excitation in the polyene chain.

Hereinafter only varying part of the Hamiltonian (14.8) is considered:

$$\Delta E(\{a\}) \equiv E(\{a\}) - E_c - W^{(0)}.$$



Under approximation of the nearest neighbors, determined in (14.3)–(14.7), it takes the form of

$$\begin{aligned}
 \Delta E(\{a\}) = & \frac{1}{2} \sum_n \left\{ w(\mathbf{R}_{1n} - \mathbf{R}_{0n}) + w(\mathbf{R}_{0,n+1} - \mathbf{R}_{1n}) + \left[ W_{0n}^{(1)} + D(\mathbf{R}_{1n} - \mathbf{R}_{0n}) \right] |a_{0n}|^2 \right. \\
 & + \left[ W_{1n}^{(1)} + D(\mathbf{R}_{0,n+1} - \mathbf{R}_{1n}) \right] |a_{1n}|^2 \\
 & + M(\mathbf{R}_{1,n+1} - \mathbf{R}_{0n}) (a_{0n}^* a_{1,n+1} + a_{1,n+1}^* a_{0n}) \\
 & + M(\mathbf{R}_{0,n+1} - \mathbf{R}_{0n}) (a_{0n}^* a_{0,n+1} + a_{0,n+1}^* a_{0n}) \\
 & + M(\mathbf{R}_{1,n+1} - \mathbf{R}_{1n}) (a_{1n}^* a_{1,n+1} + a_{1,n+1}^* a_{1n}) \\
 & + M(\mathbf{R}_{1n} - \mathbf{R}_{0n}) (a_{0n}^* a_{1n} + a_{1n}^* a_{0n}) \\
 & \left. + M(\mathbf{R}_{0,n+1} - \mathbf{R}_{1n}) (a_{1n}^* a_{0,n+1} + a_{0,n+1}^* a_{1n}) \right\}. \quad (14.9)
 \end{aligned}$$

In this Hamiltonian, designations of the dependence of energies on vectors means the compact records of their dependence on the components of these vectors. Proceeding from the designations (14.1)–(14.7), it is rather obvious that everything reduces itself to the dependence of energies on values  $d, b, \varphi, \psi$ . It is seen from Fig. 14.1 that angles  $\psi$  and  $\varphi$  are not independent, but are connected by sinus theorem. In this sense all energies in the last Hamiltonian in the most general case depend on three parameters only,  $d, b, \varphi$ , and taking into account that  $d \approx b$  in fact on two:  $b$  and  $\varphi$ . However, hereinafter for preservation of some generality (at least in zero approximation), we, after all, will take into account values  $d$  and  $b$  as different ones, using their approximate equality only in the cases when their relation is comparable with one, or their difference is comparable with themselves.

Now we must take into account that at the appearance of the injected electron in the chain, its equilibrium state, which is caused by the requirement of the energy minimality  $\frac{1}{2} \sum_{\alpha n} \sum_{\beta m} w(\mathbf{R}_{\alpha n} - \mathbf{R}_{\beta m})$  ( $\alpha n \neq \beta m$ ) by the components of the subtractive vectors  $\mathbf{R}_{\alpha n} - \mathbf{R}_{\beta m}$ , is violated. Hence, now we must perform repeated minimization of energy, already taking into account the existence of the injected electron, which violates the equilibrium of the system. To do that, in the approximation of the nearest neighbors, it is possible to consider the parameters  $d, b, \varphi$  as distributed by the space of the polyene change. Then Hamiltonian (14.9) takes the form

$$\begin{aligned}
\Delta E(\{d\}, \{b\}, \{\varphi\}, \{a\}) = & \frac{1}{2} \sum_n \left\{ w(b_n, \varphi_n) + w(d_n, \varphi_n) \right. \\
& + \left[ W_{0n}^{(1)} + D(b_n, \varphi_n) \right] |a_{0n}|^2 + \left[ W_{1n}^{(1)} + D(d_n, \varphi_n) \right] |a_{1n}|^2 \\
& + M_{01}^{\text{in}} (a_{0n}^* a_{1,n} + a_{1,n}^* a_{0n}) + M_{10}^{\text{out}} (a_{1n}^* a_{0,n+1} + a_{0,n+1}^* a_{1n}) \\
& + M_{01}^{\text{out}} (a_{0n}^* a_{1,n+1} + a_{1,n+1}^* a_{0n}) + M_0 (a_{0n}^* a_{0,n+1} + a_{0,n+1}^* a_{0n}) \\
& \left. + M_1 (a_{1n}^* a_{1,n+1} + a_{1,n+1}^* a_{1n}) \right\}. \tag{14.10}
\end{aligned}$$

It is taken into account in this presentation that the input of the energy of the resonant exchange interaction  $M(\mathbf{R}_{\alpha n} - \mathbf{R}_{\beta m})$  into the response of the “crystal lattice” of the considered chain on the electron injection is small enough with regard to energies  $w(\mathbf{R}_{\alpha n} - \mathbf{R}_{\beta m})$  and  $D(\mathbf{R}_{\alpha n} - \mathbf{R}_{\beta m})$ , so we can neglect by them. As a result, the last presentation contains matrix elements  $M(\mathbf{R}_{\alpha n} - \mathbf{R}_{\beta m})$  in the form of constants. The explicit form of designations for these constants can be easily obtained from the comparison of (14.9) and (14.10).

For final definition of the Hamiltonian (14.10), it is necessary to specify energies  $W_{0n}^{(1)}$  and  $W_{1n}^{(1)}$ , which are connected with the influence of the external field on the injected electron. Proceeding from the general definition for them [28, p. 51] and also introducing more compact designations for them, it is possible to obtain

$$W_{0n}^{(1)} = -2e(\mathbf{F} \cdot \mathbf{R}_{0n}) \equiv W_n^{(I)}; \quad W_{1n}^{(1)} = -2e(\mathbf{F} \cdot \mathbf{R}_{1n}) \equiv W_n^{(II)}$$

Here  $F$  is the vector of the strength of the external electrical field, and values  $W_n^{(I)}$  and  $W_n^{(II)}$ , taking into account (14.1) and (14.2), have the following explicit form:

$$W_n^{(I)}(d_n, b_n, \varphi_n) = -nW(d_n, b_n, \varphi_n); \tag{14.11}$$

$$W_n^{(II)}(d_n, b_n, \varphi_n) = -nW(d_n, b_n, \varphi_n) - W_x(d_n, \varphi_n) - W_y(d_n, \varphi_n). \tag{14.12}$$

Here  $W(d_n, b_n, \varphi_n) \equiv W_x(d_n, b_n, \varphi_n) + 2eF_x b_n \cos \psi_n$ ;  $W_x(d_n, b_n, \varphi_n) \equiv 2eF_x d_n \cos \varphi_n$ ;  $W_y(d_n, b_n, \varphi_n) \equiv 2eF_y d_n \sin \varphi_n$ . Therefore, finally the Hamiltonian (14.10) takes the form (14.15) with the approximation (14.13) and Taylor minimization series

$$W(d_n, b_n, \varphi_n) \equiv W_x(d_n, b_n, \varphi_n) + 2eF_x b_n \cos \psi_n \tag{14.13}$$

Further this Hamiltonian should be minimized, first of all, by the set of variables  $\{d\}, \{b\}, \{\varphi\}$  that will be done in the following section.

Taking into account conditions (14.28), (14.29), and (14.30), Equations (14.26) and (14.27) (with zero approximation in relation to the ratio of energy minimization {Taylor series formula is too long to show it in this work}), are transformed into nonlinear Hamiltonian.

To perform the energy minimization (14.13) by the set of variables  $\{d\}, \{b\}, \{\varphi\}$ , first of all represent them in the following form:

$$d_n = d + \xi_n; \quad b_n = b + \eta_n; \quad \varphi_n = \varphi + \chi_n. \quad (14.14)$$

Such representation always admits that changes of the "lattice constants"  $\xi_n$ ,  $\eta_n$ , and angular "lattice constants"  $\chi_n$  are considerably less than the corresponding equilibrium values  $d, b, \varphi$ . Substitution of (14.14) in (14.13) and (14.13) in (14.10) reduces this Hamiltonian to the form

$$\begin{aligned} \Delta E(\{\xi\}, \{\eta\}, \{\chi\}, \{a\}) = & \frac{1}{2} \sum_n \left\{ w(b + \eta_n, \varphi + \chi_n) + w(d + \xi_n, \varphi + \chi_n) \right. \\ & + \left[ W_{||n}^{(I)}(d + \xi_n, b + \eta_n, \varphi + \chi_n) + D(b + \eta_n, \varphi + \chi_n) \right] |a_{0n}|^2 \\ & + \left[ W_{||n}^{(II)}(d + \xi_n, b + \eta_n, \varphi + \chi_n) + D(d + \xi_n, \varphi + \chi_n) \right] |a_{1n}|^2 \\ & + M_{01}^{in}(a_{0n}^* a_{1n} + a_{1n}^* a_{0n}) + M_{10}^{out}(a_{1n}^* a_{0,n+1} + a_{0,n+1}^* a_{1n}) \\ & + M_{01}^{out}(a_{0n}^* a_{1,n+1} + a_{1,n+1}^* a_{0n}) + M_0(a_{0n}^* a_{0,n+1} + a_{0,n+1}^* a_{0n}) \\ & \left. + M_1(a_{1n}^* a_{1,n+1} + a_{1,n+1}^* a_{1n}) \right\}. \end{aligned} \quad (14.15)$$

Now, taking into consideration the smallness of shifts  $\xi_n$ ,  $\eta_n$ , and  $\chi_n$ , let us expand all energies, which contain them, into the Taylor series. In such a case, all inputs not higher than linear or squared, if the linear is absent, are preserved (which takes place in the energy  $w$ ).

Performing after that the operation of minimization according to conditions  $\frac{\partial}{\partial \xi_n}(\Delta E) = 0$ ;  $\frac{\partial}{\partial \eta_n}(\Delta E) = 0$ ;  $\frac{\partial}{\partial \chi_n}(\Delta E) = 0$  (14.16), we obtain the set of three connected linear equations for determination of values  $\xi_n$ ,  $\eta_n$  i  $\chi_n$  and, after solving it, obtain (14.16), where

$$\begin{aligned} \xi_n = & \lambda_n^{(I)} |a_{0n}|^2 + \mu_n^{(II)} |a_{1n}|^2; & \eta_n = & \mu_n^{(I)} |a_{0n}|^2 + \lambda_n^{(II)} |a_{1n}|^2; \\ \chi_n = & -\gamma \left[ \left( \mu_n^{(I)} - \nu_n^{(I)} \right) |a_{0n}|^2 + \left( \mu_n^{(II)} - \nu_n^{(II)} \right) |a_{1n}|^2 \right], \end{aligned} \quad (14.16)$$

$$\begin{aligned}
\lambda_{\parallel n}^{(I,II)} &= g_{\parallel n}^{(I,II)} + f \dot{W}_{\parallel n}^{(I,II)}; & \mu_{\parallel n}^{(I,II)} &= q_{\parallel n}^{(I,II)} + h \dot{W}_{\parallel n}^{(I,II)}; \\
v_{\parallel n}^{(I,II)} &= \frac{\dot{W}_{\parallel n}^{(I,II)}}{\dot{w}_{\parallel}}; & \gamma &= \frac{\ddot{w}_{\parallel}}{\ddot{w}_{\diamond}}; \\
g_{\parallel n}^{(I,II)} &= -\frac{\dot{D}_{\parallel n}^{(I,II)}}{2\ddot{w}_{\parallel}} + \frac{\ddot{w}_{\diamond} \dot{D}_{\perp n}^{(I,II)} - \ddot{w}_{\perp} \dot{D}_{\parallel n}^{(I,II)}}{2(\ddot{w}_{\parallel} \ddot{w}_{\perp} - \ddot{w}_{\diamond}^2)}; & q_{\parallel n}^{(I,II)} &= \frac{\ddot{w}_{\diamond} (\ddot{w}_{\parallel} \dot{D}_{\perp n}^{(I,II)} - \ddot{w}_{\diamond} \dot{D}_{\parallel n}^{(I,II)})}{2\ddot{w}_{\parallel} (\ddot{w}_{\parallel} \ddot{w}_{\perp} - \ddot{w}_{\diamond}^2)}; .
\end{aligned} \tag{14.17}$$

The simplifying designation is also used:

$$h = \frac{2\ddot{w}_{\perp} \ddot{w}_{\parallel} - \ddot{w}_{\diamond}^2}{2\ddot{w}_{\parallel} (\ddot{w}_{\parallel} \ddot{w}_{\perp} - \ddot{w}_{\diamond}^2)}; \quad f = \frac{\ddot{w}_{\diamond}^2}{2\ddot{w}_{\parallel} (\ddot{w}_{\parallel} \ddot{w}_{\perp} - \ddot{w}_{\diamond}^2)}. \tag{14.18}$$

Substituting values (14.16) into the Hamiltonian, which can be obtained from (14.15) by expansion of its matrix elements in the Taylor series (it is not presented here because of its bulkiness), after not complex, but rather awkward transformations, it is possible to formulate nonlinear Hamiltonian with regard to plurality of complex conjugate pairs of variables  $\{a\}$ :

$$\begin{aligned}
\Delta E(\{a\}) &= \frac{1}{2} \sum_n \left\{ M_0 (a_{0n}^* a_{0,n+1} + a_{0,n+1}^* a_{0n}) + M_1 (a_{1n}^* a_{1,n+1} + a_{1,n+1}^* a_{1n}) \right. \\
&\quad + M_{01}^{\text{in}} (a_{0n}^* a_{1n} + a_{1n}^* a_{0n}) + M_{10}^{\text{out}} (a_{1n}^* a_{0,n+1} + a_{0,n+1}^* a_{1n}) \\
&\quad + M_{01}^{\text{out}} (a_{0n}^* a_{1,n+1} + a_{1,n+1}^* a_{0n}) - G_{00}^{(n)} |a_{0n}|^4 - G_{11}^{(n)} |a_{1n}|^4 \\
&\quad \left. - G_{10}^{(n)} |a_{0n}|^2 \cdot |a_{1n}|^2 - W \cdot n (|a_{0n}|^2 + |a_{1n}|^2) - (W_x + W_y) |a_{1n}|^2 \right\},
\end{aligned} \tag{14.19}$$

where

$$\begin{aligned}
G_{00}^{(n)} &= \frac{1}{2} \ddot{w}_{\parallel} (\lambda_n^{(I)2} + \mu_n^{(I)2}) - \ddot{w}_{\diamond} (v_n^{(I)} \lambda_n^{(I)} + v_n^{(I)} \mu_n^{(I)}) + \frac{1}{2} \ddot{w}_{\perp} v_n^{(I)2} + \dot{D}_{\parallel} \lambda_n^{(I)} \\
&\quad - \dot{D}_{\perp} v_n^{(I)} + \dot{W}_{\parallel n}^{(I)} (\lambda_n^{(I)} + \mu_n^{(I)}) - \dot{W}_{\perp n}^{(I)} v_n^{(I)};
\end{aligned} \tag{14.20}$$

$$\begin{aligned}
G_{11}^{(n)} &= \frac{1}{2} \ddot{w}_{\parallel} (\lambda_n^{(II)2} + \mu_n^{(II)2}) - \ddot{w}_{\diamond} (v_n^{(II)} \lambda_n^{(II)} + v_n^{(II)} \mu_n^{(II)}) + \frac{1}{2} \ddot{w}_{\perp} v_n^{(II)2} + \dot{D}_{\parallel} \lambda_n^{(II)} \\
&\quad - \dot{D}_{\perp} v_n^{(II)} + \dot{W}_{\parallel n}^{(II)} (\lambda_n^{(II)} + \mu_n^{(II)}) - \dot{W}_{\perp n}^{(II)} v_n^{(II)};
\end{aligned} \tag{14.21}$$

$$\begin{aligned}
G_{01}^{(n)} &= \ddot{w}_{\parallel} (\lambda_n^{(I)} \mu_n^{(II)} + \mu_n^{(I)} \lambda_n^{(II)}) - \ddot{w}_{\diamond} (v_n^{(I)} \lambda_n^{(II)} + v_n^{(II)} \mu_n^{(I)}) - \ddot{w}_{\diamond} (v_n^{(II)} \mu_n^{(I)} + v_n^{(I)} \mu_n^{(II)}) \\
&\quad + \ddot{w}_{\perp} v_n^{(I)} v_n^{(II)} + \dot{D}_{\parallel} (\mu_n^{(I)} + \mu_n^{(II)}) - \dot{D}_{\perp} (v_n^{(I)} + v_n^{(II)}) + \dot{W}_{\parallel n}^{(I)} (\lambda_n^{(II)} + \mu_n^{(II)}) \\
&\quad - \dot{W}_{\perp n}^{(II)} v_n^{(I)} + \dot{W}_{\parallel n}^{(II)} (\lambda_n^{(I)} + \mu_n^{(I)}) - \dot{W}_{\perp n}^{(I)} v_n^{(II)},
\end{aligned} \tag{14.22}$$

and also definitions (14.11) and (14.12) for the external electric field are taken into account.

Proceeding from the definitions (14.17) and (14.18), one can easily reassure himself that under the absence of the external field ( $F=0$ ), the symmetry is realized at which nonlinearity parameters  $G_{00}^{(n)}$  and  $G_{11}^{(n)}$ , first, lose dependence on  $n$  variable and, secondly, coincide. Hence, the equality  $G_{00} = G_{11}$  is fulfilled. It will be important at consideration of the base properties of the states under investigation.

## 14.4 Work System of Equations and Analysis of Its Solution

The Hamiltonian (14.19) can be considered as a form, which by its structure reminds the classical Hamiltonian form for an arbitrary system of the harmonic oscillators, formulated in the “normal coordinates”  $a_{\alpha n}$  and “normal impulses”  $i\hbar a_{\alpha n}^*$ . It can be done as they satisfy classical Poisson brackets just as it may do canonically conjugated pair of variables [29, pp. 201–202]. Hence, it is possible to write Hamilton equation:  $i\hbar \frac{\partial a_{\alpha n}}{\partial t} = \frac{\partial \Delta E(\{a\})}{\partial a_{\alpha n}^*}$ ;  $i\hbar \frac{\partial a_{1n}}{\partial t} = \frac{\partial \Delta E(\{a\})}{\partial a_{1n}^*}$  substituting which in (14.19) we obtain the system

$$i\hbar \frac{\partial a_{\alpha n}}{\partial t} = \frac{1}{2} M_{\alpha} (a_{\alpha, n+1} + a_{\alpha, n-1}) + \frac{1}{2} \left( M_{01}^{in} a_{\beta n} + M_{\alpha\beta}^{out} a_{\beta, n+1} + M_{\beta\alpha}^{out} a_{\beta, n-1} \right) - 2G_{\alpha\alpha}^{(n)} |a_{\alpha n}|^2 a_{\alpha n} - G_{\alpha\beta}^{(n)} |a_{\beta n}|^2 a_{\alpha n} - nW a_{\alpha n} - \delta_{1\alpha} (W_x + W_y) a_{\alpha n};$$

$$\{\alpha, \beta\} = \{0; 1\}; \quad \alpha \neq \beta.$$

$$i\hbar \frac{\partial a_{\alpha n}}{\partial t} = \frac{1}{2} M_{\alpha} (a_{\alpha, n+1} + a_{\alpha, n-1}) + \frac{1}{2} \left( M_{01}^{in} a_{\beta n} + M_{\alpha\beta}^{out} a_{\beta, n+1} + M_{\beta\alpha}^{out} a_{\beta, n-1} \right) - 2G_{\alpha\alpha}^{(n)} |a_{\alpha n}|^2 a_{\alpha n} - G_{\alpha\beta}^{(n)} |a_{\beta n}|^2 a_{\alpha n} - nW a_{\alpha n} - \delta_{1\alpha} (W_x + W_y) a_{\alpha n};$$

$$\{\alpha, \beta\} = \{0; 1\}; \quad \alpha \neq \beta.$$

(14.23)

It is taken into account in this system that for  $G$ -factors, the symmetry relationship  $G_{01}^{(n)} \equiv G_{10}^{(n)}$  is fulfilled. We shall search solution of the system (14.23) in the form

$$a_{\alpha n}(t) = A_{\alpha n}(t) \exp [i(p(t)n - \gamma(t))], \quad (14.24)$$

where  $A_{\alpha n}(t)$  is a real function. Then Eq. (14.23), after substitution of (14.24) in it, division of real and imaginary parts, and introduction of designations,

$$\begin{aligned}
v_\alpha &\equiv \frac{|M_\alpha|}{\hbar}; & v_{\alpha\beta}^{out} &\equiv \frac{|M_{\alpha\beta}^{out}|}{\hbar}; & v_{\beta\alpha}^{out} &\equiv \frac{|M_{\beta\alpha}^{out}|}{\hbar}; & v_{01}^{in} &\equiv \frac{|M_{01}^{in}|}{\hbar}; & \tau_\alpha &\equiv \frac{1}{v_\alpha}; \\
\Pi_\alpha &\equiv \frac{W}{|M_\alpha|}; & \Pi_x &\equiv \frac{W_x}{|M_\alpha|}; & \Pi_y &\equiv \frac{W_y}{|M_\alpha|}; & g_{\alpha\alpha}^{(n)} &\equiv \frac{G_{\alpha\alpha}^{(n)}}{|M_\alpha|}; & g_{\alpha\beta}^{(n)} &\equiv \frac{G_{\alpha\beta}^{(n)}}{|M_\alpha|},
\end{aligned}
\tag{14.25}$$

and also using a continual (long-wavelength) approximation  $A_{\gamma n}(t) \Rightarrow A_\gamma(t, x)$ ,  $A_{\gamma, n\pm 1}(t) \Rightarrow A_\gamma(t, x \pm 1) = A_\gamma(t, x) \pm \frac{\partial A_\gamma(t, x)}{\partial x} + \frac{1}{2} \frac{\partial^2 A_\gamma(t, x)}{\partial x^2}$  reduces itself to the system:

$$\frac{\partial A_\alpha}{\partial t} + v_\alpha \sin(p) \frac{\partial A_\alpha}{\partial x} + \frac{1}{2} (v_{\alpha\beta}^{out} + v_{\beta\alpha}^{out}) \sin(p) \frac{\partial A_\beta}{\partial x} + \frac{1}{2} (v_{\alpha\beta}^{out} - v_{\beta\alpha}^{out}) \sin(p) A_\beta = 0
\tag{14.26}$$

$$\begin{aligned}
&\frac{1}{2} \cos(p) \frac{\partial^2 A_\alpha}{\partial x^2} + 2g_{\alpha\alpha}(x) A_\alpha^3 + \left[ \tau_\alpha \dot{\gamma} + \cos(p) + x (\Pi_\alpha - \tau_\alpha \dot{p}) + \delta_{1\alpha} (\Pi_x^\alpha + \Pi_y^\alpha) \right] A_\alpha \\
&+ \frac{1}{4} \tau_\alpha (v_{\alpha\beta}^{out} + v_{\beta\alpha}^{out}) \cos(p) \frac{\partial^2 A_\beta}{\partial x^2} + \frac{1}{2} \tau_\alpha (v_{\alpha\beta}^{out} - v_{\beta\alpha}^{out}) \cos(p) \frac{\partial A_\beta}{\partial x} \\
&+ \frac{1}{2} \tau_\alpha \left[ v_{01}^{in} + (v_{\alpha\beta}^{out} + v_{\beta\alpha}^{out}) \cos(p) \right] A_\beta + g_{\alpha\beta}(x) A_\beta^2 A_\alpha = 0.
\end{aligned}
\tag{14.27}$$

Here is designated  $\dot{p} \equiv \frac{dp}{dt}$  and  $\dot{\gamma} \equiv \frac{d\gamma}{dt}$ . Herewith the first equation has dimensionality of frequency, and the second one is dimensionless. Hereinafter we shall consider a problem in zero approximation with regard to the ratio  $\frac{v_{\alpha\beta}^{out} - v_{\beta\alpha}^{out}}{v_{\alpha\beta}^{out} + v_{\beta\alpha}^{out}}$ . It is seen from Eqs. (14.26) and (14.27) that this ratio can play the role of a small parameter, as for  $\pi$ -bonds, which are typical for polyenes, the level of this ratio is estimated as the value  $0.2 \pm 0.05$ . Restriction by zero approximation here is aimed at finding of the solution of the system (14.26) and (14.27) in the analytical form for its further use for improvement of solutions concerning polyenes. In such zero approximation  $(v_{\alpha\beta}^{out} = v_{\beta\alpha}^{out})$ , the following designations may be introduced:

$$v_{\alpha\beta}^{out} = v_{\beta\alpha}^{out} = v_\perp.
\tag{14.28}$$

As follows from designations for the matrix elements and frequencies, presented in (14.25), zero approximation (14.28) means the equity of the processes of the resonance exchange between lattice cells with the numbers  $n$  and  $n+1$  with simultaneous change of the chain numbers. In this sense condition (14.28) is reasonably rigid. Besides that, the condition of the equality of the  $v_\alpha$  frequencies shall be used:

$$v_0 = v_1 = v_\parallel.
\tag{14.29}$$

Equality (14.29), by contrast with (14.28), is fulfilled practically precisely, because frequency factors  $v_\alpha$  are connected with description of the processes of the resonance exchange along each of two chains, which are physically equivalent in polyenes. Let us also designate for the uniformity:

$$v_{01}^{in} = v_\perp^{in}. \quad (14.30)$$

Taking into account conditions (14.28), (14.29), and (14.30), Eqs. (14.26) and (14.27) in zero approximation in relation to the ratio  $\frac{v_{\alpha\beta}^{out} - v_{\beta\alpha}^{out}}{v_{\alpha\beta}^{out} + v_{\beta\alpha}^{out}}$  take the form of

$$\frac{\partial A_\alpha}{\partial t} + \sin(p) \left[ v_\parallel \frac{\partial A_\alpha}{\partial x} + v_\perp \frac{\partial A_\beta}{\partial x} \right] = 0 \quad (14.31)$$

$$\begin{aligned} & \frac{1}{2} \cos(p) \left[ \frac{\partial^2 A_\alpha}{\partial x^2} + \tau_\parallel v_\perp \frac{\partial^2 A_\beta}{\partial x^2} \right] + \left( 2g_{\alpha\alpha}(x)A_\alpha^2 + g_{\alpha\beta}(x)A_\beta^2 \right) A_\alpha \\ & + \left[ \tau_\parallel \overset{\circ}{\gamma} + \cos(p) + x \left( \Pi - \tau_\parallel \overset{\circ}{p} \right) + \delta_{1\alpha} \left( \Pi_x + \Pi_y \right) \right] A_\alpha \\ & + \tau_\parallel \left[ \frac{1}{2} v_\perp^{in} + v_\perp \cos(p) \right] A_\beta = 0. \\ & \frac{1}{2} \cos(p) \left[ \frac{\partial^2 A_\alpha}{\partial x^2} + \tau_\parallel v_\perp \frac{\partial^2 A_\beta}{\partial x^2} \right] + \left( 2g_{\alpha\alpha}(x)A_\alpha^2 + g_{\alpha\beta}(x)A_\beta^2 \right) A_\alpha \\ & + \left[ \tau_\parallel \overset{\circ}{\gamma} + \cos(p) + x \left( \Pi - \tau_\parallel \overset{\circ}{p} \right) + \delta_{1\alpha} \left( \Pi_x + \Pi_y \right) \right] A_\alpha \\ & + \tau_\parallel \left[ \frac{1}{2} v_\perp^{in} + v_\perp \cos(p) \right] A_\beta = 0. \end{aligned} \quad (14.32)$$

Due to condition (14.29) (more precisely, equality of matrix elements  $M_\alpha$ ,  $\alpha = \{0; 1\}$ ), the fields  $\Pi_x$ ,  $\Pi_y$ ,  $\Pi$  also loss indexes  $\alpha$ . With regard to the designation  $\tau_\alpha \equiv \frac{1}{v_\alpha}$ , presented in (14.25), and designation (14.29), designation

$$\tau_\parallel \equiv \frac{1}{v_\parallel} \quad (14.33)$$

is obvious as well. It is seen now that using the parameter  $\tau_\parallel$ , which has dimension of time, it is possible to reduce the last system to the completely dimensionless form, multiplying Eq. (14.31) by  $\tau_\parallel$ , introducing dimensionless time  $\tau \equiv \frac{t}{\tau_\parallel}$ , and taking into account (14.33) in the form  $\tau_\parallel v_\parallel = 1$ . At such transformation designations  $\overset{\circ}{p}$  and  $\overset{\circ}{\gamma}$  should be already understood as  $\frac{dp}{d\tau}$  and  $\frac{d\gamma}{d\tau}$ , respectively, and systems (14.31) and (14.32) take the form

$$\frac{\partial A_i}{\partial \tau} + \beta(p) \frac{\partial A_i}{\partial x} + \tau_{\parallel} v_{\perp} \beta(p) \frac{\partial A_j}{\partial x} = 0; \quad (14.34)$$

$$\begin{aligned} & \frac{1}{2} \cos(p) \left[ \frac{\partial^2 A_{\alpha}}{\partial x^2} + \tau_{\parallel} v_{\perp} \frac{\partial^2 A_{\beta}}{\partial x^2} \right] + \left( 2g_{\alpha\alpha}(x) A_{\alpha}^2 + g_{\alpha\beta}(x) A_{\beta}^2 \right) A_{\alpha} \\ & + \left[ \tau_{\parallel} \overset{\circ}{\gamma} + \cos(p) + x \left( \Pi - \tau_{\parallel} \overset{\circ}{p} \right) + \delta_{1\alpha} (\Pi_x + \Pi_y) \right] A_{\alpha} \\ & + \tau_{\parallel} \left[ \frac{1}{2} v_{\perp}^{in} + v_{\perp} \cos(p) \right] A_{\beta} = 0. \quad (i \neq j); \quad \{i, j\} = \{0; 1\}. \end{aligned} \quad (14.35)$$

In this system, in comparison with (14.31) and (14.32), the following changes took place. Firstly, Greek indexes are changed by Latin ones, as now the danger to mix up index  $i$  with the imaginary unit is absent, and, secondly, Greek letters are used for designations of dimensionless velocity:

$$\beta(p) \equiv \sin(p), \quad (14.36)$$

and dimensionless dynamic mass:

$$\mu(p) \equiv \frac{1}{\cos(p)}. \quad (14.37)$$

The following condition is also accepted:

$$v_{\perp} = v_{\perp}^{in}, \quad (14.38)$$

nonuse of which results in excess of precision in regard to condition (14.28), which determines the zero approximation, accepted here.

## 14.5 Solution and Its Analysis

Analysis of the systems (14.34) and (14.35) should be started from the subsystem (14.34), which has such an explicit form:

$$\begin{aligned} & \frac{\partial A_0}{\partial \tau} + \beta \frac{\partial A_0}{\partial x} + \tau_{\parallel} v_{\perp} \beta \frac{\partial A_1}{\partial x} = 0; \\ & \frac{\partial A_1}{\partial \tau} + \beta \frac{\partial A_1}{\partial x} + \tau_{\parallel} v_{\perp} \beta \frac{\partial A_0}{\partial x} = 0. \end{aligned} \quad (14.39)$$

The general solution of this system is two linear arbitrary functions of the variable:  $\xi = x - x_c(\tau)$ , where  $x_c(\tau)$  is the point of localization of this excitement, dynamics of which is subjected to determination. In other words,



$$A_i(\tau, x) \equiv A_i(x - x_c(\tau)) \equiv A_i(\xi); \quad i = \{0; 1\}. \quad (14.40)$$

Substitution of  $A_i(\xi)$  into the system (14.39) and the requirement of the compatibility of obtained equations result to obtaining of two values of the derivative  $\overset{\circ}{x}_c$ :

$$\overset{\circ}{x}_c^{\pm} = (1 \pm \tau_{\parallel} v_{\perp}) \beta(p). \quad (14.41)$$

Accordingly, we have two variables:

$$\xi_{\pm} = x - x_c^{\pm}(\tau). \quad (14.42)$$

Using of the eigenvalues of (14.41) in the system, which can be obtained from (14.39) by substitution of (14.40), with simultaneous change of variable  $\xi$  on the corresponding variable from (14.42) leads to both equations of this system for each of branches “ $\pm$ ” coincide, however reproduce a couple of new equations – for each branch:

$$\frac{\partial A_1^+}{\partial \xi_+} = \frac{\partial A_0^+}{\partial \xi_+}, \quad \frac{\partial A_1^-}{\partial \xi_-} = -\frac{\partial A_0^-}{\partial \xi_-}. \quad (14.43)$$

Here the situation is considered, when each of the branches from (14.43) depends on its variable only (in the general case, each of branches can have a parametric dependence on the other variable) in such a manner that

$$A_i^s(\xi_s) = B_i^s \Phi_s(\xi_s); \quad i = \{0; 1\}; \quad s = \{\pm\}. \quad (14.44)$$

Using presentation (14.44) in relations (14.43), we can, at least, formulate the following conditions for both branches:  $A_0^+(\xi_+) = A_1^+(\xi_+) = \Phi_+(\xi_+)$ ;  $A_0^-(\xi_-) = -A_1^-(\xi_-) = \Phi_-(\xi_-)$ . Or, in more compact form:

$$A_0^{\pm}(\xi_{\pm}) = \pm A_1^{\pm}(\xi_{\pm}) = \Phi_{\pm}(\xi_{\pm}). \quad (14.45)$$

In this case relationship (14.45) in fact means the transfer from the initial branches “0” and “1” to the new branches “+” and “-” (e.g., in the condition of normalization  $\sum_{in} |a_{in}|^2 = 1$  as a result of a sequence of transformations from the initial functions  $a_{in}$  to functions  $\Phi_{\pm}(\xi_{\pm})$ ).

Before starting to consider subsystem (14.35) with due regard for (14.45), let us return to conditions (14.41). By their form conditions (14.41) are equations of motion, which determine dynamics of centers of localization of the exited (injected into conduction zone) electron. In this case the dependence of the mechanically wave impulse  $p$  on time  $\tau$  should be known. Such a dependence can be both specified directly in the form of function  $p(\tau)$ , or be determined by the dynamical equation for impulse  $p$ , which completes (14.41). Looking back at the subsystem (14.35), one can immediately notice the following: in the equations of this subsystem, due to the

factor  $(\Pi - \overset{\circ}{p})x$ , there is a possibility to raise a question about the formulation of the dynamical equation for the impulse  $p$ . There are three possible situations:

1.  $|\beta(p)| \rightarrow 0$ . According to designation (14.36), this condition means also the condition  $|p| \rightarrow 0$ . And, as follows from (14.37),  $|\mu(p)| \rightarrow 1$ . In this case the desired dynamical equation, which complements the equation of motion (14.41), can be written in the form [28–30]

$$\overset{\circ}{p} = \Pi. \quad (14.46)$$

In the circumstances, different from the approximation  $|\beta(p)| \rightarrow 0$ , this condition is physically incorrect, as violates the accordance between the classical description of this object and its quantum-mechanical description in the form of the subsystem (14.35). This contradiction makes itself evident in the fact that in the classical description (14.46), the object is considered as such, which moves in the external field with the force constant  $\Pi$ , whereas in the quantum-mechanical description (14.35), the main input from the external field, which is determined just by the factor  $(\Pi - \overset{\circ}{p})x$ , disappears.

2.  $|\beta(p)| \ll 1$ . According to the definition (14.36), in the field of uniqueness of the function  $\sin(p)$  ( $|p| \leq \frac{\pi}{2}$ ), this condition also means the condition  $|p| \ll 1$ . Dynamical equation, which completes Eq. (14.41), should be already presented in the symmetrical form:

$$\overset{\circ}{p} = \frac{1}{2}\Pi \quad (14.47)$$

Symmetry of this form is connected with the fact that in the quantum-mechanical description (14.35), the factor  $(\Pi - \overset{\circ}{p})x$  also takes the form of  $\frac{1}{2}\Pi x$ . That is, both descriptions have the same force constant  $\frac{1}{2}\Pi$ . However, such a choice of the dynamical equation for the impulse  $p$  is correct only in the specified asymptotics  $|\beta(p)| \ll 1$ , as at the transfer to the variables  $\xi_{\pm} = x - x_c^{\pm}$ , the classical description (14.41) and (14.47) and quantum-mechanical one (14.35) appear to be formulated in different coordinate systems. Quantum-mechanical, in the coordinate system, connected with the point  $x_c^{\pm}$ , and the classical one, in the “laboratory” coordinate system, is connected with the polyene molecule.

3.  $|\beta(p)| \leq 1$ . In this asymptotics it is not possible already to neglect by the fact that the classical and quantum descriptions are formulated in different coordinate systems. In this case the forces should have different scales. Hence, analogue of Eq. (14.47) now should have the form  $\overset{\circ}{p} = G$ , and the factor  $(\Pi - \overset{\circ}{p})x$  the form  $\frac{1}{\mu}Fx$ . The mass factor  $\frac{1}{\mu}$  arises due to the necessity to formulate Eq. (14.35) in their own coordinate systems, connected with the points  $x_c^{\pm}(\tau)$ . In this case the forces  $F$  and  $G$  satisfy the relationship  $\frac{1}{\mu}F + G = \Pi$ . It is clear that one more relationship is necessary to determine them. This relationship can be

obtained [28, p. 4.3] already from the solution of the subsystem (14.35). In this case this solution is constructed in such a manner that the quantum and classical descriptions were successively coordinated.

## 14.6 Maximally Feeble Fields: Soliton Solution

Hereinafter only the first situation  $|\beta(p)| \rightarrow 0$  is considered in detail, for which the equation of motion (14.46) is fulfilled. In this case the subsystem (14.35) with due regard for (14.45) and condition,  $\frac{\partial}{\partial x} \equiv \frac{\partial}{\partial \xi_{\pm}}$ , resolves itself into two equations, the first of which has a form

$$\frac{1}{2\mu} [1 \pm \tau_{\parallel} v_{\perp}] \frac{\partial^2 \Phi_{\pm}(\xi_{\pm})}{\partial \xi_{\pm}^2} + (2g_{00}(\xi_{\pm} + x_c^{\pm}) + g_{01}(\xi_{\pm} + x_c^{\pm})) \Phi_{\pm}^3(\xi_{\pm}) + \left[ \Omega + \frac{1}{\mu} \pm \tau_{\parallel} v_{\perp} \left( \frac{1}{2} + \frac{1}{\mu} \right) \right] \Phi_{\pm}(\xi_{\pm}) = 0,$$

and the second one can be reduced to the form

$$\frac{1}{2\mu} [1 \pm \tau_{\parallel} v_{\perp}] \frac{\partial^2 \Phi_{\pm}(\xi_{\pm})}{\partial \xi_{\pm}^2} + (2g_{11}(\xi_{\pm} + x_c^{\pm}) + g_{10}(\xi_{\pm} + x_c^{\pm})) \Phi_{\pm}^3(\xi_{\pm}) + \left[ \Omega + (\Pi_x + \Pi_y) + \frac{1}{\mu} \pm \tau_{\parallel} v_{\perp} \left( \frac{1}{2} + \frac{1}{\mu} \right) \right] \Phi_{\pm}(\xi_{\pm}) = 0.$$

In these equations in the factors  $g_{ij}(x)$ , the designation (14.42) is taken into account, however, in the form

$$x = \xi_{\pm} + x_c^{\pm}, \text{ and the designation } : \Omega \equiv \gamma^{\circ} \quad (14.48)$$

and is also introduced.

The parameter  $\Omega$  is a dimensionless analog of the frequency constant  $\omega$  in the phase of the plane wave:  $(\mathbf{k} \cdot \mathbf{r} - \omega t)$ ; however here, due to the presence of the external field, it can have the dependence on time, and one of the problems of the construction of the solutions is the identification of this parameter with the classical Hamiltonian of the considered quasiparticle. In this case it will have the property of constant (preserves in time) and can be also identified with its eigenvalue.

As it is seen, both solutions for each from the branches “ $\pm$ ” determine one and the same function, but differ therewith. The second solution has the term  $(\Pi_x + \Pi_y)$ , which is absent in the first equation. Besides, in both equations the factors in the nonlinear terms at  $\Phi_{\pm}^3(\xi_{\pm})$  differ. Such differences are the sequences of presentation (14.44), (14.45) and approve themselves only under conditions of the external field switched on. (In general, as follows from definitions (14.11), (14.12), the external field can always be oriented in such a manner that  $\Pi_x + \Pi_y = 0$ ; however, we will not do that, as such special requirement to the external field is

a sequence of approximations made earlier) Under this approximation ( $|\beta(p)| \rightarrow 0$ ), the field is vanishingly small in the sense of conditions:  $\Pi_x \rightarrow 0$ ,  $\Pi_y \rightarrow 0$ ,  $\Pi \rightarrow 0$ . In the dimension presentation, according to designations (14.25), (14.11) and (14.12), such condition (within the accuracy unessential coefficients) can be estimated by the relationship  $(eF_i b/|M|) \rightarrow 0$ ,  $i = \{x, y\}$ . Here  $F_i$  are the components of the strength of the external field,  $b$  is longitudinal “lattice parameter” of the polymer chain (in particular, for polyenes here  $b = 1, 4\text{\AA}$  is accepted), and  $|M|$  is the numerical value of the matrix element of the energy of the longitudinal exchange resonance interaction. As the dimensionless values of the fields cannot exceed one (in this case the field starts to destroy the material), the condition  $\Pi_i < 1$  corresponds to the concept of vanishingly small fields. If, for the sake of providing estimations, we particularise this condition with the inequality  $\Pi_i \leq 10^{-2}$ , then for the dimension field we shall have the following:  $F_i \leq 10^{-2} \frac{|M|}{be}$ . Assuming for polyenes  $b = 1, 4\text{\AA}$ ,  $|M| \sim 0.2$  eV, we shall have  $F_i \sim 10^7$  V/m ( $10^5$  V/cm).

In this case in the zero approximation by the external field (or at the field switched off), both these equations for each branch “ $\pm$ ” coincide and reduce themselves to the form

$$\begin{aligned} & \frac{1}{2\mu} [1 \pm \tau_{\parallel} v_{\perp}] \frac{\partial^2 \Phi_{\pm}(\xi_{\pm})}{\partial \xi_{\pm}^2} + (2g_{11} (\xi_{\pm} + x_c^{\pm}) + g_{10} (\xi_{\pm} + x_c^{\pm})) \Phi_{\pm}^3(\xi_{\pm}) \\ & + \left[ \Omega + (\Pi_x + \Pi_y) + \frac{1}{\mu} \pm \tau_{\parallel} v_{\perp} \left( \frac{1}{2} + \frac{1}{\mu} \right) \right] \Phi_{\pm}(\xi_{\pm}) = 0. \end{aligned} \quad (14.49)$$

In this case we designate

$$g_{00} \equiv g_{11} \equiv g_{\parallel}; \quad (14.50)$$

$$g_{00} \equiv g_{11} \equiv g_{\parallel}. \quad (14.51)$$

That is under conditions of the absence of the external field or in zero approximation by it, parameters  $g_{ij}$ , as follows from their definitions (14.20)–(14.22) and (14.25), do not depend on the variable  $x = \xi_{\pm} + x_c^{\pm}$  (i.e., they are constants) and coincide by pairs according to definitions (14.50), (14.51).

In the approximation considered ( $|\beta(p)| \rightarrow 0$ ,  $|p| \rightarrow 0$   $\{\Pi\} \rightarrow 0$ ), the dependence of  $\mu$  on  $p$  is rather weak and can be neglected. In this case the functions  $\Phi_{\pm}^{(0)}(\xi_{\pm})$  do not obtain additional, besides  $x_c^{\pm}(\tau)$ , dependence on  $\tau$ , which is forbidden by the subsystem (14.39).

Introducing, for simplifications of computations, designations

$$2g_{\parallel} + g_{\perp} \equiv g, \text{ and also } \Omega + \frac{1}{\mu} \pm \tau_{\parallel} v_{\perp} \left[ \frac{1}{2} + \frac{1}{\mu} \right] \equiv \varepsilon_{\pm}; \quad (14.52)$$

$$1 \pm \tau_{\parallel} v_{\perp} \equiv s_{\pm}, \quad (14.53)$$

reduce Eq. (14.49) to the more compact form [30–29]:

$$\frac{s_{\pm}}{2\mu} \Phi_{\pm}^{(0)''}(\xi_{\pm}) + g \Phi_{\pm}^{(0)3}(\xi_{\pm}) + \varepsilon_{\pm} \Phi_{\pm}^{(0)}(\xi_{\pm}) = 0. \quad (14.54)$$

This equation is well known [28, p. 103; 11] as the soliton equation. Its solution is searched in the form of the substitution:

$$\Phi_{\pm}^{(0)}(\xi_{\pm}) = \frac{C_{\pm}}{ch(\kappa_{\pm} \xi_{\pm})}. \quad (14.55)$$

where parameters  $\kappa_{\pm}$ ,  $\varepsilon_{\pm}$ , and  $C_{\pm}$  are determined from the solution of Eq. (14.54) and the condition of normalization. The condition of normalization for  $\Phi_{\pm}^{(0)}(\xi_{\pm})$  can be obtained from the general relationship:

$$\sum_{in} |a_{in}|^2 = 1 \quad (14.56)$$

To use it, as was mentioned above, it is necessary to change over from functions  $a_{in}$  to the solutions (14.45) and simultaneously to change over from the summing up by branches “0”, “1” to the summing up by the new branches “+”, “-”.

Consecutively using in (14.56) designations (14.24), (14.40), (14.42), (14.45) (14.24), (14.40), (14.42), and (14.45) and changing over from the summing up by branches “0”, “1” to summing up by branches “+”, “-,” we shall obtain  $\int_{-\infty}^{\infty} \Phi_{-}^2(\xi_{-}) d\xi_{-} + \int_{-\infty}^{\infty} \Phi_{+}^2(\xi_{+}) d\xi_{+} = 1$ . Substituting here the explicit form of

the function  $\Phi_{\pm}^{(0)}(\xi_{\pm})$  from (14.55) and accomplishing integration, it is possible to obtain  $\frac{C_{-}^2}{\kappa_{-}} + \frac{C_{+}^2}{\kappa_{+}} = \frac{1}{2}$ . It is not difficult to see that this relationship can be satisfied if to put

$$C_{-} = \cos(\phi) \sqrt{\frac{\kappa_{-}}{2}}; \quad C_{+} = \sin(\phi) \sqrt{\frac{\kappa_{+}}{2}}. \quad (14.57)$$

where the parameter  $\phi$  changes within the limits from 0 to  $2\pi$  and still remains uncertain. Substituting (14.55) into Eq. (14.54) and differencing and taking into account the linear independence of the functions  $\frac{1}{ch(\kappa_{\pm} \xi_{\pm})}$  and  $\frac{1}{ch^3(\kappa_{\pm} \xi_{\pm})}$ , we shall obtain two more relationships:

$$\varepsilon_{\pm} = -\frac{\kappa_{\pm}^2 s_{\pm}}{2\mu}; \quad g C_{\pm}^2 = \frac{\kappa_{\pm}^2 s_{\pm}}{\mu}. \quad (14.58)$$

Introducing the obvious designation  $J_{\pm} = \left\{ \begin{array}{l} \sin \phi \\ \cos \phi \end{array} \right\}$ , which enables one to write (14.57) as the integrated relationship

$$C_{\pm} = J_{\pm} \sqrt{\frac{\kappa_{\pm}}{2}} \quad (14.59)$$

and solving Eq. (14.59) and the second (right) equation in (14.58) relative to  $C_{\pm}$  and  $\kappa_{\pm}$ , finally we find

$$\kappa_{\pm} = \frac{g\mu}{2} \cdot \frac{J_{\pm}^2}{s_{\pm}}; \quad C_{\pm} = J_{\pm}^2 \sqrt{\frac{g\mu}{4s_{\pm}}}; \quad \varepsilon_{\pm} = -\frac{g^2\mu}{8} \cdot \frac{J_{\pm}^4}{s_{\pm}}, \quad (14.60)$$

where it is obvious that

$$J_{\pm}^n = \left\{ \begin{array}{l} \sin^n \phi \\ \cos^n \phi \end{array} \right\}. \quad (14.61)$$

## 14.7 Conclusions

In the first part of the work, the general problem statement on the transfer of charge, injected into conduction zone of the polyene chain, is performed. The response of the “crystal lattice” of the crystal chain is taken into account, the system of equations for description of the charge transfer is obtained, and its solutions in the zero approximation relative to the case of maximally weak fields and condition (14.28) are found. These approximations correspond to the transfer by the mechanism of the charge soliton. It is shown that the accounting of the structural features of the “lattice” originates from two modes of the excitation. In the second part of this work, the problems connected with the soliton nanoconductivity of the polymer chain of the polyene type will be analyzed.

## References

1. Mishra A (2000) Cyanine during 1990s: a review. *Chem Rev* 100:1973–2011
2. Meyers F, Marder SR, Perry JW (1998) Chapter 6: Introducing to nonlinear optical properties organic materials. In: Interrante LV, Hampden-Smith J (eds) *Chemistry advanced materials. An overview*. Wiley-VCH. Inc, New York/Chichester/Weinheim/Brisbane/Singapore/Toronto, pp 207–268
3. Bredas JL, Street GB (1985) Polaron, bipolaron and solitons in conducting polymers. *Acc Chem Res* 18:309–315
4. Davydov AS (1973) The theory of contraction of proteins under their excitation. *J Theor Biol* 38(3):559–569. doi:10.1016/0022-5193(73)90256-7. PMID 4266326

5. Vakhnenko AA, Gaididei YB (1986) On the motion of solitons in discrete molecular chains. *TMF* 68(3):350–359
6. Gaididei YB, Petrov EG (1971) Theory of band and bound states of double triplet excitations in molecular crystals. I. *TMF* 6(3):433–444
7. Gaididei YB, Petrov EG (1971) Theory of band and bound states of double triplet excitations in molecular crystals. II. *TMF* 7(1):95–105
8. Davydov AS (1982) Solitons in quasi-one-dimension molecular structures. *Phys T* 138(4 (1.11)):603–643
9. Davydov AS (1984) Solitons in molecular systems. *Naukova doomka*, Kiev, 288 p
10. Kachkovsky OD (2005) Soliton nature of E-ion structure of linear conjugated systems. *Teoret experimental Chemistry* 41:139–164
11. Davydov AS (1973) The theory of contraction of proteins under their excitation. *J Theor Biol* 38(3):559–569. doi:10.1016/0022-5193(73)90256-7. PMID 4266326
12. Davydov AS (1974) Quantum theory of muscular contraction. *Biophysics* 19:684–691
13. Davydov AS (1977) Solitons and energy transfer along protein molecules. *J Theor Biol* 66(2):379–387. doi:10.1016/0022-5193(77)90178-3. PMID 886872
14. Brizhik L, Eremko A, Piette B, Zakrzewski W (2004) Solitons in  $\alpha$ -helical proteins. *Phys Rev E Stat Nonlin Soft Matter Phys* 70:031914, 1–16
15. Scott AS (1992) Davydov's soliton. *Phys Rep* 217:1–67. doi:10.1016/0370-1573(92)90093-F
16. Cruzeiro-Hansson L, Takeno S (1997) Davydov model: the quantum, mixed quantum-classical, and full classical systems. *Phys Rev E* 56:894–906
17. Cruzeiro-Hansson L (2005) Influence of the nonlinearity and dipole strength on the amide I band of protein  $\alpha$ -helices. *J Chem Phys* 123(23):234909, 1–7. doi:10.1063/1.2138705. PMID 16392951
18. Cruzeiro-Hansson L (1997) Short timescale energy transfer in proteins. *Solphys '97 Proceedings*
19. Petrov E (1984) Physics of charge transfer in biosystems. *Naukova Dumka*, K. 368 p
20. Ostapenko, MG, Petrov E (1990) Donor-acceptor transfer of excess electrons through a short chain magnetically. 33. Kiev, ITF
21. Davydov AS (1979) Influence of electron-phonon interaction on the motion of an electron in a one-dimensional molecular system. *TMF* 40(3):408–421
22. Bredas, JL, Belionne, D., Cornil, J., Calhert, J. Ph., Shuai, Z., Silbey, R., Electronic structure  $\pi$ -conjugated oligomers and polymers: a quantum-chemical approach to transport properties. *Synth Met*, 2002, 125, 107–116.
23. Kachkovskyy AD (1997) Nature electron transitions in linear conjugated systems. *Successes chemistry*. T.66. N 8. S.715-734; Kachkovski AD, Przhonska OV, Ryabitzki AB (2007) Symmetry breaking in cationic and anionic polymethine dyes. *J Molec Struct (THEOCHEM)* 802:75–83
24. Bach G, Daehne S. Cyanine dyes and related compounds, in ROOD'S chemistry carbon compounds, 2nd suppl. to 2nd ed., Vol. IVB, *Het. Comp.*, Sainsbury M., Ed., Elsevier science, Amsterdam, 1997, chapter 15, pp 383–481 (443)
25. Suprun AD (2008) The dynamic properties of single-electron excitations of nonlinear crystals. K.: CUP "Kyiv University". p 151. See. also electronic version: [http://www.phys.univ.kiev.ua/theory/suprun/1\\_Part1c\\_Dynam.pdf](http://www.phys.univ.kiev.ua/theory/suprun/1_Part1c_Dynam.pdf)
26. Fedorchenko A (1992) Theoretical physics. T. 1. Classical mechanics and electrodynamics. High School, K. 536 p
27. Scharf B (1995) *Phys Rev Lett* 74:1186
28. Cai B et al (1996) *Phys Rev E* 53:1202
29. Nogami Y, Toyama FM (1994) *Phys Rev E* 49:4497–4501
30. Suprun AD (2002) *Functional Materials* 9:389

# Chapter 15

## Complex Flows of Immiscible Microfluids and Nanofluids with Velocity Slip Boundary Conditions

Vitalina Cherevko and Natalya Kizilova

### 15.1 Introduction

During the last decade, the microfluids (suspensions of microparticles with  $d = 10\text{--}100\ \mu\text{m}$ ) and nanofluids (suspensions of nanoparticles with diameters  $d = 10\text{--}100\ \text{nm}$ ) have become important components of different microunits for mixing and purification of the microscopic volumes of technical and biological fluids, biochemical analysis, and medical diagnostics in the lab-on-a-chip flow systems, as well as efficient nanofluid-based microcoolers/heaters and other devices [1–3]. Numerous experiments with flows of micro- and nanofluids through the microtubes, ducts, and channels revealed that the measured pressures, velocities, volumetric flows, and shear rates had not corresponded to those values computed from classical Poiseuille and Couette flow solutions in the corresponding geometry with no-slip boundary conditions (BC) [4]. The most essential differences had been found in the flow patterns, pressure drops, early transition to turbulence, and higher friction losses that could be explained by the bigger influence of the wall roughness on the micro- and nanofluid flows [4, 5]. Therefore, reformulation of the BC problem is needed for better understanding of the differences between the flows of macroscopic fluids and micro-/nanofluids.

---

V. Cherevko

Kharkov National University, Svobody sq., 4, Kharkov, 61022, Ukraine

N. Kizilova (✉)

Warsaw University of Technology, ul. Nowowiejska 24, Warsaw, 00-665, Poland

Vilnius Gediminas Technical University, J. Basanavičiaus st. 28, Vilnius, 03224, Lithuania

e-mail: [n.kizilova@gmail.com](mailto:n.kizilova@gmail.com)

© Springer International Publishing AG 2017

O. Fesenko, L. Yatsenko (eds.), *Nanophysics, Nanomaterials, Interface Studies, and Applications*, Springer Proceedings in Physics 195,

DOI 10.1007/978-3-319-56422-7\_15



Applicability of the slip boundary conditions has already been studied for the Newtonian fluid flows [6], for macroscopic liquid flows near biological surfaces and interfaces [7], for walls with special slide coating [8], for penetrable walls [9], in polymer melts [10], and in turbulent flows with boundary slip [11]. The first formulation of the nonlinear slip BC has been proposed by Navier in 1873 in the form

$$\left(\widehat{T}\vec{n}\right)_\tau + \kappa v_\tau = 0 \text{ on } \partial\Omega$$

where  $\partial\Omega$  is the boundary of the flow domain  $\Omega$ ,  $\vec{v}$  and  $\widehat{T}$  are the fluid velocity and stress tensor,  $\vec{n}$  and  $\vec{\tau}$  are normal and tangential unit vectors to the surface, and  $\kappa$  is the “friction” coefficient. Validity of the Navier BC for the fluid flows through rigid microtubes has been studied in [12].

Nanofluids as suspensions of nanoparticles and polymer molecules exhibit high thermal and electric conductivity, low specific heat, and unique electromagnetic properties due to high strength, thermal and electric conductivity of the nanoparticles, and their magnetic properties [13]. Classical fluid dynamics and thermomechanical theories developed for the macroscopic systems are not fully applicable to the suspensions of nanoparticles as well as to uniform fluids at the micro- and nanoscales. Velocity slip, viscous dissipation, thermal creep, and non-continuum effects like scattering at the wall, adhesion, and changes in conformations must be taken into account [14–16] as well as electrokinetic phenomena [17]. For the solid nanoparticles in the concentrated ( $C > 5\%$ ) nanofluids, the shear-thickening behavior may also lead to the high-pressure gradients for the steady fluid flow than those predicted by the Poiseuille law [18]. Gas microflows in MEMS and microfluidic devices can be used for extracting biological samples, cooling integrated circuits and active control over the aerodynamic forces [19, 20].

The first experimental study conducted for the gas flow in the rectangular glass channels with hydraulic radius  $D_h = 45.5\text{--}83.1 \mu\text{m}$  and silicon channels with  $D_h = 55.8\text{--}72.4 \mu\text{m}$  of microminiature Joule–Thomson refrigerators revealed that the friction coefficient is 10–30% higher in silica channels and 3–5 times higher in glass channels than those predicted by the Moody chart for the friction factor against the Reynolds number at different relative roughness  $\varepsilon/D_h$ , where  $\varepsilon$  is the roughness height [21]. In the micro- and nanochannels due to the tremendous increase in the surface-to-volume ratio, the relative roughness becomes the most influencing factor, which must be accounted for in the BC via complex geometry of the wall with roughness, as well as complex interaction of the flow and nanoparticles with the wall.

Experimental study of the fluid flow (1-,2-propanol and 1-,3-pentanol) through silicon microchannels with  $D_h = 5;12;25 \mu\text{m}$  also demonstrated an increase in the friction coefficient by 5–30% depending on the temperature within the limits  $T = 0\text{--}85^\circ\text{C}$  compared to the classical computations on the Navier–Stokes equations with no-slip boundary conditions [22]. Water flow through rectangular stainless steel microchannels with  $D_h = 133\text{--}367 \mu\text{m}$  and width-to-height ratios

$W/H = 0.333-1$  has been studied in [23]. The friction factors for both laminar and turbulent flows have been found deviated from the classical predictions, and the geometry factor  $W/H$  was found to have important effects on the flow. The laminar to turbulence transition occurred at the critical Reynolds numbers  $Re^* = 200-700$  depending on  $D_h$  and  $W/H$ . The value  $Re^*$  becomes lower as the size of the microchannel decreases. Water flow through the stainless steel and fused silica circular microtubes with diameters  $D = 50-254 \mu\text{m}$  and  $\varepsilon/D = 0.69-3.5\%$  at  $Re = 100-2000$  also exhibited higher friction than those predicted by the classical fluid dynamics [15]. The difference increased with the decreasing  $D$  and increasing  $Re$  values. The flow transition has been observed at  $Re^* = 300-900$  depending on the microtube diameter  $D = 50-150 \mu\text{m}$ . For the fluid flows in rectangular metallic channels with widths  $W = 150-600 \mu\text{m}$  and heights  $H = 22.7-26.3 \mu\text{m}$ , an approximate 20% increase over the classical theory prediction in the friction factor at low  $H/W$  ratios has been revealed [24]. The water flow through trapezoidal silicon microchannels with  $D_h = 51.3-168.9 \mu\text{m}$  and  $\varepsilon/D = 1.76-2.85\%$  at  $Re < 1500$  demonstrated the friction factor by 8-38% higher than the classical theory prediction for laminar flows [25].

A good review of literature published between 1983 and 2005 on the experimental studies of the friction coefficient and laminar to turbulence transition  $Re^*$  values in the microchannels and tubes of different geometry and materials is given in [16]. It is shown when  $\varepsilon/D_h < 1\%$  the classical computations for the corresponding Poiseuille and Couette laminar flows remain still valid. A positive deviation of the friction factor from the conventional theory is observed due to the high roughness and compressibility effects. For instance, smaller friction factors detected in gas flows through fused silica microtubes with  $D = 10-20 \mu\text{m}$  are produced by rarefaction effect.

The results of the abovementioned experimental studies confirmed that the flow resistances are about 10-90% higher than the theoretical values for the corresponding geometry and material parameters, some of them even by 350% over the theoretical predictions [16, 21, 26].

For lower  $Re$  numbers, the required pressure drop is roughly the same as for the Poiseuille flow, but at bigger  $Re$ , the pressure gradient becomes higher than those compared to the predicted by the Poiseuille law due to higher friction at the wall or/and development of turbulence [15]. The dependence of the flow behavior on the wall material has been shown for the metal, glass, and silica tubes. At the same flow rate and tube diameter, the fluid flow through the fused silica microtube requires a higher pressure gradient than through the stainless steel microtube.

## 15.2 Problem Formulations with Slip Boundary Conditions

The wall roughness may be taken into account by modeling the fluid layer that is in contact with the wall as flow in the porous medium [27]. This approach was applied to the macroflows in [28].

The modified roughness viscosity model has been proposed in [29] for circular tubes with axisymmetric roughness. Instead of the conventional dynamic viscosity  $\mu$  in the Navier–Stokes equations, the viscosity  $\mu + \mu_R$  where

$$\mu_R = A\mu\text{Re}_\varepsilon \frac{r}{\varepsilon} \left( 1 - \exp\left(\frac{\text{Re}_\varepsilon r}{\text{Re} \varepsilon}\right) \right)^2 \quad (15.1)$$

is the so-called roughness viscosity,  $r$  is the radial coordinate,  $\text{Re} = \rho u D / \mu$ ,  $u$  is the average flow velocity,  $\rho$  is the fluid density,  $\text{Re}_\varepsilon = \rho U \varepsilon / \mu$ ,  $U$  is the velocity at the top of the roughness element, and  $A$  is the material-dependent constant. Solution of the steady incompressible Navier–Stokes equations with modified viscosity in the form (15.1) has been found numerically for the no-slip boundary conditions and compared to the experimental data in [15].

Another effective viscosity model for concentrated nanofluids has been proposed in the form [30]

$$\mu_{\text{eff}} = \frac{\mu_{\text{bf}}}{1 - \alpha (d_p / d_f)^{-0.3} C^{1.03}} \quad (15.2)$$

where  $\mu_{\text{bf}}$  is the viscosity of the base fluid,  $d_p$  is the diameter of nanoparticles,  $d_f = (6M_{\text{bf}} / \pi N_A \rho_{\text{bf}})^{1/3}$  is the base fluid equivalent diameter,  $C$  is the nanoparticle volume fraction,  $\rho_{\text{bf}}$  and  $M_{\text{bf}}$  are the density at temperature  $T = 293$  K and molecular weight of the base fluid, and  $N_A$  is the Avogadro number.

For the concentrated nanofluids, the nonlinear approximation

$$\mu_{\text{eff}} = \mu_{\text{bf}} (1 + k_1 C + k_2 C^2) \quad (15.3)$$

has also been used. For instance, in [31]  $k_1 = 39.1$ ,  $k_2 = 533.9$  values have been accepted.

The effective density of the suspension can be introduced in a usual form accepted for mixtures [32]:

$$\rho_{\text{eff}} = \rho_p C + \rho_{\text{bf}} (1 - C) \quad (15.4)$$

where  $\rho_p$  is the density of particle material: 15.4 may also be generalized for the set of particles of different densities and concentrations.

Then expressions for the effective heat conductivity  $k$  and specific heat  $c_p$  of the nanofluid have been derived in the form [33]

$$k = k_{\text{bf}} \frac{(k_p + 2k_{\text{bf}}) - 2C(k_{\text{bf}} - k_p)}{(k_p + 2k_{\text{bf}}) + C(k_{\text{bf}} - k_p)} + k_{\text{Brownian}}, \quad (15.5)$$

$$k_{\text{Brownian}} = 5 \cdot 10^4 \beta C \rho_{\text{bf}} c_{\text{bf}} \sqrt{\frac{k_B T}{d_p}} f(T, C),$$

$$c_{\text{eff}} = \frac{\rho_p c_p C + \rho_{\text{bf}} c_{\text{bf}} (1 - C)}{\rho_p C + \rho_{\text{bf}} (1 - C)}, \quad (15.6)$$

where  $k_p, k_{\text{bf}}$  and  $c_p, c_{\text{bf}}$  are heat conductivity and specific heat of the particles and base fluid,  $k_B$  is the Boltzmann constant,  $\beta$  is the constant dependent on the material, concentration of the particles and temperature, and  $f(T, C)$  is the function determined from experiments.

The heat transfer by the steady laminar nanofluid flow in the 2D microtube ( $d = 50\mu\text{m}, L = 250\mu\text{m}$ ) has been studied experimentally for the  $\text{Al}_2\text{O}_3, \text{CuO}, \text{SiO}_2,$  and  $\text{ZnO}$  nanoparticles with  $d_p = 25, 45, 65,$  and  $80$  nm and concentrations  $C = 1\text{--}4\%$  in ethylene glycol as a base fluid [34]. The corresponding steady nonlinear incompressible 2D Navier–Stokes equations and heat equation have been solved by finite volume method. It was found that the nanofluid with  $\text{SiO}_2$  particles had the highest Nusselt number, followed then by  $\text{ZnO}, \text{CuO},$  and  $\text{Al}_2\text{O}_3$  and lastly by pure ethylene glycol. The Nusselt number for all cases increased with the Reynolds number, with volume fraction  $C$  of the particles, and with decrease of the particle diameter  $d_p$ .

Steady 2D Navier–Stokes equations with no-slip boundary conditions are considered in most papers on the flows in the microchannels. The roughness is introduced as small amplitude wall waviness, and the solution is sought as power expansions over the small parameter  $\varepsilon/D$  [26]. The same approach applied to the macroflows revealed appearance of the slip flow over the wall with regular [35] and randomly rough [36] walls. The slip coefficient has been derived by using conformal mapping techniques [37] and method of matched asymptotic [38]. The numerical results show that microflows are more complex than macroflows [26], and the pressure drops are up to 65% higher than those in the classical Poiseuille flow when the roughness  $\varepsilon/D$  rises to 5%. As it was previously shown in the classic experiments by J. Nikuradse on rough pipes [39], in the macroflows the same roughness 5% had no influence on the friction factor [40]. In the microflows apparent fluctuations in flow fields have been found, and influence of the roughness on the flow profile and the friction factor was different [26].

The Maxwell first-order slip model [41] of diffusive reflection of the particles from the rough surface of the isothermal wall within the so-called Knudsen layer is

$$\left( u - u_w - \frac{2 - \sigma}{\sigma} \text{Kn} \frac{\partial u}{\partial n} \right) \Big|_{\partial\Omega} = 0, \quad (15.7)$$

where  $u_w$  is the wall velocity,  $\text{Kn} = \lambda/L$  is the Knudsen number,  $\lambda$  is the mean free path,  $L$  is the characteristic length,  $\sigma$  is the tangential momentum accommodation factor (or friction), and  $\sigma = 1$  for purely diffuse reflection, and has been used for Lattice–Boltzmann simulation of the microchannel flow [14]. In gases the mean free path is determined by the diameters of particles and their numerical concentration  $N$  (number per unit volume) as follows  $\lambda = (\sqrt{2}N\pi d_p^2)^{-1}$  [42].

The thickness of the Knudsen layer in the discrete hard sphere model can be computed as [43]

$$\delta = \frac{k_B T}{\pi d_p^2 p}, \quad (15.8)$$

where  $p$  is the pressure, while in the continuous media,

$$\delta = \mu \sqrt{\frac{\pi}{2p\rho}}. \quad (15.9)$$

A modification of (15.7) has been proposed in [44] in the form

$$\left( u - u_w - \frac{2 - \sigma}{\sigma} \frac{\text{Kn}}{1 - \text{Kn} \cdot f(\text{Kn})} \frac{\partial u}{\partial n} \right) \Big|_{\partial\Omega} = 0, \quad (15.10)$$

where  $f(\text{Kn})$  is an empirical parameter to be determined;  $|f(\text{Kn})| < 1$ .

The model (15.7) can be considered at  $0.01 < \text{Kn} \leq 0.1$  because at  $\text{Kn} < 0.01$ , the no-slip boundary conditions give good results [42, 44]. For the flow regimes with  $0.1 < \text{Kn} \leq 1$ , the second-order slip boundary condition is used in the form proposed by J.C. Maxwell:

$$\left( u - u_w - \frac{2 - \sigma}{\sigma} \text{Kn} \left( \frac{\partial u}{\partial n} + \frac{\text{Kn}}{2} \frac{\partial^2 u}{\partial n^2} \right) \right) \Big|_{\partial\Omega} = 0 \quad (15.11)$$

In that way, the boundary condition (15.7) is used for the microchannel flows, while the condition (15.11) is more exact for the nanochannel flows, as well as flows of concentrated nanofluids of nanoparticles or fullerenes ( $C_{60}$  or others). Then the diffusive reflection and free path may be related to the particles. In the general form, the second-order boundary condition (15.11) has been proposed in the form [45]

$$\left( u - u_w - C_1 \text{Kn} \frac{\partial u}{\partial n} + C_2 \text{Kn}^2 \frac{\partial^2 u}{\partial n^2} \right) \Big|_{\partial\Omega} = 0. \quad (15.12)$$

The term  $C_1 \text{Kn}$  in (15.12) is the constant slip length [19] that equals to the mean free path of the fluid particles. A good review on the experimental data of the coefficients  $C_{1,2}$  is given in [44, page 74]. Summarizing the table, we may accept  $C_1 \in [1; 1.15]$ ,  $C_2 \in [0.5; 1.31]$  for further computations.

Molecular dynamics simulations revealed that the velocity slip at the wall decreases with increase of the ratio  $\varepsilon/\lambda$  for both regular and stochastic roughness [46]. In the transition regime  $\text{Kn} > 0.1$ , the constitutive laws for the stress tensor, heat flux vector, and other parameters break down requiring higher-order correcting terms [47]. When the coupled heat and mass transfer is studied, the Navier–Stokes and heat balance equations are solved with the modified second-order boundary conditions in the form

$$\begin{aligned} \left( u - u_w - \frac{2 - \sigma}{\sigma} \text{Kn} \frac{\partial u}{\partial n} - \frac{3(\gamma - 1) \text{Kn}^2 \text{Re}}{2\pi\gamma} \frac{\partial T}{Ec} \frac{\partial T}{\partial s} \right) \Big|_{\partial\Omega} &= 0, \\ \left( T - T_w - \frac{2\gamma(2 - \tilde{\sigma}) \text{Kn}}{(\gamma + 1)\tilde{\sigma} \text{Pr}} \frac{\partial T}{\partial n} \right) \Big|_{\partial\Omega} &= 0, \end{aligned} \quad (15.13)$$

where  $T$  and  $T_w$  are temperatures in the flow and at the wall,  $s$  is the tangential direction (coordinate),  $\tilde{\sigma}$  is the energy accommodation coefficient,  $\gamma = C_p/C_v$  is the ratio of specific heats,  $\text{Re} = \rho u D/\mu$  is the Reynolds number,  $\text{Pr} = C_p \mu/k$  is the Prandtl number,  $Ec = u^2/C_p \Delta T$  is the Eckert number,  $k$  is the heat conductivity, and  $\Delta T$  is the specified temperature difference in the domain. Perfect energy exchange also corresponds to  $\tilde{\sigma} = 1$  when the energy of the reflected (scattered) particles corresponds to the wall temperature. Thermal and tangential momentum accommodation coefficients have been measured for different typical gases and surfaces and were shown to be strongly dependent on the material and surface state [48]. Their values can be reduced by applying suitable surface preparation techniques.

For the second-order slip conditions, the effective viscosity has been proposed in [44] and studied for the Navier–Stokes tube flow [49] in the form:

$$\mu_{\text{eff}} = \frac{\mu_{\text{bf}}}{1 + \alpha \text{Kn}}, \quad \alpha = \frac{2\alpha_0}{\pi \tan(\alpha_1 \text{Kn}^\beta)}, \quad (15.14)$$

where  $\alpha_1 = 4$ ,  $\beta = 0.4$ ,  $\alpha_0 = 64/3\pi(1 - 4/b)$ ,  $b = -1$ .

As it was shown in [50, 51], the experimental data on the isothermal Poiseuille flows of dilute compressible gases in the microchannels better correspond to the following velocity slip condition:

$$\left( u - u_w + \frac{\mu}{\rho} \frac{\partial}{\partial s} \ln \rho \right) \Big|_{\partial\Omega} = 0, \quad (15.15)$$

than to the Maxwell condition (15.13), because the compressible fluid always slips along the wall in the direction of diminishing density and, hence, for the case of isothermal flows, in the direction of decreasing pressure [52].

Kinematics of the nanotube's nanostructure can be modeled by Euler–Bernoulli plug flow (EBPF) beam theory which was found applicable to the pipe flows when  $L/D > 10$  [53]. Oscillations of the microtubes conveying nanofluids have been studied using the EBPF theory with no-slip velocity profiles [54].

Therefore the value  $\varepsilon/\lambda$  can be considered as a criterion for the no-slip boundary condition acceptance. When  $\varepsilon \leq \lambda$ , the no-slip condition is satisfied; otherwise, significant slip at the wall is present. As it was shown by comparative numerical simulations of the micro- and nanochannel flows in different geometries conducted by molecular dynamics simulations, numerical solutions of the Boltzmann equation, as well as direct computations on the Navier–Stokes equations, the slip flow

approach is remarkably robust in the meaning that it is qualitatively accurate and physically relevant [19]. The classical pressure-driven and shear-driven channel flows being generalized for the velocity slip and thermal jump BC have the analytical solutions [19, 44, 55]. It is convenient for the comparative studies by both experiments and numerical simulations with determination of the model coefficients in the BC formulations for diluted and concentrated micro- and nanosuspensions.

### 15.3 Analytical Solutions for the Classical Poiseuille and Couette Laminar Flows with Second-Order Velocity Slip Boundary Conditions

The analytical solutions for the Poiseuille flows in the circular pipes and between the parallel plates and coaxial cylinders [55] and for the Couette flows between the parallel plates [44] have been obtained for the surfaces with the same roughness. In this chapter similar solutions as well as a set of new ones are obtained and analyzed for different surfaces, so the BC (15.12) are accepted in the form

$$\left( u - u_w - \alpha_j \frac{\partial u}{\partial n} + \beta_j \frac{\partial^2 u}{\partial n^2} \right) \Big|_{\partial\Omega_j} = 0, \quad (15.16)$$

where  $j = 1, 2$ ,  $\alpha_j = C_1 j \text{Kn}_j$ ,  $\beta_j = C_2 j \text{Kn}_j^2$ .

#### 15.3.1 Couette Flow Between the Parallel Plates

The shear-driven laminar flow between the plates  $y=0$  and  $y=h$  moved with velocities  $\vec{V}_1 = (V_1, 0, 0)$  and  $\vec{V}_2 = (V_2, 0, 0)$  accordingly is described by the velocity distribution  $v(y) = V_1 + (V_2 - V_1)y/h$  with the volumetric rate  $Q_{\text{Couette}} = \int_0^h v(y) dy = (V_1 + V_2)h/2$  and constant shear stress  $\tau_{\text{Couette}} = \mu(V_2 - V_1)/h$ , where  $\mu$  is the fluid viscosity.

For the micro- and nanoflows, the coefficients in the same linear velocity distribution determined from (15.16) give the following results

$$\begin{aligned} v_{\text{Couette}}^{\text{slip}}(y) &= \frac{V_1 h + \alpha_2 V_1 - \alpha_1 V_2}{h + \alpha_2 - \alpha_1} + \frac{V_2 - V_1}{h + \alpha_2 - \alpha_1} y, \\ Q_{\text{Couette}}^{\text{slip}} &= \frac{(V_1 + V_2) h^2 + 2h(\alpha_2 V_1 - \alpha_1 V_2)}{2(h + \alpha_2 - \alpha_1)}, \\ \tau_{\text{Couette}}^{\text{slip}} &= \mu \frac{V_2 - V_1}{h + \alpha_2 - \alpha_1}. \end{aligned} \quad (15.17)$$

When  $\alpha_1 = \alpha_2 = 0$ , (15.17) has the form of classic Couette flow solution; at  $\alpha_1 = \alpha_2 \neq 0$  (15.17) gives the expressions presented in [44]; due to the linear velocity field, the second-order term does not influence the solution. If we assume  $V_2 > V_1$  for the sake of definiteness, then (15.17) gives

$$v_{\text{Couette}}^{\text{slip}}(0) - V_1 = \frac{-\alpha_1 (V_2 - V_1)}{h + \alpha_2 - \alpha_1}, \quad v_{\text{Couette}}^{\text{slip}}(h) - V_2 = \frac{-\alpha_2 (V_2 - V_1)}{h + \alpha_2 - \alpha_1} \quad (15.18)$$

and both differences in (15.18) are positive when  $\alpha_1 - \alpha_2 > h$ , i.e., the difference in the constant slip lengths of the two plates must exceed the distance between the plates. This condition is valid for the sufficiently high Knudsen numbers. In connection with the development of rheology of the micro- and nanofluids, the correction (15.18) must be accounted for in the viscosity estimations by the rotational viscosimeters.

Comparison of the micro (slip BC) with macro (no-slip BC) flow gives

$$Q_{\text{Couette}}^{\text{slip}} - Q_{\text{Couette}} = \frac{-(\alpha_1 + \alpha_2) (V_2 - V_1) h}{2(h + \alpha_2 - \alpha_1)} > 0 \text{ when } \alpha_1 - \alpha_2 > h, \text{ and}$$

$$\tau_{\text{Couette}}^{\text{slip}} - \tau_{\text{Couette}} = \mu \frac{(V_2 - V_1) (\alpha_1 - \alpha_2)}{h(h + \alpha_2 - \alpha_1)} < 0 \text{ when } \alpha_1 < \alpha_2 \text{ or } \alpha_1 - \alpha_2 > h.$$

In that way, when  $\alpha_1 - \alpha_2 > h$ , the slip BC flow experiences lower shear rate and lower apparent viscosity with higher flow rate than the no-slip BC flow.

### 15.3.2 Couette Flow Between Coaxial Rotating Cylinders

Two coaxial cylinders with axis  $Oz$  and radii  $R_1$  and  $R_2$  rotated at the angular velocity  $\Omega_1$  and  $\Omega_2$  (let's assume  $\Omega_2 > \Omega_1$ ) are considered (Fig.15.1). Then the known solution of the Navier–Stokes equation for the angular velocity  $v_\theta$  of the fluid at the slip BC is

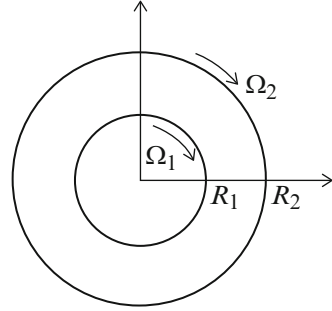
$$v_\theta(r) = \frac{\Omega_2 R_2^2 - \Omega_1 R_1^2}{R_2^2 - R_1^2} r - \frac{(\Omega_2 - \Omega_1) R_1^2 R_2^2}{R_2^2 - R_1^2} \frac{1}{r},$$

$$\tau_{\text{rot}} = \frac{\Omega_2 R_2^2 - \Omega_1 R_1^2}{R_2^2 - R_1^2} + \frac{(\Omega_2 - \Omega_1) R_1^2 R_2^2}{R_2^2 - R_1^2} \frac{1}{r^2}. \quad (15.19)$$

For the micro-/nanofluid flow, the same solution with the BC (15.16) gives



**Fig. 15.1** Couette flow between two rotating coaxial cylinders



$$\begin{aligned}
 v_{\theta}^{\text{slip}}(\mathbf{r}) &= \frac{\Omega_2 R_2^4 A_1 - \Omega_1 R_1^4 A_2}{R_2^3 (R_2 - \alpha_2) A_1 - R_1^3 (R_1 - \alpha_1) A_2} r \\
 &\quad - \frac{\Omega_2 R_1^3 R_2^4 (R_1 - \alpha_1) - \Omega_1 R_1^4 R_2^3 (R_2 - \alpha_2)}{R_2^3 (R_2 - \alpha_2) A_1 - R_1^3 (R_1 - \alpha_1) A_2} \frac{1}{r}, \\
 \tau_{\text{rot}}^{\text{slip}}(\mathbf{r}) &= \frac{\Omega_2 R_2^4 A_1 - \Omega_1 R_1^4 A_2}{R_2^3 (R_2 - \alpha_2) A_1 - R_1^3 (R_1 - \alpha_1) A_2} \\
 &\quad + \frac{\Omega_2 R_1^3 R_2^4 (R_1 - \alpha_1) - \Omega_1 R_1^4 R_2^3 (R_2 - \alpha_2)}{R_2^3 (R_2 - \alpha_2) A_1 - R_1^3 (R_1 - \alpha_1) A_2} \frac{1}{r^2},
 \end{aligned} \tag{15.20}$$

where  $A_{1,2} = R_{1,2}^2 + \alpha_{1,2} R_{1,2} - \beta_{1,2}$ .

At some sets of the parameters  $\alpha_1, \alpha_2, \beta_1, \beta_2$ , the values

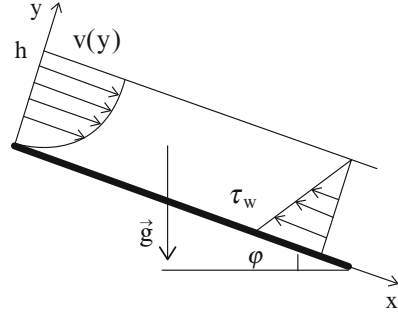
$$\begin{aligned}
 v_{\theta}^{\text{slip}}(R_{1,2}) &= \frac{\Omega_{1,2} R_{1,2}^3 (R_{2,1}^2 (R_2^2 - R_1^2) \mp \alpha_{2,1} R_{2,1} (R_1^2 + R_2^2))}{R_2^3 (R_2 - \alpha_2) A_1 - R_1^3 (R_1 - \alpha_1) A_2} \\
 &\quad \pm \frac{2\beta_{2,1} R_{1,2}^2 + 2\Omega_{2,1} R_{1,2} R_{2,1}^4 (\alpha_{1,2} R_{1,2} - \beta_{1,2})}{R_2^3 (R_2 - \alpha_2) A_1 - R_1^3 (R_1 - \alpha_1) A_2}
 \end{aligned}$$

will be bigger ( $v_{\theta}^{\text{slip}}(R_{1,2}) > \Omega_{1,2} R_{1,2}$ ) and the wall shear stress

$$\tau_{\text{rot}}^{\text{slip}}(R_{1,2}) = \frac{(\Omega_2 R_2^4 A_1 - \Omega_1 R_1^4 A_2) R_{1,2}^2 + \Omega_2 R_1^3 R_2^4 (R_1 - \alpha_1) - \Omega_1 R_1^4 R_2^3 (R_2 - \alpha_2)}{(R_2^3 (R_2 - \alpha_2) A_1 - R_1^3 (R_1 - \alpha_1) A_2) R_{1,2}^2}$$

will be smaller than in the corresponding no-slip BC flow. Using this regularity, the low and high shear stress micro-/nanofluid devices could be designed for the separated layered or intensive mixing flows between the rotating cylinders when the condition  $R_2 - R_1 \ll R_1$  is not valid.

**Fig. 15.2** Schema of the laminar flow in an inclined duct



### 15.3.3 Laminar Flow in an Inclined Duct

Laminar  $v_x = v(y)$  Couette flow in a rectangular duct  $y=0$  with sufficiently big length  $L$  and width inclined at the angle  $\varphi$  to the horizon (Fig. 15.2) is considered.

At the free surface, the kinematic BC is taken in the form

$$\left. \frac{dv(y)}{dy} \right|_{y=h} = 0. \quad (15.21)$$

The velocity, flow rate, and shear stress are determined by the well-known expressions:

$$\begin{aligned} v_{\text{incl}}(y) &= \frac{\rho g \sin \alpha}{2\mu} y (2h - y), \\ Q_{\text{incl}} &= \frac{\rho g \sin \alpha}{3\mu} h^3, \\ \tau_{\text{incl}} &= \rho g \sin \alpha (h - y) = \tau_b \left(1 - \frac{y}{h}\right), \end{aligned} \quad (15.22)$$

where  $\tau_b = \rho g h \sin \alpha$  is the shear stress at the bottom of the duct.

For the same solution with velocity slip BC, one can obtain from (15.16) and (15.21) the following expressions:

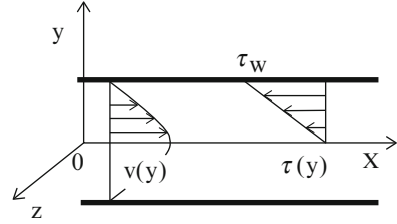
$$\begin{aligned} v_{\text{incl}}^{\text{slip}}(y) &= \frac{\rho g \sin \alpha}{2\mu} (2(\alpha h + \beta) + y(2h - y)), \\ Q_{\text{incl}}^{\text{slip}} &= \frac{\rho g \sin \alpha}{\mu} h \left( \alpha h + \beta + \frac{h^2}{3} \right), \\ \tau_{\text{incl}}^{\text{slip}} &= \tau_b \left(1 - \frac{y}{h}\right), \end{aligned} \quad (15.23)$$

where  $\alpha, \beta$  are the slip coefficients for the bottom.

Comparing (15.22) and (15.23), one may conclude that

$$\begin{aligned} v_{\text{incl}}^{\text{slip}}(0) &= \frac{\rho g \sin \alpha}{\mu} (\alpha h + \beta) > 0, \quad v_{\text{incl}}^{\text{slip}}(h) = \frac{\rho g \sin \alpha}{2\mu} (2(\alpha h + \beta) + h^2) > v_{\text{incl}}(h), \\ Q_{\text{incl}}^{\text{slip}} &> Q_{\text{incl}}, \quad \tau_{\text{incl}}^{\text{slip}} &= \tau_{\text{incl}} \end{aligned}$$

**Fig. 15.3** Poiseuille flow between the parallel plates



for positive  $\alpha, \beta$  values. Since in some papers the negative  $C_2$  coefficient in (15.12) has been reported, the comparative results are definitely valid for  $C_1 > C_2 \text{Kn}/h$ .

### 15.3.4 Poiseuille Flow Between the Parallel Plates

Laminar flow  $v_x = v(y)$  between the plates  $y = \pm h$  (Fig. 15.3) driven by the pressure drop  $\Delta p = p^+ - p^-$  between the inlet  $p|_{x=0} = p^+$  and outlet  $p|_{x=L} = p^-$  at the no-slip BC has the following distributions of the flow profiles, volumetric flow rate, and shear stress.

$$v_{\text{paral}}(y) = \frac{\Delta p h^2}{2\mu L} \left( 1 - \left( \frac{y}{h} \right)^2 \right), \quad Q_{\text{paral}} = \frac{2}{3} \frac{\Delta p h^3}{\mu L}, \quad \tau_{\text{paral}} = \frac{\tau_w}{h} y, \quad (15.24)$$

where  $\tau_w = \Delta p h/L$  is the wall shear stress.

The same parabolic velocity profile at the slip BC (15.16) and different slip coefficients of the upper and lower plates has the form

$$\begin{aligned} v_{\text{paral}}^{\text{slip}}(y) &= \frac{\Delta p}{\mu L} \left( \frac{h^2}{2} + \frac{\beta_1 \alpha_2 - \beta_2 \alpha_1 + h(\beta_1 + \beta_2 - 2\alpha_1 \alpha_2) + h^2(\alpha_1 + \alpha_2)}{2h - (\alpha_1 - \alpha_2)} \right. \\ &\quad \left. + \frac{\beta_1 - \beta_2 - h(\alpha_1 + \alpha_2)}{2h - (\alpha_1 - \alpha_2)} y - \frac{y^2}{2} \right), \\ Q_{\text{paral}}^{\text{slip}} &= \frac{2}{3} \frac{\Delta p h}{\mu L} \frac{2h^3 + 2h^2(\alpha_1 + \alpha_2) + 3h(\beta_1 + \beta_2 - 2\alpha_1 \alpha_2) + 3(\beta_1 \alpha_2 - \beta_2 \alpha_1)}{2h - (\alpha_1 - \alpha_2)}, \\ \tau_{\text{paral}}^{\text{slip}} &= \frac{\tau_w}{h} \left( \frac{\beta_1 - \beta_2 - h(\alpha_1 + \alpha_2)}{2h - (\alpha_1 - \alpha_2)} - y \right). \end{aligned} \quad (15.25)$$

Comparative study of (15.24) and (15.25) revealed that the differences in the shear rates at no-slip and slip BC are constant and become negative:

$$\tau_{\text{paral}}^{\text{slip}} - \tau_{\text{paral}} = \frac{\Delta p}{L} \frac{\beta_1 - \beta_2 - h(\alpha_1 + \alpha_2)}{2h - (\alpha_1 - \alpha_2)} < 0$$

when

$$\left[ \begin{array}{l} \alpha_1 - \alpha_2 < 2h, \\ \beta_1 - \beta_2 < h(\alpha_1 + \alpha_2) \end{array} \right] \text{ or } \left[ \begin{array}{l} \alpha_1 - \alpha_2 > 2h, \\ \beta_1 - \beta_2 > h(\alpha_1 + \alpha_2) \end{array} \right]. \quad (15.26)$$

With the constraint (15.26), the corresponding difference in the flow rates

$$Q_{\text{paral}}^{\text{slip}} - Q_{\text{paral}} = 2 \frac{\Delta p h}{\mu L} \frac{\beta_1 \alpha_2 - \beta_2 \alpha_1 + h(\beta_1 + \beta_2 - 2\alpha_1 \alpha_2) + h^2(\alpha_1 + \alpha_2)}{2h - (\alpha_1 - \alpha_2)}$$

could be either positive or negative, but a wide set of the parameters  $\alpha_1, \alpha_2, \beta_1, \beta_2$  providing the condition  $Q_{\text{paral}}^{\text{slip}} > Q_{\text{paral}}$  could be chosen among them. In that way, the shear rate and apparent viscosity could be decreased by the wall slip BC providing bigger flow rate in the channel flow at the same pressure drop  $\Delta p$ . In [44, 55] the solution of the problem is given for the plates with the same slip coefficients.

### 15.3.5 Poiseuille Flow in the Circular Tubes

The pressure-driven ( $\Delta p = p^+ - p^-$ ) axisymmetric ( $\partial/\partial\theta = 0$ ) laminar flow  $v_x = v(r)$  through the tube with axis, radius  $R$ , and length  $L$  is described by the following velocity profile, flow rate, and shear stress:

$$v_{\text{pois}} = v_{\text{max}} \left( 1 - \frac{r^2}{R^2} \right), \quad Q_{\text{pois}} = \frac{\Delta p}{8\mu L} \pi R^4, \quad \tau_{\text{pois}} = \tau_{\text{wall}} \frac{r}{R}, \quad (15.27)$$

where  $v_{\text{max}} = \Delta p R^2 / (4\mu L)$ ,  $\tau_{\text{wall}} = -\Delta p R / 2L$ .

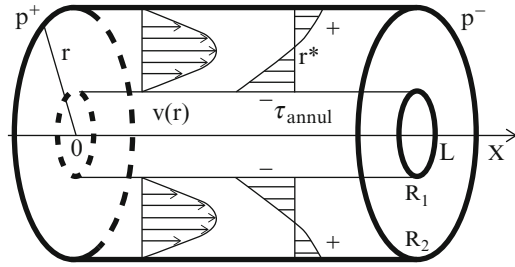
For the micro- and nanofluids with BC (15.16), the same solution has the form [19, 44, 55]

$$\begin{aligned} v_{\text{pois}}^{\text{slip}}(r) &= \frac{\Delta p R^2}{4\mu L} \left( 1 - \left(\frac{r}{R}\right)^2 + 2\frac{\beta - \alpha R}{R^2} \right), \\ Q_{\text{pois}}^{\text{slip}} &= \frac{\Delta p}{8\mu L} \pi R^2 (R^2 + 4(\beta - \alpha R)), \\ \tau_{\text{pois}}^{\text{slip}} &= \tau_{\text{pois}}, \end{aligned} \quad (15.28)$$

where  $\alpha, \beta$  are the slip coefficients for the circular wall.

Comparison of (15.27) and (15.28) demonstrates that  $Q_{\text{pois}}^{\text{slip}} > Q_{\text{pois}}$  when  $\beta/\alpha > R$  or at the high Knudsen numbers  $\text{Kn} > R \cdot C_1/C_2$ . According to the data for  $C_{1,2}$  presented in [44], the nanofluid flow benefits of higher efficiency due to bigger flow rates at the same pressure drop drive the flow. Note that for the microfluids ( $\beta = 0$ ), the slip BC flow rate is always lower than the classical flow.

**Fig. 15.4** Schema of the Poiseuille flow between coaxial cylinders



### 15.3.6 Poiseuille Flow in the Tubes of Elliptic Cross Section

Similar pressure-driven laminar flow through the tube with axis  $Oz$  and elliptic cross section  $\frac{x^2}{a^2} + \frac{y^2}{b^2} = 1$  with semimajor axes  $a$  and  $b$  is described by the following distributions:

$$v_{\text{ell}}(x, y) = V_{\text{max}} \left( 1 - \frac{x^2}{a^2} - \frac{y^2}{b^2} \right), \quad Q_{\text{ell}} = \frac{\pi a^3 b^3 \Delta p}{4\mu L (a^2 + b^2)}, \quad (15.29)$$

$$\tau_{xz} = \frac{\Delta p}{L} \frac{b^2 x}{a^2 + b^2}, \quad \tau_{yz} = \frac{\Delta p}{L} \frac{a^2 y}{a^2 + b^2},$$

where  $V_{\text{max}} = \frac{\Delta p}{2\mu L} \frac{a^2 b^2}{a^2 + b^2}$ .

In this case the solution of the Navier–Stokes equations with the slip BC (15.16) has the form

$$v_{\text{ell}}^{\text{slip}}(x, y) = V_{\text{max}} \left( 1 - \frac{x^2 + 2(\alpha a - \beta)}{a^2} - \frac{y^2 + 2(\alpha b - \beta)}{b^2} \right) \quad (15.30)$$

$$Q_{\text{ell}}^{\text{slip}} = Q_{\text{ell}} \left( 1 + \frac{\beta - \alpha a}{a^2} + \frac{\beta - \alpha b}{b^2} \right),$$

while the shear stress field keeps the same form (15.29).

Similar shift of the velocity profile and increase in the volumetric rate will be obtained when  $\beta/\alpha > \max\{a, b\}$  or  $\text{Kn} > \max\{a, b\} \cdot C_1/C_2$ .

### 15.3.7 Poiseuille Flow Between Two Coaxial Circular Tubes

The same pressure-driven flow through the annulus between the concentric tubes with long axis  $Ox$  and radii  $R_1$  and  $R_2$  is considered (Fig. 15.4).

Classical Navier–Stoke solution for the no-slip boundary conditions at both circular walls is

$$\begin{aligned}
v_{\text{annul}}(r) &= \frac{\Delta P}{4\mu L} \left( R_1^2 - r^2 + \frac{R_2^2 - R_1^2}{\ln(R_2/R_1)} \ln\left(\frac{r}{R_1}\right) \right), \\
Q_{\text{annul}} &= \frac{\pi \Delta P}{8\mu L} \left( R_2^4 - R_1^4 - \frac{(R_2^2 - R_1^2)^2}{\ln(R_2/R_1)} \right), \\
\tau_{\text{annul}} &= \frac{\Delta P}{4L} \left( \frac{R_2^2 - R_1^2}{\ln(R_2/R_1)} \frac{1}{r} - 2r \right),
\end{aligned} \tag{15.31}$$

The velocity in (15.31) is maximal and shear stress is zero:

$$v_{\text{annul}} = u_{\text{max}} \equiv \frac{\Delta P}{4\mu L} \left( R_1^2 - \frac{R_2^2 - R_1^2}{2 \ln(R_2/R_1)} \left( 1 - \ln \frac{(R_2/R_1)^2 - 1}{\ln(R_2/R_1)} \right) \right), \quad \tau_{\text{annul}} = 0,$$

$$\text{at } r = r^* = \sqrt{\frac{R_2^2 - R_1^2}{2 \ln(R_2/R_1)}} \text{ (Fig. 15.4).}$$

When the flow is subjected to the slip BC (15.16) with different slip coefficients at the inner and outer tubes, the solution has the form

$$\begin{aligned}
v_{\text{annul}}^{\text{slip}}(r) &= \frac{\Delta P}{4\mu LZ} \left( R_1 (R_1^2 - 2\alpha_1 R_1 + 2\beta_1) (R_2 \ln R_2 - \alpha_2) - R_2 (R_2^2 - 2\alpha_2 R_2 + 2\beta_2) \right. \\
&\quad \left. \times (R_1 \ln R_1 - \alpha_1) (R_2^2 - R_1^2 + 2(\alpha_1 R_1 - \alpha_2 R_2 + \beta_2 - \beta_1)) R_1 R_2 \ln(r) - r^2 \right), \\
Q_{\text{annul}}^{\text{slip}} &= \frac{\pi \Delta P}{8\mu LZ} \left( 2(R_1 (R_1^2 - 2\alpha_1 R_1 + 2\beta_1) (R_2 \ln R_2 - \alpha_2) - R_2 (R_2^2 - 2\alpha_2 R_2 + 2\beta_2) \right. \\
&\quad \left. \times (R_1 \ln R_1 - \alpha_1)) (R_2^2 - R_1^2) + \frac{R_1 R_2}{2} (R_2^2 - R_1^2 + 2(\alpha_1 R_1 - \alpha_2 R_2 + \beta_2 - \beta_1)) \right. \\
&\quad \left. \times (2R_2^2 \ln R_2 - 2R_1^2 \ln R_1 - R_2^2 + R_1^2) - (R_2^4 - R_1^4) \right), \\
\tau_{\text{annul}}^{\text{slip}} &= \frac{\Delta P}{4LZ} \left( \frac{R_1 R_2}{r} (R_2^2 - R_1^2 + 2(\alpha_1 R_1 - \alpha_2 R_2 + \beta_2 - \beta_1)) - 2r \right),
\end{aligned} \tag{15.32}$$

where  $Z = R_1 R_2 \ln(R_2/R_1) + \alpha_1 R_2 - \alpha_2 R_1$ .

In this case,  $v_{\text{annul}}^{\text{slip}}$  reaches its maximum at

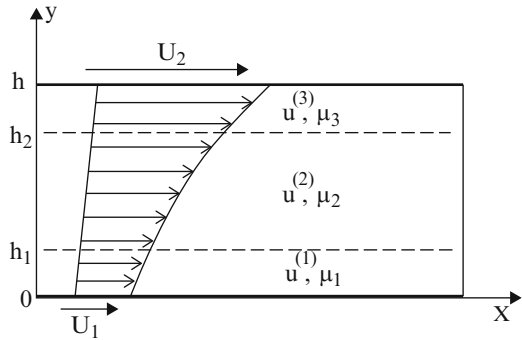
$$r = r^{**} = \sqrt{\frac{R_2^2 - R_1^2 + 2(\alpha_1 R_1 - \alpha_2 R_2 + \beta_2 - \beta_1)}{2(\ln(R_2/R_1) + \alpha_1/R_1 - \alpha_2/R_2)}} \text{ and } r^{**} > r^* \text{ or } r^{**} < r^* \text{ depending on}$$

the slip coefficients  $\alpha_{1,2}, \beta_{1,2}$  and radii  $R_{1,2}$ . Like in the circular tubes (15.27), (15.28), one can reach  $Q_{\text{annul}}^{\text{slip}} > Q_{\text{annul}}$  by a proper choice of the walls' (i.e., slip) parameters  $\alpha_1, \alpha_2, \beta_1, \beta_2$  depending on the radii  $R_1, R_2$ . In [55] the solution (15.32) is presented in the simplified form at  $\alpha_1 = \alpha_2$  and  $\beta_1 = \beta_2$ .

## 15.4 Layered Laminar Flow of Immiscible Micro-/Nanofluids Between Moving Plates

Shear-driven laminar flow of three liquids with different viscosities  $\mu_{1,2,3}$  between two parallel plates moved with velocities  $U_1$  and  $U_2 > U_1$  (Fig.15.5) is considered. The thickness of the layers  $h_1, h_2 - h_1$ , and  $h - h_2$  are assumed to be constant. The differences in the viscosities can be produced by different concentrations of the micro-/nanoparticles in the uniform suspension caused by interaction with walls.

**Fig. 15.5** Laminar flow of three fluids between moving plates



Then the layers with  $\mu_1$  and  $\mu_3$  are thin in comparison to the innermost layer of the fluid with viscosity  $\mu_2$  and can be considered as boundary layers.

The solution of the Navier–Stokes equations in this case is given by linear function (see Sect. 3.1):

$$u^{(j)} = C_1^{(j)} y + C_2^{(j)}, \tag{15.33}$$

where  $j = 1, 2, 3$  and  $C_{1,2}^{(j)}$  are constants determined from the slip conditions at the walls

$$\begin{aligned} \left( u^{(1)} - \alpha_1 \frac{du^{(1)}}{dy} + \beta_1 \frac{d^2u^{(1)}}{dy^2} \right) \Big|_{y=0} &= U_1, \\ \left( u^{(3)} - \alpha_2 \frac{du^{(3)}}{dy} + \beta_2 \frac{d^2u^{(3)}}{dy^2} \right) \Big|_{y=h} &= U_2, \end{aligned} \tag{15.34}$$

and velocity and shear stress continuity conditions at the interfaces

$$\begin{aligned} \left( u^{(1)} - u^{(2)} \right) \Big|_{y=h_1} &= 0, & \left( \mu_1 \frac{du^{(1)}}{dy} - \mu_2 \frac{du^{(2)}}{dy} \right) \Big|_{y=h_1} &= 0, \\ \left( u^{(2)} - u^{(3)} \right) \Big|_{y=h_2} &= 0, & \left( \mu_2 \frac{du^{(2)}}{dy} - \mu_3 \frac{du^{(3)}}{dy} \right) \Big|_{y=h_2} &= 0. \end{aligned} \tag{15.35}$$

Substitution of (15.33) into (15.34) and (15.35) gives the expressions for  $C_{1,2}^{(1,2,3)}$ , and finally the velocities in the non-dimensional form are

$$\begin{aligned} V_1 &= \frac{1}{\Delta_c} [\gamma_3 + \gamma_2 - \gamma_1 + \eta_2 (u - 1) Y], \\ V_2 &= \frac{1}{\Delta_c} [\gamma_3 + \gamma_2 u - \gamma_1 u + \eta_1 (u - 1) Y], \\ V_3 &= \frac{1}{\Delta_c} [\gamma_3 + \gamma_2 u - \gamma_1 + \eta_1 \eta_2 (u - 1) Y], \end{aligned} \tag{15.36}$$

where  $V_{1,2,3} = u^{(1,2,3)}/U_1$ ,  $Y = y/h$  are dimensionless coordinates,  $\Delta_c = l_1 \eta_2 (1 - \eta_1) - l_2 \eta_1 (1 - \eta_2) + \eta_1 + (a_1 \eta_2 - a_2 \eta_1) \text{Kn}$ ,  $l_{1,2} = h_{1,2}/h$ ,  $\eta_{1,2} = \mu_{1,2}/\mu_3$ ,  $a_{1,2} = \alpha_{1,2}/h$ ,  $u = U_2/U_1 > 1$ ,  $\gamma_1 = \eta_1 l_2 (1 - \eta_2)$ ,  $\gamma_2 = \eta_2 l_1 (1 - \eta_1)$ ,  $\gamma_3 = \eta_1 (1 - a_2 \text{Kn}) + u \eta_2 a_1$ .

From (15.36) one may compute the flow rate

$$Q = \int_0^{h_1} u^{(1)}(y)dy + \int_{h_1}^{h_2} u^{(2)}(y)dy + \int_{h_2}^h u^{(3)}(y)dy.$$

and obtain for the non-dimensional flow rate  $q = Q/(U_1 h)$  the following expression

$$q = \frac{1}{2\Delta} [\eta_2 (1 - \eta_1) (2u - (1 - u) l_1) l_1 - \eta_1 (1 - \eta_2) (2u - (1 - u) l_2) l_2 + \eta_1 (1 + u) + 2 (\eta_2 a_1 u - \eta_1 a_2) \text{Kn}]. \quad (15.37)$$

When  $l_1 = 0$ ,  $l_2 = 1$ ,  $\eta_1 = \eta_2 = 1$ , we have the uniform flow, and (15.36) and (15.37) coincide with (15.17).

The laminar flow between the parallel plates is the basic model for the rotational viscosimeters. Let us assume one plate corresponds to a moving wall ( $U_1$ ), while another experiences the viscous shear stress  $\tau_3$ . Then the apparent viscosity can be computed as  $\mu_{\text{app}} = h\tau_3/U_1$  which gives after the substitution of (15.37) the following dimensional expression

$$\mu_{\text{app}} = \frac{\mu_1 \mu_2 \mu_3 h}{h_1 \mu_2 (\mu_3 - \mu_1) - h_2 \mu_1 (\mu_3 - \mu_2) + h \mu_1 \mu_3 + (\alpha_1 \mu_2 - \alpha_2 \mu_1) \mu_3 \text{Kn}}. \quad (15.38)$$

## 15.5 Results and Discussions

The velocity profiles are presented schematically in Fig.15.5. Numerical calculations of the flow rate have been carried out at the following values of the parameters  $l_{1,2} = 0.1, 0.2, 0.3$ ,  $a_{1,2} = 0.5, 1, 1.5$ ,  $\eta_{1,2} = 0.25, 0.5, 1, 2, 4$ , and  $\text{Kn} = 0.02, 0.05, 0.08, 0.2, 0.5, 0.8$  and flow regimes  $u = 1; 2; 5; 8$ . The dependencies of the non-dimensional flow rate  $q$  on one of the parameters  $u, a_{1,2}, \eta_{1,2}, l_{1,2}$  while others are kept constant are presented in Fig. 15.6. Here  $\text{Kn} = 0.02, 0.05, 0.08$  correspond to the microfluids and  $\text{Kn} = 0.2, 0.5, 0.8$  for nanofluids.

When the difference between the velocities of the two plates increases, the flow rate increases proportionally to the  $\text{Kn}$  number that determines the tangential slip of the particles (Fig. 15.6a). When  $U_2/U_1 = 8$ , the maximal difference in 2 times is observed for  $\text{Kn} = 0.2$  and  $\text{Kn} = 0.8$ . When the slip coefficient  $a_2$  increases, the flow rate becomes bigger due to accumulation of the slip at lower, upper, or both plates (Fig. 15.6b).

The dependence  $q(\eta_1)$  (Fig. 15.6c) has been computed at  $\eta_2 = 1$ , while the dependence  $q(\eta_2)$  (Fig. 15.6d) has been computed at  $\eta_1 = 1$ . In both cases the two-layer flow with one boundary layer has been considered. When the viscosity is bigger in the layer which is in contact with the faster moving plate, the flow rate decreases. In that way the layer with decreased viscosity serves as a lubrication that



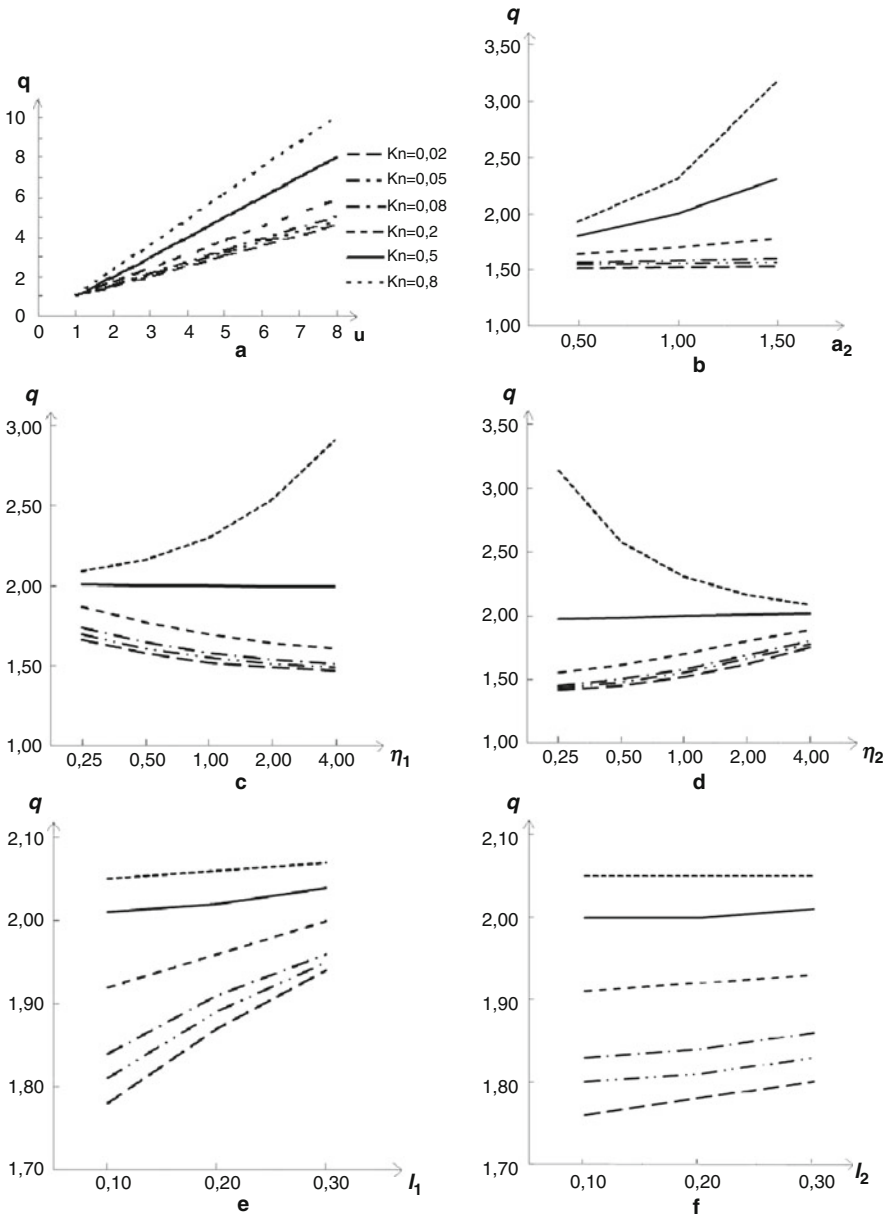


**Fig. 15.6** Dependencies  $q$  on  $u$ (a),  $a_2$ (b),  $\eta_1$ (c),  $\eta_2$ (d),  $l_1$ (e),  $l_2$ (f) for different values  $Kn = 0.02, 0.05, 0.08, 0.2, 0.5, 0.8$

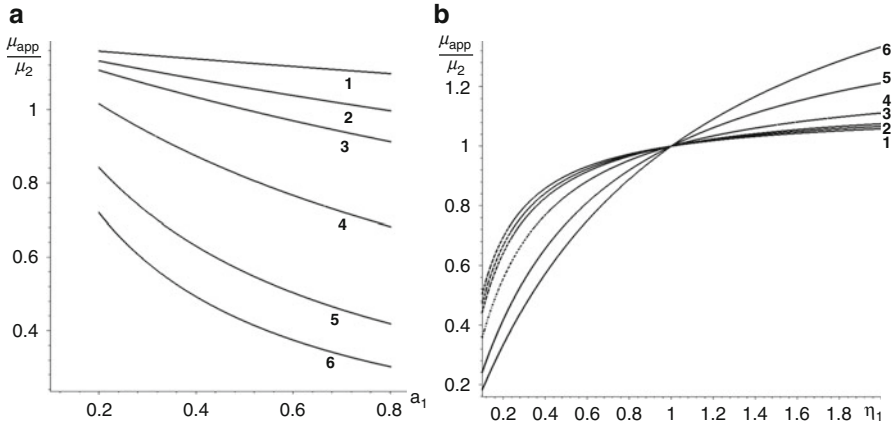


**Fig. 15.7** Dependencies  $\mu_{app}/\mu_2(a_1)$  at  $a_2 = 0.1$ ,  $\eta_2 = 0.25$  (a) and  $\mu_{app}/\mu_2(\eta_1)$  at  $a_{1,2} = 0.5$ ,  $\eta_2 = 1$  (b) when  $l_{1,2} = 0.1$ ; the curves 1–6 correspond to  $Kn = 0.02, 0.05, 0.08, 0.2, 0.5, 0.8$

decreases the resistivity to the flow and therefore increases the flow rate. Anyway, in the nanofluid flows, the opposite effect is observed (Fig. 15.6c, d at  $Kn = 0.8$ ) because the terms with  $Kn$  in (15.37) become significant. At different sets of the values  $u, l_{1,2}, \eta_{1,2}, \alpha_{1,2}$ , the sign  $\partial q/\partial \eta_{1,2}$  could be either positive or negative.

The dependencies  $q(l_{1,2})$  have been computed at  $\eta_1 = 0.25$ ,  $\eta_2 = 2$ . When the thickness of the faster layer with lower viscosity increases, the flow rate also increases (Fig. 15.6e). When the thickness of the slower layer with high viscosity increases, the flow rate varies insignificantly (Fig. 15.6f).

The computed apparent viscosity (15.38) differs from the viscosity  $\mu_2$  of the core fluid  $\mu_{app} > \mu_2$  when  $h_1\mu_2(\mu_3 - \mu_1) - h_2\mu_1(\mu_3 - \mu_2) + (\alpha_1\mu_2 - \alpha_2\mu_1)\mu_3Kn < 0$  and vice versa.

For instance, when  $\mu_2 < \mu_3 < \mu_1$  and  $\alpha_1\mu_2 < \alpha_2\mu_1$ , the accepted formula for the apparent viscosity will give the overestimated viscosity values; when  $\mu_2 > \mu_3 > \mu_1$  and  $\alpha_1\mu_2 > \alpha_2\mu_1$ , the computed values will be underestimated. In the case presented in Fig. 15.5, the Magnus forces will decrease/increase concentration of particles in the lower/upper layer. The case  $\mu_1 < \mu_2 < \mu_3$  corresponds to the velocity distributions presented in Fig. 15.5; the relationship between  $\mu_{app}$  and  $\mu_2$  will depend on the whole set of the model parameters. Some computational results are given in Fig. 15.7.

The measured apparent viscosity of the fluid will be overestimated for the microfluids with  $Kn \geq 0.7$  at different velocity slip coefficients  $a_1$  (curves 1–3 in Fig. 15.7a) and underestimated in the nanofluids with  $Kn > 0.2$  (curves 4–6 in Fig. 15.7a). When  $\eta_1 < 1$  (or  $\mu_1 < \mu_3$ ), the apparent viscosity is underestimated, while when  $\mu_1 > \mu_3$ , the viscosimeter gives correct values  $\mu_{app} \approx \mu_2$  for the microfluids (curves 1–3 in Fig. 15.7b). The obtained results allow correction of the viscosity measurements of the nanofluids and microfluids in the viscosimeters.

## 15.6 Conclusions

A review of the analytical solutions for the pressure-driven Poiseuille flow between the parallel plates, through the circular and elliptic tubes, and the annulus between the two coaxial circular tubes, as well as the shear-driven Couette flows between the moving parallel plates, rotating coaxial cylinders, and inclined duct, is generalized for the first- and second-order velocity slip BC and different slip coefficients at the opposite walls. It was found that by a proper choice of the wall coefficients, one can reach lower shear stress and bigger flow rates at the same pressure drop or shear rate at the expense of tangential velocity slip in the micro- and nanochannels.

Experimental measurements of viscosities of the microfluids and nanofluids in viscosimeters are based on accepted formulae that may be erroneous due to velocity slip BC and concentration phenomena. The Magnus forces may appear due to rotation of the moving particles as well as their interaction with the walls. Then the concentrations of the micro- or nanoparticles in the layers which are in contact with the walls may be bigger or lower than in the core of the flow. As it was shown, the apparent viscosity computed for the rotational viscosimeter accounting to the concentration effects could give overestimated and underestimated values of the viscosity. Using the obtained regularities, the proper conditions of the experiments can be developed to obtain the values  $\mu_{\text{app}} \approx \mu_2$ . The corresponding dependencies for the capillary viscosimeters can also be computed in the same way for the layered laminar Poiseuille flows in the tubes, channels, and annulus given in Chap. 3.

## References

1. Islam N (2012) Microelectromechanical systems and devices. InTech Open Access book publisher. <https://www.intechopen.com/books/microelectromechanical-systems-and-devices>
2. Ghodssi R, Lin P (2011) MEMS materials and processes handbook, vol Vol.1. Springer Series on MEMS Reference Shelf, Springer US
3. Liou W, Fang Y (2005) Microfluid mechanics: principles and modeling (nanoscience and technology). McGraw-Hill Education Publ, New York
4. Tay FEH (2002) Microfluidics and BioMEMS applications, vol Vol.10. Springer Series in Microsystems, Springer US
5. Karniadakis GE, Beskok A, Aluru N (2005) Microflows and nanoflows: fundamentals and simulation, Interdisciplinary Applied Mathematics Series, vol 29. Springer-Science, New York
6. Neto C, Evans DR, Bonaccorso E, Butt H-J, Craig VSJ (2005) Boundary slip in Newtonian liquids: a review of experimental studies. Rep Prog Phys 68:2859–2897
7. Bechert DW, Bruse M, Hage W, Meyer R (2004) Fluid mechanics of biological surfaces and their technological application. Naturwissenschaften 87:157–171
8. Christodoulou KN, Scriven LE (1992) The fluid mechanics of slide coating. J Fluid Mech 99:39–55
9. Beavers GS, Joseph DD (1967) Boundary conditions at a naturally permeable wall. J Fluid Mech 30:197–207
10. Denn MM (1990) Issues in viscoelastic fluid mechanics. Annu Rev Fluid Mech 22:13–34
11. Mohammadi B, Pironneau O (1974) Analysis of the k-epsilon turbulence model. John Wiley&Sons, Masson

12. Sbragaglia M, Prosperetti A (2007) Effective velocity boundary condition at a mixed slip surface. *J Fluid Mech* 578:435–451
13. Sidik NAC, Mohammed HA, Alawi OA, Samion S (2014) A review on preparation methods and challenges of nanofluids. *Intern Commun Heat Mass Transfer* 54:115–125
14. Lim CY, Shu C, Niu XD, Chew YT (2002) Application of lattice Boltzmann method to simulate microchannel flows. *Phys Fluids* 14:2299–2308
15. Mala GM, Li DQ (1999) Flow characteristics of water in microchannels. *Int J Heat Fluid Flow* 20:142–148
16. Tang GH, Zhuo L, He YL, Tao WQ (2007) Experimental study of compressibility, roughness and rarefaction influences on microchannel flow. *Int J Heat Mass Transfer* 50:2282–2295
17. Rice CL, Whitehead R (1965) Electrokinetic flow in a narrow cylindrical capillary. *J Phys Chem* 69:4017–4021
18. Kizilova N (2015) Space-filling trees for microfluidic applications: a review. In: Fesenko O, Yatsenko L (eds) *Nanoplasmonics, nano-optics, nanocomposites, and surface studies*. Springer Proceedings in Physics, Cham, pp 7–23
19. Gad-el-Hak M (2006) MEMS introduction and fundamentals, *The MEMS handbook*, 2nd edn. Taylor & Francis Group, LLC, Boca Raton
20. Zhang W-M, Meng G, Wei X (2012) A review on slip models for gas microflows. *Microfluid. Nano* 13:845–882
21. Wu PY, Little WA (1983) Measurement of the friction factors for the flow of gases in very fine channels used for microminiature joule–Thomson refrigerators. *Cryogenics* 23:273–277
22. Urbanek W, Zemel JN, Bau H (1993) An investigation of the temperature dependence of Poiseuille numbers in microchannel flow. *J Micromech Microeng* 3:206–208
23. Peng XF, Peterson GP, Wang BX (1994) Frictional flow characteristics of water flowing through rectangular channels. *Exp Heat Transfer* 7:249–264
24. Papautsky I, Gale BK, Mohanty S, Ameal TA, Frazier AB (1999) Effects of rectangular microchannel aspect ratio on laminar friction constant, vol vol 3877. SPIE conf. on Microfluidic Devices and Systems II, Santa Clara, pp 147–158
25. Qu WL, Mala GM, Li DQ (2000) Pressure-driven water flows in trapezoidal silicon microchannels. *Int J Heat Mass Transf* 43:353–364
26. Wang H, Wang Y (2007) Influence of three-dimensional wall roughness on the laminar flow in microtube. *Intern J Heat Fluid Flow* 28:220–228
27. Kleinstreuer C, Koo L (2004) Computational analysis of wall roughness effects for liquid flow in micro-conduits. *J Fluids Eng* 126:1–9
28. Gayev YA, Hunt JCR (2007) Flow and transport processes with complex obstructions: applications to cities, vegetation canopies and industries, vol Vol. 236. Springer Nato Science Series II: Mathematics, Physics and Chemistry, Netherlands
29. Merkle CL, Kubota T, Ko DRS (1974) An analytical study of the effects of surface roughness on boundary-layer transition. Air Force Office of Scientific Research Space and Missile System Organization, AD/A004786. Flow Research Inc. <http://www.dtic.mil/dtic/tr/fulltext/u2/a004786.pdf>
30. Corcione M (2010) Heat transfer features of buoyancy-driven nanofluids inside rectangular enclosures differentially heated at the sidewalls. *Intern J Thermal Sci* 49:1536–1546
31. Malvandi A, Ganji DD (2015) Effects of nanoparticle migration and asymmetric heating on magnetohydrodynamic forced convection of alumina/water nanofluid in microchannels. *European J Mech Ser B Fluids* 52:169–184
32. Maninen M, Taivassalo V (1996) On the mixture model for multiphase flow. *VTT Publ*, Espoo
33. Ghasemi B, Aminossadati S (2010) Brownian motion of nanoparticles in a triangular enclosure with natural convection. *Intern J Therm Sci* 49:931–940
34. Salman BH, Mohammed HA, Kherbeet AS (2012) Heat transfer enhancement of nanofluids flow in microtube with constant heat flux. *Int Comm Heat Mass Transfer* 39:1195–1204
35. Lesson M, Huang PS (1976) Poiseuille flow in a pipe with axially symmetric wavy walls. *Phys Fluids* 19:945–950

36. Jansons KM (1988) Determination of the macroscopic (partial) slip boundary condition for a viscous flow over a randomly rough surface with a perfect slip microscopic boundary condition. *Phys Fluids* 31:15–17
37. Hocking LM (1976) Moving fluid on a rough surface. *J Fluid Mech* 76:801–817
38. Michael JM, Stephen HD (1994) Slip over rough and coated surface. *J Fluid Mech* 273:801–817
39. Nikuradze J (1950) Laws of flow in rough pipes, NACA. Technical Memorandum 1292, Washington, DC
40. Kandlikar SG (2005) Roughness effects at microscale – reassessing Nikuradze’s experiments on liquid flow in rough tubes, *bull. Polish Acad Sci Tech Sci* 53:343–349
41. Maxwell JC (1879) On stresses in rarefied gases arising from inequalities of temperature. *Philos Trans R Soc* 170:231–256
42. Bird GA (1994) *Molecular gas dynamics and the direct simulation of gas flows*. Clarendon Press, Oxford
43. Gusarov AV, Smurov I (2002) Gas-dynamic boundary conditions of evaporation and condensation: numerical analysis of the Knudsen layer. *Phys Fluids* 14:4242–4255
44. Karniadakis GE, Beskok A, Aluru N (2005) *Microflows and nanoflows: fundamentals and simulation*. Interdisc Appl Math Series 29:51–77
45. Aubert C, Colin S (2001) High-order boundary conditions for gaseous flows in rectangular microducts. *Microscale Thermophys Eng* 5:41–54
46. Mo G, Rosenberger F (1990) Molecular-dynamics simulation of flow in a two-dimensional channel with atomically rough walls. *Phys Rev Ser A* 42:4688–4892
47. Chapman S, Cowling TG (1991) *The mathematical theory of non-uniform gases. An account of the kinetic theory of viscosity, thermal conduction and diffusion in gases*, Cambridge Math. Library, 3rd edn. Cambridge University Press, Cambridge
48. Seidl M, Steinheil E (1974) Measurement of momentum accommodation coefficients on surfaces characterized by Auger spectroscopy, Sims and LEED. In: Becker M, Fieberg M (eds) *Rarefied gas dynamics*, vol Vol.9. DFVLR Press, Porz-Wahn, pp E9.1–E9.2
49. Roohi E, Darbandi M (2009) Extending the Navier–Stokes solutions to transition regime in two-dimensional micro- and nanochannel flows using information preservation scheme. *Phys Fluids* 21:082001
50. Dongari N, Sharma A, Durst F (2009) Pressure-driven diffusive gas flows in micro-channels: from the Knudsen to the continuum regimes. *Microfluid Nanofluid* 6:679–692
51. Dongari N, Durst F, Chakraborty S (2010) Predicting microscale gas flows and rarefaction effects through extended Navier–Stokes–Fourier equations from phoretic transport considerations. *Microfluid Nanofluid* 9:831–846
52. Brenner H (2011) Beyond the no-slip boundary condition. *Phys Rew Ser E* 84:0463091
53. Paidoussis MD (1998) *Fluid–structure interactions: slender structures and axial flow*, vol 1. Academic Press, London
54. Rashidi V, Mirdamadi HR, Shirani E (2012) A novel model for vibrations of nanotubes conveying nanoflow. *Comput Mater Sci* 51:347–352
55. Karniadakis GE, Garimella S, Li D, Kolin S, King MN (2006) *Heat transfer and fluid flow in 545 minichannels and microchannels*. Elsevier, Singapore

**Part II**  
**Nanooptics and Photonics**

# Chapter 16

## Optimization of the Parameters of Digital Holographic Microscope

Yu. Kotsiuba, H. Petrovska, V. M. Fitio, T. Bulavinets, and Ya. V. Bobitski

### 16.1 Introduction

The modern state of micro- and nanotechnologies requires development of new approaches and methods in the diagnosis of properties of media and objects as well as research into processes and structural changes that are taking place under the influence of external factors. It is known that optical microscopy is the classical solution to these problems [1]. However, its main drawback is limited spatial resolution due to the diffraction phenomenon and the inability (or technical complexity) of the 3D visualization of the microscopic phase.

With the appearance of coherent light sources, coherent-optical methods, including methods of holographic interferometry, have become one of the most promising tools of studying the characteristics of the experimental material properties of transparent and nontransparent macro- and microobjects [2, 3]. However, application of the holographic interferometry for the study of microobjects is only possible when it is used in combination with classical microscopy. This combination allows performing qualitative and quantitative diagnosis with high sensitivity and precision, while achieving the required zoom [4, 5].

---

Y. Kotsiuba • H. Petrovska • V.M. Fitio • T. Bulavinets (✉)

Department of Photonics, Lviv Polytechnic National University, S. Bandery Str., 12, 79013, Lviv, Ukraine

e-mail: [tetiana.o.protalchuk@lpnu.ua](mailto:tetiana.o.protalchuk@lpnu.ua)

Y.V. Bobitski

Department of Photonics, Lviv Polytechnic National University, S. Bandery Str., 12, 79013, Lviv, Ukraine

Faculty of Mathematics and Natural Sciences, University of Rzeszow, Pigionia Str.1, 35959, Rzeszow, Poland

© Springer International Publishing AG 2017

O. Fesenko, L. Yatsenko (eds.), *Nanophysics, Nanomaterials, Interface Studies, and Applications*, Springer Proceedings in Physics 195,

DOI 10.1007/978-3-319-56422-7\_16

The appearance of digital recording devices significantly expanded capabilities of the holographic interferometry associated with increasing the information content and reliability of the experimental data [6–8]. Unlike the conventional interferometry, which needs two or more coherent phase fields to obtain the interferogram, digital holographic interferometry (DHI) allows, by calculation, getting the interferograms of incoherent phase fields, such as fields that existed at different times and really could not interfere with each other.

Digital double-exposure holographic interferometry allows obtaining phase difference surface that carries information about changes which occurred with the test object during the selected period of time. In this case, reconstruction of the object field and its further imaging are realized through a sequence of mathematical procedures that includes Fourier or Fresnel transform [9, 10], numerical algorithms of phase unwrapping, and digital image processing [11].

Digital holographic microscopy (DHM) is the application of DHI to microscopy. It is different from other microscopy methods in that it does not require focused recording of an object image. Object wave is projected by the microscope lens onto the detector plane. During the reconstruction with numerical methods, the focal length can be selected to obtain a clear object image. Once you've processed the image stack, you can visualize the scene in pseudo-3D. Applying the angular scan to the object, you get access to the tomographic information [12].

DHM is sensitive to deformation in the submicron range. Besides, it is a noncontact and nondestructive method for studying static and dynamic characteristics of objects in micro- and nanosystem engineering [13].

This allows creating systems for automatic measuring of thin-film thickness [14] and rapid nondestructive measurement of the form [15] and the position in space of the microscopic particle with nanometer resolution. This resolution allows studying the Brownian motion of particles in water using DHM at 30 fps (frames per second) [16].

DHM is widely used in biology and medicine [17–19]. The quantitative phase microscopy (QPM) has recently become a powerful tool in the study of living cells, which allows a noninvasive study of cellular structure and dynamics of the processes of separate cells with nanometer sensitivity [20, 21]. The results may be useful for monitoring specific cellular processes that are important to identify new biomarkers.

The combination of the methods of digital holography and fluorescent analysis made it possible to create a hybrid digital holographic microscope, with which you can get both the phase and fluorescent images of the sample [22]. Well known is its application for the study of cells of living organisms, when information about the structure of cells is obtained by using phase imaging, and fluorescent imaging is used for obtaining of the nucleus image. In [22, 23] it is reported about high reliability and speed of the new microscope and its great advantages over the common microscope.

As you can see, today the digital holographic microscopy is the most promising coherent-optical method for studying micro- and nano-objects. Its methods can be used as the basis for creating a number of measuring devices that provide unique



opportunities. But the demands imposed on the accuracy of these devices are rather high. So nowadays, improving the quality of the digital holographic interferogram is an urgent task [24].

However, despite the intensive development of modern methods of digital holographic microscopy, it is necessary to adapt holographic optical schemes depending on the specifics of the objects, optimize experimental conditions, and coordinate the parameters of digital registration devices with the characteristics of the optical system. The problems of improving the quality of digital holographic interferogram and increasing the resolution and sensitivity of measurements are also relevant.

## 16.2 Theoretical Description of DHI Method

The implementation of DHI methods is performed in two steps: during the first step, the digital hologram is recorded using optical scheme; during the second step, reconstruction of the holographic computer images, information processing, and its presentation in a user-friendly way are performed [25].

The following parameters of the optical scheme should be selected during the first step: the angle between the reference and the object beam ( $\theta$ ), the diameter of the aperture diaphragm ( $D$ ), the recording distance ( $z_0$ ) and the linear magnification ( $\beta$ ). The tasks of the next step are performed by programming.

Nowadays a large amount of specialized algorithms is developed in DHI. Below is an overview of all stages of obtaining and processing digital interferograms as well as modern methods of improving their quality.

### 16.2.1 Apparatus Part of DHI

The first step in the creation of DHI measurement systems is the selection of a digital camera to record digital holograms. Modern manufacturers of industrial digital cameras offer a range of devices with different functions. The choice of camera and manufacturer is defined by objectives of the study and functionality of the measuring system, so the users must choose their own configuration needed for a specific task. For DHI most important parameters of digital cameras are the size of pixel and the size of the photosensitive area. For example, camera KAF – 5010 has the following parameters: pixel size  $6 \times 6 \mu\text{m}^2$ , the number of pixels  $8208 \times 6144$ , frame size  $36 \times 48 \text{ mm}^2$ . It may be appropriate for all the needs, both in terms of pixel size and in terms of the size of the photosensitive area.

As digital cameras have a much lower resolution than the classic photosensitive materials, in digital holography there are substantial limitations to the angle  $\theta$ . In general, the spatial frequency of the recorded hologram is defined as

$$f_0 = \frac{2 \sin\left(\frac{\theta}{2}\right)}{\lambda} \tag{16.1}$$

where  $\lambda$  is the recording wavelength.

According to the Nyquist criterion [26], the minimal sampling rate must be at least twice bigger than the initial value  $f_0$ . On the other hand, a digital camera with a pixel size  $\Delta x$  allows maximal frequency value equal to

$$f_{\max} = \frac{1}{\Delta x} \tag{16.2}$$

where  $\Delta x$  is a digital camera pixel size.

Therefore, for constructing the scheme for DHI, it is necessary to select such an angle  $\theta$  at which frequency  $f_0$  is twice less than  $f_{\max}$ .

### 16.2.2 Recording Schemes

As for recording schemes, there are many possible configurations to be used for research of different types of objects. Depending on the optical recording scheme used, various mathematical expressions can be applied for reconstruction of the object field. The most common for DHI are digital Fresnel-Kirchhoff, Fresnel, and Fourier transforms. However, compared with others fast Fourier transform is faster and easier in implementation, and therefore it is better to use it in digital holography [27]. As an example we consider here the scheme for the focused image hologram recording (see Fig. 16.1).

During the recording of this hologram, the image of the object is projected by the objective on the recording plane, where it interferes with the reference wave. The

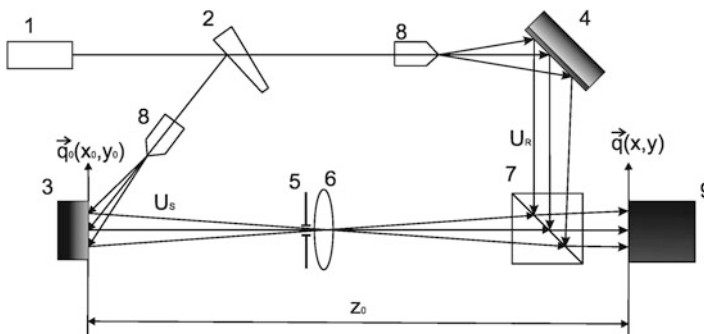


**Fig. 16.1** Optical scheme: 1 laser, 2 wedge, 3 object, 4 mirror, 5 diaphragm, 6 lens, 7 optical cube, 8 micro objective, 9 CCD

distribution of the intensity of interference between object and reference waves is recorded by using CCD or CMOS matrix.

### 16.2.3 Mathematical Description of DHI Method

Recorded digital hologram is an image having dimension of  $M \times N$  points. Depending on the chosen zoom, there is an ability to study micro or macro areas of the object. The intensity of a digital hologram at each point is determined by the expression:

$$I(\vec{q}) = |U_R(\vec{q}) + U_S(\vec{q})|^2 = |U_R|^2 + |U_S|^2 + U_R U_S^* + U_S U_R^*, \quad (16.3)$$

where  $U_S$  and  $U_R$  are the complex amplitudes of the object and reference beams, here:

$$U_R(\vec{\rho}) = A_R(\vec{\rho}) \exp[i\varphi_R(\vec{\rho})], \quad (16.4)$$

where  $A_R$  and  $\varphi_R$  represent the amplitude and phase of the reference beam;  
 $\vec{q}(x, y)$  stands for the recording plane.

The image of spatial spectrum of digital focused image hologram was obtained by Fourier transform and shown in Fig. 16.2. There are two spatial components of the object field ( $U_S(k,l)U_R^*(k,l)$  and  $U_S^*(k,l)U_R(k,l)$ ) in the spectrum of the received digital hologram, which are used during the reconstruction of the complex amplitude. After fast Fourier transform by applying the binary filter, a useful signal part should be selected.

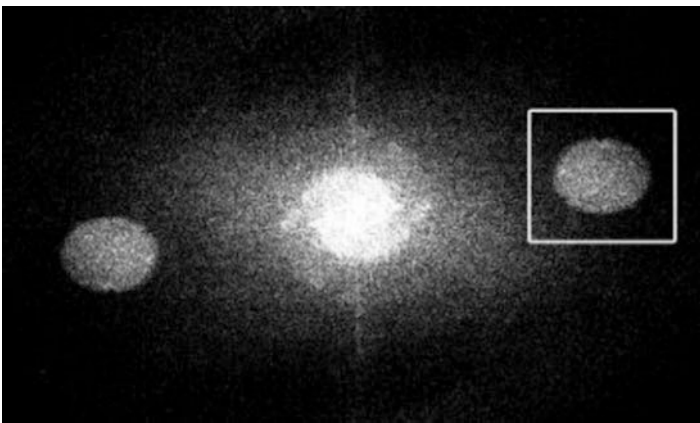


**Fig. 16.2** Spatial spectrum of a hologram (“-1” order of diffraction selected) [28]

Applying Fourier inverse transform of the selected area, we can obtain complex amplitude of the object field:

$$\Gamma(x, y) = F^{-1} \{B(x, y) \cdot F\{I(x, y)\}\}, \quad (16.5)$$

where  $B(x, y)$  represents the binary filter and

$F\{\dots\}$  is the symbol of the Fourier transform.

It should be noted that the signal selection is performed in the frequency domain by multiplying the corresponding spectrum by the specially selected binary image. The shape of useful component is similar to the image of exit pupil of the optical system. In addition, the distance of such component to the center of spectrum may vary according to the recording conditions. Therefore, one should select a special binary image for each case. The method developed in [29] allows automating the entire process of selecting the required filter to facilitate and speed up the whole process of the reconstruction of the complex amplitude of the object field. There are also algorithms, which help to determine the optimal position of the object plane [12] and to compensate phase aberrations [30] without any information about the wave vector, focal length, and recording distance.

Digital interferogram is obtained by the direct subtraction of phases:

$$\Delta\varphi = \begin{cases} \varphi_{S_2} - \varphi_{S_1}, & \text{if } \varphi_{S_2} \geq \varphi_{S_1}, \\ \varphi_{S_2} - \varphi_{S_1} + 2\pi, & \text{if } \varphi_{S_2} < \varphi_{S_1}, \end{cases} \quad (16.6)$$

where the phase is calculated from

$$\varphi_S(x, y) = \arctan \frac{\text{Im}[\Gamma(x, y)]}{\text{Re}[\Gamma(x, y)]}. \quad (16.7)$$

The obtained picture has  $2\pi$  discontinuities and is sensitive to the direction of the deformation vector.

### 16.2.4 Elimination of the Zero Order

The elimination of the zero order can significantly improve the quality of the restored digital hologram [31]. Nowadays we know several methods of its implementation, the most popular of them being the method of direct elimination and the method with a random phase shift.

In the first method [32], digital interferogram  $I(\vec{q})$ , object, and reference waves are recorded independently. So we can obtain a hologram without useless parts.

$$I'(\vec{q}) = I(\vec{q}) - |U_R(\vec{q})|^2 - |U_S(\vec{q})|^2 = U_R U_S^* + U_S U_R^* \quad (16.8)$$

In practice, the recording of such a hologram, of the reference, and then of the object waves is carried out sequentially, which generates noise fluctuations in what is obtained. That's why a slight trace of the zero order may remain.

The method with a random phase shift [33] can be used as an alternative. If we add a phase shift  $\delta$ , whose value is not a multiple of  $2\pi$ , the intensity of the hologram will correspond to

$$I''(\vec{q}) = |U_R|^2 + |U_S|^2 + U_R U_S^* \exp[i\delta] + U_S U_R^* \exp[-i\delta]. \quad (16.9)$$

By subtracting the result from the initial hologram, we obtain

$$I(\vec{q}) - I''(\vec{q}) = U_R U_S^* \exp[i\delta] + U_S U_R^* \exp[-i\delta]. \quad (16.10)$$

The exponential factor inside the brackets in (16.10) does not influence the spatial distribution of the reconstructed image.

The quality of the reconstructed hologram is identical in both methods. However, in the second method, we need two sequentially recorded images, instead of three.

### 16.2.5 Filtration of Digital Interferogram

The resulting interferogram is always modulated with speckles. The quality of the phase distribution depends on several factors such as the environmental influence, signal to noise ratio, resolution of the recording element, and fringe density. The task of filtration is to reduce the noise level without degrading the phase jumps.

Nowadays there is a great choice of adaptive and nonadaptive filtering methods. Various algorithms including median, mean, vector filtration, and multi-looking processing are used in them. In this article we consider the Fourier filtering method [34] for getting clean digital interferogram, as this method is the most effective and simple in implementation. In the proposed method, wrapped phase map is converted to fringe patterns using both cosine and sine operations. In this process, the high-frequency  $2\pi$  phase jumps in the wrapped cosine and phase map are replaced by low-frequency continuous fringes due to the periodic feature of sine functions. The resultant fringe patterns  $f(x, y)$  and  $g(x, y)$  can be expressed as

$$\begin{aligned} f(m, n) &= \cos[\Delta\varphi(m, n)] + r(m, n) \\ g(m, n) &= \sin[\Delta\varphi(m, n)] + r'(m, n) \end{aligned} \quad (16.11)$$

where  $r(m, n)$  and  $r'(m, n)$  correspond to the noise.

When applying a fast Fourier transform to the fringe patterns (here useful signal part is located in the low-frequency domain of the spectrum), using an appropriate low-pass filter, and applying Fourier inverse transform to the result, we will get clean

cosine and sine fringe patterns. Based on the reconstructed parts, a new wrapped phase map can be reconstructed by the pixel-wise function  $\arctan2(y, x)$ .

A more detailed review of spatial filtering methods based on statistical analysis is given in [35, 36]. In addition to spatial filtering improvement, the image quality in digital holographic interferometry can be achieved with the use of partially coherent illumination instead of fully coherent light. The relevant theoretical models to quantify the noise reduction depending on the spatial coherence of light are presented in [37].

### **16.2.6 Phase Unwrapping**

Next step in the digital processing is elimination of the phase discontinuities (phase unwrapping). This problem exists in DHI for a long time and today many methods of its solution are known. The main task of phase unwrapping algorithms is to find the place in the phase map, where appropriate phase shift is needed. At this moment we consider Goldstein method [38], method of phase unwrapping via graph cuts [39], and phase unwrapping method by a shift of the reconstructed field [40].

So using computer processing, we can get high-quality digital interferograms, despite the small resolution of the digital matrix compared with photosensitive media used in analog holographic interferometry.

## **16.3 Results and Discussion**

In this section we consider the application of methods intended to improve the quality of digital interferogram by applying them to interferograms obtained by the simulation of the recording process. The software was developed in the LabView 13.0 programming environment to carry out simulations. It allows simulation of digital focused image hologram recording and interferogram forming. The program allows you to set quantitative and qualitative parameters of deformations, to choose parameters of hologram recording scheme. To perform the computer processing, there were realized two methods of eliminating zero order, namely, filtration method discussed earlier and Goldstein method for phase unwrapping.

### **16.3.1 Example of the Zero-Order Elimination**

The process of improving the quality of digital interferogram starts at the stage of reconstruction of the digital hologram by eliminating zero order. This procedure eliminates unnecessary spectrum components of the digital hologram, so the contrast of the restored object image increases. To demonstrate the influence of

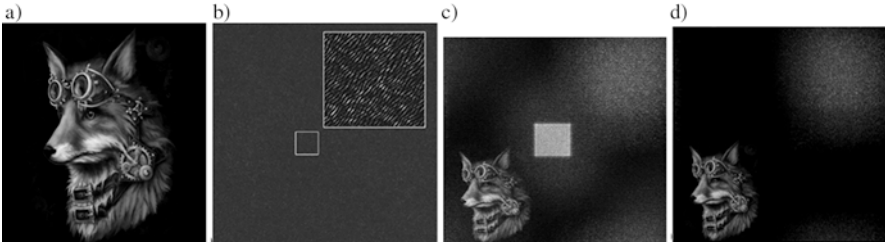


**Fig. 16.3** Digital hologram forming stages: test image (a); digital hologram (b); reconstructed image (c); reconstructed image without zero order (d)

this procedure on the quality of the restored digital hologram, the following option including both elimination methods was added to the software.

As an example, the image with size  $512 \times 512$  shown in Fig. 16.3a is the object. With the recording distance  $z_0 = 2000$  mm, pixel size  $\Delta x = 0.00001$  mm, and wavelength  $\lambda = 0.0006328$  mm, we have calculated the digital hologram shown in Fig. 16.3b. The width of the figure must be less than a quarter of the object plane so that the reconstructed image might be separated from the parasitic orders [41], so we added some zeros to form  $1024 \times 1024$  image. An example of the reconstruction is shown in Fig. 16.2c.

In Fig. 16.3d, one can see that elimination of zero order increases the image quality.

### 16.3.2 Example of Filtration in Frequency Domain

To show the quality of the filtration method proposed in the previous section, several different digital interferograms were formed using the developed software for cases of transparent and nontransparent objects. However, in this method for each single digital interferogram, you need to have a special filter, since the shape of the useful signal depends on the quantitative and qualitative changes in the state of the object. This issue greatly complicates the work of the whole algorithm. So it was proposed to use automatic binarization of spatial spectrum image with a choice of threshold to select the needed component. This solution greatly simplified the work of the algorithm and allowed better and faster filtering.

For the case of nontransparent objects, the model of a square plate divided into  $M \times N$  pixels was used as the object of study. Each pixel “emitted light” with the magnitude equal to “1,” the phase of each pixel being randomly and uniformly distributed in the range of  $[-\pi; \pi]$ . During the simulation, the “object” was deformed in different ways.

As a result of the simulation for different types of “object” deformation, we have received two holograms: in the initial state and after the deformation. Digital interferograms were calculated using Eq. (16.4) (see Fig. 16.4).



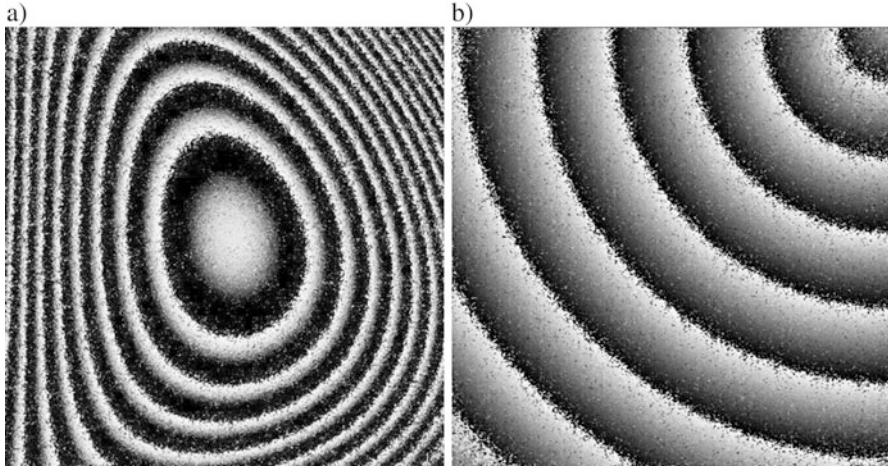


**Fig. 16.4** Digital interferograms of the object deformation

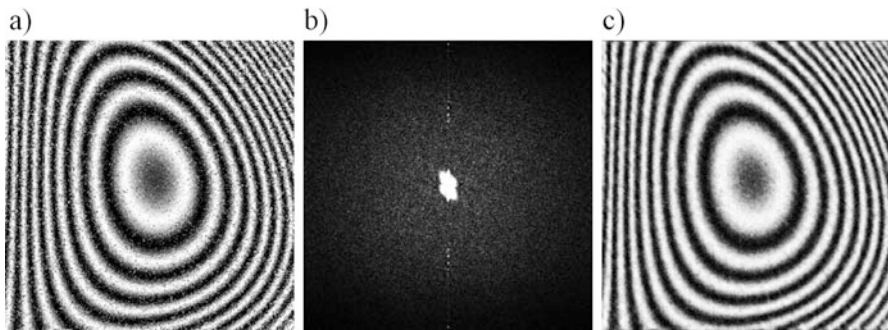


**Fig. 16.5** Cosine fringe map obtained from the wrapped phase map (a); Fourier spectrum of cosine fringe maps (b); clean cosine image (c)

As shown in Fig. 16.4, interferograms are modulated with speckles. The filtration procedure was performed by the method described earlier. A typical rewrapped fringe pattern is shown in Fig. 16.5. When applying a Fourier two-dimensional transform to the fringe patterns (Fig. 16.5b shows the Fourier spectrum of the cosine image), using appropriate low-pass filter, and applying an inverse Fourier transform to the result, we will get clean cosine and sine fringe patterns (see Fig. 16.5c). Based on both the reconstructed parts, a new wrapped phase map (see Fig. 16.6) can be reconstructed with the pixel-wise function  $\arctan_2(y, x)$ .

For the case of transparent objects as the objects of study, there were taken models of spherical (a) and cylindrical (b) microlenses. The size of raster was chosen  $5 \times 5$  mm, refracting index was 1.52, and the heights of lenses were 4.2 and 3  $\mu\text{m}$ . As a result of the simulation for different types of “object” deformation, we have received two holograms: with and without raster included in the object



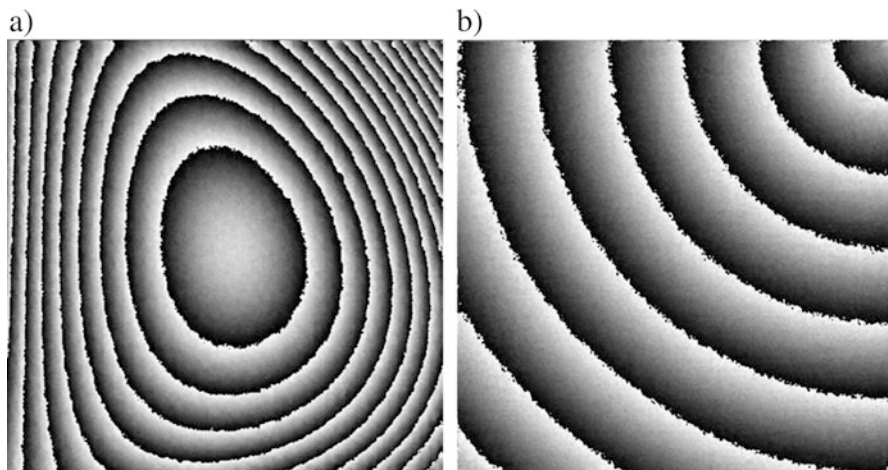


**Fig. 16.6** Filtered digital interferograms

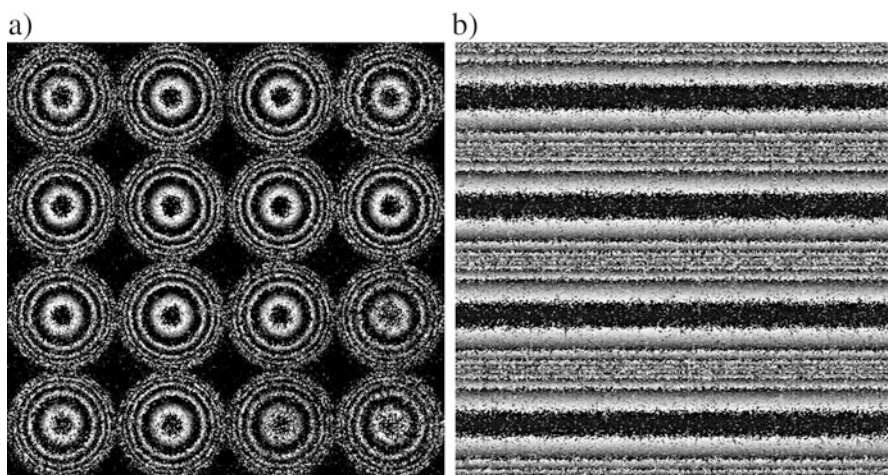


**Fig. 16.7** Digital interferograms of spherical (a) and cylindrical (b) optical rasters

beam. As for the previous case, digital interferograms were calculated using Eq. (16.4) (see Fig. 16.7).

The filtration was performed in the same way as for nontransparent objects. Examples of the cosine part, its spectrum, and filtered cosine image are shown in Fig. 16.8. The result of the filtration is shown in Fig. 16.9.

After the filtration done with the help of Goldstein method, we have visualized the received information in 3D (see Fig. 16.9a, b).

As shown in Figs. 16.6 and 16.9, speckle noise is fully eliminated, so our filtration method is suitable for different types of the studied object and deformation.

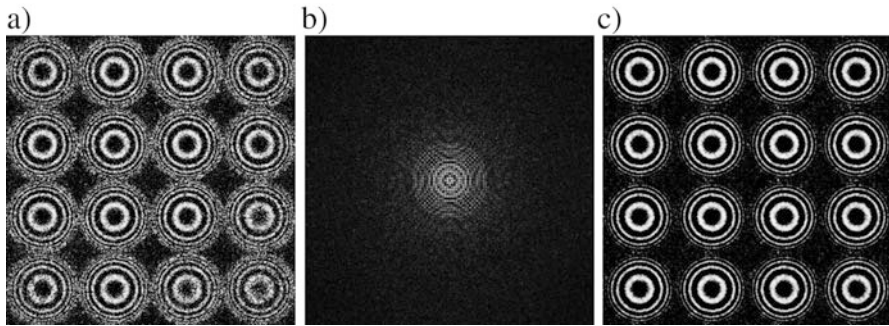


**Fig. 16.8** Cosine fringe map obtained from the wrapped phase map (a); Fourier spectrum of cosine fringe maps (b); clean cosine image (c)

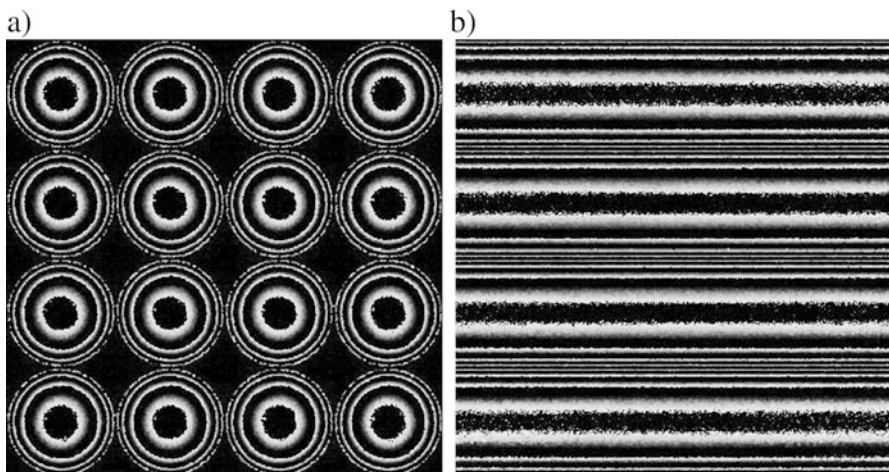


**Fig. 16.9** Filtered digital interferograms of spherical (a) and cylindrical (b) optical rasters

### 16.3.3 Drawback of the Filtration Method

Despite all the advantages, the method is not suitable for all possible cases of the studied object. For example, if there are some deviations in lenses size or refractive index in raster, the result of filtering will be unsatisfactory (Fig. 16.11b).

It is not possible to perform the unwrapping procedure in this case. Thus other approaches are needed to use in filtering of sine and cosine components of the interferogram.

The main drawback of the proposed method is that it is not possible to filter the interferogram when there occurs less than one whole fringe on it [42]. After filtering the cosine component of the interferogram (see Fig. 16.12a) by the following

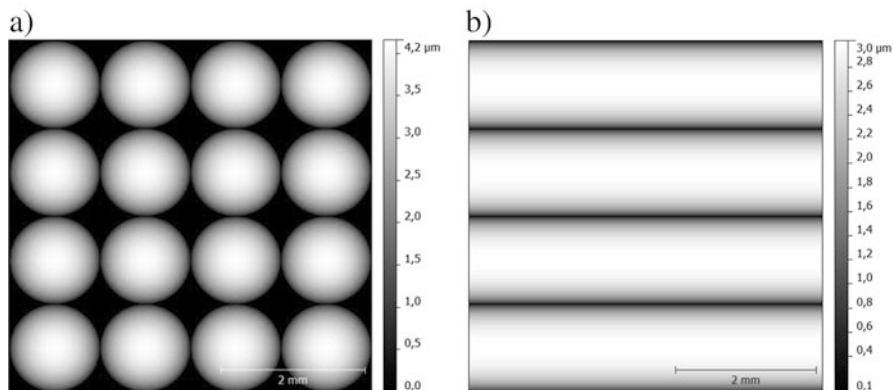


**Fig. 16.10** The result of phase unwrapping for the first (a) and the second (b) digital interferogram

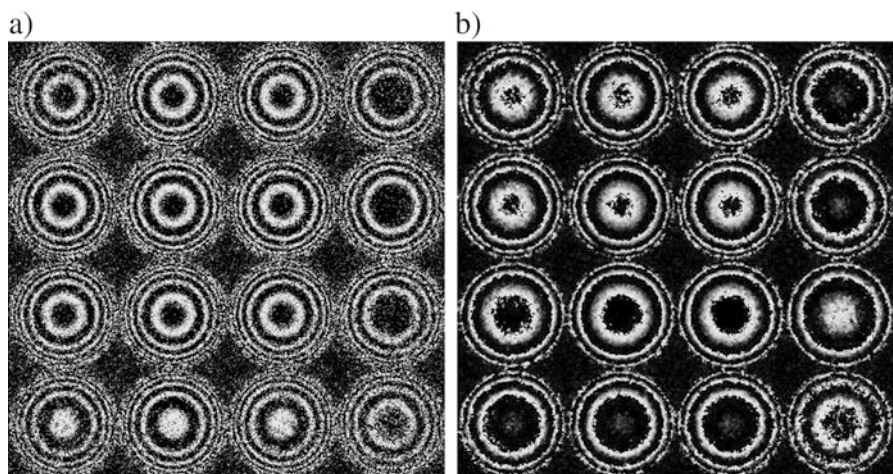


**Fig. 16.11** Digital interferogram of the optical raster with deviation in lenses size (a); the result of filtering (b)

method, the picture quality is sure to be distorted (see Fig. 16.12c, d). Apparently, instead of a half of the fringe, the whole period is formed at the exit. This imposes significant limitations on the value of the minimum deformation, which can be measured by DHI. In this case, the sensitivity can be increased by using a larger photosensitive matrix or laser with a shorter wavelength.

For this case, it was suggested to use a median filter with an appropriately chosen filtering window. Then the result should be approximated by a certain sine or cosine function, and the phase distribution should be calculated.

This method can give a two-time increase in the sensitivity.



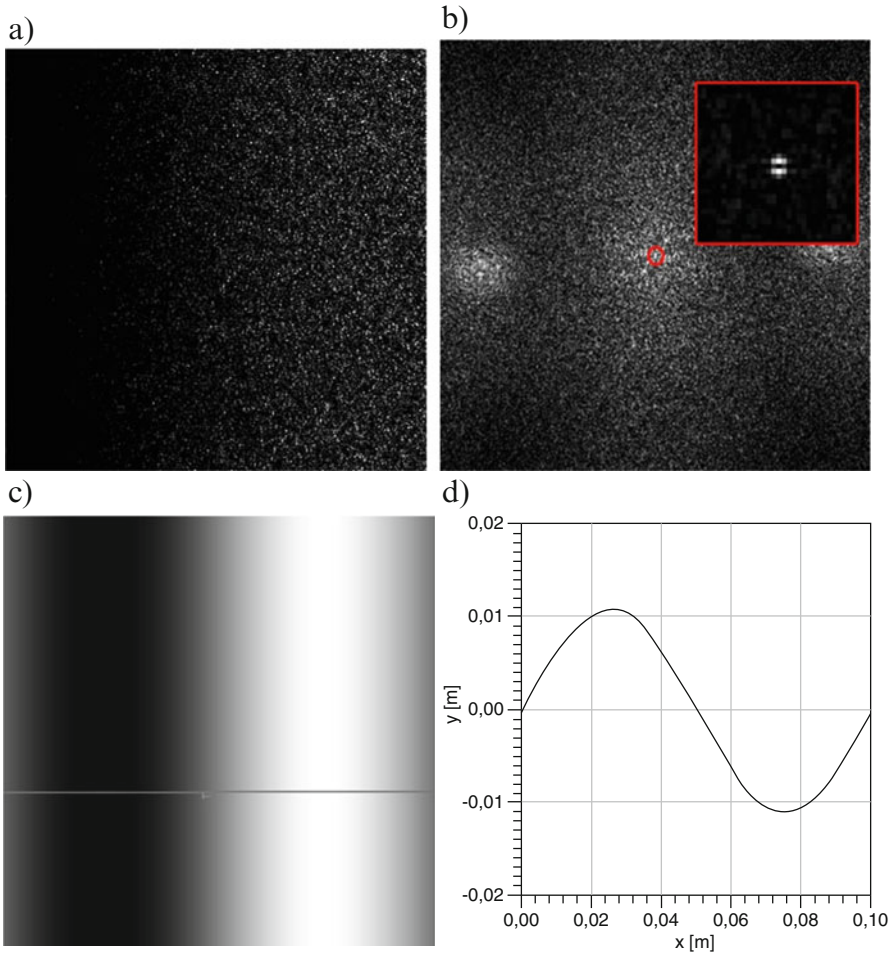


**Fig. 16.12** Cosine fringe map, with half of the fringe (a); spectrum of (a, b); result of the filtration (c); intensity graph of (c, d) [42]

## 16.4 Conclusion

It is obvious that improving the quality of digital interferogram is a necessary condition for reliable results in the study of materials, their properties, and structural changes, especially when it comes to micro- and nanotechnology. Thus in this paper we made the review of modern methods of improving the quality of digital interferograms, including methods of eliminating zero order and filtrating the resulting hologram phase map. Elimination of zero order can increase the quality of



**Fig. 16.13** An example of approximation application [42]

the reconstructed image still at the stage of the digital hologram reconstruction. The results showed that the best quality of the reconstructed holograms can be obtained by using the direct elimination method and the method with random phase shift of the reference wave.

The method of filtering in the frequency domain using Fourier transform and binarization of the spectrum image was proposed for filtering digital interferograms. Some interferograms of typical transparent and nontransparent objects were filtered to show the capability of our method. Test interferograms were obtained by simulation with the developed software. As a result, there were complete removals of speckle noise for the simplest cases, indicating high efficiency of the proposed method. However, in the case of real periodic structures with certain parameters deviation, the frequency spectrum becomes more complicated, and the quality of the interferograms filtered by the proposed method is unsatisfactory. This demonstrates the need for new approaches and further research to improve the presented method.

Speaking about the research of objects in micro- and nanotechnology, an important criterion is sensitivity. Therefore, for the filtering method, the maximum sensitivity has been considered, and the approach for its increase by approximation with the sine function has been proposed.

## References

1. Born M, Wolf E (1973) Basics of the optics. *M. Science* 2:719
2. Soroka LM (1996) Holography and interference data processing. *Uspekhi Fizicheskikh Nauk* 1(90):3–45
3. Petrovska HA, Kotsiuba YM, Fitio VM, Bobitski YV (2016) Optimization of the parameters of digital holographic microscope, 4-th International research and practice conference. *Nanotechnology and Nanomaterials (NANO-2016)* 24–27 August, Lviv
4. Inkyu M, Mehdi D, Arun A, Bahram J (2011) Cell Identification with computational 3-DHolographic microscopy. *Opt Photonics News* 22(6):18–23
5. Tishko TV, Titar VP, Tishko DN (2009) Holographic microscopy. Three-dimensional visualization of microscopic phase objects. *Applied radio electronics* 8(1):40–45
6. Petrovska HA, Kotsiuba YM, Fitio VM, Bobitski YV (2015) Digital holographic interferometry, VII International conference on Optoelectronic Information Technologies «PHOTONICS-ODS 2015», 21–23 April 2015, Vinnytsia, p 97
7. Abramov AY, Savonin SA, Dikov OV, Perepel'nitsina OA, Ryabukho VP (2010) Digital focused image holographic interferometry of microscopic transparent objects, Collection of works of international conference «FOP-2010». *Saint-Petersburg* 1:272–274
8. Schwider J, Burow R, Elssner K-E, Grzanna J, Spolaczyk R, Merkel K (1983) Digital wavefront measuring interferometry: some systematic error sources. *Appl Opt* 22:3421
9. Schnars U, Jueptner W (1994) Direct recording of holograms by a CCD-target and numerical reconstruction. *Appl Opt* 33(2):179–181
10. Schnars JU (2004) *Digital holography*. Springer, Berlin
11. Vizilter Y, Zhellow SY, Kniaz VA, Khodarev AN, Morzhin FV (2007) Processing and analysis of digital images with examples in Lab VIEW and IMAQ Vision. *DMK Press, Moscow*
12. Picart P (2015) *New techniques in digital holography*. Wiley, Inc., p 318
13. Asundi A (2011) *Digital holography for MEMS and microsystem metrology*. Wiley, p 232
14. Lai YW, Hamann S, Ehmann M, Ludwig A (2011) High through put characterization of stresses in thin film materials libraries using Si cantilever array wafers and digital holographic microscopy. *Rev Sci Instrum* 82:063903
15. Wen Y, Qu W, Wang Z, Yang F, Cheng CY (2015) Shape measurement of micro-objects using a common-path digital holographic microscopy (CDHM) with dual wavelength. In: *Proceedings SPIE 9524, international conference on optical and photonic engineering (icOPEN 2015)*, 17 July 2015, p 952422
16. Bae Y-S, Jeon P-J, Lee H-J (2015) Observation of Brownian motion of a micrometer-size bead in water by off-axis digital holographic microscopy. In: *Proceedings SPIE 9523, international conference on nano-bio sensing, imaging, and spectroscopy 2015*, 8 July 2015, p 95230A
17. Benzerdjeb N, Garbar C, Camparo P, Sevestre H (2016) Digital holographic microscopy as screening tool for cervical cancer preliminary study. *Cancer Cytopathol* 124:573–580
18. Savoia R, Memmolo P, Merola F, Miccio L, D'Ippolito G, Fontana A, Ferraro P (2015) Full 3D morphology of diatoms flowing in a microfluidic channel by digital holographic microscopy. In: *Amelink A, Vitkin I (eds) Novel biophotonics techniques and applications III, vol 9540 of SPIE Proceedings (Optical Society of America, 2015)*, pp 95400J
19. Rappaz B, Moon I, Yi F, Javidi B, Marquet P, Turcatti G (2015) Automated multi-parameter measurement of cardiomyocytes dynamics with digital holographic microscopy. *Opt Express* 23:13333–13347
20. Marquet P, Depeursinge C, Magistretti PJ (2014) Review of quantitative phase-digital holographic microscopy: promising novel imaging technique to resolve neuronal network activity and identify cellular biomarkers of psychiatric disorders. *Neurobiologia* 1(2):020901
21. Marquet P, Rothenfusser K, Rappaz B, Depeursinge C, Jourdain P, Magistretti PJ (2016) Quantitative phase-digital holographic microscopy: a new imaging modality to identify original cellular biomarkers of diseases. In: *Proceedings. SPIE 9718, quantitative phase imaging II*, 2 May 2016, p 97180K

22. Matoba O, Quan X, Xia P, Awatsuji Y (2015) A hybrid digital holographic microscopy for biological applications. In: Proceedings SPIE 9659, international conference on photonics solutions (29 July 2015), p 965903
23. Quan X, Nitta K, Matoba O et al (2015) Phase and fluorescence imaging by combination of digital holographic microscopy and fluorescence microscopy. *Opt Rev* 22:349
24. Kotsiuba YM, Petrovska HA, Fitio YVM, Bobitski YV (2016) Improving digital holographic interferogram quality by frequency filtering, 7-th International Conference on Advanced Optoelectronics and Lasers Accompanying (CAOL\*2016) events 13-th International Conference on Laser and Fiber-Optical Networks Modeling (LFNM\*2016), Odessa, 12–15 September 2016
25. Gusev ME, Voronin AA, Gurevich VS, Isaev AM, Alexeenko IV (2012) Modern methods of registration, reconstruction and representation of results in digital holographic interferometry, 7-th international scientific-practical conference «Holography – study and practice», Moscow, 28–30 september 2010, p 83
26. Nyquist H (1928) Certain topics in telegraph transmission theory. *Trans AIEE* 47(2):617–644
27. Gusev ME, Voronin AA, Gurevich VS, Isaev AM, Alexeenko IV, Redkorechev VI (2011) Methods of digital holographic interferometry and its application to measurement displacement. *Nanosystems Phys Chem Math* 2(1):23–39
28. Savonin SA, Ryabukho PV, Ryabukho VP (2015) Post-processing of a focused-image hologram in the digital holographic interferometry. *Comput Opt* 39(1):26–35
29. He X, Nguyen CV, Pratap M, Zheng Y, Wang Y, Nisbet DR, Williams RJ, Rug M, Maier AG, Lee WM (2016) Automated Fourier space region-recognition filtering for off-axis digital holographic microscopy. *Biomed Opt Express* 7:3111–3123
30. Colomb T, Cuche E, Charrière F, Kühn J, Aspert N, Montfort F, Marquet P, Depeursinge C (2006) Automatic procedure for aberration compensation in digital holographic microscopy and applications to specimen shape compensation. *Appl Opt* 45:851–863
31. Li JC, Xiong B (2009) Information optics theory and computation. Science Press, Pekin
32. Zhang Y, Lu Q, Ge B (2004) Elimination of zero-order diffraction in digital off-axis holography. *Opt Commun* 240:261–267
33. Yamaguchi I, Zhang T (1997) Phase-shifting digital holography. *Opt Lett* 22:1268–1270
34. Huang Y, Janabi-Sharifi F, Liu Y, Hung YY (2011) Dynamic phase measurement in shearography by clustering method and Fourier filtering. *Opt Express* 19:606–615
35. Dohet-Eraly J, Yourassowsky C, El Mallahi A, Dubois F (2016) Partial spatial coherence illumination in digital holographic microscopy: quantitative analysis of the resulting noise reduction, Proceedings SPIE 9890, optical micro- and nanometrology VI, 26 April 2016, p 989004
36. Dohet-Eraly J, Yourassowsky C, El Mallahi A, Dubois F (2016) Quantitative assessment of noise reduction with partial spatial coherence illumination in digital holographic microscopy. *Opt Lett* 41:111–114
37. Montresor S, Picart P (2016) Quantitative appraisal for noise reduction in digital holographic phase imaging. *Opt Express* 24:14322–14343
38. Goldstein R, Zebreker H, Werner C (1988) Satellite radar interferometry- two-dimensional phase unwrapping. *Radio Sci* 23(4):713–720
39. Bioucas-Dias JM, Valadao G (2007) Phase unwrapping via graph cuts. *Image Proceeding IEEE Transactions on* 2007 16(3):698–709
40. Shevkunov IA (2015) Phase unwrapping method by a shift of the reconstructed field. *Vestnik of Saint-Petersburg University, Series 4. Physics. Chemistry*
41. Li J-c, Picart P (2013) Digital holography. Wiley, Inc., p 350
42. Kotsiuba YM, Petrovska HA, Fitio VM (2016) Improving digital holographic interferogram quality by frequency filtering, 8th Ukrainian-Polish Scientific and Practical Conference “Electronics and information technologies” (ELIT-2016), (Methods and means of the information processing), 27–30 August, Chynadiyevo

# Chapter 17

## Computer Simulation of Collision-Induced Absorption Spectra of Confined Argon-Xenon Mixture

A. Dawid and Z. Gburski

### 17.1 Introduction

When two different atoms of noble gas are in the collision state, the short-time dipole moment is generated. These dipoles are able to absorb the infrared electromagnetic radiation. This phenomenon should be taken into account when it comes to design the double glazing windows [1, 2] or new cooling systems for electronic devices [3]. The collision-induced light absorption (CILA) phenomenon in noble gases has been studied for a long time, both in the theoretical and experimental works [4–9]. In the recent years, the computer simulation methods become valuable for the study of this phenomenon. The first simulations of CILA spectra concentrated on the small number of noble gas atoms grouped in the form of clusters [10–12]. The sensitivity of interaction-induced spectra to the phase transition in small Ar<sub>13</sub> cluster has been proved in those studies [8]. By studying clusters, we can also better understand the origins of collective behavior in bulk systems [13–17]. Further development of computer technology allowed simulation of CILA spectra in bulk noble gas samples [18]. The dynamical and structural properties of noble gas binary mixtures in a confined space become more important due to its potential applications in nanoelectronic devices, nanoscale molecule sensors [3], and gas storage containers. The new allotropes of carbon-like fullerene, graphene, or nanotubes are new promising material in nanoscale electronics. The adsorption of noble gases on the carbon structures has been simulated by molecular

---

A. Dawid  
Department of Computer Science, The University of Dąbrowa Górnicza, ul. Ciepłaka 1c,  
Dąbrowa Górnicza, Poland

Z. Gburski (✉)  
Institute of Physics, University of Silesia, Uniwersytecka 4, 40-007 Katowice, Poland  
e-mail: [zygmunt.gburski@us.edu.pl](mailto:zygmunt.gburski@us.edu.pl)



dynamics (MD) methods. There are some valuable works about the dynamics of a thin layer of noble gas atoms adsorbed on fullerene [19–24] and carbon nanotube [25–28]. The monoatomic thin layer of noble gas atoms between graphite slabs was also simulated. The interaction-induced light scattering was investigated in these systems for the various densities and temperatures of noble gases [29–31].

In this work we have concentrated on the system of argon-xenon binary mixture confined between graphite slabs. We have calculated the temperature dependence of Ar-Xe CILA spectra. We have also shown how these spectra are related to other dynamical and structural properties of argon-xenon binary mixture confined between graphite plates.

## 17.2 Simulation Protocol

The layer of graphene sheet was created by multiplying the elementary cell in  $x$  and  $y$  direction. This cell was constructed from six hexagonal carbon rings with the distance between near carbon atoms equal to 1.42 Å and the angle between two vectors drawn from one atom to nearby atoms equals to 120 degrees. The graphite in our simulations consists of two layers of graphene with the interlayer distance equal to 3.4 Å. In order to simulate narrow slot between very heavy graphite walls, we have assumed that carbon atoms are not moving during the simulations. It approximates bulk sample of graphite sheets. The interaction potential between noble gases and between noble gases and carbon was taken to be Lennard-Jones (LJ) potential with the usual form

$$V(r_{ij}) = 4\varepsilon_{ij} \left[ \left( \frac{\sigma_{ij}}{r_{ij}} \right)^{12} - \left( \frac{\sigma_{ij}}{r_{ij}} \right)^6 \right], \quad (17.1)$$

where  $r_{ij}$  is the distance between atoms and  $\varepsilon_{ij}$  and  $\sigma_{ij}$  are the LJ potential parameters listed in Table 17.1. The parameters between unlike atoms were calculated using Lorentz-Berthelot mixing rule [32]. Simulations were performed with the three-dimensional orthogonal periodic boundary conditions (PBC) using minimum image convention algorithm. The master simulation cell was of the edge size  $x = 28.31$  Å,  $y = 25.73$  Å, and  $z = 60$  Å. The potential cutoff distance between all unlike atoms was set to 20 Å. The size of master cell in  $z$  direction and potential cutoff distance were chosen so to not disturb the dynamics of noble gas atoms by periodic boundary conditions. In all our simulations, the distances between the slabs were set to  $d = 25.2$  Å. The system was simulated using classical equations of motion. The equations were integrated up to 5 ns by the velocity Verlet algorithm [33]. The integration time step used in simulation is 5 fs which ensures total energy conservation within 0.01%. The average temperature was adjusted as desired by a process of velocity scaling using Berendsen algorithm [33]. The system was equilibrated for  $5 * 10^6$  MD steps. All simulations have been performed using our own developed simulation program RIGMD [34].

**Table 17.1** Lennard-Jones potential parameters

Atom	$\varepsilon$ [meV]	$\sigma$ [Å]
Carbon	2.413	3.400
Argon	10.341	3.400
Xenon	22.180	3.924

### 17.3 General Relations

The mutual distortion of the atomic charge cloud occurs when two dissimilar rare gas atoms are in the collision state. During this process, a dipole moment is generated. These dipoles interact with the incident light beam generating absorption spectrum. The corresponding spectrum lies in the far infrared, typically in the range 0–250  $\text{cm}^{-1}$ . Computationally, the interaction-induced absorption spectrum is related to the Fourier transform of the time correlation function  $G(t)$

$$G(t) = \sum \langle \mu_{ij}(t) \mu_{kl}(0) \rangle, \quad (17.2)$$

where  $\mu_{ij}$  is the dipole moments induced in a pair of dissimilar atoms and the sum is over all pairs of unlike atoms in the mixture containing  $c_A$  and  $c_B$  concentrations of atoms types  $A$  and  $B$ ,  $c_A + c_B = c$ . The correlation function  $G(t)$  of the total dipole moment  $\mu = \sum_{ij} \mu_{ij}$  can be decomposed into pair, triplet, and quadruplet contributions [35],

$$G(t) = G_2(t) + G_{3a}(t) + G_{3b}(t) + G_4(t), \quad (17.3)$$

where eventual irreducible three-body dipole moments have been neglected. In the following, the two-body dipole moments  $\mu_{ij}$  are identified with dipole functions available in the literature [9, 36]:

$$\vec{\mu}_{ij} = \mu(r_{ij}) \hat{n}_{ij}, \quad (17.4)$$

$$\mu(r) = \mu_0 e^{-\alpha r - \beta(r-r_0)^2} + D_7/r, \quad (17.5)$$

where  $\mu_0$ ,  $\alpha$ ,  $\beta$ ,  $r_0$  and  $D_7$  are parameters evaluated for different rare gas pairs. The dynamics of argon or xenon atoms was studied by the mean square displacement function

$$MSD(t) = \langle |r_{ij}(t)|^2 \rangle, \quad (17.6)$$

where  $r_{ij}$  is the distance between noble gas atoms.

## 17.4 Results

In the argon-xenon mixture we have used 208 argon atoms and 48 xenon atoms which give 19% concentration of xenon in argon. The density of noble gases mixture inside the slot was  $\rho = 1.604 \text{ g/cm}^2$ . The initial locations of argon and xenon atoms between graphite walls were chosen to fulfill its uniform distribution. The instantaneous configuration of the system is shown in Fig. 17.1. The parameters of  $\mu(r)$  were estimated using the values of dipole moments between argon and xenon atoms obtained from ab initio calculations. The CC method was used for exchange-correlation potential expression with 6-31G(d,p) basis set. This method was chosen because it gives good results at the higher distances between atoms, covering van

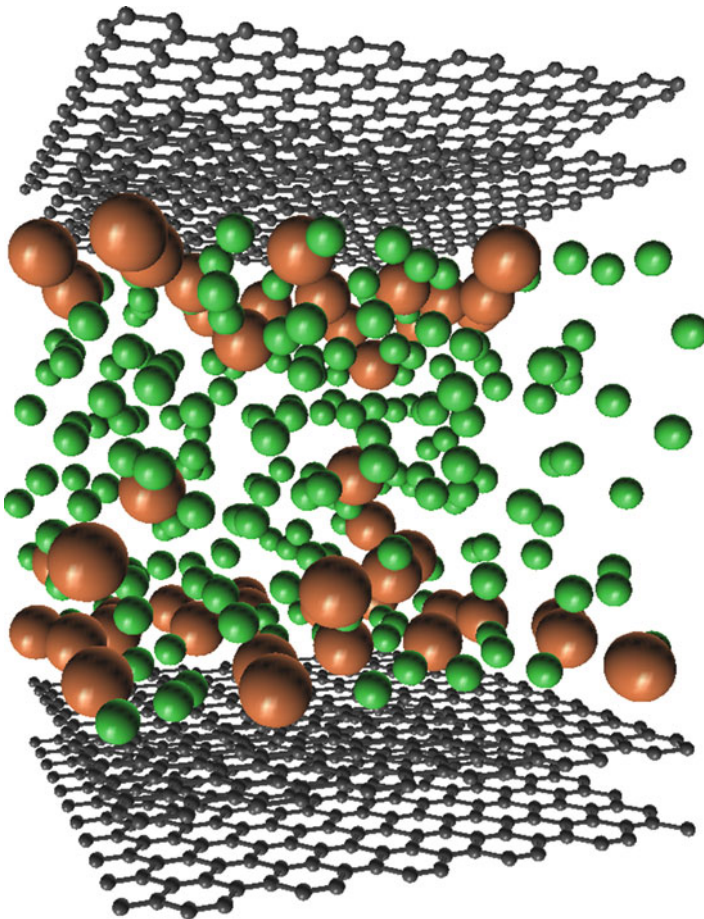


**Fig. 17.1** The instantaneous configuration of argon-xenon mixture between graphite walls at  $T = 140.0 \text{ K}$

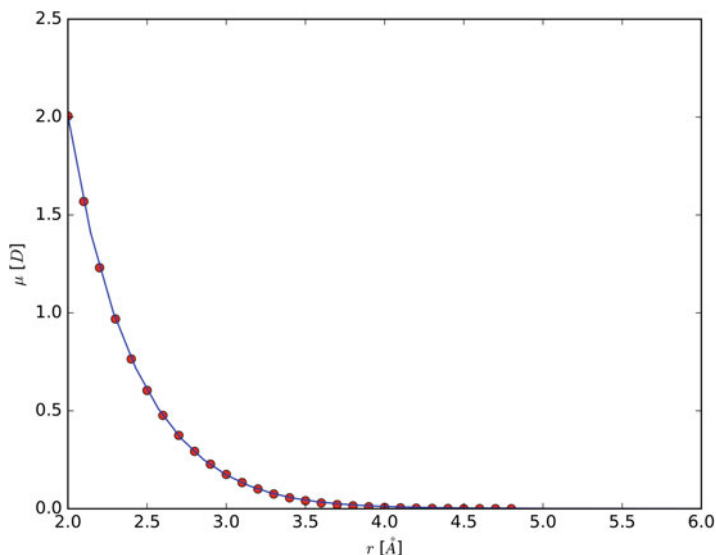


**Fig. 17.2** The interaction-induced dipole moment dependence of the distance between interacting centers of argon and xenon atoms. The *red circles* represent quantum mechanical calculations and *solid line* represents fitted model

**Table 17.2** The DFT calculated parameters for the Ar-Xe induced dipole

$\mu_0$ (Debye)	$r_0$ (Å)	$\alpha$ (Å <sup>-1</sup> )	$\beta$ (Å <sup>-1</sup> )	$D_7$ (Debye)
1.425	0.088	-1.01	0.658	132.257

der Waals dispersion potential [37]. All quantum mechanical calculations were done using GAMESS software [38]. The calculated quantum mechanical data fit well to Eq. 17.5 (Fig. 17.2). The set of parameters fitted for that equation is shown in Table 17.2 We have used the parameters to simulate collision-induced absorption spectra in argon-xenon binary mixture. In order to calculate the spectra, we had to calculate appropriate correlation functions first. We know that dipole moment correlation function can be decomposed into two-, three-, and four-body contributions (Eq. 17.3). The two-body contribution functions at three temperatures are shown in Fig. 17.3. At low temperature  $T = 80$  K, the function decays rapidly within 0.3 ps reaching local minimum and then decays slowly to zero within 500 ps. The initial rapid decay is caused by ballistic movement of atoms (before any collisions occur). The slow decay of  $G_2(t)$  function can be connected with reduced mobility of argon and xenon atoms. When the temperature increases, the  $G_2(t)$  function decays smoothly to zero within 120 ps at  $T = 140$  K and 30 ps at  $T = 220$  K. The initial ballistic region is invisible. The three-body contribution to the correlation function is of two kinds. The first situation is when argon is in collision state with two xenon atoms (Fig. 17.4). The  $G_{3a}(t)$  function is at the beginning negative. Once again we

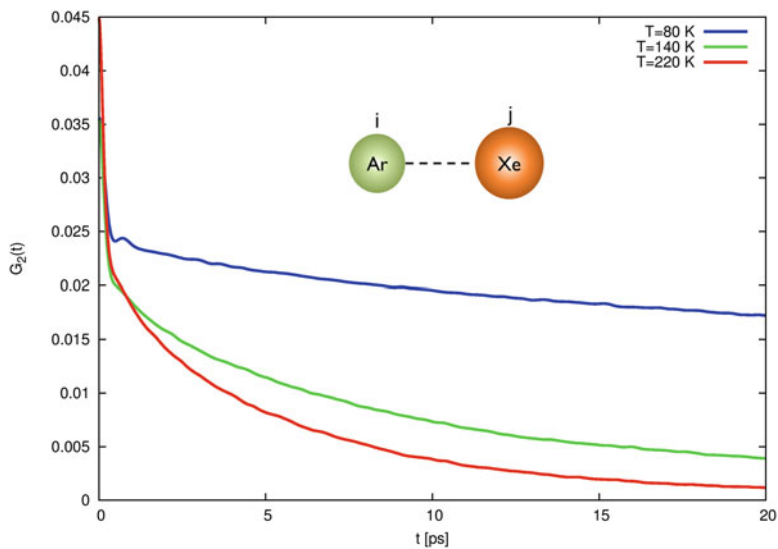


**Fig. 17.3** The two-body correlation function of induced dipole moment between argon and xenon atoms at three temperatures

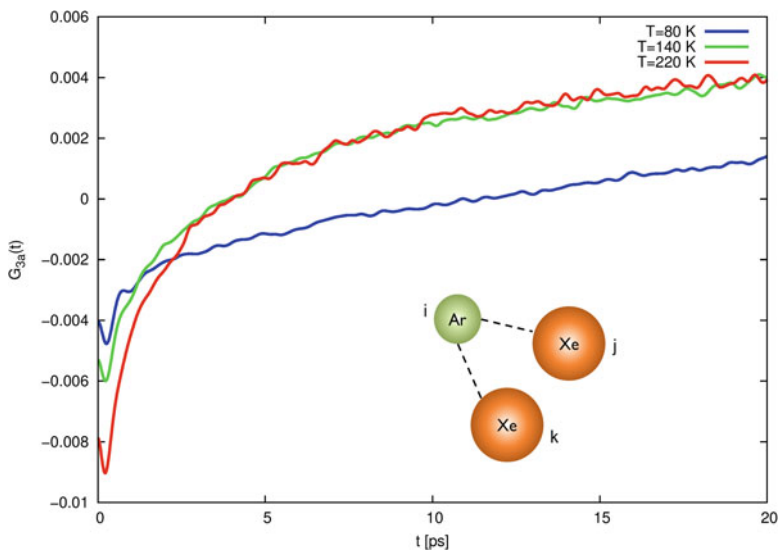


**Fig. 17.4** The three-body correlation function of induced dipole moment between one argon atom and two xenon atoms at three temperatures

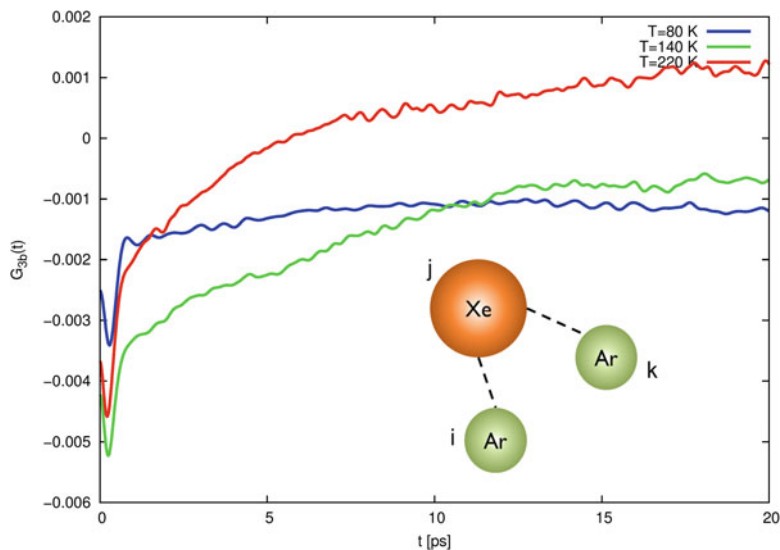


**Fig. 17.5** The three-body correlation function of induced dipole moment between two argon atoms and one xenon atom at three temperatures

can distinguish two regions on this plot, the short-time ballistic region with the minimum at 0.3 ps and smooth long-lasting region. The depth of the first minimum depends on the temperature. The first dip is getting deeper with the increase of the temperature. The  $G_{3a}(t)$  function at  $T = 80$  K is becoming positive within 13.5 ps, and functions at  $T = 140$  and 220 K are becoming positive within 4 ps. The function reaches its maximum at 28 ps and then slowly decays to zero. In the second situation, one xenon collide with two argon atoms. The  $G_{3b}(t)$  functions at  $T = 80$  K and  $T = 140$  K are negative; only at  $T = 220$  K function becomes positive within 5 ps (Fig. 17.5). The difference between  $G_{3a}(t)$  and  $G_{3b}(t)$  comes from the fact of lower concentration of xenon. Heavy xenon atoms are less mobile than argon atoms. Its phase is similar to dense fluid. The  $G_4(t)$  functions have mainly oscillatory character (Fig. 17.6). The average value of the function is negative for temperatures  $T = 80$  K and  $T = 140$  K. Only the function at temperature  $T = 220$  K has the positive value. This situation can be explained by freeing xenon atoms from graphite surfaces.  $G_{3b}(t)$  and  $G_4(t)$  functions seem to be the xenon atom mobility indicators. The total collision-induced dipole moment correlation function at three temperatures is shown in Fig. 17.7. Note the that first dip reaches its higher value at  $T = 140$  K. All total

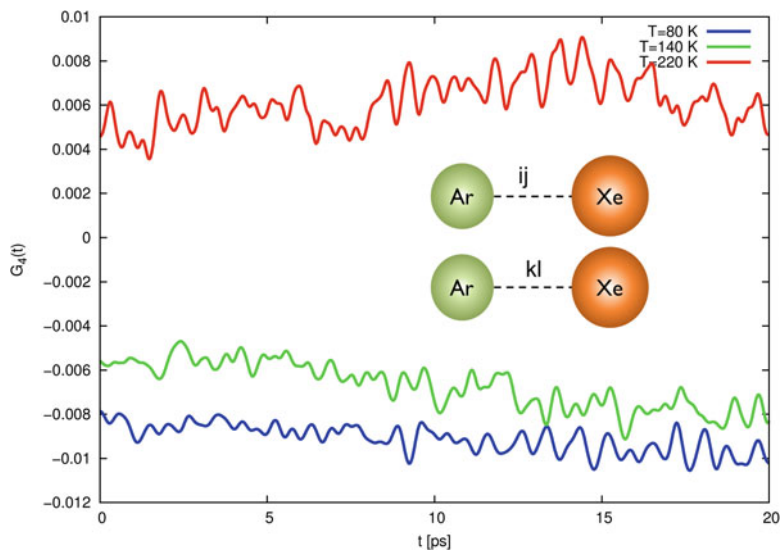


**Fig. 17.6** The four-body correlation function of induced dipole moment between two argon atoms and two xenon atom at three temperatures

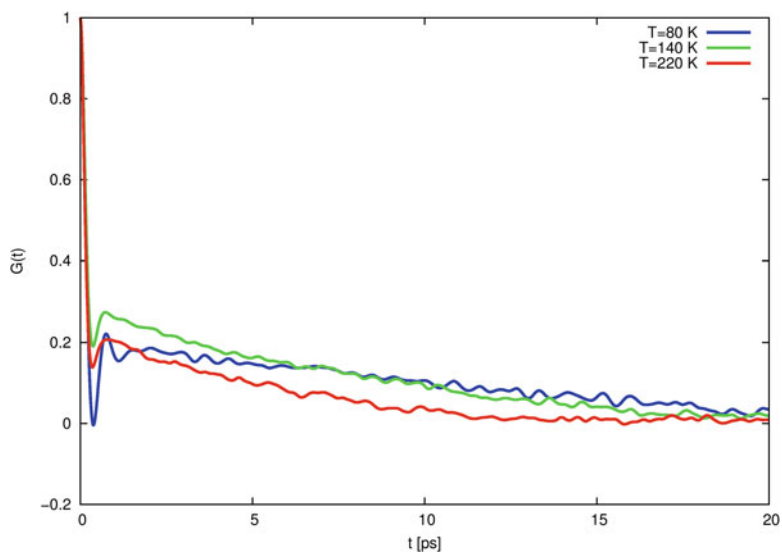


**Fig. 17.7** The total correlation function of induced dipole at three temperatures

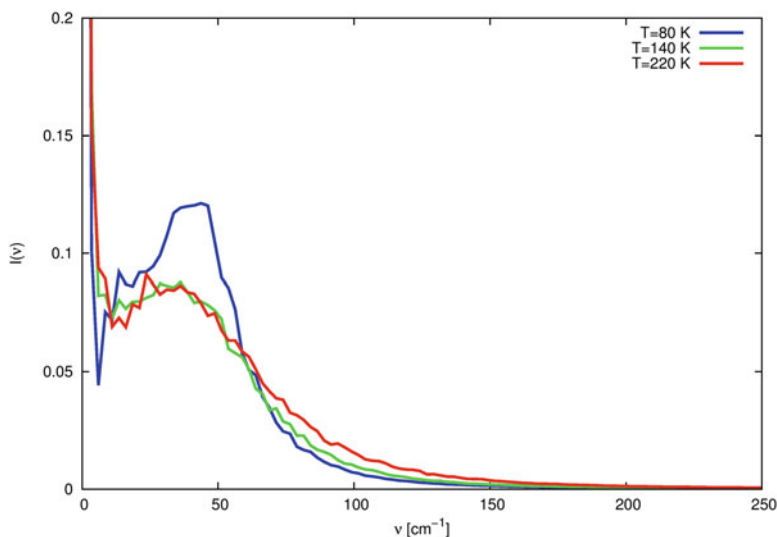


**Fig. 17.8** The total intensity  $I(\nu)$  of confined argon-xenon mixture at three temperatures

functions decay to zero within 20 ps. There probably exists the critical temperature in the system where the ballistic region reaches its higher value. Increasing of collisions with incompact heavy xenon atoms can be a reason it. The absorption spectra of binary mixture are calculated as Fourier transform of  $G(t)$  functions. The broadening of spectra is observed with increase of temperature (Fig. 17.8). The maximum absorption induced by collision of atoms in confined space is observed at wavenumber  $\nu = 35 \text{ cm}^{-1}$ . The amplitude of spectra reaches its higher value at low temperatures  $T = 80 \text{ K}$ . In our study we also want to confront obtained collision-induced results with diffusion in the system. The mean square displacement functions for argon (Fig. 17.9) and xenon (Fig. 17.10) at  $T = 80 \text{ K}$  show that heavy xenon atoms almost did not move at that temperature. Further investigations by calculation of distribution of xenon atoms between graphite plates in  $z$  direction proved that there are some places where xenon atoms have never been during the simulation at temperature  $T = 80 \text{ K}$  (Fig. 17.11). It looks that xenon atoms are concentrated mostly near graphite plates. The light argon atoms are able to penetrate the entire slot between graphite slabs even at  $T = 80 \text{ K}$  (Fig. 17.12). The calculated  $z$ -profile also showed the layered structure of argon-xenon mixture between graphite walls.



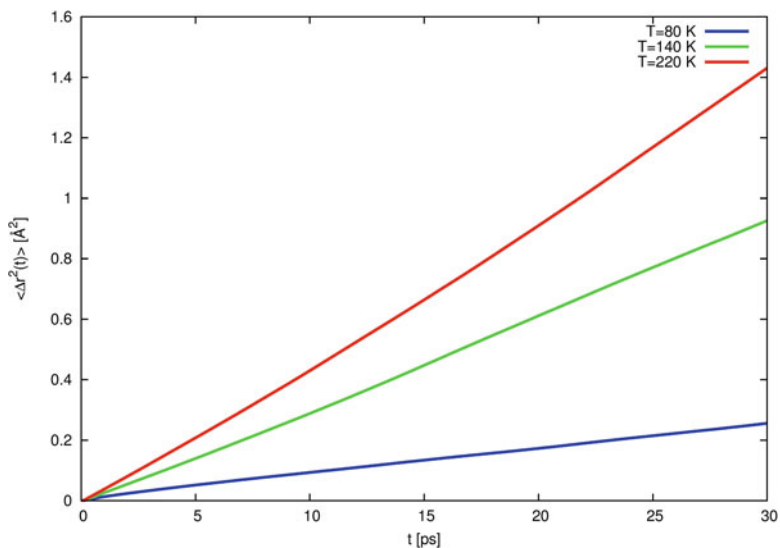


**Fig. 17.9** The mean square displacement functions of argon in Ar-Xe binary mixture confined between graphite walls at three temperatures

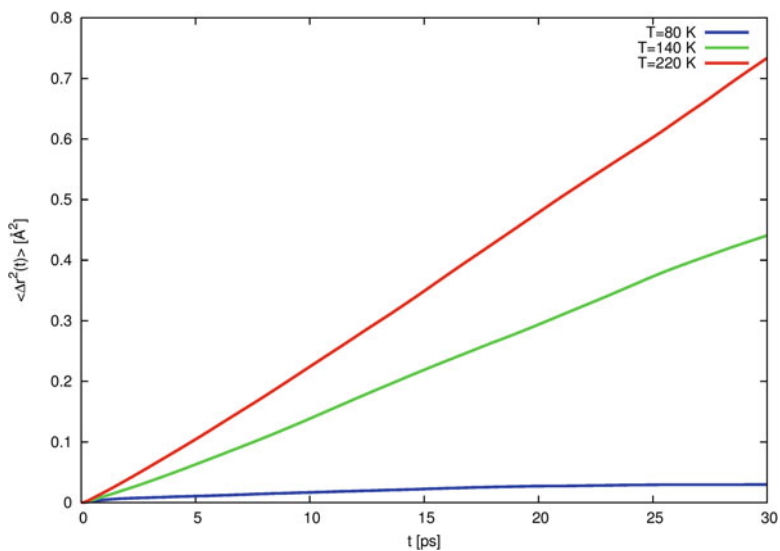


**Fig. 17.10** The mean square displacement functions of xenon in Ar-Xe binary mixture confined between graphite walls at three temperatures

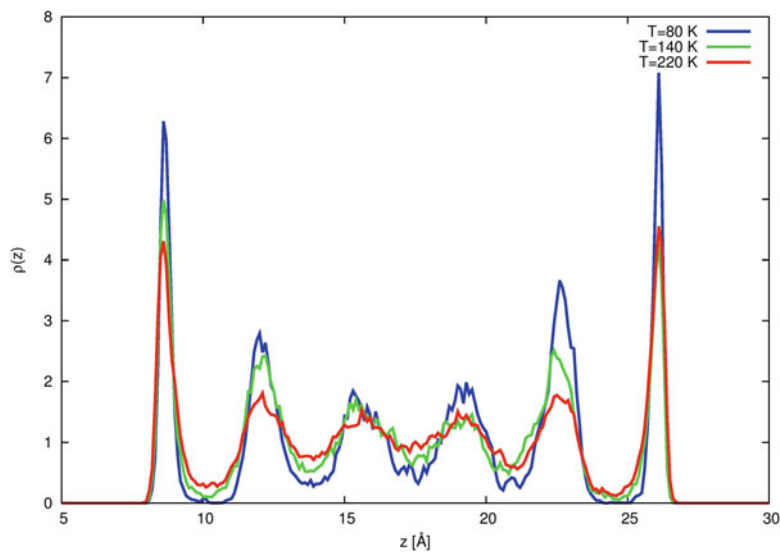


**Fig. 17.11** The  $z$ -profile distribution of argon atoms in Ar-Xe binary mixture confined between graphite walls at three temperatures

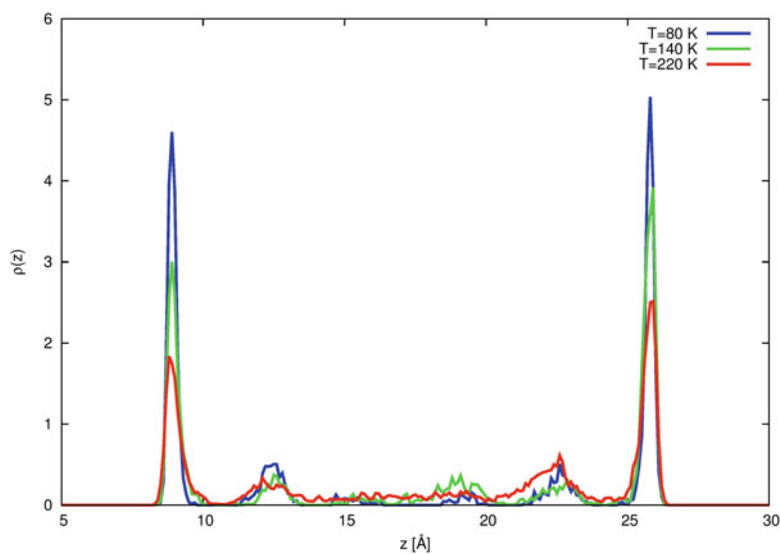


**Fig. 17.12** The  $z$ -profile distribution of xenon atoms in Ar-Xe binary mixture confined between graphite walls at three temperatures

## 17.5 Conclusions

We have observed that the interaction-induced absorption spectrum of confined Ar-Xe mixture is broadening with the increase of temperature. The difference in mobility of two constituents of noble gas binary mixture can be seen in collision-induced dipole moment correlation function. We have found the layered structure of argon-xenon binary mixture between graphite slabs. The separation of phases in binary mixture is also visible at low temperatures. The simulations reported here might encourage the future research of the noble gas mixtures confined between graphite walls.

**Acknowledgment** This research was supported in part by PL-Grid Infrastructure (grant IDs: molinter2015 and fulinter2016).

## References

1. Weir G, Muneer T (1998) Energy and environmental impact analysis of double-glazed windows. *Energy Convers Manag* 39:243–256. doi:[10.1016/S0196-8904\(96\)00191-4](https://doi.org/10.1016/S0196-8904(96)00191-4)
2. Clarke JA, Janak M, Ruyssevelt P (1998) Assessing the overall performance of advanced glazing systems. *Sol Energy* 63:231–241. doi:[10.1016/S0038-092X\(98\)00034-6](https://doi.org/10.1016/S0038-092X(98)00034-6)
3. Huang B, Li Z, Liu Z et al (2008) Adsorption of gas molecules on graphene nanoribbons and its implication for Nanoscale molecule sensor. *J Phys Chem C* 112:13442–13446. doi:[10.1021/jp8021024](https://doi.org/10.1021/jp8021024)
4. Guillot B (1989) Triplet dipoles in the absorption spectra of dense rare gas fluids. II. Long range interactions. *J Chem Phys* 91:3456–3462. doi:[10.1063/1.456874](https://doi.org/10.1063/1.456874)
5. Gburski Z (1985) Convergence of memory functions for the vibrational dephasing process in liquids. *Chem Phys Lett* 115:236–240. doi:[10.1016/0009-2614\(85\)80687-4](https://doi.org/10.1016/0009-2614(85)80687-4)
6. Krauss M, Regan RM, Konowalow DD (1988) Rare-gas interaction energy curves. *J Phys Chem* 92:4329–4333. doi:[10.1021/j100326a018](https://doi.org/10.1021/j100326a018)
7. Gburski Z, Zerda T (1980) Vibrational dephasing and intermolecular interactions in liquids. *Acta Phys Pol Ser A* 57:447–454
8. Gburski Z, Gray CG, Sullivan DE (1984) Lineshape in collision-induced absorption. *Mori Theory Chem Phys Lett* 106:55–59. doi:[10.1016/0009-2614\(84\)87010-4](https://doi.org/10.1016/0009-2614(84)87010-4)
9. Guillot B (1987) Theoretical investigation of the dip in the far infrared absorption spectrum of dense rare gas mixtures. *J Chem Phys* 87:1952–1961. doi:[10.1063/1.453167](https://doi.org/10.1063/1.453167)
10. Dawid A, Gburski Z (1998) Interaction-induced absorption in argon-krypton mixture clusters: molecular-dynamics study. *Phys Rev A* 58:740–743. doi:[10.1103/PhysRevA.58.740](https://doi.org/10.1103/PhysRevA.58.740)
11. Dawid A, Gburski Z (1997) Interaction-induced light scattering in Lennard-Jones argon clusters: computer simulations. *Phys Rev A* 56:3294–3296. doi:[10.1103/PhysRevA.56.3294](https://doi.org/10.1103/PhysRevA.56.3294)
12. Dawid A, Gburski Z (1999) Interaction-induced light scattering in xenon clusters: molecular dynamics study. *J Mol Struct* 482–483:271–276. doi:[10.1016/S0022-2860\(98\)00668-1](https://doi.org/10.1016/S0022-2860(98)00668-1)
13. Dawid A, Gburski Z (2002) Interaction-induced absorption in liquid argon–xenon mixture cluster: MD simulation. *J Mol Struct* 614:177–182. doi:[10.1016/S0022-2860\(02\)00243-0](https://doi.org/10.1016/S0022-2860(02)00243-0)
14. Piatek A, Dawid A, Gburski Z (2006) The existence of a plastic phase and a solid–liquid dynamical bistability region in small fullerene cluster (C60)<sub>7</sub>: molecular dynamics simulation. *J Phys Condens Matter* 18:8471. doi:[10.1088/0953-8984/18/37/006](https://doi.org/10.1088/0953-8984/18/37/006)
15. Dawid A, Gburski Z (1997) Dynamical properties of the argon-krypton clusters: molecular dynamics calculations. *J Mol Struct* 410–411:507–511. doi:[10.1016/S0022-2860\(96\)09512-9](https://doi.org/10.1016/S0022-2860(96)09512-9)

16. Piatek A, Dawid A, Gburski Z (2011) The properties of small fullerene cluster (C-60(OH)(24))(7): computer simulation. *Spectrochim Acta Part Mol Biomol Spectrosc* 79:819–823. doi:[10.1016/j.saa.2010.08.059](https://doi.org/10.1016/j.saa.2010.08.059)
17. Raczyński P, Dawid A, Gburski Z (2005) Depolarized light scattering in small fullerene clusters—computer simulation. *J Mol Struct* 744–747:525–528. doi:[10.1016/j.molstruc.2004.12.064](https://doi.org/10.1016/j.molstruc.2004.12.064)
18. Abdel Kader MS (2008) Collision-induced light scattering spectra and ground state potential of gaseous xenon. *Chem Phys* 352:311–319. doi:[10.1016/j.chemphys.2008.07.004](https://doi.org/10.1016/j.chemphys.2008.07.004)
19. Dawid A, Dendzik Z, Gburski Z (2004) Molecular dynamics study of ultrathin argon layer covering fullerene molecule. *J Mol Struct* 704:173–176. doi:[10.1016/j.molstruc.2004.01.065](https://doi.org/10.1016/j.molstruc.2004.01.065)
20. Kachel A, Gburski Z (1997) Chain formation in a model dipolar liquid: computer simulation study. *J Phys-Condens Mat* 9:10095–10100. doi:[10.1088/0953-8984/9/46/007](https://doi.org/10.1088/0953-8984/9/46/007)
21. Dawid A, Gburski Z (2003) Rayleigh light scattering in fullerene covered by a spherical argon film – a molecular dynamics study. *J Phys Condens Matter* 15:2399–2405. doi:[10.1088/0953-8984/15/14/315](https://doi.org/10.1088/0953-8984/15/14/315)
22. Gruszka M, Gburski Z (1992) Interaction-induced light scattering in atomic fluids — a two-body contribution studied by MD simulations. *J Mol Struct* 275:129–133. doi:[10.1016/0022-2860\(92\)80188-N](https://doi.org/10.1016/0022-2860(92)80188-N)
23. Dawid A, Gburski Z (2003) Interaction-induced light scattering in a fullerene surrounded by an ultrathin argon “atmosphere”: molecular dynamics simulation. *Phys Rev A* 68:065202. doi:[10.1103/PhysRevA.68.065202](https://doi.org/10.1103/PhysRevA.68.065202)
24. Skrzypek M, Gburski Z (2002) Fullerene cluster between graphite walls – computer simulation. *Eurphys Lett* 59:305–310. doi:[10.1209/epl/i2002-00242-8](https://doi.org/10.1209/epl/i2002-00242-8)
25. Dawid A, Gburski Z (2007) Dielectric relaxation of 4-cyano-4-n-pentylbiphenyl (5CB) thin layer adsorbed on carbon nanotube – MD simulation. *J Non-Cryst Solids* 353:4339–4343. doi:[10.1016/j.jnoncrsol.2007.02.072](https://doi.org/10.1016/j.jnoncrsol.2007.02.072)
26. Dendzik Z, Kosmider M, Dawid A, Gburski Z (2005) Interaction induced depolarized light scattering from ultrathin n film covering single-walled carbon nanotubes of different chiralities. *J Mol Struct* 744:577–580. doi:[10.1016/j.molstruc.2004.12.049](https://doi.org/10.1016/j.molstruc.2004.12.049)
27. Kośmider M, Dendzik Z, Pałucha S, Gburski Z (2004) Computer simulation of argon cluster inside a single-walled carbon nanotube. *J Mol Struct* 704:197–201. doi:[10.1016/j.molstruc.2004.02.050](https://doi.org/10.1016/j.molstruc.2004.02.050)
28. Dendzik Z, Kosmider M, Dawid A et al (2005) Interaction-induced depolarized light scattering spectra of exohedral complexes of Ne and Ar with fullerenes and nanotubes. *Mater Sci-Pol* 23:457–466
29. Dawid A, Raczynski P, Gburski Z (2014) Depolarised Rayleigh light scattering in argon layer confined between graphite plains: MD simulation. *Mol Phys* 112:1645–1650. doi:[10.1080/00268976.2013.853111](https://doi.org/10.1080/00268976.2013.853111)
30. Dawid A, Wojcieszek D, Gburski Z (2016) Collision-induced light scattering spectra of krypton layer confined between graphite slabs – MD simulation. *J Mol Struct* 1126:103–109. doi:[10.1016/j.molstruc.2016.01.063](https://doi.org/10.1016/j.molstruc.2016.01.063)
31. Dawid A, Gorny K, Wojcieszek D et al (2014) Collision-induced light scattering in a thin xenon layer between graphite slabs – MD study. *Spectrochim Acta Part Mol Biomol Spectrosc* 129:594–600. doi:[10.1016/j.saa.2014.03.101](https://doi.org/10.1016/j.saa.2014.03.101)
32. Allen MP, Tildesley DJ (1989) *Computer simulation of liquids*. Oxford University Press, New York
33. Rapaport DC (2004) *The art of molecular dynamics simulation*. Cambridge University Press, Cambridge
34. Dawid A (2012) RIGid Molecular Dynamics (RIGMD) – simulation software. In: <http://prac.us.edu.pl/~dawid/RIGMD/rigmdUS.php>. <http://prac.us.edu.pl/~dawid/RIGMD/rigmdUS.php>
35. Mountain RD, Birnbaum G (1987) Molecular dynamics study of intercollisional interference in collision-induced absorption in compressed fluids. *J Chem Soc Faraday Trans 2* 83:1791. doi:[10.1039/f29878301791](https://doi.org/10.1039/f29878301791)

36. Birnbaum G, Krauss M, Frommhold L (1984) Collision-induced dipoles of rare gas mixtures. *J Chem Phys* 80:2669–2674. doi:[10.1063/1.447062](https://doi.org/10.1063/1.447062)
37. Piecuch P, Kucharski SA, Kowalski K, Musiał M (2002) Efficient computer implementation of the renormalized coupled-cluster methods: the R-CCSD[T], R-CCSD(T), CR-CCSD[T], and CR-CCSD(T) approaches. *Comput Phys Commun* 149:71–96. doi:[10.1016/S0010-4655\(02\)00598-2](https://doi.org/10.1016/S0010-4655(02)00598-2)
38. Gordon MS, Schmidt MW (2005) Chapter 41 – Advances in electronic structure theory: GAMESS a decade later A2 – Dykstra, Clifford E. In: Frenking G, Kim KS, Scuseria GE (eds) *Theory application computational chemistry*. Elsevier, Amsterdam, pp 1167–1189

# Chapter 18

## Electromagnetic Modes Inside the Island Kind 2D Photonic Crystal Resonator

E. Ya. Glushko and A. N. Stepanyuk

### 18.1 Introduction

The existing terminology distinguishes several kinds of photonic structures: photonic crystals, photonic membranes and photonic crystal resonators. An infinite 2D structure periodically ordered in  $ZY$  plane and having also infinite size in  $Z$  direction is called a photonic crystal whereas the photonic crystal resonator has finite sizes in  $ZY$  plane and perfectly smooth boundaries with external medium. This circumstance generates a clear expressed angular area of total internal reflection of field inside the resonator for in-plane geometry. In general case, a resonator has infinite size in  $X$  direction. The only way to excite a standing wave inside exists through the input prisms due to that the external beam may hit into the total internal reflection area of the resonator. The photonic membrane may be treated as a thin photonic crystal dividing the external medium into two parts and transmitting radiation from one medium to another [1]. At the present time the photonic crystals (PhC) have been widely investigated as perspective objects of optical technologies in computing, signal processing, telecommunication, sensing, etc. [2, 3] though in the main, the 2D PhC is considering only as a perfect reflecting medium surrounding an optical waveguide. Therefore the conditions of omnidirectional gaps in photonic spectrum are of interest for the determination of the optimal wavelength range of optical devices [4–7]. Meanwhile optical properties of photonic crystals may be

---

E.Y. Glushko (✉)

Institute of Semiconductor Physics, National Academy of Sciences of Ukraine, 41 Nauki Prsp,  
Kyiv 03028, Ukraine

e-mail: [scientist.com\\_eugene.glushko@mail.com](mailto:scientist.com_eugene.glushko@mail.com)

A.N. Stepanyuk

Kryvyi Rih State Pedagogical University, Gagarin pr., 54, 50086 Kryvyi Rih, Ukraine

© Springer International Publishing AG 2017

O. Fesenko, L. Yatsenko (eds.), *Nanophysics, Nanomaterials, Interface Studies, and Applications*, Springer Proceedings in Physics 195,

DOI 10.1007/978-3-319-56422-7\_18

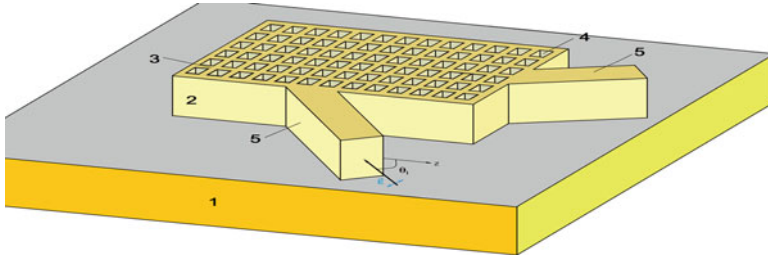


**Fig. 18.1** Sketch of the island type binary  $13 \times 6$  period 2D photonic crystal resonator (ICPR). 1 substrate, 2 covering layer, 3 matrix material, 4 accompanying material (shown air wells), 5 input-output waveguides,  $\theta_1$ , angle of incidence,  $p$ -polarized plane wave

important for a wide area of applications in optoelectronic and all-optical devices. Further development of this area may be related to more detailed consideration of the influence of a resonator's finite sizes on the modal structure and features of field modal distribution inside a finite photonic crystal. A number of FDTD investigations exist devoted to wave transmission through the infinite 2D PhCr of various symmetries (see review [8]) whereas resonators of finite sizes need a more adequate mathematical model. The proposed island 2D resonator is a generalized kind of the 2D photonic crystal, ( $N_z, N_y \rightarrow \infty$ ) which, the resonator, has finite sizes in two directions and perfect external faces (Fig. 18.1). In [8, 9] the properties of finite resonators were estimated in the framework of perturbation theory. It was found there that small parameter exists for the problem of captured within the total internal reflection (TIR) domain electromagnetic field in a finite dielectric structure with spatially piecewise alternating index of refraction. The condition of small parameter existence is based on demand electromagnetic energy inside the resonator which is much more than energy of the mode tails outside the resonator. Therefore, the number of periods in both directions should be more than 10–12. The small parameter existence and an appropriate realization of the perturbation theory were demonstrated in [9, 10] for the case of weak intrinsic optical contrast of the dielectric photonic structure (see [11]).

In Fig. 18.1, a binary island kind  $N_z \times N_y$  period photonic crystal resonator (ICPR) grown on a substrate 1 and consisting of matrix material 3 with refractive indices  $n_1$  pierced with a regular system of wells/bars 4 having refractive indices  $n_2$ . If the external covering layer 2 consists of the optically nonlinear material, an opportunity arises to control the beam entrance angle into the resonator. It is worth noting that matrix material is topologically connected whereas the embedded into the matrix ordered bars or wells of a concomitant material are disconnected. This circumstance is important for the method to calculate field in a finite resonator developed below.

The resonator in-plane standing modes can be excited by an external source through the special inputs 5 and may be controlled due to their nonlinear properties. The photonic modes differ in terms of field density distribution inside the resonator,

their dependence on frequency and geometry of incidence that may be used in optical devices to control light energy flows and perform logic operations.

In this work, a binary island kind photonic crystal resonator is investigated analytically and numerically in the framework of standing wave expansion (SWE) method. We have calculated parametric dependencies of modes energy for silicon glass resonator and considered a way to classify the resonator's eigenstates. The field distribution inside the resonator is calculated at different parameters, and ways of use the switching states in optical devices are discussed.

## 18.2 SWE Theory for Electromagnetic Field in a Finite 2D Photonic Crystal

The standing wave expansion (SWE) approach is based on the representation of a 2D eigenstate of a resonator as the expansion in eigenstates produced by two crossed in  $Z$  and  $Y$  directions and superposed finite binary 1D photonic crystals. The eigenvalue problem is analytically solved separately for two probe 1D PhCrS and resulting 2D basis is generated as a direct production of separated 1D bases  $\{|s\rangle_z\}$  and  $\{|g\rangle_y\}$  [6], where  $s, g = 1, 2, \dots, m$ , correspondingly the 2D basis size is  $m^2$ . Due to the rectangular form of the resonator, the incident angles of waves united in a 2D basis function  $|s(\theta_1)g(\theta_1')\rangle$  are correlated  $\theta_1 = \pi/2 - \theta_1'$ , where the subscript ( $'$ ) refers to the optically more dense matrix medium,  $\theta_1$  is the wave angle of incidence relatively  $Z$ -axis in matrix material. Suppose the materials constituting the photonic crystal are optically linear, isotropic and nonmagnetic and free charges are absent, the following equation for electromagnetic field in a continuous medium with piecewise constant refractive index

$$\frac{1}{\varepsilon(z, y)} \Delta \vec{E} + \frac{\omega^2}{c^2} \vec{E} = 0 \quad (18.1)$$

can be expanded into the 2D basis  $|s(\theta_1)g(\theta_1')\rangle$  series. The piecewise constant dielectric function  $\varepsilon(z, y)$  is factored out through the Laplace operator, therefore solutions of both probe 1D problems are the plane wave based standing modes. In the considered case of p-polarization, a convenient basis of functions  $M^{sg}(z, y)$  may be built in several ways: on the magnetic field components, on tangential components of electric field and on normal components of the electrical induction. A set of eigenfunctions based on magnetic field was investigated in [8, 9]. Here we consider the normal components of electrical induction as the modes  $M^{sg}(z, y)$  of initial basis, where  $s = 1, s_{\max}$ ,  $g = 1, g_{\max}$ . The physical restrictions demand the mode to be a continuous function of variables  $z$  and  $y$  but the derivatives may have a jump because the standing waves do not convey energy. Below, we study the rectangular photonic crystal resonator based on a 2D terminated binary



structure consisting of the topologically connected matrix material and another one – disconnected material 4 (Fig. 18.1), which looks like a system of rectangular bars. Therefore the resonator may be divided into  $ij$  areas by the number of periods  $N_z, N_y$  in  $Z$  and  $Y$  directions, where  $i = 0, 1, \dots, 2N_z + 2, j = 0, 1, \dots, 2N_y + 2$ . The outside areas are described by indices  $i = 0, 2N_z + 2, j = 0, 2N_y + 2$  and the solution of (18.1) contains here at least one exponentially decreasing with distance factor. Inside the IPCR body, the indices  $i, j$  run from 1 to  $N_z + 1$  or  $N_y + 1$ . Then a mode in an intrinsic area  $ij$  may be presented in a view:

$$\begin{aligned} M_{ij}^{sg}(z, y) &= A_{zi} \bullet \sin \theta_i \bullet \varepsilon_i \bullet \cos(k_{is}z + \psi_{is}) \bullet \\ &A_{yj} \sin \theta_j \bullet \varepsilon_j \bullet \cos(k_{jg}y + \psi_{jg}), \end{aligned} \quad (18.2)$$

where  $\varepsilon_{i,j}$  denotes dielectric function in matter of the resonator area  $i$  or  $j$ . The amplitudes  $A_{zi}, A_{yj}$  and phases  $\psi_{is}, \psi_{jg}$  are analytically obtained in the framework of the 1D problem for two probe crossed photonic crystals inside intrinsic areas  $j, i = 1, 2, \dots, 2N + 1$ , whereas for outside areas where  $i = 0$  or  $j = 0$  the cosines should be replaced by  $\exp(-k_{is}z)$  or  $\exp(-k_{jg}y)$ , correspondingly. The wave front orientation with respect to OX axes is given by angle  $\theta_i = \theta_1$  or  $\theta_2$  for odd or even layers of a probe 1D PhCr with the same materials and appropriate geometry [8]. The angles  $\theta_j$  presented in Y-part of the basis function are  $\pi/2 - \theta_1$  and  $\pi/2 - \theta_2$  for odd or even layers, respectively. Here, the index 1 corresponds to matrix material and index 2 denotes the embedded into the matrix ordered bars of another material. The indices  $s, g$  enumerate eigenstates of two probe 1D problems solved for  $Z$  degrees of freedom at the incident angle  $\theta_1$  and for  $Y$  direction at the incident angle  $\theta'_1$ .

$$\begin{aligned} \vec{E}_i &= (\sin \theta_i, \cos \theta_i) A_{zi} e^{ik_{iz}z} + \\ &(\sin \theta_i, -\cos \theta_i) B_{zi} e^{-ik_{iz}z} \\ \vec{E}_j &= (\sin \theta'_j, \cos \theta'_j) A_{yj} e^{ik_{jy}y} + \\ &(\sin \theta'_j, -\cos \theta'_j) B_{yj} e^{-ik_{jy}y} \end{aligned} \quad (18.3)$$

The amplitudes  $A, B$  ( $A^* = B$  in the considered case) are found in the framework of both probe problems from the system of boundary conditions taken at  $2N_{z(y)} + 1$  alternating boundaries [8–10]. Further, the boundary conditions of continuity for the normal component of electrical induction (mode) at both surfaces of each layer of the probe 1D PhCr lead to the system of equations for unknown amplitudes. In matrix view we have the system of equations

$$\left\{ \begin{array}{l} \widehat{R}_l \begin{pmatrix} A_l \\ B_l \end{pmatrix} = \widehat{L}_l \begin{pmatrix} A_l \\ B_l \end{pmatrix} = \\ \widehat{R}_1^{-1} \bullet \widehat{L}_2 \begin{pmatrix} A_2 \\ B_2 \end{pmatrix} = \\ \widehat{R}_2^{-1} \bullet \widehat{L}_3 \begin{pmatrix} A_3 \\ B_3 \end{pmatrix} = \dots \\ = \widehat{R}_{2N}^{-1} \bullet \widehat{L}_{2N+1} \begin{pmatrix} A_{2N+1} \\ B_{2N+1} \end{pmatrix} = \\ A_r \widehat{R}_{2N+1}^{-1} \bullet \widehat{L}_r \begin{pmatrix} \cos \theta_r \\ \varepsilon_r \sin \theta_r \end{pmatrix} \end{array} \right. , \quad (18.4)$$

where  $\widehat{L}, \widehat{R}$  are binary matrices of boundary conditions of probe problem for a layered photonic crystal, indices  $l$  ( $ij = 0$ ) and  $r$  ( $ij = 2N_{z(y)} + 2$ ) describe the external medium and topology demands  $\varepsilon_l = \varepsilon_r$ . The set of 1D functions  $\{|s > z\}$  and  $\{|g > y\}$  should possess the properties of a basis: completeness, orthogonality, right position and number of nodal points. Nevertheless, we observed the affinity of the calculated basis expressed in a weak (5%) non-orthogonality between states of the same parity. We suppose that the 1D basis affinity is caused by dielectric function jumps at the layer boundaries. Further, using the Gram-Schmidt procedure of orthogonalization separately for odd and even subgroups of states, the basis is transformed to the needed orthogonal form.

The expansion of a mode  $\sigma$  into the series gives

$$M_\sigma(z, y) = \sum_{s, g} h_{sg}^\sigma \cdot |s, g > \quad (18.5)$$

Then, Eq. (18.1) generates the system of equations for expansion amplitudes  $h_{sg}$ :

$$\left\{ \begin{array}{l} \sum_{s, g} \left[ \langle q | \frac{k_{sg}^2}{\varepsilon(x, y)} |s, g > - \frac{\Omega^2}{c^2} \delta_{q, sg} \right] h_{sg} \\ q = 1..N_m \end{array} \right. , \quad (18.6)$$

where  $q$  numbers state the 2D basis,  $N_m = s_{\max} \cdot g_{\max}$ ; matrix element  $\langle q | k_{sg}^2 / \varepsilon(x, y) |s, g >$  means the integral is over the resonator and surrounding medium; wave vector  $k_{sg}$  is also a piecewise continuous constant. It should be noted that matrix elements have the analytical form in our approach because the modes  $M$  presented in formula (18.2) are described by amplitudes  $A_{zi}(s)$ ,  $A_{yj}(g)$  and phases  $\psi_{is}$ ,  $\psi_{is}$  found in two 1D problems for crossed layered structures [8]. These two problems play the part of a 2D basis generator. The full solution of the IPCR system is given by a multitude of eigenvalues  $\Omega_q^2$  and corresponding standing waves, resonator modes.

$$\left\{ \Omega_\sigma^2, \begin{pmatrix} h_1^\sigma \\ \dots \\ h_{N_m}^\sigma \end{pmatrix} \right\}, \quad (18.7)$$

where  $\sigma$  enumerates standing waves inside the total internal reflection area of the resonator and  $h^\sigma_m$  are coefficients of the 2D state  $\sigma$  expansion into initial basis  $|s, g\rangle$  series.

The developed approach differs from the calculation methods for infinite structures like the plane wave expansion method (PWEM) due to the essential non-periodicity of integrals  $\langle q | k^2_{sg} / \epsilon(x, y) | s, g \rangle$  in (18.6) that leads to additional  $4(N_z + 1)(N_y + 1)$  separate integrals for the total number of  $ij$  areas. As a result, the modes  $q$  described by expansion coefficients  $h^q_{sg}$  are far from periodicity along the IPCR body. As an advantage of this method, one can note that the number of states  $|s, g\rangle$  taken to form the 2D basis may be essentially less than in the case of PWEM due to their initial nearness to needed solutions. Especially when it concerns the local states and low-energetic modes with small number of knot lines. Besides, the multitude of states  $|s, g\rangle$  can be formed in accordance with the energy interval under consideration.

To analyse eigenstates inside the IPCR, we have calculated the  $19 \times 19$ -period ( $\text{SiO}_2/\text{SiO}_2$ ) 2D IPCR consisting of rectangular glass wells with sides  $b_z = 1.0 \mu\text{m}$ ,  $b_y = 1.1 \mu\text{m}$  and  $\epsilon_2 = 2.25$  periodically distributed in the optically more dense glass matrix with dielectric function  $\epsilon_1 = 3.61$ . The optically lesser contrast IPCR (Fig. 18.2a–c) has the period along  $Z$  axis  $d_z = a_z + b_z = 3.0 \mu\text{m}$  as well as along  $Y$  axis  $d_y = a_y + b_y = 3.0 \mu\text{m}$ . The total sizes of the IPCR in this case are  $59 \times 58.9 \mu$  including the covering layer. The optically bigger contrast IPCR (Fig. 18.2d)

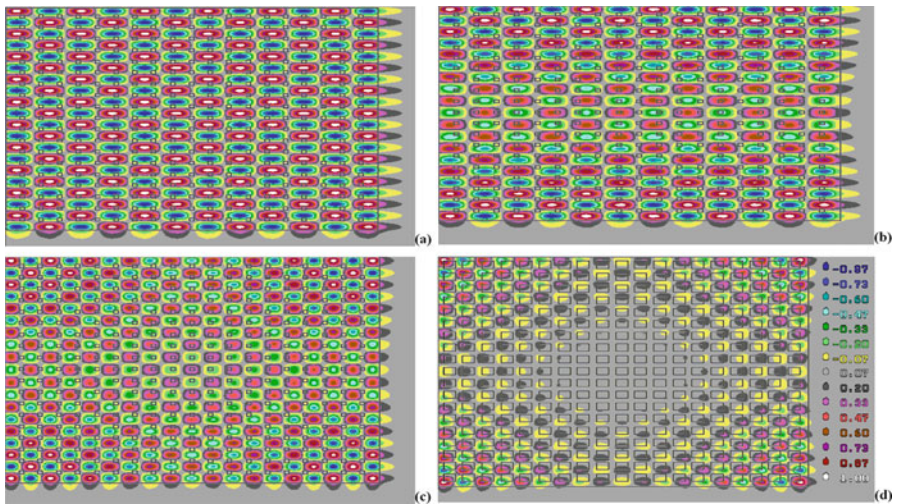


**Fig. 18.2** Photonic mode distribution patterns for the  $19 \times 19$  period 2D IPCR (*left and upper* external parts are cut).  $\text{SiO}_2/\text{SiO}_2$  structure  $b_z = 0.5 \mu\text{m}$ ,  $b_y = 0.6 \mu\text{m}$ ,  $d_z = 2.0 \mu\text{m}$ ,  $d_y = 1.8 \mu\text{m}$ . Modal Msg distribution (a) band mode  $s = 12$ ,  $g = 20$ ,  $\theta_1 = \pi/4$ ; (b) local surface mode  $s = 12$ ,  $g = 19$ ,  $\theta_1 = \pi/4$ ; (c) local edge mode,  $s = 19$ ,  $g = 19$ ,  $\theta_1 = \pi/4$  (lower contrast); (d) local edge mode,  $s = 19$ ,  $g = 19$ ,  $\theta_1 = \pi/4$  (higher contrast,  $b_z = 1.0 \mu\text{m}$ ,  $b_y = 1.1 \mu\text{m}$ ,  $d_z = 3.0 \mu\text{m}$ ,  $d_y = 3.0 \mu\text{m}$ )

has the period along  $Z$  axis  $d_z = a_z + b_z = 2.0 \mu\text{m}$  as well as along  $Y$  axis  $d_y = a_y + b_y = 1.8 \mu\text{m}$ , then we have total sizes of the IPCR  $39.5 \times 35.4 \mu\text{m}$  including the covering layer. The difference in optical contrasts for structures based on the same materials is explained by wider gaps for this geometry [10]. In Fig. 18.2a, shown is a typical band mode, energy  $\Omega_{sg} = 0.333 \text{ eV}$ ,  $s = 12$ ,  $g = 20$ , uniformly distributed inside the resonator's body. The part of field energy outside the IPCR in mode  $M_{sg}$  tails is small in comparison with the bulk part. This circumstance is the reason of small parameter existence and serves as a base of perturbation theory for field in a resonator of finite sizes [11]. In Fig. 18.2b, field amplitude distribution is shown for the local surface mode  $s = 12$ ,  $g = 19$  with energy  $\Omega_{sg} = 0.327 \text{ eV}$  which is characterized by dominating density of electromagnetic energy near both resonator surfaces parallel to  $OZ$  axis (Fig. 18.1). The case of edge local modes is presented in Fig. 18.2c (lower contrast,  $s = 19$ ,  $g = 19$ ,  $\Omega_{sg} = 0.378 \text{ eV}$ ) and Fig. 18.2d (higher contrast,  $s = 19$ ,  $g = 19$ ,  $\Omega_{sg} = 0.306 \text{ eV}$ ). Depending on the intrinsic optical contrast, the edge-kind local mode concentrates its density mainly near the edges inside the IPCR.

### 18.3 Mode Energy Angular Diagram for an Island Resonator

The island kind photonic resonator being principally a finite size object serving to concentrate the electromagnetic energy inside should be described by a basis set of 2D eigenfunctions which have finite amplitudes in the resonator's volume with decreasing to zero outside the IPCR. The electromagnetic flow of resonance frequency passes into the IPCR through the input and go out through the output prism (Fig. 18.1). The gain may be reached due to an appropriate ratio of input-output sections. One more circumstance is that the IPCR is a convenient system to operate the separate modes due to distinctive difference in their energies and wave vectors.

We have calculated the  $6 \times 7$ -period ( $\text{SiO}_2/\text{SiO}_2$ ) 2D IPCR consisting of rectangular glass wells with sides  $b_z = 1.0 \mu\text{m}$ ,  $b_y = 2.0 \mu\text{m}$  and  $\varepsilon_2 = 2.25$  periodically distributed in the optically more dense glass matrix with dielectric function  $\varepsilon_1 = 3.24$  so that the period along  $Z$  axis is  $d_z = a_z + b_z = 2.5 \mu\text{m}$  and along  $Y$  axis is  $d_y = a_y + b_y = 3.0 \mu\text{m}$ . The total sizes of the IPCR are  $16 \times 22$  microns including the covering layer.

The multitude of modes having the given number of nodal lines forms a branch in the TIR domain ( $\Theta_{\text{TIR}}, \pi/2 - \Theta_{\text{TIR}}$ ). In Fig. 18.3, 10 lowest mode branches were calculated for 30 angles  $\theta_1$  in interval  $0.589 < \theta_1 < 0.982$  (14 mode points at  $\theta_1 = \pi/4$ ). The basis contained 100 eigenfunctions,  $s_{\text{max}} = g_{\text{max}} = 10$ . The branches 1, 2... 10 are highlighted by colour. The inclined arrows show angles of strengthened Bragg diffraction along the symmetry directions: 0.629, 0.657, 0.695 radians and three symmetrically reflected points with respect to the  $\Gamma\text{M}'$  direction ( $\theta_1 = 0.785$ ). The calculated lowest energy is  $\Omega_{\text{min}} \approx 0.006 \text{ eV}$  (branch 1) and the maximal energy 0.372 eV is reached by mode of branch 9 at  $\theta_1 \approx 0.973$ , whereas

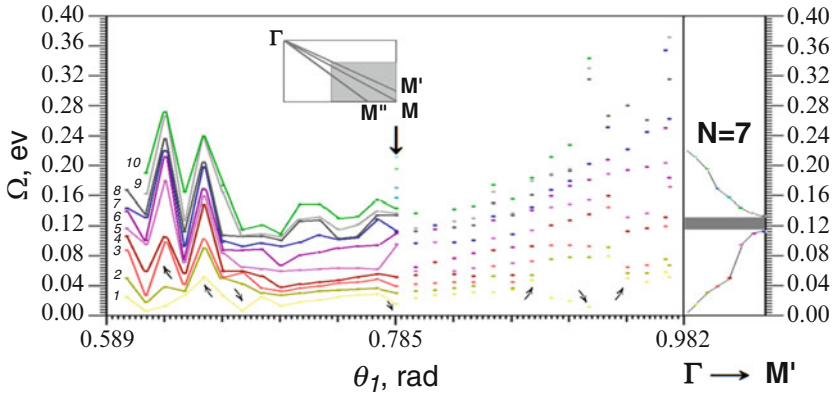


**Fig. 18.3** Mode energy angular diagram of the  $6 \times 7$ -period ( $\text{SiO}_2/\text{SiO}_2$ ) 2D IPCR. *Inset:* rectangular reciprocal lattice cell, symmetry directions:  $M'$ , corresponds to  $\theta_1 = \pi/4$ ;  $M$ , the resonator diagonal;  $M''$ , elementary cell symmetry direction. *Mode energy diagram.*  $\theta_1$ , plane wave incidence angle in the silicon glass matrix material within the TIR domain  $0.589 < \theta_1 < 0.982$ ; 1,2...10, conventional lines (branches) uniting modal points at different  $\theta_1$  by increased number of nodal lines;  $a_y = 1.5 \mu\text{m}$ ,  $a_z = 1.0 \mu\text{m}$ , well sizes  $b_z = 1.0 \mu\text{m}$ ,  $b_y = 2.0 \mu\text{m}$  (bar material 4, Fig. 18.1); dielectric functions  $\epsilon_1 = 3.24$  (matrix);  $\epsilon_2 = 2.25$  (bar material 4); *inclined arrows* show angles of strengthened Bragg diffraction, *vertical arrow*, direction  $\Gamma M'$ . *Right panel:* generalized bandgap diagram for  $\Gamma M'$  direction ( $N = 7$ ), first band, seven points, second band, seven points; gap is between 0.116 and 0.132 eV

in interval (0.922, 0.966) both branches 9 and 10 exceed the interval of calculation 0.4 eV. The calculations show that if  $N_z$  and  $N_y$  increase then all branches shift down and density of branches becomes larger. Therefore, the states existing in an infinite PhCr may be forbidden in a finite resonator.

In some sense the considered IPCR represents a generalization of a partial case of infinite PhCr when  $N_z, N_y$  should tend to infinity. The local density of modal points along energy axis increases with increasing  $N_z$  and  $N_y$  and simultaneously the all modal branches go down. Let us take into account that the number of eigenstates forming the band varies from 0 to  $N$  (number of periods in this direction) for the first band, from  $N$  to  $2N$  for the second and so on. Therefore, to transfer from the modal branches representation to the conventional description of the bandgap structure we should step by step select  $N$  points

$$N = \text{Int} \left( \sqrt{N_z^2 \cos^2 \theta_1 + N_y^2 \sin^2 \theta_1} \right) \tag{18.8}$$

corresponding to the chosen angle  $\theta_1$ . For the  $\Gamma M'$  direction ( $\theta_1 = \pi/4$ ) the lowest  $p$ -polarized band of the generalized bandgap diagram is shown at the right side of Fig. 18.2. As far as the number of states in this direction  $N = 7$ , the first band consists of seven points projected from the  $\Gamma M'$  column of mode points (vertical arrow) to right in order of the mode energy and wave vector growth.

In a conventional case of an infinite photonic crystal, when the number of periods along the chosen direction  $\Gamma M'$  goes to infinity the number of points forming the curve also goes to infinity. The second band contains the next 7 modes numbered from 8 to 14 with energy growth. A partial gap arises between 0.116 and 0.132 eV. In the case of an infinite resonator, the modes became allocated along the band line everywhere densely though the point's density is expressed by the same formula "crystal size/ $2\pi$ ". Here, we are considering  $p$ -polarized modes of the resonator. The linearly independent set of  $s$ -polarized modes form their own structure of branches and an additional band line arises in the  $\Gamma M'$  direction for each band.

If the resonator has the shape of a square and elementary cells are also squares, the calculated branches became allocated symmetrically as to the bisector  $\theta_1 = \pi/4$ . Besides, due to symmetry the modal branches are doubly degenerated. The decrease of symmetry leads to splitting of branches like what we can see for the considered IPCR. The SWE approach gives a smooth transformation of the considered IPCR (Fig. 18.1) to a structure with extremely increased  $d_y$  when the system becomes indistinguishable from a layered structure. Since the angular discreteness of spectrum arises due to the finite size of the resonator, we have got  $N$  angular-dependent mode branches inside every band of states [1, 9, 10].

## 18.4 Mode Energy Distribution Throughout the Island Resonator

The classification of the trapped inside the resonator modes is ruled by the Courant nodal line theorem [12, 13] claiming that for the system defined in the space  $R^m$ , the nodal set of eigenfunctions (modes) of Eq. (18.1) are locally composed of hypersurfaces of dimensions  $m-1$ . In particular, we have for  $m = 2$  a set of nodal lines which are either closed or having their ends at the definitional domain. Due to the principally unlimited definitional domain of the problem under consideration, the nodal lines must be also nonrestricted. Several topology features should be noted for the modes of a 2D island kind resonator.

- The node lines of a mode reflects symmetry of the system and are divided into two types: longitudinally (along  $Z$  axis) and transversely oriented.
- The node lines of both types are infinite.
- The energy hierarchy of modes correlates with number of node lines within a given type.
- If one of two modes has one node line more, it has higher energy, *ceteris paribus*.

The latter statement is the consequence of the easy proven theorem: between the two nodal lines of a mode one can find a node line of the older mode with higher energy. The Courant nodal line theorem gives a base to test the results of calculation both the set of mode branches (eigenvalues) and mode coordinate dependencies (eigenfunctions). In general, the structure of island resonator modes

shows the expected similarity to that existing for transverse electromagnetic waves in rectangular and cylindrical waveguides [14, 15]. In Fig. 18.4a, the classification of lowest eigenstates in the IPCR is presented. Two factors influence the classification: number of node lines and correlation between them. The first circumstance leads to the shell structure of states when a shell unites modes with the same number of node lines. It is obvious that two types of node lines produce three kinds of modes: with node lines along  $Z$  axis, along  $Y$  axis and containing both transverse and longitudinal node lines. In Fig. 18.4a, the ground state is represented by a mode without nodal lines, first shell consists of two modes with one node line, second shell contains three two-node line states and so on. In accordance with the Courant theorem, every added node line, even of another type, increases energy of state. Nevertheless in a binary structure with rectangular (non-square) lattice, the modes containing node lines of one kind may form more or less densely the ladder of energy levels. In particular, if period  $d_y > d_z$ , then modes with transverse node lines have softer spectrum. Mixed modes occupy intermediate position. Therefore the shells have a tilt that makes energy hierarchy of states more complicate like it is shown in Fig. 18.3a. The discussed above smooth transformation of the IPCR to a structure with extremely large magnitudes  $d_y$ , will express here in an essential reconstruction of modal structure: the left column remains the same, soft modes containing transverse node lines become practically indistinguishable from the left column modes with the same number of longitudinal nodal lines and vanish. As the result, the 2D energy angular diagram coincides with the spectrum angular diagram of a layered photonic crystal. The mode amplitudes  $h_m^\sigma$  have a sense of a mode expansion coefficients in the  $|s, g\rangle$  basis. Following (18.5) and (18.6), we calculated the complete eigenvalue problem including both energies and eigenfunctions in basis  $s_{\max} = g_{\max} = 10$ . In Fig. 18.4b, spatial distribution for the lowest 6 modes  $\sigma = 1, 2, \dots, 6$  at  $\theta_1 = 0.785$  is shown. The calculated energies of states  $\Omega_\sigma$  are 0.0116 eV, 0.031 eV, 0.040 eV, 0.052 eV, 0.096 eV and 0.112 eV. Though the nodal lines allocate in accordance with the Courant theorem (arrows), small deviations of symmetry in the distribution of modal amplitudes arise due to not too high accuracy of calculations (0.01).

To know the distribution of field density in the IPCR may be of importance in two aspects. First, pumping of a separate mode inside the resonator's TIR domain leads to accumulation of energy distributed throughout the IPCR. Therefore the output beam may be made of much more intensity than the input one. One more circumstance concerns an opportunity to use the distributed active impurities matching to a chosen mode.

## 18.5 Summary

Here the theory of a binary island kind photonic crystal resonator has been developed in the framework of standing wave expansion method. The 2D basis formation procedure was implemented with the use of analytically obtained two



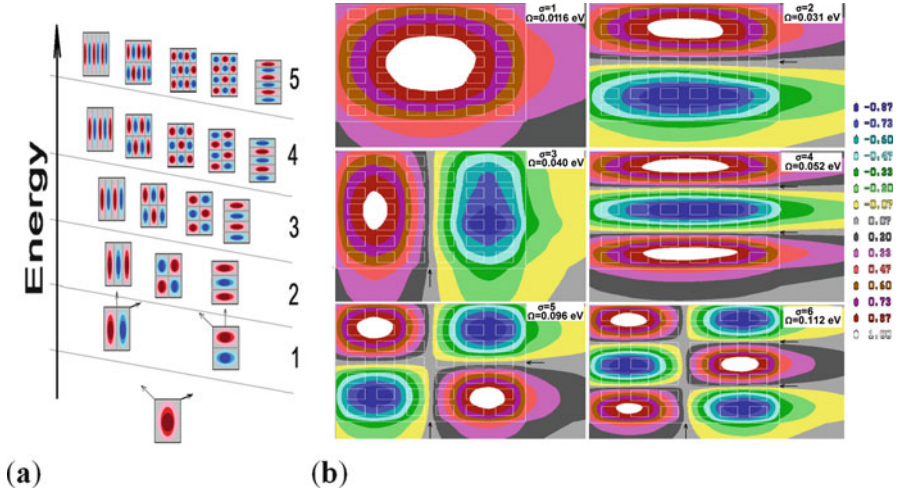


**Fig. 18.4** (a) The eigenstates classification in an island kind 2D photonic crystal resonator, lowest 20 modes. Two systems of nodal lines, oriented along  $Z$  and  $Y$  axis; it is taken that  $Y$  direction has softer spectrum,  $1, 2 \dots 5$  shells of states; (b) Calculated field amplitude distribution for 6 lowest p-polarized modes  $\sigma = 1..6$ , of the  $6 \times 7$ -period ( $\text{SiO}_2/\text{SiO}_2$ ) 2D IPCR (parameters are described in Fig. 18.3), ICPR mask, white lines,  $\theta_1 = \pi/4$

1D basis sets for the two probe 1D structures and Courant's nodal line theorem in the process of basis generation. Electromagnetic energy distribution for some typical band, surface and edge modes of a  $19 \times 19$  period photonic resonator were calculated. The procedure of the transfer to conventional band structure description was considered for a  $6 \times 7$  period finite structure was investigated analytically and numerically. The classification concept of island kind resonator's modes is proposed. It worth noting that though the rectangular lattice was considered, the proposed SWE method for finite resonators may be adapted for any symmetry of the lattice as well as for any shape of bars in matrix.

## References

1. Glushko EY, Glushko OE, Karachevtseva LA (2012) Photonic Eigenmodes in a photonic crystal membrane. ISRN Optics 2012:Article ID 373968:6p. doi:10.5402/2012/373968
2. Yablonovich E (1987) Inhibited spontaneous emission in solid state physics and electronics. Phys Rev Lett 58:2059
3. John S, Joannopoulos D, Johnson SG, Winn JN, Meade RD (2008) Photonic crystals: molding the flow of light, 2nd edn. Princeton University Press, Princeton
4. Sakoda K (2001) Optical properties of photonic crystals. Springer, Berlin
5. Winn NY, Fink S, Fan Y, Joannopoulos JD (1998) Omnidirectional reflection from a one-dimensional photonic crystal. Opt Lett 23:1573–1575



6. Deopura M, Ullal CK, Temelkuran B, Fink Y (2001) Dielectric omnidirectional visible reflector. *Opt Lett* 26:1197–1199
7. Loncar M, Doll T, Vuchkovich J, Scherer A (2000) Design and fabrication of silicon photonic crystal optical waveguides. *J Lightwave Technol* 18:1402–1411
8. Jamois C, Wehrspohn RB, Andreani LC, Hermann C, Hess O, Gosele U (2003) Silicon-based two-dimensional photonic crystal waveguides. *Photonics Nanostruct Fundam Appl* 1:1–13
9. Glushko EY, Glushko AE, Karachevtseva LA (2010) Photonic membranes and photonic crystal resonators for all-optical signal processing. *Proc SPIE* 7713:77131D
10. Glushko EY (2014) Influence of oxidation on the spectrum of a ternary comb-like silicon photonic crystal: intrinsic modes, reflection windows and intrinsic contrastivity. *Eur Phys J D* 68:264
11. Glushko EY, Glushko AE, Evteev VN, Stepanyuk AN (2008) Electromagnetic eigenwaves in metastructures: perturbation theory method. *Proc. SPIE*. 6888:69880J–69880J-11
12. Courant R, Hilbert D (1953) *Methods of mathematical Physics*, vol 1. Interscience, New York
13. Gladwell GML, Zhu H (2002) Courant's nodal line theorem and its discrete counterparts. *Q J Mech Appl Math* 55(1):1–15
14. Orfanidis SJ *Electromagnetic waves and antennas*, Chapter 9. Online book: <http://eceweb1.rutgers.edu/~orfanidi/ewa/ch09.pdf>
15. Oron R, Davidson N, Friesem AA (2001) Transverse mode shaping and selection in laser resonators. In: Wolf E (ed) *Progress in optics* 42. Elsevier Science, Burlington

# Chapter 19

## Dynamic Light Scattering with Nanoparticles: Setup and Preliminary Results

G. Derkachov, D. Jakubczyk, K. Kolwas, Y. Shopa, and M. Woźniak

### 19.1 Experimental Method and DLS Setup

Dynamic light scattering (DLS) method for particle size determination is based on the measurement of scattered light intensity fluctuations on a micro- and millisecond time scale in a volume containing particles in suspension or solution [1–3]. The motion of particles is diffusion controlled and is characterized by the diffusion coefficient  $D$ . For noninteracting spherical Brownian particles in suspension characterized with a low Reynolds number, the Stokes-Einstein equation holds:

$$D = \frac{kT}{6\pi\eta R_h}, \quad (19.1)$$

where  $R_h$  is the so-called hydrodynamic radius,  $\eta$  is the dynamic viscosity of the dispersion medium,  $T$  is the absolute temperature, and  $k$  is the Boltzmann constant. The obtained optical signal shows random changes due to the Brownian motions of the particles. This signal can be interpreted in terms of an autocorrelation function (ACF). Incoming signal is processed in real time with a digital correlator, and the ACF versus the delay time  $\tau$  is extracted. Time-dependent autocorrelation function

---

G. Derkachov • D. Jakubczyk • K. Kolwas • M. Woźniak  
Institute of Physics, Polish Academy of Sciences, Aleja Lotników 32/46, PL-02668,  
Warsaw, Poland  
e-mail: [derkaczg@ifpan.edu.pl](mailto:derkaczg@ifpan.edu.pl)

Y. Shopa (✉)  
Cardinal Stefan Wyszyński University in Warsaw, ul. Dewajtis 5, PL-01815, Warsaw, Poland  
e-mail: [i.shopa@uksw.edu.pl](mailto:i.shopa@uksw.edu.pl)

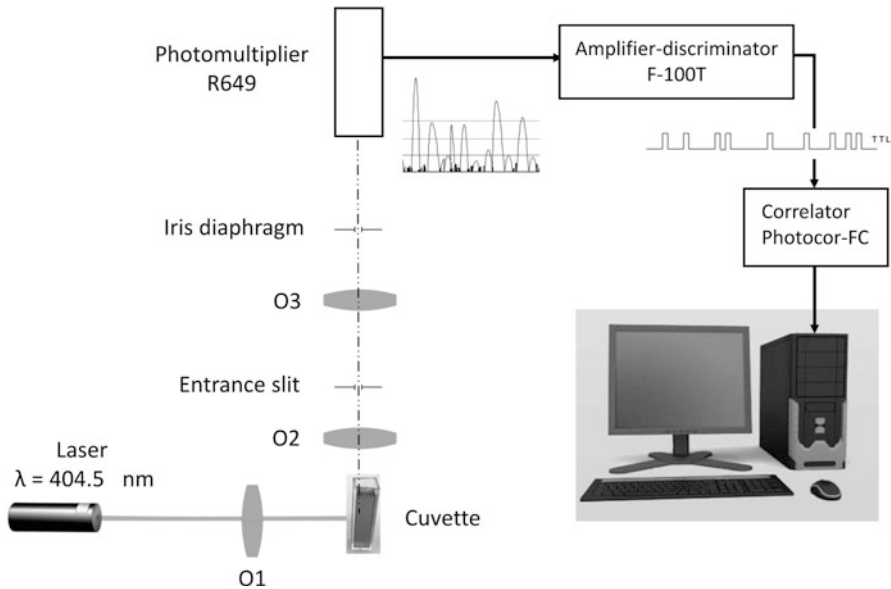


**Fig. 19.1** Schematic diagram of the DLS experimental setup

$G(\tau)$ , which is measured experimentally, typically is decaying exponentially with a decay constant  $\Gamma$

$$G(\tau) = B_0 + B_1 \exp(-2\Gamma\tau), \quad (19.2)$$

where  $B_0$  and  $B_1$  are constants independent of time. In such case, after processing the experimental data, the diffusion coefficient  $D$  can be found from  $\Gamma = Dq^2$  relation, where  $q = \frac{4\pi}{\lambda} n \sin(\theta/2)$  is the scattering number,  $\theta$  is the angle between the incident and the scattered light wave vectors, and  $n$  is the refractive index. Inserting  $D$  into the Stokes-Einstein equation (19.1) yields the particle size.

The schematic diagram of the experimental setup for DLS measurements is presented in Fig. 19.1. As the light source we chose 404.5 nm laser with 22 mW output power, because violet light gives higher scattering intensity than the more commonly used red. Laser light passes through a 60-mm focal range lens that focuses the beam into the cell with the investigated liquid placed in the temperature-stabilized cylindrical jacket. In order to minimize the effect of stray light and maximize the signal to noise ratio, the scattered light is collected at  $\theta = 90^\circ$  to the incident beam with a confocal lens system and fed into a photomultiplier tube (Hamamatsu R649 in a C10372 dedicated housing).

The signal from the photomultiplier is converted with transimpedance preamplifier/discriminator (Advanced Research Instruments Corporation, F-100T) to TTL level 10-ns pulses and sent to real-time correlator (Photocor-FC) built with a software-configurable FPGA circuits [4]. The DLS setup (with a single photomulti-

plier) outputs the count rate and the autocorrelation function. The results are stored in an ASCII data file and analyzed with Alango DynaLS software [5–7].

In order to find ACF reliably, the signal must be measured over a relatively long time (>60 s). The scattered light intensity (count rate) depends on the number of particles diffusing within the sample volume. The dark current pulses in our experiments did not exceed 150 cps level.

## 19.2 DLS Setup Calibration with Gold and Silicon Dioxide Nanoparticles

First DLS measurements were performed with ultrapure water suspensions of highly monodisperse gold and SiO<sub>2</sub> spheres with diameters of 30 and 445 nm, respectively. The samples were loaded into a 3-mL cuvette with 10-mm square cross section.

The measurements of ACF of monodisperse gold particles with a diameter of 30 nm (given by the manufacturer) show single exponential decay with the relaxation time  $1/2\Gamma = \tau_0 = 0.068$  ms (Fig. 19.2). Using the physical parameters of the experiment, we obtained the nanoparticles diameter of 30.8 nm, which is in good agreement with the value given by the manufacturer. DLS measurement of SiO<sub>2</sub> spheres in water gives 1.16 ms and 452 nm, which is also in agreement with the diameter given by the manufacturer. In case of monodisperse particles, the hydrodynamic diameter DLS measurement error does not exceed several percent.

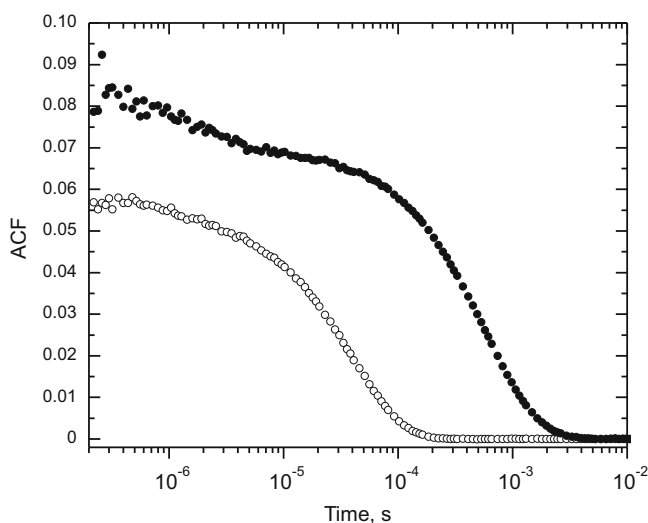


**Fig. 19.2** The measured ACF for 30 nm gold ( $\circ$ ) and 445 nm SiO<sub>2</sub> ( $\bullet$ ) particles in water

The presented measurements indicate that our setup was properly calibrated and that it should produce reliable results.

### 19.3 Study of Aqueous Solutions of Sodium Dodecyl Sulfate

Our further studies were focused on sodium dodecyl sulfate (SDS), a synthetic organic compound with the formula of  $\text{CH}_3(\text{CH}_2)_{11}\text{SO}_4\text{Na}$ . We have measured dynamic light scattering on aqueous solutions of SDS as a function of SDS concentration and temperature. Samples were prepared from commercial SDS product (Sigma-Aldrich, ACS reagent,  $\geq 99.0\%$ ) with ultrapure water produced in-lab (Millipore, Simplicity UV) few day before the experiments, with concentrations of 5, 12, 20, 30, 40, 60, 80, and 100 mM/L. On loading into the cuvette, a 0.2-micron filter was used. The temperature was stabilized down to  $\pm 0.5$  K in 295–340 K range.

In order to calculate  $R_h$  from the Stokes-Einstein equation, the refractive index of dispersion medium/solvent and its viscosity must be known. The refractive index of 100 mM/L SDS solution differs by less than 0.001 from that of pure water. Thus for finding  $q$  we used the  $n$  value for water and its respective temperature dispersion from [8] and [9]. Considering the low SDS concentration, the dynamic viscosity  $\eta$  and its temperature dependence were also taken for pure water.

For the SDS solution concentrations used in experiment, the measured scattered light intensities were exceptionally small: from 5000 to 50,000 cps. In consequence, obtaining an ACF suitable for interpretation required long accumulation times. We found that SDS formed relatively very large, non-spherical aggregates in water [10–12], which manifested in ACF (Fig. 19.3) as a slope around 400 ms. Filtering did not remove these SDS aggregates. They weakly depended on SDS concentration, while they seemed to diminish with growing temperature. Due to high non-sphericity calculating of hydrodynamic radius made no sense.

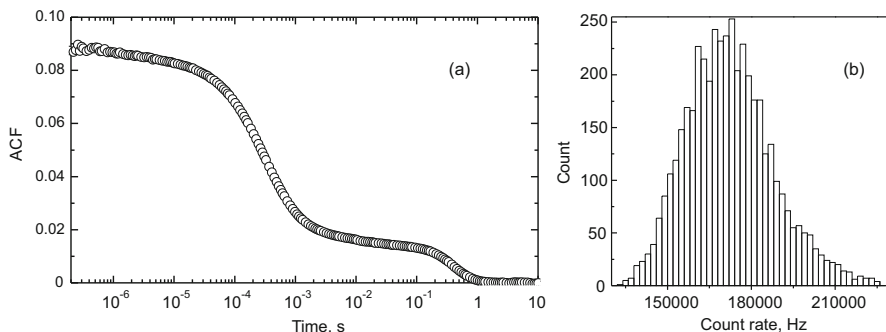


**Fig. 19.3** Results from dynamic light scattering experiments on 12 mM/L SDS solution, which shows high values of correlation time. The corresponding count rate histogram exhibits a classical gaussian-like shape

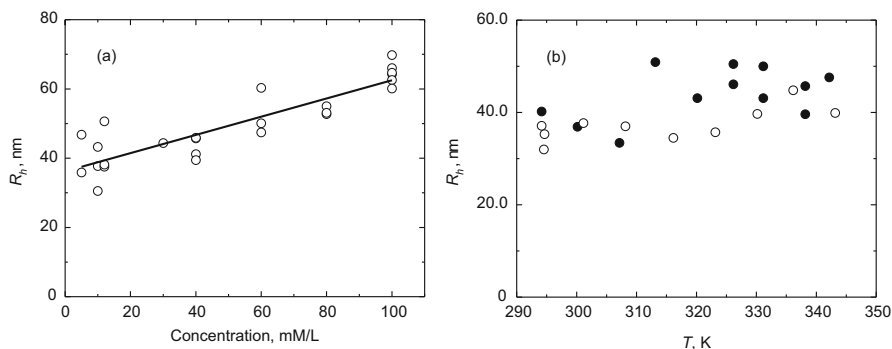


**Fig. 19.4** Hydrodynamic radius  $R_h$  as a function of SDS concentration in water (a) and as a function of temperature (b) for concentrations of 12 (○) and 20 mM/L (●)

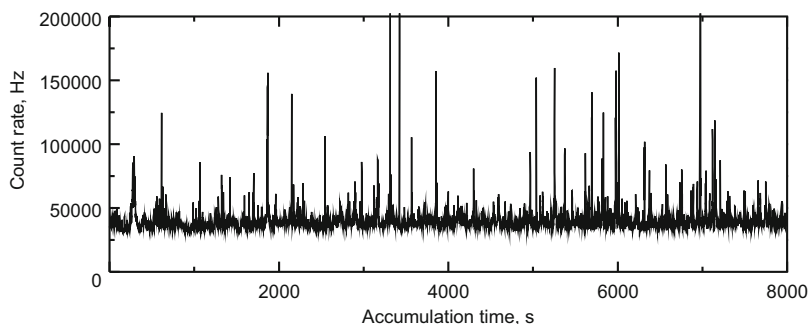


**Fig. 19.5** Count rate monitor for 20 mM/L SDS concentration, at 295.5 K and 8000 s accumulation time

On the other hand, the relaxation time of  $\sim 0.3$  ms would correspond to aggregates of several dozen nanometers in size, which is much larger than the micelle size [13, 14]. Their size depended on the SDS concentration; however, we did not observe any phase transition versus the concentration. The corresponding relaxation time depended on the temperature, but due to the opposite temperature dependence of  $D$ , the aggregate size hardly exhibited any temperature dependence. Both dependencies – versus concentration and versus temperature – are shown in Fig. 19.4.

Count rate monitor shown in Fig. 19.5 exhibits short-lasting high-value intensity deviations from the average scattering intensity of a long measurement. It seems to indicate the presence of ultra-large aggregates in the SDS solution, which scatter light very intensively. Such scattering episodes preclude accessing short relaxation times in the correlation function.

## 19.4 First ACF of the Single Droplet

Our ultimate goal is the application of DLS to single, freely suspended multi-component droplets. Our preliminary experimental results confirm the possibility of such DLS usage.

We applied the DLS technique to single droplets levitated in an electrodynamic quadrupole trap. Electrodynamic trapping is a well-established experimental technique [15–17] using a combination of alternating (AC) and static (DC) electric fields to constrain particle to a small volume, ideally to a point. The droplet was illuminated with 458-nm vertically polarized Ar<sup>+</sup> laser light, and the scattered light was collected around the right angle in the horizontal scattering plane. The droplet was in the focus of an objective, and the collected light was introduced into an optical fiber and fed to a photomultiplier. For higher scattered light intensity, the scattered light might also be collected directly into an optical fiber. Using an optical fiber for the collection of scattered light (in the Mie regime) has an advantage over a lens optics [18, 19] since the fiber entrance aperture works as a good spatial filter and ensures a small area of coherence which is important for ACF quality.

In experiments presented in this work, we used several micron-sized droplets of pure diethylene glycol in a dry nitrogen atmosphere. An example of ACF obtained with the described method is presented in Fig. 19.6.

The first results were obtained within a 30-s interval, which was found sufficient to calculate the ACF. Due to the evaporation of the droplet, there is a decrease of the scattered light intensity, and the collection interval must be appropriately short in order to obtain a sensible ACF. However, the amplitude of ACF was very large in comparison to the results obtained for a bulk solution/suspension in a cuvette.

We expect that, in general, characteristic times found from ACF can be attributed to different phenomena associated with the droplet, for instance, macro- and

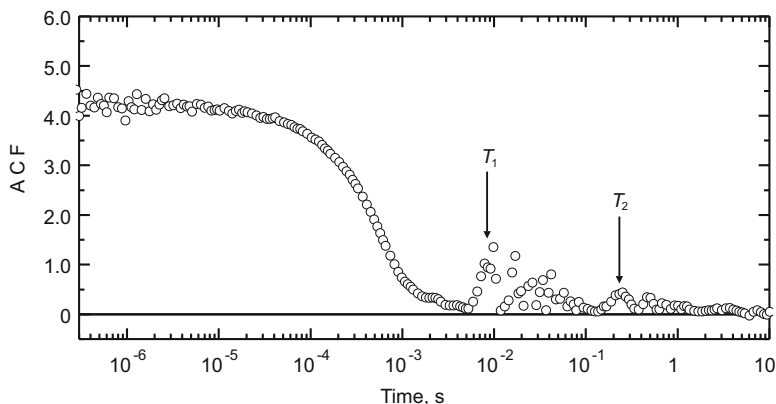


**Fig. 19.6** The measured correlation function for a pure diethylene glycol droplet. Characteristic times  $T_1 = 8.4$  ms and  $T_2 = 0.23$  s of droplet motion are indicated with arrows

micromotion of the droplet in the trap and rotations of the droplet. For a droplet of suspension, the motions of particles inside the droplet should be visible as well, since their characteristic time is much different from the mentioned above. For a droplet of a pure liquid (diethylene glycol) and the light collection with the lens, the micromotion of the droplet with the drive frequency of the trap at 120 Hz was plainly visible (Fig. 19.6). The second type of droplet motion at 4.3 Hz could be possibly associated with the secular (macro) motion in the trap.

## 19.5 Conclusions

The DLS setup was designed, built, and used for studying diverse solutions and suspensions of nanoparticles. It was tested with bulk gold and silica nanosuspensions in a cuvette and produced good results. Next, we tried to apply the DLS method to sodium dodecyl sulfate solution in cuvette versus temperature and SDS concentration. We found aggregates of various sizes and probably complex morphology. However, the interpretation of the results in detail seems hardly possible. In general, the preliminary results showed that the sensitivity of the DLS setup is sufficient for detection of light scattered by a single micron-sized droplet. We started our experiments with droplets of diethylene glycol and obtained an ACF exhibiting at least two characteristic times, corresponding to motions of the droplet in the trap. We expect that for a droplet of suspension, there is a possibility to find characteristic times corresponding to the evolution of suspension in the droplet and its internal structure.

**Acknowledgements** The authors acknowledge financial support from the National Science Centre, Poland, grants number 2014/13/D/ST3/01882 and 2014/13/B/ST3/04414.

## References

1. Chu B (1974) *Laser light scattering*. Academic Press, New York
2. Brown W (1993) *Dynamic light scattering: the method and some applications*. Oxford University Press, New York
3. Frisken BJ (2001) Revisiting the method of cumulants for the analysis of dynamic light scattering data. *Appl Opt* 40:4087–4091
4. Multi-angle dynamic and static light scattering instrument Photocor complex. [www.photocor.com](http://www.photocor.com). Cited 7 Dec 2016
5. Koppel DE (1972) Analysis of macromolecular polydispersity in intensity correlation spectroscopy: the method of cumulants. *J Chem Phys* 57:4814–4820
6. Provencher SW (1979) Inverse problems in polymer characterization: direct analysis of polydispersity with photon correlation spectroscopy. *Macromol Chem Phys* 180:201–209
7. Software for particle size distribution analysis in photon correlation spectroscopy. <http://www.softscientific.com/science/WhitePapers/dynals1/dynals100.htm>. Cited 12 Dec 2016



8. Harvey AH, Gallagher JS, Levelt Sangers JMH (1998) Revised formulation for the refractive index of water and steam as function of wavelength, temperature and density. *J Phys Chem Ref Data* 27:761–775
9. Bashkatov AN, Genina EA (2003) Water refractive index in dependence on temperature and wavelength: a simple approximation. *Proc SPIE* 5068:393–395
10. Hayashi S, Ikeda S (1980) Micelle size and shape of sodium dodecyl sulfate in concentrated sodium chloride solutions. *J Phys Chem* 84:744–751
11. Ikeda S, Hayashi S, Imae T (1981) Rodlike micelles of sodium dodecyl sulfate in concentrated sodium halide solutions. *J Phys Chem* 85:106–112
12. Almgren M, Swarup S (1982) Size of sodium dodecyl sulfate micelles in the presence of additives. 2. Aromatic and saturated hydrocarbons. *J Phys Chem* 86:4212–4216
13. Mukerjee P, Mysels KJ (1971) Critical micelle concentration of aqueous surfactant systems. NSRDS-NBS series, vol 36. U.S. National Bureau of Standards, Washington, DC
14. Kenneth G, Norelus A (1993) Determining the critical micelle concentration of aqueous surfactant solutions: using a novel colorimetric method. *J Chem Educ* 70:254–257
15. Woźniak M, Derkachov G, Kolwas K, Archer J, Wojciechowski T, Jakubczyk D, Kolwas M (2015) Formation of highly ordered spherical aggregates from drying microdroplets of colloidal suspension. *Langmuir* 31(28):7860–7868
16. Major F, Gheorghe V, Werth G (2005) Charged particle traps. Springer, Berlin
17. Arnold S (1991) A three-axis spherical void electrodynamic levitator trap for micro-particle experiments. *Rev Sci Instrum* 62:3025–3028
18. MacFadyen AJ, Jennings BR (1990) Fibre-optic systems for dynamic light scattering – a review. *Opt Laser Technol* 22:175–187
19. Goldburg WI (1999) Dynamic light scattering. *Am J Phys* 67:1152–1160

# Chapter 20

## Application of Nanofilled Polymer Coatings for Increasing Radiation Resistance of Solar Cells

L. P. Steblenko, A. A. Podolyan, L. N. Yashchenko, D. V. Kalinichenko, A. N. Kuryliuk, Yu. L. Kobzar, L. A. Voronzova, V. N. Kravchenko, S. N. Naumenko, and A. N. Krit

### 20.1 Introduction

Nowadays silicon dominates in solar power engineering since the efficient techniques of manufacturing solar cells (SCs) of it are well-known [1–3]. At the same time, for the silicon SCs to remain competitive, one should search for the ways of increasing their long-term stability.

As is known, one of the main functional characteristics of SCs is the carrier lifetime. It is also known that the concentration of recombination centers determining the carrier lifetime can change due to a variety of factors. Redistribution of carrier lifetime determining recombination centers in a Si crystal can be caused by not only certain treatments (chemicals, radiation, magnetic fields) but also such processes as impurity gettering and adsorption by the surface as well as deposition of various coatings. The above-listed treatments and processes are directly related to SC operation stability.

It should be noted that various antireflection films being deposited on the front surface of SCs in order to increase the efficiency can also be a high-quality protective and passivating coating [4], which allows one to reduce the degrading action of an aggressive environment.

---

L.P. Steblenko (✉) • A.A. Podolyan • D.V. Kalinichenko • A.N. Kuryliuk • Y.L. Kobzar  
V.N. Kravchenko • S.N. Naumenko • A.N. Krit  
Faculty of Physics, Taras Shevchenko National University of Kyiv, vul. Volodymyrska 64/13,  
01601, Kyiv, Ukraine  
e-mail: [kurylyuk\\_a2008@ukr.net](mailto:kurylyuk_a2008@ukr.net)

L.N. Yashchenko • L.A. Voronzova  
Institute of Macromolecular Chemistry, National Academy of Sciences of Ukraine, Harkivske  
shose, 48, 02160, Kyiv, Ukraine

For the modern solar power engineering, an issue of the day is increasing the radiation resistance of silicon-based semiconductor devices. Phenomena related to solar Si (s-Si) device functional parameter degradation can occur in subjecting the devices to ionizing radiation with both superthreshold and subthreshold energies. The latter case is most interesting because, on the one hand, it has not been practically studied yet and, on the other hand, it is important for understanding the nature of degradation processes under low-energy irradiation.

Gaps in the field of studying the radiation effect on carrier lifetime in SCs point to the urgency of this problem and to the need for accumulating experimental data on the ways of preventing SC electrophysical parameter degradation under the action of ionizing radiation. In this connection, the aim of our work was to investigate the possibilities of optimal combination of passivating nanofilled polymer coating and low-energy X-ray irradiation which together reduce degradation of the photovoltage determining electrophysical parameters of s-Si crystals.

## 20.2 Experimental

Boron-doped s-Si crystals with specific resistance of  $5 \Omega \cdot \text{cm}$  and crystallographic surface orientation  $\{100\}$  were used.

The coatings on the basis of both unfilled and nanofilled epoxy-urethane polymers were applied on the surface of the s-Si samples. The synthesis of the unfilled epoxy-urethane oligomer was carried out through the stage of obtaining the prepolymer on the basis of toluylenediisocyanate (2,4–2,6 TDI) and polyoxypropyleneglycol (POPG MM 1052) with subsequent addition of epoxy oligomer ED-20. The synthesis of the inorganic component (filler) was carried out by the reaction of hydrolysis and condensation of tetraethoxysilane (TEOS) directly in the environment of polyoxypropyleneglycol (nPOPG). The content of the polysiloxane particles (PSPs) in terms of  $\text{SiO}_2$  was 0.001, 0.5, and 1.0 wt. %. According to the small-angle X-ray scattering, the sizes of the synthesized primary PSPs were from 5 to 80 nm. The IR spectroscopy of the obtained structures has shown that the PSPs formed in nPOPG are associated with POPG by both hydrogen and covalent bonds.

Both types of epoxy-urethane polymers (unfilled and nanofilled) were obtained by mixing the respective epoxy-urethane oligomers with a hardening agent (isomethyltetrahydrophthalic anhydride (iso-MTHPA)) taken in a certain ratio. 2,4,6-Tris-(N, N-dimethylaminomethyl)phenol (UP-606/2) was used as a hardening accelerant. The thickness of the coatings deposited on the s-Si surface was  $20 \mu\text{m}$ .

Soft X-rays with the photon energy  $W = 8 \text{ keV}$  (Cu  $K_\alpha$  line) and exposure dose  $D = 0.3 \cdot 10^2 \text{ Gy}$  were used in our study. Fast ( $\tau_1$ ) and slow ( $\tau_2$ ) photovoltage decay components were used as a response of “s-Si + uEU” and “s-Si + nEU” to X-ray irradiation. Photovoltage decay kinetics was studied by means of capacitance technique [5].

In studying the aggressive action of irradiation solved was a problem of obtaining a correlation between the irradiation-stimulated changes in the electrophysical parameters and the charge state evolution in *s*-Si crystals.

The charge state of the surface was determined using a technique based on the local measurements of photovoltage at each point of the sample; these data were then used to reconstruct the maps of the surface electric potential distribution. To excite the charge carriers, we used pulses from a LED, with pulse duration of a few microseconds and the spectral emission peak at 650 nm. This provided generation of charge carriers on the surface. The photovoltage was generated by applying the emission of a red LED laser (wavelength of 650 nm, power 7 mW), focused into a light spot of approx. 100  $\mu\text{m}$  in diameter. The photovoltage signal was scanned across the surface of the sample with the step size of 100  $\mu\text{m}$ . Thus, the essence of the method of the surface charge state investigation was to measure the local kinetics of photovoltage decay and to build the surface potential maps on the basis of photovoltage decay curves.

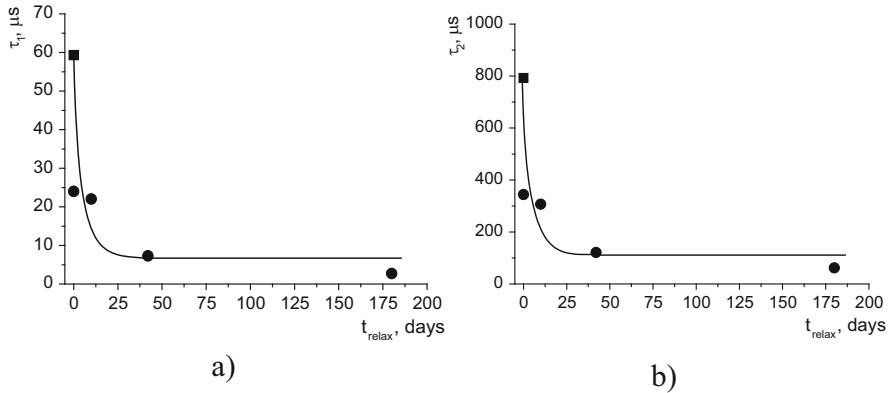
The EPR spectra of silicon samples were recorded at room temperature using a “BRUKER ELEXSYS E580” EPR spectrometer. The microwave frequency was 9.81 GHz, the modulation frequency was 100 kHz, and the microwave power was varied from 20 to 40 mW. The spectra were recorded in the scanning range of permanent magnetic field  $B_0 = 3480\text{--}3540$  Oe.

The ellipsometric measurements of the phase shift  $\Delta$  between the *p*- and *s*-components of the polarization vector and the azimuth  $\psi$  of the restored linear polarization as a function of the angle of incidence  $\varphi$  for the Si samples were carried out on a standard laser ellipsometer LEF-3 M-1 with an operating wavelength of the helium-neon laser  $\lambda = 632.8$  nm. From the angular dependences  $\cos\Delta(\varphi)$  and  $\text{tg}\psi(\varphi)$  determined were the principal angle of incidence  $\varphi_0$  ( $\cos\Delta = 0$ ) and  $\text{tg}\psi$  at that angle.

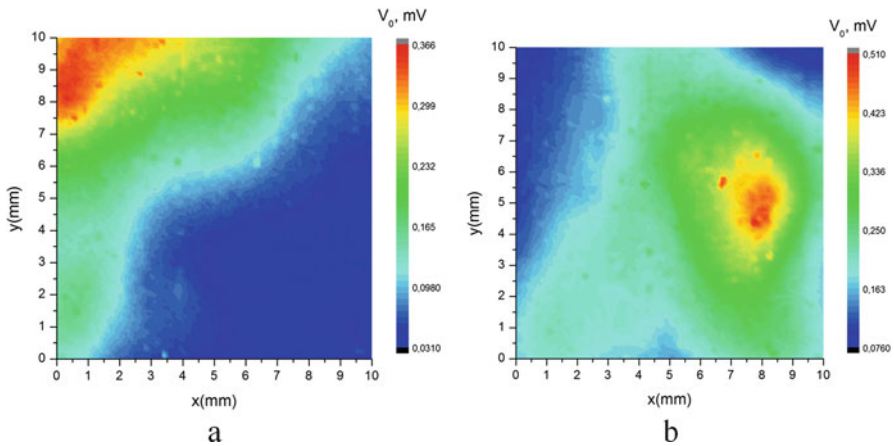
### 20.3 Experimental Results and Discussion

Figure 20.1a, b shows the values of  $\tau_1$  and  $\tau_2$  parameters calculated from the curves of photovoltage decay recorded just after termination of X-ray treatment and after a certain period of time. One can see that the values of both components of the photovoltage decay decrease after X-ray treatment, which indicates the radiation-stimulated changes in the decay kinetics.

As is known, the fast decay component  $\tau_1$  is determined by the surface electronic states and thus corresponds to the lifetime of charge carriers at the surface. The slow decay component  $\tau_2$  is associated with the presence of the near-surface potential barrier for charge carriers and, in fact, is identified with the carrier lifetime in the near-surface layer. On this basis, the results of our study indicate a decrease in the carrier lifetime under X-ray irradiation both at the surface and in the near-surface layer. This may be due to a significant increase in the number of charged centers at the surface and in the near-surface region, which act as recombination centers



**Fig. 20.1** The dependence of fast (a) and slow (b) photovoltage decay time constants in *s-Si* crystals on the time elapsed after termination of X-ray treatment: ■, control samples; ●, silicon samples after X-ray treatment with a dose of  $D = 3 \cdot 10^4$  Gy

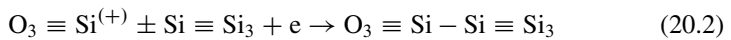
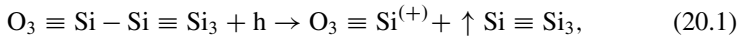


**Fig. 20.2** Distribution of surface electrostatic potential in *s-Si* samples: (a) before X-ray treatment (control samples); (b) after X-ray treatment ( $D = 3 \cdot 10^4$  Gy)

and traps. Additional studies of the surface distribution of electrostatic potential have confirmed this assumption. It has been established that, after X-ray treatment, the surface regions with a higher potential expand, while the surface regions with a lower potential shrink in size (Fig. 20.2). The latter indicates that the absolute value of the surface electrostatic potential increases after X-ray irradiation. So, the changes in the kinetics of photovoltage decay, which are detected in *s-Si* crystals after X-ray treatment, correlate well with the change in the charge state of the surface and near-surface layers.

Our results agree well with the experimental results and conclusions presented in [6]. The authors of [6] have investigated the influence of soft X-ray radiation

with photon energies up to 20 keV on the change of the limiting voltage in MOS components of integrated circuits. According to [6], X-ray irradiation led to the accumulation of positive (hole) charge in the bulk of the MOS structure oxide and stimulated generation of the surface states (SS). A characteristic feature of the relaxation process which was observed in [6] was a synchronous change of the charge in the oxide and at the SS. The results obtained in [6] reveal the common mechanism of generation of radiation-induced electric charge for the SS and for the space charge. This mechanism is explained by the authors of [6] using the following reactions:



The first reaction describes the breakage of strained Si-Si bonds at the Si-SiO<sub>2</sub> interface during the capture of radiation-generated holes. This leads to formation of the SS in the form of dangling bonds (*p<sub>b</sub>*-centers) and generation of the positively charged E'-centers in the oxide. The reverse reaction takes place in case of an electron tunnel transition from silicon to E'-center followed by restoration of Si-Si bond. As noted in [6], the tunneling mechanism is confirmed by the logarithmic dependence of slow relaxation of space charge in the oxide. Approximating the conclusions of the authors of [6] to our experimental results, we can assume that, after the X-ray treatment at the Si-SiO<sub>2</sub> interface of the studied s-Si crystals (where SiO<sub>2</sub> is a natural oxide which is always present at the silicon surface), the density of the SS is increased due to the breakage of strained Si-Si bonds and the space charge is accumulated. The latter affects the processes of recombination and carrier capture and correspondingly changes the photovoltage decay kinetics, which manifests itself in a decrease in the fast and slow decay time constants.

Applying the EPR method, the authors of [7] have shown that the radiation treatment (in particular, ion irradiation) of silicon leads to the formation of defects in its crystal lattice, which are usually described as certain vacancy-like centers (V<sub>V</sub>-centers) or as dangling bonds (D-centers). According to [7], the accumulation of such defects leads to structure amorphization, the mentioned centers remaining in amorphous phase as well. The conclusions drawn by the authors of [7] whose study was focused on the effects of radiation (ion) treatment on the changes of the defect structure of silicon used for microelectronics have encouraged us to conduct similar studies on Si crystals used for solar power applications. One of the scientific problems which required solution was to detect changes in the structural state of s-Si crystals upon the action of low-energy X-rays and to find a correlation between changes of the structural and electrophysical parameters.

Our experimental data obtained using the EPR method (Fig. 20.3) indicate that the low-energy X-ray treatment of s-Si crystals results in increasing the intensity of the spectral line which characterizes the paramagnetic centers with a g-factor of 2.0055. These centers correspond to dangling bonds. So, the X-ray irradiation

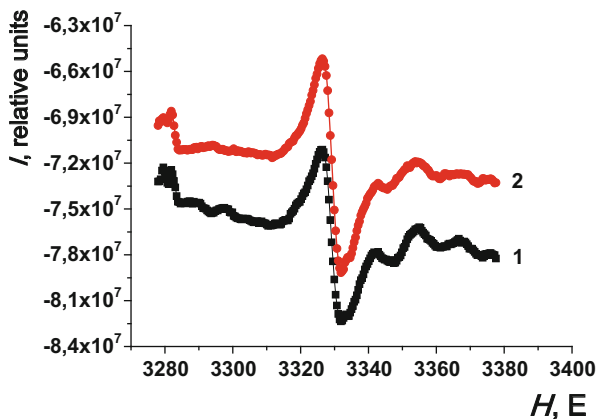


**Fig. 20.3** EPR spectra of s-Si crystals: (1) control samples; (2) samples after X-ray treatment ( $D = 3.7 \cdot 10^4$  Gy)

can lead not only to formation of radiation-induced defects in crystals but also to breakage of chemical bonds, in particular, to breakage of Si-O-Si bonds in silicon. A consequence of this can be the formation of radicals of broken bonds of  $\equiv\text{Si} \bullet$  type and  $\equiv\text{SiO} \bullet$  type that resonate as paramagnetic centers, which is characteristic of broken bonds. We have suggested that, after the s-Si crystals are X-ray irradiated, there can occur interdefect interactions between the radiation defects formed during the process of bond breaking ( $\equiv\text{Si} \bullet$  and  $\equiv\text{SiO} \bullet$  radicals) and paramagnetic oxygen atoms which are the main impurity in silicon. These interdefect interactions may result in the formation of amorphous oxide layer on the silicon surface. Our assumptions were confirmed by ellipsometric measurements.

The results of our studies presented in Fig. 20.4 indicate that, prior to X-ray exposure, the thickness of the natural oxide layer on the s-Si surface was  $\sim 5$  nm and increased to  $\sim 9.5$  nm after the X-ray irradiation. The X-ray treatment thereby induces oxidation processes on the surface of s-Si crystals. It has been found that these processes lead not only to formation of additional oxide layer at the surface but also to a decrease in the refractive index of s-Si crystals by a value of 0.03.

Summing up this discussion, we can draw the following conclusion.

The changes in the photovoltage decay kinetics which we observed in s-Si crystals after termination of X-ray treatment may be attributed to the influence of two factors, namely, to a change in the charge state of the surface and near-surface layers and to the surface substructure evolution. These factors of influence have appeared due to X-ray-induced breakage of stressed Si-Si bonds and due to formation of an oxide additional to a natural one at the layer surface.

The analysis of the results obtained on investigating the role of radiation treatment in changing the electrophysical characteristics of “s-Si + nanofilled polymer coating” structures allowed one to conclude the following:

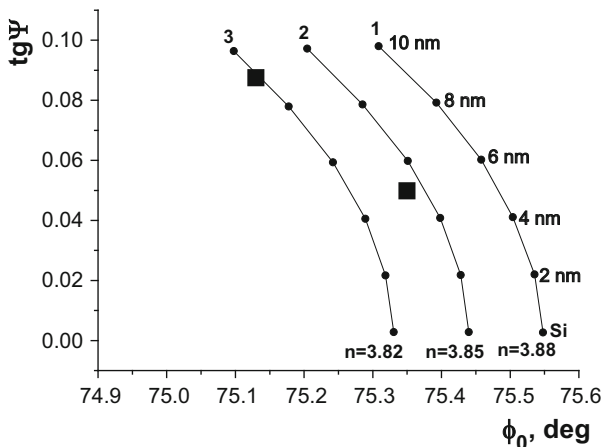


**Fig. 20.4** Dependence of the restored linear polarization azimuth ( $\text{tg } \psi$ ) on the principal angle of incidence ( $\phi_0$ ): (1) literature data for the  $\text{Si-SiO}_2$  system (where  $\text{SiO}_2$  is a natural oxide film); (2) control  $s\text{-Si}$  sample, not treated by X-rays; (3)  $s\text{-Si}$  sample after X-ray treatment ( $D = 3 \cdot 10^4$  Gy)

1. After deposition of nEU coatings on the  $s\text{-Si}$  surface, the carrier lifetime for the surface and the near-surface region of the  $s\text{-Si}$  crystals characterized by parameters  $\tau_1$  and  $\tau_2$ , respectively, exceeds the carrier lifetime measured for “ $s\text{-Si} + \text{uEU}$ ” structures as well as uncoated  $s\text{-Si}$  crystals (Fig. 20.5). The maximum difference is herewith observed for the structures with 0.001 and 1.0 wt. % PSP content in coatings, whereas the minimum difference occurs for structures with 0.5 wt. % PSP content.
2. The character of the dependences of  $\tau_1$  and  $\tau_2$  parameters on the PSP content in nEU coatings after X-ray treatment is diametrically opposite to that of similar structures which were not subjected to irradiation (Fig. 20.5).

At minimum (0.001 wt. %) and maximum (1.0 wt. %) PSP contents in nEU coatings, the values of  $\tau_1$  and  $\tau_2$  in the studied structures just after X-ray treatment decrease in comparison with the unirradiated structures. At the same time, at 0.5 wt. % PSP content, one can observe irradiation-stimulated rise of  $\tau_1$  and  $\tau_2$  parameters.

3. The character of relaxation curves for “ $s\text{-Si} + \text{uEU}$ ” and “ $s\text{-Si} + \text{nEU}$ ” measured for a long period of time ( $\sim 250$  days) after X-ray treatment termination points to the fact that  $\tau_1$  and  $\tau_2$  parameters in the structures with nEU coatings after irradiation remain greater compared to those in “ $s\text{-Si} + \text{uEU}$ ” structures during the entire period of observation (Fig. 20.6). The latter indicates a higher efficiency of nanofilled polymers when they are applied as protective coating for increasing radiation resistance of solar cells.



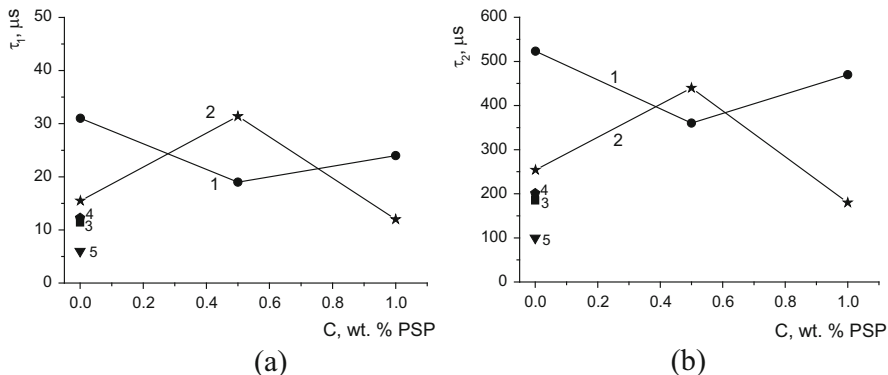


**Fig. 20.5** Dependences of fast ( $\tau_1$ ) (a) and slow ( $\tau_2$ ) (b) photovoltage decay time constants on the PSP content in epoxy-urethane matrix measured in the studied structures: control (initial) “s-Si + nEU” structures (1); “s-Si + nEU” structures subjected to X-ray treatment (2); “s-Si + uEU” structure (3); “s-Si + uEU” structure subjected to X-ray treatment (4); uncoated s-Si samples after X-ray treatment (5)

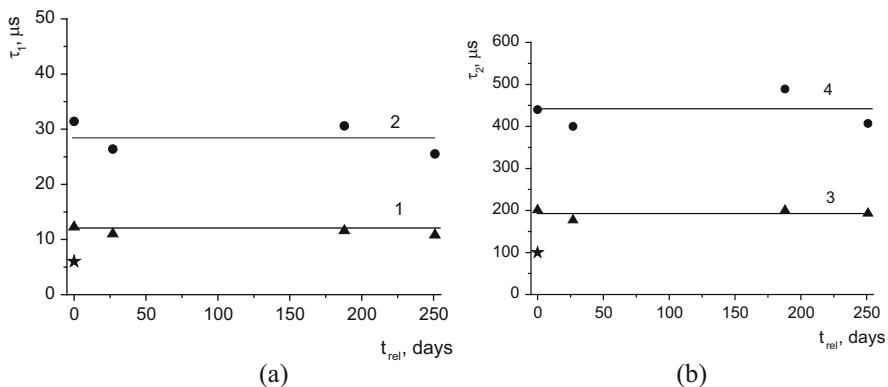


**Fig. 20.6** Dependences of  $\tau_1$  (a) and  $\tau_2$  (b) parameters in nEU structures on time that elapsed after termination of X-ray treatment: “s-Si + uEU” structures (1, 3); “s-Si + nEU” structures containing 0.5 wt. % PSP (2, 4);  $\xi$  – uncoated s-Si samples after X-ray treatment

4. The dependences shown in Fig. 20.7 allowed us to analyze the results obtained from a viewpoint of the efficiency of filled polymers with various PSP contents and from a viewpoint of reduction of recombination losses induced by X-ray irradiation. The mentioned analysis points to the fact that, under action of X-rays, the efficiency of nEU coatings with 1.0 wt. % PSP does not practically differ from that of uEU coatings (compare dependences 1 and 3 in Fig. 20.6 with dependences 3 and 6 in Fig. 20.7).

X-ray treatment proves to have a stronger effect on  $\tau_1$  and  $\tau_2$  in nEU coatings with 0.5 wt. % PSP content than in nEU coatings with 0.001 and 1.0 wt. % PSP

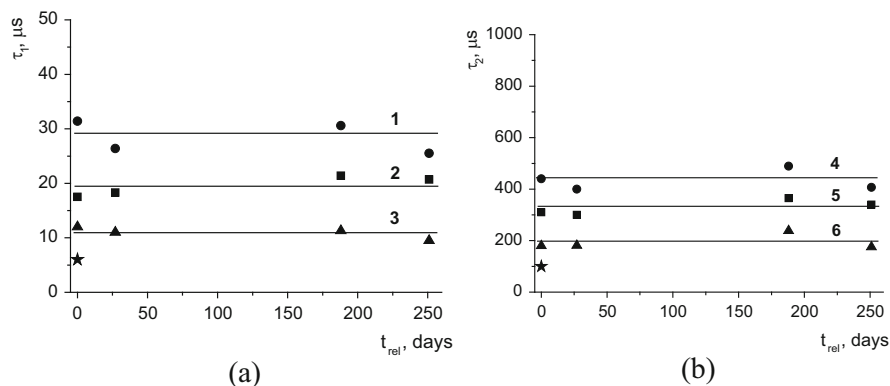


**Fig. 20.7** Dependences of  $\tau_1$  and  $\tau_2$  parameters in “s-Si + nEU” structures (a, b) on time that elapsed after termination of X-ray treatment: “s-Si + nEU” structures containing 0.5 wt. % PSP (1, 4); “s-Si + nEU” structures containing 0.001 wt. % PSP (2, 5); “s-Si + nEU” structures containing 1.0 wt. % PSP (3, 6);  $\xi$  – uncoated s-Si samples after X-ray treatment

contents. It is found that, under X-ray irradiation, the best passivating functions are exhibited by nEU coatings with 0.5 wt. % PSP content.

As follows from the results described in the present paper, covering s-Si crystals with polymer coatings in the form of certain nanocompositions reduces the processes induced in s-Si crystals under X-ray irradiation to zero as well as eliminates irradiation-induced degradation owing to the surface passivation. Differences in the character of passivating functions exhibited by coatings with different nanofiller (PSPs) contents may be related to both different structural features of the nanocompositions and different extent of their destruction under X-ray irradiation. It is not excluded that structure features and destruction peculiarities of nanofilled polymers affect the adhesive properties of the coatings. Therefore it determines their ability to efficiently passivate the surface.

## 20.4 Conclusions

A search for the possibilities of optimal combination of passivating nanofilled epoxy-urethane coating and soft X-ray irradiation providing a minimum degradation of functional characteristics of solar Si-based cells is carried out. It is found that the highest radiation resistance is exhibited by coatings containing a nanofiller (polysiloxane particles (PSPs)) in the epoxy-urethane matrix in the amount of 0.5 wt. %. So, incorporation of 0.5 wt. % PSPs into a polymer matrix eliminates radiational damage of s-Si crystals. At the same time, at 0.001 and 1.0 wt. % PSP contents in polymer matrix in s-Si crystals, quite big recombination losses are observed after X-ray irradiation.

## References

1. Mukashev BN, Betekbaev AA, Kalygulov DA, Pavlov AA, Skakov DM (2015) Issledovaniya protsessov polucheniya kremniya i razrabotka tehnologii izgotovleniya solnechnykh elementov. *Fiz Tekh Poluprovodn* 49:1421
2. Yarovoy GP, Latushina NV, Rogozhin AS, Gurtov AS, Ivkov SV, Minenko SI (2012) Silicon photoelectric converters for space and aviation industry. *Izvestiya SNTs RAN* 14:521
3. Nikolaenko YE, Vakiv NM, Krukovskiy SI, Erohov VY, Melnik II, Zaverbnyiy IR (2001) The state and tendencies of development of solar power solid-state phototransmitters. *Tehnologiya i konstruirovaniye v elektronnoy apparature* 3:21
4. Koltun MM (1985) *Optika i metrologiya solnechnykh elementov*. (Nauka M)
5. Munakata C, Nishimatsu S, Honma N, Yagi K (1984) Ac Surface Photovoltages in strongly-inverted oxidized p-type silicon wafers. *Jpn J Appl Phys* 23:1451
6. Kadenskii AG, Kadenskii SG, Levin MN, Maslovskii VM, Chernyshev VE (1993) Relaksatsionnyie protsessyi v MDP-elementah integralnykh shem, vyizvannyie ioniziruyuschim izlucheniem i impulsnyim magnitnyim polem. *Pisjma v Zh Tekhn Fiz* 19:41
7. Tetelbaum DI, Yezhevskii AA, Mikhailov AN (2003) Ekstremalnaya dozovaya zavisimost kontsentratsii paramagnitnykh tsevtrov, obuslovlennykh oborvannyimi svyazyami v Si, pri ionnom obluchenii, kak svidetelstvo nanostrukturirovaniya. *Fiz Tekh Poluprovodn* 37:1380

# Chapter 21

## Two-Dimensional Periodic Structures Recorded in Nanocomposites by Holographic Method: Features of Formation, Applications

V.O. Hryn, P.V. Yezhov, and T.N. Smirnova

### 21.1 Introduction

Two-dimensional (2D) photonic crystal structures based on polymers have attracted much attention of researchers in recent years due to their potential application as a modern element base of optoelectronics and quantum electronics.

Although the phase contrast of polymer structures is relatively small ( $\Delta n \leq 0.04$ ), the resulting group velocity anomaly provides a significant increase in the local field in such structures. Therefore, 2D structures are most widely studied as effective cavities for lasers with distributed feedback (DFB) [1–12]. Moreover, in comparison with 1D cavities, the use of 2D structures with the same contrast can increase the selectivity of the resonator, reduce the oscillation threshold, and improve the differential efficiency of DFB laser. Two-dimensional photonic crystals can also be used as Bragg diffraction elements for optical signal processing, for example, [13] and photonic crystal sensors [14, 15].

The use of polymer nanocomposites comprising nanoparticles (NPs) of different nature for manufacturing of photonic crystals can significantly change their properties. First of all, the refractive index of NPs material ( $n_{NP}$ ) usually considerably differs from the refractive index of polymer matrix ( $n_P$ ) that will lead to an increase in structure contrast. On the other hand, the use of metal, metal oxide, and semiconductor NPs possessing specific physical properties opens the possibility to produce photonic crystals with nonlinear optical, plasmonic, fluorescent, and laser properties that significantly expand the range of photonic crystal applications. Two-dimensional periodic polymer/metal nanostructures serving as laser cavities can

---

V.O. Hryn (✉) • P.V. Yezhov • T.N. Smirnova  
Institute of Physics, National Academy of Sciences of Ukraine, Prospect Nauki, 46, 03680,  
Kiev, Ukraine  
e-mail: [mrvolodymyr91@gmail.com](mailto:mrvolodymyr91@gmail.com); [yezhov@iop.kiev.ua](mailto:yezhov@iop.kiev.ua); [smirnova@iop.kiev.ua](mailto:smirnova@iop.kiev.ua)

significantly reduce the lasing threshold in DFB lasers due to the enhancement of the pumping radiation caused by the excitation of local surface plasmons [16]. The exploration of periodically ordered metal microstructures opens new application possibilities providing the coupling between light waves and surface plasmons. A properly structured medium can convert an incoming light wave to a surface plasmon-polariton wave and *vice versa* that can serve as a powerful basis for designing new optical diffractive elements with ultrahigh spectral dispersion [17]. In addition, structuring of plasmonic nanocomposites significantly impacts the decay dynamics of induced changes in the vicinity of surface plasmon absorption resonance [18, 19]. It was found [19] that the complication of the structure and increase of its order of symmetry, in a series of 1D–2D structures, result in the enhancement of induced absorption and increase in the relaxation time of electron excitation defined by electron thermalization.

Both relief and volume 2D structures are used for a variety of applications. Relief structures are manufactured with the help of various lithography techniques (UV, electron beam), nanoimprint, hot embossing, micromolding, reactive ion etching, and others. These methods include the sequence of operations and in many cases require a number of wet technological steps typical for photoresist technology.

The cheapest and simple method of 2D and 3D structure formation in the volume of photosensitive material is one-step holographic lithography method, which allows to obtain large enough, highly efficient structures of high uniformity with easily variable period [20–22]. Periodic distribution of the field, forming a structure, is created as a result of interference of multiple coherent laser beams. An interference field of desired configuration is obtained from a single laser beam, by splitting it up into a system of beams and varying their number, direction, phase, and polarization [22–25]. Diffractive beam splitter or prism system is used for the splitting of the original laser beam, for example [4, 8, 26, 27].

In this paper we study the peculiarities of 2D structures formation in nanocomposites with NPs of different nature, using multibeam recording scheme. We propose a modified scheme of the interference pattern creation that enables smooth change of the phase shift between the recording beams and easy change of the field period. We explore the properties of the structures and possibility of their use in the DFB lasers.

## 21.2 Experimental Technique

### 21.2.1 Materials

We used two types of photopolymerizable compositions for manufacturing of 2D polymer/NPs structures. In the first case, the *ex situ* synthesized NPs were introduced into a monomer mixture. Volume structure is formed as a result of local polymerization and diffusive redistribution of the mixture components in

interference field [28]. In the second case, the NPs synthesis occurs after the recording from the metal precursor, spatially distributed in polymer matrix under interference pattern. We produced periodic structures with  $\text{LaPO}_4$  and Ag NPs. We used nanocomposite developed in [29] to manufacture structures with  $\text{LaPO}_4$  NPs.

The pre-polymer syrup is a homogenous mixture of mono- and multifunctional acrylate monomers (70:30) isobutyl acrylate (IBA) and pentaerythritol triacrylate (sartomer SR444). Photoinitiators camphorquinone (5 wt.%) and Michler's ketone (1 wt.%) were added to the syrups to provide the sensitivity to 441–488 nm light.  $\text{LaPO}_4$  NPs were purchased from Nanogate AG as a white powder. According to the manufacturer data, the average particle size is of about 7 nm, size distribution is 15%, and specific gravity is  $5 \text{ g/cm}^3$ . The weight fraction of the inorganic core (according to TGA) was found to be ca. 83 wt.%. The monomer–NPs nanocomposites were prepared by adding the pentane dispersion of the NPs to the monomer blend.

Structures with metal NPs can also be manufactured by introducing the *ex situ* synthesized NPs into monomer mixture. However, such blends possess high absorption in visible spectral range that prevents the use of vis-emissive laser sources for the holographic recording and limits the concentration of NPs in the matrix material. Besides that, it is always difficult to disperse metal NPs homogeneously into a polymer matrix or in monomers because of the easy aggregation of the NPs. Therefore, we have proposed a new method of the formation of periodic polymer/metal NPs structures [30]. During the first step – photopolymerization in the interference pattern – a stable volume periodical structure polymer/metal precursor is formed. Reduction of the precursor and the formation of metal NPs occur mainly during the stage of photo- or heat-processing. Since the solution of the precursor, for example, gold or silver, absorbs light in the spectral range  $<350 \text{ nm}$ , the holographic photopolymerization can be carried out in a vis spectral range. From the other hand, this method allows increasing the NP concentration in the final structure compared to the *ex situ* method for the nanocomposite preparation. In this case the mixture of triethylene glycol dimethacrylate (70 w.%) and  $\alpha, \omega$ -akrylbis(propylene glycol)2,4-toluylene diurethane was used as pre-polymer composite. Solution of  $\text{AgNO}_3$  in acetonitrile as metal (Ag) precursor was added to the mixture. Camphorquinone and Michler's ketone were also used as photoinitiating system. Manufacturing technology of photopolymerizable compositions and synthesis of Ag NPs in periodic structures are described in detail in [29, 30].

To obtain a recording layer, liquid mixture was placed between glass substrates, separated by calibrated spacers with a thickness  $d = 10\text{--}30 \text{ }\mu\text{m}$ .

### 21.2.2 System Design

Holographic lithography methods are well developed nowadays. As mentioned above, a system of prisms or diffraction splitter consisting of a number of diffraction gratings is used to implement a multibeam recording. Parameters of gratings and

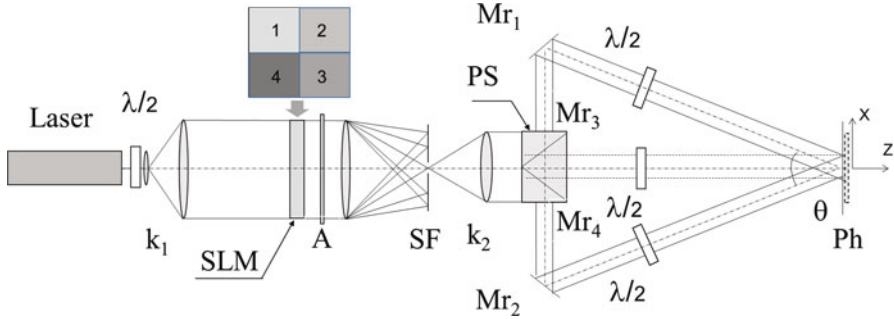


**Fig. 21.1** Experimental setup for four-beam holographic recording of 2D structures: *Laser* is the  $\text{Ar}^+$  laser,  $\lambda/2$  are the  $\lambda/2$  waveplates,  $k_1$ ,  $k_2$  are the collimators, *SLM* is the spatial light modulator, *A* is the analyser, *SF* is the spatial filter, *PS* is the laser beam splitter prism system,  $M_{r1-4}$  are the mirrors,  $\theta$  is the total internal angle, *Ph* is the photopolymer layer

their relative position are selected so as to provide the necessary quantity and geometry of the interfering beams [23].

The recording field for hexagonal 2D photonic crystals creation is obtained by the interference of three (or six) laser beams. The simplest diffraction splitter was proposed in [8]. It consisted of an opaque mask with three Bragg gratings deployed by  $120^\circ$  relative to each other. It should be noted that while using a prism or grating beam splitter, it is quite difficult to change the convergence angles of the interfering beams or, in other words, parameters of a crystal cell of a photonic crystal. In each case it is necessary to fabricate a new set of optical elements with the necessary parameters.

We propose a more flexible recording scheme, in which a spatial light modulator (SLM) is used for formation of the recording plane waves. This scheme is an improved modification of the scheme presented in [31]. It allows a rather simple modification of the crystal-structure parameters of 2D and 3D photonic crystals. An example of a four-wave recording scheme is shown in Fig. 21.1.

Collimated beam of the recording laser radiation passes through a transmission-type SLM, which alters the phase distribution in such a way that four waves with a determined phase shift are created. Analyzer *A* and five half-wave plates ensure the operation of SLM in phase mode. A spatial filter *SF* separates the main order of SLM. The system of prisms *PS*, whose number corresponds to the number of recording waves, directs them to the mirrors  $M_{1-4}$  that form an interference pattern with the required period.

The same principle can be implemented in the recording scheme with a different number of waves. The wave vector  $\mathbf{k}_j$  for each  $j$  wave lies on a surface of cone with opening angle  $\theta$  and has components  $\mathbf{k}_{j,x}$ ,  $\mathbf{k}_{j,y}$ , and  $\mathbf{k}_{j,z}$ , where the  $Z$ -axis coincides with the axis of the cone. Interference of waves forms transverse field distribution in the plane ( $X,Y$ ) and longitudinal field distribution in the plane ( $X,Z$  or  $Y,Z$ ). By varying the phase difference between the recording waves with help of an SLM, we can form crystals with different symmetry and change the period of their structure.

It should be noted that for a certain fixed ratios of wave phases, we can form a family of discrete nondiffracting beams [32]. They result from the interference of plane waves and have no diffraction divergence in the overlap area along the axis  $Z$ . Recording by nondiffracting waves ensures the invariance of the structural parameters over the depth with high accuracy. Below we consider examples of such structures.

### 21.3 Simulation of a Pattern Profile

The distribution of complex field  $\Psi_{n,m}$  in plane of interference Ph can be presented in Cartesian coordinates as:

$$\Psi_{n,m}(\mathbf{r}) = \sum_{j=1}^n \Psi_j \cdot \exp \left\{ i \left( k_{x,j}x + k_{y,j}y + k_{z,j}z + j \frac{\Phi_m}{n} \right) \right\} \quad (21.1)$$

with

$$\Phi_m = 2\pi m, \quad 0 \leq m \leq \frac{n}{2}, \quad m \in \mathbb{R},$$

where  $\Psi_j$  is the amplitude of  $j$ -component of field;  $n$  is the number of plane waves;  $\Phi_m$  is the total initial phase shift between all participating plane waves;  $m$  is the positive integer; and  $\mathbb{R}$  is the set of real numbers.

As indicated in [32],  $m$  can take integer as well as fractional values and ensures the calculation of the same absolute phase values  $\Phi_m/n$  for each of the  $j$  waves so that the full phase incursion of all  $n$  plane waves  $\Phi_m$  was an integer of  $\pi$  ( $\Phi_m = 2\pi m$ ).

Using (21.1) we calculated the intensity distribution  $|\Psi_{n,m}|^2$  in the interference pattern formed by three, four, and six beams. Figure 21.2 shows the intensity distribution for the cases (1)  $\Psi_{6,0}$  and  $\Psi_{6,3}$ ; (2)  $\Psi_{4,0}$  and  $\Psi_{4,1}$ . For cases  $\Psi_{n,0}$  the total initial phase shift  $\Phi_m = 0$ , for  $\Psi_{4,1} - \Phi_m = 2\pi$  and for  $\Psi_{n,3} - \Phi_m = 6\pi$ . The results correspond to the structures obtained in [31].

### 21.4 Results and Discussion

By using the six-beam scheme, we manufactured 2D photonic crystals with a hexagonal structure ( $\Psi_{6,0}$ ;  $\Psi_{6,3}$ ), formed by Ag NPs in the polymer matrix. Photomicrographs of the crystals are shown in Fig. 21.3a, b. Images were obtained by focusing on the crystal surface. Figure 21.3c shows real space lattice. Mirror planes that form gratings with periods shown in the figure are marked here as well.



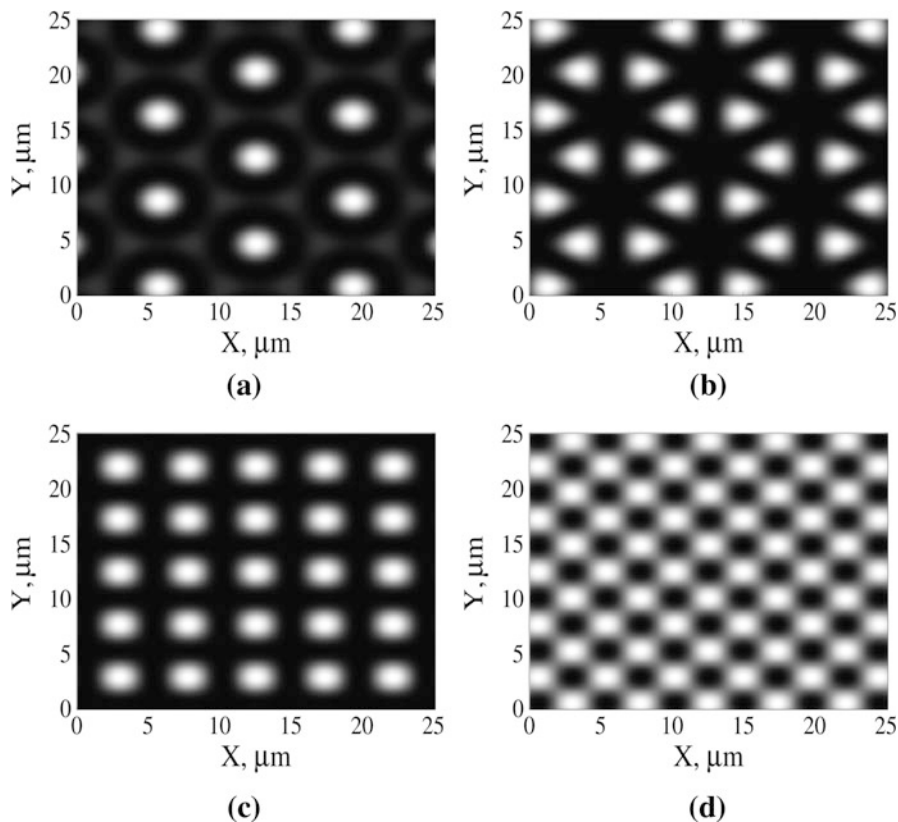


**Fig. 21.2** Calculated intensity distribution in interference pattern: (1)  $\Psi_{6,0}$  (a) and  $\Psi_{6,3}$  (b); (2)  $\Psi_{4,0}$  (c) and  $\Psi_{4,1}$  (d) with absolute phase values  $\Phi_m/n$ :  $0, \pi, 0, \pi/2$ , respectively

We found that the areas of primary localization of polymer and NPs are redistributed when changing the phase shift between recording beams. As has been shown previously [30], Ag NPs are localized in regions corresponding to minima of the interference field, in which  $\text{AgNO}_3$  solution diffuses during polymerization of composite. By comparing the distribution of the field and the picture of the structure, we found that light areas in the image correspond to field maxima, i.e., to the areas of preferred polymer concentration, whereas Ag NPs are concentrated in dark areas of the image. Thus, at a zero phase shift ( $\Psi_{6,0}$ ), polymer-rich regions form hexagonal structures, being located in the corners and in the center of hexagons. When the full phase incursion is  $6\pi$  (case  $\Psi_{6,3}$ ), hexagons are formed by the areas enriched with Ag NPs.

As can be seen from Figs. 21.2b and 21.3b, the polymer phase corresponding to illuminated areas is also structured and forms hexagons around the areas enriched with Ag NPs (dark areas in Fig. 21.2b). Since Ag NPs are formed directly in the

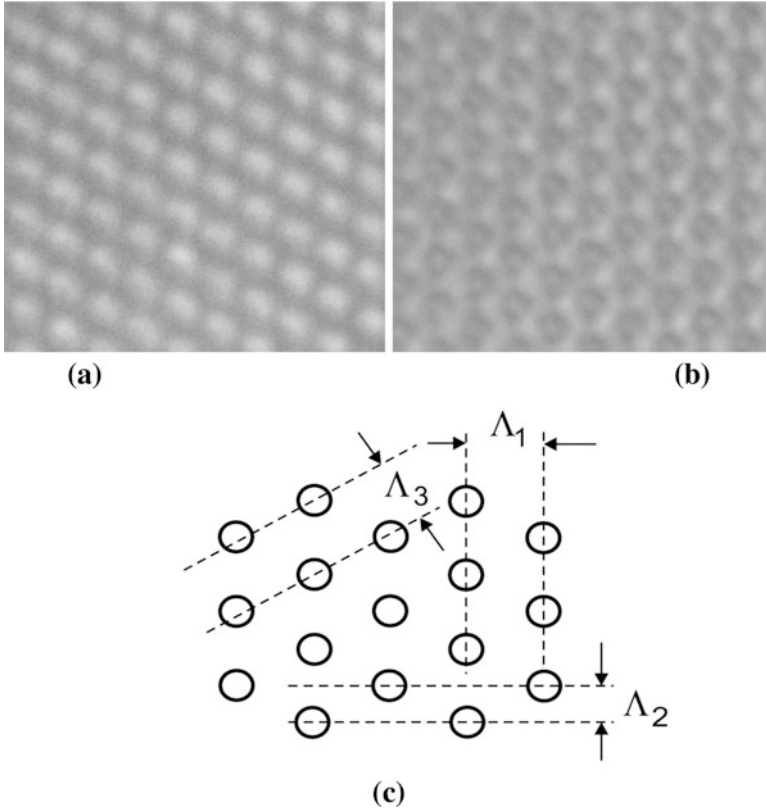


**Fig. 21.3** Photomicrographs of 2D photonic crystals with a hexagonal structure formed by Ag NPs distribution in polymer matrix:  $\Psi_{6,0}$  (a),  $\Psi_{6,3}$  (b); crystal lattice for  $\Psi_{6,0}$  (c) with periods of the real space lattices  $\Lambda_1 = \Lambda_3 = 3.39 \mu\text{m}$ ,  $\Lambda_2 = 1.96 \mu\text{m}$

crystal, the change of a size of the zones of their formation can affect the size and concentration of NPs and accordingly the dynamics of electronic excitations in Ag NPs [19]. These issues are the subject of further research.

Two-dimensional photonic crystals polymer/LaPO<sub>4</sub> NPs are manufactured using four-beam recording scheme ( $\Psi_{4,0}$ ). Atomic force microscope image of the photonic crystal surface is shown in Fig. 21.4. Similar to a composite with Ag NPs, LaPO<sub>4</sub> NPs are also displaced from the polymer phase and diffuse into the regions corresponding to the minima of interference pattern during recording. As a result, a horizontal section of 2D crystal is a square lattice formed by polymer zones and zones enriched by NPs. The surface of the crystal is almost flat; relief height does not exceed a few nanometers. Depressions correspond to the regions of NPs primary localization. We used the present 2D crystals with square lattice to achieve distributed feedback in the DFB laser described below.

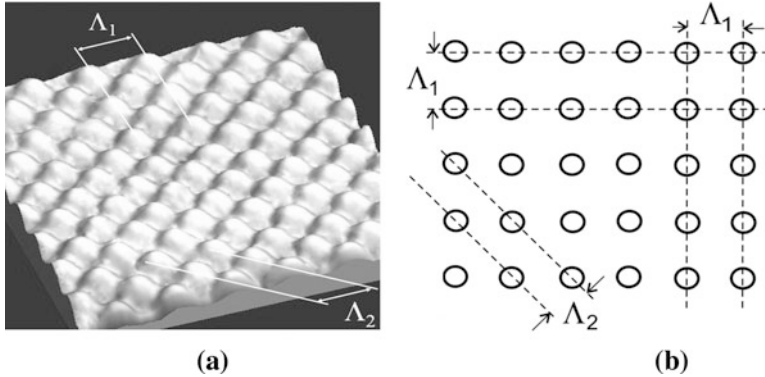


**Fig. 21.4** Atom force microscope image of the surface of the Bragg nanocomposite grating formed by  $\text{LaPO}_4$  NPs distribution in polymer matrix (a); crystal lattice with periods of the real space lattices  $\Lambda_1 = 0.40 \mu\text{m}$ ,  $\Lambda_2 = 0.28 \mu\text{m}$

## 21.5 DFB Laser Based on 2D Volume Structure

In this section we consider a DFB laser as an example of application of obtained 2D photonic crystals. It consists of a planar waveguide with volume 2D structure activated by laser dye.

Our studies [33, 34] have shown that the DFB laser based on the volume grating is the simplest to manufacture and has excellent characteristics: low lasing threshold and narrow-band illumination with low divergence. For the manufacturing of laser, we used a nanocomposite with  $\text{LaPO}_4$  NPs, containing laser dye pyrromethene 567 (Pyr567). Properties of the DFB laser based on a nanocomposite with 1D structure providing feedback were investigated in [33, 34]. It was found that introduction of a dye in the nanocomposite does not lead to a reduction of a 1D structure contrast ( $n_1$  value) but only slightly increases the time of grating formation. Our experiments confirmed that the same situation prevails also when recording 2D structures. In accordance with the results of [34], the dye concentration was chosen so that optical density  $D$  of the active layer was 0.4 at the laser pumping wavelength.

Figure 21.5a shows the schematic structure of the DFB laser under study, direction of the optical pumping, and the output of laser emission. Figure 21.5b shows the absorption and fluorescence spectra of the dye in the nanocomposite film. The devices were pumped with a frequency-doubled Nd:YAG laser which emits 500 ps long pulses with maximum pulse energy of  $30 \mu\text{J}$  at a wavelength of 532 nm. The pump radiation was directed perpendicularly to the surface of the waveguide along the Z-axis. The pump beam was shaped as a stripe (approx.  $(4 \times 0.5) \text{mm}^2$ ) oriented along the grating vector  $G_1$  (Y-axis). The laser output from the edge of the sample was directed into a charge-coupled device spectrometer Horiba Jobin-Yvon (the spectral resolution is 0.2 nm).

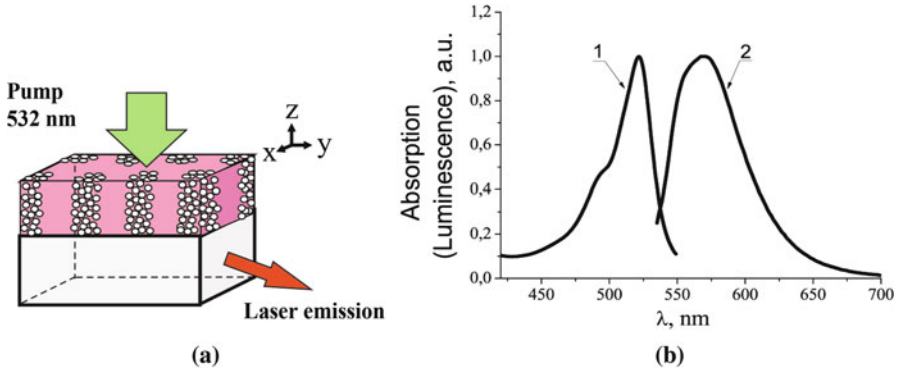


**Fig. 21.5** Sketch of the DFB laser based on 2D crystal with square lattice activated by laser dye Pyr567 and the geometry of the lasing experiment (a). The spectra (b) of absorbance (1) and luminescence (2) of Pyr567 in nanocomposite layer

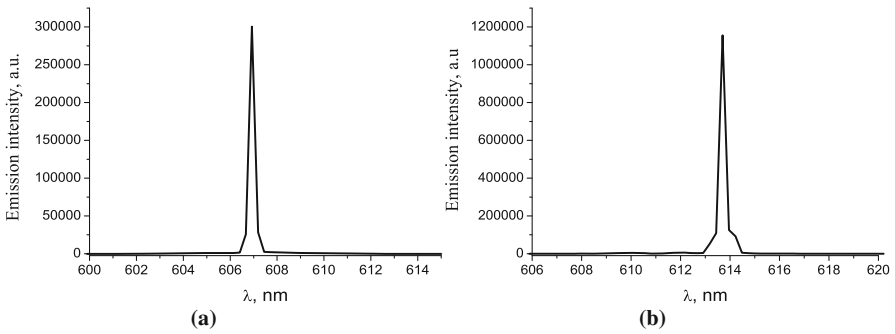


**Fig. 21.6** DFB-laser emission spectra for  $\Lambda_1 = 400$  nm (a) and 407 nm (b)

The out-coupling of the emission from the volume DFB laser is demonstrated in Fig. 21.6. It was found that for 2D DFB structures, the lasing emission propagates inside the substrates and then couples out from substrate edges at the certain angle  $\theta_{out}$ .

Figure 21.6 shows the emission spectrum of the DFB laser. Structure period was selected so as to ensure lasing in the second order of diffraction at the wavelength corresponding to the emission spectrum of the dye.

For the structures with  $\Lambda_1 = 400$  nm, pump stripe was oriented along the Y-axis; vector  $\mathbf{E}$  was directed along the X-axis. A narrow peak with a maximum at 606.9 nm was observed in the spectrum of emission coupled out from the end face perpendicular to the Y-axis. The spectral position and the shape of the emission band are not changed after rotation of the sample by  $90^\circ$  around the Z-axis. For the structure with  $\Lambda_1 = 407$  nm, the wavelength of emission peak was 613.7 nm.

For DFB laser with the optimized parameters  $n_{at} = 1.517$  (the average refractive index of active waveguide with grating),  $D \cong 0.4$ ,  $n_1 = 0.0098$ ,  $\Lambda = 401, 407$  nm, and

$d = 10 \mu\text{m}$ , the following output characteristics were measured: threshold energy is  $0.1 \mu\text{J/pulse}$  ( $5 \mu\text{J/cm}^2$ ) and the lasing line width  $\leq 0.2 \text{ nm}$ . It is important to underline that the shape and the width of the lasing lines remain constant even at a pump energies 5 times higher than the corresponding threshold ones. For all measurements the spectral width was kept at the limit of spectrometer resolution. For comparison we shall point out that for a laser based on 1D grating with practically the same contrast ( $n_1 = 0.011$ ) and identical other parameters, lasing threshold was  $0.48 \mu\text{J/pulse}$ . Thereby, the use of 2D DFB cavity results in about 5 times reduction of lasing threshold. The far-field beam divergence of the 2D DFB laser was of about 6 mrad that almost coincides with that obtained for the DFB laser based on a 1D structure ( $\approx 5 \text{ mrad}$ ).

## 21.6 Conclusions

A modified multibeam scheme of interference field formation was developed. A spatial light modulator ensures continuous phase shift between the interfering beams and therefore formation of interference patterns of different geometry. This allowed simplifying the method of holographic lithography and making it more versatile.

Numerical simulation of the intensity distribution in the interference pattern formed by three, four, and six laser beams showed that the phase shift between the interfering beams leads to a change in the structure of the light field.

Two-dimensional photonic crystals based on polymer/NPs were recorded in the nanocomposites of two types. In the first case, *ex situ* synthesized NPs were introduced into the photosensitive nanocomposite. The structure was formed by polymerization and diffusion redistribution of NPs in periodic light field. We also obtained 2D structures by *in situ* synthesis of metal NPs from the metal precursor spatially distributed in a polymer matrix beforehand. Two-dimensional photonic crystals of different symmetries (hexagonal, tetragonal) were manufactured. We demonstrated variations in the localization of polymer- and NP-enriched regions, when changing the phase shift between recording beams.

Output characteristics of the DFB laser based on the manufactured 2D photonic crystal structure were investigated. The 2D cavity generated laser emission with the same spectral bandwidth ( $\leq 0.2 \text{ nm}$ ) and divergence (6 mrad), as for a DFB laser with the corresponding 1D structure. The lasing threshold decreases of about 5 times.

Fabricated 2D photonic crystals are characterized by a high temporal stability of parameters (not less than 5 years) and are potentially usable as elements of photonic devices.

**Acknowledgements** This work was supported by the grant of the Target Comprehensive Program of Fundamental Research of National Academy of Sciences of Ukraine "The Fundamental Problems of Creation of New Nanomaterials and Nanotechnologies" (Project 3/16-H).

## References

1. Riechel S, Kallinger C, Lemmer U, Feldmann J (2000) A nearly diffraction limited surface emitting conjugated polymer laser utilizing a two-dimensional photonic band structure. *Appl Phys Lett* 77:2310–2312
2. Vasdekis A, Turnbull G, Samuel I, Andrew P, Barnes W (2005) Low threshold edge emitting polymer distributed feedback laser based on a square lattice. *Appl Phys Lett* 86:161102
3. Turnbull G, Andrew P, Barnes W, Samuel I (2003) Operating characteristics of a semiconducting polymer laser pumped by a microchip laser. *Appl Phys Lett* 82:313–315
4. Jakubiak R, Tondiglia VP, Natarajan LV, Sutherland RL, Lloyd P, Bunning TJ, Vaia R (2005) Dynamic lasing from all-organic two-dimensional photonic crystals. *Adv Mater* 17:2807–2811
5. Heliotis G, Xia R, Turnbull GA, Andrew P, Barnes WL, Samuel IDW, Bradley DDC (2004) Emission characteristics and performance comparison of polyfluorene lasers with one- and two-dimensional distributed feedback. *Adv Func Mater* 14:91–97
6. Harbers R, Strasser P, Caimi D, Mahrt RF, Moll N, Offrein BJ, Erni D, Bachtold W, Scherf U (2005) Enhanced feedback in organic photonic-crystal lasers. *Appl Phys Lett* 87:151121
7. Raineri F, Vecchi G, Yacomotti AM, Seassal C, Viktorovitch P, Raj R, Levenson A (2005) Doubly resonant photonic crystal for efficient laser operation: pumping and lasing at low group velocity photonic modes. *Appl Phys Lett* 86:011116
8. Liu YJ, Sun XW (2006) Electrically tunable two-dimensional photonic crystal fabricated by a single diffractive element. *Appl Phys Lett* 89:171101
9. Luo D, Sun XW, Dai HT, Demir HV, Yang HZ, Ji W (2010) Temperature effect on the lasing from a dye-doped two-dimensional hexagonal photonic crystal made of holographic polymer-dispersed liquid crystals. *J Appl Phys* 108:013106
10. Luo D, Sun XW, Dai HT, Demir HV, Yang HZ, Ji W (2010) Electrically tunable lasing from a dye-doped two-dimensional hexagonal photonic crystal made of holographic polymer-dispersed liquid crystals. *Appl Phys Lett* 97:081101
11. Jørgensen MM, Petersen SR, Christiansen MB, Buß T, Smith CLC, Kristensen A (2010) Influence of index contrast in two dimensional photonic crystal lasers. *Appl Phys Lett* 96:231115
12. Ge C, Lu M, Tan Y, Cunningham BT (2011) Enhancement of pump efficiency of a visible wavelength organic distributed feedback laser by resonant optical pumping. *Opt Exp* 19:5086–5092
13. He Q, Zaquine I, Maruani A, Frey R (2006) Band-edge-induced Bragg diffraction in two-dimensional photonic crystals. *Opt Lett* 31:1184
14. Nair RV, Vijaya R (2010) Photonic crystal sensors: an overview. *Progr Quant Electr* 34:89–134
15. Endo T (2014) Polymer-based two dimensional photonic crystal for biosensing application. In: *Symposium proceedings progress in electromagnetic research, Guangzhou, 25–28 Aug 2014*
16. Stehr J, Grewett J, Shimdler F, Sperling R, Plessen G, Lemmer U, Lupton JM, Klar TA, Feldman J, Holleitner AW, Forster M, Scherf U (2003) A low threshold polymer laser based on metallic nanoparticle gratings. *Adv Mater* 15:1726–1729
17. Mikhailov V, Elliott J, Wurtz G, Bayvel P, Zayats AV (2007) Dispersing light with surface plasmon polaritonic crystals. *Phys Rev Lett* 99:083901
18. Lamprecht B, Schider G, Lechner RT, Ditlbacher H, Krenn JR, Leitner A, Aussenegg FR (2000) Metal nanoparticle gratings: influence of dipolar particle interaction on the plasmon resonance. *Phys Rev Lett* 84:4721–4724
19. Tikhomirov SA, Buganov OV, Ponyavina AN, Yezhov PV, Kokhtich LM, Smirnova TN (2014) Time-dependent absorption spectra of photopolymeric films with periodic structure of silver. *J Appl Spectr (Belarus)* 81:710–716
20. Berger V, Gauthier-Lafaye O, Costard E (1997) Photonic band gaps and holography. *J Appl Phys* 82:60–64
21. Campbell M, Sharp DN, Harrison MT, Denning RG, Turberfield A (2000) Fabrication of photonic crystals for the visible spectrum by holographic lithography. *Nature* 404:53–56

22. Maldovan M, Thomas E (2009) Periodic materials and interference lithography. Wiley-VCH Verlag GmbH & Co/KGaA, Weinheim
23. Kondo T, Juodkazis S, Mizeikis V, Misawa H (2006) Holographic lithography of periodic two- and three-dimensional microstructures in photoresist SU-8. *Opt Expr* 14:7943–7953
24. Su H, Zhong YC, Wang X, Zheng XG, Xu JF, Wang HZ (2003) Effects of polarization on laser holography for microstructure fabrication. *Phys Rev E* 67:056619
25. Moon JH, Yang SM, Pine D, Chang W (2004) Multiple-exposure holographic lithography with phase shift. *Appl Phys Lett* 85:4184–4186
26. Kondo T, Matsuo S, Juodkazis S, Misawa H (2001) A novel femtosecond laser interference technique with diffractive beam splitter for fabrication of three-dimensional photonic crystals. *Appl Phys Lett* 79:725–727
27. Yang Y, Wang GP, Xie J, Zhang S (2005) Metal nanoparticles-embedded three-dimensional microstructures created by single-beam holography. *Appl Phys Lett* 86:173108
28. Sakhno OV, Goldenberg LM, Stumpe J, Smirnova TN (2009) Effective volume holographic structures based on organic-inorganic photopolymer nanocomposites. *J Opt A Pure Appl Opt* 11:024013
29. Sakhno OV, Smirnova TN, Goldenberg LM, Stumpe J (2008) Holographic patterning of luminescent photopolymer nanocomposites. *Mater Sci Eng C* 28:28–35
30. Smirnova TN, Kokhtych LM, Kutsenko AS, Sakhno OV, Stumpe J (2009) Fabrication of periodic polymer/silver nanoparticles structures: *in situ* reduction of silver nanoparticles from precursor spatially distributed in polymer using holographic exposure. *Nanotechnology* 20:405301
31. Boguslawski M, Rose P, Denz C (2011) Increasing the structural variety of discrete nondiffracting wave fields. *Phys Rev A* 84:013832
32. Durnin J (1987) Exact solutions for nondiffracting beams. I. The scalar theory. *J Opt Soc Am A* 4:651–654
33. Sakhno OV, Smirnova TN, Stumpe J (2011) Distributed feedback dye laser holographically induced in improved organic-inorganic photocurable nanocomposites. *Appl Phys B* 103:907–916
34. Smirnova TN, Sakhno OV, Fitio VM, Gritsai Yu, Stumpe J (2014) Simple and high performance DFB laser based on dye-doped nanocomposite volume grating. *Laser Phys Lett* 11:125804

# Chapter 22

## Spinel Ferrite Nanoparticles: Synthesis, Crystal Structure, Properties, and Perspective Applications

Tetiana Tatarchuk, Mohamed Bououdina, J. Judith Vijaya,  
and L. John Kennedy

### 22.1 Introduction

Spinel ferrite nanomaterials (SFNs) have gained huge attention in modern days from fundamental science point of view owing to their unique properties and promising applications such as high-density data storage, catalysts, gas sensors, rechargeable lithium batteries, information storage systems, magnetic bulk cores, magnetic fluids, microwave absorbers and medical diagnostics and therapy, etc. [1–5]. The fundamental understanding of crystal chemistry in SF nanomaterials is very essential, and the proper choice of synthesis route will determine its well-defined crystal lattice structure and chemical composition, leading to enhanced/excellent physical and chemical properties. With the general molecular formula  $MFe_2O_4$  (where  $M = Mn$ ,

---

T. Tatarchuk (✉)

Department of Inorganic and Physical Chemistry, Faculty of Natural Science, Vasyl Stefanyk Precarpathian National University, 57, Shevchenko Str., Ivano-Frankivsk, 76018, Ukraine  
e-mail: [tatarchuk.tetyana@gmail.com](mailto:tatarchuk.tetyana@gmail.com)

M. Bououdina

Department of Physics, College of Science, University of Bahrain, PO Box 32038, Southern Governorate, Bahrain  
e-mail: [mboudina@gmail.com](mailto:mboudina@gmail.com)

J. Judith Vijaya

Catalysis and Nanomaterials Research Laboratory, Department of Chemistry, Loyola College, Chennai, 600034, India  
e-mail: [jjvijaya78@gmail.com](mailto:jjvijaya78@gmail.com)

L. John Kennedy

Materials Division, School of Advanced Sciences, Vellore Institute of Technology (VIT) University, Chennai Campus, Chennai, 600127, India  
e-mail: [ljkennedy14@gmail.com](mailto:ljkennedy14@gmail.com)



Fe, Co, Ni, Cu, and Zn), the majority of SFs exhibit superparamagnetic (SPM) properties at the nanoscale dimensions of diameter below or about 20 nm [1–7].

The metal cations in both sites are distributed based on their affinity to occupy the positions which in turn are significantly dependent on the stabilization energy, ionic radii of metal cations, size of interstitial site, synthesis technique, and their synthesis reaction conditions [1–7]. In addition, the development of suitable synthesis routes which can control the morphological properties of SFs becomes much more important, since there is a correlation between the catalytic activity and the morphological properties, and thus it is revealed that the catalytic activity of SFs also depends upon the adopted synthesis method. The structural, magnetic, electronic, and optical properties of SFs are significantly enhanced in the nanoscale regime with the reduction in crystallite size and increase in specific surface area. The size and shape of the SFs can modulate their physical and chemical properties, and consequently extensive researches have been devoted to the fabrication of SFs with controlled morphological properties.

In the past decade, various methods of synthesizing SFs have been addressed and reported in the literature, but there is a requirement for the commercially reliable methods, since every synthesis method has its own advantages and disadvantages. Henceforth, the design of new synthesis method for SFs which also utilizes less hazardous and commercially available low-cost precursor materials requires greater attention.

The present chapter focuses on highlighting the successful synthesis methods for SFs with few examples and pointing out their advantages and disadvantages. Meanwhile, particular attention will be given to in-depth understanding of the spinel crystal structure and its correlation with magnetic/optical properties. Finally, potential applications of SFs are presented and discussed.

## 22.2 Synthesis Methods of Spinel Ferrites

### 22.2.1 *Microemulsion Method*

This method involves the dispersion of two relatively immiscible liquids which is thermodynamically feasible and stabilized by added surfactant molecules [8]. The advantages of this method include changing the surfactants and co-surfactant combination and oil-to-water ratio, and thus the particle size can be controlled [8, 9]. This reaction is known for being eco-friendly and favorable at low temperature and reuse of surfactants for several cycles during the synthesis and possibility of commercial production [9]. Nevertheless, the major disadvantage is the poor crystalline nature of synthesized SFs, requirement of larger amounts of solvents and high polydispersion due to the slower nucleation rate at low temperature. The two major classifications of this method are reverse water-in-oil and normal oil-in-water [8], and some SFs synthesized by this method include  $\text{Fe}_2\text{Mn}_{0.5}\text{Zn}_{0.5}\text{O}_4$ ,  $\text{Ni}_{0.6}\text{Fe}_{2.4}\text{O}_4$ , and  $\text{Fe}_3\text{O}_4$  [8, 9].

### **22.2.2 Ultrasonic (Sonochemical) Method**

The sonochemical route is widely employed nowadays for the synthesis of SFs due to the facile control of reaction conditions. This method particularly targets in achieving homogeneous mixing and controlling the particle size distribution. Therefore, the temperature and the intensity of ultrasonic waves are major factors which can have a direct impact on the particle size of SFs. During the synthesis, as a resultant of the ultrasonic wave irradiation, the bubbles are formed in the reaction medium, and SFs undergo in situ calcination due to the induced high-energy collisions between the particles [1, 10]. By means of ultrasonication, mixing at the atomic level can be achieved so that the formation of crystalline phase is possible by annealing at relatively low temperatures [11]. Some SFs synthesized by this method include  $\text{CuFe}_2\text{O}_4$  and  $\text{Fe}_3\text{O}_4$  [10, 11].

### **22.2.3 Non-hydrolytic Method**

The synthesis of SFs via non-hydrolytic process using suitable organic solvents at elevated temperatures is proved to be an effective method to obtain high-quality and well-controlled sized nanoparticles [7]. Generally, the inorganic coordination complexes or organometallic compounds are used as molecular precursors because they play a key factor in achieving well-crystalline SFs [7]. SFs are commonly considered as ternary metal oxides ( $\text{MFe}_2\text{O}_4$ ), and hence in non-hydrolytic method, two different kinds of molecular precursors have been used. Some of the reported molecular precursors are manganese(II) acetylacetonate,  $(\text{Mn}(\text{acac})_2)$ , and iron(III) acetylacetonate,  $(\text{Fe}(\text{acac})_3)$ . Some SFs synthesized by this method include  $\text{CoFe}_2\text{O}_4$  and  $\text{MnFe}_2\text{O}_4$  [12].

### **22.2.4 Solvothermal Method**

The solvothermal method (or hydrothermal if water is solvent) is one of the most eco-friendly and promising synthesis methods which is available and employs the usability of aqueous or nonaqueous solvents for a better control on particle size distribution and morphology [1]. Also, the shape, size, and morphology of SFs were altered by adjusting the experimental reaction conditions, such as temperature, time, solvent, precursor materials, and surfactant [1]. Due to its simplicity in procedure, commercial production of SFs is feasible with enhanced physical and chemical properties [1, 13–15]. A wide range of SFs have been synthesized, and some examples are MWCNT/ $\text{CoFe}_2\text{O}_4$ ,  $\text{Co}_3\text{O}_4$ ,  $\text{Fe}_3\text{O}_4$ ,  $\text{CoFe}_2\text{O}_4$  [1], Ni–Zn ferrite [13],  $\text{MnFe}_2\text{O}_4$  [14], and metal-doped  $\text{MgFe}_2\text{O}_4$  [15].

### 22.2.5 Coprecipitation Method

The synthesis of SFs by coprecipitation method is the most convenient, economic, and less time-consuming, has high mass production, and is frequently employed among all other methods in order to achieve uniform-sized particles [1]. This method is also commonly used to synthesize biocompatible SFs, which have applications in in vivo biomedical field [1]. This method employs the mixing of aqueous solutions of divalent and trivalent transition metal salts that are uniformly mixed together in 1:2 mole ratios with continuous and vigorous stirring in an alkaline medium. The coprecipitation method needs careful monitoring of pH in order to achieve high-quality SFs [4, 16]. The common disadvantage of this method is that relatively low crystallinity of synthesized SFs and hence a subsequent thermal treatment is necessary in order to achieve better crystallinity. This method is preferred to be the suitable route for synthesizing water-dispersible SFs [16], and a variety of SFs have been synthesized by coprecipitation method including  $\text{CoFe}_2\text{O}_4$  [2, 16],  $\text{MnFe}_2\text{O}_4$  [16],  $\text{Fe}_3\text{O}_4$  [4, 16], and Sn-doped  $\text{MnFe}_2\text{O}_4$  [4].

### 22.2.6 Sol-gel Method

The sol-gel synthesis method is widely employed for the SFs, in which the metal alkoxide solution undergoes hydrolysis and condensation polymerization reactions to produce gels and any volatile impurities are removed by heat treatment after the synthesis reaction [1]. The advantages of this method include low-cost, simple, carried out at a relatively low temperature without the need of special equipment, and achievable of narrow particle size distribution [17–20]. However, particular care should be taken for a better control of reaction parameters such as stirring rate, concentration of sol, and annealing temperature [1, 6]. The major limitation of this method is the lack of purity of the final product, and thus thermal treatment is required after the synthesis to achieve the high purity [1]. Nevertheless, the homogeneity, composition control, particle size, and particle distribution can be well achieved by sol-gel method, and nanocomposites based on SFs dispersed in silica gel matrix have been synthesized by this method, and some SFs synthesized by this method are  $\text{Ni}_{0.4}\text{Zn}_{0.6-x}\text{Co/Mn}_x\text{Fe}_2\text{O}_4$  [1],  $\text{CoFe}_2\text{O}_4$  [2, 17],  $\text{MnFe}_2\text{O}_4$  [6],  $\text{NiFe}_2\text{O}_4$  [17–19], Pr-substituted Mg-Zn ferrites [18],  $\text{CuFe}_2\text{O}_4$  [19], and  $\text{ZnFe}_2\text{O}_4$  [20].

### 22.2.7 Microwave-Assisted Method

The microwave-assisted method is a new technique which emerges rapidly for the synthesis of SFs. The advantages of this method are generally fast, simple, lower reaction time, high-energy efficiency, good yield, cost-effective, and appropriate

dielectric loss of the as-synthesized SFs [20]. Moreover, this method can be employed to synthesize SFNs on a commercial scale, but a low yield can be obtained when compared to other methods such as coprecipitation, hydrothermal, or thermal decomposition methods [1, 20]. In this method, heating energy is internal rather than external as in the case of conventional combustion reactions, and microwave energy is utilized for the combustion of precursors to form SFs. Heat generation is due to the conversion of microwave energy to thermal energy, and the temperature usually ranges from 100 to 200 °C for the shorter period of time. The gases produced during the reaction were eliminated through an exhaust drain connected with Teflon vessel [1]. Some SFs synthesized by this method are  $\text{Fe}_3\text{O}_4$  [1],  $\text{Co}_2\text{Fe}_2\text{O}_4$  [1],  $\text{Mn}_{1-x}\text{Ni}_x\text{Fe}_2\text{O}_4$  [20], and  $\text{ZnFe}_2\text{O}_4$  [21].

### 22.2.8 Mechanical Milling Method

Mechanical milling is a top-down approach method used for the synthesis of SFs by means of high-energy shaker, planetary ball mill, and sometimes tumbler mills [1, 22]. Some of the advantages of this method are low-cost, short time, simple, and large-scale production, and SFs obtained from this method have an ordered ferromagnetic core and a random shell [1]. The major disadvantage of this method is frequent contamination by milling tools during longtime milling, which in turn will change the stoichiometry of the as-obtained SFs [1, 22]. Some SFs synthesized by this method include  $\text{CoFe}_2\text{O}_4$  [1],  $\text{CuFe}_2\text{O}_4$  [1],  $\text{NiFe}_2\text{O}_4$  [1], and  $\text{Ni}_{1-x}\text{Mn}_x\text{Fe}_2\text{O}_4$  [22].

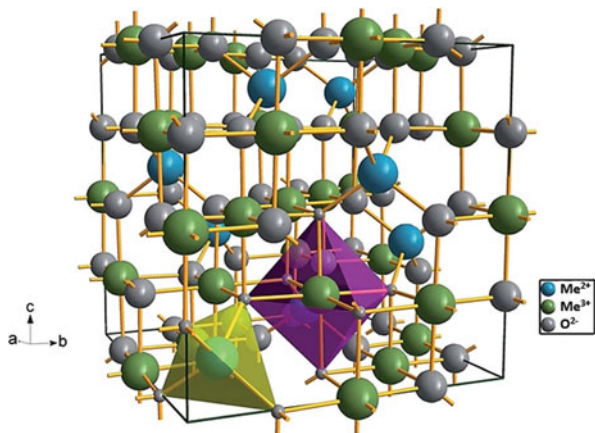
### 22.2.9 Other Methods

Numerous other methods frequently employed for the synthesis of SFs have been reported in the literature, including combustion [23], reverse micelle [24], spray pyrolysis [25], electrospinning [26], self-reactive quenching [27], double sintering ceramics [28], powder metallurgy [29], self-propagating high temperature [30], thermal decomposition [31], liquid exchange [32], and solid-state reaction [33].

## 22.3 Crystal Structure and Properties of Spinel Ferrites

Among different magnetic materials, SF nanoparticles have attracted particular considerations. SFs are a class of compounds of general formula  $\text{MFe}_2\text{O}_4$  (where  $\text{M} = \text{Zn}^{2+}$ ,  $\text{Mg}^{2+}$ ,  $\text{Mn}^{2+}$ ,  $\text{Fe}^{2+}$ ,  $\text{Co}^{2+}$ ,  $\text{Ni}^{2+}$ ,  $\text{Cu}^{2+}$ ,  $(0,5\text{Li}^+ + 0,5\text{Fe}^{3+})$ , etc.), which are of great interest for their remarkable magnetic, catalytic, optical, and electrical properties [34–37].

**Fig. 22.1** The unit cell of spinel structure  $\text{MeFe}_2\text{O}_4$



In the spinel structure with general formula  $\text{AB}_2\text{O}_4$ , oxygen atoms form cubic close packing where A and B cations occupy tetrahedral and octahedral lattice sites. The crystal structure has a space group  $\text{Fd}\bar{3}\text{m}$  [38]. The cubic unit cell is formed by 56 atoms: 32 oxygen anions distributed in a cubic close-packed structure and 24 cations occupying 8 of the 64 available tetrahedral sites (A sites) and 16 of the 32 available octahedral (B sites). Thus, the cell contains eight formula units ( $Z = 8$ ) corresponding to  $(\text{Me}_8^{2+})_A[\text{Me}_{16}^{3+}]_B(\text{O}_{32}^{2-})_O$ . The divalent metal ions commonly used in ferrites can be classified into those preferring B sites (Co, Fe, Ni, Cr) and those preferring A sites (Mn, Zn) (Fig. 22.1).

The crystal chemistry of spinels is described by the general formula  $(\text{Me}_{1-x}^{2+}\text{Fe}_x^{3+})_A[\text{Me}_x^{2+}\text{Fe}_{2-x}^{3+}]_B\text{O}_4$ , where  $x$  refers to the *inversion parameter or degree of inversion*, and  $\gamma$  depends from several factors, such as site preferences of ions in terms of size, covalent bonding effects, and crystal field stabilization energies (CFSE). In general, the inversion parameter of a given nanostructured ferrite is quite different from that of the bulk counterpart and varies with the preparation method. In the ideal *normal structure* ( $x = 0$ ),  $\text{Me}^{2+}$  cations are found at the A sites, and  $\text{Me}^{3+}$  cations are found at the B sites. Whereas in the *inverse structure* ( $x = 1$ ), half  $\text{Me}^{3+}$  cations are found at the A sites with consequent migration of all the  $\text{Me}^{2+}$  cations to the octahedral sites. Spinels can also display a *partially inverted structure*, which is described by means of the  $x$ -parameter, corresponding to the occupancy of  $\text{Me}^{3+}$  cations on the A sites.

In order to accommodate larger cations such as Co, Cu, Mn, Mg, Ni, and Zn, the lattice has to be expanded. The difference in the expansion of the tetrahedral and octahedral sites is characterized by a parameter called *oxygen parameter or anion parameter* ( $u$ ). The oxygen parameter ( $u$ ) is a quantity which represents the movement of  $\text{O}^{2-}$  ion due to the substitution of cation at tetrahedral A site. As  $u$  increases, oxygen ions move in such a way that the distance between A and O ions ( $R_A$ ) is increased while that between B and O ions ( $R_B$ ) is decreased, and when  $u$  parameter decreases, the  $\text{O}^{2-}$  ions are displaced in such a way that  $R_A$

decreases and  $R_B$  increases [39]. In all ideal spinels, the parameter  $u$  has a value in the neighborhood of 0.375 ( $u = 3/8$ ). But in the actual spinel lattice, this ideal pattern is slightly deformed and usually corresponds to  $u > 0.375$ .

The theoretical lattice constant ( $a_{th}$ ), radius of the ions at octahedral site ( $r_B$ ), and radius of the ions at tetrahedral site ( $r_A$ ) for spinel systems have been calculated on the basis of the cation distribution by the next relation [38]:

$$a_{th} = \frac{8}{3\sqrt{3}} \left[ (r_A + R_O) + \sqrt{3} (r_B + R_O) \right]$$

$$r_B = a \left( \frac{5}{8} - u \right) - R_O \qquad r_A = a\sqrt{3} (u - 0, 25) - R_O$$

where  $R_O$  is the radius of oxygen ion  $O^{2-}$  (1.38 Å);  $r_A$  and  $r_B$  are the ionic radii of tetrahedral (A) and octahedral (B) sites, respectively; and  $u$  is the anion (oxygen) parameter.

For example, for  $Zn_{1-x}Co_xFe_2O_4$  system [40], the average cation radii at the tetrahedral and octahedral sites,  $r_A$  and  $r_B$ , were calculated according to the following cation distribution:

$$\left( Zn_{1-x}^{2+} Fe_{x+y}^{3+} Co_y^{2+} \right)_A \left[ Co_{x-y}^{2+} Fe_{2-x-y}^{3+} \right]_B (O_4^{2-})_O \quad (0 \leq x \leq 1, 0 \leq y \leq 0,21)$$

$$r_A = C (Zn_A^{2+}) \cdot r (Zn_A^{2+}) + C (Fe_A^{3+}) \cdot r (Fe_A^{3+}) + C (Co_A^{2+}) \cdot r (Co_A^{2+})$$

$$r_B = \frac{C (Co_B^{2+}) \cdot r (Co_B^{2+}) + C (Fe_B^{3+}) \cdot r (Fe_B^{3+})}{2}$$

where  $C$  is the ionic concentration at the tetrahedral and octahedral sites;  $r (Zn_A^{2+})$ ,  $r (Fe_A^{3+})$ ,  $r (Co_A^{2+})$  are the ionic radii of  $Zn^{2+}$  (0.60 Å),  $Fe^{3+}$  (0.49 Å), and  $Co^{2+}$  (0.58 Å) ions in the tetrahedral sites, respectively; and  $r (Co_B^{2+})$ ,  $r (Fe_B^{3+})$  are the ionic radii of  $Co^{2+}$  (0.745 Å) and  $Fe^{3+}$  (0.645 Å) ions in the octahedral sites, respectively [40].

It can be seen that  $r(A)$  decreases while  $r(B)$  increases with increasing  $Co^{2+}$  concentration. This is due to the fact that  $Zn^{2+}$  ions (0.60 Å) with larger ionic radius are replaced by  $Co^{2+}$  ions (0.58 Å) with smaller ionic radius. Some of  $Fe^{3+}$  ions (0.49 Å) also migrate to (A) sites as a result of the substitution process. However, in (B) sites,  $Fe^{3+}$  ions with smaller ionic radius are replaced by  $Co^{2+}$  ions with larger ionic radius, so the values of radii of octahedral sites will be increased [40].

A recent published paper [39] also reports a decrease in cationic distribution parameters such as site radii ( $r_A$ ,  $r_B$ ) in the  $Zn_{0.85-x}Ni_xMg_{0.05}Cu_{0.1}Fe_2O_4$  ferrites ( $x = 0.00, 0.17, 0.34, 0.51, \text{ and } 0.85$ ), prepared by sol-gel auto-combustion method, with Ni doping. The parameters obtained by cationic distribution are reported. The cationic distribution can give a better understanding of the magnetic interaction in spinel ferrites, because there exists a strong correlation between magnetic properties and cation distribution of spinel ferrite [39].

In addition, the substitution (doping) of rare earth metal ions ( $\text{Sc}^{3+}$ ,  $\text{Dy}^{3+}$ ,  $\text{Sm}^{3+}$ ,  $\text{Gd}^{3+}$ , etc.) at  $\text{Fe}^{3+}$  site significantly affects the structural, microstructural, optical, electrical, and magnetic properties in the nanostructured ferrites [41]. Both magnetic and electrical properties of SFs are found to be strongly dependent on their chemical composition, method of preparation, grain/particle size, and distribution of cation between two interstitial sites. The structural and the magnetic environments of these two sites are quite different [41]. The doping of nonmagnetic ions, for example, the transition metal/rare earth-doped ferrites, has been extensively studied. It was found that the presence of nonmagnetic ions reduces the magnetic interactions between the two interstitial sites and leads to a decrease in hyperfine magnetic fields and hence changes observed in magnetic and electronic properties [41]. Table 22.1 illustrates some characteristics of selected SFs systems reported in the literature.

It can be seen from Table 22.1 that the decrease in lattice constant in SF systems can be explained by several mechanisms: (i) ionic radius reduction due to the fact that the doping cation has a smaller ionic radius compared to that of being cation; (ii) a possible redistribution of  $\text{Me}^{2+}$  and  $\text{Me}^{3+}$  ions within the tetrahedral/octahedral ionic sites, which will be followed by important changes in the magnetic properties; (iii) a fraction of  $\text{Me}^{2+}$  ions occupying the octahedral sites and forcing  $\text{Me}^{3+}$  to the tetrahedral sites against their chemical preferences [54].

Thus the cation distribution between tetrahedral (A) and octahedral (B) sites greatly influences the structural, electrical, optical, and magnetic properties of SFs [48]. In general, the magnetic behavior of spinel ferrites is dependent on the physical properties of individual particles and their environments. The most important physical characteristics include chemical composition, particle size, particle morphology, intrinsic material parameters (e.g., magnetocrystalline anisotropy, saturation magnetization, etc.), surfaces/interfaces, and particle size distribution. Most of these parameters are easily obtained (or are relatively non-important) for bulk magnetic materials; however, this is not necessarily true for nanoparticles.

The magnetic properties of SFs are classified as intrinsic and extrinsic. *Intrinsic magnetic parameters* depend mainly on the crystal structure and chemical composition of the material. Examples of intrinsic magnetic properties include Curie temperature  $T_c$ , saturation magnetization  $M_s$ , exchange stiffness  $A$ , and magnetocrystalline anisotropy  $K$ . On the other hand, *extrinsic magnetic parameters* depend upon the microstructure of the material and are naturally affected by the size and shape of particles. Extrinsic magnetic properties include coercivity  $H_c$ , remanent magnetization  $M_r$ , and magnetic susceptibility  $\chi$ . The concentration and types of cations substitution also have very dominant effect on the magnetic properties. According to the Neel's two-sublattice model of ferrimagnetism, the magnetic moment per formula unit is expressed as:

$$M(X) = M_{B(x)} - M_{A(x)}$$

where  $M_B$  and  $M_A$  are the B and A sublattice magnetic moment in  $\mu_B$ , respectively. Actually, the net magnetic moment determines the  $M_s$  value.

**Table 22.1** Composition and crystal chemical parameters for several ferrites with a cubic spinel structure

Compound	Synthesis method	Lattice constant (Å)	Size, nm	Strain, $\epsilon$	Ref.
ZnFe <sub>2</sub> O <sub>4</sub>	MCM	8.4410	5–15 <sup>b</sup>	0.034	[34]
ZnFe <sub>2</sub> O <sub>4</sub>	CCM	8.4429	30–50 <sup>b</sup>	0.038	[34]
ZnFe <sub>2</sub> O <sub>4</sub>	HEBM	8.448	9 <sup>a</sup>	–	[42]
CoFe <sub>2</sub> O <sub>4</sub>	MM	–	85 <sup>a</sup>	–	[43]
Co <sub>1-x</sub> Zn <sub>x</sub> Fe <sub>2</sub> O <sub>4</sub> (0 ≤ x ≤ 0.5, L-arginine as a fuel)	MCM	8.3799–8.3959	45–32 <sup>a</sup>	0.035–0.043	[44]
Zn <sub>1-x</sub> Co <sub>x</sub> Fe <sub>2</sub> O <sub>4</sub> (x = 0; 0.1; 0.2; 0.3; 0.4; 0.5; 0.6; 0.7; 0.8; 0.9; 1.0)	CM	8.4392–8.3536	37–25 <sup>a</sup>	–	[40]
Mn <sub>0.5</sub> Zn <sub>0.5</sub> Sc <sub>y</sub> Fe <sub>2-y</sub> O <sub>4</sub> (y = 0.00, 0.01, 0.03, and 0.05)	SCM	8.434–8431	20–22 <sup>a</sup> 20–23 <sup>c</sup>	–	[41]
Mn <sub>0.5</sub> Zn <sub>0.5</sub> Fe <sub>2</sub> O <sub>4</sub>	SCM	8.4339	25 <sup>a</sup>	0.0009	[45]
Mn <sub>1-x</sub> Zn <sub>x</sub> Fe <sub>2</sub> O <sub>4</sub> (x = 0, 0.1, 0.3, 0.5, 0.7, 0.9, 1.0)	SCM	8.432–8.372	25–35 <sup>c</sup>	–	[46]
Mn <sub>1-x</sub> Ni <sub>x</sub> Fe <sub>2</sub> O <sub>4</sub> (x = 0.0, 0.1, 0.2, 0.3, 0.4, 0.5)	MCM	8.477–8.419	–	0.412–0.200	[20]
Co <sub>x</sub> Ni <sub>0.6-x</sub> Zn <sub>0.4</sub> Fe <sub>2</sub> O <sub>4</sub> (x = 0.0 to 0.6)	PCM	8.3763–8.4002	–	–	[47]
Mg <sub>x</sub> Zn <sub>1-x</sub> Fe <sub>2</sub> O <sub>4</sub> (x = 0.5, 0.6, 0.7)	CM	8.422–8.438	6.3–14.6 <sup>a</sup>	~0.005	[48]
Co <sub>1-x</sub> Zn <sub>x</sub> Fe <sub>2</sub> O <sub>4</sub> (0 ≤ x ≤ 0.5, urea as a fuel)	MCM	8.284–8.356	3.07–11.3 <sup>a</sup>	–	[49]
Fe <sub>3</sub> O <sub>4</sub>	MCM	8.393	25 <sup>a</sup>	0,143	[50]
Fe <sub>3</sub> O <sub>4</sub>	SGM	8.3639	8 <sup>c</sup>	–	[51]
Zn <sub>1-x</sub> Mg <sub>x</sub> Fe <sub>2</sub> O <sub>4</sub> (x = 0.0, 0.1, 0.2, 0.3, 0.4, 0.5, 0.6, 0.7, and 0.8)	MCM	8.443–8.427	41.20–15.87 <sup>a</sup>	0.067–0.047	[52]
Zn <sub>1-x</sub> Sr <sub>x</sub> Fe <sub>2</sub> O <sub>4</sub> (x = 0.0, 0.1, 0.2, 0.3, 0.4, and 0.5)	MCM	8.443–8.451	42 – 25 <sup>a</sup>	0.067–0.077	[53]
Zn <sub>1-x</sub> Cu <sub>x</sub> Fe <sub>2</sub> O <sub>4</sub> (x = 0.0, 0.1, 0.2, 0.3, 0.4, and 0.5)	MCM	8.443–8.413	43–54 <sup>a</sup>	0.067–0.056	[54]
Zn <sub>1-x</sub> Ni <sub>x</sub> Fe <sub>2</sub> O <sub>4</sub> (x = 0.0, 0.1, 0.2, 0.3, 0.4, and 0.5)	MCM	–	43–49 <sup>a</sup>	–	[55]
Zn <sub>0.85-x</sub> Ni <sub>x</sub> Mg <sub>0.05</sub> Cu <sub>0.1</sub> Fe <sub>2</sub> O <sub>4</sub> (x = 0.00, 0.17, 0.34, 0.51, 0.85)	SGM	8.412–8.352	34–42 <sup>a</sup>	–	[39]
Li <sub>0.5-x/2</sub> Zn <sub>x</sub> Fe <sub>2.5-x/2</sub> O <sub>4</sub> (x = 0, 0.1, 0.25, 0.3, 0.5, 0.7, 0.9, 1.0)	SGM	8311–8.423	–	–	[56]
Mg <sub>1-x</sub> Zn <sub>x</sub> FeCrO <sub>4</sub> (0.0 ≤ x ≤ 1.0)	CCM	8.3610–8.3820	20.1–28.7 <sup>a</sup>	–	[57]
MnFe <sub>2-x</sub> Mn <sub>x</sub> O <sub>4</sub> (x = 0.0, 0.25, 0.5, 1.0)	RMM	8369–8379	23–28 <sup>a</sup> 4–22 <sup>c</sup>	–	[58]
NiFe <sub>2-x</sub> Ga <sub>x</sub> O <sub>4</sub> (x = 0.0, 0.2, 0.4, 0.6, 0.8, 1.0)	SGM	8.3491–8.3313	13.8–5.5 <sup>a</sup>	–	[59]
Mn <sub>1-x</sub> Mg <sub>x</sub> Fe <sub>2</sub> O <sub>4</sub> (0.0 ≤ x ≤ 1.0)	HTM	8.471–8.443	20–30 <sup>a</sup>	–	[60]

MCM microwave combustion method, CCM conventional combustion method, SCM solution combustion method, PCM precursor combustion method, CM coprecipitation method, SGMsol-gel method, MM mechanical milling, HEBM high-energy ball milling, CCM conventional ceramic method, RMM reverse microemulsion method, HTM hydrothermal method  
a, b, and c are sizes from XRD [<sup>a</sup>], SEM [<sup>b</sup>], and TEM [<sup>c</sup>]



**Table 22.2** Magnetic properties (magnetization Ms, remanence Mr, and coercivity Hc) and optical data (band gap) as a function of cation substitution at some SF systems

Compound	Magnetic properties			Optical properties	Ref.
	Ms (emu/g)	Hc (Oe)	Mr (emu/g)	Band gap (eV)	
ZnFe <sub>2</sub> O <sub>4</sub> -MCM	31.96	119.7	0,5247	2.08	[34]
ZnFe <sub>2</sub> O <sub>4</sub> - CCM	149.1	46.96	1.358	2.03	[34]
ZnFe <sub>2</sub> O <sub>4</sub>	30	–	–	2.13	[42]
CoFe <sub>2</sub> O <sub>4</sub>	72.1	1517	37.7	–	[43]
Co <sub>1-x</sub> Zn <sub>x</sub> Fe <sub>2</sub> O <sub>4</sub> (0 ≤ x ≤ 0.5)	–	–	–	1.88–2.10	[44]
Mn <sub>1-x</sub> Ni <sub>x</sub> Fe <sub>2</sub> O <sub>4</sub> (x = 0.0, 0.1, 0.2, 0.3, 0.4, 0.5)	67.79–35.09	48.25–99.26	11.94–6.425	1.56–1.83	[20]
Co <sub>x</sub> Ni <sub>0.6-x</sub> Zn <sub>0.4</sub> Fe <sub>2</sub> O <sub>4</sub> (x = 0.0 to 0.6)	63.5–74.8	75–150	8.8–10.2	–	[47]
Mg <sub>x</sub> Zn <sub>1-x</sub> Fe <sub>2</sub> O <sub>4</sub> (x = 0.5, 0.6, 0.7)	38.46–44.03	18.67–23.52	1.303–1.471	–	[48]
Co <sub>1-x</sub> Zn <sub>x</sub> Fe <sub>2</sub> O <sub>4</sub> (0 ≤ x ≤ 0.5, urea as a fuel)	14.26–29.61	–	–	2.56–2.17	[49]
Fe <sub>3</sub> O <sub>4</sub>	66.12	65.89	10.2	2.12	[50]
Fe <sub>3</sub> O <sub>4</sub>	47	0.655	–	–	[51]
Zn <sub>1-x</sub> Co <sub>x</sub> Fe <sub>2</sub> O <sub>4</sub> (x = 0.0 to 0.5)	1.638–65.20	5.027–66.36	0.0016–10.862	2.10–1.71	[52]
Zn <sub>1-x</sub> Mg <sub>x</sub> Fe <sub>2</sub> O <sub>4</sub> (x = 0.0, 0.1, 0.2, 0.3 0.4, 0.5, 0.6, 0.7, 0.8)	1.638–64.98	5.027–65.96	0.0016–11.565	2.15–1.42	[61]
Zn <sub>1-x</sub> Sr <sub>x</sub> Fe <sub>2</sub> O <sub>4</sub> (x = 0.0, 0.1,0.2, 0.3,0.4, 0.5)	1.638–59.581	5.027–30.152	0.0016–4.6562	2.1–1.72	[53]
Zn <sub>1-x</sub> Cu <sub>x</sub> Fe <sub>2</sub> O <sub>4</sub> (x = 0.0, 0.1, 0.2, 0.3, 0.4, 0.5)	1.638–58.58	5.027–29.15	0.0016–4.9361	2.1–1.95	[54]
Zn <sub>1-x</sub> Ni <sub>x</sub> Fe <sub>2</sub> O <sub>4</sub> (x = 0.0, 0.1, 0.2, 0.3, 0.4, 0.5)	1.681–57.89	5.034–30.14	0.0018–4.8953	2.11–1.96	[55]
Zn <sub>0.85-x</sub> Ni <sub>x</sub> Mg <sub>0.05</sub> Cu <sub>0.1</sub> Fe <sub>2</sub> O <sub>4</sub> (x = 0.00, 0.17, 0.34, 0.51, 0.85)	47.63–136.93	0.97–167.5	0.27–11.87	–	[39]
MnFe <sub>2-x</sub> Mn <sub>x</sub> O <sub>4</sub> (x = 0.0, 0.25, 0.5, 1.0)	16–30	115–223	–	–	[58]

A few most representative examples of the magnetic SFs with their magnetic and optical properties are given in Table 22.2.

As can be seen from Table 22.2, there is some correlation between the structural properties of the materials (difference in the cation sharing at the A and B sites) and their magnetic results. The magnetic properties of nanoparticles are determined by their physical structure: the size and shape of the particles, their microstructure, the chemical phase or phases that are present, the defects, and differences between the crystal structure of nanoscale phases and their bulk counterparts. For example, the magnetic properties of zinc ferrite systems are influenced by the preparation route,

cation distribution, grain size, and sintering conditions [34]. The smaller value of saturation magnetization in  $\text{ZnFe}_2\text{O}_4$ -CCM is due to the differences in inversion parameter, which indicates the distribution of cations between A and B sites of the spinel lattice [34]. Moreover, the very low values of  $H_c$  and  $M_r$  indicate that the ferrites are soft magnets. Magnetic SFs with the same chemical composition often differ markedly from one another due to a different distribution of ions among the sublattice (Table 22.2).

For example, zinc ferrite is a normal spinel and nonmagnetic ion  $\text{Zn}^{2+}$  and magnetic ion  $\text{Fe}^{3+}$  are distributed in A and B sites, respectively [18]. But the lower magnitudes of magnetization and occurrence of a net magnetic moment of the order of 10.73 emu/g in zinc ferrite (for  $x = 1$ ) at room temperature in the reference [46] are indicative of the presence of  $\text{Zn}^{2+}$  ions on the octahedral sites in nanoregime. It can alter the cation distribution to a greater extent which is an influential factor in determining the overall magnetic properties in the nanoregime. The small values of coercivity indicate that the synthesized ferrites can be used for low- and high-frequency applications [46].

In Mg-Zn ferrites [48], both  $\text{Zn}^{2+}$  and  $\text{Mg}^{2+}$  are diamagnetic, and therefore the distribution of  $\text{Fe}^{3+}$  between tetrahedral (A) and octahedral (B) sites will determine the magnetization. In the present ferrite systems,  $\text{Zn}^{2+}$  substantially occupies tetrahedral (A) site, and  $\text{Mg}^{2+}$  occupies octahedral (B) sites along with inversion to tetrahedral (A) sites accompanied with an increase of  $\text{Mg}^{2+}$  ion concentration leading to the formula unit  $(\text{Zn}_{1-x}\text{Mg}_x\text{Fe}_{x-\delta})[\text{Mg}_{x-\delta}\text{Fe}_{2-x+\delta}]\text{O}_4$ . Therefore the increase of  $\text{Mg}^{2+}$  in B sites pushes the  $\text{Fe}^{3+}$  to A sites, thereby strengthening A-B exchange interaction and finally resulting in the increase of saturation magnetization [48].

The preparation of ferrite nanoparticles with controlled particle sizes leading to the appearance of a superparamagnetic behavior remains a challenging task. On the other hand, the magnetic anisotropy of ferrite nanoparticles can be controlled by a proper selection of divalent dopants in the spinel structure [48]. When particle size reaches to a critical size ( $D_c$ ), in such ferrite nanoparticles, thermal fluctuations disorganize the magnetic spins in random way like paramagnetic state, and this state is termed as superparamagnetism. The ferrite nanoparticles with superparamagnetic behavior are suitable for biomedical applications like targeted drug delivery, cancer treatment by hyperthermia, etc. [48]. For example, magnetic measurements of  $\text{Zn}_{1-x}\text{Sr}_x\text{Fe}_2\text{O}_4$  nanoparticles [53] revealed that, at lower Sr concentration ( $x < 0.2$ ), the system shows a superparamagnetic behavior, whereas, at higher concentration ( $x > 0.2$ ), it becomes ferromagnetic. The samples  $\text{ZnFe}_2\text{O}_4$ ,  $\text{Zn}_{0.9}\text{Mg}_{0.1}\text{Fe}_2\text{O}_4$ , and  $\text{Zn}_{0.8}\text{Mg}_{0.2}\text{Fe}_2\text{O}_4$  [61] with lesser Mg concentration ( $x = 0.0, 0.1$  and  $0.2$ ) also showed superparamagnetic behavior. This indicates that  $\text{Zn}^{2+}$  ions occupied the tetrahedral sites and  $\text{Fe}^{3+}$  ions at the octahedral sites, whereas the dopant  $\text{Mg}^{2+}$  ions occupied either octahedral or tetrahedral sites, thus showing superparamagnetic behavior.

It is known that in SFs, the saturation magnetization depends on the exchange interaction between the A and B sites, i.e., A-B exchange interaction [39, 40] (Fig. 22.2). The different types and amount of magnetic or nonmagnetic cationic

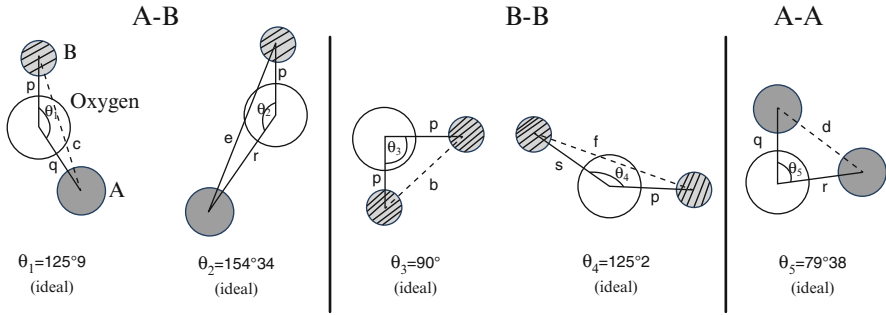


**Fig. 22.2** Configuration of the ion pairs in SFs with favorable distances and angles for effective magnetic interactions

substitution on A and B sites strongly affect the exchange interactions among them [39]. In ferrites, the exchange interaction occurs by the contribution of oxygen “anions” which is called superexchange interaction. There are three probable superexchange interactions in the ferrites as follows: A–A, B–B, and A–B interactions. The inter-sublattice interactions (A–O–B) are much stronger than the intra-sublattice interactions (A–O–A and B–O–B) in SFs with collinear ferrimagnetic structure. The inter-sublattice interaction (A–O–B) is accountable for the discrepancy of initial permeability and Curie temperature of SFs [39].

The bond distances between cations (Me–Me) ( $b$ ,  $c$ ,  $d$ ,  $e$ , and  $f$ ) and cation–anion (Me–O) ( $p$ ,  $q$ ,  $r$ , and  $s$ ) are estimated using the following relations [40]:

Me–O	Me–Me
$p = a \left( \frac{5}{8} - u \right)$	$b = \sqrt{2} \left( \frac{a}{4} \right)$
$q = a\sqrt{3} \left( u - \frac{1}{4} \right)$	$c = \sqrt{11} \left( \frac{a}{8} \right)$
$r = a\sqrt{11} \left( u - \frac{1}{4} \right)$	$d = \sqrt{3} \left( \frac{a}{4} \right)$
$s = a\sqrt{3} \left( \frac{u}{3} + \frac{1}{8} \right)$	$e = \sqrt{3} \left( \frac{3a}{8} \right)$
	$f = \sqrt{6} \left( \frac{a}{4} \right)$

The overall strength of the magnetic interactions (A–B, B–B, and A–A) depends upon the bond lengths and bond angles between the cations and cation–anion. The strength is directly proportional to bond angle but inversely proportional to bond length. The bond angles ( $\theta_1$ ,  $\theta_2$ ,  $\theta_3$ ,  $\theta_4$ , and  $\theta_5$ ) between the cations and cation–anion are estimated using the following relations [40]:

$$\theta_1 = \cos^{-1} \left( \frac{p^2 + q^2 - c^2}{2pq} \right)$$

$$\theta_2 = \cos^{-1} \left( \frac{p^2 + r^2 - e^2}{2pr} \right)$$

$$\theta_3 = \cos^{-1} \left( \frac{2p^2 - b^2}{2p^2} \right)$$

$$\theta_4 = \cos^{-1} \left( \frac{p^2 + s^2 - f^2}{2ps} \right)$$

$$\theta_5 = \cos^{-1} \left( \frac{r^2 + q^2 - d^2}{2rq} \right)$$

For example, the estimated bond angles for the spinel system  $\text{Zn}_{1-x}\text{Co}_x\text{Fe}_2\text{O}_4$  [40] indicate that  $\theta_1$ ,  $\theta_2$ , and  $\theta_5$  increase while  $\theta_3$  and  $\theta_4$  decrease with increasing  $\text{Co}^{2+}$  concentration. The decrease in  $\theta_3$  and  $\theta_4$  suggests a strengthening of B–B interactions, while  $\theta_1$ ,  $\theta_2$ , and  $\theta_5$  increase, which is indicative of weakening A–B and A–A interactions with decreasing  $\text{Zn}^{2+}$  concentration. In reference [39], it is also reported that the magnetic exchange (A–B, A–A, and B–B) strength depends upon the bond distance and bond angles. The strength varies directly with bond angle and varies inversely with bond length for the  $\text{Zn}_{0.85-x}\text{Ni}_x\text{Mg}_{0.05}\text{Cu}_{0.1}\text{Fe}_2\text{O}_4$  spinel nanoferrites for different compositions ( $x = 0.00, 0.17, 0.34, 0.51, 0.85$ ).

Furthermore, ferrites are one of the most promising photocatalysts, with the characteristic behavior of absorbing visible light, and possess band gap in the range 1.1–2.5 eV (Table 22.2). The optical properties of ferrite nanoparticles can be investigated by UV–visible absorption spectroscopy. The band gap energy can be evaluated from the  $E_g$  measurements using Kubelka–Munk (K–M) model, and the  $F(R)$  value is estimated from the following equation:

$$F(R) = (1 - R)^2 / 2R$$

where  $F(R)$  is the Kubelka–Munk function and  $R$  is the diffuse reflectance. A graph is plotted between  $[F(R)h\nu]^2$  and  $h\nu$ ; the intercept value is the band gap energy.

For example, the estimated values of the band gap of  $\text{Zn}_{1-x}\text{Cu}_x\text{Fe}_2\text{O}_4$  ( $x = 0.0, 0.1, 0.2, 0.3, 0.4, \text{ and } 0.5$ ) system are 2.1, 2.07, 2.05, 2.03, 2.0, and 1.95 eV, respectively [54]. The band gap energy decreases with increasing Cu content, which may be associated with various parameters including the crystallite size, structural parameter, carrier concentrations, presence of very small amount of impurities which are not detectable by XRD and SEM/EDX techniques, and lattice strain. Interestingly, a possible correlation between the band gap and the lattice parameter can be highlighted; it was noticed that both values of band gap as well as lattice parameter decrease with increasing Cu concentration [54].

## 22.4 Applications

SFs offer numerous applications in wide-range fields, including biomedical, sensors and biosensors, high-frequency components, low-temperature co-fired ceramic (LTCC) devices, supercapacitors, microwave absorption, and photocatalytic activity.

### 22.4.1 *Biomedical*

Magnetic nanoparticles possess great potential for innumerable applications like magnetic carriers in bio-screening, magnetic resonance imaging (MRI), cell separation, contrast enhancement, tissue repair, cancer treatment and controlled drug delivery, hyperthermia, and related biomedical areas [62]. SFs have exclusively gained importance in magnetic hyperthermia applications. Magnetic hyperthermia treatment is a technique whereby spherically shape-controlled ferrite nanoparticles are targeted through the bloodstreams which can selectively kill cancer cells and tumors by raising their temperature in the range 41–46 °C by noninvasive manner [63].

Spherical uniform-sized ferrite particles having an average diameter between 50 and 150 nm are used in biomedical applications to achieve high throughput. This facilitates a uniform immobilization of bio-functional molecules on the shape-controlled ferrite particles so as to bestow unvarying magnetic, hydrodynamic, biocompatibility, and colloidal stability properties. Ruthradevi and co-workers [64] attempted nickel ferrite nanoparticles in calcium phosphate nanostructure exhibiting ferromagnetic behavior with coercivity of 0.045 T at 5 K and the superparamagnetic behavior with zero coercivity at 300 K giving a scope for hyperthermia treatment. Magnetic fluid obtained by colloidal suspension of manganese/zinc ferrite nanoparticles (15–17 nm) were stabilized through steric repulsion by coating with biologically compatible carboxymethyl dextran (CMDx) [65]. Cell viability measurements showed that the magnetic fluid is nontoxic to MCF-7 and CaCo-2 cell lines at concentrations of up to 7.5 mg/mL of particle fraction for a contact time of up to 48 h. The stability and nontoxicity, superparamagnetic behavior, and cytotoxic effects show a possibility for biomedical applications. Calcium-doped zinc ferrite within the range of 12–14 nm employed for hemolysis testing demonstrated that the ferrite material was not cytotoxic when using 10 mg of ferrite/mL of solution. Accordingly  $\text{Zn}_{0.50}\text{Ca}_{0.50}\text{Fe}_2\text{O}_4$  was found to be a potential material for cancer treatment by magnetic hyperthermia therapy [63]. Likewise, many spherical-shaped, uniform-sized, and colloidal stable dispersions employing ferrite particles showcase as promising magnetic carriers for biomedical applications.

### 22.4.2 *Sensors and Biosensors*

Ferrite nanoparticles are widely used as sensor materials for detecting different analytes at the trace levels.  $\text{CoFe}_2\text{O}_4$  plays an important role in the fabrication of gas sensors. A simple conductometric sensor has been fabricated using samarium (Sm)-doped cobalt ferrite for the detection of hydrogen leaks [66]. Cobalt–manganese ferrite appears to be quite suitable for an application as  $\text{CO}_2$  gas sensors [67].

Ferrites have also proved as excellent materials for electrochemical biosensor because of their sensing accuracy, low detection levels of the analyte, and quick analysis time. Some of the examples include  $\text{Fe}_3\text{O}_4$ ,  $\gamma\text{-Fe}_2\text{O}_3$ ,  $\text{CoFe}_2\text{O}_4$ ,  $\text{MnFe}_2\text{O}_4$ , and  $\text{ZnFe}_2\text{O}_4$ . Among these, gold (Au)-coated  $\text{Fe}_3\text{O}_4$  nanoparticle-based biosensors are widely studied and used for detection of a number of biochemical moieties [8]. Nanostructured  $\text{ZnFe}_2\text{O}_4$  ionic liquid carbon paste electrode sensor exhibited low interfacial resistance and fast electron transfer capacity, high sensitivity to trace level, good detection limits, and excellent reproducibility for the determination of 5-fluorouracil anticancer drug and real pharmaceutical and human urine samples even at trace level [68].

### 22.4.3 High-Frequency Components

$\text{MFe}_2\text{O}_4$  ( $\text{M} = \text{Mn, Fe, Co, etc.}$ ) spinels have attracted much consideration in the recent years in applications such as computers, communications, office automation, remote monitoring, audio and video equipment, household appliances, and industrial automation technology. At present, electronic industries are in need of magnetic materials especially ferrite-based compounds. Nevertheless, with the arrival of high-frequency applications, the regular techniques of reducing eddy current losses, using iron cores which are in practice, become less efficient and not cost-effective. Moreover, the existing switched mode power supplies industries required even low energy losses in power conversion with maintenance of adequate initial permeability. Manganese–zinc ferrite with low magnetic loss, high saturation magnetization, high permeability, and high magnetic domain relaxation frequency was achieved. This type of ferrite material finds use in electronic and electrical industries especially for manufacturing deflection yoke rings, memory chips, magnetic recording heads, transformers, transducers, and other devices [69].

### 22.4.4 LTCC Devices

By the advent of miniaturization of electronic products, the low temperature co-fired ceramic (LTCC) materials and chip devices have gained importance due to their small volume and mass. NiCuZn ferrite and M-type barium ferrite play a dominant role in the manufacture of components in miniature form. These ferrites led to surface mounting devices and are used as multilayer chip inductor and wire wound chip inductor. Specifically, NiCuZn ferrites are best suited magnetic materials for capacitors, transformers, microwave gyromagnetic devices, and components in electronic products like cell phones, video cameras [70], laptops, and wireless communication systems [71, 72].

### 22.4.5 Supercapacitors

$\text{CoFe}_2\text{O}_4$ ,  $\text{SnFe}_2\text{O}_4$ , and many other metal ferrites have been largely used for charge storage applications. Recently, doped manganese ferrite nanoparticles chemically anchored on graphene nanosheets exhibited an enhanced capacitive performance as compared to individual components due to the synergistic effect of faradic behavior and electric double layer capacitance. The ferrites in various morphologies have influence in varying the surface area of the material leading to different supercapacitance values. The higher the surface area, the higher the charge storage capacity becomes. The ferrites are observed to have a specific capacitance value around 50–400 F/g. The fascinating electrochemical activity of several ferrite nanocomposites makes them a potential candidate for supercapacitor applications [73–75].

### 22.4.6 Microwave Absorption

In the day-to-day life applications, radio broadcasting, satellite communications, radars, GPS, cell phones, and wireless networks operate at microwave frequency range 1–18GHz. The efficiency of these systems can be severely affected by unwanted reflections or emissions in addition to associated health risks. In this context, ferrites play a predominant role in reflection suppression or damping of free space electromagnetic waves [76].

Various compounds mainly based on planar M-, W-, Y-, Z-, and U-type hexagonal ferrite structures are extensively employed as electromagnetic (EM) wave absorbers. Some of the widely discussed materials are lithium–zinc ferrite doped with La and Mg,  $\text{SrFe}_{12}\text{O}_{19}/\text{TiO}_2$  nanocomposites, doped barium ferrite, Ce-substituted barium ferrite, nickel- and zinc-substituted strontium hexaferrite,  $\text{MnFe}_2\text{O}_4/\text{wax}$ ,  $\text{RGO}/\text{MnFe}_2\text{O}_4/\text{wax}$ , and the  $\text{RGO}/\text{MnFe}_2\text{O}_4/\text{PVDF}$ ; these are some of the most excellent wave absorbing ferrites in the microwave frequency range of 8–12 GHz (X band). All the above materials have been evaluated with a minimum reflection loss observed at the studied frequency range. In addition, similar substituted hexagonal ferrites are also tested for broadband absorption between 12 and 30 GHz and thus suiting application in RADAR absorption [77–81].

### 22.4.7 Photocatalytic Activity

Ferrites are one of the most promising photocatalysts, with the characteristic behavior of absorbing visible light, and possess a band gap in the range 1.1–2.3 eV. Besides, ferrites overcome the technical problem of separation and reuse as they

are magnetically separable. The spinel structure of metal ferrites provides extra catalytic reaction sites resulting in enhanced photocatalytic degradation efficiency. Ferrites possess important photocatalytic properties for many industrial processes, including the oxidative dehydrogenation of hydrocarbons; photo-Fenton-like process; decomposition of alcohols and hydrogen peroxide; the treatment of exhaust gases; the oxidation of compounds such as CO, H<sub>2</sub>, CH<sub>4</sub>, and chlorobenzene; the hydroxylation of phenol; alkylation reactions; the hydrodesulphurization of crude petroleum; the catalytic combustion of methane; degradation of toxic dyes; elimination of contaminants from water and air; odor control; bacterial inactivation; water splitting to produce H<sub>2</sub>; the inactivation of cancer cells; and many others. Numerous studies have focused on potential ferrite catalyst such as meso-CuFe<sub>2</sub>O<sub>4</sub>, meso-CoFe<sub>2</sub>O<sub>4</sub>, GO-NiFe<sub>2</sub>O<sub>4</sub>, BiFeO<sub>3</sub>, ZnFe<sub>2</sub>O<sub>4</sub>, Fe<sub>3</sub>O<sub>4</sub>, MnFe<sub>2</sub>O<sub>4</sub> with activated carbon, BaFe<sub>2</sub>O<sub>4</sub>, BaFeO<sub>3-x</sub>, ZnFe<sub>2</sub>O<sub>4</sub>-graphene, mesoporous-ZnFe<sub>2</sub>O<sub>4</sub>, CuFe<sub>2</sub>O<sub>4</sub>, CoFe<sub>2</sub>O<sub>4</sub>, MnFe<sub>2</sub>O<sub>4</sub>, NiFe<sub>2</sub>O<sub>4</sub> CoFe<sub>2</sub>O<sub>4</sub>-graphene, SrFe<sub>12</sub>O<sub>19</sub>, etc. Utilizing ferrite-based photocatalytic studies for wider applications promotes sustainable eco-friendly and cleaner technologies [44, 82, 83].

## 22.5 Conclusions

In this chapter, synthesis methods, crystal structure, properties, and perspective applications of SFs are summarized. Magnetic spinel nanoparticles gained a lot of interest due to their ability to be manipulated upon application of an external magnetic field and thereby can be utilized as gas sensors, catalysts, photocatalysts, adsorbents, electronic devices, etc. The specific focus was on the methods of preparation (microemulsion, ultrasonic, non-hydrolytic, solvothermal, coprecipitation, sol-gel, microwave-assisted, mechanical milling, etc.), the crystal structure, magnetic and optical properties, and different application of SFs. The influence of the synthesis method on the ferrite particle size was also described. The crystal structure, cationic distribution, and exchange interaction between the magnetic ions are responsible for the magnetic behavior in SFs. Finally, it can be concluded that SFs are suitable materials for many technological applications.

## References

1. Yan Z, Gao J, Li Y, Zhang M et al (2015) Hydrothermal synthesis and structure evolution of metal-doped magnesium ferrite from saprolite laterite. *RSC Adv* 5:92778–92787
2. Olsson RT, Salazar-Alvarez G, Hedenqvist SM et al (2005) Controlled synthesis of near-stoichiometric cobalt ferrite nanoparticles. *Chem Mater* 17:5109–5118
3. Latham AH, Williams ME (2008) Controlling transport and chemical functionality of magnetic nanoparticles. *Acc Chem Res* 41:411–420
4. Moussaoui HE, Mahfoud T, Habouti S et al (2016) Synthesis and magnetic properties of tin spinel ferrites doped manganese. *J Magn Magn Mater* 405:181–186
5. Mathew DS, Juang R (2007) An overview of the structure and magnetism of spinel ferrite nanoparticles and their synthesis in microemulsions. *Chem Eng J* 129:51–65



6. Carta D, Casula MF, Falqui A et al (2009) A structural and magnetic investigation of the inversion degree in ferrite nanocrystals  $MFe_2O_4$  ( $M = Mn, Co, Ni$ ). *J Phys Chem C* 113:8606–8615
7. Song Q, Ding Y, Wang ZL et al (2007) Tuning the thermal stability of molecular precursors for the nonhydrolytic synthesis of magnetic  $MnFe_2O_4$  spinel nanocrystals. *Chem Mater* 19:4633–4638
8. Kefeni KK, Msagati TAM, Mamba BB (2017) Ferrite nanoparticles: synthesis, characterisation and applications in electronic device. *Mater Sci Eng B* 215:37–55
9. Pang YL, Lim S, Ong H et al (2016) Research progress on iron oxide-based magnetic materials: synthesis techniques and photocatalytic applications. *Ceram Int* 42:9–34
10. Goswami PP, Choudhury HA, Chakma S et al (2013) Sonochemical synthesis and characterization of manganese ferrite nanoparticles. *Ind Eng Chem Res* 52:17848–17855
11. Kurikka JL, Shafi VPM, Ulman A et al (2004) Mixed iron–manganese oxide nanoparticles. *J Phys Chem B* 108:14876–14883
12. Song Q, Zhang ZJ (2012) Controlled synthesis and magnetic properties of bimagnetic spinel ferrite  $CoFe_2O_4$  and  $MnFe_2O_4$  nanocrystals with core–shell architecture. *J Am Chem Soc* 134:10182–10190
13. Ni D, Lin Z, Xiaoling P et al (2015) Preparation and characterization of nickel-zinc ferrites by a solvothermal method. *Rare Metal Mater Eng* 44:2126–2131
14. Li Z, Gao K, Han G, Wang R et al (2015) Solvothermal synthesis of  $MnFe_2O_4$  colloidal nanocrystal assemblies and their magnetic and electrocatalytic properties. *New J Chem* 39:361–368
15. Yin Y, Liu W, Huo N et al (2016) Synthesis of vesicle-like  $MgFe_2O_4$ /Graphene 3D network anode material with enhanced lithium storage performance. *ACS Sustain Chem Eng*. doi:10.1021/acssuschemeng.6b01949
16. Pereira C, Pereira AM, Fernandes C et al (2012) Superparamagnetic  $MFe_2O_4$  ( $M = Fe, Co, Mn$ ) nanoparticles: tuning the particle size and magnetic properties through a novel one-step coprecipitation route. *Chem Mater* 24:1496–1504
17. Carta D, Loche D, Mountjoy G et al (2008)  $NiFe_2O_4$  nanoparticles dispersed in an aerogel silica matrix: an X-ray absorption study. *J Phys Chem C* 112:15623–15630
18. Mukhtar MW, Irfan M, Ahmad I et al (2015) Synthesis and properties of Pr-substituted  $MgZn$  ferrites for core materials and high frequency applications. *J Magn Magn Mater* 381:173–178
19. Sharma R, Bansal S, Singhal S (2015) Tailoring the photo-Fenton activity of spinel ferrites ( $MFe_2O_4$ ) by incorporating different cations ( $M = Cu, Zn, Ni$  and  $Co$ ) in the structure. *RSC Adv* 5:6006–6018
20. Jesudoss SK, Vijaya JJ, Kennedy LJ et al (2016) Studies on the efficient dual performance of  $Mn_{1-x}Ni_xFe_2O_4$  spinel nanoparticles in photodegradation and antibacterial activity. *J Photochem Photobiol B* 165:121–132. doi:10.1016/j.jphotobiol.2016.10.004
21. Tadjarodi A, Imani M, Salehi M (2015)  $ZnFe_2O_4$  nanoparticles and a clay encapsulated  $ZnFe_2O_4$  nanocomposite: synthesis strategy, structural characteristics and the adsorption of dye pollutants in water. *RSC Adv* 5:56145–56156
22. Marinca TF, Chicinaş I, Isnard O et al (2016) Nanocrystalline/nanosized manganese substituted nickel ferrites –  $Ni_{1-x}Mn_xFe_2O_4$  obtained by ceramic-mechanical milling route. *Ceram Int* 42(4):4754–4763. doi:10.1016/j.ceramint.2015.11.155
23. Angadi VJ, Rudraswamy B, Sadhana K et al (2016) Effect of  $Sm^{3+}$ – $Gd^{3+}$  on structural, electrical and magnetic properties of Mn–Zn ferrites synthesized via combustion route. *J Alloys Compd* 656:5–12. doi:10.1016/j.jallcom.2015.09.222
24. Singh C, Jauhar S, Kumar V et al (2015) Synthesis of zinc substituted cobalt ferrites via reverse micelle technique involving in situ template formation: a study on their structural, magnetic, optical and catalytic properties. *Mater Chem Phys* 156:188–197. doi:10.1016/j.matchemphys.2015.02.046
25. Kotsikau D, Ivanovskaya M, Pankov V et al (2015) Structure and magnetic properties of manganese–zinc-ferrites prepared by spray pyrolysis method. *Solid State Sci* 39:69–73. doi:10.1016/j.solidstatesciences.2014.11.013

26. Cortes MS, Martínez-Luevanos A, García-Cerda LA et al (2015) Nanostructured pure and substituted cobalt ferrites: fabrication by electrospinning and study of their magnetic properties. *J Alloys Compd* 653:290–297. doi:[10.1016/j.jallcom.2015.08.262](https://doi.org/10.1016/j.jallcom.2015.08.262)
27. Cai X, Wang J, Li B et al (2016) Microwave absorption properties of LiZn ferrites hollow microspheres doped with La and Mg by self-reactive quenching technology. *J Alloys Compd* 657:608–615. doi:[10.1016/j.jallcom.2015.10.153](https://doi.org/10.1016/j.jallcom.2015.10.153)
28. Ishaque M, Khan MA, Ali I et al (2015) Investigations on structural, electrical and dielectric properties of yttrium substituted Mg-ferrites. *Ceram Int* 41(3):4028–4034. doi:[10.1016/j.ceramint.2014.11.093](https://doi.org/10.1016/j.ceramint.2014.11.093)
29. Anjum S, Hameed S, Bashir F (2015) Microstructural, structural, magnetic and optical properties of antimony doped cobalt spinel ferrites. *Mater Today Proc* 2(10):5329–5336. doi:[10.1016/j.matpr.2015.11.045](https://doi.org/10.1016/j.matpr.2015.11.045)
30. Cross WB, Affleck L, Kuznetsov MV et al (1999) Self-propagating high-temperature synthesis of ferrites  $MFe_2O_4$  ( $M = Mg, Ba, Co, Ni, Cu, Zn$ ): reactions in an external magnetic field. *J Mater Chem* 9:2545–2552. doi:[10.1039/A904431K](https://doi.org/10.1039/A904431K)
31. Peng E, Ding J, Xue JM (2014) Concentration-dependent magnetic hyperthermic response of manganese ferrite-loaded ultrasmall graphene oxide nanocomposites. *New J Chem* 38:2312–2319. doi:[10.1039/C3NJ01555F](https://doi.org/10.1039/C3NJ01555F)
32. Leal MP, Rivera-Fernández S, Franco JM et al (2015) Long-circulating PEGylated manganese ferrite nanoparticles for MRI-based molecular imaging. *Nanoscale* 7:2050–2059. doi:[10.1039/C4NR05781C](https://doi.org/10.1039/C4NR05781C)
33. Kaiser M (2016) Magnetic and electric modulus properties of In substituted Mg–Mn–Cu ferrites. *Mater Res Bull* 73:452–458. doi:[10.1016/j.materresbull.2015.09.015](https://doi.org/10.1016/j.materresbull.2015.09.015)
34. Kombaiah K, Vijaya JJ, Kennedy LJ, Bououdina M (2017) Optical, magnetic and structural properties of  $ZnFe_2O_4$  nanoparticles synthesized by conventional and microwave assisted combustion method: a comparative investigation. *Optik Int J Light Electron Optics* 129:57–68. doi:[10.1016/j.ijleo.2016.10.058](https://doi.org/10.1016/j.ijleo.2016.10.058)
35. Kurta SA, Mykytyn IM, Tatarchuk TR (2014) Structure and the catalysis mechanism of oxidative chlorination in nanostructural layers of a surface of alumina. *Nanoscale Res Lett* 9:357. doi:[10.1186/1556-276X-9-357](https://doi.org/10.1186/1556-276X-9-357)
36. Tatarchuk T (2014) Catalytic oxidation of carbon monoxide on lithium-zinc ferrites with a spinel structure. *Ekologia i Technika* 32(2):70–75
37. Tatarchuk TR, Boyko EV, Yaremij IP et al (2014) Synthesis crystal chemistry and antistructure modelling of  $CoFe_2O_4$  nanoparticles prepared by citrate sol-gel method. *Phys Chem Solid State* 15(4):792–797
38. Sickafus KE, Wills JM, Grimes NW (1999) Structure of spinel. *J Am Ceram Soc* 82:3279–3292. doi:[10.1111/j.1151-2916.1999.tb02241.x](https://doi.org/10.1111/j.1151-2916.1999.tb02241.x)
39. Kane SN, Satalkar M (2017) Correlation between magnetic properties and cationic distribution of  $Zn_{0.85-x}Ni_xMg_{0.05}Cu_{0.1}Fe_2O_4$  nanospinel ferrite: effect of Ni doping. *J Mater Sci* 52(6):3467–3477. doi:[10.1007/s10853-016-0636-7](https://doi.org/10.1007/s10853-016-0636-7)
40. Tatarchuk TR, Bououdina M, Paliychuk ND et al (2017) Structural characterization and antistructure modeling of cobalt-substituted zinc ferrites. *J Alloys Compd* 694(15):777–791. doi:[10.1016/j.jallcom.2016.10.067](https://doi.org/10.1016/j.jallcom.2016.10.067)
41. Angadi VJ, Choudhury L, Sadhana K et al (2017) Structural, electrical and magnetic properties of  $Sc^{3+}$  doped Mn-Zn ferrite nanoparticles. *J Magn Magn Mater* 424:1–11. doi:[10.1016/j.jmmm.2016.10.050](https://doi.org/10.1016/j.jmmm.2016.10.050)
42. Lemine OM, Bououdina M, Sajieddine M et al (2011) Synthesis, structural, magnetic and optical properties of nanocrystalline  $ZnFe_2O_4$ . *Physica B* 406(10):1989–1994. doi:[10.1016/j.physb.2011.02.072](https://doi.org/10.1016/j.physb.2011.02.072)
43. Al-Saie AM, Bououdina M, Jaffar A et al (2011) The effect of annealing on the structure, magnetic properties and AC heating of  $CoFe_2O_4$  for biomedical applications. *J Alloys Compd* 509:S393–S396. doi:[10.1016/j.jallcom.2011.02.024](https://doi.org/10.1016/j.jallcom.2011.02.024)
44. Sundararajan M, Sailaja V, Kennedy LJ, Vijaya JJ (2017) Photocatalytic degradation of rhodamine B under visible light using nanostructured zinc doped cobalt ferrite: kinetics and mechanism. *Ceram Int* 43(1A):540–548. doi:[10.1016/j.ceramint.2016.09.191](https://doi.org/10.1016/j.ceramint.2016.09.191)

45. Angadi VJ, Anupama AV, Choudhary HK et al (2017) Mechanism of  $\gamma$ -irradiation induced phase transformations in nanocrystalline  $Mn_{0.5}Zn_{0.5}Fe_2O_4$  ceramics. *J Solid State Chem* 246:119–124. doi:[10.1016/j.jssc.2016.11.017](https://doi.org/10.1016/j.jssc.2016.11.017)
46. Angadi VJ, Rudraswamy B, Sadhana K et al (2016) Structural and magnetic properties of manganese zinc ferrite nanoparticles prepared by solution combustion method using mixture of fuels. *J Magn Magn Mater* 409:111–115. doi:[10.1016/j.jmmm.2016.02.096](https://doi.org/10.1016/j.jmmm.2016.02.096)
47. Gawas SG, Meena SS, Yusuf SM et al (2016) Anisotropy and domain state dependent enhancement of single domain ferrimagnetism in cobalt substituted Ni–Zn ferrites. *New J Chem* 40:9275–9284. doi:[10.1039/C6NJ02121B](https://doi.org/10.1039/C6NJ02121B)
48. Singh SB, Srinivas C, Tirupanyam BV et al (2016) Structural, thermal and magnetic studies of  $Mg_xZn_{1-x}Fe_2O_4$  nanoferrites: study of exchange interactions on magnetic anisotropy. *Ceram Int* 42(16):19179–19186. doi:[10.1016/j.ceramint.2016.09.081](https://doi.org/10.1016/j.ceramint.2016.09.081)
49. Sundararajan M, Kennedy LJ, Vijaya JJ et al (2015) Microwave combustion synthesis of  $Co_{1-x}Zn_xFe_2O_4$  ( $0 \leq x \leq 0.5$ ): structural, magnetic, optical and vibrational spectroscopic studies. *Spectrochim. Acta Part A* 140:421–430. doi:[10.1016/j.saa.2014.12.035](https://doi.org/10.1016/j.saa.2014.12.035)
50. Manikandan A, Vijaya JJ, Mary JA et al (2014) Structural, optical and magnetic properties of  $Fe_3O_4$  nanoparticles prepared by a facile microwave combustion method. *J Ind Eng Chem* 20(4):2077–2085. doi:[10.1016/j.jiec.2013.09.035](https://doi.org/10.1016/j.jiec.2013.09.035)
51. Lemine OM, Omri K, Zhang B et al (2012) Sol–gel synthesis of 8 nm magnetite ( $Fe_3O_4$ ) nanoparticles and their magnetic properties. *Superlattice Microst* 52(4):793–799. doi:[10.1016/j.spmi.2012.07.009](https://doi.org/10.1016/j.spmi.2012.07.009)
52. Manikandan A, Kennedy LJ, Bououdina M et al (2014) Synthesis, optical and magnetic properties of pure and Co-doped  $ZnFe_2O_4$  nanoparticles by microwave combustion method. *J Magn Magn Mater* 349:249–258. doi:[10.1016/j.jmmm.2013.09.013](https://doi.org/10.1016/j.jmmm.2013.09.013)
53. Manikandan A, Vijaya JJ, Kennedy LJ et al (2013) Microwave combustion synthesis, structural, optical and magnetic properties of  $Zn_{1-x}Sr_xFe_2O_4$  nanoparticles. *Ceram Int* 39(5):5909–5917. doi:[10.1016/j.ceramint.2013.01.012](https://doi.org/10.1016/j.ceramint.2013.01.012)
54. Manikandan A, Vijaya JJ, Kennedy LJ et al (2013) Structural, optical and magnetic properties of  $Zn_{1-x}Cu_xFe_2O_4$  nanoparticles prepared by microwave combustion method. *J Mol Struct* 1035:332–340. doi:[10.1016/j.molstruc.2012.11.007](https://doi.org/10.1016/j.molstruc.2012.11.007)
55. Manikandan A, Vijaya JJ, Kennedy LJ (2013) Comparative study of pure and Ni-doped  $ZnFe_2O_4$  nanoparticles for structural, optical and magnetic properties. *Adv Mater Res* 699:524–529
56. Panchal S, Raghuvanshi S, Gehlot K et al (2016) Cationic distribution assisted tuning of magnetic properties of  $Li_{0.5-x/2}Zn_xFe_{2.5-x/2}O_4$ . *AIP Adv* 6(5):055930. doi:[10.1063/1.4944517](https://doi.org/10.1063/1.4944517)
57. Khalaf KAM, Al-Rawas AD, Widatallah HM et al (2016) Influence of  $Zn^{2+}$  ions on the structural and electrical properties of  $Mg_{1-x}Zn_xFeCrO_4$  spinels. *J Alloys Compd* 657:733–747. doi:[10.1016/j.jallcom.2015.10.157](https://doi.org/10.1016/j.jallcom.2015.10.157)
58. Hashim M, Shirsath SE, Meena SS et al (2015) Manganese ferrite prepared using reverse micelle process: structural and magnetic properties characterization. *J Alloys Compd* 642:70–77. doi:[10.1016/j.jallcom.2015.04.085](https://doi.org/10.1016/j.jallcom.2015.04.085)
59. Heiba ZK, Mohamed MB, Ahmed MA et al (2014) Cation distribution and dielectric properties of nanocrystalline gallium substituted nickel ferrite. *J Alloys Compd* 586:773–781. doi:[10.1016/j.jallcom.2013.10.137](https://doi.org/10.1016/j.jallcom.2013.10.137)
60. Hemedi OM, Mostafa NY, Abd Elkader OH et al (2014) Solubility limits in Mn–Mg ferrites system under hydrothermal conditions. *J Magn Magn Mater* 364:39–46. doi:[10.1016/j.jmmm.2014.03.061](https://doi.org/10.1016/j.jmmm.2014.03.061)
61. Manikandan A, Vijaya JJ, Sundararajan M et al (2013) Optical and magnetic properties of Mg-doped  $ZnFe_2O_4$  nanoparticles prepared by rapid microwave combustion method. *Superlattice Microst* 64:118–131. doi:[10.1016/j.spmi.2013.09.021](https://doi.org/10.1016/j.spmi.2013.09.021)
62. Tanaka T, Shimazu R, Nagai H et al (2009) Preparation of spherical and uniform-sized ferrite nanoparticles with diameters between 50 and 150 nm for biomedical applications. *J Magn Magn Mater* 321:1417–1420

63. Jasso-Terán RA, Cortés-Hernández DA, Sánchez-Fuentes HJ et al (2017) Synthesis, characterization and hemolysis studies of  $Zn_{(1-x)}Ca_xFe_2O_4$  ferrites synthesized by sol-gel for hyperthermia treatment applications. *J Magn Magn Mater*. doi:[10.1016/j.jmmm.2016.10.099](https://doi.org/10.1016/j.jmmm.2016.10.099) (in press)
64. Ruthradevi T, Akbar J, Kumar GS et al (2017) Investigations on nickel ferrite embedded calcium phosphate nanoparticles for biomedical applications. *J Alloys Compd* 695:3211–3219. doi:[10.1016/j.jallcom.2016.11.300](https://doi.org/10.1016/j.jallcom.2016.11.300)
65. Latorre-Esteves M, Cortés A, Torres-Lugo M et al (2009) Synthesis and characterization of carboxymethyl dextran-coated Mn/Zn ferrite for biomedical applications. *J Magn Magn Mater* 321:3061–3066
66. Falsafi F, Hashemi B, Mirzaei A et al (2017) Sm-doped cobalt ferrite nanoparticles: a novel sensing material for conductometric hydrogen leak sensor. *Ceram Int* 43:1029–1037. doi:[10.1016/j.ceramint.2016.10.035](https://doi.org/10.1016/j.ceramint.2016.10.035)
67. Sandu I, Presmanes L, Alphonse P et al (2006) Nanostructured cobalt manganese ferrite thin films for gas sensor application. *Thin Solid Films* 495:130–133
68. Wen T, Zhu W, Xue C et al (2014) Novel electrochemical sensing platform based on magnetic field-induced self-assembly of  $Fe_3O_4$ @Polyaniline nanoparticles for clinical detection of creatinine. *Biosens Bioelectron* 56:180–185
69. Praveena K, Chen H-W, Liu H-L et al (2016) Enhanced magnetic domain relaxation frequency and low power losses in  $Zn^{2+}$  substituted manganese ferrites potential for high frequency applications. *J Magn Magn Mater* 420:129–142
70. Li B, Yue Z-X, Qi X-W et al (2003) High Mn content NiCuZn ferrite for multiplayer chip inductor application. *Mater Sci Eng B* 99:252–254
71. Yang Q, Zhang H, Liu Y et al (2009) Microstructure and magnetic properties of microwave sintered M-type barium ferrite, for application in LTCC devices. *Mater Lett* 63:406–408
72. Reddy NR, Ramana MV, Rajitha G et al (2009) Stress insensitive NiCuZn ferrite compositions for microinductor applications. *Curr Appl Phys* 9:317–323
73. Kumbhar VS, Jagadale AD, Shinde NM et al (2012) Chemical synthesis of spinel cobalt ferrite ( $CoFe_2O_4$ ) nano-flakes for supercapacitor application. *Appl Surf Sci* 259:39–43
74. Bashir B, Shaheen W, Asghar M et al (2016) Copper doped manganese ferrites nanoparticles anchored on graphene nano-sheets for high performance energy storage applications. *J Alloys Compd* 695:881–887. doi:[10.1016/j.jallcom.2016.10.183](https://doi.org/10.1016/j.jallcom.2016.10.183)
75. Bindu K, Sridharan K, Ajith KM et al (2016) Microwave assisted growth of stannous ferrite microcubes as electrodes for potentiometric nonenzymatic  $H_2O_2$  sensor and supercapacitor applications. *Electrochim Acta* 217:139–149
76. Charalampos AS, Litsardakis G (2016) Y-type hexagonal ferrites for microwave absorber and antenna applications. *J Magn Magn Mater* 405:54–61
77. Dadfar MR, Ebrahimi SAS, Masoudpanah SM (2015) Sol-gel synthesis and characterization of  $SrFe_{12}O_{19}/TiO_2$  nanocomposites. *J Supercond Nov Magn* 28(1):89–94
78. Meng P, Xiong K, Ju K (2015) Wideband and enhanced microwave absorption performance of doped barium ferrite. *J Magn Magn Mater* 385:407–411
79. Zhang X-J, Wang G-S, Cao W-Q et al (2014) Enhanced microwave absorption property of reduced graphene oxide (RGO)- $MnFe_2O_4$  nanocomposites and polyvinylidene fluoride. *ACS Appl Mater Interfaces* 6:7471–7478
80. Chang S, Kangning S, Pengfei C (2012) Microwave absorption properties of Ce-substituted M-type barium ferrite. *J Magn Magn Mater* 324(5):802–805
81. Tyagi S, Baskey HB, Agarwala RC et al (2011) Development of hard/soft ferrite nanocomposite for enhanced microwave absorption. *Ceram Int* 37(7):2631–2641
82. Casbeer E, Sharma VK, Li X-Z (2012) Synthesis and photocatalytic activity of ferrites under visible light: a review. *Sep Purif Technol* 87:1–14
83. Valero-Luna C, Palomares-Sánchez SA, Ruíz F (2016) Catalytic activity of the barium hexaferrite with  $H_2O_2$ /visible light irradiation for degradation of methylene blue. *Catal Today* 266:110–119. doi:[10.1016/j.cattod.2015.08.049](https://doi.org/10.1016/j.cattod.2015.08.049)

# Chapter 23

## Study of MAX Phase-Based Compacts Obtained by Shock-Wave Loading Method

Larysa Sudnik, Aleksey Luchenok, Yuliya Kaladkevich, Victor Tkachuk, Tatiana Prikhna, and Artem Kozyrev

### 23.1 Introduction

Interest to the MAX phases (ternary compounds with general formula  $M_{n+1}AX_n$ , where M is early-transition metal, A is element of A group, X is carbon or nitrogen) [1] is determined by combining the properties of metal and ceramic, what makes these materials promising for use in mechanical engineering, energetic, and aviation industry [2]. MAX phases have both metallic and ceramic properties due to their nanolaminate structure of elementary crystal lattice, where layers of octahedral  $M_6X$  are alternate with atoms of A element. In results, MAX phases have low density, high heat resistance, resistance to oxidation, high thermal and electrical conductivity, and the toughness at high temperature [3, 4].

Nonporous material with high volume of MAX phase may be obtained by compacting MAX phase powder by shock-wave loading method.

Shock-wave loading method is impact of explosion energy on materials through any obstacle. Traditional technique of explosive compression is based on shock-wave loading of prepared samples by planar or cylindrical configuration. The mechanism of this method is activation of the powder grains and subsequently milling them during the loading. This increases the crystal lattice defects, the surface area of the powder, and the area of contact between the grains. All these lead to the activation of the sintering of material [5].

In this paper, we evaluated the possibility of using this technique for compacting powders of the MAX phases  $Ti_2AlC$  and  $Ti_3AlC_2$ .

---

L. Sudnik • A. Luchenok • Y. Kaladkevich (✉) • V. Tkachuk  
Research Institut of Pulse Processes with Pilot Plant, Minsk, Belarus  
e-mail: [juliakolodkevich@gmail.com](mailto:juliakolodkevich@gmail.com)

T. Prikhna • A. Kozyrev  
Institut for Superhard Materials NAS of Ukraine, Kyiv, Ukraine

## 23.2 Methodology of the Experiments

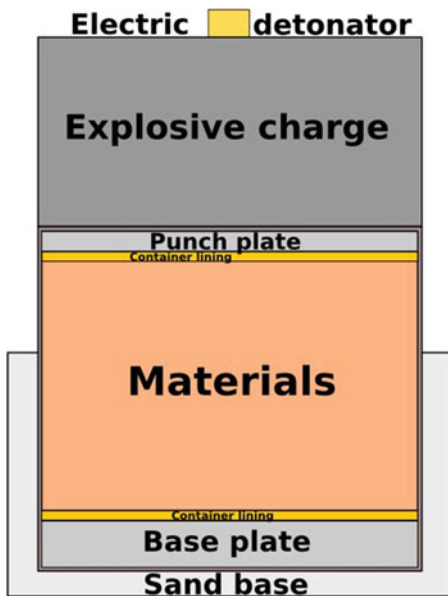
MAX phase-based materials of Ti-Al-C system were synthesized at the Institute for Superhard Materials from mixture of the powders TiC/TiH<sub>2</sub>/Al in ratio 2/2/1.25 for Ti<sub>2</sub>AlC and 2/1/1.25 for Ti<sub>3</sub>AlC<sub>2</sub>. Excessive amounts of aluminum were 25%, because Al evaporates at high temperature. All samples were obtained by free sintering method in vacuum at 1350 °C and different duration of the synthesis process. Ti<sub>2</sub>AlC and Ti<sub>3</sub>AlC<sub>2</sub> powders were carried out on a planar configuration (Fig. 23.1) by using a pulse industrial explosive.

The process of compacting involves three steps. At first, the powder is dried and homogenized. Then material is placed in shaping elements in the container between plates of base and punch (steel sheets 2 and 8 mm). This equipment is placed on sand base, explosive charge is set on top (ammonite 6GV), height of charge is 32 mm, and weight is 4 kg. After charge, detonation compressing the material by a shock wave occurs. Parameters of loading were detonation velocity  $D = 4 \times 10^3$  m/s and pressure  $p = 2.5\text{--}3.5$  GPa. Obtained compacts were treated at 950 °C for 90 min.

Phase composition of compacts was analyzed by X-ray (CuK<sub>α</sub> emitting in the range of angles  $2\Theta$  18–88°). Data processing was carried out using full-profile Rietveld method. Measurement error for this system was 3%.

Density and porosity of the samples were determined by hydrostatic weighing method. Calculation was carried out based on the results of quantitative X-ray analysis. In calculating, such values of theoretical density were used: Ti<sub>2</sub>AlC, 4.10 g/cm<sup>3</sup>; Ti<sub>3</sub>AlC<sub>2</sub>, 4.24 g/cm<sup>3</sup>; TiC, 4.93 g/cm<sup>3</sup>; and Al<sub>2</sub>O<sub>3</sub>, 3.98 g/cm<sup>3</sup>.

**Fig. 23.1** Scheme of the shock-wave compression (planar configuration)



Microhardness measurements were carried out using a Vickers indenter on PMT-3 at loading 1.96 N (200 g).

Microhardness was calculated by Eq. (23.1):

$$H\mu = \frac{1854 * P}{C^2} * 10 \quad (23.1)$$

where:

$H\mu$  is microhardness, MPa.

$P$  is loading on indenter, g.

$C$  is indentation diagonal,  $\mu\text{m}$ .

Microhardness was measured on the surface, which was in contact with the base plate.

### 23.3 Experimental Data and Discussion of the Results

Six compacts of MAX phase of the system Ti-Al-C were obtained by compacting the powders during shock-wave loading. Two of them were  $\text{Ti}_2\text{AlC}$ , and four were  $\text{Ti}_3\text{AlC}_2$ . The samples were flat cylinders, with a diameter of 30 mm and a height of 5 mm (Fig. 23.2). One of the tasks of the study was to obtain compacts with high volume of MAX phase. Comparative analysis of phase composition of materials before and after compacting was carried out. Results of X-ray analysis are shown in Table 23.1.

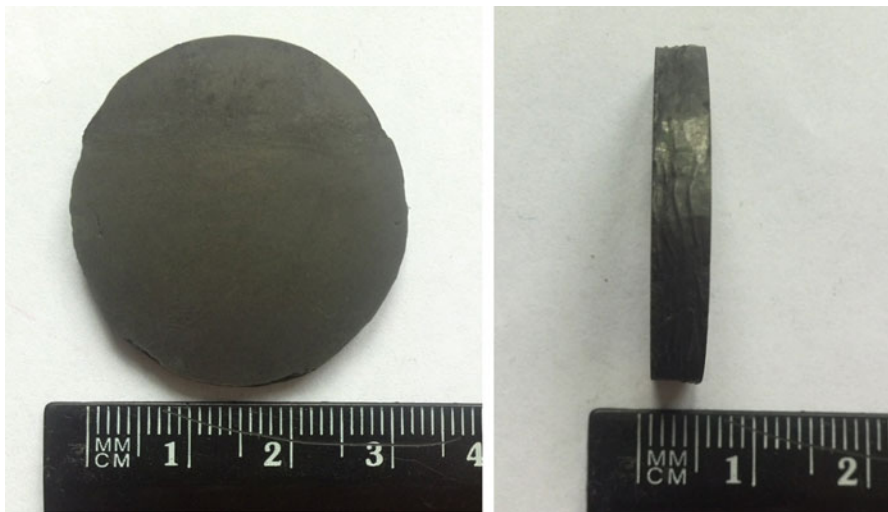


Fig. 23.2 Compacts of MAX phases after shock-wave loading



**Table 23.1** Characteristics of the materials before and after compacting

Sample	MAX phase formula	Time of synthesis, min	Stage of compacting	The phase composition, wt.%				
				Ti <sub>2</sub> AlC	Ti <sub>3</sub> AlC <sub>2</sub>	TiC	Al <sub>2</sub> O <sub>3</sub>	Impurities
1	Ti <sub>2</sub> AlC	30	Before	86	–	11	–	(Ti <sub>4</sub> N <sub>3</sub> ) 3
			After	97	–	3	–	–
2	Ti <sub>2</sub> AlC	120	Before	97	–	3	–	–
			After	96	–	4	–	–
3	Ti <sub>3</sub> AlC <sub>2</sub>	30	Before	–	98	2	–	–
			After	17	79	3	1	–
4	Ti <sub>3</sub> AlC <sub>2</sub>	30	Before	–	94	6	–	–
			After	–	92	6	2	–
5	Ti <sub>3</sub> AlC <sub>2</sub>	30	Before	–	96	4	–	–
			After	–	90	6	4	–
6	Ti <sub>3</sub> AlC <sub>2</sub>	180	Before	–	64	36	–	–
			After	3	54	43	–	–

High amount of Ti<sub>2</sub>AlC was found in samples 1 and 2. In sample 1, during compacting, the amount of MAX phase increases from 86 to 97 wt.%, and the amount of titanium carbide decreases from 11 to 3 wt.%. In sample 2, changes of phase composition were in the range of 1%. Impurities of Ti<sub>4</sub>N<sub>3</sub> are present in sample 1 due to the presence of impurities in starting materials.

In samples 3, 4, and 5, before compacting, content of Ti<sub>3</sub>AlC<sub>2</sub> was in the range 90–98 wt.%. In sample 6, content of Ti<sub>3</sub>AlC<sub>2</sub> was 64 wt.%. It may be due to the synthesis conditions (synthesis time was 180 min for sample 6, whereas synthesis time for samples 3, 4, and 5 was only 30 min). During loading, decrease in amount of MAX phase occurred. In samples 4 and 5, change of content was 2–6 wt.%. But in sample 3, content of Ti<sub>3</sub>AlC<sub>2</sub> was decreased from 98 to 79 wt.%. 17 wt.% Ti<sub>2</sub>AlC was observed in this sample after compacting. The observed phenomenon is probably due to the use of different titanium carbide as starting powder.

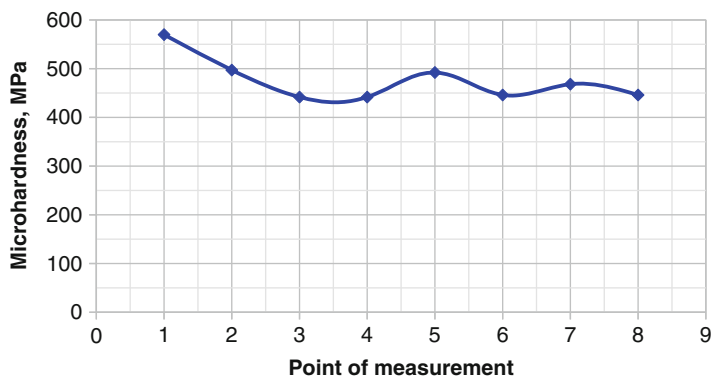
Samples 1 and 3 were compacted from powders with carbon-deficient titanium carbide. The material has a high content of MAX phase, but demonstrates low stability of phase composition. Activation of powder grains during shock-wave loading leads to rearrangement of the atoms in the crystal lattice, achieving equilibrium composition. In the case of sample 1, this phenomenon has positive effect and is accompanied by an increase of amount of Ti<sub>2</sub>AlC phase of 11 wt.%. In sample 3, on the contrary, it leads to a decreased amount of phase Ti<sub>3</sub>AlC<sub>2</sub> due to the decomposition. Results of investigation of phase composition, density, porosity, and microhardness of obtained compacts are shown in Table 23.2.

Analysis of the density and porosity of the compacts showed that theoretical density has not been achieved. Densities of samples 1 and 2 were 3.36 and 3.40 g/cm<sup>3</sup>, respectively, but theoretical density for Ti<sub>2</sub>AlC is 4.10 g/cm<sup>3</sup>. Thus, porosity of samples 1 and 2 was about 18%. Densities for samples 3, 4, and 5 was



**Table 23.2** Characteristics of MAX phase compacts

Sample	Ti <sub>2</sub> AlC	Ti <sub>3</sub> AlC <sub>2</sub>	TiC	Al <sub>2</sub> O <sub>3</sub>	$\gamma$ , g/cm <sup>3</sup>	$\Pi$ , %	H $\mu$ , MPa
1	97	–	3	–	3.36	18.4	547
2	96	–	4	–	3.40	17.6	605
3	17	79	3	1	3.67	13.3	619
4	–	92	6	2	3.70	13.3	605
5	–	90	6	4	3.67	13.6	456
6	3	54	43	–	3.59	18.7	690

**Fig. 23.3** Change microhardness over the surface (sample 5)

in the range from 3.67 to 3.70 g/cm<sup>3</sup>, whereas theoretical density for Ti<sub>3</sub>AlC<sub>2</sub> is 4.24 g/cm<sup>3</sup>. Porosity of these three samples is less than samples 1 and 2 and was 13.3–13.6%.

Thus, we can say that a relatively effective compression is observed only for materials based on Ti<sub>3</sub>AlC<sub>2</sub>. The exception was sample 6, where porosity was 18.7%. Probably this phenomenon is a consequence of significant amount of titanium carbide. It increases during compacting due to decomposition of Ti<sub>3</sub>AlC<sub>2</sub>.

All samples were characterized by approximately the same mean values of microhardness, which were low than literature data. Microhardness of compacts was in the range from 450 to 690 MPa. It was observed that when compared to microhardness, values were different between maximum and minimum values for samples 1, 3, and 6 (45, 55, and 40%, respectively). Sample 5 was characterized with most uniform distribution of microhardness over surface (Fig. 23.3). The difference between maximum and minimum values was 23% (442–570 MPa).

Also, it was noted that samples with porosity ~18% (samples 1, 2, and 6) have uneven distribution of microhardness over surface. MAX phase structural type 211 prevails in samples 1 and 2 (97 and 96 wt.%, respectively). In sample 6, significant amount of titanium carbide (almost 43 wt.%) were present, but this did not caused increase of microhardness in relatively other samples.

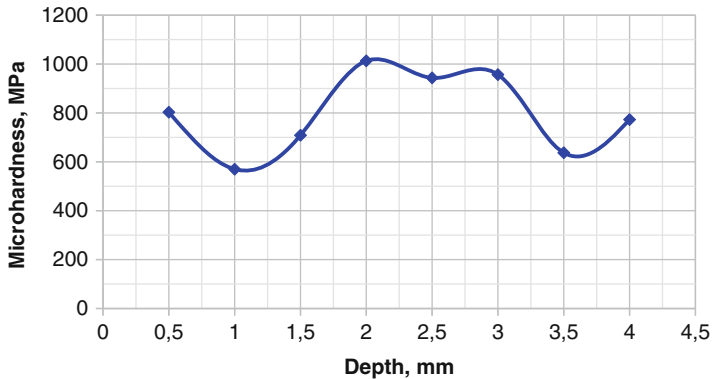


Fig. 23.4 Change microhardness over the depth (sample 4)

The depth distribution of microhardness at loading 200 g for sample 4 is shown in Fig. 23.4. Measuring was carried out in eight points with steps 0.5 mm and depth 4 mm. The average microhardness value was 801 MPa.

## 23.4 Conclusion

As can be seen, the method of the shock-wave loading can be used for compacting materials based on Ti-Al-C system MAX phases. Study of phase composition of materials showed that destruction of MAX phase during loading doesn't occur. However, ratio of titanium and carbon play important role in starting powder of titanium carbide. Deficient in carbon during loading, occurs formation phase  $Ti_2AlC$  as the closer on stoichiometry in the case of material synthesis from titanium carbide.

A relatively effective compression was achieved only to materials based on phase structural type 312. However, this consolidation was uneven. Harder area was in the depth of the sample, whereas the layer near the surface was characterized by high porosity.

Powder of  $Ti_2AlC$  at the same conditions of compacting was compressed worse, and obtained materials have strong homogeneity. Probably it was due to the insufficient pressure and short time of shock-wave action on compacted materials.

## References

1. Barsoum W (2000) The  $M_{n+1}AX_n$ : a new class of solids; thermodynamically stable nanolaminates. *Prog in Solid State Chem* 28:201–281
2. Anirudh C, Vaibhav Koushik AV, Kempaiah UN (2014) MAX phase materials - Review of an exciting class of ternary carbides and nitrides. *IJETAE* 4(8):624–628

3. Prikhna T, Starostina A, Basyuk T et al (2014) Studies of the oxidation stability, mechanical characteristics of materials based on MAX phases of the Ti–Al–(C, N) systems, and of the possibility of their use as tool bonds and materials for polishing. *Journal of Superhard Materials* 1:3–14
4. Prikhna T, Ostash O, Basyuk T, Ivasyshyn A, Sverdun V, Loshak M, Dub S, Podgurska V, Moshchil V (2015) Cabioc'h T., Chartier P., Karpets M., Kovylaev V., Starostina O., Kozyrev a. Thermal stability and mechanical characteristics of densified Ti<sub>3</sub>AlC<sub>2</sub>-based material. *Solid State Phenom* 230:140–143
5. Khasanov O, Dvilis E, Bikbaeva Z (2008) *Methods of compaction and consolidation of nanostructured materials and products*. Tomsk. 212 p. (in russian)

# Chapter 24

## Standard Si Photovoltaic Devices Improved by ZnO Film Obtained by Pulsed Laser Deposition

G. Wisz, I. Virt, P. Sagan, I. Hatala, Ł. Głowa, M. Kaczor, and R. Yavorskyi

### Abbreviations

CVD	Chemical vapor deposition
ITO	Indium tin oxide
PLD	Pulsed laser deposition
PV	Photovoltaic cell
PVD	Physical vapor deposition
SEM	Scanning electron microscope
TCO	Transparent conducting oxide

---

**Authors' Contributions** GW has grown thin films, has performed and determined the problem, and has defined the methods and subjects of investigation. IV characterizes measurement and data analysis as well as SEM cross-sectional images. PS has obtained SEM. IH performed the experimental works and analyzed the results. ŁG, MK, and RY carried out the experiments and drafted the manuscript. All authors have read and approved the final version of the manuscript.

**Authors' Information** GW is a Doctor of Physical Sciences and President of the Board of Subcarpathian Renewable Energy Cluster, University of Rzeszow, Rzeszow, Poland. IV is a Professor of Physical Sciences, Laboratory Research and Environmental Monitoring, University of Rzeszow, Rzeszow, Poland, and a Professor of Engineering and Technology Fundamentals Department, Drohobych State University, Drohobych, Ukraine. PS is a Doctor of Physical Sciences, Laboratory Research and Environmental Monitoring, University of Rzeszow, Rzeszow, Poland. IH is a Master of Physical Sciences, University of Rzeszow, Rzeszow, Poland. ŁG is a physics student at the University of Rzeszow, Rzeszow, Poland. MK is a physics student at the University of Rzeszow, Rzeszow, Poland. RY is a Master of Physical Sciences, University of Rzeszow, Rzeszow, Poland, and a PhD student at the Physics and Chemistry of Solid State Department, Vasyl Stefanyk Precarpathian National University, Ivano-Frankivsk, Ukraine.

G. Wisz (✉) • P. Sagan • I. Hatala • Ł. Głowa • M. Kaczor  
Faculty of Mathematics and Natural Sciences, University of Rzeszow, 1 Pigonia Str.,  
35-959 Rzeszow, Poland  
e-mail: [gwisz@ur.edu.pl](mailto:gwisz@ur.edu.pl)

## 24.1 Introduction

Photovoltaics is intensively developed as an alternative renewable energy source and may replace conventional energy sources based on fossil fuels in the nearest future [1–3]. For further development and worldwide market growth of photovoltaic power generation, a cost reduction of the PV systems is one of the major issues [4, 5]. Among the approaches followed in thin film photovoltaics, solar cells based on hydrogenated amorphous (*a-Si:H*) or microcrystalline (*pc-Si:H*) silicon offer specific advantages. Earlier and recent studies indicate a substantial cost reduction potential [6] compared to the conventional crystalline silicon wafer technology. The low material costs and proven manufacturability of *a-Si:H* solar modules make them ideally suited for low-cost application on large scale. An integral part of these devices are the transparent conductive oxide (TCO) layers used as a front electrode and as part of the back side reflector. When applied at the front side, the TCO has to possess a high transparency in the spectral region, where the solar cell is operating, a high electrical conductivity, and a surface structure, which leads to sufficient scattering of the incoming light into the silicon absorber layer [7]. The scattering at interfaces between neighboring layers with different refractive indices and subsequent trapping of the incident light within the silicon absorber is crucial for all thin film silicon solar cells to gain high efficiency. For amorphous or microcrystalline cells, light scattering is usually achieved by nanotexturing the front TCO electrodes (with a typical root mean square surface roughness of 40–150 nm) and/or nanotextured back reflectors. In the ideal case, these rough layers can introduce nearly completely diffuse transmission or reflection of light, leading to very effective light trapping. TCO is also used between silicon and the metallic contact as a part of the back reflector to improve its optical properties and to act as a diffusion barrier [8]. Furthermore, applied in *a-Si:H/pc-Si:H* “micromorph” tandem solar cells, TCO can be used as an intermediate reflector between top and bottom cell to increase the current in the thin amorphous silicon top cell [6, 8, 9]. As a result the thickness of the *a-Si:H* top cell can be decreased to improve the stability of the cell against light-induced degradation. Finally, nano-rough TCO front contacts act as an efficient antireflection coating due to the refractive index grading at the rough

---

I. Virt

Faculty of Mathematics and Natural Sciences, University of Rzeszow, 1 Pignonia Str.,  
35-959 Rzeszow, Poland

Drohobych State University, I. Franko 24, 82-100 Drohobych, Ukraine

R. Yavorskyi

Faculty of Mathematics and Natural Sciences, University of Rzeszow, 1 Pignonia Str.,  
35-959 Rzeszow, Poland

Vasyl Stefanyk PreCarpathian National University, T. Shevchenko 57, 76-018 Ivano-Frankivsk,  
Ukraine

TCO/*Si* interface. In summary, TCOs play an important role in thin film silicon solar cell structure and have a decisive influence on the efficiencies presently achievable in state-of-the art amorphous, microcrystalline, or micromorph solar cells [10].

Basic types of photovoltaic cells, such as crystalline, microcrystalline, and amorphous silicon based [11], were already examined and optimized in many aspects. At the same time, a necessity appears to search for new solutions to rising efficiency of solar cells. One of the most promising directions for optimization of the cells is the surface texturization. The Bragg reflection is connected with planar, untexturized surface, which restricts penetration of photons into *p-n* junction. Vice versa, the texturization provides trapping the solar light inside the cell structure, catching the photons, and, as a result, increasing the conversion of solar energy.

Zinc oxide is a wide-bandgap semiconductor of the II–VI semiconductor groups with *n*-type conductivity. It is considered as one of the best materials as a texture on silicon cells [12, 13], due to its chemical and thermal stability, large exciton binding energy (60 meV), and large bandgap energy at room temperature of about 3.37 eV [14, 15]. The most used methods for obtaining thin films of zinc oxide are chemical vapor deposition (CVD) or physical vapor deposition (PVD) [16, 17].

In present work pulsed laser deposition (PLD) method was used to improve the standard *Si* photovoltaic devices by *ZnO* thin films due to wide variation of technological capabilities [18].

## 24.2 Experimental

The modular platform of PREVAC company was used for deposition of thin films of zinc oxide (Fig. 24.1). There are five main components of the platform: (1) processing chamber PVD, (2) processing chamber PLD, (3) distribution chamber (UFO) connected with sluice to contain the samples and deliver them to PLD and PVD chambers, (4) sluice chamber, and (5) storing chamber. From the beginning of the experiment, the samples were cut and fitted to sample holder. Then, substrate was cleaned and degreased physically and chemically to improve adhesive parameters of samples and to avoid falling apart the deposited films. Each sample was placed in holder disposed in load sluice. Finally, the appropriate experiment conditions (laser power and temperature of substrate) were set on the control panel. The process of thin *ZnO* film growth on silicon substrate and ITO/glass is realized by PLD method.

The most important factors influencing the properties of thin films obtained by PLD technique are temperature of substrate, power of laser, and time of deposition. Zinc oxide thin films were grown at various substrate temperatures  $T_s$  in the range between 25 and 300 °C using pulse laser YAG:Nd<sup>3+</sup> of 532 nm wavelength (second harmonics) with impulse time of 6 ns and fluence of 16 J/cm<sup>2</sup>. The laser beam was focused on the pressed *ZnO* powder target using a quartz lens with focal distance of 600 mm. The pressure in the processing chamber was about 10<sup>-8</sup> mbar. The technological parameters of obtained samples are presented in Table 24.1.



**Fig. 24.1** The modular platform for thin film deposition

**Table 24.1** Technological parameters of manufactured samples

Sample	Sample code	Vacuum $p$ , mbar	Fluence, $J/cm^2$	Substrate	Substrate temperature $T_p$ , °C	Time of manufacturing $t$ , min
P1	16-01-26	$1.29 \cdot 10^{-8}$	11	Si	25	20
P2 PLD-200A	16-02-01	$1.16 \cdot 10^{-8}$	11	Si	200	20
P3 PLD- 200B	16-03-10	$1.16 \cdot 10^{-8}$	16	Si	200	20
P4 PLD-300	16-03-15	$1.16 \cdot 10^{-8}$	16	Si	300	20

Structural parameters and cross section of samples were characterized by scanning electron microscopy (SEM) Vega3 Tescan. The cross-sectional study was carried out on the structures with the substrate temperature of 200 and 300 °C.

To measure current-voltage characteristic (CVC) of cell, each sample was connected by soldering with silver wires. Samples were soldered by standard soldering station. Characterization of samples was made using solar simulator at standard conditions. CVC measurements were carried out in dark and light conditions. Illumination was obtained using halogen lamp with power density of  $850 W/m^2$ .

## 24.3 Results

### 24.3.1 Morphology

Figure 24.2 shows SEM images of surface of  $ZnO/Si$  structure. Sample P1 (Fig. 24.2a) was deposited on the silicon substrate at 25 °C, and its surface had been modified into pyramid-like surface. It is observed that condensation of  $ZnO$  layers has got the biggest intensity on the tops of pyramids. For sample P2 (Fig. 24.2b) obtained at 200 °C, we can see the homogenous structure with a small amount of spherical precipitates. There are a few precipitates with a size of 400 nm on the surface. It is interesting to note the presence of nanowire-like element with a diameter of 150 nm and length of 500 nm (Fig. 24.2c). For sample P3 (Fig. 24.2d),

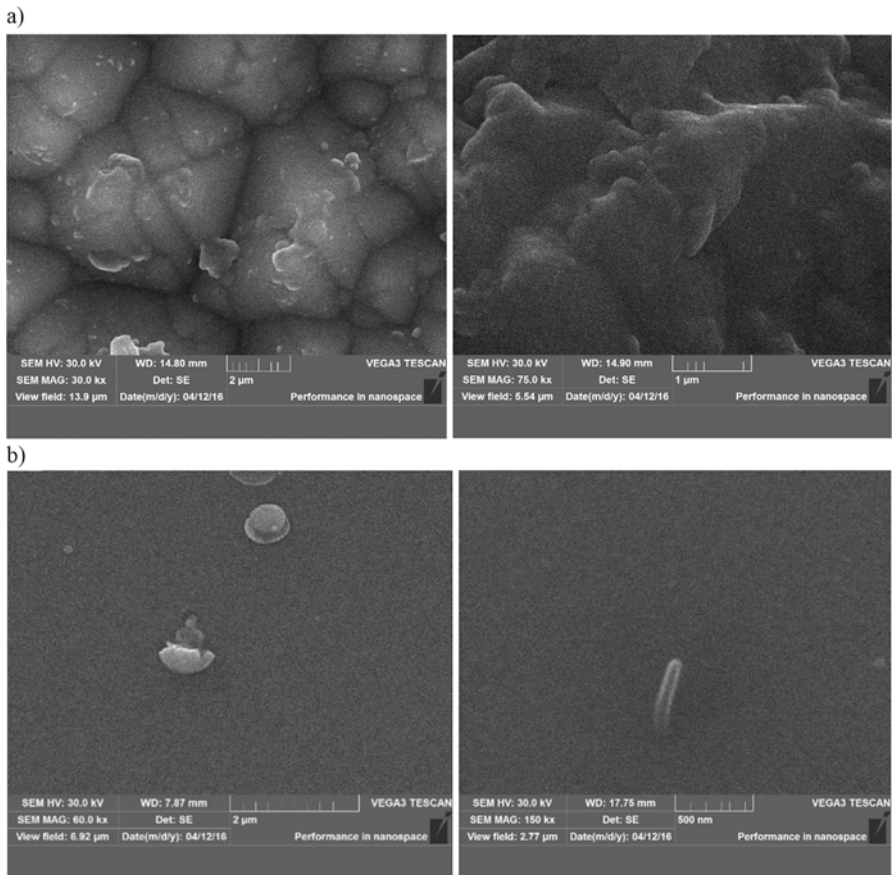
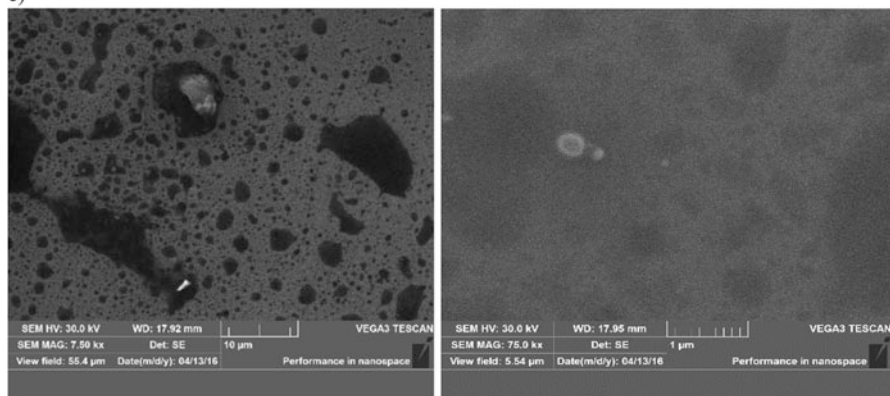


**Fig. 24.2** Morphology of  $ZnO/Si$  thin films for samples: (a) P1 PLD, (b) and (c) P2 PLD-200A, (d) P3 PLD-200B, and (e) P4 PLD-300



c)



d)

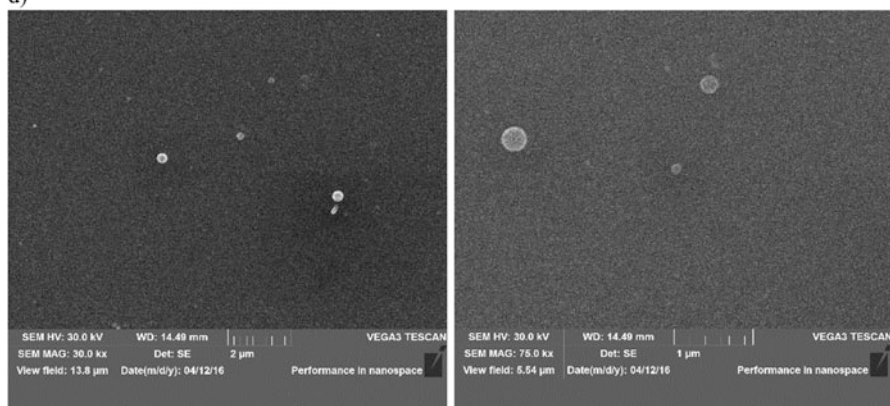


**Fig. 24.2** (continued)

the increase of fluence from 11 to 16 J/cm<sup>2</sup> leads to a big amount of defects with irregular shapes. Sample P4 (Fig. 24.2d) is characterized by regular surface with a small amount of spherical precipitates, with a size up to 250 nm. It can be concluded that increasing the substrate temperature significantly affects the surface structure, reducing the number of defects and making the surface more uniform.

On cross-sectional morphology of sample P3 (Fig. 24.3), we observed the condensed film in planar mode. It has the layered structure with clearly visible phase boundaries. Interlayers located closer to the substrate are characterized by bigger amount of defects. For sample P4 (Fig. 24.4), columnar type of growth oriented in *c* direction of hexagonal structure of wurtzite is noticed. In this case, type of growth is oriented by temperature of the substrate.

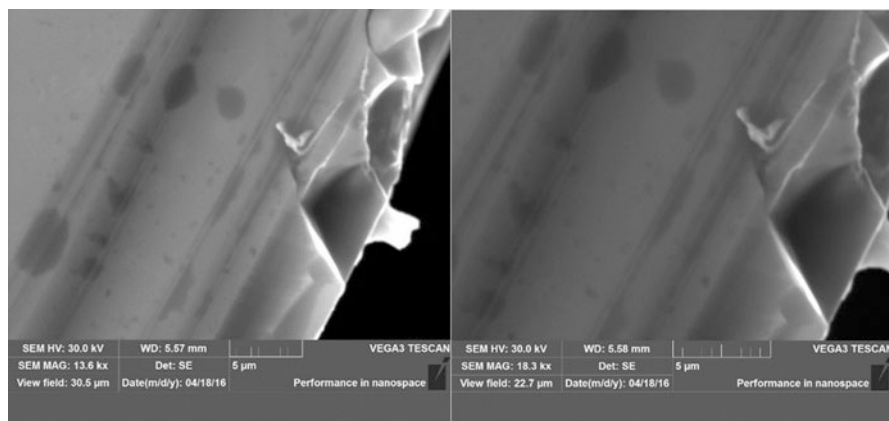


Fig. 24.3 Cross-sectional morphology of P2 PLD-200A sample

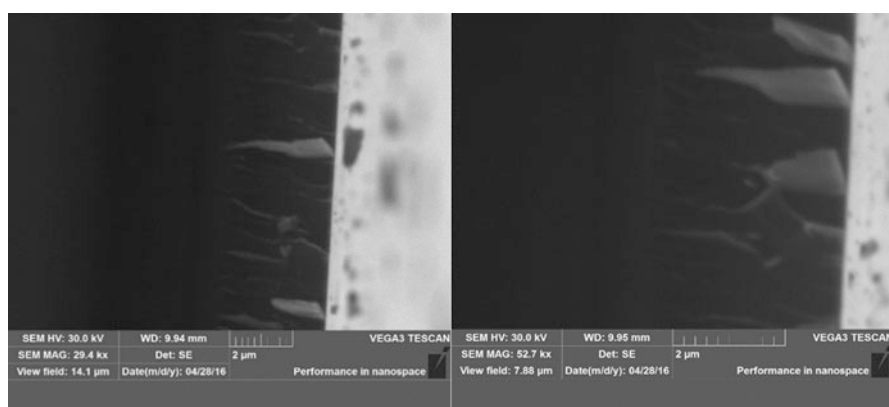
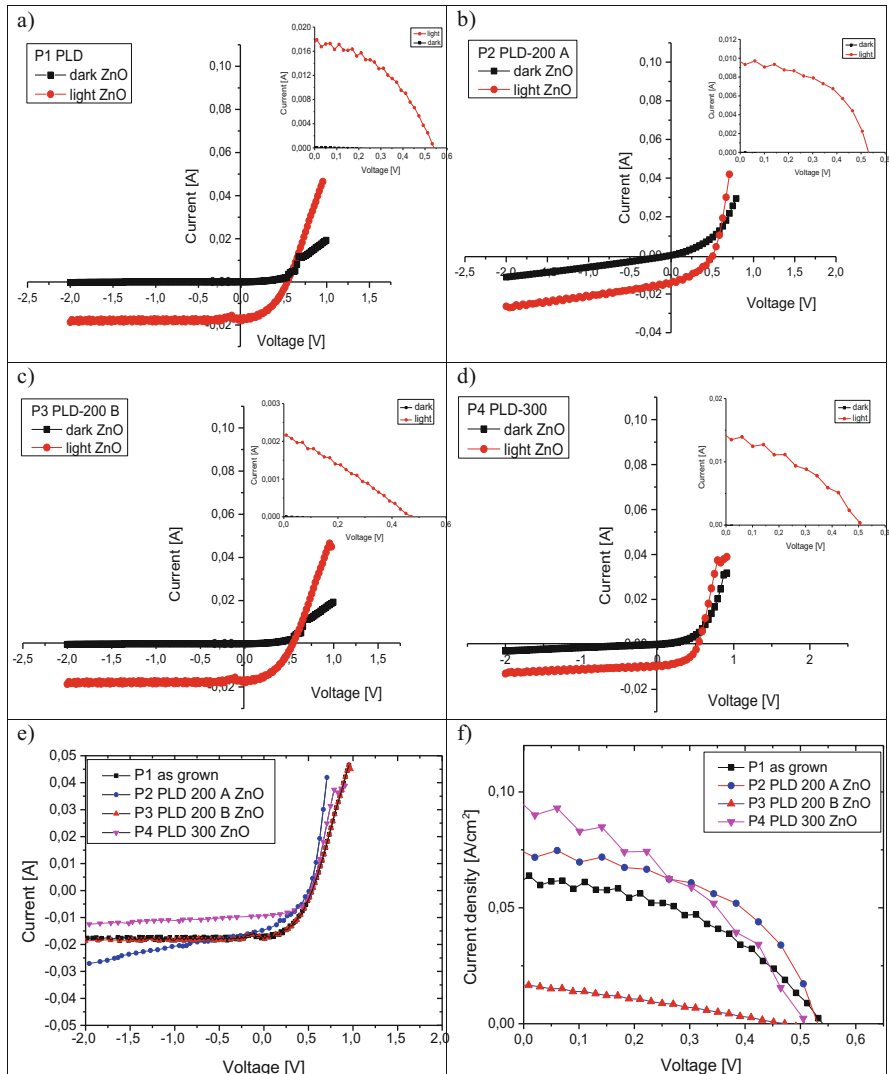


Fig. 24.4 Cross-sectional morphology of P4 PLD-300 sample with two magnifications

### 24.3.2 Current-Voltage Characteristics

Figure 24.5 shows current-voltage characteristics for the  $ZnO/Si$  samples measured under the illumination of  $850 \text{ W/m}^2$ . In the case of sample P1, we observed classical plot for light conditions. For the P2 sample with  $ZnO$  film deposited in temperature  $200 \text{ }^\circ\text{C}$ , the change of characteristics is observed. It is noticed that current increases rapidly in reverse bias. What is more, in the forward bias, change of the current is also visible. Intensity of current through the junction at light conditions increases much rapidly than intensity of current in the junction investigated in dark conditions. For the P3 sample, cleaning of the surface in the vacuum conditions with halogen lamp was not accomplished. CVCs in the reverse bias are similar to the characteristics of cell without  $ZnO$  deposition. Decreasing of



**Fig. 24.5** Current-voltage characteristics for samples P1 (a), P2 (b), P3 (c), and P4 (d) measured in the dark and under illumination and current density for all samples under illumination (e, f)

the energy parameters of junction is clearly visible. For sample P4 with zinc oxide film deposited at 300 °C, the CVCs are similar to the P2 sample characteristics, although the current flowing through the junction in the reverse bias increases slowly than in the case of P2 sample.

**Table 24.2** PV properties of obtained solar cell samples

Sample	$V_{oc}$ , V	$J_{sc}$ , A	$J_{sc}/cm^2$ , A/cm <sup>2</sup>	FF, %	$\eta$ , %
P1 PLD	0.53240	0.01700	0.06389	42	16
P2 PLD-200A	0.50536	0.00933	0.07177	38	17
P3 PLD-200B	0.62576	0.01055	0.01665	15	14
P4 PLD-300	0.50514	0.01350	0.09027	36	19

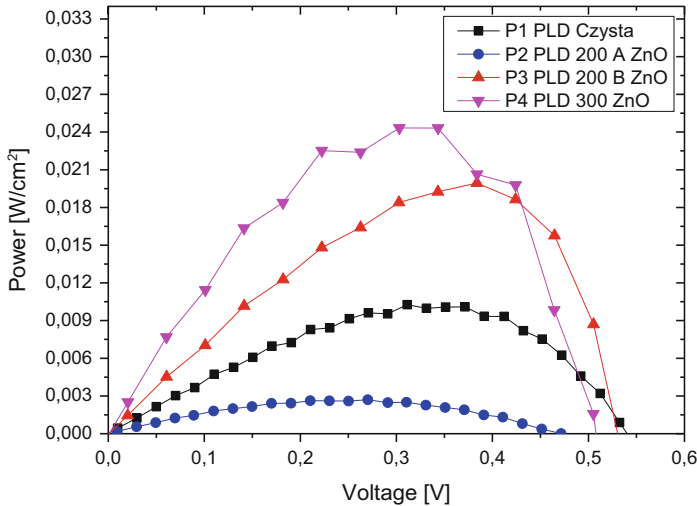


**Fig. 24.6** Power corresponding to appropriate voltage of cell

### 24.3.3 Maximal Powers and Efficiency

On the chart, power generated by unit of surface for each sample is presented. The photovoltaic parameters obtained from the fit are summarized in Table 24.2. Notable differences are clearly visible for each of the case, for example, for the P3 sample, decreasing of generated power is noticed. Maximal value of power density is observed for the junction with film deposited with 300 °C temperature of substrate and can be observed on Fig. 24.6. Appointed efficiencies are 16% for P1, 17% for P2 PLD-200A, 14% for P3 PLD-200B, and 19% for P4 PLD-300.

## 24.4 Conclusion

The thin films of zinc oxide were obtained on the standard silicon cells. Different types of ZnO layer growth were observed depending on deposition parameters. Two types of growth were indicated: planar and columnar mode. Based on voltage-current characteristics generated per unit by the individual structures, the

improvement of photovoltaic efficiency for samples P4 PLD-300 and P2 PLD-200A was noticed. For the P3 PLD-200B sample, efficiency decreased distinctly. It was found that increasing of efficiency is connected with columnar type of growth. Layer with this structure is characterized by lower reflectance and acts as fiber, causing the increasing of the amount of photons reaching the active region of *p-n* junction of silicon cells. For the samples with planar type of thin *ZnO* film growth, it was observed that power generated in cells highly decreased. It is caused by decreasing of the amount of absorbed photons as a result of increasing of reflectance for this layer.

## References

1. Green MA, Emery K, Hishikawa Y, Warta W, Dunlop ED (2016) Solar cell efficiency tables (version 47). *Prog Photovolt Res Appl* 24:3–11. doi:[10.1002/pip.2728](https://doi.org/10.1002/pip.2728)
2. Connolly D, Lund H, Mathiesen BV (2016) Smart energy Europe: the technical and economic impact of one potential 100% renewable energy scenario for the European Union. *Renew Sust Energy Rev* 60:1634–1653. doi:[10.1016/j.rser.2016.02.025](https://doi.org/10.1016/j.rser.2016.02.025)
3. Torani K, Rausser G, Zilberman D (2016) Innovation subsidies versus consumer subsidies: a real options analysis of solar energy. *Energy Policy* 92:255–269. doi:[10.1016/j.enpol.2015.07.010](https://doi.org/10.1016/j.enpol.2015.07.010)
4. Kang MH, Rohatgi A (2016) Quantitative analysis of the levelized cost of electricity of commercial scale photovoltaics systems in the US. *Sol Energy Mater Sol Cells* 154:71–77. doi:[10.1016/j.solmat.2016.04.046](https://doi.org/10.1016/j.solmat.2016.04.046)
5. Louwen A, Sark W, Schropp R, Faaij A (2016) A cost roadmap for silicon heterojunction solar cells. *Sol Energy Mater Sol Cells* 147:295–314. doi:[10.1016/j.solmat.2015.12.026](https://doi.org/10.1016/j.solmat.2015.12.026)
6. Ramanathan K, Keane J, Noufi R (2005) Properties of high-efficiency CIGS thin-film solar cells. Conference Record of the Thirty-first IEEE, Lake Buena Vista, p 195. doi:[10.1109/PVSC.2005.1488103](https://doi.org/10.1109/PVSC.2005.1488103)
7. Brongersma M.L., Cui Yi & Fan Sh (2014) Light management for photovoltaics using high-index nanostructures. *Nat Mater* 13:451–460. doi:[10.1038/nmat3921](https://doi.org/10.1038/nmat3921)
8. Rau U, Schmidt M (2001) Electronic properties of ZnO/CdS/cu(in,Ga)Se<sub>2</sub> solar cells – aspects of heterojunction formation. *Thin Solid Films*. doi:[10.1016/S0040-6090\(00\)01737-5](https://doi.org/10.1016/S0040-6090(00)01737-5)
9. Ellmer K, Klein A, Rech B (2008) Transparent conductive zinc oxide. Springer, Berlin/Heidelberg. Chapter 8. doi:[10.1007/978-3-540-73612-7](https://doi.org/10.1007/978-3-540-73612-7)
10. Sommer N, Hüpkens J, Wilck N, Pieters BE, Lentz F, Rau U (2014) ZnO:Al for thin-film solar cell application: optimization and prediction of conductivity on textured substrates. 42nd IEEE Photovoltaic Specialists Conference, New Orleans, pp 1–3. doi:[10.1109/PVSC.2015.7356299](https://doi.org/10.1109/PVSC.2015.7356299)
11. Wurfl IP, Hao X, Gentle A, Kim DH, Conibeer G, Green MA (2009) Si nanocrystal p-i-n diodes fabricated on quartz substrates for third generation solar cell applications. *Appl Phys Lett*. doi:[10.1063/1.3240882](https://doi.org/10.1063/1.3240882)
12. Pietruszka R, Schifano R, Krajewski TA, Witkowski BS, Kopalko K, Wachnicki L, Zielony E, Gwozdz K, Bieganski P, Placzek-Popko E, Godlewski M (2016) Improved efficiency of n-ZnO/p-Si based photovoltaic cells by band offset engineering. *Sol Energy Mater Sol Cells*. doi:[10.1016/j.solmat.2015.12.018](https://doi.org/10.1016/j.solmat.2015.12.018)
13. Hussain B, Ebong A, Ferguson I (2015) Zinc oxide as an active n-layer and antireflection coating for silicon based heterojunction solar cell. *SolEnergy Mater Sol Cells*. doi:[10.1016/j.solmat.2015.03.017](https://doi.org/10.1016/j.solmat.2015.03.017)
14. Hsueh T-J, Lin S-Y, Weng W-Y, Hsu C-L, Tsai T-Y, Dai B-T, Shieh J-M (2012) Crystalline-Si photovoltaic devices with ZnO nanowires. *Sol Energy Mater Sol Cells*. doi:[10.1016/j.solmat.2011.11.029](https://doi.org/10.1016/j.solmat.2011.11.029)

15. Morkoç H, Özgür Ü (2009) Zinc oxide: fundamentals, materials and device technology. Wiley-VCH, Weinheim. doi:[10.1002/9783527623945](https://doi.org/10.1002/9783527623945)
16. Ellmer K, Klein A, Rech B (2008) Transparent conductive zinc oxide. Springer, Berlin/Heidelberg. doi:[10.1007/978-3-540-73612-7](https://doi.org/10.1007/978-3-540-73612-7)
17. Kozarsky E, Yun J, Tong C, Hao X, Wang J, Anderson WA (2012) Thin film ZnO/Si heterojunction solar cells: design and implementation. In: Proceedings of the 38TH IEEE photovoltaic specialists conference (PVSC), Austin. doi:[10.1109/PVSC.2012.6317821](https://doi.org/10.1109/PVSC.2012.6317821)
18. Schou J (2009) Physical aspects of the pulsed laser deposition technique: the stoichiometric transfer of material from target to film. Appl Surf Sci. doi:[10.1016/j.apsusc.2008.10.101](https://doi.org/10.1016/j.apsusc.2008.10.101)

# Chapter 25

## Influence of Growth Condition and Thermal Treatment of Thin Copper Oxide Films Obtained by Magnetron Sputtering on Their Transmission Spectra

G. Wisz, P. Potera, Ł. Głowa, and M. Kaczor

### 25.1 Introduction

At present intensive research is under way on developing technology that makes it possible to produce low-cost solar panels for the mass market. The research has been focused on about 10 chemical compounds, of which the most promising is cuprous oxide (II) –  $\text{Cu}_2\text{O}$ . Cuprous oxide (II) ( $\text{Cu}_2\text{O}$ ) has occasionally been investigated as a possible nontoxic, earth-abundant photovoltaic material with a high absorption coefficient in the visible region and large exciton binding energy [1, 2]. A photovoltaic effect was observed, for example, for  $\text{ZnO}/\text{Cu}_2\text{O}$ ,  $\text{Ga}_2\text{O}_3/\text{Cu}_2\text{O}$ , and  $\text{TiO}_2/\text{Cu}_2\text{O}$  structures [3]. However, relatively few attempts have been made to fabricate photovoltaic cells with cuprous oxide. The optimization of  $\text{Cu}_2\text{O}$  solar cells is slowed down by the lack of clear understanding of its electronic and thermodynamic properties and by the difficulties in the doping process.

It is commonly known that conditions of growth and thermal treatment after growth can affect the physicochemical properties of thin layers [4]. One of the characteristic parameters of films is their transmission, which describes their optical quality. Copper oxide is a semiconductor that shows varying optical behavior because of the stoichiometric deviations arising from the methods of its preparation and its parameters [5]. It has been reported that many of the methods of growing a copper oxide layer result in a combined growth of  $\text{Cu}_2\text{O}$  and  $\text{CuO}$  [5].

In this work, the results of research on the dependence of the transmission spectrum of copper oxide thin films on glass versus conditions of growth and heating in air will be presented.

---

G. Wisz • P. Potera (✉) • Ł. Głowa • M. Kaczor  
Faculty of Mathematics and Natural Sciences, University of Rzeszow, 1 Pigionia Str, 35-959  
Rzeszow, Poland  
e-mail: [ppotera@ur.edu.pl](mailto:ppotera@ur.edu.pl)

## 25.2 Experimental Setup

Copper oxide thin films on a glass substrate were obtained in a mixed argon–oxygen atmosphere by magnetron sputtering using a modular PREVAC platform at Rzeszow University.

Thin films of copper oxide were deposited on microscope glass substrates ( $25 \times 25 \times 0.1$  mm). The distance between the source and substrate was 2.6 cm. The starting materials were a solid copper target (99.995% purity) and two gases, oxygen (reactive gas) and argon (sputtering gas). The deposition chamber was evacuated to a base pressure of  $5 \times 10^{-6}$  mbar. The pressure during deposition was maintained at  $5.5 \times 10^{-3}$  mbar. Sputtering was done for 10 min. Copper oxide thin films were prepared under various oxygen flow rates (sample 3:  $4 \text{ cm}^3/\text{s}$ ; samples 1 and 2:  $8 \text{ cm}^3/\text{s}$ ), while the other deposition parameters, such as power (sample 2: 55 W; sample 1 and 3: 70 W), substrate temperature (297 K), argon flow rates ( $4 \text{ cm}^3/\text{s}$ ), and sputtering pressure, were held constant. The flow of oxygen into the deposition chamber was monitored using mass flow controllers and gas regulators interfaced to a computer.

The transmission spectra of thin films were recorded using a CARY 5000 spectrophotometer immediately after growth and 6 months after growth. After an additional 6 months following growth the samples were annealed in air for 30 min in temperatures of 150 °C, 300 °C, and 450 °C. After each annealing step, the transmission spectra were obtained.

## 25.3 Results

The transmission of samples (Figs. 25.1, 25.2, and 25.3) depended strongly on growth conditions (oxygen flow, power of deposition). The samples had an average optical transparency of 50–85% in the region from 800 to 1100 nm. This indicates a low amount of impurities and a few lattice defects in the obtained films. Also, the flat range of the transmission curves without interference fringes emphasized the surface uniformity with a small crystallite size. In addition, the lack of interference fringes in the transmission spectra was due to surface roughness, tower height, and scattering at the grain boundaries.

For the same gas flow and different power (samples 1 and 2) very different transmission spectra were obtained (Figs. 25.1 and 25.2). At a higher deposition power (70 W) the minimum transmission near 750 nm was observed, but at a lower power (55 W), only a slight decrease in transmission above 900 nm was detected. A similar situation was observed for sample growth at the same deposition power and different gas flows (samples 1 and 3). For smaller flow the minimum transmission was not observed (Figs. 25.1 and 25.3). The change in optical transmittance with an increase in oxygen flow rate during deposition was also observed in [6] at a sputtering power of 200 W.



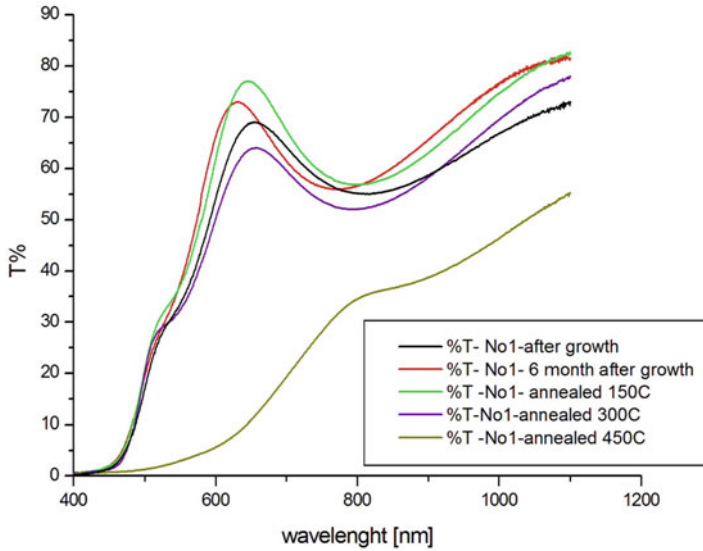


Fig. 25.1 Transmission spectra of the sample No 1

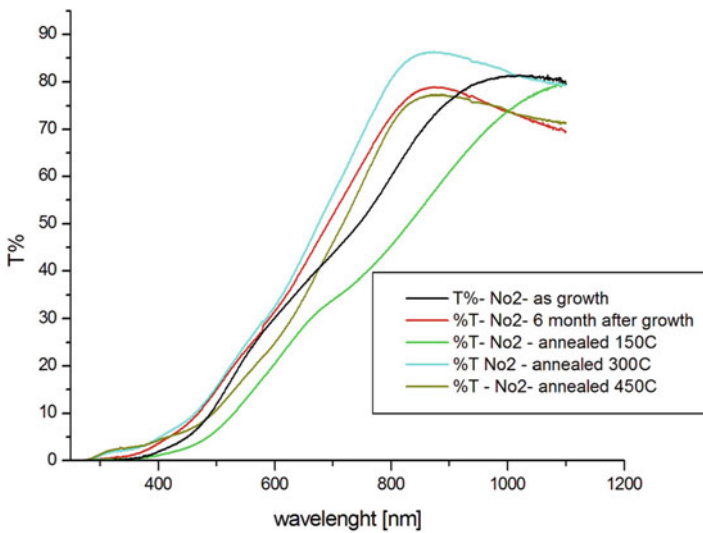
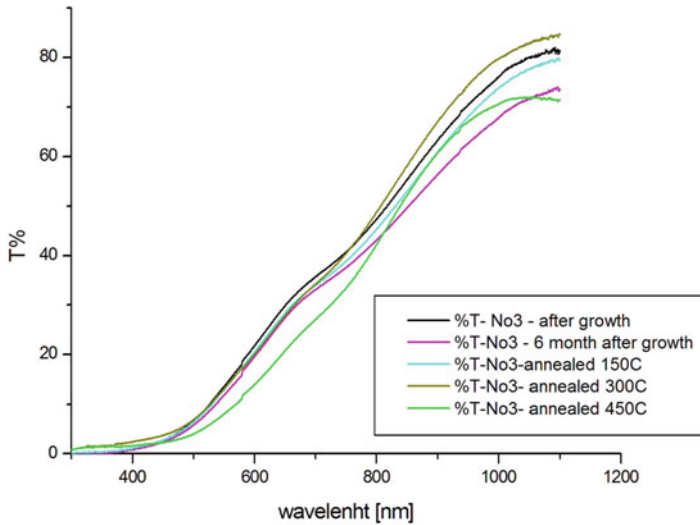


Fig. 25.2 Transmission spectra of the sample No 2

For all samples we observed that changes in transmission with time. The transmissions measured immediately after growth and 6 months after growth (e.g., right before annealing) were different; for samples 1 and 2 the average transmission value increased slightly with time, but for sample 3 the opposite effect was observed.



**Fig. 25.3** Transmission spectra of the sample No 3

Samples were annealed at temperatures of 150, 300, and 450 °C for 30 min. The transmission spectra changed for all samples. For sample 1 a slight increase in transmission at 150 °C was observed and a decrease at 300 and 450 °C took place. A particularly strong change was observed at 450 °C. For sample 2, an increase in transmission was observed only at 300 °C (Fig. 25.2), but for sample 3 an increase of transmission took place with a partial decrease only below 800 nm at an annealing temperature of 450 °C (Fig. 25.3). A decrease in transmission with annealing temperature was also observed for copper oxide thin film prepared by chemical deposition [7].

The absorption edge of the samples can be approximated by a Tauc relation [8]:

$$\alpha h\nu = B(h\nu - E_g)^\gamma,$$

where  $E_g$  is the optical band gap,  $h$  is Planck's constant,  $\nu$  is the frequency of incident photons,  $B$  is a constant, and  $\gamma$  is the index, which can have different values (2, 3,  $\frac{1}{2}$ , and  $\frac{1}{3}$ ) denoting indirect allowed, indirect forbidden, direct allowed, and direct forbidden transitions, respectively. In our case, the approximation at  $\gamma = 1/2$  was satisfactory for all samples, which corresponded with direct allowed transitions.

For direct transition, the optical band gap energy of films was determined using the equation [8]

$$(\alpha h\nu)^2 = A (h\nu - E_g).$$

**Table 25.1** The  $E_g$  and  $E_u$  values for investigated samples

Tauc	Sample 1		Sample 2		Sample 3	
	$E_g$ , eV	$E_u$ , eV	$E_g$ , eV	$E_u$ , eV	$E_g$ , eV	$E_u$ , eV
As-grown	2.44	0.67	2.07	1.07	2.23	–
After 6 months (immediately before annealing)	2.46	1.00	2.05	1.21	2.18	–
Annealing at 150 °C	2.46	0.98	1.87	0.92	2.23	–
Annealing at 300 °C	2.46	0.88	1.97	1.37	2.20	–
Annealing at 450 °C	1.77	0.42	1.93	1.22	2.11	–

The band gap values for all samples and annealing temperatures are given in Table 25.1.

According to the literature, cupric oxide (CuO) has a band gap of 1.21–2.1 eV and cuprous oxide (Cu<sub>2</sub>O) has a band gap of approximately 2.2–2.9 eV [9]. Our results are in good agreement with the value for cuprous oxide.

The energy gap value decreases with decreases in power or oxygen flow. Annealing did not change this tendency. Additionally, a strong decrease in  $E_g$  values compared with the values obtained for samples before annealing was observed for annealing at 450 °C. This suggests that at this temperature, the production of cupric oxide is more effective than at lower temperatures. It was early observed that the kinetics of CuO formation is much slower than that of Cu<sub>2</sub>O [6], which gives an advantage to the Cu<sub>2</sub>O phase in comparison to the CuO phase. At 450 °C, substantial oxidation of Cu<sub>2</sub>O takes place, and the creation of CuO is more effective than at lower temperatures.

The incorporation of impurities into a semiconductor often reveals the formation of band tailing in the band gap, interactions with phonons, and the presence of a tail absorption profile that follows the empirical Urbach law [10]:

$$\begin{cases} \alpha(h\nu) = \alpha_0 e^{\frac{h\nu}{E_U}} \\ E_U = \alpha(h\nu) \left[ \frac{d[\alpha(h\nu)]}{d[h\nu]} \right]^{-1} = h \left[ \frac{d}{d\nu} (\ln \alpha(h\nu)) \right]^{-1}. \end{cases}$$

The absorption tails can be observed also for disordered systems, for example, glasses. In our experiment, absorption tails were observed for samples 1 and 2, but for sample 3 none was observed. The approximate values of the Urbach energy for samples 1 and 2 are given in Table 1. The Urbach energy strongly depends on time—growth with time. For sample 1 the Urbach energy strongly decreased with annealing temperature, but for sample 2, a lowering of  $E_u$  values from baseline at 150 °C and an increase at 300 and 450 °C were observed.

## 25.4 Conclusion

The transmission spectra of copper oxide film obtained by magnetron sputtering depend on growth conditions (oxygen content, power of deposition) and changes during annealing with annealing temperatures. The absorption spectra of layers change over time. Growth and annealing conditions affect the value of the optical energy band gap and the Urbach energy.

**Acknowledgment** This work was supported by a Dean's grant (WMP/GD-32/2016).

## References

1. Mittiga A, Salza E, Sarto F, Tucci M, Vasanthi R (2006) Heterojunction solar cell with 2% efficiency based on a  $\text{Cu}_2\text{O}$  substrate. *Appl Phys Lett* 88:163502
2. Rakhshani AE (1986) Preparation, characteristics and photovoltaic properties of cuprous oxide – a review. *Solid State Electron* 29:7–17
3. Pavan M, Rühle S, Ginsburg A, Keller DA, Barad H, Sberna PM, Nunes D, Martins R, Anderson AY, Zaban A, Fortunato E (2015)  $\text{TiO}_2/\text{Cu}_2\text{O}$  all-oxide heterojunction solar cells produced by spray pyrolysis. *Sol Energy Mater Sol Cells* 132:549–556
4. Usikov AS, Lundin WV, Bedarev DA, Zavarin EE, Sakharov AV, Tsatsul'nikov AF, Alferov Zh I, Ledentsov NN, Hoffmann A, Bimberg D (2000) Influence of the thick GaN buffer growth conditions on the electroluminescence properties of GaN/InGaN multilayer heterostructures. *Proceedings of IWN2000*, Nagoya, September 24–27, 2000. pp 875–877
5. Ogwu AA, Bouquerel E, Ademosu O, Moh S, Crossan E, Placido F (2005) The influence of rf power and oxygen flow rate during deposition on the optical transmittance of copper oxide thin films prepared by reactive magnetron sputtering. *J Phys* 38:266
6. Mugwang'a FK, Karimi PK, Njoroge WK, Omayio O, Waita SM (2013) Optical characterization of copper oxide thin films prepared by reactive dc magnetron sputtering for solar cell applications. *Int J Thin Film Sci Tec* 2:15–24
7. Johan MR, Suan M, Hawar NL, Ching HA (2011) Annealing effects on the properties of copper oxide thin films prepared by chemical deposition. *Int J Electrochem Sci* 6:6094–6104
8. Viezbicke BD, Patel S, Davis BE, Birnie DP (2015) Evaluation of the Tauc method for optical absorption edge determination: ZnO thin films as a model system. *Phys Status Solidi B* 252:1700–1710
9. Balamurugan B, Mehta BR (2001) Optical and structural properties of nanocrystalline copper oxide thin films prepared by activated reactive evaporation. *Thin Solid Films* 396:90–96
10. Mimouni R, Kamoun O, Yumak A, Mhamdi A, Boubaker K, Petkova P, Amlouk M (2015) Effect of Mn content on structural, optical, opto-thermal and electrical properties of ZnO:Mn sprayed thin films compounds. *J Alloys Compd* 645:100–111

**Part III**  
**Nanostructured Interfaces and Surfaces**

# Chapter 26

## Structural, Catalytic, and Thermal Properties of Stainless Steel with Nanoscale Metal Surface Layer

V. Honcharov, V. Zazhigalov, Z. Sawlowicz, R. Socha, and J. Gurgol

### 26.1 Introduction

Modern catalyst systems should have the high activity, selectivity, mechanical strength, thermal stability, and so on. One of the directions providing these requirements is the creation of catalytic systems with a low content of active elements (their nanolayers) deposited on supports.

Analysis of the literature [1–6] demonstrates that the use of different metal structures, metal foams, sheets, fibers, foils, etc. as the supports, is the most promising pathway for catalyst preparation. Catalytic systems based on metallic supports have high strength, heat resistance, and thermal and electrical conductivity. These facts determine the possibility of their use as neutralizer combustion engine gas, oxidation catalysts of hydrocarbon, hydrogen generation catalyst, components of thermal power plants, etc. Various methods are used for catalyst production on metal supports. Broad prospects have ion-plasma methods [4, 7–11]. In particular, the technology of ionic implantation has significant advantages [12–15]. Ionic implantation, due to local influence and high controllability of process, permits to

---

V. Honcharov (✉)  
Institute of Chemical Technology, V. Dal' East-Ukrainian National University, Rubizhne, Ukraine  
e-mail: [gonch\\_vit@rambler.ru](mailto:gonch_vit@rambler.ru)

V. Zazhigalov  
Institute for Sorption and Problems of Endoecology, National Academy of Sciences of Ukraine,  
Kyiv, Ukraine  
e-mail: [zazhigal@ispe.kiev.ua](mailto:zazhigal@ispe.kiev.ua)

Z. Sawlowicz  
Jagellonian University, Krakow, Poland

R. Socha • J. Gurgol  
J. Haber Institute of Catalysis and Surface Chemistry, PAS, Krakow, Poland

obtain nanolayers of active components, to reduce the costs of the catalyst, and to increase the level of compatibility of components by forming the intermediate layer with the introduction of metal ions in the support [16–18]. It is necessary to note that this method practically was not used in catalyst preparation. Therefore, the studies of the application of ionic implantation in supported metal-based catalyst synthesis are very topical.

## 26.2 The Experimental Part

The low-temperature ionic implantation method was used for preparation of nanocomposites on the base of stainless steel with a low content of active components. The essence of this method is to introduce metal ions accelerated to an energy of 20–40 keV in an electrically conductive support (Fig. 26.1).

The composites containing Al, Ni, Cr, Ti, Mo, and Zr based on stainless steel foil (SSF) were prepared in the installation of low-temperature implantation (Fig. 26.2) with one- or two-element (step-by-step) deposition. The implantation dose was  $D \approx 5 \cdot 10^{17} \text{ cm}^{-2}$ , which corresponds to the penetration of target ions to a depth of support on the order of hundreds of nanometers. The synthesized composites were studied by means of traditional XRD and XRD of thin films, SEM, AFM, and XPS methods.

The temperature of the composite surface at their heating by electric current was determined. The catalytic properties of the samples in hydrogen production from ethanol were determined in traditional catalytic reactor (with reaction mixture heating) and in reactor with catalyst heating by electric current only.

**Fig. 26.1** Scheme of ionic implantation

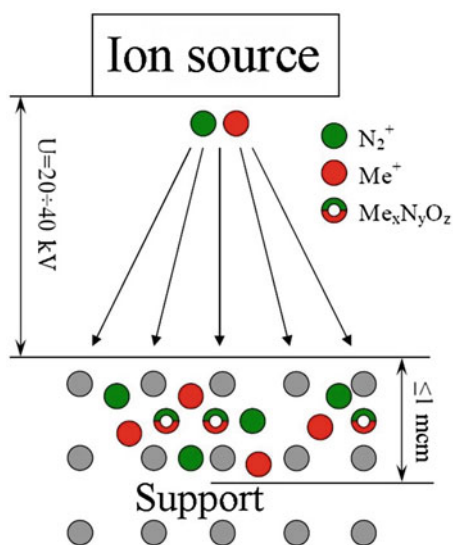


**Fig. 26.2** Installation of the ionic implantation



## 26.3 Results and Discussion

The results of XRD study of the prepared composites show the presence of austenite phase, characteristic for the stainless steel support (SS) only (Fig. 26.3). So, the metal implantation procedure does not lead to the formation of metal or its compound crystalline phase.

The results obtained with the help of XRD of thin films method (Fig. 26.4) also showed the absence of crystalline phases and introduced implants, which can be connected with their amorphous state, and the presence of the austenite phase only belong to the original support. It should be noted that the secondary implantation (first aluminum and then nickel) also is not accompanied by the change of the structural state of the composite surface.

The data obtained by SEM method (Figs. 26.5 and 26.6, cross section of the samples) show the formation of implant (e.g., Al) surface layer as a result of implantation with the thickness of this cover near 100 nm.

The AFM data demonstrate that the ionic bombardment essentially changes the support surface morphology. The surface roughness increases after the metal implantation. This parameter depends on the implanted metal nature and presence of the first introduced metal layer (Fig. 26.7).

The fact of sample roughness increase after implantation determines the possibility of the use of traditional impregnation method for additional deposition of other metals (e.g., Pd, Pt, etc.) effective in environment protection processes.

The formation of  $\text{MeN}_x$  (BE = 116.3 eV for Al/SS or 854.9 eV for Ni/Al/SS),  $\text{MeO}_x\text{N}_y$  (BE = 122.4 eV or 8723.4 eV, correspondingly), and  $\text{MeO}_x$  (BE = 119.1 eV or 869.1 eV, correspondingly) compounds on the surface layer of synthesized composites was established by XPS method (Fig. 26.8).

It was established that at the heating of the prepared composites by electric current, the temperature of their surface has higher values than in the case of industrial electric heating element or initial support (SS) use (Fig. 26.9).



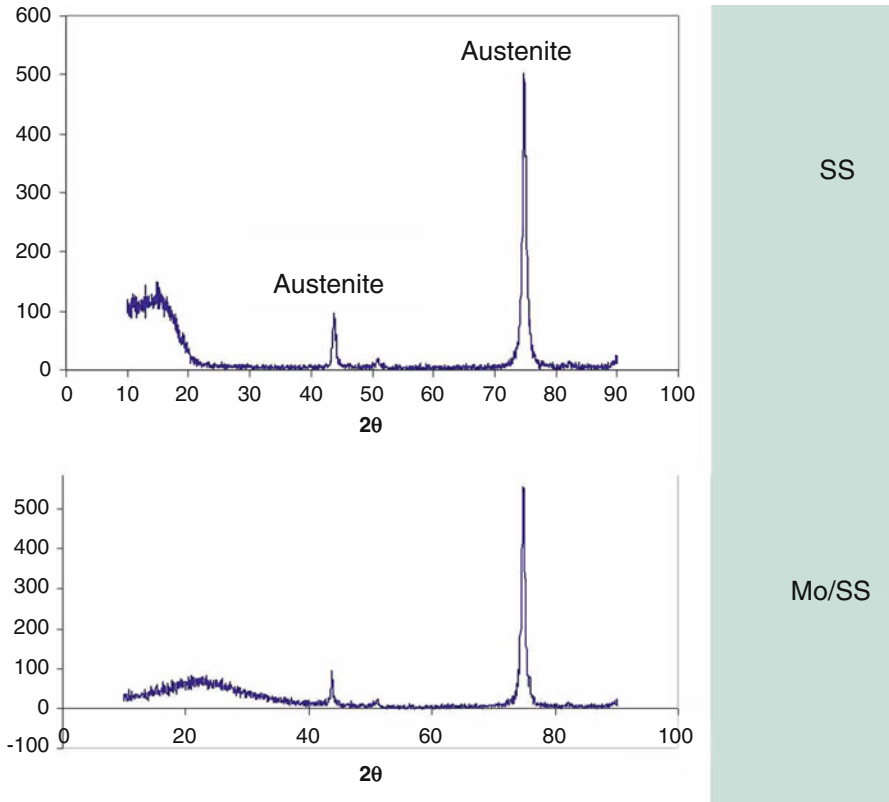


Fig. 26.3 The data of XRD analysis

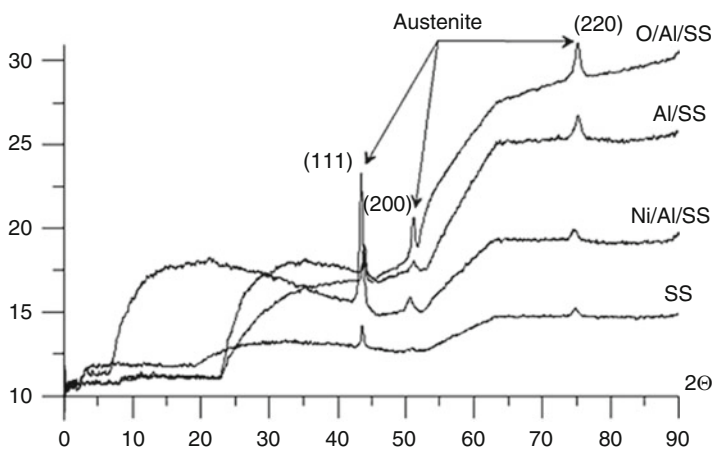
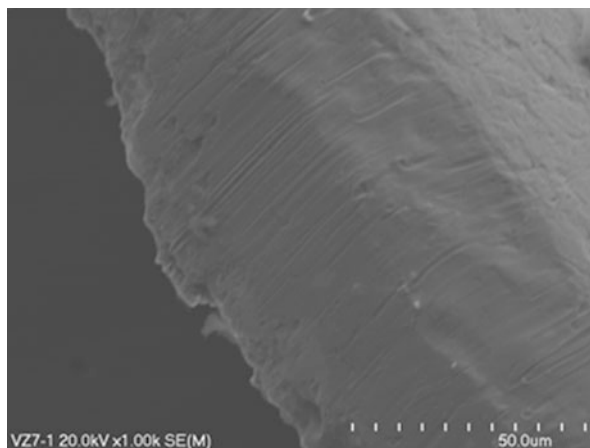
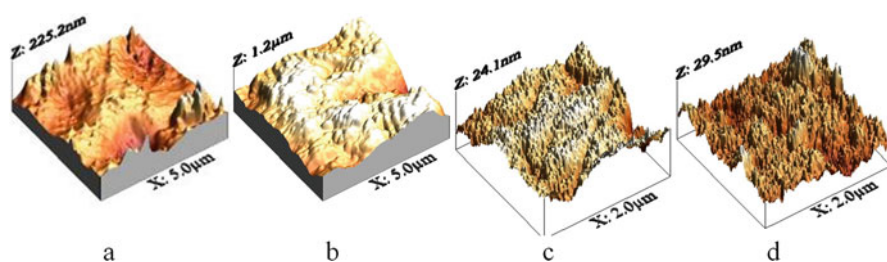
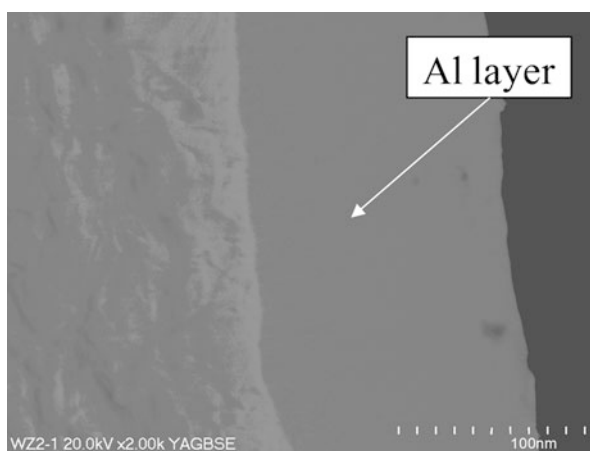


Fig. 26.4 The data of XRD of thin films

**Fig. 26.5** The data of SEM (cross section) of initial sample (SS)



**Fig. 26.6** The data of SEM (cross section) of composite with supported Al



**Fig. 26.7** Surface morphology of the samples by AFM data: (a) SS, (b) Mo/SS, (c) Ni/SS, and (d) Ni/Al/SS

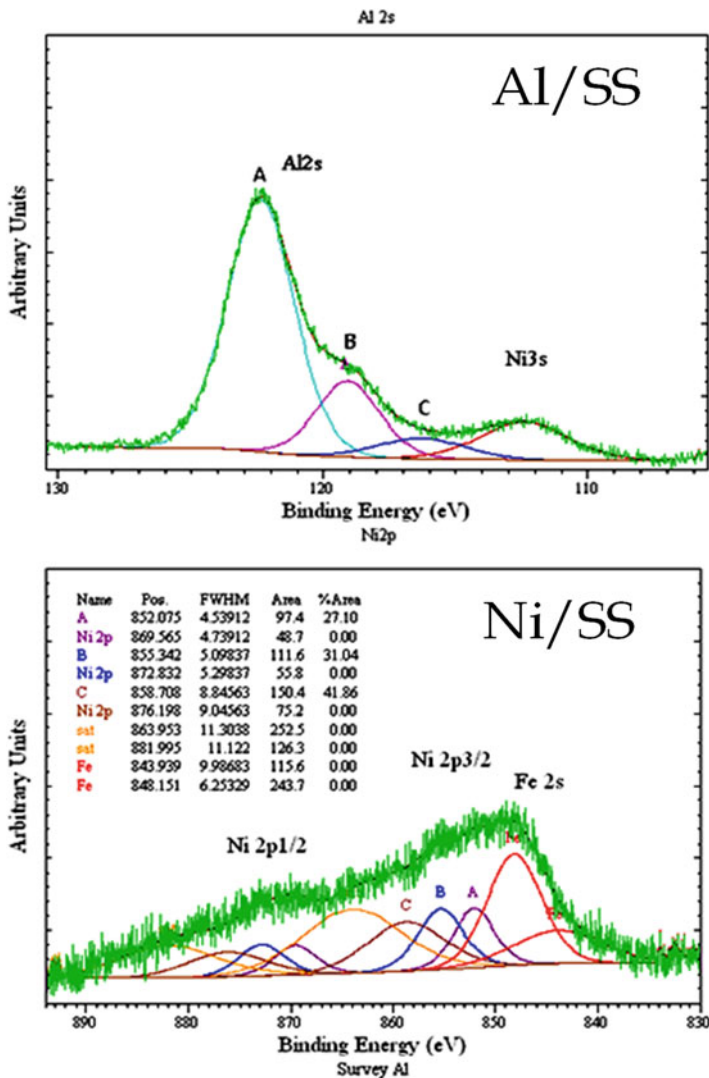


Fig. 26.8 The XPS spectra of the synthesized composites with different implants

The obtained results show the perspective of development of new electric heating elements on the base of these synthesized composites and the possibility of their use in nontraditional catalysis with electric heating of the catalyst, only.

The high effectivity of the synthesized implanted samples in hydrogen production from ethanol (Fig. 26.10) at reaction realization in traditional conditions (heating of reaction mixture) was shown. At same time, the use of nontraditional

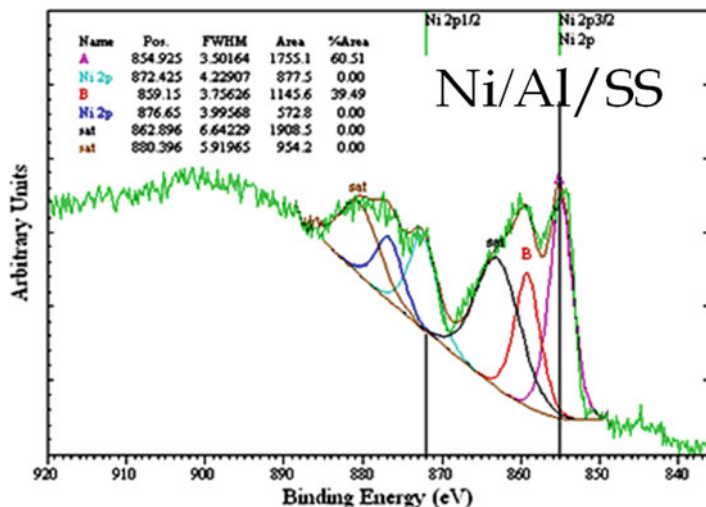


Fig. 26.8 (continued)

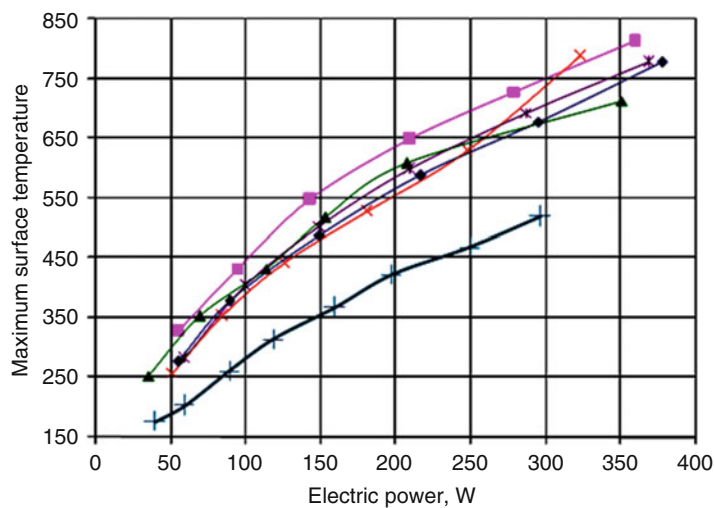
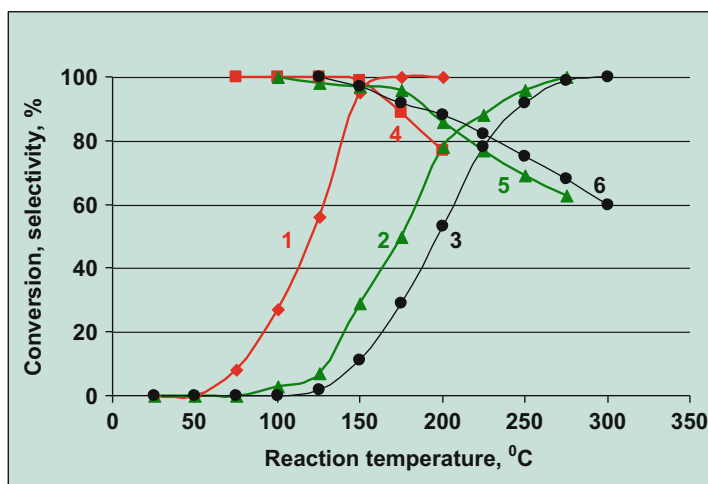
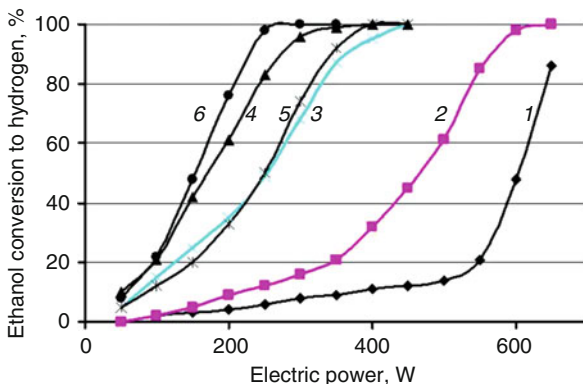


Fig. 26.9 Temperature on the implanted sample surface at their heating by electric current; ♦ SS; ■ Cr/SS; ▲ Ti/SS; \* Mo/SS; × Zr/SS; + industrial electric element (Ni-Cr-Fe)

technology of this process (with electric heating of the catalyst only) permits to the essential increase of the catalytic activity and realizes the energy saving.

It was determined that prepared composites demonstrate high activity and selectivity to acetaldehyde in the reaction of ethanol selective oxidation by air (Fig. 26.11). The parameters of this reaction depend on implant nature. Composite Mo/SS is more active and selective.

**Fig. 26.10** Ethanol transformation to hydrogen in traditional reactor (1, 3, 5) with reaction mixture heating and nontraditional reactor (2, 4, 6) with catalyst heating by electric current only. 1 and 2, SS; 3 and 4, Ni/SS; 5 and 6, Ti/SS



**Fig. 26.11** Catalytic activity (1, Mo/SS; 2, Ni/SS; 3, Ti/SS) and selectivity (4, Mo/SS; 5, Ni/SS; 6, Ti/SS) of the composites in ethanol oxidation vs reaction temperature

**Table 26.1** The rate constants ( $K_d \cdot 10^4$ ) of safranin T photocatalytic decomposition

Ti/SS after treatment at temperature			TiO <sub>2</sub> P-25
200 C	400 C	600 C	
0.8	4.3	6.2	5.4

Photocatalytic activity of the samples Ti/SS after air thermal treatment at different temperature was determined in the dye safranin T decomposition in water according to the protocol [19]. The rate constants ( $K_d$ ) were compared with the activity of traditional photocatalyst TiO<sub>2</sub> P-25 (Degussa). The obtained results (Table 26.1) show the synthesized Ti/SS composite after thermal treatment demonstrates more activity than known catalyst TiO<sub>2</sub>.

**Table 26.2** Strength of surface for composites (GPa)

Composites	SS	Al/SS	Ti/SS	Mo/SS
Strength	1.7	5.7	5.3	6.8

The presented results in Table 26.2 demonstrate the process of metal implantation on stainless steel surface accompanied by increase of the strength of surface in comparison with initial support.

## 26.4 Conclusions

It was established that implantation of the metal on stainless steel leads to formation of X-ray amorphous layer of implant with the thickness near to 100 nm. The implant in surface layer exists in the form of oxide, nitride, and oxynitride compounds. The increase of the roughness of the stainless steel after implantation permits to use obtained composite as support for deposition of other metals by traditional impregnation. The ionic implantation permits to obtain materials with high thermal and mechanical characteristics. The synthesized materials demonstrate high electric conductivity, and their surface temperature at electric current heating exceeds the temperature obtaining on industrial heating element. High activity of synthesized composites in ethanol decomposition to hydrogen, ethanol selective oxidation to acetaldehyde, and dye photodecomposition in water was shown. The possibility of energy-saving catalytic technology was based on direct heating of the catalyst (composite) by electric current.

**Acknowledgments** The investigations were realized with partial financial support of NAS of Ukraine Fundamental Programme “Fine Chemicals” Project 20-(14-16).

## Literature

1. Giornelli T, Lofberg A, Bordes-Richard E (2006) Preparation and characterization of  $\text{VO}_x/\text{TiO}_2$  catalytic coatings on stainless steel plates for structured catalytic reactors. *Appl Catal A Gen* 305:197–203
2. Vaneman GL (1991) Comparison of metal foil and ceramic monolith automotive catalytic converters. *Catal Automot Pollut Control II* 71:537–555
3. Muraoka S, Kitamura K, Kishi S et al (2007) Development of efficient metal catalyst support. *Mater Sci Forum* 561-565(1):547–550
4. Wyrwa DW, Schmid G (2007) Metal nanoparticles on stainless steel surfaces as novel heterogeneous catalysts. *J Clust Sci* 18(3):476–493
5. Kaltner W, Veprek-Heijman M, Jentys A et al (2009) Effect of chromium migration from metallic supports on the activity of diesel exhaust catalysts. *Appl Catal B Environ* 89:123–127
6. Zamaro JM, Ulla MA, Miro EE (2008) ZSM5 growth on a FeCrAl steel support. Coating characteristics upon the catalytic behavior in the  $\text{NO}_x$  SCR. *Microporous Mesoporous Mater* 115:113–122

7. Magali BK, Sven GJ (1996) A review of the use of plasma techniques in catalyst preparation and catalytic reactions. *Appl Catal A Gen* 147:1–21
8. Liu CJ, Vissokov G, Jang BWL (2002) Catalyst preparation using plasma technologies. *Catal Today* 72:173–184
9. Durme JV, Dewulf J, Leys C et al (2008) Combining non-thermal plasma with heterogeneous catalysis in waste gas treatment: a review. *Appl Catal B Environ* 78:324–333
10. Łojewska J, Kołodziej A, Łojewski T et al (2009) Structured cobalt oxide catalyst for VOC combustion. Part I: catalytic and engineering correlations. *Appl Catal A Gen* 366:206–211
11. Schmidt B, Wetzig K (2012) Materials processing. In: Schmidt B, Wetzig K (ed) *Ion beams in materials processing and analysis*. Springer, Vienna, pp 117–251
12. Kalin BA (2001) Radiatsionno-puchkovyye tekhnologii obrabotki konstruktsionnykh materialov. *Fizika i khimiya obrabotki materialov* 4:5–16
13. Dudognon J, Vayer M, Pineau A et al (2008) Grazing incidence X-ray diffraction spectra analysis of expanded austenite for implanted stainless steel. *Surf Coat Technol* 202(20):5048–5054
14. Dudognon J, Vayer M, Pineau A et al (2008) Mo and Ag ion implantation in austenitic, ferritic and duplex stainless steels: a comparative study. *Surf Coat Technol* 203:180–185
15. Khirvonen DK (1985) *Ionnaya implantatsiya*. Metallurgiya, Moskva
16. June KT, Jeong-Gil K, Lee H-Y et al (2014) Modification of optical and mechanical surface properties of sputter-deposited aluminum thin films through ion implantation. *Int J Precis Eng Manuf* 15(5):889–894
17. Zazhigalov VA, Honcharov VV (2014) Formirovaniye nanorazmernogo pokrytiya na stali 12H18N10T pri ionnoy implantatsii. *Metallofizika i Noveishie Tekhnologii* 6(36):757–766
18. Cherny AA, Maschenko SV, Honcharov VV et al (2015) Nanodimension layers on stainless steel surface synthesized by ionic implantation and their simulation. *Nanoplasmonics, Nanooptics, Nanocomposites and surface studies*. Springer, Ukraine, pp 203–213
19. Sidorchuk VV, Khalameida SV, Skubiszewska-Zieba J et al (2012) Mechanochemical degradation of safranin T catalysed by oxides. *Russ J Appl Chem* 85:187–190

# Chapter 27

## Thermal Effects at Nano-sized Pattern Formation in Surface Layers

Dmitrii O. Kharchenko and Vasyl O. Kharchenko

### 27.1 Introduction

Nano-sized patterning in thin films attains an increasing interest from theoretical and practical viewpoints due to usage of nano-sized objects in new electronic devices and, generally, in optoelectronics. During the last few decades, it was shown experimentally and by theoretical modeling that nano-sized objects can be produced at vapor or ion-beam deposition [1–4], ion-beam sputtering [5–9], pulsed laser irradiation [10–12], and molecular beam epitaxy [13–19]. It was shown that the continuous approach related to reaction-diffusion models is able to study dynamics of formation of spatial objects on wide range of time scales and considers dynamics of pattern formation on length scales from nano- to micrometers (see, e.g., Refs. [20–28]).

By studying processes of nano-sized pattern formation at deposition from gaseous phase, one usually assumes that a temperature of the surface remains a constant during adsorption/desorption processes. From a physical viewpoint, one should take into account energetic exchanges during adsorption/desorption processes. It leads to local change in temperature of the surface. These effects result in temperature field patterning at formation of spatial structures of adsorbate [17, 29]. Therefore, distribution of temperature field over the surface in above microscopic processes can affect on formation of islands of adsorbate and, hence, influence the dynamics of patterning. A description of these processes allows to understand pattern formation processes in adsorptive layers in details.

---

D.O. Kharchenko (✉) • V.O. Kharchenko  
Institute of Applied Physics, National Academy of Sciences of Ukraine, 58 Petropavlovskaya St.,  
40000, Sumy, Ukraine  
e-mail: [dikh@ipfcentr.sumy.ua](mailto:dikh@ipfcentr.sumy.ua); [vasiliy@ipfcentr.sumy.ua](mailto:vasiliy@ipfcentr.sumy.ua)



In problems related to studying formation of nano-sized clusters of point defects at irradiation of metallic foils, the related dynamical models incorporate the defect ensemble environment changes (emergence of uncompensated stresses caused by defect formation, local temperature variations in processes of defect formation, their interactions, and rearrangement). It was shown that dynamics of point defect concentration interacting with a deformation of the stretched surface layer can be described by nonlinear equation of reaction-diffusion kind, where no sputtering and erosion of the surface is assumed [30–33]. During the system evolution, self-organization of ensemble of defects can be seen through spatiotemporal instabilities leading to pattern formation, oscillatory dynamics of main variables, and change in geometrical characteristics of point defects patterns. Experimental observations of self-organization of point defects in solids with spatiotemporal oscillations of point defect concentration illustrate void size oscillations observed in irradiated nickel samples [34]; temperature oscillations of crystals  $CH_4$  were reported in Ref. [35]; periodic variations of microhardness of Nimonic 90 with  $\gamma$ -precipitates with radiation dose growth were discussed in Ref. [36]; periodic variation of electric resistivity of irradiated copper and aluminum was shown in Refs. [37–39]. Therefore, coupling of defect concentration and temperature of a surface layer leading to energetic exchange effects should be considered in order to get detail description of the above phenomena.

In this work we are aimed to describe influence of local changes in the temperature field onto self-organization processes accompanied by formation of adsorbate islands during vapor deposition and at defect clusters formation during irradiation of thin metallic foils. We introduce, initially, a general approach used in our study. Application of this approach is provided by considering temperature effects at adsorbate islands formation and vacancy clusters patterning. Here we discuss delaying and oscillatory dynamics of pattern formation caused by energetic exchanges emergent at microscopic processes, where needed estimation and comparison with experiments and real system behavior are given.

## 27.2 Generalized Model for Patterning

In the framework of mesoscopic approach used to study pattern formation phenomena, one deals with spatially inhomogeneous scalar fields such as local concentration, local coverage of the surface, etc. Dynamics of the scalar field  $c = c(\mathbf{r}, t)$  in time  $t$  ( $\mathbf{r}$  is the spatial coordinate), as usual, is governed by the reaction-diffusion equation of the form

$$\partial_t c = f(c) - \nabla \cdot \mathbf{J}. \quad (27.1)$$

The form of the reaction term  $f(c)$  corresponding to local dynamics is described usually by special kind of system and quasi-chemical reactions or related birth and death processes. The diffusion flux  $\mathbf{J}$  representing the mass transport is

defined by the linear Onsager theory, where one can write  $\mathbf{J} = -L\nabla(\mu/T)$ , where  $L$  is the kinetic coefficient,  $T$  is the temperature, and  $\mu = \delta\mathcal{F}/\delta c$  is some kind of chemical potential obtained through the free energy  $\mathcal{F}$ ;  $\nabla \equiv \partial_{\mathbf{r}}$ . By taking into account that temperature is changed locally, one gets  $\mathbf{J} = -LT^{-1}(\partial_c\mu|_T \nabla c + \partial_T\mu|_c \nabla T - \mu T^{-1} \nabla T)$ .

By taking into account that local change in the temperature occurs in time in spatially extended systems (at annihilation/recombination of point defects in crystalline matrix, in adsorption/desorption processes), one should take into account dynamics of the temperature field  $T = T(\mathbf{r}, t)$  described by general equation of the form

$$\partial_t T = \gamma(T_0 - T) + \chi \Delta T + \mathcal{G}(c, T). \quad (27.2)$$

Here  $\gamma$  and  $\chi$  relate to heat transfer coefficient and thermal conductivity, respectively;  $T_0$  is temperature of the bath. The term  $\mathcal{G}(c, T)$  describes other sources and mechanisms responsible for local variations of the temperature.

Therefore, a model to study pattern formation with temperature variations is described by the system of two Eqs. (27.1) and (27.2). Formally, this system is constructed by using mesoscopic level of description. At the same time, by introducing microscopic interaction mechanisms of mobile species characterized by the scalar field  $c(\mathbf{r}, t)$  and accounting the corresponding energetic effects, one can study formation of spatial patterns on nano-scale and reproduce local temperature variations in the corresponding processes of pattern formation. Next, we consider two typical cases, where microscopic processes of particle interactions change the local temperature of the system leading to patterning of the temperature field. These two cases correspond to the formation of nano-sized islands of adsorbate at vapor deposition and emergence of nano-clusters of point defects at irradiation of thin foils.

### 27.3 Adsorptive Layer Temperature Variations at Vapor Deposition

Let us consider temperature effects in processes of formation of nano-sized islands of adatoms at vapor deposition. To study an influence of local temperature changes onto nano-sized pattern formation at condensation from gaseous phase, we consider dynamics of local coverage  $c(\mathbf{r}, t)$  in two-dimensional system. It is assumed that particles (atoms/molecules of one sort) can be adsorbed by the substrate (become adatoms), can desorb back into gaseous phase from a substrate, interact among themselves, and diffuse along a substrate. Dynamics of adsorbate concentration (coverage) is described by Eq. (27.1).

The adsorption rate, i.e., the probability of the arrival of an atom/molecule from the gas phase at a given vacant site of the lattice  $(1 - c)$  is  $\varpi_a = k_a P$ , where  $k_a$  is the sticking coefficient and  $P$  is the partial pressure of the gaseous phase.

Hence, adsorption processes are defined as:  $k_a P(1 - c)$ . The desorption rate, i.e., the probability per unit time that an atom/molecule leaves its site  $\mathbf{r}$  and goes into the gas phase, is  $k_d = k_d^0 \exp(U(\mathbf{r})/T)$ , where  $k_d^0$  is the desorption rate for noninteracting particles (atoms/molecules) which relates to the lifetime scale of adatoms  $\tau_d = [k_d^0]^{-1}$ . We admit that only substratum-mediated interactions are possible, where  $U(\mathbf{r})$  is the interaction potential. Therefore, the desorption processes are defined by a contribution  $-k_d c$ . Adsorption and desorption are equilibrium reactions related to exchange of particles between the substrate and a large gas reservoir. In such closed system short time instabilities resulting in formation of transient patterns only can be observed. At large time intervals, such system will tend to have thermal equilibrium with uniform adsorbate coverage. Transient patterns are stabilized by nonequilibrium quasi-chemical reactions responsible for dimers formation in the form  $-k_r c^2$ , where  $k_r$  is the corresponding rate constant [40]. These dimers, formed on the substrate, are stable, and therefore, they reduce free sites for adsorption. By combining all above components, one gets  $f(c) = k_a P(1 - c) - k_d c - k_r c^2$  in Eq. (27.1).

The corresponding diffusion flux is defined in the standard way, where free energy of the system is of the form  $\mathcal{F} = \int d\mathbf{r} \{ T [c(\mathbf{r}) \ln(c(\mathbf{r})) + (1 - c(\mathbf{r})) \ln(1 - c(\mathbf{r}))] - \int d\mathbf{r}' c(\mathbf{r}) u(\mathbf{r} - \mathbf{r}') c(\mathbf{r}') \}$ . Here  $-u(r)$  is the binary attraction potential for two adsorbate particles separated by the distance  $r$ ; it is of symmetrical form, i.e.,  $\int d\mathbf{r} r^{2n+1} u(\mathbf{r}) = 0$ ,  $n = 1, \dots, \infty$ . Following Ref. [23] as a simple approximation for the interaction potential, we choose the Gaussian profile  $u(r) = 2\epsilon / \sqrt{4\pi r_0^2} e^{-r^2/4r_0^2}$ , where  $\epsilon$  is the interaction strength and  $r_0$  is the interaction radius. Assuming that the coverage  $c$  does not vary significantly within the interaction radius, one can expand the corresponding integral in series up to the second order. In such a case we arrive at  $\mathcal{F} = \int d\mathbf{r} \{ -\frac{\epsilon}{2} c^2 + T [c \ln c + (1 - c) \ln(1 - c)] - \frac{\epsilon}{2} c (1 + r_0^2 \nabla^2)^2 c \}$ . The diffusion flux takes the form  $\mathbf{J} = -D \nabla c + D \epsilon T^{-1} M(c) [\nabla c + \nabla \mathcal{L} c - c T^{-1} \nabla T]$ , where  $M(c) = c(1 - c)$  takes into account that the flow of adsorbate is possible only onto free sites.

The temperature of the growing surface can be changed locally at adsorption/desorption processes: when atom becomes adatom, the temperature of the surface increases locally, and it decreases when the desorption of adatom occurs. By using above mechanisms for the temperature variations, one can write an evolution equation for the temperature field in the form

$$C \rho \partial_t T = -\frac{\gamma_0}{h} (T - T_0) + \chi \Delta T + \eta \partial_t c. \quad (27.3)$$

Here  $C$  is the specific heat,  $\rho$  is the density,  $\gamma_0$  is the heat transfer coefficient,  $h$  is the thickness of the film,  $\chi$  is the thermal conductivity, and  $\eta$  is the reheat efficiency. The first term in the right-hand side in Eq. (27.3) corresponds to the relaxation of the surface temperature toward equilibrium value  $T_0$ . The second term corresponds to the standard diffusion, and the last term relates with the local heating/cooling of the surface during adsorption/desorption processes.

Therefore, one gets the model of two close loop equations describing reaction-diffusion dynamics of the coverage and coverage temperature. Next, it will be more convenient to measure time in units  $k_d$  and introduce the diffusion length  $L_d \equiv \sqrt{D/k_d}$  and dimensionless quantities  $\theta = T/T_0$ ,  $\varepsilon = \epsilon/T_0$ ,  $\alpha \equiv k_a p/k_d$ ,  $\beta \equiv k_r/k_d$ ,  $\nu = k_d C \rho h/\gamma_0$ ,  $\chi' = \chi h/\gamma_0$ ,  $\eta' = \eta h/\gamma_0 T_0$ . Next, we drop primes for convenience. In our consideration we pay attention onto competition between the local temperature relaxation and energy release due to an adsorbate concentration increase. Main parameters controlling above processes are  $\nu$ ,  $\eta$ ; the quantity  $\nu/\eta$  relates to specific physical systems.

Considering homogeneous system in stationary regime, we obtain a phase diagram  $\alpha(\varepsilon^{-1})$  related to the phase diagram in plane temperature–pressure ( $\varepsilon^{-1} \propto T$ ,  $\alpha \propto p$ ) shown in Fig. 27.1a. Inside the bounded domain, the system is bistable. An increase in the rate  $\beta$  leads to reducing the bistability domain. Under the bistability domain, the monostable system is in the low-density state, whereas above the bounded domain, the high-density state is realized. Hence, at constant pressure (fixed  $\alpha$ ) with an increase in equilibrium temperature  $T_0$ , one has the first-order phase transition from the high-density state toward the low-density state. At constant temperature  $T_0$ , an increase in pressure leads to the first-order phase transition from the low-density state toward the high-density state. The corresponding dependencies of the stationary coverage  $c_{st}$  on  $\varepsilon^{-1}$  and  $\alpha$  are shown in Fig. 27.1a in top and bottom insertions, respectively. Considering stability of the system to inhomogeneous perturbations, we obtain a stability diagram shown in Fig. 27.1b. It is seen that an increase in the rate  $\beta$  extends the domain of patterning (cf. solid and dash curves). In the case of small  $\beta$  and fixed  $\varepsilon_f^{-1} < \varepsilon_0^{-1}$  with an increase in adsorption coefficient  $\alpha$ , one has following changes of the surface morphology (see solid curve in Fig. 27.1b): (i) at small  $\alpha \in [0, \alpha_1)$  the uniform low-density state is realized; (ii) if condition  $\alpha_1 < \alpha < \alpha_2$  holds, then stable adsorbate structures appear; (iii) at  $\alpha > \alpha_2$  the high-density state with uniform distribution of the coverage field is realized. For the limit of constant temperature, the domain of spatially modulated phases is larger comparing to the actual system (cf. solid and dot curves in Fig. 27.1b). This effect is caused by the last term in the total adsorbate flux leading to stabilization of the system. It should be noted that neither thermal conductivity  $\chi$ , reheat efficiency  $\eta$ , nor relaxation time for the temperature field  $\nu$  does influence onto dependencies  $\alpha(\varepsilon^{-1})$  in the linear stability analysis.

According to linear stability analysis, one can choose the system parameters to analyze dynamics of adsorbate temperature field numerically. In our study all numerical simulations were done on the triangular lattice of the size  $L = 12.8L_d$  with periodical boundary conditions. In the case of hexagonal symmetry, there are three wave vectors separated by  $2\pi/3$  angles. This simulation procedure allows one to describe a formation of islands with more symmetrical shape, comparing to ones on square lattice (see discussion in Refs. [41–43]). Therefore, interactions of islands occur preferably in directions of these wave vectors according to the position of nearest neighbors on the lattice. We will fix adsorption coefficient  $\alpha = 0.1$ , interaction energy of adsorbate  $\varepsilon = 3.0$ , rate of stable dimers formation  $\beta = 0.1$ , thermal conductivity  $\chi = 10$  and vary relaxation time for the temperature field  $\nu$ , and reheat efficiency  $\eta$ ;  $r_0 = 0.25$ .

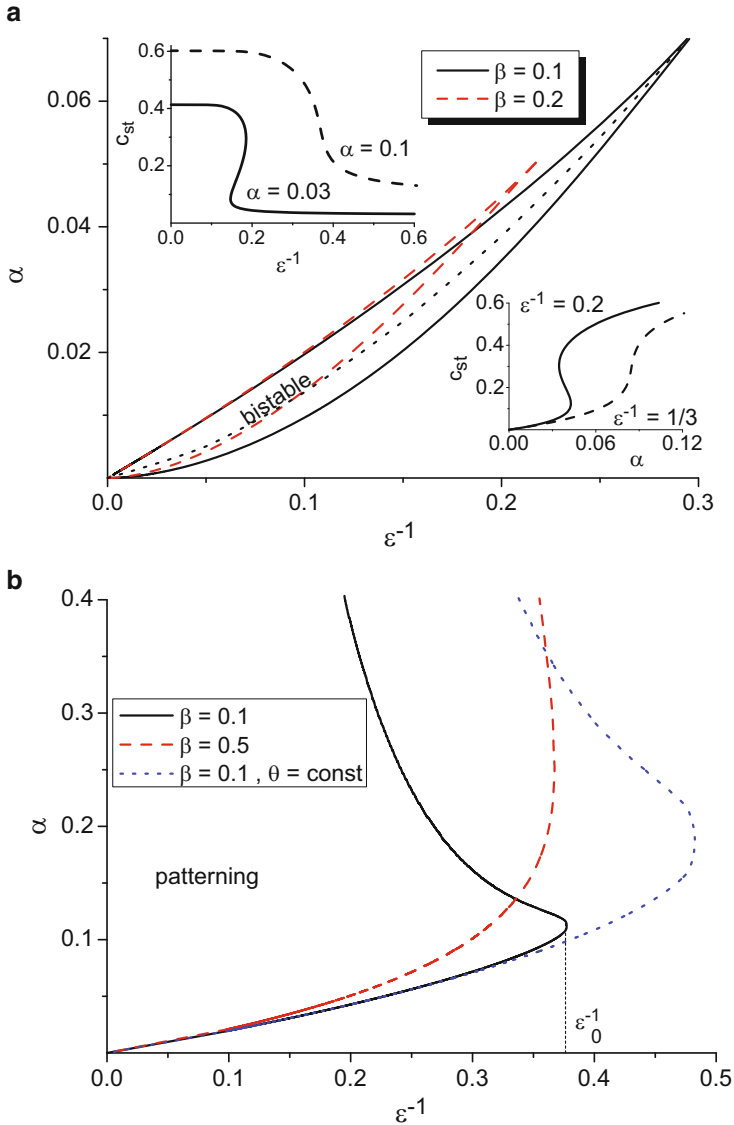


**Fig. 27.1** (a) Phase diagram for homogeneous system. Binodals are shown by *solid* (for  $\beta = 0.1$ ) and *dash* (for  $\beta = 0.2$ ) curves. Dependencies of stationary coverage  $c_{st}(\varepsilon^{-1})$  and  $c_{st}(\alpha)$  are shown in insertions. (b) Stability diagram at different values of nonequilibrium chemical reactions rate  $\beta$

To study dynamics of the adsorbate clusters formation, we consider main statistical moments,  $\langle c(\mathbf{r}, t) \rangle$ ,  $\langle \theta(\mathbf{r}, t) \rangle$ , and corresponding dispersions  $\langle (\delta c(\mathbf{r}, t))^2 \rangle$ ,  $\langle (\delta \theta(\mathbf{r}, t))^2 \rangle$  which can be considered as the corresponding order parameters for patterning of the related fields. Temporal dependencies of  $\langle c \rangle$ ,  $\langle \theta \rangle$ ,  $\langle (\delta c)^2 \rangle$  and

$\langle(\delta\theta)^2\rangle$  are shown in Fig. 27.2 at different values of relaxation time  $\nu$  of temperature field and reheat efficiency  $\eta$ . From obtained numerical results it follows, that both  $\nu$  and  $\eta$  do not influence the averaged coverage  $\langle c(t) \rangle$  shown in insertion in Fig. 27.2a for the case  $\nu = 0.1$  and  $\eta = 0.1$ . The averaged coverage grows in time until it attains the stationary value. The averaged surface temperature increases until it reaches the maximal value and then decreases to the stationary value. It follows that the averaged surface temperature  $\langle \theta \rangle$  depends on both  $\nu$  and  $\eta$  at initial stages of the system evolution.

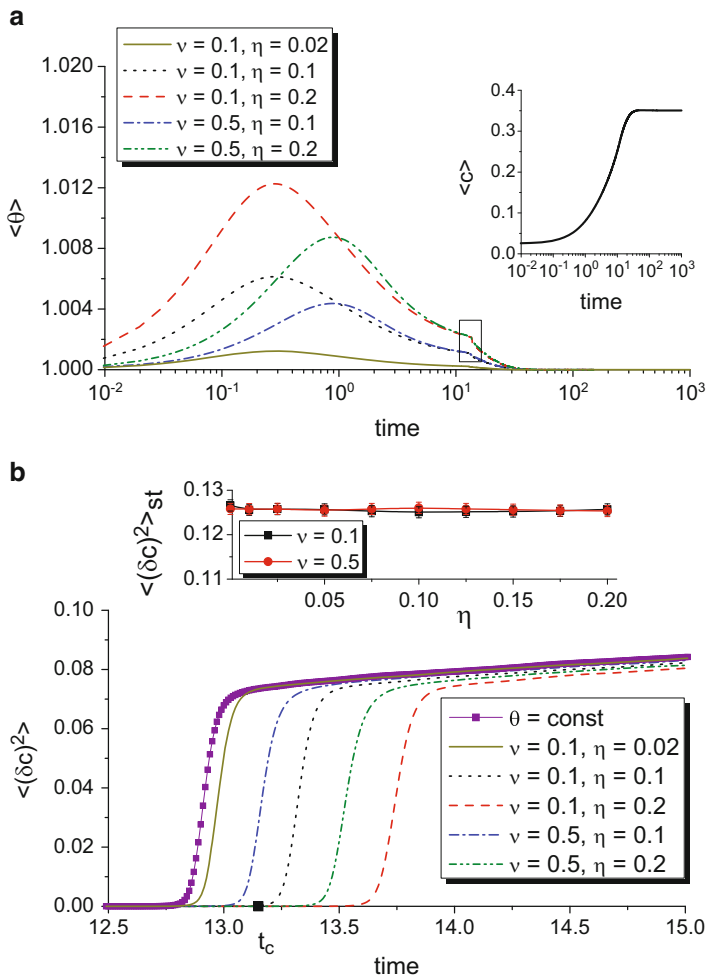


**Fig. 27.2** (Color online) Evolution of: (a) the averaged temperature  $\langle \theta \rangle$  (the averaged coverage  $\langle c \rangle$  is shown in insertion and does not depend essentially on both  $\eta$  and  $\nu$ ); (b) order parameter  $\langle(\delta c)^2\rangle$ ; (c) dispersion of the temperature field  $\langle(\delta\theta)^2\rangle$ . (d) Snapshots of the system evolution (coverage is shown in the left panel; temperature is shown in the right panel) at  $\nu = 0.1$  and  $\eta = 0.2$

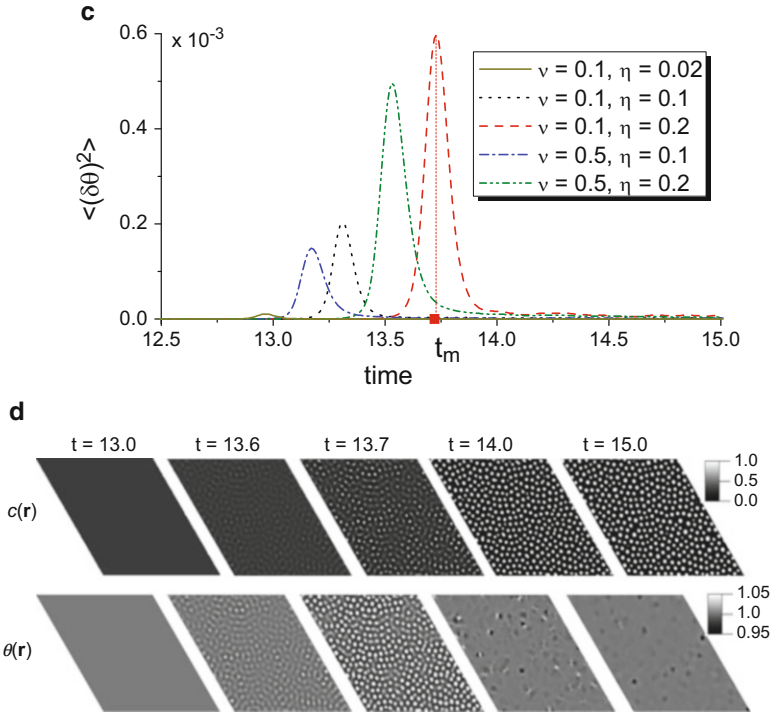


**Fig. 27.2** (continued)

Considering transient dynamics of  $\langle\theta(t)\rangle$  it follows that with an increase in the reheat efficiency  $\eta$  the maximal value of the averaged surface temperature increases (see solid, dot and dash curves for small  $\nu$ ; dash-dot and dash-dot-dot curves for elevated  $\nu$ ). An increase in  $\nu$  leads to a decrease in the maximal value of  $\langle\theta\rangle$ . Moreover, at elevated  $\nu$  surface temperature reaches its maximum later than at small  $\nu$ . The transient regime of  $\langle\theta(t)\rangle$  to the stationary value is characterized by the step-like form (see marked region in Fig. 27.2a). After the step the averaged surface temperature monotonically tends to  $\theta_{st} = 1$  depending on reheat efficiency  $\eta$  but not relaxation time  $\nu$ . Considering dynamics of the order parameter  $\langle(\delta c)^2\rangle$  shown in Fig. 27.2b it follows that at  $t > t_c$  interactions of adatoms lead to formation of separated adatom clusters. At further system evolution the order parameter  $\langle(\delta c)^2\rangle$  increases, small islands disappear and large ones grow in time. At large times  $\langle(\delta c)^2\rangle$  takes constant value indicating a realization of stationary pattern. From Fig. 27.2b it follows, that with an increase in reheat efficiency  $\eta$  the critical time  $t_c$  increases meaning a delay in the ordering processes. An increase in the relaxation time  $\nu$  at fixed  $\eta$  acts in opposing manner. In the stationary limit both  $\eta$  and  $\nu$  do not affect the order parameter  $\langle(\delta c)^2\rangle$  (see insertion in Fig. 27.2b). From the obtained numerical data for the dispersion of the temperature field shown in Fig. 27.2c it follows, that in the time interval  $t \in [0, t_c)$  one has  $\langle(\delta\theta)^2\rangle \simeq 0$  and, therefore, temperature does not essentially differ at any point of the surface. Starting from the

threshold  $t = t_c$  the quantity  $\langle(\delta\theta)^2\rangle$  starts to grow. It means that it is possible to distinguish domains characterized by elevated and lower temperature. At the time instant  $t = t_m$  a dispersion of the temperature field takes the maximal value and next it decreases toward zero. Hence, one can conclude that the ordering processes of the temperature field are reentrant. They are realized in a narrow time interval, when adsorbate structures are form and reorganize. It follows, that an increase in  $\eta$  leads to delay of the ordering processes and increases the maximal value of the quantity  $\langle(\delta\theta)^2\rangle$ ; relaxation time  $\nu$  acts in opposing manner.

Snapshots of the system evolution at time domain corresponding to the marked region in Fig. 27.2a are shown in Fig. 27.2d (see dash curve in Fig. 27.2a–c). It is seen, that at time instant  $t < t_c$  no spatial instabilities on both coverage and temperature fields are realized. Both fields are homogeneously distributed (see snapshots at  $t = 13.0$ ). With an increase in exposing time self-organization processes start to play a major role and at  $t = t_c$  with  $t_c \simeq 13.6$  one observes small clusters of adsorbate (see panel  $c(\mathbf{r})$ ). These clusters are hotter than substrate (see distribution of the temperature field in the right column in Fig. 27.2d at  $t = 13.6$ ). At the time instant  $t = t_m$ , with  $t_m \simeq 13.7$ , mean size of adsorbate islands grows and the temperature of adsorbate clusters increases comparing to the substrate temperature. With further exposing the temperature of the surface layer becomes homogeneously distributed. Therefore, both reheat efficiency  $\eta$  and relaxation time of the temperature field  $\nu$  govern transient dynamics of pattern formation at vapor deposition.

Evolution of the averaged linear size  $\langle R \rangle$  of adsorbate spherical islands in units of diffusion length, and the averaged number of adsorbate clusters  $\langle N \rangle$  at different values of  $\eta$  and  $\nu$  are shown in Fig. 27.3a, b, respectively. From obtained results it follows, that both dependencies  $\langle R(t) \rangle$  and  $\langle N(t) \rangle$  can be divided into two stages: (i) islands formation and (ii) coarsening. It is seen that the adsorbate islands formation stage is characterized by the power-law dependence  $\langle R \rangle \sim t^{0.82}$  independently on both  $\eta$  and  $\nu$ . At the same time the averaged number of adsorbate clusters here falls down in the power-law form  $\langle N \rangle \sim t^{-1.44}$ . It follows that an increase in  $\eta$  leads to a decrease in a linear size and to an increase in a number of islands;  $\nu$  acts in opposing manner. In the stationary limit both these parameters do not affect crucially the averaged liner size of adsorbate islands  $\langle R \rangle \simeq 0.53L_d$  and their number  $\langle N \rangle \simeq 70$ . Previously it was shown that the linear size of spherical adsorbate islands depends on adsorption coefficient, nonequilibrium chemical reaction rate, and adatom interaction strength [42].

Finally, let us study distributions  $f(R)$  at different values of  $\eta$  and  $\nu$  in the stationary limit shown in Fig. 27.4. By using fitting procedure, we have found that: (i) at  $\eta/\nu \ll 1$  ( $\theta = const$ ) the stationary distribution is characterized by the Lorentzian; (ii) if  $\eta/\nu < 1$  (adsorption/desorption processes weakly influence surface temperature), then the distribution of adsorbate clusters becomes broadened (see filled circles and diamonds); (iii) if relation  $\eta/\nu \geq 1$  holds (reheat of the surface leads to reorganization of adsorbate islands), then the distribution of adsorbate islands over sizes corresponds to Gaussian distribution (see filled and empty triangles).



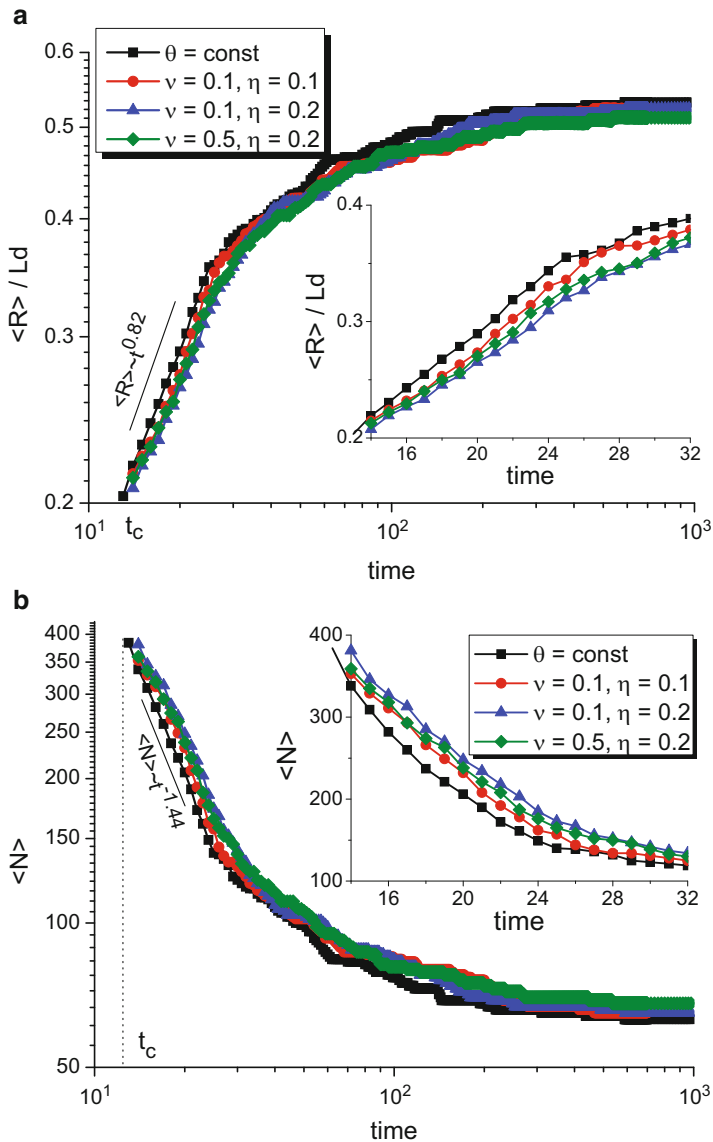


**Fig. 27.3** (Color online) Evolution of (a) the averaged linear size (radius) ( $R$ ) of adsorbate spherical islands in units of diffusion length; (b) the averaged number of adsorbate clusters ( $N$ ) at different values of  $\eta$  and  $\nu$

To estimate linear size of adsorbate islands, we consider a prototype system  $Ge/Si(100)$ , where the activation energy of adatom formation is  $E_a = 0.6$  eV,  $E_d = 1.3$  eV is the activation energy for desorption,  $E_D = 0.65$  eV is the activation energy for diffusion, and  $\omega = 10^{12} \text{ s}^{-1}$  is the lattice oscillation frequency. Using

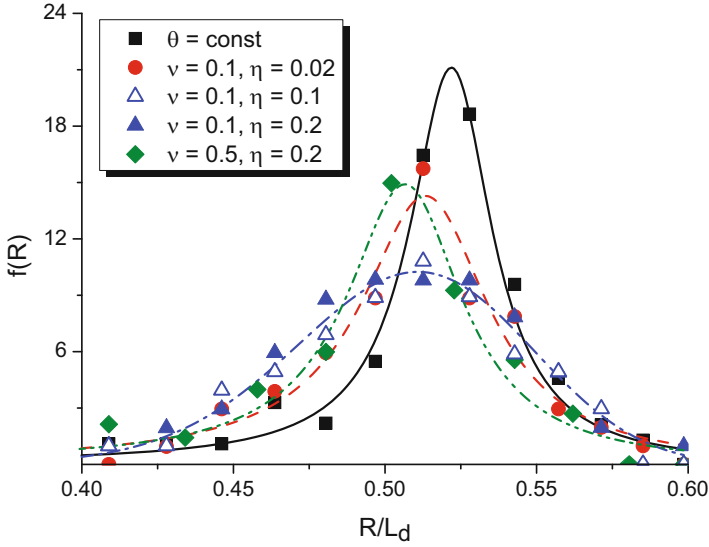


**Fig. 27.4** (Color online) Stationary distributions of adsorbate islands sizes at  $t = 1000$  and different  $\eta$  and  $\nu$

lattice constant  $a = 5.6 \times 10^{-10}$  m for *Ge* and taking adatom interaction energy  $\epsilon \approx 0.27$  eV at temperature  $T_0 = 773$  K, one gets:  $\tau_d = \omega^{-1} e^{E_d/T_0} \approx 3 \times 10^{-4}$  s,  $D = a^2 \omega e^{-E_d/T_0} \approx 1.8 \times 10^{-9}$  m<sup>2</sup>/s,  $L_d = 7.4 \times 10^{-8}$  m. According to obtained data for the mean linear size (radius) of adsorbate islands, we get  $\langle R \rangle \approx 0.53 L_d \approx 40$  nm.

## 27.4 Temperature Effects at Point Defects Patterning

In this section we pay attention on studying influence of local temperature variation onto formation of nano-sized clusters of point defects. By considering point defect rearrangement in a surface layer of irradiated thin foils of the thickness  $\sim 0.5$   $\mu$ m in an environment characterized by a constant temperature  $T_0$ , one deals with concentrations  $c_{v,i}(\mathbf{r}, t)$  of vacancies  $v$  and interstitials  $i$  obeying following set of equations

$$\partial_t c_{v,i} = \mathcal{K} - \beta_{v,i} c_{v,i} - \alpha c_i c_v - \nabla \cdot \mathbf{J}_{v,i}. \quad (27.4)$$

Here  $\mathcal{K}$  is the defect production rate;  $\beta_{i,v} = \rho_d D_{i,v}$  is the inverse lifetime of defects of  $i/v$  type defined through the dislocation density  $\rho_d$ , and diffusion coefficient  $D_{i,v}$ ,  $c_v^0$  is the equilibrium vacancy concentration;  $\alpha = 4\pi r_0 (D_i + D_v) / \Omega$  is the recombination rate defined through the atomic volume  $\Omega$  and the interaction radius  $r_0$  taken as initial vacancy loop radius. As far as  $D_i/D_v \gg 1$ , therefore, one can

exclude fast variable  $c_i$  by assuming  $\partial_t c_i \simeq 0$ . By taking into account homogeneous distribution of interstitials, one can neglect contribution of  $\mathbf{J}_i$  and exclude interstitial concentration adiabatically.

Defects production leads to deformation of the surface layer depending on the defect concentration [31]. It causes deformation-induced motion of defects resulting in determination of the diffusion flux of vacancies in the form  $\mathbf{J}_v = -D_v \nabla c_v + \nu \theta_d^2 \sigma_{||}^{-1} c_v D_v T^{-1} (\nabla \mathcal{L} c_v - \mathcal{L} c_v T^{-1} \nabla T)$ . Here  $\theta_d \equiv \Omega K$  is the strain potential of defect;  $K$  is the elasticity modulus;  $\mathcal{L} \equiv (1 + l_{||}^2 \Delta)$ ;  $\nu \in [0, 1/2]$  is the Poisson ratio ( $\nu \simeq 0.3$  for metals);  $c_{||}^2 = \sigma_{||}/\rho$  is the bending stiffness;  $\rho$  is the density;  $\sigma_{||}$  is the tensile isotropic stress in the defect-enriched surface layer of the height  $h$ ;  $l_{||} = h/2\sqrt{3}$ . The first part in the vacancy flux is responsible for free diffusion; the second one relates to deformation-induced transport.

Due to defect rearrangement, one gets the sample temperature change due to heating, production of defects, and their annihilation (a range of ionizing particles is smaller than thickness of the sample). A local increase in the sample temperature results in defects annealing. It leads to defect energy release into a heat increasing the temperature of the sample. As a result a number of defects decreases with increasing the heat transfer. Next, the sample cools, heat transfer decreases, and new defects accumulate. A repetition of this scenario leads to self-oscillations of the sample temperature and point defects concentration. According to above shown mechanisms of temperature change, one can write an evolution equation for the temperature of a sample in the form:

$$C\rho\partial_t T = \chi\Delta T - \frac{\gamma_0}{h}(T - T_0) + \zeta E_f \mathcal{K} + E_f[\beta_v(c_v - c_v^0) + \alpha c_i c_v], \quad (27.5)$$

where  $\zeta \gg 1$  is the ratio of energy of irradiation which transforms into heating and energy of irradiation which transforms into defect generation;  $E_f$  is the energy of defect formation; the last term defines energy release when defects are captured by dislocations and due to recombination with interstitials. Here we assume that a substrate for the layer location does not affect the irradiation influence, or its influence on substrate is negligibly small and is not considered. This assumption is valid only if the thickness of foils is larger than the ionization depth (low intensities of laser pulses or low energy of bombarding particles).

According to the relation  $D_i/D_v \gg 1$ , one can use  $\mu \equiv \alpha/\beta_i$  as a temperature-independent scaling quantity. Measuring time in units of vacancy lifetime  $\tau_d \equiv (\rho_d D_v^0)^{-1}$ , spatial coordinate in units  $L_D \equiv (\rho_d)^{-1/2}$ , one can introduce dimensionless quantities  $t' \equiv t/\tau_d$ ,  $\mathbf{r}' \equiv \mathbf{r}/L_D$ ,  $\ell \equiv l_{||}/L_D$ ,  $\epsilon \equiv \nu \theta_d^2 / \mu \sigma_{||} T_0$ ,  $\Theta \equiv T/T_0$ ,  $P \equiv \mu \mathcal{K} \tau_d$ ,  $\eta \equiv C\rho h / \tau_d \gamma_0$ ,  $\kappa \equiv \chi h / L_D^2 \gamma_0$ ,  $\varpi \equiv E_f h / T_0 \mu \tau_d \gamma_0$ ,  $\varepsilon \equiv E_v / T_0$ . To study the much more realistic system, we use the typical set of the system parameters:  $\mathcal{K} \sim 10^{-3}$  dpa/s,  $T_0 \in [300, 900]$  K,  $L_D \simeq 10^{-7}$  m,  $\tau_d \simeq 10^{-6}$  s,  $E_f = 1.6$  eV,  $\eta = 100$ ,  $\kappa = 1$ ,  $\ell = 0.7$ ,  $\zeta = 7$ ,  $\varpi = 0.1$ , and  $\mu \simeq 10^8$ .

In linear stability analysis by considering  $\mathcal{K}$  and  $T_0$  as independent parameters, one can obtain phase diagram illustrating domain, where short-time spatial instabilities emerge in the vicinity of the homogeneous stationary state  $c_{st}$  (see

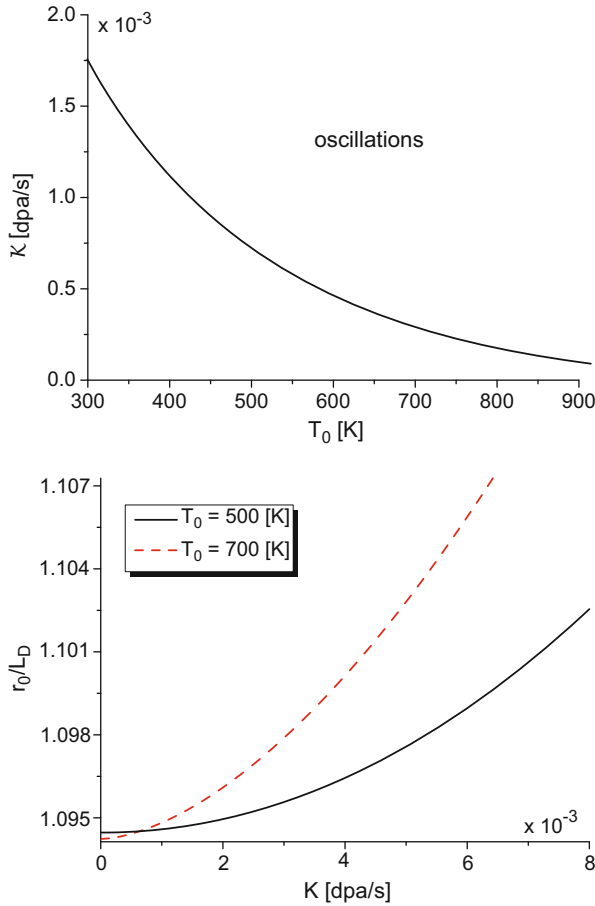


**Fig. 27.5** (a) Phase diagram for linear stability analysis. Domain of oscillatory dynamics is above the *solid curve*. (b) Dependencies of period of patterns calculated at different  $T_0$

Fig. 27.5a). According to obtained results one finds that oscillatory dynamics is realized at values of  $\mathcal{K}$  and  $T_0$  lying above the solid line. This oscillatory dynamics corresponds to pattern selection processes, when during the system evolution it selects among others only pattern characterized by most unstable mode. According to obtained data for the most unstable mode, one can estimate period of patterns  $r_0$  (see Fig. 27.5b). It is seen that with an increase in the rate  $\mathcal{K}$  the period of patterns slightly increases. Exposing (irradiating) the target at elevated environment temperature  $T_0$ , one can generate patterns with larger period.

In numerical simulations we study the system on a quadratic grid  $L \times L$  with  $L \simeq 9.2L_D$  and periodic boundary conditions. Typical patterns of both defect concentration field and temperature of the target at different times are shown in Fig. 27.6a, b at  $\mathcal{K} = 3 \times 10^{-3}$  dpa/s and  $\mathcal{K} = 5 \times 10^{-3}$  dpa/s, respectively. It is well

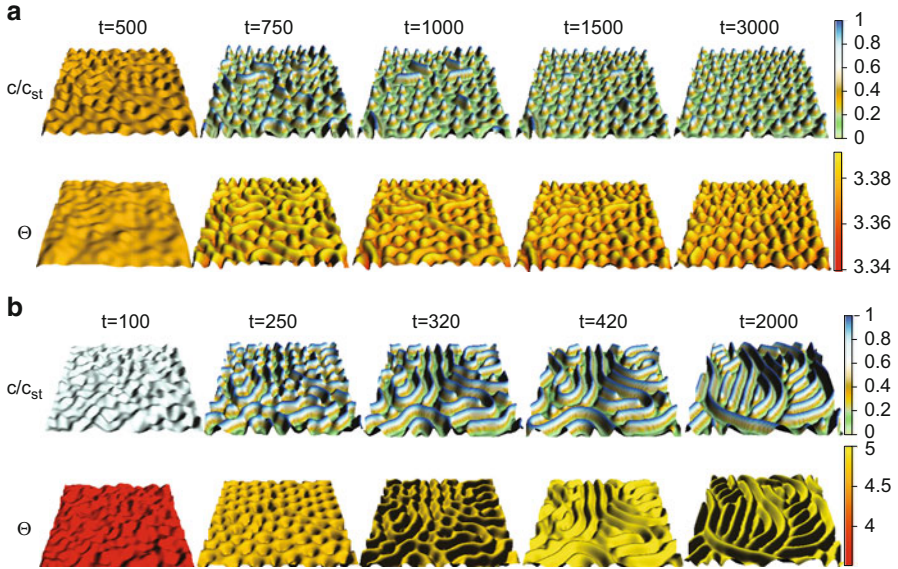


**Fig. 27.6** Snapshots of vacancy concentration field  $c/c_{st}$  and temperature field  $\Theta$  at  $T_0 = 500$  K: (a)  $\mathcal{H} = 3 \cdot 10^{-3}$  dpa/s; (b)  $\mathcal{H} = 5 \cdot 10^{-3}$  dpa/s

seen that during the system evolution, one can observe formation of vacancy patterns with nonuniform distribution of the temperature field. The local temperature is larger in domains with vacancy clusters. Comparing patterns at different damage rates, one finds that morphology of patterns depends essentially on the damage rate  $\mathcal{H}$ . At lower  $\mathcal{H}$  one gets dot-like patterns, where vacancies are concentrated in spherical clusters forming voids/holes on the surface of the target. Increasing the damage rate, one induces a formation of nonequilibrium vacancies able to form elongated clusters transformed into ripples. Analysis of the obtained patterns and the corresponding protocols for mean vacancy concentrations, mean temperature, and the corresponding dispersions allows one to elucidate that obtained numerical results for point defect patterning are well related to well-known theoretical and experimental studies concerning this problem (see, for example, Refs. [44–47]).

In order to illustrate spatial oscillations indicating pattern selection processes, let us consider a structure function as a Fourier transform of a two-point correlation function. In our computations we use spherically averaged structure function  $S_c(k, t)$ . Its dependence at fixed time moments at different damage rates is shown in Fig. 27.7a. Here one can see the main peak at small wave-number  $k$  related to period of spatial patterns and weak oscillations at large  $k$  (see insertion in Fig. 27.7a). These oscillations mean that the system selects structures with different lengths (spherical and non-spherical structures). At large time interval these oscillations disappear and only major peak remains. It means that structures with fixed length scale are selected. At the top of Fig. 27.7a typical snapshots of the defect concentration

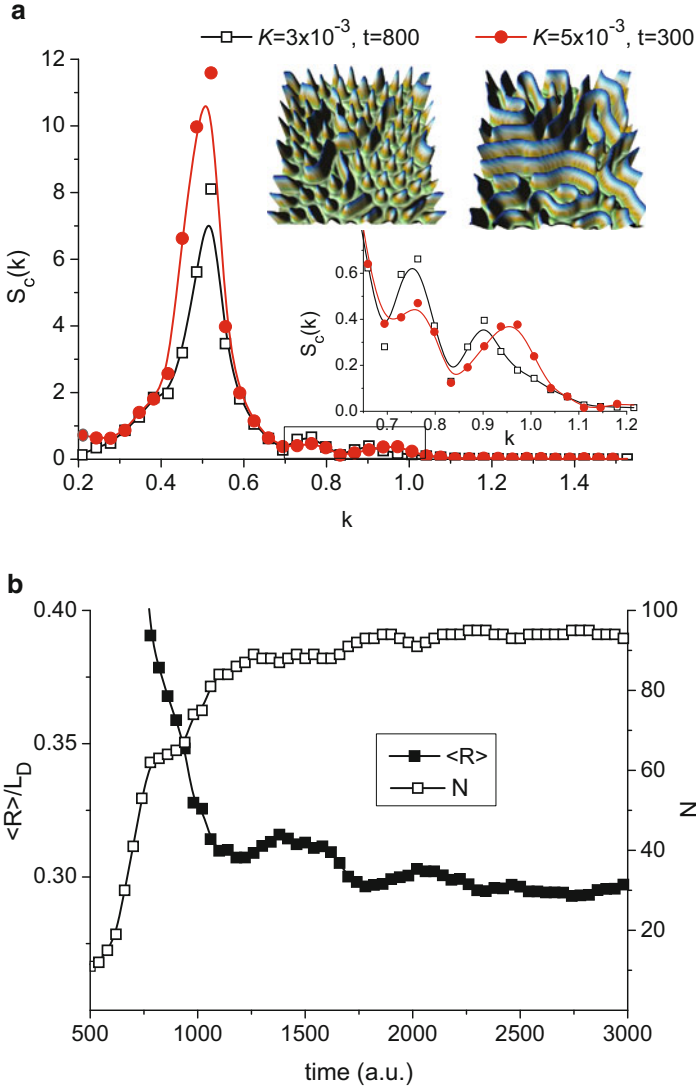


**Fig. 27.7** (a) Structure function  $S_c(k)$  illustrating pattern selection processes. Curves are obtained at  $T_0 = 500$  K and  $\mathcal{K} = 3 \cdot 10^{-3}$  dpa/s,  $t = 800$  (line with empty squares),  $\mathcal{K} = 5 \cdot 10^{-3}$  dpa/s,  $t = 300$  (line with filled circles). Corresponding configurations of vacancy concentration are shown at the top. (b) Evolution of the mean radius  $\langle R \rangle$  of spherical vacancy clusters (filled squares) with the corresponding number of clusters (empty squares) at  $\mathcal{K} = 3 \cdot 10^{-3}$  dpa/s and  $T_0 = 500$  K

field at different damage rate are shown. From the obtained results it follows that pattern selection processes are well related to dynamics of the sample temperature coupled with the defect concentration. In our previous studies it was shown that these processes in systems with constant temperature were related

to finite propagation speed of atomic disturbances, i.e., when diffusion flux is a time-dependent quantity [48–51]. Described oscillations of the mean vacancy concentration and temperature of the studied system were studied previously in a homogeneous limit [52]. Experimental results concerning oscillations of resistivity related to mean vacancy concentration in a copper samples irradiated with electrons were discussed in Ref. [53]. Our numerical data relate quantitatively well to the abovementioned theoretical and experimental results.

Finally, let us study dynamics of a mean radius of vacancy islands  $\langle R(t) \rangle$  and their number  $N(t)$  shown in Fig. 27.7b. According to obtained data, a behavior of both  $\langle R(t) \rangle$  and  $N(t)$  illustrates that pattern formation starts from organization of small amount of vacancy clusters having large characteristic lengths. These initial clusters are of elongated form. During the system evolution these structures break into small ones: some of them dissolve, some new clusters can emerge due to interactions in supersaturated vacancy ensemble. With an increase in the irradiation dose, most of the clusters become identical and are characterized by the constant averaged radius at large time scales. This stationary averaged radius is less than diffusion length  $L_D$ . To estimate  $\langle R \rangle$  we take  $L_D \simeq (\rho_d)^{-1/2}$  with  $\rho_d \simeq 10^{14} \div 10^{12} \text{ m}^{-2}$ . It gives typical size of vacancy clusters  $\langle R \rangle \simeq 0.3L_D \simeq 30 \div 300 \text{ nm}$ ; the related distance between them is around diffusion length. Dynamics of  $\langle R \rangle$  is accompanied by an increase in the number of islands toward the corresponding stationary value. Considering dependencies  $\langle R(t) \rangle$  and  $N(t)$  in detail, one finds oscillatory behavior of the mean radius and number of islands. Obtained oscillatory behavior of vacancy cluster size qualitatively relates to well-known experimental observation of vacancy cluster oscillations in nickel samples irradiated with self-ions discussed in Refs. [53, 54].

## 27.5 Conclusions

We have considered effects of temperature influence onto dynamics of patterning with formation of nano-sized objects during vapor deposition and particle irradiation of thin foils. It was shown that local variations in the temperature field are able to change dynamics leading to delaying pattern formation processes and emergence of oscillatory behavior of observable quantities.

By considering adsorptive system where local changes in the surface layer temperature are caused by adsorption/desorption processes, we have found a domain of reduced pressure of gaseous phase and equilibrium temperature, when first-order phase transitions type of gas–solid can be realized. We have shown that local changes in surface temperature lead to shrink the domain of main system parameters, when pattern formation is possible. By using numerical simulations, we have shown that a competition between temperature relaxation and reheat processes affects the behavior of the system at stages of adsorbate islands formation: increase in reheat efficiency leads to delay in ordering processes; relaxation time of surface temperature acts in opposing manner. At narrow time interval, when adsorbate islands start to organize, their temperature increases comparing to the substrate, that

leads to pattern formation in temperature field. A competition between relaxation and reheat processes defines the form of adsorbate sizes distribution. Estimation of the linear size of stationary adsorbate islands gives typical size of islands  $\simeq 40$  nm.

By considering spatiotemporal evolution of both vacancy concentration and temperature of irradiated surface layer by high-energy particles, it was shown that pattern selection processes are realized due to coupling between defect concentration and surface layer temperature. It was found that pattern selection processes are accompanied by decaying oscillatory dynamics of dispersions of both vacancy concentration and temperature. We have shown that morphology of vacancy islands emergent due to generation of nonequilibrium defects and nonlinear dynamics of the system can be controlled by positive feedback of the surface layer temperature, defect production rate, and environment temperature. At low defect production rate, spherical vacancy islands (holes) are realized, whereas at elevated defects rate, elongated patterns (type of ripples) emerge. Using typical data for bcc metals irradiated by self-ions (with damage rate  $\simeq 10^{-3}$  dpa/s), it was shown that the averaged size of vacancy islands varies in the interval  $30 \div 300$  nm depending on the defect production rate.

We expect that our nontrivial findings can be used to manufacture surface nano-sized structures at vapor deposition, irradiation by laser pulses, or particle irradiation and will stimulate further theoretical and experimental studies of nano-sized pattern formation.

## References

1. Wadley HNG, Zhou X, Johnson RA et al (2001) *Prog Mater Sci* 46:329
2. Sree Harsha KS (2006) *Principles of physical vapor deposition of thin films*. Elsevier, London
3. Perotto G, Bello V, Cesca T et al (2010) *Nucl Instr Meth Phys Res B* 268:3211
4. Bernas H (2010) *Nucl Instr Meth Phys Res B* 268:3171
5. Mark Bradley R, Harper JME (1988) *J Vac Sci Technol A* 6(4):2390
6. Karmakar P (2013) *Nanostructures in thin films by keV ion beams*. In: Som T, Kanjilal D (eds) *Nanofabrication by ion-beam sputtering*. Taylor&Francis Group/LLC, Boca Raton
7. Lian J, Zhou W, Wei QM et al (2006) *Appl Phys Lett* 88:093112
8. Kharchenko DO, Kharchenko VO, Lysenko IO et al (2010) *Phys Rev E* 82:061108
9. Kharchenko VO, Kharchenko DO (2011) *Cond Mat Phys* 14(N2):23602
10. Yutakam Y, Norihito S, Seiichi W et al (2011) *Appl Phys Expr* 4(5):055202
11. Huang SM, Hong MH, Lu YF et al (2002) *J Appl Phys* 91(5):3268
12. Lu Y, Chen SC (2003) *Nanotechnology* 14:505
13. Venables JA, Spiller GDT, Hanbücken M (1984) *Rep Prog Phys* 47:399
14. Pimpinelli A, Villian J (1998) *Physics of crystal growth*. Cambridge University Press, Cambridge
15. Caffisch RE (2006) *Proceedings of the international congress of mathematicians, Madrid*, p 1419
16. Kharchenko DO, Kharchenko VO, Lysenko IO (2011) *Phys Scr* 83:045802
17. Kharchenko DO, Kharchenko VO, Zhylenko TI et al (2013) *Eur Phys Jour B* 86(4):175
18. Kharchenko DO, Kharchenko VO, Kokhan SV (2014) *Cond Mat Phys* 17:33004
19. Kharchenko VO, Kharchenko DO, Dvornichenko AV (2015) *Eur Phys Jour B* 88:3
20. Mikhailov A, Ertl G (1994) *Chem Phys Lett* 238:104



21. Batogkh D, Hildebrand M, Krischer F, Mikhailov A (1997) *Phys Rep* 288:435
22. Hildebrand M, Mikhailov AS, Ertl G (1998) *Phys Rev Lett* 81(4):2602
23. Hildebrand M, Mikhailov AS, Ertl G, (1998) *Phys Rev E* 58(11):5483
24. Mangioni SE, Wio HS (2005) *Phys Rev E* 71:056203
25. Mangioni SE (2010) *Phys A* 389:1799
26. Casal SB, Wio HS, Mangioni S (2002) *Phys A* 311:443
27. Wolgraef D (2002) *Phys E* 15:33
28. Wolgraef D (2004) *Int J Quantum Chem* 98:248
29. Kharchenko VO, Kharchenko DO, Dvornichenko AV (2016) *Phys A* 444:689
30. Emel'yanov VI (2006) *Quantum Electron* 36(6):489
31. Emel'yanov VI (2009) *Laser Phys* 19:538
32. Emel'yanov VI, Seval'nev DM (2011) *Laser Phys* 21:566
33. Kharchenko DO, Kharchenko VO, Bashtova AI (2016) *Phys A* 463:152
34. Steel JK, Potter DI (1995) *J Nucl Mat* 218:95
35. Carpenter JM (1987) *Nature* 36:358
36. Varatharajan K, Nandedkhar RV (1989) Microhardness-microstructure study of aged Nimonic 90 irradiated with helium In: Stoller RE (ed) *Effects of radiation on materials*. ASTM, Philadelphia, pp 263–270
37. Farnum EH, Clinard FW Jr, Sommer WF et al (1994) *J Nucl Mat* 1128:212–215
38. Schule W (1996) *J Nucl Mat* 964:233–237
39. Sen P, Aggarwal G, Tiwari U (1998) *Phys Rev Lett* 80:1128
40. Kharchenko VO, Kharchenko DO, Kokhan SV, Vernyhora IV, Yanovsky VV (2012) *Phys Scr* 86:055401
41. Kharchenko VO, Kharchenko DO (2012) *Phys Rev E* 86:041143
42. Kharchenko VO, Kharchenko DO, Dvornichenko AV (2014) *Surf Sci* 630:158
43. Kharchenko VO, Kharchenko DO (2015) *Surf Sci* 90:637–638
44. Krishan K (1983) *Rad Eff* 66:121
45. Abromeit C (1989) *Int J Modern Phys B* 3:1301
46. Cahn RW, Haasen P (1996) *Physical metallurgy*. Elsevier Science B.V., Amsterdam/Lausanne/New York/Oxford/Shannon/Tokyo
47. Was GS (2007) *Fundamentals of radiation material science*. Springer, Berlin/Heidelberg
48. Galenko PK, Kharchenko D, Lysenko I (2010) *Phys A* 389:3443
49. Kharchenko D, Kharchenko V, Lysenko I (2011) *Centr Eur J Phys* 9(3):698
50. Kharchenko DO, Lysenko IO, Kharchenko VO (2010) *Ukr J Phys* 55(N11):1225
51. Kharchenko D, Lysenko I, Galenko PK (2011) Fluctuation effects on pattern selection in the hyperbolic model of phase decomposition. In: Halidias N (ed) *Stochastic differential equations*. Nova Science, New York, pp 97–127
52. Selischev PA, Sugakov VI (1995) *Rad Eff Def Solids* 237:133
53. Schule W (1996) *J Nucl Matter* 964:233–237
54. Steele JK, Potter DI (1995) *J Nucl Matter* 218:95

# Chapter 28

## The Effect of the Fermi Velocity on the Conductivity of the Graphene-Superconductive Graphene Junction

A. M. Korol, S. I. Litvynchuk, N. V. Medvid, and V. M. Isai

### 28.1 Introduction

In recent years, much attention has been paid to the study of graphene and various graphene-based structures. This is due to nontrivial properties of graphene, such as a linear dispersion law for the quasiparticles, whose behavior at low energies is described by an equation similar to the Dirac-Weyl one, unusual quantum Hall effect, the property of chirality, the Klein tunneling, high mobility, ballistic transport, etc. [1, 2]. It should also be borne in mind that graphene is a promising material in modern electronics in terms of replacing the silicon technology, the development of which has reached its limit, for the graphene one. One of the priority directions is to study the various possibilities of controlling the energy spectrum of the graphene-based structures.

Recently one new method for this purpose was proposed. The Fermi velocity of charge carriers in these structures is made to vary in space by some special techniques, e.g., by placing a grounded metal plane close to graphene sheet (which makes electron-electron interactions weaker and thereby modifies the Fermi velocity), by the appropriate doping, imprinting on graphene a lateral superlattice with hexagonal symmetry. The electron wave propagation in the graphene-based structures with the tunable Fermi velocity was investigated in [3–11] including the effect of the magnetic and the electric field. At the same time, the pristine

---

A.M. Korol (✉)

Laboratory on Quantum Theory in Linköping, ISIR, P.O. Box 8017, S-580, Linköping, Sweden

National University for Food Technologies, Volodymyrska str. 68, Kyiv, Ukraine

e-mail: [korolam@ukr.net](mailto:korolam@ukr.net)

S.I. Litvynchuk • N.V. Medvid • V.M. Isai

National University of Food Technologies, Volodymyrska str. 68, Kyiv, Ukraine

© Springer International Publishing AG 2017

O. Fesenko, L. Yatsenko (eds.), *Nanophysics, Nanomaterials, Interface Studies, and Applications*, Springer Proceedings in Physics 195,

DOI 10.1007/978-3-319-56422-7\_28

graphene can also be induced by the external forces to become the superconducting material, for example, superconductivity can be induced in a graphene layer in the presence of a superconducting electrode near it due to the proximity effect. That's why a lot of works were devoted to exploring of the properties of such structures as the graphene-superconductive graphene, graphene-insulator-superconductive graphene, and graphene-based Josephson junctions. However, the effect of tuning of the Fermi velocity on the characteristics of these contacts has not been investigated so far. Motivated by these circumstances, in this paper we consider the normal graphene-superconductive graphene (NG-SG) contact with various values of the Fermi velocity and analyze its transmission properties.

## 28.2 Model and Formulae

Let the normal and the superconductive parts of the junction studied be placed along the  $0x$  axis so that their interface locates at a point  $x = 0$ . The superconducting order parameter has the form

$$\Delta(x) = \Delta_S e^{i\varphi} \Theta(x) \quad (28.1)$$

where  $\varphi$  is the superconductive phase and  $\Theta(x)$  is the Heaviside unit step function. The eigenfunctions which describe the quasiparticle in this system are subjected to the Dirac–Bogolyubov–de Jennes equation

$$\begin{bmatrix} H - U(x) & \Delta(x) \\ \Delta^*(x) & -H + U(x) \end{bmatrix} \Psi(x) = E\Psi(x) \quad (28.2)$$

where  $H = -i\hbar v_F(\sigma_x \partial_x + \sigma_y \partial_y)$  is the Dirac Hamiltonian,  $U$  the external electrostatic potential applied to the superconducting region,  $v_F$  the Fermi velocity, and  $\sigma_x, \sigma_y$  Pauli matrices for the pseudospin. The solution of Eq. (28.2) is the four-component electron and hole spinors which are of the following form:

In NG region

$$\begin{aligned} \Psi_N(x) = & \begin{pmatrix} 1 \\ e^{i\Theta_N} \\ 0 \\ 0 \end{pmatrix} e^{ik_N e x} + r_n \begin{pmatrix} 1 \\ -e^{-i\Theta_N} \\ 0 \\ 0 \end{pmatrix} e^{-ik_N e x} \\ & + r_a \begin{pmatrix} 0 \\ 0 \\ 1 \\ e^{i\Theta_N} \end{pmatrix} e^{-ik_N h x} \end{aligned} \quad (28.3)$$

In SG region

$$\begin{aligned}
\Psi_S(x) &= t \begin{pmatrix} 1 \\ e^{i\Theta_S} \\ e^{-i\beta} e^{-i\varphi} \\ e^{i\Theta_S} e^{-i\beta} e^{-i\varphi} \end{pmatrix} e^{ik_S x - kx} \\
&+ t' \begin{pmatrix} 1 \\ -e^{-i\Theta_S} \\ e^{i\beta} e^{-i\varphi} \\ -e^{-i\Theta_S} e^{i\beta} e^{-i\varphi} \end{pmatrix} e^{-ik_S x - kx} \\
k_{Ne(h)} &= \frac{\cos \Theta_{Ne(h)}}{v_{FN}} \sqrt{[E_{FN} + (-)E]^2 - \Delta_N^2} \\
k_S &= (E_{FN} + U) \frac{\cos \Theta_S}{v_{FS}} \\
k^{-1} &= \frac{v_{FS}^2 k_S}{(U + E_{FN}) \Delta_S \sin \beta} \\
\beta &= \cos^{-1} \left( \frac{E}{\Delta_S} \right) \text{ if } |E| < \Delta_S \\
\beta &= -i \cosh \left( \frac{E}{\Delta_S} \right) \text{ if } |E| > \Delta_S
\end{aligned} \tag{28.4}$$

Units  $\hbar = v_0 = 1$  are adopted,  $v_0$  being the Fermi velocity in the pristine graphene.

The coefficients in (28.3 and 28.4) can be found by applying the following appropriate boundary conditions on the wave functions:

$$\sqrt{v_{FN}} \Psi_N(x=0) = \sqrt{v_{FS}} \Psi_S(x=0) \tag{28.5}$$

As a result we obtain for the coefficients of the Andreev and normal reflections, respectively,

$$r_a(E, \Theta_N, E_{FN}, U) = \frac{v(E)u(E)e^{-i\varphi} A_5(\Theta_N, E_{FN}, U) A_6(\Theta_N, E_{FN}, U)}{B(E, \Theta_N, E_{FN}, U)} \tag{28.6}$$

$$\begin{aligned}
r_n(E, \Theta_N, E_{FN}, U) \\
&= A_7(\Theta_N, E_{FN}, U) \left[ \frac{A_7(\Theta_N, E_{FN}, U) u(E)^2 + A_8(\Theta_N, E_{FN}, U) v(E)^2}{B(E, \Theta_N, E_{FN}, U)} \right] - 1
\end{aligned} \tag{28.7}$$

where we account for the condition

$$E_{FN}, \Delta_N \gg E, \Omega$$

and we use the following significations:

$$\Omega(E) = \sqrt{E^2 - \Delta_S^2}, u(E) = \sqrt{0,5 \left(1 + \frac{\Omega(E)}{E}\right)}, v(E) = \sqrt{0,5 \left(1 - \frac{\Omega(E)}{E}\right)}$$

$$A_N(\Theta_N, E_{FN}, U) = \frac{E_{FN} - \Delta_N}{v_{FN} k_N(\Theta_N, E_{FN})} e^{i\Theta_N}$$

$$A_{N-}(\Theta_N, E_{FN}, U) = \frac{E_{FN} - \Delta_N}{v_{FN} k_N(\Theta_N, E_{FN}, U)} e^{-i\Theta_N}$$

$$A_S(\Theta_N, E_{FN}, U) = \frac{E_{FN} + U - \Delta_N}{v_{FS} k_S(\Theta_N, E_{FN}, U)} e^{i\Theta_S}$$

$$A_{S-}(\Theta_N, E_{FN}, U) = \frac{E_{FN} + U - \Delta_N}{v_{FS} k_S(\Theta_N, E_{FN}, U)} e^{-i\Theta_S}$$

$$A_1(\Theta_N, E_{FN}, U) = A_{N-}(\Theta_N, E_{FN}, U) + A_S(\Theta_N, E_{FN}, U)$$

$$A_2(\Theta_N, E_{FN}, U) = A_N(\Theta_N, E_{FN}, U) + A_{S-}(\Theta_N, E_{FN}, U)$$

$$A_3(\Theta_N, E_{FN}, U) = A_{N-}(\Theta_N, E_{FN}, U) - A_{S-}(\Theta_N, E_{FN}, U) \quad (28.8)$$

$$A_4(\Theta_N, E_{FN}, U) = A_N(\Theta_N, E_{FN}, U) - A_S(\Theta_N, E_{FN}, U)$$

$$A_5(\Theta_N, E_{FN}, U) = A_{N-}(\Theta_N, E_{FN}, U) + A_N(\Theta_N, E_{FN}, U)$$

$$A_6(\Theta_N, E_{FN}, U) = A_S(\Theta_N, E_{FN}, U) + A_{S-}(\Theta_N, E_{FN}, U)$$

$$A_7(\Theta_N, E_{FN}, U) = A_{N-}(\Theta_N, E_{FN}, U) + A_N(\Theta_N, E_{FN}, U)$$

$$A_8(\Theta_N, E_{FN}, U) = A_S(\Theta_N, E_{FN}, U) - A_N(\Theta_N, E_{FN}, U)$$

$$B(E, \Theta_N, E_{FN}, U) = u(E)^2 A_1(\Theta_N, E_{FN}, U) \\ \times A_2(\Theta_N, E_{FN}, U) - v(E)^2 A_3(\Theta_N, E_{FN}, U) A_4(\Theta_N, E_{FN}, U)$$

$$k_N(\Theta_N, E_{FN}) = \cos(\Theta_N) \sqrt{E_{FN}^2 - \Delta_N^2} \frac{1}{\sqrt{v_{FN} v_{FS}}}$$

Angles of incidence of the quasiparticle wave on the normal and the superconductive regions of the junction considered are associated by the following condition

$$k_N \sin \Theta_N = k_S \sin \Theta_S$$

The conductivity  $G$  of the junction investigated can be found due to known Blonder-Tinkham-Klapvijk formalism [12] which expresses  $G$  in terms of  $r_a$  and  $r_n$ :

$$G(E, E_{FN}, U) = G_0 \int_0^{\frac{\pi}{2}} \left[ 1 + |r_a(E, \Theta_N, E_{FN}, U)|^2 - |r_n(E, \Theta_N, E_{FN}, U)|^2 \right] \cos(\Theta_N) d\Theta_N \quad (28.9)$$

where  $G_0$  is the ballistic conductivity of the normal graphene [13]. Equation (28.9) yields the conductivity of the structure under consideration for arbitrary parameter values.

### 28.3 Results and Discussion

Figure 28.1 shows the dependence of the normalized (dimensionless) conductivity  $G^* = G/G_0$  on the dimensionless energy of quasiparticles  $E' = E/\Delta_S$  in the case in which a normal part of the considered contact is the gapless graphene ( $\Delta_N = 0$ ). Curves 1, 2, and 3 correspond to the values of the Fermi velocity in the superconductor  $v_{FS} = 1; 1.5; 2$ . (We put the angle of incidence of the quasiparticle wave on the normal region to be equal to  $\pi/6$  throughout the text, the superconductive parameter  $\Delta_S = 0.0025$ ). Curve 1 shows that the calculations of our work are in agreement with the results of previous studies [13, 14] according to which conductivity  $G^*$  is not dependent on energy  $E$  in the range where it does not exceed the size of the superconducting gap. However, we see that in the case of different values of the Fermi velocity  $v_{FN}$  and  $v_{FS}$ , the dependence of conductivity on the excitation energy of quasiparticles in the above energy range  $0 < E < \Delta_S$  takes place. This result is qualitatively different from that obtained in papers [13, 14], and it shows that the value of the conductivity of the system under investigation depends on energy  $E$  throughout its whole range.

The larger is the difference between the Fermi velocities in the normal and the superconductor areas, the more substantial effect on the conductivity we observe (compare curves 2 and 3 in Fig. 28.1). For all the cases considered in which  $v_{FS} \neq v_{FN}$ , the magnitude of conductivity has a peak-like maximum at a point  $E = \Delta_S$ ; the maximum value of  $G^*$  grows with  $v_{FS}$  decreasing (if  $v_{FS} > v_{FN}$ ).

Consider further the results obtained for contacts: the gapped normal graphene-superconducting graphene. First of all, note that the conductivity of this system  $G^*$  reveals a complicated dependence on its parameters, and the results of calculation of  $G^*$  essentially depend on the interplay between the parameters such as the Fermi velocity in the normal and the superconducting regions (ratio  $v_{FN}/v_{FS}$ ), the magnitude of a gap in the normal area  $\Delta_N$ , an external electrostatic potential  $U$ , and the Fermi energy  $E_F$ . As for the case of  $\Delta_N = 0$ , the larger the difference between the

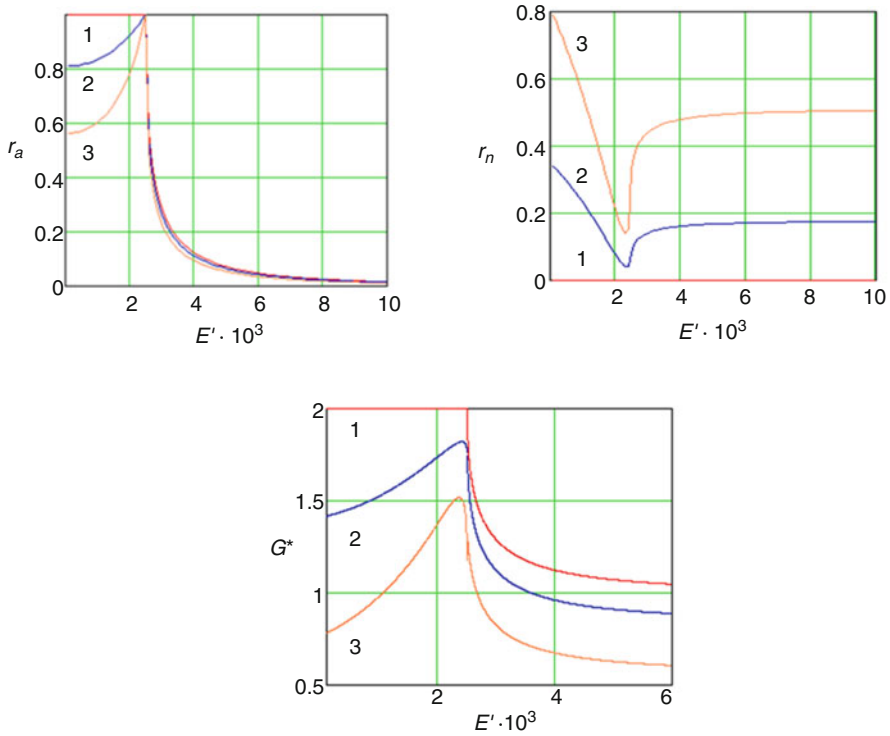


**Fig. 28.1** Functions of  $r_a(E'), r_n(E'), G^*(E')$  for the gapless normal region of the junction considered ( $\Delta_N = 0$ ). Curves 1, 2, and 3 refer to values of the Fermi velocity  $v_{FS} = 1, 1.5, 2$ , respectively (other values in the text)

Fermi velocities in the normal and the superconductor areas, the more substantial the effect on the conductivity we observed.

Note also that the examined characteristics of the *NS* contact containing the gapped graphene in the *N* region have some quality differences from the case of a contact with the gapless graphene. So in the former case, there is a significant functional dependence of conductivity on the potential  $U$ , as well as on the Fermi level  $E_F$ , while the conductivity of the system which includes the gapless graphene is independent of variables  $U$  and  $E_F$ . Because of this, in particular, in subsequent figures, we present the results of our calculations for two different values of  $U$ , namely,  $U_1 = 0$  and  $U_2 = 100$ .

Figure 28.2 shows the dependence of the normal, of the Andreev reflection, and of the dimensionless conductivity  $G^*$  on the excitation energy  $E$  for *NS* contact for the following parameters: Fermi velocity in *N* region  $v_{FN} = 1$ , the gap width in *N* region  $\Delta_N = 1$ , and curves 1 and 2 in the figures corresponding to values of potential  $U$ :  $U_1 = 0$  and  $U_2 = 100$ . It is evident that the functions  $r_a(E)$  and  $r_n(E)$ , i.e., the rates of the Andreev and the normal reflection, respectively, have the peak-like extremes at a point  $E = \Delta_S$ , which is equal to the width of the superconducting

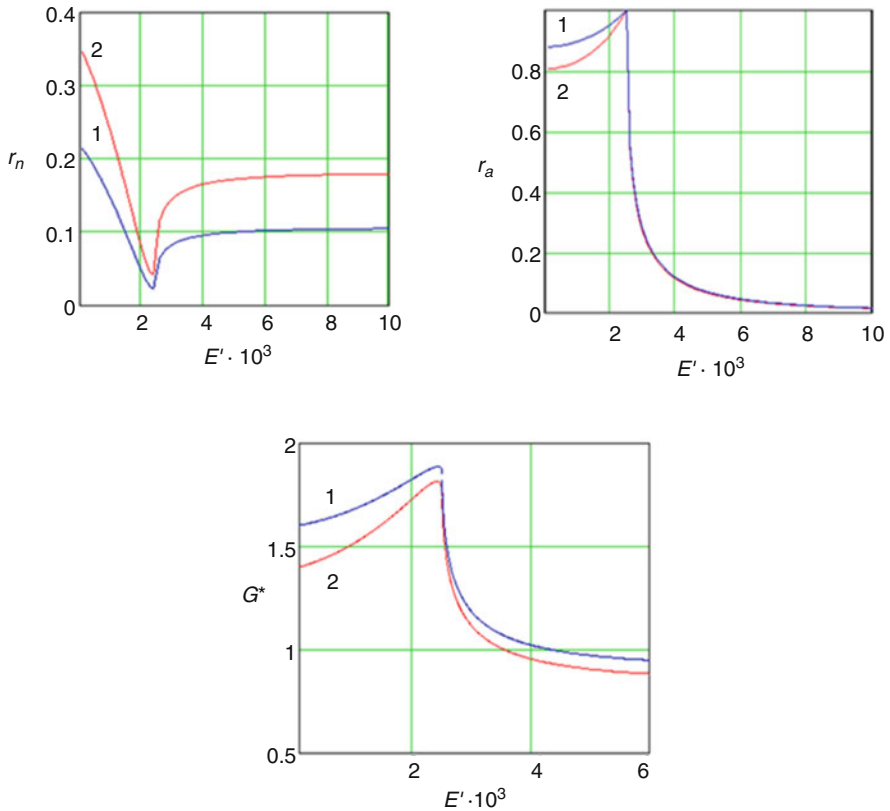


**Fig. 28.2** Plots of  $r_a(E')$ ,  $r_n(E')$ ,  $G^*(E')$  dependencies for the gapped normal region with the values of  $\Delta_N = 1$ ,  $v_{FS} = 1.5$ . Curves 1 and 2 refer to values of  $U = 0, 100$ , respectively (other values in the text)

gap. It is true for arbitrary values of the potential  $U$ . However, the behavior of the Andreev and the normal reflection rates has the opposite character, namely, the function  $r_a(E)$  increases with energy  $E$  from zero and reaches a maximum at a point  $E = \Delta_S$ ; instead the function  $r_n(E)$  decreases with  $E$  increasing, reaches a minimum value at a point  $E = \Delta_S$ , and then grows. The value of conductivity  $G^*(E)$  is mainly determined by the Andreev reflection process and the shape of the corresponding curve is similar to that of the function  $r_a(E)$ . We would like to emphasize here two important facts: (1) conductivity depends on the potential  $U$  (unlike for the case where  $\Delta_N = 0$ ,  $v_{FS} = 1$ ); (2) increasing in potential  $U$  leads to higher values of the conductivity unlike for the case of identical values Fermi velocity in  $N$  and  $S$  contact regions ( $v_{FS} = v_{FN} = 1$ ,  $\Delta_N \neq 0$ ). This behavior is due to the process of the Andreev reflection. Note also that the conductance increases with decreasing of the Fermi velocity in the superconducting region  $v_{FS}$ .



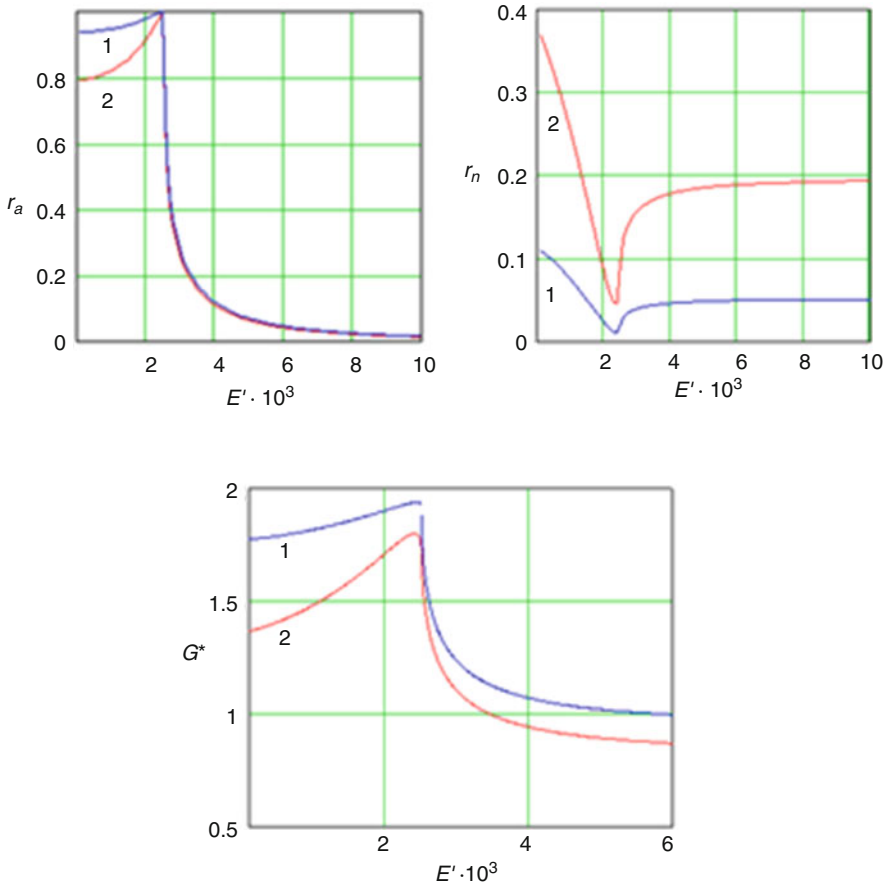


**Fig. 28.3** Plots of the Andreev, of the normal reflections, and of the conductivity dependencies on energy for the values of  $\Delta_N = 2$ ,  $v_{FS} = 1.5$ . Curves 1 and 2 refer to values of  $U = 0, 100$ , respectively (other values in the text)

Figure 28.3 presents the same functions as in Fig. 28.2 but for the case of the bigger gap in the normal region  $\Delta_N = 2$ . For larger values of  $\Delta_N$ , there is an interesting result: the conductivity reveals the non-monotonic dependence on the Fermi velocity values in the superconductors region  $v_{FS}$ . In this case, contrary to the case of smaller values  $\Delta_N$ , the conductivity increases with increasing  $v_{FS}$  and then reaches its maximum at the value  $v_{FS}$  which is approximately equal to 1.6, then  $G^*$  is reduced. This behavior of the conductivity as a function of the Fermi velocity is again due to the process of Andreev reflection.

Figures 28.4 and 28.5 illustrates the dependence of the Andreev, of the normal reflections, and of the conductivity on the Fermi energy  $E_F$  for the following values of the parameters involved:  $\Delta_N = 1$ ,  $v_{FS} = 2$ .

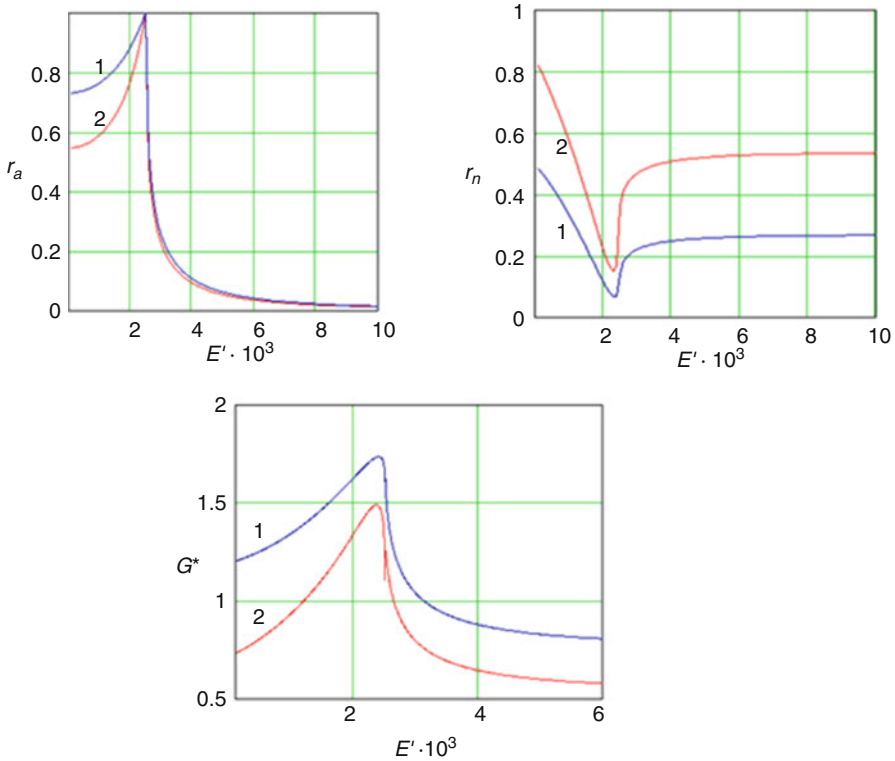


**Fig. 28.4** Dependencies of the Andreev, of the normal reflections, and of the conductivity on energy for the value of  $E_F = 5$ . Curves 1 and 2 refer to values of  $U = 0, 100$  respectively,  $v_{FS} = 2$  (other values in the text)

The main features of these relationships are as follows:

1. Unlike for the case of  $\Delta_N = 0, v_{FS} = 1$ , these functions depend essentially on the Fermi level  $E_F$ .
2. Decreasing in  $E_F$  leads to the increased conductivity and not to its decrease as for the case  $v_{FS} = 1, \Delta_N \neq 0$ .
3. Functions  $r_a(E'), r_n(E'), G^*(E')$  become practically independent on  $U$  for sufficiently large values of  $E_F$ .

## 28.4 Conclusions

We consider the nanoscale structure: the superconducting graphene in contact with the normal graphene and two options are considered – cases of the gapped and the gapless graphene. It is believed that the Fermi velocity value in the superconducting graphene may differ from that in the pristine graphene.

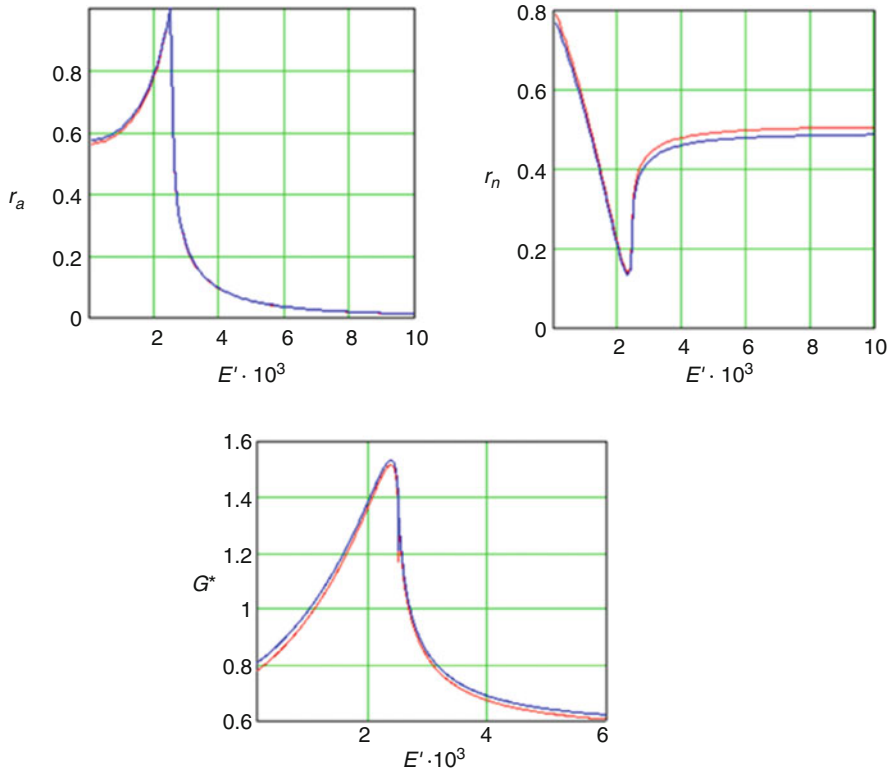


**Fig. 28.5** Dependencies of the Andreev, of the normal reflections, and of the conductivity on energy for the value of  $E_F = 50$ ,  $v_{FS} = 2$  (other values in the text)

With the help the Blonder-Tinkham-Klapwijk formalism, the conductivity  $G$  is calculated taking into account the fact that the external potential  $U$  is applied to the superconducting part of the given structure. The coefficients of both the normal and the Andreev reflection are evaluated within the framework of the Dirac-Bogoliubov-de Gennes equations.

It is shown that the determining factor in the formation of the conductivity is the process of the Andreev reflection. A characteristic feature of the  $G(E)$  dependence is the presence of a peak at a point  $E = \Delta_S$ ,  $\Delta_S$  being the superconducting energy gap in graphene. The value of the maximum (peak), value of  $G(E)$ , and the  $G(E)$  curve steepness essentially depend on the value of the Fermi velocity  $v_F$ . The dependence of the conductivity on the potential  $U$  as well as on the Fermi level  $E_F$  is analyzed. The obtained results may be useful for applications in the graphene-based electronics.

## References

1. Geim AK, Novoselov KS (2007) The rise of graphene. *Nat Mater* 6:183
2. Castro Neto AN, Guinea F, Peres NMR, Novoselov KS, Geim AK (2009) The electronic properties of graphene. *Rev Mod Phys* 81:109
3. Liu L, Li Y-X, Liu J (2012) Transport properties of Dirac electrons in graphene based double velocity-barrier structures in electric and magnetic fields. *Phys Lett A* 376:3342–3350
4. Wang Y, Liu Y, Wang B (2013) Resonant tunneling and enhanced Goos-Hänchen shift in graphene double velocity barrier structure. *Physica E* 53:186–192
5. Sun L, Fang C, Liang T (2013) Novel transport properties in monolayer graphene with velocity modulation. *Chin Phys Lett* 30(4):047201
6. Raoux A, Polini M, Asgari R, Hamilton AR, Fasio R, MacDonald AH (2010) Velocity – modulation control of electron-wave propagation in graphene. *Phys Rev B* 81:073407. arXiv:0912.2608v1 [cond-mat.mes-hall]
7. Concha A, Tešanović Z (2010) Effect of a velocity barrier on the ballistic transport of Dirac fermions. *Phys Rev B* 82:033413–033421
8. Yuan JH, Zhang JJ, Zeng QJ, Zhang JP, Cheng Z (2011) Tunneling of Dirac fermions in graphene through a velocity barrier with modulated by magnetic fields. *Physica B* 406:4214–4220
9. Krstajic PM, Vasilopoulos P (2011) Ballistic transport through graphene nanostructures of velocity and potential barriers. *J Phys Condens Matter* 23:000000 (8 pp)
10. Korol AM, Medvid' NV, Litvynchuk SI (2015) Transport properties of the Dirac-Weyl electrons through the graphene-based superlattice modulated by the Fermi velocity barriers. *Springer Proc Phys* 167:215–221
11. Korol AN, Litvynchuk SI, Baglyuk SV, Isai VN (2016) Energy spectra of the graphene-based Fibonacci superlattice modulated by the Fermi velocity barriers. *Phys Sci Int J* 9(3):1–8
12. Blonder GE, Tinkham M, Klapwijk TM (1982) Transition from metallic to tunneling regimes in superconducting microconstrictions: excess current, charge imbalance, and supercurrent conversion. *Phys Rev B* 25:4515–4524
13. Bhattacharjee S, Sengupta K (2006) Tunneling conductance of graphene NIS junctions. *Phys Rev Lett* 97:217001–217006
14. Goudarzi H, Sedghi H, Khezrou M, Mabhouti KH (2010) Tunneling conductance in gapped graphene-based normal metal-insulator-superconductor junctions: case of massive Dirac electrons. *Physica C* 470:1981–1987

# Chapter 29

## On the Possibility of Carbon Atoms' Drift to the Surface of a FCC Iron Nanocluster Through Tetrahedral Interstice

A.V. Nedolya and N.V. Bondarenko

### List of Abbreviations

COIS	Central octahedral interstitial site
FCC	Face-centered cubic
MM	Molecular mechanic
PB	Potential barrier
TIS	Tetrahedral interstitial site

### 29.1 Introduction

Usually, the nanostructured materials and nanoparticles are created from traditional metal alloys under the influence of the extreme conditions: extrusion, multiple phase transitions, laser surface treatment, metal particles deposition from the vapor phase, etc. [1–3]. As a result, the metastable phases can be obtained because of the high-cooling rate, high degrees of deformation, or both [4–6].

In any case, the obtained nanostructures are quasi-stable and change their properties over time [7–9].

The study of the metastable nanostructures and nanoclusters can help solve the problem of their stabilization using the atoms of other types. Also, it is possible to control the properties of nanoparticles by changing the spatial configuration of other type of atoms.

---

A.V. Nedolya (✉) • N.V. Bondarenko  
Applied Physics Department, Zaporizhzhya National University, 66 Zhukovsky Street, 69600,  
Zaporizhzhya, Ukraine  
e-mail: [avnedolya@hotmail.com](mailto:avnedolya@hotmail.com)

## 29.2 Method

For the study, we chose a FCC Fe-Ni-C nanocluster containing 15 atoms. We assumed that such a cluster forms randomly at initial time and contains one carbon atom and one nickel atom, that substitutes iron atom. The system was considered to be quasi-stable and quasi-isolated, that is why it was only statics that we took into account when estimating energy changes using molecular mechanic method (MM+ algorithm) [10–12]. We chose the FCC cluster because all the atoms in it are located on the surface or form the surface, which simplified interpretation of calculation results.

We performed an evaluation of energy empirically using the solution of the Newton system of equations:

$$m_i \frac{d^2 \vec{r}_i(t)}{dt^2} = - \frac{\partial U(\vec{r}_i, \dots, \vec{r}_n)}{\partial \vec{r}_i} + \vec{F}_i^{ex}, \quad (29.1)$$

where Lennard-Jones potential was:

$$U(r_{ij}) = 4\epsilon_{kl} \sum_{i < j} \left[ \left( \frac{\sigma_{kl}}{r_{ij}} \right)^{12} - \left( \frac{\sigma_{kl}}{r_{ij}} \right)^6 \right] \quad (29.2)$$

and where ( $\epsilon_{kl} = \sqrt{\epsilon_{kk}\epsilon_{ll}}$  – the bond energy and  $\sigma_{kl} = \frac{\sigma_{kk} + \sigma_{ll}}{2}$  – the measure of the atomic size, were calculated using Lorenz-Berthelot mixing rule of atoms of  $k$ -th and  $l$ -th classes) [13–15];  $F_i^{ex}$  – the force that determines intermolecular interactions;  $r_i$  and  $r_j$  – the coordinates of the interacting atoms  $r_{ij} = |\vec{r}_i - \vec{r}_j|$ .

Due to the fact that the energy in such calculations is determined up to a constant, we calculated the energy difference between the position of atom of carbon inside of the nanocluster (octahedral interstice) and the current position during its drift to the surface:

$$\Delta u = u(L) - u(0), \quad (29.3)$$

where  $L$  is a length of the carbon atom path,  $u$  – specific potential energy. Position of the carbon atom in the central octahedral interstitial site (COIS) of a cluster was chosen as null (0) of the path length ( $L$ ), conforming to central symmetry of the nanocluster.

We considered the movement of carbon atom as similar to the drift to surface due to the influence of surface energy nanocluster. We examined every possible position of nickel atom, which replaced the iron atom, as an analog of random diffused jumps of nickel atom. Also we selected the temperature of  $T = 300$  K and the distances

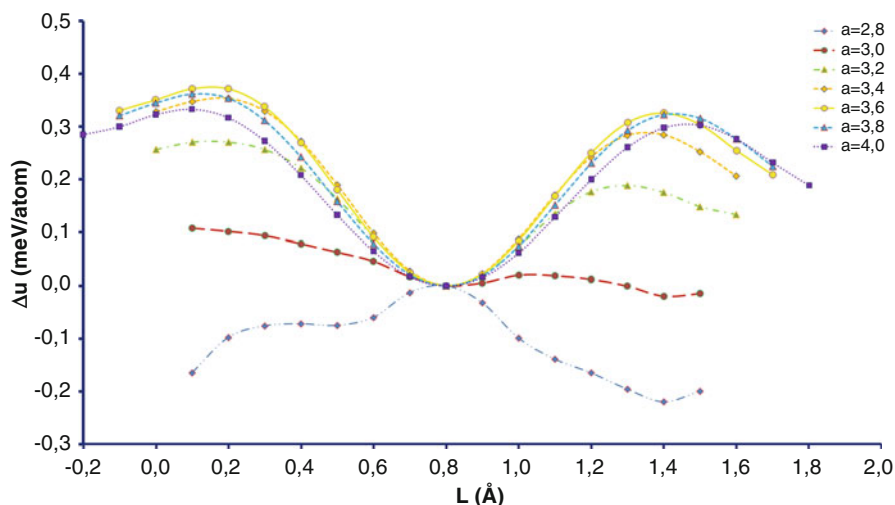
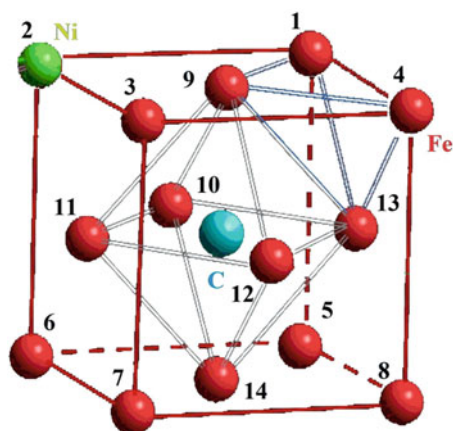


**Fig. 29.1** Change of specific energy iron FCC nanocluster depending on the distance between atoms (from 2.8 to 4.0 Å)

**Fig. 29.2** Numbering scheme of nickel atom positions in iron nanocluster



between atoms of 3.6 Å (angstroms), because the optimal interatomic distances of Fe-Ni-C nanocluster was chosen for simulation in which height of a potential barrier was maximal and FCC nanocluster was the most stable (see Fig. 29.1) [16–18]. We numbered their positions for convenience (see Fig. 29.2). In such a system, any changes of energy can be made only by changing positions of impurity atoms.

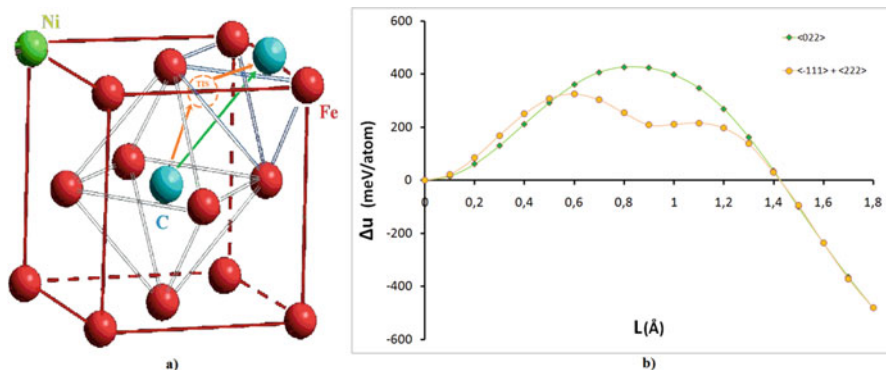


**Fig. 29.3** The scheme of carbon atom's drift (a) and specific energy change of the iron nanocluster (b): green arrow – the direction  $\langle 022 \rangle$ , orange arrows –  $\langle 111 \rangle$  plus  $\langle 222 \rangle$

## 29.3 Result and Discussion

### 29.3.1 The Case of One Ni Atom

Nanocluster's energy was calculated based on the location of the carbon atom, taking into account the nickel atom's position. We chose two directions of a carbon atom drift to the surface: direction  $\langle 022 \rangle$  (green arrow) and the way  $\langle 111 \rangle$  plus  $\langle 222 \rangle$  (orange arrows) for calculation, which formed a triangle (Fig. 29.3a). Choice of the way  $\langle 111 \rangle$  plus  $\langle 222 \rangle$  was associated with the fact that it was able to pass through the tetrahedral interstice (TIS). Both directions were energetically favorable for a carbon atom, because the cluster energy was almost twice smaller when the carbon atom was on the surface ( $L = 1.8$ ) compared to its position in the central octahedral interstice ( $L = 0$ ), due to influence of the surface as indicated in Fig. 29.4. However, in case when the carbon atom drifted toward  $\langle 022 \rangle$  direction, the potential barrier ( $\Delta$ ) was higher than two potential barriers ( $\Delta_1$ ,  $\Delta_2$ ) in  $\langle 111 \rangle$  plus  $\langle 222 \rangle$  directions (see Fig. 29.3b). We had calculated the energy of a FCC nanocluster of iron at all possible position of a nickel atom, in order to determine its effect on the potential barriers height (see Table 29.1).

If the lowest potential barrier was in the direction of  $\langle 022 \rangle$  when the nickel atom held positions 1 and 4, in the case of drift toward  $\langle 111 \rangle$  plus  $\langle 222 \rangle$  the potential barrier's configuration was more complex.

There are three potential barriers' ratios which a carbon atom can overcome using a tetrahedral interstice to reach the surface: (a)  $\Delta_1 \approx \Delta_2$ ; (b)  $\Delta_1 > \Delta_2$  and (c)  $\Delta_1 < \Delta_2$  (see Fig. 29.4).

Both of potential barriers with accuracy of 5% had an equal height when they corresponded to 11, 12, and 14 positions of nickel atom (see Fig. 29.5, green). In these cases, the heights of potential barriers on the way to the surface



**Table 29.1** Nanocluster energy at different positions of a carbon and a nickel atom at sequential drift of carbon atom in the direction  $\langle -111 \rangle$  and  $\langle 222 \rangle$  to the surface: (a)  $\Delta u_1 \approx \Delta u_2$  (with an accuracy of 5%); (b)  $\Delta u_1 > \Delta u_2$ ; (c)  $\Delta u_1 < \Delta u_2$

Equivalent Ni atom positions	Symbol	$\Delta u_1 \left( \frac{\text{meV}}{\text{atom}} \right)$	$\Delta u_2 \left( \frac{\text{meV}}{\text{atom}} \right)$	$\Delta u_{\text{min}1,2} / \Delta u_{\text{max}1,2} \%$	$\Delta \left( \frac{\text{meV}}{\text{atom}} \right)$	$\Delta - \Delta u_{\text{max}1,2} \left( \frac{\text{meV}}{\text{atom}} \right)$	$(\Delta - \Delta u_{\text{max}1,2}) / \Delta \%$
11 = 14 = 12	a	440	425	3.4	534 506	94 66	17.6 13.0
2 = 5 ≈ 3 = 8 = 6 = 7	b	368	343	6.8	457 458	89 90	19.5 19.7
4	b	368	335	9.0	427	59	13.8
1 = 9 = 13	b	326	216	33.7	427 462	101 136	13.8 20.3
10	c	326	362	-9.9	506	144	28.5

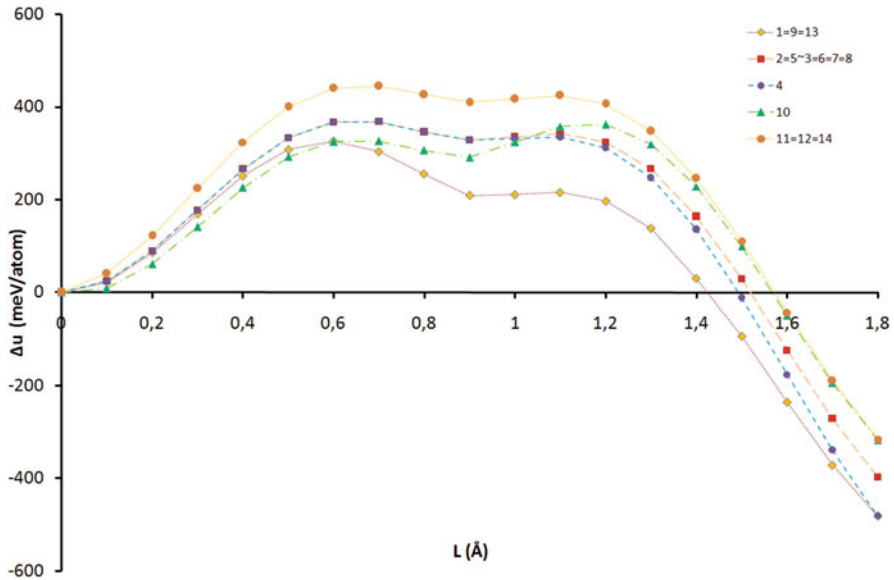
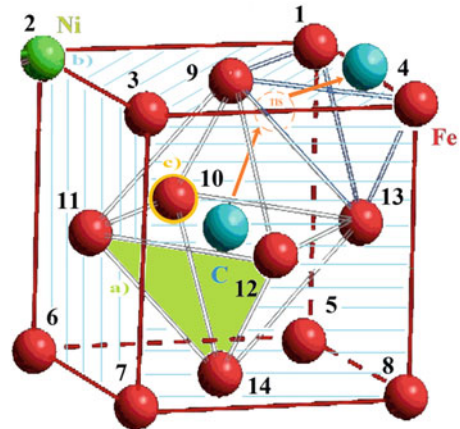


**Fig. 29.4** Change of specific energy of the iron nanocluster depending on the position of nickel atom

**Fig. 29.5** Scheme the nickel atom's positions that affect the height of potential barriers the tetrahedral interstice



through tetrahedral interstice were 13–18% less than in the direction  $\langle 022 \rangle$  (see Table 29.1a). Energy depth of tetrahedral interstices did not exceed 40 meV/atom or 11% between the maximum and the minimum. This position was the most stable of the three cases, although it was considerably unstable in comparison to the case when a carbon atom occupied the octahedral interstice.

In the second case (b), which included the majority of positions of a nickel atom (1/9, 13), the first barrier was higher than the second potential barrier (see Fig. 29.5, blue hatch). This created an energy condition for carbon atom to drift to the surface

in order to reduce the nanocluster energy. The energy advantage was from 14 to 20% in comparison to the direction  $\langle 222 \rangle$ . For the carbon atom, the most energetically favorable was position 1 of a nickel atom.

There was a case where the height of the second potential barrier of tetrahedral interstice was larger than the first barrier's by 10% (see Fig. 29.5 orange). In our opinion, although this height was significantly lower than the potential barrier of an octahedral interstice (by 29%), the carbon atom drift to the surface through TIS was not energetically favorable, because conditions for returning of a carbon atom to the central octahedral interstice were created.

### 29.3.2 *The Case of Two Ni Atoms*

In case when the FCC nanocluster contains two atoms of nickel, energy picture becomes more complex as shown on Table 29.2a, b.

Table 29.2a contains all possible positions of the pair of Ni atoms where the potential barriers of tetrahedral interstice have the same height  $\Delta u_1 \approx \Delta u_2$  (accurate to 5%). Table 29.2b contains all possible positions of the pair of Ni atoms where the first potential barrier of tetrahedral interstice is higher than the second  $\Delta u_1 > \Delta u_2$  (accurate to 5%). These are the best configurations of nickel atoms when the drift of carbon atom to the surface through tetrahedral interstice is more favorable.

The third case is given in Table 29.2b, and it collects all possible configurations of nickel atoms in which the second potential barrier is higher than the first barrier. In this case, the condition for a return of carbon atom to the central octahedral interstice has been formed.

## 29.4 Conclusions

Thus, there are two ways for carbon atom to drift to the surface of the iron FCC nanocluster: short direction of  $\langle 022 \rangle$  with high potential barrier and long direction  $\langle 111 \rangle$  plus  $\langle 222 \rangle$ , which potential barrier is lower by 13–29%. The carbon atom position in tetrahedral interstice is unstable, so it can be considered as a transit way of the carbon atom to the surface of the nanocluster.

The position of nickel atom affects the height of potential barriers and determines which of the two potential barriers of the tetrahedral interstice is higher. This can be considered as a method to control the interstitial atom's motion using the substitutional atom in nanocluster.

**Table 29.2** Nanocluster energy at different positions of a pair of nickel atoms at sequential drift of carbon atom by tetrahedral interstitial space in case of (a)  $\Delta u_1 \approx \Delta u_2$  (with an accuracy of 5); (b)  $\Delta u_1 > \Delta u_2$ ; (c)  $\Delta u_1 < \Delta u_2$

Equivalent positions of the Ni atom when a C atom occupies the TIS	Symbol	$\Delta u_1 \left( \frac{\text{meV}}{\text{atom}} \right)$	$\Delta u_2 \left( \frac{\text{meV}}{\text{atom}} \right)$	$\frac{\Delta u_{\text{min}1,2}}{\Delta u_{\text{max}1,2}} \%$	$\Delta \left( \frac{\text{meV}}{\text{atom}} \right)$	$\Delta^- \frac{\Delta u_{\text{max}1,2}}{\left( \frac{\text{meV}}{\text{atom}} \right)}$	$\Delta / \Delta u_{\text{max}1,2} \%$
<b>(a)</b>							
11.12 = 12.14 = 11.14	a <sub>1</sub>	520	507	2.5	585 613	65 93	11.0 15.0
2.12 = 3.12 = 5.12 = 6.12 = 7.12 = 8.12 = 2.11 = 3.11 = 5.11 = 6.11 = 7.11 = 8.11 = 5.14 = 8.14 = 6.14 = 7.14 = 2.14 = 3.14	a <sub>2</sub>	443	423	4.5	507 ÷ 509 536 ÷ 537 688	64 ÷ 66 93 ÷ 94 245	13.0 17.5 35.5
9.12 = 12.13 = 9.11 = 9.14 = 13.14 = 11.13 =	a <sub>3</sub>	401	381	5.0	513 541	112 98	22.0 26.0
<b>(b)</b>							
4.12 = 4.11 = 4.14	b <sub>1</sub>	443	418	5.5	475 503	32 60	7.0 12.0
1.12 = 1.11 = 1.14	b <sub>2</sub>	397	297	25.0	475 503	78 106	16.5 21.0
2.3 = 2.5 = 2.6 = 2.7 = 2.8 = 3.5 = 3.8 = 5.8 = 3.7 = 5.6 = 7.8 = 3.6 = 5.7 = 6.8 = 6.7	b <sub>3</sub>	370	345	7.0	458 ÷ 461	88 ÷ 91	19.0 ÷ 19.5
2.4 = 3.4 = 4.5 = 4.8 = 4.6 = 4.7	b <sub>4</sub>	326	216	8.0	429 ÷ 430	103 ÷ 104	24.0
2.9 = 3.9 = 5.13 = 8.13 = 5.9 = 6.9 = 7.9 = 8.9 = 6.13 = 7.13 = 4.10 = 2.13 = 3.13	b <sub>5</sub>	324	299	7.0	464 ÷ 465 475 536	140 ÷ 141 151 212	30.0 32.0 40.0

4.9 = 4.13			324	292	10.0	431	107	25.0
1.2 = 1.3 = 1.5 = 1.6 = 1.7 = 1.8	$b_6$		324	216	33.5	429 ÷ 430	105 ÷ 106	24.5
1.4	$b_8$		324	209	35.5	402	78	19.5
9.13	$b_9$		282	255	9.5	469	187	40.0
1.10	$b_{10}$		282	236	16.5	475	193	40.5
1.9 = 1.13	$b_{11}$		282	172	39.0	431	149	34.5
(c)								
10.12 =	$c_1$		401	445	-10.0	556 585	111 140	20.0 24.0
10.11 = 10.14								
2.10 = 3.10 = 5.10 = 8.10 = 6.10 = 7.10	$c_2$		324	363	-10.5	507 ÷ 509	144 ÷ 146	28.5 ÷ 29.0
9.10 = 10.13	$c_3$		282	318	-11.0	513	195	38.0

## References

1. Sree Harsha KS (2006) Principles of physical vapor deposition of thin films. Elsevier Ltd., Oxford
2. Smirnov BM (2010) Cluster processes in gases and plasmas. Wiley-VCH Verlag GmbH & Co, KGaA, Weinheim. doi:[10.1002/9783527628650.ch5](https://doi.org/10.1002/9783527628650.ch5)
3. Sagaradze VV, Danilchenko VE, L'Heriter PH, Shabashov VA (2002) The structure and properties of Fe-Ni alloys with a nanocrystalline austenite formed under different conditions of  $\gamma$ - $\alpha$ - $\gamma$  transformations. Mater Sci Eng A. doi:[10.1016/S0921-5093\(02\)00023-0](https://doi.org/10.1016/S0921-5093(02)00023-0)
4. Dai ZR, Sun S, Wang ZL (2002) Shapes, multiple twins and surfaces structures of monodisperse Fe-Pt magnetic nanocrystals. Sur Sci 505:325–335
5. Diao J, Gall K, Dunn ML (2003) Surface-stress-induced phase transition in metal nanowires. Nat Mater 2:656–660
6. Xia Y, Xiong Y, Lim B, Skrabalak SE (2009) Shape-controlled synthesis of metal nanocrystals: simple chemistry meets complex physics. Angew Chem Int Ed Engl. doi:[10.1002/anie.200802248](https://doi.org/10.1002/anie.200802248)
7. Johnston RL, Wilcoxon J (eds) (2012) Metal particles and nanoalloys, vol 3. Elsevier Ltd., Amsterdam
8. Pachon LD, Rothenberg G (2008) Transition-metal nanoparticles: synthesis, stability and the leaching issue. Appl Organomet Chem. doi:[10.1002/aoc.1382](https://doi.org/10.1002/aoc.1382)
9. Singh AK (2016) Engineered nanomaterials: structure, properties and mechanism of toxicity. Academic Press/Elsevier Inc., Amsterdam
10. Lewars EG (2011) Computational chemistry: introduction to the theory and applications of molecular and quantum mechanics, 2nd edn. Springer Science Business Media BV, Berlin. doi:[10.1007/978-90-481-3862-3](https://doi.org/10.1007/978-90-481-3862-3)
11. Ramachandran KI, Deepa G, Namboori K (2008) Computational chemistry and molecular modelling. Principles and applications. Springer, Heidelberg. doi:[10.1007/978-3-540-77304-7](https://doi.org/10.1007/978-3-540-77304-7)
12. Yang Q, To AC (2015) Multiresolution molecular mechanics: a unified and consistent framework for general finite element shape function. Comput Methods Appl Mech Eng. doi:[10.1016/j.cma.2014.09.031](https://doi.org/10.1016/j.cma.2014.09.031)
13. Ledbetter HM, Reed RP (1973) Elastic properties of metals and alloys, 1. Iron, nickel, and iron-nickel alloys. J Phys Chem Ref Data 2(3):531–617
14. Halicioğlu T, Pound GM (1975) Calculation of potential energy parameters from crystalline state properties. Phys Status Solidi A. doi:[10.1002/pssa.2210300223](https://doi.org/10.1002/pssa.2210300223)
15. Riech M (2003) Nano-engineering in science and technology. An introduction to the world nano-design. World Scientific Publishing Co Pte Ltd., Singapore
16. Ridley N, Stuart H, Zwell L (1969) Lattice parameters of Fe-C austenites at room temperature. Trans IAME 245:1834–1840
17. Diesburg DE (1971) The elastic constants of Fe-Ni-C alloys. Retrospective Theses and Dissertations. Digital Repository @ Iowa State University. 4446; [http://lib.dr.iastate.edu/mse\\_etd](http://lib.dr.iastate.edu/mse_etd). Accessed 23 Dec 2015
18. Swartzendruber LJ, Itkin VP, Alcock CB (1991) The Fe-Ni (iron-nickel) system. JPE 12:288. doi:[10.1007/BF02649918](https://doi.org/10.1007/BF02649918)

# Chapter 30

## Nanostructuring Surfaces of HgCdTe by Ion Bombardment

A. B. Smirnov and R. K. Savkina

### 30.1 Introduction

A wide spectrum of topological features of a semiconductor surface can be developed by ion bombardment [1]. It is known that low-energy ion processing (from hundreds of eV to tens of keV) creates peculiar surface morphologies, such as nanoripples and nanodots, ranging from random to regular structures, whose electronic and optical properties are different from those of bulk materials and might find technological application for nanophotonics and nanoscale magnetism. For example, the implantation of ions of magnetic (or nonmagnetic) metals makes it possible to synthesize nanostructured layers exhibiting both diamagnetic and superparamagnetic, or even ferromagnetic, properties in a thin subsurface layer of an irradiated matrix [2].

Roles of implantation parameters such as ion energy, fluence, and angle of the ion beam incidence are observed to be significant to optimize the evolution of such nanostructures. In particular, the length scales of nanoripples are found to be mainly dependent on ion energy [3]. It was shown that normal-incidence (NI) ion beam can result in the formation of nanoscale objects on the surface of both elemental (Si [4, 5], Ge [5, 6]) and compound semiconductor (GaSb [7, 8]). At the same time, well-ordered hexagonal arrays of InP nanodots [9] and well-aligned ripple structures on the surface of a single crystal of 3C-SiC [10] were created by oblique-incidence (OI) ion bombardment. It should be also noted that ripples formed by OI processing of binary compounds can have a much higher degree of order than those formed by

---

A.B. Smirnov • R.K. Savkina (✉)

V. Lashkaryov Institute of Semiconductor Physics, NAS of Ukraine, 41 Nauki Av., Kyiv 03028, Ukraine

e-mail: [alex\\_tenet@isp.kiev.ua](mailto:alex_tenet@isp.kiev.ua); [r\\_savkina@lycos.com](mailto:r_savkina@lycos.com)

© Springer International Publishing AG 2017

O. Fesenko, L. Yatsenko (eds.), *Nanophysics, Nanomaterials, Interface Studies, and Applications*, Springer Proceedings in Physics 195,

DOI 10.1007/978-3-319-56422-7\_30

bombardment of elemental materials [11]. In other words, interest in developing techniques for fabricating nanostructured semiconductor surfaces having varied textures is increasing.

Most commonly irradiation-driven surface nanostructuring is understood as interplay between surface reorganization processes such as roughening and smoothing due to erosion and diffusion correspondingly. The widely accepted Bradley–Harper theory [12] explains pattern formation by the curvature dependence of the sputtering yield. An alternative approach is based on the theory (R. Cuerno [13] and S. Norris [14]) of the stress relaxation. In particular, R. Cuerno and coauthors show that nonuniform generation of stress across the damaged amorphous layer induced by their radiation is a key factor behind the range of experimental observations. Thus, the formulation of the generalized mechanisms of the ion nanostructuring of solid (in particular, semiconductor) surface faces with certain difficulties and requires further research.

The present investigation has been carried out on HgCdTe (MCT) alloys because MCT is one of the basic semiconductors for photon detectors from near IR (wavelength  $\lambda \sim 1.5 \mu\text{m}$ ) to long IR ( $\lambda \sim 20 \mu\text{m}$ ) and is used in large-scale arrays with silicon CMOS readouts. Sub-terahertz radiation detectors based on HgCdTe semiconductor are discussed also [15]. Ion implantation of MCT structures is the commonly used method for the fabrication of the IR devices. The advantages of this technique in producing a uniform and shallow junction are recognized. An implant, getting into the epitaxial layer, initiates an active restructuring of the defect structure of MCT, which change the epilayer carrier type. As a result, n-on-p (boron-implanted) [16] and p-on-n (arsenic-implanted) [17] photodiodes are fabricated. At the same time, it is well known that ion implantation induces mechanical stress in MCT layers, which is a matter of paramount importance for solid-state devices, and has been exploited to improve their electrical and optical properties. It was shown that implantation-induced stress is an important factor influencing the depth of p–n junctions in MCT-based structures [18].

This work aimed at studying the investigation of nanostructuring surfaces of a ternary chalcogenide semiconductor compound  $\text{Hg}_{1-x}\text{Cd}_x\text{Te}/\text{Cd}_{1-y}\text{Zn}_y\text{Te}$  ( $x = 0.223, y = 0.04$ ) performed using the processing with  $\text{B}^+$  and  $\text{Ag}^+$  ions. Effect of stress on defect transformation in  $\text{B}^+$  and  $\text{Ag}^+$  implanted HgCdTe/CdZnTe structure will be discussed.

## 30.2 Experiment

### 30.2.1 Materials

Materials used in this study were *p*- $\text{Hg}_{1-x}\text{Cd}_x\text{Te}$  ( $x \sim 0.223$ ) epilayers grown on [111]-oriented semi-insulating  $\text{Cd}_{1-y}\text{Zn}_y\text{Te}$  ( $y = 0.04$ ) substrates from a Te-rich solution at 450 °C by liquid-phase epitaxy. Specimens  $1 \times 1 \text{ cm}$  in size were cut



for measurements from wafers. An optical microscope was used to determine the thickness of grown layers, which was about 17  $\mu\text{m}$ .

### 30.2.2 Ion Beam Processing of HgCdTe

The working surface of structures investigated (on the side of the MCT layer) was implanted with the boron  $\text{B}^+$  and silver  $\text{Ag}^+$  ions. The implantation has been carried out by means of a Vezuvii-5 implanter allowing to work in the energy range from 100 up to 140 keV with normal- and oblique-incidence ion bombardment. To avoid the oxidation of the distorted layer [19], the specimens were annealed in the chamber at excess argon pressure four bars in the argon atmosphere at temperatures of 75  $^{\circ}\text{C}$  for 5 h.

The mathematical simulation of the process of ion implantation with the use of the software package TRIM\_2008 allowed the parameters of the radiation-induced disordering region of MCT to be determined. The energy and dose of implanted ions as well as parameters of the MCT region subjected to the ion-induced disordering are presented in Table 30.1.

Usually,  $p$ - $n$  junctions have been produced on a MCT substrate by ion bombardment with beam fluence ranging from  $10^{13}$  ions/ $\text{cm}^2$  to  $10^{15}$  ions/ $\text{cm}^2$  and ion energy ranging from 100 keV to 300 keV. At that, appearance of the extended defects in addition to the point defects occurs at a higher dose [20]. Therefore, a low dose ( $\sim 10^{13}$   $\text{cm}^{-2}$ ) has been chosen. At such dose, the near-surface region of the MCT target becomes saturated with point defects only. In particular, there are vacancies and mercury interstitial sites.

Another feature of MCT solid solution is the weakness of the Hg-Te bond compared to the Cd-Te bond resulted in the greater ion sputter yield of HgTe to CdTe. The enthalpy of Hg-Te bond formation is about 0.33 eV and for the Cd-Te bond –  $\sim 1.044$  eV [21]. It causes Hg to have large relative ion sputter

**Table 30.1** Parameters of the MCT region subjected to the ion-induced disordering

Type of implanted ions and Ion beam incidence angle $\theta$ , $^{\circ}$	$\text{B}^+$ , 0	$\text{Ag}^+$ , 0	$\text{Ag}^+$ , 0	$\text{Ag}^+$ , 45
Energy of implanted ions, keV	100	100	140	140
Dose of implanted ions, $\text{cm}^{-2}$	$3 \times 10^{13}$	$3 \times 10^{13}$	$4.8 \times 10^{13}$	$4.8 \times 10^{13}$
Projected range $R_p$ , $\mu\text{m}$	0.22	0.0365	0.045	0.04
Straggling $\Delta R_p$ , $\mu\text{m}$	0.17	0.024	0.028	0.0186
Maximal mechanical stresses $\sigma$ , Pa	$1.4 \times 10^3$	$2.2 \times 10^5$	$2.9 \times 10^5$	$1.28 \times 10^5$
Maximum doping $C_{\text{max}}$ , $\text{m}^{-3}$	$9.5 \times 10^{23}$	$5 \times 10^{24}$	$5.25 \times 10^{24}$	$3.38 \times 10^{24}$
Vacancy concentration $C_v$ , $\text{N}/\text{\AA}^3$	20	4.5	4.67	4.68
ion The coefficient of crystal lattice contraction $\beta$ , $\text{m}^3$	$3.51 \times 10^{-31}$	$1.25 \times 10^{-32}$	$1.25 \times 10^{-32}$	$1.25 \times 10^{-32}$

yields compared to the other elements and, most likely, plays a dominant role in the preferential sputtering of Te in HgCdTe [22].

### **30.2.3 Material Characterization**

All processed surfaces were examined after ion bombardment using atomic force microscopy (Digital Instruments NanoScope IIIa operating in the tapping mode). The surface morphology of the MCT samples investigated was characterized by a scanning electron microscope (SEM) (MIRA3 TESCAN). The optical characteristics were studied by ellipsometry. The measurements were performed on a laser ( $\lambda = 632.8$  nm) photoelectric compensation null ellipsometer (LEF 3G-1). The ellipsometric parameters  $\Delta$  and  $\psi$  were determined from the results of multi-angle measurements in a range of incidence angle  $\phi = 50/75^\circ$ .

The structural characterization of the MCT samples was performed by X-ray diffraction (XRD) using a Panalytical X'Pert Pro triple-axis X-ray diffractometer. X-rays were generated from copper linear fine-focus X-ray tube. The  $\text{CuK}_{\alpha 1}$  line with a wavelength of 0.15418 nm was selected using a four-bounce (440) Ge monochromator. The experimental schemes allowed two cross sections of reciprocal lattice sites to be obtained: normally ( $\omega$ -scanning) and in parallel ( $\omega/2\theta$ -scanning) to the diffraction vector.

## **30.3 Results and Discussions**

### **30.3.1 Surface Topometry Investigation**

It was found that the ion bombardment of the samples investigated has resulted in the essential change of the physical and structural properties of MCT surface. The character of implantation-induced changes depended both on the type of implanted ions and on the implantation parameters such as ion energy, fluence, and angle of the ion beam incidence. Note that the high-energy ion processing of ternary compound was carried out, whereas the structures obtained were similar to those that are formed by ion sputtering on elemental and binary semiconductors.

It was found that in the range of nanoscale, arrays of holes and mounds are generated on a (111) MCT surface as a result of the normal-incidence ion bombardment. Nano-objects on the surface of semiconductor films were researched within the atomic force and scanning electron microscopy methods. We also constructed the histograms which present the superposition of the distribution functions of lateral dimensions in the X – Y plane. The most probable size of nano-objects was determined as the position of the major maximum in the distribution histogram.

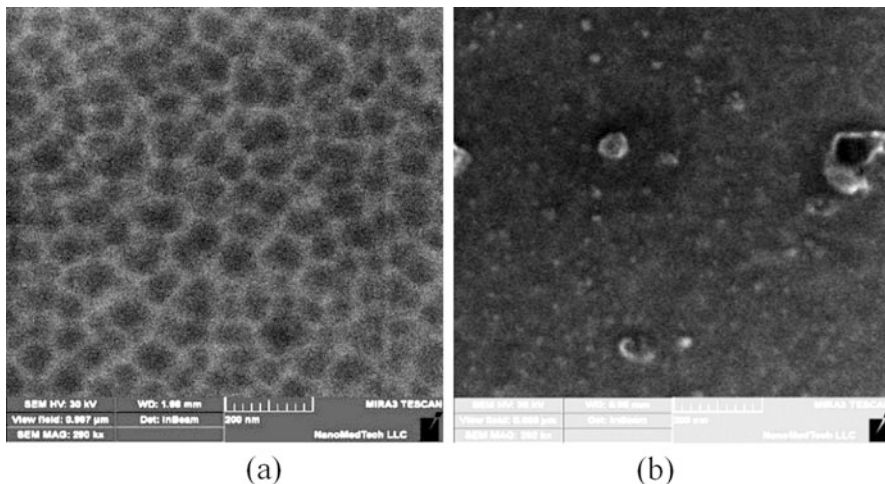


**Fig. 30.1** Typical SEM images of a (111) MCT surface generated as a result of the normal-incidence ion bombardment with boron (a) and silver (b) ions with 100 keV

SEM image of a periodic height modulation induced on a (111) MCT surface by 100 keV  $B^+$  and  $Ag^+$  ions is shown in Fig. 30.1a, b. AFM results of the initial specimen topometry (Fig. 30.2a) show that the surface plane is densely and regularly packed with round-shaped grains with preferred size of 25 nm in diameter. This means that the studied epitaxial film is characterized by a considerable nonequilibrium resource. As a rule, this state is concentrated in mechanical stresses of the local character (grains–pores), which is confirmed by the presence of a network of quasipores 3.5–10 nm in depth and 50–160 nm in diameter. The root-mean-square (RMS) roughness parameter for  $1 \times 1 \mu m^2$  initial surface fragments was in the energy range 2.45–3.34 nm.

After the double implantation with silver ions at NI regime (Fig. 30.2f), the MCT surface undergoes an essential transformation. RMS parameter reduced to 2.17 nm at the initial value 3.34 nm. The quasipores are almost unobservable, the grain boundaries are strongly smeared, and some grains, keeping their sizes in variable, form chains with channels between them.

Figure 30.2b shows AFM reconstruction of periodic height modulations (“nanohole” pattern) induced on a (111) MCT surface with 100 keV NI  $B^+$  ion processing. After low-temperature annealing, MCT surface became denser. The study of the microhardness with the use of a Shimadzu HMV-2000 pointed to increase of its value to 12%. The ordered grid of quasipores is not observed (see Fig. 30.2c). At the same time, some grains become consolidated.

NI  $Ag^+$  ion bombardment gives rise to emergence of a uniform array of nano-islands 5–25 nm in height and with a base diameter of 13–35 nm (see Fig. 30.2d). With increasing fluence from  $3 \times 10^{13} \text{ cm}^{-2}$  to  $4.8 \times 10^{13} \text{ cm}^{-2}$  and at OI regime, the diameter of nano-islands is found to increase, and the conjoined structure has

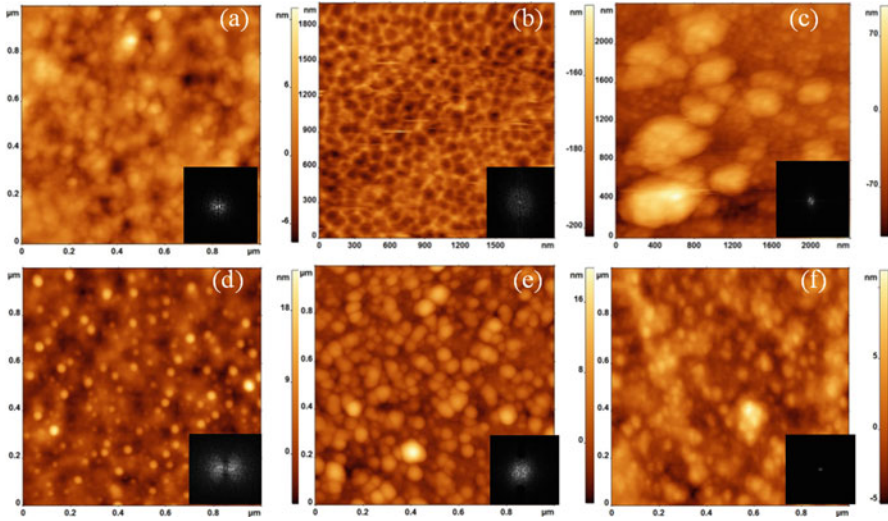


**Fig. 30.2** AFM images of a (111) MCT surface generated as a result of the ion bombardment with  $B^+$  and  $Ag^+$  ions: (a) typical virgin surface, (b)  $B^+$  ( $\theta = 0^\circ$ , 100 keV,  $3 \times 10^{13} \text{ cm}^{-2}$ ), (c)  $B^+$  ( $\theta = 0^\circ$  and postimplantation annealing, 100 keV,  $3 \times 10^{13} \text{ cm}^{-2}$ ), (d)  $Ag^+$  ( $\theta = 0^\circ$ , 100 keV,  $3 \times 10^{13} \text{ cm}^{-2}$ ), (e)  $Ag^+$  ( $\theta = 45^\circ$ , 140 keV,  $4.8 \times 10^{13} \text{ cm}^{-2}$ ), (f)  $Ag^+$  ( $\theta = 0^\circ$ , 140 keV, two doses of  $4.8 \times 10^{13} \text{ cm}^{-2}$ ). *Inset*: Fourier transforms of AFM images

been formed as shown in Fig. 30.2e. The size distribution histogram for nano-objects on the specimen surface irradiated at OI regime has a linear section (on the logarithmic scale). The presence of such a section means that the structures with fractal geometry are formed on the surface of a semiconductor compound epitaxial film [23].

The corresponding 2D fast Fourier transformation (FFT) has been depicted in insets of Fig. 30.2. They reveal that there is no signature of ordering of nanostructures over the surfaces for all regimes.

Thus, it was found that in the range of nanoscale, arrays of holes and mounds on (111) MCT surface have been fabricated using 100–140 keV  $B^+$  and  $Ag^+$  ion beam irradiation. In addition, after NI irradiation with  $Ag^+$  ions, a uniform array of nano-islands 5–25 nm in height was obtained, while the topometry investigation after OI irradiation with  $Ag^+$  ions points to the nanostructures with fractal geometry.

### 30.3.2 Subsurface Region Investigation

The optical characteristics of the subsurface region of implanted MCT samples were carried out by ellipsometry. It was observed the formation of the complex optical system [24] after NI ion bombardment and annealing. In particular, a two-layer

model of the refracting system, namely, damaged layer on MCT/substrate, was engaged for samples processed with  $B^+$  ions. For the samples implanted with  $Ag^+$ , the interpretation of the ellipsometry measurements became possible only by introducing an additional layer, which is associated with a specific character of damage in the MCT matrix induced by silver ions. The values of refractive indexes ( $n$ ) and extinction coefficients ( $k$ ) in the damaged layers turned out anomalously small [25] with respect to the corresponding value for MCT ( $n = 3.87$ ,  $k = 1.1$ ). The thickness of a damaged layer determined from the results of ellipsometry measurements was about  $0.38 \mu\text{m}$  for boron and  $0.1 \mu\text{m}$  for silver implanted samples. These findings are consistent with the simulation of the implantation process using the TRIM\_2008 program package which allowed us to state that the introduced impurity is mainly localized in the subsurface region of MCT [25]. Damages revealed in the near-surface region of MCT form a layer not thicker than  $\sim 0.4 \mu\text{m}$  and  $\sim 0.1 \mu\text{m}$  in the case of implantation with boron and silver, respectively.

### 30.3.3 XRD Investigation

X-ray rocking curves (RC) obtained in the coherent-scattering region from the symmetrical  $\omega/2\theta$ -scanning for MCT-based structures before and after implantation point out to the compression of the boron implanted MCT and tension of the silver implanted MCT layers.

The structural properties of the MCT epilayers were also investigated using X-ray high-resolution reciprocal space mapping (HR-RSM). The maps are a bonded set of scans perpendicular ( $q_x$ ) and parallel ( $q_z$ ) to the diffraction vector. The observed distribution of the intensity along axis  $q_z$  indicates the existence in the initial material of some structural heterogeneity caused by the existence of the vacancies ( $q_z < 0$ ) and interstitials ( $q_z > 0$ ) (Fig. 30.3a). The micro-defect system in the initial material is apparently compensated that is confirmed by the symmetric form of the initial RC and RSM. Implantation with boron results in insignificant changes in the RSMs. At the same time, two-dimensional RSMs of the intensity distribution around (111) sites for the MCT layer implanted by silver ions have shown following results depicted in Fig. 30.3b–d.

First of all, the formation of the significant halo in the central part of the map of the implanted sample (Fig. 30.3b–d) indicates the increase in the MCT film imperfection after the implantation performed. After processing both with NI (Fig. 30.3c) and with OI (Fig. 30.3d) geometry, the significant increase in the half-width of the  $\omega$ -scan ( $q_x$  direction) in the central part of the RSMs is observed. It can mean the formation of misorientation-type defects as a result of the ion bombardment. Moreover, the appearance of asymmetry in the  $q_z$  direction points out to the initiation of the tensile deformation in the samples investigated after  $Ag^+$  implantation.



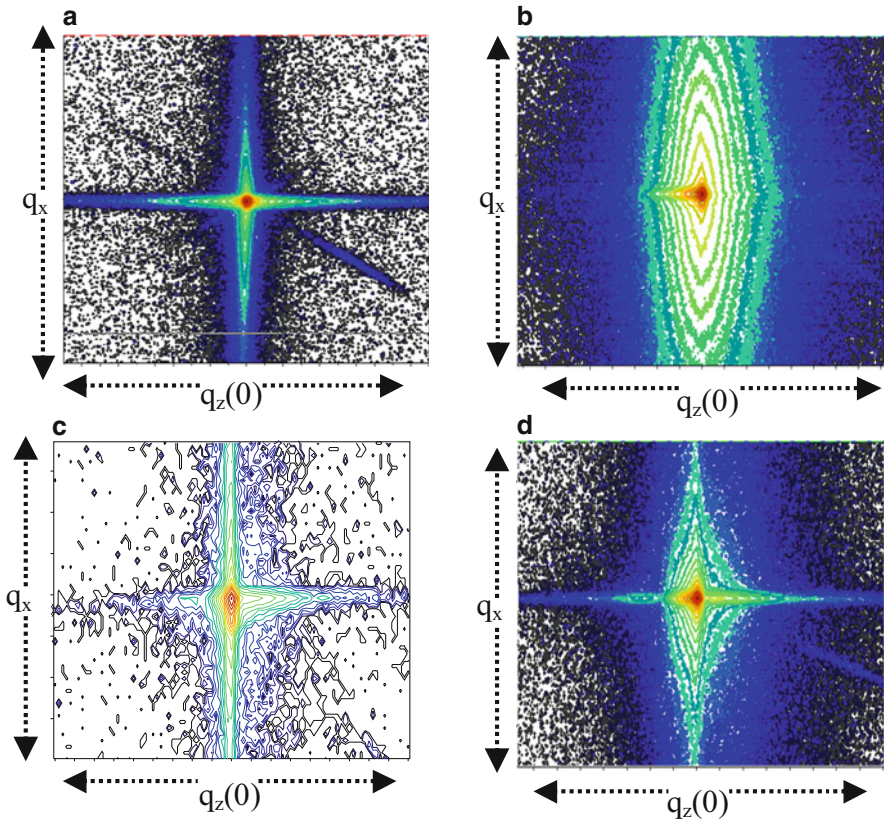


**Fig. 30.3** Reciprocal space maps of MCT-based heterostructure obtained from the combined  $\omega$  and  $(\omega-2\theta)$  scans using high-resolution modules: (a) before implantation, (b)  $\text{Ag}^+$  ( $\theta = 0^\circ$ , 140 keV, two doses of  $4.8 \times 10^{13} \text{ cm}^{-2}$ ), (c)  $\text{Ag}^+$  ( $\theta = 0^\circ$ , 100 keV,  $3 \times 10^{13} \text{ cm}^{-2}$ ), (d)  $\text{Ag}^+$  ( $\theta = 45^\circ$ , 140 keV,  $4.8 \times 10^{13} \text{ cm}^{-2}$ )

It should be also noted that peculiarity at  $q_z < 0$  on the reciprocal space map of MCT-based heterostructure (Fig. 30.3d) can mean the formation of the new phase. XRD investigation in the grazing-incidence (GI) scheme has confirmed the formation of the new phase after NI [26] and OI [27] silver implantation. This is the polycrystalline phase of the MCT (ICDD PDF 00-051-1122) and (111)  $\text{Ag}_2\text{O}$  phase (ICDD PDF 00-041-1104) in the near-surface region. The GI diffractograms have been collected by irradiating the samples at an incident angle ( $\theta_{\text{inc}}$ ) of  $1^\circ$ . The penetration depth at this incidence angle was  $\sim 400 \text{ nm}$ .

### 30.3.4 MCT Nanostructuring Mechanism Discussion

Thus, the experimental study demonstrates the nanostructurization as well as change of the chemical composition on the MCT surface after NI and OI ion beam

irradiation. As discussed in the introduction, a lot of experimental as well as theoretical efforts have been devoted to understand the mechanism of nanoscale structure formation on surfaces subjected to energetic ion bombardment. According to the Bradley–Harper theory [12], pattern formation is related to the curvature dependence of the sputtering yield. At that, if a binary compound is subjected to the ion beam processing, one of the components is preferentially sputtered, yielding a thin surface layer of altered stoichiometry. For example, due to preferential sputtering of As from GaAs during ion beam processing, its surface is enriched by Ga [28].

The two main physical mechanisms to explain preferential sputtering effects in alloy systems are differences in the masses of the atoms in the sample, so-called mass effects, and differences in the surface binding energies between atoms, so-called bonding effects. In the case of MCT ternary compound under ion bombardment, Hg, the heaviest element, is preferentially sputtered in both HgCdTe and HgTe [22] so mass effects were not the dominant preferential sputter mechanism. Thus, for MCT alloy sputtered surfaces must be depleted in Hg and enhanced in Te and Cd through the weakness of the Hg–Te bond compared to the Cd–Te bond. However, this scenario conflicts with the results of X-ray diffraction analysis of MCT films with the composition 0.23 irradiated with 100 keV silver ions [26], which proved the formation of polycrystalline MCT layer with  $x = 0.2$  on the surface. According to Sigmund theory [29], the sputtering yield for MCT is about 11, and effective sputtering depth is about 14 Å. In conformity with our experimental results, RMS parameter undergoes changes during ion processing in the range of the sputtering depth, and significant erosion is observed after double impact with 140 keV only.

At the same time, knowing that the deformation accumulation is found to lead to the topological instability of the irradiated surface and being based on our investigations, we can assume that the deformation fields appearing upon implantation of the MCT-based structures are a significant factor of the observed transformation of its surface.

The magnitude of mechanical stresses created in the MCT layer after implantation can be determined from the relation [30]:

$$\sigma(z) = \frac{C_V(z)\beta E}{(1-\nu)}$$

$$C_V(z) = \left( \frac{\Phi}{\sqrt{2\pi\Delta z}} \right) \exp \left[ \frac{(z - \bar{z})^2}{2\Delta z^2} \right]$$

$$C_V(z, \theta) = \left( \frac{\Phi \cos(\theta)}{\sqrt{2\pi\Delta z}} \right) \exp \left[ \frac{(z - R_p \cos(\theta))^2}{2\Delta z^2} \right]$$

where  $\nu$  is Poisson's ratio,  $E$  is the Young modulus,  $z$  is the coordinate,  $\Phi$  is a fluence,  $R_p$  is the projected range,  $C_V(z)$  is the distribution profile of an impurity

introduced into the target, and  $C_V(z, \theta)$  is the distribution profile of an impurity for OI regime of the ion bombardment. The coefficient of MCT crystal lattice contraction by the introduced implant,  $\beta$ , was determined using the results of X-ray diffraction studies of samples investigated [25]. The mechanical stresses that arise in the near-surface layer of an epitaxial MCT layer attain the maximal value of  $1.4 \times 10^3$  Pa for boron and  $(2.2\text{--}2.9) \times 10^5$  Pa for silver implanted structure (see Table 30.1).

As we know, the deformation sign is dependent on the ratio of ionic radii of the matrix atoms and introduced impurity [18]. Implantation with ions of small radius (such as  $B^+$ ,  $r_B \sim 0.97 \text{ \AA}$ ) stimulates the compression of the damaged layer, whereas the implantation with ions of radius comparable with that of Hg (in our case, these are  $Ag^+$  ions,  $r_{Ag} \sim 1.44 \text{ \AA}$ ,  $r_{Hg} \sim 1.55 \text{ \AA}$ ) gives rise to tensile stress in the damaged layer, as confirmed by the X-ray diffraction data obtained in this work and in our previous work [25–27]. As a result, each of the local volumes (blocks) of the crystal undergoes an action of forces from the neighboring blocks, and their resulting force and its impulse will not be zero because of fluctuations. When the stress will be higher than the ultimate strength of MCT, the action of the forces can bring about the rotation of small crystalline blocks and the structuring of the material.

## 30.4 Conclusions

In conclusion, the evolution of surface morphology of (111)  $Hg_{1-x}Cd_xTe$  ( $x \sim 0.223$ ) epilayers due to ion irradiation in the energy range 100–140 keV was studied. Modification of this ternary compound was performed using the method of normal- ( $\theta = 0^\circ$ ) and oblique-incidence ( $\theta = 45^\circ$ ) ion bombardment. The character of implantation-induced changes depended both on the type of implanted ions and on the implantation parameters such as ion energy, fluence, and angle of the ion beam incidence. Note that the high-energy ion processing of ternary compound was carried out, whereas the structures obtained were similar to those that are formed by ion sputtering on elemental and binary semiconductors.

We have shown that in the range of nanoscale, arrays of holes and mounds on (111) MCT surface have been fabricated using  $B^+$  and  $Ag^+$  ion beam irradiation, respectively. In addition, after NI irradiation with  $Ag^+$  ions, a uniform array of nano-islands 5–25 nm in height was obtained, while the topometry investigation after OI irradiation with  $Ag^+$  ions points to the structures with fractal geometry.

The deformation fields appearing upon implantation of the studied heterostructure are a significant factor of the observed transformation of its surface. It was found that processing of MCT films with ions of different radii ( $B^+$  and  $Ag^+$ ) leads to the formation of surface layers which are significantly different in thickness (400 nm and 100 nm, respectively), as well as with maximum mechanical stresses that differ by two orders of magnitude ( $1.4 \times 10^3$  Pa and  $2.2 \times 10^5$  Pa, respectively). XRD investigations point out to the compression of the boron implanted MCT



and tension of the silver implanted MCT layers. It was supposed that nano-relief character induced by ion beam irradiation of the MCT depends on the sign of the surface layer deformation.

The observed effect of nanostructuring can be useful from the viewpoint of developing a new class of electro-optical facility based on MCT that possesses a necessary combination of optical, electro-physical, and photoelectric properties. It was found also a surprising sensitivity of MCT-based heterostructures for sub-THz radiation after the oblique-incidence ( $45^\circ$ ) bombardment with silver ions (140 keV) [15]. The signal was detected without antenna and amplification, and NEP at  $\nu \approx 140$  GHz and 296 K reaches  $4.5 \cdot 10^{-8}$  W/Hz $^{1/2}$ .

**Acknowledgment** The authors gratefully acknowledge Dr. O. Lytvyn, Dr. A. Korchevyi, and Dr. A. Gudymenko for helpful cooperation in the surface characterizations.

## References

1. Malherbe JB (2003) In: Chakraborty P (ed) Ion beam analysis of surfaces and interfaces of condensed matter systems. Nova Science, New York, p 357
2. Battle X, Labarta A (2002) Finite-size effects in fine particles: magnetic and transport properties. *J Phys D Appl Phys* 35:R15; Holdenried M, Micklitz H (2000) Tunneling magnetoresistance in granular films made of well-defined Co clusters embedded in an inert-gas matrix. *Eur Phys J* 13(2):205–208
3. Chini TK, Sanyal MK, Bhattacharyya SR (2002) Energy-dependent wavelength of the ion-induced nanoscale ripple. *Phys Rev B* 66:153404
4. Gago R, Vázquez L, Cuerno R, Varela M, Ballesteros C, Albella JM (2001) Production of ordered silicon nanocrystals by low-energy ion sputtering. *Appl Phys Lett* 78(21):3316–3318
5. Ziberi B, Cornejo M, Frost F, Rauschenbach B (2009) Highly ordered nanopatterns on Ge and Si surfaces by ion beam sputtering. *J Phys Condens Matter* 21:224003
6. Wei Q, Zhou X, Joshi B, Chen Y, Li K-D, Wei Q, Sun K, Wang L (2009) Self-assembly of ordered semiconductor nanoholes by ion beam sputtering. *Adv Mater* 21:2865–2869
7. Facsko S, Dekorsy T, Koerdt C, Trappe C, Kurz H, Vogt A, Hartnagel HL (1999) Formation of ordered nanoscale semiconductor dots by ion sputtering. *Science* 285:p1551–p1553
8. Plantevin O, Gago R, Vázquez L, Biermanns A, Metzger TH (2007) In situ X-ray scattering study of self-organized nanodot pattern formation on GaSb (001) by ion beam sputtering. *Appl Phys Lett* 91:113105
9. Frost F, Schindler A, Bigl F (2000) Roughness evolution of ion sputtered rotating InP surfaces: pattern formation and scaling laws. *Phys Rev Lett* 85:4116
10. Jiaming Z, Qiangmin W, Ewing RC, Jie L, Weilin J, Weber WJ (2008) Self-assembly of well-aligned 3C-SiC ripples by focused ion beam. *Appl Phys Lett* 92(19):3107
11. Motta FC, Shipman PD, Bradley RM (2012) Highly ordered nano-scale surface ripples produced by ion bombardment of binary compounds. *J Phys D Appl Phys* 45(12):122001–1224pp
12. Bradley RM, Harper JME (1988) Theory of ripple topography induced by ion bombardment. *J Vac Sci Technol A* 6(4):2390–2395
13. Moreno-Barrado A, Castro M, Gago R, Vázquez L, Muñoz-García J, Redondo-Cubero A, Cuerno R (2015) Nonuniversality due to inhomogeneous stress in semiconductor surface nanopatterning by low-energy ion-beam irradiation. *Phys Rev B* 91(15):155303

14. Norris SA (2012) Stress-induced patterns in ion-irradiated silicon: model based on anisotropic plastic flow. *Phys Rev B* 86(23):235405
15. Kryshab T, Savkina RK, Smirnov AB, Kladkevich MD, Samoylov VB (2016) Multi-band radiation detector based on HgCdTe heterostructure. *Phys Stat Solidi (c)* 13(7–9):639–642
16. Holander-Gleixner S, Williams BL, Robinson HG, CRJ H (1997) Modeling of junction formation and drive-in in ion implanted HgCdTe. *J Electron Mater* 26(6):629–634
17. Mollard L, Destefanis G, Baier N, Rothman J, Ballet P, Zanatta JP, Pautet C (2009) Planar p-on-n HgCdTe FPAs by arsenic ion implantation. *J Electron Mater* 38(8):1805–1813
18. Ebe H, Tanaka M, Miyamoto Y (1999) Dependency of pn junction depth on ion species implanted in HgCdTe. *J Electron Mater* 28(6):854–857
19. Nemirovsky Y, Bahir G (1989) Passivation of mercury cadmium telluride surfaces. *J Vac Sci Technol A* 7(2):450–459
20. Williams BL, Robinson HG, Helms CR, Zhu N (1997) X-ray rocking curve analysis of ion implanted mercury cadmium telluride. *J Electron Mater* 26:600–605
21. Novoselova AV, Lazarev VB (eds) (1979) *Physicochemical properties of semiconductors. Handbook* [in Russian]. Nauka, Moscow
22. Stahle CM, Helms CR (1992) Ion sputter effects on HgTe, CdTe, and HgCdTe. *J Vac Sci Technol A* 10:3239–3245
23. Barabasi A-L, Stanley HE (1995) *Fractal concepts in surface growth*. Cambridge University Press, Cambridge
24. Klyui NI, Lozinskii VB, Luk'yanov AN, Morozhenko VA, Savkina RK, Sizov FF, Smirnov AB, Deriglazov VA (2012) Ion-plasma treatment of Cd $_{1-x}$ Zn $_x$ Te ( $x \sim 0.04$ ) single crystals and application of antireflection diamond-like carbon films. *Tech Phys* 57(8):1121–1126
25. Smirnov AB, Litvin OS, Morozhenko VO, Savkina RK, Smoliy MI, Udovytska RS, Sizov FF (2013) Role of mechanical stresses at ion implantation of CdHgTe solid solution. *Ukr J Phys* 58(9):872–880
26. Sizov FF, Savkina RK, Smirnov AB, Udovytska RS, Kladko VP, Gudimenko AI, Safruk NV, Lytvyn O (2014) Structuring effect of heteroepitaxial CdHgTe/CdZnTe systems under irradiation with silver ions. *Phys Solid State* 56(11):2160–2165
27. Sizov FF, Savkina RK, Smirnov AB, Udovytska RS (2016) Patent of Ukraine UA 112999 C2. *Buletyn Promyslova vlasnist'* (3) (in Ukrainian)
28. Kumar T, Khan SA, Singh UB, Verma S, Kanjilal D (2012) Formation of nanodots on GaAs by 50keV Ar $^+$  ion irradiation. *Appl Surf Sci* 258(9):4148–4151
29. Carter G (2001) The physics and applications of ion beam erosion. *J Phys D Appl Phys* 34(3):R1
30. Cerutti A, Ghezzi C (1973) X-ray observations of induced dislocations at simple planar structures in silicon. *Phys Stat Solidi (a)* 17:273–245

# Chapter 31

## The Plasmon-Polariton Mirroring Due to Strong Fluctuations of the Surface Impedance

Yu.V. Tarasov, O.V. Usatenko, and D.A. Iakushev

### 31.1 Introduction

The complexity of electromagnetic phenomena in the study of surface polariton waves has led in due time to the need for determining some simple parameters that would allow for easy modeling, calculations, and design of electromagnetic (EM) devices. Among these simple and reliable parameters, the impedance is most commonly used. It allows to greatly simplify the solution of the problem and circumvents the necessity to study the solution of electrodynamic equations directly in a metal. A brief review of the work on the development of the impedance concept, different from that of Leontovich, can be found in paper [1].

Regardless of the method of solving the problem—either accurately taking into account the surface topography or modeling it through an impedance condition—there appears a need to study an integral equation describing the PPW scattering processes. In particular, the integral equation arises from the use of the Leontovich boundary condition (functional equation) after substituting the solution of the Helmholtz equation in the form of an expansion into eigenwaves (in the simplest case, plane waves) and switching to the momentum representation, see Eq. (31.11) below or the paper by Depine [2].

In the present study, we examine plasmon-polariton scattering by a metal strip of a finite width  $L$  with fluctuating impedance (see Fig. 31.1). The wave vector of the plasmon-polariton lies in the plane of the metal and is directed perpendicular to the scattering section of the surface. The radiation arising due to the fluctuations of the surface impedance is considered with the account of the absorption due to the finite

---

Y.V. Tarasov • O.V. Usatenko • D.A. Iakushev (✉)  
A.Ya.Usikov Institute for Radiophysics and Electronics of the NAS of Ukraine, 12,Proskura Str.,  
61085, Kharkov, Ukraine  
e-mail: [daniely@ukr.net](mailto:daniely@ukr.net)

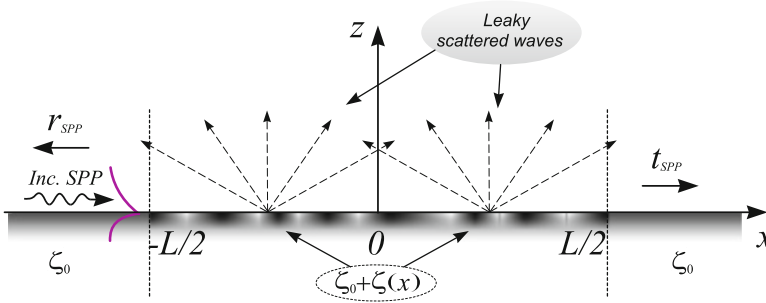


**Fig. 31.1** The geometry of the PPW scattering on a flat boundary with the surface impedance randomly modulated over a segment of finite length  $L$

conductivity of the metal. For the analysis of the problem, we apply a standard approach consisting in the analysis of the integral equation for the scattered field expressed through the Fourier components of the EM field on the metal surface. The main difficulty in solving this equation is associated with the presence of the integral term, which is usually considered as a small perturbation, in powers of which the solution is sought. We propose and justify the criterion for the evaluation of the PPW scattering intensity, which is the Hilbert norm of the mixing operator for the intermediate scattering states. A rough qualitative assessment of the norm is that it is proportional to the mean square fluctuation of the impedance and inversely proportional to its real part (the accurate estimate is given by expression (31.20)). We calculated the scattered radiation pattern and showed that for the weak scattering the radiated energy is proportional to the Fourier transform of the binary correlation function of the impedance, the argument of which is equal to the difference between the wave number of the surface polariton and the projection of the wave vector of the scattered field harmonic directed toward the observation point. This dependence has an obvious resemblance to the angular dependence of the field scattered by reflective gratings, where Wood found the anomalies [3].

We pay special attention to another limiting case, where the integral term in the master equation is major compared to those outside the integral. We show that with increasing the metal conductance, the fraction of the field scattered into vacuum increases compared to the PPW ohmic losses in the metal. Simultaneously, the contribution of the integral term grows with respect to that of the nonintegral term. For strong impedance fluctuations, the scattered field becomes almost deterministic in nature, and in the limit, when the dissipation of charge carriers in the metal completely vanishes, the PPW is totally reflected backward by the surface region containing the fluctuating impedance. Thus, we show that in the model of perfectly conductive metal the integral term is the primary one, and the starting point for solving any equation containing inhomogeneity should be the solution of the integral rather than algebraic equation. In other words, in the model of a dissipation-free metal, the standard plasmon-polariton solution is unstable with respect to infinitesimal perturbations.

## 31.2 Problem Statement

Let us consider the two-dimensional problem of scattering of a surface plasmon-polariton wave excited by a certain source (e.g., a slit [4, 5]) on the impedance boundary between a metal and vacuum. A finite section of the boundary is assumed to have random impedance. We assume also that the impedance depends on one coordinate only and describe it with a function consisting of two complex terms:

$$Z_s(x) = \zeta_0 + \zeta(x) , \quad (31.1)$$

of which the first term,  $\zeta_0$ , is constant, while the second term,  $\zeta(x)$ , is a random function of the  $x$ -coordinate. This function is assumed to have nonzero value solely in the interval  $\mathbb{L} : x \in [-L/2, L/2]$  and to have zero average value within this interval,  $\langle \zeta(x) \rangle = 0$ .

The surface plasmon-polariton is a  $p$ -polarized (TM) wave with the only nonzero component of the magnetic field  $H_y \equiv H(\mathbf{r})$  that satisfies Helmholtz equation:

$$(\Delta + k^2) H(\mathbf{r}) = 0 , \quad (31.2a)$$

and boundary condition

$$\left( \frac{\partial H}{\partial z} + ik[\zeta_0 + \zeta(x)]H \right) \Big|_{z=0} = 0 . \quad (31.2b)$$

Symbol  $\Delta$  in (31.2a) denotes the (two-dimensional) Laplace operator;  $k = \omega/c$  and  $\mathbf{r} = (x, z)$  are the wave number and two-dimensional radius-vector, respectively. Due to the complexity of random function  $\zeta(x)$ , we set its binary correlation properties by Eq. (31.13) below.

For the coordinate-independent surface impedance, problem (31.2) is easily solved and provided  $\text{Im } \zeta_0 < 0$  has, in general, two solutions of the following form:

$$H_{\text{SPP}}^{(\pm)}(\mathbf{r}) = \mathcal{A}^{(\pm)} \exp(\pm ik_{\text{SPP}}x - i\zeta_0 kz) , \quad (31.3)$$

$$k_{\text{SPP}} = k \sqrt{1 - \zeta_0^2} .$$

We are interested in polaritons propagating *quasi-freely* along the interface between two media for distances much greater than their wavelength. As it follows from Eq. (31.3), for this the following inequality should hold:

$$\zeta_0' \ll |\zeta_0''| . \quad (31.4)$$

For real metals, the imaginary part of the impedance is negative, and its absolute value does not exceed unity (see, e.g., Ref. [6]). The attenuation length of PPW due

to the dissipation in the metal half-space under condition (31.4) is represented by the following formula:

$$L_{\text{dis}}^{(\text{SPP})} = |k_{\text{SPP}}''|^{-1} = \frac{\sqrt{1 + \zeta_0''^2}}{k\zeta_0'\zeta_0''}. \quad (31.5)$$

Assuming that all the conditions necessary for the existence of a quasi-free PPW in the case of a homogeneous impedance ( $\zeta(x) \equiv 0$ ) are fulfilled, we seek a solution of the problem (31.2) as a sum of certain unperturbed plasmon-polariton-type solution  $H_0(\mathbf{r})$  and “scattered” field  $h(\mathbf{r})$ :

$$H(\mathbf{r}) = H_0(\mathbf{r}) + h(\mathbf{r}). \quad (31.6)$$

It is convenient to model the solution  $H_0(\mathbf{r})$  in the form commonly adopted for one-dimensional scattering problems. In the region  $x < -L/2$ , we take it in the form of a sum of a plasmon-polariton incident from the left, which has the unit amplitude at the left point of the segment  $\mathbb{L}$ , and the reflected PPW, which propagates and is dissipatively attenuated in the opposite direction:

$$H_0^{(l)}(\mathbf{r}) = \exp [ik_{\text{SPP}}(x + L/2) - i\zeta_0 kz] + r_- \exp [-ik_{\text{SPP}}(x + L/2) - i\zeta_0 kz]. \quad (31.7a)$$

To the right of  $\mathbb{L}$ , we choose the unperturbed field  $H_0(\mathbf{r})$  in the form of transmitted PPW only:

$$H_0^{(r)}(\mathbf{r}) = t_+ \exp [ik_{\text{SPP}}(x - L/2) - i\zeta_0 kz]. \quad (31.7b)$$

And finally, in the intermediate region  $x \in \mathbb{L}$ , we set the unperturbed field in the form of a superposition of the field transmitted through the left boundary of  $\mathbb{L}$  and the PPW reflected from its right boundary:

$$H_0^{(in)}(\mathbf{r}) = t_- \exp [ik_{\text{SPP}}(x + L/2) - i\zeta_0 kz] + r_+ \exp [-ik_{\text{SPP}}(x - L/2) - i\zeta_0 kz]. \quad (31.7c)$$

Note here an excessive amount of arbitrary constants in the “seed” solutions (31.7). Below we impose two additional conditions (in the form of continuity of the  $y$ -components of the scattered magnetic field), which eliminate this redundancy.

The scattered field  $h(\mathbf{r})$  from representation (31.6) satisfies Helmholtz equation (31.2a), but with the boundary condition on the surface  $z = 0$ , which is different from the condition (31.2b), viz.,

$$\left( \frac{\partial h(\mathbf{r})}{\partial z} + ik[\zeta_0 + \zeta(x)]h(\mathbf{r}) \right) \Big|_{z=0} = -ik\zeta(x) \left\{ t_- \exp[ik_{\text{SPP}}(x + L/2)] + r_+ \exp[-ik_{\text{SPP}}(x - L/2)] \right\}. \quad (31.8)$$

Moreover, since in the regions  $|x| > L/2$  condition (31.8) allows for the wave equation solution in the form of surface polaritons only, and such solutions have already been taken into account in Eq. (31.7), we can assume that in these areas the function  $h(\mathbf{r})$  is identically equal to zero at  $z = 0$ . As for the conditions which the scattered field should satisfy in the region  $z > 0$ , given the finite size of the surface section considered as the source of this field, we assume that at large distances the field  $h(\mathbf{r})$  fulfills the radiation conditions.

The choice of the unperturbed solution for the Helmholtz equation in the form of the set of functions (31.7) associated with different sections of the  $x$ -axis allows us to couple the elements of the scattering matrix of a plasmon-polariton with its radiation in vacuum and dissipation in the conductive substrate. The dissipative losses are incorporated into the imaginary part of the surface plasmon wave number,  $k_{\text{SPP}}$ . As for the radiation losses, they are determined by the harmonics of the field  $h(\mathbf{r})$  which leak into the upper half-space. If the field  $h(\mathbf{r})$  is found, then by joining the values of the total field at the metal-vacuum interface at the inner side of the end points of the segment  $\mathbb{L}$  with the plasmon-polariton solutions (31.7) taken along the same border at points  $x = \pm(L/2 + 0)$ , we obtain the following set of equations relating the scattering coefficients  $r_{\pm}$  and  $t_{\pm}$ :

$$1 + r_- = t_- + r_+ e^{ik_{\text{SPP}}L} + h(-L/2, 0), \quad (31.9a)$$

$$t_+ = t_- e^{ik_{\text{SPP}}L} + r_+ + h(L/2, 0). \quad (31.9b)$$

From these equations it follows that the scattering coefficients of the ‘‘unperturbed’’ PPW appearing in Eq. (31.7) are directly related to the yet unknown scattered field  $h(\mathbf{r})$ , so they should be determined self-consistently.

### 31.3 General Solution for the Scattered Field

To find the field  $h(\mathbf{r})$ , we do not restrict ourselves to specific regions on the  $x$ -axis and consider the perturbed section of the conductor as a source of the field for the entire upper half-space. Let us seek for the scattered field in the form of an integral:

$$h(\mathbf{r}) = \int_{-\infty}^{\infty} \frac{dq}{2\pi} \tilde{\mathcal{R}}(q) \exp \left[ iqx + i(k^2 - q^2)^{1/2} z \right], \quad (31.10)$$

which satisfies by construction both the wave equation in free space and the radiation conditions at infinity. To determine the scattering amplitude  $\tilde{\mathcal{R}}(q)$ , we use boundary condition (31.8) making its Fourier transform with respect to  $x$ . In this way we arrive at the following integral equation:

$$\begin{aligned} & \left[ \zeta_0 + \sqrt{1 - (q/k)^2} \right] \tilde{\mathcal{R}}(q) + \int_{-\infty}^{\infty} \frac{dq'}{2\pi} \tilde{\mathcal{R}}(q') \tilde{\zeta}(q - q') = \\ & - e^{ik_{\text{SPP}}L/2} \left[ t_- \tilde{\zeta}(q - k_{\text{SPP}}) + r_+ \tilde{\zeta}(q + k_{\text{SPP}}) \right]. \end{aligned} \quad (31.11)$$

If the real part of the surface impedance is not equal to zero ( $\zeta'_0 \neq 0$ ), the expression in the square brackets on the left-hand side of Eq. (31.11) does not vanish on the real frequency axis. By dividing both sides of the equation by this factor, we can rewrite it in the form of the standard Fredholm integral equation of the second kind [7]:

$$\tilde{\mathcal{R}}(q) + \int_{-\infty}^{\infty} \frac{dq'}{2\pi} \mathcal{L}(q, q') \tilde{\mathcal{R}}(q') = -e^{ik_{\text{SPP}}L/2} \left[ t_- \mathcal{L}(q, k_{\text{SPP}}) + r_+ \mathcal{L}(q, -k_{\text{SPP}}) \right]. \quad (31.12a)$$

The kernel of the integral operator on the left-hand side of Eq. (31.12a) has the form

$$\mathcal{L}(q, q') = \left[ \zeta_0 + \sqrt{1 - (q/k)^2} \right]^{-1} \tilde{\zeta}(q - q'). \quad (31.12b)$$

With our assumptions, it is the Hilbert-Schmidt kernel, which ensures the uniqueness of the solution of Eq. (31.12a).

In what follows, we are interested not in the actual field  $h(\mathbf{r})$ , which is, due to the problem statement, a random function of the coordinates, but only in its statistical moments. In the general case, we assume that function  $\zeta(x)$  is complex-valued and set its average value equal to zero,  $\langle \zeta(x) \rangle = 0$ , while its binary correlation functions will be taken in the form

$$\langle \zeta(x) \zeta(x') \rangle = \Xi^2 W(x - x'), \quad (31.13a)$$

$$\langle \zeta(x)^* \zeta(x') \rangle = |\Xi|^2 W(x - x'). \quad (31.13b)$$

The angle brackets  $\langle \dots \rangle$  here and below denote statistical averaging over the realizations of random function  $\zeta(x)$ . Complex parameter  $\Xi = \sigma_R + i\sigma_I$  appearing in Eq. (31.13) is called the (complex) variance of this function. The real parameters  $\sigma_{R,I}$  denote the variances of real and imaginary parts of the impedance, respectively. Function  $W(x)$  is assumed to be real, even, and normalized to unity at the maximum located at  $x = 0$ , and sufficiently rapidly decaying to negligible values at the interval  $|\Delta x| \sim r_c$  (correlation radius).



Equation (31.12a) can be formally solved with the use of the operator approach. With Fredholm operator  $\hat{\mathcal{L}}$ , the kernel of which is represented by Eq. (31.12b), the solution of Eq. (31.12a) can be written as

$$\widetilde{\mathcal{R}}(q) = -e^{ik_{\text{SPP}}L/2} \langle q | (\hat{\mathbf{1}} + \hat{\mathcal{L}})^{-1} \left[ t_- \hat{\mathcal{L}} |k_{\text{SPP}}\rangle + r_+ \hat{\mathcal{L}} |-k_{\text{SPP}}\rangle \right]. \quad (31.14)$$

Here we use Dirac notation for the matrix elements of the operator through bra- and ket-vectors. Operator  $\hat{\mathcal{L}}$  appearing in Eq. (31.14), in its turn, is represented as a product of two operators,  $\hat{\mathcal{L}} = \hat{G}^{(\text{CP})} \hat{\zeta}_L$ , where the operator factors  $\hat{G}^{(\text{CP})}$  and  $\hat{\zeta}_L$  are given by matrix elements:

$$\langle q | \hat{G}^{(\text{CP})} | q' \rangle = \left[ \zeta_0 + \sqrt{1 - (q/k)^2} \right]^{-1} 2\pi \delta(q - q'), \quad (31.15a)$$

$$\langle q | \hat{\zeta}_L | q' \rangle = \widetilde{\zeta}(q - q'). \quad (31.15b)$$

The first of the above operators,  $\hat{G}^{(\text{CP})}$ , is the propagator of a certain wave excitation which will be denoted as a composite plasmon in what follows (the reader can find justification of this term in Ref. [8]). The second factor,  $\hat{\zeta}_L$ , will be called the operator of the impedance perturbation.

Scattering amplitude (31.14) is written as a linear combination of matrix elements of a certain complex-valued operator:

$$\hat{\mathcal{T}} = (\hat{\mathbf{1}} + \hat{\mathcal{L}})^{-1} \hat{\mathcal{L}}. \quad (31.16)$$

These matrix elements play the role of the propagators of the initial states described by vectors  $|\pm k_{\text{SPP}}\rangle$  into the final state of scattering, which corresponds to vector  $|q\rangle$ . In this notation, the operator  $\hat{\mathcal{L}}$  introduced in Eq. (31.12b) can be interpreted as the operator of onefold scattering of the mode with an arbitrary  $x$ -component of the momentum from its “initial” state corresponding to the right mode index into the “final” (left) mode determined by propagator (31.15a). It is natural to associate the intensity of the scattering with the operator  $\hat{\mathcal{L}}$  norm. Depending on the value of this norm, we will define and consider the limiting cases of weak and strong inter-mode scattering below.

We define the norm of the operator  $\hat{\mathcal{L}}$  in a standard way, in terms of the vector norm defined in corresponding Banach space:

$$\begin{aligned} \|\hat{\mathcal{L}}\varphi\|^2 = (\hat{\mathcal{L}}\varphi, \hat{\mathcal{L}}\varphi) &= \iint_{-\infty}^{\infty} \frac{dk_1 dk_2}{(2\pi)^2} \widetilde{\varphi}^*(\kappa_1) \widetilde{\varphi}(\kappa_2) \\ &\times \int_{-\infty}^{\infty} dx \iint_{\mathbb{L}} dx_1 dx_2 \langle x | \hat{\mathcal{L}} | x_1 \rangle^* \langle x | \hat{\mathcal{L}} | x_2 \rangle e^{-ik_1 x_1 + ik_2 x_2}. \end{aligned} \quad (31.17)$$

Here  $\varphi$  stands for a normalized trial function from the respective functional space. We assume that characteristic “microscopic” scales of spatial variation of this function are small as compared with length  $L$ , or at least do not exceed this length by order of magnitude. Given this assumption, it follows immediately that Fourier transforms of the trial functions alter significantly at characteristic scales large (or, at least, of the same order) in comparison with  $1/L$ , which is the characteristic width of prelimit  $\delta$ -functions arising when correlation relations (31.13) are translated to momentum representation. Then, equality (31.17) is reduced to the following approximate form:

$$\langle \|\hat{\mathcal{L}}\varphi\|^2 \rangle \approx |\Xi|^2 \int_{-\infty}^{\infty} \frac{d\kappa}{2\pi} \left| \zeta_0 + \sqrt{1 - (\kappa/k)^2} \right|^{-2} \int_{-\infty}^{\infty} \frac{d\kappa_1}{2\pi} |\tilde{\varphi}(\kappa_1)|^2 \tilde{W}(\kappa - \kappa_1). \quad (31.18)$$

The factors in the integral over  $\kappa_1$  in Eq. (31.18), both  $|\tilde{\varphi}(\kappa_1)|^2$  and  $\tilde{W}(\kappa - \kappa_1)$ , have some scales of variation (localization). For function  $\tilde{\varphi}(\kappa)$  these may be  $1/L$ ,  $1/L_{\text{dis}}^{\text{(SPP)}}$  and  $1/L^{\text{(loc)}}$ , where under  $L^{\text{(loc)}}$  we mean the length of *one-dimensional* Anderson localization, which coincides, by the order of magnitude, with the extinction length. All the above scales are small compared with the inverse correlation length  $1/r_c$ . This suggests that one can calculate the integral over  $\kappa_1$  in Eq. (31.18) by taking correlation function  $\tilde{W}$  out of this integral at point  $\kappa_1 = 0$ . We thus arrive at equality:

$$\langle \|\hat{\mathcal{L}}\|^2 \rangle = |\Xi|^2 \int_{-\infty}^{\infty} \frac{d\kappa}{2\pi} \left| \zeta_0 + \sqrt{1 - (\kappa/k)^2} \right|^{-2} \tilde{W}(\kappa), \quad (31.19)$$

where function  $\tilde{W}(\kappa)$ , based on the above made assumptions, may be taken out of the integral over  $\kappa$  at the maximum points of the first integrand factor, viz., at  $\kappa_{\pm} = \pm k'_{\text{SPP}}$ . As a result, we obtain the following expression for the operator  $\hat{\mathcal{L}}$  norm squared:

$$\langle \|\hat{\mathcal{L}}\|^2 \rangle \approx |\Xi|^2 \frac{k|\zeta'_0|}{\zeta'_0 \sqrt{1 + \zeta''_0{}^2}} \cdot \frac{1}{2} \sum_{\pm} \tilde{W}(\pm k'_{\text{SPP}}). \quad (31.20)$$

### 31.4 Weak Inter-mode Scattering

In the parameter range where the inequality holds

$$\langle \|\hat{\mathcal{L}}\|^2 \rangle \ll 1, \quad (31.21)$$

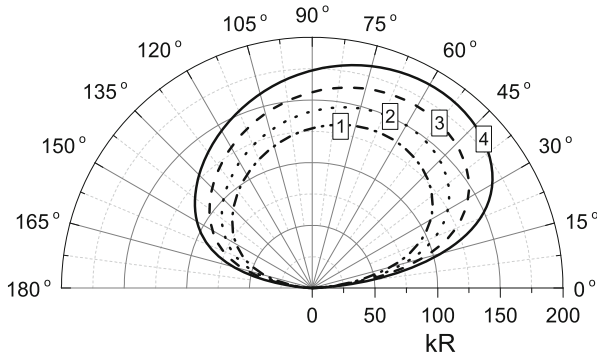


**Fig. 31.2** Radiation patterns for  $\|\hat{L}\| \ll 1$  at different values of the real part of the surface impedance. Curve 1— $\zeta'_0 = 0, 1$ ; curve 2— $\zeta'_0 = 0, 07$ ; curve 3— $\zeta'_0 = 0, 04$ ; curve 4— $\zeta'_0 = 0, 01$ . Other parameters are identical for all the diagrams:  $\zeta''_0 = -0, 25$ ;  $\Xi = 0, 125$ ;  $kr_c = 0, 5$ ;  $kL = 7$

the scattering will be considered as weak. Expanding the inverse operator on the right-hand side of Eq. (31.14) into the operator power series and retaining only the first term of this series, we can write the scattering amplitude in the following approximate form:

$$\tilde{\mathcal{R}}(q) \approx -e^{ik_{SPP}L/2} \{q| (t-\hat{L}|k_{SPP}) + r_+\hat{L}| -k_{SPP} \rangle \} . \quad (31.22)$$

Obviously, in Eq. (31.22) only onefold scattering through composite plasmons is taken into account.

The result obtained thereby consists in that the parent plasmon-polariton incident onto the surface region with modulated impedance passes through this region being scattered into the bulk modes relatively weakly. In this work, we do not dwell on this limiting case, referring the interested reader to paper [8]. We only provide here in Fig. 31.2 the radiation diagram obtained in that paper. Note especially that if the dissipation in the metallic part of the considered medium is gradually reduced, the PPW scattering into the upper (dielectric) half-space in the form of spatial harmonics quasi-isotropically distributed over the angle variable increases, while it does not undergo essential variation within the plane of the primordial PPW propagation.

### 31.5 Strong Mixing of Scattered Modes

The scattering cannot be considered as weak, and, correspondingly, one cannot limit oneself to single scattering, if the norm of the operator  $\hat{L}$  becomes of the order of unity or a fortiori when it exceeds it. We will consider the case where the inequality holds

$$\|\hat{\mathcal{L}}\|^2 \gg 1 \quad (31.23)$$

as the limit of strong inter-mode scattering. If the above inequality is satisfied, expression (31.14) for the scattering amplitude can be rearranged by simple algebraic manipulation with operator (31.16) and converted to the following approximate (in parameter  $\|\hat{\mathcal{L}}\|^{-1}$ ) form:

$$\begin{aligned} \tilde{\mathcal{R}}(q) &= -e^{ik_{\text{SPP}}L/2} \langle q | (\hat{\mathbf{1}} + \hat{\mathcal{L}})^{-1} [t_- \hat{\mathcal{L}} |k_{\text{SPP}}\rangle + r_+ \hat{\mathcal{L}} | -k_{\text{SPP}}\rangle] \\ &= -e^{ik_{\text{SPP}}L/2} \left[ \langle q | \hat{\mathbf{1}} - (\hat{\mathbf{1}} + \hat{\mathcal{L}})^{-1} \right] [t_- |k_{\text{SPP}}\rangle + r_+ | -k_{\text{SPP}}\rangle] \\ &\approx -e^{ik_{\text{SPP}}L/2} \left\{ t_- \Delta_L(q - k_{\text{SPP}}) + r_+ \Delta_L(q + k_{\text{SPP}}) \right. \\ &\quad \left. - \langle q | \hat{\mathcal{L}}^{-1} [t_- |k_{\text{SPP}}\rangle + r_+ | -k_{\text{SPP}}\rangle] \right\}. \end{aligned} \quad (31.24)$$

From Eq. (31.24), in the leading approximation in  $\|\hat{\mathcal{L}}\|^{-1} \ll 1$  the scattered field is

$$\begin{aligned} h^{(0)}(\mathbf{r}) &= -e^{ik_{\text{SPP}}L/2} \int_{-\infty}^{\infty} \frac{dq}{2\pi} \left[ t_- \Delta_L(q - k_{\text{SPP}}) + r_+ \Delta_L(q + k_{\text{SPP}}) \right] \\ &\quad \times \exp\left( iqx + i\sqrt{k^2 - q^2}z \right). \end{aligned} \quad (31.25)$$

Setting  $z = 0$  in Eq. (31.25), we immediately obtain the value of the scattered field at the metal-insulator interface inside segment  $\mathbb{L}$ :

$$h^{(0)}(x, 0) \approx -e^{ik_{\text{SPP}}L/2} \left( t_- e^{ik_{\text{SPP}}x} + r_+ e^{-ik_{\text{SPP}}x} \right) \quad (x \in \mathbb{L}). \quad (31.26)$$

Matching the values of this field with the zero values outside segment  $\mathbb{L}$ , we obtain a set of two equations for determining the coefficients  $t_-$  and  $r_+$ . If the lower medium is dissipative and the wave number  $k_{\text{SPP}}$  is, accordingly, complex, the system has only the trivial solution,  $t_- = r_+ = 0$ . Instead, if we assume zero dissipation, a nontrivial solution with arbitrary  $t_- = \pm r_+$  becomes possible. In this case the polariton propagation parameter is quantized through the condition  $k_{\text{SPP}}L = n\pi$ , which corresponds to the formation of a resonator (standing waves) inside disordered segment of the interface. Formally, the resonant reflection occurs due to the mismatch of the wave states within the “disordered” segment and outside it [9]. But regardless of whether or not there is dissipation in the conductor, in both cases the matching conditions (31.9) lead to the equations

$$1 + r_- = 0, \quad t_+ = 0, \quad (31.27)$$

meaning that in the leading approximation in the inverse norm of the operator  $\mathbb{L}$ , the segment of the boundary with the perturbed impedance acts as an almost perfect reflector for the incident PPW.

In the region  $kz \gg 1$ , where it does not altogether make sense to talk about plasmon-polaritons, the scattered field can be calculated with asymptotic accuracy far away from the scattering source, i. e., the segment of the perturbed boundary. Assuming that inequality  $|\mathbf{r}| = \sqrt{x^2 + z^2} \gg L$  is fulfilled and using the stationary phase method, we arrive at the following formula for the scattered field in the Fraunhofer zone:

$$h^{(0)}(\mathbf{r}) \approx -\sin\phi \sqrt{\frac{2\pi k}{R}} \exp\left[i(kR + k_{\text{SPP}}L/2 - \pi/4)\right] \times \left[t_- \Delta_L(q_0 - k_{\text{SPP}}) + r_+ \Delta_L(q_0 + k_{\text{SPP}})\right]. \quad (31.28)$$

Here,  $q_0 = kx/R = k \cos\phi$  is the stationary phase point. Since accounting for even weak dissipation in the conductor leads to the vanishing coefficients  $t_-$  and  $r_+$ , the field (31.28), which forms the scattering diagram, is zero in the leading approximation. The suppression of the leaking waves, in conjunction with Eq. (31.27), leads to an effectively one-dimensional scattering of surface polaritons in an open and essentially non-1D system. Yet, one should keep in mind that this effect can only occur under strong scattering of the PPW, which actually corresponds to inequality:

$$|\Xi|^2 k^2 L_{\text{dis}}^{(\text{SPP})} \widetilde{W}(k'_{\text{SPP}}) \gg 1. \quad (31.29)$$

This relation is certainly satisfied in the dissipation-free limit, since in this case  $L_{\text{dis}}^{(\text{SPP})} \rightarrow \infty$ .

## 31.6 Discussion

To conclude, in this study a detailed theory of the scattering of plasmon-polariton waves by a segment of the metal-dielectric (vacuum) interface with randomly distributed surface impedance is developed. The applied operator approach made it possible to analyze the scattered fields for any scattering intensity, from weak scattering, commonly considered in the other theories, to extremely strong scattering. To estimate the level of scattering we proposed and justified a suitable criterion based on the Hilbert norm of the mixing operator for the intermediate scattering states—composite polaritons. The term composite refers to the mixed states, which represent a weighted sum of true surface polaritons and specific bulk (quasi-Norton) waves responsible for the energy leakage into the dielectric upon scattering of the PPW by the defective segment of the interface.

Under conditions when the plasmon-polariton scattering is regarded as weak, which is only possible in the case of a sufficiently high level of dissipation in the conductor, the main result of the scattering, except for the dissipative loss, is the radiation of some fraction of PPW energy from the surface of the conductor into the bulk of the dielectric. We have succeeded in calculating the radiation pattern and shown that the radiated energy is proportional to the Fourier transform of the binary correlation function of the impedance, which is taken at a point equal to the difference between the wave number of the surface polariton and the projection on the boundary plane of the wave vector of quasi-Norton harmonics directed toward the (remote) position of the detector (see Ref. [8] for details). This dependence has an obvious resemblance to the angular dependence of the fields scattered by reflective gratings, in which Wood [3] once discovered the anomalies in the form of reflection resonances and the origin of which has been later explained by Fano [11]. The role of such resonances in the PPW scattering by an interface segment with random impedance should be played by the maxima of the impedance correlation function. For generic random processes such maxima are usually located near zero argument of the correlation function, and the abovementioned difference between the wave numbers typically does not coincide with them.

If the parameters of the impedance and the plasmon-polariton wave are such that the scattering is not weak but rather is strong (in the sense of inequality (31.29)), the result of the scattering is reduced to almost mirror reflection of the incident surface polariton and the suppression of the quasi-Norton (bulk) component of its radiation. It should be noted that the PPW scattering can become strong not only through an increase in the impedance variance but also due to the reduction in the dissipative loss in the underlying conductor. The norm of the mixing operator for the scattered modes is inversely proportional to the dissipative part of the impedance and can become arbitrarily large even for small but finite values of its reactive component. The situation here is reminiscent of that occurring at normal incidence of a plane wave on a semi-bounded one-dimensional disordered medium, in which, due to the Anderson (interference) localization of states, further penetration of the field becomes impossible. The incident wave is completely (yet again, in the absence of dissipative losses) reflected in backward direction.

Meanwhile, the propagation medium we have chosen for analysis is not one-dimensional. Moreover, the system considered here is non-Hermitian, and in such systems the Anderson localization is known to be, as a rule, rather weak. The effective “one-dimensionalization” of the system and, as a consequence, the absence of waves leaking to the upper half-space arise in our case as a result of wave interference upon their *multiple* scattering on the impedance fluctuations. In view of this, the fact that the effectiveness of the interference, along with the intensity of the scattering, reduces with the increase in the dissipation within the conducting substrate seems to be completely natural.

The fact that under strong scattering the plasmon-polariton energy leakage into the bulk of the dielectric is suppressed should, of course, play a positive role in plasmonics. Purposeful turning the obstacles along the propagation path of the surface wave into reflectors allows to effectively control its propagation direction, hence creating open-type surface waveguides.

## References

1. Kaiser T, Bin Hasan S, Paul T, Pertsch T, Rockstuhl C (2013) Impedance generalization for plasmonic waveguides beyond the lumped circuit model. *Phys Rev B* 88:035117
2. Depine RA (1992) Backscattering enhancement of light and multiple scattering of surface waves at a randomly varying impedance plane. *J Opt Soc Am A* 9:609
3. Wood RW (1902) On a Remarkable Case of Uneven Distribution of Light in a Diffraction Grating Spectrum. *Proc Phys Soc London* 18:269
4. López-Tejiera F, García-Vidal FJ, Martín-Moreno L (2005) Scattering of surface plasmons by one-dimensional periodic nanoindented surfaces. *Phys Rev B* 72:161405(R)
5. López-Tejiera F, García-Vidal FJ, Martín-Moreno L (2007) Normal-incidence scattering of surface plasmon polaritons by one-dimensional nanoindentations: a multimodal description. *Appl Phys A* 89:251
6. Palik ED (1998) *Handbook of optical constants of solids*. Academic Press, San Diego
7. Courant R, Hilbert D (1966) *Methods of mathematical physics, vol I*. Interscience Publishers, New York
8. Tarasov YV, Usatenko OV, Iakushev DA (2016) Plasmon-polaritons on a surface with fluctuating impedance: Scattering, localization, stability. *Low Temp Phys* 42:685
9. Resonance oscillations of a similar nature have been described in Ref. [10], where the problem of wave propagation in waveguides containing a segment with weakly corrugated boundaries was solved
10. Tarasov YV, Shostenko LD (2015) Dual nature of localization in guiding systems with randomly corrugated boundaries: Anderson-type versus entropic. *Ann Phys* 356:95
11. Fano U (1941) The Theory of Anomalous Diffraction Gratings and of Quasi-Stationary Waves on Metallic Surfaces (Sommerfeld's Waves). *J Opt Soc Am* 31:213

# Chapter 32

## Influence of Solution pH on the Nanostructure of Adsorption Layer of Selected Ionic Polyamino Acids and Their Copolymers at the Solid-Liquid Interface

Małgorzata Wiśniewska, Iwona Ostolska, and Agnieszka Nosal-Wiercińska

### 32.1 Introduction

Adsorption of polymer macromolecules at the solid-liquid interface is a very sophisticated process [1–3]. The polymer chains' arrangement depends on various factors which can be derived into three main groups. The first one includes the parameters associated with the adsorbent such as surface active group quantity, presence of net impurities, and pore size characteristics. The next group contains the factors directly related to the adsorbed species, mainly the adsorbate molecule structure. The last class refers to the adsorption process parameters. Thus, one can distinguish the temperature, solution strength, background electrolyte type, pH changes, and presence of additional substances (e.g., surfactants) [4–10].

The aqueous suspensions of metal oxide nanoparticles are extensively used in medicine [11–13]. Rapid development of nanotechnology contributes to the essential growth of inorganic substance utilization especially in the diagnostic and therapeutic applications. The main areas of usage include enhancing the contrast imaging technique in magnetic resonance imaging systems, controlled drugs release systems and radioisotopes therapy with the assisted magnetic field [14, 15]. Depending on the specific purpose as well as to prevent the immune response, the solid particle surface is modified by coating with a suitable polymer layer. Moreover, the presence of the adsorbed macromolecules on the solid surface enhances the system

---

M. Wiśniewska (✉) • I. Ostolska  
Department of Radiochemistry and Colloids Chemistry, Faculty of Chemistry, Maria Curie-Skłodowska University, M. Curie-Skłodowska Sq. 3, 20-031, Lublin, Poland  
e-mail: [wisniewska@hektor.umcs.lublin.pl](mailto:wisniewska@hektor.umcs.lublin.pl)

A. Nosal-Wiercińska  
Department of Analytical Chemistry and Instrumental Analysis, Faculty of Chemistry, Maria Curie-Skłodowska University, M. Curie-Skłodowska Sq. 3, 20-031, Lublin, Poland



wettability and stabilizes dispersion. In addition, functionalization of nanoparticles with the biocompatible molecules minimizes biofouling and nonspecific aggregation under physiological conditions. Modification of nanoparticles by proper polymer adsorption allows for biological active attachment to the previously formed coating layer [2, 16].

Polyamino acids are classified as synthetic polymers whose chain structure is very similar to natural proteins. Despite artificial origins, they reveal several interesting features. First of all, the polyamino acid macromolecules are fully biodegradable which is an important advantage with respect to the medical applications. Furthermore, these macromolecular compounds are nontoxic and exhibit high intrinsic stability through the presence of the amine bonds between the structural units. Modification of the side chain introducing different alkyl substituents linked with ester or amide bonds allows to obtain polymers characterized by a wide range of properties. It is possible to get the linear structure of hydrophilic macromolecule of ionic (or nonionic) character adopting the random coil conformation in the solution. On the other hand, the use of different reactants leads to production of hydrophobic substances dissolving only in nonpolar organic liquids whose macromolecules can form domains structurally similar to the liquid crystal. Due to the chemical and structural similarity to proteins, polyamino acids are often used as a simple model for more complex naturally occurring biopolymers [17–21].

Searching for new materials has led to the increased interest in the copolymers consisting of two (or more) types of monomers. These compounds have significantly different properties compared with the corresponding homopolymers. Due to the presence of different ionic or polar nature fragments, copolymers can variously interact with the solid surface molecules or drugs. With the ability to modify the amphiphilic mechanical and physical properties of block copolymers by precisely adjusting the amount of the appended segments or blocks, these materials have been successfully used in medical, pharmaceutical, and medical engineering. One of the best known groups of compounds includes copolymers having the structure of macromolecules of a nonionic block poly(ethylene glycol) [22–24].

Due to the differences in the ionic character of copolymer constituents and affinity for the solid surface, the polymer adsorption film structure is strongly influenced by the solution pH. Therefore the aim of the present study is determination of adsorption behavior of simple polyamino acid and their copolymers in the systems containing the colloidal solid particles dispersed in the aqueous solution of different pH values. Comparison of the obtained data allows to define precisely the polymer binding mechanism. Moreover, the application of the electrokinetic measurements (surface charge density and zeta potential tests) enables the macromolecule layer nanostructure arrangement. In addition, the stability studies using the turbidimetric method result in the calculation of the average aggregates size parameter. Analysis of the aforementioned factors as well as the Turbiscan Stability Index leads to the determination of the solution pH impact on the suspension stability.

## 32.2 Materials

Chromium (III) oxide ( $\text{Cr}_2\text{O}_3$ ) (POCh Gliwice) was used as an adsorbent. The  $\text{Cr}_2\text{O}_3$ -specific surface area determined by the BET method was found to be  $7.12 \text{ m}^2/\text{g}$  (Micromeritics ASAP 2405 analyzer). The point of charge ( $\text{pH}_{\text{pzc}}$ ) and the isoelectric point ( $\text{pH}_{\text{iep}}$ ) were 7.6 and 6, respectively [25]. The average  $\text{Cr}_2\text{O}_3$  particles size (dynamic light scattering, Zetasizer 3000, Malvern) was 265 nm. The diameters are calculated on the basis of the Brownian motions. The detector (at the angle of  $90^\circ$ ) analyzes the scattered light fluctuations intensity. The dependency between the size and the particle velocity is given by the Stokes-Einstein equation:

$$r = \frac{kT}{6\pi\eta D} \quad (32.1)$$

where  $r$ , the radius of the spherical particle;  $k$ , the Boltzmann's constant;  $T$ , the absolute temperature;  $\eta$ , the dynamic viscosity;  $D$ , the diffusion coefficient.

As macromolecular compounds, two classes of polymers were applied (all from Alamanda Polymers, USA). Two of them are poly(L-lysine hydrochloride) – denoted as LYS and poly(L-aspartic acid sodium salt) – ASP which are simple polyamino acids. The second group consists of the symmetric triblock copolymers: poly(L-lysine hydrochloride)–block–poly(ethylene glycol)–block–poly(L-lysine hydrochloride), designated as LPL, and poly(L-aspartic acid sodium salt)–block–poly(ethylene glycol)–block–poly(L-aspartic acid sodium salt) – APA.

The polydispersity index (PDI) which is a measure of the molecular weight distribution in the polymer is in the range from 1.02 to 1.1. Therefore polymers exhibit a uniform chain length. The polydispersity index is measured by the gel permeation chromatography (GPC) in DMF with 0.1 M LiBr at  $60^\circ\text{C}$ ; a calibration curve constructed from narrow polydispersity PEG standards is used. The average molecular weight is provided by the proton NMR spectroscopy using the amino acid repeating unit to the incorporated initiator peaks integration ratio. The average molecular weights of the respective copolymer structural units are presented in Table 32.1. The structural units' molecular weight was selected in such a way as to provide almost the same total molecular weight of all homopolymers and copolymers. The dissociation constant value ( $\text{pK}_a$ ) determined by the potentiometric titration was equal to 10.55 [26]. All measurements were performed in the pH range 3–10 at room temperature ( $\approx 25^\circ\text{C}$ ). NaCl of the concentration  $0.01 \text{ mol/dm}^3$  was used as a background electrolyte.

**Table 32.1** Average size of aggregates formed in the absence and presence of selected polymers

	Average aggregate's size [ $\mu\text{m}$ ]			
	pH 3	pH 4	pH 7.6	pH 10
$\text{Cr}_2\text{O}_3$	0.077	0.0592	0.0509	0.575
ASP	0.0726	–	0.085	0.0745
APA	0.581	–	0.579	0.5
LYS	–	0.106	0.125	0.135
LPL	–	0.485	0.223	0.133

The aggregate size's for  $\text{LYS}/\text{Cr}_2\text{O}_3$  and  $\text{LPL}/\text{Cr}_2\text{O}_3$  at pH 3 and  $\text{ASP}/\text{Cr}_2\text{O}_3$  and  $\text{APA}/\text{Cr}_2\text{O}_3$  at pH 4 were not calculated

## 32.3 Experimental Methods

### 32.3.1 Stability Tests

Stability measurements were conducted using a turbidimeter Turbiscan LabExpert connected to the cooling module TLab Cooler. This device possesses an electroluminescence diode which emits a collimated light beam ( $\lambda = 880 \text{ nm}$ ), passing through the studied suspension and two synchronized detectors. The transmission detector records the light passing through the sample at the angle of  $0^\circ$  in relation to the incident light direction. The second one is the backscattering detector which registers the light scattered at the angle of  $135^\circ$ . The obtained results are presented in the form of transmissions and backscattering curves as a function of time. The analysis of the turbidimetric data allows for the assessment of processes dynamics occurring in the sample during the measurement. Moreover, due to the specialized computer software connected with Turbiscan, it was possible to calculate the TSI parameter (Turbiscan Stability Index) that is very useful in the evaluation of colloidal system stability.

### 32.3.2 Potentiometric Titration

In order to obtain the potentiometric curves in the absence of the polymer,  $50 \text{ cm}^3$  of the supported electrolyte and  $0.2 \text{ cm}^3$  of  $0.1 \text{ mol/dm}^3$  HCl were placed into the thermostated Teflon vessel containing  $50 \text{ cm}^3$  of supporting electrolyte solution or polymer solution with a fixed concentration. A thermostated Teflon vessel with a stirrer, an automatic burette (Dosimat 765, Methrom), glass and calomel electrodes (Beckman Instruments), and the pH meter PHM 240 (Radiometer) were the parts of the measurement set. The process was controlled by a computer. The initial pH value was in the range of 3–3.5. After reaching the equilibrium,  $1.5 \text{ g}$  of  $\text{Cr}_2\text{O}_3$  was added. The obtained suspension was titrated by NaOH at a concentration of  $0.1 \text{ mole/dm}^3$ . The surface charge density of the adsorbent was calculated using the

“Titr\_v3” program written by W. Janusz. The tests were performed three times; the measurement uncertainty was at the level of 2%.

Surface charge density of silicon dioxide was determined by potentiometric titration [27]. The surface charge density was calculated from the dependence between the volume of base added to the suspension in order to obtain the desired pH value:

$$\sigma_0 = \frac{\Delta VcF}{mS} \quad (32.2)$$

where  $\Delta V$ , the difference between the volume of base added to the suspension to obtain the desired pH of the solution;  $c$ , the molar concentration of base;  $F$ , the Faraday constant ( $9.648 \times 10^4$  C/mol);  $m$ , the mass of the metal oxide;  $S$ , the specific surface area of applied metal oxide.

### 32.3.3 *Electrokinetic Potential Measurements*

The zeta potential measurements were made using Zetasizer Nano ZS (Malvern). To obtain a solid suspension in the background electrolyte solution, 0.06 g of  $\text{Cr}_2\text{O}_3$  was added to a 100  $\text{cm}^3$  beaker containing a suitable amount of NaCl. The suspension was further sonicated for 3 min, and the test pH was fixed. The zeta potential measurements were carried out up to pH 10. The samples with polymers were prepared in the same way; the polymer concentration range was 0.1–1 ppm. The electrokinetic potential values were calculated using the Henry equation. Each average value is the result of eight repetitions. The measurement error did not exceed 3%.

### 32.3.4 *Adsorption Measurements*

Adsorption measurements were conducted by the static method. The polymer concentration after the adsorption process was estimated using the UV-Vis spectrometer (Cary 100, Varian) at a wavelength of 210 nm. This wavelength was chosen after the UV-Vis absorption tests. The peptide bonds began to absorb at 280 nm and were most sensitive in the range of 210–230 nm. However, in that region, a severe interference from the absorption of  $\text{OH}^-$  ions was observed. Thus 210 nm was picked and the absorption of “blank” samples without polymers at the same pH was subtracted. A linear calibration curve was obtained from the standard solution, and it was used to determine the unknown polymer concentrations in the supernatants [10]. In order to eliminate the interferences originating from the hydroxyl ions, the calibration curves were made as a function of the solution pH. A suitable amount of  $\text{Cr}_2\text{O}_3$  was added into the Erlenmeyer flasks containing 10  $\text{cm}^3$  of polymer solution

with fixed concentrations. After adjusting the appropriate pH values, the samples were shaken in water bath (OLS 200, Grant) for 24 h in order to obtain the polymer adsorption equilibrium. Then the sediments were centrifuged twice (MPW-223e, Centrifuge), and 5 cm<sup>3</sup> of the polymer solution was taken for the spectrophotometric analysis. Each average value is the result of five repetitions. The measurement error did not exceed 5%.

## 32.4 Results and Discussion

The adsorption data are presented in Figs. 32.1 and 32.2. As one can see in both cases, the polymer adsorbed amount significantly depends on the solution pH value. In order to better understand the binding process of the selected ionic polyamino acids, it is necessary to explain the solution pH impact on the polymer functional groups dissociation degree ( $\alpha$ ). Thus, on account of the  $\alpha$  value changes the polymer macromolecules can adopt various conformations both in the solution and at the solid surface. For the carboxylic groups located in the ASP and APA chains structure, the dissociation constant ( $pK_a$ ) is equal to 3.73. As a consequence, the increasing of the solution pH above the mentioned value leads to the rapid dissociation of this moiety. In addition, the polyamino acid chains' arrangement varies from coiled under acidic conditions to highly extended at pH 10. The contrary situation takes place in the case of polylysine containing the primary amino groups ( $pK_b = 10.55$ ). This type of the polymer functional group becomes protonated at pH 3 causing macromolecules stretching. The lysine unit dissociation degree gradually decreases with the solution pH growth providing the more compact

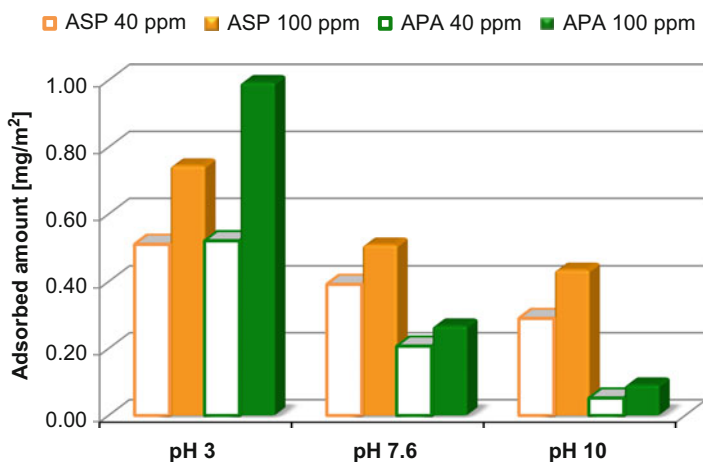


**Fig. 32.1** Adsorbed amount of the anionic homopolymer and block copolymer as a function of the solution pH and the polymer concentration

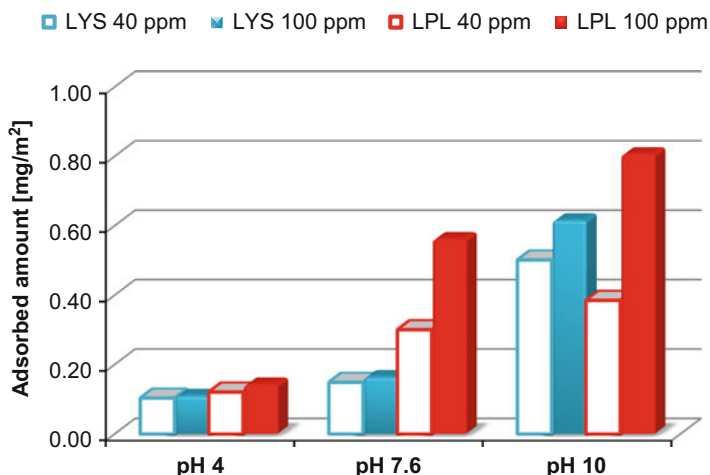


**Fig. 32.2** Adsorbed amount of the cationic homopolymer and block copolymer as a function of the solution pH and the polymer concentration

polymer chains conformation. Furthermore, the alternation of the functional groups ionic nature contributes to the marked changes in the macromolecular compound binding mechanism. It is worth noting that the surface active group ionization varies with the increasing solution pH. The point of zero charge for the  $\text{Cr}_2\text{O}_3$  particles in the presence of  $\text{NaCl}$  at a concentration  $0.01 \text{ mole/dm}^3$  (as a background electrolyte) is equal to 7.6 which means that the concentrations of positively and negatively charged surface groups are identical.

Analysis of the adsorption data obtained for the anionic homopolymer and block copolymer (Figs. 32.1 and 32.2) indicates that the quantity of the macromolecules bound to the solid surface depends not only on the solution pH, but it is determined by the polymer chain structure. For the ASP and APA substances containing the carboxylic groups, the adsorption maximum is reached at pH 3. Under these conditions, the solid surface active groups are mainly positively charged. Hence the attractive coulombic forces between the dissociated polymer functional moieties and the  $\text{Cr}_2\text{O}_3$  surface are responsible for macromolecule binding. The growth of adsorbed amount noticed for the APA block copolymer in comparison to the homopolymer can be related to two effects. First of all, the PEG unit present in the copolymer macromolecule interacts with the solid particles via the hydrogen bonds leading to the adsorption rise. Secondly, two ASP fragments belonging to the APA macromolecule are more effectively bound forming an adsorption layer rich in loops and tails in relation to the one long polyamino acid chain in ASP.

At higher pH (7.6 and 10), the APA copolymer adsorption drops distinctly with regard to the simple polymer. In both cases, the dissociation degree of the carboxylic groups is almost 100% contributing to the increase in the electrostatic repulsive forces between the suspension constituents. Moreover, the highly extended

macromolecule conformation hinders the hydrogen bridge formation. It should be also noted that the PEG chains exhibit lower affinity for the solid surface under basic pH conditions. As a consequence, the nonionic unit located in the APA copolymer macromolecules becomes directed toward the bulk solution forming the long loop acting like the steric hindrance.

The opposite dependency comes from the adsorption data collected from the systems containing the polylysine or its triblock copolymer (Fig. 32.2). The adsorption minimum for both analyzed polymers is reached at pH 4. This is a consequence of the electrostatic repulsion interactions between the totally ionized amino groups and the positively charged  $\text{Cr}_2\text{O}_3$  surface. It is worth noting that for more acidic solution, the LYS or LPL adsorption is not observed. Under these circumstances, the hydrogen bridges are driving force for the polymer binding. The solution pH increase up to 7.6 leads to the attractive force appearance between the  $\text{CrO}^-$  active sites and polylysine chains. As at pH 10, the higher value for polymer macromolecules concentrated on the solid surface is measured in the samples containing the LPL triblock copolymer. This results from the different polymer conformation. The simple polyamino acid chains adopt more flat arrangement at the solid–liquid interface. Displacing the PEG fragment toward bulk solution (as it takes place in the case of LPL) contributes to more effective polylysine units binding through the electrostatic interactions with the  $-\text{CrO}^-$  surface groups. Comparison of the data obtained for the samples including the anionic polymers at pH 3 and the systems with polylysine (or LPL) under basic conditions leads to the conclusion that the existence of two smaller polyamino acid blocks in macromolecule facilitates the polymer adsorption on the  $\text{Cr}_2\text{O}_3$  surface.

In order to prepare a comprehensive analysis of the polymer film nanostructure, the measurements involving the electrokinetic test were carried out. As follows from the results presented in Figs. 32.3, 32.4, 32.5, and 32.6, the addition of the tested polymers evidently influences both surface charge density ( $\sigma_0$ ) and zeta potential ( $\zeta$ ) curves course. Changes in the density of the solid particle surface active groups in the absence and presence of the polymer molecules are related to the amount of the charges accumulated in the layer close to the adsorbent surface. In turn, comparison of the electrokinetic potential values (measured for the samples before and after the macromolecular compound adsorption process) enables the estimation of polymeric chains spatial arrangement in the solid diffusion layer.

Experimental data referred to the samples containing the anionic polymers (Figs. 32.3 and 32.4) point out that the introduction of any analyzed polymeric species results in the obtained parameter reduction. In the case of the surface charge density, adsorption of the triblock copolymer contributes to the  $\sigma_0$  drop up to pH 10 in comparison to the  $\text{Cr}_2\text{O}_3$  particles dispersed in the ASP solution. At pH 3, the main reason for such a behavior is larger number of the  $-\text{COO}^-$  groups belonging to the APA macromolecules located in the solid surface layer. Another conclusion that might be drawn during analyzing these results is that the adsorbed polyaspartic blocks from the copolymer chains adopt a more coiled conformation under acidic conditions. Moreover, the slipping plane offset by the spatially extended simple polyamino acid macromolecules induces the distinct decrease in the zeta potential

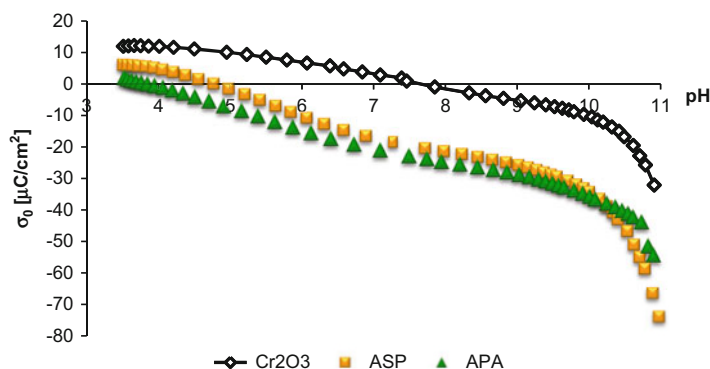


**Fig. 32.3** Surface charge density of the chromium (III) oxide particles in the absence and presence of the anionic polymers ( $C_{\text{polymer}} = 100$  ppm)

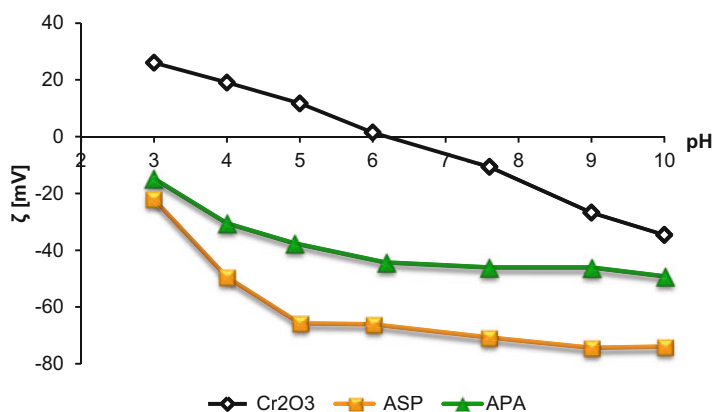


**Fig. 32.4** Zeta potential obtained for the  $\text{Cr}_2\text{O}_3$  suspensions in the absence and presence of the anionic polymers ( $C_{\text{polymer}} = 1$  ppm)

values (as regards to the suspension containing APA at pH 3) which confirms this thesis. In the neutral and basic solutions, the arrangement of the triblock copolymer chains associated to the  $\text{Cr}_2\text{O}_3$  surface is responsible for the higher surface charge density reduction. The electrostatic repulsion existence between the almost identically charged adsorbent and macromolecules favors the flatter polymer chains conformation. Furthermore, the loss of affinity for the surface by the nonionic PEG units causes the  $\text{Cr}_2\text{O}_3$  active centers blockade. This phenomenon is also clearly visible in the form of the higher absolute zeta potential value in comparison to those for the polyaspartic acid homopolymer (through the pH range from 7.6 to 10).

The electrokinetic data obtained for the systems containing the cationic polyamino acid (LYS) or triblock copolymer (LPL) adsorbed on the  $\text{Cr}_2\text{O}_3$  surface are shown in Figs. 32.5 and 32.6. It is worth noting that the presence of the positively



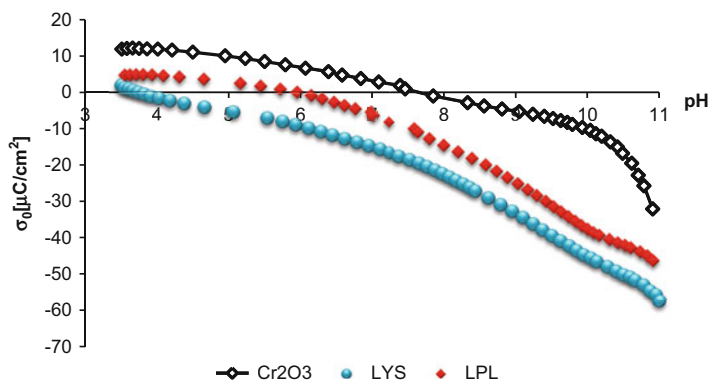


**Fig. 32.5** Surface charge density of the chromium (III) oxide particles in the absence and presence of the cationic polymers ( $C_{\text{polymer}} = 100$  ppm)

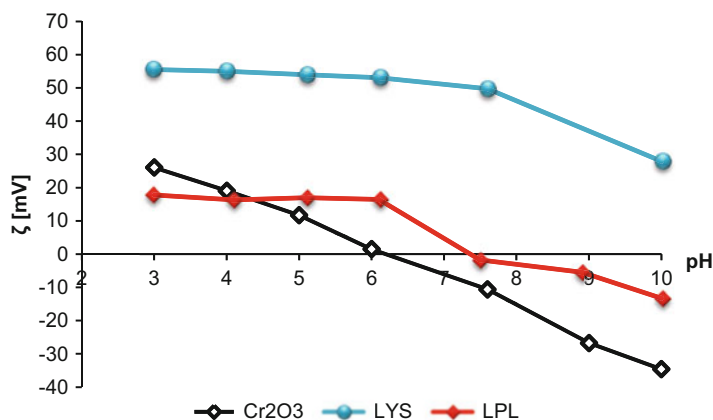


**Fig. 32.6** Zeta potential obtained for the  $\text{Cr}_2\text{O}_3$  suspensions in the absence and presence of the cationic polymers ( $C_{\text{polymer}} = 1$  ppm)

charged polymeric species leads to the decrease in the density of the solid surface charges and simultaneously contributes to the zeta potential growth (compared to the values measured for the adsorbent particles dispersed in the supporting electrolyte). In the first case, the reason responsible for such a behavior is the negative charge induction on account of the interactions between the amino moieties and the  $-\text{CrOH}$  surface centers. As a result of the proton disconnection, the negative  $-\text{CrO}^-$  groups are formed on the adsorbent surface. As regards to the electrokinetic potential, the  $\zeta$  values increase comes from the protonated polylysine functional groups occurrence in the diffusion part of the electrical double layer.

At pH 4, the adsorption of both polymers is very similar. Hence, the differences observed in the electrokinetic results follow from distinct conformation of the macromolecules accumulated on the  $\text{Cr}_2\text{O}_3$  surface. The lower absolute value of

the surface charge calculated for LPL can be explained as a result of adsorption due to the hydrogen bridges formation by the nonionic PEG fragment. Moreover, the spatially extended polyamino acid blocks directed toward the bulk solution prove the more effective slipping plane shifting in relation to the simple homopolymer causing the zeta potential drop. Increasing the solution pH accompanies the larger number of macromolecules adsorbed at the solid–liquid interface, however the quantity of polymer chains linked to the adsorbent surface is considerably higher for the symmetric triblock copolymer. Reasons for such a behavior may be found in the electrokinetic attractive forces present in the measuring system. Under these conditions, the adsorption layer formed in the presence of the LPL copolymer is characterized by numerous loops and tails, while the LYS macromolecules adopt more flat conformation. A larger number of the amino groups located on the solid surface favors the formation of the negative charges contributing to the surface charge density decrease. Simultaneously, the existence of nanostructure rich in the structures directed toward aqueous phase proves the effective solid particle slipping plane shifting evidences as the zeta potential drop.

Determination of the TSI (Turbiscan Stability Index) parameter is a convenient method used to the colloidal suspension stability investigation. Analysis of the TSI values and the average size of aggregates and their average velocity (Fig. 32.7, Table 32.1) indicates that the  $\text{Cr}_2\text{O}_3$  suspensions are relatively unstable throughout measured pH range, except pH 3 where the solid particles are stabilized by the positively charged surface groups. At point of zero charge, the  $\text{Cr}_2\text{O}_3$  stability in the background electrolyte is the lowest. It is clearly reasonable because of the larger number of the electrostatic interactions providing to the sample aggregation. In alkaline conditions, stability of the  $\text{Cr}_2\text{O}_3$  dispersed in the NaCl solution is slightly

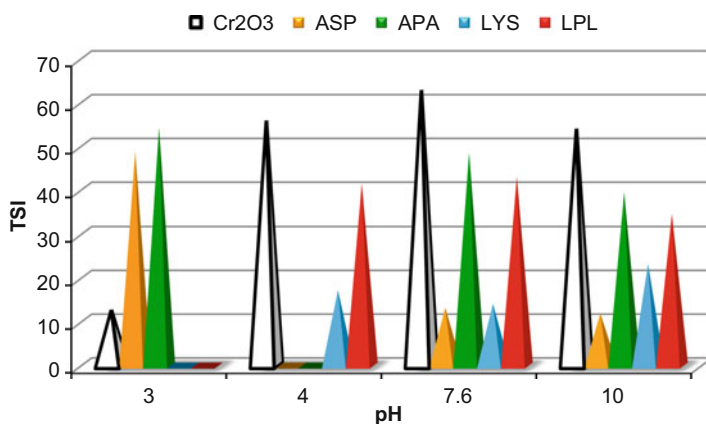


**Fig. 32.7** TSI values for the chromium (III) oxide suspension in the absence and presence of selected polymers ( $C_{\text{polymer}} = 100$  ppm). The TSI values for the LYS/ $\text{Cr}_2\text{O}_3$  and LPL/ $\text{Cr}_2\text{O}_3$  at pH 3 and ASP/ $\text{Cr}_2\text{O}_3$  and APA/ $\text{Cr}_2\text{O}_3$  at pH 4 were not measured

improved due to the growth of repulsion forces between identically charged surface groups located on the different particles surface.

Another conclusion that can be drawn from this data concerns impact of the polymer chains structure on the sample stability. At pH 3, introduction of the anionic polymers to the solid suspension causes the considerable sample stability decrease. The highest solid particle coverage noted under these circumstances contributes to the surface charge neutralization and favors the sedimentation process occurrence. As one can see, larger aggregates are formed in the presence of the APA triblock copolymer. This comes from the presence of two polyaspartic acid blocks enabling the polymer bridges' formation between the adjacent particles which explains the higher polymer adsorption. In the case of ASP, the lower zeta potential values evidence both the larger number of negative charges accumulated in the solid diffusion layer and the greater contribution originating from slipping plane offset. At  $pH_{pzc}$  and in alkaline solution, the addition of the anionic polymers improves the sample stability in comparison to the  $Cr_2O_3$  suspended in NaCl. Reason can be found in effect related to the electrosteric repulsion increase caused by the spatially extended polymer macromolecules adsorbed on the  $Cr_2O_3$  surface. The simple polyamino acid acts as a definitely better stabilizer in relation to the APA block copolymer (average aggregate size equal to 0.085 and 0.0745  $\mu m$  at pH 7.6 and 10, correspondingly). This arises from the hydrogen bond formation ability characteristic for the nonionic PEG fragment stretched toward the aqueous solution.

Regardless the solution pH, the cation polymer adsorption process significantly improved the samples stability (compared to the samples in the background electrolyte). At pH 4, reason for such a situation can be found in the adjacent solid particles' electrostatic repulsion on account of presence of the totally protonated amino groups belonging to the polylysine chains of highly extended conformation. Similarly as in the acidic solution, at higher pH conditions, the least aggregation is observed for the homopolymer regardless its lowest adsorption. The zeta potential and  $\sigma_0$  values measured for that system evidence the large number of the polymer functional groups accumulated on the solid surface. The slight increase in the TSI for  $Cr_2O_3$ /LYS suspension at pH 10 results from drop of the amino groups' dissociation degree. The neutralization of the particles' surface charge due to the adsorption of macromolecules characterized by the coiled conformation provides to the particles attraction growth. The considerably less stable sample was obtained after the addition of the LPL triblock copolymer. In this case, larger aggregates are formed on account of the symmetrical macromolecules structure – each of the polyamino acid block can adsorb on the different  $Cr_2O_3$  particles. Moreover, in alkaline medium, the PEG chains lose the affinity for the solid surface, and they are extended toward the bulk solution where they can form the hydrogen bonds with the polylysine segments accumulated on the adjacent particles.

## References

1. Wiśniewska M, Chibowski S, Urban T (2012) Effect of the type of polymer functional groups on the structure of its film formed on the alumina surface – suspension stability. *React Funct Polym* 72:791–798
2. Louget S, Kumar AC, Sigaud G, Duguet E, Lecommandoux S, Schatz C (2011) A physico-chemical investigation of poly(ethylene oxide)-block-poly(L-lysine) copolymer adsorption onto silica nanoparticles. *J Colloid Interface Sci* 359:413–422
3. Hoogeveen NG, Stuart MAC, Fleer GJ (1994) Adsorption of charged block copolymers with two adsorbing blocks. *Faraday Discuss* 98:161–172
4. Chaplain V, Janex ML, Lafuma F, Graillat C, Audebert R (1995) Coupling between polymer adsorption and colloidal particle aggregation. *Colloid Polym Sci* 273:984–993
5. Tiraferri A, Borkovec M (2015) Probing effects of polymer adsorption in colloidal particle suspensions by light scattering as relevant for the aquatic environment: an overview. *Sci Total Environ* 535:131–140
6. Chibowski S (1996) Investigation of the mechanism of polymer adsorption on a metal oxide/water solution interface. *Adsorpt Sci Technol* 14:179–188
7. Grządka E (2013) Influence of surfactants on the adsorption and elektrokinetic properties of the system: guar gum/manganese dioxide. *Cellulose* 20:1313–1328
8. Moody G (1992) The use of polyacrylamides in mineral processing. *Min Eng* 5:479–492
9. Liufu S, Xiao H, Li Y (2005) Adsorption of poly(acrylic acid) onto the surface of titanium dioxide and the colloidal stability of aqueous suspension. *J Colloid Interface Sci* 281:155–163
10. Wang X, Lee BI, Mann L (2002) Dispersion of barium titanate with polyaspartic acid in aqueous media. *Colloids Surf A* 202:71–80
11. Katsnelson BA, Privalova LI, Sutunkova MP, Gurchik VB, Loginova NV, Minigalieva IA, Kireyeva EP, Shur VY, Shishkina EV, Beikin YB, Makeyev OH, Valamina IE (2015) Some inferences from in vivo experiments with metal and metal oxide nanoparticles: the pulmonary phagocytosis response, subchronic systemic toxicity and genotoxicity, regulatory proposals, searching for bioprotectors (a self-overview). *Int J Nanomedicine* 10:3013–3029
12. Premanathan M, Karthikeyan K, Jeyasubramanian K, Manivannan G (2011) Selective toxicity of ZnO nanoparticles toward gram-positive bacteria and cancer cells by apoptosis through lipid peroxidation. *Nanomedicine* 7:184–192
13. Kumar N, Ravikumar MNV, Domb AJ (2001) Biodegradable block copolymers. *Adv Drug Deliv Rev* 53:23–44
14. Kumagai M, Imai Y, Nakamura T, Yamasaki Y, Sekino M, Ueno S, Hanaoka K, Kikuchi K, Nagano T, Kaneko E, Shimokado K, Kataoka K (2007) Iron hydroxide nanoparticles coated with poly(ethylene glycol)-poly(aspartic acid) block copolymer as novel magnetic resonance contrast agents for in vivo imaging. *Colloids Surf B Biointerfaces* 56:74–181
15. Boyer C, Whittaker MR, Bulmus V, Liu J, Davis TP (2010) The design and utility of polymer-stabilized iron-oxide nanoparticles for nanomedicine applications. *NPG Asia Mater* 2:23–30
16. Estelrich J, Escibano E, Queralt J, Busquets MA (2015) Iron oxide nanoparticles for magnetically-guided and magnetically-responsive drug delivery. *Int J Mol Sci* 16:8070–8101
17. Yang HM, Park CW, Ahn T, Jung B, Seo BK, Park JH, Kim JD (2013) A direct surface modification of iron oxide nanoparticles with various poly(amino acid)s for use as magnetic resonance probes. *J Colloid Interface Sci* 391:158–167
18. Obst M, Steinbüchel A (2004) Microbial degradation of poly(amino acid)s. *Biomacromolecules* 5:1166–1176
19. Kunioka M (2004) Biodegradable water absorbent synthesized from bacterial poly(amino acid)s. *Macromol Biosci* 4:324–329
20. Studenová H, Vodicka P, Proks V, Hlucilová J, Motlík J, Rypáček F (2010) Synthetic poly(amino acid) hydrogels with incorporated cell-adhesion peptides for tissue engineering. *J Tissue Eng Regen Med* 4:454–463

21. Yan L, Jiang D (2015) Study of bone-like hydroxyapatite/polyamino acid composite materials for their biological properties and effects on the reconstruction of long bone defects. *Drug Des Devel Ther* 9:6497–6508
22. Osada K, Christie RJ, Kataoka K (2009) Polymeric micelles from poly(ethylene glycol)–poly(amino acid) block copolymer for drug and gene delivery. *J R Soc Interface* 6:S325–S339
23. Ostolska I, Wiśniewska M (2015) The impact of polymer structure on the adsorption of ionic polyamino acid homopolymers and their diblock copolymers on colloidal chromium(III) oxide. *RSC Adv* 5:28505–28514
24. Song Z, Deng P, Teng F, Zhou F, Zhu W, Feng R (2016) Development on PEG-modified poly (amino acid) copolymeric micelles for delivery of anticancer drug. *Anticancer Agents Med Chem*. doi:[10.2174/1871520616666160817110753](https://doi.org/10.2174/1871520616666160817110753)
25. Wiśniewska M, Szewczuk-Karpisz K (2012) Removal possibilities of colloidal chromium (III) oxide from water using polyacrylic acid. *Environ Sci Pollut R* 20:3657–3669
26. Ostolska I, Wiśniewska M (2014) Comparison of the influence of polyaspartic acid and polylysine functional groups on the adsorption at the Cr<sub>2</sub>O<sub>3</sub>—aqueous polymer solution interface. *Appl Surf Sci* 311:734–739
27. Janusz W (1999) *Electrical double layer at metal oxide-electrolyte interface in “interfacial forces and fields theory and applications”*. M. Dekker, New York

# Chapter 33

## Grain Size Effect on Crystal Microstructure of the Nanoparticle TbMnO<sub>3</sub> Manganite

Wiesława Bażela, Marcin Dul, Andrzej Szytuła, and Volodymyr Dyakonov

### 33.1 Introduction

Physical properties of the RMnO<sub>3</sub> manganites, where R is the rare earth atom, have been in recent years a subject of intensive investigations because their magnetic properties are dependent on the radius of the rare earth elements R (see Fig. 33.1 in Ref. [1, 2]). Also the grain size strongly influences the physical properties. As the grain size becomes comparable to the critical length scales, interesting mechanical, optical, electric, and magnetic properties occur that are significantly different from those of the bulk materials.

The explanation of the complex magnetic interactions and correlation of the magnetic, structural, and electron properties of the RMnO<sub>3</sub> manganites is then of fundamental interest [3]. Especially TbMnO<sub>3</sub> has been attracted a lot of attention in recent years because of its strong coupling between ferroelectricity and magnetism [4]. Additional data concerning the magnetic ordering, particularly in the Mn sublattice, were reported in the few papers [5–8]. Results of these investigations indicate complex-modulated magnetic ordering.

---

W. Bażela (✉) • M. Dul

Institute of Physics, Cracow University of Technology, Podchorążych 1, 30-084, Cracow, Poland  
e-mail: [wbazela@pk.edu.pl](mailto:wbazela@pk.edu.pl); [dulmarcin@gmail.com](mailto:dulmarcin@gmail.com)

A. Szytuła

M. Smoluchowski Institute of Physics, Jagiellonian University, Łojasiewicza 11, 30-348, Cracow, Poland

e-mail: [andrzej.szytula@uj.edu.pl](mailto:andrzej.szytula@uj.edu.pl)

V. Dyakonov

Institute of Physics, Polish Academy of Science, Al. Lotników 32/46, 02-668, Warsaw, Poland  
e-mail: [dyakon@ifpan.edu.pl](mailto:dyakon@ifpan.edu.pl)

© Springer International Publishing AG 2017

O. Fesenko, L. Yatsenko (eds.), *Nanophysics, Nanomaterials, Interface Studies, and Applications*, Springer Proceedings in Physics 195,

DOI 10.1007/978-3-319-56422-7\_33

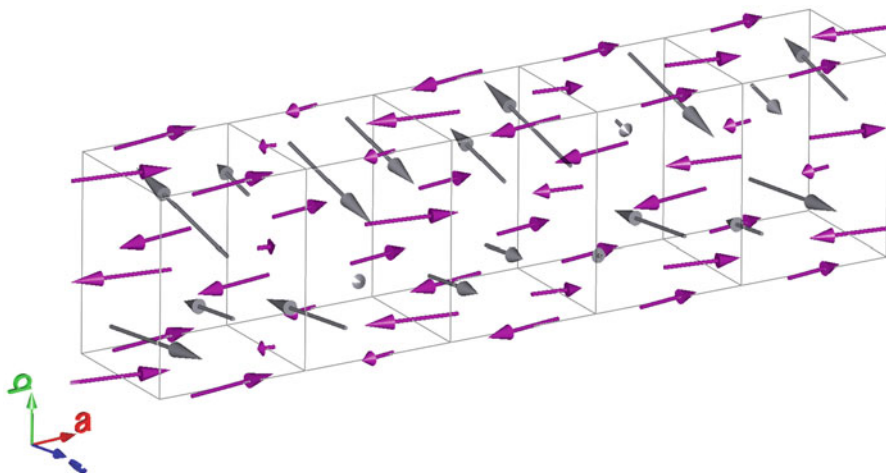


**Fig. 33.1** Sinusoidal magnetic ordering in Mn sublattice, violet ( $C_xA_z$  mode,  $k_x = 0.282(1)$ ), and in Tb sublattice, black ( $F_yA_z$  mode,  $k_x = 0.423(1)$ ), for the polycrystalline  $TbMnO_3$  sample

Discussed in this paper, the  $TbMnO_3$  compound crystallizes in the orthorhombically distorted perovskite crystal structure (space group  $Pnma$ , No. 62).

Low-temperature neutron diffraction data indicate that the magnetic ordering of Mn and Tb sublattice for polycrystalline  $TbMnO_3$  is sinusoidal modulated described by the propagation vector  $\mathbf{k} = (k_x, 0, 0)$ . The magnetic moments in the Mn sublattice order below 41 K, while in Tb they order below 9 K. The Mn magnetic moments, parallel to the  $a$ -axis, form a collinear incommensurate structure of  $C_x$  mode. At  $T = 16$  K, a noncollinear magnetic structure described by  $C_xA_z$  mode with the Mn moment in the  $a$ - $c$  plane was observed (see Fig. 33.1). The Tb sublattice exhibits the antiferromagnetic incommensurate ordering of the  $F_yA_z$  type at  $T = 5$  K. The Tb magnetic structure is described by the propagation vector  $\mathbf{k} = (k_x, 0, 0)$  where  $k_x$  is equal to 0.423(1) (Fig. 33.1). At the same temperature, the Mn moments still form the  $C_xA_z$  structure described by propagation vector  $\mathbf{k} = (k_x, 0, 0)$  where  $k_x$  is equal to 0.282(1) [9–11].

For the nano-800 and nano-850 samples below  $T_N$ , the Mn moments form a collinear incommensurate magnetic structure of  $C_x$  type described by the propagation vector  $\mathbf{k} = (k_x, 0, 0)$  (see Fig. 33.2).

Magnetic structures of the polycrystalline and nanoparticle  $TbMnO_3$  compounds are incommensurate in comparison with the crystal one. The periods of modulation of the magnetic structure are equal to  $3.54a$  (Mn sublattice) and  $2.36a$  (Tb sublattice) for the polycrystalline sample and  $3.06a$  (Mn) and  $2.25a$  (Tb) for the nano-samples, respectively (Figs. 33.1 and 33.2).

The nanomaterials of  $TbMnO_3$  are also antiferromagnets. The grain size slightly changes the Néel temperatures and sine-modulated magnetic ordering. In the case of  $TbMnO_3$ , an increase of the values of  $k_x$  components for both sublattices

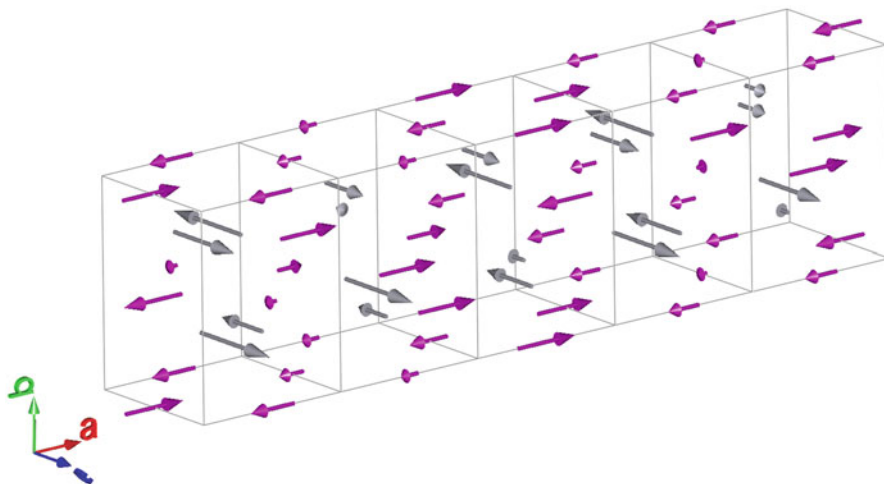


**Fig. 33.2** Sinusoidal magnetic ordering in Mn sublattice, violet ( $C_x$  mode,  $k_x = 0.326(4)$ ), and in Tb sublattice, black ( $A_z$  mode,  $k_x = 0.443(5)$ ), for the 800 nano- $\text{TbMnO}_3$  sample

(Mn and Tb) is detected. The peaks corresponding to the magnetic order in  $\text{Tb}^{3+}$  sublattice are broadening (see Fig. 33.5 in Ref. [11]) which suggest the cluster-like character of the magnetic ordering in the Tb sublattice.

In order to explain these differences, the detail analysis of the crystal structure parameters determined from the X-ray and neutron diffraction data [11] has been performed.

In this paper, we have discussed the influence of the internal structural parameters (Mn-O bond lengths and Mn-O-Mn bond angles) on magnetic behavior of the polycrystalline and nanopowder  $\text{TbMnO}_3$  samples. The structural distortion parameters, i.e., Jahn-Teller distortion (JT),  $\text{MnO}_6$ -octahedron distortion ( $\delta$ ), and unit cell volume distortion ( $D$ ), were found for all the samples. The obtained data are analyzed from the point of view of grain size value.

## 33.2 Experiment and Results

The polycrystalline  $\text{TbMnO}_3$  manganite was prepared by the solid-state reaction and annealed at 1150 °C. For preparation of the nanosize  $\text{TbMnO}_3$  samples, the sol-gel method has been used. The  $\text{TbMnO}_3$  nano-samples were obtained after annealing at 800 and 850 °C, respectively [12].

The analysis presented in this paper was based on the neutron diffraction powder data collected using the E2 and E6 diffractometers installed at the BERII reactor (Helmholtz-Zentrum Berlin) within the temperature range from 1.6 to 260 K and



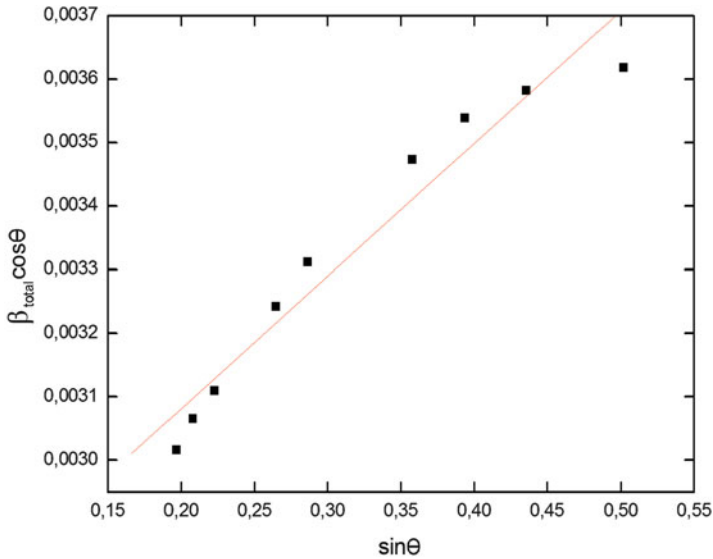


**Fig. 33.3** Williamson-Hall diagram:  $\beta_{\text{total}} \cos \theta$  versus  $\sin \theta$  plot for the  $\text{TbMnO}_3$  sample annealed at  $800^\circ\text{C}$

X-ray powder diffraction data at the room temperature using the Philips PW-3710 X'PERT diffractometer with  $\text{CuK}_\alpha$  radiation.

The grain sizes of the  $\text{TbMnO}_3$  nano-samples were determined using the Scherrer relation  $d = \lambda/B\cos\theta_B$ , where  $d$  is the grain size,  $\lambda$  is the X-ray's wavelength,  $\theta_B$  is the corresponding angle of the Bragg diffraction, and  $B$  is the difference between half-widths of the Bragg reflex of the nanopowder and the standard sample. The grain sizes were calculated using the experimental X-ray data and the following relation,  $B = \beta - \beta_0$ , where  $\beta$  is the half-width of the Bragg reflex of the investigated sample and  $\beta_0$  is the similar value for the standard sample of the Si powder with the grain size of  $10\ \mu\text{m}$  [13]. The average grain size values determined are 60 and 45 nm for 850 and 800 nano-samples of the  $\text{TbMnO}_3$ , respectively.

The grain sizes also were determined based on the Williamson-Hall method [14]. In this method, the broadening of Bragg peak is a sum of grain size broadening  $\beta_d = K\lambda/d\cos\theta$  and strain broadening  $\beta_s = \epsilon \, tg\theta$ , where the shape factor  $K$  is close to 1,  $d$  is the value of the grain size, and  $\epsilon$  is the strain constant.

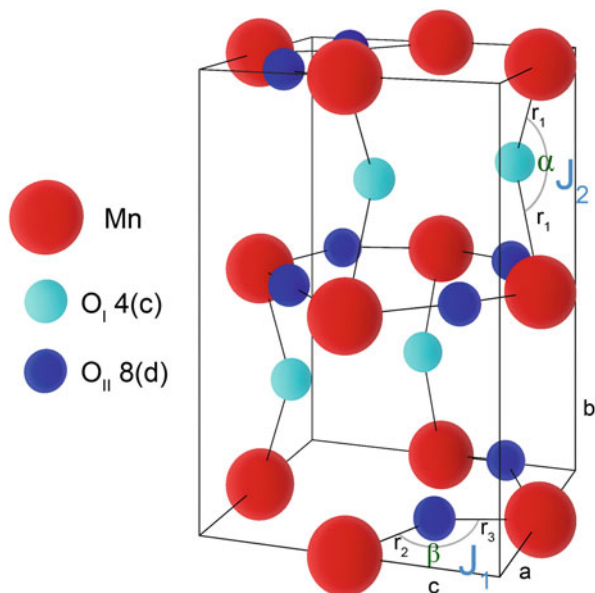
Thus, the resulting total broadening is  $\beta_{\text{total}} = \beta_s + \beta_d = \epsilon \, tg\theta + K\lambda/d\cos\theta$ .

Multiplication of the above equation by  $\cos\theta$  leads to

$$\beta_{\text{total}} \cos \theta = \epsilon \sin \theta + K\lambda/d.$$

Therefore, the grain size  $d$  can be determined from the intercept of the line fitted with linear regression as applied to the  $\beta_{\text{total}} \cos \theta$  versus  $\sin \theta$  data (Fig. 33.3).

**Fig. 33.4** The orthorhombic crystal unit cell with the marked Mn-O bond lengths ( $r_1$ ,  $r_2$ ,  $r_3$ ) and Mn-O-Mn bond angles ( $\alpha$ ,  $\beta$ ) and the exchange integrals  $J_1$  and  $J_2$



The experimental  $\beta_{\text{total}}$  values have been determined from the relation,  $\beta_{\text{total}} = [(\beta_{\theta})_{\text{sample}}^2 - (\beta_{\theta})_{\text{Si}}^2]^{1/2}$ , where  $(\beta_{\theta})_{\text{sample}}$  is the half-width of the selected Bragg reflection of the investigated sample, while  $(\beta_{\theta})_{\text{Si}}$  is the similar value found for the standard sample of Si powder.

The grain size values  $d$  are equal to 57 and 51 nm for 850 and 800 nano- $\text{TbMnO}_3$  samples, respectively. Presented data indicate that the grain size value decreases with decreasing annealing temperature.

The X-ray and neutron diffraction data indicate that all the samples studied have orthorhombically distorted perovskite crystal structure (space group  $Pnma$ , No. 62). In this structure the Tb and O1 atoms occupy 4(c) site,  $(x, y, 1/4)$ ; O2 atoms are in 8(d) site,  $(x, y, z)$ ; and Mn atoms are in 4(b) site,  $(1/2, 0, 0)$ .

In the orthorhombic unit cell, there are the three crystallographically independent bond lengths: apical Mn-O1 (4c) =  $r_1$  and two equatorial Mn-O2 (8d)<sub>1</sub> =  $r_2$  and Mn-O2 (8d)<sub>2</sub> =  $r_3$  and the two bond angles, (Mn-O1-Mn) =  $\alpha$  and (Mn-O2-Mn) =  $\beta$  (Fig. 33.4). The temperature dependences of the Mn-O bond lengths and Mn-O-Mn bond angles for the polycrystalline and two nanoparticle  $\text{TbMnO}_3$  samples are presented in Figs. 33.5 and 33.6.

The temperature dependences of the  $r_1$  and  $r_2$  bond lengths show that  $r_1$  and  $r_2$  are smaller for the nanosize samples as compared to the polycrystalline sample (see Fig. 33.5). This suggests that in these samples, there is a greater overlap of p and d orbitals. We have observed an increase of the  $r_1$  and  $r_2$  bond lengths for the nanosize samples with approaching the Néel temperature. For the polycrystalline sample, the stabilization of all three  $r_1$ ,  $r_2$ , and  $r_3$  bond lengths is visible above  $T = 50$  K. The dependence of  $r_3(T)$  exhibits an inverse behavior as compared to  $r_2(T)$  (see Fig. 33.5).

Figure 33.6 presents a gradual increase of the  $\alpha$  bond angle versus temperature for the polycrystalline sample, whereas for the nanosize samples, a decrease of  $\alpha$  till the Néel temperature and an increase beyond  $T_N$  are observed. The  $\alpha$  bond angles are larger for the nanoparticle samples as compared to  $\alpha$  for the polycrystalline sample. This suggests an increase of the superexchange interactions along the  $b$ -axis. The values of  $\beta$  bond angle are similar for the nano- and poly-TbMnO<sub>3</sub> samples. For both types of samples, an increase of  $\beta$  is observed till the Néel temperature for Mn sublattice. Beyond this temperature the  $\beta$  bond angle value substantially drops.

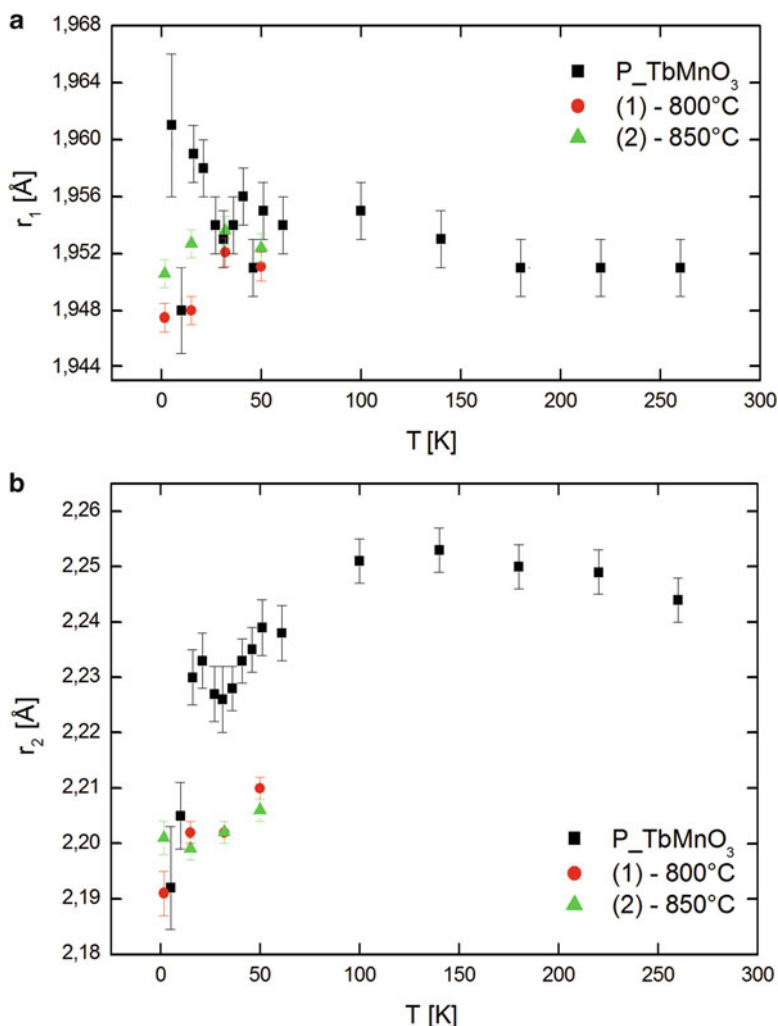


**Fig. 33.5** Temperature dependences of Mn-O bond lengths:  $r_1$  (a),  $r_2$  (b), and  $r_3$  (c) for the polycrystalline and 800 and 850 nano-TbMnO<sub>3</sub> samples

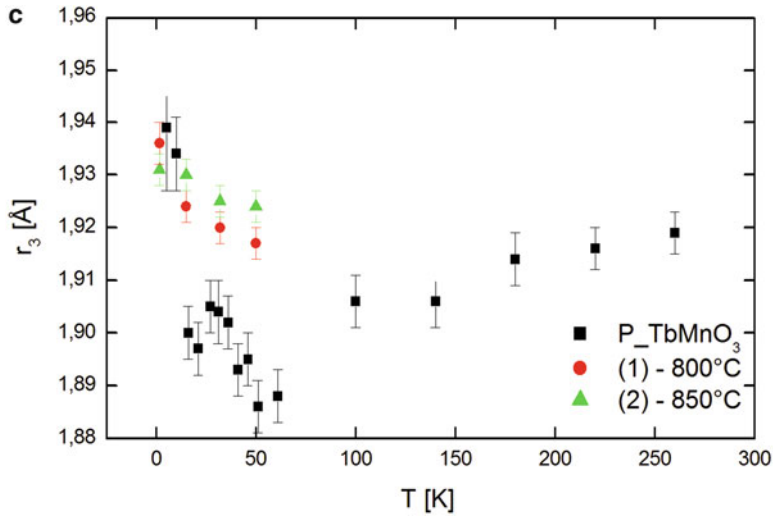


Fig. 33.5 (continued)

Using the  $r_1$ ,  $r_2$ , and  $r_3$  bond lengths, the Jahn-Teller parameter [15] for the polycrystalline and nanosize samples has been determined according to the formula [16]:

$$JT = \sqrt{\frac{1}{3} \sum_{i=1}^3 [(r_i) - \langle r \rangle]^2}$$

where  $r_i$  is the experimentally determined values of (Mn-O) interatomic lengths (see Fig. 33.5) and  $\langle r \rangle$  is the average value of these lengths.

The parameter delta, which describes the distortion of MnO<sub>6</sub> octahedron, is calculated using the formula:

$$\text{delta} = \frac{1}{3} \sum_{i=1}^3 \left[ \frac{r_i - \langle r \rangle}{\langle r \rangle} \right]^2$$

Temperature dependences of the Jahn-Teller parameter (JT) and the delta parameter for the polycrystalline and nanosize TbMnO<sub>3</sub> samples are presented in Fig. 33.7. The values of both the parameters indicate the MnO<sub>6</sub> octahedron distortion. Distortion is much smaller for the nanocrystalline samples than for polycrystalline one. For polycrystalline sample the Jahn-Teller parameter exhibits anomaly at Néel temperature.

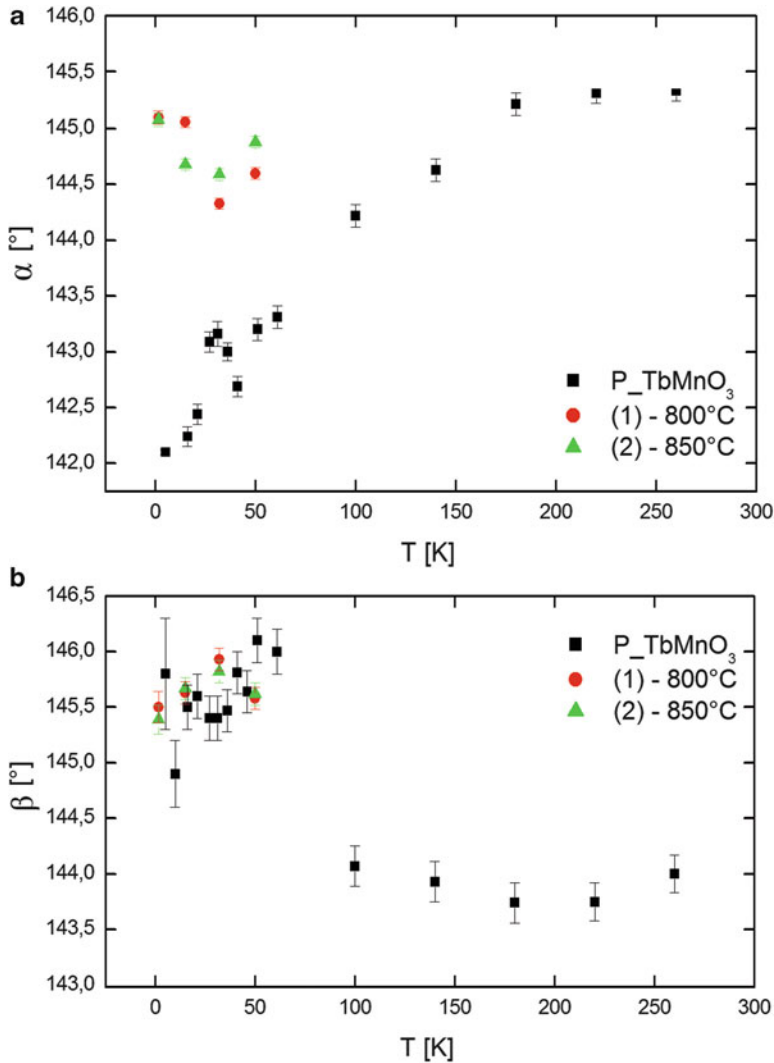


**Fig. 33.6** Temperature dependences of Mn-O-Mn bond angles:  $\alpha$  (a) and  $\beta$  (b) for the polycrystalline and 800 and 850 nano-TbMnO<sub>3</sub> samples

Unit cell volume distortion parameter  $D$  was determined according to the formula:

$$D = \frac{\sum |a_i - \langle a \rangle|}{3 \langle a \rangle}$$

where  $\langle a \rangle = \left( a \frac{b}{\sqrt{2}} c \right)^{\frac{1}{3}}$ ,  $a_1 = a$ ,  $a_2 = \frac{b}{\sqrt{2}}$ ,  $a_3 = c$ .

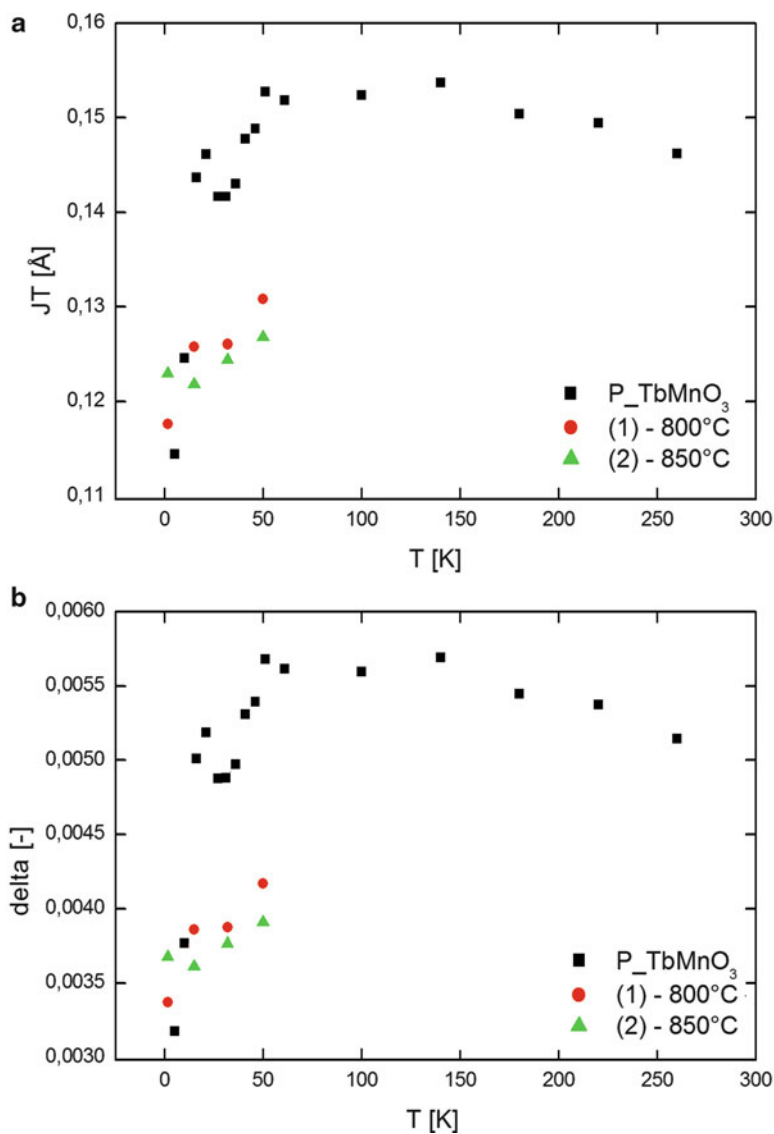


**Fig. 33.7** Temperature dependences of the Jahn-Teller parameter (a) and the delta parameter (b) for the polycrystalline and nanosize samples of  $\text{TbMnO}_3$

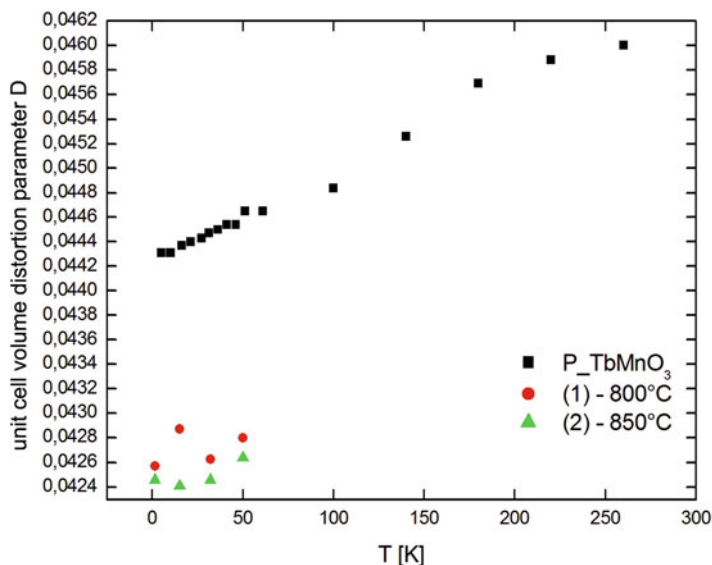


**Fig. 33.8** Unit cell volume distortion parameter  $D$  versus temperature plot for the polycrystalline and nanoparticle samples of  $\text{TbMnO}_3$

The temperature dependences of the  $D$  parameter for poly- and nano- $\text{TbMnO}_3$  samples are presented in Fig. 33.8. The orthorhombic distortion parameter  $D$  for the polycrystalline  $\text{TbMnO}_3$  sample slowly increases with increasing temperature. The values of  $D$  parameter for nano-samples are considerably smaller (see Fig. 33.8).

### 33.3 Discussion

Investigated  $\text{TbMnO}_3$  nano-samples have the orthorhombic crystal structure which is similar to that for bulk sample. The nano-samples are characterized by the lesser values of the lattice parameters [11].

The grain size values determined from X-ray data for the  $\text{TbMnO}_3$  nano-samples are lower than 100 nm. The macroscopic magnetic and microscopic neutron diffraction data indicate similar antiferromagnetic properties. In all the nano- and polycrystalline samples, the magnetic order is sinusoidally modulated described by the propagation vector  $\mathbf{k} = (k_x, 0, 0)$ . The values of  $k_x$  are higher for nano-samples than for polycrystalline one.

Observed antiferromagnetic order in the Mn sublattice is result of the superexchange mechanism (cation-anion-cation) which exists in manganites. The superexchange interaction depends on the Mn-O-Mn bond angles ( $\alpha$ ,  $\beta$ ) and is joined with partial overlap of the p(O) and d(Mn) orbitals. The interactions between Mn moments are based on the exchange integrals discussed by Bertaut [17].

At temperature 1.6 K, the values of  $\alpha$  and  $\beta$  bond angles are equal to 142° and 146° for the polycrystalline TbMnO<sub>3</sub> while they are equal to 145° and 145.5° for the nanoparticle samples, respectively. The obtained values of the Mn-O-Mn bond angles ( $\alpha$ ,  $\beta$ ) are smaller than 180°. This fact indicates the moderate ferro- or antiferromagnetic interaction between magnetic moments of Mn according to the Goodenough-Kanamori rules [18, 19].

In these compounds the Mn<sup>3+</sup> ions have electronic configuration 3d<sup>4</sup>. The exchange interactions between Mn magnetic moments are described by the exchange integrals:

- $J_1$ :  $t_{2g}(\text{Mn})/2p_{\pi}(\text{O})/t_{2g}(\text{Mn})$  in the  $a$ - $c$  plane determined by the  $\beta$  angle
- $J_2$ :  $e_g(\text{Mn})/2p_{\sigma}(\text{O})/e_g(\text{Mn})$  along the  $b$ -axis determined by the  $\alpha$  angle

The interactions between the Mn moments have been discussed in Ref. [17]. Analysis of those interactions gives the following dependence between  $k_x$  and exchange integrals:  $\cos(nk_x) = J_{\text{eff}} \approx (2J_2 - J_1)$  [20]. The inelastic neutron scattering for TbMnO<sub>3</sub> poly-sample gives the positive value of  $J_1 = 0.15(1)$  meV which corresponds to the ferromagnetic interactions and negative one of  $J_2 \approx -0.31(2)$  meV which corresponds to the antiferromagnetic interactions [21]. Observed increase of the  $k_x$  component of propagation vector for the TbMnO<sub>3</sub> nano-samples indicates the decrease of both  $\cos(nk_x)$  and the effective exchange integrals  $J_{\text{eff}}$ .

The  $r_1$  values do not change, while  $r_2$  are smaller and  $r_3$  ones are higher for the TbMnO<sub>3</sub> nano-samples. The values of  $\beta$  angles are similar for the nano- and poly-samples, while  $\alpha$  ones are larger for the TbMnO<sub>3</sub> nano-samples. Above data suggest that the decrease of the grain size results in the change in antiferromagnetic interactions along the  $b$ -axis.

The presented results suggest that the nanoparticle size plays an important role in the formation of magnetic properties.

## References

1. Balcells L, Fontcuberta J, Martínez B, Obradors X (1998) High-field magnetoresistance at interfaces in manganese perovskites. Phys Rev B 58:R14697. doi:10.1103/PhysRevB.58.R14697
2. Kimura T, Lawes G, Goto T, Tokura Y, Ramirez AP (2005) Distorted perovskite with configuration as a function as frustrated spin system. Phys Rev B 71:224425. doi:10.1103/PhysRevB.71.224425
3. Dagotto E (2001) Nanoscale phase separation and colossal magnetoresistance. Springer, Berlin
4. Kimura T, Goto T, Shintani H, Ishizaka K, Arima T, Tokura Y (2003) Magnetic control of ferroelectric polarization. Nature 426:55. doi:10.1038/nature02018
5. Kajimoto R, Yoshizawa H, Shintani H, Kimura T, Tokura Y (2004) Erratum: Magnetic structure of TbMnO<sub>3</sub> by neutron diffraction. Phys Rev B 70:012401-1-4. <https://doi.org/10.1103/PhysRevB.70.219904>
6. Blasco J, Ritter C, Garcia J, de Teresa JM, Perez-Cacho J, Ibarra MR (2000) Structural and magnetic study of Tb<sub>1-x</sub>Ca<sub>x</sub>MnO<sub>3</sub> perovskites. Phys Rev B 62:5609–5617. <https://doi.org/10.1103/PhysRevB.62.5609>
7. Prokhenenko O, Feyerherm R, Mostovoy M, Aliouane N, AUB D, Wolter A, Maljuk A, Argyrion DN (2007) Coupling of frustrated Ising spins to the magnetic cycloid in multiferroic TbMnO<sub>3</sub>. Phys Rev Lett 99:177206. doi:10.1103/PhysRevLett.99.177206



8. Kenzelmann M, Haris AB, Jones S, Broholm C, Schefer J, Kim SB, Zhang CL, Cheong S-W, Vajk OP, Lynn JW (2005) Magnetic inversion Symmetry breaking and ferroelectricity in  $\text{TbMnO}_3$ . *Phys Rev Lett* 95:087206-1-4. <https://doi.org/10.1103/PhysRevLett.95.087206>
9. Kimura T, Ishihara S, Shintani H, Arima T, Takahashi KT, Ishizaka K, Tokura Y (2003) Distorted perovskites with configuration as a frustrated spin system. *Phys Rev B* 68:060403. doi:10.1103/PhysRevB.68.060403
10. Quezel S, Tcheou F, Rossat-Mignod J, Quezel G, Roudaut E (1977) Magnetic structure of the perovskite-like compound  $\text{TbMnO}_3$ . *Physica B* 86–88:916 doi:10.1016/0378-4363(77)90740-9
11. Bazela W, Dul M, Dyakonov V, Gondek Ł, Hoser A, Hofmann J-U, Penc B, Szytuła A, Kravchenko Z, Nosalev I, Zarzycki A (2012) Magnetic and neutron diffraction studies of the polycrystalline and nanoparticle  $\text{TbMnO}_3$ . *Acta Phys Polon A* 122:384. doi: <http://dx.doi.org/10.12693/APhysPolA.122.384>
12. Dyakonov V, Szytuła A, Szymczak R, Zubov E, Szewczyk A, Kravchenko Z, Bazela W, Dyakonov K, Zarzycki A, Varyukhin V, Szymczak H (2012) Phase transitions in  $\text{TbMnO}_3$  manganites. *Low Temp Phys*. 38:216. doi: 10.1063/1.3691530
13. Rasberry SD, (1987) Bureau of standards certificate-standard reference material. 640b
14. Williamson GK, Hall WH (1953) X-ray line broadening from filled aluminium and wolfram. *Acta Metallurgica* 1:22–31. doi:10.1016/0001-6160(53)90006-6
15. Radaelli PG, Iacone G, Marezio M, Hwang HY, Cheong S-W, Jorgensen JD, Argyrion DV (1997) Structural effects on the magnetic and transport properties of perovskite  $\text{A}_{1-x}\text{A}'_x\text{MnO}_3$  ( $x = 0.25, 0.30$ ). *Phys Rev B* 56:8265. <https://doi.org/10.1103/PhysRevB.56.8265>
16. Radaelli PG, Marezio M, Hwang HY, Cheong S-W, Batlogg B (1996) Charge localization by static and dynamic distortions of the  $\text{MnO}_6$  octahedral in perovskite site manganites. *Phys Rev B* 54:8992. <https://doi.org/10.1103/PhysRevB.54.8992>
17. Bertaut EF (1963) Spin configurations of ionic structures: theory and practice. In: Rado GT, Shul H (eds) *Magnetism, a treatise on modern theory and materials*, vol 3. Academic, New York, p 149
18. Goodenough JB (1958) An interpretation of the magnetic properties of the perovskite-type mixed crystals  $\text{La}_{1-x}\text{Sr}_x\text{CoO}_{3-\lambda}$ . *Phys A Chem Solids* 6:287. doi:10.1016/0022-3697(58)90107-0
19. Kanamori J (1959) Superexchange interaction and symmetry properties of electron orbitals. *Phys a Chem Solids* 10:87. doi:10.1016/0022-3697(59)90061-7
20. Brinks HW, Rodriguez-Carvajal J, Fjellåg H, Kjekshus A, Hauback BC (2001) Crystal and magnetic structure of orthorhombic  $\text{HoMnO}_3$ . *Phys Rev B* 63:094411. doi:10.1103/PhysRevB.63.094411
21. Senff D, Link P, Hradil K, Hiess A, Regnault LP, Sidis Y, Aliouane N, Argyrion DN, Braden M (2007) Magnetic excitations in multiferroic  $\text{TbMnO}_3$ : evidence for a hybridized soft mode. *Phys Rev Lett* 98:137206. doi:10.1103/PhysRevLett.98.137206

# Chapter 34

## Influence of Annealing in Vacuum on Dispersion Kinetics of Palladium and Platinum Nanofilms Deposited onto Oxide Materials

Y. V. Naidich, I. I. Gab, T. V. Stetsyuk, B. D. Kostyuk, and V. V. Kavelin

### 34.1 Introduction

An in-depth study of the physical properties of thin metal films is stimulated by wide application of metal condensates in many areas of technology. In particular, to join such nonmetallic materials as oxide and non-oxide ceramics, single crystals, materials based on carbon, etc., using brazing or welding by pressure methods and metal coating of different thickness are often deposited onto these materials [1–5]. Metallization of the surfaces of such materials provides their sufficient wettability by molten metals determining the very technological possibility of solder joints formation and causing strength and other properties of the joints.

For brazing of nonmetallic materials, the most commonly used adhesively active materials are titanium, niobium, and hafnium [2–14].

Platinum and palladium coatings at the nonmetallic surfaces are also widely used in engineering [15–20]. These metals are interesting by fact that joints made with their use can work in an oxidizing atmosphere at high temperatures. Since metalized nonmetal parts have to be heated to sufficiently high temperatures (1300–1600 °C) for pressure welding or brazing, study of dispersion processes occurring during the

---

Y.V. Naidich • I.I. Gab (✉) • T.V. Stetsyuk • B.D. Kostyuk  
Frantsevich Institute for Problems of Materials Science, National Academy of Sciences  
of Ukraine, 3 Krzhyzhanovskogo st., Kyiv 03142, Ukraine  
e-mail: [gab@materials.kiev.ua](mailto:gab@materials.kiev.ua)

V.V. Kavelin  
Institute of Physics, National Academy of Sciences of Ukraine, 46 Nauky ave.,  
Kyiv 03680, Ukraine

annealing of these metal nanofilms 100 nm in thickness is not only of scientific interest but also of practical value for the development of technological regimes for joining of nonmetallic materials.

The metal coating thickness value equal to 100 nm was chosen by us because of the fact that, as it was demonstrated by our previous studies, good wettability by molten metal solders is provided by films 60–80 nm in thickness. Usage of films more than 120 nm in thickness leads to significant problems, including weak initial adhesion of the deposited film to the substrate at low temperatures, usually no higher than  $\cong 100$  °C (thus, only weak physical forces are involved, such as Van der Waals interaction). Besides, stresses at the film-substrate interface area (of crystallization and other origin) lead to spontaneous detachment of the film from the substrate, in particular, due to the difference of the thermal expansion coefficients of the film and the substrate materials.

## 34.2 Materials and Experimental Methods

Substrates samples were made of quartz glass, leucosapphire, and ZrO<sub>2</sub>-based ceramics. They were little thin plates sized  $4 \times 3 \times 1$  mm. One of the flat surfaces of each sample was well polished to a roughness degree  $R_z = 0.03 \div 0.05$   $\mu\text{m}$ . After polishing, all samples were carefully degreased with acetone and alcohol and annealed in a vacuum at 1100 °C for 1 h.

Onto the annealed samples surfaces, palladium and platinum films 100 nm in thickness were applied by electron beam sputtering during 10 min. During the film deposition, samples were heated up to no more than 100 °C. The coating thickness was measured with a special quartz resonator located in a vacuum chamber of electron beam apparatus ELU-2 along with samples. The quality of the deposited films was monitored by metallographic microscope XJL-17. Samples coated with palladium and platinum films were annealed in a vacuum chamber for various periods of time (from 2 up to 20 min) at different temperatures (1000  $\div$  1600 °C) in a vacuum not worse than  $2 \times 10^{-3}$  Pa.

The annealed samples were studied using scanning electron microscopes NeoScope JCM-5000, ZEISS EVO SO XVP, and atomic force microscope NanoScope IIIa with the ability of photomicrograph retention. Using these photomicrographs, percentages of metal film islet areas to the entire surface of samples were calculated by planimetric weighing method, i.e., through the weight of the images of the elements of metalized coatings at the samples surface cut out from photomicrographs [21]. The experimental data were processed graphically which has demonstrated the dependence of the sample surface areas coated with niobium and hafnium films on the annealing parameters (temperature, time).

### 34.3 Results and Discussion

Originally, films of both metals at all three oxides were continuous without any significant defects. Micrographs obtained using scanning electron microscope show only the dark field of uniform dark gray color. Because of films annealing, differences were observed in the behavior of films deposited onto leucosapphire, quartz glass, and  $ZrO_2$  ceramics.

Both palladium and platinum films at the quartz glass surface start to disintegrate as a result of annealing at 1000 °C. After a five-minute exposure, films of both metals were almost completely disintegrated into a rather large solid “drops” covering only about 40% of the quartz substrate. Besides, some interaction is already seen, particularly of palladium with quartz glass (Figs. 34.1 and 34.2). The word “drop” is written in quotes because, at such temperature (1000 °C), which is much lower than the melting point of both metals, and with rather high initial film thickness (100 nm), the formation of liquid drops is not possible. Increasing the annealing temperature up to 1100 °C practically does not change the nature of both the character of the disintegration of films and the area value of the quartz substrate covered with metal (Figs. 34.2, 34.3, and 34.4).

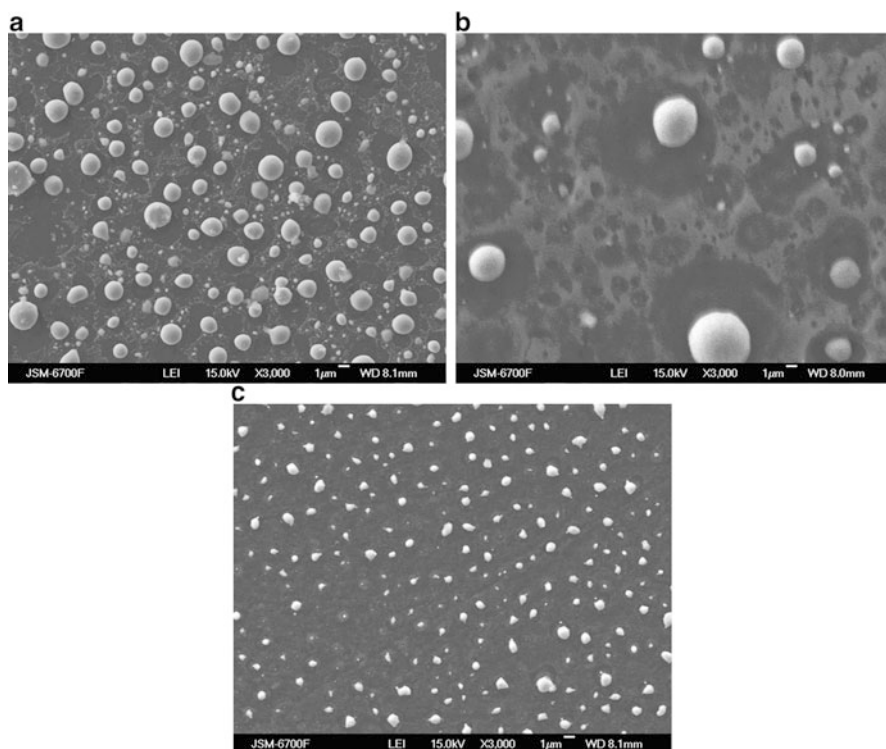


**Fig. 34.1** Palladium film 100 nm in thickness onto quartz glass (a, b) and onto leucosapphire (c) annealed at different temperatures during different times in vacuum,  $\times 3000$ : **a** 1000 °C, 5 min; **b** 1200 °C, 20 min; **c** 1400 °C, 2 min

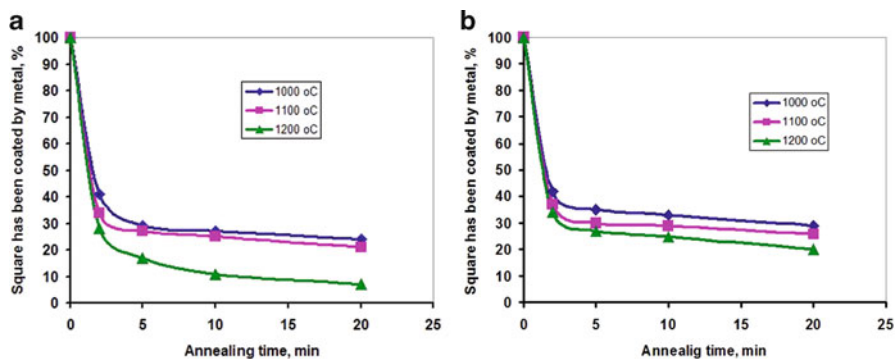


**Fig. 34.2** Quartz glass area covered by metal film dependence on annealing time at various temperatures (1000–1200 °C): (a) palladium; (b) platinum

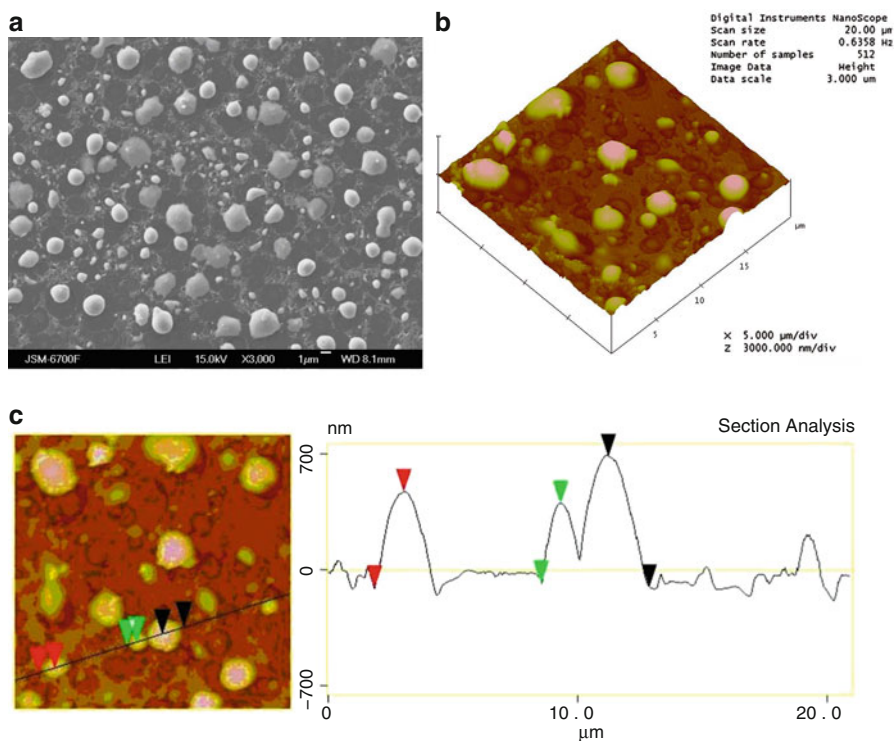


**Fig. 34.3** Palladium film 100 nm in thickness onto quartz glass annealed at 1100 °C during 10 min in vacuum: (a) film under scanning microscope,  $\times 3000$ ; (b) film under atomic force microscope; (c) profilogramma film

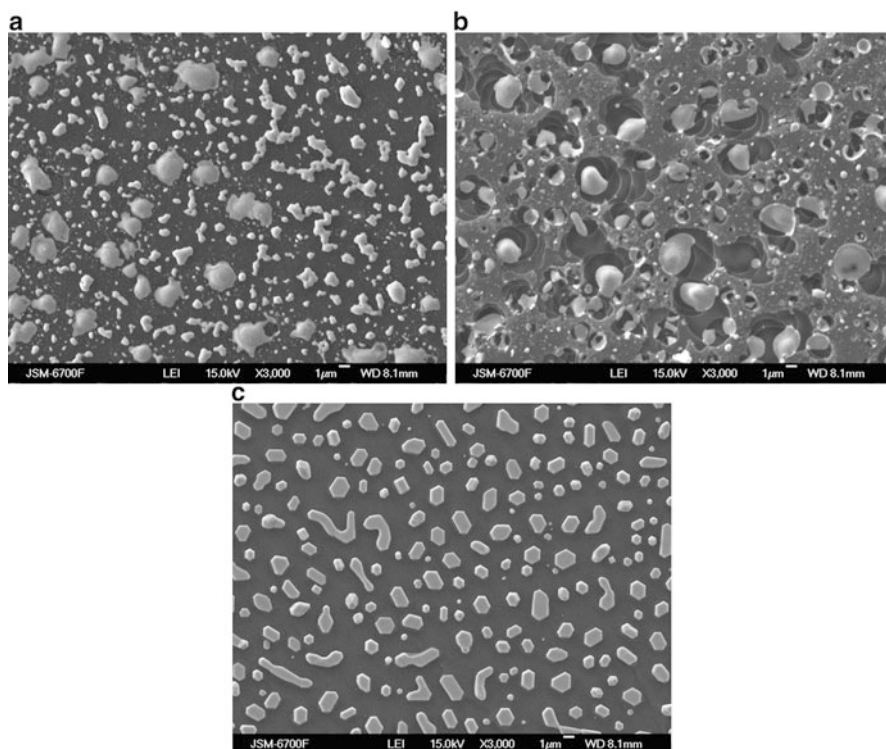


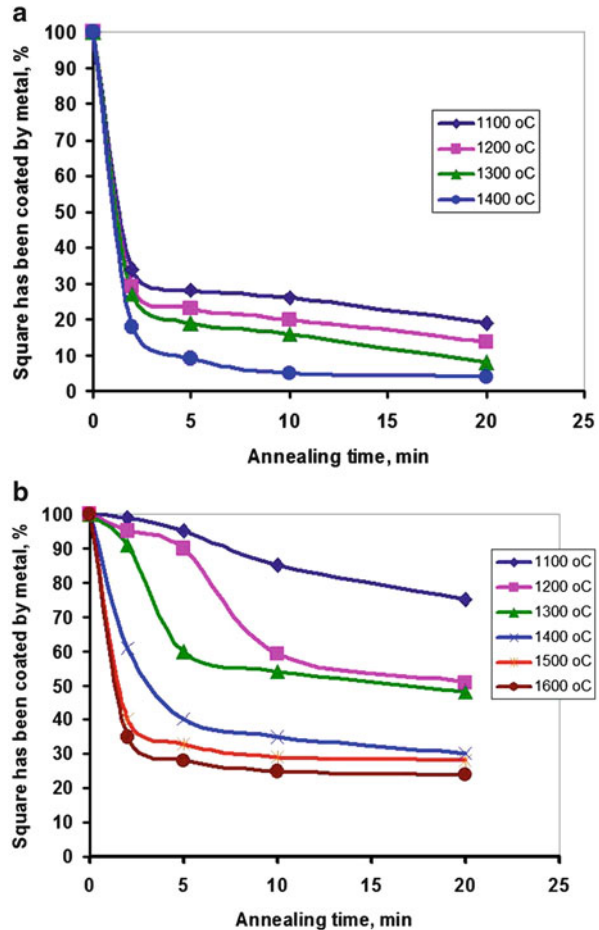
**Fig. 34.4** Platinum film 100 nm in thickness onto quartz glass (a, b) and onto leucosapphire (c) annealed at different temperatures during different times in vacuum,  $\times 3000$ : a 1100 °C, 5 min; b 1200 °C, 5 min; c 1500 °C, 10 min

The photo of palladium film annealed at 1100 °C for 10 min taken with atomic force microscope (Fig. 34.3a) clearly shows the large “drops” of palladium 700 nm high (Fig. 34.3b, c) located at a considerable distance from each other and covering about 25% of the substrate area.

As a result of films annealing at 1200 °C, they disintegrate even more intensively (Fig. 34.1b), and the degree of interaction of metals with quartz glass is significantly increased. The fragmentation process of these films was completed already after 10 min of annealing at such temperature, and subsequent exposure for 20 min at this temperature barely changes the area of substrates coated with metals (Fig. 34.2), with “drops” of lower-melting palladium covering only about 7% of the quartz substrate area, and with “drops” of more heat-resistant platinum covering 20% of the substrate surface area.

Annealing of palladium film on leucosapphire showed rapid fragmentation of the film in the first 2 min within the temperature range 1100–1400 °C (Fig. 34.5a). Further exposure at any temperature within this range leads only to regrouping of “drops” by number and size and also to slight decreasing of the

**Fig. 34.5** Leucosapphire area covered by metal film dependence on annealing time at various temperatures (1100–1600 °C): (a) palladium; (b) platinum



leucosapphire surface area covered with them (Fig. 34.1c). As a result of annealing at temperatures 1300–1400 °C, partial evaporation of palladium and its interaction with leucosapphire to the some degree take place (Fig. 34.6). Photomicrograph of palladium film deposited onto the leucosapphire surface and annealed in vacuum at 1400 °C for 10 min, taken with the atomic force microscope, shows that the film converts into separate individual significant height “drops” (from 300 up to 1000 nm) (Fig. 34.6b, c), covering only about 5% of the leucosapphire substrate area.

Annealing behavior of more heat-resistant platinum nanofilm deposited onto leucosapphire surface differs slightly from that of the palladium film. Platinum film fragments much slower than palladium one and covers much larger substrate area even at very high annealing temperatures (1500–1600 °C) (Fig. 34.5b). Intensive fragmentation of the heat-resistant platinum film at the leucosapphire surface within the first 2 min of exposure occurs at higher temperatures (1400–1600 °C) compared



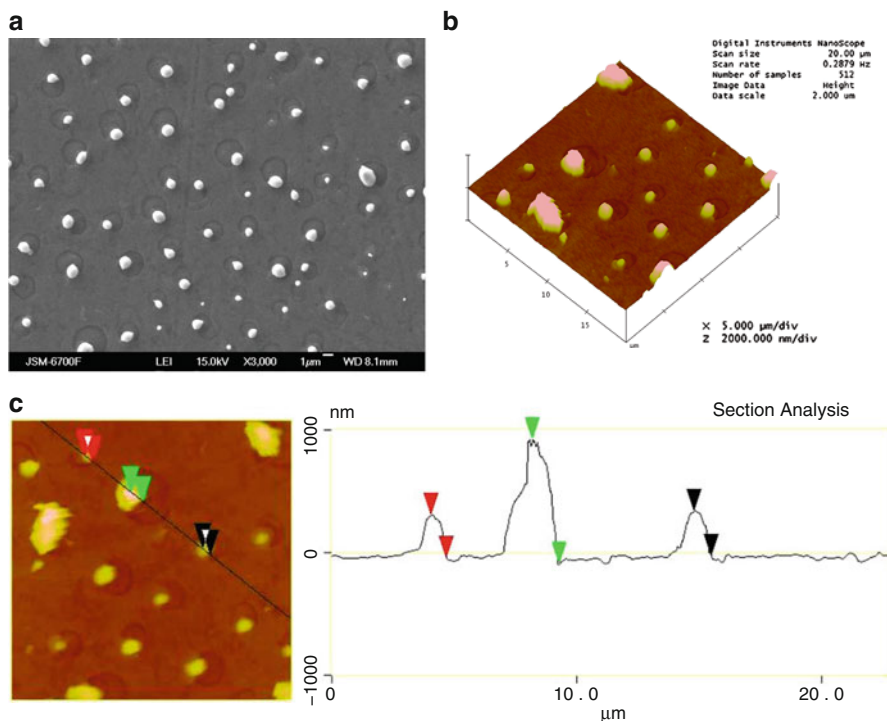


**Fig. 34.6** Palladium film 100 nm in thickness onto leucosapphire annealed at 1400 °C during 2 min in vacuum: (a) film under scanning microscope,  $\times 3000$ ; (b) film under atomic force microscope; (c) profilogram film

to the palladium film. At the temperature 1400 °C, after 10-min annealing, the platinum film was completely disintegrated into fragments of different shapes with the height of some of them reaching 400 nm (Fig. 34.7). After annealing at 1500 °C for 10 min, film fragments begin to crystallize (Fig. 34.4c), and, with further increase of temperature and crystallization annealing time, this process becomes even more pronounced.

The nature of the fragmentation during the annealing of palladium and platinum nanofilms deposited onto the  $ZrO_2$  substrate is similar to those at the quartz glass surface (Fig. 34.8), except for it is slightly slower. As it follows from the presented charts, the fragmentation character during the annealing of the palladium and platinum nanofilms at the quartz glass (Fig. 34.2) is the same, i.e., starting from annealing temperature 1000 °C, intense disintegration of films occurs within 3–5 min with formation of separate fragments and “drops” covering 30–40% of the substrate.

A further increase in the annealing time leads to a redistribution of the number and size of “drop” and to a slight reduction of the area of the substrate covered with the metal film at each temperature.



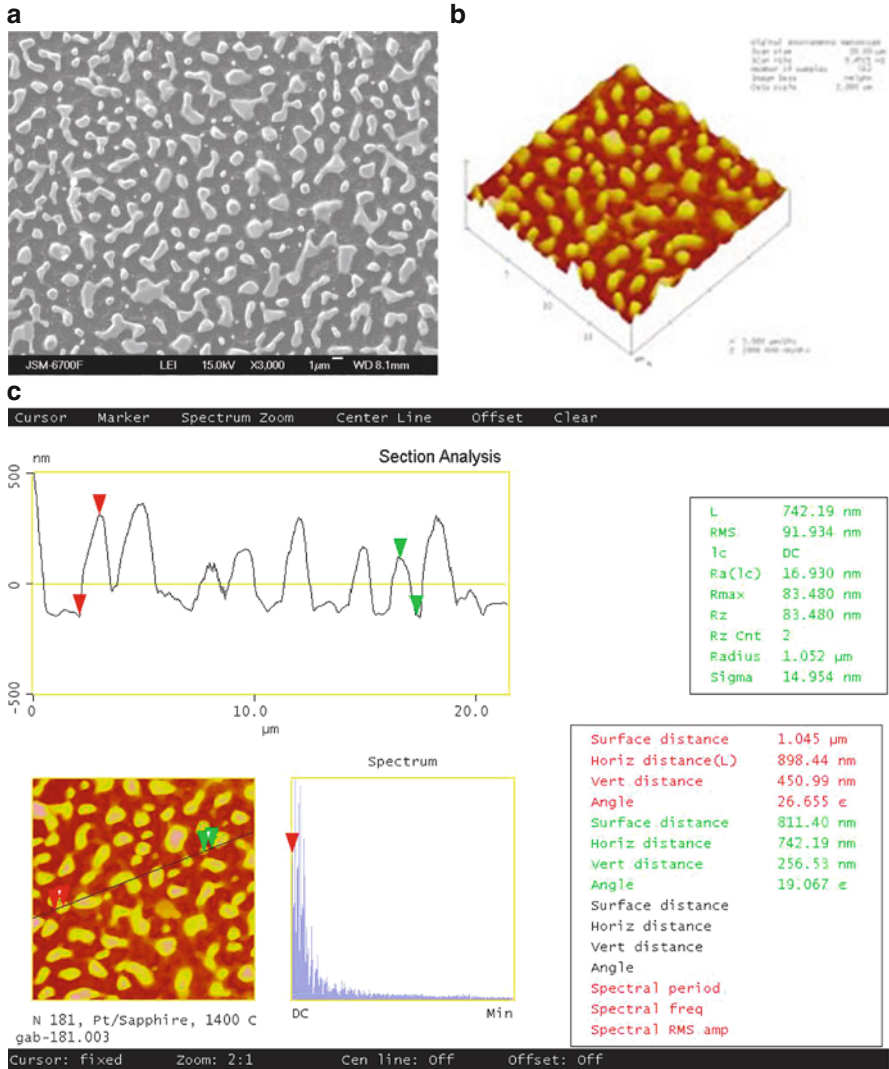


**Fig. 34.7** Platinum film 100 nm in thickness onto leucosapphire annealed at 1400 °C during 10 min in vacuum: (a) film under scanning microscope, ×3000; (b) film under an atomic force microscope; (c) profilogram film

With increasing of annealing temperature up to 1200 °C, films of both metals disintegrate completely. There is interaction of film fragments with quartz glass substrate surface which becomes almost completely naked from the remnants of palladium film. In case of platinum film  $\approx 25\%$  area of the substrate remains covered with its fragments under such conditions.

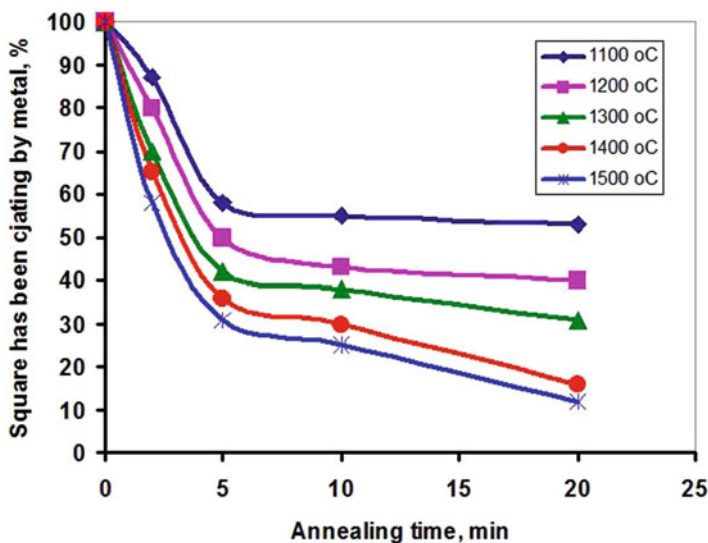


**Fig. 34.8** ZrO<sub>2</sub> ceramic areas covered by platinum film dependence on annealing time at various temperatures (1100–1500 °C)

In case of ZrO<sub>2</sub> ceramics, platinum film (Fig. 34.8) fragmentation is slower than in case of quartz glass. So, more or less substantial disintegration of film can be seen only after 5 min of annealing at all temperatures of given investigation.

After such exposure, platinum film fragments cover 60% of surface with the annealing temperature 1100 °C and 30% of surface with the annealing temperature 1500 °C. With 10 min exposure, naked surface area increases insignificantly. So, one can say that platinum film is suitable for use in the manufacture of high-temperature brazed joints of ZrO<sub>2</sub> ceramics with small exposure time at temperatures 1100–1500 °C.

In case of leucosapphire substrate, palladium film which does not react with the substrate material is also fragmenting rapidly within the first 3–5 min of annealing (Fig. 34.5a) but covering about 20% of the substrate surface at 1200 °C; and, only after annealing at 1400 °C, palladium film-covered area decreases down to about 5% of the substrate surface.

Much more heat-resistant platinum film at the leucosapphire substrate behaves a different way during the annealing (Fig. 34.5b). Thus, after annealing at temperatures up to 1300 °C, film fragments not as rapidly as at the quartz glass and thus covers more than half the surface area of the substrate. The rapid disintegration of the film takes place only after annealing at 1400 °C, and, even after annealing at 1600 °C, film fragments cover about a third of the area of the substrate. So, platinum nanofilm at the leucosapphire surface is the most suitable for use to make high-temperature brazed joints of leucosapphire devices.

## 34.4 Conclusions

As a result of annealing in vacuum, platinum and palladium nanofilms at the quartz glass surface disintegrate very rapidly into separate pieces and “drops.” After annealing at 1200 °C, they completely disintegrated covering a small area of the substrate and also interacting with quartz glass surface. So, in terms of quartz glass brazing, these films are not suitable as metalizing materials.

Platinum film deposited onto the ZrO<sub>2</sub> ceramics disintegrates much more slowly than at the quartz glass surface. With the temperatures of annealing 1100–1200 °C, platinum film covers about 50% of the ZrO<sub>2</sub> ceramic substrate with exposures up to 10 min. So it can be recommended for metallization of devices made from this ceramics for brazing at the temperature up to 1200 °C.

In case of leucosapphire substrate, palladium film is rapidly disintegrating during the annealing, exposing more than 70% of the substrate in the first minutes of annealing. During annealing, platinum nanofilm deposited onto leucosapphire disintegrates much more slowly and at higher temperatures unlike palladium one. Since, with the annealing temperatures up to 1300 °C, platinum nanofilm covers almost 60% of the leucosapphire substrate even at very long exposures at these temperatures, it can be recommended for metallization of leucosapphire devices in order to further braze them at temperatures up to 1300 °C.

## References

1. Batygin VN, Metelkin II, Reshetnikov AM (1982) *Vacuumnopltnaya keramika i yeyo spai s metallami*. Energiya, Moscow (in Russian)
2. Metelkin II, Pavlov MA, Pozdeeva NV (1977) *Svarka keramiki s metallami*. Metallurgia, Moscow (in Russian)
3. Shalz ML, Dalgleish BJ, Tomsia AP, Cannon RM, Glaesser AM (1994) Ceramic joining III. Bonding of alumina via Cu/Nb/Cu interlayers. *J Mater Sci* 29(14):3678
4. Marks RA, Sugar JD, Glaeser AM (2001) Ceramic joining IV. Effect of processing conditions on the properties of alumina joined via Cu|nb|Cu interlayers. *J Mater Sci* 36(23):5609
5. Marks RA, Chapmen DR, Danielson DT, Glaeser AM (2000) Joining of alumina via copper/niobium/copper interlayers. *Acta Mater* 48(18):4425
6. Koganitskaya EV (1959) Spai keramiki s aktivnymi metallami. *Elektronika* 4:86 (in Russian)
7. Harding FL, Rossington DR (1970) Wetting of ceramic oxides by molten metals under ultrahigh vacuum. *J Am Ceram Soc* 53(2):87
8. Naydich YV, Gab II, Zhyravlev VS, Dubrova VF, Gordynya AN (1989) Brazing nonmetallic materials to metals in vacuum brazing solder filled gap. *J Welding Tech* 2:12 (in Russian)
9. Rhee SK (1971) Wetting ceramic by liquid metals. *J Am Ceram Soc* 54(7):332
10. Melnikov VV, Ereemeev SV, Kulkova SE (2011) Izuchenie adhezii plenok niobiya na razno-orientirovanyh poverhnostyah  $\alpha$ -Al<sub>2</sub>O<sub>3</sub>. *J Tech Phys* 81(10):114 (in Russian)
11. Qiao-ying T, Lai-fei C, Li-tong Z (2004) Infiltration bonding C/SiC composite and niobium [J]. *J Aviat Mater* 24(1):53
12. Masaaki N, Tohru S, Ikuo O (1988) Bonding behavior between niobium and reaction-sintered SiC. *Trans JWRI* 17(2):67

13. Gab II, Zhyravlev VS, Kurkova DI, Stetsyuk TV, Naidich YV (1997) Contact interaction of oxide materials with refractory metals with high-temperature solid phase pressure welding. *J Powder Metall* 7–8:69 (in Ukrainian)
14. Karakozov ES, Kotelkin IS, Matveev GN, Merkulov AL, Shorshorov MH (1968) The formation mechanism of the compound at the solid state welding of ceramics from al with Nb. *J Phys Chem Treat* 3:123 (in Russian)
15. Ciftiyurek E, Sabolsky K, Sabolsky EM (2013) Platinum thin film electrodes for high-temperature chemical sensor applications. *Sens Actuators B Chem* 181:702
16. Wrbanek JD, Laster KLH (2005) Preparation and analysis of platinum thin films for high emperature sensor applications. *NASA/TM* 213433:1–19
17. Amirov II, Naumov VV, Szyumov MO, Selyukov RS (2013) Effect of ion energy on the surface morphology of the platinum film at a high-frequency ion-plasma sputtering. *Lett JTP* 39(2):68
18. Nowakowski R, Grzeszczak P, Duś R (2002) AFM studies of the catalytic reaction of hydrogen with oxygen on thin Pd and Pt films under pressure 101 kPa. *Surf Sci* 507:813
19. Ramaswamy V, Phillips MA, Nix WD, Clemens BM (2001) Observation of the strengthening of Pt layers in Ni/Pt and Pd/Pt multilayers by in-situ substrate curvature measurement. *Mater Sci Eng A* 319:887
20. Shim JY, Lee JD, Jin JM, Cheong H, Lee S (2009) Pd–Pt alloy as a catalyst in gasochromic thin films for hydrogen sensors. *Solar Energy Mater Solar Cells* 93(12):2133
21. Naydich YV, Gab II, Kostyuk BD, Stetsyuk TV, Kurkovf DI, Dukarov SV (2007) Investigation of the ceramic materials connection processes (soldering) using metal nanofilms. *J Rep Natl Acad Sci Ukr* 35:97

# Chapter 35

## Nematic Twist-Bend Phases of Liquid Crystals

Agnieszka Chrzanowska

### 35.1 Introduction

Banana-shaped molecules attract a lot of attention of researchers in recent years because of the unusual properties and novel phase structures they may form. When the system is dilute, they form simple nematic phase, in which there is no long positional order but long axes of molecules are positioned toward one direction – the director  $\mathbf{n}$ . Upon changing the density or temperature, such systems can form a new phase – the twist-bend nematic phase. This phase became famous because it exhibits, probably, the smallest spiral structure in the nanoworld.

The  $N_{TB}$  phase is in a sense very similar to the cholesteric nematic phase ( $N_{Ch}$ ) in which the director rotates on the spiral. The difference is that in cholesterics the director is positioned strictly in the plane perpendicular to the modulation axis (usually taken as the  $Z$  direction) and in the  $N_{TB}$  phase the director is tilted at a constant angle toward this axis. Another important difference is a significant change in the magnitude of the spiral pitch: in the  $N_{TB}$  phase the pitch is much shorter, about at least one order, as in the cholesteric phase. In most cases it is even comparable with molecular dimensions. The  $N_{TB}$  phase is especially interesting since the constituent banana molecules are achiral and the resultant phase is chiral. This is also the main difference as compared to the cholesteric phase, where the molecules must be chiral. The nematic director  $\mathbf{n}$  arrangement in the  $N_{TB}$  and in the cholesteric phase has been presented in Figs. 35.1 and 35.2.

---

A. Chrzanowska (✉)  
Institute of Physics, Kraków University of Technology, ul. Podchorążych 1, 30-084, Kraków,  
Poland  
e-mail: [achrzano@usk.pk.edu.pl](mailto:achrzano@usk.pk.edu.pl)

**Fig. 35.1** View of the  $\mathbf{n}$  director behavior in the  $N_{TB}$  twist-bend nematic liquid crystal phase

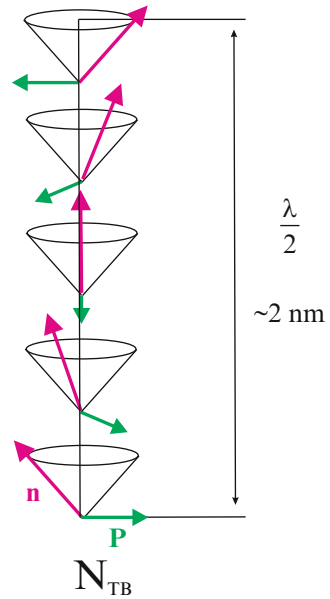
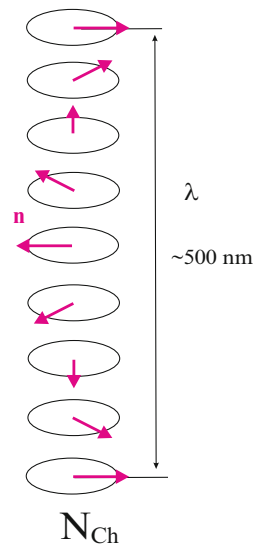


**Fig. 35.2** View of the  $\mathbf{n}$  director behavior in the  $N_{Ch}$  cholesteric nematic liquid crystal phase



The possibility of the existence of the  $N_{TB}$  phase has been suggested already in 1973 by Meyer [1]. This idea has been backed up almost 30 years later by Lorman [2], Dozov [3], and Memmer [4], who showed that to obtain a twist-bend phase, the molecules do not have to exhibit molecular chirality. The main reason for a spontaneous deformation of the director field is here the shape of the molecules – of the boomerang or the banana shape. Besides the  $N_{TB}$  phase Dozov

predicted also the splay-bend nematic  $N_{SB}$  phase. It has turned out later that achiral molecules can form also another modulated phases. In 1990, due to the suggestion of Sokalski, Chrzanowska [5] showed that the systems with negative twist elastic constant can also form spontaneously twisted nematic phase. Recently, Longa and Pająk [6], performing a detailed study of the symmetry elements, proposed a new form of the Landau-de Gennes free energy, which contains the minimum number of components that lead to the formation of the nematic modulated phases. In particular they showed that inclusion of the polarization field leads to two other new modulated nematic phases that exhibit longitudinal ( $N_{LP}$ ) and transverse ( $N_{TP}$ ) periodic waves, where the polarization field stays parallel and perpendicular to the wave vector.

From the experimental point of view, so far only the  $N_{TB}$  phase attracts the most attention, since it has been discovered in real systems. Experimental evidence of such phases is rapidly accumulating [7–22]. Experimental works are followed by theoretical explanations which comprise the mean field approaches [23–25], the Onsager theory [26], and the classical elasticity analysis of the Frank type [27]. Also molecular dynamics simulation [26] predicts the  $N_{TB}$  phase.

## 35.2 Model

We consider the Landau-de Gennes free energy of the form according to the model based on the order parameter tensor  $\mathbf{Q}$  and the polarization vector  $\mathbf{P}$ , which has been proposed in [6] by Longa and Pająk:

$$F_{LDG} = \int f_{LDG} dz = \int (f_Q + f_{QP} + f_P) dz \quad (35.1)$$

where

$$f_Q = f_{2Q} + f_{3Q} + f_{4Q} \quad (35.2)$$

with

$$f_{2Q} = \frac{1}{4} [t_Q \text{Tr}(\mathbf{Q}^2) + (\nabla \otimes \mathbf{Q}) \cdot (\nabla \otimes \mathbf{Q}) + \rho (\nabla \cdot \mathbf{Q}) \cdot (\nabla \cdot \mathbf{Q}) - 2\kappa \mathbf{Q} \cdot (\nabla \times \mathbf{Q})] \quad (35.3)$$

and

$$f_{3Q} + f_{4Q} = -\sqrt{6}B \text{Tr}(\mathbf{Q}^3) + \text{Tr}(\mathbf{Q}^2)^2 \quad (35.4)$$

and

$$f_P = \frac{1}{4} [t_p \mathbf{P}^2 + (\nabla \otimes \mathbf{P}) \cdot (\nabla \otimes \mathbf{P}) + A_C (\nabla \cdot \mathbf{P})^2 - 2\kappa_P \mathbf{P} \cdot (\nabla \times \mathbf{P})] + a_4 (\mathbf{P}^2)^2, \quad (35.5)$$

$$f_{QP} = -\frac{1}{4} [e_P \mathbf{P} \cdot (\nabla \cdot \mathbf{Q}) + 2\kappa_{QP} (\nabla \cdot \mathbf{Q}) \cdot (\nabla \times \mathbf{P})] \\ - \lambda P_\alpha Q_{\alpha\beta} P_\beta + \lambda_1 P_\alpha Q_{\alpha\beta}^2 P_\beta + \lambda_2 \mathbf{P}^2 Tr(\mathbf{Q}^2) \quad (35.6)$$

In [6] it has been shown that this type of energy contains the minimum number of components which can support occurrence of the modulated nematic structures.

The order parameter tensor which is the main property in the above free energy has to be symmetric and traceless:

$$\mathbf{Q} = \begin{bmatrix} Q_{xx} & Q_{xy} & Q_{xz} \\ Q_{xy} & Q_{yy} & Q_{yz} \\ Q_{xz} & Q_{yz} & -(Q_{xx} + Q_{yy}) \end{bmatrix} \quad (35.7)$$

and the polarization vector has three components:

$$\mathbf{P} = [P_x, P_y, P_z]. \quad (35.8)$$

Finding numerically the minimum of this energy for the parameters

$$\rho = 1, \quad \kappa = 0, \quad A_C = 2, \quad e_P = -4.0, \\ B = 1/\sqrt{6}, \quad t_q = 0.1, \quad t_p = 0.8, \quad \lambda = -\frac{1}{2}, \\ \lambda_1 = \lambda_2 = \kappa_{QP} = \kappa_P = 0 \quad (35.9)$$

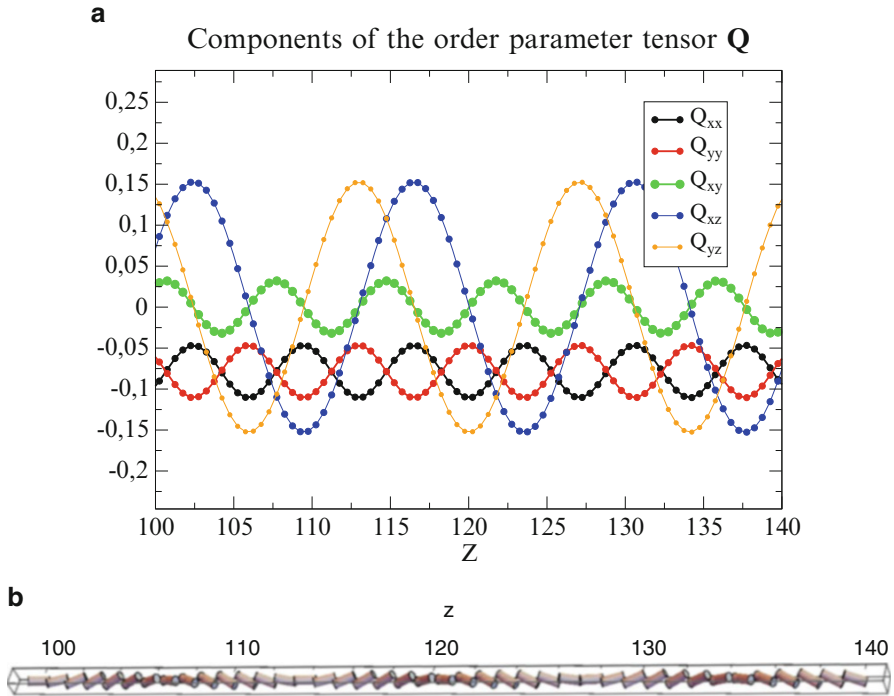
one can obtain the following profiles of the  $\mathbf{Q}$  and  $\mathbf{P}$  components.

Figure 35.3 presents *five* components of the order tensor  $\mathbf{Q}$ . It turns out that the profiles represent simple characteristics:  $Q_{xx} \sim \cos^2(Az)$ ,  $Q_{yy} \sim \sin^2(Az)$ , and  $Q_{xy} \sim \sin(Bz)\cos(Bz)$ .

Nonzero sinusoidal behavior of  $Q_{xz}$  and  $Q_{yz}$  indicates that the projection of the director on the  $Z$  axis is nonzero; hence the phase is of the nematic twist-bend type. In contrast, such projection in cholesterics would be at the zero level. The component  $P_z$  (see Fig. 35.4) is equal to zero; hence the polarization vector lies in the plane perpendicular to the  $Z$  axis. At the same time  $P_x$  and  $P_y$  are given by the sine function indicating uniform rotation about  $Z$  axis.

To assess the behavior of the  $N_{TB}$  phase it would be illustrative to see also its temperature dependence. In the Landau energy the parameter responsible for the temperature changes is given by  $t_Q$ . As an example we choose the behavior of the  $Q_{xx}$ . Figure 35.5 shows its changes versus temperature. In general all values





**Fig. 35.3** Components of the tensor  $\mathbf{Q}$  (a), behavior of the director  $\mathbf{n}$  (b).

obtained for  $Q_{xx}$  are negative. Upon increasing temperature, values of  $Q_{xx}$  increase and diminish in magnitude, being at first at low level, and then upon approaching the phase transition point, the changes are getting larger.

Figure 35.6, on the other hand, shows the changes of the  $Q_{xx}$  amplitude.

Upon approaching the phase transition point to the isotropic phase one observes diminishing of the mean average order level (illustrated either by maximum or minimum of  $Q_{xx}$ ) as well as the  $Q_{xx}$  amplitude. Finally, the first-order transition to the isotropic phase occurs.

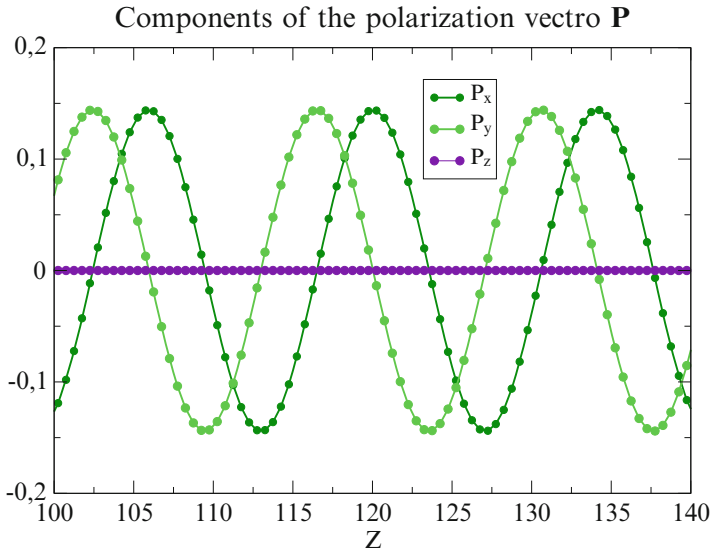


Fig. 35.4 Components of the polarization vector  $\mathbf{P}$

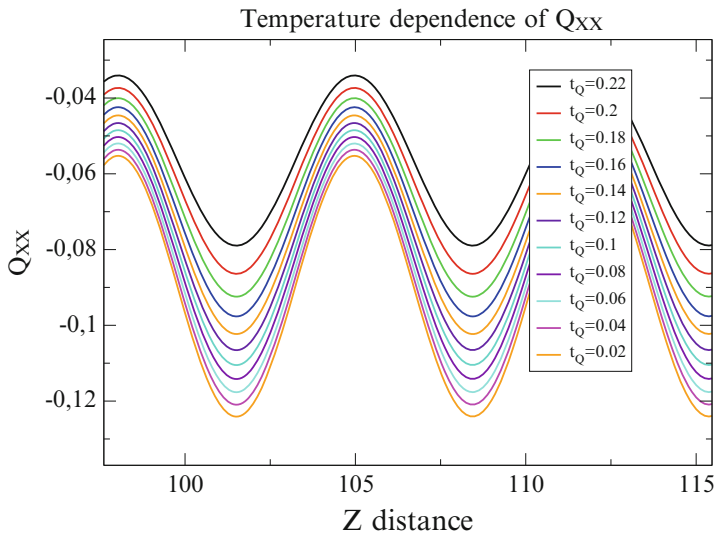


Fig. 35.5 Temperature dependence of  $Q_{xx}$

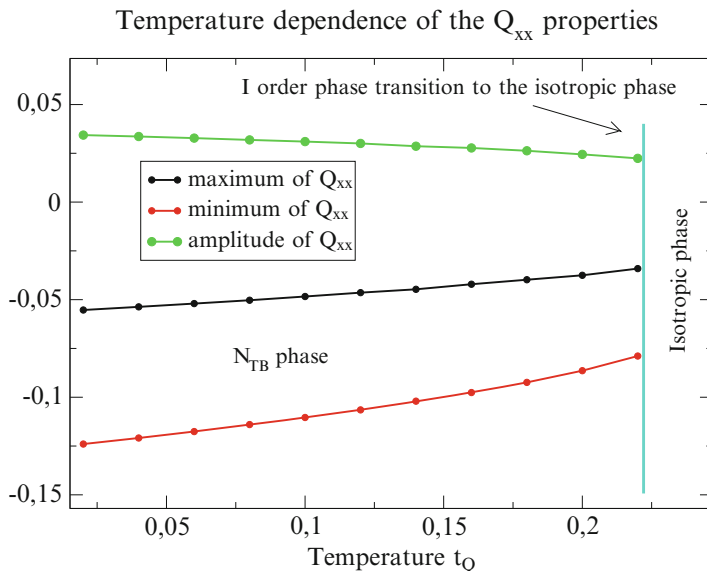


Fig. 35.6  $Q_{xx}$  amplitude properties versus temperature

### 35.3 Summary

Within the framework of the Landau-de Gennes theory we show an example of the properties of the twist-bend phase  $N_{TB}$ . Order parameter tensor  $\mathbf{Q}$  and polarization vector  $\mathbf{P}$  modulations have been presented together with their changes upon approaching the transition point to the isotropic phase.

**Acknowledgements** This work was supported by Grant No. DEC-2013/11/B/ST3/04247 of the National Science Center in Poland.

### References

1. Meyer RB (1976) Molecular fluids. Les houches summer school in theoretical physics. In: Balian R, Weill G (eds) XXV-1973 of Les houches summer school in theoretical physics. Gordon and Breach, New York, pp 273–373
2. Lorman VL, Mettout B (1999) Unconventional mesophases formed by condensed vector waves in a medium of achiral molecules. *Phys Rev Lett* 82:940–943
3. Dozov I (2001) On the spontaneous symmetry breaking in the mesophases of achiral banana-shaped molecules. *Europhys Lett* 56:247–253
4. Memmer R (2002) Liquid crystal phases of achiral banana shaped molecules: a computer simulation study. *Liq Cryst* 29:483–496
5. Chrzanowska A (1990) Spontaneously twisted nonchiral nematic liquid crystals. *Z Naturforsch* 45a:783–789

6. Longa L, Pająk G (2016) Modulated nematic structures induced by chirality and steric polarization. *Phys Rev E* 93:040701(R)
7. Šepelj M, Lesac A, Baumeister U, Diele S, Nguyen HL, Bruce DW (2007) Intercalated liquid-crystalline phases formed by symmetric dimers with an alpha, omega-diiminoalkylene spacer. *J Mater Chem*. 17:1154–1165
8. Imrie CT, Henderson PA (2007) Liquid crystal dimers and higher oligomers: between monomers and polymers. *Chem Soc Rev* 36:2096–2124
9. Panov VP, Nagaraj M, Vij JK, Panarin YP, Kohlmeier A, Tamba MG, Lewis RA, Mehl GH (2010) Spontaneous periodic deformations in nonchiral planar-aligned bimesogens with a nematic-nematic transition and a negative elastic constant. *Phys Rev Lett* 105:167801-1-4
10. Henderson PA, Imrie CT (2011) Methylene-linked liquid crystal dimers and the twist-bend nematic phase. *Liq Cryst* 38:1407–1414
11. Cestari M, Frezza E, Ferrarini A, Luckhurst GR (2011) Crucial role of molecular curvature for the bend elastic and flexoelectric properties of liquid crystals: mesogenic dimers as a case study. *J Mater Chem* 21:12303–12308
12. Panov VP, Balachandran R, Nagaraj M, Vij JK, Tamba M, Kohlmeier A (2011) Microsecond linear optical response in the unusual nematic phase of achiral bimesogens. *Appl Phys Lett* 99:261903
13. Beguin L, Emsley JW, Lelli M, Lesage A, Luckhurst GR, Timimi BA, Zimmermann H (2012) The chirality of a twist-bend nematic phase identified by NMR spectroscopy. *J Phys Chem B* 116:7940–7951
14. Panov VP, Balachandran R, Vij JK, Tamba MG, Kohlmeier A, Mehl GH (2012) Field-induced periodic chiral pattern in the N-x phase of achiral bimesogens. *Appl Phys Lett* 101:234106
15. Šepelj M, Baumeister U, Ivšić UT, Lesac A (2013) Effects of geometry and electronic structure on the molecular self-assembly of Naphthyl-based dimers. *J Phys Chem B* 117:8918–8929
16. Copic M (2013) Nematic phase of achiral dimers spontaneously bends and twists. *Proc Natl Acad Sci USA* 110:15855–15856
17. Borshch V, Kim yK, Xiang J, Gao M, Jáklí A, Panov VP, Vij JK, Imrie CT, Tamba MG, Mehl GH (2013) Nematic twist-bend phase with nanoscale modulation of molecular orientation. *Nat Commun* 4:2635-1-8
18. Chen D, Porada JH, Hooper JB, Klittnick A, Shen Y, Tuchband MR, Korblova E, Bedrov D, Walba DM, Glaser MA (2013) Chiral heliconical ground state of nanoscale pitch in a nematic liquid crystal of achiral molecular dimers. *PNAS*. 110:15931–15936
19. Mandle RJ, Davis EJ, Lobato SA, Voll CCA, Cowling SJ, Goodby JW (2014) Synthesis and characterisation of an unsymmetrical, ether-linked, fluorinated bimesogen exhibiting a new polymorphism containing the NTB or twist-bend phase. *Phys Chem Chem Phys* 16:6907–6915
20. Chen D, Nakata, Shao R, Tuchband MR, Shuai M, Baumeister U, Weissflog W, Walba DM, Glaser MA, MacLennan JE (2014) Twist-bend heliconical chiral nematic liquid crystal phase of an achiral rigid bent-core mesogen. *Phys Rev E* 89:022506
21. Robles-Hernández B, Sebastián N, Rosario de la Fuente M, López DO, Diez-Berart S, Salud J, Ros MB, Dunmur DA, Luckhurst GR, Timimi BA (2015) Twist, tilt, and orientational order at the nematic to twist-bend nematic phase transition of 1,9-bis(4-cyanobiphenyl-4-yl) nonane: a dielectric, H-2 NMR, and calorimetric study. *Phys Rev E* 92:062505
22. Yun C-J, Vengatesan MR, Vij JK, Son J-K (2015) Hierarchical elasticity of bimesogenic liquid crystals with twist-bend nematic phase. *Appl Phys Lett* 106:173102
23. Greco C, Luckhurst GR, Ferrarini A (2013) Enantiotopic discrimination and director organization in the twist-bend nematic phase. *Phys Chem Chem Phys* 15:14961–14965
24. Greco C, Luckhurst GR, Ferrarini A (2014) Molecular geometry, twist-bend nematic phase and unconventional elasticity: a generalized Maier-Saupe theory. *Soft Matter* 10:9318–9323
25. Tomczyk W, Pająk G, Longa L (2016) Twist-bend nematic phases of bent-shaped biaxial molecules. *Soft Matter* 1:7445

26. Greco C, Ferrarini A (2015) Entropy-driven chiral order in a system of achiral bent particles. *Phys Rev Lett* 115:147801
27. Barbero G, Evangelista LR, Rosseto P, Zola RS, Lelidis I (2015) Elastic continuum theory: towards understanding of the twist bend nematic phases. *Phys Rev E* 92:030501

# Chapter 36

## Influence of Free Volumes on Functional Properties of Modified Chalcogenide Glasses and Oxide Ceramics

H. Klym, O. Shpotyuk, A. Ingram, L. Calvez, I. Hadzaman, Yu. Kostiv, A. Ivanusa, and D. Chalyy

### 36.1 Introduction

An important area of electronic technology is the use of physical phenomena on nano- and subnanometer levels of structural organization of functional materials [1–3]. Transformation to these levels is achieved due to nanostructurization, i.e., formation of nanoobjects with the individual components (atoms or molecules) by their agglomeration or massive dissociation into individual components [4, 5]. In the case of disordered solids with full or partial absence of atomic structural correlations and excess free-volume configuration entropy or enthalpy, these processes occur in transformation of atom and void structures.

---

H. Klym (✉) • Y. Kostiv

Lviv Polytechnic National University, S. Bandery Str., 12, 79013, Lviv, Ukraine

e-mail: [halyna.i.klym@lpnu.ua](mailto:halyna.i.klym@lpnu.ua)

O. Shpotyuk

Vlokh Institute of Physical Optics, 23, Dragomanov Str, 79005, Lviv, Ukraine

Jan Dlugosz University in Czestochowa, 13/15, Armii Krajowej Str., 42200, Czestochowa, Poland

A. Ingram

Opole University of Technology, Ozimska Str., 75, 45370, Opole, Poland

L. Calvez

Equipe Verres et et Céramiques, UMR-CNRS 6226, Institute des Sciences chimiques de Rennes, Université de Rennes 1, 35042, Rennes Cedex, France

I. Hadzaman

Drohobych State Pedagogical University, I. Franko Str., 24, 82100, Drohobych, Ukraine

A. Ivanusa • D. Chalyy

Lviv State University of Life Safety, Kleparivska Str., 35, 79000, Lviv, Ukraine

© Springer International Publishing AG 2017

O. Fesenko, L. Yatsenko (eds.), *Nanophysics, Nanomaterials, Interface Studies, and Applications*, Springer Proceedings in Physics 195,

DOI 10.1007/978-3-319-56422-7\_36

From the standpoint of modern electronic technology, structural disordering is the basis of efficient and controlled process of obtaining various functional materials and flexible management of their functional properties due to reliable, efficient, and predictable physical and technological modifications, the possibility of additional pre- and post-process optimization processes [6–8]. Typical representatives of such materials are glasses and ceramics [9–12]. The structural disordering of these materials is impossible without the stabilization process of inner free volume. In addition, their functionality is closely related to nanostructurization under technological modifications and external factors.

An important role is void structure in chalcogenide glasses (ChG) which have a network structure with saturated covalent chemical bonds [13, 14]. Modern chalcogenide photonics [15] requires modification of disordered materials to ensure their functionality in a wide spectral range, which covers the area in both IR atmospheric windows and space telecommunications window [16]. Such modification of ChG is performed by injection of addition components (halide, metal activators, rare earth ions, etc.) into base matrix that destroy their network structure making local heterogeneity at nanolevel [17, 18]. This process is accompanied by not only the evolution of the atomic subsystem of glass materials but also the relevant changes in inner free-volume structure. Such modifications are characteristic for glass-ceramics due to process of controlled ceramization (i.e., formation of the inner structure of grains, pores, and grain boundaries) and functional ceramics for temperature- and umidity-sensitive elements [19, 20]. The main feature that combines ChG and oxide ceramics is disordering caused by nanostructurization of their inner free volumes.

The aim of this work is the investigation of inner free-volume structure and functional properties of row functional materials (chalcogenide  $\text{GeSe}_2\text{-Ga}_2\text{Se}_3$  and  $\text{GeSe}_2\text{-Ga}_2\text{S}_3\text{-CsCl}$  glasses as well as oxide  $\text{Cu}_{0.4}\text{Co}_{0.4}\text{Ni}_{0.4}\text{Mn}_{1.8}\text{O}_4$  and  $\text{MgO-Al}_2\text{O}_3$  ceramics) caused by their modifications.

## 36.2 Preparation of Glasses and Ceramics

The  $80\text{GeSe}_2\text{-}20\text{Ga}_2\text{Se}_3$  chalcogenide glasses were prepared from highly pure raw materials Ge, Ga, and Se (99.999%) [18, 21, 22]. The materials were heated from 20 to 850 °C using 2 °C/min rate. Then, the silica tube was quenched in water at room temperature, annealed at 30 °C below the glass transition temperature ( $T_g = 370$  °C) for 3 h, and finally slowly cooled down to room temperature [18]. The crystallization of the  $80\text{GeSe}_2\text{-}20\text{Ga}_2\text{Se}_3$  ChG was performed at optimal temperature of ceramization ( $T_g + 10$  °C) [21–23]. Thus, glass samples were placed in a ventilated furnace where the accuracy of temperature is  $\pm 2$  °C for 25 and 50 h.

The  $\text{GeSe}_2\text{-Ga}_2\text{S}_3\text{-CsCl}$  ChG were sintered from Ge, Ga, S, and CsCl compounds, as described in details elsewhere [24–26]. The glass transition temperatures  $T_g$  are 442 and 396 °C for  $(80\text{GeSe}_2\text{-}20\text{Ga}_2\text{S}_3)_{100-x}(\text{CsCl})_x$ ,  $x = 0$  and  $x = 10$  glasses,

respectively [24, 26]. The obtained  $(80\text{GeS}_2\text{-}20\text{Ga}_2\text{S}_3)_{100}(\text{CsCl})_0$  and  $(80\text{GeS}_2\text{-}20\text{Ga}_2\text{S}_3)_{90}(\text{CsCl})_{10}$  glasses are referred as  $(\text{CsCl})_0$  and  $(\text{CsCl})_{10}$ , respectively.

The  $\text{Cu}_{0.1}\text{Ni}_{0.8}\text{Co}_{0.2}\text{Mn}_{1.9}\text{O}_4$  ceramics were prepared from high purity carbonate salts [27–29]. The mixture was thermally decomposed in the air at  $700 \pm 5^\circ\text{C}$  for 4 h. The prepared blanks were sintered in the air with respect to special time-temperature regimes, as described in details elsewhere [30–32]. It should be noted that the sintering route of ceramics was performed to ensure necessary conditions for inhibition effect in degradation [29, 33], the content of additional NiO phase with NaCl-type structure having decisive role in the final ceramics structure. The  $\text{Cu}_{0.1}\text{Ni}_{0.8}\text{Co}_{0.2}\text{Mn}_{1.9}\text{O}_4$  ceramics with 1% and 8% NiO phase were prepared owing to different amounts of thermal energy transferred during the sintering [27, 29].

The  $\text{MgO-Al}_2\text{O}_3$  ceramics were sintered at maximal temperature ( $T_s$ )  $1300^\circ\text{C}$  for 2 h, as it was described elsewhere [34–36]. With respect to X-ray diffraction measurements [36], the ceramics contain main spinel and additional MgO (3.5%) phases.

### 36.3 Experimental Details

The PAL spectra for ChG and oxide ceramics were measured using ORTEC system of 230 ps resolution at the temperature  $T = 22^\circ\text{C}$  and relative humidity  $\text{RH} = 35\%$  [21, 22, 35, 37]. For  $\text{MgO-Al}_2\text{O}_3$  ceramics, PAL measurements were performed after initial drying, 7 days of water exposure (water vapor in desiccator at  $\text{RH} = 100\%$ ), and further final drying in a vacuum at  $120^\circ\text{C}$  for 4 h [35]. Isotope  $^{22}\text{Na}$  of slow activity ( $\sim 50$  kBq) sandwiched between two identical tested samples was used as a source of positrons.

Each spectrum was measured with a channel width of 6.15 ps (the total number of channels was 8000) and contained at least  $\sim 10^6$  coincidences in a total, which can be considered as conditions of normal PAL measurement statistics. To obtain data on longest-lived PAL components for  $\text{MgO-Al}_2\text{O}_3$  ceramics, these ceramics were studied within a channel width of 61.5 ps [35]. The measured PAL spectra of glasses and ceramics were processed with standard LT 9.0 computer program [38]. The obtained curves were fitted by two components with lifetimes  $\tau_1$  and  $\tau_2$  and intensities  $I_1$  and  $I_2$  for  $\text{Cu}_{0.1}\text{Ni}_{0.8}\text{Co}_{0.2}\text{Mn}_{1.9}\text{O}_4$  ceramics [39]; by three components with lifetimes  $\tau_1$ ,  $\tau_2$ , and intensities  $\tau_3$  and  $I_1$ ,  $I_2$ , and  $I_3$  for  $80\text{GeS}_2\text{-}20\text{Ga}_2\text{S}_3$  and  $(80\text{GeS}_2\text{-}20\text{Ga}_2\text{S}_3)_{100}(\text{CsCl})_0$  ( $x = 0$  and  $x = 10$ ) glasses [22, 25, 26]; and by four components with lifetimes  $\tau_1$ ,  $\tau_2$ ,  $\tau_3$ , and  $\tau_4$  and intensities  $I_1$ ,  $I_2$ ,  $I_3$ , and  $I_4$  for  $\text{MgO-Al}_2\text{O}_3$  ceramics [34, 35].

The positron trapping modes in the studied samples such as average positron lifetimes  $\tau_{\text{av}}$ , positron lifetime in defect-free bulk  $\tau_{\text{b}}$ , positron trapping rate in defects  $\kappa_{\text{d}}$ , and fraction of trapped positrons  $\eta$  (for  $80\text{GeS}_2\text{-}20\text{Ga}_2\text{S}_3$  glasses) were calculated using a formalism of two-state trapping model [21, 40, 41].



Optical transmission spectra of ChG were measured by Shimadzu UV-3600 spectrophotometer operated at room temperature in the visible and near-IR spectral region [21, 26, 42].

The humidity sensitivity of MgO-Al<sub>2</sub>O<sub>3</sub> ceramics was determined by dependence of electrical resistance  $R$  on relative humidity  $RH$  of environment. The electrical resistance of the studied spinel ceramics was measured in the heat and humidity chamber PR-3E “TABAI” at 20 °C for  $RH$  in range 31–96% [34, 36]. The electrodes were attached to the connecting cables of M ohmmeter working at the fixed frequency of 500 Hz. The maximal overall uncertainties in the electrical measurements did not exceed approximately  $\pm(0.02\text{--}0.04)$  MOhm in electrical resistance. The confidence interval in  $RH$  measuring bar restricted by equipment accuracy was no worse than  $\pm 1\%$  [36].

The degradation tests for Cu<sub>0.1</sub>Ni<sub>0.8</sub>Co<sub>0.2</sub>Mn<sub>1.9</sub>O<sub>4</sub> ceramics were performed at temperature of 170 °C lasting defined time intervals (within 10 time domains from 24 to 500 h) [27, 29, 33]. The results of aging tests were controlled by relative resistance drift ( $RRD$ ) defined as changes in electrical resistance  $\Delta R/R_0$  measured in the normal conditions (near 25 °C and 35% of relative humidity) using digital multimeter. The confidence interval in the  $RRD$  measuring error bar restricted by equipment inaccuracy was no worse than  $\pm 0.2\%$ . The maximal overall uncertainties in the electrical measurements did not exceed approximately  $\pm(0.4\text{--}0.5)\%$  [27].

## 36.4 Results and Discussion

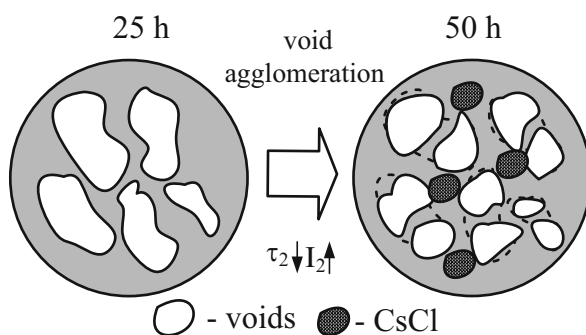
### 36.4.1 The Ge-Ga-Se Glasses Modified by Crystallization Process

With respect to XRD data, as it was noted earlier [21, 22], with increasing annealing time to 25 and 50 h at 380 °C, the well-pronounced crystalline peaks at  $2\theta \sim 28^\circ$  appear. The positions of these peaks are in agreement with GeGa<sub>4</sub>Se<sub>8</sub> and Ga<sub>2</sub>Se<sub>3</sub> phase indexation [22]. In fact, all principal XRD peaks of GeGa<sub>4</sub>Se<sub>8</sub> and Ga<sub>2</sub>Se<sub>3</sub> phases coincide, so we consider them in crystallized 80GeSe<sub>2</sub>-20Ga<sub>2</sub>Se<sub>3</sub> glass as signatures of both these phases (Ga<sub>2</sub>Se<sub>3</sub> and GeGa<sub>4</sub>Se<sub>8</sub>). The width of this peak ( $2\theta \sim 28^\circ$ ) confirms the presence of nanoparticles in a glassy matrix in the form of nanocrystallites with 9–10 nm in sizes [21].

The changes in the atomistic structure of 80GeSe<sub>2</sub>-20Ga<sub>2</sub>Se<sub>3</sub> ChG from amorphous to crystallized one are accompanied by transformations in the void structure. The results of PAL measurements confirm such diversity of void evolution processes in the studied glasses. Fitting parameters and corresponding positron trapping modes for PAL spectra of 80GeSe<sub>2</sub>-20Ga<sub>2</sub>Se<sub>3</sub> glasses are given in Table 36.1. As was described earlier in [22], the first component ( $\tau_1, I_1$ ) has no physical meaning for chalcogenide glasses. With respect to two-state positron trapping model for ChG [40], the  $\tau_2$  lifetime is directly related to the size of free volumes (trapping centers),

**Table 36.1** Fitting parameters and positron trapping modes for PAL spectra of 80GeSe<sub>2</sub>-20Ga<sub>2</sub>Se<sub>3</sub> glasses before (0 h) and after (25 h and 50 h) thermal annealing

Annealing duration	Fitting parameters					
	$\tau_1$ , ns	$I_1$ , %	$\tau_2$ , ns	$I_2$ , %	$\tau_3$ , ns	$I_3$ , %
0 h	0.209	0.610	0.426	0.360	1.967	0.030
25 h	0.215	0.633	0.432	0.337	2.038	0.030
50 h	0.210	0.605	0.424	0.365	2.159	0.030
Annealing duration	Positron trapping modes					
	$\tau_{av.}$ , ns	$\tau_b$ , ns	$\kappa_d$ , ns	$\tau_2 - \tau_b$ , ns	$\tau_2/\tau_b$	$\eta$
0 h	0.290	0.258	0.91	0.17	1.65	0.19
25 h	0.291	0.261	0.82	0.17	1.66	0.18
50 h	0.292	0.260	0.92	0.16	1.63	0.19

**Fig. 36.1** Schematic illustration of free-volume void fragmentation during crystallization process in the 80GeSe<sub>2</sub>-20Ga<sub>2</sub>Se<sub>3</sub> chalcogenide glasses caused by annealing from 25 to 50 h

and intensity  $I_2$  is proportional to the number of such defects under condition of the same defect-free bulk annihilation lifetime. The third component ( $\tau_3$ ,  $I_3$ ) in the fitting curves corresponds to ortho-positronium *o-Ps* formation on level of 3%.

With extending the annealing duration to 25 h, the lifetime  $\tau_2$  increases, and  $I_2$  intensity decreases due to void agglomeration. This trend reduces the positron trapping rate  $\kappa_d$  without significant changes in  $\tau_{av.}$  and  $\tau_b$  lifetimes. With further extension of annealing duration to 50 h, the  $I_2$  intensity increases, while lifetime  $\tau_2$  decreases to 0.424 ns. These changes result in increased positron trapping rate  $\kappa_d$ . Other positron trapping parameters such as  $\tau_2/\tau_b$  and  $\eta$  behave under annealing in line with these changes (Table 36.1). The fraction of trapped positrons  $\eta$  decreases in the initial stage of treatment to 25 h and increases at further annealing to 50 h.

During the crystallization process at annealing for 50 h, the glass structure relaxes toward more thermodynamically favorable state [22, 43]. It means that free-volume nanovoids can be essentially transformed in this process. In the case of the studied ChG, the fragmentation of larger free-volume entities into smaller ones occurs (Fig. 36.1). Such process is accompanied by a decrease in  $\tau_2$  lifetime and a corresponding increase in  $I_2$  intensity.

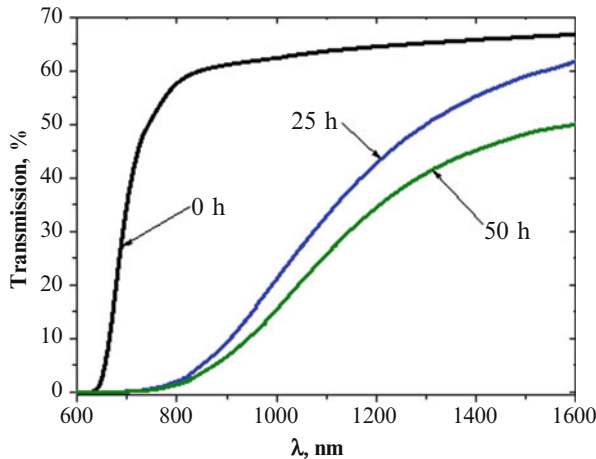


**Fig. 36.2** Optical transmission spectra for  $80\text{GeSe}_2\text{-}20\text{Ga}_2\text{Se}_3$  glass before (0 h) and after heat treatment times at  $380^\circ\text{C}$  during 25 and 50 h

Thus, nearly the same  $\tau_b$  and  $\tau_{av}$  values are characteristic for all ChG samples, while the positron trapping rate in extended defects  $\kappa_d$  decreases with nucleation of crystallized phases (annealing for 25 h) and increases with crystallization (annealing at 50 h). The crystal growth is accompanied by network shrinkage of  $80\text{GeSe}_2\text{-}20\text{Ga}_2\text{Se}_3$  glass, the agglomeration of free-volume voids occurring more rapidly than their appearance due to mismatch between growing crystallites and remainder of the glass matrix [21, 22].

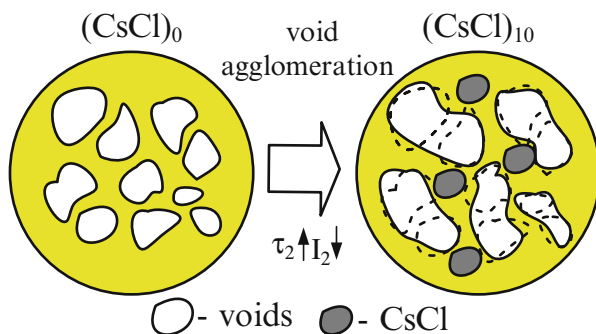
The process of crystallization in the  $80\text{GeSe}_2\text{-}20\text{Ga}_2\text{Se}_3$  glasses influences their functionality, i.e., optical transmission spectra. The non-annealed glassy samples (0 h) show maximum optical transmittance at the level of 65% (Fig. 36.2). Annealing at  $380^\circ\text{C}$  for 25 and 50 h decreases this transmittance and shifts optical transmission edge toward long-wave side. The appearance of growing of  $\text{Ga}_2\text{Se}_3$  and  $\text{GeGa}_4\text{Se}_8$  nanocrystals inside glassy matrix induces light scattering at shorter wavelengths [21].

### 36.4.2 The Ge-Ga-S Glasses Modified by CsCl Additives

Fitting parameters and positron trapping modes calculated within three-component fitting procedure for PAL spectra of  $(80\text{GeS}_2\text{-}20\text{Ga}_2\text{S}_3)_{100-x}(\text{CsCl})_x$ , ( $0 = 0$ ,  $x = 10$ ) glasses are given in Table 36.2. As was shown previously, the  $\tau_2$  lifetime shows the size of free voids where positrons are trapped, and the intensity  $I_2$  is proportional to the number of these voids. The positronium trapping in the third component ( $\tau_3$ ,  $I_3$ ) is estimated at the level of 1–3% [16, 25, 26]. We analyze the PAL results with respect to the second defect-related component ( $\tau_2$ ,  $I_2$ ) reflecting

**Table 36.2** Fitting parameters and positron trapping modes for PAL spectra of  $(80\text{GeS}_2-20\text{Ga}_2\text{S}_3)_{100-x}(\text{CsCl})_x$ , ( $0 = 0, x = 10$ ) glasses

Sample	Fitting parameters						Positron trapping modes		
	$\tau_1$ , ns	$I_1$ , a.u.	$\tau_2$ , ns	$I_2$ , a.u.	$\tau_3$ , ns	$I_3$ , a.u.	$\tau_{av}$ , ns	$\tau_b$ , ns	$\kappa_d$ , ns <sup>-1</sup>
(CsCl) <sub>0</sub>	0.201	0.581	0.426	0.387	1.958	0.032	0.310	0.279	0.59
(CsCl) <sub>10</sub>	0.249	0.696	0.499	0.290	2.029	0.014	0.313	0.282	0.73

**Fig. 36.3** Schematic illustration of free-volume void agglomeration in  $(80\text{GeS}_2-20\text{Ga}_2\text{S}_3)_{100-x}(\text{CsCl})_x$ , ( $0 = 0, x = 10$ ) glasses

evolution of voids in  $\text{GeS}_2\text{-Ga}_2\text{S}_3\text{-CsCl}$  ChG caused by CsCl presence in the glass matrix. These nanovoids have the same meaning as atomic vacancies [23].

Thus, the lifetime  $\tau_2$  increases from 0.426 ns for  $(\text{CsCl})_0$  to 0.499 for  $(\text{CsCl})_{10}$  ChG samples, while the intensity  $I_2$  decreases (Table 36.2). Consequently, positron trapping rate  $\kappa_d$  correlates with  $\tau_2$  and  $I_2$  parameters and decreases due to the drop of the intensity  $I_2$ . Such changes of PAL parameters describe the agglomeration of free-volume nanovoids in the inner structure of ChG (Fig. 36.3). The positron trapping rate in defects  $\kappa_d$  increases from 0.59 ns<sup>-1</sup> for  $(\text{CsCl})_0$  to 0.73 ns<sup>-1</sup> in  $(\text{CsCl})_{10}$ , and the density  $\rho$  of these glasses also increases with CsCl content [25, 26].

The CsCl additives in the base  $\text{GeS}_2\text{-Ga}_2\text{S}_3$  glassy matrix have influence on their optical transmission spectra. The transmission in the visible region of spectra for studied ChG is shown in Fig. 36.4.

The  $(\text{CsCl})_0$  samples are essentially transparent down to 500 nm, and CsCl content in the glassy matrix results in the shift of the absorption edge toward shorter wavelengths (similar effect is described in [24, 25, 44]). The transmission increases with CsCl from 77% in  $\text{CsCl}_0$  to 83% in  $\text{CsCl}_{10}$ . From a structural point of view, the addition of CsCl in  $\text{GeS}_2\text{-Ga}_2\text{S}_3$  glasses is characterized by the formation of  $\text{GaS}_{4-x}\text{Cl}_x$  tetrahedra that are dispersed in the glass network [24]. So, the average number of Ga-S bonds decreases for the benefit of the average number of Ga-Cl bonds.

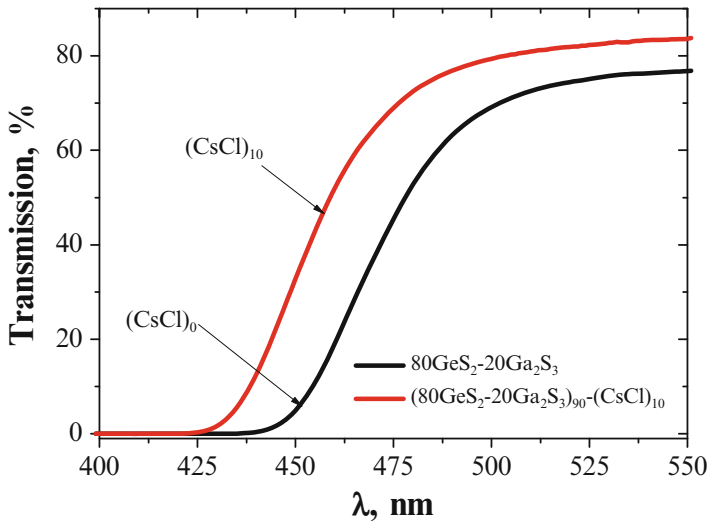


**Fig. 36.4** Optical transmission spectra of  $(80\text{GeS}_2\text{-}20\text{Ga}_2\text{S}_3)_{100-x}(\text{CsCl})_x$  ( $x = 0$  and  $x = 10$ ) chalcogenide glasses

**Table 36.3** Fitting parameters and positron trapping modes for PAL spectra of  $\text{Cu}_{0.4}\text{Co}_{0.4}\text{Ni}_{0.4}\text{Mn}_{1.8}\text{O}_4$  ceramics mathematically treated within two-component fitting procedure

NiO amount	Fitting parameters				Positron trapping modes		
	$\tau_1$ , ns	$I_1$ , a.u.	$\tau_2$ , ns	$I_2$ , a.u.	$\tau_{\text{av}}$ , ns	$\tau_b$ , ns	$\kappa_d$ , $\text{ns}^{-1}$
1% NiO	0.19	0.82	0.38	0.18	0.23	0.21	0.48
8% NiO	0.17	0.79	0.36	0.21	0.21	0.19	0.62

### 36.4.3 The $\text{Cu}_{0.1}\text{Ni}_{0.8}\text{Co}_{0.2}\text{Mn}_{1.9}\text{O}_4$ Ceramics Modified by NiO Phase

As was shown previously in [39], for oxide spinel-type ceramic materials, the first component of spectra was connected with main spinel structure and the second one with extended defects located near grain boundaries in the vicinity of additional extracted phases. The intensity  $I_1$  corresponds to the amounts of the main spinel phase, while the  $I_2$  intensity to the amount of additional NiO phase near grain boundaries.

The lifetime of the first and second components for  $\text{Cu}_{0.1}\text{Ni}_{0.8}\text{Co}_{0.2}\text{Mn}_{1.9}\text{O}_4$  ceramics is typical for spinel-structured materials and equals 0.38 ns (Table 36.3). The lower  $\tau_1$  value in ceramics with 1% NiO (0.17 ns) is well correlated with this NiO content in different crystallographical positions. Since the amount of grain/pores in these samples was larger [45], the process of positron trapping in these ceramics was more intensive (the positron trapping rate of defects increased from 0.48 to 0.62  $\text{ns}^{-1}$ ).

The intensity of the second component for ceramics with 1% NiO is 0.18 a.u. This additional NiO phase is localized near grain boundaries and partly fills pores [45]. Then the intensity  $I_2$  increases to 0.21 a.u. correspondingly to the increasing amount of NiO phase near grain boundaries and the size of defects increases ( $\tau_2$  reduces from 0.38 to 0.36 ns). These transformations were in good agreement with positron trapping parameters. Nevertheless, there were no significant changes in  $\tau_{av}$  and  $\tau_b$  parameters. In all cases, the same type of positron trapping center is formed [46].

The changes in microstructure of  $\text{Cu}_{0.1}\text{Ni}_{0.8}\text{Co}_{0.2}\text{Mn}_{1.9}\text{O}_4$  ceramics are reflected in their stability in time (electronic relaxation kinetics). Kinetic curves illustrating the *RRD* defined by  $\Delta R/R_0$  values in  $\text{Cu}_{0.1}\text{Ni}_{0.8}\text{Co}_{0.2}\text{Mn}_{1.9}\text{O}_4$  ceramics with 1% and 8% NiO phase are shown in Fig. 36.5.

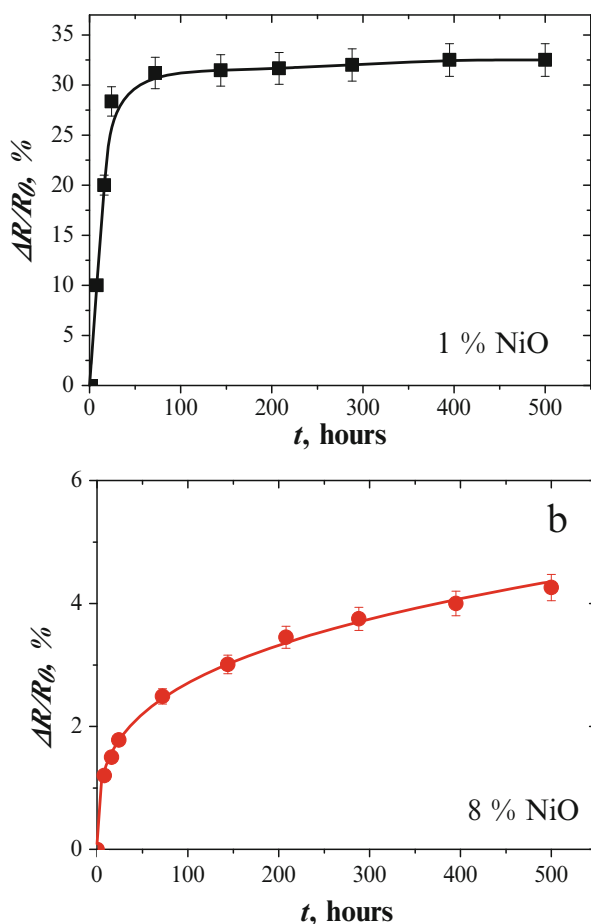


**Fig. 36.5** The *RRD* ( $\Delta R/R_0$ ) in  $\text{Cu}_{0.1}\text{Ni}_{0.8}\text{Co}_{0.2}\text{Mn}_{1.9}\text{O}_4$  ceramics (**a** – 1% NiO; **b** – 8% NiO) caused by prolonged storage at 170 °C (with error bar data)

The ceramic samples with 1% NiO phase are characterized by the largest value of *RRD* reaching more than 30% (Fig. 36.5a). With the increase in the amount of NiO phase to 8%, the saturated *RRD* value decreased to 4.3% (Fig. 36.5b). Obviously, increasing of NiO amount is needed for stabilization of electrical parameters of these ceramics.

### 36.4.4 Water Vapor Sorption Processes in the MgO-Al<sub>2</sub>O<sub>3</sub> Ceramics

As it was shown earlier [34–36, 47], the positron annihilation in humidity-sensitive MgO-Al<sub>2</sub>O<sub>3</sub> ceramics is revealed through two different channels related to positron trapping (component with lifetime  $\tau_2$ ) and *o*-Ps decaying (two long-lived components with  $\tau_3$  and  $\tau_4$  lifetimes). The first component with parameters  $\tau_1$  and  $I_1$  reflects mainly microstructure specificity of spinel ceramics along with input from annihilation of para-Ps atoms [34]. The lifetime  $\tau_2$  is related to the size of free-volume nanodefects near grain boundaries, and  $I_2$  intensity reflects their amount [41]. The third and the fourth components ( $\tau_3$ ,  $I_3$ ) and ( $\tau_4$ ,  $I_4$ ) correspond to annihilation of *o*-Ps in intrinsic nanopores of MgO-Al<sub>2</sub>O<sub>3</sub> ceramics [35, 48].

PAL parameters obtained within four-component treatment of the PAL spectra of initial, water-vapored, and dried MgO-Al<sub>2</sub>O<sub>3</sub> ceramics sintered at 1300 °C are shown in Table 36.4.

Decreasing the lifetime  $\tau_2$  in water-vapored MgO-Al<sub>2</sub>O<sub>3</sub> ceramics and increasing their intensity  $I_2$  show intensification of positron trapping in defects near grain boundaries filled with water. After drying, the intensities  $I_2$  almost completely return to the initial values (characteristic for initially dry samples). Thus, the water adsorption processes in MgO-Al<sub>2</sub>O<sub>3</sub> ceramics are accompanied by fragmentation of positron trapping sites near grain boundaries, and, respectively, the water desorption processes are accompanied by agglomeration of free-volume voids.

**Table 36.4** Fitting parameters and positron trapping modes for PAL spectra of MgO-Al<sub>2</sub>O<sub>3</sub> ceramics sintered at 1300 °C obtained from four-component procedure

Sample	Fitting parameters							
	$\tau_1$ , ns	$I_1$ , a.u.	$\tau_2$ , ns	$I_2$ , a.u.	$\tau_3$ , ns	$I_3$ , a.u.	$\tau_4$ , ns	$I_4$ , a.u.
Initial	0.155	0.82	0.414	0.16	2.426	0.008	68.74	0.014
Water vapor	0.161	0.76	0.400	0.21	2.619	0.018	58.33	0.007
Drying	0.156	0.82	0.421	0.15	2.448	0.007	68.17	0.014
	Positron trapping modes					Pore radius		
	$\tau_{av.}$ , ns	$\tau_b$ , ns			$\kappa_d$ , ns <sup>-1</sup>	$R_3$ , nm	$R_4$ , nm	
Initial	0.197	0.17			0.66	0.325	1.818	
Water vapor	0.213	0.19			0.80	0.340	1.630	
Drying	0.198	0.17			0.63	0.327	1.807	

Water vapor sorption processes in the studied MgO-Al<sub>2</sub>O<sub>3</sub> ceramics result in essential evolution of the third and fourth *o*-Ps-related components. The intensity  $I_3$  increases in initially dry samples after water vapor exposure, thus confirming *o*-Ps annihilation in water-filled nanopores through a “bubble” mechanism (with corresponding *o*-Ps lifetime close to 1.8 ns) [49–51]. After drying, the intensities of the third and fourth components return to the initial value, confirming high efficiency of water adsorption-desorption processes. The intensity  $I_4$  decreases in water vapor exposed ceramics samples. After drying (in a vacuum at 120 °C for 4 h) of the ceramic samples previously exposed to water vapor, the initial pore size tends to be restored (Table 36.4).

Additionally, the radii  $R_3$  and  $R_4$  of spherical nanopores were calculated using *o*-Ps-related  $\tau_3$  and  $\tau_4$  lifetimes in known Tao-Eldrup model [52, 53]. The decreased  $\tau_4$  value for ceramics dried after water vapor exposure can be connected with formation of thin layers of water molecules covering the walls of pores with radii of 1.8 nm, which are not completely removed after vacuum annealing at 120 °C for 4 h.

Changes caused by inner nanoporous structure of MgO-Al<sub>2</sub>O<sub>3</sub> ceramics were reflected in their humidity sensitivity. In spite of a small amount of transporting pores [34, 36, 53], ceramics are characterized by linear dependence of electrical resistance  $R$  vs.  $RH$  in the entire studied region (from 30% to 98% of  $RH$ ) without significant hysteresis in absorption-desorption cycles (Fig. 36.6). Humidity sensitivity of ceramics sintered at 1300 °C results in increased amount of open water-exchange outside-delivering macropores [36]. They provide efficient sorption processes of water through small amount of communication mesopores.

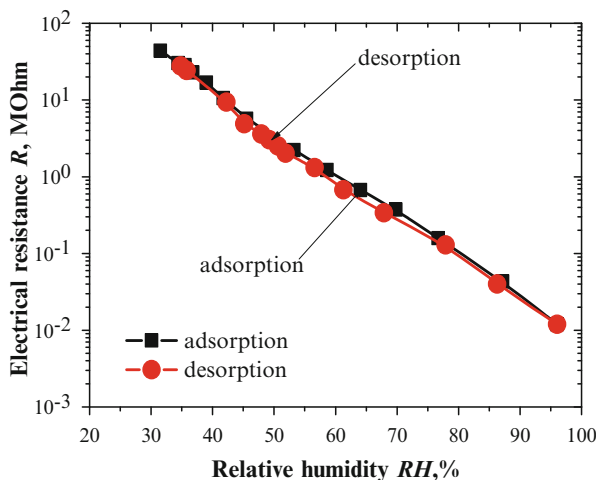


**Fig. 36.6** Exploitation properties of MgO-Al<sub>2</sub>O<sub>3</sub> ceramics sintered at 1300 °C in absorption-desorption cycle



## 36.5 Conclusions

Influences of inner free-volume structure on the functional properties of chalcogenide  $\text{GeSe}_2\text{-Ga}_2\text{Se}_3$  and  $\text{GeSe}_2\text{-Ga}_2\text{S}_3\text{-CsCl}$  glasses as well as oxide  $\text{Cu}_{0.4}\text{Co}_{0.4}\text{Ni}_{0.4}\text{Mn}_{1.8}\text{O}_4$  and  $\text{MgO-Al}_2\text{O}_3$  ceramics caused by their different modifications are investigated.

In the case of  $80\text{GeSe}_2\text{-}20\text{Ga}_2\text{Se}_3$  glasses, it was shown that crystallization process during annealing at  $380^\circ\text{C}$  for 25 and 50 h indicates specific fragmentation of larger free-volume nanovoids into a greater number of smaller ones. Annealing at  $380^\circ\text{C}$  for 25 and 50 h results in the decreasing of transmittance and shifts optical transmission edge toward long-wavelength region.

For  $\text{GeSe}_2\text{-Ga}_2\text{S}_3\text{-CsCl}$  ChG, it is established that CsCl additives transform free volume (void agglomeration in ChG with 10% mol. of CsCl) and optical properties of glass matrix. The shift of the absorption edge toward shorter wavelengths is observed in Ge-Ga-S ChG with CsCl content.

In  $\text{Cu}_{0.1}\text{Ni}_{0.8}\text{Co}_{0.2}\text{Mn}_{1.9}\text{O}_4$  ceramics with 8% of NiO phase addition, positron trapping defects (or free volumes) near grain boundaries are formed. The character of thermally induced electronic degradation in structurally modified  $\text{Cu}_{0.1}\text{Ni}_{0.8}\text{Co}_{0.2}\text{Mn}_{1.9}\text{O}_4$  ceramics shows stretched exponential behavior.

In modified  $\text{MgO-Al}_2\text{O}_3$  ceramics sintered at  $1300^\circ\text{C}$ , it is shown that drying of ceramics in vacuum at  $120^\circ\text{C}$  previously exposed to water vapor does not restore initial pore size, confirming sensitivity of PAL method to amount of water molecules adsorbed in nanopores. The water vapor modifies defects in ceramics located near grain boundaries, and this process is accompanied by void fragmentation at water adsorption with further void agglomeration at water desorption after drying. Using lifetimes of the third and fourth components of PAL spectra, the radii of nanopores were calculated using Tao-Eldrup model. The  $\text{MgO-Al}_2\text{O}_3$  ceramics sintered at  $1300^\circ\text{C}$  are humidity sensitive from 30% to 98% of *RH*.

**Acknowledgment** H. Klym thanks the Ministry of Education and Science of Ukraine for the support (grant No 0116U004411).

## References

1. Zhao X, Ren X, Sun C, Zhang X, Si Y, Yan C, Xu J, Xue D (2008) Morphology evolution at nano- to micro-scale. *Funct Mater Lett* 1(03):167–172. <http://dx.doi.org/10.1142/S1793604708000393>
2. Wilson SA, Jourdain RP, Zhang Q, Dorey RA, Bowen CR, Willander M, Al-hilli SM, Nur O, Quandt E, Johansson C, Pagounis E, Kohl M, Matovic J, Samel B, Wijngaart W, Jager EWH, Carlsson D, Djinovic Z, Wegener M, Moldovan C, Iosub R, Abad E, Wendlandt M, Rusu C, Persson K (2007) New materials for micro-scale sensors and actuators: an engineering review. *Materials Science and Engineering: R: Reports* 56(1):1–129. <http://dx.doi.org/10.1016/j.mser.2007.03.001>

3. Cain M, Morrell R (2001) Nanostructured ceramics: a review of their potential. *Appl Organomet Chem* 15(5):321–330. doi:[10.1002/aoc.153](https://doi.org/10.1002/aoc.153)
4. Dutta J, Hofmann H (2003) *Nanomaterials*. Swiss Federal Institute of Technology. Lausanne, pp 9–20
5. Gabor L, Hornyak JJ, Moore HF, Dutta J (2008) *Fundamentals of nanotechnology*. CRC Press, Boca Raton, p 786
6. Donth EJ (2013) *The glass transition: relaxation dynamics in liquids and disordered materials*, vol 48. Springer Science & Business Media, Berlin, p 418
7. Kierlik E, Monson PA, Rosinberg ML, Sarkisov L, Tarjus G (2001) Capillary condensation in disordered porous materials: hysteresis versus equilibrium behavior. *Phys Rev Lett* 87(5):055701. <https://doi.org/10.1103/PhysRevLett.87.055701>
8. Holand W, George H, Beall GH (2012) *Glass ceramic technology*. Wiley, Hoboken, p 440
9. Seddon AB (1995) Chalcogenide glasses: a review of their preparation, properties and applications. *J Non-Cryst Solids* 184:44–50. [http://dx.doi.org/10.1016/0022-3093\(94\)00686-5](http://dx.doi.org/10.1016/0022-3093(94)00686-5)
10. Zakery A, Elliott SR (2003) Optical properties and applications of chalcogenide glasses: a review. *J Non-Cryst Solids* 330(1):1–12. <http://dx.doi.org/10.1016/j.jnoncrsol.2003.08.064>
11. Li JG, Ikegami T, Lee JH, Mori T (2000) Fabrication of translucent magnesium aluminum spinel ceramics. *J Am Ceram Soc* 83(11):2866–2868. doi:[10.1111/j.1151-2916.2000.tb01648.x](https://doi.org/10.1111/j.1151-2916.2000.tb01648.x)
12. Dorey RA, Rocks S, Dauchy F, Navarro A (2006) New advances in forming functional ceramics for micro devices. *Advances in Science and Technology* 45:2440–2447. doi:[10.4028/www.scientific.net/AST.45.2440](https://doi.org/10.4028/www.scientific.net/AST.45.2440)
13. Zakery A, Elliott SR (2007) Optical switching in Chalcogenide glasses. In: *Optical nonlinearities in chalcogenide glasses and their applications*. Springer, Berlin/Heidelberg, pp 129–150. doi:[10.1007/978-3-540-71068-4\\_6](https://doi.org/10.1007/978-3-540-71068-4_6)
14. Elliott SR (1977) A theory of ac conduction in chalcogenide glasses. *Philos Mag* 36(6):1291–1304. <http://dx.doi.org/10.1080/14786437708238517>
15. Eggleton BJ, Luther-Davies B, Richardson K (2011) Chalcogenide photonics. *Nat Photonics* 5(3):141–148. doi:[10.1038/nphoton.2011.309](https://doi.org/10.1038/nphoton.2011.309)
16. Klym H, Ingram A, Shpotyuk O (2016) Free-volume nanostructural transformation in crystallized  $\text{GeSe}_2\text{-Ga}_2\text{S}_3\text{-CsCl}$  glasses. *Mater Werkst* 47(2–3):198–202. doi:[10.1002/mawe.201600476](https://doi.org/10.1002/mawe.201600476)
17. Ren J, Wagner T, Bartos M, Frumar M, Oswald J, Kincl M, Frumarova B, Chen G (2011) Intense near-infrared and midinfrared luminescence from the  $\text{Dy}^{3+}$ -doped  $\text{GeSe}_2\text{-Ga}_2\text{Se}_3\text{-MI}$  (M= K, Cs, Ag) chalcogenide glasses at 1.32, 1.73, and 2.67  $\mu\text{m}$ . *J Appl Phys* 109(3):033105. <http://dx.doi.org/10.1063/1.3531555>
18. Calvez L, Lucas P, Rozé M, Ma HL, Lucas J, Zhang XH (2007) Influence of gallium and alkali halide addition on the optical and thermo-mechanical properties of  $\text{GeSe}_2\text{-Ga}_2\text{Se}_3$  glass. *Applied Physics A* 89(1):183–188. doi:[10.1007/s00339-007-4081-y](https://doi.org/10.1007/s00339-007-4081-y)
19. Arai H, Seiyama T (2008) Humidity sensors. In: *Sensors set: a comprehensive survey*. Wiley-VCH Verlag GmbH, Weinheim, pp 981–1012. doi:[10.1002/9783527619269.ch7b](https://doi.org/10.1002/9783527619269.ch7b)
20. Fraden J (2004) *Handbook of modern sensors: physics, designs, and applications*. Springer Science & Business Media, Cham
21. Klym H, Ingram A, Shpotyuk O, Calvez L, Petracovschi E, Kulyk B, Serkiz R, Szatanik R (2015) ‘Cold’ crystallization in nanostructured  $80\text{GeSe}_2\text{-}20\text{Ga}_2\text{Se}_3$  glass. *Nanoscale Res Lett* 10(1):1–8. doi:[10.1186/s11671-015-0775-9](https://doi.org/10.1186/s11671-015-0775-9)
22. Shpotyuk O, Calvez L, Petracovschi E, Klym H, Ingram A, Demchenko P (2014) Thermally-induced crystallization behaviour of  $80\text{GeSe}_2\text{-}20\text{Ga}_2\text{Se}_3$  glass as probed by combined X-ray diffraction and PAL spectroscopy. *J Alloys Compd* 582:323–327. <http://dx.doi.org/10.1016/j.jallcom.2013.07.127>
23. Shpotyuk O, Filipecki J, Ingram A, Golovchak R, Vakiv M, Klym H, Balitska V, Shpotyuk M, Kozdras A (2015) Positronics of subnanometer atomistic imperfections in solids as a high-informative structure characterization tool. *Nanoscale Res Lett* 10(1):1–5. doi:[10.1186/s11671-015-0764-z](https://doi.org/10.1186/s11671-015-0764-z)

24. Masselin P, Le Coq D, Calvez L, Petracovschi E, Lépine E, Bychkov E, Zhang X (2012) CsCl effect on the optical properties of the  $80\text{GeS}_2\text{-}20\text{Ga}_2\text{S}_3$  base glass. *Applied Physics A* 106(3):697–702. doi:[10.1007/s00339-011-6668-6](https://doi.org/10.1007/s00339-011-6668-6)
25. Klym H, Ingram A, Shpotyuk O, Karbovnyk I (2016) Influence of CsCl addition on the nanostructured voids and optical properties of  $80\text{GeS}_2\text{-}20\text{Ga}_2\text{S}_3$  glasses. *Opt Mater* 59:39–42. <http://dx.doi.org/10.1016/j.optmat.2016.03.004>
26. Klym H, Ingram A, Shpotyuk O, Hotra O, Popov AI (2016) Positron trapping defects in free-volume investigation of Ge-Ga-S-CsCl glasses. *Radiat Meas* 90:117–121. <http://dx.doi.org/10.1016/j.radmeas.2016.01.023>
27. Shpotyuk O, Balitska V, Brunner M, Hadzaman I, Klym H (2015) Thermally-induced electronic relaxation in structurally-modified  $\text{Cu}_{0.1}\text{Ni}_{0.8}\text{Co}_{0.2}\text{Mn}_{1.9}\text{O}_4$  spinel ceramics. *Phys B Condens Matter* 459:116–121. <http://dx.doi.org/10.1016/j.physb.2014.11.023>
28. Klym H, Hadzaman I, Shpotyuk O, Fu Q, Luo W, Deng J (2013) Integrated thick-film p-i-p+ structures based on spinel ceramics. *Solid State Phenom* 200:156–161. <http://www.scientific.net/SSP.200.156>
29. Klym H, Balitska V, Shpotyuk O, Hadzaman I (2014) Degradation transformation in spinel-type functional thick-film ceramic materials. *Microelectron Reliab* 54(12):2843–2848. <http://dx.doi.org/10.1016/j.microrel.2014.07.137>
30. Klym H, Hadzaman I, Ingram A, Shpotyuk O (2013) Multilayer thick-film structures based on spinel ceramics I. *Can J Phys* 92(7/8):822–826. doi:[10.1139/cjcp-2013-0597](https://doi.org/10.1139/cjcp-2013-0597)
31. Klym H, Hadzaman I, Shpotyuk O, Brunner M (2014) Integrated thick-film nanostructures based on spinel ceramics. *Nanoscale Res Lett* 9(1):1–6. doi:[10.1186/1556-276X-9-149](https://doi.org/10.1186/1556-276X-9-149)
32. Vakiv M, Hadzaman I, Klym H, Shpotyuk O, Brunner M (2011) Multifunctional thick-film structures based on spinel ceramics for environment sensors. *J Phys Conf Ser* 289(1):012011. <http://dx.doi.org/10.1088/1742-6596/289/1/012011>
33. Shpotyuk O, Brunner M, Hadzaman I, Balitska V, Klym H (2016) Analytical description of degradation-relaxation transformations in nanoinhomogeneous spinel ceramics. *Nanoscale Res Lett* 11(1):499. doi:[10.1186/s11671-016-1722-0](https://doi.org/10.1186/s11671-016-1722-0)
34. Klym H, Ingram A, Shpotyuk O, Hadzaman I, Hotra O, Kostiv Y (2016) Nanostructural free-volume effects in humidity-sensitive  $\text{MgO-Al}_2\text{O}_3$  ceramics for sensor applications. *J Mater Eng Perform* 25(3):866–873. doi:[10.1007/s11665-016-1931-9](https://doi.org/10.1007/s11665-016-1931-9)
35. Klym H, Ingram A, Shpotyuk O, Hadzaman I, Solntsev V (2016) Water-vapor sorption processes in nanoporous  $\text{MgO-Al}_2\text{O}_3$  ceramics: the PAL spectroscopy study. *Nanoscale Res Lett* 11(1):1. doi:[10.1186/s11671-016-1352-6](https://doi.org/10.1186/s11671-016-1352-6)
36. Klym H, Hadzaman I, Shpotyuk O (2015) Influence of sintering temperature on pore structure and electrical properties of technologically modified  $\text{MgO-Al}_2\text{O}_3$  ceramics. *Mater Sci* 21(1):92–95. <http://dx.doi.org/10.5755/j01.ms.21.1.5189>
37. Karbovnyk I, Bolesta I, Rovetskii I, Velgosh S, Klym H (2014) Studies of  $\text{CdI}_2\text{-Bi}_3$  microstructures with optical methods, atomic force microscopy and positron annihilation spectroscopy. *Materials Science-Poland* 32(3):391–395. doi:[10.2478/s13536-014-0215-z](https://doi.org/10.2478/s13536-014-0215-z)
38. Kansy J (1996) Microcomputer program for analysis of positron annihilation lifetime spectra. *Nucl Instrum Methods Phys Res, Sect A* 374(2):235–244. [http://dx.doi.org/10.1016/0168-9002\(96\)00075-7](http://dx.doi.org/10.1016/0168-9002(96)00075-7)
39. Klym H, Ingram A, Shpotyuk O, Filipecki J, Hadzaman I (2011) Structural studies of spinel manganite ceramics with positron annihilation lifetime spectroscopy. *J Phys Conf Ser* 289(1):012010. <http://iopscience.iop.org/article/10.1088/1742-6596/289/1/012010/meta>
40. Shpotyuk O, Filipecki J (2003) Free volume in vitreous chalcogenide semiconductors: possibilities of positron annihilation lifetime study. *Wyd-wo WSP w Czestochowie, Czestochowa*
41. Klym H, Ingram A (2007) Unified model of multichannel positron annihilation in nanoporous magnesium aluminate ceramics. *J Phys Conf Ser* 79(1):012014. <http://dx.doi.org/10.1088/1742-6596/79/1/012014>
42. Klym H, Karbovnyk I, Guidi MC, Hotra O, Popov AI (2016) Optical and vibrational spectra of CsCl-enriched  $\text{GeS}_2\text{-Ga}_2\text{S}_3$  glasses. *Nanoscale Res Lett* 11(1):1–6. doi:[10.1186/s11671-016-1350-8](https://doi.org/10.1186/s11671-016-1350-8)

43. Ingram A, Golovchak R, Kostrzewa M, Wacke S, Shpotyuk M, Shpotyuk O (2012) Compositional dependences of average positron lifetime in binary as-S/se glasses. *Phys B Condens Matter* 407(4):652–655. <http://dx.doi.org/10.1016/j.physb.2011.11.052>
44. Calvez L, Lin C, Rozé M, Ledemi Y, Guillevic E, Bureau B, Allix M, Zhang X (2010) Similar behaviors of sulfide and selenide-based chalcogenide glasses to form glass-ceramics. *Proc SPIE* 7598:759802-1-16. doi:10.1117/12.840968
45. Klym H, Ingram A, Shpotyuk O, Hadzaman I, Solntsev V, Hotra O, Popov AI (2016) Positron annihilation characterization of free volume in micro-and macro-modified  $\text{Cu}_{0.4}\text{Co}_{0.4}\text{Ni}_{0.4}\text{Mn}_{1.8}\text{O}_4$  ceramics. *Low Temperature Phys* 42(7):601–605. <http://dx.doi.org/10.1063/1.4959021>
46. Krause-Rehberg R, Leipner HS (1999) Positron annihilation in semiconductors. Defect studies. Springer, Berlin/Heidelberg/New York, p 378
47. Klym H, Ingram A, Shpotyuk O, Filipecki J (2010) PALS as characterization tool in application to humidity-sensitive electroceramics. 27th international conference on microelectronics proceedings (MIEL). Proceedings of the 27th International Conference, pp 239–242. doi:10.1109/MIEL.2010.5490492
48. Nambissan PMG, Upadhyay C, Verma HC (2003) Positron lifetime spectroscopic studies of nanocrystalline  $\text{ZnFe}_2\text{O}_4$ . *J Appl Phys* 93:6320. <http://dx.doi.org/10.1063/1.1569973>
49. Leifer I, Patro RK (2002) The bubble mechanism for methane transport from the shallow sea bed to the surface: a review and sensitivity study. *Cont Shelf Res* 22(16):2409–2428. [http://dx.doi.org/10.1016/S0278-4343\(02\)00065-1](http://dx.doi.org/10.1016/S0278-4343(02)00065-1)
50. Ljunggren S, Eriksson JC (1997) The lifetime of a colloid-sized gas bubble in water and the cause of the hydrophobic attraction. *Colloids Surf A Physicochem Eng Asp* 129:151–155. [http://dx.doi.org/10.1016/S0927-7757\(97\)00033-2](http://dx.doi.org/10.1016/S0927-7757(97)00033-2)
51. Grosman A, Ortega C (2005) Nature of capillary condensation and evaporation processes in ordered porous materials. *Langmuir* 21:10515–10521. doi:10.1021/la051030o
52. Tao SJ (1972) Positronium annihilation in molecular substance. *J Chem Phys* 56(11):5499–5510. <http://dx.doi.org/10.1063/1.1677067>
53. Eldrup M, Lightbody D, Sherwood JN (1981) The temperature dependence of positron lifetimes in solid pivalic acid. *Chem Phys* 63:51–58. [http://dx.doi.org/10.1016/0301-0104\(81\)80307-2](http://dx.doi.org/10.1016/0301-0104(81)80307-2)

**Part IV**  
**Nanochemistry and Biotechnology**

# Chapter 37

## Preparation of Nanocellulose from Organosolv Straw Pulp Using Acid Hydrolysis and Ultrasound

V. A. Barbash, O. V. Yaschenko, O. M. Shniruk, and V. O. Kovalchuk

### 37.1 Background

In recent years, there has been a significant increase in scientific research in the field of nanomaterials and nanotechnologies [1]. Nanocellulose is a group of nanomaterials that consists of the nanosized cellulose particles. Characteristics of nanocellulose particles depend on properties of plant raw materials and methods used in the production [2]. Nanocellulose from the renewable lignocellulose materials has improved mechanical properties, such as high surface area-to-volume ratio and high aspect ratio [3]. Nanocellulose often replaces well-known material such as glass and certain polymers, which are not biodegradable at ambient conditions, in order to create new specific nanocomposites, adsorbents, and functional materials for the electrodes in the chemical sources of power and optoelectronic devices [4–6], biodegradable plastics, and paper with special characteristics [7]. Nanocellulose finds its application in nanocomposites [8–11], to increase their strength and thermal resistance [12], to stabilize the emulsions [13], in the preparation of bio-basic films [14].

The raw material that is generally used for obtaining nanocellulose is wood bleached sulfate and sulfite pulp [15, 16]. Timber resources decrease every year and it takes a long time to renew them. In addition, there is competition between the industries, which use wood in large quantities (construction, furniture, pulp, and paper). Given these factors, there is a need to find alternative sources of pulp, for example, from non-wood plant raw materials. In world practice, there are methods of obtaining nanocellulose from kenaf [17], oat husk [18], coconut fibers [19], and

---

V.A. Barbash (✉) • O.V. Yaschenko • O.M. Shniruk • V.O. Kovalchuk  
National Technical University of Ukraine “Igor Sikorsky Kyiv Polytechnic Institute”, Peremogy  
Ave. 37, Kyiv, 03056, Ukraine  
e-mail: [v.barbash@kpi.ua](mailto:v.barbash@kpi.ua)

other cellulose-containing materials [20–22]. It formed fibers, during the processing of grain and industrial crops and plant, which can be used as an alternative for the wood pulp. Wheat straw can be attributed as a prospective representative of non-wood plant raw material for pulp, and it is produced in the vast volumes in countries with developed agriculture annually.

In the world pulp and paper industry, for pulp production the technologies of sulfate and sulfite pulping and bleaching using chlorine and sulfur compounds are dominant. Increased environmental requirements to the quality of wastewater and gas emissions of the industrial enterprises require the development of new technologies for the processing of plant raw materials with the use of organic solvents [23, 24].

Previously we have demonstrated the possibility of obtaining straw pulp by organosolv method with delignification in the system isobutyl alcohol–H<sub>2</sub>O–KOH–hydrazine, which has the possibility of reuse of the organic component in the pulping liquor without regeneration [25]. Thus, the spent cooking liquor is divided into two layers: an upper organic solvent layer and a lower aqueous layer, which has moved in the bulk of soluble minerals and organic substances from plant raw materials (lignin, hemicelluloses, and extractives). The use of potassium and nitrogen compounds in the pulping liquor allows the use of black liquor in the manufacture of fertilizers [25].

Previously, in an article [26] we have obtained nanofibrillated cellulose (NFC) from the air-dry bleached softwood sulfate pulp using the mechanochemical treatment. This treatment performed with the use of a standard for the pulp and paper industry milling equipment. In the present study, to reduce the energy consumption, preparation of NFC from wet after cooking and bleaching organosolv straw pulp (OSP) with using of only sulfuric acid hydrolysis and ultrasound treatment as an effective chemo-mechanical process were investigated.

## 37.2 Methods

In order to obtain pulp, stalks of wheat straw from Kiev region harvested in 2015 were used. Average chemical composition related to absolutely dry raw material (a.d.r.m.) was 46.2% cellulose; 20.2% lignin; 25.2% pentosans; 6.6% ash; 5.2% resins, fats, and waxes; and 74.1% holocellulose. Values of chemical composition in wheat straw stalks according to standard methods were identified [27]. The raw plant material reduced in size to 2–5 mm and stored in desiccator for maintaining constant humidity and chemical composition.

Cooking of straw stalks in the system isobutyl alcohol–H<sub>2</sub>O–KOH–hydrazine was carried out according to the procedure described in [25]. Received organosolv pulp had the following quality indicators: yield of pulp, 49%; residual lignin, 1.1%; ash, 1.63%; pentosans, 0.93% to a.d.r.m.; and whiteness, 51%.

In order to bleaching and remove residual lignin, hemicellulose and minerals from OSP, the thermochemical treatment of OSP with acetic acid and hydrogen

peroxide in a volume ratio of 70:30% with the catalyst – the sulfuric acid 15% to mass a.d.r.m. – was carried out. Treatment with a mixture was carried out at a temperature of  $95 \pm 2$  °C and duration was 180 min. Received bleached OSP has ash content of 0.2%, lignin less than 0.2%, degree of polymerization 400, and whiteness 83% and was used for preparation of nanocellulose.

Hydrolysis of the bleached OSP by sulfuric acid with concentration of 43% at the liquid-to-solid ratio 10:1 at temperature  $60 \pm 1$  °C within 30 min was carried out. The hydrolyzed cellulose washed three times by the centrifugation at 8000 rev/min and subsequent dialysis until reaching neutral pH. Ultrasound treatment of hydrolyzed cellulose was performed using ultrasound disintegrator UZDN-A (SELMI, Ukraine) with 22kGz at 30–60 min. The cellulose dispersion was placed in an ice bath to prevent overheating during treatment. Eventually, the suspension had taken the form of a homogenous gel-like dispersion.

The prepared dispersions were poured into Petri dishes and dried at room temperature in air to obtain nanocellulose films. Their density was determined according to the ISO 534:1988. The degree of polymerization by the viscosity of the samples dissolved in copper ethylenediamine solution according to ISO 5351 was determined.

Scanning electron microscope (SEM) analyses were performed with a PEM-106I (SELMI, Ukraine) microscope to observe the morphology of OSP and NFC films. Transmission electron microscopy (TEM) images were obtained using electron microscope TEM125K (SELMI, Ukraine) operating at a potential of 100 kV. A dilute suspension (0.1 wt.%) was dropped onto a thin scaffoldings Lacey Formvar/Carbon, 400 mesh, copper approx. grid hole size 42  $\mu\text{m}$  (TED PELLA, Inc., USA). Electron absorption spectra of the nanocellulose films in UV, visible, and near-infrared regions were registered on two-beam spectrophotometer 4802 (UNICO, USA) with resolution of 1 nm. X-ray diffraction patterns of the different cellulose samples were obtained by Ultima IV diffractometer (Rigaku, Japan). The method proposed in [28] was used to determine the crystallinity degree (CD) of the samples, in which  $\text{CD} = (I_{200} - I_{\text{am}})/I_{200} \times 100\%$ , where  $I_{200}$  is an intensity of (200) reflex about 23° and  $I_{\text{am}}$  intensity of amorphous scattering at 18.5°.

The thermal degradation behavior of OSP and NFC film samples by heating using Netzsch STA-409 thermoanalyzer was explored. The samples at a rate of 5 °C/min, from 25 to 450 °C, were heated.

### 37.3 Results and Discussion

Morphology of bleached OSP and obtained therefrom nanocellulose films by SEM was studied. Figure 37.1 presents electron micrographs of the surface of the initial organosolvent straw pulp and after hydrolysis and sonication.

As shown in Fig. 37.1, the length of the fibers of initial OSP is more than 100  $\mu\text{m}$  and width from 10 to 20  $\mu\text{m}$  (Fig. 37.1a). Hydrolysis of the bleached OSP leads to a significant decrease in the length and diameter of its fibers (Fig. 37.1b), and



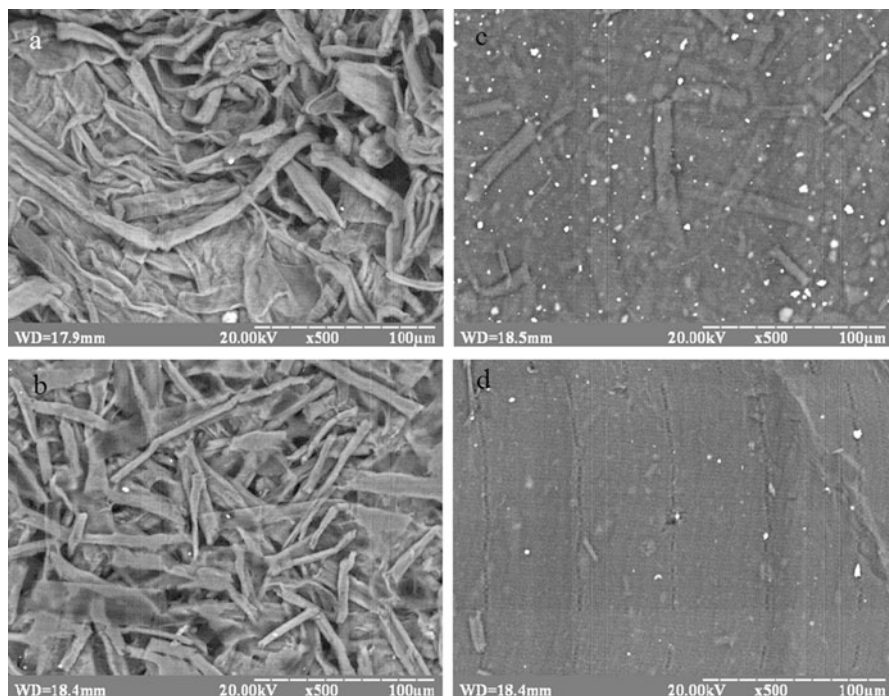


**Fig. 37.1** SEM image of organosolv straw pulp: the initial (a), after hydrolysis (b) after sonication (c), and after hydrolysis and sonication (d)

sonication of hydrolyzed cellulose significantly reduces the length of the fibers to 50  $\mu\text{m}$ . As can we see from Fig. 37.1c, the ultrasound treatment of OSP forms a film with a dense structure. Further sonication of blending pulp slurry contributes to formation of transparent films with homogeneous structure (Fig. 37.1d). These results indicate that the chemical treatment and sonication of organosolv straw pulp lead to the formation of homogeneous nanocellulose films with high transparency up to 60%.

Reducing of OSP fiber size by sequential acid treatment and sonication confirmed by a decrease in the degree of polymerization of OSP (Fig. 37.2).

As can be seen from Fig. 37.2, sonication of organosolv pulp acts more intensely on reducing the degree of polymerization of cellulose and hence on the dimensions of the fibers, compared with the hydrolysis, and the joint action of sulfuric acid and sonication leads to a substantial reduction of the size of the cellulose macromolecules.

Next, the morphology of the nanocellulose samples, in order to assess the changes in the particle size induced by hydrolysis and sonication, using TEM, was examined (Fig. 37.3). As can be seen from Fig. 37.3, organosolv straw nanocellulose obtained in the hydrolysis with sulfuric acid and sonication is nanofibrillated cellulose (NFC) with a multilayer structure. Nanofibers form a delicate mesh as

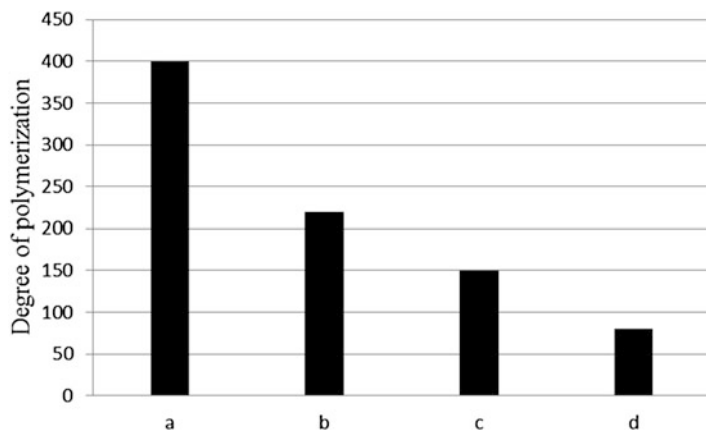


**Fig. 37.2** The dependence of the degree of polymerization of organosolv straw pulp from the processing stages: the initial pulp (a), after hydrolysis (b), after sonication (c), and after hydrolysis and sonication (d)

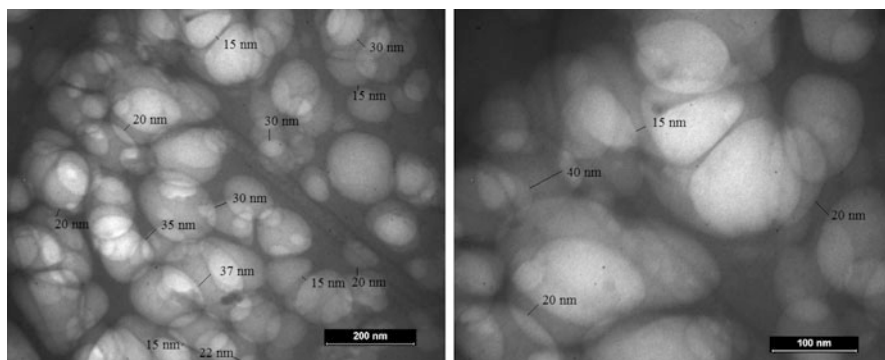


**Fig. 37.3** TEM pictures of organosolv straw nanocellulose suspension at different magnification

a result of interaction between the particles of nanocellulose. In addition, it was experimentally found that the diameters of the individual particles of nanocellulose are in the range from 20 to 40 nm, and their lengths are up to several micrometers. This result confirmed the data of dimensions of NFC obtained by mechanochemical method for bleached softwood sulfate pulp [26].

We have also investigated the change in the ratio of amorphous and crystalline parts of OSP during its chemical and physical treatments. The analysis of X-ray diffraction patterns was carried out (Fig. 37.4), and the degree of crystallinity of the initial OSP and cellulose after the hydrolysis and after the sonication was defined. The crystallinity degree of bleached OSP is significantly reduced during the sonication from 72.5% to 57.8%, due to the partial destruction of crystalline macromolecules areas under the high energy of ultrasound. At the same time,

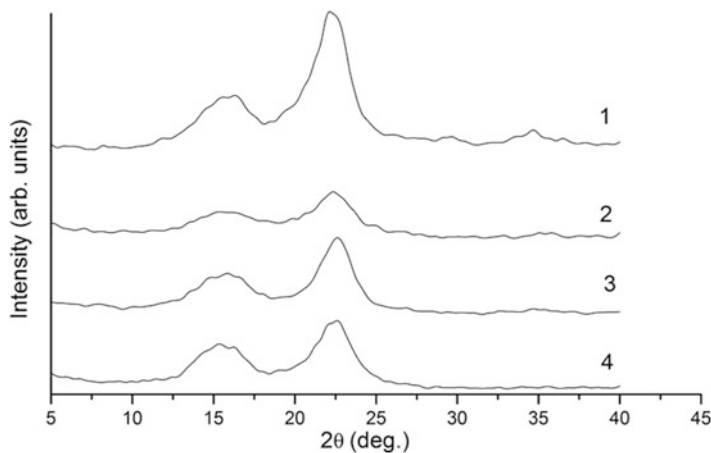


**Fig. 37.4** X-ray diffraction patterns of organosolv straw pulp: the initial (1), after sonication (2), and after hydrolysis (3), after hydrolysis and sonication (4)

hydrolysis of initial OSP increases the crystallinity to 76.3% due to the removal of amorphous parts of the cellulose. The additional sonication after hydrolysis leads to a partial degradation of crystalline parts of macromolecules and to a slight decrease in the crystallinity degree of nanocellulose to 72.2%.

The results of thermogravimetric analysis (TGA) of OSP and nanocellulose films (Fig. 37.5) confirm the fact that treatment of the initial OSP by acid hydrolysis and ultrasound an increase its crystallinity degree.

Figure 37.5 shows the change of the thermal stability of the OSP samples after the first stage of pulping in isobutanol (1), after the second stage of thermos-chemical treatment in mixture of peracetic acid (2), and nanocellulose films after hydrolysis with 43% sulfuric acid and sonication (3). As seen from the thermogravimetric curves (Fig. 37.5), for all OSP samples, weight loss begins at a temperature about 80 °C, which is due to the evaporation of residual moisture from the fibers. The main weight loss after the first stage of pulping in thermal degradation begins at temperatures between 220 and 240 °C and continues up to 300 °C. Sample (2) is characterized with weight loss about 60% in temperature ranging 220–260 °C and continues up to 400 °C as the second stage of pumping with elements of hydrolysis increases the amount of crystalline part of cellulose, and it is the reinforcing of hydrogen bonds between cellulose macromolecules. Destruction of nanocellulose films (curve 3) has a different way. Loss of 10% of nanocellulose film is at a temperature of 160 °C and at 240 °C – another 10% losses. For nanocellulose films, abrupt weight loss in temperature ranging 220–260 °C is not typical, and it happens gradually to 400 °C. This can be explained by the formation of dense structure between pulp molecules during the chemical treatment and sonication by increasing the share of crystallinity of the cellulose.

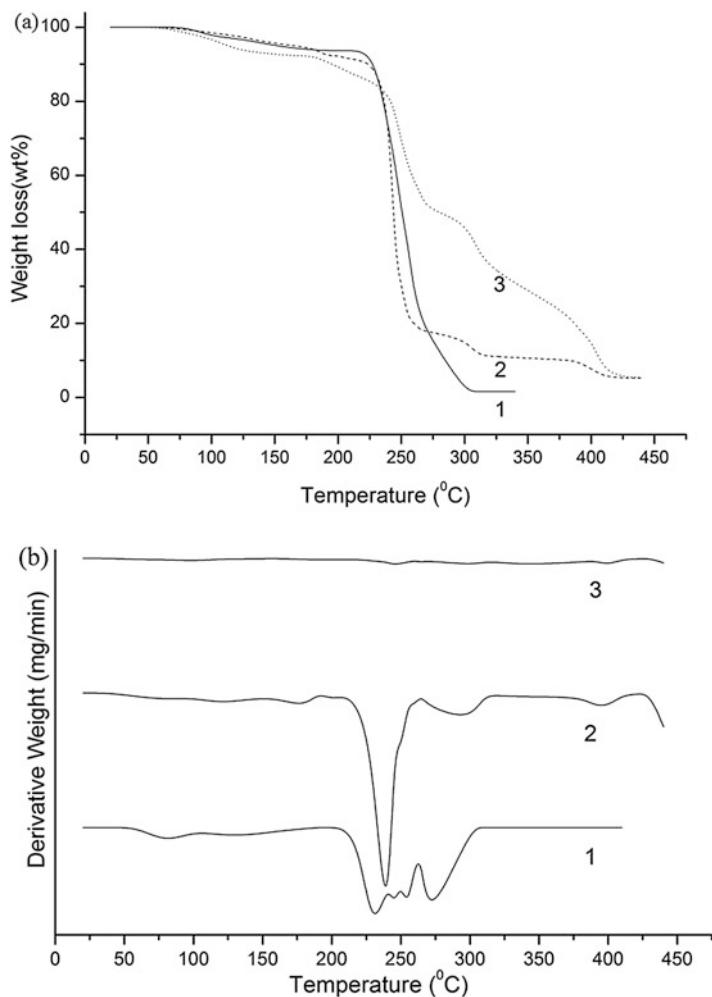


**Fig. 37.5** Gravimetric (a) and differential thermal (b) analysis curves: pulp after the first stage of pulping in isobutanol (1), pulp after the second stage of thermochemical treatment in mixture of peracetic acid (2), and nanocellulose films (3)

## 37.4 Conclusions

In the present study, organosolv pulp and nanocellulose from the wheat straw were obtained. It has been proved that delignification in isobutanol system is effective in the removal of lignin and hemicelluloses components. Organosolv pulping allows obtaining straw pulp with low lignin and mineral content. Subsequent processes of hydrolysis with sulfuric acid and sonication lead to the formation of nanofibrillated straw cellulose. The structural change and crystallinity degree of OSP and NFC were

studied by the SEM and XRD techniques. It has been established that NFS has a density up to  $1.3 \text{ g/cm}^3$ , transparency up to 60%, and crystallinity up to 72.2%. The TEM showed that NFC forms the mesh with diameter of fiber in the range from 20 to 40 nm. The method of thermogravimetric analysis confirmed that NFC films have more dense structure and smaller mass loss in temperature ranging  $220\text{--}260^\circ \text{C}$  compared with OSP.

## References

1. Szczęsna-Antczak M, Kazimierczak J, Antczak T (2012) Nanotechnology – methods of manufacturing cellulose nanofibres. *Fibres Text East Eur* 20: 2(91):8–12
2. Klemm D, Kramer F, Moritz S, Lindström T, Ankerfors M, Gray D, Dorris A (2011) Nanocellulose: a new family of nature-based materials. *Angew Chem Int Ed* 50:5438–5466
3. Liu S, Liu Y-J, Deng F, Ma M-G, Bian J (2015) Comparison of the effects of microcrystalline cellulose and cellulose nanocrystals on  $\text{Fe}_3\text{O}_4/\text{C}$  nanocomposites. *RSC Adv* 5:74198–74205
4. Thiemann S, Sachnov SJ, Pettersson F, Bollström R, Österbacka R, Wasserscheid P, Zaumseil J (2014) Cellulose-based ionogels for paper electronics. *Adv Funct Mater* 24:625–634
5. Gao K, Shao Z, Li J, Wang X, Peng X, Wang W, Wang F (2013) Cellulose nanofiber–graphene all solid-state flexible supercapacitors. *J Mater Chem A* 1:63–67
6. Burrs SL, Bhargava M, Sidhu R, Kiernan-Lewis J, Gomes C, Claussen JC, McLamore ES (2016) A paper based graphene-nanocauliflower hybrid composite for point of care biosensing. *Biosens Bioelectron* 85:479–487
7. Majoinen J, Kontturi E, Ikkala O, Gray DG (2012) SEM imaging of chiral nematic films cast from cellulose nanocrystal suspensions. *Cellulose* 19:1599–1605
8. Lavoine N, Desloges I, Dufresne A, Bras J (2012) Microfibrillated cellulose – Its barrier properties and applications in cellulosic materials: A review. *Carbohydr Polym* 90:735–764
9. Pillai KV, Rennecker S (2016) Dynamic mechanical analysis of layer-by-layer cellulose nanocomposites. *Ind Crop Prod* 93:267–275
10. Robles E, Czubak E, Kowaluk G, Labidi J (2016) Lignocellulosic-based multilayer self-bonded composites with modified cellulose nanoparticles. *Compos Part B* 106:300–307
11. Le D, Kongparakul S, Samart C, Phanthong P, Karnjanakom S, Abudula A, Guan G (2016) Preparing hydrophobic nanocellulose-silica film by a facile one-pot method. *Carbohydr Polym* 153:266–274
12. Rowe A, Tajvidi M, Gardner D (2016) Thermal stability of cellulose nanomaterials and their composites with polyvinyl alcohol (PVA). *J Therm Anal Calorim* 126(3):1371–1386
13. Mikulcová V, Bordes R, Kašpárková V (2016) On the preparation and antibacterial activity of emulsions stabilized with nanocellulose particles. *Food Hydrocoll* 61:780–792
14. Santucci BS, Bras J, Belgacem MN, Curvelo AADS, Pimenta MTB (2016) Evaluation of the effects of chemical composition and refining treatments on the properties of microfibrillated cellulose films from sugarcane bagasse. *Ind Crop Prod* 9:238–248
15. Potulski DC (2016) Characterization of fibrillated cellulose nanofilms obtained at different consistencies. *Forest Sci* 44(110):361–372
16. Dai L, Long Z, Lv Y, Feng Q-C (2014) The role of formic acid pretreatment in improving the carboxyl content of TEMPO-oxidized cellulose. *Cellul Chem Technol* 48(5–6):469–475
17. Kim D-Y, Lee B-M, Koo DH, Kang P-H, Jeun J-P (2016) Preparation of nanocellulose from a kenaf core using E-beam irradiation and acid hydrolysis. *Cellulose* 23(5):3039–3049
18. Qazanfarzadeh Z, Kadivar M (2016) Properties of whey protein isolate nanocomposite films reinforced with nanocellulose isolated from oat husk. *Int J Biol Macromol* 91:1134–1140
19. Machado BAS, Reis JHO, da Silva JB, Cruz LS, Nunes IL, Pereira FV, Janice ID (2014) Obtaining nanocellulose from green coconut fibers and incorporation in biodegradable films of starch plasticized with glycerol. *Quím Nova* 37(8):1275–1282

20. Travalini A, Prestes E, Pinheiro L, Demiate I (2016) High crystallinity nanocellulose extracted from cassava bagasse fiber. *O Papel* 77(1):73–80
21. Bansal M, Chauhan GS, Kaushik A, Sharma A (2016) Extraction and functionalization of bagasse cellulose nanofibres to Schiff-base based antimicrobial membranes. *Int J Biol Macromol* 91:887–894
22. Kunaver M, Anžlovar A, Žagar E (2016) The fast and effective isolation of nanocellulose from selected cellulosic feedstocks. *Carbohydr Polym* 148:251–258
23. Saberikhan E, Rovshandeh JM, Rezayati-Charani P (2011) Organosolv pulping of wheat straw by glycerol. *Cellul Chem Technol* 45(1–2):67–75
24. Correia VC, dos Santos V, Sain M, Santos SF, Leão AL, Savastano JH (2016) Grinding process for the production of nanofibrillated cellulose based on unbleached and bleached bamboo organosolv pulp. *Cellulose* 23:2971–2987
25. Barbash V, Yashchenko O (2015) Obtaining a straw pulp in the isobutanol medium. *Res Bull NTUU “KPI”* 6(104):80–86
26. Barbash VA, Yaschenko OV, Alushkin SV, Kondratyuk AS, Posudievsky OY, Koshechko VG (2016) The Effect of Mechanochemical Treatment of the Cellulose on Characteristics of Nanocellulose Films. *Nanoscale Res Lett* 11:410
27. TAPPI (2004) *Test Methods*. Tappi Press, Atlanta, Georgia
28. Costa LA, Fonseca AF, Pereira FV, Druzian JI (2015) Extraction and characterization of cellulose nanocrystals from corn stover. *Cellul Chem Technol* 49:127–133

# Chapter 38

## Nanoscale Oxide PEO Coatings Forming from Diphosphate Electrolytes

Nikolay D. Sakhnenko, Maryna V. Ved, and Ann V. Karakurkchi

The widespread use of aluminum, titanium, and alloys in various industries (air and mechanical engineering, medicine, chemical industry) and innovative technologies puts forward a number of requirements for their corrosion resistance, mechanical strength, tribological characteristics, catalytic activity, and others.

Environmental and technical problems arising in the operation of internal combustion engines (ICEs) are associated with the incomplete combustion of fuel and, accordingly, the inevitable formation of toxic components, such as CO, NO<sub>x</sub>, and soot [1]. One of the possible ways to improve the performance of ICEs can be the use of catalysis in situ in the combustion chamber [2]. Since catalytic processes are characterized by a decrease in the activation energies of intermediate stages, the combustion process and the fuel combustion completeness occur at lower temperatures (650–1200 K); this feature must lead to a decrease in the maximum pressure in the combustion chamber and, hence, in the severity of engine operation and to the minimization of emissions of hazardous substances with exhaust gases.

The currently available hydrocarbon fuel combustion catalysts are divided into two groups: catalysts based on noble metals (most commonly Pd and Pt) and transition metal oxides (Mn, Co, Fe, etc.), particularly those with a complex composition (spinel, perovskite, hexa-aluminates) [3]. At high temperatures, significant advantages are shown by a family of catalysts based on manganese oxides, which exhibit high thermal stability and oxygen affinity [4]. The formation of high-temperature manganese oxides not only provides the thermal stability of the catalysts but also leads to a significant improvement of the catalyst reactivity.

---

N.D. Sakhnenko (✉) • M.V. Ved • A.V. Karakurkchi  
National Technical University “Kharkiv Polytechnic Institute”, 21, Frunze Str, Kharkiv, 61002,  
Ukraine  
e-mail: [anyutikukr@gmail.com](mailto:anyutikukr@gmail.com)

In terms of rational designing and effective technology, it seems appropriate to deposit a catalytic layer directly on the surface of ICE pistons manufactured using AK12M2MgN cast complex-alloyed silumins with an optimal combination of physico-mechanical and performance properties [5]. The most promising method for the formation of thin layers on passive metal surfaces, in particular, silumins, is plasma electrolytic oxidation (PEO). This method provides the incorporation of catalytically active components into an alumina matrix owing to the implementation of both electrochemical and thermochemical reactions in high-energy modes [6, 7]. However, it should be taken into account that the PEO of silumins is complicated because these materials contain a large number of alloying components and intermetallic compounds with different chemical properties of oxides. On the basis of the above, the main task that has predetermined the aim of this study is to substantiate the electrolyte composition and the PEO modes for the formation of a mixed oxide layer with high manganese and cobalt content on the surface of the AK12M2MgN alloy.

Titanium and its alloys are justly referred to the most popular construction materials that are diversely used due to their physicochemical and operational characteristics. However, there are several factors limiting the applicability of these materials: in particular, their poor sliding properties entail problems when titanium alloys are used in friction pairs or high chemical reactivity arises from welding operations. Many problems, however, can be effectively solved due to the surface modification. From this perspective, the most rational approach seems to be based on galvanochemical technologies, including covering the surface with coatings of various compositions for different purposes. When it concerns valve metals, the most appropriate coatings seem to be conversion and composite ones [8, 9]. They are important to consider not only because they are able to diversify the functional properties of products but also because they increase the reliability and service life under operating conditions [10, 11].

It is much interesting to consider studies that are aimed at improving the technologies of producing oxide coatings. However, a vast majority of traditional methods cannot provide sufficiently strong adhesion, wear resistance, and corrosion resistance combined with a certain set of properties that provide for the functional purposes of materials and products. The method of plasma electrolytic oxidation (PEO), which is also called microarc or anode spark oxidation, allows creating strong adhesion to the substrate of oxide coatings that have dielectric [12], protective [13], catalytic, antifriction [14], antiseptic [15], and other properties [16, 17].

A distinctive feature of the PEO method is the possibility to form conversion layers that incorporate both oxides of a refined metal and electrolyte components or products of their electrochemical and thermochemical transformations. The chemical composition of the coatings formed by PEO determines the nature of the oxidizable metal, the process parameters, and the electrolyte components, so that controlling the chemical composition of anode layers can significantly improve their physical and chemical properties [9, 18] as well as significantly expand the functional uses of valve metals and alloys with them.



The relevance of the work in this direction is due to the present lack of effective solutions that would allow combining the advantages of titanium-based alloys as promising carriers and the catalytic activity of manganese oxides in O–O bond cleavage reactions while ensuring strong adhesion to the substrate. It is especially important in this case to carry out the oxidation process in a single step, eliminating the thermochemical reaction of nitrates decomposition that would release toxic nitrogen oxides.

### 38.1 Experimental

The studies were conducted using A99 aluminum and AK12M2MgN (AL25) alloy samples with a working surface of  $0.5 \text{ cm}^2$  (Table 38.1). The surface preparation included sequential procedures of mechanical grinding, etching in an alkaline solution, thorough washing with distilled water, and drying. Electrolyte solutions for the pretreatment and PEO were prepared from certified reagent-grade reactants and distilled water.

The composition of titanium VT1-0 alloy in wt.% was as follows: Ti = 99.2–99.7, Fe < 0.25, C < 0.07, Si < 0.1, N < 0.04, O < 0.2, and impurities – 0.3. The pretreatment of the samples included mechanical cleaning from the process contaminants, degreasing in a 0.2–0.3 M NaOH, etching in a mixture of a 0.1–0.3 M HF and 0.3–0.9 M HNO<sub>3</sub>, and rinsing with distilled water.

Coatings were formed in an electrolyte based on potassium diphosphate with MnSO<sub>4</sub> and KMnO<sub>4</sub> as additives (Table 38.2). The pretreatment solutions and the oxidation diphosphate electrolytes in the concentration of 0.1–1.0 mol/dm<sup>3</sup> were prepared from certified reagents graded as “chemically pure” and “analytical grade” with distilled water.

The anodic behavior of aluminum alloys in solutions of different compositions was studied by linear voltammetry at different polarization rates using an IPC Pro-M potentiostat. Polarization measurements were conducted in a standard thermostatic electrochemical cell at a temperature of  $20 \pm 1 \text{ }^\circ\text{C}$  using a cathode of Kh18N10T stainless steel. The working electrolytes based on aqueous solutions of sodium hydroxide or potassium diphosphate with a concentration of 0.005–1.0 mol·dm<sup>-3</sup>

**Table 38.1** Content of alloying elements in the aluminum alloys (wt %)

Alloy grade	Si	Cu	Ni	Mg	Mn	Fe	Zn	Ti	Other elements
A99	0.5	–	–	–	–	0.5	–	–	–
AK12M2MgN	11.0–13.0	1.5–3.0	0.8–1.3	0.8–1.3	0.3–0.6	<0.8	<0.5	<0.2	Pb < 0.1 Sn < 0.02 Cr < 0.2

**Table 38.2** The composition of the titanium PEO electrolytes

Component	Component concentration, mol·dm <sup>-3</sup>				
	1	2	3	4	5
K <sub>4</sub> P <sub>2</sub> O <sub>7</sub>	1.0	1.0	1.0	1.0	1.0
KMnO <sub>4</sub>	–	0.1	0.3	–	–
MnSO <sub>4</sub>	–	–	–	0.1	0.3
pH of the solution	9.15	9.0	9.0	8.65	9.0

were admixed with potassium permanganate in a concentration range of 0.05–0.20 mol·dm<sup>-3</sup>; the pH value was 10–12. The electrode potentials were measured with respect to an EVL-1M1 silver–silver chloride reference electrode connected to the working cell through a salt bridge filled with a saturated solution of potassium nitrate thickened with agar-agar. The potentials given in this study were converted with respect to a normal hydrogen electrode (NHE).

The PEO of AK12M2MgN and VT1-0 alloy was conducted using a B5-50 stabilized power supply that maintained voltage up to 300 V. PEO was implemented in an electrolytic cell under conditions of forced cooling of the electrolyte to a temperature of 25–30 °C and stirring the electrolyte. A current density varied in a range of 5–25 A·dm<sup>-2</sup> for AK12M2MgN and 1–5 A·dm<sup>-2</sup> for VT1-0, and the processing time was 30–60 min. Since the kinetics of the plasma electrolytic oxidation of metals can very significantly depending on the acidity of the electrolyte, an important element of the process was monitoring of the electrolytes pH.

The chemical composition of the coatings was determined by X-ray photoelectron spectroscopy on an INCA Energy 350 energy-dispersive spectrometer; X-ray radiation was excited via exposing the samples to a 15 keV electron beam. In addition, X-ray fluorescence analysis was conducted using a SPRUT portable spectrometer with a relative standard deviation of 10<sup>-3</sup>–10<sup>-2</sup>; the error in determining the component content was ±1 wt %. The surface morphology of the coatings was studied using a Zeiss EVO 40XVP scanning electron microscope (SEM). Images were recorded by the registration of secondary electrons (BSEs) via scanning with an electron beam; this mode made it possible to study the topography with a high resolution and contrast ratio.

The surface morphology of coatings was studied by an atomic force microscopy AFM using NT-206 microscope. The tapping mode was conducted to measure sample surface morphology. Scanning was performed by using the contact probe CSC-37 (lateral and vertical resolutions 2 and 0.2 nm, respectively; 1024 × 1024 scanning matrix, CSC cantilever B as probe, probe tip radius 10 nm).

The phase composition and the structure of the synthesized oxide coatings were analyzed, using the X-ray diffractometer DRON-2.0 in the emission of an iron anode. The diffraction patterns were recorded in a discrete time interval of 0.1° at exposure of 15–20 s in each point. The elemental composition of the coatings was determined by the X-ray fluorescence method with the use of a portable X-ray spectrometer, which was the universal technical fluorescent device “SPRUT,” with the relative standard deviation of 10<sup>-3</sup>–10<sup>-2</sup>.

The catalytic properties of the oxide systems were studied in the oxidation of carbon (II) oxide to carbon (IV) oxide [19]. The studies were conducted on a laboratory bench in a tubular flow reactor made of silica glass with a coaxially wound heating coil. The initial mixture of air and carbon (II) oxide with a concentration of 1.0 vol % was fed to a reactor with a volume of  $1.5 \times 10^{-2} \text{ dm}^3$  at a rate of  $1.5 \text{ dm}^3 \cdot \text{h}^{-1}$ . The reactor temperature was gradually increased from 20 to 450 °C at a rate of  $1 \text{ °C} \cdot \text{s}^{-1}$ . The CO concentration at the inlet and outlet of the reactor was recorded using Dozor signaling–analyzing devices. The catalytic activity was evaluated by the following parameters: the initial temperature of the oxidation process (the ignition temperature,  $T_i$ ) and the conversion extent ( $X$ , %). The extent of conversion was calculated by the following equation:

$$X = \frac{c(\text{CO})_i - c(\text{CO})_f}{c(\text{CO})_i} \cdot 100\%,$$

where  $c(\text{CO})_i$  and  $c(\text{CO})_f$  are the initial and the final concentrations of carbon (II) oxide, %.

The abrasion rate for the materials  $\Delta l / \Delta t$  was determined by the Calotte method on the calotester [20].

### 38.1.1 Aluminum Alloy

The efficiency of the anodic oxidation of aluminum alloys containing transition metals or intermetallic compounds Al–Cu–Ni and Al–Cu–Mn–Fe, in particular, AK12M2MgN, depends on the ratio between the electrical resistivity of oxides of the base metal and the alloying components [21]. Under conditions of formation of local temperature gradients during PEO, the thermal resistance and temperature dependence of the electrical conductivity of the oxides become of special significance; close values of quantitative indicators of these properties guarantee a uniform distribution of the components in the bulk and on the surface of the oxide matrix and the reproducibility of the results. However, the anodic oxidation of the multicomponent AK12M2MgN alloy is accompanied by the formation of oxides that exhibit not only different conductivity [22, 23] but also differentiated thermal stability (Table 38.3); this feature considerably limits the possibility of forming high-quality coatings of a specified composition.

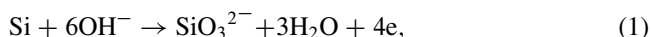
The main components of the AK12M2MgN alloy – aluminum and silicon – form thermally resistant oxides; however, the conductivity of these materials at high temperatures that occur in the zone of spark discharges sharply increases (see Table 38.3). At the same time, at high temperatures, oxides of the alloying components (Cu, Ni, Mn, Fe) undergo decomposition to evolve oxygen and form either a metal phase (Cu, Ni, Fe) or mixed-valence oxides exhibiting low resistivity (see Table 38.3). These factors lead to the heteroresistance of the treated surface and a decrease in the duration of thermochemical reactions involving the electrolyte

**Table 38.3** Characteristics of alloying metal oxides in AK12M2MgN

Metal	Oxide	Electrical resistivity ( $\Omega \cdot \text{cm}$ ) at $T$ (K)		Thermal resistance
		293	1873	
Al	$\text{Al}_2\text{O}_3$	$3 \cdot 10^{14}$	10–20	–
Si	$\text{SiO}_2$	$10^{16}$	0.9	–
Cu	$\text{CuO}$	$10^5$		1324–1398 K $4\text{CuO} \rightarrow 2\text{Cu}_2\text{O} + \text{O}_2$
	$\text{Cu}_2\text{O}$	$1 \cdot 10^4$ – $3 \cdot 10^4$		2098 K $2\text{Cu}_2\text{O} \rightarrow 4\text{Cu} + \text{O}_2$
Mg	$\text{MgO}$	$10^{14}$		–
Mn	$\text{MnO}$	$10^9$ – $10^{12}$		–
	$\text{Mn}_2\text{O}_3$	$10^5$		1238–1388 K $6\text{Mn}_2\text{O}_3 \rightarrow 4\text{Mn}_3\text{O}_4 + \text{O}_2$
	$\text{Mn}_3\text{O}_4$	$10^4$ – $10^5$		1858 K $2\text{Mn}_3\text{O}_4 \rightarrow 6\text{MnO} + \text{O}_2$
	$\text{MnO}_2$	$10^{-1}$ – $2.8 \cdot 10^{-3}$		828–883 K $4\text{MnO}_2 \rightarrow 2\text{Mn}_2\text{O}_3 + \text{O}_2$
Fe	$\text{FeO}$	$10^5$ – $10^8$		858–998 K $4\text{FeO} \rightarrow \text{Fe}_3\text{O}_4 + \text{Fe}$
	$\text{Fe}_2\text{O}_3$	$10^5$ – $10^8$		1498–1688 K $6\text{Fe}_2\text{O}_3 \rightarrow 4\text{Fe}_3\text{O}_4 + \text{O}_2$
	$\text{Fe}_3\text{O}_4$	$4 \cdot 10^{-3}$		>1835 K $2\text{Fe}_3\text{O}_4 \rightarrow 6\text{FeO} + \text{O}_2$
Ni	$\text{NiO}$	$10^{13}$ – $10^{15}$		>1528 K $2\text{NiO} \rightarrow 2\text{Ni} + \text{O}_2$
Zn	$\text{ZnO}$	$(6\text{--}9) \cdot 10^4$		–

components in the sparking zones. Under these conditions, the resulting PEO coatings have a thickness of no more than 10–20  $\mu\text{m}$  and contain a low amount of dopants. An increase in the coating thickness or in the concentration of the catalytically active component in the matrix of the basic oxide can be provided by surface homogenization. It is convenient to represent this procedure in the form of a scheme (Fig. 38.1) which takes into account the simultaneous occurrence of two processes, i.e., the formation of oxide of the basic component of the alloy ( $\text{Al}$ )<sub>S</sub> and the oxidation of intermetallic compounds ( $\text{Si}$ ,  $\text{CuAl}_2$ )<sub>S</sub> and the alloying components of the alloy ( $\text{Fe}$ ,  $\text{Cu}$ ,  $\text{Ni}$ ) to form soluble anions and complexes.

The ability of silicon to undergo oxidation in an alkaline medium during anodic polarization in a potential range of – 0.3 to 0.0 V [25, 26] does not give rise to doubt, formation of oxide films on the metal surface through the following chemical reaction:



whereas the formation of soluble iron and manganese oxo-anions in which transition metals exhibit the highest degree of oxidation is hindered; for copper and nickel,

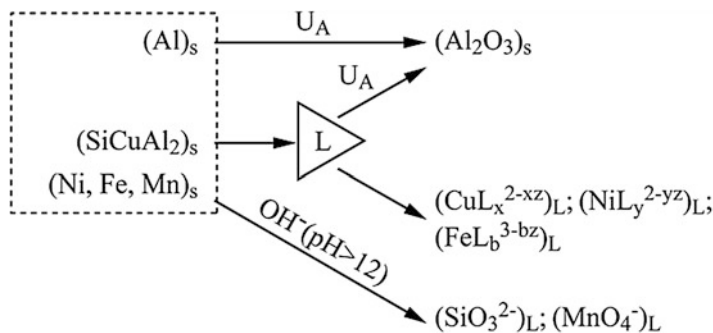


**Fig. 38.1** Scheme of parallel reactions during the anodic oxidation of the AK12M2MgN alloy at voltage  $U_A$  in an alkaline solution ( $pH > 12$ ) in the presence of ligand L

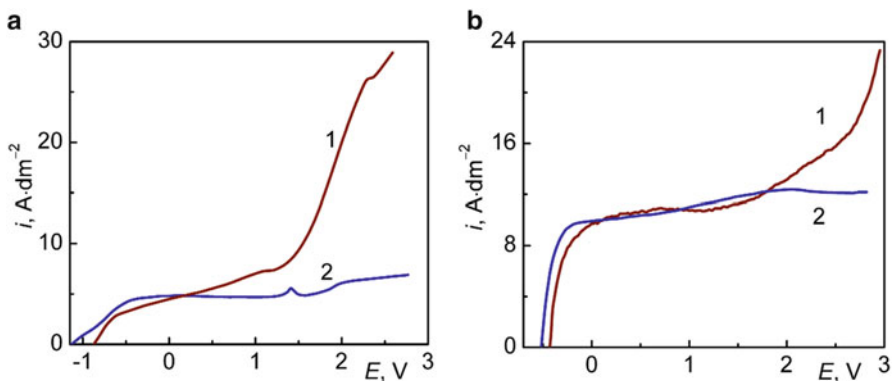


**Fig. 38.2** Anodic voltammograms of the AK12M2MgN alloy (1) and A99 aluminum (2) in solutions of the composition, at  $mol \cdot dm^{-3}$ :  $K_4P_2O_7$ , 0.5 (a);  $K_4P_2O_7$ , 0.5; and  $KMnO_4$ , 0.1 (b). Potential scanning rate,  $10 \text{ mV} \cdot \text{s}^{-1}$ ; the potentials are given vs. SHE

this process is completely excluded. Therefore, for the homogenization of the surface composition of the treated alloy, a diphosphate ion was introduced into the electrolyte as a ligand; the degree of protonation of this ion decreases with increasing pH, while the stability of the complexes with the main components of the alloy is fairly high [24]. In addition, during the hydrolysis of diphosphate solutions, the pH value increases to 9–10; this effect contributes to the oxidation of Si and Mn to form soluble oxo-anions.

Analysis of the anodic behavior of the AK12M2MgN alloy and A99 aluminum in a potassium diphosphate solution suggests that the active dissolution of the intermetallic compounds and the alloying components of the alloy begins at a potential of 1.2 V, whereas on the surface of pure aluminum, an oxide film is formed and no active process is observed in the studied potential range (Fig. 38.2a).

The introduction of potassium permanganate into the basic diphosphate solution leads to an increase in the current density of aluminum oxidation (Fig. 38.2b), while the oxidation of the AK12M2MgN alloying components is considerably slowed

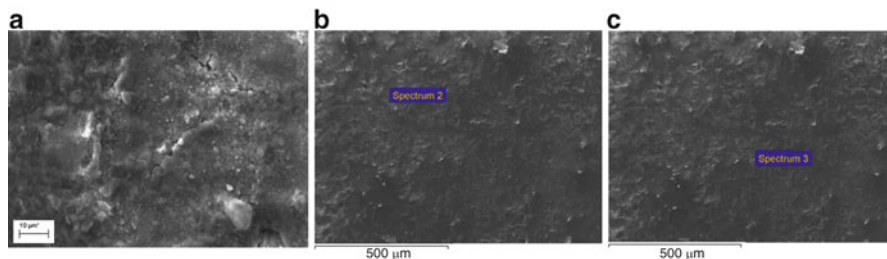
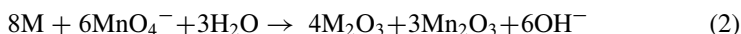


**Fig. 38.3** Micrograph (a) and composition of the oxide coatings after the PEO of AK12M2MgN in the diphosphate–permanganate electrolyte for 60 min. Composition for different places, at %: (b) O, 55.44; Mg, 0.31; Al, 41.04; Si, 1.39; Mn, 1.72; Fe, 0.09; and Cu, 0.00; (c) O, 61.24; Mg, 0.32; Al, 19.95; Si, 13.41; Mn, 5.04; Fe, 0.05; and Cu, 0.00

down. This character of voltammograms can be explained if one takes into account the fact that potassium permanganate is a strong oxidizing agent that provides the reaction



where M is the alloy component.

It was found that the PEO of the AK12M2MgN alloy in a solution of 0.5 M  $K_4P_2O_7$  and 0.1 M  $KMnO_4$  can be implemented only in a step mode:

First step – at a current density of  $i_1 = 2 \text{ A/dm}^2$  for 30 min

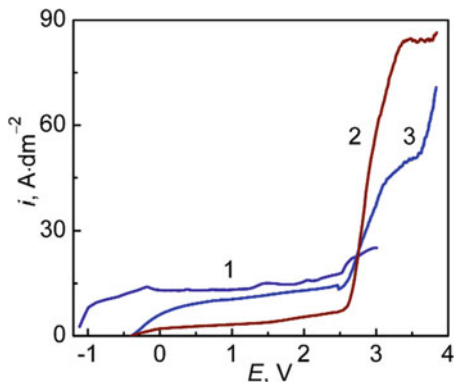
Followed by the second step at higher current  $i_2 = 20 \text{ A/dm}^2$  for the same time

A stable sparking level providing the simultaneous occurrence of the electrochemical formation of oxides and the thermochemical reactions involving water and permanganate [6] was observed at voltage  $U_s$  of 80–90 V; the final forming voltage  $U_{fn}$  did not exceed 140–180 V. Taking into account the fact that, for pure aluminum, the PEO parameters are higher by 50–70 V, one can assume that the mixed oxides formed on the alloy surface exhibit a lower electrical conductivity than that of  $Al_2O_3$ .

In fact, electron probe microanalysis results show that alumina and silica are dominant in the surface layers (Fig. 38.3), while alloying components (copper, nickel, iron, etc.) are either practically absent or present in trace amounts. In addition, the manganese content in the coating increases compared to the substrate material; however, the amount of it (12.4 wt % or 5 at %) is obviously insufficient to provide high catalytic activity. Other negative factors are a significant difference in the composition of the oxide layers and uneven distribution of the components at different surface places (Fig. 38.3b, c).

Thus, unlike the PEO of the D16 alloy with the same copper content [25], an effective oxidation of the AK12M2MgN alloy in electrolytes based on potassium diphosphate is not provided. Apparently, this fact can be attributed to the fairly high silicon content and the unstable temperature dependence of the electrical resistance of silica (Table 38.2). A decrease in the electrical resistivity of  $SiO_2$  by 16 orders of

**Fig. 38.4** Anodic voltammograms of the AK12M2MgN alloy in solutions, at mol·dm<sup>-3</sup>: (1) NaOH, 0.005; (2) NaOH, 0.005; KMnO<sub>4</sub>, 0.05; and (3) NaOH, 0.005. KMnO<sub>4</sub>, 0.2



magnitude in the zone of a local breakdown of the oxides and respective heating leads to the cessation of sparking, a decrease in the forming voltage, and the retardation of the thermochemical reactions. On the basis of the above, to decrease the silica content in the surface layers, the PEO process was conducted in a solution based on sodium hydroxide.

Analysis of the voltammograms of the AK12M2MgN alloy in a sodium hydroxide solution shows an increase in the current density and, consequently, in the oxidation rate compared with the values for the diphosphate electrolyte, particularly in the presence of potassium permanganate (Fig. 38.4). However, with an increase in the concentration of both the alkali and KMnO<sub>4</sub>, the oxidation current density decreases.

This behavior of the alloy can be attributed to the competition of the electrochemical and chemical oxidation (2) of the substrate; an increase in the alkali concentration provides the dissolution of amphoteric alumina and thereby deteriorates the oxidation efficiency. A confirmation of this assumption is the mass reduction in the samples oxidized at a NaOH concentration greater than 0.005 mol·dm<sup>-3</sup>. In this context, the electrolyte for PEO with the following composition is recommended: 0.005 M NaOH and 0.05 M KMnO<sub>4</sub>. The possibility of using higher current density, which is evident from the voltammograms (Fig. 38.4), provides almost a twofold decrease in the PEO time compared to the permanganate–diphosphate electrolyte used for the formation of coatings with identical thickness.

It was also found that PEO of the AK12M2MgN alloy in the alkaline permanganate is more efficient by maintaining effective oxidation in sparking – microarc zone using step mode:

First step – at initial current  $i_0$  of 20 A·dm<sup>-2</sup>

Followed by decreasing current density at the second step to 5–10 A·dm<sup>-2</sup> after the sustainable sparking establishment (Fig. 38.5a)

Sparking voltage increases to 140–150 V as one can see from the voltage variation dependence (Fig. 38.5b), and the final oxidation voltage is 220–240 V; these features indicate the formation of more perfect oxide coatings with higher resistance to local overheating (Fig. 38.6).

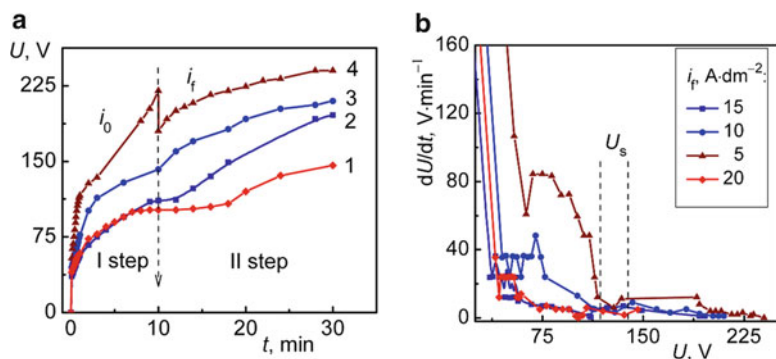


**Fig. 38.5** Voltage chronograms (a) and voltage variation (b) in plasma electrolytic oxidation of AK12M2MgN in electrolyte 0.005 M NaOH and 0.05 M  $\text{KMnO}_4$  at initial current density  $i_0 = 20 \text{ A}\cdot\text{dm}^{-2}$  following by final current density  $i_f$ ,  $\text{A}\cdot\text{dm}^{-2}$ : 1–20; 1–15; 1–10; 1–5

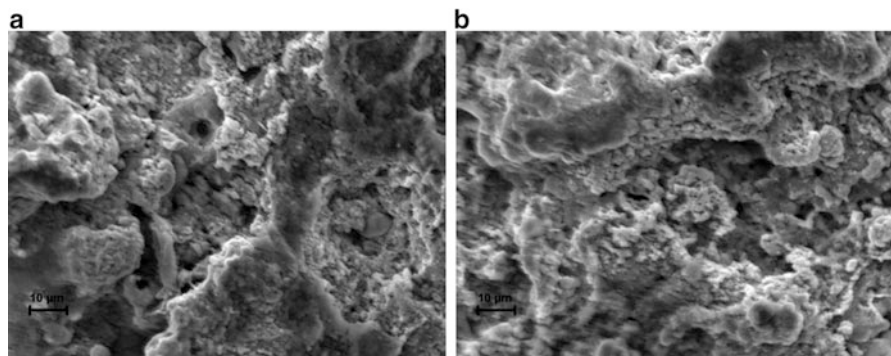
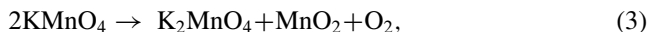


**Fig. 38.6** Micrographs and composition of the coatings after the PEO of AK12M2MgN in the alkaline permanganate electrolyte at a current density of (a) 15 and (b) 20  $\text{A}/\text{dm}^2$  for 30 min. Composition, at. %: (a) O, 62.06; Al, 3.82; Si, 0.87; and Mn, 33.25; (b) O, 61.04; Al, 2.75; Si, 0.41; and Mn, 35.80

The surface composition and morphology of the oxide coatings formed in the alkaline permanganate electrolyte differ significantly from the parameters obtained in the diphosphate–permanganate electrolyte (Fig. 38.5). Primarily, it should be noted that the distribution of the elements in the coating is more uniform apparently owing to the high oxidation rate. In addition, the surface layers are characterized not only by the absence of traces of alloying metals but also by a significantly lower content of aluminum and silicon, whereas the manganese concentration increases almost by an order of magnitude; an increase in the current density leads to an increase in the manganese content. These results suggest that manganese oxides  $\text{MnO}_x$  for which the oxygen index is  $x = 1.71\text{--}1.87$  are incorporated into the



alumina matrix and form the outer layer of the coating. The simultaneous occurrence of the oxidation and the thermochemical reactions involving permanganate in the sparking zone,



provides both high adhesion and the manganese concentration at a level of 60–70 wt %.

The thickness of the oxide layer depends on the electrolyte composition, the current density, and the PEO time; for the studied samples, it is 15–30  $\mu\text{m}$ .

The surface of  $\text{Al} \mid \text{Al}_2\text{O}_3 \cdot \text{MnO}_x$  becomes more developed and nanoglobular as it was established by AFM analysis (Fig. 38.7a, b). We observe the formation on the surface of the cone-shaped conglomerates with an average diameter of 80–100 nm, and the difference of hills and valleys does not exceed 200 nm (Fig. 38.7c). The surface is characterized by the sufficiently uniform distribution of manganese at hills and valleys (Fig. 38.7c), while aluminum content is substantially lower and oxygen content is significantly higher at hills than at valleys (Fig. 38.7c). Such a distribution of elements on the surface is completely natural and reflects proposed mechanism of the processes taking place during plasma electrolytic oxidation.

Analysis of the AK12M2MgN alloy anodic behavior in a potassium diphosphate-containing cobalt (II) (Fig. 38.8) reveals that the oxidation rate is lower an order of magnitude compared to the permanganate–diphosphate electrolyte. This difference may be attributed with variation in electrical resistivity and thermal stability of manganese (Table 38.3) and cobalt (Table 38.4) oxides formed on the AK12M2MgN surface by anodic oxidation.

Experimental data indicate that the oxidation current density increases with polarization rate and is virtually independent of the concentration of cobalt or diphosphate. Considering the fact of PEO process intensification in dilute solutions, mixed cobalt oxides in alumina matrix formation were performed in electrolyte composition – 0.4 M  $\text{K}_4\text{P}_2\text{O}_7$  and 0.1 M  $\text{CoSO}_4$ .

The results of experimental studies found that PEO process of alloy AK12M2MgN in diphosphate electrolytes containing cobalt (II) is a classic case. It was also established that PEO must be performed in the incident power mode. Initial current density  $i_0$  is higher for forming barrier aluminum oxide film on the AK12M2MgN substrate, which is accompanied by oxidation of the alloying components and particularly silicon with forming soluble substances and promotes homogenization of the alloy surface. After the process enters a mode of stable arcing current density for the following stages,  $i_f$  is reduced to ensure a formation of the mixed oxide layer. The current density for the first PEO stage in cobalt diphosphate solution does not exceed the interval 5–10  $\text{A} \cdot \text{dm}^{-2}$  (Fig. 38.9), while the second stage is advisable to hold at current density of 2.0–4.0  $\text{A} \cdot \text{dm}^{-2}$ . Characteristic parameters of the voltage PEO process also depend on the composition of the

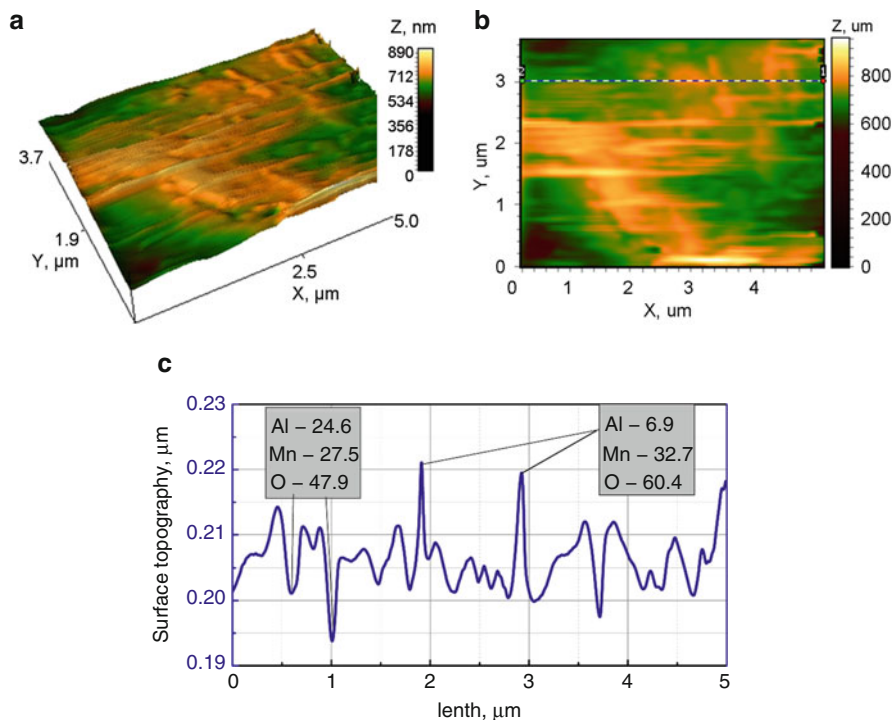
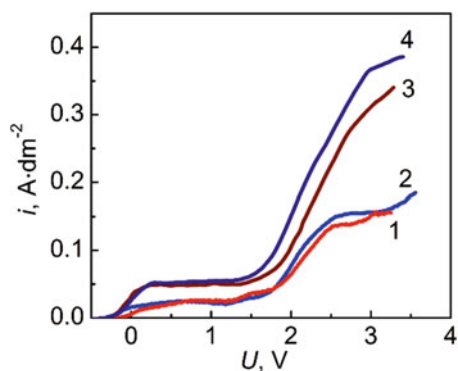


**Fig. 38.7** 3D (a) and 2D (b) maps of the surface and cross-sectional profile (c) between markers 1 and 2 for mixed oxide system Al |  $\text{Al}_2\text{O}_3\cdot\text{MnO}_x$  with manganese content 30.8 at.%. Scanning area  $5 \times 5 \mu\text{m}$

**Fig. 38.8** Anodic voltammograms of the AK12M2MgN in solutions of the composition, at  $\text{mol}\cdot\text{dm}^{-3}$ : (1, 3)  $\text{K}_4\text{P}_2\text{O}_7$ , 0.2,  $\text{CoSO}_4$ , 0.05; (2, 4)  $\text{K}_4\text{P}_2\text{O}_7$ , 0.4,  $\text{CoSO}_4$ , 0.1. Potential scanning rate, at  $\text{mV}\cdot\text{s}^{-1}$ : (1, 2) 10; (3, 4) 50. The potentials are given vs. SHE

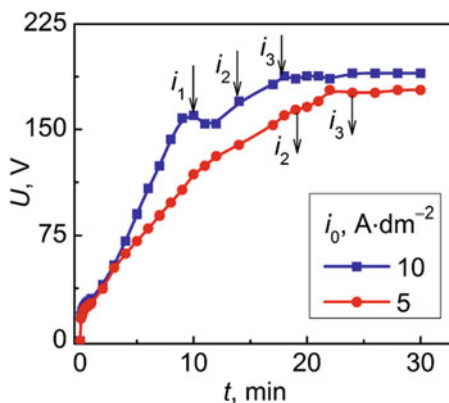


electrolyte: sparking voltage  $U_s$  is 115–120 V, and the resulting formation voltage is  $U_f$  140–160 V. It should be noted that all voltage parameters rising with the electrolyte dilution and with increasing current density as well as the cobalt content in the mixed oxides increase with the current density, and uniformity of its distribution on the surface is improved.

**Table 38.4** Characteristics of cobalt oxides

Oxide	Electrical resistivity ( $\Omega\cdot\text{cm}$ ) at 293 K	Thermal resistance
CoO	$10^6\text{--}10^{10}$	–
Co <sub>2</sub> O <sub>3</sub>	$10^5$	538 K $6\text{Co}_2\text{O}_3 \rightarrow 4\text{Co}_3\text{O}_4 + \text{O}_2$
Co <sub>3</sub> O <sub>4</sub>	$4\cdot 10^3 - (1.05\text{--}1.6)\cdot 10^4$	1178–1213 K $2\text{Co}_3\text{O}_4 \rightarrow 6\text{CoO} + \text{O}_2$

**Fig. 38.9** PEO voltage chronograms in electrolyte 0.4 M  $\text{K}_4\text{P}_2\text{O}_7$  and 0.1 M  $\text{CoSO}_4$  at initial current density  $i_0$  followed by step current density  $i_i$ , at  $\text{A}\cdot\text{dm}^{-2}$ : (1) 4; 3 (2); 2 (3)



Composition of multicomponent oxides depends both on the concentration ratio of the electrolyte components and the oxidation current density. Thus, the oxide system is logically enriched with cobalt by increasing its content in the solution, but the electrolyte stability as well as service time is reduced. At the same time, increasing the diphosphate concentration in the bath is not desirable because it leads to a decrease of PEO efficiency.

Surface morphology and composition of PEO coatings doped with cobalt oxides depend both on the concentration of electrolyte and oxidation conditions – current density, voltage, and time of formation (Fig. 38.10). The incorporation of the cobalt in oxide systems affects the formation of separate spheroid islets of characteristic blue-purple color. During the treatment, the number of islet structures significantly increases; some of the islets grow together, agglomerated, and form ceramic-like mosaic patterns (Fig. 38.10b, c).

The higher the content of cobalt is, the more developed but at the same time less uniform is the surface of coating. Formed oxide systems have high developed microglobular surface with cobalt content 8–30 at.% and lower concentration of impurities compared with  $\text{Al} | \text{Al}_2\text{O}_3$  coating synthesized in pure diphosphate electrolyte (Fig. 38.10a), which is essential for the high catalytic properties of the material [3]. Analysis of the composition of oxide systems indicates nonstoichiometric ratio of cobalt and oxygen which is favorable for the implementation of catalytic processes involving oxygen.

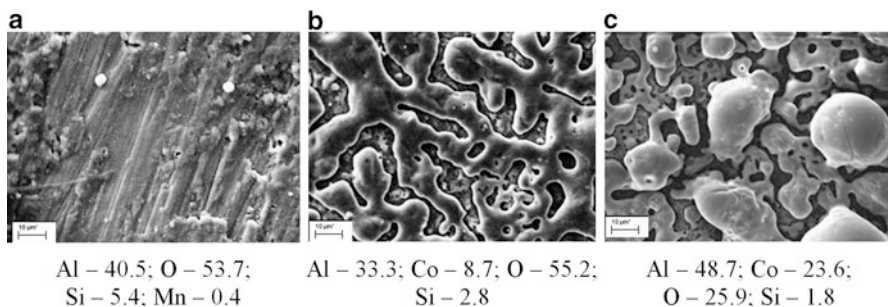


**Fig. 38.10** Surface morphology and composition (at.%) of PEO coatings on AK12M2MgN: (a) Al | Al<sub>2</sub>O<sub>3</sub> obtained in electrolyte 0.4 M K<sub>4</sub>P<sub>2</sub>O<sub>7</sub> with current density  $i_0 = 8 \text{ A}\cdot\text{dm}^{-2}$ ; (b, c) mixed oxide systems Al | Al<sub>2</sub>O<sub>3</sub>·CoO<sub>x</sub> obtained in PEO two-stage mode ( $i_0 = 8 \text{ A}\cdot\text{dm}^{-2}$ ,  $i_t = 2.5 \text{ A}\cdot\text{dm}^{-2}$ ) in diphosphate electrolyte with CoSO<sub>4</sub> addition of concentration (b) 0.05 and (c) 0.2 mol·dm<sup>-3</sup>. Magnification 1000

It was established by AFM analysis that the surface of Al | Al<sub>2</sub>O<sub>3</sub>·CoO<sub>x</sub> system with cobalt content of 8–12 at.% (Fig. 38.11) is microglobular characterized by the high roughness and larger conglomerate sizes compared to the Al | Al<sub>2</sub>O<sub>3</sub>·MnO<sub>x</sub>.

Mixed oxide coatings are composed from the set of spheroid conglomerates with an average size of 1–2 μm which gather and form the parts of smooth surface with the spherical agglomerates of 6–8 μm (Fig. 38.11a). The surface roughness may be characterized with the spread of conglomerate size on the cross section between markers 1 and 2 (Fig. 38.11b). In addition, the surface morphology of oxides is characterized by rather large difference between hills and valleys (Fig. 38.11c) of 0.3 μm up to 1.2 μm and alternating the spheroid- and torus-shaped structures (Fig. 38.10c).

The anodic oxidation of the AK12M2MgN cast aluminum alloy as the main structural material of reciprocating ICEs is complicated by the presence of significant amounts of alloying elements, such as silicon, copper, and iron subgroup metals; therefore, satisfactory-quality coatings of a considerable thickness can be obtained only in the PEO mode. In the PEO mode, a variation in the ratio between hydroxide and permanganate ions leads to a variation in the sparking and forming voltage for the oxides; this feature makes it possible to control the process and prepare more perfect oxide coatings resistant to local overheating. An increase in the coating thickness and the manganese oxide content in the coating is achieved by the homogenization of the treated surface owing to the parallelization of the anodic process that provides the simultaneous occurrence of the formation of mixed oxides in the presence of hydroxide ions and the dissolution of the alloying components of the alloy. Mixed oxide systems Al<sub>2</sub>O<sub>3</sub>·CoO<sub>x</sub> with cobalt content of 8–30 at.% were obtained on aluminum alloy AK12M2MgN by two-step plasma electrolytic oxidation in a diphosphate electrolyte added with cobalt (II) sulfate. It has been found that surface concentration of silicon dopant in mixed coatings is two to three times less than in the system Al | Al<sub>2</sub>O<sub>3</sub> or treated alloy AK12M2MgN.

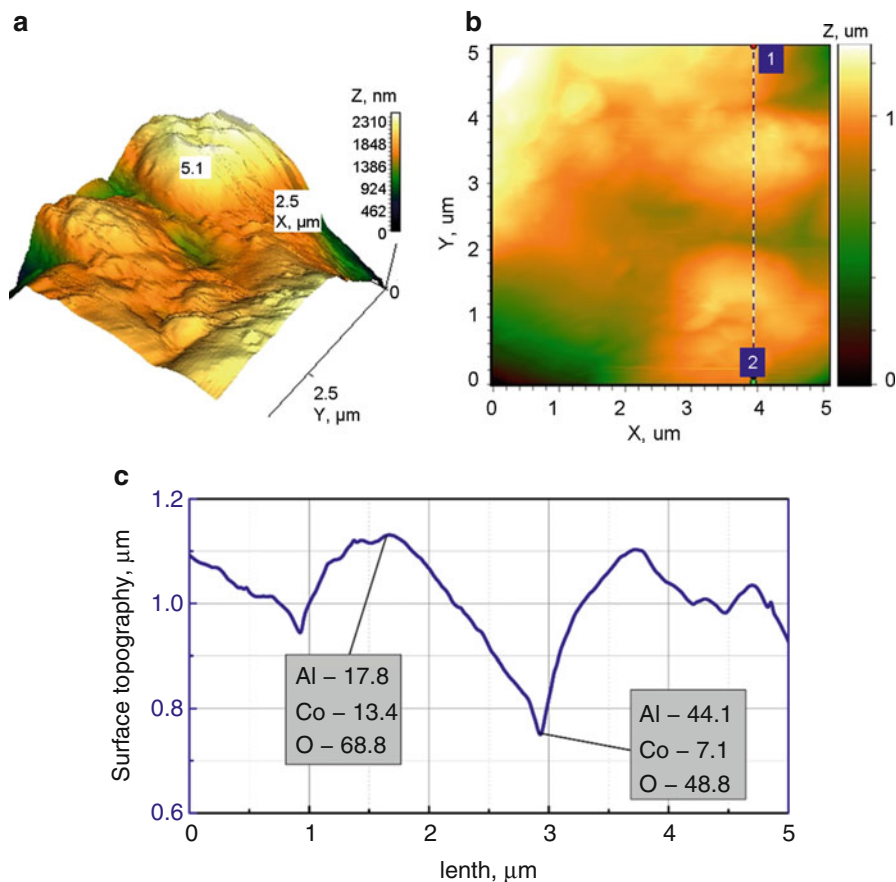


**Fig. 38.11** 3D (a) and 2D (b) maps of the surface and cross-sectional profile (c) between markers 1 and 2 for mixed oxide system Al |  $\text{Al}_2\text{O}_3\text{-CoO}_x$  with cobalt content 8.7 at.%. Scanning area  $5 \times 5 \mu\text{m}$

It was shown nonstoichiometric ratio of cobalt and oxygen in deposits as well as the cobalt content in mixed oxide increases regularly with concentration of cobalt ions in the electrolyte. At the same time, the morphology of Al |  $\text{Al}_2\text{O}_3\text{-CoO}_x$  surface changes from the uniformly roughened to microglobular containing sufficiently large spheroids characterized by elevated concentrations of cobalt.

Taking into account the nanoglobular surface pattern of Al |  $\text{Al}_2\text{O}_3\text{-MnO}_x$  and microglobular of Al |  $\text{Al}_2\text{O}_3\text{-CoO}_x$  as well as the composition of the oxide coatings, one can reasonably expect that the resulting materials will exhibit catalytic activity in redox reactions involving oxygen [26].

Testing of oxide system in the model reaction of carbon (II) oxide conversion to  $\text{CO}_2$  showed (Table 38.5) that their activity (both ignition and complete conversion temperature) is close to platinum catalyst.

**Table 38.5** Characteristics of the CO conversion to CO<sub>2</sub>

Material	Active metal content, at %	Ignition temperature $T_i$ , K	Complete conversion temperature $T_c$ , K
Pt	100	490	570
Al Al <sub>2</sub> O <sub>3</sub> ·MnO <sub>x</sub>	30.8	495	570
Al Al <sub>2</sub> O <sub>3</sub> ·CoO <sub>x</sub>	8.7	505	580

This can be attributed to several factors: Firstly, this is due to a high affinity of nonstoichiometric cobalt oxides to oxygen and the corresponding decrease in the activation energy of double bond O = O destruction [26]. Secondly, the developed microglobular surface of oxide systems is characterized by a large number of catalytic centers and provides an increase in the number of elementary collisions and interactions.

Pilot tests of mixed oxides deposited on the surface of combustion chamber piston of the ICE showed a reduction in fuel consumption at 1–3% and NO<sub>x</sub> emission reduction at forced diesel engine operating modes. This is due to lower ignition temperature of the air–fuel mixture on the surface of Al | Al<sub>2</sub>O<sub>3</sub>·CoO<sub>x</sub> catalyst composed of nonstoichiometric oxides with developed surface.

Thus, we can conclude that the varying electrolyte concentrations and conditions of the PEO process allow formation of oxide coatings of different compositions and morphologies that are expected to affect their functional properties including catalytic activity in the process of burning fuel in internal combustion engines and reduce the toxicity of emissions improving fuel efficiency and environmental performance of engines.

### 38.1.2 Titanium Alloy

The voltage chronograms for the plasma electrolytic oxidation of the titanium alloys (Fig. 38.12a, b) in all the researched electrolytes have a classic geometry with the division into specific areas: pre-spark, spark, and microarc [27].

The sections of dependencies that correspond to the pre-spark area of the coatings forming are almost linear, which is explained by the growth of the titania film thickness and a corresponding increase in the resistance. The time before the sparks in all the investigated electrolytes is 1–2 min at a current density of 2.0–5.0 A·dm<sup>-2</sup>.

The pre-spark area for oxide films that are formed in a diphosphate electrolyte has a light gray color corresponding to the titanium (IV) oxide. The sparking voltage is in the range of 55–65 V, and the PEO process stabilization occurs at the voltages of 120–140 V (Table 38.6).

In the transition to the sparking section, the  $U$ ,  $t$  dependence stops being linear, and the voltage growth slows down significantly, apparently due to the inclusion of the electrolyte components into the coating. This is particularly evident in the

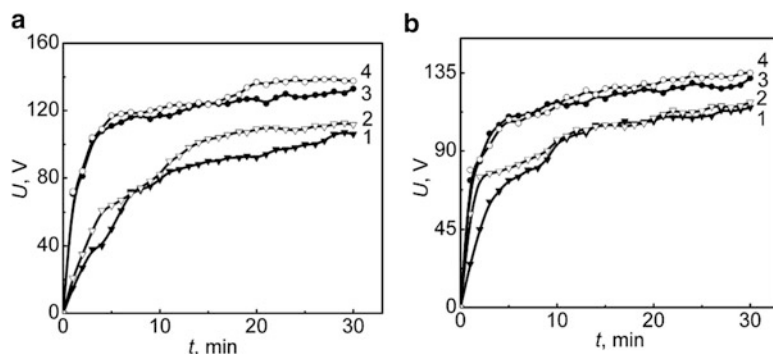


**Fig. 38.12** The voltage chronograms to form a VT1-0 alloy in a diphosphate electrolyte: (a)  $\text{KMnO}_4$  and (b)  $\text{MnSO}_4$  with different concentrations of manganese salts.  $\text{mol}\cdot\text{dm}^{-3}$ : 1.3–0.1 and 2.4–0.3 for  $i$ .  $\text{A}\cdot\text{dm}^{-2}$ : 1.2–2.0 and 3.4–4.0

**Table 38.6** Parameters of the coating formation process

Process parameters	Electrolyte				
	1	2	3	4	5
Sparking voltage $U_i$ , V	55	65	65	65	65
Forming voltage $U_f$ , V	120	130	140	130	120

**Table 38.7** The electrical resistivity and thermal stability of the titanium oxides

Oxide	Electrical resistivity $\rho$ ( $\Omega\cdot\text{cm}$ ) at 293 K	Color	Conductivity type	Thermal stability
$\text{TiO}_x$ ( $x = 0.92\text{--}1.26$ )	$3\cdot 10^{-3}$	Light bronze metal	Metallic	1198–1298 K $3\text{TiO}_2 + \text{Ti} \rightarrow 2\text{Ti}_2\text{O}_3$
$\text{Ti}_2\text{O}_3$	$10^5$	Purple	s/c <sup>a</sup> n-type	1698–1798 K $\text{TiO}_2 + \text{Ti} \rightarrow 2\text{TiO}$
$\text{TiO}_{1.75\text{--}1.97}$ $\text{TiO}_{1.98\text{--}2.00}$	$10^5\text{--}10^{13}$	From blue steel through dark blue and straw yellow to white	s/c n-type	1198–1598 K $6\text{TiO}_2 \rightarrow 2\text{Ti}_3\text{O}_5 + \text{O}_2$
$\text{TiO}_2$ (anatase and rutile)	$10^{13}$	Light gray	s/c n-type	2298–1698 K $6\text{TiO}_2 \rightarrow 2\text{Ti}_3\text{O}_5 + \text{O}_2$

<sup>a</sup>s/c semiconductor

formation of coatings in manganese-containing solutions when black free forms begin to appear in the anode areas, primarily occurring at sharp edges and in defect surface sites. On the basis of the color gamut of  $\text{MnO}_y$  (Table 38.7), we can confidently assert that the dark areas are formed by manganese oxides of different oxidation number.

In the microarc mode, the amount of inclusions increases, and they gradually cover the entire surface of the electrode, wherein the process voltage practically remains unchanged; however, in all  $U$ ,  $t$  dependencies, there are observed small



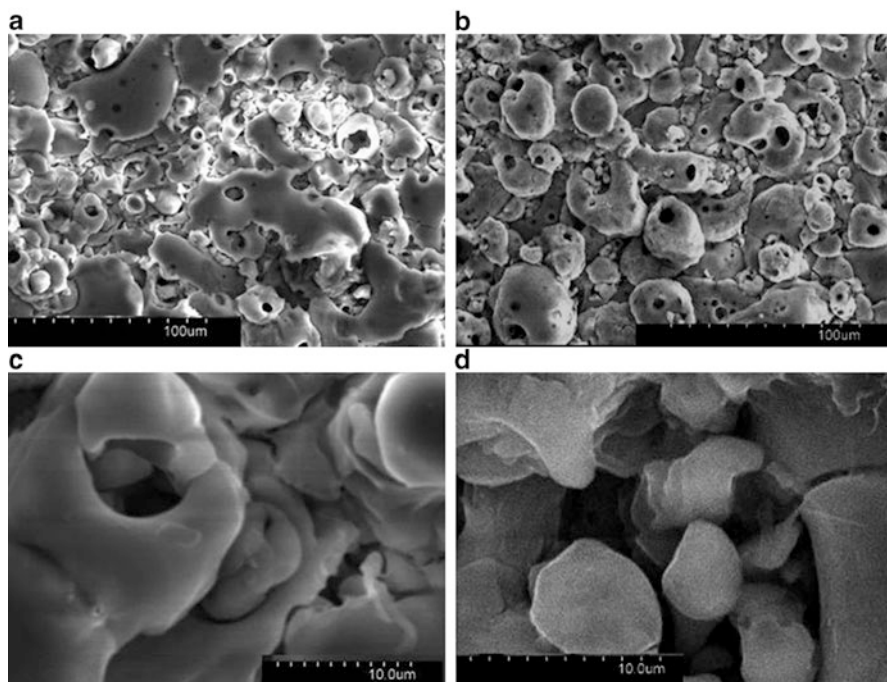


**Fig. 38.13** The morphology of PEO coatings on the VT1-0 alloy obtained from solutions, at mol/dm<sup>3</sup>: (a) and (c) K<sub>4</sub>P<sub>2</sub>O<sub>7</sub>, 1; (b) and (d) K<sub>4</sub>P<sub>2</sub>O<sub>7</sub>, 1, and KMnO<sub>4</sub>, 0.1. Magnification: *a* and *b* = 500; *c* and *d* = 5000

**Table 38.8** The phase composition of the coatings

PEO electrolyte composition, mol·dm <sup>-3</sup>	The phase composition of the coatings
K <sub>4</sub> P <sub>2</sub> O <sub>7</sub> , 1	TiO, TiO <sub>2</sub> , and Ti <sub>3</sub> O <sub>5</sub>
K <sub>4</sub> P <sub>2</sub> O <sub>7</sub> , 1 KMnO <sub>4</sub> , 0.3	TiO, TiO <sub>2</sub> , Ti <sub>3</sub> O <sub>5</sub> , MnO <sub>1.88</sub> , MnO, MnO <sub>2</sub> , and Mn <sub>2</sub> O <sub>3</sub>
K <sub>4</sub> P <sub>2</sub> O <sub>7</sub> , 1 MnSO <sub>4</sub> , 0.3	TiO, TiO <sub>2</sub> , Ti <sub>3</sub> O <sub>5</sub> , MnO <sub>1.88</sub> , Mn <sub>3</sub> O <sub>4</sub> , and Mn <sub>2</sub> O <sub>3</sub>

oscillations that appear to be associated with different electrical resistivities of the produced mixed oxides (Table 38.7).

When synthesized in the diphosphate electrolyte, oxide coatings on VT1-0 resemble enamel (Fig. 38.13a): on their surface areas of blue and golden-yellow colors appear, which correspond to the oxides of TiO<sub>2</sub>, Ti<sub>3</sub>O<sub>5</sub>, and TiO. The results of the X-ray analysis confirm that the coatings in the conversion layer contain a mixture of the titanium oxides: Ti<sub>3</sub>O<sub>5</sub>, TiO<sub>2</sub>, and TiO (Table 38.8) [28].

The incorporation of manganese oxides in the coating leads to a change in the surface morphology (Fig. 38.13b). On the surface of the oxide systems that



were formed by a plasma electrolytic oxidation in a solution of 1 M potassium diphosphate, sufficiently large areas of the amorphous glassy film alternate with tubular porous sections (Fig. 38.13a, b). The surfaces of the coatings with mixed oxides  $\text{TiO}_x \cdot \text{MnO}_y$  are more uniform; they clearly display visible spheroidal grains, and a 5000 magnification reveals the oxides' tubular structure (Fig. 38.13b, d).

It was established by AFM analysis that the surface of Ti |  $\text{TiO}_2 \cdot \text{MnO}_x$  system with manganese content of 3–4 at.% is microglobular characterized by the high roughness and larger conglomerate sizes compared to the Ti |  $\text{TiO}_2$  (Fig. 38.14).

Synthesized in diphosphate electrolyte, Ti |  $\text{TiO}_2$  coatings have developed unevenly globular surface including phosphorus and potassium. Surface relief is smoothed, and the globule size ranges from 200 to 600 nm (Fig. 38.14a).

However sample surface becomes more uniform and globular in the presence of  $\text{MnO}_x$  (3 at.% Mn) in the coating (Fig. 38.14b). This nature of the surface improves the physical and mechanical properties, chemical resistance, and increased catalytic activity of the material.

The influence of the electrolyte composition on the coating thickness obtained at the same current density relates to the formation of mixed oxide systems; moreover, in  $\text{MnSO}_4$ -containing electrolytes, the thickness and, consequently, the oxidation rate for the same final synthesis voltage are higher. The inclusion of manganese oxides into conversion coatings that are based on titanium alloys naturally affects the field strength  $E_{\text{gk}}$  in the coating (Table 38.9).

The observed decrease in the field strength  $E_{\text{gk}}$  depends on the presence, besides titanium, of manganese and phosphorus, which are fairly evenly distributed throughout the thickness of the coating (Fig. 38.15a, b) and also of trace quantities of potassium.

The amount of manganese in the oxide systems depends on the nature of the dopant: the electrolyte  $\text{K}_4\text{P}_2\text{O}_7 + \text{KMnO}_4$  was used to form coatings with an even distribution of Mn throughout the thickness at the level of 2.5–2.7 at.%, and it did not exceed 1 at.% on the surface  $\omega(\text{Mn})$ . The electrolyte  $\text{K}_4\text{P}_2\text{O}_7 + \text{MnSO}_4$  was used to obtain oxide systems containing manganese in the surface layer at 3.8–4.0 at.%, which was more conducive to the implementation of catalytic reactions. Of course, the reason of this difference is the diversification of the base metal and Mn (II) oxidation routes, whereas in the  $\text{KMnO}_4$ -contained solutions, manganese can be included in the coating only after thermochemical reactions in the arcing zone [6].

It is particularly noteworthy that the content of phosphorus in all coatings is higher at the oxide – solution interface versus lower deep down to the oxide – Ti boundary, whereas the content of titanium regularly increases in the same direction (Fig. 38.16).

It should be noted that the composition and structure of the complex oxide coatings are significantly affected by the current density of the forming. As can be seen from Fig. 38.17a, PEO at current density of 1  $\text{A} \cdot \text{dm}^{-2}$  provides uniform microporous oxide coatings, and at 1.5  $\text{A} \cdot \text{dm}^{-2}$ , the morphology changes: the roughness of the surface and the number of toroid-like coating sections increase (Fig. 38.17b). Thus, an increase in the current density during PEO allows obtaining materials with a more developed surface area, which creates conditions for increasing the catalytic activity of the materials.

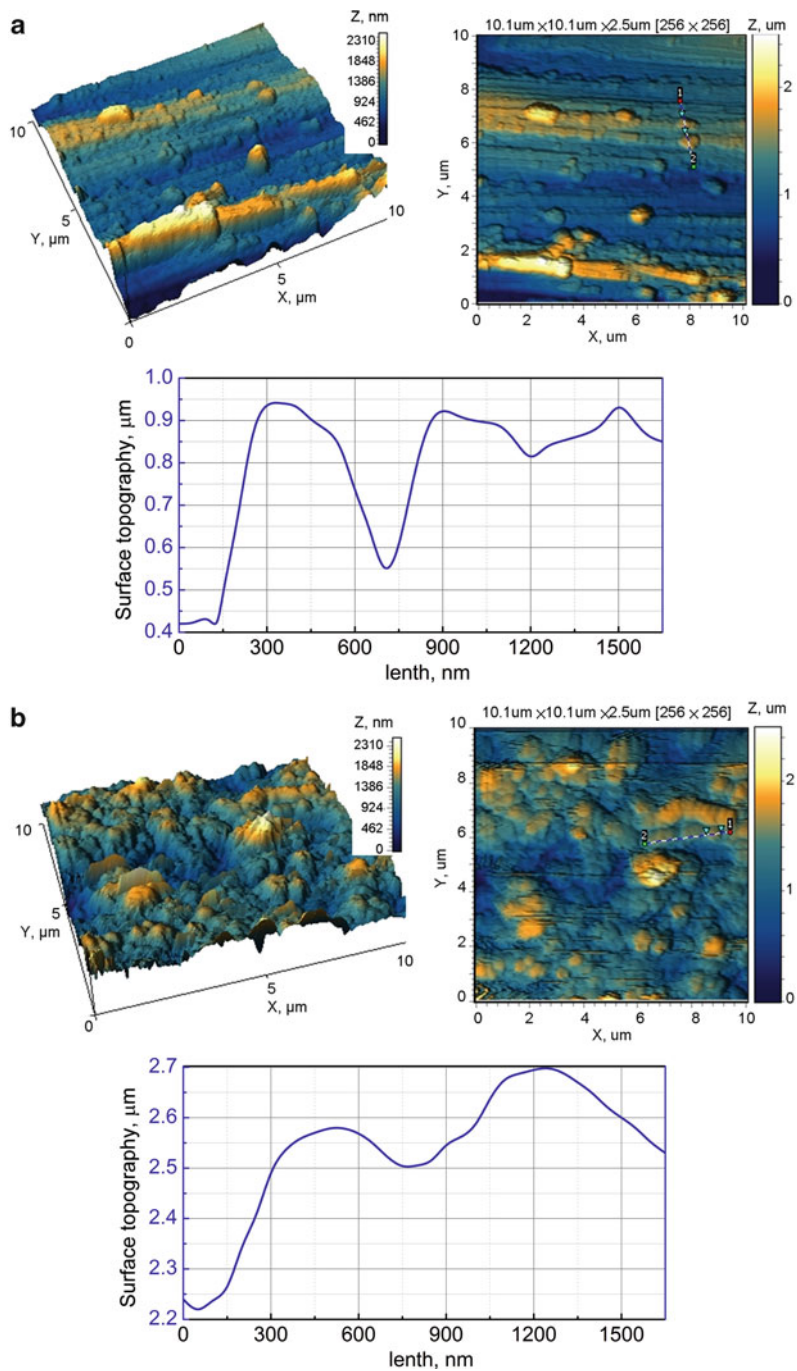


**Fig. 38.14** 3D and 2D surface maps and cross-sectional profile between markers 1 and 2 of oxide coatings on titanium alloy VT1-0: (a) Ti/TiO<sub>x</sub>; (b) Ti/TiO<sub>2</sub>·MnO<sub>x</sub> (3 at.% Mn). Scanning area 10 × 10 μm

**Table 38.9** The field strength in the PEO coatings obtained in different electrolytes at  $i = 5 \text{ A/dm}^2$

Electrolyte	1	2	3	4	5
$U_k, \text{ V}$	120	130	140	130	120
$h \cdot 10^6, \text{ m}$	45	55	45	65	80
$E_{gk} \cdot 10^{-6}, \text{ V/m}$	2.67	2.36	2.27	2	1.75

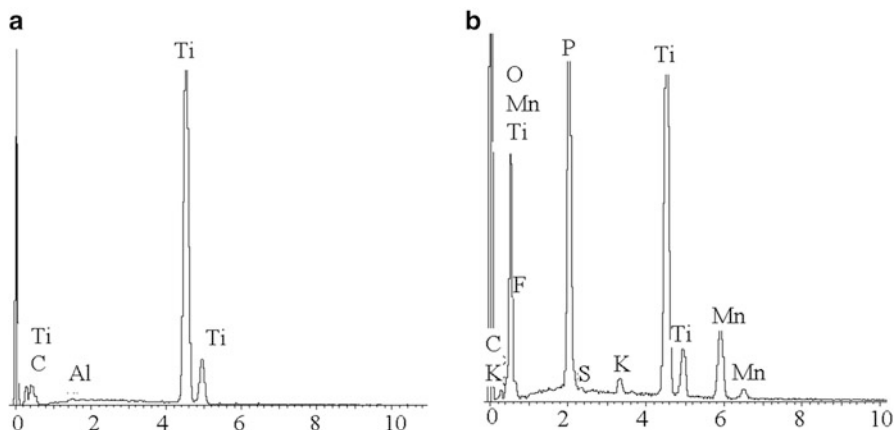


**Fig. 38.15** The radiographs and the VT1-0 alloy composition, at wt%: (a) before the PEO – C, 0.13; O, 0.27; Ti, 99.60; (b) after the PEO in the solution, at mol/dm<sup>3</sup> – K<sub>4</sub>P<sub>2</sub>O<sub>7</sub>, 1.0, MnSO<sub>4</sub>, 0.1;  $i = 1.5 \text{ A/dm}^2$ : C, 4.62; O, 48.69; P, 14.36; K, 0.96; Ti, 20.34; Mn, 11.03

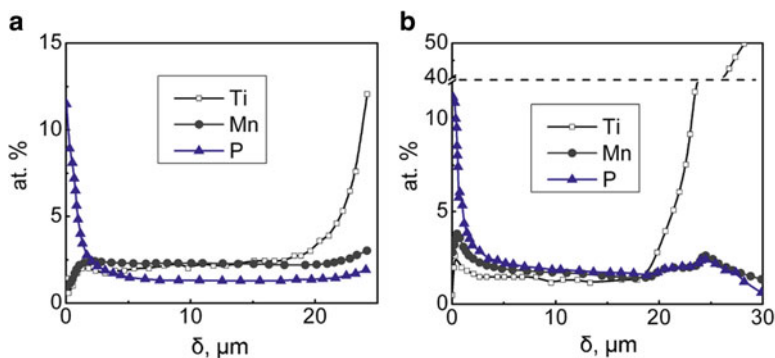


**Fig. 38.16** The distribution of the major components throughout the thickness of the PEO coatings produced in a diphosphate electrolyte that comprises (a) KMnO<sub>4</sub> and (b) MnSO<sub>4</sub>, with up to 100% of oxygen. The coordinate  $\delta = 0$  corresponds to the coating surface

The results of testing the catalytic activity of the coatings with the mixed manganese-based oxides show that the ignition temperature  $T_i$  corresponding to the top efficient operation of a catalyst for the synthesized TiO<sub>x</sub>·MnO<sub>y</sub> systems is in the range from 510 to 520 K, which is slightly higher than for platinum-based ones, and the complete conversion of CO is achieved at 670 K (Tables 38.6 and 38.10).

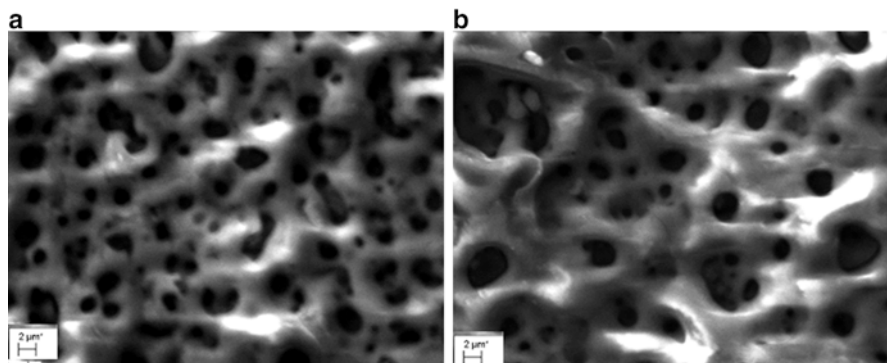


**Fig. 38.17** The photomicrographs of the surface  $\text{TiO}_x \cdot \text{MnO}_y$  formed at current densities, at  $\text{A}/\text{dm}^2$ : (a) 1.0 and (b) 1.5. Magnification by 2000

**Table 38.10** The catalytic activity of the materials in the CO oxidation reaction

Catalyst material	The content of the active ingredient $\omega$ , at. %	Ignition temperature $T_i$ , K
Pt [29]	100	490
$\text{Pt}_{\text{exp}}$	100	
$\text{TiO}_x \cdot \text{MnO}_y$	$\omega(\text{Mn}) = 7.5$	510

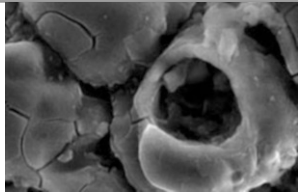
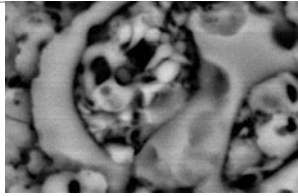
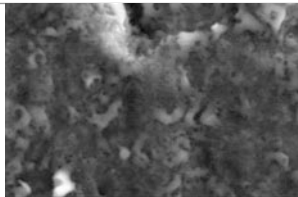
An important operational characteristic of functional materials that defines their service life under operating conditions is resistance to external influences. One of the most important indicators of reliability is resistance of coatings to abrasion, which essentially depends on their composition and surface morphology [30]. It has been determined that higher contents of manganese and titanium in mixed oxide systems decrease the grain size and facilitate formation of a microglobulin surface (Table 38.11) due to randomization of electrochemical and thermochemical reactions throughout the surface and inside the oxide layer.

The tendency to a reduced abrasive wear rate really coincides with the observed grain refinement and smoothing of the surface layers (Table 38.11). Certainly, the tribological properties of the oxide systems also increase in case of a lower content of potassium, as it is known [31] that inclusion of alkali metal oxides loosens the structure of mixed oxides.

Thus, the process of plasma electrolytic oxidation in a Mn (II)-containing solution on the surface of titanium alloys results in the formation of the complex oxide layers  $\text{TiO}_x \cdot \text{MnO}_y$ . These are the mixed oxides of titanium  $\text{TiO}$ ,  $\text{Ti}_3\text{O}_5$ , and  $\text{TiO}_2$  with manganese  $\text{MnO}_2$ ,  $\text{Mn}_2\text{O}_3$ , and  $\text{Mn}_3\text{O}_4$ , as evidenced by the results of studying the phase composition of the coatings.

It has been shown that the plasma electrolytic oxidation of the VT1-0 alloy in diphosphate solutions facilitates the formation of enamel-like oxide coatings of a microglobular morphology; according to the results of the X-ray analysis, such coatings include a mixture of the titanium oxides  $\text{Ti}_3\text{O}_5$ ,  $\text{TiO}_2$ , and  $\text{TiO}$ . By varying the concentration of the electrolyte and the current density for forming, it is possible to control the chemical and phase compositions of coatings as well as the

**Table 38.11** The resistance of the oxide coatings to abrasion

Electrolyte composition, mol·dm <sup>-3</sup>	Photomicrographs of the coating surface, magnification 2000	The coating composition, at. %	Abrasion rate, $\Delta l/\Delta t$ , $\mu\text{m}\cdot\text{h}^{-1}$
K <sub>4</sub> P <sub>2</sub> O <sub>7</sub> -1		Ti – 31.28 O – 53.40 P – 11.53 K – 3.79	2.50
K <sub>4</sub> P <sub>2</sub> O <sub>7</sub> -1 MnSO <sub>4</sub> -0.05		Ti – 40.11 Mn – 1.00 O – 48.75 P – 8.42 K – 1.72	1.85
K <sub>4</sub> P <sub>2</sub> O <sub>7</sub> -1 MnSO <sub>4</sub> -0.1		Ti – 40.73 Mn – 3.17 O – 47.42 P – 8.05 K – 0.63	0.81

topography of the surface and the grain size. The study has proved the possibility of including manganese into oxide coatings by incorporating the components of the electrolyte into the growing oxide phase and subsequent chemical and thermal transformations, which allows forming mixed conversion compositions on the VT1-0 alloy surface. Mixed oxide coatings formed in the PEO mode with reduction of the conglomerate size and formation of a microglobular structure have an increased abrasion wear resistance and an intense catalytic activity in carbon monoxide oxidation reactions. Thus, there is a prospect of using such coatings in the industrial systems of catalytic purification of exhaust gases of industrial plants and power system facilities.

## References

1. Gardiner WC (1984) Combustion chemistry. Springer, New York
2. Fong KF, Lee CK (2015) Performance analysis of internal-combustion-engine primed trigeneration systems for use in high-rise office buildings in Hong Kong. Appl Energy 160:793–801. doi:[10.1016/j.apenergy.2014.11.059](https://doi.org/10.1016/j.apenergy.2014.11.059)
3. Stiles AB (1987) Catalyst supports and supported catalysts: theoretical and applied concepts. Butterworth, Stoneham

4. Sakhnenko ND, Ved MV, Vestfrid YV, Stepanova II (1996) Predicting the catalytic activity of metal oxide systems in treatment of exhaust gases to remove nitrogen oxides. *Russ J Appl Chem* 69(9):1346–1350
5. Glazoff MV, Zolotarevsky VS, Belov NA (2007) *Casting aluminum alloys*. Elsevier, Oxford
6. Sakhnenko ND, Ved' MV, Androshchuk DS, Korniy SA (2016) Formation of coatings of mixed aluminum and manganese oxides on the AL25 alloy. *Surf Eng Appl Electrochem* 52(2):145–151. doi:[10.3103/S1068375516020113](https://doi.org/10.3103/S1068375516020113)
7. Ved' MV, Sakhnenko ND, Bogoyavlenska OV, Nenastina TO (2008) Modeling of the surface treatment of passive metals. *Mater Sci* 44(1):79–86. doi:[10.1007/s11003-008-9046-6](https://doi.org/10.1007/s11003-008-9046-6)
8. Barros AD (2010) Thin titanium oxide films deposited by e-beam evaporation with additional rapid thermal oxidation and annealing for ISFET applications. *Microelectron Eng* 87(3):443–446. doi:[10.1016/j.mee.2009.06.020](https://doi.org/10.1016/j.mee.2009.06.020)
9. Sakhnenko ND, Ved MV, Karakurkchi FV, Galak AV (2016) A study of synthesis and properties of manganese-containing oxide coatings on alloy VT1-0. *East Eur J Enterp Technol* 3(5(81)):37–43. doi:[10.15587/1729-4061.2016.69390](https://doi.org/10.15587/1729-4061.2016.69390)
10. Yerokhin A, Khan RHU (2010) Anodising of light alloys. In: Dong H (ed) *Surface engineering of light alloys: aluminium, Magnesium and Titanium Alloys*. Woodhead Publishing Ltd, Cambridge, pp 83–109
11. Yerokhin AL, Nie X, Leyland A, Matthews A, Dowe SJ (1999) Plasma electrolysis for surface engineering. *Surf Coat Technol* 122(2–3):73–93. doi:[10.1016/s0257-8972\(99\)00441-7](https://doi.org/10.1016/s0257-8972(99)00441-7)
12. Rudnev VS, Lukiyanchuk IV, Vasilyeva MS, Sergienko NV (2016) Aluminum- and titanium-supported plasma electrolytic multicomponent coatings with magnetic, catalytic, biocide or biocompatible properties. *Surf Coat Technol* 307(Part C):1219–1235. doi:[10.1016/j.surfcoat.2016.07.060](https://doi.org/10.1016/j.surfcoat.2016.07.060)
13. Gupta P, Tenhundfeld G, Daigle EO, Ryabkov D (2007) Electrolytic plasma technology: science and engineering – an overview. *Surf Coat Technol* 201(21):8746–8760. doi:[10.1016/j.surfcoat.2006.11.023](https://doi.org/10.1016/j.surfcoat.2006.11.023)
14. Krishna LR, Somaraju KRC, Sundararajan G (2003) The tribological performance of ultra-hard ceramic composite coatings obtained through microarc oxidation. *Surf Coat Technol* 163–164:484–490. doi:[10.1016/s0257-8972\(02\)00646-1](https://doi.org/10.1016/s0257-8972(02)00646-1)
15. Wu H, Zhang X, Geng Z, Yin Y, Hang R, Huang X, Yao X, Tang B (2014) Preparation, antibacterial effects and corrosion resistant of porous Cu–TiO<sub>2</sub> coatings. *Appl Surf Sci* 308:43–49. doi:[10.1016/j.apsusc.2014.04.081](https://doi.org/10.1016/j.apsusc.2014.04.081)
16. Terleeva OP, Belevantsev VI, Slonova AI (2006) Comparison analysis of formation and some characteristics of microplasma coatings on aluminum and titanium alloys. *Prot Met* 42(3):272–278. doi:[10.1134/s0033173206030106](https://doi.org/10.1134/s0033173206030106)
17. Umar AA, Rahman MYA, Saad SKM (2013) Preparation of grass-like TiO<sub>2</sub> nanostructure thin films: effect of growth temperature. *Appl Surf Sci* 270:109–114. doi:[10.1016/j.apsusc.2012.12.128](https://doi.org/10.1016/j.apsusc.2012.12.128)
18. Sakhnenko ND, Ovcharenko OA, Ved' MV (2015) Electrochemical synthesis of nickel-based composite materials modified with nanosized aluminum oxide. *Russ J Appl Chem* 88(2):267–271. doi:[10.1134/S1070427215020123](https://doi.org/10.1134/S1070427215020123)
19. Glushkova M, Bairachna T, Ved' M, Sakhnenko M (2013) Electrodeposited cobalt alloys as materials for energy technology. *MRS Proc* 1491:18–23. doi:[10.1557/opl.2012.1672](https://doi.org/10.1557/opl.2012.1672)
20. Kassman Å, Iacobson S, Ericson L, Hedenqvist P, Olsson M (1991) A new test method for the intrinsic abrasion resistance of thin coatings. *Surf Coat Technol* 50(1):75–84. doi:[10.1016/0257-8972\(91\)90196-4](https://doi.org/10.1016/0257-8972(91)90196-4)
21. Mchardy J, Ludwig F (1992) *Electrochemistry of semiconductors and electronics: processes and devices*. Noyes, Park Ridge
22. Pergament A, Stefanovich G, Malinenko V, Velichko A (2015) Electrical switching in thin film structures based on transition metal oxides. *Adv Condens Matter Phys* 2015. doi:[10.1155/2015/654840](https://doi.org/10.1155/2015/654840)
23. Patil V, Joshi P, Chougule M, Sen S (2012) Synthesis and characterization of Co<sub>3</sub>O<sub>4</sub>, thin film. *Soft Nanosci Lett* 2:1–7. doi:[10.4236/snll.2012.21001](https://doi.org/10.4236/snll.2012.21001)

24. Sillen LG, Martell AE (1965) Stability constants of metal-ion complexes. *J Chem Educ* 42(9):521. doi:[10.1021/ed042p521.1](https://doi.org/10.1021/ed042p521.1)
25. Ved' MV, Sakhnenko ND, Shtefan VV, Lyon SB, Oleinyk SV, Bilyi LM (2008) Computer modeling of the nonchromate treatment of aluminum alloys by neural networks. *Mater Sci* 44(2):216–221. doi:[10.1007/s11003-008-9066-2](https://doi.org/10.1007/s11003-008-9066-2)
26. Ivanova ND, Ivanov SV, Boldyrev EI, Sokol'skii GV, Makeeva S (2002) High-performance manganese oxide catalysts for CO oxidation. *Russ J Appl Chem* 75(9):1452–1455. doi:[10.1023/A:1022216626347](https://doi.org/10.1023/A:1022216626347)
27. Vasilyeva MS, Rudnev VS (2014) Composition, surface structure and catalytic properties of manganese- and cobalt-containing oxide layers on titanium. *Adv Mater Res* 875–877:351–355. doi:[10.4028/www.scientific.net/amr.875–877.351](https://doi.org/10.4028/www.scientific.net/amr.875-877.351)
28. Cherniayeva O, Lunarska E, Sakhnenko N, Ved M (2009) Modyfikacja powierzchni tytanu metoda elektrochemiczno plazmowa. *Inzynieria Materialowa* 5:298–301
29. Snytnikov PV, Belyaev VD, Sobyanyin VA (2007) Kinetic model and mechanism of the selective oxidation of CO in the presence of hydrogen on platinum catalysts. *Kinet Catal* 48(1):93–102. doi:[10.1134/s0023158407010132](https://doi.org/10.1134/s0023158407010132)
30. Lunarska E, Cherniayeva O, Ved M, Sakhnenko N (2007) Oxide film formed on Ti by the microark anodic method. *Ochrona przed Korozja* 11A:65–269
31. Krishna DSR, Sun Y (2005) Thermally oxidised rutile-TiO<sub>2</sub> coating on stainless steel for tribological properties and corrosion resistance enhancement. *Appl Surf Sci* 252(4):1107–1116. doi:[10.1016/j.apsusc.2005.02.046](https://doi.org/10.1016/j.apsusc.2005.02.046)



# Chapter 39

## Gold Nanoparticle/Polymer/Enzyme Nanocomposite for the Development of Adenosine Triphosphate Biosensor

Ivan S. Kucherenko, Carole Farre, Gaetan Raimondi, Carole Chaix, Nicole Jaffrezic-Renault, Oleksandr O. Soldatkin, Alexei P. Soldatkin, and Florence Lagarde

### 39.1 Introduction

Biosensors represent a group of advanced analytical devices suitable for the determination of a variety of substances in liquid or gaseous samples. Biosensors consist of a biomaterial and a transducer in close contact with each other [24]. The biomaterial (e.g., enzymes) serves as a sensing element, which selectively interacts with a target substance, while the transducer (e.g., an electrode in the case of electrochemical biosensors) records the signal issued from the biomaterial/analyte interaction.

---

I.S. Kucherenko (✉)

Laboratory of Biomolecular Electronics, Institute of Molecular Biology and Genetics, National Academy of Sciences of Ukraine, Zabolotnogo Street 150, 03143, Kyiv, Ukraine  
e-mail: [kucherenko.i.s@gmail.com](mailto:kucherenko.i.s@gmail.com)

C. Farre • G. Raimondi • C. Chaix • N. Jaffrezic-Renault • F. Lagarde  
Univ Lyon, CNRS, Université Claude Bernard Lyon1, ENS de Lyon, Institut des Sciences Analytiques, UMR5280, 5 Rue de la Doua, 69100, Villeurbanne, France  
e-mail: [carole.farre@isa-lyon.fr](mailto:carole.farre@isa-lyon.fr); [gaetan.raimondi@isa-lyon.fr](mailto:gaetan.raimondi@isa-lyon.fr); [carole.chaix@isa-lyon.fr](mailto:carole.chaix@isa-lyon.fr); [nicole.jaffrezic@isa-lyon.fr](mailto:nicole.jaffrezic@isa-lyon.fr); [florence.lagarde@isa-lyon.fr](mailto:florence.lagarde@isa-lyon.fr)

O.O. Soldatkin • A.P. Soldatkin

Laboratory of Biomolecular Electronics, Institute of Molecular Biology and Genetics, National Academy of Sciences of Ukraine, Zabolotnogo Street 150, 03143, Kyiv, Ukraine

Institute of High Technologies, Taras Shevchenko National University of Kyiv, Volodymyrska Street 64, 01601, Kyiv, Ukraine  
e-mail: [alex\\_sold@yahoo.com](mailto:alex_sold@yahoo.com); [a\\_soldatkin@yahoo.com](mailto:a_soldatkin@yahoo.com)

© Springer International Publishing AG 2017

O. Fesenko, L. Yatsenko (eds.), *Nanophysics, Nanomaterials, Interface Studies, and Applications*, Springer Proceedings in Physics 195,  
DOI 10.1007/978-3-319-56422-7\_39



The immobilization of the biological material onto the sensitive region of the electrode is a key step in biosensor development [23] as it may significantly affect analytical characteristics of the biosensor (i.e., sensitivity, linear range, reproducibility, stability, etc.).

In recent years, the capacity of a variety of nanomaterials and nanostructures to improve the biosensor performances has been demonstrated [8]. For example, porous nanomaterials like zeolites have been proposed as adsorbents for biosensing elements in electrochemical biosensors [12]. Other nanostructures as carbon nanotubes, conductive polymers, and different types of nanoparticles have been shown to be able to increase electron transfer between the biorecognition element and the transducer [2]. This is the most common approach used for the development of the third generation of electrochemical enzyme biosensors, which enables direct electron transfer from the enzymes to the electrode and operate at low potentials, limiting the risk of interference [5]. Owing to their quite simple procedure of synthesis and the excellent conducting properties, gold nanoparticles (GNPs) are often used in the elaboration of electrochemical biosensors. GNPs decrease insulating properties of the polymer/enzyme films and improve electron transfer between enzymes and the electrode. GNPs can electrically make a contact between the redox center of the enzyme and the electrodes [27].

Adenosine triphosphate (ATP) is a widespread organic molecule used as a short-term energy carrier in all living organisms. New ATP molecules are mostly created during decomposition of carbohydrates, but also in many other biochemical reactions. ATP molecules are involved (directly or indirectly) in almost all cellular processes such as molecular synthesis, transport, movements, regulation, etc. Furthermore, ATP takes part in many physiological reactions such as transmission of nerve impulses, thromboregulation, regulation of immune system, and gastrointestinal motility. Thus, monitoring the concentration of ATP, especially in the biochemical, molecular-biological, and biotechnological samples, as well as in vivo in tissues and cells, is very important [1, 7, 9].

Analytical methods available for ATP determination include luciferase assays and spectrophotometric and chromatographic techniques. These methods are sensitive, quite selective, and convenient. However, they require large and expensive equipment, and it is hard (often impossible) to use them for the real-time or in vivo measurements of the ATP concentrations [4, 10]. Development of the ATP-sensitive biosensors can help to overcome these disadvantages.

Most of the electrochemical biosensors recently reported for the ATP determination are based on the amperometric transducers and two enzyme systems: glucose oxidase (GOx)/hexokinase (HEX) and glycerol kinase-glycerol-3-phosphate oxidase [4, 11, 14, 16, 19, 22, 25]. A conductometric ATP-sensitive biosensor based on a single enzyme (HEX) has been also proposed [13]. The biosensors based on GOx/HEX generally demonstrate better analytical characteristics than those based on glycerol kinase-glycerol-3-phosphate oxidase. Various modes of immobilization have been proposed for GOx/HEX bienzymatic system, including cross-linking by

glutaraldehyde, entrapment in polyphenol films, entrapment in electropolymerized anodic electrophoretic deposition paint, and immobilization in the silica hybrid sol-gel film. Among them, entrapment in a biocompatible hydrophilic matrix is very attractive as it provides the enzyme a favorable environment able to preserve its biological activity.

In this work, we evaluated two different methods of GOx/HEX immobilization based on entrapment into cross-linked polymers (i.e., photo-cross-linked poly(vinyl alcohol) bearing styrylpyridinium groups, PVA-SbQ, and poly(vinyl alcohol)/poly(ethylenimine), PVA/PEI, chemically cross-linked with glutaraldehyde, GA). The aim was to improve the sensitivity of GOx/HEX biosensors already reported in the literature for ATP determination. These two polymer matrices have been selected because they have already been successfully used for the production of GOx-based biosensors in our group [20, 21]. For comparison, we also immobilized the enzymes using a classical method, which consists in cross-linking by glutaraldehyde (GA) in the presence of BSA [18, 26]. The effect of GNP addition into the PVA-SbQ matrix was also tested. To the best of our knowledge, this is the first time that GNPs are combined to a polymer matrix and GOx/HEX system to produce ATP biosensor.

## 39.2 Experimental

### 39.2.1 Materials

Hexokinase (HEX, EC 2.7.1.1; activity,  $\geq 25$  U/mg) from *Saccharomyces cerevisiae* and glucose oxidase (GOx, EC 1.1.3.4; activity, 128 U/mg) from *Aspergillus niger* (Sigma-Aldrich, USA) were used as biorecognition elements. Bovine serum albumin (BSA, fraction V,  $\geq 96\%$ ), glucose ( $\geq 99.5\%$ ), adenosine triphosphate (ATP, disodium salt hydrate, grade 1,  $\geq 99\%$ ), magnesium chloride ( $\geq 99\%$ ), glycerol ( $\geq 99\%$ ), HEPES ( $\geq 99.5\%$ ), polyvinyl alcohol (PVA, 87–89% hydrolyzed, Mw 85,000–124,000), polyethylenimine (PEI, 50% aqueous solution, Mw  $\sim 750,000$ , Mn  $\sim 60,000$ ), and glutaraldehyde (GA, 50% aqueous solution) have been purchased from Sigma-Aldrich company (USA). Polyvinyl alcohol bearing styrylpyridinium pendent groups (PVA-SbQ, SPP-H-13: degree of polymerization 1700, degree of saponification 88, betaine SbQ 1.3 mol%, solid content 13.35 wt%, pH 6.2) was from Toyo Gosei (Japan). All other chemicals were of analytical grade. All reagents were used without further purification. All aqueous solutions were prepared using ultrapure water (resistivity  $>18$  M $\Omega$  cm) obtained from a Milli-Q purification system.

Citrated GNPs ( $1.1 \times 10^9$  NPs/mL) were produced using the classical Turkevich and Frens method following the protocol already described elsewhere [20]. Average size of the particles, as determined by transmission electron microscopy, was 18 nm.

### **39.2.2 Design of Amperometric Transducers**

In this work, platinum disk electrodes of our own production served as amperometric transducers. A platinum wire (0.4 mm in diameter, 3 mm long) was sealed at the end of a glass capillary with an outer diameter of 3.5 mm. An open end of the wire served as working surface. An inner end of the platinum wire was connected to a copper wire, placed inside the capillary, using fusible Wood's alloy. A contact pad for connecting to the measuring setup was placed at the other end of the copper wire. The working surface of platinum electrodes was cleaned by immersing it into a concentrated sulfuric acid for 30 s and washing with water and ethanol wetted cotton swab prior to enzyme immobilization. The platinum surface was periodically renewed by grinding using a 12 $\mu$  abrasive paper disk 800/2400.

### **39.2.3 Immobilization Procedures**

Two enzymes (GOx and HEX) were immobilized onto the sensitive surface of the working electrodes following the procedures described below. Loading of both enzymes, GOx (0.5%) and HEX (2.5%), was kept constant to facilitate the comparison between different immobilization methods.

#### **39.2.3.1 Immobilization via GA Cross-Linking in the Presence of BSA**

Mother solution used for the preparation of working membranes contained 1% GOx (hereafter, w/w), 5% HEX, 3% BSA, and 10% glycerol in 20 mM phosphate buffer, pH 7.2. Glycerol was added to stabilize the enzymes and to prevent the early drying of the solution on the transducer surface. BSA helped stabilizing the enzymes through the formation of intermolecular bindings. Equivolumes of this solution and a 0.8% aqueous solution of GA cross-linking agent were mixed, and 150 nL was immediately deposited onto the transducer working surface using a 500 nL microsyringe. Afterward, the created biosensors were dried for 40 min in air at room temperature. During this time, cross-linking of the enzymes and BSA by GA occurred. The biosensors were then immersed in the working buffer for 10 min in order to stop cross-linking reaction and wash out unbound components. Biosensors prepared with other concentrations of GOx and HEX, which were used in the first part of the work, were prepared in the same way, just changing GOx and HEX concentrations of mother solutions.

#### **39.2.3.2 Immobilization in Cross-Linked PVA-SbQ Matrix**

In this case, the enzyme mother solution contained 1% GOx and 5% HEX in 20 mM phosphate buffer, pH 7.2. PVA-SbQ aqueous solution containing 6.68% of the polymer was prepared by dilution of the commercial 13.35% PVA-SbQ solution

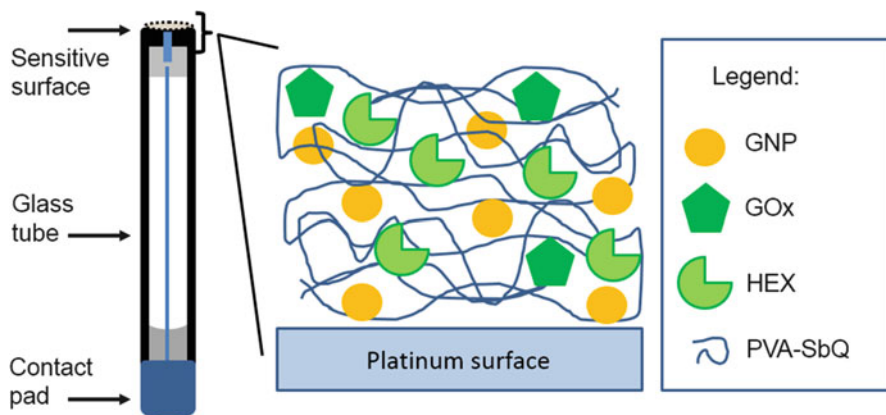


Fig. 39.1 Scheme of the PVA-SbQ/GNP biosensor

with ultrapure water followed by stirring for 2 h. The enzyme and 6.68% PVA-SbQ solutions were thoroughly mixed (1:1 volume ratio), and 150 nL of the mixture was immediately deposited onto the transducer working surface. The modified transducers were exposed to UV irradiation for 10 min at a Bio-Link BLX UV-cross-linker (Vilber Lourmat) equipped with one 100 W UV lamp (365 nm), inducing PVA-SbQ cross-linking and therefore HEX and GOx entrapment into the polymer matrix. The created biosensors were finally dried at a room temperature for 20 min and then used for measurements.

In order to prepare biosensors with GNPs, this procedure was slightly modified: the solution containing 2% GOx and 10% HEX was mixed (1:3 volume ratio) with 4.45% PVA-SbQ solution containing  $0.7 \times 10^9$  GNPs/ml. Thus the final mixture contained the same GOx and HEX amounts as in all other cases. Figure 39.1 shows the scheme of the PVA-SbQ/GNP biosensor obtained this way.

Twice higher PVA-SbQ concentration was also checked, but the obtained enzymes/PVA-SbQ mixture was too viscous for manipulations and thus was not further used.

### 39.2.3.3 Immobilization in Cross-Linked PVA/PEI Matrix

This method of immobilization was adapted from F. Dridi et al. [6]. The initial mixture contained 0.67% GOx, 3.3% HEX, 0.06% PVA, and 0.02% PEI, in 8.9 mM phosphate buffer, pH 7.2, with or without  $0.73 \times 10^9$  GNPs/ml. This solution was thoroughly mixed (3:1 volume ratio) with GA (1.6% aqueous solution), and 150 nL of the mixture was immediately deposited onto the transducer working surface. The created sensor elements were dried for 40 min in air at room temperature and then immersed in the working buffer for 10 min in order to stop cross-linking reaction and wash out unbound components.

In an alternative procedure, the same enzyme mixture was mixed (3:1 volume ratio) with ultrapure water (to obtain the same concentration of the enzymes as was used in all cases) and deposited on the electrodes. The transducers were then placed into saturated GA vapors for 30 min for cross-linking.

### 39.2.4 Working Conditions

The amperometric biosensor was placed in an electrochemical cell with an auxiliary electrode (platinum wire) and a reference electrode (saturated Ag/AgCl produced by Hach Lange, France) that were connected to a PalmSens potentiostat (Palm Instruments BV, Netherlands). The measurements were carried out at room temperature in an open measuring cell containing 5 mL of working buffer, at permanent stirring by a magnetic stirrer and at constant potential of 0.6 V versus Ag/AgCl reference electrode. Ten-mM HEPES, pH 7.4, with 3 mM of  $Mg^{2+}$  was used as the working buffer in all experiments. Magnesium ions were needed to preserve HEX biological activity. Higher concentration of HEPES (25 mM) was also tested, but the biosensor responses did not differ from those obtained in 10 mM HEPES. So, 10 mM HEPES was preferred. Substrate concentrations in the working cell were obtained by the addition of aliquots of stock solutions (100 mM and 500 mM glucose and 50 mM ATP). The value of biosensor responses were calculated after reaching steady state.

## 39.3 Results and Discussion

### 39.3.1 The Principle of Biosensor Operation

As already described in a former publication [11], GOx/HEX biosensor working principle is based on two simultaneous enzymatic reactions and the reaction of hydrogen peroxide oxidation on the working electrode, occurring when applying a suitable potential and followed with generation of electrons, which can be directly registered by the amperometric transducer:

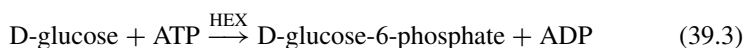
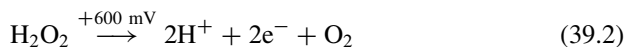
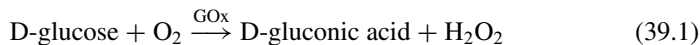
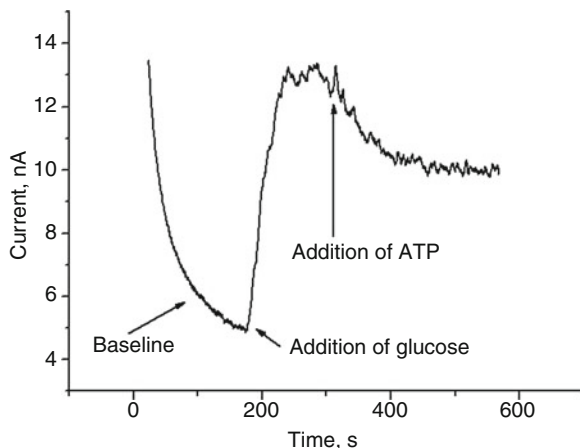


**Fig. 39.2** An example of the biosensor response to subsequent additions of glucose and ATP



In the presence of glucose and the absence of ATP, only the reactions (39.1) and (39.2) take place on the electrode surface: glucose oxidase oxidizes glucose and produces hydrogen peroxide. The latter is oxidized on the surface of the transducer, generating current that is registered as an amperometric signal. In this case, the biosensor response is directly proportional to glucose concentration. After addition of ATP to the working cell, HEX phosphorylates glucose by transferring a phosphate group from ATP (reaction (39.3)). This reaction reduces the local concentration of glucose, and, consequently, the biosensor response to glucose decreases in proportion to the ATP concentration. A typical biosensor response to glucose and ATP is shown in Fig. 39.2.

### 39.3.2 Optimization of GOx and HEX Concentrations and GOx/HEX Ratio

The biosensor response to ATP is produced as a result of competition between two immobilized enzymes (GOx and HEX) for glucose. Thus, the biomembrane composition, namely, the amount and ratio of GOx and HEX, is an important parameter, which will strongly affect the biosensor operation.

In the first stage of the work, different concentrations of GOx (from 0.25% to 2.5%) and HEX (from 1% to 5%) in biomembrane of the biosensor were tested. The study was performed by immobilizing the enzymes through cross-linking in the presence of BSA, the aim being to find the best conditions to get the highest sensitivity for both glucose and ATP. The biosensor sensitivity to glucose did not depend on the concentration of GOx in the 0.5–2.5% range and slightly decreased for 0.25% GOx. The highest sensitivity to ATP was achieved for 2.5% of HEX.

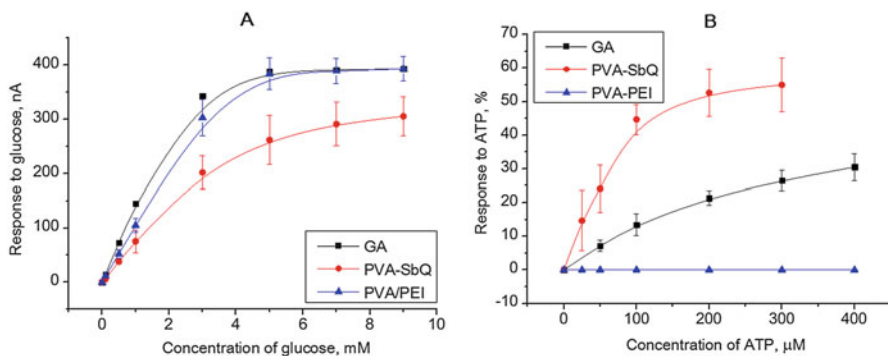


**Fig. 39.3** Calibration curves for glucose (a) and ATP (b) determination of the biosensor based on GOx and HEX immobilized via different methods. Concentration of glucose during ATP determination was 100  $\mu\text{M}$

Thus, 0.5% GOx and 2.5% HEX concentrations in the biomembrane were chosen for further experiments. Considering five times higher activity per mg of GOx, nominal activities of GOx and HEX in biomembrane were almost equal at this GOx/HEX ratio.

### 39.3.3 *Effect of Immobilization Procedure on the Analytical Characteristics of the Biosensor*

The three methods of GOx/HEX described in the experimental section were further compared. Figure 39.3 shows biosensors' response to glucose and ATP (each point represents mean values of responses of four different biosensors  $\pm$  standard deviation). The highest responses and sensitivities to glucose were obtained when enzymes were immobilized through cross-linking in the presence of BSA or entrapment into the PVA/PEI matrix. In both cases, the response to glucose was linear in the 10  $\mu\text{M}$  to 3 mM range (Fig. 39.3a). Sensitivity observed for PVA-SbQ immobilization was lower, which may be attributed to the slower diffusion of glucose through the high-density PVA-SbQ membrane, but linear range was much wider – up to 7 mM in logarithmic coordinates.

The biosensors' response to ATP, calculated as the decrease of glucose response after addition of ATP, is shown in Fig. 39.3b. Contrary to what was observed for glucose determination, the highest sensitivity to ATP and the widest linear range (up to 100  $\mu\text{M}$ ) were obtained using the PVA-SbQ immobilization matrix. Biosensors based on enzyme cross-linking in the presence of BSA exhibited a much lower sensitivity and a similar linear range, while no response was observed using the PVA/PEI immobilizing matrix.

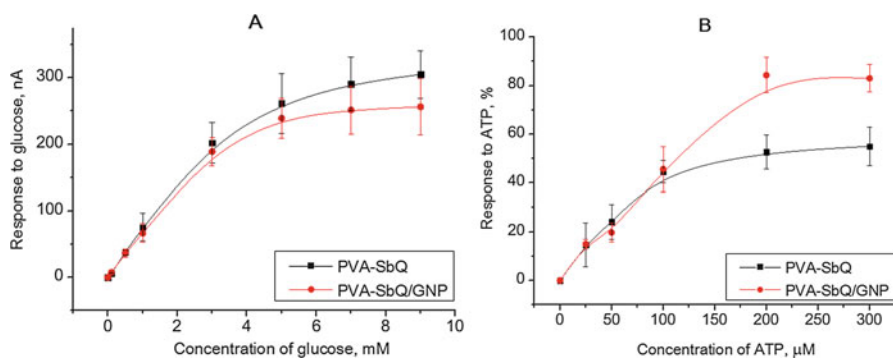


**Fig. 39.4** Calibration curves for glucose (a) and ATP (b) determination of the biosensors based on GOx and HEX immobilized in PVA-SbQ with and without GNPs

Using GA vapor instead of liquid GA for cross-linking and increasing ten times PVA/PEI concentration did not help improving the PVA-/PEI-based biosensor response to glucose or ATP. It seems that PVA/PEI blend is not suitable for immobilization of HEX in the presence of GOx, while it had been demonstrated as suitable for individual GOx immobilization [20]. This may be due to the creation of an unfavorable environment for HEX, GOx, and HEX being both negatively charged in the immobilization conditions (isoelectric point of GOx is 4.2 and isoelectric point of HEX is 4.93–5.25 depending on isozyms), with PEI being positively charged. This environment may induce a change in HEX conformation, leading to a loss in enzyme activity.

Doubling both GOX and HEX concentrations in the biomembrane (1% GOx, 5% HEX, 3.3% PVA-SbQ) led to a decrease in biosensor response, probably due to enzyme aggregation. Aggregation may hamper substrate access to the active site of the enzymes or decrease their activity by changing their conformation.

### 39.3.4 Effect of GNPs on Analytical Characteristics of the Biosensors

Since biosensors based on PVA-SbQ demonstrated the highest sensitivity to ATP, further experiments were carried out using this matrix of immobilization. GNPs were added to the enzyme/PVA-SbQ mixture, and analytical characteristics of the biosensors were compared with those of the biosensors prepared without GNPs.

As seen in Fig. 39.4, GNPs did not improve significantly the biosensor sensitivity to glucose or ATP. On the contrary, a wider linear range (up to 200  $\mu\text{M}$ ) could be achieved for ATP by adding the GNPs (Fig. 39.4b).



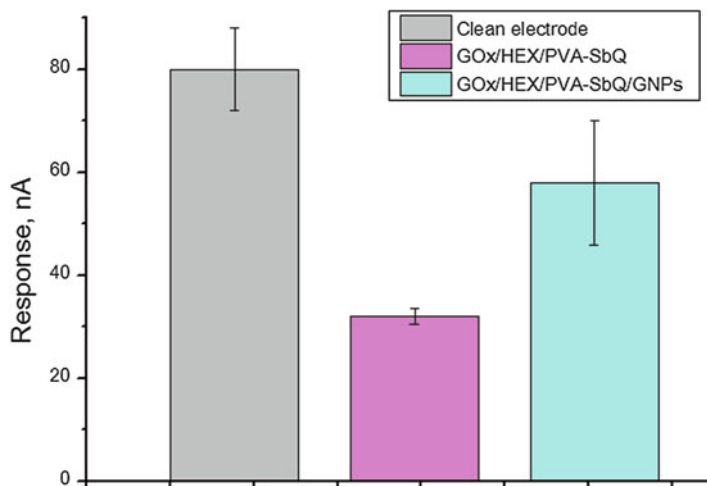


**Fig. 39.5** Comparison of the responses to hydrogen peroxide (100  $\mu\text{M}$ ) obtained with a clean working electrode and with biosensors based on enzymes immobilized in PVA-SbQ without and with GNPs

Biosensor responses were not modified by decreasing GNP concentration added to the biomembrane ( $0.36 \times 10^9$  GNPs/ml instead of  $0.73 \times 10^9$  GNPs/ml) but were higher than without GNPs.

As was described earlier, the proposed biosensor principle is based on the detection of hydrogen peroxide oxidation on the electrode surface. Thus, sensitivity of the biosensor to substrates depends on sensitivity to hydrogen peroxide. We obtained responses to 100  $\mu\text{M}$   $\text{H}_2\text{O}_2$  with a clean working electrode and with biosensors based on enzymes immobilized in PVA-SbQ without and with GNPs (Fig. 39.5). It was found that after coverage of the electrode-sensitive region with PVA-SbQ, sensor sensitivity to  $\text{H}_2\text{O}_2$  decreased threefold because of the insulating properties of PVA-SbQ. The polymer is not conductive and blocks electron transfer in the near-electrode area. On the contrary, after addition of the GNPs, the sensor sensitivity increased greatly, since GNPs actively participate in the transfer of electrons (generated from  $\text{H}_2\text{O}_2$  oxidation) to the electrode surface.

Considering all these data, we used enzyme mixture (0.5% GOx and 2.5% HEX) with PVA-SbQ (3.3%) and  $0.73 \times 10^9$  GNPs/ml for the preparation of ATP-sensitive biosensors. Although responses to glucose in the case of PVA-SbQ were lower than those for biosensors based on GA cross-linking, sensitivity to ATP was much better.

Operational and storage stabilities were further assessed as these are key parameters for long-term use of the biosensors. For operational stability, the biosensor responses to glucose and ATP were measured for several hours. One measurement of glucose and ATP took about 5–8 min (this time included baseline stabilization, steady-state response to glucose, and steady-state response to ATP), the interval between measurements was about 10 min, and during the intervals the biosensor was

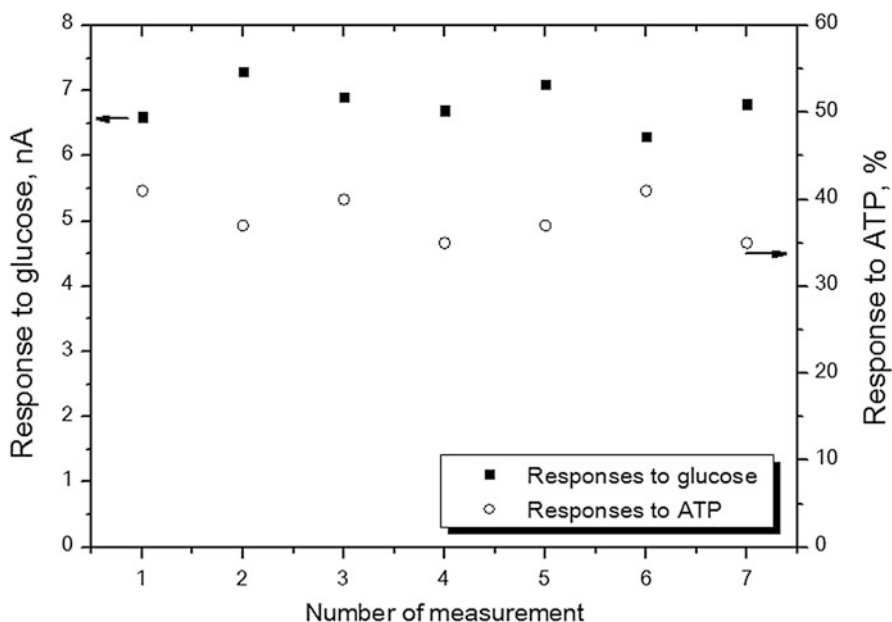


**Fig. 39.6** One-day operational stability of the biosensor responses to 100  $\mu\text{M}$  of glucose and 100  $\mu\text{M}$  of ATP

repeatedly washed with working buffer. The biosensor was stable for one working day, no significant decrease of the responses to glucose and ATP (100  $\mu\text{M}$  each) being observed (Fig. 39.6).

After storage of the biosensors for 16 days in a dry state at  $-18\text{ }^{\circ}\text{C}$ , only 7% decrease of the response to glucose and 11% of the response to ATP were observed. The proposed biosensor is much more stable than biosensors based on GOx/HEX previously reported in the literature [3, 14, 15], which may be due to the stability effect provided by the polymer/GNP environment as already shown for GOx [17].

The higher decrease in biosensor response to ATP may be assigned to the lower stability of HEX than GOx [11].

## 39.4 Conclusions

An amperometric biosensor based on a bienzyme system (GOx/HEX) for the ATP determination has been developed. Three different methods of GOx/HEX immobilization on the surface of working electrodes were investigated. The best results for the ATP determination were obtained with the biosensors based on the entrapment of GOx and HEX in photopolymerized PVA-SbQ. Addition of 18-nm GNPs to the immobilization mixture led to further increase of the biosensor

sensitivity and widening of the linear range of the ATP determination. It was demonstrated that the presence of GNPs improved sensitivity of the biosensors to the main product of the enzymatic reaction – hydrogen peroxide – which is directly detected by the working electrode during the biosensor work, which is probably caused by the improvement of the conductivity of enzymes/PVA-SbQ composite.

**Acknowledgments** The authors gratefully acknowledge the financial support of this study by Project European IRSES-318524-NANODEV. Furthermore, this study was partly supported by the NASU in the frame of Scientific and Technical Program “Sensor devices for medical-ecological and industrial purposes: metrology and trial performance.” I. Kucherenko thanks the French Ministry of Higher Education and Research and Campus France for his PhD grant.

## References

1. Alvarez A, Lagos-Cabr e R, Kong M et al (2016) Integrin-mediated transactivation of P2X7R via hemichannel-dependent ATP release stimulates astrocyte migration. *Biochim Biophys Acta, Mol Cell Res* 1863:2175–2188
2. Biloivan OA, Rogaleva NS, Korpan YI (2010) Optimization of bioselective membrane of amperometric enzyme sensor on basis of glucose oxidase using NH<sub>2</sub>-modified multi-wall carbon nanotubes. *Biopolym Cell* 26:56–63
3. Compagnone D, Guilbault G (1997) Glucose oxidase/hexokinase electrode for the determination of ATP. *Anal Chim Acta* 340:109–113
4. Dale N, Frenguelli B (2012) Measurement of purine release with microelectrode biosensors. *Purinergic Signal* 8:S27–S40
5. Das P, Das M, Chinnadayala S et al (2016) Recent advances on developing 3rd generation enzyme electrode for biosensor applications. *Biosens Bioelectron* 79:386–397
6. Dridi F, Marrakchi M, Gargouri M et al (2015) Thermolysin entrapped in a gold nanoparticles/polymer composite for direct and sensitive conductometric biosensing of ochratoxin a in olive oil. *Sensors Actuators B Chem* 221:480–490
7. Fuentes E, Palomo I (2015) Extracellular ATP metabolism on vascular endothelial cells: a pathway with pro-thrombotic and anti-thrombotic molecules. *Vasc Pharmacol* 75:1–6
8. Hayat A, Catanante G, Marty J (2014) Current trends in nanomaterial-based amperometric biosensors. *Sensors* 14:23439–23461
9. Kennedy C (2015) ATP as a cotransmitter in the autonomic nervous system. *Auton Neurosci* 191:2–15
10. Khlyntseva S, Bazel’ Y, Vishnikin A et al (2009) Methods for the determination of adenosine triphosphate and other adenine nucleotides. *J Anal Chem* 64:657–673
11. Kucherenko I, Didukh D, Soldatkin O et al (2014) Amperometric biosensor system for simultaneous determination of adenosine-5'-triphosphate and glucose. *Anal Chem* 86:5455–5462
12. Kucherenko I, Soldatkin O, Kasap BO et al (2015) Nanosized zeolites as a perspective material for conductometric biosensors creation. *Nanoscale Res Lett* 10:209
13. Kucherenko IS, Kucherenko DY, Soldatkin OO et al (2016) A novel conductometric biosensor based on hexokinase for determination of adenosine triphosphate. *Talanta* 150:469–475
14. Kueng A, Kranz C, Mizaikoff B (2004) Amperometric ATP biosensor based on polymer entrapped enzymes. *Biosens Bioelectron* 19:1301–1307
15. Liu S, Sun Y (2007) Co-immobilization of glucose oxidase and hexokinase on silicate hybrid sol-gel membrane for glucose and ATP detections. *Biosens Bioelectron* 22:905–911

16. Llaudet E, Hatz S, Droniou M et al (2005) Microelectrode biosensor for real-time measurement of ATP in biological tissue. *Anal Chem* 77:3267–3273
17. Luo X-L, Xu J-J, Du Y, Chen H-Y (2004) A glucose biosensor based on chitosan–glucose oxidase–gold nanoparticles biocomposite formed by one-step electrodeposition. *Anal Biochem* 334:284–289
18. Migneault I, Dartiguenave C, Bertrand M (2004) Glutaraldehyde: behavior in aqueous solution, reaction with proteins, and application to enzyme crosslinking. *BioTechniques* 37:790–802
19. Patel B, Rogers M, Wieder T et al (2011) ATP microelectrode biosensor for stable long-term in vitro monitoring from gastrointestinal tissue. *Biosens Bioelectron* 26:2890–2896
20. Sapountzi E, Braiek M, Farre C et al (2017) Gold nanoparticles assembly on electrospun poly(vinyl alcohol)/poly(ethyleneimine)/glucose oxidase nanofibers for ultrasensitive electrochemical glucose biosensing. *Sens Actuators B Chem* 238:392–401
21. Sapountzi E, Braiek M, Farre C et al (2015) One-step fabrication of electrospun photo-cross-linkable polymer nanofibers incorporating multiwall carbon nanotubes and enzyme for biosensing. *J Electrochem Soc* 162:B275–B281
22. Soldatkin O, Schuvailo O, Marinesco S et al (2009) Microbiosensor based on glucose oxidase and hexokinase co-immobilised on platinum microelectrode for selective ATP detection. *Talanta* 78:1023–1028
23. Teles FRR, Fonseca LP (2008) Applications of polymers for biomolecule immobilization in electrochemical biosensors. *Mater Sci Eng C* 28:1530–1543
24. Thevenot D, Toth K, Durst R, Wilson G (1999) Electrochemical biosensors: recommended definitions and classification. *Pure Appl Chem* 71:2333–2348
25. Vanegas D, Clark G, Cannon A et al (2015) A self-referencing biosensor for real-time monitoring of physiological ATP transport in plant systems. *Biosens Bioelectron* 74:37–44
26. Walt D, Agayn V (1994) The chemistry of enzyme and protein immobilization with glutaraldehyde. *TrAC Trends Anal Chem* 13:425–430
27. Xiao Y, Patolsky F, Katz E et al (2003) “plugging into enzymes”: nanowiring of redox enzymes by a gold nanoparticle. *Science* 299:1877–1881

# Chapter 40

## Novel Ferromagnetic Iron-Based Nanocomposite Powders with High Magnetic Characteristics

N. F. Kuschevskaya, V. V. Malyshev, D. B. Shakhnin, and E. A. Paprotskaya

### 40.1 Introduction

Problems of development of new nanoscale ferromagnetic composite powders for biology, medicine, microengineering, and electrical engineering, as well as the development of improved technologies based on nanoscale materials are urgent problems of our time. Magnetic iron-based powders are used, e.g., in pharmacology to produce a new class of biologically active substances, in medicine to create a magnetically controlled carrier formulations to deliver them to the target organ which greatly increases the effectiveness of medicines while reducing their adverse side effects, in immunology as markers to study cellular and humoral immunity and natural resistance, in food processing and veterinary medicine for the prevention and treatment of diseases of different etiology associated with iron deficiency, in biology to determine the effects of iron on the processes of respiration and photosynthesis of plants in order to improve the nutritional and energy value of forage crops, in the chemical industry as dyes for food and cosmetic preparations, and also as catalysts for chemical reactions.

For the use of iron-based composite nanomaterials, powders for medicine, biology, food, and chemical industries should have the necessary complex of physicochemical and medico-biological properties, such as high specific surface area; good magnetic characteristics; high corrosion resistance, particularly in biological media of the body; adsorption capacity; absence of pyrophorosity and harmful impurities; hypoallergenicity; and antibacterial properties [1, 4].

---

N.F. Kuschevskaya (✉) • V.V. Malyshev • D.B. Shakhnin • E.A. Paprotskaya  
University “Ukraine”, Kyiv, Ukraine  
e-mail: [kushchevskaya@email.ua](mailto:kushchevskaya@email.ua)

As food supplements, iron powders are produced for a long time by such large companies as “Hoganas” (Holland), “QMP” (Canada), “OMG” (USA), BASF (Germany), and “Industrial Metal Powders” (India) [5].

However, until now, the question remains actual on the development and preparation of nano-sized iron powders with preset complex of physicochemical and medico-biological properties required for use in biology and medicine.

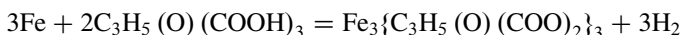
The aim of this work is to develop and to obtain iron-based nano-dispersed magnetic powders of controlled phase composition with high specific surface area and good magnetic characteristics.

## 40.2 Materials and Methods

In this paper, for the synthesis of nano-sized iron-based powder, a combination of method of decomposition and reduction of iron citrate  $\text{Fe}_3\{\text{C}_3\text{H}_5(\text{O})(\text{COO})_3\}_2$  by hydrocarbons mixture and of modified procedure including further prolonged surface passivation of obtained iron powder was used.

In certain process conditions, thermal decomposition of the iron citrate  $\text{Fe}_3\{\text{C}_3\text{H}_5(\text{O})(\text{COO})_2\}_3$  in a reducing atmosphere produces a nano-sized iron powder.

Iron citrate  $\text{Fe}_3\{\text{C}_3\text{H}_5(\text{O})(\text{COO})_3\}_2$  was prepared by the following reaction:



Decomposition of iron citrate was carried out in the hydrocarbons mixture atmosphere within the temperature range 250–500 °C in a specially designed protective sealed muffle providing a controlled gas medium. Muffle was equipped with a system of molds in the form of boats in which the layer thickness and the area of the powder to be treated are controlled.

X-ray diffraction studies of obtained powders were performed using X-ray diffractometer DRON-3.0 in  $\text{Co K}_\alpha$  radiation. The phase composition of the powders was determined by comparing the lattice spacing set calculated from the experimentally recorded diffraction patterns with those given in the international tables of diffraction data [3]. The relative quantities of found phases were defined from the heights ratio of the most intense lines of these phases at the diffraction patterns. Dimensions of coherent scattering regions (CSR),  $D$ , were calculated from the broadening of lines at the diffraction patterns with the use of Selyakov-Scherrer formula [2].

Measurements of magnetic characteristics of the obtained powder, namely, of specific saturation magnetization  $\sigma_s$ , of residual induction  $B_r$ , and of coercivity  $H_c$ , were carried out using the ballistic magnetometer within the field's strength range up to 10 kOe at room temperature.

Electron microscopy studies of the resulting powders were carried out with a scanning electron microscope JSM 6360 LA equipped with a system of X-ray spectral microanalysis JED-2200 with accelerating voltage 15 kV and with the electron probe diameter 4 nm.

### 40.3 Results and Discussion

Figure 40.1 shows the dependence of the degree of decomposition of iron citrate on the process temperature.

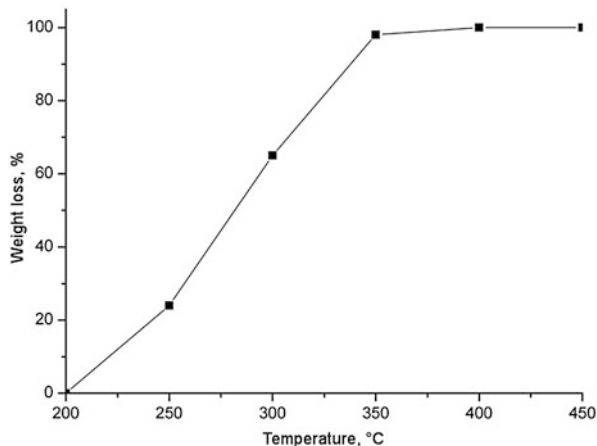
To control the phase composition and dispersion degree of the obtained powder, samples of synthesized product were collected at 250, 300, 325, 400, and 450 °C. Figure 40.1 shows that decomposition process and further weight loss is virtually finished after the 350 °C. The loss of weight of the product was calculated from the mass of the powder synthesized at 450 °C which was taken as 100%.

Figures 40.2, 40.3, and 40.4 show X-ray diffraction data of the powders obtained at different decomposition temperatures in hydrocarbons atmosphere. It has been shown that the powders produced by the decomposition-reduction of iron citrate contain three crystalline phases, namely, iron oxycarbide  $\text{FeC}_2\text{O}_4$ ,  $\alpha\text{-Fe}$ , and magnetite  $\text{Fe}_3\text{O}_4$ . The relative content of these phases, as well as the CSR size, depends on the temperature of these powder syntheses (see Figs. 40.2, 40.3, and 40.4). Thus, powders synthesized at 250 and 300 °C comprise only the crystalline phase of iron oxycarbide  $\text{FeC}_2\text{O}_4$  (Fig. 40.2).

As it can be seen from the data obtained, powders synthesized at 325 °C contain phase  $\text{FeC}_2\text{O}_4$ ,  $\alpha\text{-Fe}$ , and  $\text{Fe}_3\text{O}_4$  (Fig. 40.3a).

Synthesis temperature rise up to 350 °C leads to the disappearance of the crystal phase of iron oxycarbide  $\text{FeC}_2\text{O}_4$  from the powders' X-ray patterns (Fig. 40.3b). According to X-ray diffraction data, powders synthesized at 400 and 450 °C consist only of the crystalline phase  $\alpha\text{-Fe}$  (Fig. 40.4).

**Fig. 40.1** Mass loss of iron powder obtained from iron citrate salt during the reduction within the temperature range 250, 300, 325, 400, and 450 °C



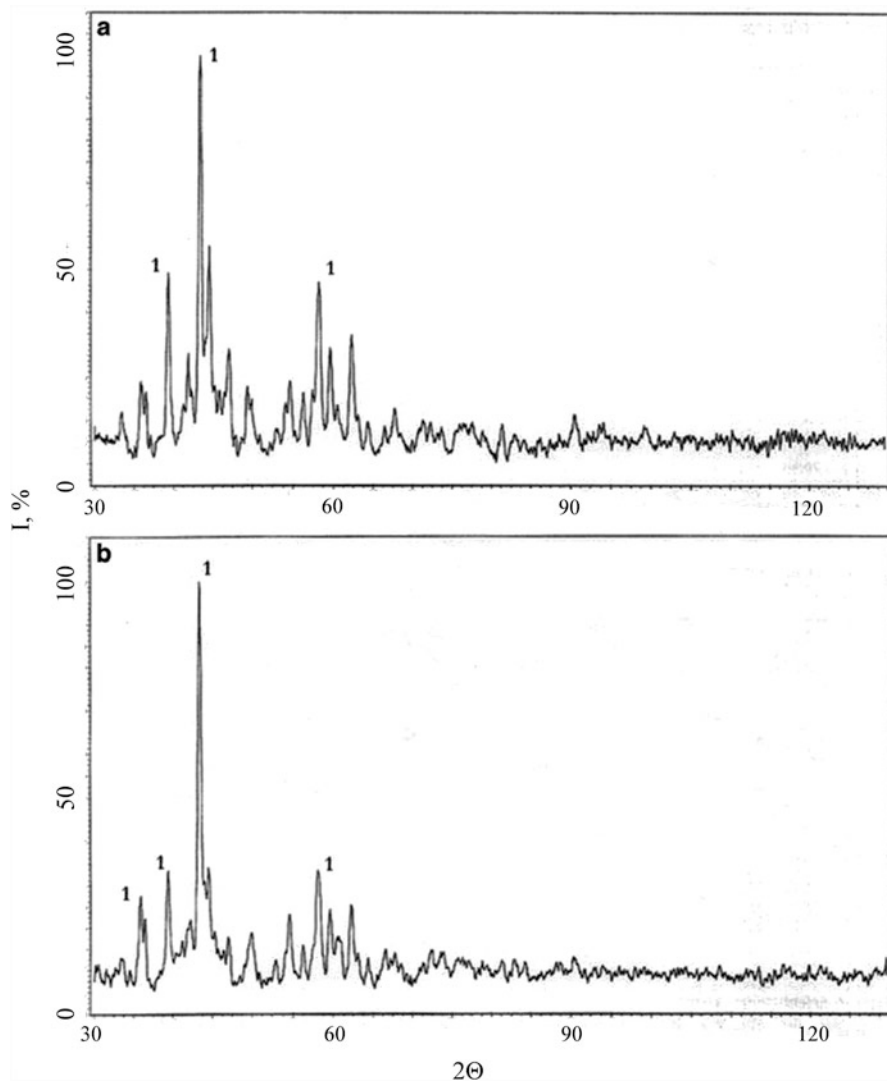


**Fig. 40.2** XRD patterns of powders produced by decomposition-reduction of iron citrate salt at temperatures (a) 250 °C and (b) 300 °C, 1 iron oxycarbide  $\text{FeC}_2\text{O}_4$

It should also be noted that the amount of the oxycarbide  $\text{FeC}_2\text{O}_4$  decreased and of  $\alpha\text{-Fe}$  (Table 40.1) increased with the increase of the synthesis temperature due to the intensification of processes of diffusion leading to the formation of aforementioned crystalline phases. Average size of CSR of magnetite  $\text{Fe}_3\text{O}_4$  is not possible to calculate because of the low intensity of the respective diffraction patterns.



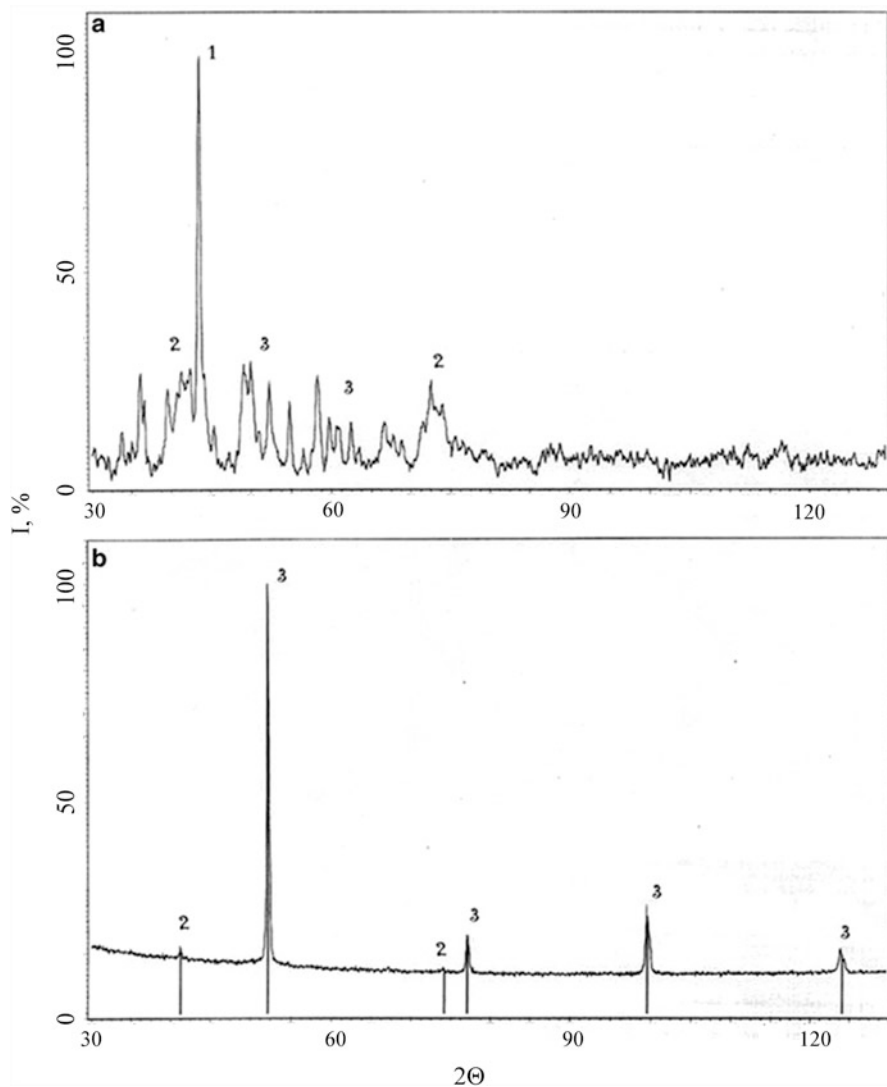


**Fig. 40.3** The XRD patterns of powders produced by decomposition-reduction of iron citrate salt at temperatures (a) 325 °C and (b) 350 °C; 1 iron oxycarbide  $\text{FeC}_2\text{O}_4$ , 2 magnetite  $\text{Fe}_3\text{O}_4$ , 3  $\alpha$ -Fe

As it can be seen from the data obtained, the powder's surface area increases with the increase of decomposition temperature due to the formation of multiple phases and slightly decreases with the transition to a single-phase system at 400–500 °C.

Dependence of the specific magnetization of the powders obtained by decomposition-reduction of iron citrate salt within a temperature range of 250, 300, 325, 400, and 500 °C on the magnetic field intensity is shown in Fig. 40.5.

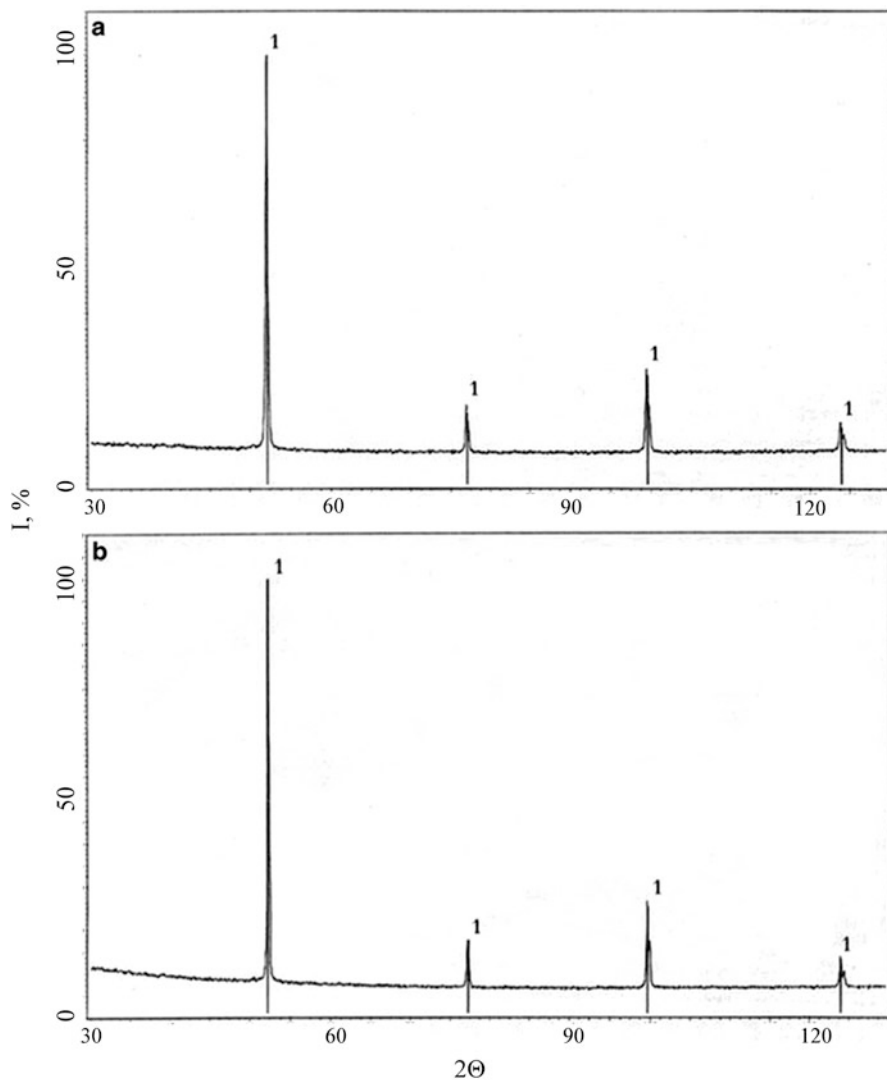


**Fig. 40.4** XRD patterns of powders produced by decomposition-reduction of iron citrate salt at temperatures: (a) 400 °C and (b) 450 °C;  $I$   $\alpha$ -Fe

The resulting curves have a shape characteristic for ferromagnetic materials, except powders synthesized at 250 and 300 °C (curves 2 and 3) which do not contain a ferromagnetic phase. With the increasing of the synthesis temperature, curves of dependence of the specific magnetization on field intensity move up along the y-axis toward the increase of their absolute values which also corresponds to the increase in the value of the specific saturation magnetization of obtained powders. This experimental finding is in full agreement with the results of X-ray phase analysis and caused by the increase of the content of the ferromagnetic  $\alpha$ -phase in powders with the increase of the synthesis temperature (Table 40.1). The increase in the

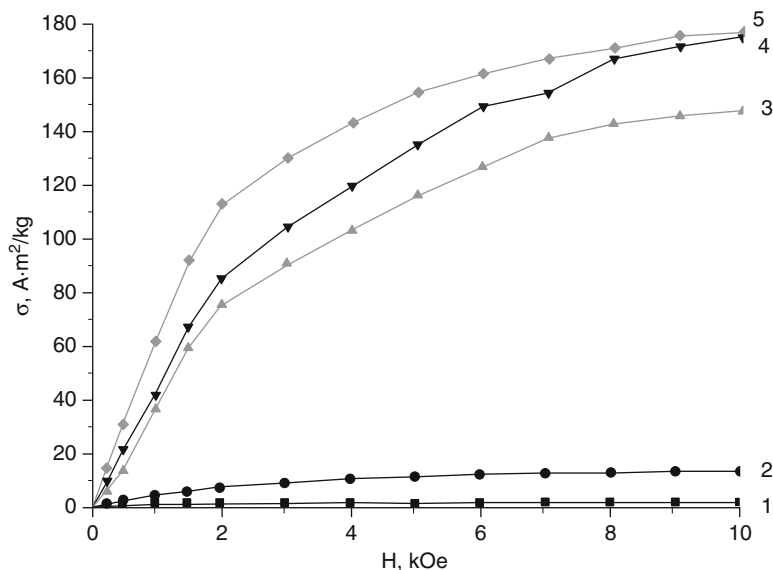


**Fig. 40.5** Dependence of the specific magnetization of the powders obtained by the decomposition-reduction of iron citrate salt on the magnetic field strength at temperatures 1 250; 2 300; 3 325; 4 400; and 5 500 °C

**Table 40.1** Phase composition and average size of CSR of powders obtained by decomposition and subsequent reduction of iron citrate

Sample	Phase composition	Phase content, %	D, nm	Specific surface area <sup>a</sup> , m <sup>2</sup> /g
1	FeC <sub>2</sub> O <sub>4</sub>	100	50	9.88
2	FeC <sub>2</sub> O <sub>4</sub>	100	50	15.07
3	FeC <sub>2</sub> O <sub>4</sub>	70	60	
	α-Fe	10	50	28.9
	Fe <sub>3</sub> O <sub>4</sub>	20	–	
4	α-Fe	98	150	31.8
	Fe <sub>3</sub> O <sub>4</sub>	2	–	
5	α-Fe	100	180	31.4
6	α-Fe	100	1100	30.5

<sup>a</sup>The specific surface area of powders synthesized at various temperatures was determined by the method of thermal desorption of nitrogen

synthesis temperature of the obtained powders results also in the increase in the residual induction  $B_r$  (Table 40.2). Coercive force  $H_c$  associated with the powders' particles size is increasing up to 350 °C synthesis temperature (CSR size, 150 nm) and reaching its maximum value of 120 Oe. At 400 °C, when a slight increase in particle size is observed (CSR size, 180 nm), coercive force begins to decrease, and its value becomes 65 Oe. Residual induction  $B_r$  is the highest at the temperature of 400 °C, at which only nanoscale phase α-Fe is present in the system. With

**Table 40.2** Magnetic properties of the powders produced by decomposition-reduction of iron citrate

Sample	$\sigma_S$ , A·m <sup>2</sup> /kg	$H_C$ , Oe	$B_r$ , Gs
1	0.5	–	–
2	4.1	–	–
3	15.8	20	58.8
4	150	120	666
5	177.6	100	1522
6	179.6	65	1599

**Table 40.3** Phase and elemental composition (wt. %) of Fe powders synthesized at various temperatures

Sample	$T_c$ , °C	C, %	O, %	Fe, %	Other impurities, %
1	250	11.84	26.43	59.40	1.33
2	300	9.85	22.56	63.07	4.52
3	325	6.10	19.64	72.41	1.85
4	350	1.65	4.50	91.72	2.13
5	400	0.65	2.44	94.58	2.33
6	450	0.67	1.99	96.15	1.19

further increase of the synthesis temperature up to 450 °C, values of the specific magnetization  $\sigma_S$  and of the residual induction  $B_r$  of the synthesized powders, associated with the content of the ferromagnetic phase in them, remain virtually unchanged, and the coercive force  $H_C$  continues to decrease because of increased powders particles average size (see Table 40.2). Thus, the powder produced at the synthesis temperature 400–500 °C has the highest magnetic performance.

X-ray spectral analysis results are shown in Table 40.3 and Figs. 40.6 and 40.7. As it can be seen in Table 40.3, powders synthesized at different temperatures contain iron, carbon, oxygen, and also minor amounts of chromium, nickel, calcium, and sulfur (generally, not more than 4.5 mass %) which probably appeared in the powders during the preparation process. Elemental analysis results given in Table 40.3 show that the content of the main elements in the obtained powders depends on the synthesis temperature: the higher it is, the lower is the carbon and oxygen content, and the higher is the iron content in these powders. This finding is entirely consistent with the results of X-ray analysis and is connected with the decomposition of iron oxides and carbides and with the increase of  $\alpha$ -Fe phase amount in powders (Table 40.1).

The results of electron-microscopic examination of the microstructure of the powders obtained are shown in Figs. 40.6 and 40.7. As it follows from these results, the powders are conglomerates sizes of which depend on the synthesis temperature and are situated within the range from 0.1 up to 10 microns. At low synthesis temperatures (250–325 °C), conglomerate sizes are between 2 and 10 microns (Fig. 40.6a–c), and the main phase component in these powders is iron oxycarbide  $\text{FeC}_2\text{O}_4$  (Table 40.1). With an increase of the synthesis temperature, conglomerates sizes decrease, and the surface becomes more developed and porous (Fig. 40.6d–f).

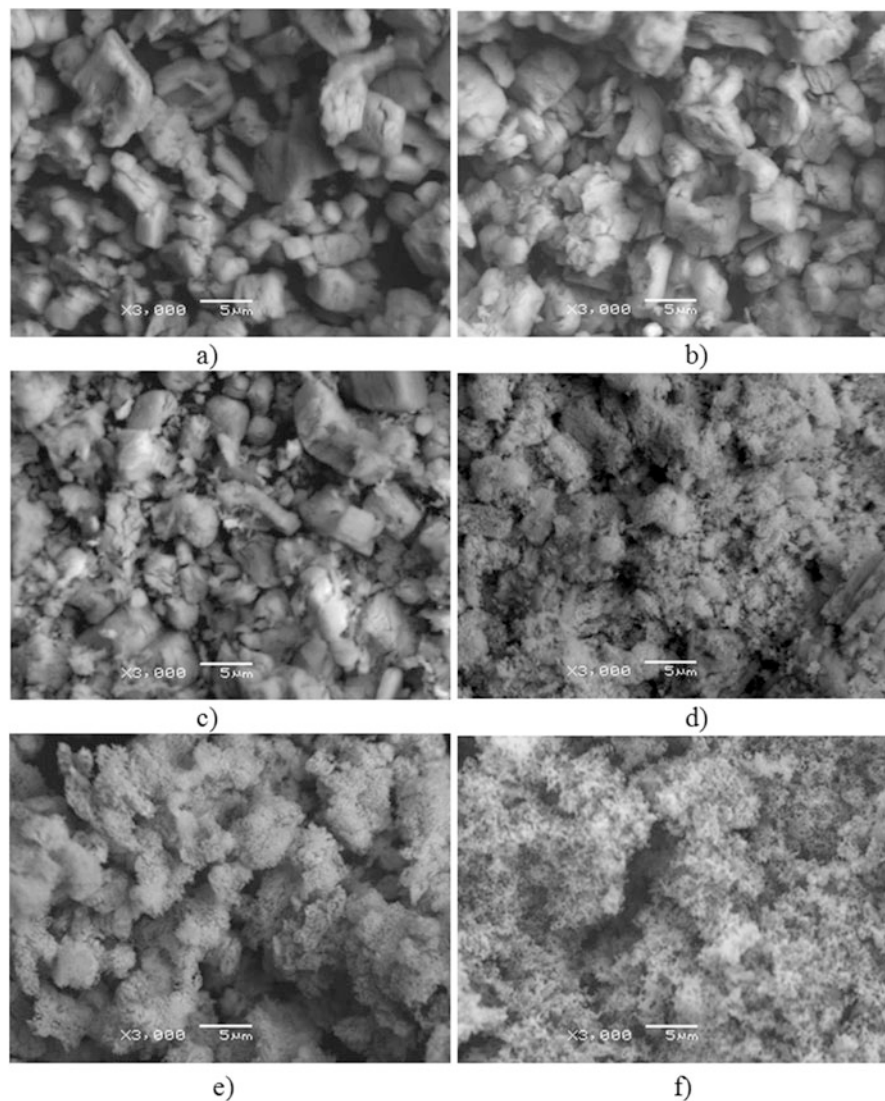


**Fig. 40.6** The micrographs of iron powder synthesized at different temperatures ( $\times 3000$ ): (a) 250 °C, (b) 300 °C, (c) 325 °C, (d) 350 °C, (e) 400 °C, and (f) 450 °C

The powder obtained by annealing at 400 °C is a porous multiply connected structure with dimensions of some structural elements within 0.1–0.2 micrometer range (Fig. 40.7) close to the CSR sizes measured by X-ray method (Table 40.1).

Thus, thermal decomposition of the citrate salt of iron  $\text{Fe}_3\{\text{C}_3\text{H}_5(\text{O})(\text{COO})_3\}_2$  in a protective hydrocarbons mixture atmosphere at certain process conditions allows to obtain nano-sized iron powder. During the synthesis of powders within the

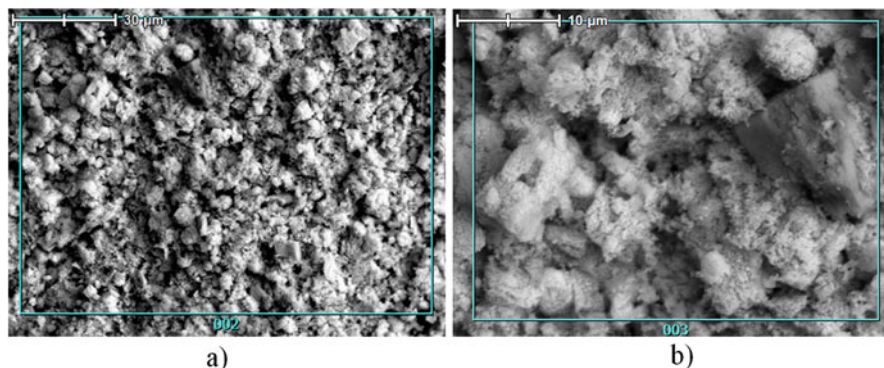


**Fig. 40.7** Photomicrographs of Fe powder synthesized at 400 °C at different magnifications: (a)  $\times 1000$ ; (b)  $\times 5000$

temperature range 250–500 °C, an increase in the amount of the ferromagnetic  $\alpha$ -phase therein occurs. According to the X-ray diffraction data, powders synthesized at 350, 400, and 500 °C consist of the crystalline phase  $\alpha$ -Fe. Iron powder's synthesis temperature increase leads to an increase of the value of their specific saturation magnetization and residual induction due to an increase of the amount of the ferromagnetic  $\alpha$ -phase in these powders.

Nanodispersed iron powder produced at 400 °C consists of ferromagnetic phase of  $\alpha$ -iron; has an optimum specific surface area 31.4 m<sup>2</sup>/g and high magnetic characteristics,  $\sigma_s$ , 177.6 A·m<sup>2</sup>/kg;  $H_c$ , 100 Oe; and  $B_r$ , 1522 G; and is the most promising material for use in the chemical industry, the medicine, and the food industry.

## References

1. Boshitskaya NV, Kushchevskaya NF (2015) Nanodispersni poroshki feromagnetnykh biomedichnogo pryznachennya (Nanodispersed ferromagnetics powders for biomedical purposes). *Visnyk NAN Ukrainy* 2:92–97
2. Gorelik SS, Skakov YA, Rastorguev LN (1994) *Rentgenograficheskii i elektronno-opticheskkii analiz (X-ray diffraction and electron-optical analysis)*. MISIS, Moscow
3. Guinier A (1961) *Rentgenografiya kristallov (X-ray crystallography)*. Fizmatlit, Moscow
4. Kovalenko LV, Folmanis GE (2006) *Biologicheskii aktivnyye nanoporoshki zheleza (Biologically active iron nanopowders)*. Nauka, Moscow
5. Ranum P (2001) Elemental iron powder for food fortification. *General Foods Word* 46:137–138

# Chapter 41

## Electrochemical Formation of Multilayer Metal and Metal Oxide Coatings in Complex Electrolytes

Antonina Maizelis and Boris Bairachniy

### 41.1 Introduction

Interest in the multilayer coatings is caused by possibility of improving surface physical properties and enhancing application scope of the goods with coated details. Metal multilayer coatings with alternating copper and nickel layers with thickness of up to 100 nm possess improved functional properties, compared to the corresponding metals: magnetic [1, 2], mechanical [3–7], and anticorrosive [8] properties.

Various nickel-copper materials possess catalytic activity in the reactions of organic compounds electrooxidation [9–12] and have good corrosion resistance in alkaline environment of carbohydrates [13, 14]. They are promising electrode materials to replace platinum-containing catalysts in alkaline direct methanol fuel cells, which have advantages over acid fuel cells [13, 15]. Nickel-copper alloys [16–18] and coatings by these alloys [15, 19] with oxyhydroxide films formed on the surface [13, 20] have a wider range of potentials of substance selective oxidation, compared to nickel, due to the greater polarization of the oxygen evolution [17].

Cu/Ni multilayer coatings are produced by various physical methods. The electrochemical method allows to obtain Cu/(Ni–Cu) coatings, where layers of nickel contain impurities of copper. It depresses magnetic properties of coatings, but improves such properties as ductility and corrosion resistance. The advantages of this method are the low cost, wide range of coating thicknesses, simplicity of composition regulation, and exception of metal interdiffusion at room temperature [21].

---

A. Maizelis (✉) • B. Bairachniy  
National Technical University, “Kharkov Polytechnic Institute”, 21 Frunze Street,  
Kharkov, 61002, Ukraine  
e-mail: [a.maizelis@gmail.com](mailto:a.maizelis@gmail.com); [b.bayrachny@gmail.com](mailto:b.bayrachny@gmail.com)

The basic principles of development of monobaths for multilayer metal coating electrodeposition by programmed current are given in [22]. The monobath technique can also be realized using classical pulsed current [23, 24]. Analysis of state-of-the-art multilayer coating formation methods is given in works by Baconyi I, Peter L [25, 26], and Podlaha EJ et al. [27]. Besides sulfate electrolytes, Cu/(Ni–Cu) multilayer coatings are deposited mainly from sulfamate [4–7] and citrate electrolytes [21, 28, 29]. The limiting factor of obtaining the compact thick multilayer coating is quality deterioration of nickel-enriched layers, while their thickness increases or the cupric ion concentration grows in electrolyte. This occurs because the cupric ions are reduced in the conditions of the limiting diffusion current during copper and nickel codeposition in these acid electrolytes.

The problem of improving the coating quality in the alloy deposition technique is solved by making the metal deposition potentials as close as possible binding ions of electropositive metal in a more stable complex than ions of electronegative metal. However, such complex electrolytes are not suitable for electrodeposition of multilayer coatings since the condition for the multilayer coating formation is the difference of metal deposition potentials as high as 200 mV.

In our opinion, the perspective way of formation of multilayer metal coatings is control of metal deposition conditions by changing the ratio of metal ions and ligand concentration in polyligand electrolytes. However, there is lack of information about the use of polyligand electrolytes for metal and metal oxide multilayer coating formation.

For copper-nickel multilayer coating deposition, we consider here pyrophosphate and ammonia ligands [30], since both monoligand and mixed complexes with cupric and nickel ions are formed in this system [31]. In this chapter we analyze the properties of metal and metal oxide multilayer nickel-copper coatings, obtained in pyrophosphate-ammonium polyligand electrolyte.

## 41.2 Experimental

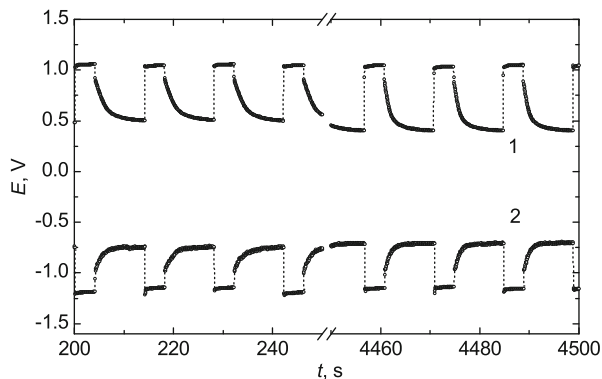
### 41.2.1 Methods of Coating Deposition

All solutions were prepared from analytical grade chemicals and distilled water without further treatment. Pyrophosphate-ammonium polyligand electrolyte for the multilayer coating deposition contained  $0.02\text{--}0.1\text{ mol L}^{-1}$   $\text{CuSO}_4 \cdot 5\text{H}_2\text{O}$ ,  $0.25\text{--}0.70\text{ mol L}^{-1}$   $\text{NiSO}_4 \cdot 7\text{H}_2\text{O}$ ,  $0.25\text{--}1.0\text{ mol L}^{-1}$   $\text{K}_4\text{P}_2\text{O}_7$ ,  $1.0\text{--}3.2\text{ mol L}^{-1}$   $\text{NH}_3(\text{NH}_4^+)$  as a mixture of  $(\text{NH}_4)_2\text{SO}_4$ ,  $0.2\text{ mol L}^{-1}$   $\text{NH}_4\text{Cl}$ , and  $\text{NH}_4\text{OH}$  to  $pH$  8.7–9.4.

For electrodeposition of Cu/(Ni–Cu) multilayer coatings, we used DC power supply BP-5 with converter of constant current into two-pulse current. At the first impulse, the copper layer was deposited at a current density corresponding



**Fig. 41.1** Chronopotentiograms of anodic (1) and cathodic (2) processes of multilayer Cu/(Ni-Cu) coating formation in electrolyte containing  $0.02 \text{ mol L}^{-1} \text{ Cu}^{2+}$ ,  $0.70 \text{ mol L}^{-1} \text{ Ni}^{2+}$ ,  $1.0 \text{ mol L}^{-1} \text{ P}_2\text{O}_7^{4-}$ ,  $2.8 \text{ mol L}^{-1} \text{ NH}_3(\text{NH}_4^+)$ ,  $0.2 \text{ mol L}^{-1} \text{ Cl}^-$ , and  $pH$  9, at  $J_{\text{Cu}} = 4 \text{ mA cm}^{-2}$  and  $J_{\text{Ni-Cu}} = 28 \text{ mA cm}^{-2}$



to the range of potentials from  $-0.65$  to  $-0.9 \text{ V}$  (vs saturated Ag/AgCl reference electrode) with agitation by cathodic bar moving with a frequency of  $2 \text{ s}^{-1}$ . At the second impulse, the Ni-Cu alloy layer was deposited at a current density corresponding to the potential range from  $-1.1$  to  $-1.2 \text{ V}$ . The time of layer deposition of the given thickness (from 5 to 100 nm) was calculated by Faraday's law, taking into account that the copper current efficiency is 99% and alloy current efficiency is 92.5%. Time of the copper layer deposition was in the range of 5–50 s. Time of Ni-Cu layer deposition was in the range of 2–5 s. The combined nickel-copper anode was used. Chronopotentiograms of the electrode processes are shown in Fig. 41.1.

The catalytically active metal oxide nickel-copper multilayer coating (MNCO) was formed in three stages on a substrate made of copper with dendritic structure:

1. Deposition of Cu/(Ni-Cu) multilayer coating underlayer with the thickness of  $2 \mu\text{m}$  from polyligand electrolyte. Due to the compact underlayer deposition at the first step, the catalytically active coating has strong adhesion to the substrate.
2. Deposition of multilayer nickel-copper hydroxide coating (MNCH) layer from the same polyligand electrolyte using a two-pulse mode. At the first current impulse, compact nickel-copper alloy is deposited in the range of current densities corresponding to the potential range from  $-1.1$  to  $-1.2 \text{ V}$ . At the second current pulse, a mixture of metals and their hydroxides is deposited in the range of current densities corresponding to the potential range from  $-1.3$  to  $-1.5 \text{ V}$ . The alternating deposition of the layers of compact alloy and mixtures of metals with their hydroxy compounds allows formation of mechanically strong dendritic structure with the developed surface.
3. Obtaining multilayer nickel-copper metal oxide coating (MNCO) containing nickel oxyhydroxide NiOOH and copper hydrated oxides. The MNCH coating is oxidized in 1M KOH solution in the potential range of  $0.1$ – $0.7 \text{ V}$  at this stage.

### 41.2.2 *Methods of the Electrode Processes Study*

Electrochemical measurements were carried out in the three-electrode cell using a potentiostat PI-50.1. The results were transferred from analogue form to digital by means of the two-channel voltmeter and Telemax program for PC (5–100 signals per second). Voltammograms were obtained at a potential scan rate of 0.2–1000 mV s<sup>-1</sup>. The working electrodes were made of platinum, nickel, copper, and steel 08KP. Its area was 1–12 cm<sup>2</sup>. Before each measurement, the electrode surface was updated by the treatment with carbide-silicone paper (500, 1000, 2000, and 3000 grit, sequentially) and cathodically polarized to obtain reproducible results in the range of the potentials corresponding to the surface oxide reduction process. The saturated Ag/AgCl reference electrode was used in the measurements, and all the potentials are given in the reference to this electrode.

The buffer capacity of the solutions was determined by potentiometric titration of solution (25 ml) using *pH* meter pH-150 in the cell equipped with a magnetic stirrer. Solutions of 2 mEq L<sup>-1</sup> sulfate acid and 4 mEq L<sup>-1</sup> potassium hydroxide were used as titrant solutions.

### 41.2.3 *Methods of Determining the Coating Properties*

Morphology of the multilayer coating surface was observed using scanning electron microscope LEO 1420.

The Vickers microhardness of the coatings with a thickness of 28–33 μm was measured using PMT-3 microhardness tester as the average of 10 measurements. The load on diamond pyramid was 10–50 g.

The coating ductility was evaluated by bending coated samples on a cylindrical holder. The multilayer coating thickness was 15 μm and the holder diameter was 3–46 mm. The appearance of cracks was controlled using microscope of PMT-3 microhardness tester (×400 magnification). The coating adhesion strength was estimated according to the minimal diameter of the cylinder, when bending of the coated samples leads to the partial exfoliation of the coating.

The internal stresses *IS* of coatings were determined using the method of flexible cathode. The deformation of the cathode was fixed using a device with an inductive sensor according to equation:

$$IS = \frac{h_e (h_e \varepsilon_e - h_c \varepsilon_c) x}{3 l^2 h_c}, \quad (41.1)$$

where  $h_e$ ,  $h_c$  are thicknesses of cathode and coating, respectively, m;  $\varepsilon_e$ ,  $\varepsilon_c$  are the elastic modules of cathode and coating materials, respectively, N m<sup>-2</sup>;  $l$  is the length of the coated part of the cathode, m; and  $x$  is the deviation of the end of the cathode, m.

## 41.3 Experimental Results and Discussion

### 41.3.1 Kinetic Regularities of Copper and Nickel Deposition from Polyligand Electrolyte

The cathodic polarization curve obtained in pyrophosphate (monoligand) electrolyte for deposition of nickel-copper alloy is presented in Fig. 41.2 (curve 2). Only one region of limiting current of copper and nickel codeposition as an alloy can be observed there. It is in the range from  $-1.1$  to  $-1.2$  V. Addition of the second ligand (ammonia) to this electrolyte composition (curve 1) leads to the appearance of the limiting current of copper deposition in the wide area of potential (from  $-0.4$  to  $-0.9$  V). Therefore, it appears possible to deposit the alternating layers of Cu and Ni-Cu alloy in polyligand electrolyte. Moreover, the value of limiting current of alloy deposition increases due to the depolarization of nickel reduction in the polyligand electrolyte in comparison with pyrophosphate electrolyte. At the potentials above this limiting current (more negative than  $-1.3$  V), a mixture of metals and metal hydroxides is deposited.

Cyclic voltammogram (CVA) dependencies are presented in Fig. 41.3. They start from the cathodic polarization up to different potentials corresponding to the potential range of Ni-Cu alloy deposition. After that, the electrode was polarized in the anodic direction leading to the complete dissolution of the obtained deposit. Two peaks of consecutive dissolution of copper and nickel are observed on the anodic branch. The height of these peaks increases when the cathodic border of the range of potential scan is getting lower. Since the potentials of copper deposition and nickel dissolution do not overlap, there are no prerequisites of the contact displacement

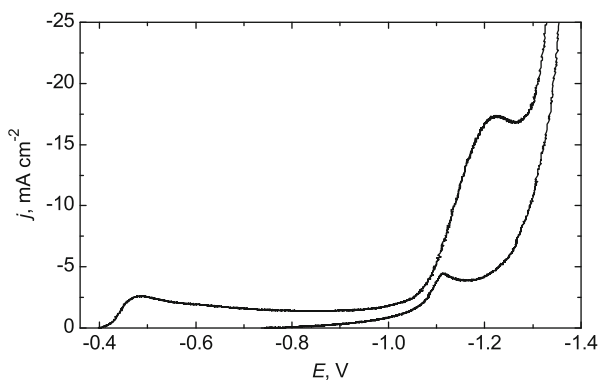


**Fig. 41.2** Cathodic polarization curve on Cu electrode in electrolytes containing  $0.05 \text{ mol L}^{-1} \text{ Cu}^{2+}$ ,  $0.25 \text{ mol L}^{-1} \text{ Ni}^{2+}$ ,  $0.35 \text{ mol L}^{-1} \text{ P}_2\text{O}_7^{4-}$ ,  $1.0 \text{ mol L}^{-1} \text{ NH}_3(\text{NH}_4^+)$ ,  $0.1 \text{ mol L}^{-1} \text{ Cl}^-$ ,  $\text{pH } 9$  (1);  $0.05 \text{ mol L}^{-1} \text{ Cu}^{2+}$ ,  $0.25 \text{ mol L}^{-1} \text{ Ni}^{2+}$ ,  $1.0 \text{ mol L}^{-1} \text{ P}_2\text{O}_7^{4-}$ ,  $0.1 \text{ mol L}^{-1} \text{ Cl}^-$ ,  $\text{pH } 9$  (2). Potential scan rate is  $50 \text{ mV s}^{-1}$

**Fig. 41.3** CVA on Pt electrode in electrolyte containing  $0.05 \text{ mol L}^{-1} \text{ Cu}^{2+}$ ,  $0.25 \text{ mol L}^{-1} \text{ Ni}^{2+}$ ,  $0.35 \text{ mol L}^{-1} \text{ P}_2\text{O}_7^{4-}$ ,  $1.0 \text{ mol L}^{-1} \text{ NH}_3(\text{NH}_4^+)$ ,  $0.1 \text{ mol L}^{-1} \text{ Cl}^-$ ,  $pH 9$ . Potential scan rate is  $50 \text{ mV s}^{-1}$

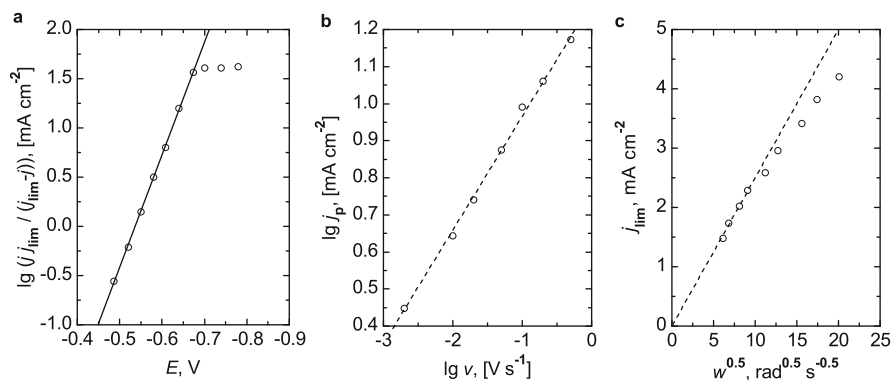
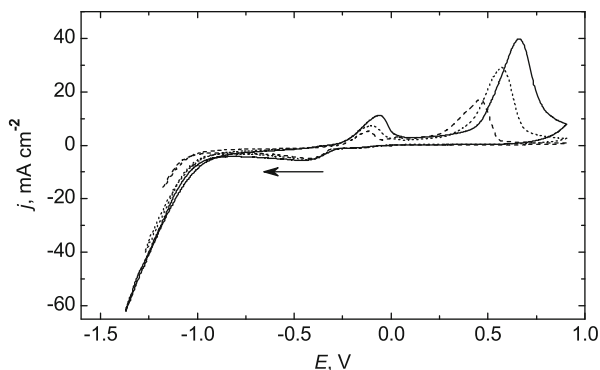


**Fig. 41.4** Copper deposition dependences in electrolyte containing  $0.013 \text{ mol L}^{-1} \text{ Cu}^{2+}$ ,  $0.067 \text{ mol L}^{-1} \text{ Ni}^{2+}$ ,  $0.173 \text{ mol L}^{-1} \text{ P}_2\text{O}_7^{4-}$ ,  $0.267 \text{ mol L}^{-1} \text{ NH}_3(\text{NH}_4^+)$ ,  $pH 9$ : (a) steady-state  $j$ - $E$  curve in coordinates of mixed kinetics, (b) current peak  $j_p$  vs potential scan rate  $v$  in logarithmic coordinates, (c) limiting current  $J_{lim}$  vs speed of RDE rotation  $w^{0.5}$  at the potential  $-0.75 \text{ V}$

of copper ions by nickel in polyligand electrolyte. Due to the contact displacement in acidic electrolytes, the ratio of copper content to nickel content in the coating is overestimated.

Steady-state polarization dependence of Cu(II) reduction in the polyligand electrolyte becomes linear in the coordinates corresponding to the mixed kinetics (Fig. 41.4a), i.e., the cupric ion discharge is limited by the concentration overpotential. The slope of the logarithmic dependence of the peak current on potential scan rate  $k = 0.31$  is less than 0.5 (Fig. 41.4b). In addition, the dependence of the limiting current of Cu(II) reduction  $j_{lim}$  on the rotation speed of rotating disk electrode  $w^{0.5}$  deviates from the straight line (Fig. 41.4c). Therefore, the speed of cupric ion reduction is limited by both diffusion and the rate of a previous chemical reaction of complex decomposition.

To estimate the influence of changes of solution  $pH$  near the electrode during prolonged electrolysis, the resistance of polyligand and pyrophosphate electrolytes

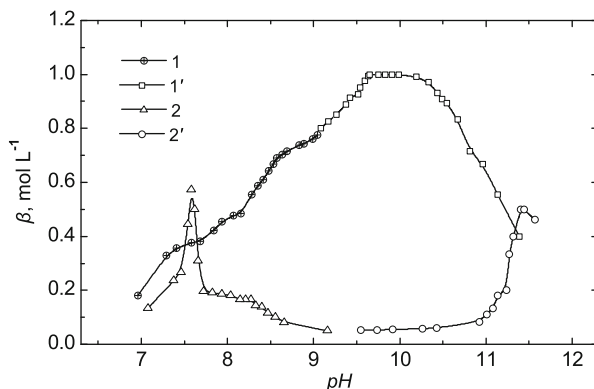


**Fig. 41.5** Dependences of buffer capacity  $\beta$  on electrolyte  $pH$  during acidic (1, 2) and alkalic (1', 2') titration of solutions containing  $0.02 \text{ mol L}^{-1} \text{ Cu}^{2+}$ ,  $0.35 \text{ mol L}^{-1} \text{ Ni}^{2+}$ ,  $0.37 \text{ mol L}^{-1} \text{ P}_2\text{O}_7^{4-}$ ,  $2.4 \text{ mol L}^{-1} \text{ NH}_3(\text{NH}_4^+)$  (1);  $0.02 \text{ mol L}^{-1} \text{ Cu}^{2+}$ ,  $0.35 \text{ mol L}^{-1} \text{ Ni}^{2+}$ ,  $0.74 \text{ mol L}^{-1} \text{ P}_2\text{O}_7^{4-}$  (2)

to both acid and alkaline titration was determined by potentiometric titration. Figure 41.5 shows the curves of the true buffer capacity  $\beta$ ,  $\text{mol L}^{-1}$ . The value of  $\beta$  was determined by numerical differentiation of titration curves according to the equation:

$$\beta = \frac{c \Delta V}{V_s \Delta pH}, \quad (41.2)$$

where  $c$  is the concentration of sulfate acid (or potassium hydroxide),  $\text{mol L}^{-1}$ ;  $\Delta V$  is the volume of the added acid (or alkali), ml;  $V_s$  is solution volume, ml; and  $\Delta pH$  is the change in the  $pH$  of the solution.

Significant increase in the resistance to both alkalization and acidification is observed (curve 1) in the presence of two ligands (pyrophosphate-ammonia solution), compared to pyrophosphate solution (curve 2). Buffer capacity of polyligand electrolyte is  $0.8\text{--}1.0 \text{ mol L}^{-1}$  in an operating region of  $pH$ . High buffer capacity of the electrolyte in a combination with a mixed nature of limiting current of  $\text{Cu(II)}$  reduction provides the higher quality of copper coating deposited at the potentials of the limiting current, in comparison with the coating obtained in electrolytes with the diffusion limiting current.

Despite the fact that the nickel and copper have the same type of the lattice (face-centered cubic), and the lattice parameters are close, the nickel surface is foreign for copper. Therefore copper nuclei of new phase form on nickel surface at the more negative potentials than on the copper electrode. That is, in the case of thin layer electrodeposition, each layer starts with formation of new nuclei. That leads to decrease of the coating grain size and improvement of the functional properties of final coating.

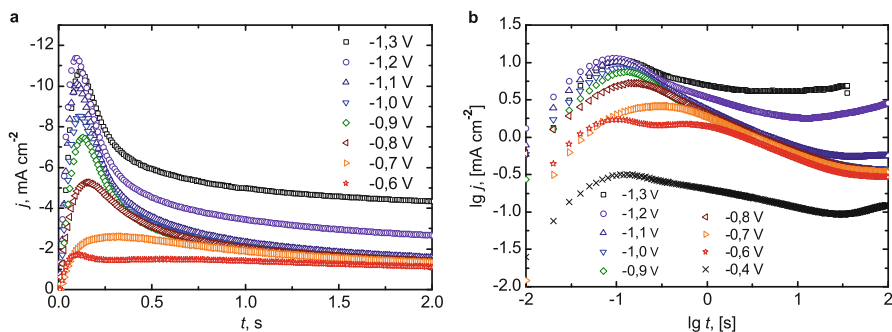


**Fig. 41.6** Current transients of Cu(II) reduction in the electrolyte containing  $0.1 \text{ mol L}^{-1} \text{ Cu}^{2+}$ ,  $0.22 \text{ mol L}^{-1} \text{ P}_2\text{O}_7^{4-}$ ,  $0.77 \text{ mol L}^{-1} \text{ NH}_3(\text{NH}_4^+)$ ,  $pH$  9.25, at different potential values  $E$ , in  $j - t$  (a) and logarithmic (b) coordinates

**Table 41.1** The time and thickness of the continuous layer formation and fractal parameters of crystal growth

$E$ , V	Time of layer formation, s	Layer thickness, nm	Fractal parameter $\alpha$	Fractal dimensionality $D_f$
-0.6	3.53	1.49	0.495	1.990
-0.7	2.37	1.46	0.520	2.040
-0.8	1.33	1.19	0.520	2.040
-0.9	1.31	1.16	0.521	2.043
-1.0	1.10	1.13	0.542	2.084
-1.1	0.99	1.20	0.587	2.174

The mathematical models of nucleation and growth of copper nuclei on nickel and nickel nuclei on copper in polyligand electrolyte are proposed in [32], and a number of parameters are identified. Coating uniformity is extremely important for the deposition of nano-sized layers of multilayer coatings. The time of formation of continuous layers and their thickness were determined by the analysis of current transients. They were obtained by the change of the potential from open circuit potential to the potential of copper deposition (Fig. 41.6a). In logarithmical coordinates (Fig. 41.6b), the current transients obtained at the potential from  $-0.6$  to  $-1.1$  V are linearized with a slope of about 0.5. This indicates instantaneous nucleation with the limiting stage of diffusion of adatom to the site of crystal growth.

In the case of instantaneous nucleation, the copper layer is accumulated completely in  $6t_{\text{max}}$  seconds [33]. This time in the studied electrolyte decreases with the increase of overpotential (see Table 41.1). The layer thickness in a wide range of potentials of deposition does not exceed 1.5 nm.

Fractal dimensionality ( $D_f$ ) of a surface was determined from the slope of current transients in logarithmic coordinates (fractal parameter  $\alpha$ ):  $D_f = 2\alpha + 1$  [33]. Values of fractal parameter and fractal dimensionality at copper deposition at the

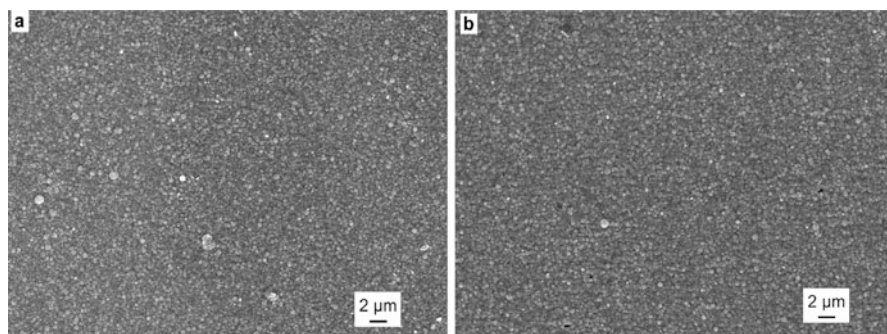
different potentials are represented in Table 41.1. In the potential range from  $-0.6$  to  $-0.9$  V, the fractal dimensionality is close to 2. This indicates the formation of smooth 2D surface of copper. In the case of copper deposition at  $-0.6$  V, fractal dimensionality is slightly less than 2. This indicates the possible appearance of islands in the layer of 2D crystals. At the greater overpotential (at  $-1.1$  V), the fractal parameter slightly increases. That is apparently due to the onset of rough continuous surface formation.

### 41.3.2 Study of the Multilayer Metal Cu/(Ni–Cu) Coating Properties

Compact thick multilayer Cu/(Ni–Cu) coatings are deposited under the optimum conditions of electrolysis from the polyligand pyrophosphate-ammonium electrolyte. The coatings have fine crystalline globular structure (Fig. 41.7) in the cases of thicker (about 300 nm) both copper (Fig. 41.7a) and Ni–Cu (Fig. 41.7b) outer layers.

The porosity of the multilayer coatings obtained on the carbon steel surface decreases by four–six times with the increase of the copper layer thickness  $d_{\text{Cu}}$  from 6 to 25 nm (the thickness of alloy layers was constant,  $d_{\text{Ni–Cu}} = 25$  nm), depending on the coating thickness. At the same time, the thickness of nonporous coatings decreases from 3.7 to 2  $\mu\text{m}$  [34, 35]. The coatings are nonporous at 4–4.5  $\mu\text{m}$  thickness when they are deposited without stirring.

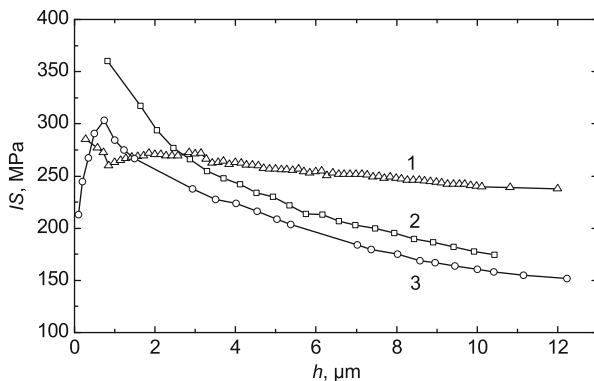
The ductility of the multilayer coatings and their adhesion strength were estimated by bending the coating of 15  $\mu\text{m}$  thickness on cylinders with different diameters. When the cylinder diameter was decreased to  $d_1$ , cracks appeared (became visible using optical microscope of PMT-3 tester), and when the cylinder diameter was decreased to  $d_2$ , the coating was partially exfoliated (complete exfoliation did not occur). The changes of  $d_1$  and  $d_2$  represented changes of the



**Fig. 41.7** The surface morphology ( $\times 5000$  magnification) of Cu/(Ni–Cu) multilayer coating of 17  $\mu\text{m}$  thickness in the case of upper Cu (a) and Ni–Cu (b) layer

**Table 41.2** Characteristics of Cu/(Ni–Cu) coating ductility and their strength of adhesion to the substrate

Characteristics	1	2	3	4	5	6
$d_{\text{Cu}}/d_{\text{Ni–Cu}}$ , nm/nm	8.5/29.6	11.1/30	11.8/29.9	13.7/29.8	18.7/21.7	25.2/19.6
$d_1$ , mm	46	33	24	15	13	8
$d_2$ , mm	8	3	3	—	—	—

**Fig. 41.8** Internal stresses of nickel (1) and Cu/(Ni–Cu) (2, 3) coatings. The microhardness of coatings is 360 HV (1), 670 HV (2), and 520 HV (3)

ductility and adhesion strength of the coatings, respectively. The data in Table 41.2 show the positive effect of increasing the thickness of the copper layers on the ductility and strength of adhesion to the substrate.

Figure 41.8 shows plots of in situ changes of internal stresses  $IS$  of coatings *vs* their thickness. The  $IS$  were calculated according to Eq. (41.1). The dependencies obtained during the deposition of multilayer coatings in polyligand electrolyte reflect the significant decrease of  $IS$  with coating thickness increase (curves 2 and 3), as compared to nickel coating deposited from the Watts electrolyte (curve 1). The  $IS$  are increased for the multilayer coatings with higher microhardness (curve 2) with thicker layers of nickel-copper alloy, but remain lower than for nickel  $IS$ . The multilayer coatings having 2–30  $\mu\text{m}$  thickness possess  $IS = 80\text{--}240$  MPa.

The obtained multilayer coatings had Vickers microhardness  $HV$  from 400 to 800 HV, depending on the parameters of electrolysis [30, 34, 35]. For comparison, the microhardness of copper coating, deposited in pyrophosphate-ammonia electrolyte (free of  $\text{Ni}^{2+}$  ions), was  $HV_{\text{Cu}} = 154$  HV, and the microhardness of nickel coating, deposited in pyrophosphate-ammonia electrolyte (free of  $\text{Cu}^{2+}$  ions), was  $HV_{\text{Ni}} = 360$  HV. Figure 41.9 shows the dependences of microhardness on the thickness of bilayer consisting of metal layers with different ratio of thickness. The microhardness decreases with the decrease of bilayer thickness below 25 nm, which is probably due to the weakening of multilayer structures with thinner layers. The maximum of the microhardness was observed, when the Ni–Cu alloy layer thickness is 1.8–2.5 times higher than the copper layer thickness in the multilayer coating. In the range of 35–75 nm bilayer thickness, microhardness of coatings is 530–740 HV.



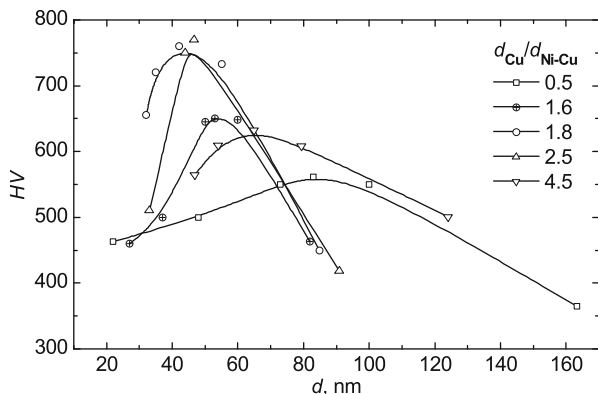
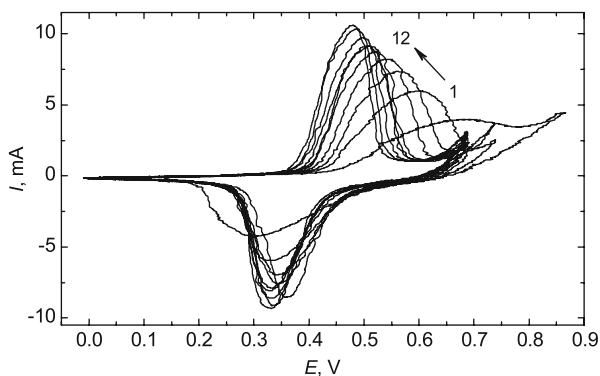


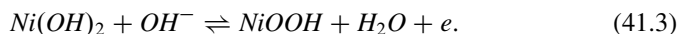
**Fig. 41.9** Dependences of Cu/(Ni-Cu) coating microhardness on bilayer thickness  $d$  at the different ratio of Ni-Cu and Cu layer thicknesses  $d_{\text{Ni-Cu}}/d_{\text{Cu}}$

**Fig. 41.10** CVA of MNCO electrode in the solutions containing KOH: 0.1 mol L<sup>-1</sup> (1), 0.2 mol L<sup>-1</sup> (2), 0.3 mol L<sup>-1</sup> (3), 0.4 mol L<sup>-1</sup> (4), 0.5 mol L<sup>-1</sup> (5), 0.6 mol L<sup>-1</sup> (6), 0.7 mol L<sup>-1</sup> (7), 0.8 mol L<sup>-1</sup> (8), 0.9 mol L<sup>-1</sup> (9), 1.0 mol L<sup>-1</sup> (10), 1.4 mol L<sup>-1</sup> (11), 2.0 mol L<sup>-1</sup> (12). Potential scan rate is 10 mV s<sup>-1</sup>



### 41.3.3 The Oxidation of Methanol on the Electrode with a Multilayer Nickel-Copper Metal Oxide Coating in KOH Solution

Cyclic voltammograms (CVA) of multilayer MNCO electrode in KOH solution (Fig. 41.10) have anodic peak of nickel hydroxide oxidation to oxyhydroxide and cathodic peak of oxyhydroxide reduction to hydroxide. These peaks correspond to the reversible reaction [17]:



The maxima of current of anodic and cathodic processes increases and potentials of cathode and anode peaks are getting closer with the increase of KOH concentrations. This indicates the growth reinforcement of the reversibility of electrode. This electrode is characterized by the wider potential window as compared to the known

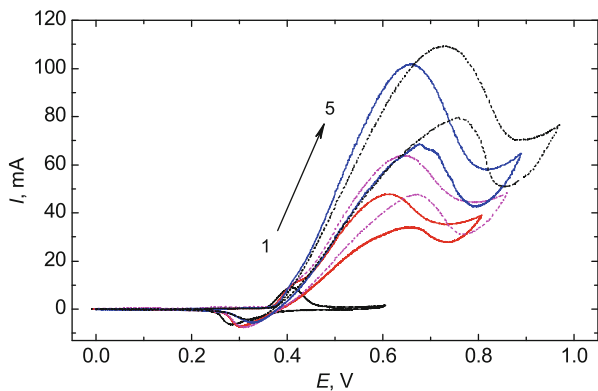


**Fig. 41.11** First cycles of CVA on MNCO electrode in the solutions containing  $1.0 \text{ mol L}^{-1}$  KOH and  $0 \text{ mol L}^{-1}$  (1),  $0.2 \text{ mol L}^{-1}$  (2),  $0.3 \text{ mol L}^{-1}$  (3),  $0.5 \text{ mol L}^{-1}$  (4),  $0.7 \text{ mol L}^{-1}$  (5) of methanol

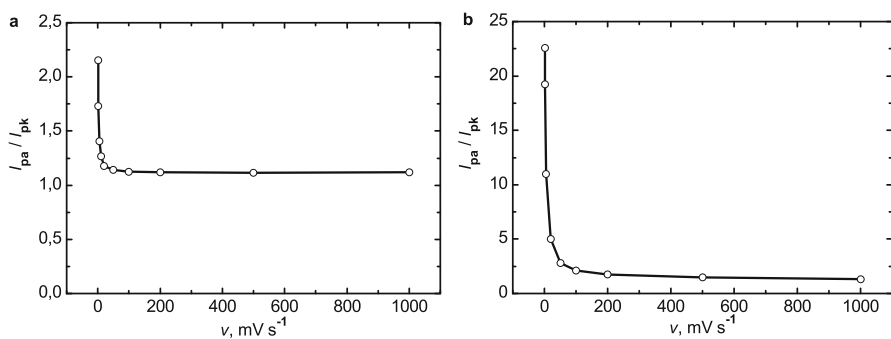


**Fig. 41.12** The  $I_{pa}/I_{pk}$  ratio in electrolyte containing (a)  $1 \text{ mol L}^{-1}$  KOH, (b)  $1 \text{ mol L}^{-1}$  KOH, and  $0.4 \text{ mol L}^{-1}$  methanol

nickel-contained electrodes [17, 19, 36]. Nickel hydroxide oxidation is almost over before the oxygen evolution potential is reached.

The peak of methanol oxidation on the MNCO electrode in the alkaline solution appears in the range of potentials of anode peak of nickel hydroxide oxidation (Fig. 41.11, curves 1 and 2–5). The height of the peak is maximal at the first cycle; at the next cycles, its height decreases and then it becomes unchanged. The height of the oxidation peak grows when the concentration of methanol in solution increases, both at the first and at the stable cycles.

The absence of the increase of cathodic peak height with increase of methanol concentration indicates the catalytic character of the irreversible process of its oxidation. The ratio of anodic  $I_{pa}$  and cathodic  $I_{pk}$  peak height decreases when potential sweep rate increases (Fig. 41.12a). This ratio increases by the order of magnitude when methanol is added in the solution (Fig. 41.12b).

Dependences of the normalized values of anodic peak current  $I_{pa}/v^{0.5}$  on the square root of potential scan rate (Fig. 41.13) have the typical shape for the electrochemical-chemical catalytic process [13, 36].

**Fig. 41.13** Plots of  $I_{pa}/v^{0.5}$  vs  $v^{0.5}$  in the electrolyte containing  $1.0 \text{ mol L}^{-1}$  KOH and  $1 \text{ mol L}^{-1}$  (1),  $0.7 \text{ mol L}^{-1}$  (2),  $0.5 \text{ mol L}^{-1}$  (3),  $0.4 \text{ mol L}^{-1}$  (4),  $0.3 \text{ mol L}^{-1}$  (5), and  $0.2 \text{ mol L}^{-1}$  (6) of methanol

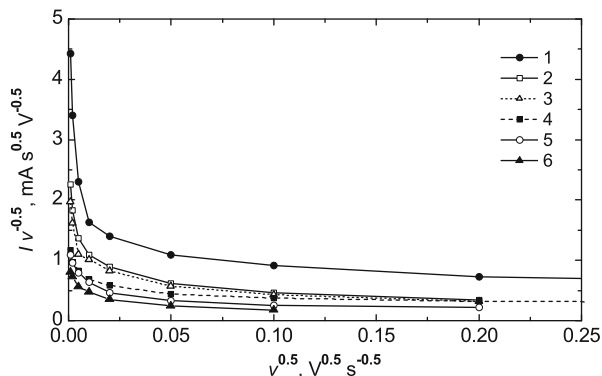
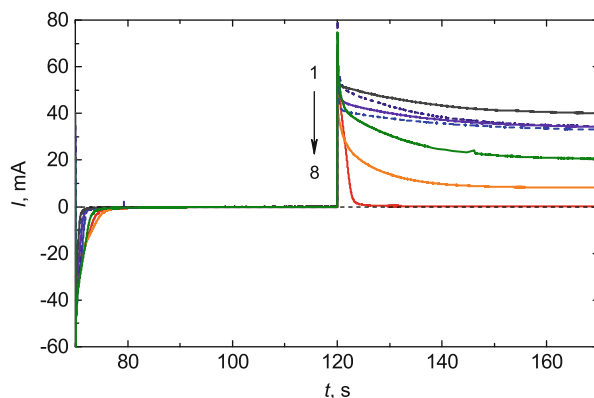


**Fig. 41.14** Combined chronoamperograms of double-stage change of potential from anodic peak potential to cathodic peak potential in the electrolytes containing  $1.0 \text{ mol L}^{-1}$  KOH and  $1.0 \text{ mol L}^{-1}$  (1),  $0.6 \text{ mol L}^{-1}$  (2),  $0.5 \text{ mol L}^{-1}$  (3),  $0.4 \text{ mol L}^{-1}$  (4),  $0.3 \text{ mol L}^{-1}$  (5),  $0.2 \text{ mol L}^{-1}$  (6),  $0.1 \text{ mol L}^{-1}$  (7), and  $0 \text{ mol L}^{-1}$  (8) of methanol



Irreversibility of methanol oxidation reaction is visually illustrated by chronoamperograms of the two-step change of the electrode potential from the potential of anodic peak to the potential of cathodic peak at various methanol concentrations (Fig. 41.14).

The quantity of electricity for methanol oxidation is much higher as compared to the quantity of electricity for reduction of nickel oxyhydroxide, which was formed during anode period, but does not take part in catalytic reaction of methanol oxidation. Cathodic regions of chronoamperograms indicate the decrease of the amount of substance that was reduced with the increase of methanol concentration. This fact confirms the nature of the methanol catalytic oxidation by means of mediator.

Methanol oxidation rate increases with the increase of solution temperature  $T$  up to 333 K. The formal activation energy of chemical reaction A for methanol oxidation by Ni(III) particles is calculated according to the equation:

$$A = R \frac{d(\ln I)}{d(T^{-1})}. \quad (41.4)$$

For calculating  $A$ , the value of the slope of dependence of the current logarithm on  $T^{-1}$  was used. The current values corresponded to the potential of 550 mV on CVA obtained at a potential scanning in the anodic direction with sweep rate of  $10 \text{ mV s}^{-1}$  in the range of  $T = 288\text{--}333 \text{ K}$ . The solution contained  $1.0 \text{ mol L}^{-1}$  KOH and  $0.1 \text{ mol L}^{-1}$   $\text{CH}_3\text{OH}$ . Formal activation energy of chemical reaction is  $9.88 \pm 0.07 \text{ kJ mol}^{-1}$ . It is significantly lower than in the case of electrode based on nickel and its hydroxide ( $43 \text{ kJ mol}^{-1}$  [37]) and nickel electrode modified with  $N,N$ -bis(salicylidene)phenylenediamine ( $44.09 \pm 0.06 \text{ kJ mol}^{-1}$  [38]). The MNCO electrode has also the advantage over the electrode made of glassy carbon with nickel-cobalt coating ( $11.41 \pm 0.25 \text{ kJ mol}^{-1}$  [39]).

## 41.4 Conclusions

It is shown that the polyligand pyrophosphate-ammonium electrolyte allows to obtain multilayer coatings both metal Cu/(Ni–Cu) and coatings consisting of metals and their hydroxides. The limiting current of cupric ion reduction has the mixed concentration nature that, together with the high buffer capacity of electrolyte ( $0.8\text{--}1.0 \text{ mol L}^{-1}$ ), leads to codeposition of Cu and Ni in the form of compact coating. This allows deposition of smooth multilayer coatings which can be thicker than the coating obtained in the acid electrolytes. The average thickness of completely accumulated layer of copper crystals does not exceed 1.5 nm, and the fractal dimension is close to 2, indicating the formation of smooth copper layers in a wide range of potentials.

Vickers microhardness of Cu/(Ni–Cu) coatings is 400–800 HV depending on the conditions of its formation. The microhardness maximum is observed for coatings with thickness ratio  $d_{\text{Ni–Cu}}/d_{\text{Cu}} = 1.8\text{--}2.5$  and bilayer thickness  $d = 40\text{--}60 \text{ nm}$ . Internal stresses of Cu/(Ni–Cu) coatings at  $10 \mu\text{m}$  thickness are 160–175 MPa.

Electrode with the multilayer nickel-copper metal oxide coating has wider potential window for the oxidation of methanol in alkaline solution and lower activation energy of the methanol oxidation reaction ( $9.88 \pm 0.07 \text{ kJ mol}^{-1}$ ) in comparison with the known nickel-containing electrodes.

## References

1. Bennett LH, Lashmore DS, Dariel MP, Kaufman MJ, Rubinstein M, Libits P, Zadok O, Yahalom J (1987) Magnetic properties of electrodeposited copper-nickel composition-modulated alloys. *J Magn Magn Mater* 67:239–245. doi:10.1016/0304-8853(87)90237-X
2. Fesharaki MJ, Peter L, Schucknecht T, Rafaja D, Degi J, Pogany L, Neurohr K, Szeles E, Nabiyouni G, Bakonyi I (2012) Magnetoresistance and structural study of electrodeposited Ni–Cu/Cu multilayers. *J Electrochem Soc* 159:D162–D171. doi:10.1149/2.090203jes
3. Barshilia HC, Rajam KS (2002) Characterization of Cu–Ni multilayer coatings by nanoindentation and atomic force microscopy. *Surf Coat Technol* 155:195–202. doi:10.1016/S0257-8972(02)00008-7

4. Cammarata RC (1994) Mechanical properties of nanocomposite thin films. *Thin Solid Films* 240:82–87. doi:10.1016/0040-6090(94)90699-8
5. Tokarz A, Fraczek T, Balaga Z, Nitkiewicz Z (2007) Structure, hardness and thermal stability of electrodeposited Cu/Ni nanostructured multilayers. *Rev Adv Mater Sci* 15:247–252.
6. Oberle RR, Cammarata RC (1995) Dependence of hardness on modulation amplitude in electrodeposited Cu–Ni compositionally modulated thin films. *Scripta Metall Mater* 32:583–588. doi:10.1016/0956-716X(95)90841-7
7. Hattori T, Kaneko Y, Hashimoto S (2007) Tribological properties of Ni/Cu multilayers. *Mater Sci Forum* 561–565:2451–2454. doi:10.4028/www.scientific.net/MSF.561-565.2451
8. Rajasekaran N, Mohan S (2009) Preparation, corrosion and structural properties of Cu–Ni multilayers from sulphate/citrate bath. *Corros Sci* 51:2139–2143. doi:10.1016/j.corsci.2009.05.052
9. Fuerte A, Valenzuela RX, Escudero MJ, Daza L, Conesa JC, Bera P, Martinez-Arias A (2009) Structural, catalytic/redox and electrical characterization of systems combining Cu–Ni with CeO<sub>2</sub> or Ce<sub>1-x</sub>M<sub>x</sub>O<sub>2-δ</sub> (M = Gd or Tb) for direct methane oxidation. *J Power Sources* 192:70–77. doi:10.1016/j.jpowsour.2008.12.015
10. Niedbala J, Budniok A, Matyja P (1994) Electro-oxidation of ethanolamine on modified layers of Cu–Ni alloys in alkaline environment. *Thin Solid Films* 237:148–154. doi:10.1016/0040-6090(94)90252-6
11. Yeo IH, Johnson DC (2001) Electrochemical response of small organic molecules at nickel-copper alloy electrodes. *J Electroanal Chem* 495:110–119. doi:10.1016/S0022-0728(00)00401-0
12. Jafarian M, Forouzandeh F, Danaee I, Gopal F, Mahjani MG (2009) Electrocatalytic oxidation of glucose on Ni and NiCu alloy modified glassy carbon electrode. *J Solid State Electrochem* 13:1171–1179. doi:10.1007/s10008-008-0632-1
13. Danaee I, Jafarian M, Forouzandeh F, Gopal F, Mahjani MG (2008) Electrocatalytic oxidation of methanol on Ni and NiCu alloy modified glassy carbon electrode. *Int J Hydrogen Energy* 33:4367–4376. doi:10.1016/j.ijhydene.2008.05.075
14. Hameed RMA, Fekry AM (2010) Electrochemical impedance studies of modified Ni–P and Ni–Cu–P deposits in alkaline medium. *Electrochim Acta* 55:5922–5929. doi:10.1016/j.electacta.2010.05.046
15. Danaee I, Jafarian M, Forouzandeh F, Gopal F, Mahjani MG (2009) Electrochemical impedance studies of methanol oxidation on GC/Ni and GC/NiCu electrode. *Int J Hydrog Energy* 34:859–869. doi:10.1016/j.ijhydene.2008.10.067
16. Gupta SS, Mahapatra SS, Datta J (2004) A potential anode material for the direct alcohol fuel cell. *J. Power Sources* 131:169–174. doi:10.1016/j.jpowsour.2004.01.009
17. Jafarian M, Moghaddam RB, Mahjani MG, Gopal F (2006) Electro-catalytic oxidation of methanol on a Ni–Cu alloy in alkaline medium. *J Appl Electrochem* 36:913–918. doi:10.1007/s10800-006-9155-6
18. Ding R, Liu J, Jiang J, Wu F, Zhu J, Huang X (2011) Tailored Ni–Cu alloy hierarchical porous nanowire as a potential efficient catalyst for DMFCs. *Catalys Sci Technol* 1:1406–1411. doi:10.1039/C1CY00164G
19. Hameed RMA, El-Khatib KM (2010) Ni–P and Ni–Cu–P modified carbon catalysts for methanol electro-oxidation in KOH solution. *Int J Hydrog Energy* 35:2517–2529. doi:10.1016/j.ijhydene.2009.12.145
20. Shobha T, Aravinda CL, Devi LG, Mayanna SM (2003) Preparation and characterization of oxides of Ni–Cu: anode material for methanol oxidative fuel cells. *J Solid State Electrochem* 7:451–455. doi:10.1007/s10008-002-0327-y
21. Dulal SMSI, Charle EA (2008) Electrodeposition and composition modulation of Co–Ni(Cu)/Cu multilayers. *J Alloys Compd* 455:274–279. doi:10.1016/j.jallcom.2007.01.020
22. Gabe DR, Wilcox GD (2002) Underlayered and multilayered electrodeposits. *Met Finish* 100:18–27. doi:10.1016/S0026-0576(02)80242-2
23. Roy S (1998) Electrodeposition of compositionally modulated alloys by a electrodeposition-displacement reaction method. *Surf Coat Technol* 105:202–205. doi:10.1016/j.jallcom.2007.01.020

24. Ghosh SK, Grover AK, Dey GK, Totlani MK (2000) Nanocrystalline Ni–Cu alloy plating by pulse electrolysis. *Surf Coat Technol* 126:48–63. doi:10.1016/S0257-8972(00)00520-X
25. Peter L, Bakonyi I (2007) Electrodeposition and properties of nanoscale magnetic/non-magnetic metallic multilayer films, Chapter 12, pp 242–260. In: Staikov G (ed) *Electrocrystallization in nanotechnology*. Wiley-VCH, Weinheim, p 265. doi:10.1002/9783527610198.fmatter
26. Bakonyi I, Peter L (2010) Electrodeposited multilayer films with giant magnetoresistance (GMR): progress and problems. *Prog Mater Sci* 55:107–245. doi:10.1016/j.pmatsci.2009.07.001
27. Podlaha EJ, Li Y, Zhang J, Huang Q, Panda A, Lozano-Morales A, Davis D and Gu Z (2006) Electrochemical deposition of nanostructured metals, Chapter 16, pp 484–504. In: Gogotsi Yu (ed) *Handbook of nanomaterials*. CRC Press, New York, p 788
28. Lebbad N, Voiron J, Nguyen B, Chainet E (1996) Electrodeposition of metallic multilayers with modulated electric regimes. *Thin Solid Films* 275:216–219. doi:10.1016/0040-6090(95)07047-8
29. Wang L, Fricoteaux P, Yu-Zhang K, Troyon M, Bonhomme P, Douglade J, Metrot A (1995) Growth mechanism and structure of electrodeposited CuNi multilayers. *Thin Solid Films* 261:160–167. doi:10.1016/S0040-6090(95)06538-5
30. Maizelis AA, Bairachniy BI, Trubnikova LV, Savitsky BA (2012) The effect of architecture of the Cu/(Ni–Cu) multilayer coatings on their microhardness. *Funct Mater* 19(2):238–244
31. Orehova VV, Andriushenko FK (1979) Poliligandnye jelektrolity v gal'vanostegii [Polyligand electrolytes in electroplating]. *Vishha shkola, Har'kov*, p 144 (in Russian)
32. Maizelis AA, Bairachniy BI, Trubnikova LV (2011) Features of nucleation during electrochemical formation of Cu/(Ni–Cu) multilayer coatings. *Abstrakt book*. In: XIX Mendeleev Congress on general and applied chemistry, Volgograd, 25–30 Sept, 4:85
33. Nouri E, Dolati A (2007) The fractal study of Cu–Ni layer accumulation during electrodeposition under diffusion-controlled condition. *Mater Res Bull* 42:1769–1776. doi:10.1016/j.materresbull.2006.11.039
34. Trubnikova LV, Bairachniy BI, Maizelis AA (2010) The influence of multilayered copper-nickel coatings formation circumstances on the corrosion resistance and mechanical properties. *Abstrakt book*. In: *Electrochemical technologies and materials for 21st century: 9th international Frumkin symposium*, Moscow, 24–29 Oct, p 172
35. Maizelis AA, Bairachniy BI, Trubnikova LV (2012) The influence of architecture of the Cu/(Ni–Cu) multilayer coatings on their corrosion and mechanical properties. In: *Sviridov readings 2012: book of abstracts of 4-th international conference on chemistry and chemical education*, Minsk, 9–13 Apr, p 58
36. Norouzi B, Norouzi M (2012) Methanol electrooxidation on novel modified carbon paste electrodes with supported poly(isonicotinic acid) (sodium dodecyl sulfate)/Ni–Co electrocatalysts. *J Solid State Electrochem* 16:3003–3010. doi:10.1007/s10008-012-1736-1
37. Oleksy M, Budniok A, Matyja P (1993) Electrolytic composite layers based on nickel with nickel oxide addition. *Thin Solid Films* 235:96–100. doi:10.1016/0040-6090(93)90249-o
38. Golikand AN, Raouf J, Baghayeri M, Asgari M, Irannejad L (2009) nickel electrode modified by N,N-bis(salicylidene)phenylenediamine (salophen) as a catalyst for methanol oxidation in alkaline medium. *Russ J Electrochem* 45(2):192–198. doi:10.1134/S1023193509020104
39. Asgari M, Maragheh MG, Davarkhah R, Lohrasbi E, Golikand AN (2012) Electrocatalytic oxidation of methanol on the nickel-cobalt modified glassy carbon electrode in alkaline medium. *Electrochim Acta* 59:284–289. doi:10.1016/j.electacta.2011.10.091

## Chapter 42

# Development of a New Biosensor by Adsorption of Creatinine Deiminase on Monolayers of Micro- and Nanoscale Zeolites

Svitlana V. Marchenko, Ihor I. Piliponskiy, Olha O. Mamchur, Oleksandr O. Soldatkin, Ivan S. Kucherenko, Berna Ozansoy Kasap, Burcu Akata Kurç, Sergei V. Dzyadevych, and Alexei P. Soldatkin

### 42.1 Introduction

In recent years, scientists are very active in the study of nanoparticles because of their unique properties, significantly different than those of the same materials at the bulk scale, which offers potential applications of nanoscaled materials in various fields [1, 2]. Production of these new materials and structures should be low cost and safe for the environment. An application of nanomaterials for the development of biosensors is getting more and more popular and widespread.

The application of different nanotechnologies for elaboration of optimal method of immobilization is very important for the development of new biosensors and improvement of their analytical characteristics. The simplest method of enzyme

---

S.V. Marchenko (✉) • I.S. Kucherenko

Laboratory of Biomolecular Electronics, Institute of Molecular Biology and Genetics, National Academy of Sciences of Ukraine, Zabolotnogo Street 150, 03143, Kyiv, Ukraine  
e-mail: [svmarchenkosv@ukr.net](mailto:svmarchenkosv@ukr.net); [kucherenko.i.s@gmail.com](mailto:kucherenko.i.s@gmail.com)

I.I. Piliponskiy • O.O. Mamchur

Faculty of Biotechnology and Environmental Control, National University of Food Technologies, Volodymyrska Street 68, 01601, Kyiv, Ukraine  
e-mail: [igorpiliponskiy@gmail.com](mailto:igorpiliponskiy@gmail.com); [oliyamamchur17@gmail.com](mailto:oliyamamchur17@gmail.com)

O.O. Soldatkin • S.V. Dzyadevych • A.P. Soldatkin

Laboratory of Biomolecular Electronics, Institute of Molecular Biology and Genetics, National Academy of Sciences of Ukraine, Zabolotnogo Street 150, 03143, Kyiv, Ukraine

Institute of High Technologies, Taras Shevchenko National University of Kyiv, Volodymyrska Street 64, 01601, Kyiv, Ukraine

e-mail: [alex\\_sold@yahoo.com](mailto:alex_sold@yahoo.com); [dzyad@yahoo.com](mailto:dzyad@yahoo.com); [a\\_soldatkin@yahoo.com](mailto:a_soldatkin@yahoo.com)

B.O. Kasap • B.A. Kurç

Central Laboratory, Middle East Technical University, 06531, Ankara, Turkey  
e-mail: [bernaozansoy@gmail.com](mailto:bernaozansoy@gmail.com); [akata@metu.edu.tr](mailto:akata@metu.edu.tr)

© Springer International Publishing AG 2017

O. Fesenko, L. Yatsenko (eds.), *Nanophysics, Nanomaterials, Interface Studies, and Applications*, Springer Proceedings in Physics 195,  
DOI 10.1007/978-3-319-56422-7\_42

immobilization is an adsorption on insoluble carrier [3]. Any solid material with microporous structure can serve as an adsorbent. The most important features of any adsorbent are its surface area and structure. Additionally, the adsorbent chemical nature and surface polarity can influence the gravity between the adsorbent and the substance absorbed [4–6].

Zeolites, microporous aluminosilicate minerals of natural or synthetic origin, are one of the most commonly used adsorbents due to their porous structure, catalytic activity, and hydrothermal stability. They are used as adsorption carriers for a large number of organic and inorganic materials in various advanced areas: electrochemistry, electrocatalysis, dispersion electrolysis, biosensorics, potentiometry, accumulation of energy, and photoelectrochemistry. The process of adsorption using zeolites depends on a number of factors, including temperature, pH, time of contact, and substance concentration. Recently, nanoscaled zeolite crystals (nanozeolites) provoke increasing interest due to their unique efficiency in catalysis and immobilization of enzymes [6, 7].

To date using zeolites of various types, the biosensors have been developed based on enzymes glucose oxidase [8–12], urease [13–21], acetylcholinesterase [22], butyrylcholinesterase [23, 24], and creatinine deiminase [25]. Three-enzyme system, glucose oxidase/mutarotase/invertase, was also immobilized using silicalite [26].

This study was aimed at developing creatinine-sensitive biosensor based on pH-sensitive field-effect transistors, in which the following zeolites were used as adsorbents for creatinine deiminase: silicalite, zeolite beta (BEA), zeolite nano-BEA, BEA modified with gold particles (BEA-gold), and BEA modified with ionic gold ( $\text{Au}^{3+}$ ) (BEA-Au). Creatinine deiminase is quite widely applied for creatinine quantification in real biological samples. Determination of creatinine in human blood and urine is important in clinical practice, as it partly reflects the function of kidney, muscles, and thyroid. It is also useful for biomedical diagnosis of acute myocardial infarction and quantitative description of hemodialysis therapy [27]. Every year, millions of patients die from the initial acute heart attacks, which are a consequence of undiagnosed renal disease. Therefore, the patients suffering from kidney disease need a device for daily measurement of the creatinine concentration in the blood [28, 29]. Here, we assumed to develop the method for rapid analysis of creatinine concentration in model and real samples.

## 42.2 Experimental

### 42.2.1 Materials

In experiments the following reagents were used: creatinine deiminase (CD) of microbial origin (EC 3.5.4.21) and activity of 36 U/mg (“Sigma-Aldrich,” Japan); creatinine, bovine serum albumin (BSA, fraction V), and 25% aqueous solution of glutaraldehyde (“Sigma-Aldrich Chemie,” Germany); DEAE-Dextran (“Fluka Biochemika,” France); lactitol (“Fluka,” Switzerland); and working phosphate buffer



( $\text{KH}_2\text{PO}_4\text{-NaOH}$ ), pH 7.4, prepared from reagents manufactured by “Helicon” (Moscow, Russia). For zeolite synthesis, we used tetraethyl orthosilicate (TEOS) 98% and 25% aqueous solution of tetrapropylammonium hydrochloride (TPAOH) (both from “Acros Organics,” Belgium), 98% sodium hydroxide (NaOH) (“J. T. Baker,” USA), and 35% aqueous solution of tetraethylammonium hydrochloride (TEAOH) (“Aldrich,” USA). Other inorganic substances used were of analytical grade of purity.

## 42.2.2 Potentiometric Transducers

In the work, we used sensor chips with a differential pair of pH-sensitive field-effect transistors, developed at the V.Ye. Lashkarev Institute of Semiconductor Physics, NASU. Two identical p-channel transistors were placed on a single crystal of a total area 8x8 mm. The transistors were separated via a 50- $\mu\text{m}$ -wide protective  $\text{n}^+$ -region contacting with the substrate. The crystal included also  $\text{p}^+$ -diffusion buses with contacts to drain and source, which are connected to the chip edge, output cable to the embedded reference microelectrode, and two test MOS-transistors with metal gates for checking electrical parameters of the structures prepared.

Ion-selective properties of transistors are determined by a silicon nitride layer, deposited in their subgate area. pH sensitivity of the elements was about 30–40  $\mu\text{A}/\text{pH}$ . The general and schematic views of pH-sensitive field-effect transistors are presented in Fig. 42.1.

**Fig. 42.1** General and schematic views of pH-sensitive field-effect transistor. 1, 2 sensitive areas (transistors), 3 working enzyme membrane, 4 BSA-based reference membrane, 5 contacts

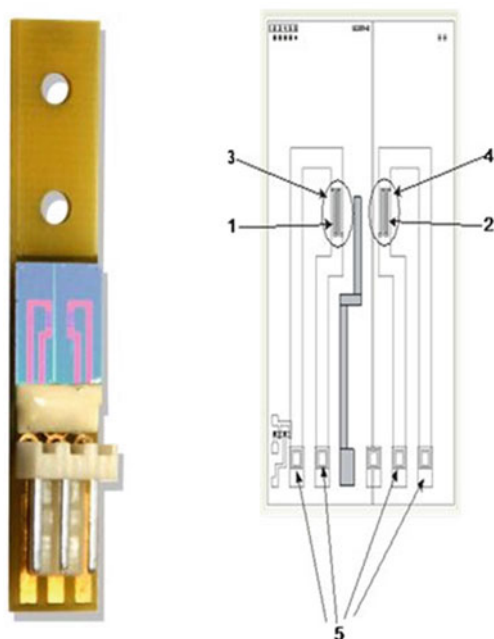
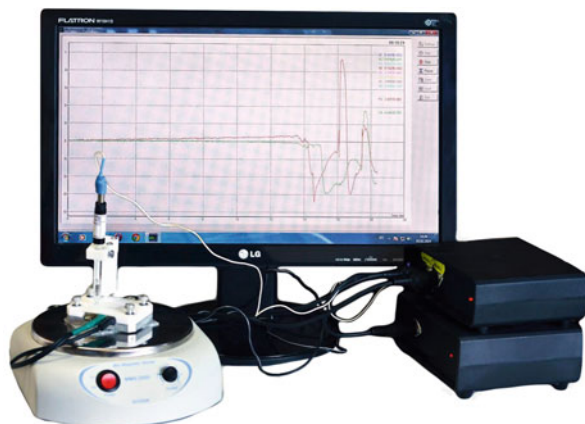


**Fig. 42.2** General view of measurement setup used with pH-FET-based biosensors



The pH sensitivity of sensor elements was about 40 mV/pH. At the given slope of transfer current-voltage characteristic of the transistor, ranging from 400 to 500  $\mu\text{A}/\text{V}$ , it provided the dependence of the channel current on pH of approximately 15–20  $\mu\text{A}/\text{pH}$ .

The response of pH-FET was measured using direct detection of current in the channel of field-effect transistor with an active load. The threshold voltage for the pH-FET used was about  $-2.5$  V. Measurements were carried out under the following conditions: channel current about 500  $\mu\text{A}$ , and drain-source voltage about 2 V; the substrate is connected to drain.

The measuring device, which was used in the work, comprised an analog-to-digital electrochemical apparatus; an Ag/AgCl reference electrode; an electrochemical cell volume of 1.5–2 ml, into which pH-FET was placed and fixed; and PC. Its image is presented in Fig. 42.2.

The process of receiving and processing analytical signals from the biosensor was automated using a specially developed program “Multisensor Workstation.”

### **42.2.3** *Synthesis of Zeolite Particles and Their Characteristics*

#### **42.2.3.1** *Synthesis of Silicalite*

The molar ratio of initial substances in the gel for synthesis was as follows: 1 TPAOH:4 TEOS:350  $\text{H}_2\text{O}$ . Tetrapropylammonium hydrochloride (TPAOH) served as a source of OH groups and tetraethyl orthosilicate (TEOS) as a source of silicon. TEOS was added to the TPAOH solution at vigorous stirring, and this process lasted at room temperature for 6 h. Then the mixture was placed in an incubator for 18 h at 125 °C. The obtained solid particles were centrifuged at 7500 rpm, washed with deionized water, and dried at 50 °C for 12 h. The particles size was about 450 nm.

### 42.2.3.2 Synthesis of Zeolite BEA

An optimized molar composition of the gel used for the synthesis of zeolite beta (BEA) was as follows: 1.92 Na<sub>2</sub>O:1 Al<sub>2</sub>O<sub>3</sub>:60 SiO<sub>2</sub>:444 H<sub>2</sub>O:4.6 (TEA)<sub>2</sub>O. A mixture of sodium aluminate, sodium hydroxide, and distilled water was stirred for 40 min and then placed in an oven at 100 °C for 50 min. Next, TEOH was added to the cooled mixture and stirred for 15 min, and SiO<sub>2</sub> was added and stirred again for 15 min. The obtained mixture was placed in a Teflon-lined autoclave for crystallization. The static synthesis was carried out for 14 days at 120 °C. The product was centrifuged three times at 7500 rpm and dried overnight at 50 °C. As a result, the mixture of zeolite particles 700 and 1300 nm in size was obtained.

### 42.2.3.3 Synthesis of Nano-BEA

The molar composition of nano-BEA was 0.25 Al<sub>2</sub>O<sub>3</sub>:25 SiO<sub>2</sub>:490 H<sub>2</sub>O:9 TEOH. TEOS was a source of silica. Aluminum isopropoxide, TEOH, and distilled water were used as additional reagents. The synthesis of nanoparticles lasted under static conditions for 4 h in a clean solution. The crystallization was completed during 14 days under static conditions at 100 °C in a Teflon-lined autoclave. The product was purified three times by centrifugation at 7500 rpm. The nano-BEA particles were approximately 100 nm in size.

### 42.2.3.4 Synthesis of BEA-Gold and BEA-Au<sup>3+</sup>

Prior to the procedure of ion exchange, the synthesized BEA zeolites were calcined at 500 °C in air for 12 h. 400 mg of calcined BEA were added to 100 ml of aqueous solution of gold chloride (III) to obtain substituted zeolite BEA (Au(III)BEA) and stirred at 50 °C. In one day, the obtained Au(III)BEA samples were washed and centrifuged four times at 7500 rpm and afterward dried in air at 50 °C. The nanoclusters Au(0)BEA were produced by reduction of gold ions at 50 °C in a suspension of sodium borohydride. The stage of regeneration was completed when the hydrogen evolution stopped. The Au(0)BEA samples were then centrifuged, washed four times at 7500 rpm, and dried at 50 °C.

### 42.2.3.5 Characteristics of Synthesized Zeolites

X-ray diffraction patterns of silicalite, nano-BEA, BEA, and BEA-gold are presented in Fig. 42.3. The Si/Al ratio for all types of zeolite was 20.8 to 21.5. The size of nanoparticles of BEA was on average 100 nm, silicalite 470 nm, and BEA and BEA-gold 1.2 μm. The external surface ( $S_{\text{ext}}$ ) of silicalite was 96 m<sup>2</sup>/g, BEA 128 m<sup>2</sup>/g, BEA-gold 160 m<sup>2</sup>/g, and nano-BEA, 183 m<sup>2</sup>/g. Zeta potential of silicalite was -62.6 mV, BEA -47.9 mV, BEA-gold -47.2 mV, and nano-BEA -36.6 mV.

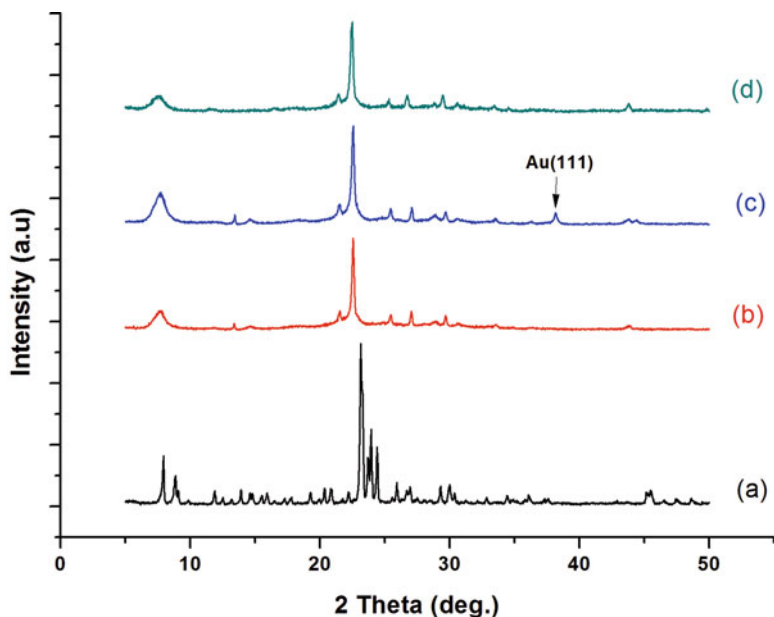


**Fig. 42.3** The XRD spectrum of (a) silicalite, (b) nano-BEA, (c) BEA, and (d) BEA-gold

#### **42.2.4** *Modification of pH-FET Surface with Monolayers of Zeolites*

To prepare the zeolite monolayers, the electrode surfaces were first treated for 15 min in the Mucosal solution, then were washed with distilled water, and air-dried. Next, a homogeneous polyethylenimine layer was formed on the transducers by spin coating. The polyethylenimine layer served to separate the electrode surface and zeolites. The best conditions of polyethylenimine deposition for following formation of zeolite monolayers were: 1% alcoholic solution of polyethylenimine, centrifugation for 15 min at 3000 rpm, and burning for 30 min at 100 °C. The obtained transducers, modified with zeolite monolayers, were used for CD adsorption.

#### **42.2.5** *Creatinine Deiminase Adsorption on Surface of Transducers, Modified with Various Zeolites*

The previously prepared working and reference gels (0.1  $\mu$ l each) were deposited onto the sensors, modified with zeolites. The working gel based on CD was prepared as follows: the enzyme sample of final concentration 20% was dissolved in 20 mM potassium phosphate buffer, pH 7.4, with addition of 10% of glycerol, 20% of BSA,

4% of lactitol, and 0.4% of DEAE-Dextran. Glycerol was added to stabilize the enzyme during immobilization and to prevent early drying of the solution on the transducer surface. Bovine serum albumin and lactitol were also used as stabilizing agents. To prepare the reference gel, we used 40% of BSA and 10% of glycerol in 20 mM potassium phosphate buffer, pH 7.4.

### **42.2.6 Immobilization of Creatinine Deiminase in Glutaraldehyde Vapors**

To immobilize CD via GA, the solution of 10% CD and 10% BSA was prepared in 20 mM phosphate buffer, pH 7.5. Glycerol was added to the enzyme-BSA mixture to a final concentration of 10% to stabilize the enzyme during immobilization and to prevent early drying of the solution on the transducer surface. A drop of this mixture was deposited on one sensitive surface of transducer (transistor) and 20% BSA solution without enzyme on another (in that way the reference membrane was formed). For membrane immobilization, the transducers were placed in saturated GA vapor for 15–30 min and then air-dried and washed from excess glutaraldehyde solution in 5 mM buffer, pH 7.5, for 10–20 min.

### **42.2.7 Measurement Procedure**

Determination of creatinine in the model solutions was performed in 5 mM potassium phosphate buffer, pH 7.4, at room temperature. The working cell of open type, volume 1.5 ml, with intensive stirring by a magnetic stirrer was used. Prior to the work, the transducers with immobilized membranes were washed for 20–30 min from unbound GA until the baseline became stable. The substrate concentration was changed by adding certain aliquots of stock solution. After each response, the biosensor was washed from the reaction products, changing the working buffer every 2 min at least three times.

## **42.3 Results and Discussion**

The function of developed biosensor for creatinine determination is based on the reaction of creatinine hydrolysis catalyzed by creatinine deiminase, which is contained in a sensitive element of the biosensor:

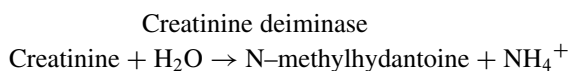
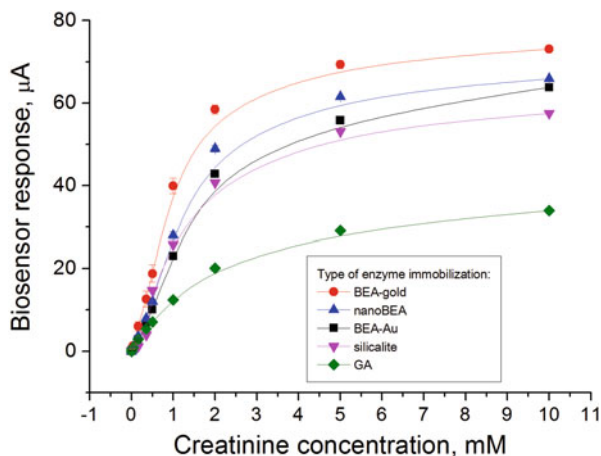


**Fig. 42.4** Calibration curves for determination of creatinine concentration obtained by biosensors based on CD adsorption on zeolites of four types (BEA-gold, nano-BEA, BEA-Au, silicalite) and covalent CD-BSA cross-linking in GA vapor



The transducer of biosensor registers the changes in pH induced by creatinine hydrolysis, which are proportional to the substrate concentration in the analyzed solution.

The basic idea of the work presented was to compare analytical characteristics of the biosensors based on the proposed method of immobilization, i.e., enzyme adsorption on monolayers of zeolites of different types, with those of biosensors based on traditional technique, i.e., immobilization in GA vapor. The calibration curves were obtained for the biosensors under investigation, i.e., dependence of the responses on creatinine concentration in the working buffer (Fig. 42.4).

It was shown that CD was successfully adsorbed on zeolites of all types, which is evidenced by effective operation of biosensors with zeolite monolayers. Here, the biosensor based on CD adsorption on pH-FET modified with BEA-gold was characterized by the best sensitivity to creatinine, whereas the worst was typical for the biosensors, in which the covalent cross-linking of CD with BSA in saturated GA vapor was used. This can be explained by a softer technique of enzyme immobilization by adsorption on zeolites, at which the CD activity losses are less than in the case of covalent cross-linking CD using GA.

As known, a disadvantage of absorption is probable leaching of enzymes into the working buffer due to a weak binding between the enzyme and adsorbent [3]. Therefore, at the next stage, the operational stability of the developed biosensors was tested. To explore this important analytical characteristic, the signals of all biosensors to the same concentration of creatinine were measured over one working day, the working surface of biosensors being kept during intervals between measurements in the working buffer (Fig. 42.5). As seen, all biosensors, both those based on immobilization with zeolites and in GA vapor, had good signal reproducibility over 8 working hours. This is confirmed by a slight relative standard deviation (RSD) of responses, which was 2–3% for all biosensors (except nano-BEA) indicating quite stable binding of CD with zeolites.

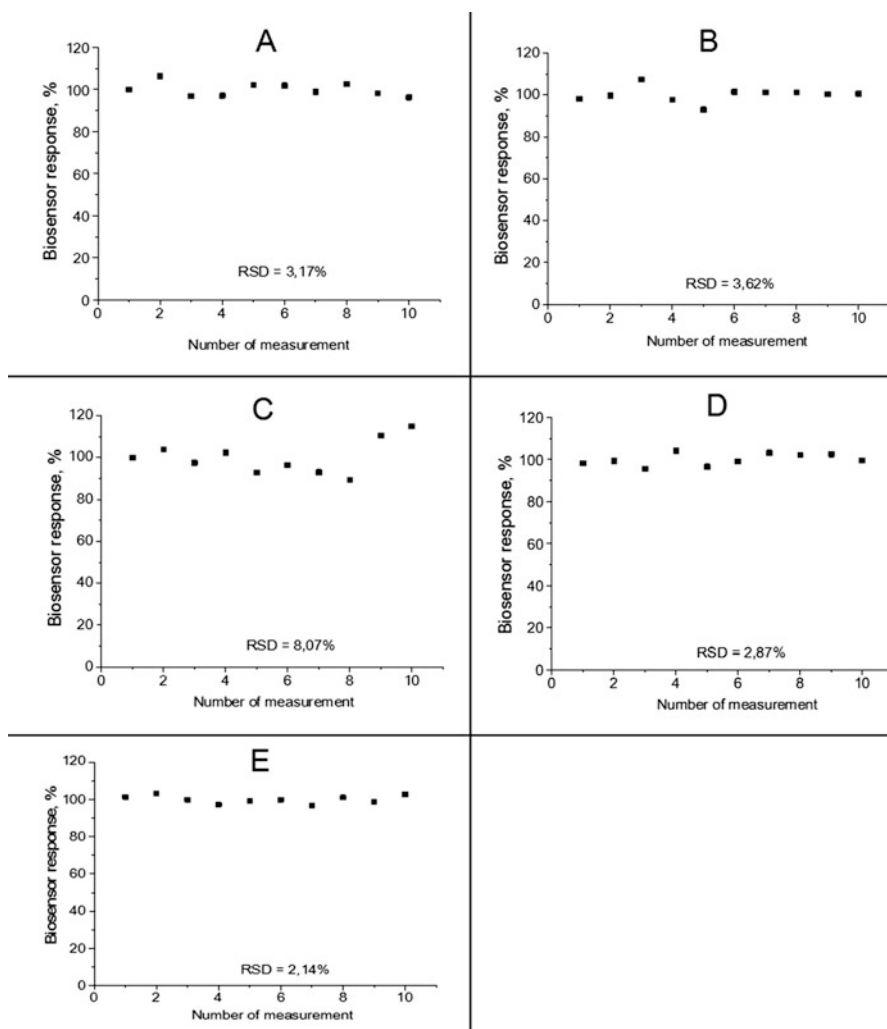


**Fig. 42.5** Reproducibility of signals of biosensors manufactured using CD adsorption on zeolites (a, BEA-Au; b, BEA-gold; c, nano-BEA; d, adsorption on silicalite) and by covalent cross-linking in GA vapor (e). Measurements were carried out in 5 mM phosphate buffer, pH 7.4, at room temperature. Creatinine concentration was 1 mM

At the next stage, we investigated reproducibility of the biosensor preparation (inter-reproducibility, i.e., a deviation between the responses of different biosensors). Three transducers with similar working characteristics were modified in the same way, the membranes were deposited on their surfaces, and the responses of the biosensors to 1 mM creatinine were measured three times for each biosensor. The comparison of inter-reproducibility was carried out by calculating RSD.

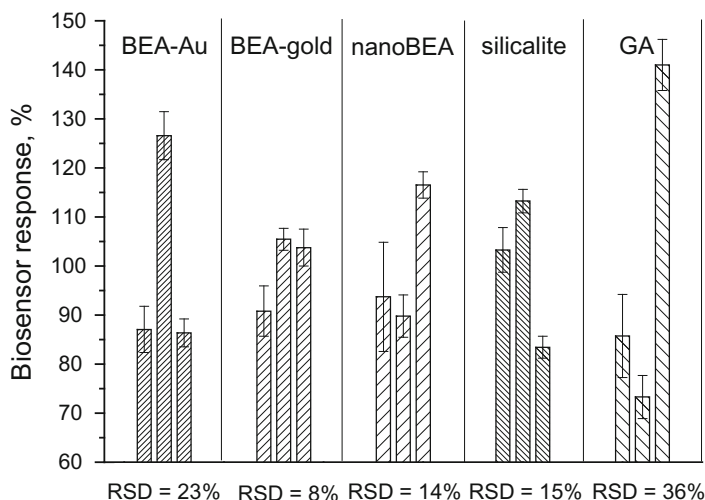


**Fig. 42.6** Reproducibility of preparation of various biosensors. Three adjacent columns correspond to responses of three different biosensors prepared by the same technique. In each three-column part, the average value was taken for 100%. Measurements were carried out at room temperature in 5 mM phosphate buffer, pH 7.4. Creatinine concentration was 1 mM

**Table 42.1** Basic analytical characteristics of biosensors prepared using adsorption (monolayer method of zeolite deposition) and covalent cross-linking in GA vapor

Parameter	Limit of detection, $\mu\text{M}$	Linear dynamic range, $\mu\text{M}$	Response time, s	Regeneration time, s
Material for immobilization				
GA	10	10–2000	240	300
Silicalite	2	5–2000	30	60
BEA	5	5–2000	150	120
BEA-Au	5	5–2000	60–90	60–120
BEA-gold	1	5–2000	60	60–120
Nano-BEA	1	3–2000	60–120	60

As seen in Fig. 42.6, the best inter-reproducibility was revealed in the case of CD adsorption on pH-FET modified with BEA-gold, nano-BEA, and silicalite and the worst for covalent cross-linking with BSA in saturated GA vapor.

Given the calibration curves and typical responses to the substrate addition, the basic analytical characteristics were calculated as follows: a limit of detection, linear dynamic range, response time, and regeneration time. The data are presented in Table 42.1.

Comparing the results obtained, a conclusion can be made that the use of monolayer method of zeolite deposition for the development of creatinine-sensitive biosensors leads to the improvement of their analytical characteristics: a decrease of



the minimum limit of creatinine detection for zeolites BEA-Au, BEA-gold, nano-BEA, and silicalite as well as a decrease in overall response time, which is a significant positive effect on the biosensor creation.

## 42.4 Conclusions

Novel bioselective elements of the biosensor based on creatinine deiminase immobilized on pH-sensitive field-effect transistors were developed using different types of zeolites: silicalite, BEA, nano-BEA, BEA-Au<sup>3+</sup>, and BEA-gold. It was shown that application of the adsorption method for immobilization of creatinine deiminase on the surfaces of pH-FET, modified with zeolites, leads to the improvement of basic analytical characteristics, as compared with the method of covalent cross-linking with glutaraldehyde in BSA membrane. In particular, it resulted in a decrease of the response time and thus of the overall time of analysis; an increase in sensitivity and, in some cases, a reduction in the minimum limit of detection; and a reduction of the measurement error.

**Acknowledgments** The authors gratefully acknowledge the financial support of this study by the Ministry of Education and Science of Ukraine (project DZ/45-2015) and STCU Project 6052 “Enzyme multibiosensor system for renal dysfunction diagnosis and hemodialysis control.”

## References

1. Adhikari R (2016) Applications of upconversion nanoparticles in nanomedicine. *J Nanomed Nanotechnol* 7:e141
2. Krejčová L, Michálek P, Rodrigo MM et al (2015) Nanoscale virus biosensors: state of the art. *Nanobiosensors in Disease Diagnosis* 4:47–66
3. Bonnet C, Andreescu S, Marty JL (2003) Adsorption: an easy and efficient immobilisation of acetylcholinesterase on screen-printed electrodes. *Anal Chim Acta* 481:209–211
4. Wu J, Li X, Yan Y (2013) Protein adsorption onto nanozeolite: effect of micropore openings. *J Colloid Interface Sci* 406:130–138
5. Bhakta SA, Evans E (2015) Protein adsorption onto nanomaterials for the development of biosensors and analytical devices: a review. *Anal Chim Acta* 872:7–25
6. Bacakova L, Vandrovčova M, Jirka I (2016) Biomedical applications of zeolites – a review. *J Material Sci Eng* 5:4
7. Kabwadza-Corner P, Johan E, Matsue N (2015) pH dependence of lead adsorption on Zeolites. *J Environ Prot* 6:45–53
8. Soldatkin O, Shelyakina M, Arkhypova V et al (2015) Nano- and micro-sized zeolites as a perspective material for potentiometric biosensors creation. *Nanoscale Res Lett* 10:59
9. Pyeshkova VN, Dudchenko OY, Soldatkin OO et al (2014) Application of silicalite for improvement of enzyme adsorption on the stainless steel electrodes. *Biopolym. Cell* 30:462–468
10. Nenkova R, Wu J, Zhang Y et al (2013) Influence of different nanozeolite particles on the sensitivity of a glucose biosensor. *Anal Biochem* 439:65–72

11. Soldatkin OO, Kucherenko IS, Shelyakina MK et al (2014) Elaboration of new method of enzyme adsorption on silicalite and nano beta zeolite for amperometric biosensor creation. *Biopolym Cell* 30:291–298
12. Dudchenko OY, Pyeshkova VM, Soldatkin OO et al (2016) Development of silicalite/glucose oxidase-based biosensor and its application for glucose determination in juices and nectars. *Nanoscale Res Lett* 11:59
13. Hamlaoui ML, Reybier K, Marrakchi M (2002) Development of a urea biosensor based on a polymeric membrane including zeolite. *Anal Chim Acta* 466:39–45
14. Shelyakina MK, Soldatkin OO, Arkhypova VM et al (2014) Study of zeolite influence on analytical characteristics of urea biosensor based on ion-selective field-effect transistors. *Nanoscale Res Lett* 9:124–132
15. Soldatkin OO, Kucherenko IS, Marchenko SV et al (2014) Application of enzyme/zeolite sensor for urea analysis in serum. *Mater Sci Eng C* 42:155–160
16. Kucherenko IS, Soldatkin OO, Kasap B et al (2012) Elaboration of urease adsorption on silicalite for biosensor creation. *Electroanalysis* 24:1380–1385
17. Soldatkin OO, Soy E, Errachid A et al (2011) Influence of composition of zeolite/enzyme nanobiocomposites on analytical characteristics of urea biosensor based on ion-selective field-effect transistors. *Sens Lett* 9:2320–2326
18. Soldatkin OO, Kucherenko IS, Shelyakina MK et al (2013) Application of different zeolites for improvement of the characteristics of a pH-FET biosensor based on immobilized urease. *Electroanalysis* 25:468–474
19. Kucherenko IS, Soldatkin OO, Soy E et al (2012) Effect of different modifications of BEA-zeolites on operational characteristics of conductometric biosensor. *Mater Sci Eng C* 32:1648–1653
20. Kirdeciler SK, Soy E, Öztürk S et al (2011) A novel urea conductometric biosensor based on zeolite immobilized urease. *Talanta* 85:1435–1441
21. Saiapina OY, Pyeshkova VM, Soldatkin OO et al (2011) Conductometric enzyme biosensors based on natural zeolite clinoptilolite for urea determination. *Mater Sci Eng C* 31:1490–1497
22. Kucherenko I, Soldatkin O, Kasap BO et al (2015) Nanosized zeolites as a perspective material for conductometric biosensor creation. *Nanoscale Res Lett* 10:209
23. Soy E, Arkhypova V, Soldatkin O et al (2012) Investigation of characteristics of urea and butyrylcholine chloride biosensors based on ion-selective field-effect transistors modified by the incorporation of heat-treated zeolite Beta crystals. *Mater Sci Eng C* 32:1835–1842
24. Soy E, Galioglu S, Soldatkin OO et al (2013) Direct evidence of advantage of using nanosized zeolite Beta for ISFET-based biosensor construction. *J Nanopart Res* 15:1645
25. Marchenko SV, Soldatkin OO, Kasap OB et al (2016) Creatinine deiminase adsorption onto silicalite-modified pH-FET for creation of new creatinine-sensitive biosensor. *Nanoscale Res Lett* 11:173
26. Pyeshkova VM, Dudchenko OY, Soldatkin OO et al (2015) Application of silicalite-modified electrode for the development of sucrose biosensor with improved characteristics. *Nanoscale Res Lett* 10:149
27. Pundir CS, Yadav S, Kumar A (2013) Creatinine sensors. *TrAC Trends Anal Chem* 50:42–52
28. Marchenko SV, Kucherenko IS, Soldatkin OO et al (2015) Potentiometric biosensor system based on recombinant urease and creatinine deiminase for urea and creatinine determination in blood dialysate and serum. *Electroanalysis* 27:1699–1706
29. Nanda SS, An SSA, Yi DK (2015) Measurement of creatinine in human plasma using a functional porous polymer structure sensing motif. *Int J Nanomedicine* 10:93–99

# Chapter 43

## Nanostructured Dextran-Graft-Polyacrylamide Flocculants: Effect of Internal Molecular Structure on Flocculative Efficiency

N. V. Kutsevol, V. A. Chumachenko, A. V. Balega, O. M. Nadтока, and A. P. Naumenko

### 43.1 Introduction

Water treatment represents one of the most important problems caused by environmental pollution and increased worldwide demand for pure water. Water, usually surface water and industrial water, contains many impurities in the form of very fine suspended solids, dissolved solids, inorganic and organic particles, metals, and others. The very small size of the particles and the presence of surface charge cause the difficulties to settle down of impurities [1, 2]. Flocculation is a physical and chemical process that is used for the removal of colloid, visible sediments, and some dissolved impurities from water [3]. In the flocculation process, the polymers are used as flocculating agent for the formation of bridges between the colloidal particles or other impurities that form clusters [4–7]. Moreover, the flocculating agents can remove some dissolved impurities by reacting with a functional group of the flocculant. Polyacrylamide is a common type of polymeric flocculant that is used because of its low cost and because it allows for synthesizing polyacrylamide with variable functionality (positive, neutral, negative). In recent years, many investigations have focused on replacing linear flocculants with branched polymers [7, 8].

Branched polymers have attracted special interest because of their controlled internal molecular structure, which results from the fact that the number of variable

---

N.V. Kutsevol (✉) • V.A. Chumachenko • O.M. Nadтока  
Faculty of Chemistry, Taras Shevchenko National University of Kyiv, Kyiv, Ukraine  
e-mail: [kutsevol@ukr.net](mailto:kutsevol@ukr.net)

A.V. Balega  
Institute of Biology, Taras Shevchenko National University of Kyiv, Kyiv, Ukraine

A.P. Naumenko  
Faculty of Physics, Taras Shevchenko National University of Kyiv, Kyiv, Ukraine

parameters is overwhelmingly large, that is, the initial polymer architecture, average degree of polymerization, solubility properties, distance between grafts, nature and flexibility of backbone and grafts, and so forth [9, 10].

The additional factors affecting the internal structure appear for branched polyelectrolytes: for example, the charge density or pH, the nature of the charge distribution, and the valence and nature of counterions. Owing to structural peculiarities, the local concentration of functional groups in branched polymers is notably higher than in linear ones, so they should be promising materials for technological applications, in particular for issues related to pollution: the sorption of toxic metal ions [11] from a water medium or the regulation of stability of dispersed systems.

Starlike and linear polyacrylamides (PAAs) in nonionic and anionic forms were tested as flocculants in the polydispersed kaolin dispersion model. Also, the advantage of using branched-polymer flocculants to remove heavy metal ions from water containing clay particles and metal ions simultaneously has been shown.

## 43.2 Experimental Setup

### 43.2.1 Materials

Dextran-g-polyacrylamide (D-g-PAA) copolymers consist of a dextran core ( $M_w = 20,000$  or  $M_w = 70,000$ ), and polyacrylamide grafts were synthesized by radical polymerization [12]. The theoretical number of grafting sites per dextran backbone for both series of copolymers according to synthesis conditions was equal to  $n = 20$ . The samples were designed as D20-g-PAA20 and D70-g-PAA20. Linear PAA with  $M_w = 1.4 \times 10^6$  was synthesized for comparative investigations.

The samples were characterized using self-exclusion chromatography coupled with light scattering (LS) and refractometry (Rf). The features of their molecular structure were analyzed in detail in [12].

Alkaline hydrolysis was used to obtain the branched polyelectrolytes dextran-graft-polyacrylamide/polyacrylic acid (D20(70)-g-PAA20(PE)) and linear anionic PAA(PE). The synthesis and characterization of polyelectrolytes were described in [13]. Branched and linear polyelectrolytes and linear PAA were tested as flocculants in model kaolin polydispersed dispersion ( $C = 30$  g/L) containing  $\text{Cu}^{2+}$ ,  $\text{Co}^{2+}$ , and  $\text{Ni}^{2+}$  ions.

### 43.2.2 Methods

#### 43.2.2.1 Self-exclusion Chromatography

Self-exclusion chromatography (SEC) analysis was carried out using a multidetection device consisting of an LC-10 AD Shimadzu pump (throughput  $0.5 \text{ mL min}^{-1}$ ), a WISP 717+ automatic injector from WATERS, three coupled 30 cm-Shodex OH-pak columns (803HQ, 804HQ, 806HQ), a multiangle light scattering detector

DAWN F from Wyatt Technology (Goleta, CA), and a differential refractometer R410 from WATERS. Distilled water containing 0.1 M  $\text{NaNO}_3$  was used as eluent. The polymer concentrations in solutions prepared for the SEC analysis ( $C = 1 \text{ g/L}$ ) were below overlap concentration  $C^* = 1/[\eta]$ ; therefore, the intermolecular interactions can be neglected.

#### 43.2.2.2 Potentiometry

Potentiometric titration was performed using a pH meter pH-340 (СПеЛ, Тех-НоРесуьс, Moscow, Russia). Solutions of HCl (0.2 N) and NaOH (0.2 N) as titrates were used. Polymer concentration was 2 g/L. The measurements were performed at 25.0°C under argon, with constant stirring.

#### 43.2.2.3 Flocculation Ability Test

Flocculation tests were performed in 50 mL graduated cylinders. Kaolin KOM (Poland) with high content of 2  $\mu\text{m}$  particles (more than 60%) was applied in 30  $\text{g}\cdot\text{L}^{-1}$  suspensions. Polymer concentrations were varied in a range from  $C = 1 \cdot 10^{-4}$  to  $1 \cdot 10^{-1} \text{ g/L}$ . The cylinders were inverted 12 times to mix the kaolin suspension with a dose of flocculant solution. The kaolin sedimentation was measured by observing the height of clarified liquid versus time and the sedimentation rate ( $V$ , mm/s) was analyzed. The supernatant clarity was analyzed by measuring the absorbance at 540 nm (D) in 20 min of flocculation using Varian Cary 50 Scan UV-Visible spectrophotometer.

#### 43.2.2.4 Test for Heavy Ion Removal from [Kaolin Dispersion/Polymer/ $\text{Me}^{2+}$ ] Systems

5 mL of water solution of  $\text{CuSO}_4$ ,  $\text{NiSO}_4$ , or  $\text{CoSO}_4$  ( $C = 0.60 \text{ g/L}$ ) were added to 1.5 g of kaolin, mixed for 10 s, then 45 mL of water solution of polymer-flocculant was added. In 20 min 1 mL of the supernatant was diluted ten times and analyzed by atomic absorption on the "AAS-1 N" (Carl Zeiss, Jena, Germany) with an acetylene torch. The source of the radiation was a lamp with a hollow cathode. Terms of atomic-absorption determination: copper – wavelength 324.7 nm, cobalt – 240 nm, nickel – 341,5 nm; spectral slit 0.2 nm, lamp current of 8.0 mA, acetylene flow rate  $0.5 \text{ L min}^{-1}$ , air flow rate –  $4.0 \text{ L min}^{-1}$ .

### 43.3 Results and Discussion

Molecular parameters of graft copolymers obtained by SEC are represented in Table 43.1.

**Table 43.1** Polymer characteristics determined by SEC:  $M_w$  is the average molecular weight;  $M_w/M_n$  the polydispersity index, and  $R_g$  the radius of gyration

Sample	$M_w \times 10^{-6}$	$R_g$	$M_w/M_n$	$(R_g^2/M_w) \times 10^3$
	mol g <sup>-1</sup>	nm		m <sup>2</sup> mol g <sup>-1</sup>
D70-g-PAA20	1.43	64	1.98	2.85
D20-g-PAA20	0.77	46	1.81	2.75
PAA	1.40	68	2.40	–

**Table 43.2** Sedimentation rate ( $V$ ) of kaolin dispersion after treatment with different concentrations of polymer-flocculant

Flocculant	$V$ , mm/s			
	$C_{\text{polymer}}$ , g/L			
	$1 \cdot 10^{-4}$	$1 \cdot 10^{-3}$	$1 \cdot 10^{-2}$	$1 \cdot 10^{-1}$
D20-g-PAA20	1.04	1.46	3.20	6.15
D70-g-PAA20	0.98	1.55	3.18	6.18
PAA	0.93	1.75	3.60	6.91
D20-g-PAA20(PE)	0.95	1.72	4.79	10.89
D70-g-PAA20(PE)	0.76	2.18	5.10	11.34
PAA(PE)	1.01	2.27	4.20	10.14

Synthesized samples are branched starlike copolymers with a dextran core and PAA arms [12, 14]. They are characterized by higher compactness in comparison with linear analogs. Compactness can be estimated as  $R_g^2/M_w$  [12] (Table 43.1). A lower  $R_g^2/M_w$  value means higher compactness. The compactness becomes higher with a decreasing distance between grafts (as for D20-g-PAA20 sample).

The branched and linear samples were saponified to obtain branched polyelectrolyte flocculants. The degree of conversion of acrylamide groups to carboxylate groups after 30 min of hydrolysis was equal to 37% for D70-g-PAA20(PE), 36% for D20-g-PAA20(PE), and 28% for PAA(PE). This confirms that the local concentration of functional groups is higher for branched polymers than their linear analogs.

D20(70)-g-PAA20, D20(70)-g-PAA20(PE), and their linear analogs PAA and PAA (PE) were analyzed as flocculants within a wide concentration range. The resulting analysis, presented in Table 43.2, shows that increasing the concentration of polymer-flocculant led to an enhancement of flocculation ability of the nonionic and anionic branched flocculants as well as their linear analogs. To conduct a correct analysis of the polymer-flocculant internal molecular structure's effect on the sedimentation rate of clay dispersion, a comparison of parameter  $V$  (Table 43.2.) at  $C_{\text{polymer}} = 1 \cdot 10^2$  g/L was carried out (Fig. 43.1). At higher concentrations of flocculant the sedimentation rate was so high that the effect of falling snow was observed (Fig. 43.2).

It is evident that nonionic flocculants with linear structure reveal a higher sedimentation rate in comparison with branched flocculants. Linear macromolecules can easily form bridges between kaolin particles because of their greater flexibility in comparison with branched macromolecules (Fig. 43.3) [14]. For flocculants

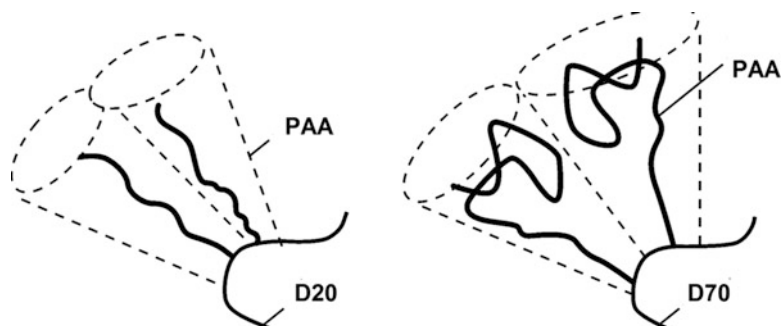
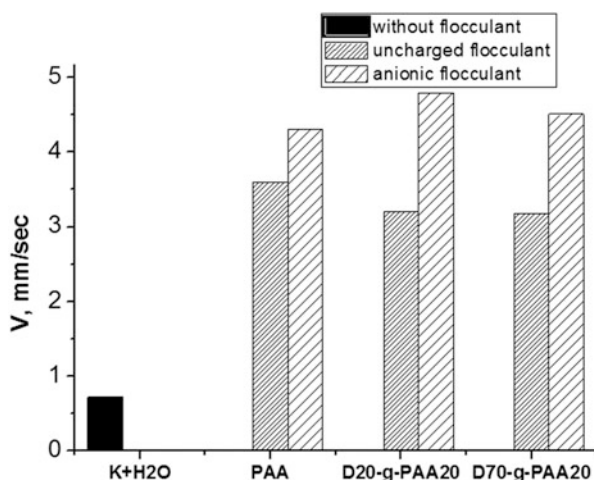


**Fig. 43.1** Scheme of conformation of grafts in branched copolymers D20-g-PAA20 and D70-g-PAA20

**Fig. 43.2** Suspension settling rate in flocculation by uncharged and anionic polymer-flocculants.

$C_{\text{floc}} = 1 \times 10^{-2}$  g/L



in anionic form, branched flocculants are more efficient in terms of the rate of suspension sedimentation. The higher value of  $V$  was observed for copolymer D20-PAA(PE) with the most extended PAA(PE) grafts. Obviously, when a polymer chain becomes very rigid the branched architecture confers some advantages to forming bridges between clay particles.

The ability to remove the smallest kaolinite particles (colloid clay particles) is the most important characteristic of the flocculants used in mineral industry wastewater recycling. Uncharged branched flocculants are more efficient at supernatant clearing in comparison with linear PAA (Table 43.3).

It was discovered that the branched anionic polymer-flocculant at  $C_{\text{floc}} = 1 \cdot 10^{-3}$  g/L stabilized the smallest particles of clay dispersion (Table 43.3, Fig. 43.4). This effect was not observed for linear PAA(PE). The stabilizing effect increases for starlike copolymers with smaller distances between PAA grafts (or higher compactness of the macromolecules). Obviously, this can be explained by the different molecular structure of the polymer-flocculant. Branched macromolecules

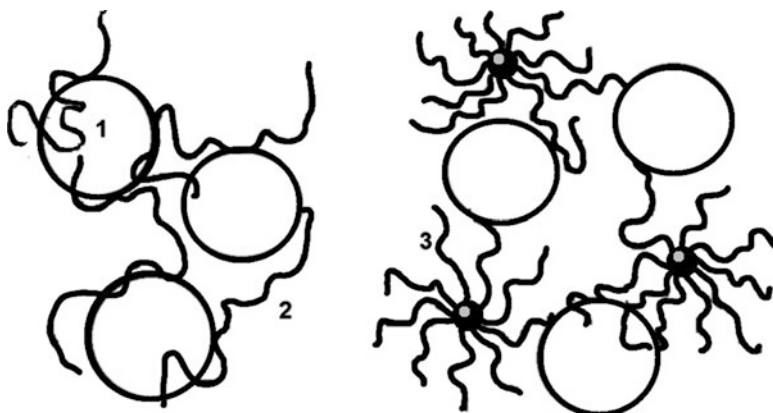


**Fig. 43.3** Scheme of floccule formation in system of uncharged flocculant/large particles of kaolin dispersion. 1: particles of kaolin, 2: linear flocculant, 3: branched flocculant

**Table 43.3** Optical density (D) of supernatant after treatment of kaolin dispersion at different concentrations ( $C_{\text{floc}}$ ) of flocculant

Sample	D			
	$C_{\text{floc}}, \text{g/L}$			
	$1 \cdot 10^{-4}$	$1 \cdot 10^{-3}$	$1 \cdot 10^{-2}$	$1 \cdot 10^{-1}$
D20-g-PAA20	0.815	0.385	0.229	0.059
D70-g-PAA20	1.000	0.517	0.261	0.081
PAA	1.287	0.990	0.282	0.240
D20-g-PAA20(PE)	0.645	0.826	0.228	0.199
D70-g-PAA20(PE)	0.879	0.954	0.221	0.158
PAA(PE)	0.734	0.481	0.265	0.191

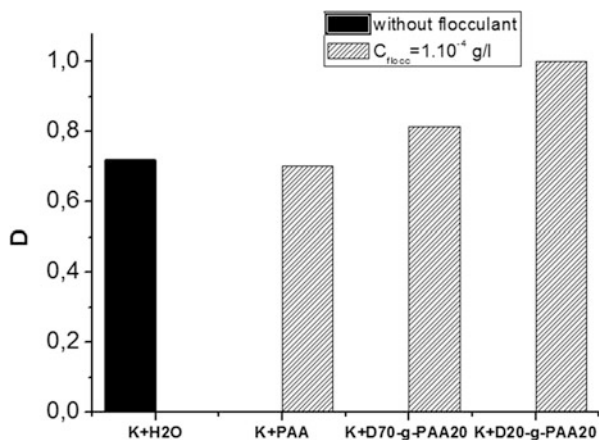
can “trap” more small colloidal particles of polydispersed kaolin dispersion than linear macromolecules (Fig. 43.5).

Increasing the concentration of polymer-flocculant makes possible two processes in parallel: capturing the smallest clay particles and forming a bridge between large kaolin particles. In the concentration range  $1 \times 10^{-3} < C \leq 1 \times 10^{-1}$  (g/dL) both uncharged and anionic flocculants of various molecular architectures have revealed a greater clearing ability with concentration growth. The most efficient for the removal of the smallest and large clay particles was branched polymer D70-g-PAA20 in nonionic and anionic forms (Fig. 43.6).

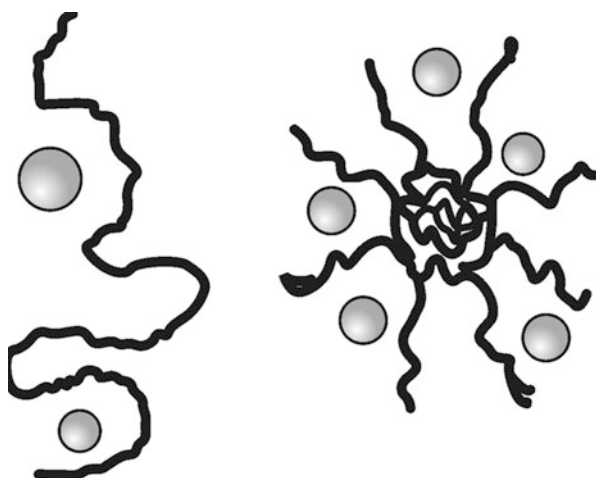
The removal of  $\text{Cu}^{2+}$ ,  $\text{Co}^{2+}$ , and  $\text{Ni}^{2+}$  ions from a ternary system [kaolin dispersion/polymer/ $\text{Me}^{2+}$ ] was tested. The content of  $\text{Me}^{2+}$  ions in the supernatant was analyzed by atomic absorption (Fig. 43.7). It was proved that kaolin itself could remove metal ions from aqueous medium by adsorbing them during the process of clay particle sedimentation. The first column of the diagram represents the initial



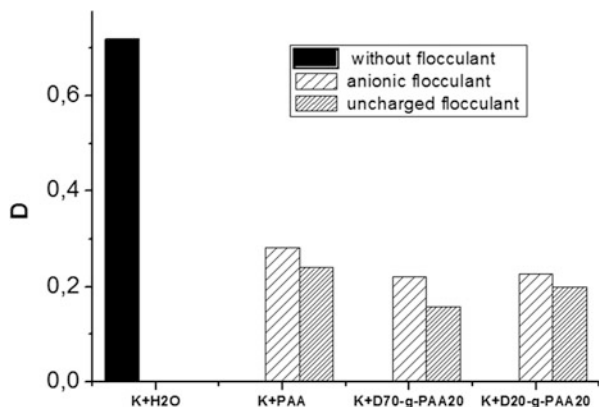
**Fig. 43.4** Supernatant clarity in 20 min after kaolin dispersion treatment by uncharged polymer-flocculants,  $C_{\text{floc}} = 1 \times 10^{-4}$  g/L



**Fig. 43.5** Scheme for trapping colloidal particles of kaolin dispersion by linear and branched flocculants



**Fig. 43.6** Supernatant clarity in 20 min after kaolin dispersion treatment by noncharged and polymer-flocculants,  $C_{\text{floc}} = 1 \times 10^{-1}$  g/L



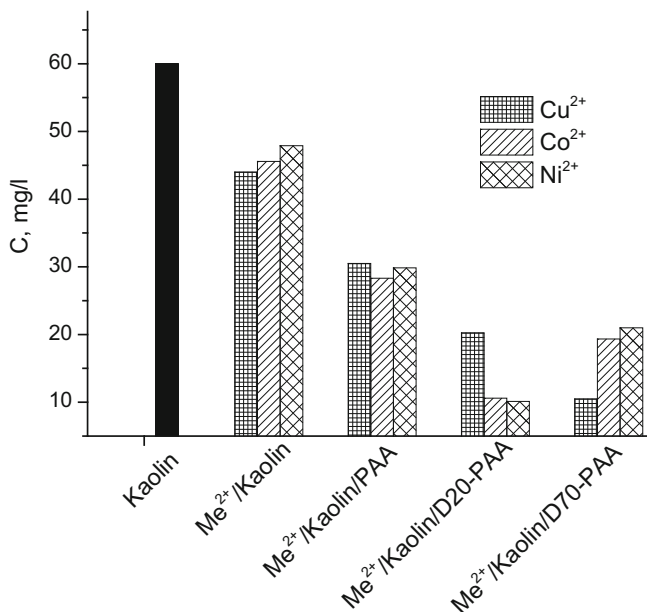


**Fig. 43.7** Content of  $\text{Cu}^{2+}$ ,  $\text{Co}^{2+}$ , and  $\text{Ni}^{2+}$  in supernatant after sedimentation in [kaolin (K)/polymer(PE)/ $\text{Me}^{2+}$ ] ternary system,  $C_{\text{polym}} = 1 \cdot 10^{-2}$  g/L

content of  $\text{Cu}^{2+}$  for all experiments. Kaolin dispersion can reduce by half the metal ion content in water after clay particle precipitation.

Branched polymers D20-g-PAA20(PE) and D70-g-PAA(PE) are more efficient at heavy metal ion trapping in comparison with linear PAA(PE). The ability to remove  $\text{Me}^{2+}$  ions from clay dispersion is highest for D70-g-PAA20(PE).

## 43.4 Conclusions

Analysis of the kinetics of the flocculation process revealed that flocculation activity was more significant for the branched sample having greater compactness. It was shown that at low concentrations of branched flocculants ( $C_{\text{floc}} = 1 \times 10^{-4}$  g/L), residues of the kaolin suspension stabilize. The degree of supernatant clarification for branched polymers at optimal flocculant concentrations is comparatively higher than for linear PAA. The branched polyelectrolytes dextran-graft-(polyacrylamide-co-polyacrylic acid) are less efficient at clarification but more effective in sedimentation rate in the flocculation process of polydispersed kaolin suspension in comparison with noncharged D-g-PAA copolymers. In the case of 20–34% conversion degree of the branched samples, the sedimentation rate increases, but further conversion of amide groups into carboxylate groups does not influence

the flocculation substantially. Nevertheless, the best supernatant clarification was achieved for less compact branched polyelectrolytes at a flocculant concentration of  $10^{-2} \div 10^{-1}$  g/L. Branched polyelectrolytes D-g-PAA and PAA in anionic form were tested and compared with respect to the flocculation of the setting of kaolin dispersions as well as for efficiency at removing  $\text{Cu}^{2+}$ ,  $\text{Co}^{2+}$ , and  $\text{Ni}^{2+}$  ions during the flocculation process. It was shown that the flocculation parameters (setting rate and degree of supernatant clarification) depend on the polymer-flocculant molecular structure. Branched polymers D20-g-PAA20(PE) and D70-g-PAA(PE) are more efficient for heavy metal ions trapping in comparison with linear PAA(PE). The ability to remove  $\text{Me}^{2+}$  ions from clay dispersions is highest for D70-g-PAA20(PE).

**Acknowledgments** The authors are grateful to M. Rawiso and A. Rameau for the SEC experiment at Institute Charles Sadron, Strasbourg, France.

## References

1. Teh CY, Budiman PM, Shak KPY, Wu TY (2016) Recent advancement of coagulation–flocculation and its application in wastewater treatment. *Ind Eng Chem Res* 55(16):4363–4389
2. Brostow W, Hagg Lobland HE, Pal S, Singh RP (2009) Polymeric flocculants for wastewater and industrial effluent treatment. *J Mater Educ* 31(3-4):157–166
3. Kim M, Kim S, Kim J, Kang S (2013) Sangbong lee factors affecting flocculation performance of synthetic polymer for turbidity control. *J Agric Chem Environ* 2(1):16–21
4. Bersa L, Sengupta DK, Roy SK, Ay P (2004) Influence of polymer adsorption and conformation of flocculation and dewatering of kaolin suspension. *Sep Purif Technol* 37(3):231–246
5. Fleer GJ, Scheutjens JM, Cohen MA (1988) Theoretical progress in polymer adsorption, steric stabilization and flocculation. *Smart Coll Surf* 31:1–29
6. Ghimici L, Morariu S, Nichifor M (2009) Separation of clay suspension by ionic dextran derivatives. *Sep Purif Technol* 68:165–171. Blanco Á, Fuente E, Concepción Monte M, Cortés N, Negro C (2009) Polymeric branched flocculant effect on the flocculation process of pulp suspensions in the papermaking industry. *Eng Chem Res* 48(10):4826–4836
7. Blanco Á, Fuente E, Concepción Monte M, Cortés N, Negro C (2009) Polymeric branched flocculant effect on the flocculation process of pulp suspensions in the papermaking industry. *Ind Eng Chem Res* 48(10):4826–4836
8. Sun WM, Zhang GC, Li HL, Li DD, Li PP, Liu BC, Zhang D, Lei X, Zhao QR (2012) Synthesis, characterization, and flocculation properties of branched polyacrylamide. *Adv Mater Res* 476-478:2311–2316
9. Grest GS, Fetters LJ, Huang JS, Richter D (1996) Star polymers: experiment, theory and simulation, Chapter 2. In: Prigogine I, Rice SA (eds) *Polymeric systems*, volume XCIV in *advances in chemical physics*. Wiley, New York
10. Borisov OV (1996) Conformations of star-branched polyelectrolytes. *J Phys II (France)* 6(1): 1–19
11. Rivas BL, Pereira I, Moreno-Villoslada ED (2003) Water-soluble polymer–metal ion interactions. *Prog Polym Sci* 23:173–208
12. Kutsevol N, Bezugla T, Bezuglyi M, Rawiso M (2012) Branched dextran-graft-polyacrylamide copolymers as perspective materials for nanotechnology. *Macromol Symp* 317-318(1):82–90
13. Kutsevol N, Bezuglyi M, Rawiso M, Bezugla T (2014) Star-like Dextran-graft-(polyacrylamide-co-polyacrylic acid) copolymers. *Macromol Symp* 335:12–16
14. Kutsevol N, Guenet JM, Melnyk N, Sarazin D, Rochas C (2006) Solution properties of dextran-polyacrylamide graft copolymers. *Polymer* 47:2061–2068

# Chapter 44

## Molecular Dynamics Simulations of the Dynamics of Small Cholesterol Systems

Przemysław Raczyński and Z. Gburski

### 44.1 Introduction

Cholesterol is an important sterol present in all mammalian cell membranes due to its functional ability to modulate their physical properties [1–5]. It is well known, for instance, that the cell plasma membrane is characterized by its fluidity and just that the cholesterol concentration in bilayer regulates the fluidity. On the other hand, the excess of cholesterol is unhealthy because it starts to form plaque in blood vessels, in consequence leading to the atherosclerosis disease.

The molecular structure of cholesterol consists of steroid and alcohol components. Four linked hydrocarbon rings form bulk part of cholesterol. The single hydrocarbon tail is connected to the one end of the bulk part and the hydroxyl polar (–OH) group to the other one.

In our previous studies, we widely investigated the properties of cholesterol in various systems, e.g., we investigated the process of extraction of cholesterol molecules from the small deposit located on protein surface by nanotubes [6–8] or impact of nanotube on cholesterol cluster [9]. Unfortunately, we have never studied the behavior of cholesterol in small systems, like these we placed on a protein surface [6–8].

In this paper we refine our studies by investigation of the properties of cholesterol in two small systems composed of  $n = 15$  and  $n = 30$  molecules. Through the analysis of MD simulation results, we describe the differences between systems with water and without it as well as the impact on the temperature on the dynamics of molecules in such small systems.

---

P. Raczyński (✉) • Z. Gburski  
Institute of Physics, University of Silesia, Uniwersytecka 4, 40-007, Katowice, Poland  
e-mail: [przemyslaw.raczynski@us.edu.pl](mailto:przemyslaw.raczynski@us.edu.pl)

## 44.2 Simulation Details

All MD simulations were performed using NAMD 2.9b2 program [10, 11] with the all-atom CHARMM force field [12]. The TIP3P CHARMM adapted model was applied for the aqueous samples [13]. The initial configurations of all systems were obtained from the series of NVT simulations. Next, the systems with water were additionally simulated in NPT ensemble over  $2 \cdot 10^6$  time steps and with the reference pressure set to 1 atm. We controlled the pressure using Langevin barostat implement in NAMD. Next we returned to equilibration of these in the NVT ensemble over  $10^6$  time steps.

After these preliminary simulations, we started to appropriate simulations, where the data to be analyzed were collected every 200 simulation steps. Each run of these simulations takes  $10^7$  time steps with the time step equal to 0.5 fs (totally 5 ns).

The cholesterol molecules were modelled on the full atomistic level. All interactions between cholesterols in the simulated systems were described with adapted form of CHARMM potential. Atomic charges on cholesterol molecules were taken from [14].

## 44.3 Results and Discussion

First, we would like to show the impact of water on the cholesterol molecules. Figure 44.1 shows the snapshots of the larger system ( $n = 30$  molecules), with water and without it. To better visualize the impact of water, we additionally marked OH groups.

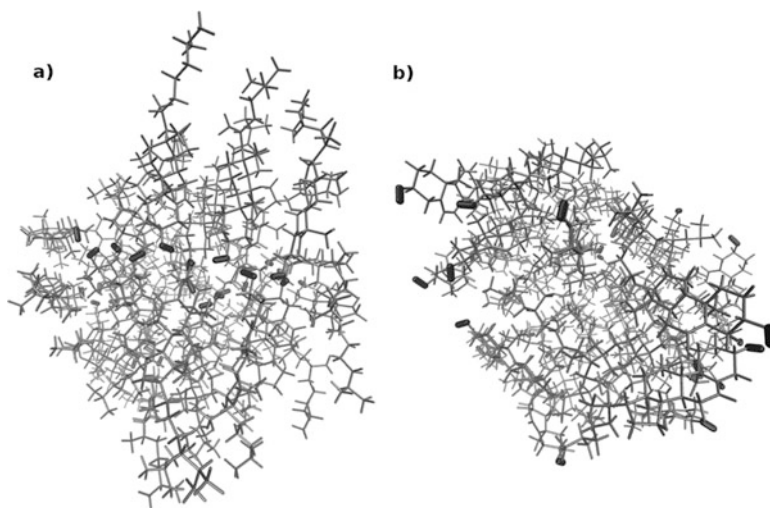


**Fig. 44.1** The instantaneous configurations of the systems composed of  $n = 30$  molecules without water (a) and in water ensemble (b), at  $T = 310$  K. OH groups are additionally marked

The orientation of the molecules in the system with water and without it varies considerably. It reflects the nature of cholesterol, consisted of two parts: larger hydrophobic and smaller hydrophilic. In the system without water, the hydrophilic OH groups of molecules are oriented toward each other. The polar alcohol components prefer neighborhood of other OH groups. In water the orientation of cholesterol is quite different, long nonpolar chains are turned to the center of the system, whereas OH groups are directed outside of it, to the polar environment. Because the significant part of cholesterol molecule is a hydrophobic region, water does not dissolve the system.

Figure 44.2 shows the mean square displacement  $\langle |\Delta \vec{r}(t)|^2 \rangle$  plots of the center of mass of cholesterol.  $\Delta \vec{r}(t) = \vec{r}(t) - \vec{r}(0)$  [10], where  $\vec{r}$  is the position of the center of mass of a single molecule. In this paper we present only the initial, most significant part of  $\langle |\Delta \vec{r}(t)|^2 \rangle$  for the system consisted of  $n = 15$  molecules in water environment.

None of the plots shown in Fig. 44.2 exhibit behavior characteristic for the solid state. All of them indicate on liquid state of the system at the given temperature. Although there are differences between plots for  $T = 320$  K and other temperatures, the plot features at the highest temperature are typical for a liquid phase.

To refine our discussion regarding the mobility of cholesterol molecules in the studied systems, we have calculated translational diffusion coefficient  $D$ , where  $\langle |\Delta \vec{r}(t)|^2 \rangle \approx 6Dt$  [15]. Nonzero slope of  $\langle |\Delta \vec{r}(t)|^2 \rangle$  is an indicator of translational diffusion of molecules.

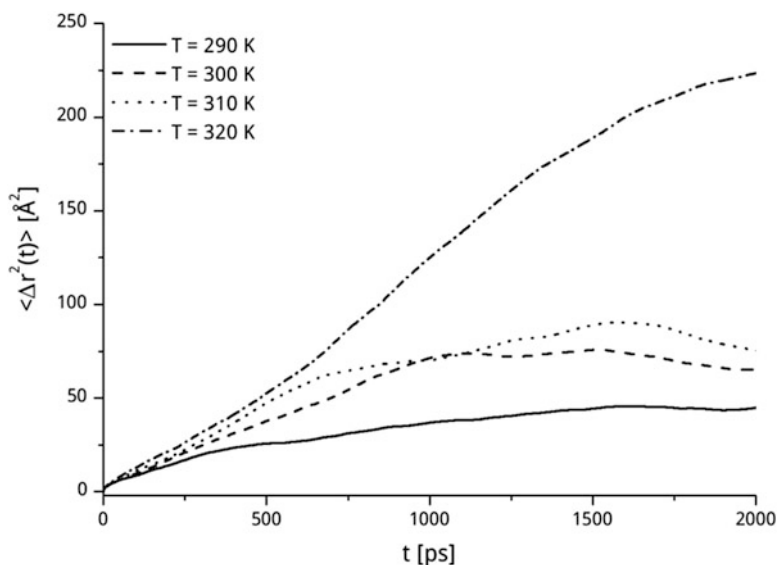


**Fig. 44.2** The mean square displacement of the center of mass of cholesterol for the system composed of  $n = 15$  molecules, in water environment

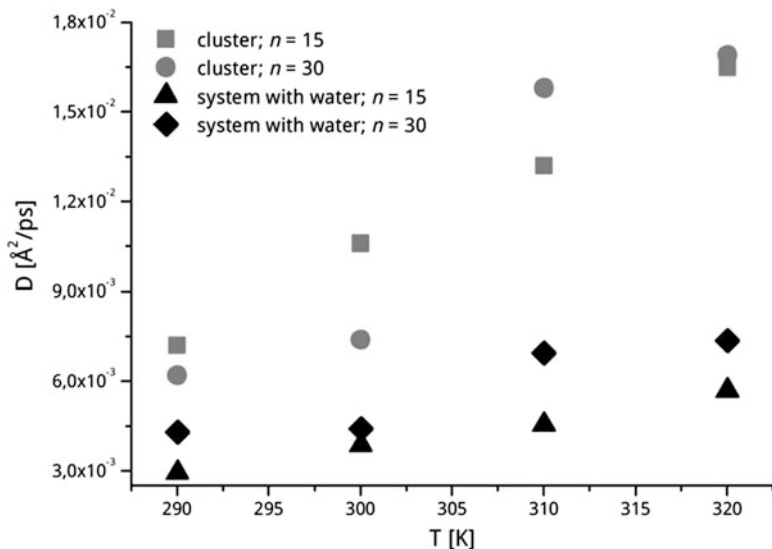


**Fig. 44.3** The temperature dependence of diffusion coefficient for all systems studied

Figure 44.3 shows the comparison of  $D$  for all systems and at all temperatures studied. In the systems with water, the dynamic of cholesterol molecules is lower. As we pointed before, in water environment, cholesterol molecules are oriented to each other with long tails. Meshing with larger hydrophobic parts of cholesterol means stronger interactions comparing to small OH groups. That is why the dynamics of the cholesterol molecules is lower in systems with water.

It seems that differences between  $D$  values are smaller in case of the systems with water, comparing to systems without it. Note that in water environment, cholesterol molecules are surrounded by polar HOH molecules, whereas hydrophobic cholesterol molecules keep together. It is the reason for the similar mobility of cholesterol molecules in the different systems in case of the aqueous samples. Figure 44.3 shows that with the heating of the cluster, the dynamics of molecules grows.

Previously we have concluded that there is no phase transition in the aqueous system consisted of  $n = 15$  cholesterol molecules. To confirm this conclusion, we have calculated the values of the Lindemann indexes.

Lindemann index  $\delta_L$  is defined as [16]

$$\delta_L = \frac{2}{N(N-1)} \sum_{i < j}^N \frac{\left( \langle r_{ij}^2 \rangle - \langle r_{ij} \rangle^2 \right)^{\frac{1}{2}}}{\langle r_{ij} \rangle},$$

where  $r_{ij}$  is the distance between the center of mass of  $i$ th and  $j$ th molecules.

The comparison of the obtained values of  $\delta_L$  for all systems and for all temperatures is shown in Fig. 44.4. For all systems studied, there is no significant

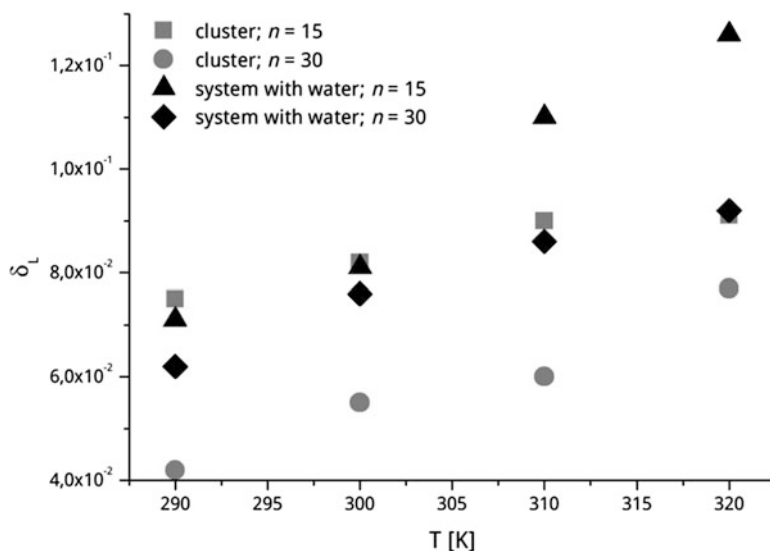


**Fig. 44.4** The temperature dependence of Lindemann index for all systems studied

discontinuity; if it would appear, it would be the indicator of the phase transition. The values of  $\delta_L$  become larger with the heating of the system, but the differences for successive values are not significant. Connecting these conclusions with the previous, we can point out that all systems are in the liquid state at the temperatures studied although there are differences between molecular mobility of individual samples.

The last comparison we would like to discuss is a comparison of radial distribution function  $g(r)$  plots. In Fig. 44.5 the similarities between the nonaqueous and aqueous  $n = 30$  systems, at  $T = 310$  K, are shown.

There are no strong differences in plots of these two systems. One sharp peak associated with the nearest neighbors can be observed at the distance approximately  $r = 6.2$  Å. No more clearly defined peaks can be observed, and this confirms the absence of a solid phase.

## 44.4 Conclusions

The clusters composed of  $n = 15$  and  $n = 30$  cholesterol molecules were studied, pure as well as in water environment. Water impacts the behavior of the cholesterol molecules. In systems without water, the molecules orient their polar groups toward the interior of the cluster, while in water environment the opposite orientation prevails and hydrophobic tails intermingle.



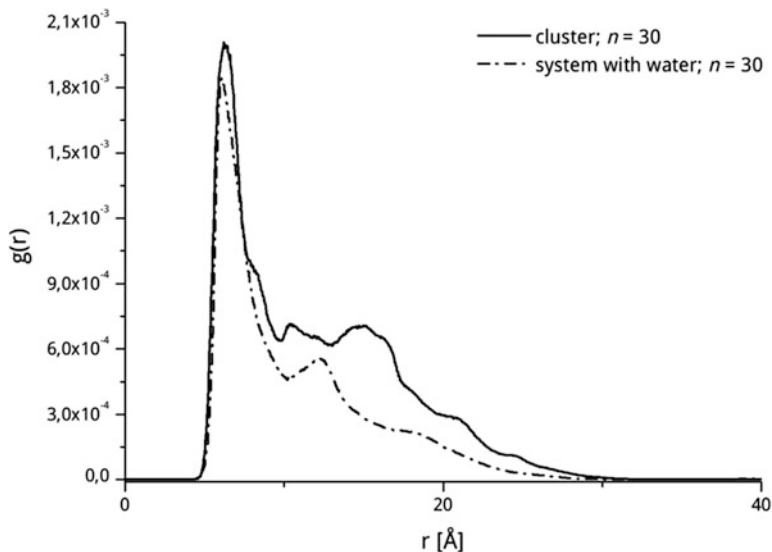


**Fig. 44.5** The comparison of the radial distribution function of the center of mass of cholesterol for the cluster and aqueous system composed of  $n = 30$  cholesterol, at  $T = 310$  K

The dynamics of cholesterol molecules in water environment is lower comparing to these in clusters. The molecules in all systems and temperatures studied are in the liquid state. No phase transition occurs.

Our studies complement our previous simulations and describe the behavior of cholesterol molecules in small systems. It can be potentially interesting in the context of forming the incipience of cholesterol deposit in blood vessels.

## References

1. Lusis AJ (2000) Atherosclerosis. *Nature* 407:233–241. doi:[10.1038/35025203](https://doi.org/10.1038/35025203)
2. Alberts B (2008) *Molecular biology of the cell*. Garland Science, New York. [etc.]
3. Scott HL (2002) Modeling the lipid component of membranes. *Curr Opin Struct Biol* 12:495–502. doi:[10.1016/S0959-440X\(02\)00353-6](https://doi.org/10.1016/S0959-440X(02)00353-6)
4. Feller SE (2000) Molecular dynamics simulations of lipid bilayers. *Curr Opin Colloid Interface Sci* 5:217–223. doi:[10.1016/S1359-0294\(00\)00058-3](https://doi.org/10.1016/S1359-0294(00)00058-3)
5. Róg T, Pasenkiewicz-Gierula M, Vattulainen I, Karttunen M (2009) Ordering effects of cholesterol and its analogues. *Biochim Biophys Acta Biomembr* 1788:97–121. doi:[10.1016/j.bbame.2008.08.022](https://doi.org/10.1016/j.bbame.2008.08.022)
6. Raczyński P, Górny K, Samios J, Gburski Z (2014) Interaction between silicon-carbide nanotube and cholesterol domain. A molecular dynamics simulation study. *J Phys Chem C* 118:30115–30119. doi:[10.1021/jp505532f](https://doi.org/10.1021/jp505532f)
7. Gburski Z, Gorny K, Raczynski P, Dawid A (2011) Impact of the carbon allotropes on cholesterol domain: MD simulation. *Carbon Nanotub. Growth Appl. InTech*. doi:[10.5772/18039](https://doi.org/10.5772/18039)

8. Gburski Z, Gómy K, Raczynski P (2010) The impact of a carbon nanotube on the cholesterol domain localized on a protein surface. *Solid State Commun* 150:415–418. doi:[10.1016/j.ssc.2009.12.005](https://doi.org/10.1016/j.ssc.2009.12.005)
9. Raczynski P, Raczynska V, Gorny K, Gburski Z (2015) Properties of ultrathin cholesterol and phospholipid layers surrounding silicon-carbide nanotube: MD simulations. *Arch Biochem Biophys* 580:22–30. doi:[10.1016/j.abb.2015.06.008](https://doi.org/10.1016/j.abb.2015.06.008)
10. Kale L, Skeel R, Bhandarkar M, Brunner R, Gursoy A, Krawetz N, Phillips J, Shinozaki A, Varadarajan K, Schulten K (1999) NAMD2: greater scalability for parallel molecular dynamics. *J Comput Phys* 151:283–312. doi:[10.1006/jcph.1999.6201](https://doi.org/10.1006/jcph.1999.6201)
11. Phillips JC, Braun R, Wang W, Gumbart J, Tajkhorshid E, Villa E, Chipot C, Skeel RD, Kalé L, Schulten K (2005) Scalable molecular dynamics with NAMD. *J Comput Chem* 26:1781–1802. doi:[10.1002/jcc.20289](https://doi.org/10.1002/jcc.20289)
12. MacKerell BD, Bellott D, Evanseck JD, Field MJ, Fischer S, Gao J, Guo H, Ha S, Joseph-McCarthy D, Kuchnir L, Kuczera K, Lau FTK, Mattos C, Michnick S, Ngo T, Nguyen DT, Prodhom B, Reiher WE, Roux B, Schlenkrich M, Smith JC, Stote R, Straub J, Watanabe M, Wiórkiewicz-Kuczera J, Yin D, Karplus M (1998) All-atom empirical potential for molecular modeling and dynamics studies of proteins†. *J Phys Chem B* 102:3586–3616. doi:[10.1021/jp973084f](https://doi.org/10.1021/jp973084f)
13. Jorgensen WL, Chandrasekhar J, Madura JD, Impey RW, Klein ML (1983) Comparison of simple potential functions for simulating liquid water. *J Chem Phys* 79:926. doi:[10.1063/1.445869](https://doi.org/10.1063/1.445869)
14. Henin J, Chipot C (2006) Hydrogen-bonding patterns of cholesterol in lipid membranes. *Chem Phys Lett* 425:329–335. doi:[10.1016/j.cplett.2006.04.115](https://doi.org/10.1016/j.cplett.2006.04.115)
15. Allen MP, Tildesley DJ (1989) *Computer simulation of liquids*. Clarendon Press/Oxford University Press, Oxford, UK/New York
16. Jena P, Rao BK, Khanna SN (2013) *Physics and chemistry of small clusters*. Springer, New York

# Chapter 45

## Quantum Chemical Study of Water Molecule Adsorption on the Nitrogen-Doped Titania Thin Films

O. Smirnova, A. Grebenyuk, O. Linnik, and V. Lobanov

### 45.1 Introduction

Metal oxides ZnO, SnO<sub>2</sub>, Fe<sub>2</sub>O<sub>3</sub>, CdO, WO<sub>3</sub>, In<sub>2</sub>O<sub>3</sub>, and TiO<sub>2</sub> are generally used as photocatalytic substances [1]. They are used in many processes, including water and air purification from organic impurities [2], and to destroy bacteria [3]. Titanium dioxide (anatase) has a high photosensitivity toward UV light and a band gap  $E_g = 3.2$  eV. It is also chemically and biologically inert and low-cost material, used for photocatalytic sterilization in the medical and food industries and for environmental purification [4].

TiO<sub>2</sub> generally exists as three polymorphs: rutile, anatase, and brookite. The brookite phase is unstable, so it is rarely used in the photocatalytic studies. Most of the studies are conducted with pure anatase, rutile, or pure mixture of the two phases [5]. Often the most photocatalytic anatase phase is considered [6–10]. However, a mixture of anatase with rutile exhibits better photocatalytic properties for a large number of organic compounds [11, 12]. The process of photocatalytic oxidation over TiO<sub>2</sub> surface occurs only if the film is irradiated with light (or other radiation sources) with energy above the band gap [13].

Broadening the titania absorption towards the visible part of the solar spectrum can be achieved due to the modification of titania films by urea [14]. Doping of TiO<sub>2</sub> by nonmetals is based on:

- (a) Band gap narrowing proposed by Asahi et al. [15].
- (b) Impurity energy level formation above the valence band as a result of the substitution of oxygen atom by nitrogen in titania stated by Irie et al. [16].

---

O. Smirnova (✉) • A. Grebenyuk • O. Linnik • V. Lobanov  
Chuiiko Institute of Surface Chemistry, National Academy of Sciences of Ukraine, 17 General Naumov Str., Kyiv 03164, Ukraine  
e-mail: [olsmirnova2001@ukr.net](mailto:olsmirnova2001@ukr.net)

- (c) Formation of oxygen vacancies concluded by Ihara et al. [17]. It is reported that  $\text{TiO}_2$  doped with substitutional nitrogen has shallow acceptor states above the valence state, while doping with interstitial nitrogen leads to isolated impurity states in the middle of the band gap where energy levels of the impurity are mainly hybridized by  $\text{N}2p$  states and  $\text{O}2p$  states [18]. The nature of the nitrogen species is under discussion in numerous scientific publications.

This paper is intended to provide the relationship between the theoretical and experimental investigation of nitrogen-doped titania films.

## 45.2 Experimental

Quantum chemical calculations were carried out within the frameworks of the so-called cluster approximation [19]. Computations on the total energy values of the optimized geometrical structures of different sized  $\text{TiO}_2$ - $\text{TiO}_2(\text{N})$  cluster models (including 14 to 21 titanium atoms) were performed using density functional theory (DFT) method [20] and the hybrid B3LYP [21] potential with basis set 6-31G(d, p). Calculations were carried out by means of the software package PC GAMESS [22] (version Firefly 8.1.0 by A. Granovsky <http://classic.chem.msu.su/gran/firefly/index.html>).

$\text{TiO}_2$  thin films were synthesized by the sol-gel method using titanium tetraisopropoxide as a titania source and a three-block copolymer of polyethyleneoxide and polypropyleneoxide (PEO)20(PPO)70(PEO)20 (Pluronic P-123) as a template in alcoholic medium. Concentrated  $\text{HClO}_4$  and acetylacetone were added to the precursor as stabilizers. The molar ratio of the components in the sol for film deposition was as follows:  $\text{Ti}(\text{Oi-Pr})_4$ : P123: acetylacetone:  $\text{H}_2\text{O}$ :  $\text{C}_2\text{H}_5\text{OH}$ :  $\text{HClO}_4$  = 1: 0.05: 0.5: 1: 40: 1. A solution of urea ( $\text{CO}(\text{NH}_2)_2$ ) with 5 mol. % was added under vigorous stirring. The one-layered films were deposited by dip-coating procedure at a withdrawal rate 1.5 mm/s. The films were left for 1 h for hydrolysis and heated in air at 450 °C for 1 h with the heating rate of 3 °C/min. Photocatalytic activity of the films was assessed via tetracycline hydrochloride (TC) degradation. The film was immersed in 40 ml of an aqueous solution of  $2 \times 10^{-5}$  mol/L TC. The reaction temperature was kept constant (20 °C) during the experimental procedure. The change of TC concentration was monitored with a Lambda 35 UV-Vis spectrophotometer (PerkinElmer) every 20 min at  $\lambda = 357$  nm. The film was immersed in the solution until complete adsorption in the dark occurred and then irradiated by a 1000 W middle-pressure mercury lamp for 90 min. The distance lamp reactor was set at 90 cm. A blank experiment was carried out where a bare glass was used instead of film. No significant changes in the absorption spectra of the liquid were observed for the blank. For testing the visible light sensitivity, a filter transmitting light with  $\lambda > 380$  nm was introduced into the photocatalytic setup.

### 45.3 Results and Discussion

Previously [23] we examined titanium oxide clusters considered both theoretically and experimentally. The energy difference from the HOMO–LUMO gap is defined as the difference between the ionization potential and the electron affinity. Here we analyze the atomic and electronic properties of both pure and nitrogen-doped  $\text{TiO}_2$  clusters of different compositions (14 or 21 Ti atoms, stoichiometric, and having oxygen vacancies). The effect of nitrogen incorporation on the adsorption of water molecules was also studied.

Various kinds of pure clusters are given in Fig. 45.1.

Molecular models for probable adsorption complexes of water on the surfaces of pure and nitrogen-doped titania are given in Fig. 45.2.

In addition, cluster models of titania including more 21 Ti atoms (pure and nitrogen-doped) were examined (see Fig. 45.3).

The calculated values of band gaps along with respective total energies for all the clusters examined are summarized in Table 45.1.

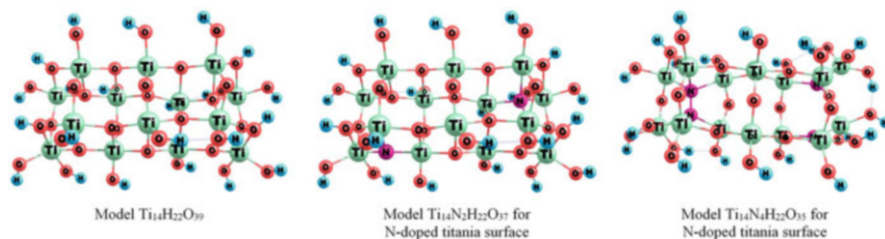


Fig. 45.1 Cluster models for pure and N-doped titania

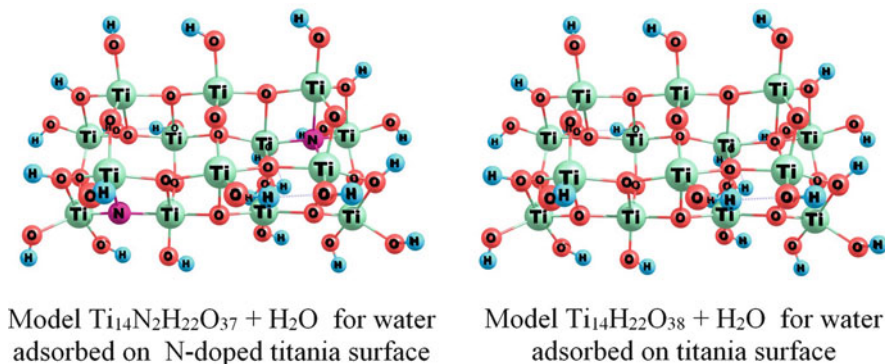
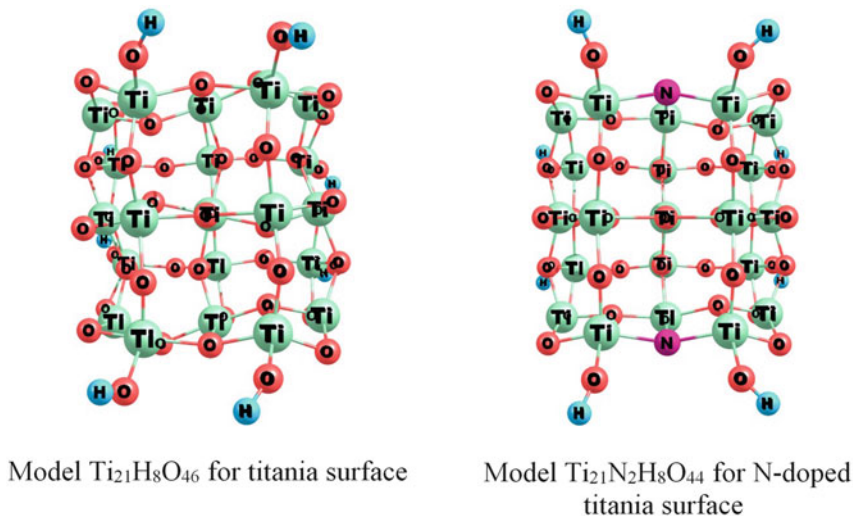


Fig. 45.2 Cluster models for adsorbed water molecules on surface defects (oxygen vacancies) of pure and N-doped titania



**Fig. 45.3** Expanded cluster models of pure and N-doped titania

**Table 45.1** Effect of composition of the molecular models on the value of band gap width

Molecular model	Theoretical band gap $E_g$ , eV	$E_{\text{total}}$ , a.u.
<b>Ti<sub>14</sub>-family</b>		
$\text{Ti}_{14}\text{H}_{22}\text{O}_{39}$	5.23	-14842.51877
$\text{Ti}_{14}\text{N}_2\text{H}_{22}\text{O}_{37}$	4.00	-14801.36164
$\text{Ti}_{14}\text{N}_4\text{H}_{22}\text{O}_{35}$	3.40	-14760.25821
$\text{Ti}_{14}\text{H}_{22}\text{O}_{38} + \text{H}_2\text{O}$	1.90	-14843.41766
$\text{Ti}_{14}\text{H}_{22}\text{O}_{38}$	2.48	-14767.17117
$\text{Ti}_{14}\text{N}_2\text{H}_{22}\text{O}_{36}$	0.10	-14726.00093
$\text{Ti}_{14}\text{N}_2\text{H}_{22}\text{O}_{37} + \text{H}_2\text{O}$	0.17	-14802.27852
<b>Ti<sub>21</sub>-family</b>		
$\text{Ti}_{21}\text{H}_8\text{O}_{46}$	3.78	-21207.82324
$\text{Ti}_{21}\text{H}_{24}\text{O}_{54}$	4.16	-21815.40622
$\text{Ti}_{21}\text{N}_2\text{H}_8\text{O}_{44}$	4.05	-21266.95149
$\text{Ti}_{21}\text{N}_2\text{H}_8\text{O}_{40}$	0.30	-20965.54102
$\text{Ti}_{21}\text{H}_8\text{O}_{42}$	1.45	-21006.620663
$\text{Ti}_{21}\text{H}_{32}\text{O}_{58}$	4.50	-22119.41492
$\text{H}_2\text{O}$	9.73	-76.41973

One can see from the data listed in Table 45.1 that substitution of nitrogen atoms for oxygen ones in the titania structure (in the case of  $\text{Ti}_{14}$ -family of clusters) decreases the  $E_g$  value. In case of  $\text{Ti}_{21}$ -family, no analogous tendency is observed.

The inclusion of the more number of OH-groups in the cluster models also increases the band gap width. Thus, the increase in the number of atoms in the model does not improve the coincidence between experimental and theoretical data. That is why we have to examine the effect of the oxygen vacancies and the adsorption of water molecules via testing the clusters from  $\text{Ti}_{14}$ -family.

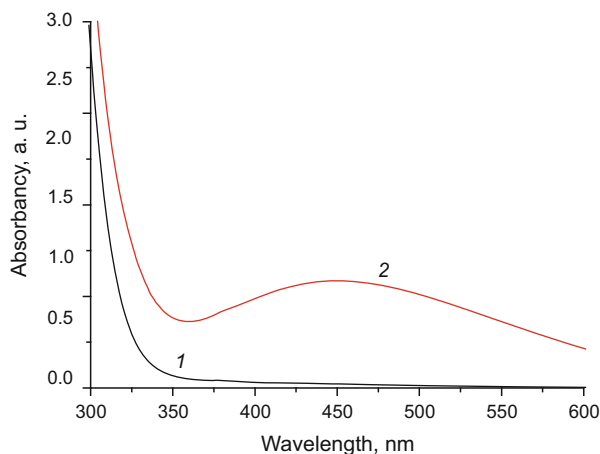


**Fig. 45.4** Absorption spectra of  $\text{TiO}_2$  (1) and  $\text{TiO}_2(\text{N})$  (2)

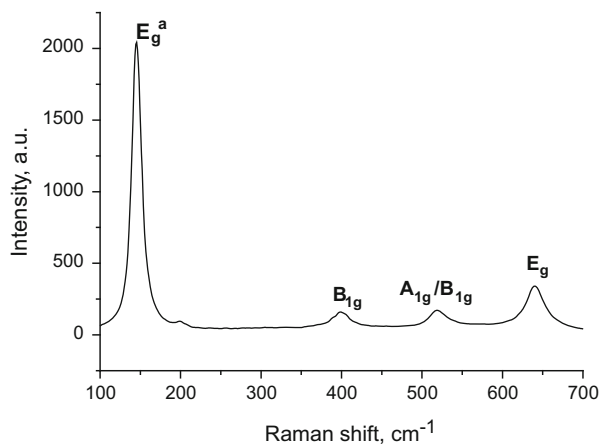


**Fig. 45.5** Raman spectra of  $\text{TiO}_2(\text{N})$  treated at  $450^\circ\text{C}$

Calculated values of the Gibbs free energy of adsorption increase for  $\text{TiO}_2$  clusters from  $\text{Ti}_{14}$ -family doped with nitrogen (from 454.84 to 373.21 kJ/mol). This fact demonstrates the hydrophobic surface properties of the film. In all the cases, the presence of oxygen vacancies decreases the  $E_g$  value.

The experimental results show that high absorption intensity in the visible region and significant shift of absorption edge to the longer wavelengths in the absorption spectra (Fig. 45.4) and the decrease in band gap energy values (3.6 and 3.3 eV for the pure and nitrogen-doped titania films) clearly indicate the effective nitrogen incorporation into the titania matrix.

**Table 45.2** The conversion percentage of TC over the films after UV and visible irradiation

Film	UV, %	Vis., %
Blank (glass)	6	2
TiO <sub>2</sub>	11	5
TiO <sub>2</sub> (N)	30	16

As a proof of anatase formation in nitrogen-containing films, the Raman spectrum of TiO<sub>2</sub>(N) is presented in Fig. 45.5. The high intensive Raman peaks at 145, 398, 518, and 640 cm<sup>-1</sup> are observed for TiO<sub>2</sub>(N) films. These peaks are related to the formation of photocatalytically active anatase phase.

The photocatalytic activity of TiO<sub>2</sub>(N) films is increased in three times comparing with pure TiO<sub>2</sub> film under both UV and visible light (Table 45.2). This could point on the change in the electronic structure as a result of nitrogen incorporation in the semiconductive matrix.

## 45.4 Conclusions

The calculations have shown that the introduction of two nitrogen atoms into the matrix reduces the band gap from 5.23 eV (Ti<sub>14</sub>H<sub>22</sub>O<sub>39</sub>) to 4.00 eV (Ti<sub>14</sub>N<sub>2</sub>H<sub>22</sub>O<sub>37</sub>). Increasing the cluster size (Ti<sub>21</sub>H<sub>8</sub>O<sub>46</sub>) brings the calculated value (3.16 eV) to the experimental one of 3.2 eV.

Nitrogen doping leads to growth of the hydrophobic properties of surface of the titania films.

Thus, the experimental data show that the photocatalytic activity is sharply increased for N-doped films as a result of nitrogen introduction in semiconductor. It is also shown that TiO<sub>2</sub>(N) possessed by high absorption in the visible part of the spectrum and contained the photocatalytically active anatase phase.

## References

1. Hangfeldt A, Gratzel M (1995) Light-induced redox reactions in nanocrystalline systems. *Chem Rev* 95:49–68
2. Ollis DF, Al-Ekabi H (eds) (1993) Photocatalytic purification of water and air. Elsevier, Amsterdam, 432 p
3. Xu M, Huang N, Xiao Z, Lu Z (1998) Photoexcited TiO<sub>2</sub> nanoparticles through \*OH-radicals induced malignant cells to necrosis. *Supramol Sci* 5:449–451
4. Kim B, Kim D, Cho D, Cho S (2003) Bactericidal effect of TiO<sub>2</sub> photocatalyst on selected food-borne pathogenic bacteria. *Chemosphere* 52:277–281
5. Kominami H, Kato JI, Murakami S, Ishii Y, Kohno M, Yabutani K, Yamamoto T, Kera Y, Inoue M, Inui T, Ohtani B (2003) Solvothermal syntheses of semiconductor photocatalysts of ultra-high activities. *Catal Today* 84:181–189



6. Ohno T, Sarukawa K, Matsumura M (2001) Direct observation of suppressed recombination of electron-hole pairs in the TiO<sub>2</sub> nanopowders with anatase-rutile interface: in-situ NEXAFS study under UV irradiation. *J Phys Chem* 105:2417–2425
7. Tanaka K, Capule MFV, Hisanaga T (1991) Effect of crystallinity of TiO<sub>2</sub> on its photocatalytic action. *Chem Phys Lett* 29:73–78
8. Scalfani A, Herrmann JM (1996) Comparison of the photoelectronic and photocatalytic activities of various anatase and rutile forms of titania in pure liquid organic phases and in aqueous solutions. *J Phys Chem* 100:13655–13661
9. Rao MV, Rajeshwar K, Verneker VR (1980) Photosynthetic production of H<sub>2</sub> and H<sub>2</sub>O<sub>2</sub> on semiconducting oxide grains in aqueous solutions. *J Phys Chem* 84:1987–1991
10. Nishimoto S, Ohtani B, Kaijiwara H, Kagiya T (1985) Correlation of the crystal structure of titanium dioxide prepared from titanium tetra-2-propoxide with the photocatalytic activity for redox reactions in aqueous propan-2-ol and silver salt solutions. *J Chem Soc, Faraday Trans I* 81:61–68
11. Guillard C, Disdier J, Herrmann J-M, Lechaut C, Chopin T, Malato S, Blanco J (1999) Comparison of various titania samples of industrial origin in the solar photocatalytic detoxification of water containing 4-chlorophenol. *Catalysis Today* 54:217–228
12. Heintz O, Robert D, Weber JV (2000) Comparison of the degradation of benzamide and acetic acid on different TiO<sub>2</sub> photocatalysts. *J Photochem Photobiol A Chem* 135:77–80
13. Suche M, Christoulakis S, Tudose IV, Vernardou D, Lygeraki MI, Anastasiadis SH, Kitsopoulos T, Kiriakidis G (2007) Pure and Nb<sub>2</sub>O<sub>5</sub> - doped TiO<sub>2</sub> amorphous thin films grown by dc magnetron sputtering at room temperature: surface and photo-induced hydrophilic conversion studies. *Materials Science and* 144:54–59
14. Shestopal NA, Linnik OP, Smirnova NP (2015) Influence of metal and non-metal ions doping on the structural and photocatalytic properties of titania films. *Chem Phys Technol Surf* 6(2):203–210
15. Asahi R, Morikawa T, Ohwaki T et al (2001) Visible-light photocatalysis in nitrogen-doped titanium dioxide. *Science* 293:269
16. Irie H, Watanabe Y, Hashimoto K (2003) Nitrogen-concentration dependence on photocatalytic activity of TiO<sub>2-x</sub>N<sub>x</sub> powders. *J Phys Chem B* 107:5483
17. Ihara T, Miyoshi M, Triyama Y et al (2003) Visible-light-active titanium oxide photocatalyst realized by an oxygen-deficient structure and by nitrogen doping. *Appl Catal* 42:403
18. Zhao Z, Liu Q (2008) Mechanism of higher photocatalytic activity of anatase TiO<sub>2</sub> doped with nitrogen under visible-light irradiation from density functional theory calculation. *J Phys D Appl Phys* 41:1
19. Sauer J (1989) Molecular models in ab initio studies of solids and surfaces: from ionic crystals and semiconductors to catalysts. *Chem Rev* 89(1):199–255
20. Becke A et al (1993) Density-functional thermochemistry. III. The role of exact exchange. *J Chem Phys* 98:5647–5652
21. Cohen AJ, Mori-Sanchez P, Yang W (2012) Challenges for density functional theory. *Chem Rev* 112:289–320
22. Schmidt M, Baldridge K, Boatz J et al (1993) General atomic and molecular electronic structure system. *J Comput Chem* 14:1347–1359
23. Smirnova OV, Grebenyuk AG, Linnik OP, Chorna NO, Lobanov VV (2016) Effect of nitrogen doping on the spatial and electronic structure of TiO<sub>2</sub> thin films and on the efficiency of water molecules adsorption onto their surfaces. *Scientific papers of NAUKMA* 183:67–72

# Chapter 46

## Effect of Chemical Vapor Deposition on the Morphology of the Nanocomposite Layer in the Complex Method

Andrew E. Stetsko

### 46.1 Introduction

Machine parts of the future must be more powerful, faster and very easy to use. This requires a significant increase in the functional reliability and durability of parts and equipment assemblies, leading to increased operational efficiency.

The operating properties depend not only on the physical and mechanical characteristics of the material from which they are made, but also on the state of the surface layer, and the manufacture of other material using different modes results in significant changes in the surface layer properties and parts durability. During manufacturing operations, irreversible processes of adaptivity and self-organization take place on the surface layer, which as a result of the imposition of joint and actions made and transformed flow of energy and matter lead to the formation of complex structures. The management of this process and energy absorption of a layered substance with the passage of high-intensity effects allows one to create needed layers in details for the future structure and operation of the surface.

*Objective:* To investigate the influence of previous chemical sedimentation for the formation and morphology of composite layer hardening using a complex method of chemical sedimentation and chromium diffusion.

---

A.E. Stetsko (✉)  
Ukraine Academy of Printing, Lviv, Ukraine  
e-mail: [andrew73@ukr.net](mailto:andrew73@ukr.net); <http://www.lnu.edu.ua/en/>

## 46.2 Materials and Methods

A variety of methods have been developed for strengthening the surfaces of machine details. The continued development of one of the traditional methods of surface hardening – induction heating – is ongoing [1, 2].

This hardening is achieved by high-frequency heating. The main advantage of induction heating is that it allows for strengthening of the surface layer only in certain places at a certain penetration depth. This is done by modifying the shape of the induction coil, which controls the magnitude and frequency of the current in the coil. This process is commonly used in steel alloys to improve fatigue durability and wear resistance. The disadvantage of this method is that its effectiveness varies depending on the surface properties of the material, which significantly limits its potential for development and improvement.

Studies have been carried out using high-strength materials in order to reduce grain size [3]. These efforts have made possible the dispersion of ultra-fine-grained microstructures and highly reinforced construction. But these studies are limited by the physical properties of the material.

Methods involving microalloying [4, 5] along with fractional-jet treatment, provide a surface with good yield strength and tensile strength, but sufficient durability.

Good experimental results [6] for strengthened alloys have been obtained from nitrogen and carbon diffusive at the  $\gamma/\alpha$  transformation. Material durability is provided by carbides and nitrides, but this also increases the brittleness of the materials, thus limiting the use of this method.

The solution to these issues is provided by the manufacturing process for machine parts.

## 46.3 Discussion

The technology involved in creating heterogeneous chromium coatings uses the effect of liquid metal phase [7], which contributes significantly to the acceleration process forming a resistant coating of machine parts. Results of this investigation showed intensification of the diffusive process of steel (0.45% C).

The initial conditions at the very beginning of the investigations demonstrated that just by using chemical sedimentation before thermochemical treatment, chromium diffusivity gives a new layer of hardness (Fig. 46.1).

In general, the complex method has three stages: previous tooling, chemical sedimentation and thermochemical treatment delay, and final tooling (Fig. 46.2).

To investigate impact of chemical sedimentation for repaired machine parts, we verified [8–15] five recipes (Table 46.1) and used thermochemical treatment of chromium diffusion. Five additional recipes were developed for the diffusion of chromium and titanium, and we determined the best results (Table 46.2, Fig. 46.3).

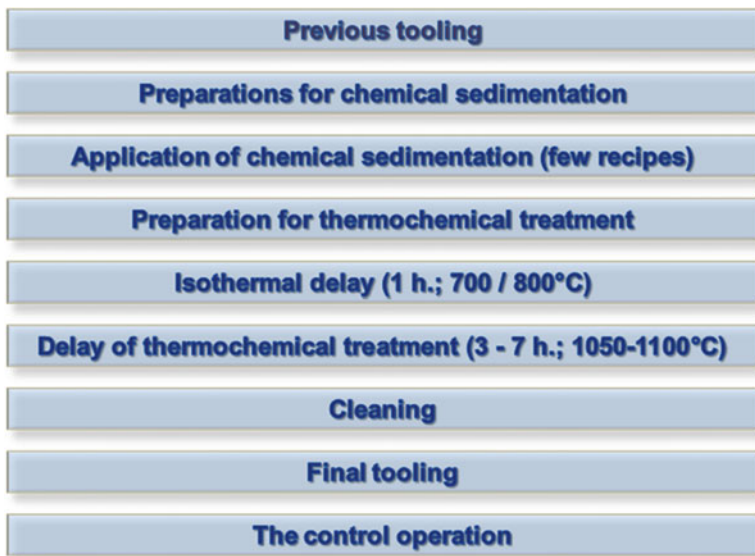


Fig. 46.1 Complex method

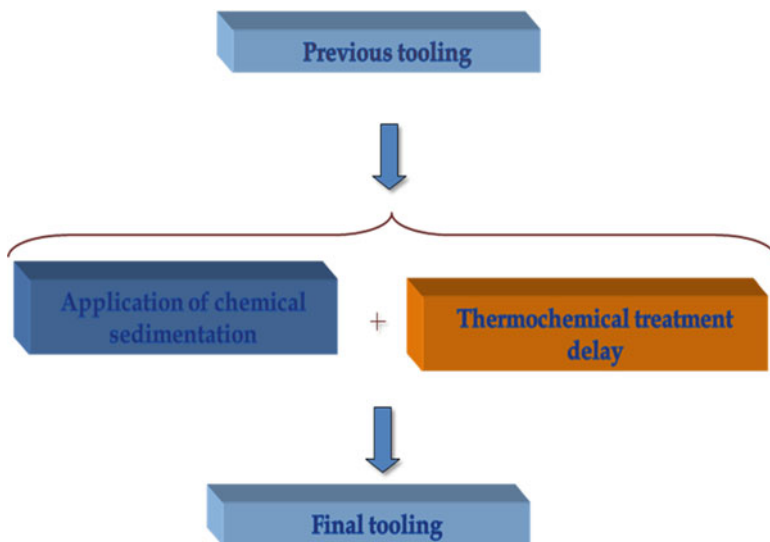


Fig. 46.2 Stages of the complex method

The impact of thermochemical treatment depends on the liquid of chemical sedimentation on the cover of parts details. After the molten state of chemical sedimentation we have intensification of adsorption on details and intensification of the diffusion process.

**Table 46.1** Elements of chemical Ni-Co-P sedimentation and diffusion saturation of Cr

Chemical element	#1	#2	#3	#4	#5
CoCl <sub>2</sub> , (g/l)	–	15	15	30	–
NiCl <sub>2</sub> , (g/l)	–	30	30	30	–
Na <sub>3</sub> C <sub>6</sub> H <sub>5</sub> O <sub>7</sub> , (g/l)	84	100	100	80	–
NaH <sub>2</sub> PO <sub>2</sub> , (g/l)	30	20	60	10	25
NH <sub>4</sub> Cl, (g/l)	–	50	50	50	50
CoCO <sub>3</sub> , (g/l)	7	–	–	–	–
CoSO <sub>4</sub> , (g/l)	–	–	–	–	30
NiSO <sub>4</sub> , (g/l)	15	–	–	–	30
CH <sub>3</sub> COONa, (g/l)	–	–	–	–	100
H <sub>2</sub> SO <sub>4</sub> , (g/l)	15	–	–	–	–
NH <sub>4</sub> OH, (ml)	90	60	60	60	50

**Table 46.2** Elements of chemical Ni-Co-P sedimentation and diffusion saturation of Cr–Ti

Chemical element	#6	#7	#8	#9	#10
CoCl <sub>2</sub> , (g/l)	15	30	–	–	–
NiCl <sub>2</sub> , (g/l)	30	30	–	–	–
Na <sub>3</sub> C <sub>6</sub> H <sub>5</sub> O <sub>7</sub> , (g/l)	90	–	–	–	–
NaH <sub>2</sub> PO <sub>2</sub> , (g/l)	25	25	25	30	–
K <sub>2</sub> H <sub>2</sub> PO <sub>2</sub> (g/l)	–	–	–	–	30
NH <sub>4</sub> Cl, (g/l)	–	50	50	45	–
CoCO <sub>3</sub> , (g/l)	–	–	–	15	–
NiCO <sub>3</sub> , (г/л)	–	–	–	30	–
CoSO <sub>4</sub> , (g/l)	–	–	20	–	–
NiSO <sub>4</sub> , (g/l)	–	–	30	–	–
Co(NO <sub>3</sub> ) <sub>2</sub> (g/l)	–	–	–	–	18
Ni(NO <sub>3</sub> ) <sub>2</sub> (g/l)	–	–	–	–	30
CH <sub>3</sub> COONa, (g/l)	–	90	–	90	–
(CHCOONa) <sub>2</sub> ,(g/l)	–	–	90	–	–
C <sub>4</sub> H <sub>6</sub> O <sub>6</sub> , (g/l)	15	–	–	–	–
CH <sub>2</sub> NH <sub>2</sub> COOH, (g/l)	25	–	–	–	–
Na <sub>2</sub> C <sub>4</sub> H <sub>4</sub> O <sub>4</sub> (g/l)	–	–	–	–	100
NH <sub>3</sub> (ml)	50	50	50	50	60

According to the investigated peculiarities of structuring [16, 17], first we formed the base zone of solid solution Cr in  $\alpha$ -Fe or Cr and Ti in  $\alpha$ -Fe. This zone is based in zones 1 and 2.

To investigate the molten state of chemical sedimentation we heat details from 640 to 1100 °C in increments of 20 °C. After heating, the details were cooled in air.

Details that were heated to temperatures of 640, 660, 680, 700 and 720 °C showed characteristic discoloration only on the covering (the color of metallic luster to the metal dark gray), which is typical for all samples. At a temperature of 740 °C, the formation of small (1–2 mm in diameter) bubbles on the surface could be observed.

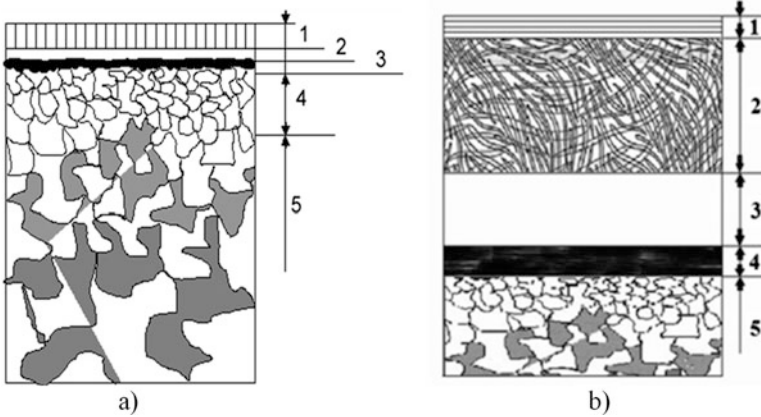


**Fig. 46.3** The structure of the diffusion layer after (a) diffusion saturation of Cr and (b) diffusion saturation of Cr and Ti: (a) 1 chromium carbides in solid solution Cr in  $\alpha$ -Fe, 2 solid solution Cr in  $\alpha$ -Fe, 3 eutectoid layer, 4 without carbon layer, 5 inner part. (b) 1 titanium carbides, 2 titanium and chromium carbides in solid solution Cr and Ti in  $\alpha$ -Fe, 3 solid solution Cr and Ti in  $\alpha$ -Fe, 4 eutectoid layer, 5 without carbon layer, 6 inner part

The remaining samples, which were heated to higher temperatures, including up to 1050 °C and some with isothermal holding at 800 °C for 1 h, were characterized by the formation of bubbles with a larger diameter (3–5 mm) and swelling of surface chemical sedimentation in the form of randomly directed “swollen veins” 20–25 mm in length and 5 mm wide. Additionally, changes were observed on the sample surface in the form of “ripples on water”.

The application of Ni-Co-P chemical sedimentation and heating from 700 °C to the upper liquid alloy on the surface accelerates the adsorption process and subsequently accelerates the diffusion of Ni, Co, Cr and other elements.

To study this process, one may consider forming fusible alloys with low melting points (below 1000 °C) in this system. Testing showed that implementation is likely to melt the surface to form reinforced outer layers of the composite area involving phosphoric eutectic alloys [18], which have a low melting point. Among these, the lowest temperature should highlight phosphoric eutectic Ni-P, which has a melting point of 870 °C (Fig. 46.4), and in the presence of other elements (Co, P, etc.), the melting temperature decreases.

Among the recipes considered, five were selected (Table 46.1). Formula #1 is Ni and Co salts of various acids (sulfuric and carbon), which also require the use of sulfuric acid substitution reaction of carbon cobalt sulfate. Accordingly, in order to obtain a chemical solution with pH 9–10, the amount of ammonia is increased to 90 ml. As a result of these steps (including isothermal holding for 1 h at 800 °C), composite layers of thickness are about 150  $\mu$ ; increasing the size of the workpiece to 80  $\mu$ , the total thickness of the diffusion layer was 190  $\mu$ .

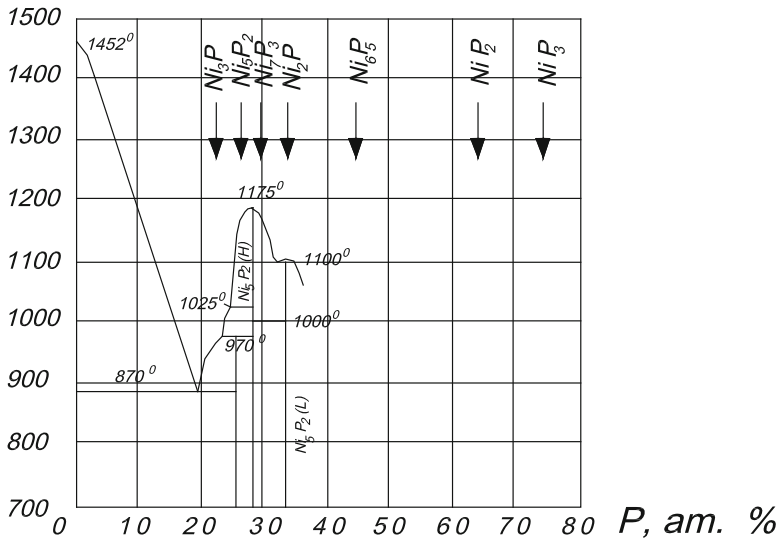


Fig. 46.4 The phase diagram of the Ni-P system

The composite zone is riddled with small pores (basically 10  $\mu$  in diameter) that are located between the carbide grains in a matrix of a solid solution of chromium in  $\alpha$ -iron. The surface roughness is Rz 40.

Different results were obtained when using the complex method of production and recovery solution for chemical coating formula #5 (Table 46.1). The composite area of the hardened layer is smaller than the thickness (averaging about 100  $\mu$ ), because of the high carbide component of a solid solution of chromium in  $\alpha$ -iron with a high microhardness, which averaged up to 14 GPa.

When carrying out research by the complex method of chemical processing and diffusion plating solutions using recipes #2, #3 and #4 (Fig. 46.4), hardened layers are obtained, and the composite zones are characterized by advanced carbide components in a columnar carbide grain structure.

The same solution composition for chemical sedimentation was used for all three recipes, changing only quantitative elements. The results revealed that the composite zone with the greatest thickness (250  $\mu$ ) was obtained for the sample using strengthening of chemical depositions solution for recipe #3 (Fig. 46.4b) using the complex method. This formulation is characterized by the use of salt Ni and Co hydrochloric acid (sulfuric is weaker by chemical action) in a ratio of 1:2, and high (up to 60 g/l) sodium hypophosphite content. This is a key element in the solution, because sodium hypophosphite conducts Ni and Co salt recovery. This sample is also characterized by the development of a composite zone – first, a typical columnar carbide grain structure composite zone. The microstructure shows that these grains are predominantly perpendicular to the physical surface. It should also be noted that the area riddled with these grains is not at the physical surface, but begins at a

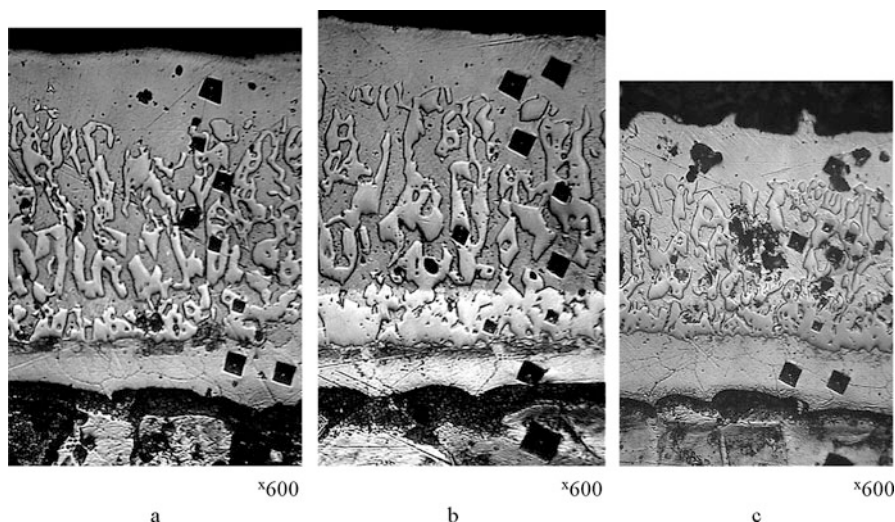


**Fig. 46.5** The microstructure of a hardened diffusion layer of chemical Ni-Co-P coating for recipes #2 (a), #3 (b), and #4 (c), and for the diffusion Cr modes: isothermal holding 1 h at 800 °C, diffusive saturation of Cr 7 h at a temperature of 1050 °C; magnification  $\times 600$

depth of 30–50  $\mu\text{m}$ . Accordingly, composite zone 1 is divided into two subzones: a solid solution of chromium in  $\alpha$ -iron and subdivisions – carbide grains located in a matrix of a solid solution of chromium in  $\alpha$ -iron – actually, a composite component of a composite zone, which is 200–220  $\mu\text{m}$ . The existence of the surface subzone solid solution of chromium in  $\alpha$ -iron is clear evidence of the lack of either of the elements – carbon or chromium – making the formation of chromium carbide grains impossible. Since the source of chromium (the outside air) is continuously active throughout the process of diffusion plating, the deficit eventually becomes part of carbon (Fig. 46.5).

Thus, during thermochemical processing, carbon was in a near-surface zone or in contact with chromium or diffused out. But over time, Carbide formation became so intense that a continuous layer of carbide grains was formed on the border area of a solid solution of chromium in  $\alpha$ -iron, blocking carbon access from inside. It is also possible that access to “deep” carbon under the temperature-diffusive physical surface prevented many other diffusive elements from moving to the core, and they remained closer to the area of the solid solution of chromium in  $\alpha$ -iron.

In studying the kinetics of the formation of hardened layers on steel with 0.45% carbon for other modes of chemical and thermal processing, with exposure at 700 °C, reducing the temperature of isothermal holding to 100 °C and reducing the duration of thermochemical treatment from 7 to 5 h drastically affected the morphology of the obtained layers (Fig. 46.6a–d).

The first effect is the relatively small thickness of the layers themselves, which are reduced by more than 100  $\mu\text{m}$ . Second, carbide colonies are still in the formative



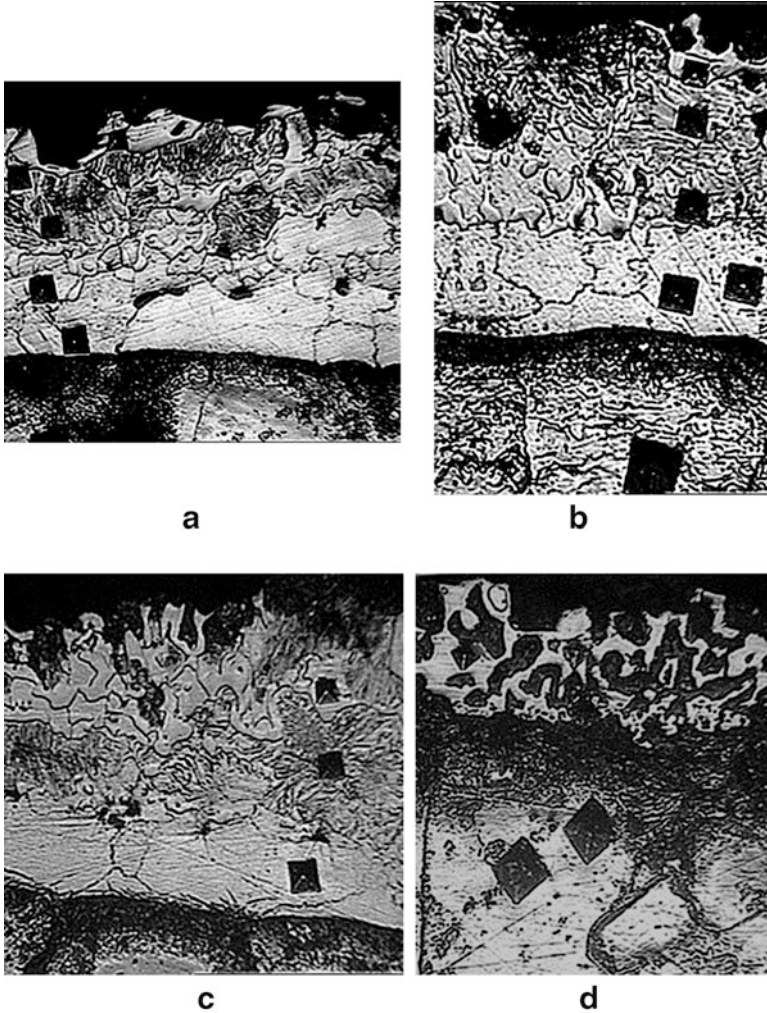


**Fig. 46.6** The microstructure of strengthened diffusion layer of chemical sedimentation of Ni-Co-P for recipe #1 – (a), recipe #2 – (b), recipe #3 – (c), recipe #5 – (d); and diffusion Cr regimes: 1 h isothermal delay at 700 °C, 5 h diffusive Cr saturation at 1050 °C

stage and are dominated by micrograin carbide chromium, and individual carbide grains are small and are located mostly along the grain boundaries of ferrite and pearlite, where, according to the classical theory of diffusion processes, diffusion occurs more readily, creating the best conditions for their formation and growth. As in previous samples, the most developed hardened layer is observed in the sample in which the previous chemical coating was obtained by compound #3. This layer thickness has the greatest and most integrated microhardness as a result of a dense

**Fig. 46.7** The microstructure of the hardened diffusion layer of chemical Ni-Co-P coating for recipe #3 and for the Cr-Ti diffusion modes: isothermal holding for 1 h at 700 °C, diffusive saturation Cr 5 h at a temperature of 1050 °C; magnification  $\times 600$



mesh of carbide micrograins and a certain number of existing chromium carbide grains. For the modes for this complex method, see the sample (Fig. 46.6d), as noted above, which is the zone 2 solid solution of chromium in  $\alpha$ -iron, a chemical coating that used recipe #5.

It should be mentioned that the sample in Fig. 46.7 has continuous stretches along the border area with two carbide micrograin colonies directed mainly perpendicular to the physical surface. If we compare this sample with the sample shown in Fig. 46.3, we can clearly see that the above colony micrograin plot is similar to the solid carbide grain colony chromium, which further covers the access to the carbon carbide composite zone 1.

Because of its accessibility and universality, the complex method that includes a surface treatment by chemical vapor deposition developed for recipes and thermochemical treatment by accepted modes enables new qualitative characteristics of surface-hardened layers of machine parts, instruments and tools, allowing the expansion of its scope.

Using a number of new chemical formulations developed to cover certain modes and methods of chemical and thermochemical treatment with Cr and Cr-Ti, we obtained positive experimental results, with improved physical and mechanical properties of iron alloy surfaces, namely:

- (a) Considerable thickness of diffusion layers (within 200  $\mu$  of the working area);
- (b) Sufficient hardness of diffusion layers, which is about 20 GPa of working area.

The results of scientific developments set the stage for more advanced research and analysis, which will aid the development and implementation of practical recommendations for strengthening concrete machinery parts, equipment and tools (Figs. 46.8 and 46.9).

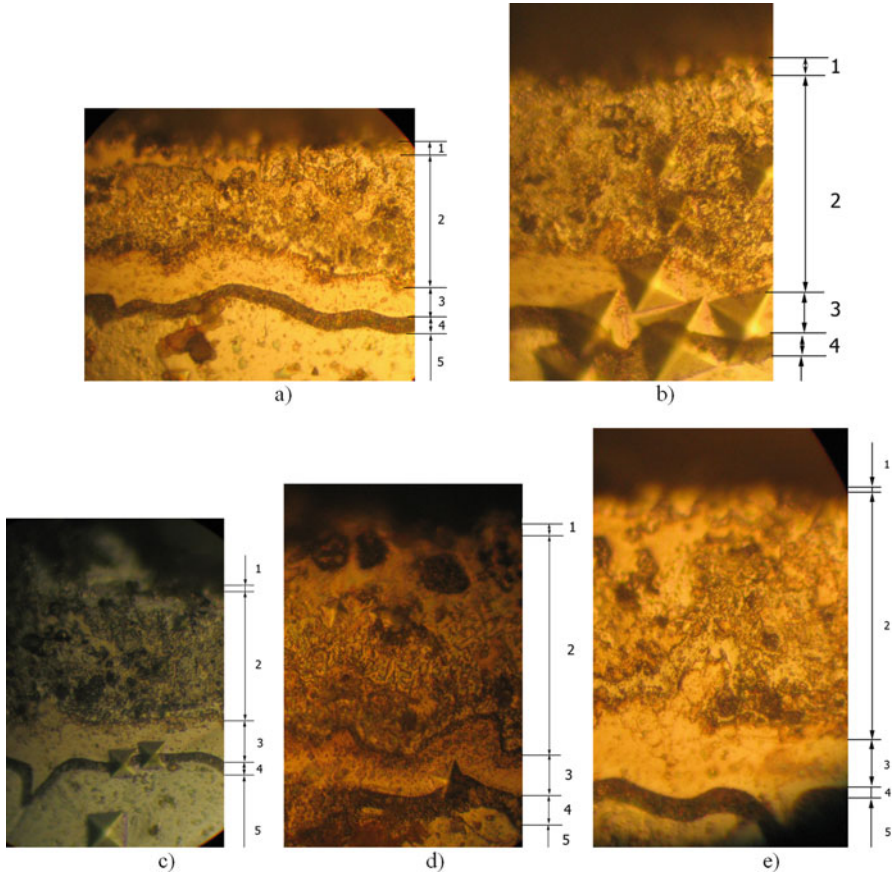


**Fig. 46.8** The microstructure of the hardened diffusion layer of chemical Ni-Co-P coating for recipe #1 (a), recipe #2 (b), recipe #3 (c), recipe #4 (d), recipe #5 (e) and for the diffusion Cr-Ti modes: isothermal holding 1 h at 800 °C, diffusive saturation Cr-Ti 7 h at a temperature of 1100 °C; magnification  $\times 600$

## 46.4 Conclusions

In this work, the complex method for strengthening machine surface details is improved and extended. The method consists of a few stages, with the basic stages comprising chemical Ni-Co-P sedimentation and thermochemical treatment (diffusion of Cr or Cr-Ti).

The application of the different recipes for chemical sedimentation provides hardness layers with the requisite structure.

The method is inexpensive, simple and flexible for application across a number of industry sectors.

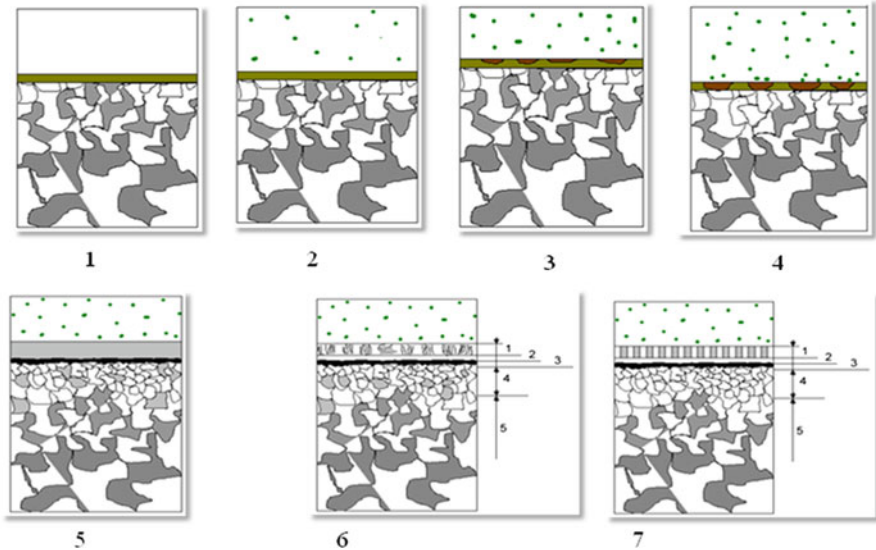


**Fig. 46.9** The model of diffusion Cr/Cr-Ti saturation. 1 Chemical Ni-Co-P sedimentation, 2 Beginning of diffusion of atoms of Cr or Cr-Ti, 3 Appearance of spots of fusion of Ni-Co-P chemical sedimentation, 4 Acceleration of adhesion of atoms Cr or Cr-Ti, 5 Formation of primary zone of solid solution of Cr or Cr-Ti in  $\alpha$ -Fe, 6 Formation of composite zone with nanodispersible carbide grains, 7 Completion of formation of composite zone with carbide grains in the solid solution of Cr or Cr-Ti in  $\alpha$ -Fe

Because of its accessibility and universality, the complex method that includes surface treatment by chemical vapor deposition developed for recipes and thermochemical treatment by accepted modes is able to achieve new qualitative characteristics of surface-hardened layers of machine parts, instruments and tools, thus expanding its scope.

Using a number of new chemical formulations developed for certain modes and methods of chemical and thermochemical treatment with Cr and Cr-Ti, we obtained positive experimental results, with improved physical and mechanical properties of iron alloy surfaces, namely:

- (a) Considerable thickness of diffusion layers (within 200  $\mu$  of the working area);
- (b) Sufficient hardness of diffusion layers, which is about 20 GPa of working area.

## References

1. Rudnev V, Loveless D, Cook R, Black M (2003) Handbook of induction heating. Marcel Dekker, New York/Basel
2. Hetnarski RB (2014) Encyclopedia of thermal stresses, covers thermal stresses, mathematical preliminaries, thermodynamics and heat conduction. Springer, Dordrecht/Heidelberg/ New York/London. doi:10.1007/978-94-007-2739-7

3. Hodgson PD, Beladi H, Barnett MR (2005) Grain refinement in steels through thermomechanical processing. *Mater Sci Forum* 500–501:39–48
4. Chaudhury JN (2013) Effect of heat treatment, pre-stress and surface hardening on fracture toughness of micro-alloyed steel. *J Mater Eng Perform* 23(1):152–168
5. Matlock DK, Krauss G, Speer JG (2005) New microalloyed steel applications for the automotive sector. *Mater Sci Forum* 500–501:87–96
6. Zajac S (2005) Precipitation of microalloy carbo-nitrides prior, during and after  $\gamma/\alpha$  transformation. *Mater Sci Forum* 500–501:75–86
7. Stetsko A (2013) Technological support resource of manufactured and remanufactured parts. Monograph, Lviv, p 240. ISBN 978-966-2739-29-9
8. UA 109283, C23C 10/32, C23C 22/62, C23C 22/05, C23C 10/02, 10 Aug 2015
9. UA 112714, C23C 22/63, C23C 22/52, 19 Oct 2016
10. UA 112601, C23C 22/63, C23C 22/52, 18 Sep 2016
11. UA 110684, C23C 10/58, C23C 10/18, C23C 10/02, 2 Jun 2016
12. UA 111034, C23C 22/60, C23C 22/14, C23C 22/22, 5 Mar 2016
13. UA 112605, C23C 10/02, C23C 10/32, C23C 10/40, C23C 22/05, 18 Sep 2016
14. UA 110046, C23C 8/70, C23C 10/32, 10 Nov 2015
15. UA 109285, C23C 10/32, C23C 22/62, C23C 22/05, C23C 10/02, 10 Aug 2015
16. Stetsko AE (2016) Composite coatings are formed by complex methods. *Universal J Mater Sci* 4:75–81. doi:[10.13189/ujms.2016.040401](https://doi.org/10.13189/ujms.2016.040401)
17. Andrew Stetsko (2016) Chapter 12: Composite coatings formed by complex methods of surface hardening. Nanophysics, nanophotonics, surface studies, and applications. Springer Proceeding in Physics 183, Part III. Nanostructured interface and surfaces, pp 145–154. doi:[10.1007/978-3-319-30737-4\\_12](https://doi.org/10.1007/978-3-319-30737-4_12)
18. Okamoto H (2000) Desk handbook: phase diagrams for binary alloys. American Society for Metals, Materials Park, p 828

# Chapter 47

## Effect of Water Vapor Amount in Hydrogenous Atmospheres on Reducing Ability of the YSZ–NiO Fuel Cell Anode Material

B. D. Vasyliv, V. Ya. Podhurska, and O. P. Ostash

### 47.1 Introduction

It is known that temperatures within the 550–600 °C range are the most effective for the reduction of NiO powders [1]. However, exposition of NiO ceramics in Ar–5 vol% H<sub>2</sub> mixture, which can be used for gradual reduction of SOFC anodes, for 4 h at 600 °C causes partial reduction of the NiO particles forming thin edgings of metallic Ni (of thickness of 0.1–0.3 μm) around them [2]. During redox treatment of NiO ceramics, structural transformation of boundaries of contacting nickel phase particles occurs causing increase in strength.

It was revealed for ScCeSZ–NiO anode ceramics that at certain redox treatment regimes, substantial improvements in strength (up to 112%) and electrical conductivity can be reached [3]. It was also found that after the redox treatment of YSZ–NiO anode ceramics at certain regimes, improvements in physical and mechanical properties occur [4, 5].

The efficiency of the fuel cell is known to rely significantly on fuel gas composition. It is known that the electrochemical oxidation of H<sub>2</sub> is strongly influenced by the steam content in the fuel. It has been reported that a small amount of water (few %) significantly helps decrease anode polarization resistance, while too large an amount of water can degrade anode performance, especially at high electrical load and low concentrations of H<sub>2</sub> in the fuel [6]. The mechanism by which the steam content in fuels promotes the H<sub>2</sub> oxidation reaction is still not well established. There is contradictory evidence as to whether adsorption of oxygen

---

B.D. Vasyliv (✉) • V.Y. Podhurska • O.P. Ostash  
Karpenko Physico-Mechanical Institute of the NAS of Ukraine, 5 Naukova Str, Lviv 79060,  
Ukraine  
e-mail: [frankivsk@email.ua](mailto:frankivsk@email.ua)

species from water on the ceramic part of a cermet anode or the metal part of the anode plays the key role in promoting the reaction.

It is also known that under anodic operation in the presence of high water vapor pressures, redistribution of Ni in the YSZ–Ni cermet occurs [7].

The aims of this work are to study an effect of water vapor amount in a hydrogenous medium on structure and physical and mechanical properties of YSZ–Ni anode materials for solid oxide fuel cells (SOFCs) after various kinds of preconditioning and also to find out microstructural changes causing resulting properties of the material.

## 47.2 Material and Methods

Anode ceramics of YSZ–NiO system sintered of zirconium oxide powder stabilized with 8 mol%  $Y_2O_3$ , with the addition of 50 wt% NiO, has been investigated. A series of specimens of the size of  $1 \times 5 \times 25$  mm were subjected to one-time reduction in hydrogenous atmosphere (the Ar–5 vol%  $H_2$  mixture) for 4 h at  $600^\circ C$  under the pressure of 0.15 MPa or to “reduction in the mixture–oxidation in air” (redox) cycling at  $600^\circ C$  according to [5, 8] (see Table 47.1). The preconditioned specimens and the as-received ones were then subjected to dwell for 4 h in “water vapor–Ar–5 vol%  $H_2$  mixture” atmosphere at  $600^\circ C$  under the pressure of 0.15 MPa. In order to reach the pressure of 0.15 MPa, the test chamber was degassed and filled with water vapor of a certain pressure (0.03 or 0.148 MPa) and then filled up to the pressure of 0.15 MPa with the Ar–5 vol%  $H_2$  mixture. The test conditions were divided into three modes, and the names of samples contained designations of preconditioning and treatment modes (see Table 47.1).

**Table 47.1** The treatment regimes for the materials tested

Name of a series	Preconditioning	Test mode
A1	A	1
R1	R	1
RO1	RO	1
A2	A	2
R2	R	2
RO2	RO	2
A3	A	3
R3	R	3
RO3	RO	3

A as-received material, *R* one-time reduction in the Ar–5 vol%  $H_2$  mixture for 4 h at  $600^\circ C$  under the pressure of 0.15 MPa, *RO* redox treatment for five cycles (reduction in the Ar–5 vol%  $H_2$  mixture–oxidation in air), *mode 1* no treatment, *mode 2* dwelling for 4 h in “water vapor–Ar–5 vol%  $H_2$  mixture” atmosphere at  $600^\circ C$  under the pressure of 0.15 MPa (water vapor pressure, 0.03 MPa), *mode 3* dwelling for 4 h in “water vapor–Ar–5 vol%  $H_2$  mixture” atmosphere at  $600^\circ C$  under the pressure of 0.15 MPa (water vapor pressure, 0.148 MPa)



Ultimate fracture stresses of materials in the initial state,  $\sigma_{f0}$ , and after the corresponding treatment,  $\sigma_f$ , were determined during the three-point bending test of the specimens in air at 20°C. Based on these data, the relative strength,  $\sigma_f/\sigma_{f0}$ , of the material treated was evaluated.

Specific electrical conductivity of material,  $\sigma$ , was determined in air at 20°C using the Van der Pauw method [9]. Fracture surface morphology of the specimens was studied using SEM with secondary electron images. For this purpose, the electron microscope Carl Zeiss EVO-40XVP was used.

### 47.3 Results and Discussion

It is known [2, 8] that exposition of YSZ–NiO ceramics at the temperature 600°C for 4 h in the Ar–5 vol%H<sub>2</sub> mixture causes formation of thin Ni edgings (of thickness of 0.1–0.3 μm) around NiO particles. As compared to as-received material, residual stresses have not changed, and no noticeable change of zirconia skeleton has been found. But reduction in strength to 84% of the value for the as-received YSZ–NiO ceramics, caused by partial structural transformation of nickel phase, has been found for this mode of the treatment. The network of united Ni shells allows the electrical conductivity to be satisfactory. In pure hydrogen, nanopores on Ni particles formed due to their shrinkage and the pores between the particles prevent the rise of residual tensile stresses, but the nickel phase transformation followed by volume change and formation of pores causes the loss of a significant percentage of particle bonds and violates material integrity. Thus, reduction in strength to 48% of the value for the as-received YSZ–NiO ceramics was found.

Taking into account the mentioned peculiarities, we used in this work the Ar–5 vol%H<sub>2</sub> mixture for gradual reduction of SOFC anode material.

A strong tendency to increase the strength of material after both the one-time and redox preconditioning has been observed (mode 1 in Fig. 47.1a, b). Electrical conductivity of material has increased to a quite appropriate level as a result of reduction of a nickel phase (mode 1 in Fig. 47.1c).

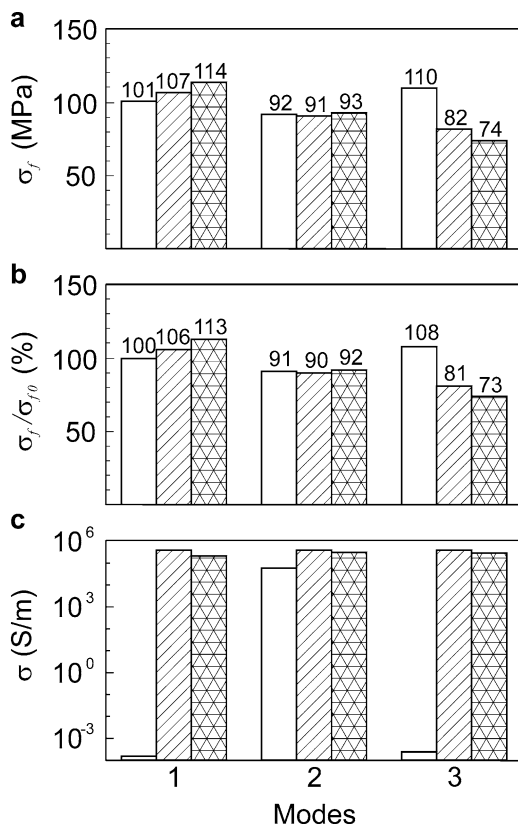
A coarse agglomerate fracture was observed for R series (Fig. 47.2d) without the next treatment (of mode 1). It means that thin Ni edgings around NiO particles (Fig. 47.2a) do not affect structural integrity of the material. We can observe signs of ductile elongation of the nickel phase particles for R series (Fig. 47.2d) contrary to their brittle debonding for A series.

No discernible difference in mechanical behavior was found for R series tested in mode 2 (see Fig. 47.1a, b). A small amount of water vapor in Ar–5 vol% H<sub>2</sub> mixture (water vapor pressure below 0.03 MPa) causes some changes in the YSZ–Ni cermet structure (Fig. 47.2b, e), in particular, growth of nanopores on tiny Ni particles. Resulting strength of the YSZ–Ni cermet decreases by 10–12% as compared to the material reduced in the atmosphere without water vapor. Electrical conductivity of material is of about the same level as for preconditioned series in mode 1 (see Fig. 47.1c).

For as-received material (A series), high concentration of water vapor in Ar–5 vol% H<sub>2</sub> mixture (water vapor pressure 0.148 MPa) is an obstacle for its reduction.



**Fig. 47.1** Ultimate fracture stresses,  $\sigma_f$  (a); relative strength,  $\sigma_f/\sigma_{f0}$  (b); and specific electrical conductivity,  $\sigma$  (c), for materials tested in modes 1–3 (see Table 47.1). *White bars* – A series (no preconditioning); *hatched bars* – R series (preconditioning by one-time reduction); *cross-hatched bars* – RO series (preconditioning by redox cycling). The numbers above the bars indicate the values of corresponding parameters



As a result no satisfied value of electrical conductivity for A series was reached (mode 3 in Fig. 47.1c). A particular increase in strength (mode 3 in Fig. 47.1a, b) is probably caused by water vapor assisted lowering the residual stresses in YSZ–NiO ceramics [10, 11] because no visible signs of structural degradation are observed. At the same water vapor concentration, a drop of strength of preconditioned material was revealed (mode 3 in Fig. 47.1a, b). Such an atmosphere does not allow the reduction of a nickel phase to occur. In the presence of water vapor of high pressure, reoxidation of a nickel phase occurs at 600°C, and, finally, degradation of YSZ–Ni cermet takes place by debonding smaller particles of nickel phase (Fig. 47.2c, f), accompanied with slight lowering of the conductivity (by 3%). The strength of the one-time-reduced material (R series) is lowered by 19% as compared to the as-received ceramics (mode 3 in Fig. 47.1b).

We did not find any difference in mechanical behavior for R and RO series tested in mode 2 (see Fig. 47.1a, b). As compared to the cermet structure formed during the redox treatment (Fig. 47.3a, d), a small amount of water vapor in Ar–5 vol% H<sub>2</sub> mixture (water vapor pressure below 0.03 MPa) causes growth of nanopores (Fig. 47.3b, e), similarly to R series. In all the cases of testing in mode 2, resulting

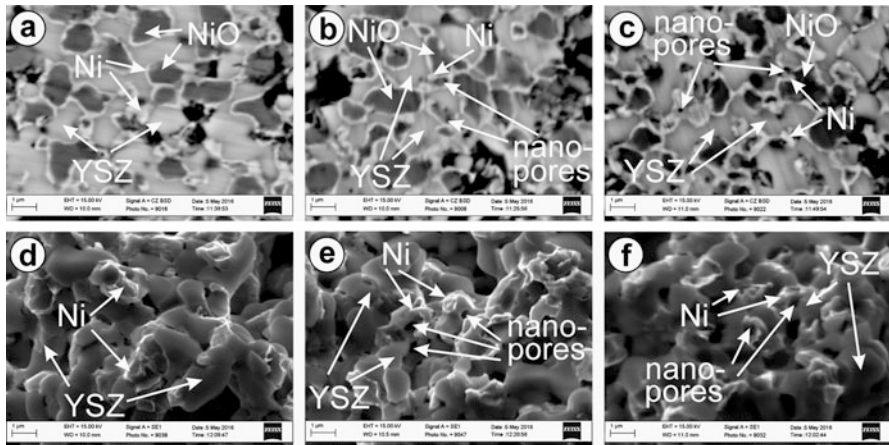


**Fig. 47.2** Observations of (a–c) the structure and (d–f) fracture surface morphology of specimens preconditioned by one-time reduction, with the following treatment in (a, d) mode 1, (b, e) mode 2, and (c, f) mode 3 (see Table 47.1)

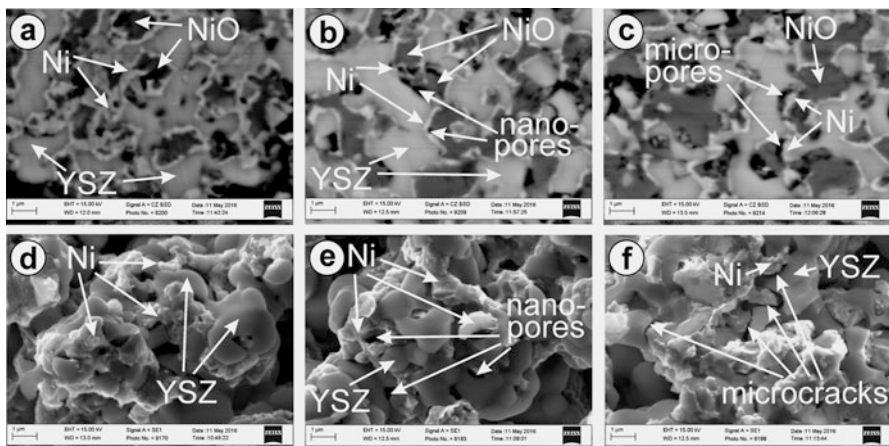


**Fig. 47.3** Observations of (a–c) the structure and (d–f) fracture surface morphology of specimens preconditioned by redox treatment for five cycles, with the following treatment in (a, d) mode 1, (b, e) mode 2, and (c, f) mode 3 (see Table 47.1)

strength of the YSZ–Ni cermets is of about the same level. Electrical conductivity for RO series in mode 2 is of about the same level as for R series in mode 1 (see Fig. 47.1c).

At high water vapor concentration (water vapor pressure, 0.148 MPa), a drastic drop of strength for RO series was revealed (mode 3 in Fig. 47.1a, b). Such an atmosphere causes reoxidation of the nickel phase. Degradation of YSZ–Ni cermet structure occurs with formation of microcracks on the boundaries between the YSZ

and nickel phases (Fig. 47.3c, f). The strength of the cyclically treated material (RO series) is lowered by 27% as compared to the as-received ceramics (mode 3 in Fig. 47.1a, b).

Thus, we revealed a positive effect of high amount of water vapor at 600°C on the strength of the as-received ceramics. But in all the cases of preconditioned specimens, deterioration of the physical and mechanical properties affected by water vapor of high pressure was observed. We suppose that such a dual effect of water vapor on durability of a nickel–zirconia anode needs to be an object of forthcoming thorough investigations.

## 47.4 Conclusions

Based on the experimental data, the dual effect of water vapor on durability of nickel–zirconia SOFC anodes has been revealed. Small amount of water vapor in Ar–5 vol% H<sub>2</sub> mixture (water vapor pressure below 0.03 MPa) does not affect the reduction of a nickel phase in YSZ–NiO ceramics but causes some changes in the YSZ–Ni cermet structure, in particular, growth of nanopores on tiny Ni particles. Resulting strength of the YSZ–Ni cermet decreases by 10–12% as compared to the material reduced in the atmosphere without water vapor. A higher concentration of water vapor in the mixture (water vapor pressure above 0.03–0.05 MPa) causes a converse change in the reduction kinetics. For as-received material, such an amount of water vapor in the mixture is an obstacle for its reduction. It also causes reoxidation of a nickel phase in the YSZ–Ni cermet at 600°C. For the material treated by redox cycling, better physical and mechanical properties were revealed after dwelling at 600°C in a water-depleted gas mixture. Contrary to this, after dwelling at 600°C in a water-enriched gas mixture, the material showed lower resistance against reoxidation and the lowest strength. We suggest that amount of water vapor in operating hydrogenous media of SOFCs should be limited and water vapor pressure should be below 0.03–0.05 MPa.

## References

1. Utigard T, Wu M, Plascencia G et al (2005) Reduction kinetics of Goro nickel oxide using hydrogen. *Chem Eng Sci* 60(7):2061–2068
2. Podhurs'ka VY, Vasyliv BD, Ostash OP et al (2014) Structural transformations in the NiO-containing anode of ceramic fuel cells in the course of its reduction and oxidation. *Mater Sci* 49(6):805–811
3. Ostash OP, Vasyliv BD, Podhurs'ka VY et al (2011) Optimization of the properties of 10Sc1CeSZ–NiO composite by the redox treatment. *Mater Sci* 46(5):653–659
4. Wood A, Waldbillig D (2011). Preconditioning treatment to enhance redox tolerance of solid oxide fuel cells. US Patent 8,029,946 B2, 4 Oct 2011

5. Vasyliv BD, Podhurs'ka VY, Ostash OP et al (2013) Influence of reducing and oxidizing media on the physicochemical properties of ScCeSZ–NiO and YSZ–NiO ceramics. *Mater Sci* 49(2):135–144
6. Kim P, Brett D, Brandon N (2009) The effect of water content on the electrochemical impedance response and microstructure of Ni-CGO anodes for solid oxide fuel cells. *J Power Sources* 189(2):1060–1065
7. Primdahl S (1999) Nickel/yttria-stabilised zirconia cermet anodes for solid oxide fuel cells. Dissertation, University of Twente, Faculty of Chemical Technology, The Netherlands, and Riso National Laboratory, Materials Research Department, Denmark
8. Podhurska V, Vasyliv B, Ostash O et al (2016) Influence of treatment temperature on microstructure and properties of YSZ–NiO anode materials. *Nanoscale Res Lett* 11:93. doi:[10.1186/s11671-016-1306-z](https://doi.org/10.1186/s11671-016-1306-z)
9. Van der Pauw L (1958) A method of measuring specific resistivity and hall effect of discs of arbitrary shape. *Philips Res Rep* 13(1):1–9
10. Jin HM, Shen MS (2009) Study of integrity of NiO oxide film by acoustic emission method. In: Proceedings of the fifth international conference on natural computation, Tianjian, vol 6. Conference Publishing Services, Los Alamitos, California, 14–16 August 2009, p 252. doi:[10.1109/ICNC.2009.133](https://doi.org/10.1109/ICNC.2009.133)
11. Zhou XW, Shen YF, Jin HM (2011) Effect of deposition mechanism and microstructure of nano-ceria oxide addition on Ni-P coating by pulse electrodeposition. *Adv Mater Res* 326:151–156. doi:[10.4028/www.scientific.net/AMR.326.151](https://doi.org/10.4028/www.scientific.net/AMR.326.151)

# Chapter 48

## Sol-gel Synthesis and Conductivity

### $\text{NaLn}_9(\text{SiO}_4)_6\text{O}_2$

K. V. Borysova and E. I. Getman

#### 48.1 Introduction

Compounds with the structure of apatite have found applications in various fields of science and technology. The urgency in obtaining silicate apatites is that the introduction of silicon into the apatite structure significantly increases the biocompatibility and bioactivity of the materials for use in medicine. Apatites containing silicon and rare earth elements (REEs) can be used, for example, as selective catalysts in organic synthesis reactions, electrolytes for solid oxide fuel cells, and luminescent materials.

The aluminosilicate and germanosilicate apatites can play the role of electrolytes in solid oxide fuel cells, which will become important components for a future of clean energy. The main advantage of solid oxide cells is that they do not require an expensive catalyst (platinum) and can run on many types of fuel. For a long time, the problems with using solid oxide fuel cells (SOFCs) were the high process temperature (700–1000 °C) and the need to disperse the heat.

A promising development in media is the use of a SOFC solid electrolyte with higher ionic conductivity at low temperatures compared to YSZ. Despite numerous studies aimed at finding and studying new electrolytes, the problem remains unresolved and open, which is due to the additional requirements for the electrolyte material, such as low electronic conductivity, mechanical strength, structural stability, and chemical stability in oxidizing and reducing environments at temperatures of assembly and operation of the component. In this regard, among the most promising oxygen ion conductors are silicates and germanates REE apatite structure. The features of the structure of these compounds ensure their high oxygen

---

K.V. Borysova (✉) • E.I. Getman  
Donetsk National University, Ukraine. 600-richya Street, 21, Vinnytsia, 21021, Ukraine  
e-mail: [k.borysova@donnu.edu.ua](mailto:k.borysova@donnu.edu.ua)

conductivity at moderate temperatures, low conductivity activation energy, stability in reducing environments, and the possibility of isomorphous substitution (doping) of the different elements, which allows them to modify the transport properties [1–3].

However, the use of oxyapatites as electrolytes requires the development of simple and inexpensive methods of synthesis and studies of the systematic structural and transport properties of materials to obtain compounds with optimal physicochemical characteristics.

Already in the early papers on the conductivity of silicate and germanate REEs, a dependence of the transport properties on the composition of the samples and the structural features of oxyapatites was observed. For example, works on single crystals show the anisotropy of the transport properties of silicon apatite owing to the anisotropy of the hexagonal lattice of apatite, which is manifested in the fact that the conductivity of oxygen oxyapatites parallel to the *c* axis is almost one order of magnitude higher than the conductivity in the perpendicular direction [4, 5].

There was a marked increase in the ionic conductivity and reduced activation energy with increasing radius of REE ions (REE = La, Nd) [4]. In a series REE<sub>10</sub>(RO<sub>4</sub>)<sub>6</sub>O<sub>3</sub> samples of polycrystalline composition, REE = La, Pr, Nd, Sm, Gd, and Dy, the maximum conductivity value at 700 °C, equal to  $1,4 \cdot 10^{-3}$  S/cm, was obtained for La<sub>10</sub>(SiO<sub>4</sub>)<sub>6</sub>O<sub>3</sub>. Later, a similar relationship was also obtained by a number of other investigators for samples containing less REE, such as RE<sub>9,6</sub>(SiO<sub>4</sub>)<sub>6</sub>O<sub>2,4</sub> (REE = La, Nd, Gd), and for RE<sub>9,33</sub>(SiO<sub>4</sub>)<sub>6</sub>O<sub>2</sub> (REE = La, Pr, Nd, Sm, Eu, Gd) [6–8].

The observed behavior associated with changes in the composition of the samples and the stoichiometry of the apatite in them reflect well on modern concepts of the oxygen conductivity of silicates of REEs, according to which high ionic conductivity is typical for samples with a hexagonal lattice of apatite and associated with the presence in it of channels, cation vacancies, and interstitial oxygen atoms [9]. Tolerance to the apatite structure of isomorphous substitutions in a wide range elements and compounds can adjust the number of cation vacancies and interstitial oxygen atoms and thus modify the transport properties of the electrolyte putting bifunctional atoms into the lattice in place of lanthanum or silicon. In addition, the introduction of isovalent atoms also makes it possible to change the conductivity of the oxyapatites, for example, by stabilizing the apatite structure with excess oxygen atoms [10, 11].

## 48.2 Experimental Setup

A sample of NaNd<sub>9</sub>(SiO<sub>4</sub>)<sub>6</sub>O<sub>2</sub> was prepared by the method of solid phase synthesis. At first, oxides were chosen as the starting materials; their elemental composition corresponds to silicate apatite. According to the synthesis procedure, the resulting mixture was calcined at 800 °C, then the temperature was raised to 1100 °C. The sample was calcined for 10 h.

The same compound was obtained by the synthesis of  $\text{NaGd}_9(\text{SiO}_4)_6\text{O}_2$ . The sample was calcined at 800 °C (16 h) and 1100 °C with intermediate abrasion every 20 h to obtain a single phase apatite (of 120 h).

The sol-gel method was used on the sample of  $\text{NaEu}_9(\text{SiO}_4)_6\text{O}_2$ . For this synthesis the starting materials were tetraethoxysilane, carbonate, and oxide corresponding to the elemental composition of the apatite; they were then added dropwise to the required amount of concentrated nitric acid, distilled water, and ethyl alcohol. The resulting sol was dried. Solids of this sol were calcined at a temperature of 550 to 1100 °C. In accordance with the method, the powders were pressed into pellets, calcined at 900 °C, and sintered at 1100 °C for 30 h.

Powder diffraction analysis was performed on DRON-3 (NPO «TsNYYTMASH» Russia) X-ray diffractometers using  $\text{CuK}_\alpha$  radiation and Ni filter. The angular scan rate for the determination of the phase content of the samples was 1–2°/min ( $2\theta$ ). A Rietveld refinement was then used to determine the crystalline structure by powder diffraction data. The angular range chosen for calculations was from 15 to 95° ( $2\theta$ ). The angle increment and exposure time were 0.05° and 3 s, respectively.

### 48.3 Results

Powder diffraction revealed that the apatite structures appeared in the samples after calcination at 800 °C, but the phase composition was not yet uniform, as the lines corresponding to the  $\text{Eu}_2\text{O}_3$  phase were still quite visible. Figure 48.1 shows phase compositions for the samples sintered at temperatures ranging from 800 to 1100 °C.

The intensity of europium oxide lines during the synthesis of  $\text{NaEu}_9(\text{SiO}_4)_6\text{O}_2$  drops considerably only after calcination at 1000 °C. The single phase  $\text{NaEu}_9(\text{SiO}_4)_6\text{O}_2$  was obtained after calcination at 1100 °C.

The elemental composition in  $\text{NaEu}_9(\text{SiO}_4)_6\text{O}_2$ , determined at over 60 points (surface regions) on 8 thin sections is satisfactorily consistent with the calculated data (Table 48.1). This indicates that  $\text{Na}_2\text{O}$  has not undergone sublimation during the apatite synthesis.

The foregoing X-ray diffraction analysis for  $\text{NaNd}_9(\text{SiO}_4)_6\text{O}_2$  and  $\text{NaGd}_9(\text{SiO}_4)_6\text{O}_2$  also indicated that the apatite began to form at 800 °C and retained its structure up to 1100 °C. When the temperature rose above this range, sodium sublimation occurred and the samples did not correspond to the elemental composition.

For samples in the studied temperature range of 320–750 °C, the temperature dependence of conductivity obeys the Arrhenius equation with an inflection at 420–450 °C, caused, apparently, by the transition from extrinsic to intrinsic conduction, and is linear in each of the areas. Therefore, the graph in the coordinates  $\lg\rho$  was built to process the data from  $1/T$ , and calculated activation energies of conduction.

For  $\text{NaNd}_9(\text{SiO}_4)_6\text{O}_2$  the lower temperature range is 320–420 °C, and the upper range is 430–750 °C (Fig. 48.2). In both areas the dependence is close to linear.

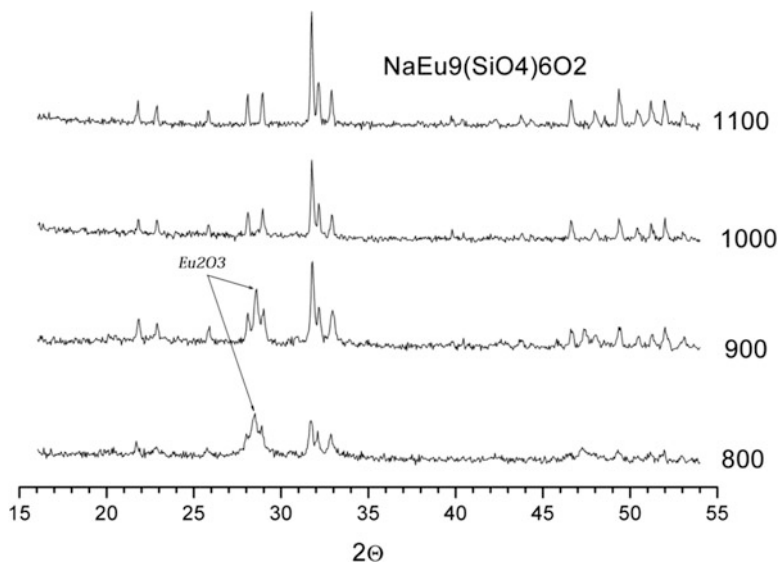


**Fig. 48.1** X-ray diffraction spectra for  $\text{NaEu}_9(\text{SiO}_4)_6\text{O}_2$  samples after calcination at 800, 900, 1000 and 1100 °C

**Table 48.1** Element analysis results for  $\text{NaEu}_9(\text{SiO}_4)_6\text{O}_2$  (% by weight)

Section	Number of points (regions)	O	Na	Si	Eu
1	7	21.18	1.14	8.67	69.01
2	12	21.43	1.12	8.97	68.48
3	7	21.84	1.13	9.46	67.57
4	7	21.41	1.13	8.95	68.51
5	7	21.40	1.19	8.92	68.49
6	9	21.63	1.10	9.21	68.06
7	7	21.34	1.15	8.92	68.59
8	4	21.02	1.06	8.50	69.42
Determined		21.44	1.13	8.98	68.45
Calculated		21.06	1.16	8.53	69.25

For  $\text{NaEu}_9(\text{SiO}_4)_6\text{O}_2$  (Fig. 48.3) the lower temperature range is 300–440 °C, and the upper range is 450–750 °C.

The inflection point on the Arrhenius plot is due to a transition from extrinsic to intrinsic conductivity as the temperature increases. The values of DC and AC electrical conductance as well as activation energy were measured for this compound and are given in Table 48.2.

As can be seen from the data, the conductivity values measured at the alternating current are higher than the values measured at the direct current because both active and reactive components of the conductivity are measured at the alternating current (capacitive or inductive), and only the active component is measured at the direct current.



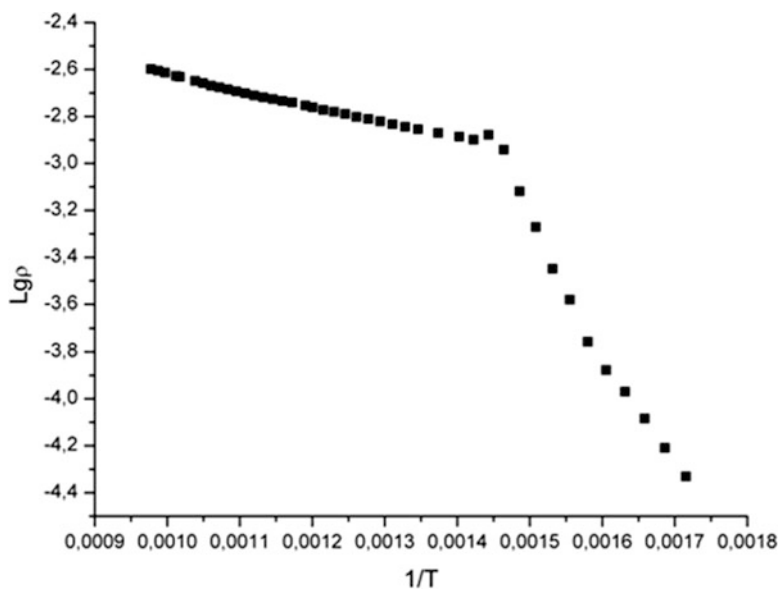


Fig. 48.2 Logarithm of conductivity,  $\sigma$  ( $\text{mScm}^{-1}$ ), as function of  $1/T$  ( $\text{K}^{-1}$ ) for  $\text{NaNd}_9(\text{SiO}_4)_6\text{O}_2$

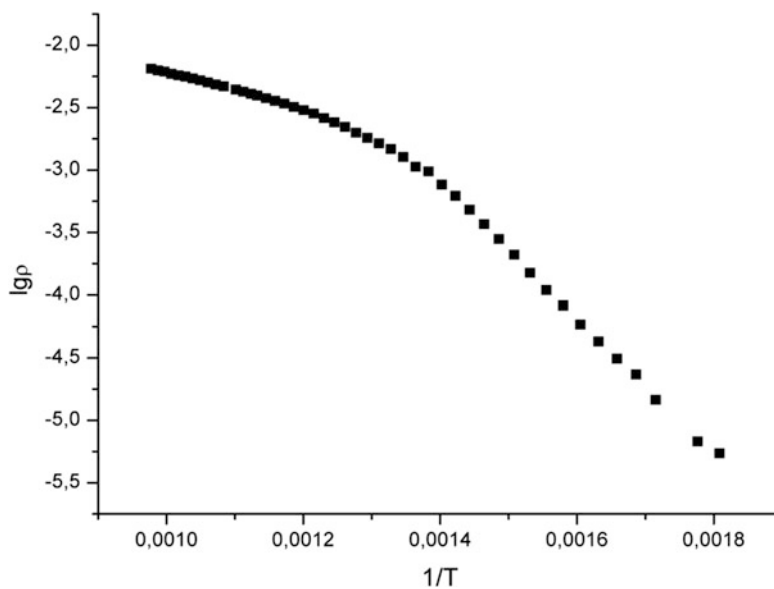


Fig. 48.3 Logarithm of conductivity,  $\sigma$  ( $\text{mScm}^{-1}$ ), as function of  $1/T$  ( $\text{K}^{-1}$ ) for  $\text{NaEu}_9(\text{SiO}_4)_6\text{O}_2$

**Table 48.2** DC and AC conductance and activation energy for the samples

Composition	$\sigma$ (500°C), mScm <sup>-1</sup>	$\sigma$ (600°C), mScm <sup>-1</sup>	$\sigma$ (700°C), mScm <sup>-1</sup>	$E_A$ , eV
NaEu <sub>9</sub> (SiO <sub>4</sub> ) <sub>6</sub> O <sub>2</sub> (direct current)	0.547	1.887	3.120	0.62
NaEu <sub>9</sub> (SiO <sub>4</sub> ) <sub>6</sub> O <sub>2</sub> (1000 Hz)	1.257	2.681	4.059	0.77
NaNd <sub>9</sub> (SiO <sub>4</sub> ) <sub>6</sub> O <sub>2</sub> (direct current)	0,461	0,782	1151	0.40
NaNd <sub>9</sub> (SiO <sub>4</sub> ) <sub>6</sub> O <sub>2</sub> (1000 Hz)	0,942	1163	1401	0.31
La <sub>9,33</sub> Si <sub>6</sub> O <sub>26</sub> [12]	0.023	–	0.26	0.84
La <sub>9</sub> Mg <sub>0,5</sub> Si <sub>6</sub> O <sub>26</sub> [12]	0.021	–	–	0.98
La <sub>8,67</sub> SrSi <sub>6</sub> O <sub>26</sub> [12]	0.083	–	–	0.87
La <sub>8,67</sub> CaSi <sub>6</sub> O <sub>26</sub> [12]	0,058	–	–	0.87

NaEu<sub>9</sub>(SiO<sub>4</sub>)<sub>6</sub>O<sub>2</sub> has greater electrical conductance and in most cases slightly lower activation energy compared to lanthanum silicates La<sub>9,33</sub>Si<sub>6</sub>O<sub>26</sub> and La<sub>9,67</sub>Si<sub>6</sub>O<sub>26,5</sub> as well as some silicates of lanthanum doped with magnesium and alkaline earth metals La<sub>9</sub>Mg<sub>0,5</sub>Si<sub>6</sub>O<sub>26</sub>, La<sub>8,67</sub>SrSi<sub>6</sub>O<sub>26</sub>, La<sub>8,67</sub>CaSi<sub>6</sub>O<sub>26</sub> [12]. An increase in electrical conductivity in compounds containing excess oxygen atoms, such as La<sub>10</sub>Si<sub>6</sub>O<sub>27</sub>, was established previously [12]. A greater electrical conductivity of NaEu<sub>9</sub>(SiO<sub>4</sub>)<sub>6</sub>O<sub>2</sub> can be explained by the local distortion of the crystal structure since it does not have excess oxygen. The alkali metal replacing europium has a much smaller charge and larger size. Some oxygen atoms of each SiO<sub>4</sub> tetrahedron surround both Eu(1) and Eu(2). This leads to a weaker electrostatic interaction of oxygen with the Eu(1) and a stronger electrostatic interaction with Eu(2).

## 48.4 Conclusions

However, solid-phase, mechanochemical, and hydrothermal methods were not able to obtain NaLn<sub>9</sub>(SiO<sub>4</sub>)<sub>6</sub>O<sub>2</sub> compounds suitable for making pottery because of uncontrolled sublimation under Na<sub>2</sub>O, no single-phase samples, and the deviation from the set of predetermined compositions. For that reason, we used the sol-gel method for the synthesis of nanoscale compounds NaLn<sub>9</sub>(SiO<sub>4</sub>)<sub>6</sub>O<sub>2</sub> by the hydrolysis of sodium tartrate solution and rare earth metals from tetraethoxysilane Si(OC<sub>2</sub>H<sub>5</sub>)<sub>4</sub>. Ceramics, obtained from polycrystalline samples at 1100 °C, had a sufficient density for measuring the electrical conductivity. It is established that electrical conductivity at 700 °C has the same order as the most-apatite REE silicates without alkali metals. The conductivity of sodium silicates of the yttrium subgroup is lower than that of cerium, which is due to the decrease in the diameters of the channels of the structure through which the ions that conduct the conductivity move, due to the decrease in the distances Ln(2) -Ln(2). The distances Ln(2) -Ln(2) where Ln - Nd, Eu, Gd are 3.94; 3.87; 3.85 to 3.81 Å.

## References

1. Tao SW, Irvine JTS (2000) Synthesis and ionic conduction of apatite-type materials. *Ionics* 6:389–396
2. Lakshminarasimhan N, Varadaraju UV (2005) Synthesis and  $\text{Eu}^{3+}$  luminescence in new oxyasilicates,  $\text{ALa}_3\text{Bi}(\text{SiO}_4)_3\text{O}$  and  $\text{ALa}_2\text{Bi}_2(\text{SiO}_4)_3\text{O}$  [a=Ca, Sr and Ba] with apatite-related structure. *J Solid State Chem* 178:3284–3292
3. Masubuchi Y, Higuchi M, Kodaira K (2003) Reinvestigation of phase relations around the oxyapatite phase in the  $\text{Nd}_2\text{O}_3$ - $\text{SiO}_2$  system. *J Cryst Growth* 247:207–212
4. Nakayama S, Sakamoto M (1998) Electrical properties of new type high oxide ionic conductor  $\text{RE}_{10}\text{Si}_6\text{O}_{27}$  (RE = La, Pr, Nd, Sm, Gd, Dy). *J Eur Ceram Soc* 18:1413–1418
5. Meis C, Gale JD, Boyer L, Carpena J, Gosset D (2000) Theoretical study of Pu and Cs incorporation in a mono-silicate neodymium fluoroapatite  $\text{Ca}_9\text{Nd}(\text{SiO}_4)(\text{PO}_4)_5\text{F}_2$ . *J Phys Chem* 104:5380–5387
6. Masubuchi Y, Higuchi M, Takeda T, Kikkawa S (2006) Oxide ion conduction mechanism in  $\text{RE}_{9.33}(\text{SiO}_4)_6\text{O}_2$  and  $\text{Sr}_2\text{RE}_8(\text{SiO}_4)_6\text{O}_2$  (RE=La, Nd) from neutron powder diffraction. *Solid State Ionics* 177:263–268
7. Sansom JEH, Tolchard JR, Slater PR, Islam MS (2004) Synthesis and structural characterisation of the apatite-type phases  $\text{La}_{10-x}\text{Si}_6\text{O}_{26+z}$  doped with Ga. *Solid State Ionics* 167:17–22
8. Li B, Liu W, Pan W (2010) Synthesis and electrical properties of apatite-type  $\text{La}_{10}\text{Si}_6\text{O}_{27}$ . *J Power Sources* 195:2196–2201
9. Jothinathan E, Vanmeensel K, Vleugels J, Kharlamova T, et al (2010) Apatite type lanthanum silicate and composite anode half cells. *Solid State Ionics* 43(12):3627–3632. doi: [10.1016/j.ssi.2010.02.009](https://doi.org/10.1016/j.ssi.2010.02.009)
10. Kendrick E, Slater PR (2008) Synthesis of Ga-doped Ge-based apatites: effect of dopant and cell symmetry on oxide ion conductivity. *Mater Res Bull* 43:3627–3632
11. Kendrick E, Slater PR (2008) Synthesis of hexagonal lanthanum germanate apatites through site selective isovalent doping with yttrium. *Mater Res Bull* 43:2509–2513
12. Yoshioka H, Nojiri Y, Tanase S (2008) *Solid State Ionics*. Ionic conductivity and fuel cell properties of apatitetype lanthanum silicates doped with Mg and containing excess oxide ions 179:2165

**Part V**  
**Nanocomposites and Nanomaterials**

# Chapter 49

## Structure, Morphology, and Properties of Copper-Containing Polymer Nanocomposites

V. Demchenko, S. Riabov, N. Rybalchenko, and V. Shtompel'

### 49.1 Introduction

In the last decade, there has been increased interest in the creation of new functional polymeric materials containing metal nanoparticles of various metals or their metal oxides [1–3].

In this connection, researches dealing with elaboration of such hybrid materials [4–8], including synthesis of Cu nanoparticles directly in a polymers film [9–11], are intensively developed. It is known that copper's nanoparticles have interesting optical properties and high catalytic, antibacterial, and fungicidal activities, and this urges an interest for design and preparing a polymer–metal and hybrid composites, having controllable structure and particles of nano-size level [4].

Cu nanoparticles have been synthesized through different methods such as thermal decomposition [12–15], metal salt reduction [16], microwave heating [17], radiation methods [18], micro emulsion techniques [19], laser ablation [20], polyol method [21], solvothermal method [22], and thermal and sonochemical reduction [23].

As an intensive expansion and steady growing of microorganisms in a various environments takes place, new efficient substances are strongly required to apply

---

V. Demchenko (✉) • S. Riabov • V. Shtompel'  
Institute of Macromolecular Chemistry, The National Academy of Sciences of Ukraine,  
Kiev, Ukraine  
e-mail: [dvaleriyl@ukr.net](mailto:dvaleriyl@ukr.net)

N. Rybalchenko  
Zabolotny Institute of Microbiology and Virology, The National Academy of Sciences of  
Ukraine, Kiev, Ukraine

in pharmacology, medicine, food industry, and for wastewater treatment as well. Nanoparticles of metals (e.g., Ag and Cu) and metal oxides (like Cu<sub>2</sub>O) possessing a biocidal activity and high stability in the extreme conditions are in the focus of researchers, developing efficient antimicrobial agents [24, 25].

So, the aim of this work is to study the structural organization, morphology, and thermomechanical and antimicrobial properties of nanocomposites prepared involving natural and synthetic polymers – pectin, polyethyleneimine, and Cu/Cu<sub>2</sub>O or Cu nanoparticles – obtained by the chemical and thermal reduction of copper ions in the interpolyelectrolyte–metal complexes.

## 49.2 Experimental

To obtain the interpolyelectrolyte complexes (IPEC), pectin–polyethyleneimine; the interpolyelectrolyte–metal complexes (IMC), pectin–Cu<sup>2+</sup>–polyethyleneimine; and nanocomposites of IPEC–Cu/Cu<sub>2</sub>O or Cu, the following reagents were used: anionic polyelectrolyte citrus pectin (Cargill Deutschland GmbH, Germany) with  $M = 3 \times 10^4$ , cationic polyelectrolyte anhydrous branched polyethyleneimine (PEI) (Aldrich) with  $M_n = 1 \times 10^4$  and  $M_w = 2.5 \times 10^4$ , copper (II) sulfate pentahydrate (CuSO<sub>4</sub> × 5H<sub>2</sub>O) (Aldrich) with  $M = 249.69$ , and sodium borohydride (NaBH<sub>4</sub>) (Aldrich) with  $M = 37.83$ .

IPEC samples were formed via mixing of 5% aqueous solutions of pectin and PEI taken at a molar ratio of 1:1, at  $T = 20 \pm 2$  °C. IPEC as films were prepared via pouring onto PTFE plates and drying up to constant masses at the same temperature. Dry IPEC films were washed in distilled water up to neutrality and dried repeatedly at 20 °C up to constant masses. The resulting films were 100 μm thick.

IMC samples were prepared via immersion of IPEC films into an aqueous solution of CuSO<sub>4</sub> with a concentration of 0.1 mol/L at  $T = 20 \pm 2$  °C for 24 h. The colorless IPEC films became dark blue.

The adsorption capacities of films,  $A$  (mmol/g), were calculated through the formula [26]

$$A = (c_{in} - c_{eq}) V/m,$$

where  $m$  is the mass of the adsorbent,  $V$  is the solution volume, and  $c_{in}$  and  $c_{eq}$  are the initial and the equilibrium concentrations of copper ions. For IMC films  $A = 2.9$  mmol/g.

The chemical reduction of Cu<sup>2+</sup> ions in the IMC was conducted with NaBH<sub>4</sub> (a molar ratio of [BH<sub>4</sub><sup>-</sup>]: [Cu<sup>2+</sup>] = 0.5–10.0) in an alkaline medium (pH 10.8) in a solvent mixture of water–isopropanol (4:1 vol %) at  $T = 20 \pm 2$  °C for 3 h (until the release of gaseous bubbles ceased). The concentration of NaBH<sub>4</sub> in the aqueous alcohol solution was 0.1 mol/L.

Thermal reduction of  $\text{Cu}^{2+}$  ions in the IMC's volume was performed by heating of films to 120–190 °C within 30 min, as well as at optimal temperature 170 °C within 5, 10, 20, and 30 min, respectively. Specimens were heated in the oven using precise thermal regulator VRT-3. Temperature regulation precision was  $\pm 0.5$  °C.

As a result of the reduction, IMC films changed color from blue to dark brown.

The features of the amorphous and amorphous–crystalline structuring of the IPEC (pectin–PEI), the IMC (pectin– $\text{Cu}^{2+}$ –PEI), and nanocomposites of IPEC–Cu/Cu<sub>2</sub>O or Cu were studied by wide-angle X-ray diffraction on a DRON-4-07 diffractometer, whose X-ray optical scheme was used to “pass” primary beam radiation through samples. X-ray diffraction studies were performed at  $T = 20 \pm 2$  °C in  $\text{CuK}\alpha$  radiation monochromated with a Ni filter.

The heterogeneous structuring of these polymeric systems (at the nanometer level) was studied via small-angle X-ray scattering with a CRM-1 camera, having a slit collimator of the primary irradiation beam made via the Kratky method. The geometric parameters of the camera satisfied the condition of infinite height of the primary beam [27]. The intensity profiles were normalized to the volume of X-ray scattering and the attenuation factor of the primary beam of the test sample.

All X-ray diffraction studies were performed at  $T = 20 \pm 2$  °C in  $\text{CuK}\alpha$  radiation monochromated with a Ni filter.

The size of the Cu/Cu<sub>2</sub>O or Cu nanoparticles and their distribution in the polymer matrix were examined with a JEM-1230 transmission electron microscope (JEOL, Japan) at a resolution of 0.2 nm.

Thermomechanical studies of polymer systems were conducted using the penetration method in the mode of a uniaxial constant load ( $\sigma = 0.5$  MPa) on a UIP-70 M device. Linear heating of samples was performed at a rate of 2.5 °C/min in the temperature range – 100 to +350 °C.

The antimicrobial activity of IPEC–Cu/Cu<sub>2</sub>O or Cu nanocomposites, prepared by chemical and thermal reduction of  $\text{Cu}^{2+}$  ions in IMC, was investigated using reference strains of opportunistic bacteria *Staphylococcus aureus* ATCC 6538 and *Escherichia coli* ATCC 35218 (as a model gram-positive and gram-negative bacteria).

Investigations were carried out by agar diffusion method on a solid LB (Luria-Bertani) nutrient medium [28]. The nanocomposite films (size 10 × 10 mm) were placed on the surface of nutrient agar, which had been previously inoculated with 10  $\mu\text{L}$  of bacterial suspension of *S. aureus* and *E. coli* at the rate of  $2 \times 10^5$  CFU/ml. The plates were incubated at 37°C for 24 h.

Clear zones, which has no bacteria around the film of composite, containing copper was the indicator of antimicrobial activity. All experiments were repeated three times. The IPEC film was applied as a control sample.

### 49.3 Structure and Thermomechanical Properties of Nanocomposites, Obtained by the Chemical Reduction of Copper Ions in the Interpolyelectrolyte–Metal Complexes

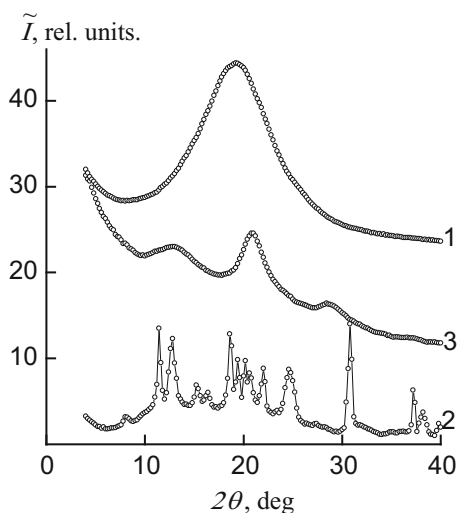
During comparison of the wide-angle X-ray diffractograms of the weak cationic and anionic polyelectrolytes on whose basis the IPEC was formed (see Fig. 49.1), it was found that PEI has only short-range ordering during translation of fragments of its macromolecular chains in space, while pectin has an amorphous–crystalline structure. This fact is confirmed by the appearance of one diffuse diffraction maximum (as judged from the angular half-width, an amorphous halo) on the diffractogram for PEI (curve 1), whose angular position ( $2\theta_m$ ) is approximately  $19.2^\circ$ . The average value of period  $d$  of the short-range ordering of fragments of PEI macrochains during their positioning in space (in a volume of PEI) according to the Bragg equation is

$$d = \lambda(2 \sin \theta_m)^{-1},$$

where  $\lambda$  is the wavelength of the characteristic X-ray radiation, which is  $4.6 \text{ \AA}$  ( $\lambda = 1.54 \text{ \AA}$  for  $\text{CuK}_\alpha$  radiation).

On the X-ray diffractogram of pectin, whose sample is a powder (curve 2), there are many singlet and multiplet diffraction maxima having an imaginary amorphous halo with a vertex at  $2\theta_m 16.8^\circ$  in the background, which implies the amorphous–crystalline structure of the polysaccharide. The estimation of the relative level of pectin's crystallinity ( $X_{\text{cr}}$ ) by Matthews method [29]

**Fig. 49.1** Wide-angle X-ray diffractograms of (1) PEI, (2) a powdered pectin sample, and (3) a pectin film obtained from a 5% aqueous solution





$$X_{cr} = Q_{cr}(Q_{cr} + Q_{am})^{-1} \cdot 100,$$

(where  $Q_{cr}$  area diffraction peaks that characterize the crystalline structure of the polymer and  $Q_{cr} + Q_{am}$  the whole area in the range of diffraction angles scattering ( $2\theta_1/2\theta_2$ )), which appears to be amorphous–crystalline polymer, showed that this value is about 65%.

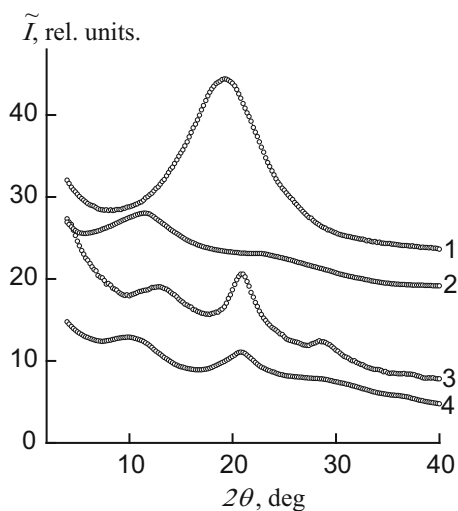
In turn, effective crystallite size  $L$  of pectin determined via the Scherrer method [30]

$$L = K\lambda(\beta \cos \theta_m)^{-1},$$

where  $K$  is a constant related to a shape of the crystallites ( $K = 0.9$  if their shape is unknown) and  $\beta$  is the angular half-width (width at a half-height) of the singlet of a discrete diffraction maximum, showed that the average value of  $L$  is 17.5 nm. (For the calculation, singlet diffraction maxima at  $2\theta_m = 18.7^\circ$  and  $30.8^\circ$  were used.) However, the X-ray diffractogram of the pectin sample film obtained with the use of a 5% aqueous solution, similar to the diffractogram for IPEC formation, has only outlines of main intensity groups of the diffraction maxima that are present on the diffractogram of the pectin powder sample (curves 2, 3), thereby indicating a slow rate of crystallization of pectin as well as a relaxed type of structure formation in the polymers.

However, the sorption of  $\text{CuSO}_4$  by the initial samples of PEI and pectin and the formation of polyelectrolyte–metal complexes, such as  $\text{PEI-Cu}^{2+}$  and  $\text{pectin-Cu}^{2+}$ , are accompanied by changing in the diffractograms (see Fig. 49.2) and emerging of an intense diffuse diffraction maximum at  $2\theta_m \sim 11.6^\circ$  and  $10.0^\circ$  on the  $\text{PEI-Cu}^{2+}$  and  $\text{pectin-Cu}^{2+}$  profiles, respectively (curves 2, 4). According to [29], these

**Fig. 49.2** Wide-angle X-ray diffractograms of (1) PEI, (2)  $\text{PEI-Cu}^{2+}$ , (3) pectin, and (4)  $\text{pectin-Cu}^{2+}$



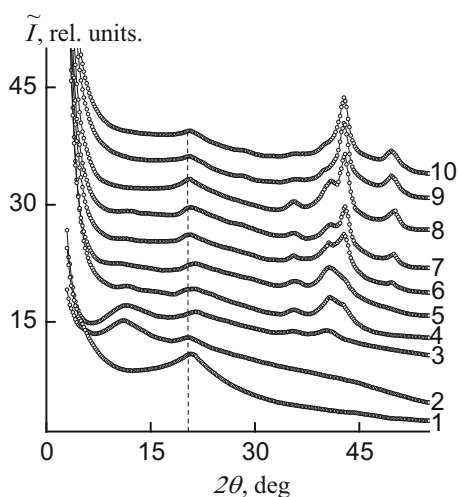
diffraction peaks characterize the existence of polyelectrolyte–metal complexes between  $\text{Cu}^{2+}$  ions and the ligands. With allowance for the angular positions of the diffraction maxima of the corresponding X-ray diffractograms, average Bragg distances  $d$  between the macromolecule chains of PEI and pectin coordinated by  $\text{Cu}^{2+}$  ions are 7.6 and 8.8 Å, respectively.

The analysis of wide-angle X-ray diffractograms has shown that IPEC formed of pectin and PEI is characterized by short-range ordering during translation of fragments of oppositely charged polyelectrolyte macromolecular chains in space. This circumstance is indicated by the appearance of one diffuse diffraction maximum with  $2\theta_m \sim 20.8^\circ$  on the X-ray diffractogram of the IPEC sample (see Fig. 49.3, curve 1). The average value of the period of short-range ordering of fragments of complementary macromolecular chains of oppositely charged polyelectrolytes in the IPEC (the Bragg distance between the macromolecule chains of anionic and cationic polyelectrolytes in the IPEC) is 4.3 Å, i.e., slightly less than that in the cationic polyelectrolyte.

However, the sorption of  $\text{CuSO}_4$  by the initial IPEC sample and formation of the IPEC– $\text{Cu}^{2+}$  IMC is accompanied by a change in the diffractogram. This result is indicated by the appearance of an intense diffuse diffraction maximum at  $2\theta_m \sim 11.2^\circ$  (curve 2) in the presence of a low-intensity amorphous halo, which, unlike that for the initial IPEC, has an angular position at  $2\theta_m \sim 20.4^\circ$  ( $d \sim 4.4$  Å). This diffraction maximum characterizes the existence of polyelectrolyte–metal complexes between the central ions ( $\text{Cu}^{2+}$ ) and ligands. With the use of the angular position of this diffraction peak on the X-ray diffractogram of the IMC, average Bragg distance  $d$  between the macromolecule chains of polyelectrolytes coordinated with  $\text{Cu}^{2+}$  ions is found to be 7.9 Å.

After the chemical reduction of the  $\text{Cu}^{2+}$  ions in the IMC with the use of sodium borohydride (a molar ratio of  $[\text{BH}_4^-]: [\text{Cu}^{2+}] = 0.5$ ) to form a nanocomposite

**Fig. 49.3** Wide-angle X-ray diffractograms of (1) the IPEC, (2) the IMC, and (3–10) the IPEC–Cu/Cu<sub>2</sub>O nanocomposites obtained via the chemical reduction of  $\text{Cu}^{2+}$  ions in the IMC at molar ratios of  $[\text{BH}_4^-]: [\text{Cu}^{2+}] =$  (3) 0.5, (4) 1, (5) 2, (6) 3, (7) 4, (8) 5, (9) 6, and (10) 10



based on the IPEC and  $\text{Cu}_2\text{O}$ , the X-ray diffractogram of the nanocomposite (Fig. 49.3, curve 3) shows a slight weakening of the intensity of the diffraction peak, characterizing the existence of polyelectrolyte–metal complexes, with an insignificant shift to the region of large angles of X-ray scattering ( $2\theta$ ), from  $11.2^\circ$  to  $11.6^\circ$ , with a decrease in the average value of the Bragg distance between the macromolecules chains coordinated with  $\text{Cu}^{2+}$  ions, from 7.9 to 7.6 Å. In addition, there is a shift in the region of large scattering angles of the amorphous halo, which characterizes the short-range ordering of the fragments of macromolecule chains of anionic and cationic polyelectrolytes during their distribution in the volume of the IPEC, from  $2\theta_m \sim 20.8^\circ$  to  $21.4^\circ$ . This result indicates the tendency for a decrease in the distance between the Bragg chains of macromolecules from 4.3 to 4.1 Å. Also, two low-intensity diffraction peaks appeared at  $2\theta_m \sim 35.6^\circ$  and  $40.8^\circ$  confirm the formation of  $\text{Cu}_2\text{O}$  nanoparticles in the IPEC.

With an increase in the amount of the reducing agent (a molar ratio of  $[\text{BH}_4^-]:[\text{Cu}^{2+}] = 1-2$ ), the X-ray diffractograms of nanocomposites based on the IPEC and  $\text{Cu}_2\text{O}$  (curves 4, 5) show a significant decrease in the intensity of the diffraction peak characterizing the existence of polyelectrolyte–metal complexes in the IPEC at  $2\theta_m \sim 11.6^\circ$ . Also, there is an increase in the intensity of the two diffraction peaks at  $2\theta_m \sim 35.6^\circ$  and  $40.8^\circ$ , an outcome that implies the formation of  $\text{Cu}_2\text{O}$  nanoparticles in the IPEC. In addition, a low-intensity diffraction peaks are fixed at  $2\theta_m \sim 42.8^\circ$ , which characterizes the metallic copper phase of  $\text{Cu}/\text{Cu}_2\text{O}$  nanoparticles.

Increasing the amount of the reducing agent (a molar ratio of  $[\text{BH}_4^-]:[\text{Cu}^{2+}] = 3-6$ ) leads to a different diffractogram; as in the case of the two previous samples of nanocomposites based on the IPEC and  $\text{Cu}_2\text{O}$  (curves 4, 5), there is a significant reduction in the intensity of the diffraction maximum at  $2\theta_m \sim 11.6^\circ$ , which characterizes the existence of polyelectrolyte–metal complexes in the IMC, that is due to the chemical reduction of  $\text{Cu}^{2+}$  ions in the IMC yielding  $\text{Cu}/\text{Cu}_2\text{O}$  nanoparticles (curves 6–9). Also, there is a shift to a region of lower angles of scattering of the amorphous halo, showing the short-range order of fragments during their distribution in macromolecular chains of PEI and pectin in the IPEC, from  $2\theta_m \sim 21.4^\circ$  to  $20.6^\circ$ . This circumstance indicates a trend toward an increase in the Bragg distance between the chains of macromolecules from 4.1 to 4.3 Å relative to that for the previous nanocomposites, where the molar ratio was  $[\text{BH}_4^-]:[\text{Cu}^{2+}] = 0.5-2.0$ . Also, the intensity of the diffraction peak increases at  $2\theta_m \sim 42.8^\circ$ , and a diffraction peak appears at  $2\theta_m \sim 49.6^\circ$  with growing intensity as the content of the reducing agent is increased. These maxima characterize the structuring of the metallic copper phase of  $\text{Cu}/\text{Cu}_2\text{O}$  nanoparticles in the IPEC. When the molar ratio  $[\text{BH}_4^-]:[\text{Cu}^{2+}] = 6$  is reached, there is weakening of the intensity of the diffraction peaks at  $2\theta_m \sim 35.6^\circ$  and  $40.0^\circ$ , suggesting the presence of  $\text{Cu}_2\text{O}$  nanoparticles in the IPEC, while the peaks at  $2\theta_m \sim 42.8^\circ$  and  $49.6^\circ$ , which identify the structure of metallic copper, are more evident.

The evaluation of an effective crystallite size of  $\text{Cu}/\text{Cu}_2\text{O}$  nanoparticles in the IPEC demonstrated that  $L \sim 4.5$  nm. (For the calculation, the diffraction peaks at  $2\theta_m = 42.8^\circ$  and  $49.6^\circ$  (curve 9) were used.)

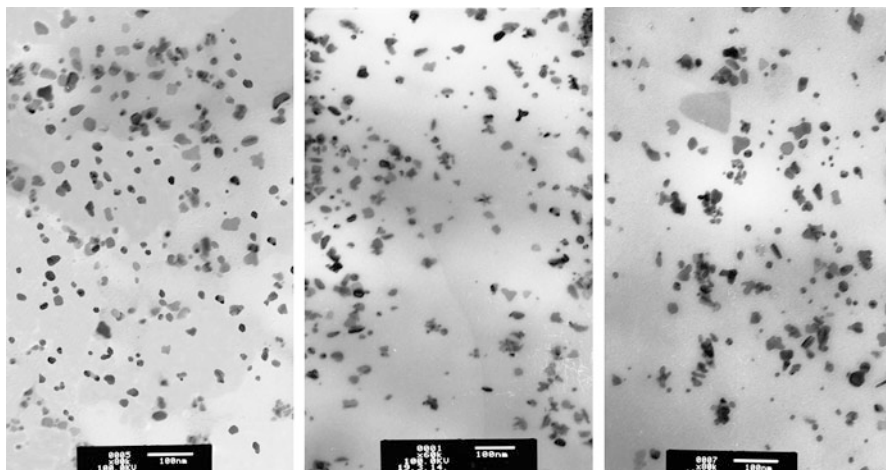


**Fig. 49.4** TEM micrograph of the IPEC–Cu/Cu<sub>2</sub>O nanocomposite obtained via the chemical reduction of Cu<sup>2+</sup> ions in the IMC at a molar ratio [BH<sub>4</sub><sup>−</sup>]: [Cu<sup>2+</sup>] = 6

A further increase in the amount of the reducing agent (a molar ratio of [BH<sub>4</sub><sup>−</sup>]: [Cu<sup>2+</sup>] = 10) does not change the structuring of the nanocomposites based on the IPEC and Cu/Cu<sub>2</sub>O nanoparticles (curves 9, 10).

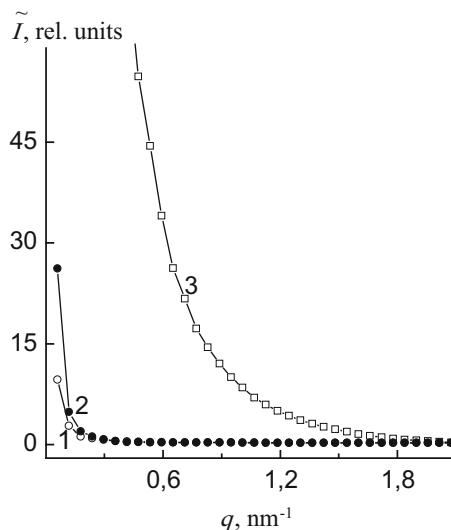
Thus, according to wide-angle X-ray diffraction, it may be concluded that the molar ratio [BH<sub>4</sub><sup>−</sup>]: [Cu<sup>2+</sup>] = 6 is optimum for the formation of IPEC–Cu/Cu<sub>2</sub>O nanocomposites.

The conversion of IPEC–Cu<sup>2+</sup> polyelectrolyte–metal complexes into nanocomposites containing Cu/Cu<sub>2</sub>O nanoparticles is confirmed by transmission electron microscopy (see Fig. 49.4), and the average size of the Cu/Cu<sub>2</sub>O nanoparticles in nanocomposites is 10 nm. Analysis of the micrographs showed that the nanoparticles are more or less evenly distributed in the IPEC.

The revealed specific features in structures at the transition from the IPEC into IMC and IPEC–Cu/Cu<sub>2</sub>O nanocomposites form the basis for the studying of heterogeneity of their structures.

Observing the profiles of small-angle X-ray scattering of the various polymeric and polymer–metal systems presented in accordance with [31, 32] as dependences of on  $\tilde{I}$  on  $q$  (Fig. 49.5) and  $s^3\tilde{I}$  on  $s^3$ , where is the intensity of scattering without the collimation correction and  $q = (4\pi/\lambda)\sin\theta = 2\pi s$ , we found out that all these systems except the IPEC have heterogeneous structuring; i.e., contrast electron densities  $\Delta\rho$  ( $\Delta\rho = \rho - \langle\rho\rangle$ , where  $\rho$  and  $\langle\rho\rangle$  are the local and average values of the electron density, respectively) are present in their volumes. This result means that in both the IMC and the nanocomposites based on the IPEC and Cu/Cu<sub>2</sub>O, there are no less than two types of region heterogeneity with different values of local electron density  $\rho$ . Nanocomposites based on IPEC–Cu/Cu<sub>2</sub>O have higher intensities of scattering and, hence, values of  $\Delta\rho$  (curves 3) than those of the polymeric systems of the IPEC and the IMC (curves 1, 2). However, the absence

**Fig. 49.5** Profiles of the intensity of small-angle X-ray scattering of (1) the IPEC, (2) the IMC, and (3) the IPEC–Cu/Cu<sub>2</sub>O nanocomposites obtained via the chemical reduction of Cu<sup>2+</sup> ions in the IMC at a molar ratio [BH<sub>4</sub><sup>−</sup>]: [Cu<sup>2+</sup>] = 6



of the interference peak from all the profiles of intensity indicates the stochastic nature of the location of various types of heterogeneity regions in space.

The values of their Porod invariants  $Q'$  were compared to semiquantitatively evaluate the relative levels of structural heterogeneity of these polymer systems [33]:

$$Q' = \int_0^{\infty} q \tilde{I}(q) dq.$$

These values are invariant with respect to the shapes of the heterogeneity regions and are directly related to the rms values of fluctuations of electron density ( $\langle \Delta \rho^2 \rangle$ ) in a two-phase system:

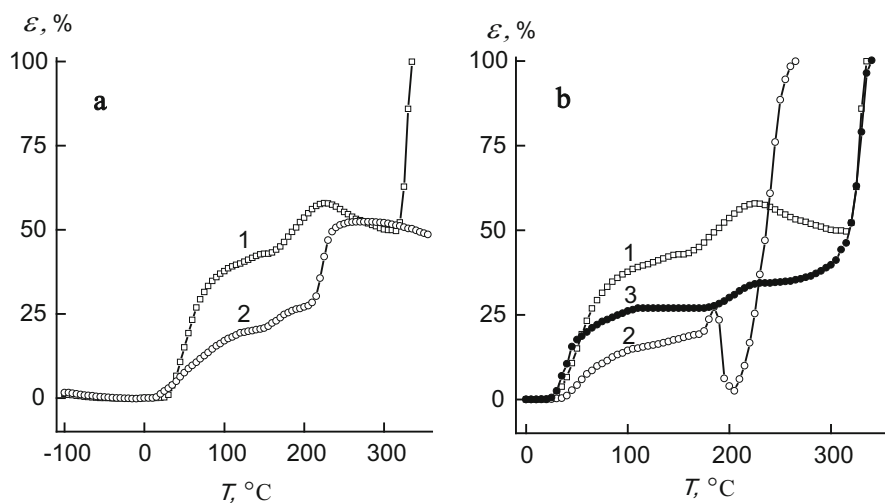
$$Q' \propto \langle \Delta \rho^2 \rangle,$$

Here,  $\langle \Delta \rho^2 \rangle = \varphi_1 \varphi_2 (\rho_1 - \rho_2)^2$ , where  $\varphi_1$  and  $\varphi_2$  are the volume ratios of heterogeneity domains in a two-phase system and  $\rho_1$  and  $\rho_2$  are the electron densities of heterogeneity domains ( $\varphi_1 + \varphi_2 = 1$ ) in a two-phase system. A comparison of the values of invariant  $Q'$  for the studied polymer systems (Table 49.1) shows that the relative level of the structural heterogeneity increases significantly during the transition from the IPEC and the IMC into the nanocomposites based on the IPEC and Cu/Cu<sub>2</sub>O.

An evaluation of the effective sizes of the heterogeneity regions existing in the IMC and the resulting IPEC–Cu/Cu<sub>2</sub>O nanocomposites was performed through the method from [31, 32] via calculation of structural parameters, such as the range of heterogeneity (range of inhomogeneity),  $l_p$ , which is directly related to the average

**Table 49.1** Some structural parameters of the studied polymeric systems

Sample	$l_p$ , nm	$Q'$ , rel. Units	$T_g$ , °C	$T_f$ , °C
IPEC	–	6.2	53	319
IMC	12	6.0	57	205
IPEC–Cu/Cu <sub>2</sub> O	4.2	251.1	44	317

**Fig. 49.6** Thermomechanical curves: (a) (1) the IPEC and (2) pectin films obtained from a 5% aqueous solution; (b) (1) the IPEC, (2) the IMC, and (3) the IPEC–Cu/Cu<sub>2</sub>O nanocomposite

diameters of heterogeneity regions,  $\langle l_1 \rangle$ ,  $\langle l_2 \rangle$ , in the two-phase system:

$$l_p = \phi_2 \langle l_1 \rangle = \phi_1 \langle l_2 \rangle.$$

As a result of the calculation of  $l_p$ , the transition from the IMC into the IPEC–Cu/Cu<sub>2</sub>O nanocomposites was found to be accompanied by an almost threefold decrease in the effective size of heterogeneity regions (Table 49.1).

Together with the structural organization of the IPEC, the IMC, and the nanocomposites based on IPEC–Cu/Cu<sub>2</sub>O, their thermomechanical behavior was studied.

The analysis of the thermomechanical curve of the IPEC (see Fig. 49.6a, curve 1) demonstrated temperature transitions that are associated with the glass-transition temperatures and flow occur in the temperature ranges 25–145 °C and 265–335 °C, respectively. Furthermore, in the range of temperatures 150–245 °C, there is a temperature transition that is likely due to the melting of the crystallites of pectin in the IPEC (curves 1, 2) [34]. Respectively, the strong deformational change has been observed in the melting process of pectin's crystalline phase in IPEC [35].

The formation of IMC leads to the appearance of a temperature transition at  $T = 205$  °C on the thermomechanical curve, which seems to be due to melting

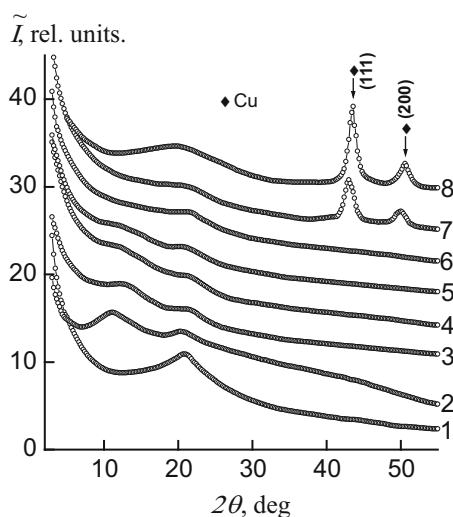
of  $\text{CuSO}_4$  in the IMC bulk that results in the transition of the polymer to the viscous-flow state (see Fig. 49.6b, curve 2). Therefore, location of the IMC's thermomechanical curve indicates that in the temperature area ranged from 170 to 205 °C (curve 2) the following successive processes occur in IMC sample: interpolyelectrolyte–metal complexes are destroyed, then the salt ( $\text{CuSO}_4$ ) transfers from its ionic form to the crystalline one, and then melts.

Analysis of the thermomechanical curves of the IPEC, the IMC, and the IPEC–Cu/Cu<sub>2</sub>O nanocomposite (see Fig. 49.6b) shows that, during the transition from the IPEC to the IMC, glass-transition temperature  $T_g$  increases and, at the next transition from the IMC to the IPEC–Cu/Cu<sub>2</sub>O nanocomposite,  $T_g$  significantly decreases (Table 49.1). Simultaneously with the decrease in  $T_g$ , a decrease in transition temperature in the viscous-flow state,  $T_f$ , occurs in the following series:  $T_{f(\text{IPEC})} > T_{f(\text{IPEC-Cu/Cu}_2\text{O})} > T_{f(\text{IMC})}$ .

#### 49.4 Structure Peculiarities and Thermomechanical Properties of Nanocomposites, Prepared by the Thermal Reduction of Copper Ions in the Interpolyelectrolyte–Metal Complexes

In the profiles of IMC, after being influenced by temperature in the range from 120 to 160 °C for 30 min (Fig. 49.7, curves 3–6), one can see a substantial weakening of the diffraction peak's intensity, characterizing the existence of polyelectrolyte–metal complexes in the IMC with its insignificant shift to the area of large angles of X-ray scattering ( $2\theta$ ) from 11.2° to 13.0° and, correspondingly, decreasing from

**Fig. 49.7** Wide-angle X-ray diffractograms of (1) the IPEC, (2) the IMC, and (3–8) the IMC, obtained at temperatures (3) 120, (4) 140, (5) 150, (6) 160, (7) 170, and (8) 190 °C for 30 min



7.9 to 6.8 Å in the average value of the Bragg distance between the macromolecules chains, coordinated by  $\text{Cu}^{2+}$  ions. Besides, there is a shift of the amorphous halo from  $2\theta_m \sim 20.5^\circ$  to  $21.6^\circ$  in the area of large scattering angles, demonstrating the short-range ordering of the macromolecular chains' fragments of anionic and cationic polyelectrolytes being distributed in the IPEC's volume. This indicates the tendency in decreasing of the Bragg distance between the chains of macromolecules from 4.3 to 4.1 Å.

In the diffractogram IPEC–Cu nanocomposite, obtained at  $T = 170^\circ\text{C}$  for 30 min (curve 7), the intense diffraction maximum at  $2\theta_m \sim 11.2^\circ$ , which is typical of the abovementioned polyelectrolyte–metal complexes, is absent, unlike the two intense maxima at  $2\theta_m = 43.0^\circ$  and  $50.0^\circ$ , corresponding to the crystallographic plan of the face-centered cubic lattice of copper with (111) and (200) indexes, respectively, and confirming the presence of metal copper in the polymeric system.

In the IPEC–Cu nanocomposite diffractogram, formed at  $T = 190^\circ\text{C}$  for 30 min (curve 8), we can see another behavior – diffraction maximum becomes wider and it means short-range ordering of macromolecular chains' fragments of anionic and cationic polyelectrolytes within IPEC, and it's shifting to the area of lower scattering angles (from  $2\theta_m \sim 21.6^\circ$  to  $19.8^\circ$ ). Respectively, enhancing of the average Bragg distance between the macromolecules', chains from 4.1 to 4.5 Å (curves 7 and 8) are fixed. This is evidence of the destruction of IPEC–metal systems. Also, diffraction maximums inherent to the metallic copper are being shifted by  $0.6^\circ$  to the area of larger angles, suggesting probable aggregation of copper nanoparticles.

Thus, according to the WAXS data, it may be concluded that  $T = 170^\circ\text{C}$  is optimum one for the  $\text{Cu}^{2+}$  ion reduction in the IMC and for further IPEC–Cu nanocomposite formation as well.

The mechanism of thermal reduction consists of electrons transfer from the nitrogen atoms of amino group of polyethyleneimine to  $\text{Cu}^{2+}$  ions during the process of IPEC–metal complexes destruction at  $T = 170^\circ\text{C}$  and higher temperature values.

The evaluation of an effective crystallite size of Cu nanoparticles in the IPEC demonstrated that  $L \sim 4.5$  nm. (For the calculation, the diffraction peaks at  $2\theta_m = 43.0^\circ$  and  $50.0^\circ$  (curve 7) were used).

The conversion of interpolyelectrolyte–metal complexes pectin– $\text{Cu}^{2+}$ –polyethyleneimine into nanocomposites containing Cu nanoparticles is confirmed by transmission electron microscopy (see Fig. 49.8).

The analysis of small-angle X-ray scattering profiles of the various polymer–metal systems, obtained by the thermal reduction of  $\text{Cu}^{2+}$  ions in the interpolyelectrolyte–metal complexes at temperatures 130, 160, and  $170^\circ\text{C}$ , shows that all mentioned systems have heterogeneous structuring – i.e., contrast electron densities  $\Delta\rho$  ( $\Delta\rho = \rho - \langle\rho\rangle$ , where  $\rho$  and  $\langle\rho\rangle$  are the local and average values of the electron density, respectively) are present in their volumes (Fig. 49.9a).



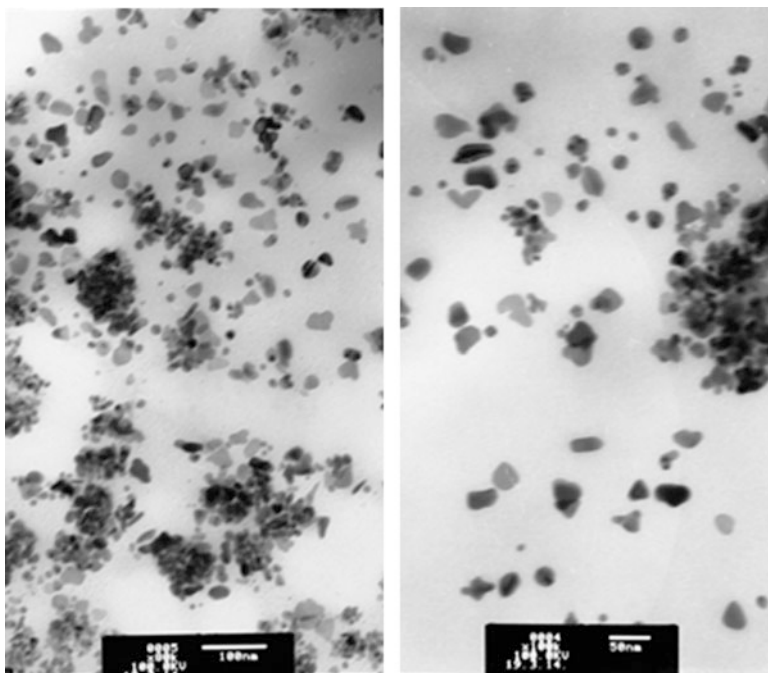


**Fig. 49.8** TEM images of the IPEC-Cu nanocomposite obtained during thermoreduction of  $\text{Cu}^{2+}$  ions in the IMC at the  $T = 170^\circ\text{C}$  for 30 min

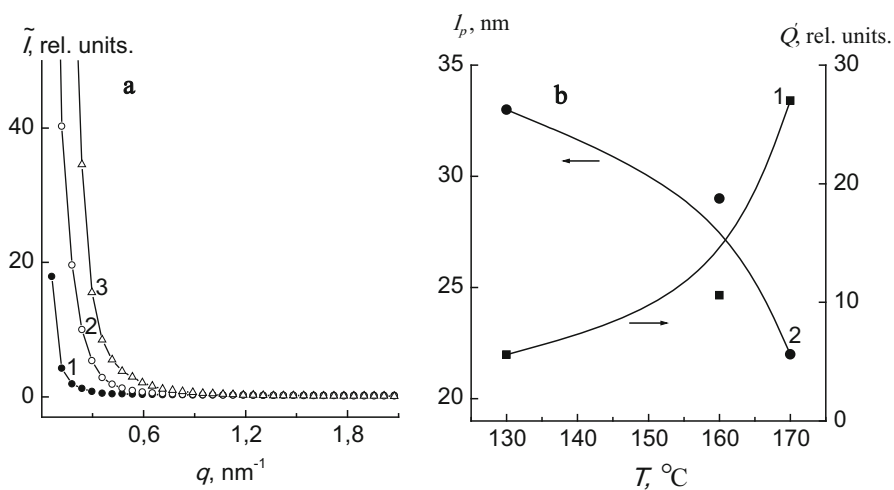


**Fig. 49.9** (a) Small-angle X-ray intensity profiles of the IMC, obtained at the temperature: (1)  $130^\circ\text{C}$ , (2)  $160^\circ\text{C}$ , and (3)  $170^\circ\text{C}$  for 30 min; (b) graphical dependence of  $Q'$  Porod invariant (1) and range of heterogeneity on the temperature of the  $\text{Cu}^{2+}$  ion reduction in the IMC

**Table 49.2** Structural parameters of the studied polymeric systems

Polymer system	Reduction temperature °C	Reduction time, xB	$l_p$ , nm	$Q'$ , rel. Units
IMC	130	30	33	5.6
IMC	160	30	29	10.6
IPEC–Cu	170	30	22	27

This result means that, in all the polymer–metal systems, there are no less than two types of region heterogeneity with different values of local electron density  $\rho$ . Nanocomposites based on IPEC–Cu, obtained at the  $T = 170$  °C (curves 3), have higher intensities of scattering and, hence, values of  $\Delta\rho$ , comparing to the polymeric systems obtained at lower temperatures (curves 1 and 2). However, the absence of the interference peak from all the profiles of intensity indicates the stochastic nature of the location of various types of heterogeneity regions in space.

Comparing values of invariant  $Q'$  for the polymer systems investigated (Fig. 49.9b, curve 1 and Table 49.2), one can observe that relative level of structure's heterogeneity dramatically grows up while transferring from IMC to IPEC–Cu nanocomposite.

As the result of  $l_p$  parameter's calculation, we have revealed that increasing of temperature reduction for  $\text{Cu}^{2+}$  ions in IMC and simultaneous formation of IPEC–Cu nanocomposite are accompanied by diminishing of heterogeneity areas' effective size (Fig. 49.9b, curve 2 and Table 49.2).

The analysis of the thermomechanical curves of the IPEC, the IMC, and IPEC–Cu nanocomposite (see Fig. 49.10a) shows that, during the transition from the IPEC to the IMC, glass-transition temperature  $T_g$  increases, and while IMC is converting into the IPEC–Cu nanocomposite,  $T_g$  significantly decreases (Table 49.3). Simultaneously, while  $T_g$  is changed, the decrease of transition temperature to the viscous-flow state ( $T_f$ ) occurs in the following row:  $T_{f(\text{IPEC})} > T_{f(\text{IMC})} > T_{f(\text{IPEC–Cu})}$ .

In the thermomechanical curve of the IPEC–Cu nanocomposite, one can see that at temperature range from 155 to 255 °C, the processes proceed in such route: IPEC destruction, melting of pectin's crystalline phase, and polymer transfer to the viscous-flow state (see Fig. 49.10a, curve 3).

In its turn, the thermal reduction of  $\text{Cu}^{2+}$  ions in the IMC bulk at 130, 150, and 160 °C, correspondingly, within 30 min results in successive decreasing of peak intensity at 210–215 °C area, which could be attributed to the salt transferring from ionic form to the crystalline one ( $\text{CuSO}_4$ ) (see Fig. 49.10b, curve 1–3). At the same time, IPEC quantity is falling down in the polymeric system. Polymer's thermal curve fixed at 170 °C is typical for the nanocomposite IPEC (pectin–PEI)–Cu [36]. These data completely correlate with X-ray diffraction analysis data (see Fig. 49.7 and Fig. 49.10b).

Additionally, thermomechanical characteristics of polymeric systems, elaborated at various time-consuming (5, 20, and 30 min correspondingly) thermoreduction

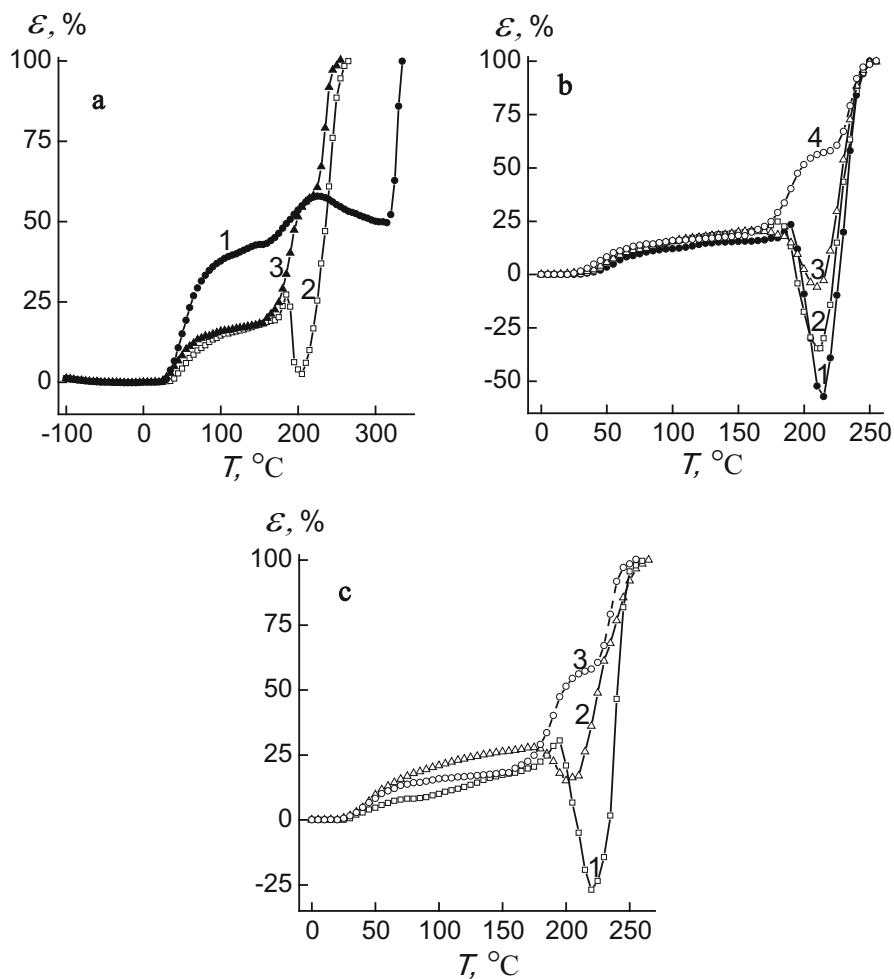


**Fig. 49.10** Thermomechanical curves: (a) (1) the IPEC, (2) the IMC, and (3) the IPEC-Cu nanocomposite, obtained via the thermoreduction of  $\text{Cu}^{2+}$  ions in the IMC at a  $T = 170^\circ\text{C}$  for 30 min; (b) the IMC, obtained at the temperatures (1) 130, (2) 150 (3) 160, and (4) 170 °C for 30 min; (c) the IMC, obtained at the temperature 170 °C for (1) 5, (2) 20, and (3) 30 min

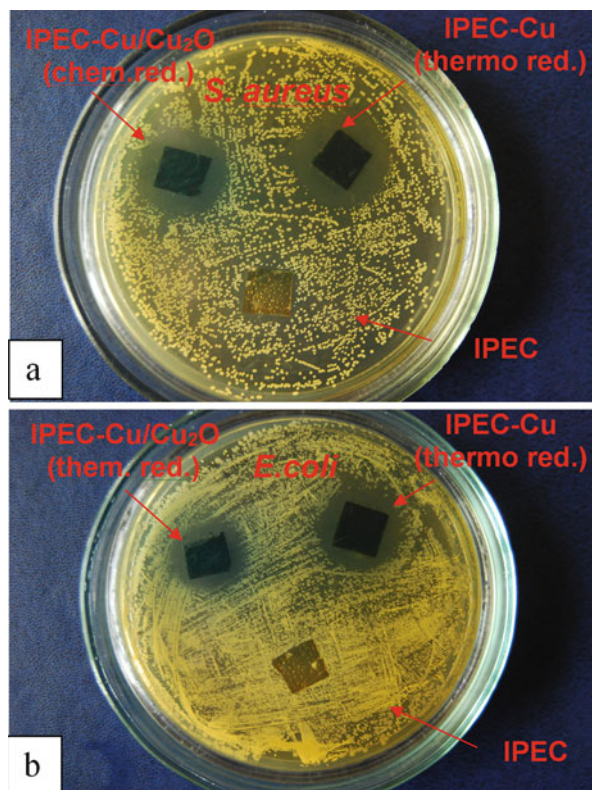
conditions for  $\text{Cu}^{2+}$  in IMC, were also studied. Figure 49.10c shows that the optimal time for complete reduction of  $\text{Cu}^{2+}$  ions to the metallic copper in polymeric systems is 30 min.

The transition temperatures of the polymer systems, prepared under various  $\text{Cu}^{2+}$  reduction conditions in IMC, are presented in Table 49.3.

**Table 49.3** Transition temperatures for the different polymer systems

Polymer system	Reduction temperature °C	Reduction time, min.	$T_g$ , °C	$T_f$ , °C
IPEC	–	–	53	319
IMC	–	–	57	205
IMC	130	30	53	215
IMC	150	30	50	211
IMC	160	30	49	210
IPEC–Cu	170	30	47	226
IPEC–Cu	170	20	47	205
IPEC–Cu	170	5	45	220

**Fig. 49.11** Images of antimicrobial test results of agar plates containing IPEC–Cu or Cu/Cu<sub>2</sub>O nanocomposites, obtained via the thermo- and chemical reduction of Cu<sup>2+</sup> ions in the IMC against *S. aureus* (a) and *E. coli* (b)



#### 49.5 Antimicrobial Properties of Nanocomposites, Elaborated Involving Chemical and Thermal Reduction of Copper Ions in the Interpolyelectrolyte–Metal Complexes

IPEC–Cu nanocomposites created by thermal reduction of Cu<sup>2+</sup> ions in IMC at  $T = 170$  °C within 30 min (Fig. 49.11) are found out to demonstrate highest antimicrobial activity against *S. aureus* and *E. coli* strains compared to IPEC–Cu/Cu<sub>2</sub>O,

**Table 49.4** Antimicrobial activity of the IPEC–Cu (Cu/Cu<sub>2</sub>O) nanocomposites, prepared via the thermo- and chemical reduction of Cu<sup>2+</sup> ions in the IMC

The method of obtaining nanocomposite films	Diameter of inhibition zone, mm	
	<i>Staphylococcus aureus</i>	<i>Escherichia coli</i>
Thermo reduction	IPEC–Cu	IPEC–Cu
	23.4 ± 1.1	22.5 ± 0.9
Chemical reduction	IPEC–Cu/Cu <sub>2</sub> O	IPEC–Cu/Cu <sub>2</sub> O
	22.4 ± 0.9	18.1 ± 0.6
Control sample	IPEC	IPEC
	0	0

synthesized by chemical reduction (the chemical reduction of Cu<sup>2+</sup> ions in the IMC was conducted with NaBH<sub>4</sub> (a molar ratio of [BH<sub>4</sub><sup>-</sup>]: [Cu<sup>2+</sup>] = 2.0).

After incubation proceeds for 24 h at 37 °C, one can observe a clear zone around the films' contours, thus confirming inhibition of bacteria growth. The growth inhibition's zone diameter for *S. aureus* was 23 mm for specimens prepared by thermal reduction and 22 mm for those obtained by chemical reduction. For *E. coli* these values are 22 mm and 18 mm, correspondingly (Table 49.4).

Active growth of the test bacteria and absence of growth inhibition have been observed in the test specimens (polymer film without nanoparticles).

## References

1. Gates BC, Guezi L, Knosinger H (1986) Metal clusters in catalysis. Elsevier, Amsterdam
2. Pomogailo AD, Rozenberg AS, Uflyand IE (2000) Metal nanoparticles in polymers. Khimiya, Moscow. [in Russian]
3. Nicolais L (2005) Metal\_polymer nanocomposites. Wiley, New York
4. Zezin AA (2016) Synthesis of hybrid materials in polyelectrolyte matrixes: control over sizes and spatial organization of metallic nanostructures. Pol Sci C 58:118–130
5. Kaur R, Giordano C, Gradzielski M, Mehta SK (2014) Synthesis of highly stable, water-dispersible copper nanoparticles as catalysts for nitrobenzene reduction. Chem Asian J 9:189–198
6. Pucek R, Kvitik L, Panacek A, Vancurova L, Soukupova J, Jancik D, Zboril R (2009) Polyacrylate-assisted synthesis of stable copper nanoparticles and copper(I) oxide nanocubes with high catalytic efficiency. J Mater Chem 19:8463–8469
7. Wang Y, Asefa T (2010) Poly(allylamine)-stabilized colloidal copper nanoparticles: synthesis, morphology, and their surface-enhanced Raman scattering properties. Langmuir 26:7469–7474
8. Bakar A, De VV, Zezin AA, Abramchuk SS, Güven O, Feldman VI (2012) Spatial organization of a metal–polymer nanocomposite obtained by the radiation-induced reduction of copper ions in the poly(allylamine)–poly(acrylic acid)–Cu<sup>2+</sup> system. Mendeleev Commun 22:211–212
9. Ruiz P, Macanas J, Munoz M, Muraviev DN (2011) Intermatrix synthesis: easy technique permitting preparation of polymer-stabilized nanoparticles with desired composition and structure. Nanoscale Res Lett 6:343–348

10. Zezin AA, Feldman VI, Dudnikov AV, Zezin SB, Abramchuk SS, Belopushkin SI (2009) Reduction of copper(II) ions in polyacrylic acid–polyethyleneimine complexes using x-ray radiation. *High Energy Chem* 43:100–104
11. Pergushov DV, Zezin AA, Zezin AB, Müller AHE (2014) Advanced functional structures based on interpolyelectrolyte complexes. *Adv Polym Sci* 255:173–226
12. Liu X, Geng B, Du Q, Ma J, Liu X (2007) Temperature-controlled self-assembled synthesis of CuO, CuO<sub>2</sub>, and Cu nanoparticles through a single-precursor route. *Mater Sci Eng A* 448:7–14
13. Kim YH, Lee DK, Jo BG, Jeong JH, Kang YS (2006) Synthesis of oleate capped Cu nanoparticles by thermal decomposition. *Colloids Surf A* 284–285:364–368
14. Nasibulin AG, Ahonen PP, Richard O, Kauppinen EI, Altman IS (2001) Copper and copper oxide nanoparticle formation by chemical vapor nucleation from copper(II) acetylacetonate. *J Nanopart Res* 3:383–398
15. Daroczi L, Beck MT, Beke DL, Kis-Varga M, Harasztosi L, Takacs N (1998) Production of Fe and Cu nanocrystalline particles by thermal decomposition of ferro- and copper-cyanides. *Mater Sci Forum* 319:269–272
16. Chen S, Sommers JM (2001) Alkanethiolate-protected copper nanoparticles: spectroscopy, electrochemistry, and solid-state morphological evolution. *J Phys Chem B* 105:8816–8820
17. Zhu H, Zhang C, Yin Y (2005) Novel synthesis of copper nanoparticles: influence of the synthesis conditions on the particle size. *Nanotechnology* 16:3079–3083
18. Johi SS, Patil SF, Iyer V, Mahumuni S (1998) Radiation induced synthesis and characterization of copper nanoparticles. *Nanostruct Mater* 10:1135–1144
19. Pileni MP, Ninham BW, Gulik-Krzywicki T, Tanori J, Lisiecki I, Filankembo A (1999) Direct relationship between shape and size of template and synthesis of copper metal particles. *Adv Mater* 11:1358–1362
20. Song RG, Yamaguchi M, Nishimura O, Suzuki M (2007) Investigation of metal nanoparticles produced by laser ablation and their catalytic activity. *Appl Surf Sci* 253:3093–3097
21. Park BK, Jeong SH, Kim DJ, Moon JH, Lim SK, Kim JS (2007) Synthesis and size control of monodisperse copper nanoparticles by polyol method. *J Colloid Interface Sci* 311:417–424
22. Xin-ling T, Ling R, Ling-na S, Wei-guo I, Min-hua C, Chang-wen H (2006) A solvothermal route to Cu<sub>2</sub>O nanocubes and Cu nanoparticles. *Chem Res Chin Univ* 22:547–551
23. Dash NA, Raj CP, Gedanken A (1998) Synthesis, characterization, and properties of metallic copper nanoparticles. *Chem Mater* 10:1446–1452
24. Banasiuk R, Frackowiak JE, Krychowiak M, Matuszewska M, Kawiak A, Ziabka M, Lendzion-Bielun Z, Narajczyk M, Krolick A (2016) Synthesis of antimicrobial silver nanoparticles through a photomediated reaction in an aqueous environment. *Int J Nanomedicine* 11:315–324
25. Garciduenas-Pina C, Medina-Ramirez IE, Guzman P, Rico-Martinez R, Morales-Dominguez JF, Rubio-Franchini I (2016) Evaluation of the antimicrobial activity of nanostructured materials of titanium dioxide doped with silver and/or copper and their effects on *Arabidopsis thaliana*. *Int J Photoenergy* 1:1–14
26. Kobylinskyi SM, Riabov SV, Kercha YY (2005) Chitosan modification by polyethyleneimines. *Vopr Khim Khim Tekhnol* 5:28–33. [in Ukrainian]
27. Kratky O, Pilz I, Schmitz PJ (1966) Absolute intensity measurement of small-angle x-ray scattering by means of a standard sample. *J Colloid Interface Sci* 21:24–34
28. Case CL, Johnson TR (1984) Laboratory experiments in microbiology. Benjamin Cummings Pub Inc., California
29. Shtompel' VI, Kercha YY (2008) Structure of linear polyurethanes. *Naukova dumka, Kiev*. [in Russian]
30. Gin'e A (1961) X-ray diffraction of crystals. Theory and practice. Fizmatgiz, Moscow. [in Russian]
31. Ruland W (1971) Small-angle scattering of two-phase systems: determination and significance of systematic deviations from Porod's law. *J Appl Crystallogr* 4:70–73
32. Perret R, Ruland W (1971) Eine verbesserte Auswertungsmethode für die Röntgenkleinwinkelstreuung von Hochpolymeren. *Kolloid Z – Z Polymere* 247:835–843

33. Porod G (1982) In: Glatter O, Kratky O (eds) Small-angle X-ray scattering. Acad. Press, London
34. Demchenko V, Shtompel' V, Riabov S (2016) Nanocomposites based on interpolyelectrolyte complex and Cu/Cu<sub>2</sub>O core-shell nanoparticles: structure, thermomechanical and electric properties. *Eur Polym J* 75:310–316
35. Teitelbaum BJ (1979) Thermomechanical analysis of polymers. Nauka, Moscow. [in Russian]
36. Demchenko VL, Shtompel' VI, Riabov SV (2015) DC field effect on the structuring and thermomechanical and electric properties of nanocomposites formed from pectin-Cu<sup>2+</sup>-polyethyleneimine ternary polyelectrolyte-metal complexes. *Pol Sci A* 57:635–643

# Chapter 50

## Nanocomposites on the Base of Synthetic Opals and Nanocrystalline Phases of Bi-containing Active Dielectrics

V. Moiseienko, M. Derhachov, B. Abu Sal, R. Holze, and M. Brynza

### 50.1 Introduction

The obtaining and investigating of novel nanocomposites on the base of synthetic opals are of fundamental interest for both nanophotonics and physics of the low-dimensional systems. Synthetic opals composed of close-packed monodisperse silica globules have a regular 3D arrangement of tetrahedral and octahedral pores connected by channels. The typical values of globule diameter and linear size of pores are hundreds and tens of nanometres, respectively. The pores can be filled with various compounds (metals, semiconductors, salts and organic materials) by employing different techniques [1, 2]. Being filled with active dielectric nanocrystals, they are expected to be very promising for applications in light beam-operating systems and nonlinear optical devices [3–7].

On the other hand, crystallisation of active dielectrics inside opal pores occurs under specific conditions. These are restricted volume, lack of atmosphere in the

---

V. Moiseienko (✉) • M. Derhachov • M. Brynza  
Oles Honchar Dnipro National University, Ave. Gagarina 72, 49010 Dnipro, Ukraine  
e-mail: [vnmois@yandex.ru](mailto:vnmois@yandex.ru); [derhachov.mp@gmail.com](mailto:derhachov.mp@gmail.com); [kolanchic@gmail.com](mailto:kolanchic@gmail.com)

B. Abu Sal  
Applied Physics Department, Tafila Technical University, P.O. Box 40, Al-Eis 66141, Tafila,  
Jordan  
e-mail: [abusal@ttu.edu.jo](mailto:abusal@ttu.edu.jo)

R. Holze  
Technische Universität Chemnitz, Institute of Chemistry, AG Elektrochemie,  
Strasse der Nationen 62, D-09111 Chemnitz, Germany  
e-mail: [rudolf.holze@chemie.tu-chemnitz.de](mailto:rudolf.holze@chemie.tu-chemnitz.de)



interior pores, enhanced internal tension and so on. Moreover, each silica globule, owing to its own substructure [8, 9], can be considered as a great number of crystallisation centres that give rise to the growth of ordered nanoclusters and nanocrystals with sizes from a few to tens of nanometres. All of these factors may result in changing interatomic distances and crystal lattice period of the embedded compound as compared to the bulk crystal parameters. In case of polymorphism, the other crystalline phases, non-obtained under usual conditions, may be formed inside opal pores, similar to the metastable  $\gamma$ -TeO<sub>2</sub> phase in paper [10].

This paper shows the possibility of growth of bismuth-containing active dielectric nanocrystals Bi<sub>12</sub>SiO<sub>20</sub>, Bi<sub>2</sub>TeO<sub>5</sub> and NaBi(MO<sub>4</sub>)<sub>2</sub> from the melts into opal pores and also discusses the features of structure and phase composition of the nanocomposites. The choice of these materials is due to their prominent photorefractive, acoustooptic and nonlinear optical properties [11–15]. It allows us to expect a wide application of the nanocomposites in the optical storage systems.

## 50.2 Properties of Initial Active Dielectric Crystals

Bi<sub>12</sub>SiO<sub>20</sub> (BSO) belongs to the sillenite-type cubic structure (space group *I23*) with the framework composed of BiO<sub>5</sub> polyhedra [16]. BSO crystals are grown by Czochralski technique from the Bi<sub>2</sub>O<sub>3</sub>–SiO<sub>2</sub> system melt at molar ratio of 6:1. In contrary to BTO, phase diagram of the Bi<sub>2</sub>O<sub>3</sub>–SiO<sub>2</sub> system is more complicated, and some metastable states are possible [17]. The second stable phase is a bismuth orthosilicate Bi<sub>4</sub>(SiO<sub>4</sub>)<sub>3</sub> realised at the 2:3 molar ratio.

Bi<sub>2</sub>TeO<sub>5</sub> (BTO) has a rhombic structure with non-centrosymmetric space group *Abm2* at room temperature. According to the *p*–*T*–*x* diagram [18], BTO melts congruently at 885 °C and undergoes diffuse structural phase transition from centrosymmetric phase to polar one in the 820 °C–780 °C range. BTO single crystal is typically grown by using Czochralski or Bridgman technique from the (Bi<sub>2</sub>O<sub>3</sub>)<sub>*x*</sub>–(TeO<sub>2</sub>)<sub>1–*x*</sub> melt with a molar ratio of 47:53 in the charge [19]. Refractive indexes in visible region are  $n_\alpha = 2.350$ ,  $n_\beta = 2.360$  and  $n_\gamma = 2.460$  [13]. The total number of Raman bands predicted by the group-theoretic analysis is  $24A_1 + 22A_2 + 25B_1 + 22B_2$ .

NaBi(MoO<sub>4</sub>)<sub>2</sub> (NBMO) belongs to the tetragonal system (space group *I4<sub>1</sub>/a*) at room temperature and undergoes a ferroelastic phase transition to monoclinic *I2/a* symmetry at 241 K [20]. NBMO crystals are grown from the melt using Czochralski technique. According to the group-theoretic analysis, there are 36 fundamental vibrations described by the representation  $6A + 10B + 10E$  and investigated in the papers [21, 22].

## 50.3 Fabrication and Characterisation of Nanocomposites

### 50.3.1 Structural Parameters of Bare Synthetic Opals

Bulk bare opals were grown by slow crystallisation of a colloidal suspension of monodisperse silica globules synthesised by using Stöber technique [23]. After drying in the air, the precipitates obtained were sequentially annealed at 125 °C and 850 °C for several hours. The arrangement of globules in real synthetic opals was found to be close to the face-centred cubic lattice formed by hexagonal close-packed (111) layers, perpendicular to the [111] growth axis of the sample [24]. Characterisation of bare opals was performed by using X-Ray microanalyzer JEOL JXA 8200 (Fig. 50.1) and by measuring the Bragg light reflection spectra in accordance with the procedure described in the paper [25]. The mean globule diameter  $D$  in the as-prepared opals was 300 nm with a variation no more than 3% in each sample. The maximum linear pore size was estimated as 120 nm. The opals to be infiltrated were as plates of about 5 mm  $\times$  8 mm in size and up to 2 mm thick.

### 50.3.2 Embedding of Active Dielectrics in Opal Pores and Experimental Technique

The melt-based technique was chosen among different methods of the opal pore filling. It meant an infiltration with wetting melt of the embedded compound by the action of capillary forces. At the previous stage, polycrystalline powders of BSO, BTO and NBMO were prepared and put on the opal growth surface. Then, the as-prepared samples were placed into the air-resistant furnace and heated up to the temperature slightly higher than the temperature of the congruent melting of corresponding embedded compound (900 °C for BSO, 885 °C for BTO and 867 °C

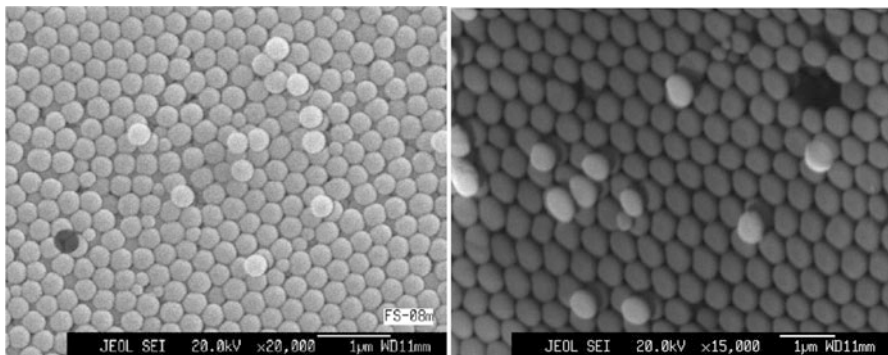


Fig. 50.1 Images of the bare opal surface in the [111] growth direction

for NBMO). The samples were held at the temperature for 15 min and then were cooled down at room temperature. The heating and cooling rates were the same and no more than 3 °C per minute.

Characterisation of the composite surface was made by employing a scanning electron microscope Nova NanoSEM. The Bragg light reflection spectra were measured by using a modified laser spectrometer based on a DFS12 double monochromator with a photon-counting system. Infrared transmission spectra were obtained with using a Fourier transform infrared (FTIR) spectrometer Bruker IFS 66.

Raman spectra were measured by employing the DFS12-based spectrometer with a 532-nm laser and two confocal Raman microscopes (LabRam HR800 with a 50 × LWD lens and UV-Visible-NIR Olympus BX41 with a triple spectrometer Horiba Jobin-Yvon T64000) both equipped with a 514.5-nm Ar–Kr laser and a liquid nitrogen-cooled CCD detector. The scattered radiation was collected along the [111] growth axis of opals in the backward geometry. The laser spot diameter on the sample surface was varied from 1 mm to 500 nm; its value was determined by the scanning edge method. All of the Raman spectra were unpolarised and measured at room temperature.

### 50.3.3 Characterisation of Nanocomposites

The visual changes in appearance of infiltrated opals were a complete vanishing of iridescence by visible light illumination and a colour tint, typical for the single crystal used for infiltration. The melt penetration into opal pores was also tested by scanning electron microscopy (SEM), Bragg light reflection and FTIR spectroscopy measurements. The SEM images of untreated surface of composites demonstrated the melt acceptance (Fig. 50.2). Thin layer formed on the surface after cooling was subjected to further grinding in order to eliminate its contribution to the reflection and Raman spectra.

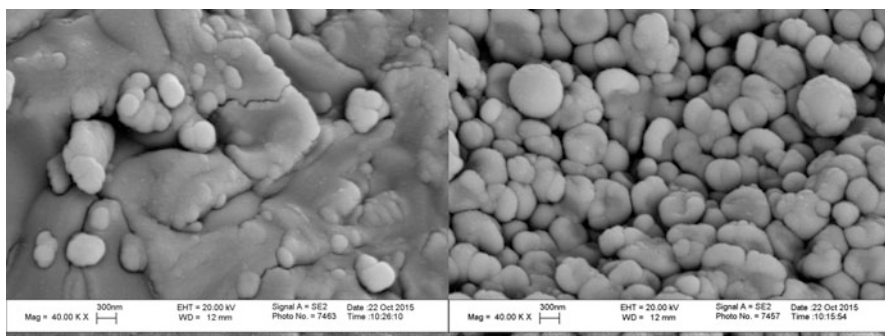
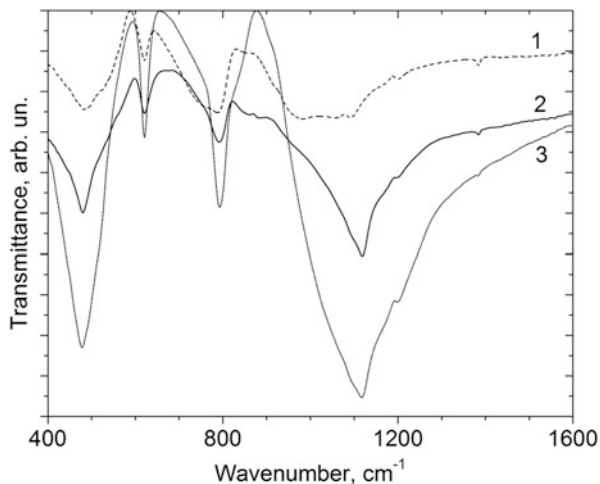


Fig. 50.2 SEM images of the untreated ‘opal–BTO’ (left) and ‘opal–NBMO’ (right) surface

**Fig. 50.3** FTIR spectra of the ‘opal–BTO’ (1), ‘opal–BSO’ (2) and ‘opal–NBMO’ (3) composites



An increase of effective refraction index of composites caused by the pore filling was revealed as an infrared shift of the Bragg diffraction maximum and detected in accordance with the measurement procedure described in the paper [26]. It allowed us to estimate the compound volume fraction inside opal. The mean value of part of the volume of the filled pores was no lower than 50% in each composite. The photonic stop-band spectral position along the [111] direction, associated with the Bragg diffraction maximum interval, was over a 650 nm–750 nm range in all composites. As it was far from the Raman spectrum region (515 nm–575 nm), the photonic stop-band effects have been excluded from further consideration.

FTIR spectra over a 400  $\text{cm}^{-1}$ –1600  $\text{cm}^{-1}$  range contained the bands caused by the opal matrix absorption (Fig. 50.3). The bands at 484  $\text{cm}^{-1}$ , 756  $\text{cm}^{-1}$  and 789  $\text{cm}^{-1}$  are typical to silicates with  $[\text{SiO}_4]$  tetrahedrons. The band at 620  $\text{cm}^{-1}$  was assigned to the cristobalite or to the other crystalline silica phases [27, 28]. The bands over a 900  $\text{cm}^{-1}$ –1100  $\text{cm}^{-1}$  range could be related to vibrations in chains of the finite number of  $[\text{SiO}_4]$  tetrahedrons combined with the common oxygen atom.

## 50.4 Raman Spectra of Nanocomposites

### 50.4.1 *Opal–Bi<sub>12</sub>SiO<sub>20</sub>*

The Raman spectra of ‘opal–BSO’ composite obtained by micro-Raman surface scanning are shown in Fig. 50.4 with the reference data on Raman spectra of  $\text{Bi}_{12}\text{SiO}_{20}$  and  $\text{Bi}_4\text{Si}_3\text{O}_{12}$  single crystals [29, 30].

The Raman spectra of infiltrated opals prove a crystalline state of the embedded substance, demonstrate spectral redistribution by scanning from point to point and

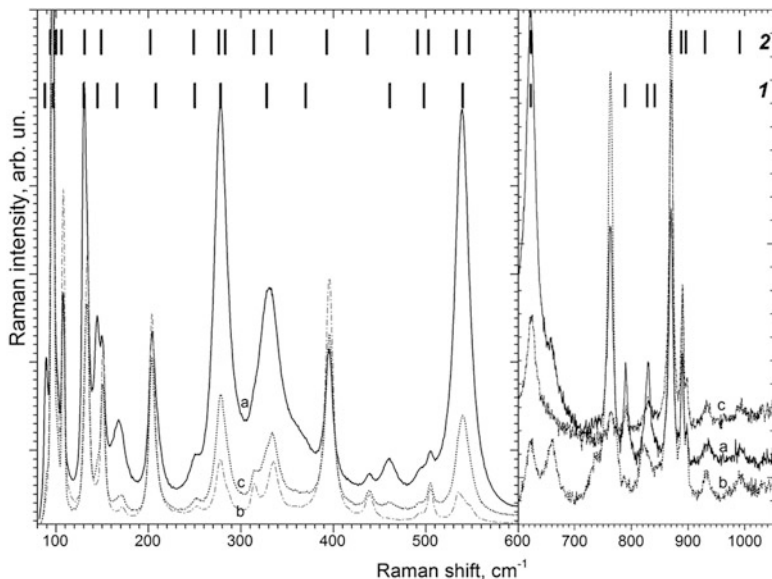


**Fig. 50.4** The Raman spectra of the ‘opal-BSO’ composite measured at different points on the treated surface (a–c). All the 600 cm<sup>-1</sup>–1050 cm<sup>-1</sup> spectra are multiplied by 10. The bars are the reference data on Raman spectra of BSO (1) [29] and Bi<sub>4</sub>Si<sub>3</sub>O<sub>12</sub> (2) [30] single crystals

have new bands compared to the BSO crystal spectrum. More detailed description of the changes in the Raman spectrum of the nanocomposite has been performed earlier [26].

A comparison with the reference data presented in Fig. 50.4 gives an evidence of several crystalline phases in opal pores, in particular bismuth silicate Bi<sub>12</sub>SiO<sub>20</sub> and bismuth orthosilicate Bi<sub>4</sub>Si<sub>3</sub>O<sub>12</sub>.

As mentioned above, bismuth orthosilicate can be grown from the melt of the Bi<sub>2</sub>O<sub>3</sub>–SiO<sub>2</sub> system at molar 2:3 ratio. At the beginning of the infiltration, a molar ratio is 6:1 because of the BSO melting. In order to satisfy the change in molar ratio, the melting of globules should be assumed. There seem to be no any way in changing molar ratio under infiltration conditions described above. Although the temperature in our infiltration cycle was lower than that of silica melting, the melting temperature of subglobules with sizes no more than 10 nm can be reached, in this case, according to the size effect of the melting temperature for nanoscaled particles [31]. Really, the estimated thickness of the globule surface layer needed to be melted in order to provide the proper 2:3 molar ratio is no more than 20 nm. It is in a good agreement with sizes of 10-nm small subglobules in silica globule structure [8]. In case of the existence of Si–O bonds in the embedding compound structure, the melt–globule interface could be served as an effective seed for formation of new structure along the whole pore volume.

Besides, there are new bands over a  $650\text{ cm}^{-1}$ – $770\text{ cm}^{-1}$  region in the ‘opal–BSO’ spectra that cannot be related to vibrations in the bismuth silicate or bismuth orthosilicate structure (Fig. 50.4). Their appearance may be explained by assuming the formation of any crystalline silica phase; however, this assumption is needed to be proved by further investigations.

### 50.4.2 *Opal–Bi<sub>2</sub>TeO<sub>5</sub>*

The total number of bands observed in Raman spectrum of BTO single crystal is lower than that predicted by the group-theoretic analysis. The bands below  $150\text{ cm}^{-1}$  are mainly due to the translations of the metal atoms and to the bending vibrations of the Bi–O–Bi, Bi–O–Te and Te–O–Te bonds. The bands above  $150\text{ cm}^{-1}$  are most probably caused by the internal vibrations of the coordination  $\text{BiO}_y$  and  $\text{TeO}_y$  polyhedrons involved in the BTO crystal structure [32, 33].

Similar to the ‘opal–BTO’ composite spectra, the Raman spectra of infiltrated opals obtained by micro-Raman surface scanning are evidence of a crystalline state of the embedded substance (Fig. 50.5). The spectra excited by laser radiation with a different spot diameter on the sample surface are not principally different. All the composite spectra are, in general, similar to the BTO spectrum, except for some features. They are as follows: (i) a spectral intensity redistribution over the  $100\text{ cm}^{-1}$ – $550\text{ cm}^{-1}$  range, while the rest of the spectrum remains unchangeable, as well as an overall increase of Raman scattering intensity in contrast to the BTO spectrum and (ii) an appearance of new bands over the  $370\text{ cm}^{-1}$ – $540\text{ cm}^{-1}$  and  $820\text{ cm}^{-1}$ – $1100\text{ cm}^{-1}$  regions and also positioned at  $207\text{ cm}^{-1}$ ,  $705\text{ cm}^{-1}$  and  $1654\text{ cm}^{-1}$ . Taking into account a good agreement between composite and BTO single-crystal Raman spectra (Fig. 50.5), BTO nanocrystals are considered as a basic phase that is formed into opal pores.

Firstly, let us clarify an origin of new bands. They appear accidentally by composite surface scanning from point to point; however, their spectral position is quite stable. Their appearance may be caused by the nanocrystal surface vibrational modes as well as by the compound–globule interface vibrational modes. The first ones are getting able to be observed owing to an increasing role of surface in forming the nanocrystal vibrational spectrum. The second ones are due to producing new chemical bonds when the melt solidification starts. At the high temperatures required for the melted-based infiltration, the Si–O–Si bridge between  $[\text{SiO}_4]$  tetrahedrons (the basic units of silica globule) may be broken and new Si–O–Bi(Te) bridges may be produced. As a Bi(Te)–O bond length in the bridge should be quite different from that in the usual BTO structure, new Raman bands due to this bond vibration can become apparent. Their occurrence is most probable in the regions typical for the Bi–O and Te–O stretching vibrations, i.e.  $370\text{ cm}^{-1}$ – $540\text{ cm}^{-1}$  and  $600\text{ cm}^{-1}$ – $810\text{ cm}^{-1}$ , respectively (Table 50.1). By following this, the  $439\text{ cm}^{-1}$ ,  $462\text{ cm}^{-1}$  and  $534\text{ cm}^{-1}$  bands can be assigned to the Bi–O stretching vibrations

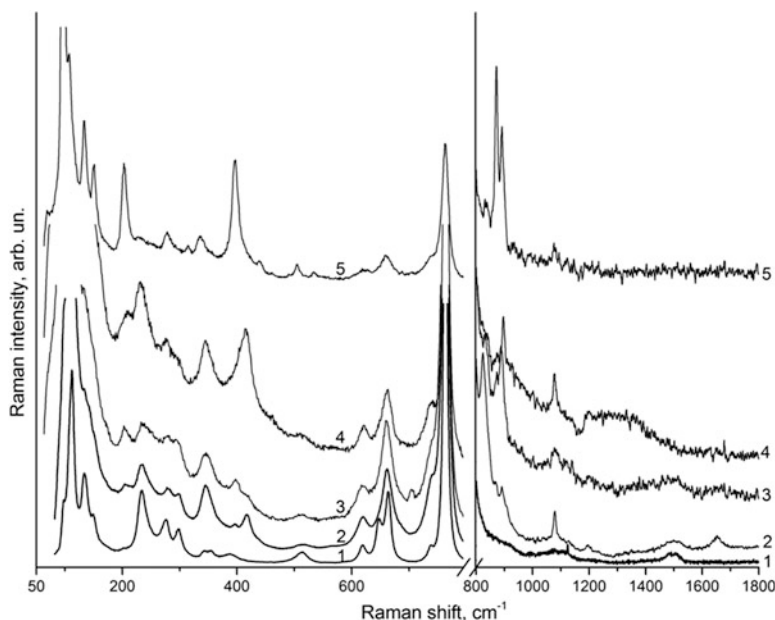


**Fig. 50.5** The Raman spectra of BTO single crystal (1) and of the ‘opal-BTO’ composite measured at different points on the treated surface (2–5). All the 800  $\text{cm}^{-1}$ –1800  $\text{cm}^{-1}$  spectra are multiplied by a factor of 12

and the 705  $\text{cm}^{-1}$  band to the Te–O stretching vibration of the  $\text{TeO}_3$  polyhedron [32]. Because of their weak relative intensity, the bands may be related to the antisymmetric vibrations involving two or more neighbouring chemical bonds. The corresponding Bi–O bond lengths calculated by using the empirical relation in the paper [33] are equal to 2.13 Å, 2.11 Å and 2.05 Å. New narrow bands over the 820  $\text{cm}^{-1}$ –1100  $\text{cm}^{-1}$  region might be also assigned to the Bi–O or Te–O stretching vibrations if there would be bonds with much shorter lengths. For example, the 828  $\text{cm}^{-1}$  band could be related to the Bi–O stretching vibration if the 1.88 Å bond would be produced. However, the values like that or lower are not typical even for diatomic BiO molecule [33]. As for the Te–O stretching vibrations, an existence of bonds with lengths shorter than 1.86 Å, as in the  $\gamma$ - $\text{TeO}_2$  single crystal (819  $\text{cm}^{-1}$ ), is required. This is possible but not provided with the known literature data [32, 34].

Another way to interpret the 828  $\text{cm}^{-1}$ , 838  $\text{cm}^{-1}$ , 870  $\text{cm}^{-1}$  and 892  $\text{cm}^{-1}$  bands is to relate them to antisymmetric Si–O stretching vibrations in  $[\text{SiO}_4]$  tetrahedrons distorted by forming new Si–O–Bi(Te) bridges. The bands at similar spectral positions are clearly observed in the BSO and  $\text{Bi}_4\text{Si}_3\text{O}_{12}$  spectra (Table 50.1).

Such assignment of the bands together with their sharpness allows us to assume the medium-range order in compound–globule interface [29]. On the other hand, the formation of any crystalline silica phase should not be excluded. The sharpened band at 1076  $\text{cm}^{-1}$  is very typical to the tridymite (Fig. 50.5, Table 50.1), and the



**Table 50.1** Frequencies ( $\text{cm}^{-1}$ ) of new Raman bands in the ‘opal–BTO’ spectrum, averaged by all measured points, and of bands in the referred material spectra

opal–BTO	$\alpha\text{-Bi}_2\text{O}_3$ [35]	$\alpha\text{-TeO}_2$ [34]	$\gamma\text{-TeO}_2$ [10]	BSO [36]	$\text{Bi}_4\text{Si}_3\text{O}_{12}$ [30]	Tridymite [28]
207	210	196	226	209	202	212
439	438		426		437	433
462	467			469	491	
534		593		546	533	
705		718	683	785		
828		806	819	827		
838				841		
870					868	
892					896	
1076					991	1078
1654						

other bands of tridymite coincide with positions of the new opal–BTO bands quite well [28]. In this case, one can assume the melting of subglobules in the bare opal structure with their following crystallisation. The  $1076\text{ cm}^{-1}$  band can be related to the stretching vibrations of Si–O–Si bridges [27]. This band appears against the weak diffuse band at approximately  $1095\text{ cm}^{-1}$  that can be related to the second-order Raman processes in the BTO single crystal, in particular to the combination of the  $345\text{ cm}^{-1}$  and  $763\text{ cm}^{-1}$  or  $741\text{ cm}^{-1}$  lattice vibrations. The next weak diffuse band at  $1495\text{ cm}^{-1}$  results from the combination of the  $763\text{ cm}^{-1}$  and  $741\text{ cm}^{-1}$  vibration. Finally, the  $1654\text{ cm}^{-1}$  band is an overtone of the  $828\text{ cm}^{-1}$  vibration.

### 50.4.3 Opal–NaBi(MoO<sub>4</sub>)<sub>2</sub>

Raman spectra of the ‘opal–NBMO’ composite have more broadened bands and do not demonstrate so drastic changes in Raman intensity redistribution and appearance of new bands as in the composite spectra described above. The changes detected in the ‘opal–NBMO’ composite spectra over a  $100\text{ cm}^{-1}$ – $1000\text{ cm}^{-1}$  range are a  $6\text{ cm}^{-1}$  shift of the  $409\text{ cm}^{-1}$  Raman band and appearance of a new band at  $232\text{ cm}^{-1}$  (Fig. 50.6). Besides, the second-order Raman spectrum related to the combination of modes from the  $680\text{ cm}^{-1}$  to  $1000\text{ cm}^{-1}$  range has been also measured (Fig. 50.7). As can be seen from Fig. 50.7, its spectral profile is slightly changed. This is correlated with no strong changes in the spectral profile over a  $680\text{ cm}^{-1}$ – $1000\text{ cm}^{-1}$  range composed of overlapping bands (Fig. 50.6).

In accordance with previous investigations of NBMO vibrational spectrum, the  $180\text{ cm}^{-1}$ – $250\text{ cm}^{-1}$  region is related to translations of Na ions [21, 22]. This is a reason to assign the  $232\text{ cm}^{-1}$  band to translations of Na ions. The shifted band at  $409\text{ cm}^{-1}$  is within the region related to asymmetric bending vibrations of  $[\text{MoO}_4]$



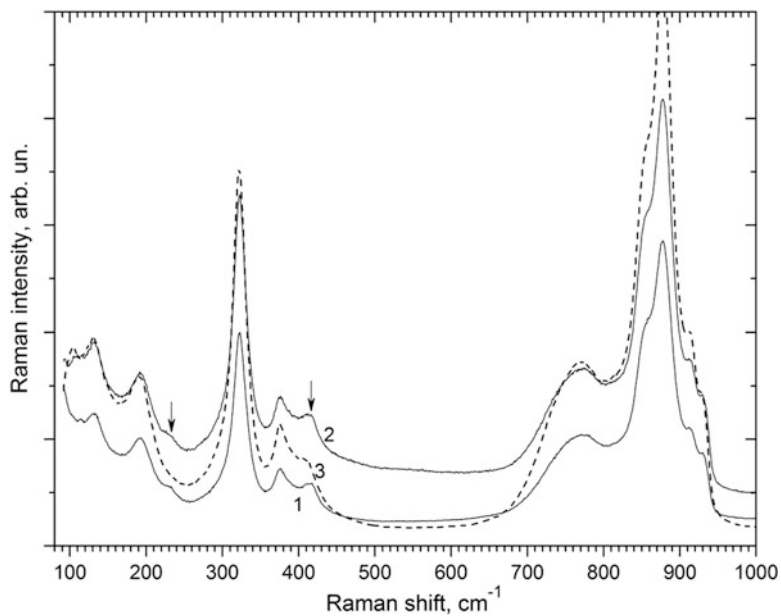


**Fig. 50.6** The Raman spectra of 'opal-NBMO' composite measured at different points on treated surface (1, 2) and of NBMO crystal (3). The arrows mark the changes in the composite spectra

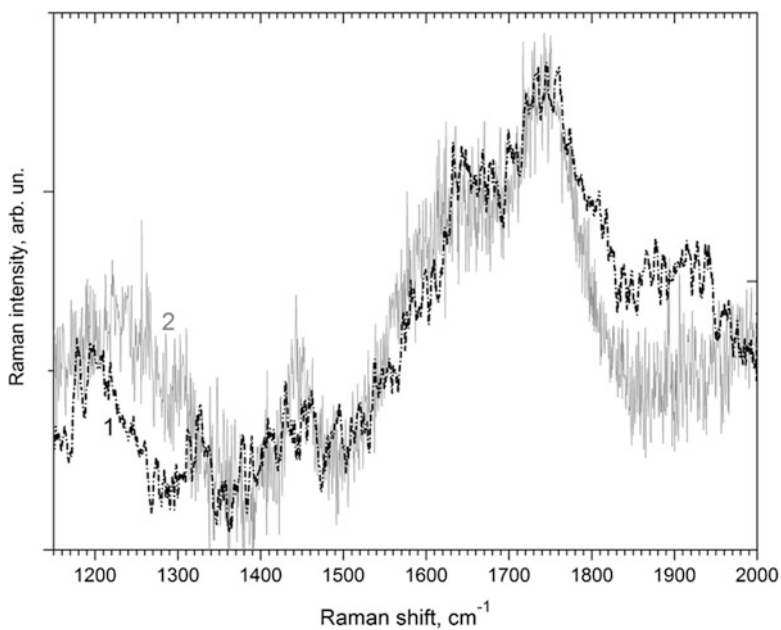


**Fig. 50.7** The second-order Raman spectra of 'opal-NBMO' composite (1) and NBMO crystal (2)

tetrahedrons with possible involving of Na ions. The  $680\text{ cm}^{-1}$ – $1000\text{ cm}^{-1}$  range is related to the stretching vibrations of  $[\text{MoO}_4]$  tetrahedrons, and the second-order Raman spectrum is caused by their interactions. Thus, the observable changes in the composite spectrum may be explained by restricting the Na ions motion parameters in nanocrystals. Deformation of  $[\text{MoO}_4]$  tetrahedrons is not excluded; however it seems to be very small.

#### ***50.4.4 Raman Spectra at Different Points of the Sample Surface***

The spectral redistribution of Raman intensity was clearly observed in the ‘opal–BTO’ and ‘opal–BSO’ Raman spectra and not so remarkable in the ‘opal–NBMO’ spectrum (Figs. 50.4, 50.5 and 50.6).

The Raman intensity variations and the overall enhancement in the composite spectrum can be explained in terms of the concentration and inhomogeneous distribution of the exciting radiation field inside the composite. The duration of the light–substance interaction inside opal can be prolonged through photon multiple scattering by the microscopic opal structure defects. It causes the enlargement of the exciting radiation density under continuous laser pumping and, hence, gives a reason to expect the enhancement of Raman scattering by the embedded substance. In addition, the light can be concentrated inside macroscopic surface and bulk structural defects filled by high-refractive substance due to the internal reflection. Finally, the structural light-focusing effect in opals is possible [4]. All of these effects can result in inhomogeneous distribution of the exciting radiation field over the opal surface and volume with a linear size of inhomogeneous domain of the order of hundreds of nanometres.

### **50.5 Conclusions**

The possibility of opal infiltration with the high-temperature melted  $\text{Bi}_{12}\text{SiO}_{20}$ ,  $\text{Bi}_2\text{TeO}_5$  and  $\text{NaBi}(\text{MO}_4)_2$  was examined, and the characterisation of the obtained composite was performed. The melt wetting and penetration into opal pores were proved by the SEM images, by the Bragg maximum spectral shift with increasing the effective refraction index as well as by Raman spectroscopy measurements. The estimated grade of pore filling was no more than 50%. The crystalline state of the substance embedded into opal pores was proved.

The basic phase formed in opal pores is the embedded substance in crystalline state, in general. However, the melting of silica subglobules, caused by the size effect of the melting temperature for nanoscaled particles [31], should be taken into account. Several ways of influence of the liquid silica phase on the final composition of nanocomposite are proposed.

The existence of liquid silica phase in the melt may result in the changing of chemical composition of finally crystallised nanocrystals, e.g. the formation of bismuth orthosilicate  $\text{Bi}_4\text{Si}_3\text{O}_{12}$  under soaking opals with the  $\text{Bi}_{12}\text{SiO}_{20}$ .

In the case of ‘opal–BTO’ composite, liquid silica phase crystallises in tridymite. The formation of ‘globule–nanocrystal’ interface composed of the medium-range ordered Si–O–Bi(Te) bridges is also proposed.

There is no clear evidence of the change in chemical composition or crystalline silica phase formation in the ‘opal–NBMO’ composite. They may be difficult to be observed in the Raman spectra that have bands broadened due to nonstoichiometric distribution of Na and Bi ions in the cation sublattice [21, 22].

Raman intensity variations by surface scanning are discussed in terms of the redistribution of the exciting radiation field. The reasons proposed for realising this effect are the multiple scattering by the surface and bulk opal structural defects together with internal reflection as well as the structural light focusing.

**Acknowledgements** Special thanks to Deutsche Forschungsgemeinschaft for the grant which offered one of us (BA) to use the Raman and infrared facilities in Technische Universität Chemnitz, Institute of Chemistry, and to Dr. Raul David Rodriguez (Institute of Physics) and to the SEM centre there. We are also thankful to Dr. Olexandr Kolomys (Institute of Semiconductor Physics of National Academy of Sciences of Ukraine) for performing micro-Raman scattering measurements.

## References

1. Kurdyukov DA, Kartenko NF, Golubev VG (2010) Infiltration of silica colloidal crystals with molten salts and semiconductors under capillary forces. *J Alloys Compd* 492(1–2):611–615. doi:[10.1016/j.jallcom.2009.11.193](https://doi.org/10.1016/j.jallcom.2009.11.193)
2. Lytle JC, Stein A (2006) Recent progress in syntheses and applications of inverse opals and related macroporous materials prepared by colloidal crystal templating. *Ann Rev Nano Res* 1:1–79
3. Zaytsev KI, Yurchenko SO (2014) Enhancement of second harmonic generation in  $\text{NaNO}_2$ -infiltrated opal photonic crystal using structural light focusing. *Appl Phys Lett* 105(5):051902(4)
4. Zaytsev KI, Katyba GM, Yakovlev EV et al (2014) Band-gap nonlinear optical generation: The structure of internal optical field and the structural light focusing. *J Appl Phys* 115(21):213505(9). doi:[10.1063/1.4880299](https://doi.org/10.1063/1.4880299)
5. Gorelik VS (2009) Optical and dielectric properties of nanostructured photonic crystals loaded by ferroelectrics and metals. *Phys Solid State* 51(7):1321–1327
6. Fedyanin AA, Aktsipetrov OA, Kurdyukov DA et al (2005) Nonlinear diffraction and second-harmonic generation enhancement in silicon-opal photonic crystals. *Appl Phys Lett* 87(15):151111(3)
7. Soljacic M, Joannopoulos J (2004) Enhancement of nonlinear effects using photonic crystals. *Nat Mater* 3:211–219. doi:[10.1038/nmat1097](https://doi.org/10.1038/nmat1097)
8. Masalov VM, Sukhinina NS, Kudrenko EA et al (2011) Mechanism of formation and nanostructure of Stöber silica particles. *Nanotechnology* 22:275718(9)
9. Kurdyukov DA, Eurov DA, Stovpiaga EY et al (2014) Photonic crystals and glasses from monodisperse spherical mesoporous silica particles filled with Nickel. *Phys Solid State* 56(5):1033–1038

10. Abu Sal B, Moiseyenko V, Dergachov M et al (2013) Manifestation of metastable  $\gamma$ -TeO<sub>2</sub> phase in the Raman spectrum of crystals grown in synthetic opal pores. *Ukr J Phys Opt* 14(3):119–124
11. Weber MJ (ed) (2003) Handbook of optical materials. CRC Press, Boca Raton
12. Horn W, Földvári I, Denz C (2008) Holographic data storage in photorefractive bismuth tellurite. *J Phys D Appl Phys* 41(22):224006
13. Ok KM, Bhuvanesh SP, Shiv Halasyamani P (2001) Bi<sub>2</sub>TeO<sub>5</sub>: synthesis, structure, and powder second harmonic generation properties. *Inorg Chem* 40(8):1978–1980
14. Shen C, Zhang H, Zhang Y et al (2014) Orientation and temperature dependence of piezoelectric properties for sillenite-type Bi<sub>12</sub>TiO<sub>20</sub> and Bi<sub>12</sub>SiO<sub>20</sub> single crystals. *Crystals* 4(2):141–151
15. Krupych O, Kushnirevych M, Mys O et al (2015) Photoelastic properties of NaBi(MoO<sub>4</sub>)<sub>2</sub> crystals. *Appl Opt* 54(16):5016–5023. doi:10.1364/AO.54.005016
16. Kargin Yu F, Burkov VI, Maryin AA et al (2005) Crystals Bi<sub>12</sub>M<sub>x</sub>O<sub>20±8</sub> with sillenite structure. Synthesis, properties. Alphabet, Moscow. (in Russian)
17. Zhereb VP, Skorikov VM (2003) Metastable states in bismuth-containing oxide systems/. *Inorg Mater* 39(S2):S121–S145
18. Dityatyev OA, Smidt P, Stefanovich SY et al (2004) Phase equilibria in the Bi<sub>2</sub>TeO<sub>5</sub>-Bi<sub>2</sub>SeO<sub>5</sub> system and a high temperature neutron powder diffraction study of Bi<sub>2</sub>SeO<sub>5</sub>. *Solid State Sci* 6(9):915–922
19. Wu A, Xu J, Qian G et al (2005) Bridgman growth of bismuth tellurite crystals. *Bull Mater Sci* 28(6):561–564
20. Waškowska A, Gerward B, Staun Olsenc J (2005) Low-temperature and high-pressure structural behaviour of NaBi(MoO<sub>4</sub>)<sub>2</sub>—an X-ray diffraction study. *J Solid State Chem* 178:2218–2224
21. Moiseyenko VN, Bogatirjov Yu I, Jeryemenko AM et al (2000) Raman spectra of acoustooptic NaBi(MoO<sub>4</sub>)<sub>2</sub>. *J Raman Spectrosc* 31:539–541
22. Hanuza J, Haznar A, Maczka M et al (1997) Structure and vibrational properties of tetragonal sheelite NaBi(MoO<sub>4</sub>)<sub>2</sub>. *J Raman Spectrosc* 28:953–963
23. Stöber W, Fink A, Bohn E (1968) Controlled growth of monodisperse silica spheres in the micron size range. *J Colloid Interface Sci* 26(2):62–69
24. Samusev KB, Yushin GN, Rybin MV et al (2008) Structural parameters of synthetic opals: statistical analysis of electron microscopy data. *Phys Solid State* 50(7):1230–1236
25. Moiseyenko V, Yevchik AV, Dergachov M et al (2015) The effects of disorder on the optical spectra of synthetic opals. *Springer Proc Phys* 167:315–327
26. Gorelik VS, Dovbeshko GI, Evchik AV et al (2013) Growth and optical properties of synthetic opal filled with Bi<sub>12</sub>SiO<sub>20</sub> and Bi<sub>12</sub>GeO<sub>20</sub> nanocrystals. *Inorg Mater* 49(8):802–806
27. Hernández-Ortiz M, Hernández-Padrón G, Bernal R et al (2015) Nanocrystalline mimetic opals: synthesis and comparative characterization vs. natural stones. *Int J Basic Appl Sci* 4(2):238–243
28. Kihara K, Hirose T, Shinoda K (2005) Raman spectra, normal modes and disorder in monoclinic tridymite and its higher temperature orthorhombic modification. *J Mineral Petrolog Sci* 100(2):91–103
29. Mihailova B, Gospodinov M, Konstantinov L (1999) Raman spectroscopy study of sillenites. I. Comparison between Bi<sub>12</sub>(Si,Mn)O<sub>20</sub> single crystals. *J Phys Chem Solids* 60:1821–1827
30. Beneventi P, Bersani D, Loticci PP et al (1995) A Raman study of Bi<sub>4</sub>(Ge<sub>x</sub>Si<sub>1-x</sub>)O<sub>12</sub> crystals. *Solid State Commun* 93(2):143–146
31. Patterson BM, Unruh KM, Shah SI (1992) Melting and freezing behavior of ultrafine granular metal films. *Nanostructured Mater* 1(1):65–70
32. Domoratskii KV, Pastukhov VI, Kudzin AY et al (2000) Raman scattering in the Bi<sub>2</sub>TeO<sub>5</sub> single crystal. *Phys Solid State* 42(8):1443–1446
33. Hardcastle FD, Wachs IE (1992) The molecular structure of bismuth oxide by raman spectroscopy. *J Solid State Chem* 97:319–331

34. Champarnaud-Mesjard JC, Blanchandin S, Thomas P et al (2000) Crystal structure, Raman spectrum and lattice dynamics of a new metastable form of tellurium dioxide:  $\gamma$ -TeO<sub>2</sub>. *J Phys Chem Solids* 61:1499–1507
35. Narang SN, Patel ND, Kartha VB (1994) Infrared and Raman spectral studies of  $\alpha$ -Bi<sub>2</sub>O<sub>3</sub>. *J Mol Struct* 327:221–235
36. Venugopalan S, Ramdas AK (1972) Raman spectra of bismuth germanium oxide and bismuth silicon oxide. *Phys Rev* 5(10):4065–4079

# Chapter 51

## Organic-Inorganic Materials for Baromembrane Separation

Yurii Zmievskii, Ludmila Rozhdestvenska, Yuliya Dzyazko,  
Ludmila Kornienko, Valerii Myronchuk, Alexander Bildukevich,  
and Anatolii Ukrainetz

### 51.1 Improvement of Antifouling Stability of Polymer Membranes

Polymer membranes are widely used for baromembrane separation, particularly for ultrafiltration due to their elasticity and mechanical stability against high pressure [1]. Due to their hydrophobicity, the membranes accumulate organics not only on their outer surface but also inside pores [2, 3]. The cake can be easily removed from the outer surface, for instance, by flow pulsation [4]. Alternatively, filling of pores requires chemical reagents [5]. This type of fouling causes shortage of separation cycle, longer period for regeneration of the membrane system, and larger volume of water for washing (as a result, significant amount of secondary wastes is formed). Moreover, chemical treatment decreases a lifetime of the membranes.

Hydrophilization of polymers allows us to overcome these difficulties. The first type of modifier is hydrophilic polymers [6, 7]. Another type is inorganic functional groups (as a rule,  $\equiv\text{SiOH}$ ) grafted to the polymer [8, 9]. The membranes obtained by this manner are related to hybrid materials. The third type of hydrophilic modifier is nanoparticles of multi-walled carbon nanotubes [10, 11], graphene

---

Y. Zmievskii • L. Kornienko • V. Myronchuk • A. Ukrainetz  
National University of Food Technologies of the Ministry of Education and Science of Ukraine,  
Kyiv, Ukraine

L. Rozhdestvenska • Y. Dzyazko (✉)  
V. I. Vernadskii Institute of General and Inorganic Chemistry of the National Academy of Science  
of Ukraine, Kyiv, Ukraine  
e-mail: [dzyazko@gmail.com](mailto:dzyazko@gmail.com)

A. Bildukevich  
Institute of Physical Organic Chemistry, National Academy of Sciences of Belarus, Minsk,  
Belarus

oxide [12], carbon nanotubes and graphene oxide simultaneously [13], dextran-grafted *halloysite* nanotubes (aluminosilicate clay mineral) [14],  $\text{SiO}_2$  [15],  $\text{Fe}_2\text{O}_3$  stabilized with chitosan [16],  $\text{ZrO}_2$  [17], and  $\text{TiO}_2$  [18]. The nanoparticles are inserted to the membrane during polymer formation. However, porosity of the membranes cannot be regulated purposefully by this manner (as well as in the case of modifiers of the first and second types). Moreover, a part of the nanoparticles occur outside the pores. Regarding carbon modifiers, some regions of nanoparticles are hydrophobic [19, 20]; they weaken hydrophilicity of the composite membranes.

Nanoparticles can be also inserted into pores of the membranes, which have been formed preliminarily. This approach was applied to zirconium hydrophosphate (ZHP). ZHP nanoparticles embedded to cation exchange resin increase its electrical conductivity [21, 22], ion exchange capacity [22], and selectivity [22, 23]. Cation and anion exchange membranes were also modified with ZHP and hydrated zirconium dioxide (HZD), respectively [24]. Non-aggregated nanoparticles have been found to improve transport of counterions through the membranes. Aggregates of the nanoparticles are barriers against organics and co-ions.

ZHP nanoparticles form agglomerates inside pores of track microfiltration membrane [25]. In opposite to the pristine polymer, no accumulation of organics has been found for the composite. However, modification with ZHP does not improve selectivity of the membrane. Thus, the problem of a choice of the modifier has to be solved. Another task is optimization of the modification conditions; they must provide mechanical stability of the particles inside the membrane against high pressure. Finally, antifouling properties of the composites have to be investigated.

Among inorganic materials, amorphous ZHP and HZD look the most attractive due to chemical stability, possibility to obtain nanoparticles, as well as cheapness of reagents for synthesis. ZHP and HZD are characterized by high content of functional groups [26–29], which could provide considerable hydrophilicity of the membrane.

## 51.2 Modification of Polymer Membrane

Polymer microfiltration membrane marked as Mifil-0.2 (Institute of Physical Organic Chemistry of the National Academy of Science of the Republic of Belarus) was applied to investigations. The membrane includes polyester (substrate) and aliphatic polyamide (active layer).

The samples of the membrane were immersed with water under vacuum conditions at 343 K and then with sol of insoluble zirconium hydroxocomplexes. Sol (1 M Zr(IV)) was prepared similarly to [30] and diluted in 10 times. HZD and ZHP were deposited using 0.1 M solutions of  $\text{NH}_4\text{OH}$  or  $\text{H}_3\text{PO}_4$ , respectively. In opposite to [31], where the ion exchangers were precipitated at 298 K, this procedure was carried out at 273 K. Further the membranes were washed with deionized water and dried at 298 K down to a constant mass. The cake was removed from the outer surface by means of ultrasonic treatment at 30 kHz.

Morphology of the membranes was investigated using SEM method. For TEM investigations, the active layer was removed from the substrate, crushed in liquid nitrogen, and treated with ultrasound. The pretreatment procedures and devices are given in [21–25].

### 51.3 Membrane Test

The stack for baromembrane separation is described in [31]. Deionized water was used for pressure test. The solution of bovine serum albumin, BSA (Merck), was applied to investigations of rejection ability of the membranes. The protein concentration was  $0.3 \text{ g dm}^{-3}$ . Wheat stillage (produced by Chervonoslobidskii state company “Ukrspirt”) was used for test of the membrane stability against fouling; earlier corn stillage was applied to investigations [25, 31, 32].

First of all, the membranes were pressed in deionized water at 298 K and 1 bar until a constant flow rate of the permeate. Then the pressure was increased up to 8 bars; the constant flow rate was reached again. Further the test was repeated at 1 bar. After the pressure test, the BSA solution was filtered at 1 bar. The protein was determined by biuret method according to [33].

Other fresh samples were pressed in water as described above. Then water was changed by wheat stillage, which circulated through the cell for 1 h at 333 K and 0.03–0.05 bar (no filtration was realized under these conditions). Further water was filtered at 333 K and 1 bar. Finally, water was filtered through the membrane again at 333 K and 1 bar.

Then wheat stillage was filtered at 1 bar and 333 K. Both permeate and concentrate were analyzed with a URL-1 model 1 refractometer (Analitpribor, Ukraine).

### 51.4 Structure of the Polymer and Organic-Inorganic Membranes: Location of the Modifier Particles

The polymer membrane consists of macroporous fibrous substrate and active layer that is attached to its outer surface. The plaited fibers form pores, a size of which is up to  $\approx 50 \text{ }\mu\text{m}$  (Fig. 51.1a); these voids provide low hydrodynamic resistance of the membrane. A size of pores of the active layer is mainly 100–300 nm (Fig. 51.1b). A shape of the holes is both irregular and close to round. These pores are either isolated or located very close to each other, when a distance between them is less than 100 nm. Pores of the active layer are responsible for rejection ability of the membrane.

Aggregates of HZD particles are precipitated both on the substrate fibers (Fig. 51.2a, b) and inside the active layer (Figs. 51.2c–e). A size of the formations on the



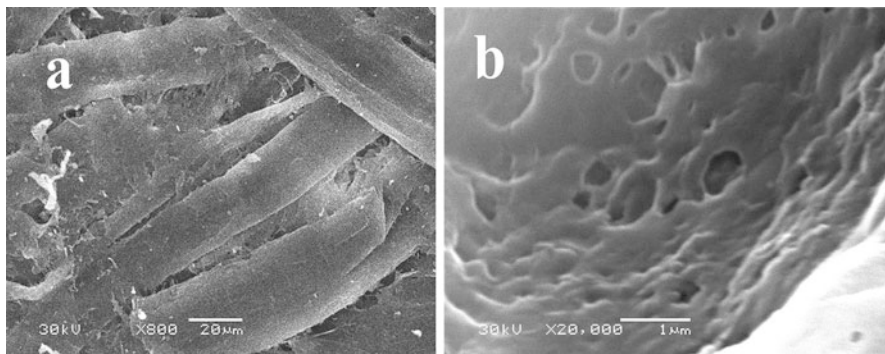


**Fig. 51.1** SEM images of macroporous substrate (a) and active layer of the Mifil-0.2 membrane

fibers is several microns. The aggregates cannot fill completely the voids between the fibers. Thus, no rejection of colloidal particles due to macroporous substrate is expected. At the same time, a change of morphology of the active layer is visible after modification. The modifier particles (up to 400 nm) inside the active layer are close to spheres; they consist of smaller particles (50–100 nm). Comparing with the modifier precipitated at 298 K [31], the aggregates in the active layer are more compact. However, the particles are larger than those obtained under higher temperature. Secondary porosity (pores between primary particles) should provide rejection of colloidal species.

No sufficient change of morphology of the active layer after modification with ZHP is visible (Fig. 51.2f). As shown with TEM technique, the modifier is absent in this region of the membrane. However, the particles were found inside the macroporous substrate.

Different location of ZHP and HZD particles is caused by the size of the particles, which are formed during precipitation, when small particles are dissolved and redeposited as larger particles. Indeed, sol of insoluble zirconium hydroxocomplexes contains nanoparticles, a size of which is mainly 6 nm [30]. Larger primary particles in the active layer indicate dissolution and reprecipitation. Dissolution of the particle, a maximal radius ( $r$ ) of which is determined by Ostwald-Freundlich equation [33]

$$\ln \frac{C}{C_{\infty}} = \frac{\beta v_m \sigma \cos \varphi}{RT r} \quad (51.1)$$

is possible. Here  $C$  is the compound concentration,  $C_{\infty}$  is the concentration of saturated solution (the  $C$  and  $C_{\infty}$  values are very low for ZHP and HZD),  $\beta$  is the shape factor,  $v_m$  is the molar volume of the compound,  $\sigma$  is the surface tension of the solvent,  $\varphi$  is the wetting angle,  $R$  is the gas constant, and  $T$  is the temperature. As follows from Eq. (51.1), a decrease in the temperature results in enlargement of

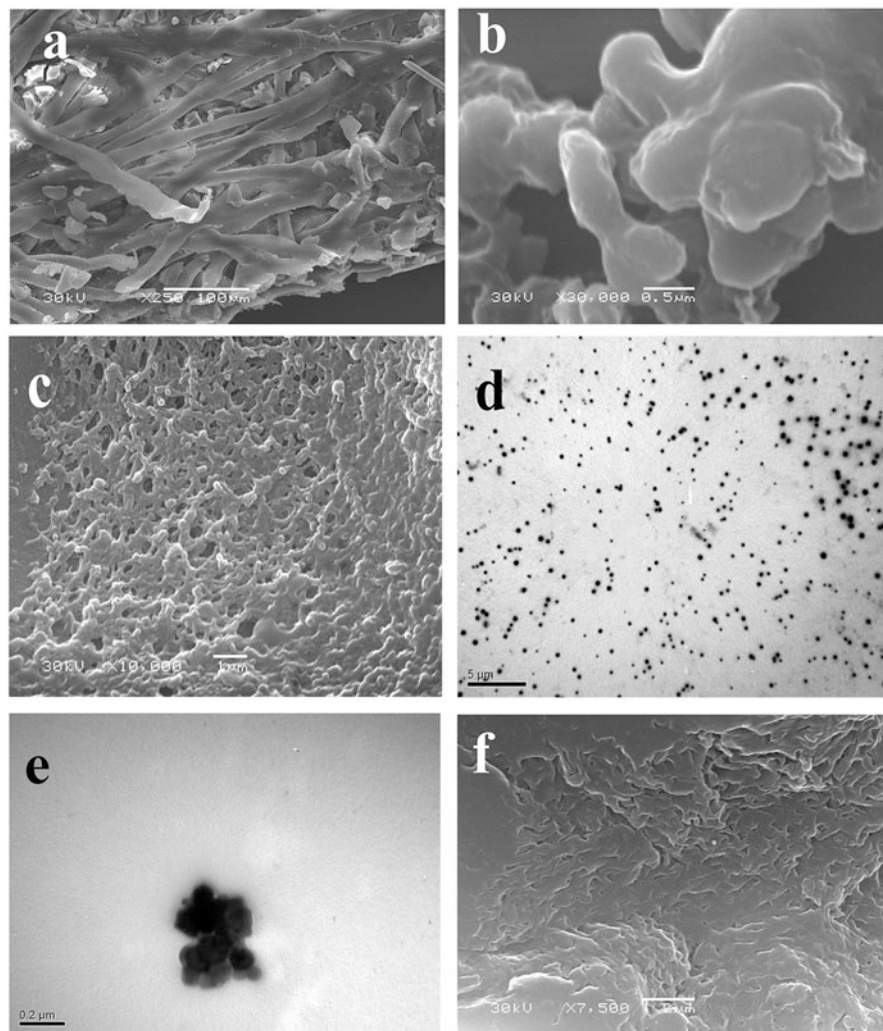


**Fig. 5.1.2** SEM (a–c, f) and TEM (d, e) images of macroporous substrate (a, b) and active layer (c–f) of the membrane modified with HZA (a–e) and ZHP (f)

the deposited particles. Simultaneously the surface tension of the solvent increases. This causes formation of larger primary particles than those deposited at 298 K [31].

Other important factor is the molar volume of the compound. Exact chemical composition of amorphous ZHP and HZA is indefinite. The  $v_m$  value can be estimated from the molar mass and particle density of crystalline materials. Regarding  $ZrO_2$ , these values are  $123.2 \text{ g mol}^{-1}$  and  $5.68 \text{ g cm}^{-3}$ , respectively [34],  $v_m = 21.7 \text{ cm}^3 \text{ mol}^{-1}$ . ZHP deposited from sol contains mainly hydrophosphate groups [23] similarly to  $\alpha$ -ZHP ( $Zr(HPO_4)_2 \cdot H_2O$ ). Molar mass and particle density

of this compound are  $301 \text{ g mol}^{-1}$  and  $3.3 \text{ g cm}^{-3}$  [34], thus,  $v_m = 91 \text{ cm}^3 \text{ mol}^{-1}$ . Larger molar volume of ZHP provides larger particles of this ion exchanger comparing with HZD. As a result, ZHP particles are precipitated only inside the macroporous substrate due to steric factor. In opposite to ZHP, HZD particles can be deposited both in the substrate and active layer.

## 51.5 Filtration of Liquids

Figure 51.3a illustrates a cumulative volume ( $V$ ) of deionized water passed through the membranes as a function of time ( $\tau$ ). The data were obtained at 1 bar after the pressure test, which was carried out preliminarily at 1 and 8 bars. The permeate rate decreases gradually and reaches constant values after predetermined times. The pristine membrane shows the highest filtration rate; the modifier particles in the substrate increase hydrodynamic resistance of the membrane (membrane modified with ZHP). At last, the membrane containing the inorganic particles inside the active layer shows the lowest filtration rate. When water is passed through the membrane containing adsorbed layers on the outer surface (after circulation of grain stillage without filtration), the rate of permeate increases due to gradual cleaning of the surface.

Regarding filtration of wheat stillage, the  $V$ - $\tau$  curves show the same order as for water filtration (Fig. 51.3b). The pristine membrane and the separator modified with ZHP demonstrate a decrease of the permeate rate over time. The flow rate through the membrane containing HZD is constant.

The permeate flux through the membrane ( $J$ ) was calculated as [1]:

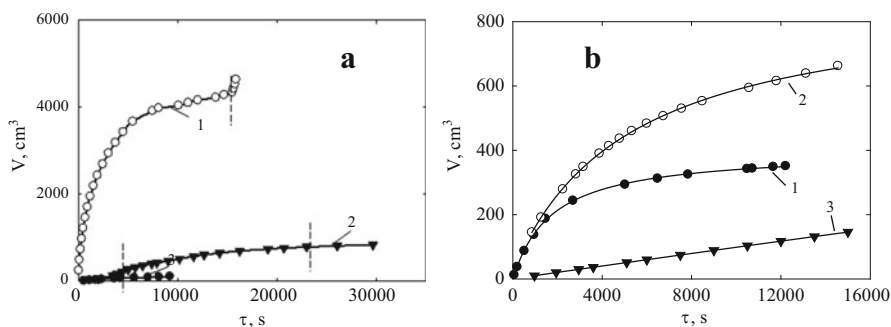


**Fig. 51.3** Cumulative volume of permeate as a function of time. Liquids: deionized water (a) and wheat stillage (b). Pressure drop was 1 bar (after the pressure testing at 1 and 8 bar). Membranes: pristine (1), modified with ZHP (2) and HZD (3). Vertical lines (a) correspond to interruption of water filtration (water was changed by wheat distillery). Further region corresponds to water filtration after the circulation of wheat distillery without applied pressure

**Table 51.1** Water flux through the membranes and their selectivity toward wheat stillage

Membrane	$J, \text{m}^3 \text{m}^{-2} \text{s}^{-1}$ (under steady state at 1 bar)		$\varphi, \%$	
	During pressure test	After pressure test performed at 1 and 8 bar	Wheat stillage	BSA
Pristine	$2.99 \times 10^{-5}$	$1.27 \times 10^{-5}$	0	0
Modified with ZHP	$7.35 \times 10^{-6}$	$1.25 \times 10^{-5}$	0	0
Modified with HZD	$6.28 \times 10^{-6}$	$1.02 \times 10^{-5}$	72	90

$$J = \frac{dV}{dt} \frac{1}{A}, \quad (51.2)$$

where  $A$  is the membrane area. As seen from Table 51.1, the permeate flux of water through the composite membranes slightly increases after the previous pressure test. This indicates that the particles can move through the membranes under the influence of pressure, form aggregates, and even be partially removed. This redistribution of the particles allows us to avoid additional tortuosity and narrowing-widening. As a result, hydrodynamic resistance of the composite membranes decreases. However, different behavior of the membranes during filtration of water and wheat stillage shows stability of the main part of the particles in the membranes.

Selectivity of the membranes ( $\varphi$ ) was found as:

$$\varphi = \left(1 - \frac{C_p}{C_f}\right) \times 100\%, \quad (51.3)$$

where the  $p$  and  $f$  indexes correspond to permeate and feed solution, respectively.

As seen from Table 51.1, only the membrane modified with HZD demonstrates high rejection toward BSA, the molecular mass of which is 69,000 Da. This is evidently caused by location of the particles, which determine functional properties of the composite membrane.

## 51.6 Intraporous Active Layer of Inorganic Particles

According to the data of BSA solution filtration, a diameter of pores ( $d_{50}$ ), which are responsible for 50% of rejection ( $\phi=50\%$ ), can be calculated from the formula [35]:

$$d_{50} = 0.11(MW_{50})^{0.46}. \quad (51.4)$$

Here  $MW_{50}$  is the molecular weight of a large organic molecule that displays 50% rejection capability. The  $d_{50}$  value has been estimated as 18 nm. Analogous membrane, which was modified with HZD under room temperature, shows 10% selectivity toward polyethylene glycol (40,000 Da). The  $d_{50}$  magnitude is 14 nm assuming 50% rejection. Thus, a size of pores that provide rejection is within the

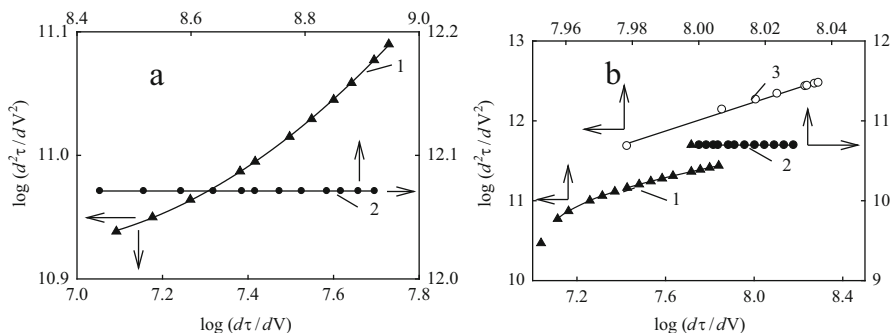


**Fig. 51.4** Dependence of  $\log\left(\frac{d^2\tau}{dV^2}\right)$  on  $\log\left(\frac{d\tau}{dV}\right)$ . Liquids: deionized water (a) and wheat stillage (b). Pressure drop was 1 bar (after the pressure testing at 1 and 8 bar). Membranes: modified with ZHP (1), HZD (2), and pristine (3)

interval of 14.4–18.5 nm. This indicates transformation of microfiltration membrane into ultrafiltration separator.

A thickness of the secondary active layer (inorganic particles) inside the pores  $l$  can be calculated from Kozeny-Carman equation [36]:

$$\frac{\Delta P}{l} = \frac{180\mu(1-\varepsilon^2)}{\Phi^2 d^2 \varepsilon^2} v_s, \quad (51.5)$$

where  $\varepsilon$  is the porosity (0.33 for compact bed of globules),  $\Phi$  is the sphericity of the particles (it is assumed that  $\Phi=1$ ),  $d$  is their diameter,  $v_s$  is the superficial flow velocity, and  $\mu$  is the dynamic viscosity ( $9 \times 10^{-3}$  Pa s at 298 K). A shape of particles is close to spherical (see Fig. 51.3); their diameter is assumed to be 50 nm. Since  $v_s$  is  $6.3 \times 10^{-6}$  m s $^{-1}$  at 1 bar for completely compacted HZD-containing membrane,  $l=43$   $\mu$ m. This is comparable with a thickness of active layer. A similar approach for the ZHP layer ( $d=300$  nm, see Fig. 51.4,  $v_s=9.2$  m s $^{-1}$ ) gives  $l=0.5$  mm; this corresponds to a thickness of the whole membrane.

Thus, hydrodynamic resistance of the membranes modified with ZHP is determined by the particles in the substrate. In the case of the membrane containing HZD, its resistance depends on the particles incorporated into the active layer.

## 51.7 Modeling of Fouling

A number of mathematical approaches for the determination of fouling model have been proposed. The approach [37] is the most widely used; it is based on a classical equation of dead-end filtration under constant pressure:

**Table 51.2** Application of fouling models to filtration of water and wheat stillage

Parameter	Deionized water		Wheat stillage		
	ZHP-containing membrane	HZD-containing membrane	Pristine membrane	ZHP-containing membrane	HZD-containing membrane
$n$	0.24	0	0.90	1.55	0
$R^2$	0.9771	1.0000	0.9936	0.9936	1.0000

$$\frac{d^2\tau}{dV^2} = k \left( \frac{d\tau}{dV} \right)^n, \quad (51.6)$$

where  $k$  is the coefficient that is related to hydrodynamic resistance of the precipitate and  $n$  is the exponent. The  $n$  value reflects the filtration model: (a)  $n=0$  corresponds to cake formation on the outer surface; (b)  $n=1$  is attributed to transition mechanism; (c)  $n=1.5$  is related to pore constriction, where species are precipitated on the pore walls and the particles are smaller than pores; and (d)  $n=2$  means pore blockage, when the particles are larger than pores (more exactly, larger than narrowing). The exponent can be determined from the logarithmic dependence of  $\frac{d^2\tau}{dV^2}$  vs  $\frac{d\tau}{dV}$  (Fig. 51.4).

In the case of water filtration through the composite membranes, incorporated particles of the modifier can be assumed as a result of fouling. As follows from Table 51.2, which illustrates the exponents under steady state conditions, the  $n$  values are close (membrane modified with ZHP) or equal to 0 (membrane containing HZD). It means stability of the particle location after the pressure test. Roughness of the particles (see Fig. 51.2e) prevents their redistribution through the polymer and removal from the membrane pores.

Fouling with components of wheat stillage is simulated by transition mechanism (pristine membrane) and pore constriction (membrane containing ZHP). Since a receiving side of the membrane is the active layer (free from ZHP), the organic species fill its pores. Alternately, fouling of the membrane modified with HZD is only due to cake formation. The cake can be easily removed from the outer surface without chemical reagents.

## 51.8 Conclusions

In accordance with Ostwald-Freundlich equation, the particles of ZHP inside the polymer membrane are larger in comparison with HZD, since the value of molar volume of ZHP is much higher. Decreasing in temperature, at which precipitation occurs, causes an increase of size of the incorporated particles. Due to steric limitations, ZHP particles are located mainly in the macroporous substrate. HZD particles (50–100 nm) occupy also the active layer transforming the microfiltration membrane into ultrafiltration separator. These particles form aggregates; their

roughness prevents movement of the particles through the membrane. Secondary porosity due to inorganic particles provides rejection ability of the membrane. The composite containing HZD shows considerable selectivity toward BSA and organic components of wheat stillage. The membranes show similar rejection ability as the materials modified at higher temperature [31]): selectivity of the membranes toward components of wheat and corn stillage is practically the same. The concentrate, which is formed during separation, can be used for alcohol production or for preparation of food for domestic animals. Deionized water can be obtained from the permeate using nanofiltration followed by reverse osmosis [38, 39].

The composite membrane containing HZD demonstrates stability against pore fouling: only cake is formed on the outer surface of the membrane. This facilitates cleaning of the membranes and provides longer time of separation and shorter period of membrane regeneration. Moreover, the absence of organics in pores allows us to minimize consumption of the reagents for regeneration. This increases lifetime of the membrane.

## References

1. Mulder M (1996) Basic principles of membrane technology, 2nd edn. Kluwer Academic Publisher, Dordrecht, Boston, London
2. Qu F, Liang H, Zhou J et al (2014) Ultrafiltration membrane fouling caused by extracellular organic matter (EOM) from *Microcystis aeruginosa*: effects of membrane pore size and surface hydrophobicity. *J Membr Sci* 449:58–66
3. Hadidi M, Zydney AL (2014) Fouling behavior of zwitterionic membranes: impact of electrostatic and hydrophobic interactions. *J Membr Sci* 452:97–103
4. Jaffrin MY (2012) Hydrodynamic techniques to enhance membrane filtration. *Annu Rev Fluid Mech* 44:77–96
5. Kazemimoghadam M, Mohammadi T (2007) Chemical cleaning of ultrafiltration membranes in the milk industry. *Desalination* 204(1–3):213–218
6. Kanagaraj P, Nagendran A, Rana D et al (2015) Influence of *N*-phthaloyl chitosan on poly (ether imide) ultrafiltration membranes and its application in biomolecules and toxic heavy metal ion separation and their antifouling properties. *Appl Surf Sci* 329:165–173
7. Susanto H, Roihatin A, Aryanti N et al (2012) Effect of membrane hydrophilization on ultrafiltration performance for biomolecules separation. *Mater Sci Eng C* 32(7):1759–1766
8. Kumar M, Lawler J (2014) Preparation and characterization of negatively charged organic–inorganic hybrid ultrafiltration membranes for protein separation. *Sep Purif Technol* 130:112–123
9. Sforça ML, Yoshida IVP, Nunes SP (1999) Organic–inorganic membranes prepared from polyether diamine and epoxy silane. *J Membr Sci* 159(1–2):197–207
10. Ma J, Zhao Y, Xu Z et al (2013) Role of oxygen-containing groups on MWCNTs in enhanced separation and permeability performance for PVDF hybrid ultrafiltration membranes. *Desalination* 320:1–9
11. Majeed S, Fierro D, Buhr K et al (2012) Multi-Walled Carbon Nanotubes (MWCNTs) mixed Polyacrylonitrile (PAN) ultrafiltration membranes. *J Membr Sci* 403–404:101–109
12. Yu L, Zhang Y, Zhang B et al (2013) Preparation and characterization of HPEI-GO/PES ultrafiltration membrane with antifouling and antibacterial properties. *J Membr Sci* 447:452–462

13. Zhang J, Xu Z, Shan M et al (2013) Synergetic effects of oxidized carbon nanotubes and graphene oxide on fouling control and anti-fouling mechanism of polyvinylidene fluoride ultrafiltration membranes. *J Membr Sci* 448:81–92
14. Yu H, Zhang Y, Sun X et al (2014) Improving the antifouling property of polyethersulfone ultrafiltration membrane by incorporation of dextran grafted halloysite nanotubes. *Chem Eng J* 237:322–328
15. Chen J, Ruan H, Wu L et al (2011) Preparation and characterization of PES-SiO<sub>2</sub> organic-inorganic composite ultrafiltration membrane for raw water pre-treatment. *Chem Eng J* 168(3):1272–1278
16. Rahimi Z, Zinatizadeh AA, Zinadini S (2014) Preparation and characterization of a high antibiofouling ultrafiltration PES membrane using OCMCS-Fe<sub>3</sub>O<sub>4</sub> for application in MBR treating wastewater. *J Appl Res Water Wastewater* 1:13–17
17. Pang R, Li X, Li J et al (2014) Preparation and characterization of ZrO<sub>2</sub>/PES hybrid ultrafiltration membrane with uniform ZrO<sub>2</sub> nanoparticles. *Desalination* 332(1):60–66
18. Kwak S-Y, Kim SH, Kim SS (2001) Hybrid organic/inorganic reverse osmosis (RO) membrane for bactericidal anti-fouling. 1. Preparation and characterization of TiO<sub>2</sub> nanoparticle self-assembled aromatic polyamide thin-film-composite (TFC) membrane. *Environ Sci Technol* 35(11):2388–2394
19. Tuseeva EK, Mayorova NA, Sosenkin VE et al (2008) Carbon nanotubes as a support for pt-and pt-Ru-catalysts of reactions proceeding in fuel cells. *Russ J Electrochem* 44(8):884–893
20. Shulga YM, Baskakov SA, Baskakova YV et al (2015) Supercapacitors with graphene oxide separators and reduced graphite oxide electrodes. *J Power Sources* 279:722–730
21. Dzyazko YS, Ponomareva LN, Volkovich YM et al (2013) Conducting properties of a gel ionite modified with zirconium hydrophosphate nanoparticles. *Russ J Electrochem* 49(3):209–215
22. Dzyazko YS, Ponomaryova LN, Volkovich YM et al (2013) Polymer ion-exchangers modified with zirconium hydrophosphate for removal of Cd<sup>2+</sup> ions from diluted solutions. *Sep Sci Technol* 48(14):2140–2149
23. Dzyazko YS, Ponomaryova LN, Volkovich YM et al (2014) Ion-exchange resin modified with aggregated nanoparticles of zirconium hydrophosphate. Morphology and functional properties. *Microporous Mesoporous Mater* 198:55–62
24. Dzyazko Y, Rozhdestvenskaya L, Zmievsii Y et al (2015) Heterogeneous membranes modified with Nanoparticles of inorganic ion-exchangers for whey demineralization. *Mater Today: Proceedings* 2(6):3864–3873
25. Dzyazko YS, Rozhdestvenskaya LM, Zmievsii YG et al (2015) Organic-inorganic materials containing nanoparticles of zirconium hydrophosphate for baromembrane separation. *Nanoscale Res Lett* 10:64
26. Amphlett CB (1964) *Inorganic ion exchangers*. Elsevier, Amsterdam
27. Clearfield A (ed) (1982) *Inorganic ion exchange materials*. CRC Press, Boca Raton
28. Dzyazko Y, Rozhdestvenska L, Palchik A et al (2005) Ion-exchange properties and mobility of Cu<sup>2+</sup> ions in zirconium hydrophosphate ion exchangers. *Sep Purif Technol* 45(2):141–146
29. Dzyazko YS, Rozhdestvenskaya LM, Vasilyuk SL et al (2009) Electrodeionization of Cr (VI)-containing solution. Part I: chromium transport through granulated inorganic ion-exchanger. *Chem Eng Commun* 196(1–2):3–21
30. Dzyazko YS, Volkovich YM, Sosenkin VE et al (2014) Composite inorganic membranes containing nanoparticles of hydrated zirconium dioxide for electrodialytic separation. *Nanoscale Res Lett* 9(1):271
31. Myronchuk VG, Dzyazko YS, Zmievsii YG et al (2016) Organic-inorganic membranes for filtration of corn distillery. *Acta Period Technol* 47:153–165
32. Kornienko L, Yu Z, Myronchuk V (2015) Investigation of ultrafiltration of grain stillage. *Ukr Food J* 4(1):131–138
33. Myerson AS, Ginde R (2002) Crystals, crystal growth, and nucleation. In: Myerson AS (ed) *Handbook of industrial crystallization*, 2nd edn. Butterworth-Heinemann, Woburn, pp 33–100



34. Gahan L, Blackman A (eds) (2014) *Aylward and Findlay's SI chemical data*, 7th edn. John Wiley & Sons, Australia
35. Arkhangelsky E, Dueka A, Gitis V (2012) Maximal pore size in UF membranes. *J Membr Sci* 394–395:89–97
36. McCabe WL, Smith JC, Harriot P (eds) (2005) *Unit operations of chemical engineering*, seventh edn. McGraw-Hill, New York
37. Hermia J (1982) Constant pressure blocking filtration laws – application to power-law non-newtonian fluids. *Chem Eng Res Des* 60a:183–187
38. Myronchuk VG, Grushevskaya IO, Kucheruk DD et al (2013) Experimental study of the effect of high pressure on the efficiency of whey nanofiltration process using an OPMN-P membrane. *Petrol Chem* 53(7):439–443
39. Zmievskii YG, Kirichuk II, Mironchuk VG (2014) Membrane treatment of wastewater obtained after the whey processing. *J Water Chem Technol* 36(6):309–316

# Chapter 52

## Chemico-metallurgical Method for Obtaining Tungsten-Based Nanopowders

N. F. Kuschevskaya, A. I. Gab, E. A. Paprotskaya, and V. V. Malyshev

### 52.1 Introduction

The use of powdered nanomaterials in technology is one of the most promising areas of modern materials science. Recently, intensive research is conducted to create tungsten alloys with a high content of tungsten and with matrices providing high capacity for adiabatic shear localization and to enhance the special properties of alloys [1–4]. One way to obtain such alloys is high-temperature electrochemical synthesis [5–7]. However, the high process temperatures (1173–1223 K) are limiting the possibilities of its practical application.

Today, for obtaining nanopowders based on tungsten, the following methods are used: arc discharge in thermal plasma, plasmochemical synthesis, chemical condensation, carbonylates thermolysis, and synthesis in aqueous solutions. Promising are works concerning methods of obtaining of nanosized tungsten-based powders from tungsten-containing wastes. Recently, much attention is given to methods of obtaining of the nanosized tungsten powders by the hydrogen reduction. Particularly, it was found that oxidation resistance and size distribution of such nanopowders are crucial for their practical application.

*The aim of the present work* was to develop low-temperature methods allowing to control the structure and properties of the final materials obtained during the process of the nanopowders manufacturing.

---

N.F. Kuschevskaya • E.A. Paprotskaya • V.V. Malyshev  
University “Ukraine”, Kyiv, Ukraine

A.I. Gab (✉)

Open International University of Human Development “Ukraine”, Kyiv, Ukraine  
e-mail: [lina\\_gab@mail.ru](mailto:lina_gab@mail.ru)

## 52.2 Materials and Methods

In this paper, for the synthesis of nanopowders of the present composition based on tungsten, combined chemico-metallurgical method is used including the deposition of metal hydroxides from solutions of their respective salts to hydrogen reduction of obtained intermediate product. Intermediate for tungsten-doped nanopowders was obtained in two ways: by mechanical mixing of nickel, iron, and cobalt hydroxides with tungsten acid and by treating tungsten acid with aqueous solutions of nickel, iron, and cobalt salts followed by evaporation of the resulting mixture while continuously stirring to dryness and washing with acetone or alcohol to remove the chlorine anions. As a result, intermediate tungsten-based powder was obtained which is a mixture of oxides according to X-ray analysis data.

Using the first method, it is difficult to control the chemical composition of the powders since during their obtaining, contamination of product by admixtures is taking place. Besides, the process is multistage which can lead to instability of characteristics of the final doped tungsten nanopowder.

The second method is notable by its technological simplicity and flexibility and does not require special process equipment. The high reproducibility of its results is found, so powders for further studies were synthesized by this method. To obtain an intermediate product, the following materials were used: tungstate acid and iron, cobalt, and nickel chlorides.

An analysis of obtained materials was conducted by the following methods. Content of nickel, iron, and cobalt was determined by atomic absorption spectroscopy (AAS) and atomic emission spectroscopy with induction-coupled plasma (ICP-AES). ICP-AES spectrometer “Ultima 2” (HORIBA Jobin Yvon, France) and AAS spectrometer “AAS-3” (Germany) were used. Content of chlorine was determined titrimetrically. Powders phase composition was determined by X-ray diffraction analysis using DRON-3 equipment (with X-rays wavelength  $1.541781 \times 10^{-10}$  m) followed by mathematical data processing and ASTM information directory data usage. Specific surface area of powders was determined by low-temperature nitrogen adsorption-desorption using GC-1 equipment.

Metallization of obtained intermediate tungsten-based product was performed using the apparatus Setaram TAG 24 within the temperature range of 293–1073 K. Electron microscope examinations of the size and morphology of the powder particles were performed using the scanning electron microscope “Leo-430i.”

## 52.3 Results and Discussion

The conditions were determined of the interaction of solid tungstate acid with solutions of salts of iron, nickel, and cobalt. Chemical composition nanocomposites based on tungsten is optimal with solution concentrations 5–75 g/l. Table 52.1 and

**Table 52.1** Phase composition of intermediate tungsten-based product

Phase	WO <sub>3</sub>	W <sub>20</sub> O <sub>58</sub>	NiO	NiFe <sub>2</sub> O <sub>4</sub>	FeWO <sub>4</sub>	Fe <sub>2</sub> O <sub>3</sub>	WOCl <sub>3</sub>	Co <sub>3</sub> O <sub>4</sub>
Content, %	64.22	22.43	1.98	3.38	1.98	3.69	0.66	1.66

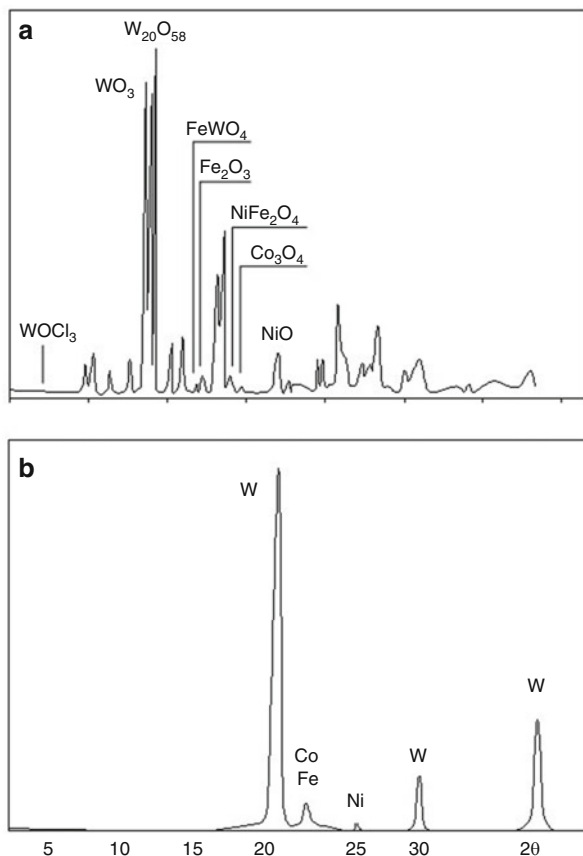
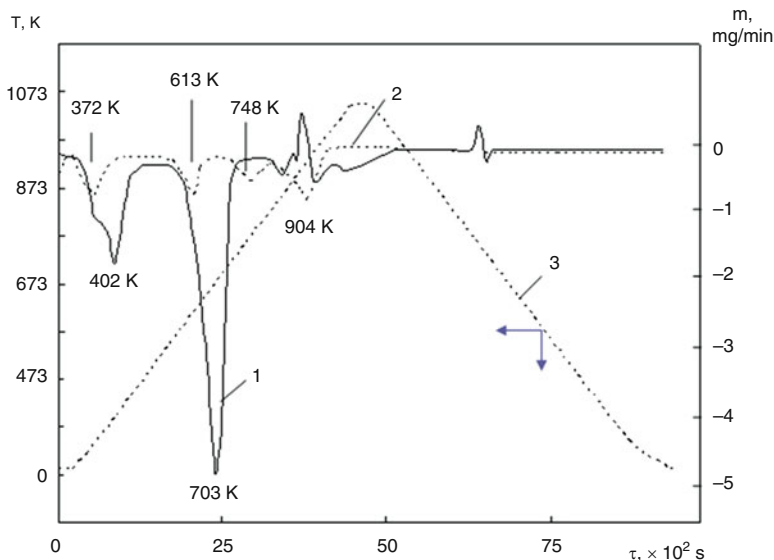
**Fig. 52.1** X-ray diffractograms of intermediate product (a) and reduced tungsten-based alloy powder (b)

Fig. 52.1 present the results of X-ray analysis and X-ray diffractogram fragments of obtained product based on tungsten, respectively.

Fig. 52.2 shows thermograms of intermediate products obtained under hydrogen and helium atmosphere. Metallization of chemical mixture occurs in several stages and within different temperature ranges. However, temperature ranges and respective peaks characterizing the reduction of both iron, nickel, cobalt, and tungsten components of the mixture are shifted into a low-temperature range. Decrease of the metallization temperature of oxides of iron, nickel, and cobalt is associated with the decrease of the contact area of individual particles of these phases, as well as



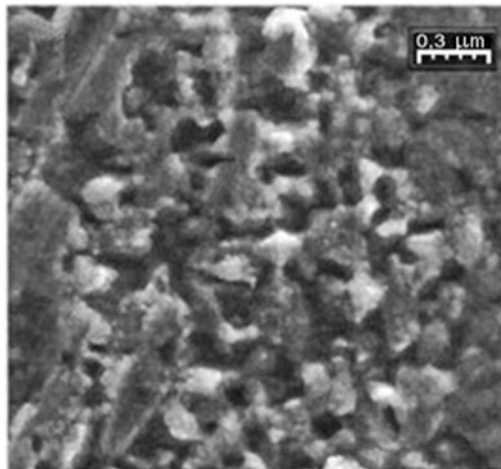
**Fig. 52.2** Thermogravimetric curves of heating of intermediate tungsten-based product under atmosphere of helium (curve 1) and hydrogen (curve 2). Curves 1 and 2 are dependences of rate of change of the mass ( $m$ ) of the sample on time; 3 – curve of temperature change from time

with the decrease of the water's partial pressure in the bulk of the charge reduced within this temperature range (473–773 K) due to the presence of tungsten oxide. In addition, oxygen-containing tungsten component can present an obstacle to an increase of size of the particles of iron, nickel, and cobalt, which can also lead to a decrease of reduction temperature of iron, nickel, and cobalt components. The latter, in turn, according to [8], can influence the electronic structure of primary tungsten oxide system, slowing the induction period of nucleation and accelerating the process of metallization of tungsten oxide. Thus, tungsten oxide reduction is affected not by oxides of iron, nickel, and cobalt, but by their reduced phases. Increasing the number of nucleation centers on the surface of tungsten oxide crystallites, which are reduced particles of iron, nickel, and cobalt, accelerates the tungsten oxide metallization process.

The experiment has tested several temperature modes of hydrogen reduction for the synthesis of powders of the following composition: W 7.2%, Ni 1.8%, Fe 1%, and Co 1%. Such reduction parameters as temperature and reduction time were varied within the range of 923–1173 K for 1–2 h. The structure, phase composition, and dispersion of synthesized powders were studied affecting the mechanism of consolidation and properties of bulk samples. Fig. 52.1b shows X-ray diffractogram of reduced nanopowder based on tungsten.

Using X-ray analysis, the phase composition of reduced tungsten-based alloy nanopowder was determined (weight %): W, 87.72; Fe, 2.63; Fe-Ni, 0.88; Ni,

**Fig. 52.3** Electron microphotograph of the tungsten-based alloy powder



6.14; and Co, 0.88. The chemical composition of reduced tungsten-based alloy nanopowder is as follows (weight %): Fe, 1.8; Ni, 7.2; Co, 1.1; and W, the rest.

The results of the phase analysis of reduced powder indicate that the oxides and intermetallides phases are absent in the samples and that powder chemical composition corresponds to a predefined ratio.

Figure 52.3 shows photomicrographs of nanopowders of doped tungsten-based alloy. Electron microscopic studies have shown that the materials consist of dense agglomerates with an average size value estimated as 300–400 nm and the individual particle size as 100 nm.

The specific surface of the tungsten-based powder was determined by BET method. It is  $0.9 \text{ m}^2/\text{g}$ , corresponding to an average particle size value (with material density  $18.6 \text{ g/cm}^3$ ) of about 300 nm.

Thus, the powder's synthesis modes were proposed providing the possibility to obtain by chemico-metallurgical method nanopowdered tungsten-based alloys with desired chemical and physicochemical properties. Based on the found patterns, approaches were developed to control the properties of tungsten-based nanopowders at the stage of their formation.

## References

1. Debata M, Upadhyaya A (2004) Effect of boron addition on sintering of tungsten based alloys. *J Mater Sci* 39:2539–2541
2. Rittel D, Weisbrod G (2001) Dynamic fracture of tungsten base heavy alloys. *Int J Fract* 12:87–98
3. Eroglu S, Erken H, Baykara T (1998) Surface hardening of tungsten heavy alloys. *Scr Mater* 38(1):131–136

4. Wei Z et al (2000) Influence of microstructure on adiabatic shear localization of pre-twisted tungsten heavy alloys. *Int J Impact Eng* 24:747–758
5. Malyshev VV, Gab AI (2005) Electrochemical synthesis of nickel (cobalt) molybdenum (tungsten) intermetallides. *Physico Chem Mech Mater* 5:61–68. [in Ukrainian]
6. Malyshev VV (2007) Electrochemical behavior of cobalt and electrodeposition of cobalt-molybdenum (tungsten) alloys from oxide melts. *Prot Met* 43(6. C):607–612. [in Russian]
7. Malyshev VV (2009) Mechanisms of electroreduction and electrodeposition of coatings of VIA group metals from ionic melts. *Physico Chem Surf Prot Met* 45(4):339–357. [in Russian]
8. Skorokhod VV, Panychkyna VV, Solonin YM, Uvarov IV (1979) Dispersed refractory metal powders. *Naukova dumka, Kiev*, p 172

# Chapter 53

## Nanoporous Thin Film VN<sub>x</sub> Hydrogen Absorbents: Method of Production, Structure Formation Mechanism, and Properties

Alexey Guglya, Alexander Kalchenko, Yury Marchenko, Elena Solopikhina, Viktor Vlasov, and Elena Lyubchenko

### 53.1 Introduction

Vacuum deposition techniques, such as magnetron sputtering and physical and chemical vapor deposition, have been successfully used for thin film creation for a long time. A characteristic feature of these techniques is that the resulting structures are formed under less than equilibrium conditions allowing the creation of materials with unique properties.

B. Movchan and A. Demchishin in 1969 [1] have shown the substrate temperature influence on the structure of Ti, Ni, W, ZrO<sub>2</sub>, and Al<sub>2</sub>O<sub>3</sub> films. Evaporation of the substances was carried out by the electron beam heating of the crucible. Three temperature zones with boundary temperatures T<sub>1</sub> and T<sub>2</sub> that are, respectively, equal to 0.3 and 0.45–0.5 of T<sub>m</sub> for metals and 0.22–0.26 and 0.45–0.5 of T<sub>m</sub> for oxides were determined. The films with certain structure and properties have been formed inside each of these zones. These studies marked the beginning of the so-called structure zone model (SZM). Later J. Thornton [2] took into account the effect of the gas environment on the film structure additionally to the influence of the substrate temperature. It was shown that the film forming mechanism at the ion bombardment was fundamentally being changed depending not only on the substrate temperature but also on the pressure of the working gas (argon). Effect

---

A. Guglya (✉) • A. Kalchenko • Y. Marchenko • E. Solopikhina • V. Vlasov  
National Science Center “Kharkov Institute of Physics and Technology”, 61108, Kharkov,  
Ukraine  
e-mail: [guglya@kipt.kharkov.ua](mailto:guglya@kipt.kharkov.ua); [alexey.guglya@springernature.com](mailto:alexey.guglya@springernature.com);  
[kalchenko@kipt.kharkov.ua](mailto:kalchenko@kipt.kharkov.ua); [ymarch@ukr.net](mailto:ymarch@ukr.net); [ellena104@rambler.ru](mailto:ellena104@rambler.ru); [vlvictorkipt@gmail.com](mailto:vlvictorkipt@gmail.com)

E. Lyubchenko  
National Technical University “Kharkov Polytechnic Institute”, 61002, Kharkov, Ukraine  
e-mail: [e\\_lyubchenko@ukr.net](mailto:e_lyubchenko@ukr.net)



of the reactive gas (oxygen) on the formation of the microstructure of thermally evaporated metal (in that case, aluminum) has been studied in detail by P. Barna and M. Adamik in [3]. Oxygen adsorbed on the surface of the forming film reduces the mobility of grain-nucleating centers and inhibits their coalescence. It results in the breaking of the columnar structure and nucleating of the grains with different texture. Eventually, at a high concentration of oxygen molecules, the formation of the aluminum oxide matrix with metallic inclusions is observed.

The substrate temperature and content of the gas atoms influence the formation of the film structure only at the initial stage. At this stage, the density of nucleation centers is determined mainly by the surface diffusion coefficient. For equiaxial nanocrystalline structure creation, it is necessary to speed up the bulk diffusion in the film at the stage of its growth. It can be achieved by ion-stimulation processing of the film.

The bombardment of the deposited film by 0.02–2 keV energy ions, the generation of the radiation-induced defects not more than 1–10 displacements per atom, takes place. It gives the intensification of diffusion processes and the introduction of gas ions to a depth of 5–10 nm. As a result, the reduced intergranular porosity and increased density of the film are observed. The additional spaces for the grains nucleation appear on the surface of the growing film, which in turn leads to grain size decrease and inhibition of columnar structure growth [4–6].

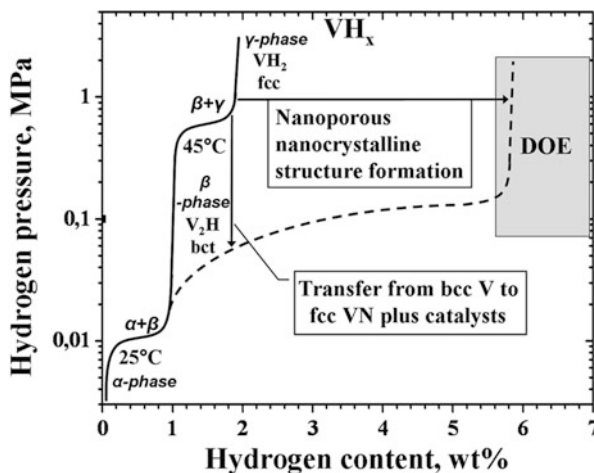
However, the best opportunities for the nanocrystalline film creation arise if the substrate is bombarded by gas ions of energies more than 10 keV during the metal vapor deposition. This combination of metal evaporation with the ion irradiation is implemented in the ion beam-assisted deposition technology, so-called IBAD method [7–11]. Ions with such energies create during bombardment of the deposited film a large number of defects, on which the grain nuclei are formed. Consequently, the nanocrystalline structures with grain size that does not exceed 10 nm are formed [10–12].

Hydrides on the base of vanadium, the, respectively, light transition metal, are considered to be perspective for usage as solid-state hydrogen storages. The total mass of stored hydrogen in them reaches the value of 2.1 wt.%. At that the amount of absorbed hydrogen atoms in  $\text{VH}_2$  is essentially more than, for example, in  $\text{MgH}_2$  hydride (11.2 in  $\text{VH}_2$  vs. 2.5 wt.% in  $\text{MgH}_2$ , at./ $\text{cm}^3$ ,  $\times 10^{22}$ ) [13].

The V-H system includes the following phases:  $\alpha$ , solid solution;  $\beta$ ,  $\text{VH}_{0.45}$ – $\text{VH}_{0.95}$ ; and  $\gamma$ ,  $\text{VH}_2$ . The  $\beta + \gamma$  phase mixture is in the  $\text{VH}_{1.0}$ – $\text{VH}_{2.0}$  concentration range. The  $\text{V}_2\text{H}$ ,  $\text{V}_3\text{H}_2$ , and  $\text{V}_4\text{H}_3$  ordered structures are revealed in the homogeneity range of the  $\beta$ -phase. The  $\beta$ -phase has the body-centered tetragonal (bct) lattice; the  $\text{VH}_{1.77}$  nonstoichiometric phase has fcc lattice.

Due to the existence of several V-H phases with different crystal structures, several plateaus related to the phase transitions have to appear on the P-C-T diagram (Fig. 53.1). The figure also shows the possible ways of the improvement of the absorptive properties of vanadium hydride, such as nanoporous structure formation (increasing of the gravimetric capacity), hydride phase stabilization by means of complex  $\text{VN}_x\text{H}_y$  hydride formation, and development of the additional hydrogen traps (the improvement of the thermodynamic and kinetic properties).

**Fig. 53.1** Pressure-concentration constitution diagram for hydride  $VH_x$  (summarized data from [14]). Dot line is related to the state when this hydride may be used as hydrogen storage. The receipts for this state achievement are shown



The aim of this study is to investigate the structure of V-N films prepared using the ion-assisted deposition technology.

## 53.2 Experimental Procedure

Nanocrystalline  $VN_x$  porous thin films were obtained by evaporation of vanadium from electron beam crucible at the simultaneous irradiation by mixed beam of helium and nitrogen ions ( $N_2^+/He^+ = 1$ ) with energy of 30 keV. The ratio between the speeds of vanadium atom deposition and gas ion implantation was 0.5 at./ion. The film deposition was conducted onto the NaCl substrate at 200 °C. Thin carbon film was deposited on the substrate before the vanadium evaporation. During the vanadium film deposition, the parts of the substrate were sequentially overlapped by shutter at regular time intervals. The set of films with a thickness from 5 up to 25 nm was obtained.

In addition, the films of 1.5  $\mu\text{m}$  thickness and  $1.5 \times 1.5$  cm area were deposited on sapphire and silicon substrates. The structure of the films deposited on silicon and NaCl substrates was investigated by means of JEM 100CX transmission and JSM 7001F scanning electron microscopes.

## 53.3 The Results of the Experiments

### 53.3.1 The Initial Stage of Film Formation

The inhomogeneity zone is always observed in the surface layer of deposited film at its bombardment by gas ions with energy of some tens of keV. The number

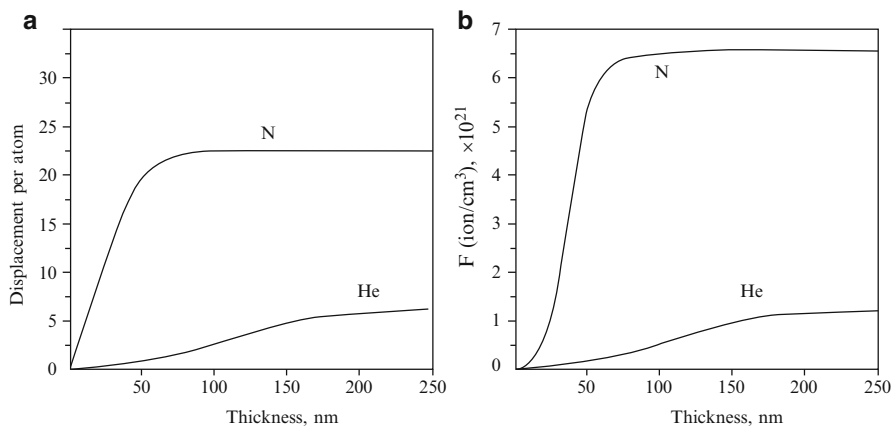


**Fig. 53.2** Thickness dependencies of damage distribution (displacement per atom) (a) and implanted helium and nitrogen atoms (b) in the V-N-He film.  $j(\text{N}_2^+, \text{He}^+) = 10^{14}$  ion/cm<sup>2</sup>·sec

of generated defects and implanted gas concentration was increased successively deep inside the zone starting from the film surface. The extent of this zone is determined by the path depth of ions used for the bombardment of deposited material. For example, an extent of this heterogeneity zones for 30 keV-nitrogen ions is  $\sim 70\text{--}80$  nm [7]. Accordingly, the structure of the film, at the nucleation stage and after its thickness has exceeded 80 nm, is different. Therefore, the zone of structural heterogeneity seems to be a good subject for investigation of the mechanisms of nanoporous structure formation at the bombardment by medium-energy gas ions.

Using SPURT program as described previously [15], we performed a mathematical modeling of the defect formation (Fig. 53.2a) and ion implantation of nitrogen and helium (Fig. 53.2b) processes in the deposited vanadium film.

Figure 53.2a shows that most of the damages in the film at all stages of deposition arise from the nitrogen ions. Moreover, the impact of the nitrogen ions on the structure and composition of the vanadium film ends at a depth of 80 nm. The level of damage at the thickness of more than 80 nm increases slightly and exclusively due to helium ions. The quantity of implanted nitrogen at such thicknesses is not changed, and the helium concentration increases almost tenfold. At a depth of 250 nm, the calculated concentration of helium in vanadium film is similar to the nitrogen concentration at a depth of  $>80$  nm, namely,  $6.5 \cdot 10^{21}$  ions/cm<sup>3</sup>. Thus, calculations show that the structure and composition of the film of less than 80 nm thickness are determined by the concentration and amount of radiation defects generated by nitrogen ions. In the thickness range of 80–250 nm, the film structure can be transformed due to implanting helium ions. Total estimated amount of nitrogen and helium in the vanadium film of the thickness  $> 250$  nm should not exceed 12.0 at.%.

Figure 53.3a–f shows the electron microscopic images of VN<sub>x</sub> films at the initial stage of their growth. Figure 53.3e demonstrates the same piece of the 20-nm-thick

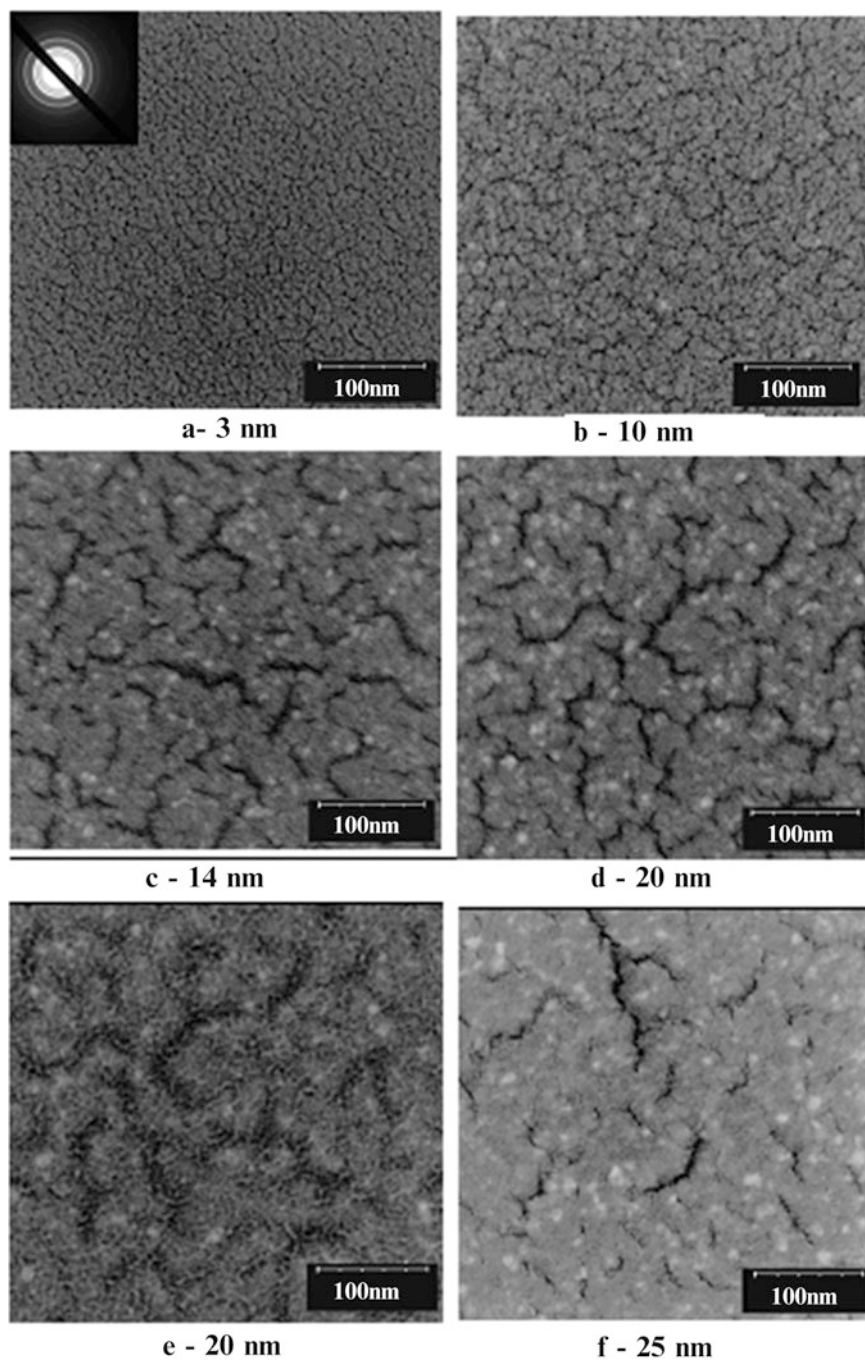


**Fig. 53.3** Electron microscopy images of VN<sub>x</sub> film structure at different deposition stages (the estimations for all film thicknesses are given)

film as the Fig. 53.3d but at the different electron beam focusing. All figures present the negative images for better visualization of the grain boundaries and pores. It is seen that the films are solid even at the thickness of 5 nm. They have nanocrystalline structure with the grain size of 10–15 nm. Grains are arranged in a single layer; 3–5 nm pores are observed almost in all triple and quartic intergranular joints.

The specific ruptures of 100 nm in length and ~10–15 nm in width appear in film starting from the thickness of 15 nm (Fig. 53.3c). There are large enough (~50–150 nm) areas (hereinafter referred to as particles) that are visible between the adjacent ruptures. Blocks display heterogeneous structure and consist of nanograins separated by porous boundaries. Filling the ruptures by the grains of new population (Fig. 53.3e–f) takes place simultaneously with the subsequent layer formation. Their average size is approximately the same as the size of the grains inside the particle, namely, ~15–20 nm. At the film thickness more than 30–40 nm, the ruptures are completely filled by nanograins, and formation of the subsequent layer of particles and grains begins.

The crystal structure of  $VN_x$  films at all stages of their formation corresponds to the fcc structure of vanadium nitride.

### 53.3.2 *The Structure of Already Formed $VN_x$ Films of 1.5 $\mu m$ Thickness*

Figure 53.4a–b shows SEM and TEM images of  $VN_x$  films deposited on silicon substrates. In the first case, the electron beam was directed at the film surface. In the second case, the research subject was prepared by ion thinning of the end face of the substrate with the deposited film. It can be seen (Fig. 53.4a) that the film structure consists of the particles with a diameter of 150–250 nm. Particles are nonhomogeneous and consist of grains of irregular shape and the size of 10–20 nm arbitrarily distributed in space.

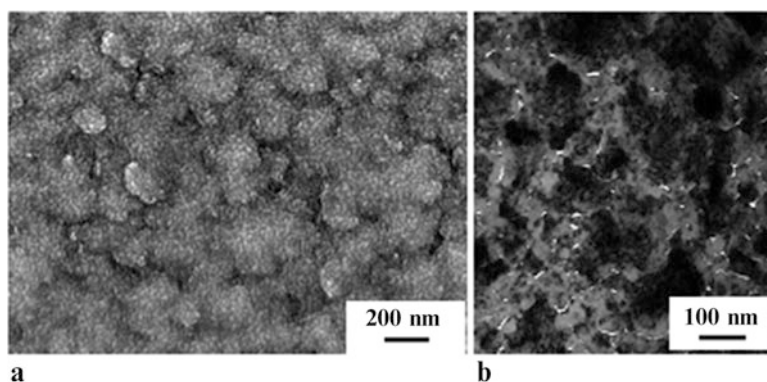


**Fig. 53.4** The structure of the surface (a), particles, and interparticle boundaries (b) of already formed  $VN_x$  of the film

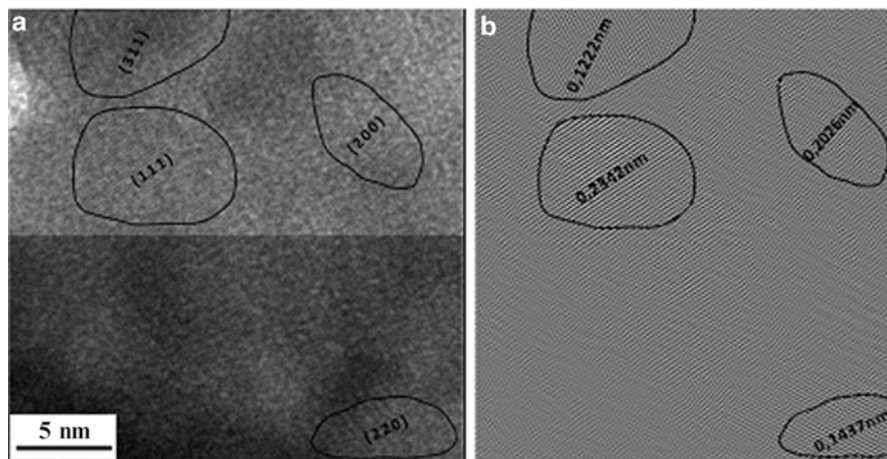


**Fig. 53.5** TEM image inside the particle structure of VN<sub>x</sub> film (a) and its Fourier transformation (b)

The results of TEM study shown in Fig. 53.4b confirm the SEM investigation data. The particles are not homogeneous formations and consist of nanograins. The boundaries between particles are loose; and the connections of 3–4 particles contain pores of 5–10 nm in size.

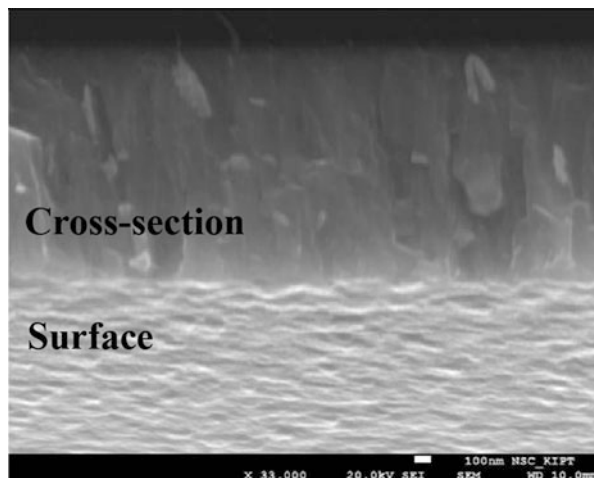
In order to explore the structure and orientation of the individual grains in detail, the high-resolution TEM was used. Figure 53.5a shows the area inside a single block. It can be seen that the block consists of nanograins of 5–15 nm size. Moreover, the crystallographic planes in each grain are arbitrarily oriented with respect to the perpendicular of the film plane.

It is difficult to calculate with high accuracy the interplanar spacings in each individual grain using Fig. 53.5a. The particle morphology and size distribution were analyzed by transmission electron microscopy (JEOL 2100) that was operated at 200 kV. Using the Digital Micrograph Ver. 3.10.0 (Gatan) program, a fast Fourier transform (FFT) pattern of the high-resolution TEM (HRTEM) image was obtained. Figure 53.5b demonstrates the results of these investigations. It can be seen that the grains are randomly distributed in the particle volume. Parameter of fcc crystal lattice of VN<sub>x</sub> film calculated on the base of interplanar spacing was 0.4052 nm.

## 53.4 Results and Discussion

Vanadium deposition under the ion-stimulated bombardment with working ion source occurs at a total pressure of nitrogen and helium in the chamber equaled to  $(1.5\text{--}2.0) \times 10^{-3}$  Pa. At this pressure, the continuous adsorption of nitrogen molecules and helium atoms by the substrate surface is taking place simultaneously

**Fig. 53.6** SEM image of the crosscut and the surface of  $\text{VN}_x$  film



with the vanadium vapor deposition. Moreover, at such experimental conditions, the rate of gas adsorption is not less than the speed of vanadium deposition. The partial dissociation of nitrogen molecules is in process at ion bombardment. Taking into account that Gibbs free energy of vanadium nitride formation is rather low [16], an ongoing chemisorption of nitrogen atoms and formation of vanadium nitride occur. This may explain the vanadium nitride appearance at very early stages of film growth.

Physical adsorption of nitrogen molecules leads to the inhibition of diffusion processes on the film surface. As a result, there is a large-scale nucleation of small grains poorly oriented relatively to each other whose boundaries are saturated with nitrogen molecules and helium atoms. Radiation-induced diffusion of adsorbed gas atoms implanted at the irradiation stimulates the steady flow of gas molecules and atoms to the grain boundaries. At a certain stage of the film growth, the amount of gas impurities in grain boundaries and in triple grain boundary intersections becomes sufficient for boundary destruction and for the formation of ruptures of 50–100 nm in length (Fig. 53.3b–d). This size is very close to the size of particles shown in Fig. 53.4. Therefore, we believe that the formation of randomly distributed particles is associated with the formation of such ruptures. The nucleation of new grain population in the fracture places prevents the formation of continuous columnar structure that is characteristic for the film deposition at a low-energy ion bombardment [4–6]. Figure 53.6 shows the corresponding image of  $\text{VN}_x$  film crosscut.

Quantitative analysis of the SEM results revealed that the nitrogen concentration in  $\text{VN}_x$  films does not exceed 10 at.%, although the selected area electron diffraction analysis shows the presence of nitride phase at all stages of film growth.

As noted above, the vanadium nitride formation at the initial stages of film growth may occur due to the adsorption of nitrogen molecules from the volume inside the vacuum chamber, their dissociation, and nitride phase formation. The structure of



VN<sub>x</sub> film forming during the ion bombardment is nanocrystalline. Therefore, it is not necessary to provide the equal amounts of vanadium and nitrogen for the nitride phase formation in such small grains.

It is known that during the transition from a polycrystalline to a nanocrystalline structure, the fraction of the grain surface area in which the equilibrium vacancy concentration is different from concentration in “bulk” sample increases. The equilibrium concentration of vacancies in the small size particle depends on the particle size (*r*) as follows [17]:

$$C_s = C_v \exp(3\sigma\Omega/rkT),$$

where  $\sigma$  is the surface energy, and  $\Omega$  is the atomic volume.

It follows from this expression that the equilibrium concentration of vacancies in small size particles may exceed significantly the concentration of vacancies in the “bulk” samples. A similar relationship exists for the diffusion coefficients too.

Increase in the equilibrium concentration of vacancies in nanograins of two-component structure, which is the vanadium nitride, can occur exclusively at the expense of nitrogen atom. Consequently, VN stoichiometric compound exists only in the central region of grains, and the nitrogen is virtually nonexistent in the grain boundaries. In this spirit, we believe that vanadium nitride with fcc lattice exists in our films in form of nonstoichiometric compound VN<sub>x</sub> ( $x < 1$ ).

Helium ions during film deposition penetrate deeper than a typical particle size, namely, up to 250 nm (Fig. 53.1b). To determine their concentration, we used the data obtained by Rutherford backscattering and the thermal desorption spectra analysis. Helium was not found. The lack of helium indicates a good gas permeability of formed porous nanocrystalline structure. The successive accumulation of helium atoms implanted by ion beam in film region which is at a distance of 80 to 250 nm from its surface takes place during VN<sub>x</sub> film growth. As a result, the local heating of the film in the damage zone and helium pressure increase in it take place. Helium implanted in nanograins can easily move to the grain and interparticle boundary surfaces and finally leave the volume of the film due to the high equilibrium concentration of vacancies in the nanograins and radiation-induced diffusion. Thus, the helium role in the creation of solid-state VN<sub>x</sub> hydrogen storage is to form the structure of nanopores united by intergranular and interparticle boundaries. The nitrogen role is to create vanadium bcc structure that is denser than nanocrystalline fcc structure of VN<sub>x</sub>.

At the physical adsorption of hydrogen by such structures, the rapid filling of grain boundaries and pores takes place. Further, a partial dissociation of the hydrogen molecules in the grain boundaries and the hydrogen atoms' diffusion into them occur with the increase of pressure in the pores. The selected area electron diffraction data have not revealed the hydride phase appearance. Therefore, the most likely and effective traps for hydrogen atoms are the vacant positions in VN<sub>x</sub> lattice. It was shown for TiC<sub>x</sub> [18, 19] that the greater the degree of deviation from stoichiometry ( $x < 0.6$ ) is observed, the greater amount of hydrogen atoms can be accumulated within the crystal lattice.



The configuration of nanopores in investigated film structures is not just a system of voids that directly traverse each other (it is peculiar for metal-organic and carbon film structures). In the present case, the pores are interconnected by relatively long intergranular boundaries of width that does not exceed 1 nm. This value is very closely related to the most optimal (0.6 nm) design size at which hydrogen will be retained in its molecular state [20]. The availability of such branched pore system connected by narrow and long channels provides the rapid delivery of molecular hydrogen to the film volume and its retention at room temperature.

### 53.5 Conclusion

The results given in this paper show that the use of IBAD method allows not only the controlled formation of nanoporosity with prescribed parameters but also the embedment of this nanoporosity into the nanocrystalline structure of a matrix. The material produced under such a method is capable to accumulate hydrogen at low pressures and room temperature. In particular, we have shown earlier that these structures can absorb the hydrogen up to 7 wt. % and release it in the temperature range of 50–275°C [12, 16]. The availability of broad channels between grains provides high diffusion mobility, which allows accumulating the hydrogen and releasing it from material within a short period of time. The formed structure accumulates hydrogen both in nanopores and in the vacant sites inside  $VN_x$  grains. Varying the basic parameters of the ion beam-assisted process and firstly its radiation component, it is possible to produce nanocrystalline porous structures in which the grain size can be both higher and lower than the pore diameter. It was the certain relationship between the sizes of the elements of crystalline structure that allows the production of solid-state hydrogen storages with required properties.

### References

1. Movchan BA, Demchishin AV (1969) Issledovanie struktury i svoystv tolstykh vakuumnykh kondensatov nikelya, titana, volframa, okisi alyuminiya i dnuokisi tsirkoniya (investigation of the structure and properties of the thick vacuum condensates of nickel, titanium, tungsten, aluminum oxide and zirconium dioxide). *ФММ (Phys Met Metallogr, Rus)* 28:653–660
2. Thornton JA (1974) Influence of apparatus geometry and deposition conditions on the structure and topography of thick sputtered coatings. *J Vac Sci Technol* 11:666–670. doi:[10.1116/1.1312732](https://doi.org/10.1116/1.1312732)
3. Barna PB, Adamik M (1998) Fundamental structure forming phenomena of polycrystalline films and the structure zone models. *Thin Solid Films* 317:27–33. doi:[10.1016/S0040-6090\(97\)00503-8](https://doi.org/10.1016/S0040-6090(97)00503-8)
4. Greene JE, Barnett SA, Sundgren JE, Rockett A (1989) Ch.5. Ion beam assisted film growth. Elsevier, Amsterdam, pp 101–152. doi:[10.1016/B978-0-444-87280-7.50010-9](https://doi.org/10.1016/B978-0-444-87280-7.50010-9)
5. Petrov I, Barnam P, Hultmann L, Greenem J (2003) Microstructural evolution during film growth. *J Vac Sci Technol A* 21:S117–S128. doi:[10.1116/1.1601610](https://doi.org/10.1116/1.1601610)

6. Dhara S (2007) Formation, dynamics and characterization of nanostructures by ion beam irradiation. *Crit Rev Solid State Mater Sci* 32(1–2):1–50. doi:[10.1080/10408430601187624](https://doi.org/10.1080/10408430601187624)
7. Guglya A, Marchenko I (2015) Ion beam-assisted deposition. In: *Comprehensive guide for nanocoatings technology*, vol 1. NOVA press, USA, pp 45–69
8. Ensinger W (1997) Low energy ion assists during deposition – an effective tool for controlling thin film microstructure. *Nucl Instr Meth Phys Res B* 127-128:796–808. doi:[10.1016/S0168-583X\(97\)00010-4](https://doi.org/10.1016/S0168-583X(97)00010-4)
9. Wolf G (1992) Modification of chemical properties of materials by ion beam mixing and ion beam assisted deposition. *J Vac Sci Tech A* 10(4):1757–1764. doi:[10.1116/1.577743](https://doi.org/10.1116/1.577743)
10. Guglya A, Marchenko I, Neklyudov I (2003) Chromium film deposition stimulated by nitrogen ions implantation with energies up to 30 keV. *Surf Coat Tech* 173-174:1248–1252. doi.org/[10.1016/S0257-8972\(03\)00605-4](https://doi.org/10.1016/S0257-8972(03)00605-4)
11. Volz K, Kiuchi M, Ensinger W (1998) Structural investigations of chromium nitride films formed by ion beam-assisted deposition. *Surf Coat Tech* 108-109:303–307. doi:[10.1016/S0257-8972\(98\)00565-9](https://doi.org/10.1016/S0257-8972(98)00565-9)
12. Goncharov A, Guglya A, Melnikova E (2012) On the feasibility of developing hydrogen storages capable of adsorption hydrogen both in its molecular and atomic states. *Int J Hydrogen Energy* 37:18061–18073. doi.org/[10.1016/j.ijhydene.2012.08.142](https://doi.org/10.1016/j.ijhydene.2012.08.142)
13. Jain I, Vijay Y, Malhotra L, Uppadhyay K (1988) Hydrogen storage in thin film metal hydride – a review. *Int J Hydrogen Energy* 13:15–23. doi:[10.1016/0360-3199\(88\)90005-5](https://doi.org/10.1016/0360-3199(88)90005-5)
14. Papathanassopoulos K, Wenzl H (1982) Pressure-composition isotherms of hydrogen and deuterium in vanadium films measured with a vibrating quartz microbalance. *J Phys F* 12:1369–1381. doi:[10.1088/0305-4608/12/7/009](https://doi.org/10.1088/0305-4608/12/7/009)
15. Bendikov V, Guglya A, Marchenko I, Malykhin D, Neklyudov I (2003) Mechanisms of forming the Cr-N composite in the unsteady-state stage of ion beam-assisted deposition process. *Vacuum* 70:331–337. doi:[10.1016/S0042-207X\(02\)00666-8](https://doi.org/10.1016/S0042-207X(02)00666-8)
16. Guglya A, Lyubchenko E, Marchenko Y, Solopikhina E, Vlasov V (2016) Crystal lattice of solid body can store simultaneously both molecules and atoms of hydrogen in quantities. *Int J Hydrogen Energy* 41:9410–9411. doi:[10.1016/j.ijhydene.2016.03.181](https://doi.org/10.1016/j.ijhydene.2016.03.181)
17. Gladkih NT (ed) (2004) *Poverhnostnyie yavleniya i fazovyye prevrascheniya v kondensirovannykh plenках* (surface phenomena and phase transitions in condensed films). Kh. Nation. Univer, Kharkov
18. Gringoz A, Glandu N, Valette S (2009) Electrochemical hydrogen storage in TiC<sub>0.6</sub>, not in TiC<sub>0.9</sub>. *Electrochem Commun* 11:2044–2047. doi:[10.1016/j.elecom.2009.08.049](https://doi.org/10.1016/j.elecom.2009.08.049)
19. Ding H, Fan X, Li C, Liu X, Jiang D, Wang C (2013) First-principles study of hydrogen storage in non-stoichiometric TiC<sub>x</sub>. *J Alloys Compd* 551:67–71. doi:[10.1016/j.jallcom.2012.10.067](https://doi.org/10.1016/j.jallcom.2012.10.067)
20. Carbia I, Lopez M, Alonso J (2007) The optimum average nanopore size hydrogen storage in carbon nanoporous materials. *Carbon* 45:2649–2658. doi:[10.1016/j.carbon.2007.08.003](https://doi.org/10.1016/j.carbon.2007.08.003)

# Chapter 54

## Magnetic Nanocomposite Sorbents on Mineral Base

Oksana Makarchuk , Tetiana Dontsova , and Anatolii Perekos 

### 54.1 General

#### 54.1.1 Introduction

Sorption purification is the most commonly used and suitable for adaptation to industrial conditions technology [1–3]. The high sorption capacity of sorbent minerals including clay minerals is provided by their colloidal dispersion. But in wastewater treatment process, the problem of removing spent sorbent particles from the aquatic environment is appeared.

Classical separation methods of sorbent sludge from purified water like centrifugation, filtration, upholding, coagulation, and flocculation processes are unacceptable in industrial-scale purification. Centrifugation is too energy intensive and, therefore, costly process. Filtration in this case is complicated from engineering and technological point of view due to the high dispersion of sorption material. Purification by upholding is a too long process. The destabilization of wastewater suspension by coagulation and flocculation processes requires the use of large number of different reagents. The cost of reagents calls into question the economic viability of this technology. In addition, none of these conventional methods can guarantee elimination of secondary water pollution risk [4].

---

O. Makarchuk (✉) • T. Dontsova  
National Technical University of Ukraine “Kyiv Polytechnic Institute”, Kyiv, Ukraine  
e-mail: [xtfhn9207@ukr.net](mailto:xtfhn9207@ukr.net); [dontsova@ua.fm](mailto:dontsova@ua.fm)

A. Perekos  
Institute of Magnetism of the NAS of Ukraine and Ministry for Education and Science of Ukraine, Kyiv, Ukraine  
e-mail: [perekos@ukr.net](mailto:perekos@ukr.net)

In [5] the profitability of magnetic separation, process in wastewater filtering of the steel-making company was calculated. It was found that the removal of suspended particles from the water medium in the magnetic filter was 24 times faster compared to conventional filter with the same level of capital expenditures, operating costs, and occupied production area.

The process of magnetic separation can be realized in a magnetic field created by a permanent magnet or an electromagnet. In implementing purification technology in industrial level, an external magnetic field created by using permanent magnets is acceptable, because in this case, the magnetic field strength does not require constant electricity consumption [6, 7].

Magnetic separation process can be adapted to the adsorption technology of purification by [8]:

Direct adsorption of pollutants on magnetic particles

Introduction of a magnetic modifier as flocculant for magnetic particle coagulation of spent sorbent

Application of magnetic composite sorbents

Magnetic iron oxides are costly and not porous sorbents. The combination of processes of contaminants adsorption on magnetic particles, magnetic separation, and flocculation is a complex problem, which includes a significant number of manufacturing operations and requires the use of a large amount of equipment and production areas. Among these methods, the most technologically and economically favorable form of magnetic support of sorption treatment is the use of magnetic composite sorbents [9, 10].

Manageability of ferromagnetic particle deposition process in a magnetic field is determined not only by their size and magnetic characteristics but the magnetic nature of the matrix in which they are stabilized [11]. The clays are paramagnetic substances, and in magnetic separator, their mineral matrices are magnetized in the direction of the external magnetic field. Such feature of clays provides the decisive influence to choose them as a basis for magnetic composite sorbent creation [12].

This study shows the results of the physical, chemical, and magnetic properties of composite magnetic-controllable sorbents based on clays, and it presents an assessment of effectiveness to their use in magnetic field.

### **54.1.2 Materials and Methods**

Magnetic composite sorbents were prepared by impregnation method. The natural saponite, palygorskite, and spondyle clays were sieved to the particle size less than 230 meshes (63  $\mu\text{m}$ ) and dispersed in magnetic fluid. The obtained mixture was mechanically stirred for 30 min in order to adsorb  $\text{Fe}_3\text{O}_4$  on the surface and pores of clay. The synthesized sorbent was separated in magnetic filter at magnetic induction of external magnetic field of 66 mT and dried at 60–80 °C for 1 day.

Thus, samples of magnetic sorbents (MC) based on saponite (MCSp-4, MCSp-7, MCSp-10), palygorskite (MCP-4, MCP-7, MCP-10), and spondyle clays (MCSd-4, MCSd-7, MCSd-10) containing 4 wt.%, 7 wt.%, and 10 wt.% of magnetite were obtained.

Measurement of mass concentration of chemical elements in sample MC was carried by nondestructive energo-dispersive roentgen analysis method without standards using analyzer EXPERT 3 L.

Powder X-ray diffractions (XRD) of all sorbent samples were recorded using a Rigaku Ultima IV diffractometer using Cu K $\alpha$  radiation at 40 KV, 30 mA. Orientated samples were scanned from 2° to 162° 2-theta at 1°/min with a scanning step of 0.0001°/step. Crystallographic Open Database (COD) was applied for phase composition definition of sorbents. The crystallite sizes and the unit cell parameters of magnetite and magnetite in magnetic composites were calculated with software package PDXL using the Scherrer's formula.

The morphologies of the synthesized products were observed using a scanning electron microscope (SEM 106 M).

Magnetic properties of nanocomposites (specific magnetization  $\sigma_s$  (A•m<sup>2</sup>/kg); magnetic field strength  $H_c$  (A/m); magnetic induction  $B_r$  (mT)) were determined by ballistic magnetometer of Steinberg.

High-gradient magnetic separation of MC and native clays was studied in magnetic filter. Magnetic induction of external magnetic field was 66 mT. The residual concentrations of suspended sorbent particles in an aqueous medium through 5, 30, and 60 min of magnetic separation were determined by turbidimetry method.

## 54.2 Experimental

### 54.2.1 Chemical Analysis

Measurements of chemical composition in the sorbent samples were carried out by nondestructive energy-dispersive XRF analysis without standards and results listed in the Table 54.1 (MCSp and saponite clay), Table 54.2 (MCP and palygorskite clay), and Table 54.3 (MCSd and spondyle clay).

The results of elemental composition analysis of MC and natural clays showed the directly proportional growth of Fe concentration in depending on the increase of Fe<sub>3</sub>O<sub>4</sub> content in composites at a relatively constant concentration of the basic elements of crystal clay lattice Mg, Al, Si, and Ca.

### 54.2.2 X-ray Analysis

Powder X-ray diffractions of magnetite, MC, and natural clays were recorded using a Rigaku Ultima IV diffractometer. The corresponding diffraction patterns are

**Table 54.1** Chemical analysis of the composites MCSp and saponite clay

Chemical element	Saponite	MCSp-4	MCSp-7	MCSp-10
	Content, % wt.			
Mg	5.34–7.18	4.09–6.23	4.69–5.61	3.64–5.14
Al	4.90–5.76	3.77–4.97	1.19–2.15	1.57–2.33
Si	20.68–22.67	20.32–22.40	18.44–20.06	15.92–17.42
S	0.00–0.18	0.14–0.36	0.02–0.04	0.02–0.04
Ca	24.57–26.86	17.83–19.84	15.54–17.81	14.27–16.17
Ti	2.22–2.98	2.38–2.59	1.22–2.43	1.35–1.97
V	0.15–0.20	0.20–0.29	0.10–0.19	0.11–0.21
Mn	0.87–1.21	0.69–0.77	0.73–0.82	0.56–0.65
<i>Fe</i>	<i>35.94–37.35</i>	<i>45.30–47.17</i>	<i>52.75–55.47</i>	<i>57.28–60.71</i>
Ni	0.05–0.12	0.05–0.07	0.06–0.09	0.06–0.08
Cu	0.11–0.14	0.08–0.10	0.07–0.10	0.09–0.11
Zn	0.09–0.18	0.10–0.11	0.10–0.12	0.10–0.12
Sr	0.05–0.1	0.03–0.05	0.05–0.06	0.02–0.03

**Table 54.2** Chemical analysis of the composites MCP and palygorskite clay

Chemical element	Palygorskite	MCP-4	MCP-7	MCP-10
	Content, % wt.			
Al	4.48–5.79	5.42–6.72	4.65–5.97	4.70–6.24
Si	52.22–55.12	42.69–45.51	43.48–45.42	41.83–44.02
S	0.20–0.50	0.15–0.20	0.05–0.09	0.07–0.15
Cl	2.36–3.37	0.37–1.59	0.84–1.05	0.52–1.14
Ca	6.56–8.75	6.07–7.93	2.58–4.97	2.42–3.72
Ti	1.79–2.03	1.13–1.56	0.72–0.99	0.63–1.26
Mn	0.15–0.22	0.20–0.26	0.19–0.26	0.11–0.15
<i>Fe</i>	<i>26.97–28.83</i>	<i>38.58–40.73</i>	<i>42.20–45.83</i>	<i>44.49–48.01</i>
Zn	0.07–0.09	0.08–0.10	0.06–0.08	0.07–0.09
Sr	0.08–0.11	0.11–0.13	0.06–0.09	0.06–0.07
Rb	0.02–0.04	0.04–0.05	0.03–0.04	0.02–0.03
Zr	0.05–0.06	0.08–0.10	0.09–0.11	0.04–0.05
Pb	0.05–0.08	0.09–0.12	0.06–0.09	0.05–0.07

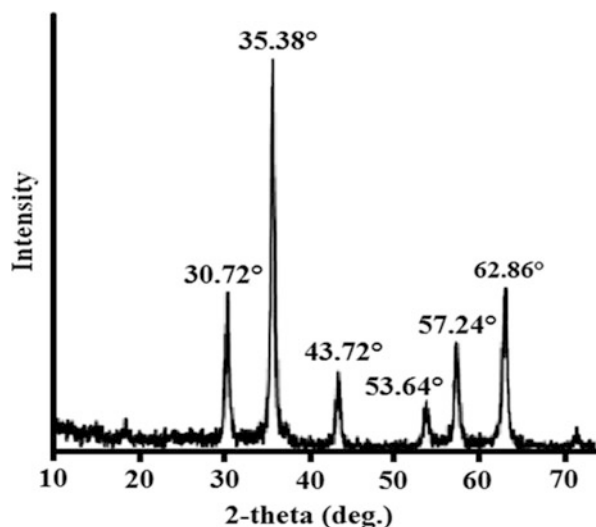
presented in Fig. 54.1 (magnetite), Fig. 54.2 (MCSp and saponite clay), Fig. 54.3 (MCP and palygorskite clay), and Fig. 54.4 (MCSd and spondyle clay).

Diffraction pattern of magnetite (Fig. 54.1) demonstrated strong peaks at 30.72 °, 35.38 °, 43.72 °, 53.64 °, 57.24 °, and 62.86 ° 2-theta attributed to the Fe<sub>3</sub>O<sub>4</sub> (card № 01–071-6336). No other impurities were observed. Hence, the method of Elmore allows obtaining the pure magnetic-modifying agent.

The XRD pattern of the native saponite (Fig. 54.2a) had indicated peaks that correspond to saponite (card № 00–013-0305), montmorillonite (card № 00–002-0014), quartz (card № 00–001-0649), and calcite (card № 00–002-0623). The crystal plane diffraction peaks of composite sorbent MCSp-4 (Fig. 54.2b), MCSp-7 (Fig. 54.2c), and MCSp-10 (Fig. 54.2d) detected the presence of inherent phases of native saponite clay and found peaks that corresponded to Fe<sub>3</sub>O<sub>4</sub>.

**Table 54.3** Chemical analysis of the composites MCSd and spondyle clay

Chemical element	Spondyle clay	MCSd-4	MCSd-7	MCSd-10
	Content, % wt.			
Si	19.26–23.08	21.37–24.34	20.25–22.53	18.35–20.93
S	1.07–1.47	0.67–0.88	0.54–0.73	0.60–0.98
Cl	1.17–1.45	0.35–0.55	0.39–0.48	0.81–1.08
Ca	56.54–59.37	45.53–49.04	40.70–45.29	36.23–39.10
K	3.59–3.72	3.16–3.95	2.81–2.91	2.51–2.62
Ti	2.01–2.23	1.61–1.81	1.38–1.52	1.07–1.25
<i>Fe</i>	<i>11.05–13.32</i>	<i>21.92–23.97</i>	<i>28.57–31.12</i>	<i>35.15–38.70</i>
Zn	0.04–0.05	0.04–0.05	0.03–0.04	0.03–0.04
Sr	0.18–0.19	0.24–0.26	0.21–0.22	0.16–0.17
Rb	0.03–0.04	0.04–0.05	0.04–0.05	0.03–0.04
Zr	0.05–0.06	0.07–0.08	0.06–0.08	0.06–0.08
Pb	0.02–0.03	0.02–0.03	0.02–0.03	0.01–0.02

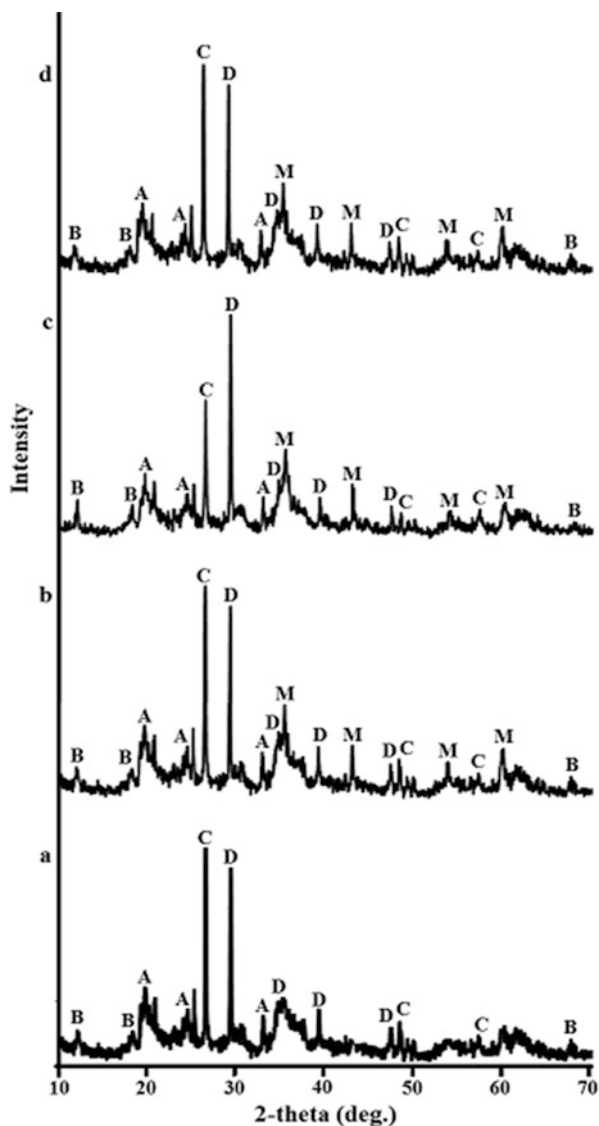
**Fig. 54.1** The XRD patterns of magnetite  $\text{Fe}_3\text{O}_4$ 

The XRD pattern of native palygorskite (Fig. 54.3a) consists of peaks that correspond to own palygorskite (card № 01–082-1872) and quartz (card № 00–001-0649). Diffraction patterns (Fig. 54.3b–d) confirmed the presence of magnetite in the presence of native clay phases in the composition of sorbents MCP-4, MCP-7, and MCP-10, respectively.

According to the X-ray diffraction analysis presented in Fig. 54.4a, spondyle clay consists of two minerals such as augite (card № 01–088-0831) and pigeonite (card № 01–087-0693). Phase composition of samples MCSd-4, MCSd-7, and MCSd-10 differs from native spondyle clays by the presence of magnetite peaks, which are identified in the Fig. 54.4b–d, respectively.

The X-ray analysis results of magnetic composites, native clay minerals, and magnetite phase confirmed stability of the mineral base and a magnetic modifier in the composition of obtained sorbents. As shown in the Figs. 54.2, 54.3, and 54.4,

**Fig. 54.2** The XRD patterns of saponite clay (**a**), MCSp-4 (**b**), MCSp-7 (**c**), and MCSp-10 (**d**): A, saponite  $\text{NaMg}_3[\text{AlSi}_3\text{O}_{10}](\text{OH})_2 \cdot 4\text{H}_2\text{O}$ ; B, montmorillonite  $\text{NaMgAlSi}_2(\text{OH}) \cdot \text{H}_2\text{O}$ ; C, quartz  $\text{SiO}_2$ ; D, calcite  $\text{CaCO}_3$ ; M, magnetite  $\text{Fe}_3\text{O}_4$

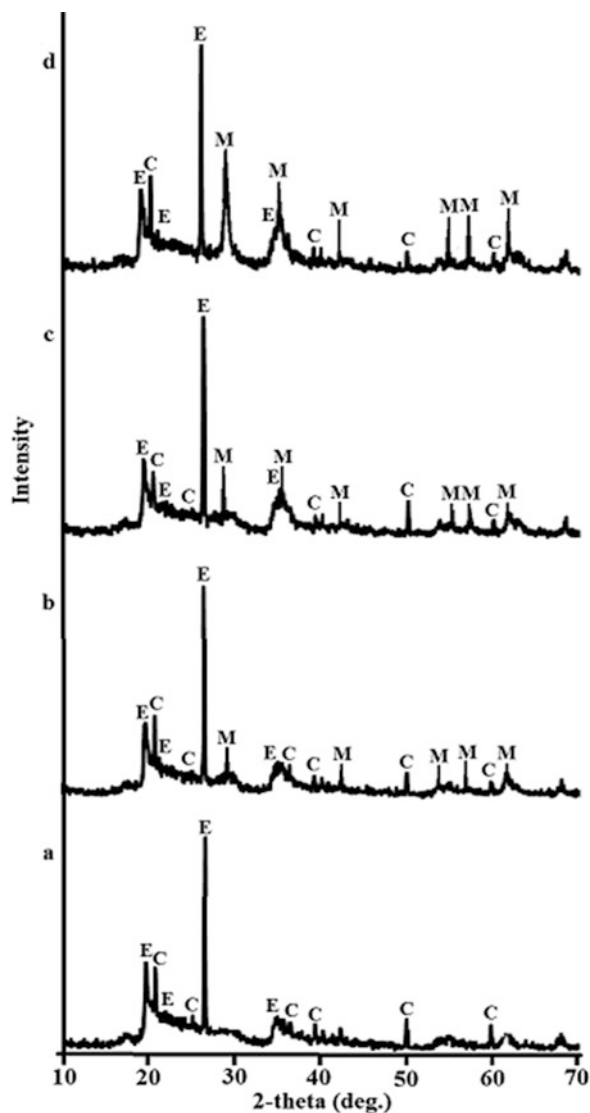


the increasing of peak intensity of magnetite is corresponded with increasing of magnetic modifier content in the MC samples from 4% wt. to 10 wt. Thus, as a result of composite synthesis, the phase composition of different natural sorption materials such as saponite, palygorskite, and spondyle clays was retained and supplemented by magnetic oxide  $\text{Fe}_3\text{O}_4$ .

The XRD patterns of MC and magnetite were automatically analyzed by software package PDXL using COD. The crystallite sizes and the unit cell parameters of



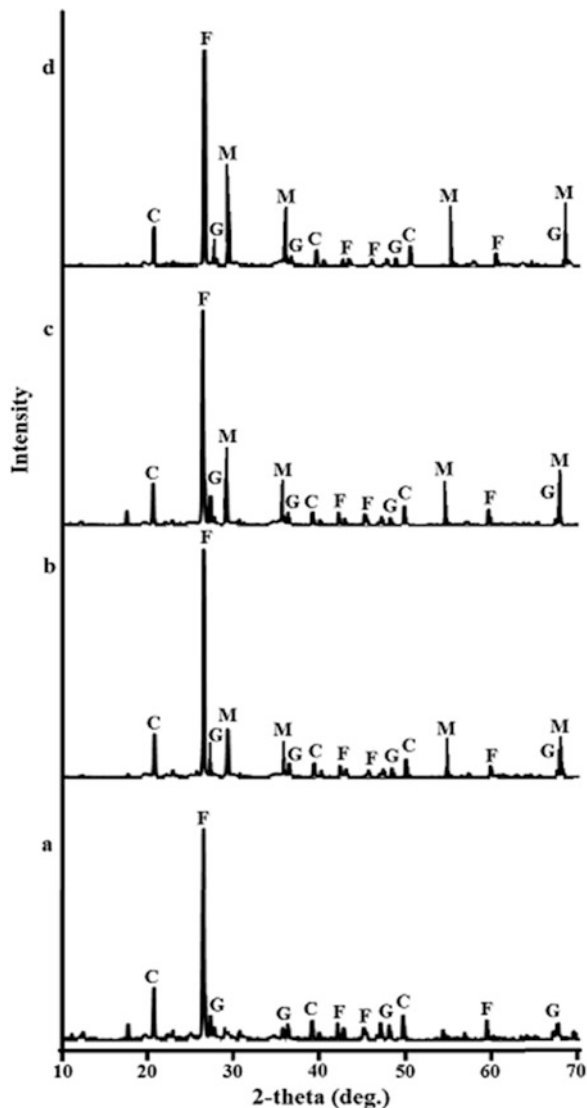
**Fig. 54.3** The XRD patterns of palygorskite clay (a), MCP-4 (b), MCP-7 (c), and MCP-10 (d): E, palygorskite ( $\text{Mg}_{0.669}\text{Al}_{0.331}\text{}_4(\text{Si}_4\text{O}_{10})_2(\text{OH})_2 \cdot 8\text{H}_2\text{O}$ ); C, quartz  $\text{SiO}_2$ ; M, magnetite  $\text{Fe}_3\text{O}_4$



magnetite and magnetite in magnetic composites were calculated and reported in Table 54.4.

As follows from the Table 54.4, magnetite in composite sorbents was obtained in the nanometer range. The average crystallite size of  $\text{Fe}_3\text{O}_4$  nanoparticles was 5–10 nm.

**Fig. 54.4** The XRD patterns of spondyle clay (a), MCSd-4 (b), MCSd-7 (c), and MCSd-10 (d): F, augite  $\text{Ca}(\text{Mg, Fe, Al})[(\text{Si, Al})_2\text{O}_6]$ ; G, pigeonite  $(\text{Ca, Mg, Fe})(\text{Mg, Fe})\text{Si}_2\text{O}_6$ ; C, quartz  $\text{SiO}_2$ ; M, magnetite  $\text{Fe}_3\text{O}_4$

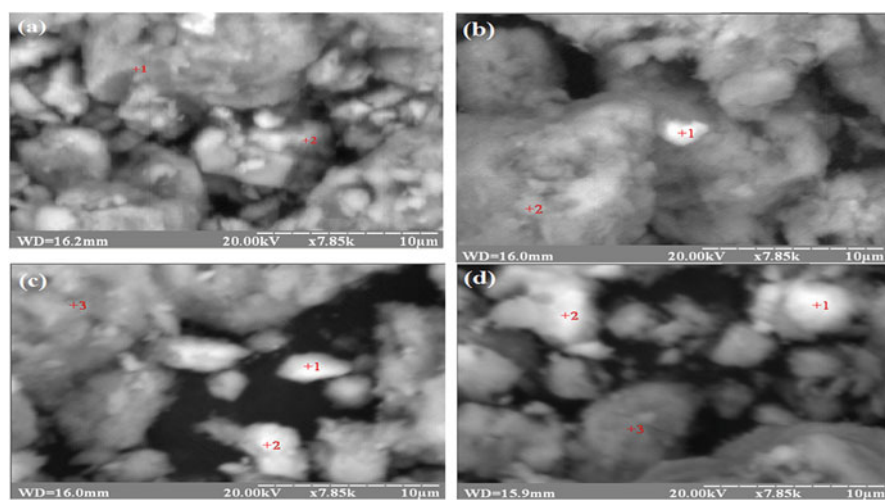


### 54.2.3 Microscopy

The SEM micrographs of saponite clay and MCSp (Fig. 54.5), palygorskite clay and MCP (Fig. 54.6), spondyle clay and MCSd (Fig. 54.7) were received and compared with an increase in 7850 times. These images show that magnetite had precipitated on the surface of clay minerals unequally. Tables 54.5, 54.6, and 54.7 present selective sorbent surface chemical analysis of the nanocomposites and natural clays.

**Table 54.4** X-ray analysis of magnetic sorbents on the base of saponite, palygorskite, spondyle clays and magnetite

Sample	Average size of Fe <sub>3</sub> O <sub>4</sub> crystallites, nm	Cell parameters, nm		
		a	b	c
MCSp-4	6.2	0.833	0.833	0.833
MCSp-7	9.6	0.833	0.833	0.833
MCSp-10	7.4	0.838	0.838	0.838
MCP-4	5.0	0.848	0.848	0.848
MCP-7	2.5	0.844	0.844	0.844
MCP-10	5.8	0.837	0.837	0.837
MCSd-4	4.9	0.856	0.856	0.856
MCSd-7	9.2	0.831	0.831	0.831
MCSd-10	10.3	0.836	0.836	0.836
Fe <sub>3</sub> O <sub>4</sub>	17.9	0.835	0.835	0.835

**Fig. 54.5** SEM images of samples surfaces: saponite clay (a), MCSp-4 (b), MCSp-7 (c), and MCSp-10 (d)

As can be seen from the data, Fe content on the surface of clay matrix is increased with increasing amounts of magnetite in the structure of composites.

#### 54.2.4 Magnetic Characteristics

The specific saturation magnetization, coercive force, and magnetic induction of saponite, palygorskite, and spondyle clays, Fe<sub>3</sub>O<sub>4</sub>, and synthesized MC samples are reported in the Table 54.8. Natural clays were characterized by specific saturation

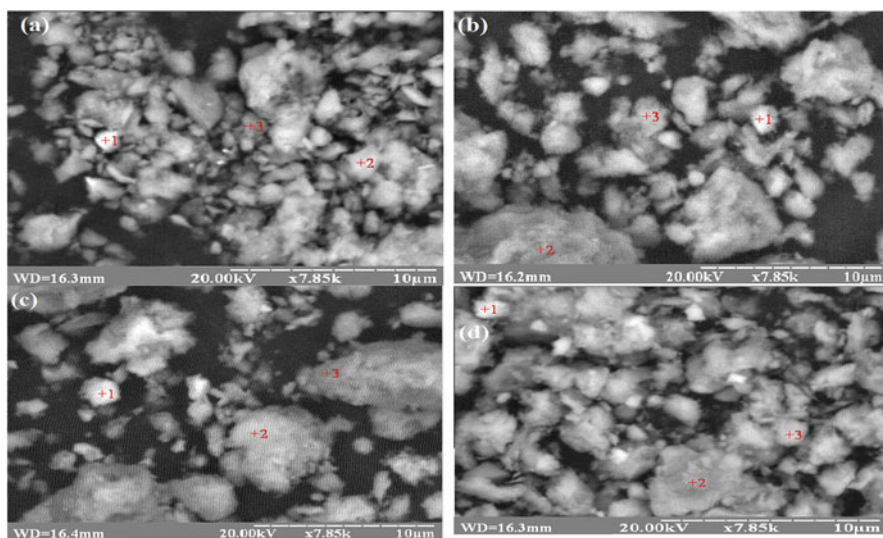


**Fig. 54.6** SEM images of samples surfaces: palygorskite clay (a), MCP-4 (b), MCP-7 (c), and MCP-10 (d)

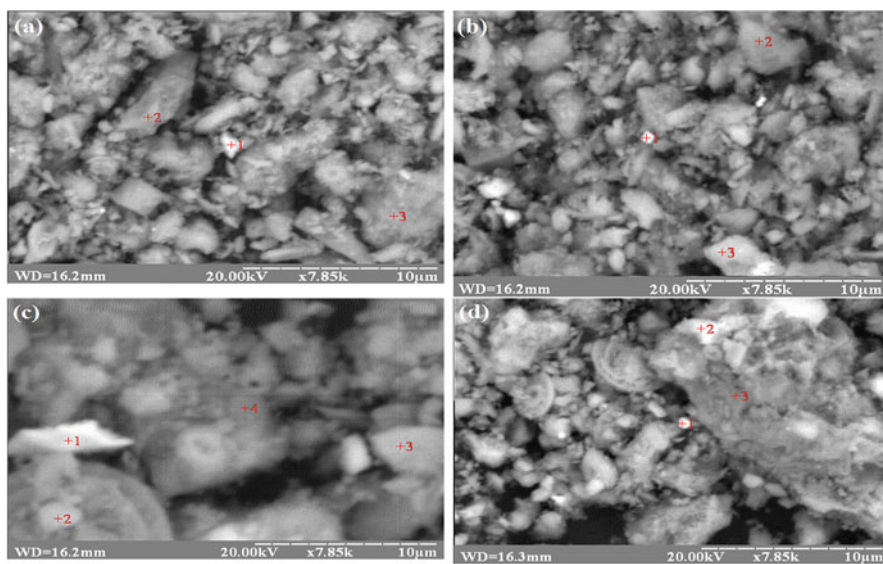


**Fig. 54.7** SEM images of samples surfaces: spondyle clay (a), MCSd-4 (b), MCSd-7 (c), and MCSd-10 (d)

**Table 54.5** Results of point chemical analysis of the saponite clay and nanocomposites MCSp

Chemical element	Contents, %			
	1	2	1	2
Point				
Sample	Saponite clay		MCSp-4	
Mg	8.52	6.3	1.8	5.7
Al	15.25	13.42	1.9	12.8
Si	39.4	40.43	6.2	36.8
Ca	4.88	5.6	1.7	3.4
Fe	31.95	34.25	88.4	41.3
Sample	MCSp-7		MCSp-10	
Mg	0.4	2.7	1.1	0.4
Al	0.7	3.0	1.6	0.7
Si	2.5	9.8	6.2	2.2
Ca	4.2	7.6	0.8	0.3
Fe	92.2	76.9	90.3	96.4

**Table 54.6** Results of point chemical analysis of the palygorskite clay and nanocomposites MCP

Chemical element	Contents, %			
	1	2	1	2
Point				
Sample	Palygorskite clay		MCP-4	
Mg	0.96	0.87	1.03	1.85
Al	11.9	9.89	8.79	11.48
Si	69.31	77.96	50.68	61.39
Ca	2.39	2.09	1.44	2.34
Fe	15.44	9.19	38.06	22.94
Sample	MCP-7		MCP-10	
Mg	0.19	1.73	0.67	0.17
Al	0.39	13.04	6.62	4.7
Si	4.56	57.82	44.39	25.16
Ca	0.41	3.34	2.21	1.31
Fe	94.45	24.07	46.11	68.66

**Table 54.7** Results of point chemical analysis of the spondyle clay and nanocomposites MCSd

Chemical element	Contents, %			
	1	2	1	2
Point				
Sample	Spondyle clay		MCSd-4	
Mg	4.26	5.72	0.43	0.37
Al	1.68	3.93	3.67	4.93
Si	16.89	15.54	19.59	17.54
Ca	71.12	68.96	36.19	48.96
Fe	6.05	5.85	40.12	28.2
Sample	MCSd-7		MCSd-10	
Mg	0.2	0.53	0.01	0.16
Al	1.43	2.4	0.84	1.38
Si	5.24	9.87	2.96	4.91
Ca	42.65	12.44	40.52	5.32
Fe	50.48	73.9	55.67	88.23

**Table 54.8** Magnetic characteristics of sorbent samples

Sample	$\sigma_{S(10)}$ , A·m <sup>2</sup> /kg	$H_c$ , A/m	$B_r$ , mT
Saponite clay	0	0	0
MCSp-4	3.0	0	0
MCSp-7	4.5	954.9	1.20
MCSp-10	6.5	954.9	1.10
Palygorskite clay	0	0	0
MCP-4	3.0	636.6	0.16
MCP-7	3.9	954.9	0.10
MCP-10	7.3	3819.7	0.57
Spondyle clay	0	0	0
MCSd-4	2.0	795.8	0.09
MCSd-7	6.3	1909.9	0.20
MCSd-10	8.3	2864.8	0.57
Fe <sub>3</sub> O <sub>4</sub>	90.0	501.3	3.50

zero magnetization; therefore, these minerals were classified as paramagnetic materials. When paramagnetic mineral matrix of composite modified by nanomagnetite enters to the magnetic separator, it is magnetized in the direction of the external magnetic field. So, controllability of magnetic separation process is determined by the properties of modifier ferromagnetic particles.

Most popular magnetic modifiers, such as magnetite Fe<sub>3</sub>O<sub>4</sub> and maghemite  $\gamma$ -Fe<sub>2</sub>O<sub>3</sub>, in the nanoscale state showed specific behavior in a magnetic field compared to monolithic magnetic materials [13]. Nanoscale magnetic modifier is characterized by super paramagnetic properties and low residual magnetization (soft magnetic materials). As is known [14], the magnetite change of reversal mechanism from reorientation of magnetic moments (single-domain state) to displacement of domain walls (poly-domain state) for magnetite occurred when the size of nanoparticles approximately 30 nm.

In the synthesis of MCSp, MCP, and MCSd in the clay matrix, the Fe<sub>3</sub>O<sub>4</sub> crystallites were formed about the same size of 2–10 nm (Table 54.4). Based on this, the specific saturation magnetization of MC samples was gradually increased with growing of magnetite content. Hence, the nanoscale magnetite particles of MC were formed with the same magnetization and arrangement of spins in one direction.

For MC samples containing magnetite in an amount of less than 7%wt., coercive force  $H_c$  and residual magnetic induction  $B_r$  are characterized by significantly lower values. Size of Fe<sub>3</sub>O<sub>4</sub> nanoparticles in the composition of these samples is smaller than 5 nm. For single-domain magnetic particles, there is some critical value of size in which the coercive force disappears, and they become superparamagnetic state. In the case of Fe<sub>3</sub>O<sub>4</sub>, this critical diameter corresponds to 5–6 nm. In a superparamagnetic state, magnetite nanoparticles behave like substance consisting of very small ferromagnetic particles, weakly interacting with each other.

**Table 54.9** The magnetic separation process of saponite, palygorskite, and spondyle clays and nanocomposites MCSp, MCP, and MCSd

Sample	C, mg/dm <sup>3</sup>		
	5 min	30 min	60 min
Saponite clay	558.8	387.7	327.1
MCSp-4	121.6	17.7	14.3
MCSp-7	32.7	1.0	<0.5
MCSp-10	16.6	<0.5	<0.5
Palygorskite clay	662.7	418.2	351.6
MCP-4	186.6	69.3	21.6
MCP-7	26.6	<0.5	<0.5
MCP-10	24.3	<0.5	<0.5
Spondyle clay	713.8	526.0	464.9
MCSd-4	126.6	37.1	23.8
MCSd-7	14.9	5.4	<0.5
MCSd-10	9.9	<0.5	<0.5

Magnetization of nanoparticles is easy for operating since it is determined by the ordering of atoms of magnetic structure [15]. Thus, magnetic particles of magnetite in the nanometer range have specific superparamagnetic properties, and MC samples belong to the soft magnetic materials. It is worth mentioning that nanosized iron oxide particles over time can aggregate and form hard magnetic materials with high value of residual magnetization. The use of hard magnetic materials complicates the regeneration of magnetic separator.

Fe<sub>3</sub>O<sub>4</sub> is introduced into the larger particles (clay matrix) for practical application in the process of magnetic separation. This is caused by the large hydrodynamic resistance and the tendency of nanoscale magnetic particles to aggregate. The interaction of magnetic nanoparticles with an applied magnetic field provides the controlled deposition of magnetic composite which dispersion can vary depending on the requirements of water purification technology [16, 17].

### 54.2.5 Magnetic Separation

Table 54.9 shows the kinetics of separation of clay minerals and magnetic composites based on them. Separation of magnetic sorbents from the purified solution in a filter equipped with permanent magnets was held in 36 times faster.

The 98% of spent magnetic sorbent mass were precipitated for the first 5 min of magnetic separation, and purified water was suitable for discharge into the centralized sewage. Application of magnetic composites has ensured the achievement of the residual concentration of suspended solids  $\leq 0.02$  mg/L for 30 min of magnetic separation.

### 54.3 Conclusions

Magnetic composite sorbents on mineral base (saponite, palygorskite, and spondyle clays) were created by impregnation method. The pure magnetic-modifying agent  $\text{Fe}_3\text{O}_4$  was obtained by method of Elmore.

In the synthesis of MCSp, MCP, and MCSd in the clay matrix, the  $\text{Fe}_3\text{O}_4$  crystallites were formed approximately in the same range (5–10 nm). The specific saturation magnetization of MC samples was approximately the same which agrees with crystallite sizes. Magnetic particles of magnetite in the nanometer range were characterized by specific superparamagnetic properties, and MC were classified to the soft magnetic materials.

The removal of spent magnetic sorbents occurred almost three times faster compared to native clay, and the residual concentration of suspended solids in the water corresponded to standards for drinking water ( $<0,5 \text{ mg/dm}^3$ ). Thus, practical effectiveness magnetic separation method for the deposition of spent sorbents from the water was confirmed.

**Acknowledgments** The authors thank the G.V. Kurdyumov Institute for Metal Physics, National Academy of Sciences of Ukraine, for their support in conducting this research.

### References

1. Mortazavi S, Farmany A (2016) High adsorption capacity of MWCNTs for removal of anionic surfactant SDBS from aqueous solutions. *J Water Supply Res Technol* 65:160–166
2. Gan F, Luo Y, Hang X, Zhao H (2016) Heterocoagulated clay-derived adsorbents for phosphate decontamination from aqueous solution. *J Environ Manage* 166:23–30
3. Elmoubarki R, Mahjoubg FZ, Tounsadj H et al (2015) Adsorption of textile dyes on raw and decanted Moroccan clays: kinetics, equilibrium and thermodynamics. *Water Resou Ind* 9:16–29
4. Wang LK, Hung Y, Lo H (2006) *T Waste treatment in the Process Industries*. Taylor & Francis Group, Boca Raton, pp 307–453
5. Yavuz CT, Prakash A, Mayo JT, Colvin VL et al (2009) Magnetic separations: from steel plants to biotechnology. *Chem Eng Sci* 64:2510–2521
6. Zhu ZQ, Howe D (2001) Halbach permanent magnet machines and applications: a review. *Proc on Electr Power Appl* 148(4):299–308
7. Li XL, Yao KL, Liu HR, Liu ZL (2007) The investigation of capture behaviors of different shape magnetic sources in the high-gradient magnetic field. *J Magn Magn Mater* 311(2):481–488
8. Ambashta RD, Sillanpaa M (2010) Water purification using magnetic assistance: a review. *J Hazard Mater* 180:38–49
9. Mykhailenko NO, Makarchuk OV, Dontsova TA et al (2015) Purification of aqueous media by magnetically operated saponite sorbents. *East Eur J Enterp Technol* 10(76):13–20
10. Makarchuk OV, Dontsova TA, Astrelin IM (2015) Magnetic clay sorbent for the removal of dyes from aqueous solutions. *Research bulletin of the National Technical University of Ukraine “Kyiv Polytechnic Institute”* 6, p 109–114
11. Makarchuk OV, Dontsova TA, Astrelin IM (2016) Magnetic nanocomposites as efficient sorption materials for removing dyes from aqueous solutions. *Nanoscale Res Lett* 161(11):1–7



12. Galindo-Gonzalez C, Vicente J, Ramos-Tejada MM et al (2005) Preparation and sedimentation behavior in magnetic fields of magnetite-covered clay particles. *Langmuir* 21(10):4410–4419
13. Sun J, Xu R, Zhang Y, Ma M, Gu N (2007) Magnetic nanoparticles separation based on nanostructures. *J Magn Magn Mater* 312(2):354–358
14. Doroshenko A, Chekman I (2014) Magnetic nanoparticles: properties and biomedical applications. *Ukrainian Med J* 4(102):10–13
15. Clime L, Drogoff BL, Zhao S et al (2008) Magnetic nanocarriers: from material design to magnetic manipulation. *Int J Nanotechnol* 5(9):1268–1305
16. Latham AH, Williams ME (2008) Controlling transport and chemical functionality of magnetic nanoparticles. *Acc Chem Res* 41(3):411–420
17. Pathak A, Panda AB, Tarafdar A et al (2003) Synthesis of nano-sized metal oxide powders and their application in separation technology. *J Indian Chem Soc* 80(4):289–296

# Chapter 55

## Measurements of Electrical Conductance in Nanostructures and Their Use in Nanotechnology

Waldemar Nawrocki

### 55.1 Introduction

In the last years, nanotechnology became the important part of high technology. The nanotechnology covers measurement methods developed for testing of nanostructures as well. Measurements of electrical conductance or resistance of nanostructures is easy to carry out and useful for estimating some physical parameters of a sample. Nanostructures made of conducting material (e.g., metal, silicon, carbon) show an effect of quantization of electrical conductance. The conductance quantization was predicted by Landauer in his new theory of electrical conductance [1], 1957. In 1987, Gimzewski and Moller [3] published results on measurements of the quantization of electrical conductance in metals at room temperature observed with a scanning tunneling microscope. In 1988, two groups [4, 5] reported the discovery of the conductance quantization in controllable two-dimensional electron gas (2DEG) in the GaAs constriction at the temperature of 4 K. Formation of nanowires in the process of breaking contact between ordinary metallic macrowires at room temperature was proposed by Costa-Kramer et al. [6] in 1995.

Many groups investigate heat exchange and thermal conductance in nanostructures as well. The first theoretical analyses of thermal conductance in structures in the ballistic regime were made by P. Streda [7]. Next papers on a quantization of thermal conductance came from several groups [e.g., 8, 12].

---

W. Nawrocki (✉)

Faculty of Electronics and Telecommunications, Poznan University of Technology, ul. Piotrowo 3, 60-965, Poznan, Poland

e-mail: [nawrocki@et.put.poznan.pl](mailto:nawrocki@et.put.poznan.pl)

© Springer International Publishing AG 2017

O. Fesenko, L. Yatsenko (eds.), *Nanophysics, Nanomaterials, Interface Studies, and Applications*, Springer Proceedings in Physics 195,  
DOI 10.1007/978-3-319-56422-7\_55

721

In this paper, electrical conductance in nanostructures is analyzed and measured, e.g., in structures like integrated circuits. An inverse problem of measurements in nanostructures is considered as well: estimation of geometrical dimensions of nanostructures on basis of measurements of electrical conductance.

## 55.2 Theory of Conductance Quantization

Transport of electrons can be described classically by the Boltzmann transport equation (Drude model) which introduces mean free path  $\Lambda$ . At relatively low temperatures, the considerable contribution to conductivity is given by electrons with energy close to Fermi surface. Hence, conductivity is given by:

$$\sigma = \frac{ne^2\tau}{m^*} \quad (55.1)$$

where  $n$  is the concentration of the carriers,  $m^*$  is the effective mass of the electron, and  $\tau$  is relaxation time.

Electrical conduction in nanometer-sized samples is described much better by a model developed by Rolf Landauer at IBM (New Jersey, USA). His theory of electrical conduction, applicable also to nanostructures and predicting conductance quantization, was first presented by Landauer in 1957 [1]. Thirty years later, Landauer published its advanced version [2]. The 1980s saw the publication of the first results of conductance quantization studies in nanostructures [3, 4]. Developed further by Markus Büttiker [9], the theory is now commonly used and known as the Landauer-Büttiker formalism.

Let us consider a constriction of length  $L$  and width  $W$  between two wide metal terminals (Fig. 55.1), referred to as electron reservoirs in the Landauer theory [11]. Let the mean free path in the conductor be denoted as  $\Lambda$  and the Fermi level as  $E_F$ . As a result of the application of a potential difference  $V$  to the ends, electrons flow through the constriction. The transport of electrons is ballistic, i.e., without collision, if the length of the constriction is shorter than the mean free path of the electrons,  $L < \Lambda$ . Under this condition, the scattering of electrons can be neglected. Electron scattering is caused by the presence of impurities and donors as well as irregularities of the surface.

The following five assumptions of the Landauer theory allow to present the above description in a synthetic manner:

- Electrons are transferred between two electron reservoirs with different chemical potentials.
- The transport of charge carriers (electrical conduction) results from a charge carrier density gradient between the reservoirs of electrons.

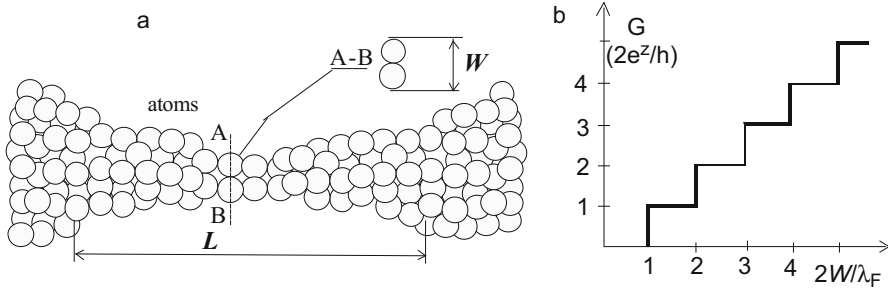


**Fig. 55.1** Conductance quantization in a nanowire (conductor with length  $L < \Lambda$  and width  $W$  comparable with the length of Fermi wave  $\lambda_F$ ): (a) nanowire outline (the third dimension is not considered); (b) conductance quantization  $G$  versus width  $W$

- Only elastic scattering of electrons, caused by their reflection from the potential barriers and the edges of the conductor, takes place in the perfect conductor.
- The observed conduction is related to the transmission probability in the conduction channels formed in the scattering.
- Power is dissipated during the transport of electrons in the reservoirs but not in the interior of the perfect guide.

Another parameter characterizing the system is Fermi wavelength  $\lambda_F = 2\pi/k_F$ , where  $k_F$  is the Fermi wavevector. For metals like copper or gold,  $\lambda_F \approx 0,5$  nm is much less than free electron path  $\Lambda$  ( $\Lambda_{Au} = 14$  nm). If the dimensions of the system are less than free electron path, the impurity scattering is negligible, so the electron transport can be regarded as ballistic. If a metal wire has outside diameter of  $W$ , comparable with Fermi wavelength  $\lambda_F$ , and the length  $L$  is less than  $\Lambda$ , the system can be regarded as one dimensional (1-D), the electron – as a wave, and one can expect quantum effects.

Let's consider perfect conductor with diameter  $W$  and the length  $L$  (Fig. 55.1) connecting two wide contacts (reservoirs of the electrons) between which the conductivity is measured. Assuming that the wide contacts are infinitely large, the electrons are in the thermodynamic equilibrium described by Fermi-Dirac statistic. When the electrons enter 1-D conductor, nonequilibrium states occur with negative and positive velocities. If there is a resultant current, the states with positive velocities correspond to higher energies [1]. According to the Büttiker [9] model, the Hamiltonian of the perfect conductor can be expressed as follows:

$$H = \frac{1}{2m^*} (\hbar^2 k_x^2 + \hbar^2 k_y^2) + V(x) \tag{55.2}$$

where  $y$  is a coordinate (a dimension along the wire),  $x$  is in the transverse direction,  $m^*$  is the effective mass,  $V(x)$  denotes the potential well of the width  $W$ ,  $k_y$  is a

wavevector along  $y$ , and  $k_x$  is a wavevector along  $x$ . Because of the narrowness of the potential wall  $V(x)$ , the energy for the transverse propagation is quantized:

$$E_{Tj} = \frac{\hbar^2 k_x^2}{2m^*} = \frac{\hbar^2}{2m^*} \left( \frac{j\pi}{W} \right)^2 \quad (55.3)$$

The formula 55.3 is valid if the potential energy tends to infinity at the quantum well boundary.

For the Fermi level  $E_F = E_j$ , there is a number  $N \sim 2W/\lambda_F$  of states  $E_{Tj}$  below Fermi surface. Let us assume that thermal energy  $k_B T$  is much smaller than the energy gap between levels and that the wide contacts are characterized by chemical potentials  $\mu_1$  and  $\mu_2$  with ( $\mu_1 > \mu_2$ ). Then current of electrons in  $j^{\text{th}}$  state equals to:

$$I_j = ev_j \left( \frac{dn}{dE} \right)_j \Delta\mu, \quad (55.4)$$

where  $v_j$  is the velocity along  $y$  and  $(dn/dE)_j$  is the density of states at the Fermi level for  $j^{\text{th}}$  state. For 1-D conductor, the density of states is

$$\frac{dn}{dk} = \frac{1}{2\pi} \text{ and } \left( \frac{dn}{dE} \right)_j = \left( \frac{dn}{dk} \frac{dk}{dE} \right)_j = \frac{2}{\hbar v_j} \quad (55.5)$$

The factor of 2 results from spin degeneracy. Hence, the current for  $j^{\text{th}}$  state  $I_j = \frac{2e^2}{\hbar} V$  does not depend on  $j$  (where the voltage difference  $V = \Delta\mu/e$ ). Total current

$I = \sum_{j=1}^N I_j$ ; hence conductivity is expressed as

$$G = \frac{2e^2}{\hbar} N \quad (55.6)$$

where the number of channels,  $N$ , depends on the width of the wire (Fig.55.1).

$$N = \text{Int} \left( \frac{2W}{\lambda_F} \right) \quad (55.7)$$

where  $\text{Int}(X)$  means the integer of the number of incomplete.

However, defects, impurities, and irregularities of the shape of the conductor can induce scattering; then conductivity is given by the Landauer equation:

$$G = \frac{2e^2}{\hbar} \sum_{i,j=1}^N t_{ij} \quad (55.8)$$

where  $t_{ij}$  denotes probability of the transition from  $j^{\text{th}}$  to  $i^{\text{th}}$  state. In the absence of scattering,  $t_{ij} = \delta_{ij}$ ; thus Eq. 55.8 is reduced to Eq. 55.6.

Measurements of electrical resistance (or conductance) of a sample of the size about  $\Lambda$ , (mesoscopic range) show that the Landauer theory better describes electrical conductance in samples than the Drude model.

### 55.3 Measurements of Electrical Conductance

The experimental setup consisted of a pair of metallic wires (they formed a nanowire), a digital oscilloscope, a motion control system (doesn't show on the picture), and a PC (see Fig. 55.2). Instruments are connected in one system using the IEEE-488 interface. There was the resistor  $R_p = 1 \text{ k}\Omega$  in series to the connected wires. The circuit was fed by the constant voltage  $V_s$ , and measurements of current  $I(t)$  have been performed. Conductance was determined by current  $I$  accordingly to:

$$G = I \frac{1}{V_s - IR_p} \quad (55.9)$$

Transient effects of making contact or breaking the contact give time-dependent current. The voltage  $V_p$  on the resistor  $R_p$  was measured with computer-controlled oscilloscope. The piezoelectric device is used to control the backward and forward movement of the macroscopic wires between which nanowires occur (QPC – quantum point contact). A high voltage amplifier controlled by a digital function generator supplies the piezoelectric device. Both electrodes of the QPC (see Fig. 55.2) are made of wire 0.5 mm in diameter or of small pieces of metal. The conductance was measured between two metallic electrodes, moved to contact by

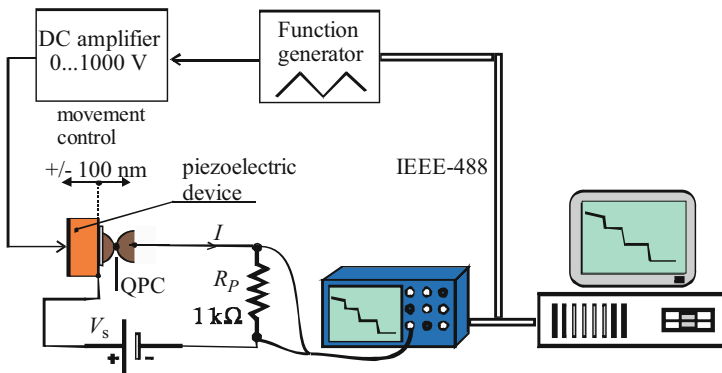


**Fig. 55.2** A system for measurements of electrical conductance quantization in nanowires (QPC) formed between two macroscopic wires

the piezoelectric tube actuator. The oscilloscope was triggered by a single pulse. All experiments were performed at room temperature and at ambient pressure.

In order to compare our results with those published before by other groups, the first experiment was performed for gold wires. Even if quantization of conductivity by  $G_0 = 2e^2/h$  does not depend on the metal and on temperature, the purpose of studying quantization for different metals was to observe how properties of the metal affect the contacts between wires. Therefore, we have investigated the conductance quantization in nanowires for three nonmagnetic metals (gold, copper, and tungsten) and for magnetic metals (cobalt and nickel) [10].

The quantization of electric conductance does not depend neither on the kind of metal nor on temperature. For nonmagnetic metals, the conductance quantization in units of  $G_0 = 2e^2/h = 7.75 \times 10^{-5} \text{ [A/V]} = (12.9 \text{ k}\Omega)^{-1}$  was previously observed for the following nanowires: Au-Au, Cu-Cu, Au-Cu, W-W, W-Au, and W-Cu. The quantization of conductance in our experiment was evident. All characteristics showed the same steps equal to  $2e^2/h$ . We observed two phenomena: quantization occurred when breaking the contact between two wires, and quantization occurred when establishing the contact between the wires. The characteristics are only partially reproducible; they differ in number and height of steps and in the time length. The steps can correspond to 1, 2, 3, or 4 quanta. It should be stated that quantum effects were observed only for some of the characteristics recorded. The conductance quantization has been so far more pronouncedly observable for gold contacts (see Fig. 55.3).

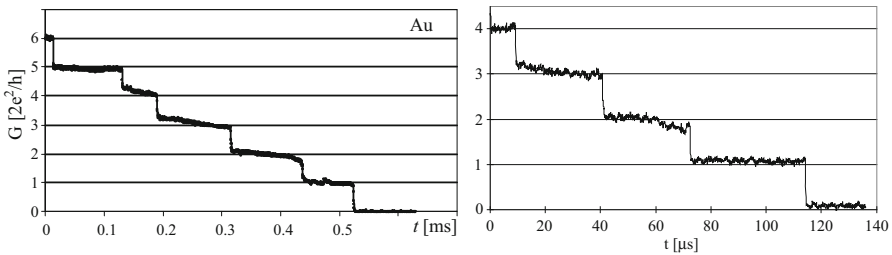
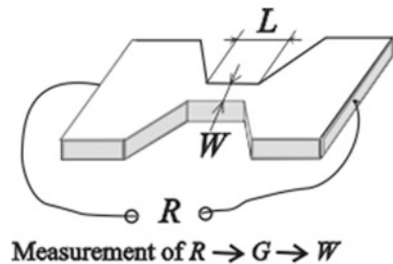


**Fig. 55.3** Quantization of electrical conductance in gold nanowires in air at room temperature (nanowires were formed by a contact between gold macrowires)

**Fig. 55.4** Measurement of a width of a nanostructure by an electrical method. The resistance of terminals  $R_{\text{term}}$  is much less than the resistance of nanostructure itself,  $R_{\text{term}} \ll R$



## 55.4 Estimation of Geometrical Dimensions of a Nanostructure by Electrical Measurements

The electrical conductivity of nanostructures with the smallest atomic size is changed stepwise as a function of the cross-section area of a nanostructure in its narrowest point. The effect of quantization of electrical conductance (resistance) with the quantum  $G_0 = 2e^2/h = (12.9 \text{ k}\Omega)^{-1}$  occurs for nanostructures under the conditions for nanostructures given by Landauer in his new definition of conductance. This effect can be used to measure the width of nanostructures (samples) or rather to estimate it. Electrical measurements of geometric sizes of nanostructures are potentially very important for nanotechnology, where other methods of measurement are very complex. One such possible method is STM microscopy. The method proposed here is based on electrical measurements (see Fig. 55.4). Therefore, the measurements are relatively simple and the results of measurement are more accurate when nanostructures are smaller.

The technical conditions necessary to carry out the measurements of the geometrical dimensions of nanostructures using electrical conductance measurements are:

- That the nanostructure is made of electrical conductor
- That the nanostructure (sample) has a constriction (wide throat) between two wide terminals
- That the thickness of the nanostructure is comparable with the Fermi wavelength  $\lambda_F$ . This means the thickness of one or numerous atoms (as it is in graphene)
- That the length of the constriction is smaller than the mean free path  $\Lambda$  in sample material

The nanowire of the smallest size forms a chain of atoms connected from one to another by path,  $L < \Lambda$ . The chain creates one transmission channel for free electrons, according to the Landauer theory. Thus, the conductance  $G_0 = 7.75 \times 10^{-5}$  [A/V] of the nanowire indicates that the nanowire contains only a single atom at its narrowest point. The cross-sectional area of such a nanowire is the area of a circle defined by  $2R$ , where  $R$  is the radius of the atom. For example, for gold, the mean free path  $\Lambda_{\text{Au}} = 14 \text{ nm}$  (at 300 K), the diameter of the atom  $R_{\text{Au}} = 0.144 \text{ nm}$ , and lattice constant  $a = 0.408 \text{ nm}$ . The chain of atoms forming a gold nanowire with conductance of  $G_0$  contains from 1 to about 34 atoms. The upper limit of number of atoms in the nanowire chain can't be given exactly. The reason is that only the *mean* free path of electrons in the material is assumed for Eqs. 55.6 and 55.7. Thus, a free path length in gold may be, e.g., 12 nm or 15 nm instead of 14 nm. One can note that a chain of atoms containing more than 30 atoms is a nanostructure unstable mechanically.

The conductance of  $2G_0$  (or  $NG_0$ ) of a nanowire means that in the nanowire, there exist two transmission channels (or  $N$  channels), respectively. The width of the nanowire at its narrowest point is  $W$ . On the basis of conductance  $G$  (or resistance  $R$ ) and the Eqs. 55.6 and 55.7, the width  $W$  of the nanostructures can be determined by formula (10).

$$W = 0.5\lambda_F [\text{Int}(G/G_0) + 1] \quad (55.10)$$



For example, a gold nanowire shows resistance  $R = 4.4 \text{ k}\Omega$ ; it means its conductance  $G = 1/R = 22.7 \times 10^{-5} \text{ [A/V]}$ . For gold, the Fermi wavelength  $\lambda_F = 0.52 \text{ nm}$ . We calculate the width of nanowire from (10):  $W = 0.5\lambda_F [\text{Int}(22.7/7.75) + 1] = 3 \times 0.52 = 1.56 \text{ nm}$ . We can estimate the length  $L$  of nanowire as well. The length  $L$  is shorter than mean free path,  $L < 14 \text{ nm}$ .

## 55.5 Conclusions

For objects about nanometer size, an influence of quantum occurrences must be taken into account. The miniaturization of devices and paths in integrated circuits and transducers has its limits. Electric and thermal parameters of electronic devices of 10 nm technology would change dramatically. For nanostructures especially essential becomes the quantization of the electrical conductance and the thermal conductance. Quantization is the non-linear effect. Therefore, it induces non-linear signals processing in nanostructures. In our measurements, quantization of electrical conductance has proved to be observable in a simple experimental setup. The new method of measuring geometric dimensions of nanostructures based on electrical measurements is described.

## References

1. Landauer R (1957) Spatial variation of currents and fields due to localized scatterers in metallic conduction, *IBM Journ. Res Dev* 1:223–231
2. Landauer R (1989) Conductance determined by transmission: probes and quantised constriction resistance, *Journ. Phys Condens Matter* 1:8099–8110
3. Gimzewski JK, Möller R (1987) Transition from the tunneling regime to point contact studied using STM. *Phys Rev B* 36:1284–1287
4. Wharam DA, Thornton TJ, Newbury R, Pepper M, Ahmed H, Frost JEF, Hasko DG, Peacock DC, Richie DA, Jones GC (1988) One-dimensional transport and the quantisation of the ballistic resistance. *J Phys C Solid State Phys* 21:L209
5. van Wees BJ et al (1988) Quantized conductance of point contacts in a two-dimensional electron gas. *Phys Rev Lett* 60:848–850
6. Costa-Krämer JL et al (1995) Nanowire formation in macroscopic metallic contacts: quantum mechanical conductance tapping a table top. *Surf Sci* 342:L1144–L1149
7. Streda P (1989) Quantised thermopower of a channel in the ballistic regime. *J Phys Condens Matter* 1:1025
8. Schwab K, Henriksen EA, Worlock JM, Roukes ML (2000) Measurement of the quantum of thermal conductance. *Nature* 404:974–977
9. Büttiker M (1988) Absence of backscattering in the quantum hall effect in multiprobe conductors. *Phys Rev B* 38:9375
10. Susła B, Wawrzyniak M, Barnaś J, Nawrocki W (2007) Conductance quantization in magnetic and nonmagnetic metallic nanowires. *Materials Sci Poland* 25:305
11. Greiner A, Reggiani L, Kuhn T, Varani L (1997) Thermal conductivity and Lorenz number for one-dimensional ballistic transport. *Phys Rev Lett* 78:1114–1117
12. Rego LGC, Kirczenow G (1998) Quantized thermal conductance of dielectric quantum wire. *Phys Rev Lett* 81:232–235

# Chapter 56

## Nano-particulate Structures with Glucose-Derived Char and Compacted Fumed Silica in Gaseous and Aqueous Media

L. V. Nosach, E. F. Voronin, E. M. Pakhlov, B. Charmas,  
J. Skubiszewska-Zięba, E. Skwarek, W. Janusz, and V. M. Gun'ko

### 56.1 Introduction

There are numerous types of composite materials with different main (host) and secondary (guest) phases prepared with polymers, metals, metal oxides, carbon, and other components. Nanocomposites include, at least, one component with nanomaterials (e.g., nanooxides, carbon nanotubes, graphenes, metal nanoparticles). Carbon/mineral nanocomposites, composed of nanosized carbon and oxide particles, possess the properties of both polar mineral and nonpolar carbon structures [1–6]. The latter can be composed of nonporous or porous nanoparticles depending on the use of porogens. These nanocomposites can effectively adsorb both polar and nonpolar compounds from aqueous solutions. This allows one to expand the range of adsorbates, which can be effectively and fast adsorbed from the solutions [7–12].

Chars and activated carbon individual or in composites can be prepared using a variety of precursors (natural biomass, polymers, and low-molecular weight organics). For effective carbonization of the precursors, they should include well-removed groups in the molecules, such as C-OH, COOH, C-Cl, and N-H; therefore, saccharides are one of the most appropriate precursors of chars [13–15].

The aim of this study was the use of the gas-phase mechano-sorption modification (GPMSM) method [16, 17] to prepare a blend of glucose (as a char precursor) with nanosilica for subsequent carbonization and preparation of powder composite containing nanoparticles of both silica and char.

---

L.V. Nosach (✉) • E.F. Voronin • E.M. Pakhlov • V.M. Gun'ko  
Chuiiko Institute of Surface Chemistry, National Academy of Sciences of Ukraine, General  
Naumov Street 17, 03164, Kyiv, Ukraine  
e-mail: [nosachlv@ukr.net](mailto:nosachlv@ukr.net)

B. Charmas • J. Skubiszewska-Zięba • E. Skwarek • W. Janusz  
Maria Curie-Skłodowska University, pl. Maria Curie-Skłodowska 2, 20031, Lublin, Poland

## 56.2 Materials and Methods

### 56.2.1 Materials

Fumed silica A-300 (pilot plant of the Chuiko Institute of Surface Chemistry, Kalush, Ukraine) was used as the initial material (bulk density  $\rho_b \approx 0.05 \text{ g/cm}^3$ , specific surface area  $S_{\text{BET}} = 330 \text{ m}^2/\text{g}$ ). Glucose (pharmaceutical grade) was used as a char precursor.

To reduce the dusty property characteristic for the initial A-300 and to change the textural characteristics, it was pretreated in a wetted state using mechanochemical activation (MCA). This dense fumed silica (labeled as densil) alone was prepared using 0.5 g of water per gram of A-300. This mixture was treated in a porcelain ball mill (volume  $\sim 1 \text{ dm}^3$  2/3 filled by porcelain balls of 2–3 cm in diameter, 60 rpm) for 1 h (final  $\rho_b = 0.21 \text{ g/cm}^3$ ). A sample with glucose/silica (Gl/DS) was prepared using 1.8 g of glucose and 0.5 g of water per gram of dry nanosilica (50 g of initial silica, 90 g of glucose, and 25 g of water). The mixture was activated during 1.5 h, and then it was dried in air at room temperature for several days.

Carbonization of glucose in the blend was performed in the nitrogen atmosphere (flow rate  $0.1 \text{ dm}^3/\text{min}$  in a flow rotary reactor) with increasing temperature from  $20 \text{ }^\circ\text{C}$  to  $500 \text{ }^\circ\text{C}$  at a heating rate of  $10 \text{ }^\circ\text{C}/\text{min}$  and heating at  $500 \text{ }^\circ\text{C}$  during 3 h. The product (char/silica) yield was 47.2% at the carbon content of 24.3 wt.%.

### 56.2.2 Characterization Methods

The morphology was analyzed using scanning electron microscopy (SEM) with a DualBeam Quanta 3D FEG FEI apparatus under conditions of low vacuum at accelerating voltage of 10 kV and magnification up to  $\times 25,000$ . Before experiments, the samples were sprayed with a very thin layer of gold and platinum.

Thermal analysis of samples (weight  $\approx 30 \text{ mg}$ ) was carried out in air at  $20\text{--}1000 \text{ }^\circ\text{C}$  using a Derivatograph C (Paulik, Paulik & Erdey, MOM, Budapest) apparatus at a heating rate of  $10 \text{ }^\circ\text{C}/\text{min}$ .

The FTIR spectra were recorded over  $4000\text{--}400 \text{ cm}^{-1}$  range using a FTIR Nicolet 8700A (Thermo Scientific) spectrophotometer in an attenuated total reflection mode using diamond crystal.

Raman spectra were recorded using an inVia Reflex (Renishaw, UK) Raman microscope with laser excitation at 514 nm.

Nitrogen adsorption-desorption isotherms were recorded at 77.4 K using a Micromeritics ASAP 2405 N adsorption analyzer. The value of  $S_{\text{BET}}$  was calculated according to the standard BET method [18]. The pore volume ( $V_p$ ) was evaluated from the nitrogen adsorption at  $p/p_0 = 0.98\text{--}0.99$  ( $p$  and  $p_0$  denote the equilibrium and saturation pressure of nitrogen at 77.4 K, respectively). The nitrogen desorption data were used to compute the pore (void) size distributions (PSD, differential

$f_V(R_p) \sim dV_p/dR_p$  and  $f_S(R_p) \sim dS/dR_p$ ) using a regularization procedure ( $f_V(R_p) \geq 0$  at any radius  $R_p$  and regularization parameter  $\alpha = 0.01$ ) with a model of cylindrical pores and voids between spherical nanoparticles (CV for silica and VCV for carbon/silica) packed in random aggregates taking into account the primary particle size distribution  $\varphi(a)$  using a self-consistent regularization (SCR) procedure [19].

To study particle size distributions (PaSD) in aqueous media (1, 2, or 30 g of a sample per 1 dm<sup>3</sup> of deionized distilled water), dynamic light scattering with a Mastersizer 2000 or a Zetasizer Nano S (Malvern Instruments) apparatuses was used. Samples were sonicated for 3 or 6 min using an ultrasonic disperser (22 kHz and 500 W). To compute the PaSD with respect to the particle volume ( $I_V$ ) and particle number ( $I_N$ ), the Malvern Instruments' software was used, assuming that particles had a roughly spherical shape.

### 56.3 Results and Discussion

Mechanochemical activation (MCA) of nanosilica with addition of water (0.5 g per gram of A-300) results in a strong increase in the value of bulk density (0.21 g/cm<sup>3</sup> instead of 0.05 g/cm<sup>3</sup> for the initial powder). The value of  $V_p$  strongly increases, but the value of  $S_{BET}$  slightly decreases (Table 56.1). Despite MCA of the wetted sample, treated nanosilica remains in the powder state (Fig. 56.1). Similar powders are also characteristic of composites with GI/DS and C/DS (Figs. 56.1 and 56.2), despite a difference in the textural characteristics of them (Table 56.1). These changes are mainly due to rearrangement of aggregates of nanoparticles and agglomerates of aggregates, because the shape of nitrogen adsorption-desorption isotherms changes at  $p/p_0 > 0.4$  with exception of GI/DS (Fig. 56.3a). Changes in the textural characteristics and organization of the secondary particles are important for composites used as adsorbents [6]. The powder state allows one to disperse the composite in the total volume of a liquid without fast sedimentation of the particles [6, 10, 17].

This provides rapid adsorption of target solutes or controlled release of bound compounds. Note that despite the reduction of the textural characteristics, GI/DS possesses aggregates/agglomerates of smaller sizes (Fig. 56.1b) than initial silica (Fig. 56.1a) or char/silica (Fig. 56.1c).

Changes in the organization of secondary particles of nanosilica during MCA lead to changes in the adsorption/desorption of water analyzed using TG data (Fig. 56.2). For A-300, desorption of water at 20–120 °C corresponds to 1.48 wt.%, 1.63 wt.% at 20–150 °C, and totally 2.84 wt.% over 20–970 °C.

For densil, these values are 14.34, 15.44, and 15.69 wt.%, respectively. Consequently, the adsorption of water from air onto densil increases approximately by order of magnitude in comparison with A-300 due to compacting of secondary particles upon MCA.

In parallel to desorption of intact water, associative desorption of water from a DS surface can increase at 120–150 °C (weight loss is 1.1 wt.%) in comparison with

**Table 56.1** Textural characteristics of silica, glucose/silica, and carbon/silica samples

Sample	$S_{\text{BET}}$ ( $\text{m}^2/\text{g}$ )	$S_{\text{nano}}$ ( $\text{m}^2/\text{g}$ )	$S_{\text{meso}}$ ( $\text{m}^2/\text{g}$ )	$S_{\text{macro}}$ ( $\text{m}^2/\text{g}$ )	$V_{\text{p}}$ ( $\text{cm}^3/\text{g}$ )	$V_{\text{nano}}$ ( $\text{cm}^3/\text{g}$ )	$V_{\text{meso}}$ ( $\text{cm}^3/\text{g}$ )	$V_{\text{macro}}$ ( $\text{cm}^3/\text{g}$ )	$\Delta w$	$\langle R_{\text{v}} \rangle$ (nm)	$\langle R_{\text{s}} \rangle$ (nm)
Initial A-300	330	29	288	13	0.826	0.012	0.621	0.193	-0.023	19.90	5.97
Dense A-300 (densil)	328	85	223	20	1.325	0.019	0.978	0.327	0.224	20.35	8.28
Glucose/densil	42	12	26	4	0.227	0.003	0.156	0.067	0.143	23.79	11.31
Carbon/densil	302	146	153	4	0.500	0.046	0.361	0.094	0.073	16.84	3.02

*Note.* The  $V_{\text{nano}}$  and  $S_{\text{nano}}$  values were calculated by integration of the  $f_{\text{v}}(R)$  and  $f_{\text{s}}(R)$  function, respectively, at  $0.35 \text{ nm} < R < 1 \text{ nm}$ ,  $V_{\text{meso}}$  and  $S_{\text{meso}}$  at  $1 \text{ nm} < R < 25 \text{ nm}$ , and  $V_{\text{macro}}$  and  $S_{\text{macro}}$  at  $25 \text{ nm} < R < 100 \text{ nm}$ ;  $\langle R_{\text{v}} \rangle$  and  $\langle R_{\text{s}} \rangle$  are the average values of the pore size calculated as a ratio of the first moment of  $f_{\text{v}}(R)$  or  $f_{\text{s}}(R)$  to the zero moment  $\langle R \rangle = \int f(R)RdR / \int f(R)dR$

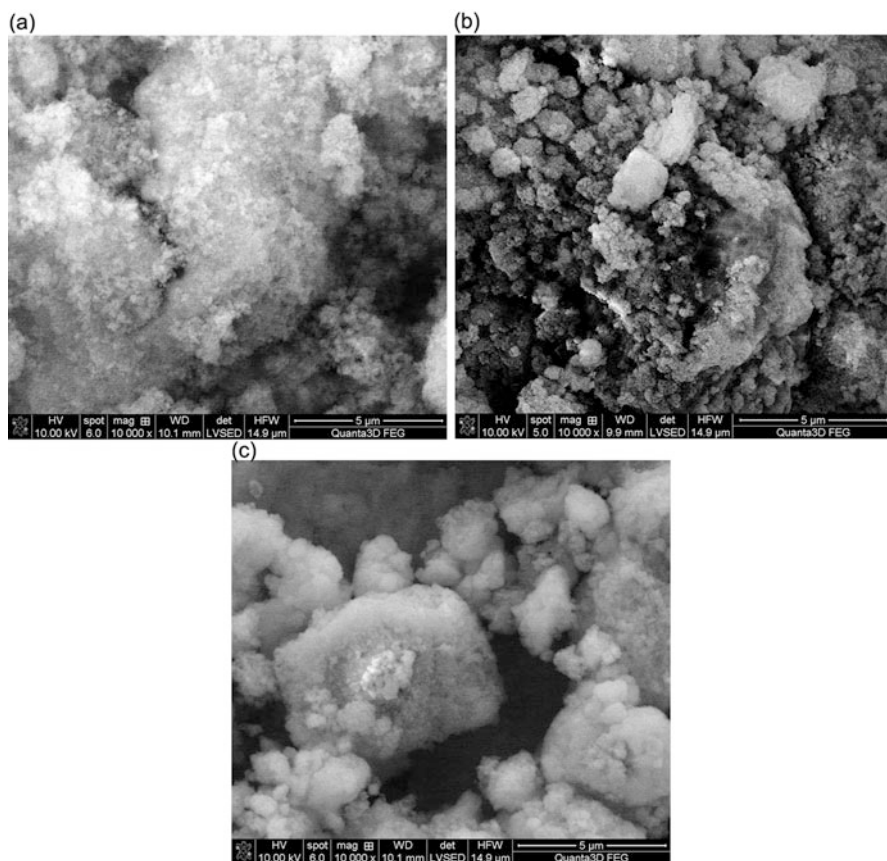


**Fig. 56.1** SEM images of (a) densil, (b) glucose/silica, and (c) char/silica (scale bar 5  $\mu\text{m}$ )

practical absence of this process for A-300 (weight loss is 0.15 wt.%). The weight loss at 150–970 °C is 1.21 wt.% and 0.25 wt.% for A-300 and DS, respectively, at close values of 1.36 and 1.35 wt.% at 120–970 °C. Thus, one can assume that the reactions with participation of surface hydroxyls and bound water during interactions of silica with glucose can occur at lower activation energy than that for the initial silica.

Pure glucose as a polar compound adsorbs a significant amount of water from air since the weight loss upon heating to 100 °C corresponds to 7.94 wt.%, and it is equal to 8.26 wt.% at 20–120 °C and 8.56 wt.% at 20–150 °C (Fig. 56.2a). The desorption water rate is maximal at 84.1 °C (Fig. 56.2b). For glucose bound to silica, this point shifts toward 117.4 °C due to (i) interactions of water and glucose molecules with silica in narrower voids in GI/DS, (ii) formation of relatively thick glucose/water adsorption layers at the silica surface, and (iii) complete filling of pores by adsorbates that decelerates desorption of water from these pores. Note that

**Fig. 56.2** Thermograms of glucose (*Gl*), initial nanosilica (*A-300*), densil (*DS*), glucose/densil (*GI/DS*), and carbodensil (*C/DS*): (a) TG, (b) differential TG (*DTG*), and (c) differential thermal analysis (*DTA*)

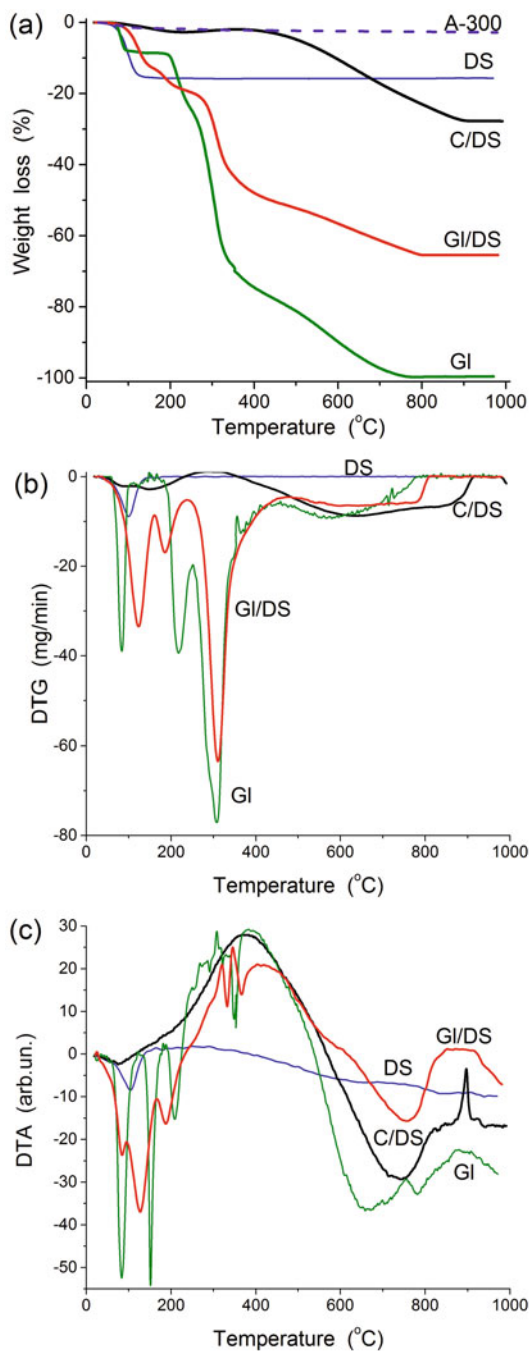
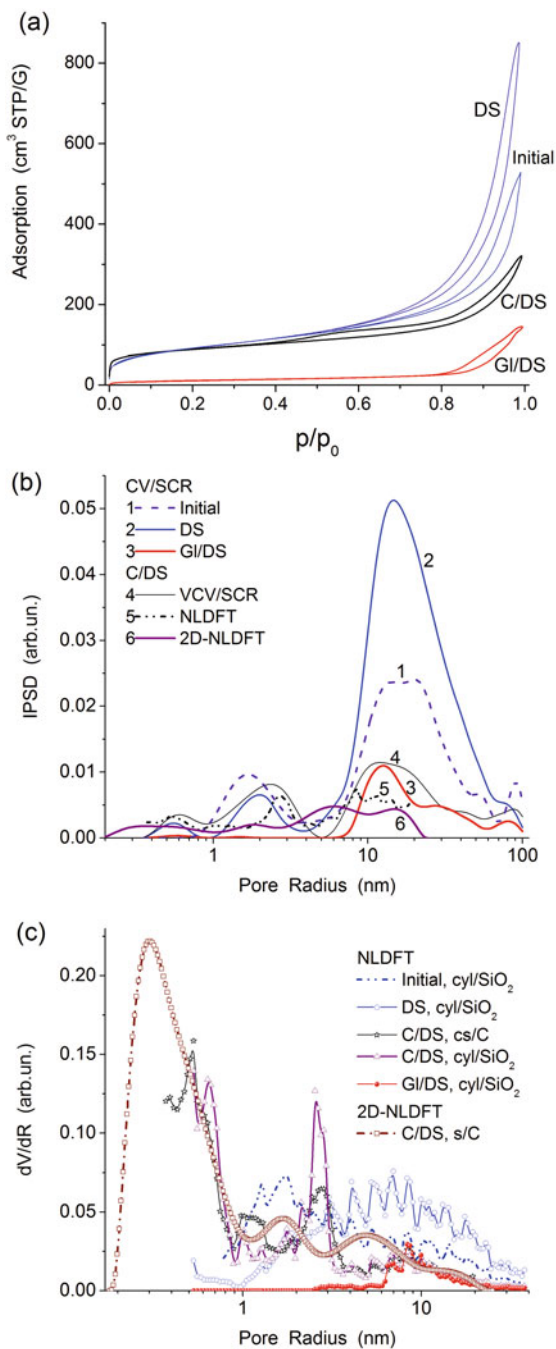


**Fig. 56.3** (a) Nitrogen adsorption-desorption isotherms for initial nanosilica (initial), densil (DS), glucose/densil (GI/DS), and carbodensil (C/DS). (b) Incremental PSD and (c) differential NLDFT or 2D-NLDFT PSD for initial nanosilica (initial), densil (DS), glucose/densil (GI/DS), and carbodensil (C/DS) calculated using (a) CV/SCR, VCV/SCR, NLDFT (cylindrical pores in silica, cyl/SiO<sub>2</sub>), and (c) NLDFT using equilibrium models with cyl/SiO<sub>2</sub> and slit-shaped and cylindrical pores in carbon (sc/C) and 2D-NLDFT with the slit-shaped pores in carbon (s/C)





for water desorbed from DS, this point is at 99.8 °C, but for A-300, it is at 72.1 °C. Consequently, compacting of secondary structures in DS decelerates desorption of water more strongly from GI/DS. The weight loss for the individual glucose (with bound water) at 20–200 °C is 9.8 wt.%, and for GI/DS, it increases to 17 wt.%. For glucose and GI/DS, two negative DTG peaks (Fig. 56.2b) correspond to three endothermic DTA peaks (Fig. 56.2c), which link to water desorption and glucose melting ( $T_m = 146$  and  $150$  °C for  $\alpha$ -D-glucose and  $\beta$ -D-glucose, respectively). At  $T > 200$  °C, thermodestruction of glucose starts. It includes such processes as dehydration (associative removal of water molecules, endothermic process), oxidation (exothermic process, TG study was carried out in air), removal of CO and CO<sub>2</sub>, and formation of polyaromatics. Some processes are completed close to 400 °C, but others (final oxidation of polyaromatics and char) occur up to 765 °C for glucose alone and 800 °C for GI/DS. Oxidation of char in C/DS finished at approximately 900 °C. Note that C/DS adsorbs water from air much smaller (desorption of 1.62 wt.% at 20–150 °C) than pure densil does (15.44 wt.%) but close to that for A-300. These amounts of adsorbed water are much smaller than the pore volume of the materials (Table 56.1,  $V_p$ , Fig. 56.3a). However, the amounts of adsorbed water correspond to the volume of nanopores ( $R < 1$  nm) and narrow mesopores ( $1 \text{ nm} < R < 3 \text{ nm}$ ) (Fig. 56.3b, c). In other words, adsorbed water (in contrast to nitrogen) weakly fill broad mesopores ( $3 \text{ nm} < R < 25 \text{ nm}$ ) and does not practically fill macropores.

Comparison of the pore size distributions (PSD, Fig. 56.3b) for DS and A-300 shows that a new peak of nanopores (pore radius  $R = 0.3$ – $0.8$  nm) arrears after MCA and a peak of narrow mesopores shifts toward larger values of  $R$  (2 nm instead of 1.67 nm for A-300). The position of a broad peak of mesopores and macropores shifts from 16.5 (A-300) to 15 nm (DS) due to powder compacting. These changes correspond to changes in the averaged values of pore radius  $\langle R_v \rangle$  (Table 56.1). For GI/DS, practically only broad mesopores and macropores are observed that result in significant diminution of the values of  $S_{\text{BET}}$  and  $V_p$  and increase in  $\langle R_v \rangle$  and  $\langle R_s \rangle$ . In other words, glucose fills narrow voids between silica nanoparticles in their aggregates (Fig. 56.3), but the agglomerates are partially destroyed (Fig. 56.1). The average size of model nonporous GI/DS aggregates corresponds to 70 nm in diameter that can include dozen nonporous nanoparticles of silica of 8.3 nm in average diameter. The glucose layer is not uniform because the textural pores filled by glucose have a complex shape as voids between nanoparticles randomly packed in secondary structures. After carbonization of glucose, the porosity of the composite increases, especially in respect to nanopores (Fig. 56.3c,  $R < 1$  nm; Table 56.1,  $S_{\text{nano}}$  and  $V_{\text{nano}}$ ). C/DS is characterized by minimal values of  $\langle R_v \rangle$  and  $\langle R_s \rangle$  (Table 56.1), i.e., it is the most compacted material. Note that the profiles of the PSD of broad mesopores ( $6 \text{ nm} < R < 25 \text{ nm}$ ) and macropores ( $R > 25 \text{ nm}$ ) are similar for C/DS and GI/DS (Fig. 56.3). This can be considered as consequence of keeping (upon carbonization) of the organization of secondary structures formed in GI/DS during MCA. SEM images (Fig. 56.1) and the textural characteristics (Table 56.1; Fig. 56.3) show that char in the C/DS composite represents weakly porous nanoparticles. Similar textural features of char

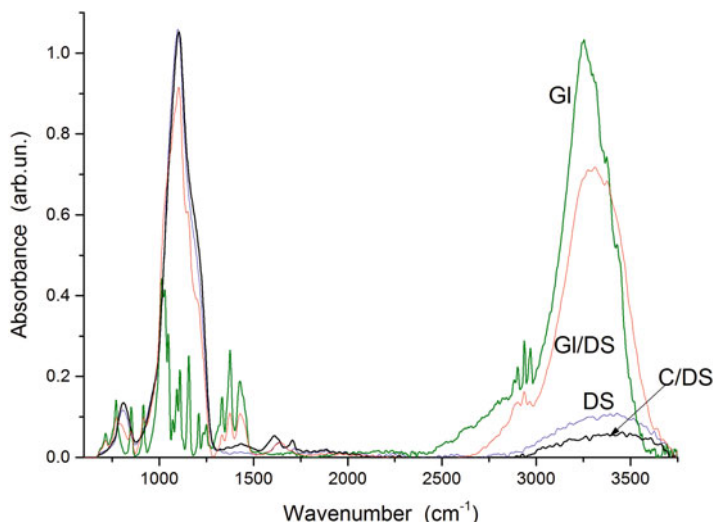


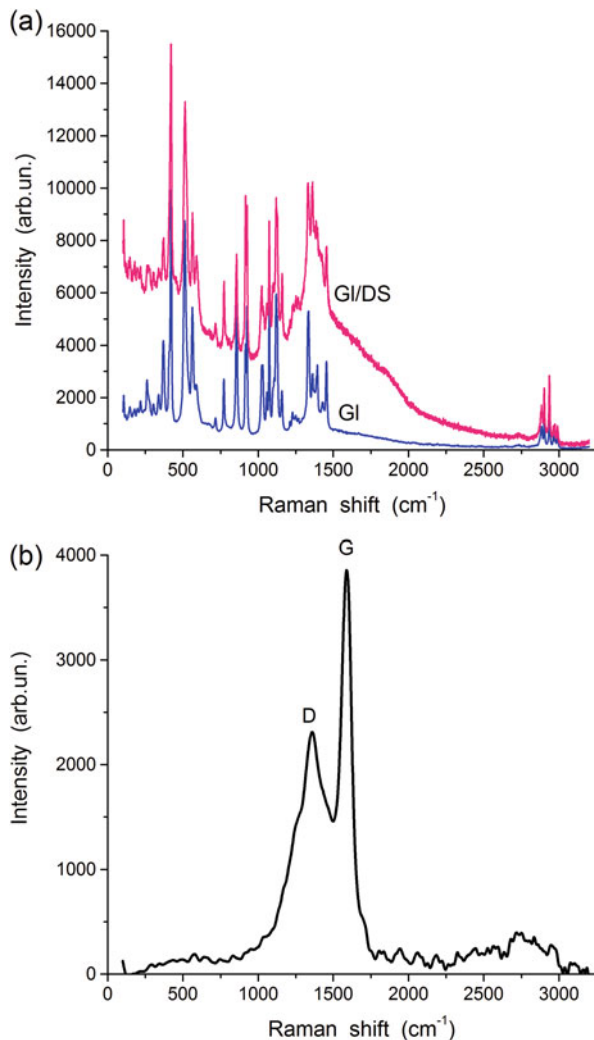
**Fig. 56.4** FTIR spectra of glucose (*Gl*), densil (*DS*), glucose/densil (*Gl/DS*), and carbodensil (*C/DS*)

are observed upon carbonization of glucose on the surface of silica gel Si-100 performed in a rotary reactor or autoclave or upon carbonization of some other precursors [2–8]. Glucose carbonization is accompanied by hydrothermal treatment of a silica surface due to the formation of water molecules upon dehydration of glucose molecules with increasing temperature (Fig. 56.2). This leads to the absence of diminution of the adsorption of nitrogen at low pressures ( $p/p_0 < 0.3$ ) (Fig. 56.3a, *C/DS*) in contrast to char/silica composites prepared using carbon precursors without O-containing functionalities in the molecules [2–8]. The model errors ( $\Delta w$ ) in CV/SCR or VCV/SCR are relatively small (2.3–22.4%, Table 56.1).

Some additional structural information on composites can be obtained from FTIR (Fig. 56.4) and Raman (Fig. 56.5) spectra. FTIR spectra (Fig. 56.4) were recorded using attenuated total reflection mode. Therefore, some bands related to bulk characteristics of particles have low intensity, e.g., the combination vibrations at  $1860\text{ cm}^{-1}$  related to siloxane bonds in the bulk of particles or bands at  $1700\text{--}1450\text{ cm}^{-1}$  related to different structures in char.

A broad band at  $3255\text{ cm}^{-1}$  in the FTIR spectrum of glucose (Fig. 56.4, *Gl*) can be attributed to the OH-stretching vibrations of both bound water and OH groups in glucose molecules disturbed by the hydrogen bonds with neighboring molecules. This band has shoulders at  $3310$ ,  $3357$ , and  $3428\text{ cm}^{-1}$  characteristic for hydroxyls in different hydrogen bonds [20]. Additionally, they appear in deformation vibrations at  $902$  and  $1428\text{ cm}^{-1}$ . Bands at  $1016$ ,  $1322$ , and  $1374\text{ cm}^{-1}$  can be attributed to the CO-stretching vibrations in the COH and COC groups of glucose. Methyl groups of glucose are characterized by bands in the  $3000\text{--}2800\text{ cm}^{-1}$  range (C-H stretching vibrations) and  $768$  and  $848\text{ cm}^{-1}$  (deformation vibrations) [21–23].

**Fig. 56.5** Raman spectra of (a) glucose (*Gl*), glucose/silica (*Gl/DS*), and (b) carbodensil



Densil containing a small amount of adsorbed water is characterized by a broad band of bound water and disturbed surface hydroxyls at  $3750\text{--}2750\text{ cm}^{-1}$ , which, however, are less intensive and broad than the bands of glucose or glucose/silica (Fig. 56.4). This difference is also dependent on a FTIR mode and sample preparation. For densil, intensive bands at  $1100$  and  $800\text{ cm}^{-1}$  correspond to asymmetric and symmetric Si-O stretching vibrations, respectively [20].

The FTIR spectrum of *Gl/DS* is close to a normalized sum of the spectra of densil and glucose. However, intensive band of the OH-stretching vibrations shifts toward greater wavenumbers by  $50\text{ cm}^{-1}$ , the asymmetry of this band decreases,

and only a shoulder is at  $3379\text{ cm}^{-1}$ . These changes correspond to diminution of the hydrogen bonding of molecules because of their non-maximum dense packing in the adsorption layer with the structure different from the structure of bulk glucose due to confined space effects and MCA.

The FTIR spectrum of C/DS (Fig. 56.4) is close to that of DS with some differences related to a smaller content of water ( $3750\text{--}2750\text{ cm}^{-1}$ ) and the presence of the char with C-C, C = C, C-O, and other bands ( $1700\text{--}1250\text{ cm}^{-1}$ ). However, intensity of the bands related to the char is low in the FTIR spectrum recorded in the attenuated total reflection mode in contrast to the Raman spectra (Fig. 56.5b) containing the most intensive D and G bands related to the char.

The Raman spectrum of char/silica (Fig. 56.5b) shows D ( $\text{sp}^3$  structures) and G ( $\text{sp}^2$  structures) bands, as well as bands at higher ( $2500\text{--}3000\text{ cm}^{-1}$ ) and lower ( $\sim 500\text{ cm}^{-1}$ ) shifts. According to this spectrum, peak intensity of a G band (corresponding to  $\text{sp}^2$  C atoms in relatively large polyaromatic graphene structures) is higher than that of the D band (disordered structures with  $\text{sp}^3$  C atoms out of planes of small carbon structures) [24–26]. However, the integral intensity of the broad D band (composed, at least, of three bands) is greater (52.2%) than that of the narrow G band (15.5%).

The shape and position of the G and D bands (and their sub-bands) depend on crystallinity or amorphism of the carbon materials. The absence of a clear picture in the spectrum (Fig. 56.5b) in the  $2500\text{--}2700\text{ cm}^{-1}$  range related to 2D band (overtone of the D band) and complex D + G band (located at  $2850\text{--}2950\text{ cm}^{-1}$  as a disorder-induced band, which would disappear with increasing crystallinity) shows that the char has rather non-ordered structure of particles bound to the silica surface but with a significant contribution of  $\text{sp}^2$  C in the graphene structures.

Glucose alone and bound to DS has similar Raman spectra (Fig. 56.5a), which correspond to typical one of glucose [27, 28]. Silica has low intensity in the Raman spectra; therefore, it is not shown here with a separate spectrum. However, the baseline in the G/DS spectrum is higher than that of pure glucose due to the effect of the silica matrix. Glucose bound to DS does not show strong disturbance in the band shapes. This can be explained by the textural characteristics of densil, which does not practically have nanopores. The absence of strong confined space effects allows us to prepare C/DS with small carbon nanoparticles, i.e., the material represents a composite with carbon and silica nanoparticles.

The aqueous suspensions of fumed silica can demonstrate one-, two-, or trimodal distributions of particle sizes (PaSD) depending on concentration, pH, salinity, sonication time, and aging time [29], and aggregates of  $50\text{--}1000\text{ nm}$  in size are most typical structures. Different treatment (e.g., 3–6 min of sonication) and varied content of silica (0.2 or 3 wt.%) weakly affect the PaSD with respect to the particle number (Fig. 56.6b). However, the PaSD with respect to the particle volume is more sensitive to the silica content (Fig. 56.6a). Compacting of A-300 in DS results in a significant increase in the size of agglomerates (Fig. 56.6a,b). Sonication can destroy only a fraction of these agglomerates (Fig. 56.6a), and sonication time (3 or 6 min) weakly affects the PaSD. Addition of glucose more strongly affects

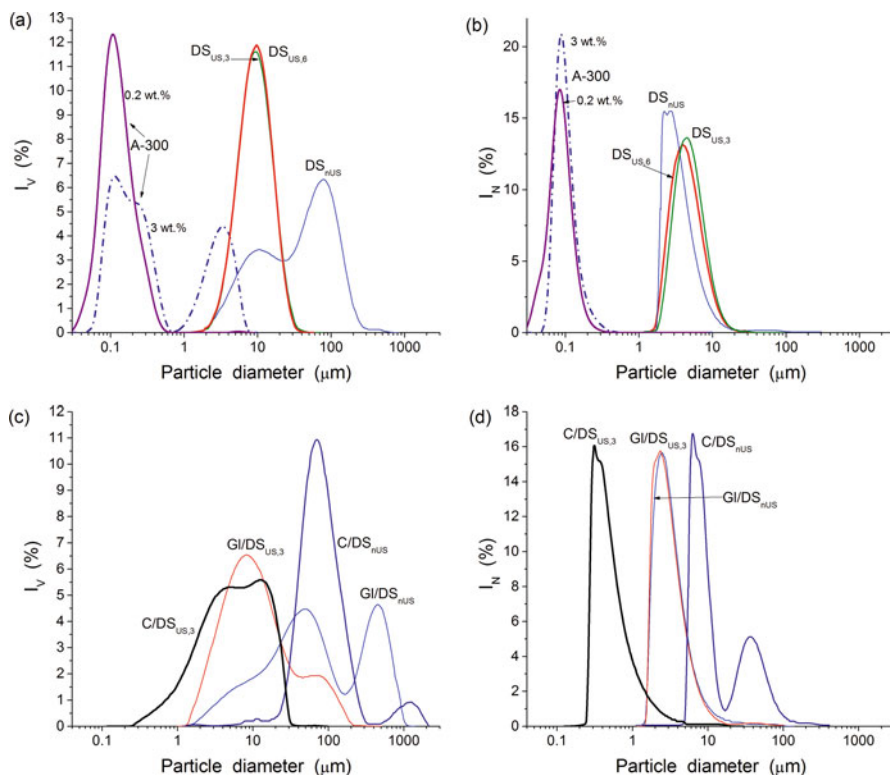


**Fig. 56.6** Particle size distributions in the aqueous suspensions with respect to particle (a, c) volume and (b, d) number for initial A-300 (obtained using Zetasizer Nano ZS) at concentration of 0.2 wt.% (shown results averaged for six measurements after sonication for 3 or 6 min) or 3 wt.% and 0.1 wt.% for other samples (Mastersizer 2000): densil (DS), densil with glucose (Gl/DS), and carbon/densil (C/DS) mechanically mixed but not sonicated (subscript 'nUS') or sonicated for 3 min ('US,3') or 6 min ('US,6')

the PaSD<sub>V</sub> (Fig. 56.6a, c) than PaSD<sub>N</sub> (Fig. 56.6b, d). After carbonization of glucose, sonication gives a maximal effect in diminution of observed aggregates in the suspension (Fig. 56.6c, d). Small aggregates, characteristic for A-300, appear.

The presence of small aggregates in the sonicated suspension of C/DS can be favorable for the use of this material as a drug carrier providing controlled release of drug molecules from a surface of relatively small particles of both carbon and silica. Desorption of drug molecules from much larger (by 3–4 orders of size magnitude) particles of AC can be very slow in comparison with the process for the C/DS materials.

## 56.4 Conclusion

Compacted fumed silica (densil, DS) was prepared using mechanochemical activation of wetted nanosilica (0.5 g of water per gram of dry silica). DS is characterized by close value of  $S_{\text{BET}} = 328 \text{ m}^2/\text{g}$  to that of initial A-300 ( $330 \text{ m}^2/\text{g}$ ) but with a greater value of pore volume ( $1.325 \text{ cm}^3/\text{g}$  vs.  $0.826 \text{ cm}^3/\text{g}$ ) and a greater bulk density ( $0.21 \text{ g}/\text{cm}^3$  vs.  $0.05 \text{ g}/\text{cm}^3$ ). Despite these textural changes, DS remains in the powder state. Fumed silica was used as a matrix for preparation of a composite with glucose (GI/DS). This composite was used for carbonization of glucose that results in the formation of weakly porous char nanoparticles. The GI/DS composite was with strongly reduced porosity ( $0.227 \text{ cm}^3/\text{g}$ ) and specific surface area ( $42 \text{ m}^2/\text{g}$ ). After carbonization of glucose, the porosity ( $0.5 \text{ cm}^3/\text{g}$ ) and  $S_{\text{BET}}$  ( $302 \text{ m}^2/\text{g}$ ) increase, and contribution of nanopores strongly grows. The composite represents a blend of silica and carbon nanoparticles in the powder state that is of importance for the use of the material as an adsorbent in the liquid media, where it represents particles mainly in the range of 1–10  $\mu\text{m}$ .

Developed method of gas-phase mechano-sorption modification of nanooxides can be useful for adsorption modification of disperse materials by nonvolatile compounds with the use of a small amount of solvent ( $\sim 30\text{--}40 \text{ wt.}\%$  in a mixture).

**Acknowledgments** The authors are grateful to the European Community, Seventh Framework Programme (FP7/2007-2013), Marie Curie International Research Staff Exchange Scheme (grant no. 612484).

## References

1. Kamegawa K, Yoshida H (1990) A method for measuring surface area of carbon of carbon-coated silica gel. *Bull Chem Soc Japan* 63:3683–3685
2. Seledets O, Leboda R, Grzegorzczak W, Zarko VI, Gun'ko VM, Janusz W, Charmas B (2006) Effect of sulphur on surface properties of complex carbon-silica adsorbents. *Microporous Mesoporous Mater* 93:90–100
3. Gun'ko VM, Skubiszewska-Zieba J, Leboda R, Zarko VI (2000) Fumed silica carbonized due to pyrolysis of methylene chloride. *Langmuir* 16:374–382
4. Gun'ko VM, Leboda R, Zarko VI, Skubiszewska-Zieba J, Grzegorzczak W, Pakhlov EM, Voronin EF, Seledets O, Chibowski E (2003) Fumed oxides modified due to pyrolysis of cyclohexene. *Colloids Surf A Physicochem Eng Asp* 218:103–124
5. Bogatyrev VM, Oranska OI, Gun'ko VM, Leboda R, Skubiszewska-Zieba J (2011) Influence of metal content on structural characteristics of inorganic Nanocomposites  $\text{M}_x\text{O}_y/\text{SiO}_2$  and  $\text{C}/\text{M}_x\text{O}_y/\text{SiO}_2$ . *Chem Phys Technol Surf* 2:135–146. (in Russian)
6. Gun'ko VM, Turov VV (2013) Nuclear magnetic resonance studies of interfacial phenomena. CRC Press, Boca Raton
7. Leboda R, Turov VV, Charmas B, Skubiszewska-Zieba J, Gun'ko VM (2000) Surface properties of mesoporous carbon-silica gel adsorbents. *J Colloid Interface Sci* 223:112–125
8. Blitz IP, Blitz JP, Gun'ko VM, Sheeran DJ (2007) Functionalized silicas: structural characteristics and adsorption of  $\text{Cu(II)}$  and  $\text{Pb(II)}$ . *Colloids Surf A Physicochem Eng Asp* 307:83–92

9. Jain A, Balasubramanian R, Srinivasan MP (2015) Production of high surface area mesoporous activated carbons from waste biomass using hydrogen peroxide-mediated hydrothermal treatment for adsorption applications. *Chem Eng J* 273:622–629
10. Mironyuk IF, Gun'ko VM, Turov V, Zarko VI, Leboda R, Skubiszewska-Zięba J (2001) Characterization of fumed silicas and their interaction with water and dissolved proteins. *Colloids Surf A Physicochem Eng Asp* 180:87–101
11. Agnieszka Ś, Wojciech S, Piotr Z, Paulina J (2015) Synthesis and characterization of carbon fiber/silica aerogel nanocomposites. *J Non-Cryst Solids* 416:1–3
12. Hoshikawa Y, Castro-Muñiz A, Komiyama H, Ishii T, Yokoyama T, Nanbu H, Kyotani T (2014) Remarkable enhancement of pyrolytic carbon deposition on ordered mesoporous silicas by their trimethylsilylation. *Carbon* 67:156–167
13. Bansal RC, Goyal M (2005) Activated carbon adsorption. CRC Press Inc., Boca Raton
14. Kumagai S, Ishizawa H, Aoki Y, Toida Y (2010) Molded micro- and mesoporous carbon/silica composite from rice husk and beet sugar. *Chem Eng J* 156:270–277
15. Sevilla M, Fuertes AB (2009) Chemical and structural properties of carbonaceous products obtained by hydrothermal carbonization of saccharides. *Chem Eur J* 15:4195–4203
16. Voronin EF, Nosach LV, Guzenko NV, Pakhlov EM, Gabchak OL (2009) Adsorption modification of nanosilica with non-volatile organic compounds in fluidized state. In: Shpak AP, Gorbyk PP (eds) *Nanomaterials and supramolecular structures: physics, chemistry, and applications*. Springer, London, pp 169–178
17. Gun'ko VM, Voronin EF, Nosach LV, Turov VV, Wang Z, Vasilenko AP, Leboda R, Skubiszewska-Zięba J, Janusz W, Mikhalovsky SV (2011) Structural, textural and adsorption characteristics of nanosilica mechanochemically activated in different media. *J Colloid Interface Sci* 355:300–311
18. Gregg SJ, Sing KSW (1982) Adsorption, surface area and porosity, 2nd edn. Academic Press, London
19. Gun'ko VM (2014) Composite materials: textural characteristics. *Appl Surf Sci* 307:444–454
20. Hair JML (1967) Infrared spectroscopy in surface chemistry. Marcell Dekker, New York
21. Brand JCD, Eglinton G (1965) Application of spectroscopy to organic chemistry. Oldbourne Press, London
22. Griffiths P, de Hasseth JA (2007) Fourier transform infrared spectrometry, 2nd edn. Wiley, New York
23. Banwell CN, McCash EM (1994) Fundamentals of molecular spectroscopy, 4th edn. McGraw-Hill, London
24. Tuinstra F, Koenig JL (1970) Raman spectrum of graphite. *J Chem Phys* 53:1126–1130
25. Galluzzi F, Barbarossa V, Polla MF, Tomaciello R (1994) Near-IR-excited Raman scattering in graphitic materials. *Mater Sci Eng B* 27:L1–L3
26. Wang Y, Alsmeyer DC, McCreery RL (1990) Raman spectroscopy of carbon materials: structural basis of observed spectra. *Chem Mater* 2:557–563
27. Kneipp K, Moskovits M, Kneipp H (2006) Surface-enhanced Raman scattering—physics and applications, topics appl. Phys Ther 103:47–66
28. Enejder AMK, Seccina TG, Oh J, Hunter M, Shih W-C, Sasic S, Horowitz GL, Feld MS (2005) Raman spectroscopy for noninvasive glucose measurements. *J Biomed Opt* 10:031114
29. Gun'ko VM, Zarko VI, Leboda R, Chibowski E (2001) Aqueous suspensions of fumed oxides: particle size distribution and zeta potential. *Adv Colloid Interf Sci* 91:1–112

# Chapter 57

## Nano- and Microdisperse Structures in Processes of Metamorphism, Reduction Sintering, and Component Separation of Iron-Oxide-Silicate Materials

A. V. Panko, I. G. Kovzun, V. A. Prokopenko, O. A. Tsyganovich,  
V. O. Oliinyk, and O. M. Nikipelova

### 57.1 Introduction

Iron-oxide-silicate ore materials (IOSOMs) and their technogenic processing products, widespread in Earth crust, including processed in reductive conditions at high temperatures are one of the natural nanostructured material groups with great practical importance. As a rule, IOSOMs contain polydispersed and polymineral formations based on iron, silicon, and aluminum oxides and containing admixtures of other inorganic and organic components [1–8]. Basic IOSOM types include nanostructured sedimentary iron ores, iron-containing clays, pelitic sediments (peloids), silica, and feldspars.

IOSOM practical importance increases constantly, and fields of their application are broadened, respectively. This fact attracts and will attract attention of many researchers to their high-temperature processing [1, 2, 4–13]. At the same time, the conceptions of physicochemical geomechanic and microbiological role in processes of nanochemical, mechanochemical, and structural IOSOM transformation

---

A.V. Panko (✉) • I.G. Kovzun • O.A. Tsyganovich • V.O. Oliinyk  
F.D.Ovcharenko Institute of Biocolloid Chemistry of NAS of Ukraine, 42, Ak.Vernadskogo Blvd,  
Kyiv, Ukraine 03680  
e-mail: [gr.k.ibcc@ukr.net](mailto:gr.k.ibcc@ukr.net)

V.A. Prokopenko  
F.D. Ovcharenko Institute of Biocolloid Chemistry of NAS of Ukraine, 42, Ak.Vernadskogo  
Blvd, Kyiv, Ukraine 03680

National technical University of Ukraine “KPI”, Peremohy Ave., 37, building 4, Kyiv,  
Ukraine 03056

O.M. Nikipelova  
State agency “Ukrainian Research Institute of Medical Rehabilitation and Balneology, Ministry of  
Health of Ukraine”, 6, Lermontovskiy Lane, Odessa, Ukraine 65014



are not quite developed enough. And the problems of IOSOM transformation and metamorphism with further nanodisperse structure formation and their high-temperature separation, concentration, purification, and practical appliance have not been discussed. The role of silicates, sulfur, phosphorus, arsenic compounds, and other admixtures in nanochemical IOSOM transformations is studied insufficiently. Thus, further investigation of the aforesaid transformations gives new opportunities for their scientifically grounded mastering.

The said reasons point on that investigations of IOSOM metamorphism and transformation along with their chemical, physical-geomechanical, microbiological, and nanochemical transformations and processes of their reduction at high temperatures and purification from admixtures of nano- and microparticles of silica, arsenic, and phosphorus are actual. It was the basis for current study increase.

## 57.2 Methods and Materials

Electron-microscopic IOSOM sample images were obtained on SELMI electron microscope in a light field mode, and the morphology of samples was studied on JEOL scanning electron microscope JSM6490LV. Thermograms of samples were obtained in inert atmosphere. XRD were done on DRON-UM1 with two Soller slits with  $\text{CuK}\alpha$  filtered emission. Rheological investigations were performed by Rheotest 2 (Germany) connected to the PC for data recording. Sample chemical composition was analyzed by X-ray fluorescence method. Physical-geomechanical and nanochemical IOSOM transformation processes in natural and technogenic conditions were modeled using physicochemical geomechanic methods [6] and their reduction up to magnetite or metallized product – in conditions described in [10, 11, 13]. Microbiological IOSOM suspension testing was performed according to methods [14]. High-dispersed pelitic iron-oxide-silicate material (Azov region) of sedimentary biocolloid origin which contain 39.87% Fe; 8.71% Mn; 0.95% Ca; 0.28% Mg; 3.89% Al; 7.81% Si; 0.45% Ti; 0.05% V; 0.98% P; 0.21% S; and 0.12% As were used as a main sample for study, and other iron-contained materials were used too [1, 9–13].

## 57.3 Experiment and Discussion

Rheological study of typical iron-oxide-silicate material [1] (Fig. 57.1) showed that its concentrated suspensions are being characterized by viscosity nonstandard hyperanomaly, being explained by influence of micro- and nanoparticles contained in zones of mechanochemically and nanochemically transforming coagulation-condensation contacts on IOSOM metamorphic processes [2]. Diffraction pattern of a sample (Fig. 57.2) points on amorphous highly dispersed IOSOM structure. Its composition was consisted of goethite, saponite, quartz, sulfides, and nanodispersed admixtures of phosphates and arsenates of aluminum and iron having microbiological origin [1, 15].

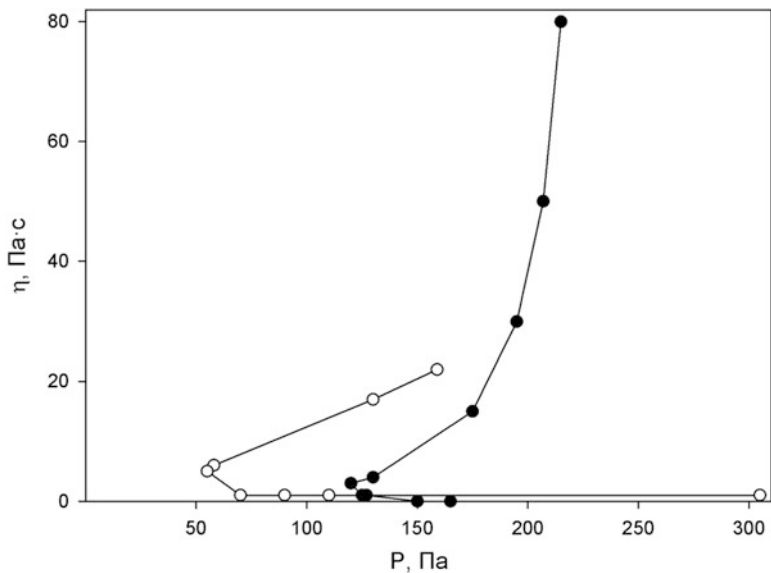


Fig. 57.1 Dependence of viscosity from shear stress (P) for sedimentary IOSOM with 46% suspension humidity. (•) – «direct» и (○) – «reversed» curve way

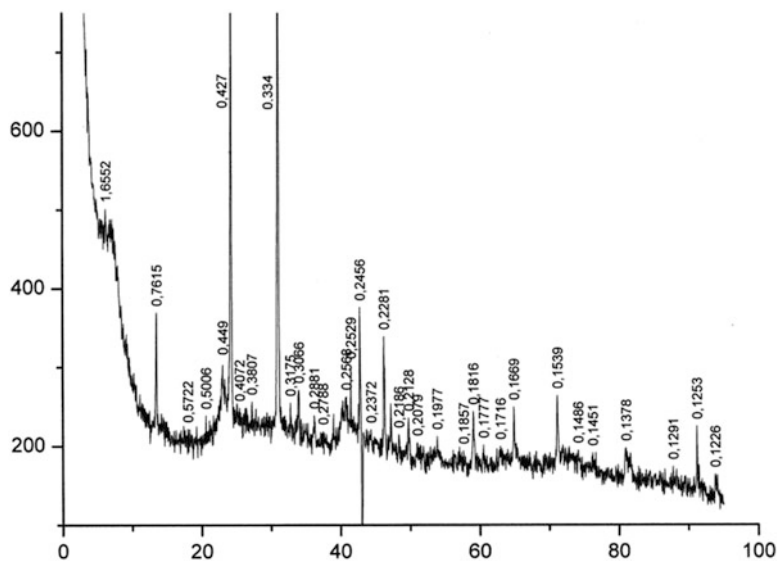
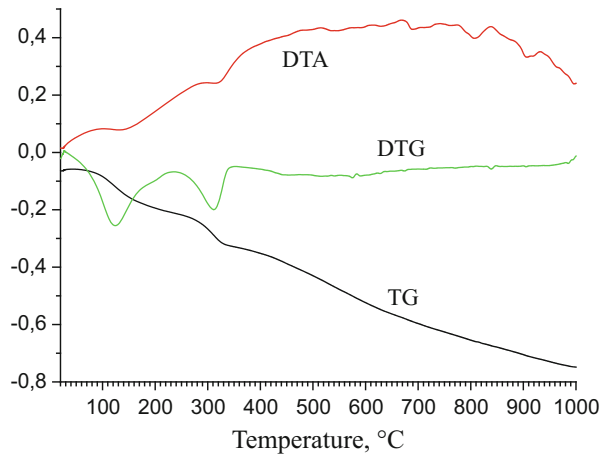


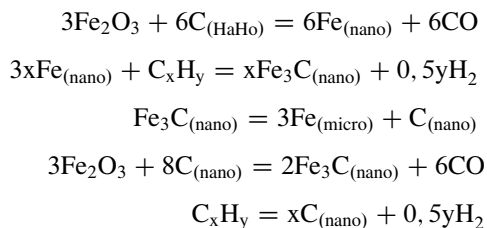
Fig. 57.2 XRD of sedimentary IOSOM

**Fig. 57.3** Thermogram of IOSOM mixed with coal powder at 4:1 ratio



According to obtained thermograms (one of which is shown on Fig. 57.3) as well as XRD investigation [11], the processes of IOSOM reduction begin at above 450°C and occur by summary reaction  $3\text{Fe}_2\text{O}_3 + \text{C} = 2\text{Fe}_3\text{O}_4(\text{nano, micro}) + \text{CO}$  up to 990–1000°C [5, 12].

Above the said temperature, magnetite is being reduced up to wustite (FeO). Then active metallization process is being held in interval of 1050–1150°C by reaction  $\text{FeO} + \text{C} = \text{Fe} + \text{CO}$ . As far as metallization process with formation of nanoparticles of metallic iron on magnetite surface begins already at 500–700°C temperatures, then such iron takes part in formation of amorphous carbon reducer ( $\text{C}_{\text{nano}}$  and  $\text{Fe}_3\text{C}_{\text{nano}}$ ) from volatile hydrocarbons formed at thermal coal decomposition [12]. The process flows by “low-temperature” (500–1000°C) carbide cycle aided with nanoparticles which in technogenic conditions promote catalytic transformation of  $\text{Fe}_2\text{O}_3$  from IOSOMs into nanodispersed and then into microdispersed magnetite, on which surface nanoparticles of arsenates and phosphates are accumulated [13]. Consequently, in natural metamorphic conditions, fine-dispersed magnetite and thermodisrupted silicates formed at first from sedimentary IOSOMs are being transformed into ferroquartzites (jaspilites) [15] or into ferrosilicates carbonized with nanocarbon particles (schungites) [16] as a result of sintering at high temperatures and pressures in Earth crust. Nanochemical processes being held in said conditions at 500–1000°C, including according to “low-temperature” carbide cycle mechanism [9], can be characterized by the following reactions [9, 13]:



Similar reactions, taking above 500°C on catalytically active surface of iron-silicate structures like saponites, nontronites, and other disperse iron-contained silicate minerals contained in IOSOM composition as admixtures, lead to formation of schungites [16] in conditions of natural metamorphism and at carbon surplus in the Earth crust and to formation of carbonized nanoporous sorbents [17] in technogenic conditions.

Given data directly points on dependence of the described processes from conditions of sediment formation usually occurring in seas and oceans [3, 4, 6–15], as far as IOSOM dispersion defines direction and efficiency of their transformation [9–13]. According to [14], such processes are also substantially depended on biocolloid (microbiological and colloid) processes in dispersions of IOSOM pelagic sediments. Biogeocenosis or bioosteal aggregates formed according to biogeochemistry laws as a result of selective microorganism with mineral particle interaction are being transformed into oolites, which are the basis of sedimentary iron-oxide-silicate and other ore deposits [7, 14, 15]. Sedimentary IOSOMs in inorganic structure of bioosteal aggregates or oolites contain also organic substances – microorganism waste products along with living organisms. Metabolic processes of the latter are accompanied with formation of variety of organic substances including nanostructured surface-active substances (SAS) [3, 15]. Such organic compounds take part in above described high-temperature reduction metamorphic processes in the Earth crust and in technogenic reduction condition of IOSOM transformations along with dispersed coal or gaseous hydrocarbons obtained from outside sources [9–13]. However, at the same time, the role of living organisms in metamorphic IOSOM sediment processes in aqueous medium and environment temperature lower than 38°C is still not quite clear.

Microorganism investigations of different eco-trophic groups [1], first of all iron-reducing bacterium, in pelitic sediment samples indicate sediment abilities to restore its physicochemical properties after their inactivation. Viscosity and yield stress change at sediment activation during 90–100 days indicate also realization of hydrolytic dispersion mechanism [6] under influence of SAS-type substances excreted by microorganisms during reduction of  $\text{Fe}^{3+}$  into  $\text{Fe}^{2+}$  processes (Fig. 57.4).

The data from Fig. 57.4 also shows that Fe(II) quantity in disperse medium increases at 0.07% during reduction processes (30–100 days). At the same time, Fe(III) concentration increases synchronously on 0.035% at the expense of reduced iron partial oxidation by oxygen from air, and it gives 0.105% in sum. Thus, at total 2.7% concentration of Fe in sediment counted by elemental iron, the part of mineral disruption mainly up to nanoparticles [13] reaches 4% in 90–100 days during the period of reduction processes. It substantively influences upon the increasing of suspension yield stress and viscosity at the same period.

High-temperature and microbiologic influence on pelitic IOSOM sediments are being preceded also by apparently connected with them physico-mechanical and geochemical transformations of iron-contained ores, which should be considered in details for discovering their role in posterior processes. Pelitic sediment formation in long-term natural geological conditions in alkaliescent disperse medium [8] is

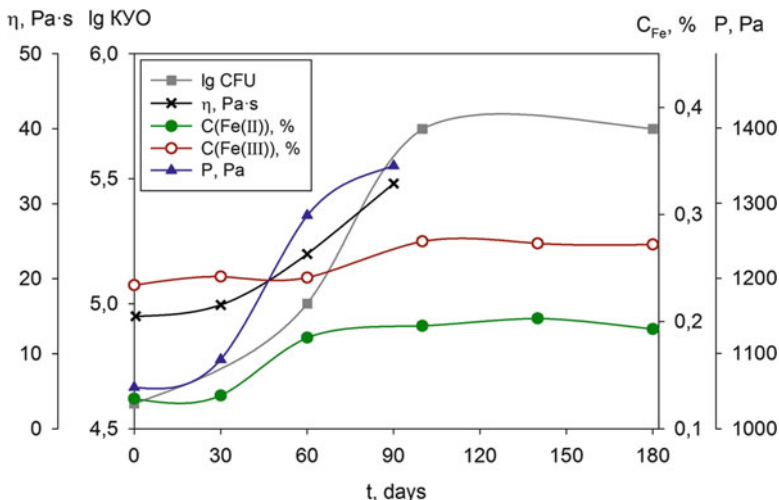
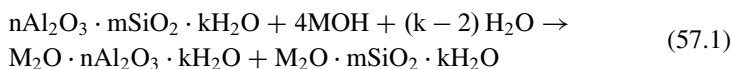
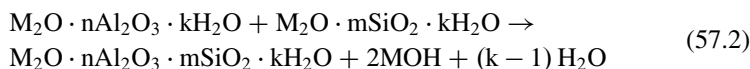


**Fig. 57.4** Change dynamics of viscosity ( $\eta$ ), of shear rate ( $P$ ), and of microbiological composition ( $lgCFU$ ) of partly deactivated iron-contained pelitic sediment suspensions during their activity further subsequent restoration, as well as change of Fe(II) and Fe(III) concentration in disperse medium

indeed being preceded by mechanical and mechanochemical transformations of iron-contained ores which are also being accompanied by formation of nano- and microparticles and which are being held according to laws of physicochemical geomechanics (PCGM) [1, 6]. Herewith, according to [6, 18–20], chemical processes can be held in nanocracks of 10–100 nm sizes as provided by the following equations:

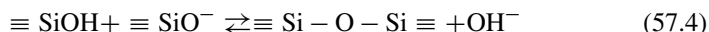
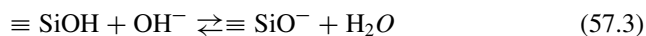


Then reaction (57.1) products react according to the following scheme:



Crystalline hydrate formed by reaction (57.2) has higher volume differing from initial product participated in the reaction (57.1). Thus, appeared crystallization pressure bursts (splits chemically) the crack subject to symbasic promotion by outer mechanical stress. Water, which additionally enters micrometer-broadened initial crack, hydrolytically destructs reaction (57.2) product at the next stage with releasing of alkali diffusing into newly formed secondary crack in the form of solution. The process goes the same way as for liquid-phase penetration into intergranular boundaries, but few grades faster, and it's now being measured not by

years but hours [2, 18, 19]. It is also promoted by nanochemical interactions adding interactions (57.1) and (57.2) being characterized by reactions [18]:



Reactions (57.3) and (57.4) are conditioned by transformations of disperse medium in soluble silicates, and they are influencing IOSOM suspension viscosity (Fig. 57.5).

Reaction (57.4) is a reaction of polymerization, and it leads to formation of insoluble polysilicate nanostructures on the surface of solid-phase crack. Released hydroxyl ions take part in reaction (57.1) or in (57.3). Therefore, reactions (57.3) and (57.4) are intermediate for processes (57.1) and (57.2), and colloid-chemical interactions held at nanolevel on solid surface of iron-contained silicate ore are closely associated with chemical transformations in disperse medium.

The process goes stepwise, and it was shown experimentally on “iron-contained aluminosilicate – alkaline component” model system. Rheological data shown in Fig. 57.6 shows that stepwise process goes more intensively in low-motion conditions of porous-dispersed ore, but for plastic flow velocity, increasing the stepwise process is being smoothed.

Formation mechanism of such process in model disperse technogenic materials in which analogues can be formed in natural conditions in zones of volcanic activity

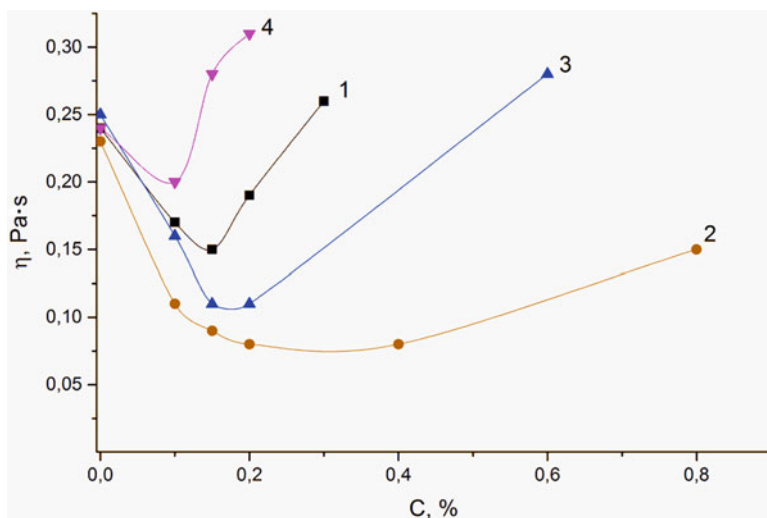
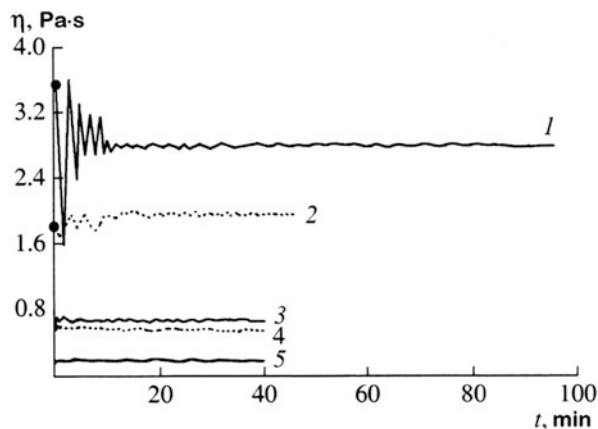


**Fig. 57.5** Influence of NaOH:Na<sub>2</sub>Si<sub>3</sub>O<sub>7</sub> ratio on IOSOM suspension viscosity ( $\eta$ ) depending on concentration (C) of alkaline mix in the following conditions: without NaOH (1); at ratio of NaOH:Na<sub>2</sub>Si<sub>3</sub>O<sub>7</sub> 1:2 (2), 1:1 (3), and 1.5:1 (4)

**Fig. 57.6** Process kinetics for iron-contained aluminosilicate ore accompanied by flowing of reactions (8) and (9) at shear rates of ( $s^{-1}$ ): 1.0 (1); 1.8 (2); 3.0 (3); 27.0 (4); and 81.0 (5)



has almost no differences from mentioned stepwise processes in rocks [18–20], and it has been proven by independent investigation [21]. The heart of the process is in fact that surface nanocracks in disperse material work as channels for penetration of reaction alkaline substance into them, i.e., they are phase-formation zones. If the volume of such new phase is bigger than phase-forming volume, then there's disjoining pressure being appeared, and it leads to disruption of initial particles by nanocracks. Then the process is being repeated on new disperse level and that is what can be seen on rheograms (Fig. 57.6) as stepwise process. As a result of new phase formation, it not only has self-activating stepwise behavior, but also it flows like mechano-geochemical and nanochemical processes described in [1, 8, 9, 18–22].

Results obtained in experimental part of the work with known ideas [1–13, 15, 18–21] taken in mind allowed proposing generalized scheme of physico-geomechanical, mechanochemical, biocolloid metamorphism and transformation processes of rock iron-oxide-silicate ore materials into pelitic (sedimentary) IOSOMs and ferroquartzites aided with nano- and microdisperse structures (Fig. 57.7). SEM images of structures formed on different process stages are presented on Fig. 57.8.

The scheme of iron-contained rock metamorphism and nanochemical transformation aided with nanostructures, microorganisms, as well as in heightened temperature conditions (Figs. 57.7 and 57.8) with formation of IOSOMs like pelitic sediments and nanocrystal jaspilites, proposed on basis of analytical-experimental investigations, allowed to provide for scientific explanation of further technological processes of high-temperature iron ore solid metallization, separation, and concentration of metallized products from nonmetallic admixtures. According to [5] the metallized product is being obtained by iron ore raw material direct reduction with carbon reducer at 900–1300°C. For example, there can be used oxidized pellets of next composition (wt%), 67.83  $Fe_{total}$ , 2.50 FeO, 94.12  $Fe_2O_3$ , 1.79  $SiO_2$ , 0.72  $Al_2O_3$ , 0.31 CaO, 0.12 MgO, 0.11 MnO, 0.31  $TiO_2$ , 0.01  $P_2O_5$ , and 0.01  $SO_3$

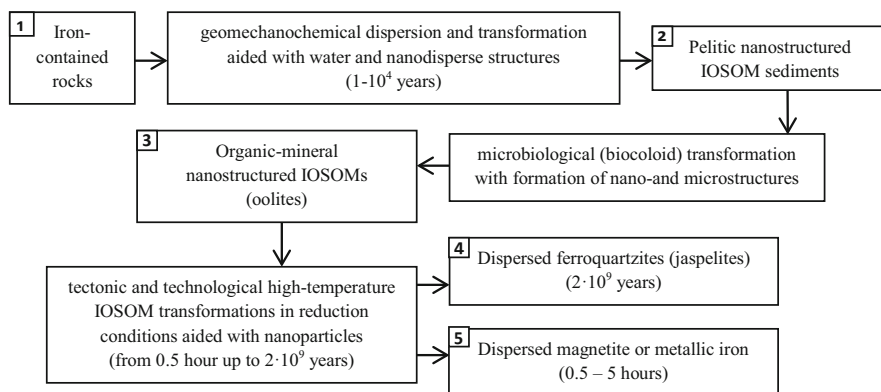


**Fig. 57.7** Scheme of natural and technogenic iron-containing rock transformation into pelitic sediments, jaspilites, and metallized materials

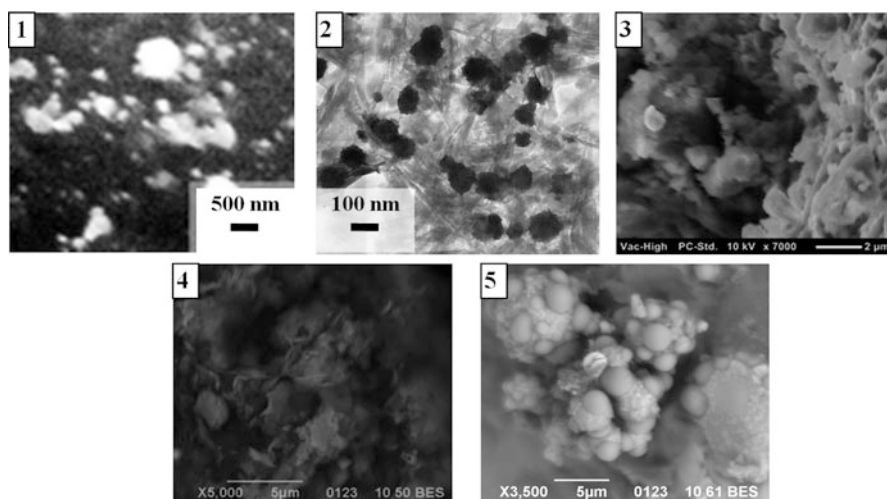


**Fig. 57.8** SEM images of structures formed on different stages (1, 2, 3, 4, 5) of processes by scheme on Fig. 57.7

(general admixture quantity is 3.38%), with flux being added for sulfur removal, for example, limestone containing (wt%) 1.59 SiO<sub>2</sub>, 0.74 Al<sub>2</sub>O<sub>3</sub>, 57.70 CaO, 0.48 MgO, 0.05 P<sub>2</sub>O<sub>5</sub>, 0.23 SO<sub>3</sub>, and 43.21 baking loss and reducer, for example, brown coal. Metallized product obtained from such mix has next composition (wt%): 92.23 Fe<sub>total</sub>, 5.93 FeO, 87.63 Fe<sub>MET</sub>, 2.43 SiO<sub>2</sub>, 0.98 Al<sub>2</sub>O<sub>3</sub>, 0.42 CaO, 0.17 MgO, 0.42 TiO<sub>2</sub>, 0.15 MnO, 0.006 P, 0.004 S, and 1.85 C (general admixture quantity is 4.58%).

Shortcoming of such process is that iron ore raw material concentrate with high content of iron (67–67) for metallization process is used, and it needs considerable

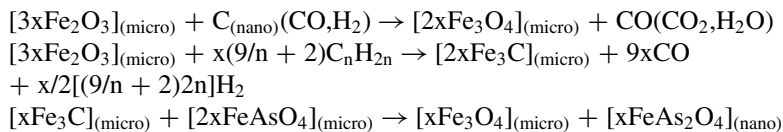


costs for preliminary grinding, concentration, and purification of iron ore raw material. Herewith, obtained metallized product contains 87.3% of metallic iron, 5.93% of FeO, 1.85% C, and 4.58% of admixtures, i.e., impurity concentration is even higher than it was in initial iron concentrate (3.38%). It means that during the process, impurity concentration in final product is increasing at 1.2% in which removal needs valuable capital, material, energetic costs and not designed yet technologies.

The proposed method of iron ore (especially of sedimentary origin) processing which considers established conditions of metamorphism and transformation of iron-contained rocks into nano- and microstructured iron oxide ore materials uses such materials without any preliminary enrichment [9–13]. Designed technology considers that obtained burnt cake can be easily cleared from general part of inorganic impurities at dry enrichment, and, in what follows, the separation process is being additionally activated during the process of wet alkaline enrichment and phosphorus and arsenic impurity separation [10, 11, 13]. Thus, for example, from arsenic- and phosphorus-contained IOSOMs reduced at 1200°C having next chemical composition (wt%) 32.88 Fe, 4.78 Mn, 1.38 P, 0.12 As, 0.09 S, 1.13 CaO, 1.88 Al<sub>2</sub>O<sub>3</sub>, and 11.11 SiO<sub>2</sub>, a high-purity concentrate can be obtained after enrichment, separation, and purification of cake; concentrate composition as given (wt%) are 95.71 Fe; 0.09 P; <0.007 As; 0.002 S; 0.23 CaO; 0.32 Al<sub>2</sub>O<sub>3</sub>; 1.73 SiO<sub>2</sub>; and 1.84 C (Table 57.1). Such results were reached also due to established fact that for iron ores contaminated with silicates, phosphorus, and arsenic, the maximal arsenic extraction and its separation from phosphorus can be reached in conditions of catalytic solid-phase carbide transformation of iron oxide at 600–980 °C with concurrent process of magnetite formation and conversion of insoluble As(V) compounds into alkali-soluble As(III) compounds, for example, by the following scheme:

**Table 57.1** Influence of NaOH and NaCl concentration on enriched metallized cake purification process

Concentration, %		Chemical composition of purified concentrate, %						
NaOH	NaCl	Fe	Mn	P	As	S	Al <sub>2</sub> O <sub>3</sub>	SiO <sub>2</sub>
4	–	91.99	0.23	0.18	0.03	0.005	0.48	2.71
6	–	93.28	0.15	0.11	0.02	0.004	0.37	2.03
8	–	95.04	0.07	0.10	0.01	0.003	0.35	1.87
12	–	95.71	0.00	0.09	0.01	0.002	0.32	1.73
14	–	95.79	0.00	0.09	0.01	0.002	0.33	1.75
12	10	95.75	–	0.10	0.009	–	–	–
12	15	95.81	–	0.08	0.007	–	–	–
12	20	95.99	–	0.07	0.007	–	–	–
12	30	96.03	–	0.06	0.007	–	–	–
12	35	95.77	–	0.07	0.008	–	–	–



Analysis of results given in Table 57.1 allows making the following conclusions: proposed technology which considers geological IOSOM transformation history can be used for component separation, enrichment, and purification of metallized iron ore raw materials of almost any composition and origin – from metallurgic sludge to rich concentrates. Most effective method application would be for sedimentary ores of biocolloid origin which usually contain 45–40% of iron and manganese and raised concentration impurities like phosphates, arsenates, and silicates. Such ore processing with other known methods is not effective due to insufficient removal of phosphorus and arsenic compounds.

Resuming the performed investigation, it should be mentioned that using advances of physicochemical geomechanics, colloid and biocolloid chemistry, and results of XRD, thermographic, SEM, rheological, and microbiologic methods, the dependences of mechanochemical, nanochemical, and microbiological metamorphism processes of rocks with their conversions into nano- and microstructured iron-oxide-silicate materials with following processes of their processing, separation, and application were established. Metamorphic processes on interim stage of rock transformation into iron ores can also be passed with formation of nanostructured pelagic sediments aided with microorganisms and their excreted surface-active metabolic products. The optimal effective ways of sedimentary nanostructured iron-silicate ores reducing burning realization with further separation and purification of obtained components were defined.

## 57.4 Conclusions

Analytical (using advances of physicochemical geomechanics) and experimental analysis of obtained data (using rheological, SEM, XRD, thermographic, chemical, and microbiologic methods) allowed to determine general role of physico-geomechanical, mechanochemical, biogeochemical, and biocolloid processes in metamorphic transformations of IOSOM rocks. It was noted a limiting influence of nano- and microstructures existed or formed during the processes on IOSOM transformation on all interrelated stages of natural metamorphism and technogenic transformations. It was shown that natural and technogenic processes in IOSOM are being held almost the same way in accordance with established relationships, and that allowed to give scientific method explanation for IOSOM processing and purification from silicate, arsenic, phosphorus, and sulfur admixtures.

Practical realization of technological methods designed based on finished investigations allowed to obtain highly enriched magnetite and iron-contained (metallized)

concentrates purified up to 90–95% from arsenic and phosphorus [9–13] from poor iron-silicate ore materials and also to design predictive recommendations for improving IOSOM processing aided with nanotechnologies.

## References

1. Panko AV, Kovzun IG, Ulberg ZR, Oleinik VA, Nikipelova EM, Babov KD (2016) Colloid-chemical modification of peloids with nano- and microparticles of natural minerals and their practical use. In: Fesenko O, Yatsenko L (eds) Nanophysics, nanophotonics, surface studies, and applications, vol 183. Springer Proceedings in Physics, Heidelberg, pp 163–177. doi:[10.1007/978-3-319-30737-4\\_14](https://doi.org/10.1007/978-3-319-30737-4_14)
2. Kovzun IG, Pertsov NV (2010) Colloid-chemical processes of contact self-organization in alkaline silicate composites and their relation to formation of nanosized surface structures (chapter 19). In: Starov VM (ed) Nanoscience: colloidal and interfacial aspects. CRC Press, London, New York, pp 523–568
3. Emel'janov VA (2003) Osnovy morskoy geojekologii (basics of marine geoecology). Naukova dumka, Kyiv
4. Shherbak NP (1990) Mineraly Ukrainy: kratkij spravochnik (minerals of Ukraine: quick-reference book). Naukova dumka, Kyiv
5. Jusfin JS, Pashkov NF (2007) Metallurgija zheleza (iron metallurgy). Akademkniga, Moscow
6. Pertsov NV (1998) Jeffekt Rebindera v zemnoj kore (fiziko-himicheskaja geomehanika) (Rebinder effect in Earth crust (physicochemical geomechanics)). Colloid J 60(5):629–640
7. Frye K (1981) The encyclopedia of mineralogy, encyclopedia of Earth sciences, vol IV B. Hutchinson Ross Publishing Company, Stroudsburg
8. Kovzun IG, Protsenko IT, Pertsov NV (2001) Rol' himicheskikh i fiziko-himicheskikh processov pri poluchenii i formirovanii svojstv silikatnyh suspenzij (role of chemical and physicochemical processes for obtaining and property formation of silicate suspensions). Colloid J 63(2):2014–2019
9. Oleinik VA, Panko AV, Kovzun IG, Ilyashov MA, Protsenko IT (2013) Nanochemical processes in solid-phase reduction of ferrioxide-silicate materials. Proceeding NAP 2(3): 03AET10
10. Kovzun IG, Ulberg ZR, Protsenko IT, Filatov YuV, Ilyashov MA, Volovik VP, Yushkov EA, Viter VG (2011) RU Patent 2412259, 20 Feb 2011
11. Kovzun IG, Ulberg ZR, Protsenko IT, Filatov YuV, Ilyashov MA, Volovik VP, Yushkov EA, Viter VG (2011) RU Patent 2413012, 27 Feb 2011
12. Panko AV, Ablets EV, Kovzun IG, Ilyashov MA (2014) Wasteless solid-phase method for conversion of iron ores contaminated with silicon and phosphorus compounds. Int J Chem Mater Sci Eng 8(1):35–37
13. Ilyashov MA, Kovzun IG, Protsenko IT, Viter VG, Panko AV (2010) UA Patent 91957, 10 Sept 2010
14. Loboda MV, Babov KD, Zolotarjova TA, Nikipelova EM (2006) Lechebnye grjazi (peloidy) Ukrainy. Chast 1 (Therapeutical muds (peloids) of Ukraine. Part 1). Kuprijanova, Kyiv
15. Rozanov AJ, Zavarzin GA (1997) Bakterial'naja paleontologija (bacterial paleontology). Vestnik RAN 67(3):241–245
16. Saranchuk VI, Ilyashov MA, Oshovskij VV (2006) Ugljerod: neizvestnoe ob izvestnom (carbon: unknown about known). UK Tsentr, Donetsk
17. Kovzun IG, Protsenko IT (1994) Hydrophilicity of disperse carbon-silicate compositions and carbonaceous materials. Colloid J 56(6):712–716

18. Kovzun IG, Pertsov NV (2005) Kolloidno-himicheskie processy kontaktnoj samoorganizacii v shhelochnyh silikatnyh kompozicijah i ih vzaimosvjaz' s obrazovaniem poverhnostnyh nano-razmernyh struktur (Colloid-chemical processes of contact self-organization in alkaline silicate compositions and their dependence with formation of surface nanosized structures). In: Kolloidno-himicheskie osnovy nanonauki (Colloid-chemical basics of nanoscience). Akademperiodika, Kyiv, p 361–412
19. Kovzun IG, Pertsov NV (2003) Colloid chemistry process contact self-organization in alkaline silicate composites and relation to formation of nanosized surface structures. In: Nanoscience: colloidal and interfacial aspects. Taylor and Francis Group, London, New York, pp 523–568
20. Kovzun IG, Korjakina EV, Protsenko IT, Pertsov NV (2003) Ковзун И.Г., Корякина Е.В., Проценко И.Т., Перцов Н.В. Kolloidno-himicheskie processy v tverdejushhijh shhelochnyh kompozicijah na osnove aljumosilikatov i shlakov. II. Reologicheskie issledovanija (Colloid-chemical processes in hardening alkaline compositions on basis of aluminosilicates and slags. II. Rheological investigations). Colloid journal 65(5): 643–647
21. Vlasova MV (1995) Fiziko-himicheskie aspekty formirovanija ul'tra- i vysokodispersnyh nemetallicheskih poroshkov (Physicochemical aspects of super- and finedispersed non-metallic powder formation). Dissertation, Власова М.В. Физико-химические аспекты формирования ультра- и высокодисперсных неметаллических порошков. Дис. ... докт. хим. наук. – Киев: Institute for Problems in Materials Science of National Academy of Sciences of Ukraine
22. Sergeev GB (2003) Nanohimija (nanochemistry). MGU, Moscow

# Chapter 58

## The Electron Radiation Effect on Polyvinylchloride (PVC) Nanocomposites with Multiwalled Carbon Nanotubes

T. M. Pinchuk-Rugal, O. P. Dmytrenko, M. P. Kulish, Yu. I. Prylutsky, O. S. Nychyporenko, M. I. Shut, V. M. Tkach, and V. V. Shlapatska

### 58.1 Introduction

Polyvinylchloride (PVC), despite a series of important physicochemical properties, such as considerable resistance against chemical agents and hydrophobic properties together with high mechanical characteristics, has a low degree of crystallinity, insufficient elasticity and frost resistance [1]. PVC is vulnerable to destruction caused by changes in chemical structure in the course of its production and use in various processes. Moreover, PVC (as with most dielectrics) is characterised with extremely low conductivity and magnetoplasticity values.

Many performance characteristics of PVC can be improved through softening, introduction of filling material and formation of polymeric mixtures. Formation of nanocomposite based on PVC with multi-walled carbon nanotubes (MWCNTs) uniformly distributed therein is one of the more efficient methods of improving electro-physical properties of PVC [2–5]. A considerable length-to-diameter ratio ( $\sim 1000$ ), specific surface area of nanotubes and their unique electrical and mechanical properties are of importance in this case [6–14]. On the other hand, ionising irradiation, which can influence the properties of the polymeric matrix, filling

---

T.M. Pinchuk-Rugal (✉) • O.P. Dmytrenko • M.P. Kulish • Y.I. Prylutsky  
O.S. Nychyporenko  
Taras Shevchenko National University of Kyiv, Kyiv, Ukraine  
e-mail: [pinchuk\\_tatiana@ukr.net](mailto:pinchuk_tatiana@ukr.net)

M.I. Shut  
National Pedagogical Dragomanov University, Kyiv, Ukraine

V.M. Tkach  
Bakul Institute for Superhard Materials of NAS of Ukraine, Kyiv, Ukraine

V.V. Shlapatska  
Pisarghevskiy Institute of Physical Chemistry of NAS of Ukraine, Kyiv, Ukraine

agent and their implantation, can be a powerful tool for efficient modification of mechanical, optical and electro-transport characteristics of polymeric composites [15, 16].

The purpose of this article is in elaborating efficient methods aimed at improvement of physical and mechanical properties of PVC nanocomposites with MWCNTs (PVC-MWCNTs) through formation/degradation of polyene sequences therein in the course of mechanical-chemical transformations and transformations stimulated by irradiation.

## 58.2 Experimental Studies

To prepare a PVC-MWCNTs nanocomposite, PVC powder of C-7058 grade with  $M_W = 157 \cdot 10^3$  has been used. MWCNTs has been synthesised by chemical vapour deposition (CVD) through decomposition of carbon-bearing compounds in the presence of highly dispersed powder of iron particles as a catalyst at the temperature of 1000–1300 K. With this end in view, some mixture of gaseous carbon and buffer gas was blown through a reaction vessel. As a result, MWCNTs with the length reaching several micrometres and external diameter up to 100 nanometres were obtained. MWNCTs were clarified from impurities by treating (etching) in  $\text{NH}_4\text{F}:\text{HF}:\text{H}_2\text{O}:\text{HCL}$  solution. PVC and MWCNTs powders were mixed in alcohol by means of an ultradisperser for 30 min. PVC-MWCNT nanocomposites were produced by pressing mixtures of powders in a cylindrical mould. Mixtures of powders were melted at a temperature of 513 K followed by pressing with a pressure of 300 atmospheres and cooling them slowly in vacuum. So obtained specimens of nanocomposites contained 0.2, 0.5, 1.0 and 2.0 wt.% of MWCNTs and were 15 mm in diameter and 1 mm thick.

Specimens were irradiated with electrons by means of a linear electron accelerator (ILU-6, Russia). Energy of electrons was  $E_e = 1.8$  MeV, while the dosage was equal to some 0.05 MGy. Temperature of specimens in the course of their irradiation did not exceed 333 K.

Morphology of PVC-MWCNT nanocomposites has been analysed by means of scanning electronic microscope (SEM Zeiss EVO 60, FRG). The voltage applied thereto was changed from 3 to 20 kV. Electron penetration depth ranged from 0.2 to 5.1  $\mu\text{m}$ .

Crystalline structure of PVC-MWCNTs nanocomposites has been determined by means of a X-ray diffractometer (DRON-3 M, Russia) with usage of monochromatic  $\text{CoK}_\alpha$  ( $\lambda = 0.179021$  nm) irradiation. X-ray diffraction patterns were taken at the tube voltage of 40 kV and the current amounting to 25 mA. Measurements were made with usage of LiF (002) flat crystals and Bragg-Brentano-type geometry.

Raman spectra and luminescence were measured with reflective geometry method at the room temperature by means of a triple spectrometer (HORIBA Jobin Yvon T64000, Japan), provided with a cooled CCD detector. To excite Raman scattering spectra, Ar-Kr ionic laser was used with the wavelength  $\lambda = 488$  nm.

The photoluminescence spectra were excited using the lines of continuous He-Cd laser with the wavelength  $\lambda = 325$  nm and Ar-Kr ionic laser with wavelength  $\lambda = 488$  nm. Exciting irradiation with 1–2 MW of power was focused at the specimen to a spot of 1  $\mu\text{m}$  in dimension.

To measure Young's modulus, a pulse measuring method for velocities of short high-frequency pulses in spring medium has been applied. Young's modulus has been determined from the formula  $E = \rho \cdot c^2$ , where  $c$  stands for the sound propagation velocity in the substance and  $\rho$  stands for the substance density.

Microhardness of PVC-MWCNT nanocomposites were determined by PMT-3 (Russia) microhardness gauge (Vickers pyramid) [17]. For each nanocomposite was obtained 50 prints. Microhardness of composites were calculated using the formula  $H = 1854 \cdot P/d$ , where  $P$  = the load on the pyramid and  $d$  = the average length of two indentation diagonal after removing the load.

### 58.3 Results and Discussion

Because of dehydrochlorination that took place owing to thermal and mechanical-chemical destruction, faulty polyene structures have been formed in polymeric PVC macro-chains. These belong to linear conjugated systems, lengths of which can vary depending on the synthesis conditions. The presence of  $\pi$ -linkages on such sections and delocalised electrons as a result influences essentially over optical properties of PVC and can also cause changes in the conductivity and mechanical characteristics. Availability of filling agents and high-energy electron irradiation, conducive to dehydrochlorination process, can also influence over formation of conjugated polyene structures, including influence over their length and content [2, 4, 5, 18, 19]. It is obvious that mechanical-chemical and irradiation-stimulated rearrangement of the said faulty structures results also in changes of their optical and physical-mechanical properties.

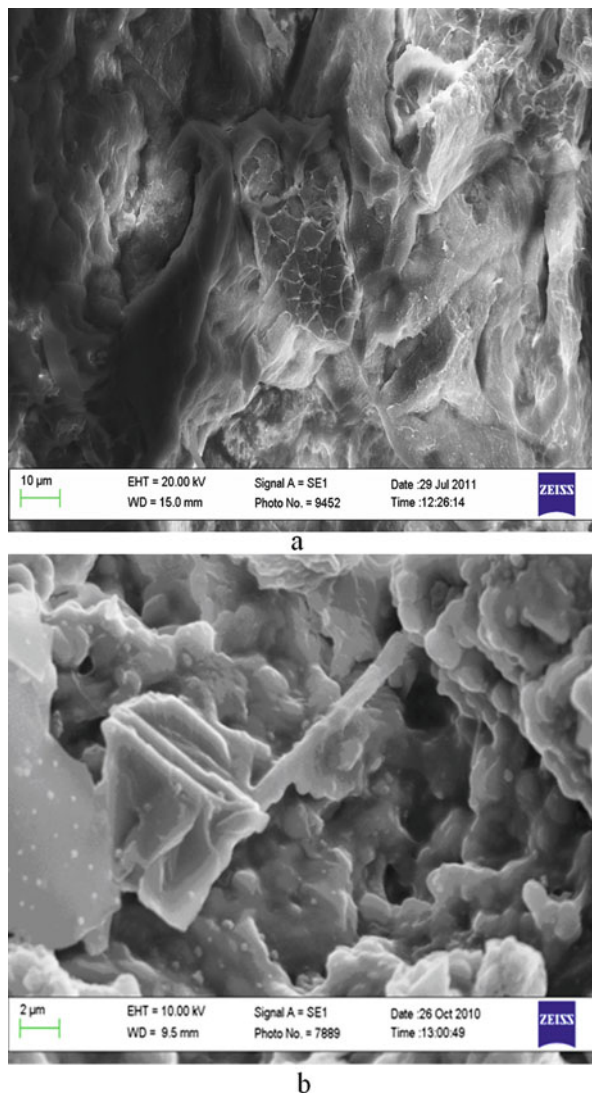
Figure 58.1 shows the SEM images of PVC and PVC-MWCNT nanocomposite.

When PVC is filled with MWCNTs, linkages between them are preserved even at small concentrations. Thickness of PVC layer covering MWCNTs is some 500 nm with MWCNTs diameter being equal to some 60–70 nm. This evidences considerable MWCNTs wetting with the polymer.

PVC has an orthorhombic structure and belongs to polymers with slight crystallinity degree. It can be seen from the behaviour of X-ray diffraction pattern for non-filled PVC (Fig. 58.2(1)): the presence of blurred halos with their maximums nearby  $2\theta = 20^\circ$  and  $2\theta = 28^\circ$ , availability of which confirms the presence of a considerable share of amorphous phase.

Diffraction patterns for PVC and PVC-MWCNT nanocomposites are similar as without exposure to electron irradiation so after it (Fig. 58.2(2); data on PVC-MWCNT nanocomposites are not shown). It evidences that neither MWCNTs as the filling agent nor electron irradiation has any effect on the crystalline structure type characteristic for PVC [20]. At the same time, depending on MWCNTs content

**Fig. 58.1** SEM images of PVC (a) and PVC-MWCNT nanocomposite with 2.0 wt.% of MWCNTs (b)



both without exposure to irradiation and after electron irradiation, changes in the crystallinity degree of PVC-MWCNT nanocomposites are observed with the said changes being especially essential under small MWCNTs concentrations (Fig. 58.3).

The maximum of crystallinity degree is apparently increased from 0.22 (without exposure to irradiation) to 0.42% (after electron irradiation) at low (0.5 wt.%) MWCNTs concentration (Fig. 58.3). The degree of arrangement of macro-chains is slowly decreasing with higher content of MWCNTs due to their aggregation. Therefore, the crystallinity degree remains low in PVC-MWCNT nanocomposites



**Fig. 58.2** X-ray diffraction spectra for non-filled PVC without exposure to irradiation (1) and after electron irradiation (2) with the dosage of 0.05 MGy ( $\lambda_{\text{CoK}\alpha} = 0.179021$  nm,  $E_e = 1.8$  MeV,  $T = 293$  K)

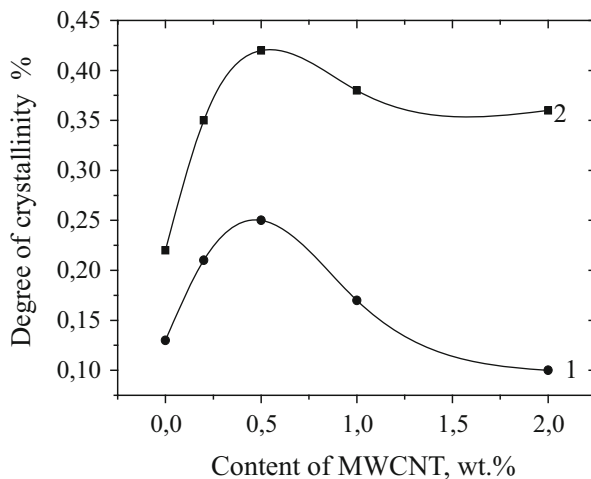
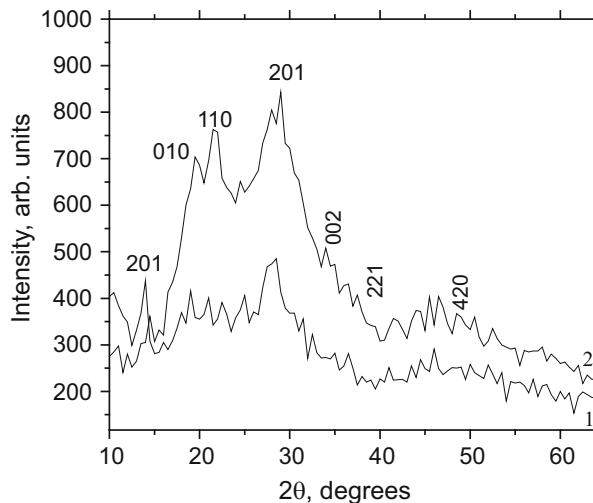


**Fig. 58.3** Crystallinity degree of PVC-MWCNT nanocomposites as a function of MWCNTs content without exposure to irradiation (1) and after electron irradiation (2) with the dosage of 0.05 MGy ( $E_e = 1.8$  MeV)

without exposure to irradiation (Fig. 58.3, graph 1) even in the presence of artificial nucleation centres represented by MWCNTs.

The crystallinity degree after electron irradiation rises sharply (Fig. 58.3, graph 2). It is apparent that any further slight (as compared with the specimen without exposure to irradiation) decrease is caused by destruction of macromolecules, including the crystalline phase spots. Maximum value of the crystallinity degree (like the nanocomposites without exposure to irradiation) is observed for PVC-MWCNT nanocomposite with MWCNTs concentration of 0.5 wt.%.

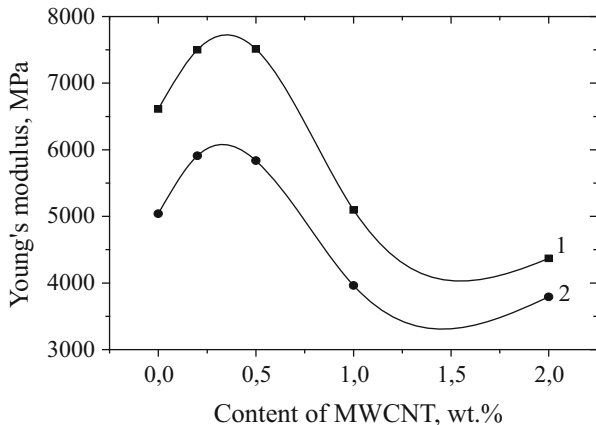


**Fig. 58.4** Young's modulus in PVC-MWCNT nanocomposites as a function of MWCNTs content either without exposure to irradiation (1) or after electron irradiation (2) with the absorption dose of 0.05 MGy ( $E_e = 1.8$  MeV,  $T = 293$  K)

Since Young's modulus is a measure of polymer rigidity to be determined with consideration of crystalline and amorphous phases, it is clear that its increase with simultaneous rise of MWCNTs content is caused by the change in the crystallinity degree.

Figure 58.4 shows the behaviour of Young's modulus in PVC-MWCNT nanocomposites as a function of MWCNTs content without exposure to irradiation and after the same.

If MWCNTs concentrations are low (0.2 and 0.5 wt.%), the crystallinity degree will rise, and Young's modulus will be increased as well. However, when MWCNTs concentration reaches 0.5 wt.%, the said increase of Young's modulus is decelerated, and it falls down abruptly at a higher MWCNTs content. Such behaviour of Young's modulus results from damage of MWCNTs macro-chains both in crystalline and amorphous phases. Electron irradiation causes a reduction of Young's modulus not only in PVC but also in PVC-MWCNT nanocomposites within the entire range of concentrations. It is apparent that dependence of Young's modulus for PVC-MWCNT nanocomposites upon MWCNTs concentration after their electron irradiation remains similar to that of specimens without exposure to irradiation in terms of quality.

Considering the applied dosage, damages of MWCNTs are slight, and therefore changes in mechanical properties of PVC-MWCNT nanocomposites are formed due to destruction of PVC macromolecules only [20].

Figure 58.5 shows the behaviour of PVC-MWCNT nanocomposite microhardness in their initial conditions and after electron irradiation.

It is obvious that the behaviours of PVC-MWCNT nanocomposite microhardness prior and after electron irradiation are similar in terms of quantity and are like to Young's modulus behaviour. At the same time, the microhardness graph for

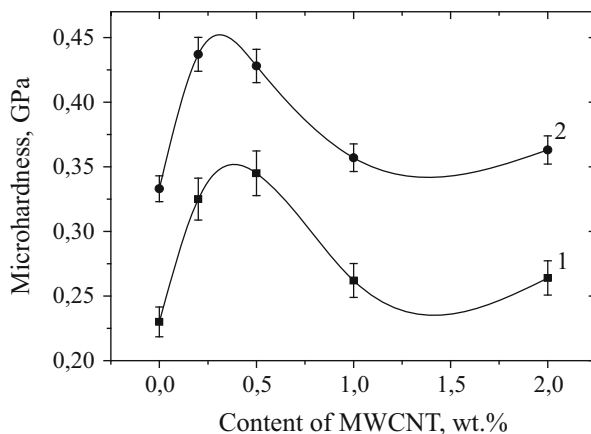


**Fig. 58.5** PVC-MWCNT nanocomposite microhardness as a function of MWCNTs content without exposure to irradiation (1) and after electron irradiation (2) at the dosage of 0.05 MGy ( $E_e = 1.8$  MeV,  $T = 293$ )

a specimen after exposure to irradiation corresponds to its higher values; it might be related to irradiation cross-linking formed between the macro-chains and MWCNTs. Such cross-links can result from formation of free radicals caused by destruction of macromolecules and radiation damages to MWCNTs surface [20, 21].

As a result of PVC (Fig. 58.6) dehydrochlorination, certain spectral bands appear in Raman spectra of such PVC with the emergence of such bands being related to nucleation of faulty polyene consequences with various lengths [20]. Bands corresponding to C-C oscillations with the frequency of  $\nu = 1125 \text{ cm}^{-1}$  and C=C nearby  $\nu = 1511 \text{ cm}^{-1}$  are the most intense. Simultaneously, higher harmonics scattering for oscillation modes  $\nu_1$  and  $\nu_2$  with frequencies of 2254 ( $2\nu_1$ ), 2636 ( $\nu_1 + \nu_2$ ) and 3360  $\text{cm}^{-1}$  ( $3\nu_1$ ) occurs. It is noteworthy that the deformational and valence oscillations are not observed for functional groups included into the structure of PVC macro-chains.

To find the length of conjugated fragments, we use an empiric relationship reflecting a correlation between the frequency  $\nu_2$  and number  $n$  of conjugated double linkages C=C in a polyene consequence [21]:

$$\nu_2 = 1461 + 151.24 \cdot \exp(-0.07808 \cdot n).$$

Thus, for non-filled PVC, band  $\nu_2 = 1511 \text{ cm}^{-1}$  includes  $n = 4$  conjugated linkages; for  $\nu_2 = 1484 \text{ cm}^{-1}$ ,  $n = 29$ ; for  $\nu_2 = 1505 \text{ cm}^{-1}$ ,  $n = 16$ ; for  $\nu_2 = 1527 \text{ cm}^{-1}$ ,  $n = 10$ , while for  $\nu_2 = 1581 \text{ cm}^{-1}$ ,  $n = 3$ . If the value of integral intensity of the aforesaid bands is taken into consideration, one can conclude that the conjugate sequences with  $n = 10$  and  $n = 16$  prevail.

**Fig. 58.6** Raman spectrum for non-filled PVC ( $\lambda_{36} = 488 \text{ nm}$ ,  $d = 15 \text{ mm}$ ,  $T = 300 \text{ K}$ )

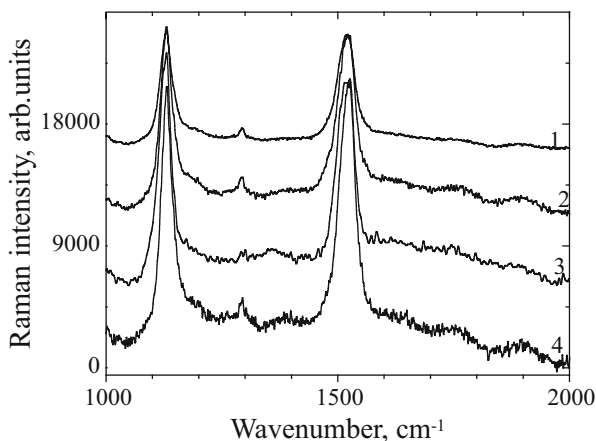
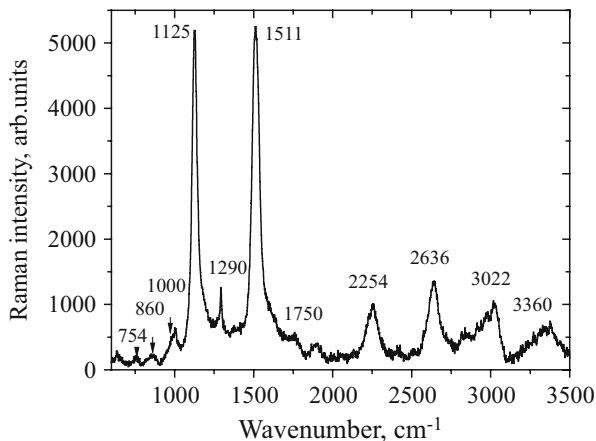


**Fig. 58.7** Raman spectra of PVC-MWCNT nanocomposites as a function of MWCNTs content: 0.2 (1), 0.5 (2), 1.0 (3) and 2.0 wt.% ( $d = 15 \text{ mm}$ ,  $\lambda = 325 \text{ nm}$ ,  $T = 300 \text{ K}$ )

In view of the availability of conjugated double linkage  $\text{C}=\text{C}$  in PVC, we can expect influence of MWCNTs over the said faulty structures and, as a result, over physical and mechanical properties of filled polymers.

Figure 58.7 shows Raman spectra of PVC with different content of MWCNTs.

As can be seen, such spectra contain oscillating modes inherent to non-filled PVC. High intensity corresponds to  $\nu_2$ ,  $(\nu_1 + \nu_2)$  and  $(2\nu_2)$ , belonging to oscillating modes of faulty conjugated consequences. At the same time, for a PVC specimen with 0.2 wt.% of MWCNTs, bands of oscillating modes  $\text{C}=\text{C}-\text{H}$ ,  $\text{C}-\text{C}$ ,  $\text{C}=\text{C}$  and their higher harmonics become more pronounced. In addition, splitting of bands with frequencies  $2\nu_2$  and  $3\nu_1$  occurs. Thus, MWCNTs influence over formation of linear conjugated structures in addition to PVC reinforcing accompanied with

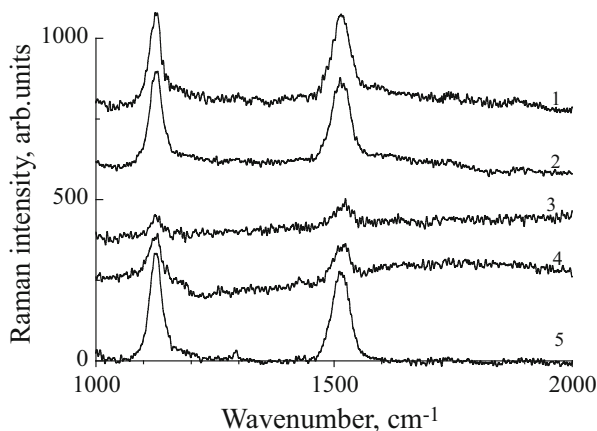


**Fig. 58.8** Raman spectra of PVC (1) and PVC-MWCNT nanocomposites as a function of concentrations amounting to 0.2 (2), 0.5 (3), 1.0 (4) and 2.0 (5) wt.% of MWCNTs after electron irradiation at the dosage of 0.05 MGy ( $d = 15$  mm,  $\lambda = 488$  nm,  $F_e = 1.8$  MeV,  $T = 300$  K)

mechanical-chemical destruction of macro-chains and changes in submolecular structure.

Due to electronic irradiation, intensity of Raman bands is decreased significantly as a result of the destruction not only of macromolecules but also of faulty linkages (Fig. 58.8).

Irradiation damages of PVC-MWCNT nanocomposite with 0.5 wt.% of MWCNTs are the most catastrophic. Obtained Raman spectrum, despite the availability of intense bands  $\nu_1(\text{C-C}) = 1125$   $\text{cm}^{-1}$  and  $\nu_2(\text{C=C}) = 1515$   $\text{cm}^{-1}$ , evidencing existence of poly-conjugated systems, hardly resembles Raman spectrum of PVC exposed to irradiation and its nanocomposite with 0.2 wt.% of MWCNTs. Raman spectrum intensity is low throughout the frequency range, but the background is also increased significantly. There are no bands caused by valence oscillations of CH and CH<sub>2</sub> groups. It is clear that the irradiation causes almost complete irradiation destruction not only of with polyvinylidenes but of polymer itself as well; such events were observed to a considerable lesser extent with PVC and its nanocomposite with 0.2 wt.% of MWCNTs. Similar destruction of the polymer takes place in PVC nanocomposite with 0.1 wt.% of MWCNTs. Raman spectrum of PVC nanocomposite with 2.0 wt.% of MWCNTs after electron irradiation is more pronounced as compared with the PVC spectrum after exposure to irradiation and includes the entirety of bands inherent to PVC, as well as  $\delta(=\text{CH})$ , which corresponds to polyene structures.

It is known that appearance of photoluminescence in PVC is caused by availability of faulty structures in the form of polyene sequences of different length and  $\pi^* \rightarrow \pi$  transition for, respective, poly-conjugated systems. Figure 58.9 shows photoluminescence spectra for non-filled PVC and its nanocomposites with

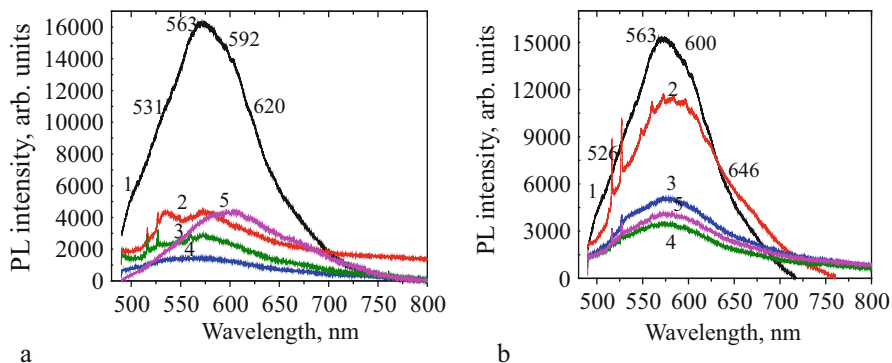


**Fig. 58.9** Photoluminescence spectra of non-filled PVC (1) and its nanocomposites with 0.2 (2), 0.5 (3), 1.0 (4) and 2.0 wt.% (5) of MWCNTs without exposure to irradiation (a) and after electron irradiation with dosage of 0.05 MGy (b) ( $\lambda = 488$  nm,  $E_e = 1.8$  MeV,  $T = 293$  K)

different content of MWCNTs without exposure to radiation and after electron irradiation with usage of exciting light with the wavelength  $\lambda = 488$  nm.

One can see that the photoluminescence is focused within the wide range of wavelengths (500–800 nm).

Several bands with their maxima located nearby 531, 563, 592 and 620 nm can be distinguished in photoluminescence spectra for PVC. The high number of conjugated sections in the spectrum corresponds to  $n = 10$  for 563 nm and to  $n = 16$  for 592 nm. One can see from such spectra that MWCNTs cause considerable quenching of PVC photoluminescence for all concentration values. At the same time, any decrease of photoluminescence with an increase of MWCNTs content does not bear monotonous character. The said photoluminescence is the least for low MWCNTs content (0.2 wt.%) and the highest for the MWCNTs concentration amounting to 0.5 Wt.%. It is obvious that such photoluminescence quenching is caused by implantation of PVC macromolecules to MWCNTs resulting in separation of photo-generating charge carriers. Polyene sequences with lengths  $n = 10$  and  $n = 13$  prevail in PVC-MWCNT nanocomposites. If photoluminescence quenching in PVC and its nanocomposite with 0.2 wt.% of MWCNTs after electron irradiation is slight, increased concentration of MWCNTs will result in abrupt fall of the integral photoluminescence intensity. Maxima of bands for PVC after exposure to irradiation correspond with positions 526, 563, 600 and 646 nm, which differ from positions of similar maxima for PVC without exposure to irradiation. Moreover, higher values of integral intensities correlate with the maxima located next to 563 and 600 nm, and not to 620 nm as it took place for the specimen without exposure to irradiation. Consequently, PVC destruction does not change the photoluminescence generation mechanism, but causes displacement of electronic transitions to other polyene sequences. Non-monotonous photoluminescence quenching with increase of MWCNTs content differs from the situation with PVC-MWCNT nanocomposites without exposure to irradiation, for which the least intensity value corresponded to

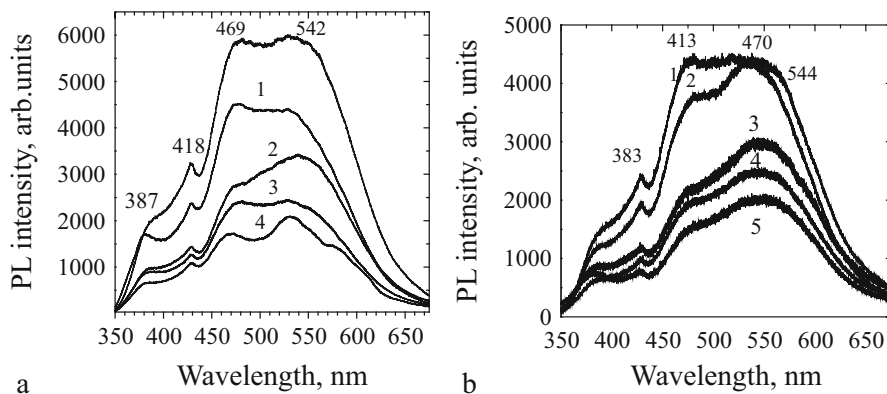


**Fig. 58.10** Photoluminescence spectra of non-filled PVC (1) and its nanocomposites with 0.2 (2), 0.5 (3), 1.0 (4) and 2.0 wt.% (5) of MWCNTs without exposure to irradiation (a) and after electron irradiation with dosage of 0.05 MGy (b) ( $\lambda = 325$  nm,  $E_e = 1.8$  MeV,  $T = 293$  K)

the specimen with 0.5 wt.% of MWCNTs. If PVC with 1.0 wt.% of MWCNTs is exposed to irradiation, Raman spectra will evidence much more considerable destruction of conjugated sections for PVC with 0.5 and 2.0 wt.% of MWCNTs, and this is the reason of the highest photoluminescence quenching for this specimen.

If light with wavelength  $\lambda = 325$  nm is used, essential rearrangement of photoluminescence spectra will be observed caused by appearance of bands not only from polyene fragments but also from C=O linkages in carbonyl groups (Fig. 58.10).

It is obvious that the photoluminescence spectrum is formed with participation of several bands, maxima of which are focused nearby wavelengths of 387, 418, 469 and 542 nm. Regardless of MWCNTs content, the set of polyene sequences in PVC-MWCNT nanocomposite is retained in the same state as for pure thermally degraded initial polymer except for PVC with 2.0 wt.% of MWCNTs. Simultaneously, displacement of maximum positions for these photoluminescence bands towards the longer wavelengths occurs together with rearrangement of relative intensities of recombination luminescence related to various emission centres represented in PVC by polyene sequences of various lengths. Any decrease of integral intensity of the emission with an increase of MWCNTs concentration in a nanocomposite proves the photoluminescence quenching at the expense of the filling agents. This bears evidence of the abatement of the recombination processes of electron-hole pairs arising due to their scattering in the course of electron transfers to MWCNTs with high acceptor properties. Such transfer of charges is accompanied with the establishment of donor-acceptor chemical interaction between macromolecules and MWCNTs, thus providing improvement of their implantation. Destruction of polyene sequences because of mechanical and chemical reactions is probably the main reason of the photoluminescence quenching [22].

As to PVC with different MWCNTs content after exposure to irradiation, pattern of spectral relationships of photoluminescence is similar to that observed for photoluminescence spectra obtained from PVC-MWCNT nanocomposites without exposure to irradiation. The increase of MWCNTs content results in non-monotonous photoluminescence quenching. If excitation is made with the light having  $\lambda = 488$  nm, the least integral photoluminescence intensity will correspond to PVC with 1.0 wt.% of MWCNTs, while excitation with the light having  $\lambda = 325$  nm will result in the least photoluminescence observed in the specimen with 2.0 wt.% of MWCNTs. It evidences the essential role in photoluminescence quenching not only of MWCNTs, their concentration, uniform dispersion, as well as destruction of polymeric chains, including the polyene structures.

## 58.4 Conclusion and Future Perspectives

1. It was demonstrated that both PVC and PVC-MWCNT nanocomposites after their electron irradiation ( $E_e = 1.8$  MeV, dosage of 0.05 MGy) retain orthorhombic structure of their crystalline lattice.
2. Crystallinity degree of PVC-MWCNT nanocomposites with low MWCNTs concentrations (0.2 and 0.5 wt.%) is increased, remaining almost constant at higher values (1.0 and 2.0 wt.%). In the event of electron irradiation, the crystallinity degree of PVC and PVC-MWCNT nanocomposites tends downwards due to destruction of macro-chains within crystalline spots and tends upwards for PVC and PVC-MWCNT nanocomposites with 0.2 and 0.5 wt.% of MWCNTs.
3. Thermal destruction of non-filled PVC and of that filled with nanotubes, manifested in generation of polyene sequences, results in appearance of pronounced bands  $\nu_1(\text{C-C})$ ,  $\nu_2(\text{C=C})$ ,  $2\nu_1$ ,  $\nu_1 + \nu_2$ ,  $2\nu_2$  in Raman spectra and weakly intense lines corresponding to deformational oscillating modes  $-\text{C}=\text{C}-\text{H}-$ . Appearance of  $\nu_2$  and  $2\nu_2$  bands indicates existence of polyene sequences of different lengths in thermally degraded specimens. When MWCNTs concentrations in nanocomposites are changed, rearrangement of all Raman bands will be observed being related to intermolecular cross-linking and destruction of main chain and faulty sections with conjugated double  $\text{C}=\text{C}$  linkages.
4. It was demonstrated that microhardness and Young's modulus values as a function of filling agent concentration in PVC-MWCNT nanocomposites are similar, while electronic irradiation causes increase of microhardness for PVC and its nanocomposite.
5. Availability of polyene sequences causes appearance of several bands in the photoluminescence spectrum of PVC. Introduction of MWCNTs into the polymer matrix and electron irradiation causes rearrangement of the photoluminescence spectrum (displacement of principal lines, in particular). On the one part, such changes can be caused by implantation of PVC macromolecules at the ends of MWCNTs lateral surface owing to the donor-acceptor interactions, while on the



other part it can be caused by destruction of faulty spots with the said destruction being accompanied with photoluminescence quenching when MWCNTs content will be increased.

Thus, usage of high-energy electron irradiation under optimal dosage and MWCNTs content in PVC is able to improve optical and mechanical performance of PVC-MWCNT nanocomposites resulting from formation or degradation of polyene sequences therein.

## References

1. Samira M, Ahmed M, Nadia N, Mohamed S, Rachida Z (2013) Thermal and mechanical properties of PVC and PVC-HDPE blends. *J Mater Sci* 1:6–11
2. Shi J-H, Yang B-X, Pramoda KP, Goh SH (2007) Enhancement of the mechanical performance of poly(vinyl chloride) using poly(n-butyl methacrylate)-grafted multi-walled carbon nanotubes. *Nanotechnology* 18:375704
3. Ye M, Boudenne A, Lebovka N, Ibos L, Candau Y, Lisunova M (2008) Electrical and thermophysical behaviour of PVC-MWCNT nanocomposites. *Comp Sci Technol* 68:1981–1988
4. O'Connor I, Hayden H, O'Connor S, Coleman JN, Gun'ko YK (2008) Kevlar coated carbon nanotubes for reinforcement of polyvinylchloride. *J Mater Chem* 18:5585–5588
5. Sterzyński T, Tomaszewska J, Piszczek K, Skórczewska K (2010) The influence of carbon nanotubes on PVC glass transition temperature. *Comp Sci Technol* 70:966–969
6. Matzui LY, Ovsienko IV, Len TA, Prylutsyy YI, Scharff P (2005) Transport properties of carbon nanotube-based composites. *Fullerenes Nanotubes Carbon Nanostruct* 13:259–265
7. Ovsienko IV, Len TA, Matzui LY, Prylutsyy YI, Ritter U, Scharff P, Le Normand F, Eklund P (2007) Resistance of nanocarbon material containing nanotubes. *Mol Cryst Liq Cryst* 468:289–297
8. Burlaka A, Lukin S, Prylutska S, Remeniak O, Prylutsyy Y, Shuba M, Maksimenko S, Ritter U, Scharff P (2010) Hyperthermic effect of multi-walled carbon nanotubes stimulated with near infrared irradiation for anticancer therapy: *in vitro* studies. *Exp Oncol* 32:48–50
9. Li J, Pandey GP (2015) Advanced physical chemistry of carbon nanotubes. *Annu Rev Phys Chem* 66:331–356
10. Peigney A, Laurent C, Flahaut E, Bacsá RR, Rousset A (2001) Specific surface area of carbon nanotubes and bundles of carbon nanotubes. *Carbon* 39:507–514
11. Korolovych VF, Bulavin LA, Prylutsyy YI, Khrapaty SV, Tsierkezos NG, Ritter U (2014) Influence of single-walled carbon nanotubes on thermal expansion of water. *Int J Thermophys* 35:19–31
12. Adamenko I, Bulavin L, Korolovych V, Moroz K, Prylutsyy Y (2009) Thermophysical properties of carbon nanotubes in toluene under high pressure. *J Mol Liq* 150:1–3
13. Korolovych VF, Nedyak SP, Moroz KO, Prylutsyy YI, Scharff P, Ritter U (2013) Compressibility of water containing single-walled carbon nanotubes. *Fullerenes Nanotubes Carbon Nanostruct* 21:24–30
14. Kim S, Polycarpou AA, Liang H (2013) Active control of surface forces via nanopore structure. *APL Mater* 1:032118
15. Ritter U, Scharff P, Siegmund C, Dmytrenko OP, Kulish NP, Prylutsyy YI, Belyi NM, Gubanov VA, Komarova LA, Lizunova SV, Poroshin VG, Shlapatskaya VV, Bernas H (2006) Radiation damage to multi-walled carbon nanotubes and their Raman vibrational modes. *Carbon* 44:2694–2700

16. Dmytrenko OP, Kulish NP, Belyi NM, Lizunova SV, Prylutskyi YI, Shlapatskaya VV, Strzhemechny YM, Ritter U, Scharff P (2009) Structure and vibrational properties of multi-walled carbon nanotubes irradiated with high-energy electrons. *Fullerenes Nanotubes Carbon Nanostruct* 17:123–134
17. Bikulčius G, Juodien T, Sūkien V (1994) Investigation of wear of alloys based on gold. *Surf Coatings Technol* 64:149–154
18. Ramesh S, Winil T, Arof AK (2010) Mechanical studies of poly(vinyl chloride)-poly(methyl methacrylate)-based polymer electrolytes. *J Mater Sci* 45:1280–1283
19. Wu XL, Liu P (2010) Poly(vinyl chloride)-grafted multi-walled carbon nanotubes via Friedel-Crafts alkylation. *Polymer Lett* 14:723–728
20. Ritter U, Scharff P, Pinchuk TM, Dmytrenko OP, Bulavin LA, Kulish MP, Prylutskyi YI, Zabolotny MA, Grabovsky YE, Bilyy MM, Rugal AG, Shut AM, Shlapatska VV (2010) Radiation modification of polyvinyl chloride nanocomposites with multi-walled carbon nanotubes. *Mat-wiss u Werkstofftech* 41:675–681
21. Ellahi S, Hester RE, Williams KPJ (1995) Waveguide resonance Raman spectroscopy of degraded PVC. *Spectrochim Acta* 51:549–553
22. Blazevska-Gilev J, Kupčik J, Šubrt J, Bastl Z, Vorlíček V, Galíková A, Spaseska D, Pola J (2006) IR laser ablation of poly(vinyl chloride): formation of monomer and deposition of nanofibres of chlorinated polyhydrocarbon. *Polymer Degrad Stab* 91:213–220

# Chapter 59

## Peculiarities of Charge Transfer in Graphite Intercalation Compounds with Bromine and Iodine Chloride

Oleksandr I. Prokopov, Irina V. Ovsienko, Lyudmila Yu. Matzui,  
Oleksandra S. Zloi, Nikolai A. Borovoy, Tatiana A. Len, and Dina D. Naumova

### 59.1 Introduction

Graphite intercalated compounds (GICs) are natural two-dimensional (2D) electronic systems in which carriers move mainly in parallel to the direction of the graphite planes. During the intercalation process there is a transfer charge from intercalate molecules to graphite layers and layers of graphite enriched with additional charge carriers. In this process, halogens and halides act as electronic acceptors, enriching the graphite layer with additional delocalized holes. Redistribution of charge between the layers of graphite and intercalate layers causes the formation of a charged layer of intercalate that contains localized electrons and acts as an electrostatic screen between the graphite layers on both sides of the intercalate layer. This high potential barrier prevents the movement of charge carriers through the intercalate layer perpendicular to the layers of graphite. The 2D properties of GICs arise from the existence of the charged intercalate layer with localized electrons. Thus, a charge carrier system in low-stage GICs is a degenerate 2D electron gas. The two-dimensionality of such electron gas is associated with structural features of the electronic structure of GICs. GICs are a perfect model to study the physical properties of 2D structures. A number of physical phenomena were investigated in acceptor GICs. Thus, the literature contains data on the study

---

O.I. Prokopov (✉) • I.V. Ovsienko • L.Y. Matzui • O.S. Zloi • N.A. Borovoy •  
T.A. Len • D.D. Naumova  
Departments of Physics and Chemistry, Taras Shevchenko National University of Kyiv,  
Volodymyrska 64/13, 01601, Kyiv, Ukraine  
e-mail: [alexprokopov@gmail.com](mailto:alexprokopov@gmail.com)

© Springer International Publishing AG 2017  
O. Fesenko, L. Yatsenko (eds.), *Nanophysics, Nanomaterials, Interface Studies,  
and Applications*, Springer Proceedings in Physics 195,  
DOI 10.1007/978-3-319-56422-7\_59

of charge carrier phonon drag, which for GICs based on high oriented pyrolytic graphite (HOPG) is manifested in a wide temperature range up to room temperature [1–4].

The quantum effects of the weak localization and interaction of charge carriers in the 2D case were investigated experimentally for GICs of the acceptor type based on fine crystalline graphite and graphite fibers [5–8]. These effects in GICs are significantly pronounced and occur at sufficiently high temperatures. Another problem that can be solved in the study of GICs is to identify the features of phase transformations in 2D systems and their effect on the transport properties of GICs. The structural peculiarities of phase transformations in GICs based on HOPG and fine-crystalline graphite upon changes in temperature and pressure have been quite thoroughly researched [9–12]. In particular, it has been revealed that phase transformations in intercalate layers can be of several types. First, it can be a phase transformation in which the intercalate layer is transformed from one commensurate with the graphite layer to another commensurate lattice. Second, it is a phase transformation in which the intercalate layer is rearranged from being commensurate with the graphite layer to being incommensurate with the lattice and vice versa. The third type of phase transformation is a transformation of the intercalate layer from a quasicrystalline state to a quasiliquid state. The types of phase transformation and their number depend on the nature of the intercalate substance, the structure of the source to the intercalation of the graphite, and the rate of change of external factors, such as temperature and pressure. The effects of phase transformations of the first and second types on transport properties have been studied well enough for intercalated compounds based on HOPG and fine crystalline graphite with, for example, antimony chloride, molybdenum chloride, and aluminum chloride.

Recently, much attention has been given to researching intercalated compounds based on nanographite, graphene, and carbon nanotubes with nonpolar intercalate molecules, such as halogens. These compounds have a number of features that distinguish them from compounds based on bulk graphite [13, 14]. For example, much greater intercalated activity of nanographite and carbon nanotubes has been found in their compounds with iodine as compared to bulk graphite [15, 16]. It has been revealed that in graphene-based intercalated compounds nonpolar molecules of intercalate during phase transformations change their orientation relative graphene layer [17].

GICs with bromine are of particular interest for researchers. Based on HOPG GICs with bromine in a temperature range of 240–333 K, a whole cascade of phase transformations of all types is observed. Additionally, the number of transformations and their types depend on the stage of the compound [18]. In [18], on the basis of detailed structural studies of GICs, a model of phase transformations in bromine layers has been proposed. According to this model, bromine atoms in the interlayer space of graphite form a chain, called polibromine anions, that consist of an even or odd number of atoms. The number of bromine atoms in a chain and the orientation of the chain depend on the phase in which there is intercalate. When changing the parity of a polibromine chain, the charge that is passed from intercalate layers

to graphite layers also changes. That is, according to this model, at the phase transformations in intercalate layers, the amount of charge that is transmitted from intercalate molecules to graphite layers changes. Obviously, such a change of the transferred charge will affect the transport properties of GICs with bromine.

The aim of this work is to present a detailed study of transport properties, namely, resistivity, thermopower, and the Hall phenomenon, in GICs with bromine in a phase transformation temperature range to determine the features of charge transfer in GICs. For comparison, in other work, analogous studies were carried out for GICs with iodine chloride, for which there is no change of transfer charge at the phase transformation.

## 59.2 Experimental Setup

### 59.2.1 Preparation and Characterization of GIC Specimens

Fine crystalline pyrolytic anisotropic graphite (FPAG) (crystallite size  $L_a \sim 30$  nm, interplanar spacing  $d_{002} = 0.34$  nm, parameter of preferred orientation of crystallites  $\eta = 10^3$ ) was used as the source material for GIC synthesis. GIC specimens were obtained using a standard two-temperature gas-phase method. The parameters of the intercalation process (temperatures of graphite  $T_{gr}$  and intercalate  $T_{int}$  and intercalation time  $t$ ) are presented in Table 59.1.

The molar concentration of intercalate  $C$  in the obtained compounds was determined by the change in mass of the specimens after intercalation:

$$C = \frac{100 (\%) }{\frac{M_{int}}{M_{gr}} \frac{m_0}{\Delta m} + 1}, \quad (59.1)$$

where  $M_{int}$  and  $M_{gr}$  are respectively the molar mass of intercalate and graphite, and  $\Delta m/m_0$  is the relative change in mass of the specimen after intercalation. From the molar concentration of intercalate  $C$  the stage of compound  $S$  (the number of graphite layers between two layers of intercalate) was defined using the formula

$$S = \frac{100 - 2}{Cp^*}, \quad (59.2)$$

where  $p^*$  is the stoichiometric index in the compound formula  $C_{p^*}X$  ( $X$  is intercalate).

**Table 59.1** Parameters of intercalation process

Specimen	$T_{gr}$ , K	$T_{int}$ , K	$t$ , h.	$S(\Delta m)$	$S(X-R)$	$I_s$ , nm	$d_i$ , nm	Stoichiometric formula
GIC-Br <sub>2</sub>	318	318	48	1.90	2	1.038	0.358	C <sub>14</sub> Br
GIC-ICl	297	297	48	1.98	2	1.040	0.360	C <sub>8</sub> ICl

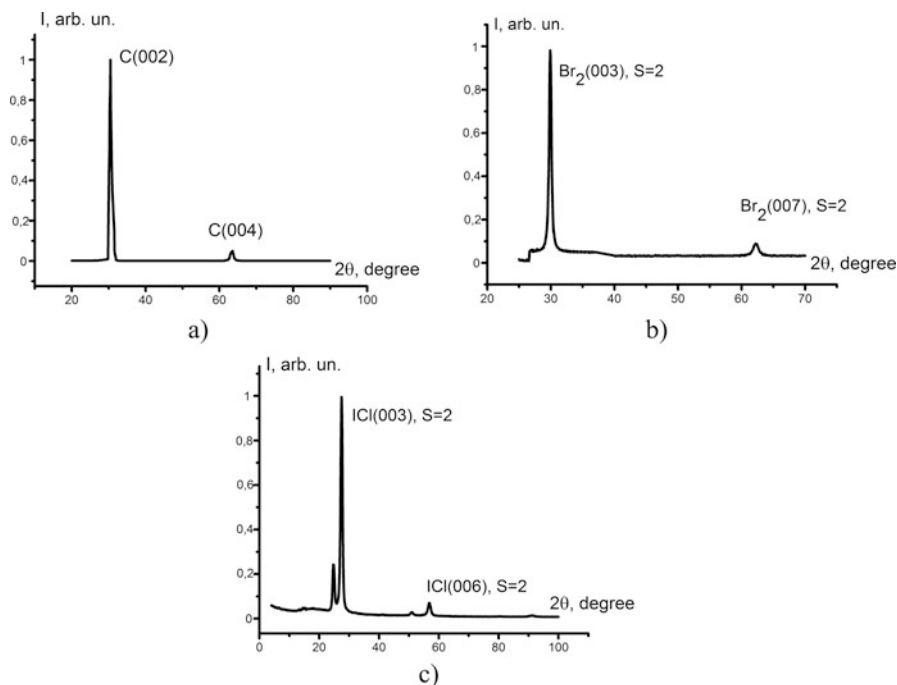


**Fig. 59.1** X-ray diffraction patterns for source FPAG (a) and for intercalated compounds with bromine (b) and iodine chloride (c)

The structure and phase composition of the synthesized GIC specimens were studied using a DRON-4-07 automated X-ray diffractometer in filter  $Ni_{K\alpha}$  radiation (wave length  $\lambda$  is 0.165791 nm). The identity period  $I_s$  of intercalated compounds ( $I_s$  is the distance between the subsequent intercalate layers separated by  $S$  graphite layers) was determined from  $00l$ -diffraction using the Wulff–Bragg formula

$$2I_s \sin \theta = l\lambda, \quad (59.3)$$

where  $2\theta$  is the angle at which a corresponding line is observed on the diffraction pattern. Identity period  $I_s$  and the stage of compounds are related using the equation

$$I_s = d_s + (S - 1) \cdot d_{002}, \quad (59.4)$$

where  $d_{002}$  is the interlayer distance in the source for intercalation FPAG, and  $d_s$  is the distance between two graphite layers that contain the intercalate layer.

Figure 59.1 displays the parts of the X-ray diffraction patterns for the source FPAG used in the intercalation process (Fig. 59.1a) as well as for the intercalated compounds with bromine (Fig. 59.1b) and iodine chloride (Fig. 59.1c).

As is easily seen from Fig. 59.1, the X-ray diffraction patterns for the GICs contain, as for the source FPAG, two intense bands whose positions are shifted somewhat compared to the source graphite. It should be noted that the distance between intercalate layers ( $\text{Br}_2$  or  $\text{ICl}$ ) and adjacent layers of graphite is about 0.35–0.36 nm, and the interlayer distance FPAG  $d_{002}$  is 0.34 nm. Therefore, the identity periods for the intercalate layers are nearly multiples  $d_{002}$  and the position of intercalate  $00l$ -lines is very close to the position of graphite  $00l$ -lines. Using the data of the X-ray diffraction, the identity parameters of the intercalated compounds  $I_s$  were determined. The calculated values of the identity parameters  $I_s$ , thickness of intercalate layer  $d_i$ , stage number  $S$  determined from the X-ray diffraction data ( $S(X-R)$ ) and from changes in the specimen mass during the intercalation ( $S(\Delta m)$ ) and stoichiometric formulas of compounds are shown in Table 59.1. As seen from the table, second-stage intercalated compounds with bromine and iodine chloride were obtained.

### 59.2.2 Characterization Methods

Resistivity along the graphite planes was investigated in a temperature interval from 77 up to 300 K with a standard four-probe method. The Hall coefficient was determined by the routine procedure at temperatures 77 and 293 K and a magnetic field up to 1.5 T. Thermopower was measured within a 77–293 K temperature range using the method described in Ref. [19]. The error of measurement for resistivity and the Hall coefficient did not exceed 0.5% and for thermopower error did not exceed 1%.

## 59.3 Results and Discussion

### 59.3.1 Resistivity of GICs with Bromine and Iodine Chloride

Figure 59.2 presents the typical temperature dependences of resistivity along graphite planes  $\rho_a(T)$  for second stage GICs with iodine chloride and bromine. For comparison there is temperature dependence of resistivity for the source FPAG in Fig. 59.1 as well.

As shown in Fig. 59.2, the character of resistivity temperature dependence  $\rho_a(T)$  for GICs is essentially different from such dependence in the source of intercalation FPAG because FPAG resistivity decreases slightly with increases in temperature ( $\rho_{a77}/\rho_{a293} \sim 1.3$ ). This, as shown in [20], is due to an increase in the charge carrier concentration in graphite with increasing temperature in conditions of preferred temperature-independent crystallite boundary charge carrier scattering. Unlike source graphite for GICs, an increase in resistivity with temperature is

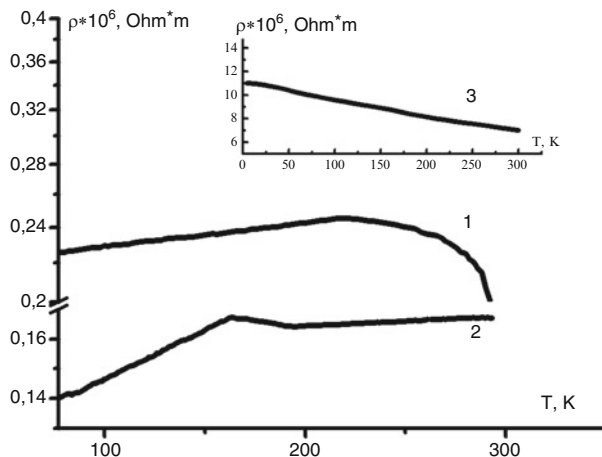


**Fig. 59.2** Dependences  $\rho_a(T)$  for second-stage GICs with iodine chloride (1) and bromine (2), for pure FPAG (3)

observed. For GICs with iodine chloride, the ratio  $\rho_{a77}/\rho_{a240}$  is  $\sim 0.92$  and for GICs with bromine this ratio  $\rho_{a77}/\rho_{a220}$  is  $\sim 0.84$ . Such resistivity temperature dependence  $\rho_a(T)$  is typical for acceptor GICs based on HOPG and FPAG [21–23].

In fact, as is known, during the intercalation process, halogens and halides are acceptors. There is a charge exchange between the layers of graphite and the intercalate layers. Graphite layers take on an additional positive charge. The quantity of this positive charge, the character of the positive charge distribution on the graphite layers, and the peculiarities of charge carrier scattering in GICs are the main factors causing some type of temperature dependence of the electrical resistivity in GICs.

However, as seen in Fig. 59.2, there are significant differences in the temperature dependence of resistivity for GICs with iodine chloride and bromine. For GICs with iodine chloride, resistivity monotonically increases with temperature up to  $T = 240$  K. With further increases of temperature, an abrupt decrease in resistivity is observed, and it continues through all measurements ranges. A similar character of the temperature dependence of resistivity and thermopower was observed in the works of Ko Sugihara [24, 25] for GICs based on HOPG with iodine chloride. For example, in [25], an abnormal increase in thermopower at 350 K has been found for GICs based on HOPG with iodine chloride. In addition, there is no explanation for this abnormal dependence of thermopower in such a temperature range.

For GICs with bromine in the temperature dependence of resistivity, two temperature intervals (77–160 K and 190–300 K) can be distinguished. In both intervals resistivity increases with temperature, but the rate of resistivity increase in each interval is different. The range 160–190 K is transitional.

Let us try to analyze the causes of such temperature dependences of resistivity of the investigated GICs. We will base our analysis on a 2D model of the



electronic structure of acceptor GICs [26], and we will take into account known data on the structural studies of phase transformations in intercalate layers for these compounds [18].

Let us consider the resistivity for acceptor GICs in terms of the 2D model of electronic structure. Within this model the 2D resistivity for a second-stage compound can be written as the sum of two terms:

$$\rho = \rho_{s0} + \rho_T, \quad (59.5)$$

where  $\rho_{s0}$  denotes temperature-independent term and  $\rho_T$  denotes temperature-dependent term. Temperature independent term or residual resistance can be written

$$\rho_{s0} = \frac{\pi \hbar}{e^2 k_F} \cdot \frac{1}{L_b}, \quad (59.6)$$

where  $L_b$  denotes charge carrier mean free path in crystallite boundary scattering,  $e$  is the electron charge, and  $k_F$  is a Fermi wave vector.

The temperature dependence term is written

$$\rho_T = \frac{\pi \hbar}{e^2 k_F} \cdot \frac{1}{L_T}, \quad (59.7)$$

where  $L_T$  denotes charge carrier mean free path of the temperature-dependent scattering mechanisms.

Let us consider the main charge carrier scattering mechanisms that give rise to the temperature dependence of the mean free path and, consequently, forming a temperature dependence of resistivity  $\rho_a$  in GICs.

First is electron–electron scattering, which leads to the quadratic dependence of resistivity on  $T$  [22]. However, according to estimates for second-stage GICs with  $\text{SbF}_5$  [27], the mean free path of carriers scattering each other is  $7 \cdot 10^{-5}$  m at 100 K, which is significantly greater than the mean free path of charge carriers scattering at phonon and crystallite boundaries (respectively  $L_{\text{ph}} \sim 10^{-7}$  m,  $L_b \sim 2 \cdot 10^{-8}$  m for FPAG and  $L_b \sim 10^{-7}$  m for HOPG). Second is charge carrier scattering on phonons, which includes scattering on different modes of graphite and intercalate.

Thus, in the first approximation, the generalized temperature dependence of the charge carriers mean free path is determined by the temperature dependence of the mean free path for scattering on phonons because with other temperature-dependent scattering mechanisms the mean free path is much larger:  $L_T = L_{\text{ph}}(T)$ . Charge carrier mean free path in phonon scattering is inversely proportional to the temperature and can be written

$$L_{\text{ph}} = L_0 T^{-c}, \quad (59.8)$$

where  $L_0$  is constant, and  $C \sim 1.6$ .

Two-dimensional resistivity for second-stage GICs in terms of 2D electron structure model can be written

$$\rho_{2S} = \frac{\pi \hbar}{e^2 k_F} \cdot \left( \frac{1}{L_b} + \frac{1}{L_{ph}(T)} \right) = \frac{3\pi \hbar a \gamma_0}{2e^2 E_F} \left( \frac{1}{L_b} + \frac{1}{L_{ph}(T)} \right). \quad (59.9)$$

Thus, the temperature dependence of GIC resistivity is determined by the ratio between the mean free paths for scattering at crystallite boundaries and phonon scattering. For GICs based on HOPG  $L_b > L_{ph}$  at all measured temperatures, that is, the temperature-dependent term (second term in 59.5) makes the main contribution to resistivity. This leads to a more pronounced temperature dependence of resistivity for GICs based on HOPG in comparison with GICs based on FPAG. For GICs based on FPAG, the temperature-independent term makes the main contribution to resistivity. This results in a weak temperature dependence of resistivity. This explains why slightly increasing the temperature dependence of resistivity for GICs based on FPAG. However, the question arises as to what happens in temperature intervals where there is a deviation from a monotonic increase in resistivity.

As is known, phase transformations in intercalate layers lead to the appearance of abnormal temperature dependences of the transport properties of GICs. In particular, there are local extremes, changes in the dependence slope angle, or sharp rises or falls of resistivity in the resistivity temperature dependence at the phase transformation temperature.

Let us consider the factors that can lead to changes in the resistivity of GIC specimens at phase transformation in intercalate layers:

- Change in the density of states at the Fermi level  $N(E_F)$  during the phase transformation that is directly linked with the accommodation coefficient;
- Change of effective relaxation time of charge carriers  $\tau_{ef}$  caused by a change in the phonon spectrum due to a structural adjustment of the intercalate layer. At phase transformation the ordering of intercalate ions or molecules in a layer changes. Transformation from one type of quasicrystalline structure to another, for example, the transformation from an incommensurate to a commensurate lattice or an intercalate transformation from a quasicrystalline to a quasiliquid state, cause a change in the electrical resistance of intercalate layers.

The temperature dependence of the resistivity of low-stage GICs below the phase transformation temperature is caused by the temperature dependence of charge carrier scattering because charge carrier concentration in these compounds is almost independent of temperature [28]. The intercalate layer is a 2D ionic crystal whose electrical resistance is several orders higher than the electrical resistance of the graphite layer. GIC conductivity is determined mainly by the conductivity of graphite layers enriched with additional charge from adjacent intercalate layers. Any structural transformation in intercalate layers changes the charge carrier mobility owing to changes in the effective relaxation time of the charge carriers. Since the value of the charge carriers' effective relaxation time upon scattering at crystallite boundaries  $\tau_b$  is constant for GICs based on a certain graphite material, the resistivity during the phase transformation can be changed only by changing the relaxation time  $\tau_{ph}$  upon charge carrier phonon scattering, in particular, the

scattering on graphite phonons  $\tau_{\text{ph0}}$  and intercalate phonons  $\tau_{\text{phi}}$ . According to [29], the value  $(\tau_{\text{ph0}})^{-1} \sim (q_0)$ , where  $q_0 = 1/(\gamma_0(\partial\gamma/\partial r))$ ;  $\gamma_0$  denotes matrix elements in the strong bond model, which characterizes the interaction of carbon atoms in a layer; and  $\partial\gamma/\partial r$  describes the change of atomic interaction with changes in interatomic distance  $r$ . This parameter also depends on the distribution of ions or molecules of intercalates in layers because molecules and ions of intercalates induce additional charge in layers of graphite.

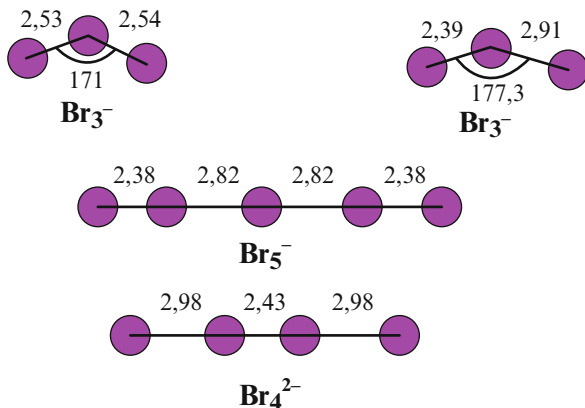
If in the intercalate layer the transformation from a quasicrystalline state to a quasiliquid state occurs, in this case the intercalate is “mobile ion liquid” that fills the space between the two layers of graphite. When a constant electric field or temperature gradient is applied in the GICs, an ordered orientation or transfer of ions occurs that results in their uneven distribution.

Let us analyze in terms of the present model changes in the character of resistivity temperature dependence in the phase transformation temperature intervals for the investigated GICs with iodine chloride and bromine.

As is known, when molecules of acceptor intercalates are injected into the interlayer space of graphite, a disproportionation reaction occurs. As a result of this reaction, neutral molecules of intercalate are transformed into negatively charged ions, and layers of graphite enriched with additional carriers are transformed into holes. Intercalate forms commensurate or incommensurate with the graphite layer lattice. A lattice type (commensurate or incommensurate) is conditioned by character of interaction between intercalate molecules and carbon atoms in a graphite layer. Such a situation is observed for GICs with iodine chloride. Polar iodine chloride molecules when injected into graphite are converted into anions, which form a lattice commensurate with the graphite layer. At a temperature of  $\sim 320$  K for GICs based on HOPG and at 240 K for GICs based on FCPG, a phase transformation of intercalate from a quasicrystalline to quasiliquid state occurs [30]. This transformation and the formation of “mobile ion liquid” are apparently the cause of the anomalous temperature dependence of the resistivity at temperatures above 240 K. In terms of the 2D model of conductivity (eq. 59.9) with use values  $\gamma_0 = 3$  eV,  $a = 0.246$  nm and  $L_b = 30$  nm Fermi energy  $E_F$ , is estimated  $E_F$  is  $\sim 0.13$  eV.

More complicated is the situation with intercalation of nonpolar molecules of bromine into graphite. X-ray diffraction data indicate that when bromine is injected into graphite, a layered structure is formed with periodic placing of bromine layers between the graphite layers. A change in the value of resistivity with bromine intercalation into graphite indicates that a transfer of additional charge occurs from intercalate molecules to graphite layers. As shown earlier [18], there is a series of structural transformation in layers of bromine connected with a different ordering of bromine in the layers. In GICs based on HOPG at  $T = 373$  K a transformation from a quasicrystalline to a quasiliquid state occurs. Below this temperature bromine forms a lattice commensurate with a layer of graphite. Diatomic molecules of bromine are connected in a chain of bromine atoms (so-called polibromine anions) composed of an odd number of bromine atoms (Fig. 59.3) [18].

**Fig. 59.3** Schematic representation of polibromine chains [18]



In this case each such chain has one extra electron. Upon further slow decrease in temperature in the bromine layers, a series of structural transformations related to the reorientation of bromine chains relative to graphite planes is observed. At the temperature  $T = 240$  K in the intercalation compound based on HOPG there is a transformation from one quasicrystalline commensurate phase to another quasicrystalline commensurate phase. In this transformation number of electrons in the polibromine chain changes from an odd to an even [18] and each chain contains two additional electrons. Thus, the important feature of such a phase transformation in bromine layers is the fact that not only the character of charge carrier scattering is changed, but also there is a change in the accommodation coefficient, that is, the amount of additional charge transferred from intercalate molecules to graphite layers. Since the phase transition temperature in GICs based on FPAG is reduced by about 80–100 K compared to GICs based on HOPG, as shown in [30], the corresponding phase transformation in GICs based on FPAG occurs at 60 K. Precisely at 160 K anomalies in the temperature dependence of resistivity are observed experimentally based on FPAG GICs with bromine. Estimated values of the Fermi energy  $E_F$  and the scattering on phonon mean free path  $L_0$  according to (59.4) and (59.5) are  $E_F = 0.22$  eV and  $L_0 = 3.25 \cdot 10^{-4}$  m below the phase transformation temperature ( $T < 160$  K) and  $E_F = 0.18$  eV and  $L_0 = 6.01 \cdot 10^{-3}$  m above the phase transformation temperature ( $T > 160$  K).

Thus, it can be assumed, based on experimental studies of the temperature dependence of resistivity, that the phase transformation in the bromine layer at  $T = 160$  K causes a change of the accommodation coefficient  $f$ . This is reflected in the change in the coefficient of linear dependence of resistivity below and above the phase transformation temperature. However, a change in the coefficient of linear dependence of resistivity can, according to (59.5), be caused by a change not only in the charge carrier concentration but also in the scattering of the phonon mean free path below and above the phase transformation temperature. It is therefore necessary to conduct a study of transport properties in which the effects of changes in charge carrier concentration and charge carrier mobility can be separated.

### 59.3.2 Effect of Thermopower GICs with Bromine and Iodine Chloride

Among other transport properties, thermopower measurements provide information about the type and concentration of charge carriers in a material, the value of Fermi energy, mechanisms of charge carrier scattering, and more. It is known that the thermopower of graphite materials and their intercalated compounds is the sum of two components: diffusive thermopower and phonon drag thermopower. Phonon drag thermopower for GICs based on HOPG is manifested in a wide temperature range, unlike GICs based on FPAG, for which phonon drag thermopower occurs at temperatures less than 90 K [23]. Thus, in the temperature range of study ( $T > 77$  K) for GICs based on FAPG thermopower is determined by only the diffusive component. For materials with one type of charge carrier, which are acceptor GICs of low stages, the diffusive thermopower complex depends on the temperature [19]. However, if charge carrier boundary scattering is preferred, as shown in [19], in the first approximation we can assume that diffusive thermopower is a linear function of temperature:

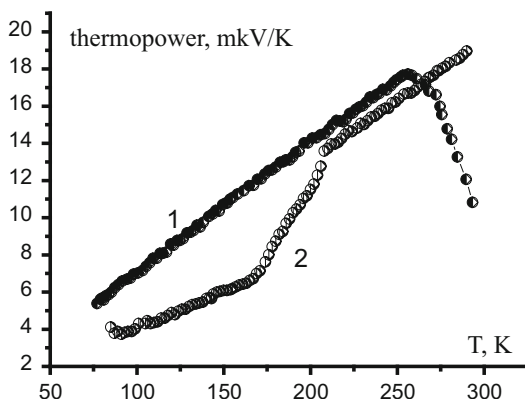
$$S_d = \frac{k_b}{e} \cdot \frac{\pi^2}{3} \cdot \frac{k_b T}{E_F} \cdot (1 + p), p = -0.5, \quad (59.10)$$

where  $K_b$  is Boltzmann's constant.

Figure 59.4 displays the typical temperature dependences of thermopower  $S(T)$  of GICs based on FPAG with iodine chloride and bromine.

As shown in Fig. 59.4, there are significant differences in the temperature dependences of thermopower for GICs with iodine chloride and GICs with bromine, which, however, fully correlates with features in the temperature dependences of resistivity for the respective intercalated compounds. For GICs with iodine chloride, thermopower increases linearly with temperature throughout all temperature ranges up to  $\sim 260$  K; then, like resistivity, there is a sharp drop in thermopower. In the

**Fig. 59.4** Temperature dependences of thermopower for GICs based on FPAG with iodine chloride (1) and bromine (2)



temperature dependence of thermopower for GICs with bromine there are two intervals, 80–170 K and 200–300 K, in which thermopower increases linearly with temperature. The temperature range 170–200 K is a transformation range, in which the angle coefficient of dependence  $S(T)$  is changed. Features in the thermopower temperature dependence for both GIC specimens (maximums and local maximums in  $S(T)$ ) cannot be associated with the manifestation of the phonon drag effect of the charge carriers because the maximum of this effect for GICs based on FPAG, as mentioned earlier [23], is at  $\sim 75$ –90 K. Therefore, these peculiarities in the thermopower temperature dependence can be associated either with change in the charge carrier concentration, leading to changes in the value of the Fermi energy, or with a change in the parameters of the relaxation time with different charge carrier scattering mechanisms, or with both of these processes simultaneously. The different character of thermopower temperature dependence in the phase transformation temperature intervals for GICs with iodine chloride and bromine obviously reflects the features of phase transformations in the layers of intercalate. For GICs with iodine chloride, as mentioned earlier, at  $T = 250$  K intercalate transformation from a quasicrystalline to a quasiliquid state with the formation of a “mobile ion liquid” occurs. Obviously this leads to a sharp change in the nature of the temperature dependence of thermopower. For GICs with bromine at  $T = 150$  K there is a transformation from one commensurate lattice to another. The only possible reason for a change in the angle coefficient of dependence  $S(T)$  is the change during the phase transformation of  $E_F$ . The estimation of values of the Fermi energy for GICs with bromine below and above the phase transformation temperature gives values of, respectively,  $E_{F77} = 0.3$  eV and  $E_{F293} = 0.187$  eV. For GICs with iodine chloride according to (59.6),  $E_F$  is 0.174 eB.

### 59.3.3 Hall Effect in GICs with Bromine and Iodine Chloride

Figure 59.5 presents the typical magnetic fields dependences of Hall coefficient  $R_H(B)$  at  $T = 77$  K and  $T = 293$  K for GICs with iodine chloride (Fig. 59.5a) and with bromine (Fig. 59.5b). For comparison, in the inset, the temperature dependence of the Hall coefficient for the source of intercalation FPAG is also presented.

The temperature dependence of the Hall coefficient of pyrolytic fine crystalline graphite is known to be rather complicated: it decreases when temperature increases from 4.2 K to an ambient value, indicating the increasing of total charge carrier concentration. The sign of the Hall coefficient remains positive within the whole temperature range. This is conditioned by the greater concentration of holes compared to that of electrons in FPAG. A characteristic feature of the Hall coefficient for lower-stage GICs is that it is independent of temperature and magnetic field, which reflects the metallic type of conductivity in such GICs.

As seen in Fig. 59.5 for the investigated GICs, the Hall coefficient is positive, which indicates a hole type conductivity for acceptor GICs. The Hall coefficient does not depend on the magnetic field. The value of the Hall coefficient for GICs

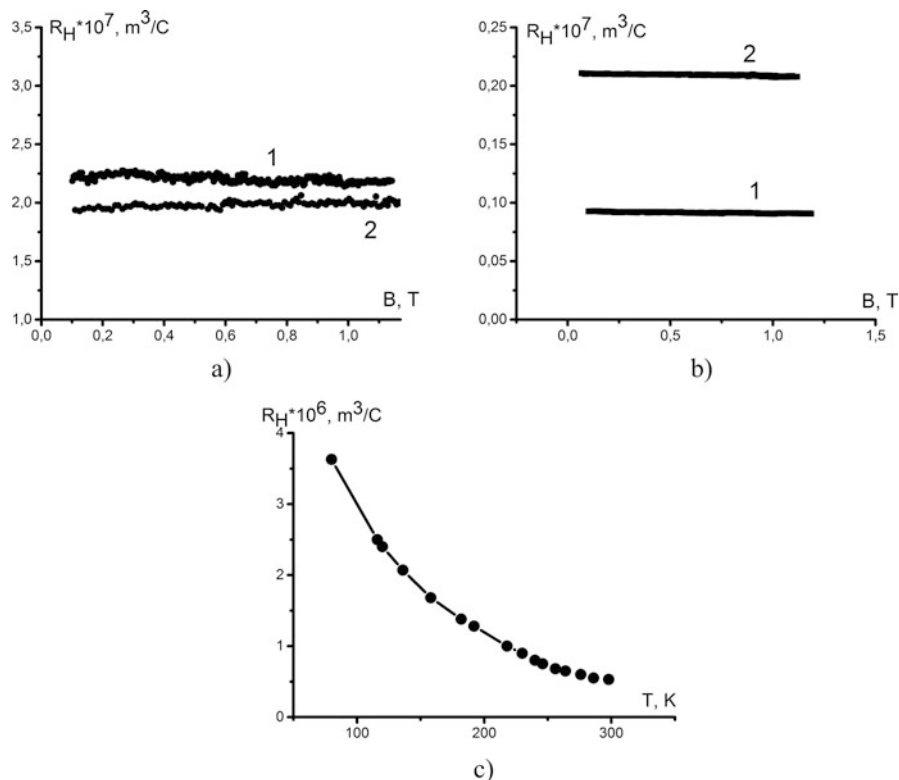


**Fig. 59.5** Magnetic field dependences of Hall coefficient at  $T = 77$  K (1) and  $T = 293$  K (2) for GICs with iodine chloride (a) and with bromine (b); source of intercalation FPAG (c).

decreases compared with source to intercalation FPAG, reflecting the increase in hole concentration in GICs after intercalation. For low-stage GICs, the Hall coefficient and bulk concentration of charge carriers are related by the simple equation

$$R = \frac{1}{e \cdot n_{e,p}}. \quad (59.11)$$

Let us analyze the Hall coefficient temperature dependence for GICs with iodine chloride and bromine. As seen in Fig. 59.5, significant differences are observed in these dependences for GICs with iodine chloride and bromine. For GICs with iodine chloride, the Hall coefficient decreases very slightly with temperature, and the  $R_{h293}/R_{h77}$  ratio is 0.93. This slight reduction in the Hall coefficient with temperature increase reveals a corresponding slight increase in the charge carrier concentration with increasing temperature in GICs with iodine chloride. The corresponding values of hole concentration are  $n_{77} = 2.88 \cdot 10^{25} \text{ m}^{-3}$  and  $n_{293} = 3.05 \cdot 10^{25} \text{ m}^{-3}$ . A completely different situation is observed in the Hall coefficient temperature dependence for GICs with bromine. For GICs with bromine, the Hall coefficient

value with increasing temperature does not decrease, which is logical, but instead almost doubles. This increase in the Hall coefficient and the corresponding reduction of the carrier concentration with increasing temperature is not typical for initial for intercalation FPAG and for intercalation compounds based on it. For low-stage acceptor GICs there are two possibilities: a charge carrier concentration is independent on temperature and a charge carrier concentration is slightly increase with temperature. However, for GICs with bromine, it has been found that above the phase transformation temperature ( $T = 293$  K), the charge carrier concentration is less than half ( $n_{293} = 2.98 \cdot 10^{25} \text{ m}^{-3}$ ) what it is at temperatures below the phase transformation ( $T = 77$  K,  $n_{77} = 6.89 \cdot 10^{25} \text{ m}^{-3}$ ). Thus, studies of the Hall coefficient have found that for GIC with iodine chloride, the Hall coefficient, and hence the concentration of holes, is almost independent of temperature and magnetic field, which is typical for low-stage GICs. For GICs with bromine there is abnormal growth of the Hall coefficient and therefore an abnormal decrease in the charge carrier concentration as temperature increases from 77 to 293 K.

### 59.3.4 Discussion

Let us analyze the obtained experimental results with changing Fermi energy and charge carrier concentration in terms of the ordinary 2D model of the electronic structure of GICs (the so-called metallic sandwich model) [31]. In this model, a GIC's electronic structure is considered to be the sequence of bands with low and high free charge carrier density along the  $c$  axis [26, 31]. One of these bands corresponds to pure 3D graphite and another to a 2D metallic sandwich consisting of an intercalate layer and two neighboring graphite layers. The bulk charge carrier concentration  $n_v$  in the metallic sandwich is determined mainly by the number of transferred charges from intercalate layers to the graphite layer:

$$n_v = \frac{N_c}{Sp^*} f \frac{d_{002}}{d_s}, \quad (59.12)$$

where  $N_c$  is the concentration of carbon atoms,  $f$  is the accommodation coefficient (charge portion transferred from intercalate layers to graphite layers in terms of one intercalate molecule),  $S$  is the stage number, and  $p^*$  is the stoichiometric index in the GIC formula. The Fermi energy  $E_F$  values are linked with the accommodation coefficient  $f$  by the following relationship:

$$E_F = \gamma_0 \left( \frac{\sqrt{3}\pi f}{pS} \right)^{\frac{1}{2}}. \quad (59.13)$$

According to Eqs. (59.12) and (59.13), the accommodation coefficient  $f$  and bulk charge carrier concentration  $n_v$  were calculated based on experimental data from electrical resistivity and thermopower studies and the accommodation coefficient  $f$  and Fermi energy  $E_F$  were calculated based on experimental studies of the Hall



**Table 59.2** Calculated values of  $E_F$ ,  $F$ , and  $n_v$  for GICs with  $\text{Br}_2$  and  $\text{ICl}$  in the approximation of the linear dependence of resistivity on temperature

Specimen	GIC-ICl		GIC- $\text{Br}_2$	
	$T = 77 \text{ K}$	$T = 293 \text{ K}$	$T = 77 \text{ K}$	$T = 293 \text{ K}$
From experimental $\rho(T)$				
$E_F$ , eV	0.13	0.13	0.22	0.18
$F$	$6.0i \cdot 10^{-3}$	$6.0 \cdot 10^{-3}$	0.016	0.011
$n_v$ , $\text{m}^{-3}$	$1.60 \cdot 10^{25}$	$1.60 \cdot 10^{25}$	$4.82 \cdot 10^{25}$	$3.23 \cdot 10^{25}$
From experimental $R_H$				
$E_F$ , eV	0.170	0.175	0.263	0.173
$F$	$9.5 \cdot 10^{-3}$	0.010	0.023	0.010
$n_v$ , $\text{m}^{-3}$	$2.80 \cdot 10^{25}$	$3.05 \cdot 10^{25}$	$6.89 \cdot 10^{25}$	$2.98 \cdot 10^{25}$
From experimental $S(T)$				
$E_F$ , eV	0.174	0.174	0.30	0.187
$F$	0.01	0.01	0.029	0.011
$n_v$ , $\text{m}^{-3}$	$3.01 \cdot 10^{25}$	$3.01 \cdot 10^{25}$	$8.96 \cdot 10^{25}$	$3.48 \cdot 10^{25}$

coefficient for GICs with both iodine chloride and bromine. Calculation results are presented in Table 59.2.

As seen from Table 59.2, for each GIC the values of the Fermi energy, accommodation coefficient, and bulk charge carrier concentration determined from experimental studies of the Hall coefficient, resistivity, and thermopower differ somewhat among themselves, but between them there is some correlation. For GICs with iodine chloride, the Fermi energy values defined by the results of various experimental studies are close to each other. For GICs with bromine, the variations in the Fermi energy values below the phase transformation temperature are higher, and the values of the Fermi energy above the phase transformation temperature almost coincide. However, for GICs with bromine, the Fermi energy values below the phase transformation temperature determined from various experimental studies are always larger than Fermi energy values defined at a temperature above the phase transformation. This fact is undisputed. Thus, for GICs with bromine, unlike other acceptor GICs with increasing temperature, the accommodation coefficient changes owing to the phase transformation of intercalate in a layer from one commensurate lattice to another. This leads to the anomalous temperature dependence of transport properties for GICs with bromine, which are not observed in other acceptor GICs based on FPAG.

## 59.4 Conclusion

The investigations carried out on the resistivity, thermopower, and Hall coefficient of GICs with bromine and iodine chloride identified significant differences in the character of the temperature dependences of these properties. In particular,

for GICs with bromine, abnormal changes in resistivity and thermopower in a temperature range of 150–240 K have been revealed. Also for GICs with bromine, abnormal growth of the Hall coefficient with increasing temperatures has been found. Established anomalies of the transport properties of GICs with bromine in the phase transformation temperature range cannot be explained in terms of changes in charge carrier relaxation time. Only a change in the accommodation coefficient can be the cause of such an abnormal dependency of transport properties in the phase transformation temperature range. The accommodation coefficient, charge carrier concentration, and Fermi energy for GICs with bromine and iodine chloride are estimated based on the obtained experimental data in terms of a simple 2D electron structure model of GICs. It is shown that the change in the carrier accommodation coefficient occurs in phase transformations in bromine layers, unlike with GICs with polar intercalate molecules.

## References

1. Issi JP (1992) Transport in acceptor GICs: have our efforts been rewarded? *Mater Sci Forum* 91:471–480
2. Piraux L, Kinany-Alaoui M, Issi JP, Perignon A (1988) Thermoelectric power and thermal conductivity of first-stage graphite-acceptor intercalation compounds. *Phys Rev B* 38(6):4329–4332
3. Matzui LY, Ovsienko IV, Vovchenko LL (2000) Thermopower of intercalated compounds based on graphite materials with different structure. *Ukrainian J Phys* 45(7):842–847
4. Matzui L, Ovsienko I, Vovchenko L (2000) Phonon drag in GIC based on disordered graphite. *Mol Cryst and Liq Cryst* 340(1):319–324
5. Piraux L, Bayot V, Michenaud JP, Issi JP (1986) The effect of disorder on weak localization and electron-electron interaction in low stage graphite intercalation compounds. *Sol St Com* 59(11):711–715
6. Piraux L, Bayot V, Michenaud JP, Issi JP (1988) Weak localization and coulomb interaction in graphite acceptor intercalation compounds. *Phys Scr* 37:942–947
7. Piraux L, Bayot V, Dresselhaus MS (1992) Influence of magnetic fields on the two-dimensional electron transport in weakly disordered fluorine-intercalated graphite fibers. *Phys Rev B* 45(24):14315–14320
8. Matzui LY, Vovchenko LL, Dvorkina IV (1994) Low temperature thermopower in disordered graphite, intercalated SbCl<sub>5</sub>. *Low Temp Phys* 5:463–468
9. Matzui L, Vovchenko L, Ovsienko I (2000) The influence of initial graphite structure on the character of phase transformations in GIC with iodine and stibium chlorides, abstracts, EuroCarbon – 2000, 1st world conference on carbon Germany, Berlin, July, 2000, 2. pp 851–852
10. Matzui LY, Vovchenko LL (1998) The shift of temperature of phase-transition in intercalant layers in GICs with chlorides, CIMTEC-World Forum on New Material. Simposium 1-Computational and Simulation of Materials'98, Florence. pp 227–234
11. Matsuzaki S, Kyouda T, Arimitsu M, Sano M (1989) Pressure-induced phase transitions of graphite-bromine intercalation compounds. *Synth Met* 34:359–364
12. Andersson OE, Sundqvist B (1988) Pressure dependence of the C-axis resistance of stage 2 SbCl<sub>5</sub> intercalated graphite to 4GPa. *Sol Stat Comun* 65(7):735–738
13. Shibayama Y, Sato H, Enoki T (2000) Novel concepts to develop carbon science and technology. *Mol Cryst Liq Cryst* 340:301–306

14. Ferrari AC (2007) Raman spectroscopy of graphene and graphite: disorder, electron–phonon coupling, doping and nonadiabatic effects. *Solid State Commun* 143:47–57
15. Prasad BLV, Sato H, Enoki T (2001) Intercalated nanographite: structure and electronic properties. *Phys Rev B* 64:1–10
16. Grigorian L, Williams KA, Fang S (1998) Reversible intercalation of charged iodine chains into carbon nanotube ropes. *Phys Rev Lett* 80:5560–5564
17. Yaya A, Ewels CP, Suarez-Martinez I, Wagner P, Lefrant S, Okotrub A, Bulusheva L, Briddon PR (2011) Bromination of graphene and graphite. *Phys Rev B* 83:045411
18. Chung DDL (1986) Structural properties and phase transitions of graphite intercalation compounds. *Phase Transit* 8:35–37
19. Matzui L, Ovsienko I, Vovchenko L (2001) Mechanisms of thermopower graphite materials with different crystalline structure. *Low Temp Phys* 27:68
20. Matzui LY, Charkov YY, Vovchenko LL (1984) Transfer phenomena in intercalated compounds of fine crystalline graphite. *Ukrainian J Phys* 29(6):1236–1289
21. Sugihara K, Matsubara K, Suzuki Itsuko S, Suzuki M (1988) Theory of the a- and c- axis resistivity and magnetoresistance in MoCl<sub>5</sub> graphite intercalation compounds. *J Phys Soc Jap* 67(12):416904177
22. Matsubara K, Sugihara K, Suzuki I-S, Suzuki M (1999) A- and c-axis resistivity and magnetoresistance in MoCl<sub>5</sub> graphite intercalation compounds. *J Phys Condens Matter* 11:3149–3160
23. Matzui LY, Vovchenko LL, Dvorkina IV (1995) Transport properties of acceptor graphite intercalated compounds. *Ukrainian J Phys* 40(1–2):107–111
24. Kobayashi K, Sugihara K, Oshima H, Tsuzuku T (1994) Thermoelectric power of graphite intercalation compounds with iodine monochloride. *J Phys Soc Jap* 63(12):4451–4455
25. Kobayashi K, Sugihara K, Oshima H (1996) C-axis thermoelectric power of graphite intercalation compounds. *J Phys Chem Solids* 57(6–8):931–933
26. Bok J (2016) The electronic structure of acceptor-type graphite intercalation compounds. *Physica* 105B(1–3):491–494
27. Piraux L, Amine K, Bayot V, Issi JP (1992) 2D electronic transport in fluorine and transition metal fluoride GICs. *Mater Sci Forum* 91–93:481–486
28. Charkov YY, Kolesnichenko LL, Matzui LY (1983) Conductivity and galvanomagnetic properties of graphite intercalated with SbCl<sub>5</sub>, FTT. *Low Temp Phys* 25(2):594–596
29. Pietronero L, Strassler S (1981) Mechanism of electron-phonon scattering and resistivity in graphite intercalation compounds. *Phys Rev B* 23(12):6793–6796
30. Matzui LY, Vovchenko LL (1998) The shift of temperature of phase-transition in intercalant layers in GICs with chlorides. *Inorganic Mater* 34(12):58–62
31. Batallan F, Bok J (1978) Electronic structure of intercalated graphite determined by magnetothermal oscillations. *Phys Rev Lett* 41:330

# Chapter 60

## Computer Simulations of the Dynamics of Cholesterol Molecules Located Between Graphene Sheets

Przemysław Raczyński, Violetta Raczyńska, and Z. Gburski

### 60.1 Introduction

Cholesterol is a sterol consisting of four hydrocarbon rings, hydrocarbon tail, and OH group. The tail is a hydrophobic part of molecule, whereas OH group is polar. Cholesterol is usually perceived as a source of health problems although its presence is essential to proper functioning of each cell in the human body. It controls the fluidity of cell membrane – the structure which protects the interior of each eukaryotic cell before the outside environment [1]. The biological role of cholesterol is well known [1–6]. However, cholesterol can exhibit other interesting undiscovered properties when interacting with nanostructures.

MD simulations have already been successfully applied to study interactions between atomic/molecular ultrathin layers surrounding carbon-based nanostructures [7–10]; therefore in this work we utilize MD approach to study the behavior of thin cholesterol film located between graphene sheets. We placed 80 cholesterol molecules between two identical graphene sheets. Graphene is only one atom thick, optically transparent, chemically inert, and very good conductor. The properties of graphene and its interactions with different molecules are intensively studied nowadays [11–17]. Thanks to its interesting properties, this material seems to make it an excellent candidate for various applications.

Our studies explore the interactions between cholesterol and graphene and the behavior of cholesterol between infinite graphene sheets.

---

P. Raczyński (✉) • V. Raczyńska • Z. Gburski  
Institute of Physics, University of Silesia, Uniwersytecka 4, 40-007, Katowice, Poland  
e-mail: [przemyslaw.raczynski@us.edu.pl](mailto:przemyslaw.raczynski@us.edu.pl)

## 60.2 Simulation Details

All full-atomistic molecular dynamics simulations were performed using NAMD 2.9b2 simulation code [18, 19], with the all-atom CHARMM force field. Simulated systems were visualized in VMD 1.9.2 [20].

The studied systems consisted of 80 cholesterol molecules located between graphene sheets. The graphene sheets were treated as infinite due to periodic boundary conditions applied on the  $y$ - and  $z$ -axis of the system. The size of simulation cell was set to accommodate graphene sheet dimension. All simulations were performed in NVT ensemble (constant volume and temperature). First, the systems were equilibrated for 2 ns, and after this equilibration phase, the simulation data were collected for the next 5 ns.

Three distances  $d$  between graphene sheets were set up ( $d = 18, 26, \text{ and } 34 \text{ \AA}$ ), and the formed cholesterol layers were studied at four temperatures ( $T = 290, 300, 310, \text{ and } 320 \text{ K}$ ).

Between neighboring temperatures, the system was slowly heated and again equilibrated for 2 ns. To ensure sufficient energy conservation, the integration time step was set to  $\Delta t = 0.5 \text{ fs}$  for all simulation runs. The standard NAMD integrator (Brünger-Brooks-Karplus algorithm) was used [21].

All interactions in the simulated systems were described with adapted form of CHARMM potential. Atomic charges on cholesterol molecule were taken from [22].

## 60.3 Results

Our simulations were performed for three different distances between graphene sheets, equal to  $d = 18, 26, \text{ and } 34 \text{ \AA}$ . The final configurations, at  $T = 320 \text{ K}$ , of all three systems are shown in Fig. 60.1. In the case of the smallest distance, the molecules are closely packed between walls, the free volume where the molecule can move is limited. When the distance between sheets grows, the cholesterol molecules group on one of the graphene surfaces, and an empty space between sheets can be observed. In the case of the largest distance between sheets, only a few molecules are localized in free space between sheets. The vast majority of cholesterol molecules is located on the graphene surface forming a thin, one-layer film. Only these molecules that do not fit on graphene begin to form a second layer or are located between sheets.

This behavior of cholesterol has an impact on all observables discussed in this work, beginning from second rank order parameter  $S_2$  defined as the highest eigenvalue of order tensor [23]:

$$Q_{\alpha\beta} = \frac{1}{N} \sum_{j=1}^N \left( \frac{3}{2} \hat{e}_{j\alpha} \hat{e}_{j\beta} - \frac{1}{2} \delta_{\alpha\beta} \right), \quad \alpha, \beta = x, y, z,$$

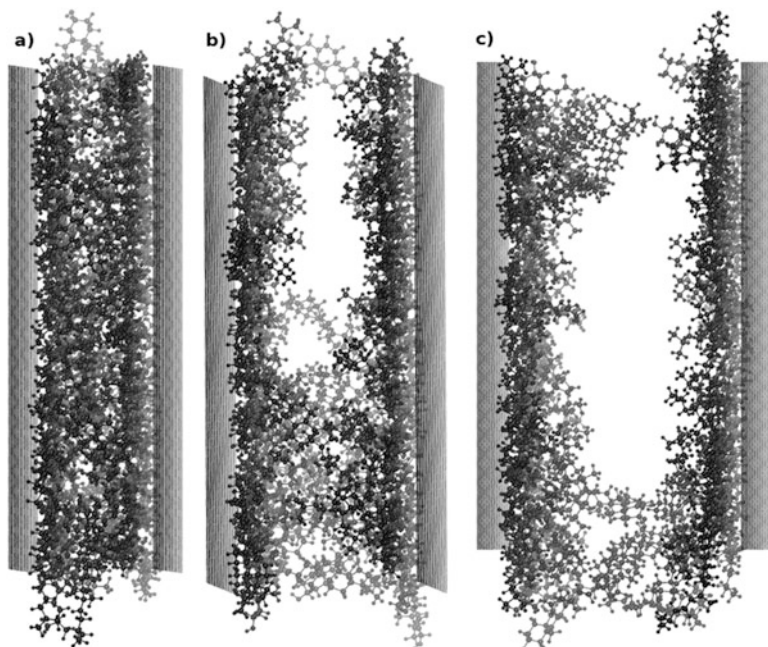


**Fig. 60.1** The instantaneous configurations, at  $T = 320$  K, of the system where the distance between graphene sheets was equal to  $d = 18$  Å (a),  $d = 26$  Å (b) and  $d = 34$  Å (c)

where  $Q$  is a second rank tensor,  $\hat{e}_j$  is a unit vector along the molecular long axis, and  $\delta_{\alpha\beta}$  is the Kronecker delta. Diagonalization of this tensor gives three eigenvalues and  $\hat{n}$  is the eigenvector associated with the largest eigenvalue. The  $\hat{n}$  vector is usually called the director of the sample. The value of  $S_2$  is usually calculated as

$$S_2 = \langle P_2(n \cdot e) \rangle = \langle P_2(\cos \theta) \rangle = \left\langle \frac{3}{2} \cos^2 \theta - \frac{1}{2} \right\rangle$$

where  $P_2$  is the second-order Legendre polynomial,  $\theta$  is the angle between molecular axes and the director  $n$ , and  $\langle \rangle$  denotes average over ensemble and time.

The obtained values of  $S_2$ , average over all timesteps, are presented in Fig. 60.2.

The highest values of  $S_2$  correspond to the system with the smallest distance between graphene sheets. In this system all cholesterol molecules are ordered in  $x, y$  plane, and there are no molecules arranged perpendicularly to this plane that can be observed in other systems (see Fig. 60.1). In the case of distance equal to  $d = 26$  Å, the values of  $S_2$  are the smallest. It can be observed in Fig. 60.1 that in this case, the large number of molecules is located between sheets and arranged perpendicularly to graphene diminishing in this way the values of  $S_2$ . When the distance between graphene sheets is large, the molecules group on its surface, as described previously.

There is one factor which diminishes the values of  $S_2$ , shown in Fig. 60.3.

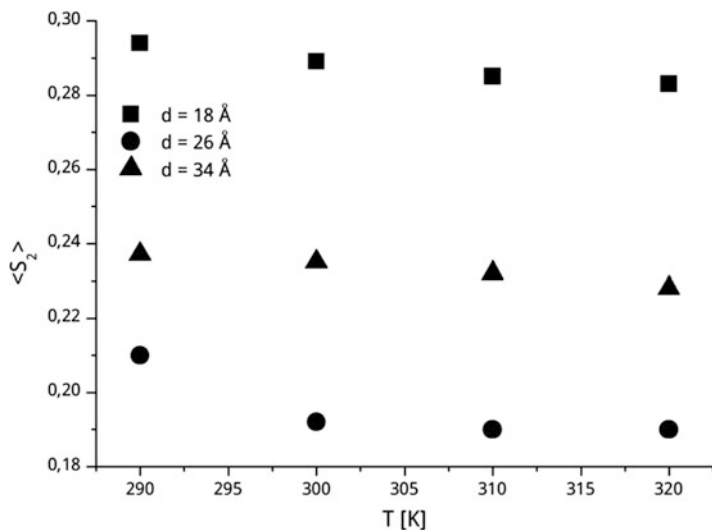
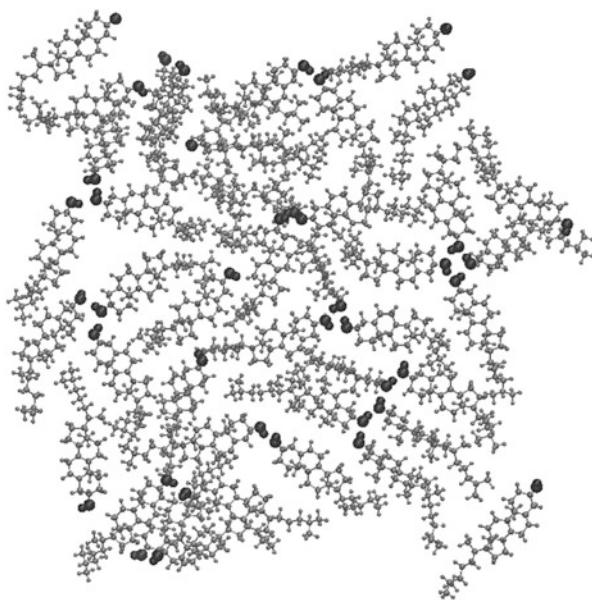


**Fig. 60.2** The comparison of the obtained values of  $S_2$  parameter

**Fig. 60.3** The snapshot of arrangement of the cholesterol on the graphene surface, for the system where  $d = 34 \text{ \AA}$  and at the  $T = 320 \text{ K}$



In this figure one can observe that molecules on graphene rearrange in a way that the OH group of cholesterol is oriented toward OH groups of neighboring cholesterols. It can be observed in each system studied, although to a different degree.

Figure 60.4a shows the mean square displacement  $\langle |\Delta\vec{r}(t)|^2 \rangle$  of the center of mass of molecule for the system with the largest distance between graphene sheets and for all temperatures. Figure 60.4b shows the comparison of  $\langle |\Delta\vec{r}(t)|^2 \rangle$  for one temperature  $T = 320$  K and for all systems studied. Mean square displacement is connected to the diffusion coefficient  $D$ , via Einstein relation:

$$\langle |\Delta\vec{r}(t)|^2 \rangle \approx 6Dt.$$

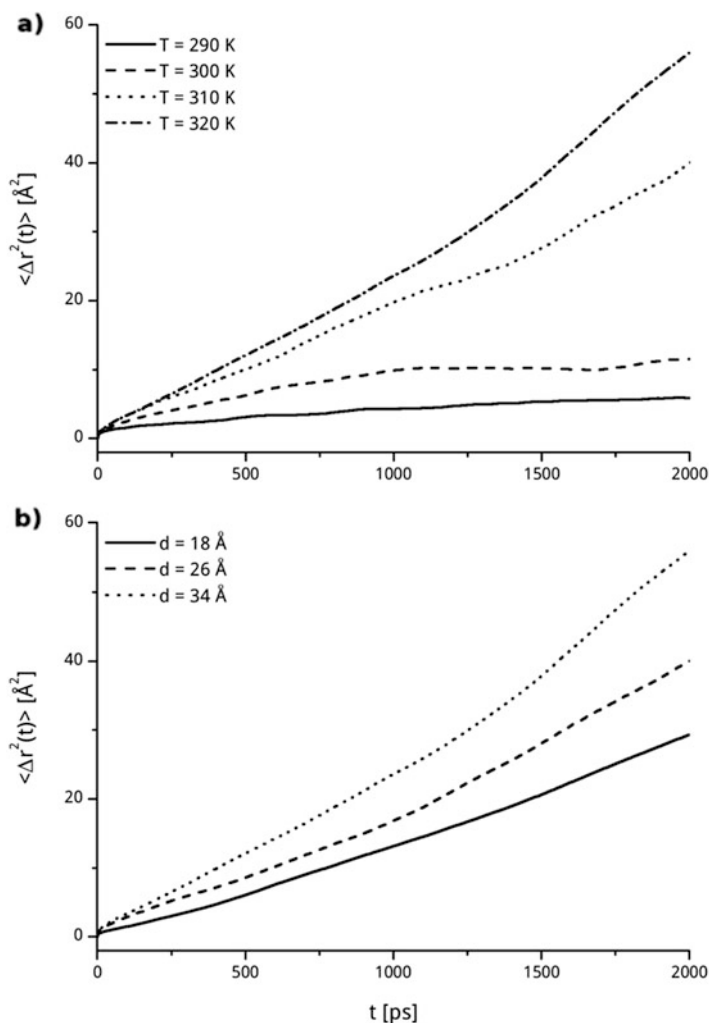


**Fig. 60.4** The mean square displacement of the center of mass of cholesterol molecules in the case of the system where the distance between graphene sheets was equal to  $d = 34 \text{ \AA}$  (a) and for all systems studied at the temperature  $T = 320$  K (b)



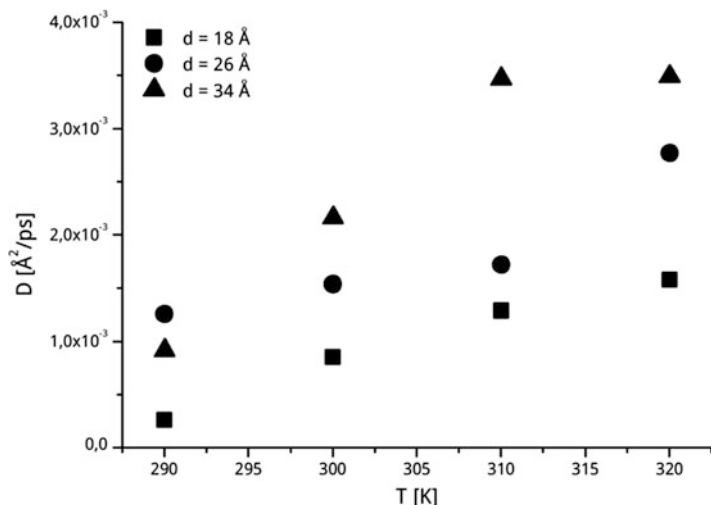


**Fig. 60.5** The comparison of the obtained values of  $D$

Obtained values of  $D$  are shown in Fig. 60.5.

Figures 60.4a and 60.5 show that the mobility of molecules grows with the heating of the system and it is a natural behavior. As observed in Figs. 60.4b and 60.5, we can conclude that the lowest mobility exhibits molecules in system where the graphene sheets are at the closest distance. As we pointed earlier, the cholesterol molecules in this system are squeezed and have limited volume to move and this restricts their mobility. When the distance between sheets grows, the free volume also grows, and as the consequence the mobility of molecules is higher. The slope of  $\langle |\Delta \vec{r}(t)|^2 \rangle$  plots allows to conclude that the system is in plastic phase.

The values of Lindemann index, shown in Fig. 60.6, indicate that there are no phase transitions. The largest difference between two subsequent temperatures can be observed in the case of system with  $d = 26 \text{ \AA}$  in the temperature range between  $T = 310$  and  $320 \text{ K}$ . However, this difference is too small to be an indicator of the phase transition. Additionally, analyzing the slopes of  $\langle |\Delta \vec{r}(t)|^2 \rangle$ , we can confirm that this system is not in liquid phase at each temperature studied.

Lastly we would like to present in this work the radial distribution function  $g(r)$ . In Fig. 60.7 the comparison of the systems with distance between graphene sheets equal to  $d = 18 \text{ \AA}$  and  $d = 34 \text{ \AA}$ , at  $T = 310 \text{ K}$ , is shown.

In the case of the system where the distance between graphene sheets is the smallest, sharp, and distinct peak can be observed at  $r = 7.2 \text{ \AA}$ . In the case of second system presented in Fig. 60.7, this peak is flat and more fuzzy. First peak shows the distance to the nearest neighbors, and it is evident that in the case of the system with smaller distance, cholesterol molecules are closer to each other and have more neighbors. Sharp and clear peaks may even somehow indicate on larger order in the system as was shown earlier. Such a shape of peaks indicates also on

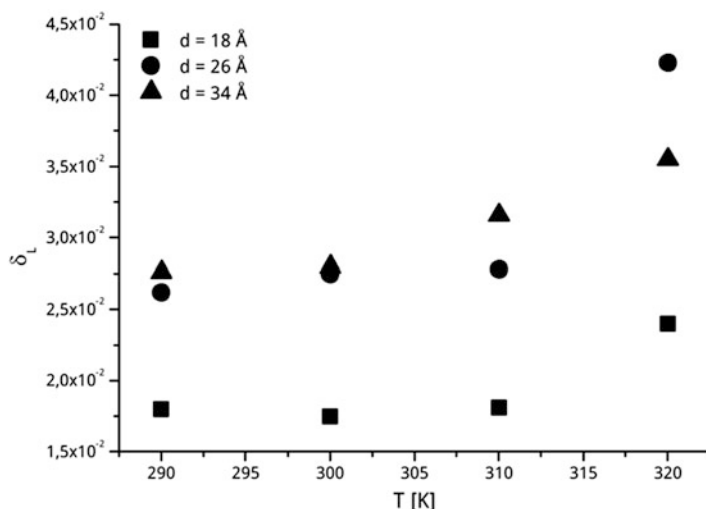


**Fig. 60.6** The comparison of the obtained values of  $\delta_L$

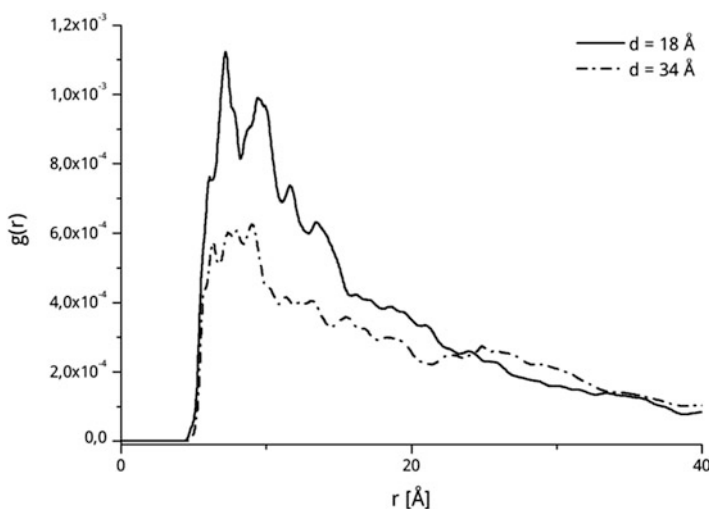


**Fig. 60.7** The comparison of radial distribution function of the systems where the distance between graphene sheets was equal to  $d = 18 \text{ \AA}$  and  $d = 34 \text{ \AA}$ , at  $T = 310 \text{ K}$

solid or amorphous phase. In the case of the system with  $d = 34 \text{ \AA}$ , sharp peaks also occur, but especially first peak is more fuzzy and smaller, compared to the second shown in the figure. We can also conclude that this system is in solid or amorphous phase, but the cholesterol molecules have smaller number of neighbors and they are not so tightly packed.

## 60.4 Conclusions

The systems of cholesterol molecules placed between graphene sheets were studied. The properties of systems varied with the distance between sheets. Cholesterol molecules in the system with  $d = 18 \text{ \AA}$  are the most ordered and the least mobile. The phase transition does not occur at the studied temperature range. The mobility of molecules becomes larger with the heating of the system. The graphene sheets modify an arrangement of cholesterol molecules, because on graphene surface they direct their hydrophilic parts toward each other.

## References

1. Alberts B (2008) *Molecular biology of the cell*. Garland Science, New York
2. Lusis AJ (2000) Atherosclerosis. *Nature* 407:233–241. doi:[10.1038/35025203](https://doi.org/10.1038/35025203)
3. Róg T, Pasenkiewicz-Gierula M, Vattulainen I, Karttunen M (2009) Ordering effects of cholesterol and its analogues. *Biochim Biophys Acta BBA Biomembr* 1788:97–121. doi:[10.1016/j.bbamem.2008.08.022](https://doi.org/10.1016/j.bbamem.2008.08.022)
4. Scott HL (2002) Modeling the lipid component of membranes. *Curr Opin Struct Biol* 12:495–502. doi:[10.1016/S0959-440X\(02\)00353-6](https://doi.org/10.1016/S0959-440X(02)00353-6)
5. Feller SE (2000) Molecular dynamics simulations of lipid bilayers. *Curr Opin Colloid Interface Sci* 5:217–223. doi:[10.1016/S1359-0294\(00\)00058-3](https://doi.org/10.1016/S1359-0294(00)00058-3)
6. Raczyński P, Górny K, Samios J, Gburski Z (2014) Interaction between silicon–carbide nanotube and cholesterol domain. A molecular dynamics simulation study. *J Phys Chem C* 118:30115–30119. doi:[10.1021/jp505532f](https://doi.org/10.1021/jp505532f)
7. Dawid A, Dendzik Z, Gburski Z (2004) Molecular dynamics study of ultrathin argon layer covering fullerene molecule. *J Mol Struct* 704:173–176. doi:[10.1016/j.molstruc.2004.01.065](https://doi.org/10.1016/j.molstruc.2004.01.065)
8. Kosmider M, Dendzik Z, Palucha S, Gburski Z (2004) Computer simulation of argon cluster inside a single-walled carbon nanotube. *J Mol Struct* 704:197–201. doi:[10.1016/j.molstruc.2004.02.050](https://doi.org/10.1016/j.molstruc.2004.02.050)
9. Dawid A, Gburski Z (2003) Interaction-induced light scattering in a fullerene surrounded by an ultrathin argon atmosphere: molecular dynamics simulation. *Phys Rev A*. doi:[10.1103/PhysRevA.68.065202](https://doi.org/10.1103/PhysRevA.68.065202)
10. Dawid A, Gburski Z (1997) Dynamical properties of the argon-krypton clusters: molecular dynamics calculations. *J Mol Struct* 410–411:507–511. doi:[10.1016/S0022-2860\(96\)09512-9](https://doi.org/10.1016/S0022-2860(96)09512-9)
11. Al Sayem A, Mahdy MRC, Jahangir I, Rahman MS (2017) Ultrathin ultra-broadband electro-absorption modulator based on few-layer graphene based anisotropic metamaterial. *Opt Commun* 384:50–58. doi:[10.1016/j.optcom.2016.09.062](https://doi.org/10.1016/j.optcom.2016.09.062)
12. Fang LJ, Wang XL, Li YH, Liu PF, Wang YL, Zeng HD, Yang HG (2017) Nickel nanoparticles coated with graphene layers as efficient co-catalyst for photocatalytic hydrogen evolution. *Appl Catal B-Environ* 200:578–584. doi:[10.1016/j.apcatb.2016.07.033](https://doi.org/10.1016/j.apcatb.2016.07.033)
13. Zhao J, Xie Y, Fang J, Ling Y, Gao Y, Liu X, Zhang Q, Xu Q, Xiong H (2016) P-phenylenediamine-benzoquinone Schiff base Ag(I) complexes chemically bonded to few-layered graphene as flexible materials for electromagnetic studies. *J Mater Sci* 51:10574–10584. doi:[10.1007/s10853-016-0277-x](https://doi.org/10.1007/s10853-016-0277-x)
14. Lan S, Song Y, Chen Q, Guo Z, Zhan H (2016) A novel platform based on defect-rich knotted graphene nanotubes for detection of small biomolecules. *Electrochim Acta* 217:47–54. doi:[10.1016/j.electacta.2016.09.029](https://doi.org/10.1016/j.electacta.2016.09.029)

15. Solookinejad G (2016) Polarized dependence of nonlinear susceptibility in a single layer graphene system in infrared region. *Phys B-Condens Matter* 497:67–70. doi:[10.1016/j.physb.2016.06.014](https://doi.org/10.1016/j.physb.2016.06.014)
16. Dawid A, Gwizdala W (2010) The dynamics of 5cb Mesogene molecules between graphite walls - an md study. *Rev Adv Mater Sci* 23:37–41
17. Gwizdala W, Górny K, Gburski Z (2011) The dynamics of 4-cyano-4-n-pentylbiphenyl (5CB) mesogen molecules located between graphene layers–MD study. *Spectrochim Acta A Mol Biomol Spectrosc*. doi:[10.1016/j.saa.2010.08.040](https://doi.org/10.1016/j.saa.2010.08.040)
18. Kale L, Skeel R, Bhandarkar M, Brunner R, Gursoy A, Krawetz N, Phillips J, Shinozaki A, Varadarajan K, Schulten K (1999) NAMD2: greater scalability for parallel molecular dynamics. *J Comput Phys* 151:283–312. doi:[10.1006/jcph.1999.6201](https://doi.org/10.1006/jcph.1999.6201)
19. Phillips JC, Braun R, Wang W, Gumbart J, Tajkhorshid E, Villa E, Chipot C, Skeel RD, Kalé L, Schulten K (2005) Scalable molecular dynamics with NAMD. *J Comput Chem* 26:1781–1802. doi:[10.1002/jcc.20289](https://doi.org/10.1002/jcc.20289)
20. Humphrey W, Dalke A, Schulten K (1996) VMD – visual molecular dynamics. *J Mol Graph* 14:33–38
21. Brunger A, Kuriyan J, Karplus M (1987) Crystallographic R-factor refinement by molecular-dynamics. *Science* 235:458–460. doi:[10.1126/science.235.4787.458](https://doi.org/10.1126/science.235.4787.458)
22. Henin J, Chipot C (2006) Hydrogen-bonding patterns of cholesterol in lipid membranes. *Chem Phys Lett* 425:329–335. doi:[10.1016/j.cplett.2006.04.115](https://doi.org/10.1016/j.cplett.2006.04.115)
23. Pasini P, Zannoni C (2013) *Advances in the Computer Simulations of liquid crystals*. Springer Science & Business Media, Dordrecht

# Chapter 61

## Structure Features, Strength, and Microhardness of Nanocomposites Obtained from Fe, Cu, and Carbon Nanotubes

S. L. Revo, M. M. Melnichenko, M. M. Dashevskiy, N. N. Belyavina,  
O. I. Nakonechna, K. O. Ivanenko, O. I. Boshko, and T. G. Avramenko

### 61.1 Introduction

Nanocomposite materials (NCMs) or nanocomposites are an important group of engineering materials that contain a combination of two or more different materials with a clear interface between them. Such structural features of NCMs as nanosize of the grains, their morphology, and the dominant role of boundaries provide the unique complex of physical properties of these materials that it is quite interesting not only in the context of their application but also to develop our knowledge on solid state.

Traditionally, the components used for synthesizing NCM are not chemically interactive but at the same time are compatible with each other or coexist in the same range of temperatures and pressures. To date, a number of methods for producing NCMs have developed, namely, physical vacuum deposition, plasma spraying, vacuum condensation, electrodeposition, pack rolling, etc. Mechanical alloying is a powder processing technique that allows production of homogeneous materials starting from blended elemental powder mixtures. Mechanical alloying involves repeated cold welding, fracturing, and rewelding of powder particles in a high-energy ball mill. This method makes it possible to obtain new materials that are difficult to produce in other ways.

Alloys of iron and copper are widely used in the industry. They have proven themselves in the creation on their base of various compositions including carbon in various modifications.

---

S.L. Revo (✉) • M.M. Melnichenko • M.M. Dashevskiy • N.N. Belyavina • O.I. Nakonechna •  
K.O. Ivanenko • O.I. Boshko • T.G. Avramenko  
Taras Shevchenko National University of Kyiv, 64/13, Volodymyrska Street, 01601, Kyiv, Ukraine  
e-mail: [s\\_revo@i.ua](mailto:s_revo@i.ua)

Microstructure of NCMs is characterized by matrix and reinforcement(s), but in a case of multilayered composite materials (MCMs), the matrix and reinforcement are placed as different layers.

Practical interest in creating multilayered composites is caused by the possibility of obtaining extraordinary complex of physical and mechanical characteristics of the material [1]. While average grain size is the main factor defining the properties of materials for usual bulk solids in a case of MCMs, its role belongs to the thickness of layer ( $h_{Me}$ ).

For these NCMs, an increase in tensile strength ( $\sigma_B$ ) with grain size decreasing (the thickness of the layers in this case) is described by the Hall-Petch law supplemented by a contribution of surface tension:

$$\sigma_B = \sigma_0 + k_b h_{Me}^{-\frac{1}{2}} + \frac{\gamma_C}{h_{Me}} A_0 \quad [2],$$

where  $\sigma_0$  is the flow stress,  $k_b$  is a blocking factor of dislocations by structural barriers,  $\gamma_C$  is the coefficient of linear tension on boundaries of adjacent lamels, and  $A_0$  is a parameter, which takes into account lamel orientation about the axis of elongation.

In addition to the grain size, a significant factor affecting the physical and mechanical properties of the materials is an introduction of high dislocation density in cold-rolling composite systems. Moreover, a unique combination of high strength and ductility is intrinsic to NCMs.

The aim of this work is the empowerment of the specified method for producing NCMs through the use of a planetary ball mill for the production of precursors, comparative analysis of the mechanisms of structure formation for nanocomposites obtained by the two abovementioned methods, and study of the effect of structural features on the physical and mechanical characteristics of the material. The effect of planetary mill to obtain a precursor in the second case is due to the fact that during components' milling occurs not only grinding the powder grains, mutual dissolution of the insoluble component under equilibrium conditions, but also changing their physicochemical characteristics. While milling, the powders of grinding material collide repeatedly in the mill, with the grinding balls and the vial. Due to these collisions, the mechanical activation of particles takes place at high accelerations; their reactivity and mutual mechanical alloying are increased. This work summarizes some results of the authors' research in this area [3–7].

It should be noted that the acceleration value (g) for widespread mills does not exceed 20 g. In this case, to obtain an effective impact on the milled material, it is necessary to process several hours [8, 9]. In our case, the planetary mill allows to get up to 50 g acceleration. So, it is possible to significantly reduce the time of processing of powders and improve its effectiveness to produce high physical and mechanical characteristics of the NCMs.

## 61.2 Methods

Elemental Fe [10], Cu [11] powders (99.6% purity) with 4:1 of weight content, particle sizes of  $\sim 100 \mu\text{m}$ , and multiwall CNTs in the amount of 0.5–2 vol. % (or 0.01–0.05 wt. %) were mixed to give the desired average composition and sealed in a vial under an argon atmosphere. Multiwalled carbon nanotubes [12] used in this study were synthesized by catalytic chemical vapor deposition (CVD) method at TM Spetzmash Ltd. (Kyiv, Ukraine). Parameters of CNTs are as follows: the average diameter is 10–20 nm, the specific surface area (determined by argon desorption method) is 200–400  $\text{m}^2/\text{g}$ , and their poured bulk density varies from 20 to 40  $\text{g}/\text{dm}^3$ . Figure 61.1 shows scanning electron microscope (SEM) images of Fe (Fig. 61.1a) and Cu (Fig. 61.1b) source powders and transmission electron microscope (TEM) image of CNTs used (Fig. 61.1c).

High-energy planetary ball mill is used for mechanochemical activation. Hardened stainless steel balls (15 units of 15 mm diameter) and vial (70 mm height, 50 mm diameter) with a ball-to-powder weight ratio of 20:1 were used. The vial temperature was held below 375 K during the experiments by air cooling. The milling process was cyclic with 5 min of treatment and 25 min of cooling time. The rotation speed was equal to 1480 rpm, the acceleration was about 50 g, and the pressure for a substance particle reached 5 GPa. An energy-dispersive X-ray spectroscopy (EDS) method using a JEOL JSM-840 microscope operated at 10 kV reveals that no additional Fe due to wear debris from the steel balls and vial are introduced into the powders after milling.

To compare the structure and properties of materials obtained, the samples with and without CNT addition have been synthesized.

Elemental powder mixture has been mechanically activated in a planetary ball mill cyclically (cycle period was 5 min). Then the mixture has been compacted in a compression mold under pressure of 30 GPa. Material compacted has been annealed in argon at temperature 950 °C for 30 min. Such treatment (compacting/annealing) was repeated several (up to three) times to get a required thickness. Next stage of the sample preparation includes rolling with relative deformation of 95%. Finally, the samples have been made from the sheets obtained.

The bulk Fe-C NCM samples have been synthesized to perform the microhardness measurements. Mechanically alloyed powder with 20 and 30 vol. % CNTs

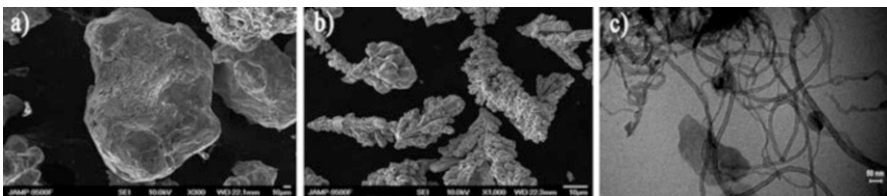


**Fig. 61.1** Microstructural characterization of source materials: SEM image of (a) Fe and (b) Cu powders; (c) TEM image of CNTs

(containing higher amounts of the  $\text{Fe}_3\text{C}$  carbides) has been compacted easily by the high-pressure high-temperature (HPHT) sintering method. The toroid-type high-pressure apparatus was used to create the pressure of 8 GPa and temperature of 850 °C (the test sample powder wrapped into the AlN foil was treated in a high-pressure cell during 40 s).

It should be noted that the samples of multilayered composite materials made of elemental powder of iron and copper have been synthesized without mechanochemical activation by simple mixing of source powders and rolling with reduction of 99.8%. At that, the intermediate annealing has been carried out at temperature which was 0.75–0.85 of melting point of copper. The proposed method has allowed to obtain samples with 20 nm of thickness of the flakes (layers) of the composite.

It should be noted that the components of such composites (Fe and Cu) are hardly soluble in each other in the solid state even at temperatures of 830–1100 °C.

X-ray powder diffraction data were collected with DRON-4 automatic diffractometer ( $\text{CoK}\alpha$  radiation). The diffraction patterns were obtained in a discrete mode under the following scanning parameters: observation range  $2\theta = 40\text{--}130^\circ$ , step scan of  $0.05^\circ$ , counting time per step at 3 s. The peak positions and integral intensities of the observed reflections were determined using full profile analysis.

The original software package elaborated for the automated DRON equipments and including full complex of the Rietveld refinement procedure (qualitative and quantitative phase analysis, lattice parameter refinement, crystal structure determination) was used [13].

The parameters of a deep structure for each  $\alpha\text{-(Fe,Cu)}$  solid solution have been defined from a pair of the 110 and 220 diffraction reflections. The physically broadened line profiles for these diffractions peaks have been splitted after their comparison with similar profiles of the annealed  $\alpha\text{-Fe}$  sample, the broadening of which was caused by the geometry of the X-ray experiment only (instrumental broadening). Each diffraction peak has been smoothed by the cubic spline method and separated into  $\text{K}\alpha_1/\text{K}\alpha_2$  components by the Reehinger method. In the next place, profile peaks have been treated using several mathematical algorithms such as approximation method (including the Cauchy or Gauss functions as well as their superpositions), the Stokes method, and the harmonic analysis method. These algorithms are described in detail [14], and their combination has been implemented in a software developed by Dr. L. Akselrud (Lviv State University, Ukraine). Usage of this software allows us to determine correctly the sizes of the coherent scattering blocks in each phase-component of the sample. The coherent scattering blocks are areas, each of which scatters the incident X-rays coherently. Whereas a set of such coherent scattering regions (or blocks of coherent scattering) composes a grain of NCMs obtained.

SEM examination of the samples was carried out using a scanning electron microscope JEOL JSM-840 [15], equipped with a system of X-ray microspectroscopy analysis (LINK add-on unit to electron microscope).

Tensile strength (for nonbreakable samples) was determined by computerized equipment of “Instron” type. The device can measure changes of tension in dependence on the strain degree  $\sigma = f(\varepsilon)$ . The rate of bursting machine is



2.5–25 mm/min. The maximum load on the sample is 200 kg. The sample studied was cut in a dumbbell-like shape with a 20-mm-wide, 4–5-mm-long working area with a thickness of 0.15–0.2 mm. Stretching speed was 5 mm/min. Average tensile strength was measured on ten samples at room temperature.

The microhardness of materials studied has been measured with PMT-3 device by Vickers method and by microindentation procedure on Micron-Gamma device at room temperature.

During the Vickers test, the diagonal of indentation has been measured. The indenter has a pyramid shape with a vertex of  $136^\circ$ . The load of 50 g has been applied to the sample for 15 s. All samples were polished by diamond paste. The number of indentations per one sample was 50. The microhardness value has been calculated by following formula:

$$H_v = \frac{1854p}{d^2},$$

where  $p$  is the load applied in grams and  $d$  is a direct average of indent's diagonals in micrometers. The microhardness value is measured in GPa.

The second method of microhardness definition is a microindentation with Micron-Gamma equipment at room temperature.

In Ref. [16], an approach to determine the level of elastic deformation in the contact area according to the indentation data has been proposed, and in Refs. [17–20], a new methodology of treatment and analysis of such indentation has been introduced. This method of automatic indentation allows us to determine the hardness ( $H_{IT}$ ), contact elastic modulus ( $E_r$ ), and the Young modulus ( $E$ ).

Local indentation on Micron-Gamma apparatus [18] has been carried out by continuous indentation (the standard Berkovich diamond pyramid) in the test material with the registration of the indentation diagram (dependence of the load ( $F$ ) on the depths of its penetration ( $h$ )) [19, 20].

This paper summarizes the data of the tests with a load varying from 20 to 300 g under the simple “loading-unloading” scheme. Each series of indentation consisted of 15 penetrations with 100  $\mu\text{m}$  step on a surface of the samples.

### 61.3 Results and Discussion

The samples of Fe-Cu (4/1) MCMs and their components were preliminary deformed (rolled) with the same level of relative strain  $\varepsilon = 70\%$ .  $\varepsilon$  value has been chosen taking into account the existing threshold for polycrystalline hardening [21]. It is known [21] that when  $\varepsilon$  reaches 30–40% and in some cases 50%, the metals almost lose the ability to further strengthening.

According to the X-ray diffraction pattern analysis, the Fe-Cu multilayered composite is a two-phase mixture of Cu and  $\alpha$ -Fe with lattice parameters close to those for raw components (Fig. 61.2).

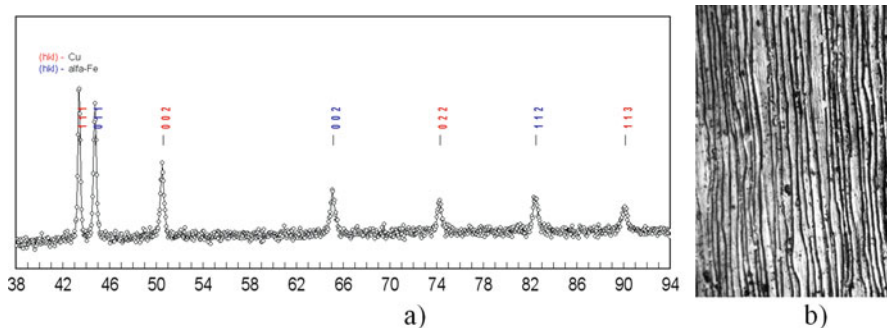


**Fig. 61.2** X-ray diffraction pattern (a) and microstructure (b) ( $\times 1500$ ) for Fe-Cu MCM

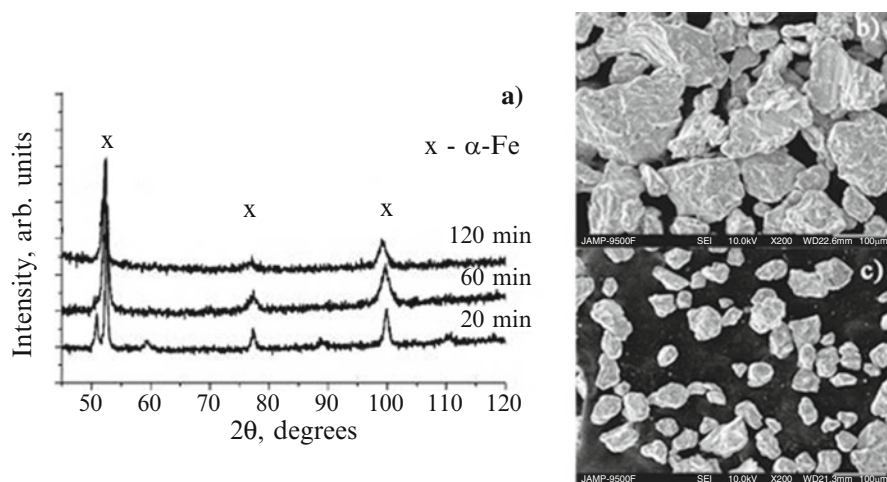


**Fig. 61.3** X-ray patterns of the powder composites obtained by mechanochemical activation of the Fe-Cu (4/1) charge in a ball mill after 20 min, 60 min, and 120 min of treatment. CoK $\alpha$  radiation (a). SEM patterns of Fe-Cu (4:1) NCM treated for 60 (b) and 120 (c) min in a ball mill

According to the X-ray diffraction data, the proof samples taken after 20 min of mechanochemical activation of the charge in a ball mill are two-phase ones and contain a mixture of  $\alpha$ -Fe and Cu in the ratio of a charge material (Fig. 61.3). The lattice constants of these phases are close to those for source powders. Further charge treatment leads to a gradual change in the lattice parameters of the phase which dominates in the charge mixture. This fact indicates the begin stage of the solid solution formation. Concurrently, this solid solution is gradually saturated by a second component that causes formation of the supersaturated solid solution on the base of  $\alpha$ -Fe or Cu. Figure 61.3 illustrates the changes occurring during treatment of the Fe-Cu (4/1) charge in a ball mill.

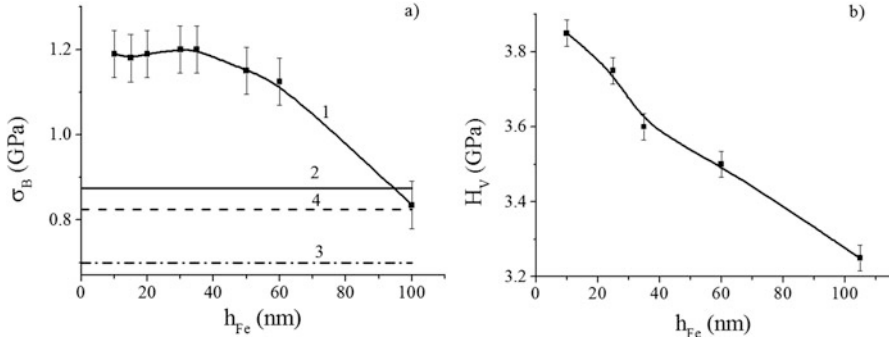


**Fig. 61.4** Dependencies of the ultimate tensile strength (a) and microhardness (b) on a thickness of iron layer. 1, Fe-Cu (4/1) MCM; 2, the deformed Fe foil; 3, the deformed Cu foil; 4, Fe-Cu (4/1) pseudoalloy

The X-ray study revealed that rolled samples obtained from Fe-Cu mixture are two-phase materials containing both  $\alpha$ -Fe phase textured in the [002] direction and Cu (Fig. 61.3).

Figure 61.4 shows the dependencies of tensile strength  $\sigma_B$  (Fig. 61.4a) and the Vickers microhardness  $H_V$  (Fig. 61.4b) on the thickness of the iron layer  $h_{Fe}$  for MCM Fe-Cu (4/1) (curve 1). To estimate a hardening effect, the same dependence for Fe (curve 2), Cu (curve 3), and pseudoalloy Fe-Cu (4/1) (curve 4) are given.

As it is clearly seen from Fig. 61.4, the thickness of layer  $h_{Me}$  decreasing results in MCMs strength and hardness increasing. Thus, the increase in strength was observed in comparison with  $\sigma_B$  of alloy and the additive strength of its components. The irregularity of curve 1 in Fig. 61.4a is obviously related to the local fragmentation of the layers as they are thinning. Besides, it is assumed that the mutual diffusion of the components and its impact on the strength are the same for this case and for the alloy. This statement is based on the fact that the alloy was received by remelting of MCM that ensured a fine structure and equal conditions for diffusion in the alloy and MCM.

As a rule, there is a correlation between strength and hardness of materials [1]. Such correlation is observed for composite components (Fig. 61.4b).

Numerically, the strength on hardness dependence for a work-hardened metal could be expressed as:

$$\sigma_B = CH_V + B, \quad (61.1)$$

where  $C$  is equal to 0.4–0.5 for annealed and 0.3 for deformed metal and  $B$  is equal to 1–3 MPa.

Substituting  $\sigma_B$  and  $H_V$  values in (61.1), one can find that coefficient  $C$  for MCM has a value greater than the value for the deformed material that is apparently due to the fact that they are less sensitive to the crack propagation compared with

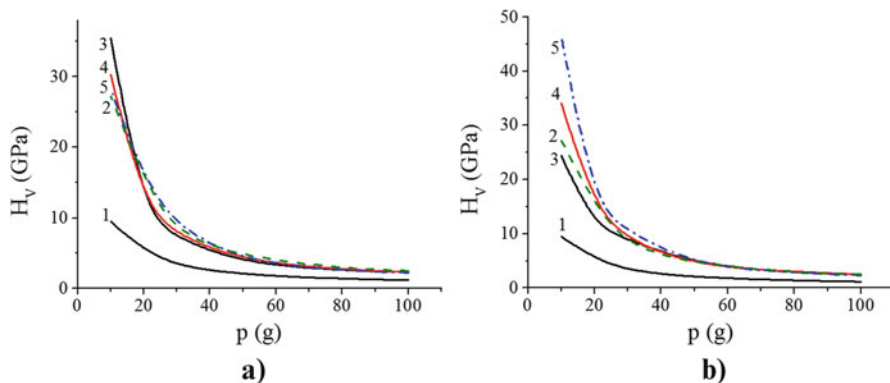


**Fig. 61.5** Microhardness dependencies on an applied load for the samples of (1) Cu and iron (2) and the systems of Fe-Cu (4:1) (a) and Fe-Cu + 1%BHT (4:1) (b) with different treatment time in a planetary ball mill 20 min (3), 60 min (4), and 120 min (5)

homogeneous materials. Therefore, multilayered composite materials have greater strength with respect to the iron samples, whereas their hardness is the same.

It is noteworthy that the maximum values of  $\sigma_B$  in this study have achieved in the direction along the plane of the layers and the microhardness – in a direction perpendicular to the layers.

Since the method of compact samples' obtaining by mechanochemical treatment of powder mixtures has not provided a creation of the regular layered system, we have analyzed  $\sigma_B$  changes on milling time increasing. Analysis of structural change caused by such treatment shows that the morphology of the particles and their phase composition are changed gradually. Besides, there is some elongation of the grain in the rolling direction after rolling the sintered mixtures. For example, both the average grain size of the powders  $\delta$  and the size  $d$  of blocks for coherent scattering for the Fe-Cu (4/1) NCMs are decreased with milling time  $t$  increasing. In particular,  $\delta$  decreases from 70 to 55 nm and  $d$  decreases from 31 to 14 nm with  $t$  increasing from 60 to 120 minutes [4, 5].  $\sigma_B$  value reaches its maximum of 140 GPa at 60 min of treatment time but decreases to 120 GPa with further milling (up to 120 min). Evidently, the prevailing significance of these changes should be attributed not only to optimization of the grain morphology and particle size of the powder mixtures but also to the degree of mutual alloying of the components, which change is also ambiguous.

For the NCMs produced by the second manner, the microhardness has been estimated by method of a continuous nanoindentation at different load. The dependencies of average microhardness estimated by Meyer's method on the load for copper (curve 1) and iron (curve 2) and samples of Fe-Cu (4:1) (a) and Fe-Cu (4:1) + 1% CNTs (b) are shown in Fig. 61.5.

Analysis of the results obtained has showed that the microhardness of samples in dependence on the load differs both by value and nature of the change in their behavior. For the Fe-Cu (4:1) system, the microhardness decreases from

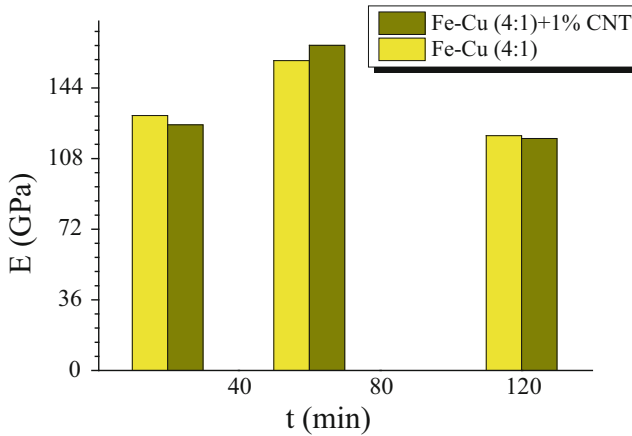


**Fig. 61.6** The Young modulus diagram for the samples of Fe-Cu (4:1) and Fe-Cu + 1%BHT (4:1) with different milling time at 20 g of loading on indenter

27–35 GPa to 2–5 GPa with load increasing, while it's difficult to trace a clear dependence of the composite hardness on milling time.  $H_V(p)$  dependencies are decreasing monotonously for the Fe-Cu (4:1) + 1% CNT system with load on the indenter increasing. Thus, when the load on the indenter is equal to 10 g, the microhardness of the Fe-Cu + 1% CNT system reaches 45 GPa after 120 min of component treatment and is equal to 33 GPa after 60 min of milling and, finally, reaches 25 GPa after 20 min of treatment. If the load on the indenter is equal to 100 g, the microhardness values are approaching 2.2 GPa. At the initial parts of the curves (indentation load is up to 30 g), a steep climb on the dependency observed indicates the fact that the material is reacting “faster” to load and depth of indentation changes. It is seen (Fig. 61.5) that microhardness of Fe is equal to 3 GPa, while  $H_V$  of Cu is half as great in a case of NCMs at indentation load of 80 g.

The indentation performed gives us a possibility to calculate the Young modulus of samples studied. The results of such calculations are presented in Fig. 61.6.

The maximum Young modulus values both for Fe-Cu and Fe-Cu + 1% CNT systems (157 and 165 GPa, respectively) have been observed at 60 min of milling time. So, the optimal (most effective) time of components' treatment in a ball mill for systems studied is 60 min. It should be noted that this result is in a good agreement with  $\sigma_B$  data.

The materials' resistance to the creep processes has been estimated by registering the changes of indentation depth at constant load on the indenter (50 and 100 g) (Fig. 61.7).

Analysis of the results obtained has shown that the penetration degree of indenter into the material is the more the longer milling time of powders' mixture. Besides, as it is seen from Fig. 61.7, the penetration is deeper for the Fe-Cu system rather than for the Fe-Cu-CNTs both after 60 and 120 mins of milling. So, one can conclude that

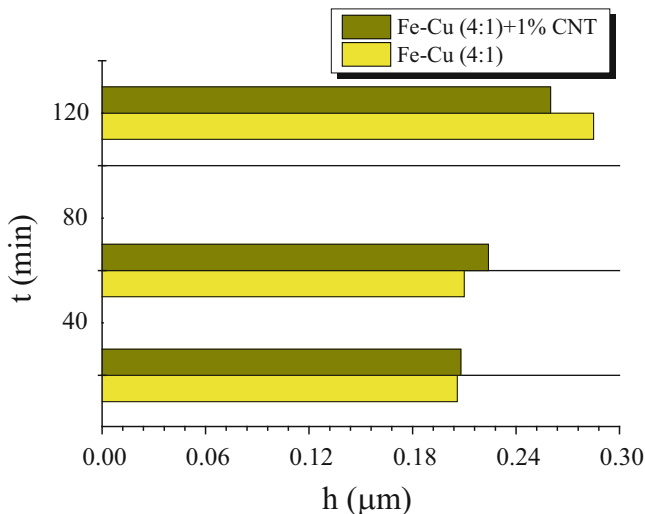


**Fig. 61.7** Dependence of indentation depth at load of 100 g and 10 s of exposition time on milling time (20, 60, and 120 min) for Fe-Cu (4:1) and Fe-Cu (4:1) + 1% CNTs

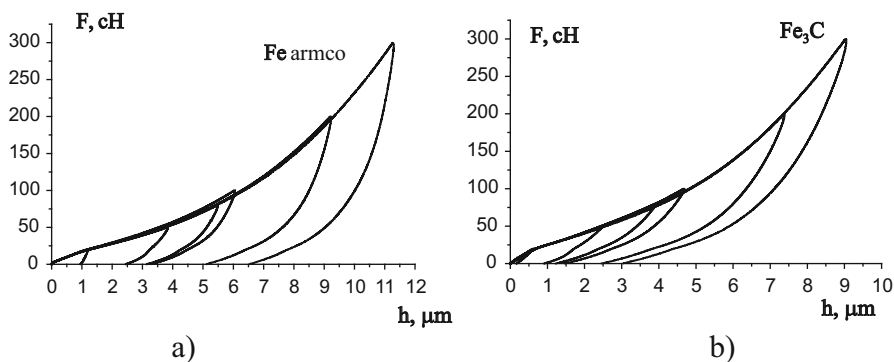


**Fig. 61.8** Dependence of indentation depth on the load applied for the samples: (a) Armco Fe, (b) Fe-CNTs

addition of the carbon nanotubes results in the material strengthening and reduces permanent deformation under long-term compressive force. Thus, the studies make it possible to define the optimum conditions of mechanochemical treatment of powder mixtures of Fe, Cu, and CNTs to synthesize nanocomposites with improved physical and mechanical features.

Indentation curves obtained on Micron-Gamma tool for Armco Fe and the Fe-CNT samples are presented in Fig. 61.8.

Analysis of these diagrams (Fig. 61.8) gives us a possibility to define directly both the maximum penetration depth of the indenter into material and residual

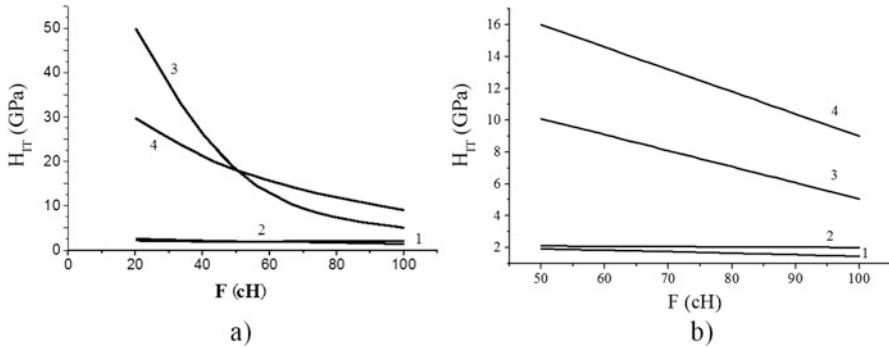


**Fig. 61.9** Dependencies of microhardness on the load applied on indenter for Armco Fe (1, 2) and Fe-CNTs (3, 4) in a range from 20 cN (a) and from 50 cN (b) obtained by Micron-Gamma apparatus (1, 3) and by Vickers method (2, 4)

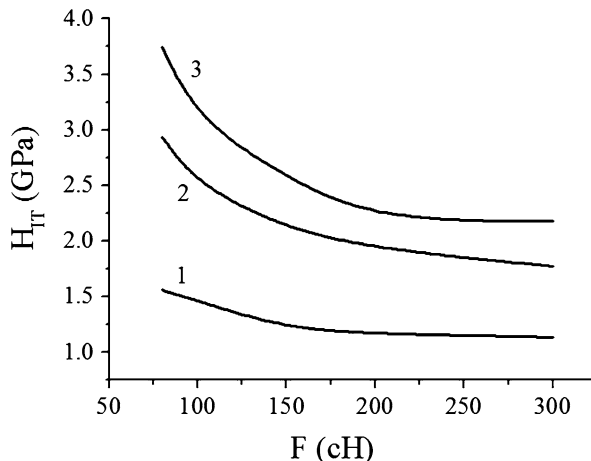
imprint of indenter after unloading. This allows us to evaluate the physical and mechanical features of the material studied.

Dependencies of average microhardness on the applied load for the samples studied by both methods (using Micron-Gamma apparatus and the Vickers method) are shown in Fig. 61.9.

Curves (Fig. 61.9) are steadily falling throughout the measuring range. Two areas can be separated for NCMs of Fe-CNT system: fast (Fig. 61.9a) and slow (Fig. 61.9b) decline of microhardness on the applied load. The beginning area with higher dynamics of microhardness changes can be connected with a size effect. The properties of any nanomaterials significantly depend on the size of structural components as well as the state of their boundaries. The grains of different rate of structural homogeneities and orientation, with different defects and chemical composition of boundaries, can be formed depending on a processing mode. A number of research have emphasized that the decisive role in the specific mechanical behavior of nanoscaled materials belongs to a near-boundary area and triple joints [22–24]. This fact is especially true for materials obtained by grinding in a planetary ball mill. For these materials, the defect structure of grain boundaries has a high level of internal elastic stresses, increased density of grain-boundary dislocations, and lattice distortion in the near-boundary regions [25].

Figure 61.9a shows that the hardness measured by Micron-Gamma tool increases from 20 to 50 GPa with load decreasing from 50 to 20 cN, but the hardness measured by the Vickers method changes from 20 to 30 GPa. Besides, for the range of  $F > 50$  cN (Fig. 61.9b), the microhardness measured by the Vickers method is significantly higher than the value obtained through Micron-Gamma apparatus. At the same time, hardness defined by continuous loading changes from 5 to 10 GPa with the loading change from 50 to 100 cN and  $H_V$  measured by PMT-3 tool increases from 7.5 to 16 GPa. This can be explained by the fact that with a decrease in the volume of a material involved in the process of deformation, the nature of the deformation mechanism is changing also, resulting in the increased hardness values. And since

**Fig. 61.10** Microhardness dependencies on the load applied obtained by Micron-Gamma apparatus for the Armco Fe (1) and Fe-CNTs milled for 150 min (2) and 500 min (3)



the value of microhardness determined by the parameters of the indent is much more higher than the value defined by continuous indentation, this is a confirmation that Fe-CNT nanocomposite demonstrates advanced elastic characteristics, which are caused by the fact that an elastic restore of indent takes place during the measurement and we get too high hardness values.

Figure 61.10 summarizes the results of microhardness average values in dependence of load (from 80 to 300 cN) for samples of Armco Fe and Fe-CNT NCMs.

Analysis of the experimental results (Fig. 61.10) shows that microhardness tends to decrease with load increasing. Moreover, for the Fe-CNTs sample  $H_V$  shifts to higher values with milling time in a planetary ball mill increasing. Apparently, this is due to the increase in the part of  $Fe_3C$  carbide phase in the material, which hardness is four times higher than the hardness of austenite.

Using the results obtained (Fig. 61.10) and the method of processing and analysis of results, the dependence of stress corresponding to the beginning of plastic deformation on the microhardness has been plotted (Fig. 61.11).

The limiting mean of  $\sigma_{TT}$  is changed from 0.34 to 0.59 GPa with load increasing from 80 to 300 cN for Armco iron whereas for samples of Fe-CNTs from 0.65 to 2.2 GPa. More intense dynamics of tension change, at which plastic deformation occurs, indicates that Fe-CNT composite reacts faster to external effects in a simple circuit of loading.

Thus, the use of continuous indentation of material by Micron-Gamma device can not only provide a nondestructive analysis of material's surface but also identify and predict its elastic properties and mechanical behavior.

**Acknowledgment** Authors would like to thank Dr. L. Kapitanchuk from Ye.O. Paton Electric Welding Institute of the National Academy of Science of Ukraine for providing SEM measurements.



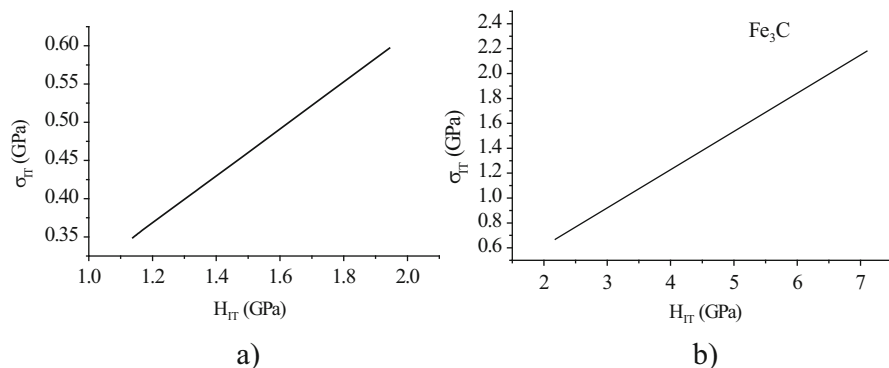


**Fig. 61.11** Dependence of  $\sigma_{TT}$  strength that corresponds to the beginning of plastic deformation process under the simple modes on microhardness  $H_{TT}$  obtained by Micron-Gamma apparatus

## References

1. Shpak AP, Mayboroda VP et al (2004) Nanolayer composite materials and coatings. Academ-periodika, Kyiv. (in Russian)
2. Kopan VS et al (1990) *MICC 90*: Microlayer composite materials. In: Fridlyander J, Kostikov VI (eds) Moscow international composites conference. Elsevier App Sci, London/New York, pp 848–850
3. Boshko OI, Dashevskiy MM, Ivanenko KO, Revo SL (2015) Metallofiz Noveishie Tekhnol 37(7):921
4. Boshko O, Dashevskiy M, Mykhaliuk O et al (2016) Structure and strength of iron-copper-carbon nanotube Nanocomposites. *Nanoscale Res Lett* 11:78. doi:10.1186/s11671-016-1298-8
5. Boshko O, Nakonechna O, Dashevskiy M et al (2016) Effect of the carbon nanotubes on structure and magnetic properties of the Fe-Cu (4:1) composites. *Adv Powder Technol* 27(4):1101–1108. <http://dx.doi.org/10.1016/j.appt.2016.03.019>
6. Revo SL, Boshko OI et al (2016) *Nanosistemi, Nanomater, Nanotehnol* 14(1):169–180. [http://www.imp.kiev.ua/nanosys/media/pdf/2016/1/nano\\_vol14\\_iss1\\_p0169p0180\\_2016.pdf](http://www.imp.kiev.ua/nanosys/media/pdf/2016/1/nano_vol14_iss1_p0169p0180_2016.pdf)
7. Nakonechna OI et al (2017) Nanocrystalline Fe-C composites obtained by mechanical alloying of iron and carbon nanotubes. *Adv Powder Technol* 28(3):964–972
8. Rajkovic Viselava, Bozic Dusan, Jovanovic Milan T (2006) Characterization of pre-alloyed copper powders treated in high energy ball mill. *Mater Charact* 57(2):94–99. <http://dx.doi.org/10.1016/j.matchar.2005.12.011>
9. Rabah Hamzaoui, Omar Elkedim (2013) Magnetic properties of nanocrystalline Fe-10%Ni alloy obtained by planetary ball mills. *J Alloys Compd* 573:157–162. <http://dx.doi.org/10.1016/j.jallcom.2013.03.183>
10. Iron Powder: GOST 9849–86 1986 [valid from 1 July 1987]. Moscow: Interstate Standard, p 9 (National Standard of Ukraine). (in Russian)
11. Copper Powder Electrodeposited. GOST 4960–2009 2009 [valid from 1 July 2010]. Moscow: Standardinform, p 16 (National Standard of Ukraine). (in Russian)
12. Carbon nanotubes: TC U 24.1–03291669-009:2009. № 02568182/095617 from 01.09.2009. Authors: Yu.I. Sementsov, O.V. Melezhik, [http://nabivka.com/ru/nanouglerodnie\\_materiali.html](http://nabivka.com/ru/nanouglerodnie_materiali.html). (in Ukrainian).
13. Markiv V, Belyavina N (1997) In: Proceedings of the Second International EFM'97, Lviv, p 260

14. Pecharsky VK, Zavalij PY (2009) Fundamentals of powder diffraction and structural characterization of materials, book, 2nd edn. Springer, New York, p 713. doi:[10.1007/978-0-387-09579-0](https://doi.org/10.1007/978-0-387-09579-0)
15. GLEEBLE – 3800. Center for shared-use of the device of Ye.O. Paton Electric Welding Institute of the National Academy of Science of Ukraine –2016. Access: <http://paton.kiev.ua/ru/o-nas/centry-kollektivnogo-polzovanija/1010-glibl-3800>
16. Galanov BA, Milman YV Chugunova SI et al (1999) Studies of mechanical properties of hard metals by indentation method, Superhard Materials, N 3, pp 25–38 (in Russian)
17. Firstov SA, Gorban VF, Pechkovsky EP et al (2007) Dopovidi NAN Ukraine. 12:100
18. Firstov SA, Gorban VF, Pechkovsky EP (2009) Mew methodology of results treatment for indentation of materials. Kyiv, Logos, (in Russian).
19. Oliver WC, Pharr GM (1992) An improved technique for determining hardness and elastic modulus using load and displacement sensing indentation measurements. J Mater Res 7(6):1564–1583
20. Oliver WC, Pharr GM (2004) Measurement of hardness and elastic modulus by instrumented indentation: Advances in understanding and refinements to methodology. J Mater Res 19(1):3–20 <http://www.msm.cam.ac.uk/mechtest/docs/untitled/MTS%20Info/Oliver%20Pharr%20Paper.pdf>
21. Cahn RW, Haasen P (eds) (1996) Physical metallurgy, vol 2, 4th edn. Elsevier, North Holland, Amsterdam
22. Van Swygenhoven H and Weertman JR (2006) Deformation in nanocrystalline metals. Materials Today 9(5):24–31. [http://dx.doi.org/10.1016/S1369-7021\(06\)71494-8](http://dx.doi.org/10.1016/S1369-7021(06)71494-8)
23. Kumar KS, Van Swygenhoven H, Suresh S (2003) Mechanical behavior of nanocrystalline metals and alloys. Acta Materialia 51(19):5743–5774. <http://dx.doi.org/10.1016/j.actamat.2003.08.032>
24. Palumbo G, Erb U, Aust KT (1990) Triple line dislocation effects on the mechanical behaviour of materials. Scr Met Mater 24:2347–2349. doi:[10.1016/0956-716X\(90\)90091-T](https://doi.org/10.1016/0956-716X(90)90091-T)
25. Horita Z, Smith D, Furuuawa M et al (1996) An investigation of grain boundaries in submicrometer-grained Al-Mg solid solution alloys using high-resolution electron microscopy. J Mater Res 11(8):1880–1890. <https://doi.org/10.1557/JMR.1996.0239>

# Chapter 62

## Influence of Radiofrequency Electromagnetic Radiation on Magnetic Properties of Magneto-Mechanochemically Synthesized Antitumor Nanocomplex

V. Orel, A. Shevchenko, O. Rykhalskyi, A. Romanov, A. Burlaka, and S. Lukin

### 62.1 Introduction

Iron oxide nanoparticles (NP) have been widely used in therapeutics of experimental tumors because of their unique size, magnetic properties, and ability to interact with a number of biomolecules [1]. We have developed a new cancer magnetic nanotherapeutic technology based on the ability of external electromagnetic field (EMF) to induce the changes in electron transitions in complex composed of semiconductor materials such as ferromagnetic iron oxide  $\text{Fe}_3\text{O}_4$  NP and antitumor drug [2]. The technology is based on known semiconductor materials' ability, in NP, to generate oxygen radicals and oxidative stress in biological media. Based on advanced studies of electromagnetic radiation (ER) on oxidative stress reactions, the potentially effect of ER on living organisms is that exposure to magnetic field can increase the activity, concentration, and life time of paramagnetic free radicals, which might cause oxidative stress, genetic mutation, and/or apoptosis [3, 4].

Primary studies were carried out to accomplish two main objectives: firstly, to observe the cytotoxic effects of iron oxide NP, and secondly, to clarify the role of iron oxide NP in reducing oxidative stress. It was confirmed that iron oxide NP can participate in cyclical regenerative or autocatalytic free radical reactions under

---

V. Orel (✉) • O. Rykhalskyi • A. Romanov  
National Cancer Institute, 33/43, Lomonosova St., 03022, Kyiv, Ukraine  
e-mail: [v-orel@voliacable.com](mailto:v-orel@voliacable.com)

A. Shevchenko  
G.V. Kurdyumov Institute for Metal Physics, 36, Academican Vernadsky Blvd., 03680, Kyiv, Ukraine

A. Burlaka • S. Lukin  
R.E. Kavetsky Institute of Experimental Pathology, Oncology and Radiobiology, 45, Vasilkovsky St., 03022, Kyiv, Ukraine

ER [5]. Thus magnetic anticancer nanocomplex regulates the redox reaction inside tumor cells. In animal models, the exposure of malignant tumor with antitumor nanocomplex to EMF consequences in significant decrease of tumor growth and dissemination as a result amplification of regulated local oxidative stress in a tumor [6].

The specified magnetic parameters in nanocomplex can be produced by magneto-mechanochemical synthesis (MMCS). This technology includes the mechanical fragmentation of separate elements and simultaneous exposure to nonhomogeneous constant magnetic and electromagnetic fields, which cause eddy currents and magnetic vortices in the areas of contact between iron oxide NP and organic compounds and initiate paramagnetic centers (free radicals) in the structure of magneto-sensitive NP complex (MNC) [2]. MMCS in magneto-mechanical nanoreactor based on the integration of two well-known technologies: mechanochemical synthesis (MCS) [7] and synthesis in the microreactor with magnetic elements [8].

MCS is the coupling of mechanical and chemical phenomena on a molecular scale. This effect is related to specific coupling of physical and chemical phenomena leading to initiation of heterogeneous chemical reactions due to mechanical action. Its top-down approach is “ball milling,” the formation of nanostructure building blocks through controlled, mechanical attrition of the bulk starting material. Those nanobuilding blocks are then subsequently assembled into a new bulk material. High-energy ball milling, the only top-down approach for NP synthesis, has been used for the generation of magnetic NP [9]. MCS activates the paramagnetic centers (free radicals) in MNC structure and is accompanied by triboemission (mechanoemission) [10]. It includes mechanical breakage and chemical behavior of mechanically stressed solids, e.g., stress corrosion cracking or enhanced oxidation. Tribolayer formation in polymers is initiated by mechanochemical reactions during friction producing free radicals that are at least partly transformed into ionic species with half-lives exceeding tens of hours and have a major if not dominating role in the formation of triboemission. Triboemission is defined as emission of electrons, charged particles, lattice components, photons, etc., under dry mechanical action, e.g., surface damage caused by fracture processes or conditions of boundary friction. The triboemission phenomena are classified into two classes by physical nature: emission of particles (“corpuscular”) and emission of energy [11].

In accordance with Lenz’s law in the areas of contacts between  $\text{Fe}_3\text{O}_4$  NP and organic compounds initiated by external ER an eddy current creates a magnetic field that opposes the magnetic field that created it, and thus eddy currents react back on the source of the magnetic field [12].

It is well known that magnetic properties of iron oxides NP include in their membership the ions with unpaired electrons on the inner orbital (3d orbital of Fe ions in  $\text{Fe}_3\text{O}_4$ ), which determine the magnetic properties of magnetite. A free radical is an atom, molecule, or ion that has unpaired valence electrons. These unpaired electrons make free radicals highly chemically reactive towards other substances, or even towards themselves. The magnetic properties of unpaired electrons of iron oxides affect an anthracycline antibiotic doxorubicin (DOXO) antitumor activity, as a result of electron transfer from to DOXO during ER. An analysis of the magnetic measurements shows that mechanochemical activation and magneto-

mechanochemical activation reduced the saturation magnetic moment of the  $\text{Fe}_3\text{O}_4$  without DOXO samples (partial demagnetization). Adding DOXO to nanocomplex naturally reduced the saturation magnetic moment. Interestingly, after MMCS the saturation magnetic moment of MNC changed as compared to particles synthesized under MCS only. This demonstrates the importance of the application of EMF during MCS. Under the influence MMCS, the complex NP with DOXO show a hysteresis curve, which is typical for soft ferromagnetic materials [2].

In cancer patients, molecular structure of malignant tumors is highly heterogenized that determines their individual chemoresistance [13]. Therefore, there is a key task to synthesize personalized antitumor nanocomplexes with specified magnetic properties. In order to evaluate the possibility of solving this problem, in this chapter we have studied the influence of different frequencies of radiofrequency ER on magnetic properties of MMCS antitumor nanocomplex.

## 62.2 Materials and Methods

### 62.2.1 Magneto-Mechanochemical Synthesis

$\text{Fe}_3\text{O}_4$  NP (International Center for Electron Beam Technologies of E.O. Paton Electric Welding Institute, Ukraine) with diameters in the range of 20–40 nm and DOXO (Actavis, Romania) were processed in high-precision magneto-mechanical milling chamber (NCI, Ukraine). The milling chamber is shown at Fig. 62.1. The samples of  $\text{Fe}_3\text{O}_4$  and DOXO were placed in the diamagnetic chamber (5) together with metallic balls (6). Mechanical processing was performed by vertical vibrations

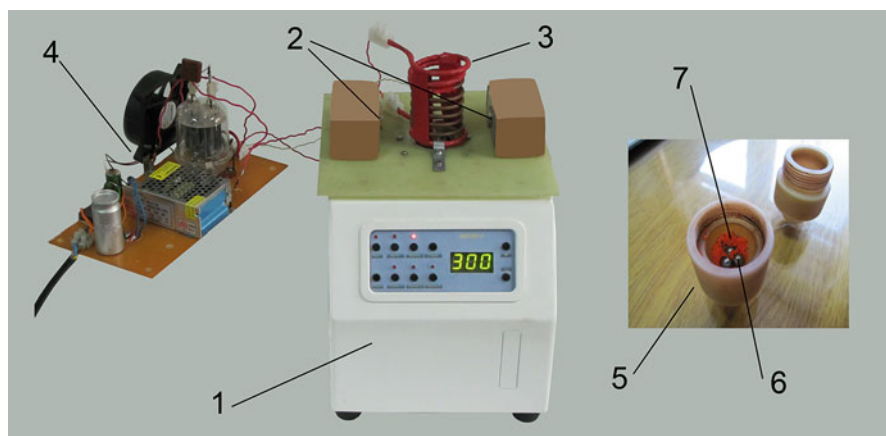


**Fig. 62.1** Magneto-mechanical milling chamber: mechanical chamber (1), permanent magnets (2), induction coil (3), frequency generator (4), diamagnetic chamber (5), metallic balls (6),  $\text{Fe}_3\text{O}_4$  NP and DOXO (7)

of the chamber at a frequency of 36 Hz and an amplitude of 9 mm for 5 min using mechanical energy of 20 W/g. Simultaneously, ER in frequency range of 0.99, 1.41, 1.84, 2.92, 5.09, 7.41, and 42 MHz was applied for 5 min with 11 W output capacity of induction coil (3) and 8 mT constant magnetic field of permanent magnets (2). Magnetically induced heating in conventional iron oxide NP or DOXO-loaded MNC was small (0.5 °C). In addition, we have investigated magnetic properties of magneto-mechanochemically activated iron oxide NP (without DOXO), MNC synthesized in MCS conditions (without ER), and NP/mixture of DOXO and Fe<sub>3</sub>O<sub>4</sub> NP without any influence.

### **62.2.2 Magnetic Studies**

The magnetic properties were studied by magnetometry using a “Vibrating Magnetometer 7404 VSM” (Lake Shore Cryotronics Inc., USA) with magnetic fields up to 13 kOe. The magnetometer’s sensitivity is  $10^{-7}$  emu, and that allowed measuring the magnetic moment of samples weighing milligrams. The mass was determined by an electronic microbalance AB135-S/FACT with auto-identification (Mettler Toledo, Switzerland) which has a sensitivity of  $10^{-5}$  g.

### **62.2.3 Electron Spin Resonance (ESR) Spectroscopy**

In order to measure the  $g$ -factor and the concentration of paramagnetic centers in the samples, ESR spectra were recorded with the spectrometer RE1307 in a cylinder resonator with the mode H<sub>011</sub> and frequency 9.15 GHz. The power of microwave radiation was 40 mW, and the magnetic field modulation frequency was 100 kHz. The samples were placed in a quartz Dewar with an inner diameter of 4.5 mm.

## **62.3 Experimental Results**

### **62.3.1 Magnetic Studies and ESR Spectroscopy of Iron Oxide NP**

Let’s analyze the first series of our research samples of iron oxide NP (Fig. 62.2 and Table 62.1) [14]. One of the important parameters is the saturation magnetic moment  $m_s$ : the state reached when an increase in applied external magnetic field  $H$  cannot increase the magnetization of the sample further. Saturation magnetic moment was maximal (46.43 emu/g) in the samples irradiated by the radio waves with the greatest frequency of 42.27 MHz. Minimal values of 27.10 emu/g and

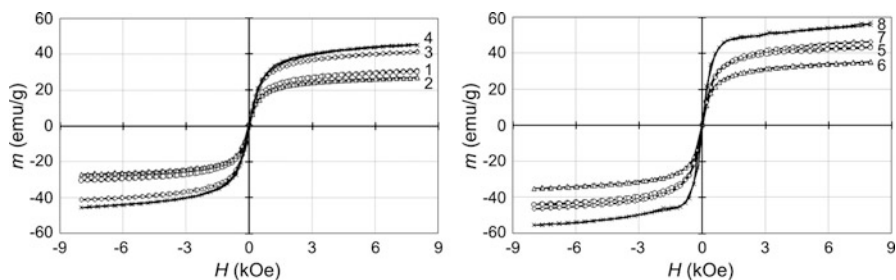


**Fig. 6.2.2** Hysteresis loops of magneto-mechanochemically activated  $\text{Fe}_3\text{O}_4$  NP at 300 K depending on ER frequency: 0.99 MHz (1), 1.41 MHz (2), 1.84 MHz (3), 2.92 MHz (4), 5.09 MHz (5), 7.41 MHz (6), 42.0 MHz (7), without influence (8).  $H$  – magnetic field

**Table 62.1** Magnetic properties of magneto-mechanochemically activated  $\text{Fe}_3\text{O}_4$  NP.  $T = 300$  K

Sample number	Frequency $f$ , MHz	Energy $W$ , $10^{-9}$ eV	Saturation magnetic moment $m_s$ , emu/g	Coercivity $H_c$ , G	Area of the hysteresis loop $S$ , erg/g
1	0.96	4	30.53	17.78	6914.5
2	1.41	6	27.10	23.30	2151.8
3	1.84	8	41.28	8.15	8915.5
4	2.92	12	45.33	4.07	13,644
5	5.09	21	44.60	7.24	17,296
6	7.41	31	35.09	11.72	7973
7	42.27	175	46.43	4.67	2235
Pearson correlation coefficient $r$			0.48	-0.44	-0.43
8	Without influence		56.194	10.20	14,394

30.53 emu/g were observed after exposure to significantly lower EMF frequency of 1.41 and 0.96 MHz, respectively.

The coercivity  $H_c$  is the intensity of the applied magnetic field required to reduce the magnetization of that material to zero after the magnetization of the sample has been driven to saturation. Thus coercivity measures the resistance of a ferromagnetic material to demagnetization. The greater the coercivity, the higher the specific absorption rate (SAR) of EMF. In our experiments, all samples exhibited low coercivity and hysteresis loops with a small area and can be classified as soft magnetic materials. The changes in coercivity depending on the ER frequency were opposite as compared to the saturation magnetic moment. Maximal coercivities of 17.78 G and 23.30 G were registered after radiation by radio waves with lowest frequencies of 1.41 and 0.96 MHz accordingly. Minimal coercivity  $H_c = 4.67$  G was observed when samples were irradiated by EMF of considerably higher frequency 42.27 MHz.

The area  $S$  of hysteresis loop showed the dependence between the induced magnetic flux density and the magnetizing force. The greatest area of hysteresis

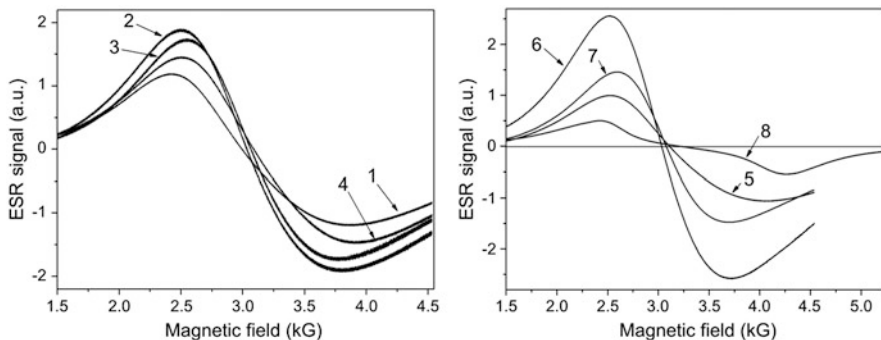


**Fig. 62.3** ESR spectrum of magneto-mechanochemically activated  $\text{Fe}_3\text{O}_4$  NP. Frequency of ER: 0.99 MHz (1), 1.41 MHz (2), 1.84 MHz (3), 2.92 MHz (4), 5.09 MHz (5), 7.41 MHz (6), 42.0 MHz (7), without influence (8).  $T = 300$  K

loop 17,296 erg/g was observed after ER by 5.09 MHz EMF. The minimal area of 2235 erg/g was in the samples irradiated by significantly greater frequency of 42.27 MHz.

We have assessed the relationship between EMF frequency and magnetic properties of investigated samples using Pearson correlation coefficient. Results demonstrated a weak straight correlation for saturation magnetic moment ( $r = 0.48$ ) and weak negative correlation for coercivity  $H_c$  ( $r = -0.44$ ) and an area  $S$  of the hysteresis loop ( $r = -0.43$ ).

We have studied the magnetic properties of NP without influence. These samples have different magnetic properties ( $m_s$ ,  $H_c$ , and  $S$ ) in comparison with NP under ER. Saturation magnetic moment ( $m_s$ ) was significantly higher.

According to ESR spectroscopy data of magneto-mechanochemically activated  $\text{Fe}_3\text{O}_4$  NP (Fig. 62.3 and Table 62.2), the maximal relative intensity 1.50 a.u. of ESR spectrum was observed after ER by 0.96 MHz EMF, and minimal value of 1.00 a.u. was registered at frequency of 42.27 MHz. Pearson correlation coefficients between ER frequency and relative intensity of ESR spectra and  $g$ -factor were, respectively,  $-0.68$  and  $-0.60$ . Conventional  $\text{Fe}_3\text{O}_4$  NP without influence had significantly lower relative intensity and different  $g$ -factors.

### 62.3.2 Magnetic Studies and ESR Spectroscopy of Magnetic Nanocomplex

Magnetic properties of MNC comprising iron oxide NP and DOXO synthesized under MMCS conditions were different as compared to conventional NP (Fig. 62.4 and Table 62.3). Maximal saturation magnetic moment  $m_s = 13.4$  emu/g was registered after ER by radio waves with the frequency of 7.41 MHz. Minimal values 4.63 emu/g and  $m_s = 9.12$  emu/g were observed similarly to the experiments



**Table 62.2** ESR spectrum of magneto-mechanochemically activated Fe<sub>3</sub>O<sub>4</sub> NP.  $T = 300$  K

Sample number	Frequency $f$ , MHz	Energy $W$ , $10^{-9}$ eV	Relative intensity, a.u.	$g$ -factor
1	0.96	4	1.50	2.40
2	1.41	6	1.22	2.46
3	1.84	8	1.39	2.41
4	2.92	12	1.19	2.39
5	5.09	21	1.24	2.44
6	7.41	31	1.49	2.42
7	42.27	175	1.00	2.37
Pearson correlation coefficient $r$			-0.68	-0.60
8	Without influence		0.52	2.73 2.07 1.56

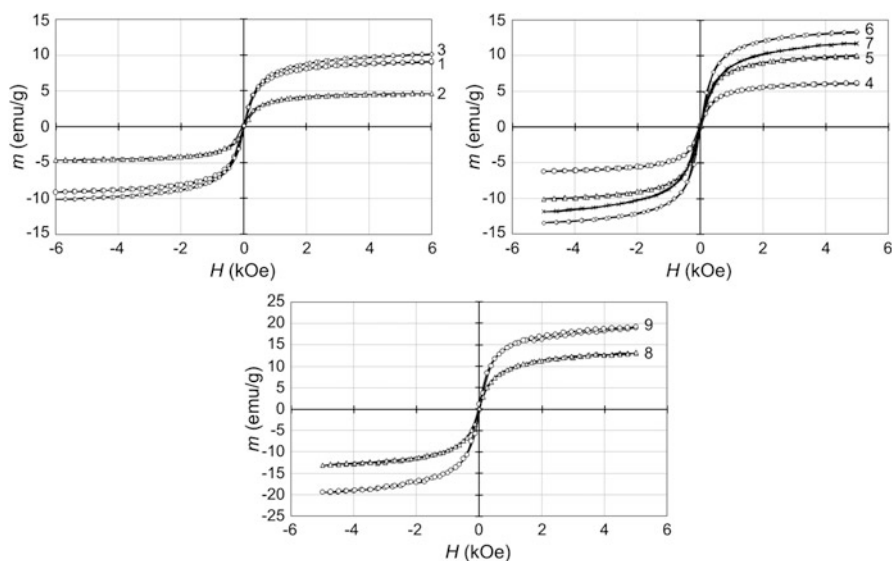


**Fig. 62.4** Hysteresis loops of MMCS nanocomplex of DOXO-loaded Fe<sub>3</sub>O<sub>4</sub> NP at 300 K depending on ER frequency: 0.96 MHz (1), 1.41 MHz (2), 1.84 MHz (3), 2.92 MHz (4), 5.09 MHz (5), 7.41 MHz (6), 42.0 MHz (7), MCS (8), the mixture of DOXO and Fe<sub>3</sub>O<sub>4</sub> NP without influence (9).  $H$  – magnetic field

with conventional iron oxide NP after radiation by EMF with significantly lower frequencies of 1.41 and 0.96 MHz accordingly. Maximal coercivity  $H_c = 40.52$  G was registered after ER by 1.41 MHz EMF. Minimal coercivity 7.16 G was observed when the samples were irradiated by radio waves of greater frequency 7.41 MHz. Maximal area of the hysteresis loop  $S = 3402$  erg/g was registered for the samples after 42.27 MHz ER; minimal area 615.6 erg/g was observed after ER by EMF with considerably lower frequency of 1.41 MHz. It was found that EMF frequency exhibits positive correlation with saturation magnetic moment ( $r = 0.45$ ) and an

**Table 62.3** Magnetic properties of MMCS nanocomplex of Fe<sub>3</sub>O<sub>4</sub> NP and DOXO.  $T = 300$  K

Sample number	Frequency $f$ , MHz	Energy $W$ , $10^{-9}$ eV	Saturation magnetic moment $m_s$ , emu/g	Coercivity $H_c$ , G	Area of the hysteresis loop $S$ , erg/g
1	0.96	4	9.12	8.07	1653.0
2	1.41	6	4.63	40.52	615.6
3	1.84	8	10.16	9.01	1561.9
4	2.92	12	6.19	22.23	1388.1
5	5.09	21	10.09	8.45	1745.7
6	7.41	31	13.4	7.16	3282.9
7	42.27	175	11.81	12.57	3402.0
Pearson correlation coefficient $r$			0.45	-0.17	0.72
8	MCS		13.14	8.33	1259.9
9	Without influence		19.39	29.91	317.5

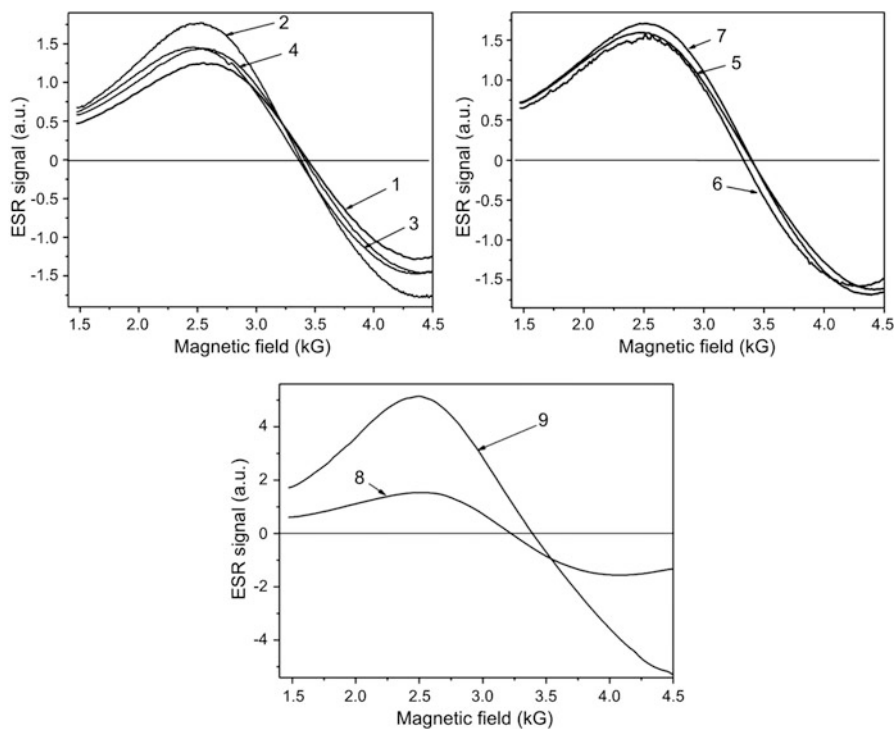
area of the hysteresis loop ( $r = 0.72$ ). The coercivity has a weak negative correlation with the frequency both in experiments with conventional iron oxide NP and iron oxide NP loaded with DOXO.

Figure 62.5 and Table 62.4 show ESR studies of DOXO-loaded iron oxide NP synthesized in MMCS conditions at different frequencies of ER. Maximal relative intensities of 1.35 a.u. and 1.41 a.u. were observed after ER with the frequencies of 0.96 and 1.41 MHz accordingly. Minimal relative intensity ( $I = 1$ ) was observed at 42.27 MHz. Negative correlations between ER frequency and relative intensity of ESR spectrum ( $r = -0.67$ ) and  $g$ -factors ( $r = -0.58$ ) were observed. Relative intensities of ESR spectra for MNC samples synthesized either in MCS conditions or without influence were different. Relative intensity was maximal ( $I = 4.65$  a.u.) after MCS. Maximal  $g$ -factor (2.56) was recorded in the samples without influence.

## 62.4 Discussion

This study demonstrates the beneficial effect of the influence of different frequencies of radiofrequency low-energy ER on magnetic properties of MMCS antitumor nanocomplex. However, it is necessary to interpret the experimental results based on previously known experimental facts or theories.

The basis of MMCS was amorphization of DOXO on the surface of iron oxide NPs. The milling of iron oxide particles did not occur in our experiments. Therefore, the problem of wide size distribution and contamination of NP during application of ball-milled synthesis was eliminated. The vibration was used only in order to form the complex of iron oxide NP core coated with amorphous DOXO shell. Because of the increased free energy, an amorphous state should have more molecular mobility and other thermodynamic properties than the crystalline molecular structures [15].



**Fig. 62.5** ESR spectrum of MMCS nanocomplex of  $\text{Fe}_3\text{O}_4$  NP and DOXO. Frequency of ER: 0.96 MHz (1), 1.41 MHz (2), 1.84 MHz (3), 2.92 MHz (4), 5.09 MHz (5), 7.41 MHz (6), 42.27 MHz (7), MCS (8), without influence (9).  $T = 77$  K

**Table 62.4** ESR spectrum of MMCS nanocomplex of  $\text{Fe}_3\text{O}_4$  NP and DOXO.  $T = 77$  K

Sample number	Frequency $f$ , MHz	Energy $W$ , $10^{-9}$ eV	Relative intensity $I$ , a.u.	$g$ -factor
1	0.96	4	1.35	2.4
2	1.41	6	1.22	2.46
3	1.84	8	1.27	2.4
4	2.92	12	1.14	2.39
5	5.09	21	1.16	2.43
6	7.41	31	1.41	2.42
7	42.27	175	1.00	2.37
Pearson correlation coefficient $r$			-0.67	-0.58
8	MCS		4.65	2.39
9	Without influence		1.06	2.56

It can be formalized by the change in free Gibbs energy  $\Delta G$ :

$$\Delta GT^{a,c} = -RT \ln (\sigma T^a / \sigma T^c), \quad (62.1)$$

where  $\sigma T^a / \sigma T^c$  is a ratio of solubility for amorphous and crystalline forms,  $R$  is gas constant, and  $T$  is the temperature.

According to the Gibbs-Helmholtz equation,

$$\Delta G = \Delta H - T\Delta S, \quad (62.2)$$

where  $\Delta H$  and  $\Delta S$  is enthalpy and entropy change. In case of small entropy  $\Delta S$  (crystal structure is not disordered) the member  $T\Delta S$  is small, and the Gibbs free energy  $\Delta G$  is determined mainly by enthalpy change  $\Delta H$ . For disordered solids, entropy increases, and  $T\Delta S$  member cannot be neglected. The change of free Gibbs energy as a result of mechanical treatment increases the deviation from equilibrium and therefore increases the chemical reaction rate [16]. Mechanochemical activation initiate the amorphization in DOXO with a disordered or defected molecular structure and increase number of paramagnetic centers [2] that can enhance drug adsorption on the surface of  $\text{Fe}_3\text{O}_4$  NP.

The inductor in magneto-mechanical milling chamber radiates electromagnetic waves with essential magnetic component [17]. It is well known that a radio wave can penetrate into depth in a magnetic field perpendicular to the surface of the metals which is conductors. In most cases, electromagnetic waves are very rapidly damped in metals (at distances of the order of the skin depth). DOXO, which is dielectric, has low attenuation coefficient, and therefore radio waves reflect from it and also easily can pass through it. It should be noted that maximal energy of ER ( $1.75 \cdot 10^{-7}$  eV) was significantly lower than  $kT$  (25.7 meV) – heat required to increase the thermodynamic entropy of a system. Therefore possible nonthermal mechanism is the absorption of electromagnetic energy at magnetic resonance. Nonthermal physical effects of eddy current on magnetic resonance in nanostructures are well known [18].

The presence of a constant magnetic field leads to the appearance of characteristic low-frequency EMF oscillations. In phenomena, which accompany the variable EMF, various kinds magnetic resonances should be observed in core and shell of the complex [19]. Iron has unpaired electrons with the same spin. Because they have no opposing fields to cancel their effects, these electrons have an orbital magnetic moment. At the same time chemically adsorbed on the NP surface atoms and molecules of DOXO with unpaired electrons during ER may attach the metal surface, lowering the number of uncompensated spins (paramagnetic centers) and therefore their a magnetic moment. In  $\text{Fe}_3\text{O}_4$  NP, it is initiated by oxide film [20]. The confirmation of the foregoing can be obtained by our results (Tables 62.1 and 62.3). These results clearly evident the decrease in saturation magnetic moment for the samples after synthesis as compared to control samples without influence both for iron oxide NP and complex in all the experiments on 42% in average. The comparison of Pearson correlation coefficients ( $r$ ) between

ER frequency and magnetic properties for magneto-mechanochemically activated  $\text{Fe}_3\text{O}_4$  NP and MMCS nanocomplex of  $\text{Fe}_3\text{O}_4$  NP and DOXO has shown the difference in correlation coefficient for coercivity and area of the hysteresis loop, but correlation coefficient for saturation magnetic moment was practically identical. It should be noted that area of hysteresis loop of MMCS nanocomplex had correlation coefficient  $r = 0.72$  with ER frequency.

Interestingly, relative ESR spectra intensities and  $g$ -factors of iron oxide NP have revealed sufficiently high negative correlation ( $r = -0.6$ ) with the ER frequencies (Table 62.2). Comparative ESR analysis between iron oxide NP and MNC indicate about  $\text{Fe}_3\text{O}_4$  properties in the spectrum in the presence on the surface of the oxide film only.

It should be noted as two related, as we think, facts concerning MNC of DOXO-loaded iron oxide NP (Tables 62.3 and 62.4): (1) positive correlation between the area of hysteresis loop and EMF frequency and (2) negative correlation between ESR relative intensity and EMF frequency. It depends on the difference in basic physical principles of vibrating magnetometry and ESR spectroscopy.

The area  $A$  contained within a hysteresis loop represents the energy that can be transferred into heat per cycle when MNC is exposed to the external alternating magnetic field and thus gives a measure of specific adsorption rate (SAR) that can be expressed as [21]:

$$\text{SAR} = Af, \quad (62.3)$$

$$A = \int_{-H_{\max}}^{+H_{\max}} \mu_0 M(H) dH, \quad (62.4)$$

where  $M(H)$  is the NP magnetization.

According to Eq. (62.3), frequency and strength of magnetic field affect at the SAR of MNC.

As stated above, an alternating electric field and associated magnetic field do not penetrate into the conductor but are concentrated mainly in a relatively thin surface layer (the so-called skin layer). The nature of the skin effect is explained as follows: free electrons in the conductor, under the impact of an external alternating field, and it creates currents which compensate the external field within the conductor's volume. Current density in skin layer increases in  $e$  times relative to current density in the whole volume of the sample. 86.4% of the total heat generation is released in skin layer. The skin depth is calculated by the formula:

$$\Delta = \sqrt{\frac{\rho}{\mu\mu_0\pi f}}, \quad (62.5)$$

where  $\mu_0 = 4\pi \cdot 10^{-7}$  H/m is the permeability of free space,  $\rho$  is resistivity of the conductor, and  $f$  is frequency of electromagnetic field.

According to the expression (62.5), the skin depth depends on the ER frequency: the higher the frequency, the thinner the skin layer. It also depends on the relative magnetic permeability  $\mu$  of material [22].

The size reduction in the magnetic NP yields higher surface/volume ratio which leads to different properties than the bulk materials.  $\text{Fe}_3\text{O}_4$  NP having the average size under 100 nm exhibited satisfying performance in electromagnetic waves attenuation and could be considered as potential candidate for electromagnetic waves absorption applications. It could be expected that the variation in the electromagnetic properties of magnetic NP with the average size of NP is mainly related to the ratio of surface and bulk atoms [23]. We believe that our results on influence of EMF frequency on MNC magnetic properties can be explained with the presence of nonthermal skin effect ( $T = 300$  K).

The skin effect of conduction electron resonance for metallic small particles has been studied thoroughly since the 1950s. [24]. The above-presented ESR data (Table 62.4) may be summarized as follows. Relative intensity in ESR spectrum of MNC of the iron oxide NP and DOXO decreased as the ER frequency increases. It is well known that the Zeeman effect is the effect of splitting a spectral line into several components in the presence of a static magnetic field [25]. This indicates that the Zeeman coupling between the field and surface spins dominates the magnetic interactions inside the particles and leads to a decrease of the paramagnetic centers (free radicals) in MNC. The effect can be interpreted in the framework of the radical pair mechanism in terms of a change in the extent of singlet–triplet interconversion in the radical pair when the oscillating field is in resonance with hyperfine splitting in the radical pairs. During ER of conventional iron oxide NP and NP loading with DOXO,  $g$ -factor is changed in different ways. The theory of paramagnetic resonance absorption by the conduction electrons in a metal is worked out, taking into account the diffusion of the electrons in and out of the thin skin into which the radiofrequency field penetrates. [26]. This indicates different ESR condition with respect to the magnetizing field. At the same time, a very important role is played by the resonance effects on the surface of ferrite NPs [27]. It is well known that an unpaired electron can move between the two energy levels by either absorbing or emitting a photon of energy  $h\nu$  such that the resonance condition  $h\nu = \Delta E$  is obeyed. The weak correlation with the frequency of the ER very logically follows from the  $g$ -factor calculated according to the fundamental equation of the ESR condition [28]:

$$h\nu = g\beta B, \quad (62.6)$$

where  $h$  is Planck constant,  $\nu$  is frequency,  $\beta$  is Bohr magneton, and  $B$  is magnetic induction.

The results of ESR spectra indicate that correlation coefficients of ER frequency with both ESR relative intensity and  $g$ -factor in the samples of magneto-mechanochemically activated  $\text{Fe}_3\text{O}_4$  NP were equal to MMCS nanocomplex of  $\text{Fe}_3\text{O}_4$  NP and DOXO. Last result can substantiate next. The recombination of the

radical pair is proportional to the probability  $\rho_S(t)$  of finding the pair in the single state. For initial triplet radical pair, it takes the form

$$\rho_S(t) = \Delta J / (2 \Omega) \sin^2 \Omega t, \quad (62.7)$$

where  $\Delta J$  is the difference of exchange energies between spin catalyst and each of the partners of the radical pair,  $\Omega$  is evolution frequency, and  $t$  is time.

The yield of reaction product generated, for instance, by recombination of the radical pair in triad, oscillates with frequency  $\Omega$  [29].

From the above, it can be noted that MMCS antitumor complex could have certain magnetic properties with the help of a fixed frequency (energy) of ER. ER can influence certain steps in the chain of free radical reactions. The fixed number of free radicals (paramagnetic centers) for the different types of malignant tumor can be generated in MMCS nanocomplex of DOXO and iron oxide NP. These effects are related to Zeeman splitting of the spin energy levels and can occur in a wide range of chemical systems and that they can be caused either by constant magnetic field or EMF. Whenever two radicals come together, either by chance or because of the form of generation, their spins can be opposite or parallel. Only in the case of opposite spins can they react to form a stable molecule that has the proper magnetic balance [30].

## 62.5 Conclusion and Future Perspectives

Based on the above interpretation, possible correlation between the frequency (energy) of ER and magnetic properties of DOXO-loaded iron oxide NP complex during MMCS can contribute to personalized treatment of cancer patients. We plan to use magnetic resonance phenomena in the development of computer-aided nanomedical equipment aimed at controlling redox reaction inside tumor cells during theranostics of cancer patients. Thus, it is potentially new method of advanced cancer treatment that could be adopted by the clinicians and minimize the side effects of conventional chemotherapy treatment [2].

It is possible that technology of MMCS can be implemented in the development of electronic components for nanoelectronics.

## References

1. Thomas R, Park I-K, Jeong YY (2013) Magnetic iron oxide nanoparticles for multimodal imaging and therapy of cancer. *Int J Mol Sci* 14:15910–15930
2. Orel V, Shevchenko A, Romanov A et al (2015) Magnetic properties and antitumor effect of nanocomplexes of iron oxide and doxorubicin. *Nanomed Nanotech Biol Med* 11:47–55
3. Barnes FS, Greenebaum B (2015) The effects of weak magnetic fields on radical pairs. *Bioelectromagnetics* 36(1):45–54
4. Valko M, Rhodes CJ, Moncol J et al (2006) Free radicals, metals and antioxidants in oxidative stress-induced cancer. *Chem Biol Interact* 160:1–40

5. Pal A, Singh A, Nag TC (2013) Iron oxide nanoparticles and magnetic field exposure promote functional recovery by attenuating free radical-induced damage in rats with spinal cord transection. *Int J Nanomedicine* 8(1):2259–2272
6. Orel V, Romanov A, Rykhalskyi O (2016) Antitumor effect of superparamagnetic iron oxide nanoparticles conjugated with doxorubicin during magnetic nanotherapy of Lewis lung carcinoma. *Mat-wiss u Werkstofftech* 47(2–3):165–171
7. Gutman EM (1998) *Mechanochemistry of materials*. Int Science Publishing, Cambridge
8. Kuramitz H (2009) Magnetic microbead-based electrochemical immunoassays. *Anal Bioanal Chem* 394(1):61–69
9. Abdi MS, Ebadzadeh T, Ghaffari A et al (2015) Synthesis of nano-sized spinel ( $MgAl_2O_4$ ) from short mechanochemically activated chloride precursors and its sintering behavior. *Adv Powder Technol* 26:175–179
10. Baláz P (2008) *Mechanochemistry in Nanoscience and Minerals Engineering*. Springer, Berlin
11. Kajdas C (2013) Ch. 11. General approach to mechanochemistry and its relation to tribochemistry. In: Pihitili H (ed) *Tribology in engineering*. Intech, Croatia, pp 209–240
12. Fink DG (1989) *Electronics engineers' handbook*, 3 Sub edn. McGraw-Hill Inc, New York
13. Dobbin ZC, Katre AA, Steg AD et al (2014) Using heterogeneity of the patient-derived xenograft model to identify the chemoresistant population in ovarian cancer. *Oncotarget* 5(18):8750–8764
14. Bertotti G (1998) *Hysteresis in magnetism*. Academic Press, San Diego
15. Hancock BC, Parks M (2000) What is the true solubility advantage for amorphous pharmaceuticals? *Pharm Res* 17:397–403
16. Greiner W, Neise L, Stöcker H (1997) *Thermodynamics and statistical mechanics*. Springer, New York
17. Nikolov NA, Orel VE, Smolanka II et al (2008) Apparatus for short-wave moderate induction therapy with increased asymmetry of electromagnetic field “Magnetotherm”. In: Katushev A, Yu D, Spigulis J (eds) *NBC 2008 Proceedings*. Springer, Berlin, Heidelberg, pp 294–298
18. Flovik V, Pettersen BH, Wahlstro E (2016) Eddy-current effects on ferromagnetic resonance: spin wave excitations and microwave screening effects. *J Appl Phys* 119:163903. <http://dx.doi.org/10.1063/1.4948302>
19. Kaner EA, Skobov VG (1964) Theory of resonance excitation of weakly decaying electromagnetic waves in metals. *J Exp Theor Phys* 18(2):419–432
20. Roduner E (2006) *Nanoscope materials size-dependent phenomena*. RSC Publishing, Cambridge
21. Carrey J, Mehdaoui B, Respaud M (2011) Simple models for dynamic hysteresis loop calculations: Application to hyperthermia optimization. *Appl Phys* 109:083921. <http://dx.doi.org/10.1063/1.3551582>
22. Hayt WH, Buck JA (2006) *Engineering electromagnetics*, 7th edn. McGraw Hill, New York
23. Durmus Z, Durmus A, Bektay MY (2016) Quantifying structural and electromagnetic interference (EMI) shielding properties of thermoplastic polyurethane–carbon nanofiber/magnetite nanocomposites. *J Mater Sci* 51(17):8005–8017
24. Feher G, Kip AF (1955) Electron spin resonance absorption in metals. I. Experimental. *Phys Rev* 98:337–348
25. Foot CJ (2005) *Atomic physics*. Oxford University Press, Oxford, United Kingdom
26. Dyson FJ (1955) Electron spin resonance absorption in metals. II. Theory of electron diffusion and the skin effect. *Phys Rev* 98:349–359
27. Gazeau F, Bacri JC, Gendron F et al (1998) Magnetic resonance of ferrite nanoparticles: evidence of surface effects. *J Magn Magn Mater* 186:175–187
28. Schweiger A, Jeschke G (2001) *Principles of pulse electron paramagnetic resonance*. Oxford University Press, Oxford
29. Buchachenko AL, Berdinsky VL (2002) Electron spin catalysis. *Chem Rev* 102(3):603–612
30. Buchachenko AL (2013) Mass-independent isotope effects. *J Phys Chem B* 117(8):2231–2238



# Chapter 63

## Continuum Modeling of Nanoelements

T. S. Nahirnyj and K. A. Tchervinka

### 63.1 Introduction

Recently nanotechnology development has been focused on investigating and using materials and systems with improved properties. At the nanoscale, the material properties are different from the properties of bulk matter. Conventional models of solid mechanics are to be substantially updated to allow describing the phenomena found at the nanoscale. The size effects of various mechanical properties occur in nanoelements, nanomaterials, and nanocomposites, and a few mathematical theories now offer an explanation.

High strength and high porosity are observed in metal foams containing ultrahigh-strength nanowires [1], size-dependent elastic properties are described in many papers [2], and the surface effects play a prominent role in the mechanical behavior of nanoelements and nanomaterials [3–5].

The nonlocal models of mechanics [6] based on a generalization of the classical Hooke's law were used to explain a number of size effects and to describe the interfacial layers' properties different from the ones of bulk matter long ago. The gradient theories [7, 8] were applied to study and model a number of effects and materials, including size effects with different scales. The gradient elasticity

---

T.S. Nahirnyj

Centre of Mathematical Modeling, Pidstryhach Institute of Applied Problems of Mechanics and Mathematics of Ukrainian NAS, Dudaeva Street 15, Lviv,-70005, Ukraine

Faculty of Mechanical Engineering, University of Zielona Góra, 65-516, Zielona Góra, Poland  
e-mail: [t.nahirnyj@gmail.com](mailto:t.nahirnyj@gmail.com)

K.A. Tchervinka (✉)

Department of Mathematical Modeling, Ivan Franko National University of Lviv, Universytetska Street 1, Lviv,-79000, Ukraine  
e-mail: [k.tchervinka@gmail.com](mailto:k.tchervinka@gmail.com)

© Springer International Publishing AG 2017

O. Fesenko, L. Yatsenko (eds.), *Nanophysics, Nanomaterials, Interface Studies, and Applications*, Springer Proceedings in Physics 195,  
DOI 10.1007/978-3-319-56422-7\_63

827

relations with thermodynamic restrictions need a set of nonstandard boundary conditions [9], and the body surfaces play an important role in understanding and explaining size effects. Some other approaches, models, and methods are used such as a semicontinuum model for ultrathin films [10], explaining size-dependent elastic moduli, strength, and other properties of nanomaterials.

Another approach to describe size effects in bodies of structurally nonhomogeneous matter such as nanomaterial is the local gradient approach in thermomechanics [11, 12]. It is based on the general principles of irreversible thermodynamics and nonlinear mechanics. The kinetic relation for mass flow is modified to account for structural changes, and the density (or the chemical potential) is introduced into the space of state parameters. The state parameters' space expansion yields mass balance equation modification with instant mass flow that is associated with transition from reference to real body. The number of models is constructed for this approach, including the models of elastic, thermoelastic, electroconductive solids, and solid solution. The models described interface phenomena, structural inhomogeneity, and size effects in solids [13–15]. The choice of boundary conditions for density is significant in problems of the local gradient approach [16].

In this paper, we consider the main key points of local gradient approach allowing it to describe in continual 3D model the locally nonhomogeneous bodies and a number of related effects including the one of specimen size. The properties of a bulk nanomaterial are determined by the structure and properties of forming its nanoelements. In the last section, we review main results of investigating the size effects in nanoelements modeled as objects of simple geometry under influence of temperature, admixture, charge, or power load.

## 63.2 Balance, Kinetic, and State Equations

We consider energy balance equation in the local form

$$\frac{\partial E}{\partial \tau} = \nabla \cdot (\boldsymbol{\sigma} \cdot \mathbf{v} - T\mathbf{j}_s - H\mathbf{j}_m) + \sigma_E. \quad (63.1)$$

Here  $E$  denotes the density of body energy;  $\boldsymbol{\sigma}$  is Cauchy stress tensor;  $T$  is temperature;  $H$  is chemical potential;  $\mathbf{j}_s$  and  $\mathbf{j}_m$  are fluxes of entropy and mass, respectively;  $\mathbf{v}$  is velocity vector;  $\tau$  is the time; and  $\sigma_E$  is energy production considering the body as an open thermodynamic system. We consider also the momentum  $\mathbf{k}_v$ , entropy  $S$ , and mass balance equations in the local form

$$\frac{\partial \mathbf{k}_v}{\partial \tau} = \nabla \cdot \boldsymbol{\sigma}, \quad \frac{\partial S}{\partial \tau} = -\nabla \cdot \mathbf{j}_s + \sigma_s, \quad \frac{\partial \rho}{\partial \tau} = -\nabla \cdot \mathbf{j}_m + \sigma_m, \quad (63.2)$$

where  $\sigma_s$  is entropy production,  $\rho$  is mass density, and  $\sigma_m$  is source of mass associated to body structure formation. We shall also assume that  $\sigma_m = \sigma_E/H$ . The role of mass sources is discussed in [14, 17].

The total energy  $E$  is the sum of internal energy  $U$  and kinetic energy  $K$ . The increase of the latter is expressed through velocity and linear momentum vectors as  $dK = \mathbf{v} \cdot d\mathbf{k}_v$ . So for  $U$  we obtain such equation

$$\frac{\partial U}{\partial \tau} = \boldsymbol{\sigma} : \frac{\partial \mathbf{e}}{\partial \tau} + T \frac{\partial S}{\partial \tau} + H \frac{\partial \rho}{\partial \tau} - T\sigma_s - \mathbf{j}_s \cdot \nabla T - \mathbf{j}_m \cdot \nabla H. \quad (63.3)$$

Here  $\mathbf{e}$  is the strain tensor, and a colon denotes contraction over two indices.

This equation is the base for equations of state and kinetic equations formulating. The gradients  $\nabla T$ ,  $\nabla H$  are usually associated with thermodynamic forces that are causes for the flows  $\mathbf{j}_s$ ,  $\mathbf{j}_m$  arising. In the classical representation we got

$$\mathbf{j}_s = -k \frac{\nabla T}{T} \equiv k_t \nabla T$$

from the law of heat conduction  $\mathbf{q} = -k \nabla T$ , also known as Fourier's law. The Fick's first law governing the transport of mass through diffusive means writes  $\mathbf{j}_m = -D \nabla C$  and leads to

$$\mathbf{j}_m = -k_m \nabla H.$$

The cross effects such as Soret, Dufour, etc. may be described as a flow dependence on a gradient of another nature. In the general case, we suppose that in the body where two forms of motion exist, the kinetic relations may be written as

$$\mathbf{j}_s = \mathbf{j}_s(\nabla T, \nabla H), \quad \mathbf{j}_m = \mathbf{j}_m(\nabla T, \nabla H), \quad (63.4)$$

where  $\mathbf{j}_s$ ,  $\mathbf{j}_m$  are functions. If there are functionals over time, then the model accounts for history of forces and depends on influence functions (kernels) of the functionals [12, 14]. If an influence function is decreasing down to zero as  $|\tau - \zeta|$  is growing, then we obtain the model suitable for describing the fading memory phenomena. If the influence function is delta-function of  $|\tau - \zeta|$ , then one says about nonfading memory. We suppose that mass flow must "remember" the events such as the surface or body structure formation and must contain at least one term proportional to the delta-function. Limiting ourselves to classical description of heat transfer and to the absence of cross effects for isotropic material, we accept the kinetic relations (63.4) in the linear form with nonfading memory term in mass flow

$$\mathbf{j}_s = -\lambda_s \frac{\nabla T}{T}, \quad \mathbf{j}_m = -g_{mm} \frac{\partial(\nabla H)}{\partial \tau}. \quad (63.5)$$

If the last relation is used in mass balance equation from (63.2), then

$$\frac{\partial}{\partial \tau} (\rho - g_{mm} \nabla^2 H) = \sigma_m, \quad (63.6)$$

and Eq. (63.3) with account to (63.5) takes the form

$$\frac{\partial}{\partial \tau} \left( U - \frac{g_{mm}}{2} \nabla H \cdot \nabla H \right) = \sigma: \frac{\partial \mathbf{e}}{\partial \tau} + T \frac{\partial S}{\partial \tau} + H \frac{\partial \rho}{\partial \tau} - T \sigma_s + \frac{\lambda_s}{T} \nabla T \cdot \nabla T \quad (63.7)$$

The Eq. (63.6) is mass balance equation modified to describe structurally nonhomogeneous materials. It contains the mass sources associated with a method of forming the body surface. It is supposed that the structure of the body material has arisen suddenly at the initial moment of time and doesn't change afterward.

Using classical expression for entropy production

$$\sigma_s = \lambda_s \frac{\nabla T}{T} \cdot \frac{\nabla T}{T} \quad (63.8)$$

we obtain that for the energy

$$F = U - \frac{g_{mm}}{2} \nabla H \cdot \nabla H - TS \quad (63.9)$$

the following Gibbs equation holds

$$dF = \sigma: d\mathbf{e} - SdT + Hd\rho. \quad (63.10)$$

The energy  $F$  differs from Helmholtz free energy  $A = U - TS$  in that it contains the term with  $\nabla H$ , gradient of chemical potential. The change in chemical potential is identified with the amend in binding energy since the parameter  $H$  in fact means the energy required to modify density by one unit. The presence of the gradient provides that it may be used efficiently for nonhomogeneous media, including the ones with a structure.

Note that here strain  $\mathbf{e}$ , temperature  $T$ , and density  $\rho$  are considered as independent parameters. While strain and temperature change occur with known deformation and heat conduction processes, the density change has another nature. It may be related to change of the structure of the body as discussed in [14].

### 63.3 Linearized Model and Key Systems of Equations

From (63.10) follows

$$\sigma = \frac{\partial F}{\partial \mathbf{e}}, \quad S = -\frac{\partial F}{\partial T}, \quad H = \frac{\partial F}{\partial \rho}.$$

If  $F(\mathbf{e}, T - T^*, \rho - \rho^*)$  is a quadratic function in the space of base state deflections  $\mathbf{e}, \theta \equiv T - T^*, \rho - \rho^*$ , then we can write linear equations of the state

$$\begin{aligned}\boldsymbol{\sigma} &= 2\mu\mathbf{e} + [\lambda e - (3\lambda + 2\mu)a_m(\rho - \rho^*) - (3\lambda + 2\mu)a_t\theta]\mathbf{I}, \\ S &= S^* + (3\lambda + 2\mu)a_t e - \alpha_{mt}(\rho - \rho^*) + \frac{c_v}{T^*}\theta, \\ H &= H^* - (3\lambda + 2\mu)a_m e + \alpha_{mm}(\rho - \rho^*) + \alpha_{mt}\theta.\end{aligned}\quad (63.11)$$

Here  $\mathbf{I}$  is the identity tensor.

This presentation implies smallness of deflections  $\mathbf{e}, \theta, \rho - \rho^*$ . In some cases, the nanomaterials are the ones we cannot accept that  $(\rho - \rho^*)/\rho^* \ll 1$ . If so then we may consider coefficient in (63.11) depending on  $\rho - \rho^*$ , and these equations of the state become nonlinear.

The complete equation system consists of equations

$$\nabla \cdot \boldsymbol{\sigma} = \frac{\partial \mathbf{k}_v}{\partial \tau}, \quad \lambda_s \nabla^2 T = T \frac{\partial S}{\partial \tau}, \quad \rho - \rho^* - g_{mm} \nabla^2 H = d_{\sigma m} \quad (63.12)$$

where  $d_{\sigma m} = \int_{-\infty}^t \sigma_m d\tau$ , along with state equations (63.11) and relations

$$\mathbf{e} = (\nabla \otimes \mathbf{u} + (\nabla \otimes \mathbf{u})^T)/2, \quad \mathbf{k}_v = \rho \mathbf{v} \equiv \rho \frac{\partial \mathbf{u}}{\partial \tau}$$

if needed.

For the steady state describing and the linear approximation, we obtain key systems of equations that can be written for displacements

$$\begin{aligned}\mu \nabla^2 \mathbf{u} + (\lambda + \mu) \nabla (\nabla \cdot \mathbf{u}) - (3\lambda + 2\mu) [a_m \nabla (\rho - \rho^*) + a_t \nabla \theta] &= 0, \\ \nabla^2 \theta = 0, \quad \nabla^2 (\rho - \rho^*) - \xi^2 (\rho - \rho^*) + \xi^2 d_{\sigma m} &= 0,\end{aligned}\quad (63.13)$$

or for stresses

$$\begin{aligned}\nabla \times \left\{ \nabla \times \left[ \frac{\boldsymbol{\sigma}}{2\mu} - \left( \frac{\lambda \sigma}{2\mu(3\lambda + 2\mu)} - a_m(\rho - \rho^*) - a_t \theta \right) \mathbf{I} \right] \right\}^T &= 0, \\ \nabla \cdot \boldsymbol{\sigma} = 0, \quad \nabla^2 \theta = 0, \quad \nabla^2 (\rho - \rho^*) - \xi^2 (\rho - \rho^*) + \xi^2 d_{\sigma m} &= 0,\end{aligned}\quad (63.14)$$

where  $\xi$  is the constant,  $\sigma = \boldsymbol{\sigma} : \mathbf{I}$ . Here the first equation of the system (63.13) was used to exclude strain (or displacements) from the equation for density.

Boundary and integral conditions for density we write as

$$\rho|_{\partial V} = \rho_a \quad (0 < \rho_a < \rho^*), \quad \int_{(V)} (\rho - \rho^*) d\mathbf{r} = \int_{(V)} d\sigma_m d\mathbf{r}, \quad (63.15)$$

if problem is formulated for the body occupying domain  $(V)$  with border  $\partial V$ .

The nonlinear problem formulation in Cartesian coordinates with local elastic moduli depending on the density

$$E = E_0 \left( \frac{\rho}{\rho^*} \right)^{\beta_E}, \quad \nu = \nu_0 \left( \frac{\rho}{\rho^*} \right)^{\beta_N}, \quad (63.16)$$

was considered in [14] to study the size effect of the effective Young's modulus and strength of the layer. The distributions of density and stresses feature two characteristic sizes: the first size can be associated with the structural non-homogeneity of the material and the second one—with geometrical irregularities of the real solid surface. The nature of the structural non-homogeneity of the bulk material and of the near-surface regions modeled by the mass sources is different. Thus, in the case of near-surface non-homogeneity, we interpret it as variable porosity. To model the distribution of mass sources, we use the solution for density in the problem without mass sources  $\sigma_m$ . The imperfect shape of the real body surface is also taken into account in the construction of mathematical models of contact interaction of solid bodies [18].

### 63.4 The Size Effects in One-Dimensional Problems

The system (63.12) in the form (63.14) along with conditions (63.15) and classical boundary conditions for temperature and stresses was used to study the stress-strain state of the bodies of simple geometry such as half-space [17], layer [12, 14], cylinder [12], solid sphere [15], etc. The more general systems were used to study state of electroconductive solids [13, 20] (the first one without mass sources) and structurally nonhomogeneous two-component solid solutions [19]. In the case of electroconductive solids, the model reveals the third characteristic size related to forces of Coulomb interaction. In the case of solid solution, the presence of admixture changes the characteristic size of near-surface non-homogeneity.

The study of the model relations and numerical simulation of the one-dimensional problems shows that in the layer  $|x| \leq l$  (thin film) with identical free surfaces the stress distribution is symmetric and depends on layer size (Fig. 63.1 solid line represents the thinnest layer with  $\xi l = 2$ ), and the surface stresses demonstrate size effects. Its value increases with the layer thickness increasing to the value of the surface stress in a half-space.

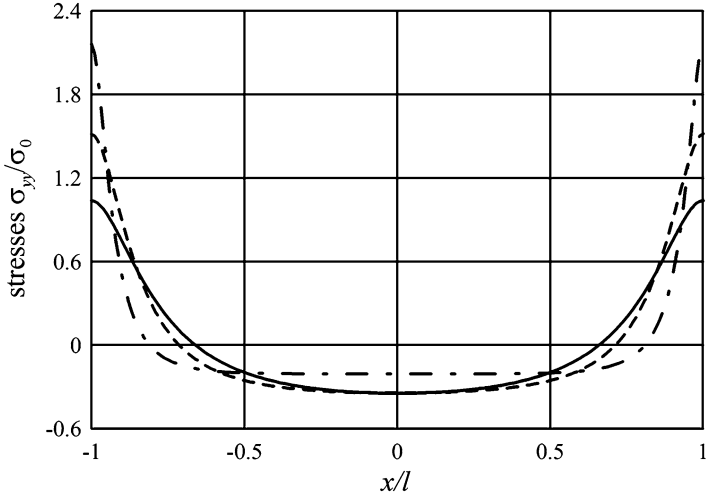


**Fig. 63.1** Stress distribution in the layer for  $\xi l = 2, 4, 20, \zeta l = 10$

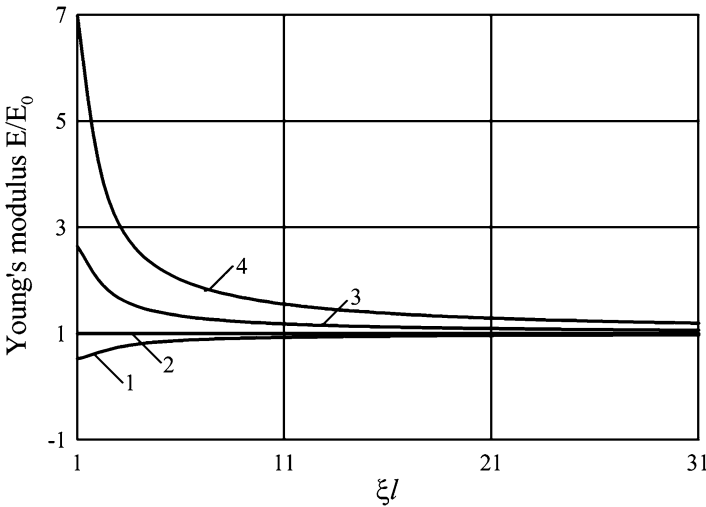


**Fig. 63.2** Size effect of effective Young's modulus

Considering stretched at infinity layer, we study effective elastic moduli and strength of the layer. The size effect of effective Young's modulus is shown in Fig. 63.2 with curves 1–4 corresponding  $\beta_E = 1, 0, -1.5, -3$  in (63.16). Postulating the local modulus  $E$  increase with the density reduction leads to experimentally observed effective Young's modulus decrease with the thin film thickness increase [4].

**Fig. 63.3** Size effect of layer strength

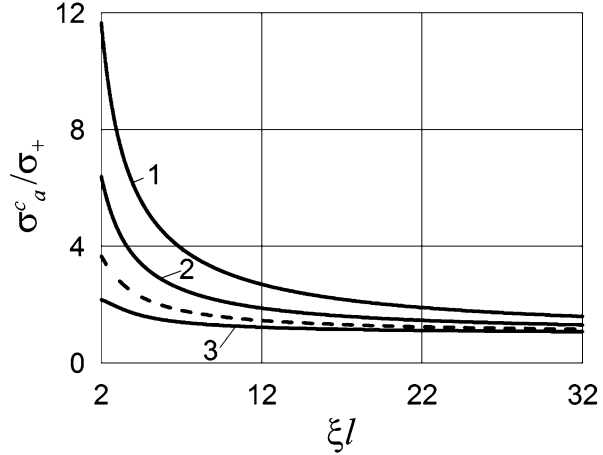
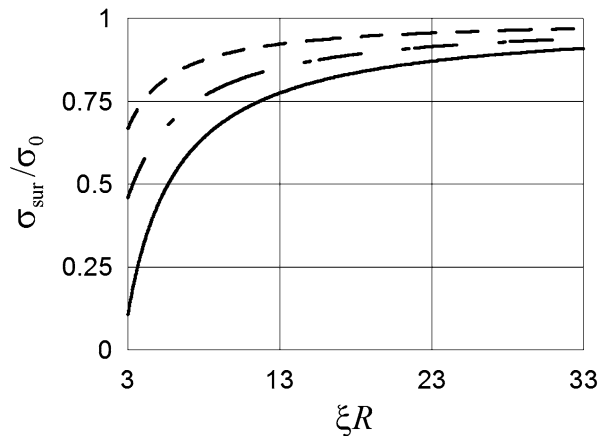


**Fig. 63.4** Comparison of surface stresses in the sphere (solid line), cylinder (dash-dotted), and layer (dashed)



Since the surface stresses demonstrate size effects and they are the greatest at the surface (see Fig. 63.1), using maximum principal stress theory reveals size effect of the strength. If  $\sigma_+$  is strength limit of thick layers, then the strength of thin films is depicted in Fig. 63.3. The curves 1–3 are for parameters  $\beta_E = -2, \beta_N = -0.5, \beta_E = -1, \beta_N = -0.25$ , and  $\beta_E = 1, \beta_N = 0.25$ , respectively; the dashed line corresponds to linear model.

The effect of body geometry (and surface curvature) for considered effects is shown in Fig. 63.4, where we can see that for the same material parameters and comparable sizes (sphere diameter = cylinder diameter = layer thickness), the surface stresses in the sphere are smallest. The similar regularity is observed for surface tension and strength [12].

The results of application of the local gradient approach to an electroconductive solid are demonstrated in Fig. 63.5 where the charge distribution in a free electroneutral layer is shown. The double electric layer is formed near the surfaces, and it affects the distribution of stresses and strain.



**Fig. 63.5** Charge distribution in a layer

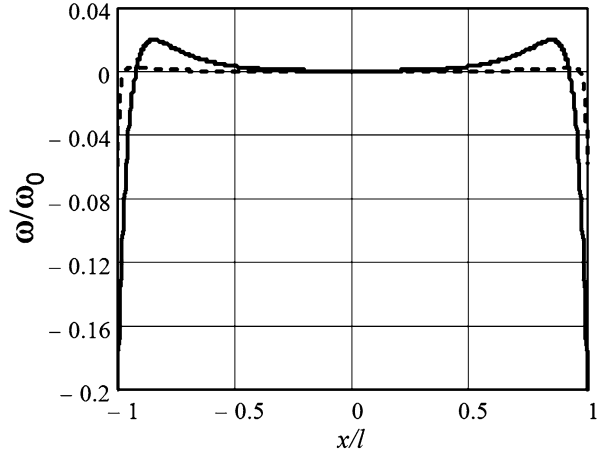
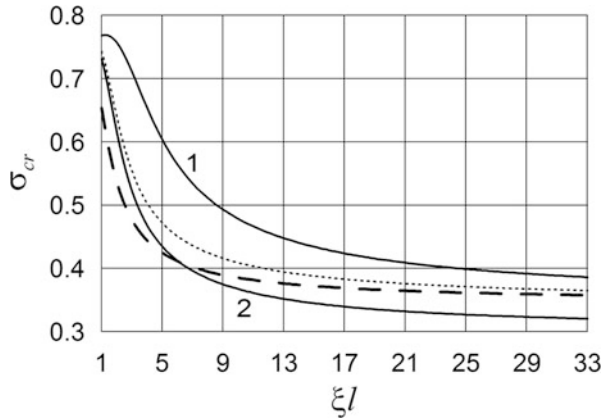


**Fig. 63.6** Size effect of strength of layer with admixtures



In the case of structurally nonhomogeneous two-component solid solution, the model approach is used to study the near-surface non-homogeneity densities of skeleton and admixture, stresses, and size effects of surface tension and strength [19]. The size effect of strength of layer with admixtures is demonstrated in Fig. 63.6 (dashed line corresponds to absence of mass sources and dotted one to absence of admixtures).

### 63.5 Conclusions

The local gradient approach allows model construction for elastic, thermoelastic, electroconductive solid, and solid solution. The model relations account for structure of locally nonhomogeneous bodies and describe various size effects that are observed in nanoelements.

## References

1. Biener J et al (2006) Size effects on the mechanical behavior of nanoporous Au. *Nano Lett* 6(10):2379–2382
2. Miller RE, Shenoy VB (2000) Size-dependent elastic properties of nanosized structural elements. *Nanotechnology* 11(3):139
3. Jing GY et al (2006) Surface effects on elastic properties of silver nanowires: contact atomic-force microscopy. *Phys Rev B* 73(23):235409
4. Guo J-G, Zhao Y-P (2005) The size-dependent elastic properties of nanofilms with surface effects. *J Appl Phys* 98(7):074306
5. Cuenot S et al (2004) Surface tension effect on the mechanical properties of nanomaterials measured by atomic force microscopy. *Phys Rev B* 69(16):165410
6. Eringen AC (2002) *Nonlocal continuum field theories*. Springer-Verlag, NewYork/Berlin Heidelberg. ISBN 0-387-95275-6
7. Askes H, Aifantis EC (2011) Gradient elasticity in statics and dynamics: an overview of formulations, length scale identification procedures, finite element implementations and new results. *Int J Solids Struct* 48(13):1962–1990
8. Aifantis EC (1999) Gradient deformation models at nano, micro, and macro scales. *J Eng Mater Technol* 121(2):189–202
9. Polizzotto C (2003) Gradient elasticity and nonstandard boundary conditions. *Int J Solids Struct* 40(26):7399–7423
10. Sun CT, Zhang H (2003) Size-dependent elastic moduli of platelike nanomaterials. *J Appl Phys* 93(2):1212–1218
11. Burak Y, Nahirnyj T, Tchervinka K (2014) Local gradient thermomechanics. In: Hetnarski RB (ed) *Encyclopedia of thermal stresses*. Springer Publishers, Netherlands, pp 2794–2801. ISBN 978-94-007-2738-0
12. Nahirnyj T, Tchervinka K (2014) Basics of mechanics of local-non-homogeneous elastic bodies. *Bases of nanomechanics II*. Rastr-7, Lviv. ISBN 978-617-7045-60-0
13. Nahirnyj T, Tchervinka K (2008) Interface phenomena and interaction energy at the surface of Electroconductive solids. *Computational Methods in Science and Technology* 14(2):105–110
14. Nahirnyj T, Tchervinka K (2015) Mathematical modeling of structural and near-surface non-homogeneities in Thermoelastic thin films. *Int J Eng Sci* 91:49–62
15. Nahirnyj T, Tchervinka K (2013) Structural inhomogeneity and size effects in thermoelastic solids. *Journal of Coupled Systems and Multiscale Dynamics* 1(2):216–223
16. Nahirnyj T, Tchervinka K, Boiko Z (2012) On the choice of boundary conditions in problems of the local gradient approach in thermomechanics. *J Math Sci* 186(1):130–138
17. Nahirnyi TS, Chervinka KA (2017) Mass sources and modeling of subsurface heterogeneities in deformable solids. *J Math Sci* 220(1):103–115
18. Shvets RM, Martynyak RM, Kryshtafovykh AA (1996) Discontinuous contact of an anisotropic half plane and a rigid base with disturbed surface. *Int J Eng Sci* 34(2):183–200
19. Bozhenko B, Nahirnyj T, Tchervinka K (2016) To modeling admixtures influence on the size effects in a thin film. *Math Model Comput* 3(1):12–22. [http://jmmc.lp.edu.ua/files/wcms\[48\]2016\\_3\\_1\\_012\\_022.pdf](http://jmmc.lp.edu.ua/files/wcms[48]2016_3_1_012_022.pdf)
20. Nahirnyj TS, Senyk YA, Tchervinka KA (2014) Modeling local non-homogeneity in electroconductive non-ferromagnetic thermoelastic solid. *Math Model Comput* 1(2):214–223

# Chapter 64

## The Electrochromic Feedback Methods for Obtaining Nanoparticles, Nanoalloys and Core-Shell Objects in Quasi-reversible Redox Systems

Yu. P. Vyshnevska and I. V. Brazhnyk

### 64.1 Introduction

Conducting polymers receiving a growing attention during past decades owe to their unique mechanical, electrical and physicochemical properties. Extensive studies of the mechanism of conductivity in such materials and specific phenomena exhibited in bulk and nanostructured forms pave the way to their application in batteries, supercapacitors, sensors, organic semiconducting and memory devices.

Even more promising are the hybrid nanostructured materials that combine metallic nanoparticles embedded into conducting polymeric matrices. High specific area of the metal-polymer interface and potentially controllable size, shape and alignment of the metallic NPs allow one to achieve an exceptional control over the functional properties of obtained hybrid material.

Conducting polymers based on aniline and aniline derivatives have been extensively studied over the past decades owing to their relative high conductivity, facile synthesis, environmental stability and unique electronic properties [1–3]. Among the most valuable features of such polymers which may be highlighted are their electrochromic properties and redox reactivity. The electrochromism phenomenon is observed in the case that material can reversibly change its light absorption spectra in response to electrochemical reaction. In particular, polymers based on aniline derivatives may exist in the different forms depending on the protonation

---

Y.P. Vyshnevska (✉)

National Technical University of Ukraine “Igor Sikorsky Kyiv Polytechnic Institute”, 37K20, Peremohy Ave., Kyiv 03056, Ukraine

Institute for Renewable Energy, 20A, H. Khotkevych str, Kyiv 02094, Ukraine

e-mail: [vishnevsk@ukr.net](mailto:vishnevsk@ukr.net)

I.V. Brazhnyk

Gimasi SA Ukraine R&D Centre, 18, Via Luigi Lavizzari, Mendrisio, 6850, Switzerland

© Springer International Publishing AG 2017

O. Fesenko, L. Yatsenko (eds.), *Nanophysics, Nanomaterials, Interface Studies, and Applications*, Springer Proceedings in Physics 195,

DOI 10.1007/978-3-319-56422-7\_64

837

state, pH and other conditions, while the transitions between oxidation states are accompanied by the electrochromism phenomena.

In the case of formation of metallic nanoparticles via reduction of metal ions due to interaction with conducting polymeric matrices, their oxidation state will change leading to a subsequent change in optical spectra. This switch may be registered using optical detector and trigger the automated control system that will apply the polarization impulse to reduce the polymer to initial state. Thus, polymeric materials that exhibit electrochromic properties and characterized by high redox reactivity may be used for optical-coupled NP synthesis.

## 64.2 Materials and Experimental Methods

The study of the morphology, structure and mechanism of formation of coatings was carried out using SEM, TEM, AFM as well as Raman and IR spectroscopy methods. Polarization measurements were carried out using a potentiostat PI-50.1 in potentiostatic and potentiodynamic (a scan rate of 1 mV/s) regimes in a three-electrode cell with separated cathodic and anodic compartments. Carbon steel 08kp was used as the working electrode, platinum as the counter-electrode and an Ag|AgCl|KCl(sat.) electrode as the reference one. The study of the structure and identification of the elemental composition of the obtained polymer coating were performed using the methods of infrared spectroscopy (Avatar 370 FT-IR, Thermo Scientific Nicolet) and Raman spectroscopy (Nanofinder, Lotis TII, Belarus). The morphological characteristics and elemental composition of the films were carried out with the scanning electron microscope (EVO-50, Zeiss, Germany) equipped with the energy-dispersive detector (INCA PENTA FET  $\times$  3, Oxford Instruments, Co., UK). Shape and size of the Ag nanoparticles were investigated by using high-resolution transmission electron microscopy (PEM-U, Selmi, Ukraine).

## 64.3 Result and Discussion

Numerous approaches for obtaining hybrid polymeric materials have been implemented, and the resulting hybrid functional coatings have been characterized. Within the two-step method, the polymeric substrate film and silver NPs have been prepared separately. Pure poly(diphenylamine) (PDPA) substrate has been obtained via in situ oxidative polymerization of diphenylamine (DPA) in sulfuric acid solutions using  $\text{Fe}^{3+}$  cations as catalyst [4]. After that the AgNP suspension has been added to a growing PDPA film. The polymerization process continued until the catalyst has been completely depleted. Poly(diphenylamine) substrate film has a domain-structured morphology with a clearly visible pattern (Fig. 64.1a).

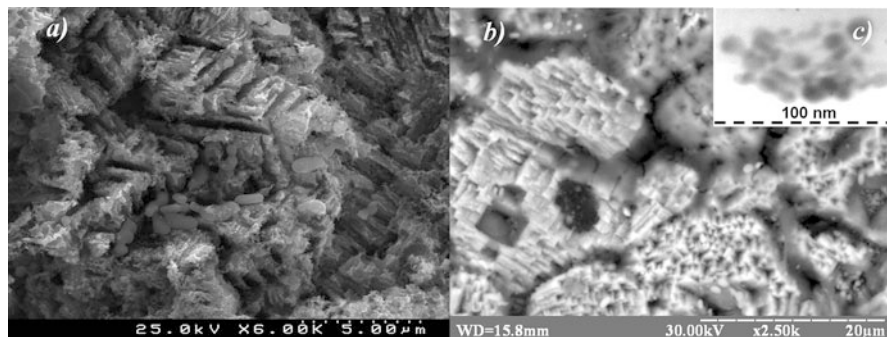


**Fig. 64.1** Morphology of the PDPA substrate film (a) and PDPA-Ag composite (b) after adding preliminary prepared silver nanoparticles (c)

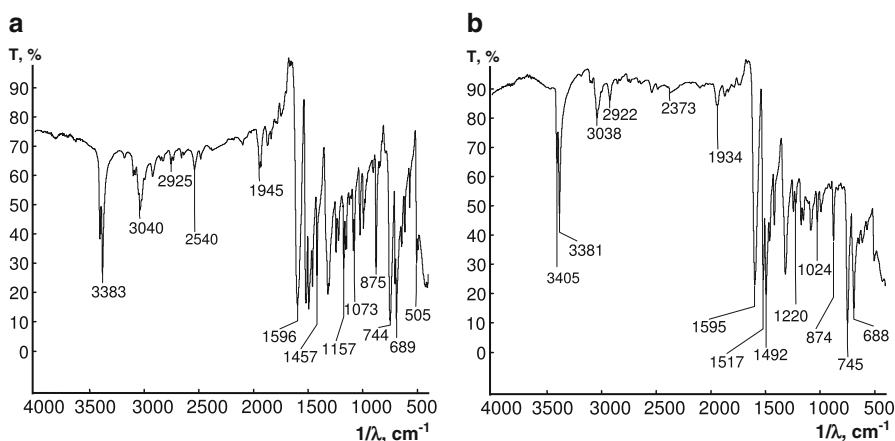
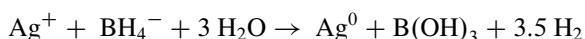


**Fig. 64.2** FTIR spectra of DPA (a) and obtained PDPA film (b)

The FTIR spectra of the pure PDPA substrate indicate that a significant amount of DPA monomer is still present in polymeric film which is required for further step of embedding the NPs to form a nanocomposite (Fig. 64.2).

Obtained polymeric film exhibits expected electrochromic behaviour under the conditions of external polarization as well as in a result of the pH change.

Silver nanoparticles have been obtained using precursor method via reduction of Ag<sup>+</sup> ions as given in [5] according to the following reaction:



The Erlenmeyer flask containing 30 ml NaBH<sub>4</sub> 0.002 M solution was cooled on the ice bath for 20 min with constant stirring using a magnetic stirrer. While the magnetic stirrer is switched on, 2 ml of AgNO<sub>3</sub> 0.001 M was added with 1 drop

per second rate. After the operation, the magnetic stirrer was switched off. PEM image shows the globular-shaped nanoparticles with nonuniform size distribution (Fig. 64.1c) [6].

Prepared AgNP suspension has been added to a growing PDPA film that results in a dramatically decreased rate of DPA polymerization. Hence, one may expect that silver NPs will have nonuniform distribution within polymeric film and would be present largely in its surface layer. The morphology of PDPA-Ag composite (Fig. 64.1b) has more strongly marked irregular domain structure compared to pure PDPA (Fig. 64.1a). It should also be noted that the presence of silver NPs has a significant influence on the conductivity of the PDPA-Ag nanocomposite due to delocalization of electrons and interfacial electronic interaction.

The advantage of such methods is a potential ability to obtain almost any kind of hybrid materials regardless of the nature of nanoparticles and the polymer itself. On the other hand, two-step methods have significant limitations in terms of fine control over obtained material and overall complexity of the preparation procedure. Furthermore, the reagents from the first step like polymerization catalysts or reducing agents for NPs and their by-products are often considered as undesired impurity for the resulting material. All these drawbacks are greatly limiting the application of the split-synthesis approaches and accelerating the development of single-step methods.

The single-step approach for obtaining the PDPA-Ag nanocomposite may be implemented owing to the fact that silver nitrate may act as an agent for oxidative polymerization of DPA. At the same time, the  $\text{Ag}^+$  ions will be reduced to the metallic state that will lead to formation of silver nanoparticles. Thus, the processes of polymerization and formation of NPs are taking place simultaneously without any other reagents that may produce undesired by-products.

The single-step synthesis of PDPA-AgNP composite has been carried out in 0.5 M sulphuric acid solution with addition of 0.0006 mol/l silver nitrate and 0.006 mol/l DPA. The products have been deposited on the steel support plate. The polymerization process has not been interrupted until silver nitrate was completely depleted.

Among other advantages, this approach allows one to obtain materials where the NP formation and polymerization processes occurred simultaneously that prevents aggregation and other undesired effects usually taking place within split approaches. We may also expect that in situ redox reaction also facilitates the formation of the well-developed NP/conducting polymer interfaces.

Obtained composite contains spherical silver nanoparticles embedded into conducting PDPA matrices. Nanoparticles have typical size in the range 40–50 nm with normal diameter distribution, while some particles reach the size of 140 nm (Fig. 64.3b). Small amount of the larger flakes may also be observed (Table 64.1).

Similar to the most precursor methods, the main approaches for controlling NP size, shape and alignment are based on determining the optimal concentrations and concentration ratios, as well as finding best suitable medium and conditions for the reaction. Such methods may deliver excellent results for mono metallic systems while facing significant difficulties in more complex cases.

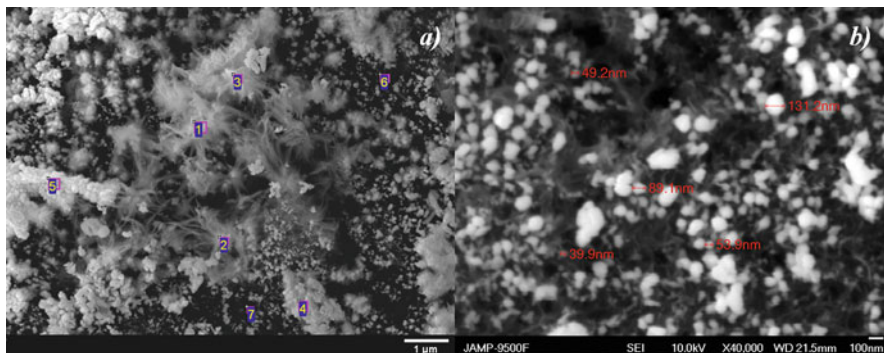


**Fig. 64.3** Morphology of the PDPA-Ag nanocomposite (a) and distribution of silver nanoparticles within surface layer (b)

**Table 64.1** Key to Fig. 64.3: elemental composition of the PDPA-Ag nanocomposite

Spectra	C	N	O	Si	S	Cl	Mn	Fe	Cu	Ag
1	2.65	0.00	59.99	0.41	0.00	0.12	0.00	22.08	0.76	13.99
2	1.84	0.00	60.98	0.32	0.00	0.15	0.00	16.20	1.39	19.11
3	2.89	1.32	58.15	0.00	0.13	0.00	0.53	14.96	0.41	21.60
4	2.86	0.00	38.35	0.00	0.00	0.54	0.17	10.80	1.76	45.51
5	1.84	6.79	30.62	0.00	0.00	0.76	1.35	7.22	1.00	50.42
6	2.84	1.70	46.65	0.13	0.85	0.00	1.38	36.27	4.71	5.47
7	2.56	1.82	51.38	0.49	0.42	0.00	0.21	35.12	5.37	2.63

. All values in atomic %

To further expand the capabilities for obtaining hybrid nanostructured materials with bimetallic NPs, nanoalloys and core-shell objects, the adaptive synthesis method with online electrochromic feedback has been developed [7].

It was found that formation of silver NPs on a preformed PDPA substrate via reduction of metal ions leads to the oxidation of the polymer and subsequent changes in optical spectra that can be registered with the optical sensor. Thus, the controlled back-coupled method for obtaining hybrid nanostructured materials may be implemented.

On the first phase, the polymeric ‘template’ film should be grown using the preferred method for a particular application. Most common polymerization methods include linear, cyclic or impulse electropolymerization, as well as radical oxidative polymerization using appropriate agent. At the same time, one of the most promising approaches for obtaining polymeric substrate is based on oxidative polymerization with insufficient amount of oxidizing agent that will lead to formation of the organized structures in a form of nanofibres and nanobrushes [8]. Combining this method with application of metal-containing oxidizer similar to a single-step approach will allow one to obtain nanostructured polymeric substrate with embedded NP seeds.

On the second phase, the metal-containing precursor should be added to the system. As a result of the redox reaction, the metal ions will be reduced to the metallic clusters and NPs, while polymeric film will be gradually transferred to an oxidized state that will indicate the end of cycle. The PDPA conductivity facilitates the charge transfer toward a growing NP seeds that also allows the distant molecules to indirectly take part in a surface redox reaction. Automated optically coupled control system may register change in optical spectra and apply external polarization to reduce film to the initial oxidation state to restart the redox cycle.

Cyclic voltammetry in the range of  $-0.2$  to  $+0.8$  V shows expected electrochromic behaviour of the polymeric film. We may also conclude that portion of the current is consumed by the process of electropolymerization of DPA that is present in the film. The remaining DPA monomers may also directly or indirectly interact with the metal ions that will facilitate the formation of nanoparticles and new portions of polymeric material.

Thus, in addition to concentrations and concentration ratios, the size and shape of nanoparticles and subsequently the functional properties of the hybrid material may be controlled by the parameters of discrete pulses of polarization.

## 64.4 Conclusions

One-step and two-step methods for obtaining PDPA-Ag nanocomposites have been studied, and resulting hybrid coatings have been characterized. In addition, the adaptive synthesis method for obtaining hybrid polymeric materials with online electrochromic feedback has been proposed.

The proposed method expands capabilities for controlling the morphological and structural parameters of the hybrid material by varying potential, duration and shape of polarization pulses as well as the relaxation time between polarization cycles.

Splitting of the process into phases also allows one to obtain the mixed NPs, core-shell and nanoalloy systems by replacing the metal containing precursor between cycles. Proposed approach can be used for both optimization of the NPs and nanocomposite preparation methods as well as fabrication of electrochemical and optoelectronic devices.

## References

1. Thummarungsan N, Pattavarakorn D (2014) Electrochromic performances of conductive polyaniline copolymer. *Int J Chem Eng Applications* 2:176
2. Molapo KM, Ndagili PM, Ajayi RF, Mbambisa G, Mailu SM, Njomo N, Masikini M, Baker P, Iwuoha EI (2012) Electronics of conjugated polymers (I): Polyaniline. *Int. J Electrochem Sci* 7:11859
3. Folarin OM, Sadiku ER, Maity A (2011) Polymer-noble metal nanocomposites: Review. *Int J Phys Sci* 21:4869



4. Vyshnevskaya YP, Brazhnyk IV, Kudrya SO (2015) Nanoplasmonics, nano-optics, nanocomposites, and surface studies. Springer International Publishing Switzerland, pp 125–133
5. Solomon SD, Bahadory M, Jeyarajasingam AV et al (2007) Synthesis and study of silver nanoparticles. *J Chem Educ* 84:322
6. Brazhnyk IV, Vyshnevskaya YP, Kudrya SA, Rumiantsev DV (2015) The 7th international conference on chemistry and chemical education “Sviridov Readings 2015”, April 7–11, 2015, Minsk. p 63
7. Vyshnevskaya YP, Brazhnyk IV (2016) The 12th international meeting on electrochromism, ISE, August 28 – September 1, 2016, Delft. p 107
8. Stratakis E, Kymakis E (2013) Nanoparticle-based plasmonic organic photovoltaic devices. *Mater Today* 4:133

# Chapter 65

## Semiconducting and Optical Properties of Compact Graphene-Like Nanoparticles of Molybdenum Disulfide

Leonid M. Kulikov, N. B. Konig-Ettel, Lyudmila Yu. Matzui, Antonina P. Naumenko, Tetyana A. Len, Iryna V. Ovsienko, and Vladimir I. Matzui

### 65.1 Introduction

Graphene-like nanoparticles (NPs) of  $2\text{H-MCh}_2$  ( $\text{M} = \text{Mo, W}$ ;  $\text{Ch} = \text{S, Se}$ ; structural type,  $2\text{H-MoS}_2$ ; «inorganic graphene-like nanoparticles») or corresponding nanosheets  $\text{Ch-M-Ch}$  and nanocomposites (nanoheterojunctions) – graphene-like  $2\text{H-MCh}_2/\text{graphene}$  – are perspective for creating new semiconducting 2D nanomaterials [1–5]. Recently, in the result of intensive qualitative studies, 2D nanomaterials have found new applications in nanoelectronics, nanooptoelectronics, nanophotovoltaics, electronic memory devices, flexible electronic systems, nanomembranes, photocatalysis on semiconducting nanoparticles, lithium sources of current with high capacity, magnetic nanomaterials, nanosensors and nanobiosensors, and nanomaterials for biomedical applications (see, e.g., [6–9]).

Until recently the changes in the properties of semiconducting graphene-like nanoparticles of d-transition metal dichalcogenides  $2\text{H-MCh}_2$  have been associated with the decrease in the number of  $\text{M-Ch-M}$  layers. However, such 2D nanoparticles, prepared by various preparative methods, are anisotropic in sizes, i.e., their dimensions in the basal plane are much greater than their “thickness” of planar

---

L.M. Kulikov • N.B. Konig-Ettel  
Frantsevich Institute for Problems of Materials Science, National Academy of Sciences of Ukraine, 3 Krzhizhanovskiy Str., 03680, Kyiv, 142, Ukraine

L.Y. Matzui • A.P. Naumenko • T.A. Len (✉) • I.V. Ovsienko  
Departments of Physics, Taras Shevchenko National University of Kyiv, Volodymyrska 64/13, 01601, Kyiv, Ukraine  
e-mail: [talen148@gmail.com](mailto:talen148@gmail.com)

V.I. Matzui  
G.V. Kurdyumov Institute for Metal Physics, National Academy of Science of Ukraine 36 Academician Vernadsky Boulevard, 03680, Kyiv,-142, Ukraine

nanoparticles (at least by an order of magnitude or more). Therefore, it is reasonable to suppose that the number of dangling bonds at the edges and, accordingly, the state of the real surface of 2D nanoparticles, as well as structure-sensitive semiconducting and optical properties, can be varied by changing the nanocrystal size in the basal plane while preserving the number of M–Ch–M nanolayers, i.e., the thickness of nanoparticles, constant.

One of the key problems that have been studied insufficiently is the state of graphene-like 2H-MCh<sub>2</sub> nanoparticles, including molybdenum disulfide. Although the researches in semiconducting properties of these were reported in a number of well-known publications [10–12], the semiconducting property studies were performed either for single nanolayers (e.g., the properties of field-effect transistors) or for nanofilms produced by depositing nanoparticles on a substrate (used as gas nanosensors). However, the compacted samples prepared by pressing (without additional binders and annealing) are also of great interest, but, to our knowledge, they have not been studied so far.

The investigation of temperature dependences of electrical conductivity for compacted samples of graphene-like nanoparticles of molybdenum disulfide can be used for comparative analysis in the study of processes and mechanisms involved in two-dimensional conductivity of monolayer (bilayers), nanofilms, and compacted samples in order to estimate the influence of surface states and degree of conductivity anisotropy. It should be noted that in most studies of graphene-like nanoparticles or nanolayers of molybdenum disulfide, only the number of S–Mo–S layers ( $L = 1, 2, 3, \dots$ ) has been taken into account, while their planar sizes have not been controlled. This has led to a noticeably ambiguous interpretation of experimental results. Therefore, the researches in electrical conductivity of graphene-like molybdenum disulfide NPs with equal number of S–Mo–S layers but significantly different sizes along the basal plane are of particular interest. Since molybdenum disulfide micron powders have been successfully used in practical applications in composite antifriction materials, this information can be used for producing electrically conductive, radiation-resistant composite antifriction nanomaterials based on graphene-like nanoparticles of molybdenum disulfide with improved performance characteristics for space and terrestrial environments at high and low temperatures.

The aim of this paper is to study the temperature dependences of electrical conductivity (77–300 K), as well as optical properties (Raman spectra) of compacted samples of graphene-like 2H-MoS<sub>2</sub> nanoparticles in order to reveal the influence of the size of basal planes and number of layers on their properties.

## 65.2 Experimental Procedure

Graphene-like nanoparticles of 2H-MoS<sub>2</sub> were synthesized from the original elements by the method of low-temperature chemical vapor deposition (CVD) under controlled kinetic characteristics of the interaction [13]. Nanosynthesis of 2H-MoS<sub>2</sub>

was implemented by the mechanism vapor–liquid–solid in self-oscillating temperatures. The flat 2H-MoS<sub>2</sub> NPs with a limited number of individual layers were formed by self-assembling S–Mo–S monolayers. To control the growth of nanoparticles in size, the additional annealing in vacuum ( $\sim 1 \cdot 10^{-3}$  Pa, 820–1120 K) was used [14].

X-ray studies were performed on an automated powder diffractometer HZG-4A (Cu–K $\alpha$  radiation) using full-profile analysis (Ritfeld method) and software package of structural calculations WinCSD. The average sizes of anisotropic nanoparticles in crystallographic directions [013] and [110] were determined by the method of X-ray line broadening (Scherrer formula) taking into account the possible impact of crystal structure distortion (Stokes' formula). Because of nanoparticles' anisotropy, we used the X-ray standard for reflex [013] and [110], which allows us to describe the function profiles more accurately comparing to the data for calculating the average size of quasi-spherical particles. The corresponding computer calculations of the nanoparticle average sizes in crystallographic directions [013] and [110] were performed with a package of advanced software WinCSD [15].

Scanning electron microscopy (SEM) of the samples was performed on JEOL JSM-820 Scanning Microscope, and transmission electron microscopy (TEM) was performed on JEM 100CXII.

The samples were compacted by cold pressing of 2H-MoS<sub>2</sub> powders by applying equilateral pressure  $(1\text{--}1.5) \cdot 10^4$  N and using a parallelepiped mold with the dimensions of  $3 \times 15 \times 2$  mm<sup>3</sup>. The porosity of the samples was about 20%.

The research in electrical resistance of the samples was carried out by the standard four-probe technique in the temperature range 77–293 K [16–18]. The dependences of the electrical resistance from temperature for graphene-like 2H-MoS<sub>2</sub> and micron powder of natural 2H-MoS<sub>2</sub> (for comparison) were studied by standard procedure (direct current, computer-controlled equipment).

Raman spectra were detected by an automated double spectrometer DFS-24 (“LOMO,” Russia), which was equipped with a cooled photomultiplier and registration system that operates in a photon-counting mode. The experiments used backscattering geometry. As a light source, a linearly polarized, cylindrical focused 488 nm Ar<sup>+</sup>-laser was used. A particular wavelength of Ar<sup>+</sup>-laser was selected by a prism located outside the laser resonator, and a cylindrical lens was used to focus light in a  $10 \times 0.1$  mm<sup>2</sup> spot.

### 65.3 Results and Discussion

According to X-ray studies and electron microscopy, the synthesized anisotropic 2H-MoS<sub>2</sub> NPs are homogeneous by chemical composition (MoS<sub>2</sub>), structural type 2H-MoS<sub>2</sub>, and type of nanostructures (2D, “inorganic graphene-like nanoparticles”), have small sizes in crystallographic direction [013] ( $\sim 1$  nm), and do not contain extraneous impurity phases, including amorphous and other nanostructures. The average sizes of anisotropic 2H-MoS<sub>2</sub> NPs are interconnected and effectively

controlled in a wide range in the subsequent annealing process. The temperature (820–1120 K) has the dominant effect on the growth of anisotropic nanoparticles, while the effect of annealing time (10–60 h) is not essential. As the annealing temperature increases from 820 K to 1120 K, the exponential increase of nanoparticle size along directions [013] and [110] is observed at that the dominant growth occurs in [110] direction:  $d_{[013]} = 2.7$  (2) –4.7 (2) nm,  $d_{[110]} = 8.5$  (4) –53 (3) nm. With decreasing the size of 2H-MoS<sub>2</sub> nanoparticles, the parameter *c* of elementary cells increases linearly in the [013] direction, while for [110] direction an exponential growth of the parameter is observed. Parameter *a* of elementary cells linearly decreases in the [013] and [110] with decreasing of the sizes of 2H-MoS<sub>2</sub> nanoparticles (obtained value of parameter *a* in this case as a rule less than the value of parameter *a* in the micron powder). It is estimated that the number of nanolayers S–Mo–S in the direction of the *Z* axis is 4–8 for annealing temperature: 820–1120 K.

According to the goals of our work, we used the samples in which nanoparticles had almost the same number of layers ( $n = 6$ –8) but were significantly different in sizes along the basal plane [110] (17 (1), 43 (3), 53 (3) nm) (see Table 65.1). For comparison the temperature dependences of electrical conductivity and Raman spectra for micron powders of natural molybdenum disulfide (see Table 65.1) were used.

The results of scanning electron microscopy of graphene-like 2H-MoS<sub>2</sub> NPs are shown in Fig. 65.1. It can be seen that 2H-MoS<sub>2</sub> nanoparticles tend to agglomerate, which results in the formation of lamella agglomerates.

The temperature dependences of normalized resistance  $R/R_{293K}(T)$  for all the samples at room temperature are presented in Fig. 65.2. One can see from Table 65.2 that for microdisperse sample 1 the resistance is rather high, while for samples 3 and 4 it is  $10^2$ – $10^4$  times lower. It is worth mentioning that for these samples, which have similar sizes of nanoparticles in crystallographic directions [110], the temperature dependences of resistance  $R/R_{293K}(T)$  are similar although these samples have different number of layers.

**Table 65.1** X-ray data of graphene-like 2H-MoS<sub>2</sub> nanoparticles

Compound	Sequence number	Unit cell parameters, nm		Average sizes of nanoparticles for [013] and [110] crystallographic directions, nm		Number of layers
		<i>a</i>	<i>c</i>	$d_{[013]}$	$d_{[110]}$	
2H-MoS <sub>2</sub>	1	0,31,601(1)	1,22,984(6)	>200	>200	–
	2	0,31,621(4)	1,2294(7)	4.2(2)	17(1)	6
	3	0,31,600(5)	1,2255(7)	4.7(2)	43(3)	8
	4	0,31,622(5)	1,2254(8)	3.9(2)	53(3)	6

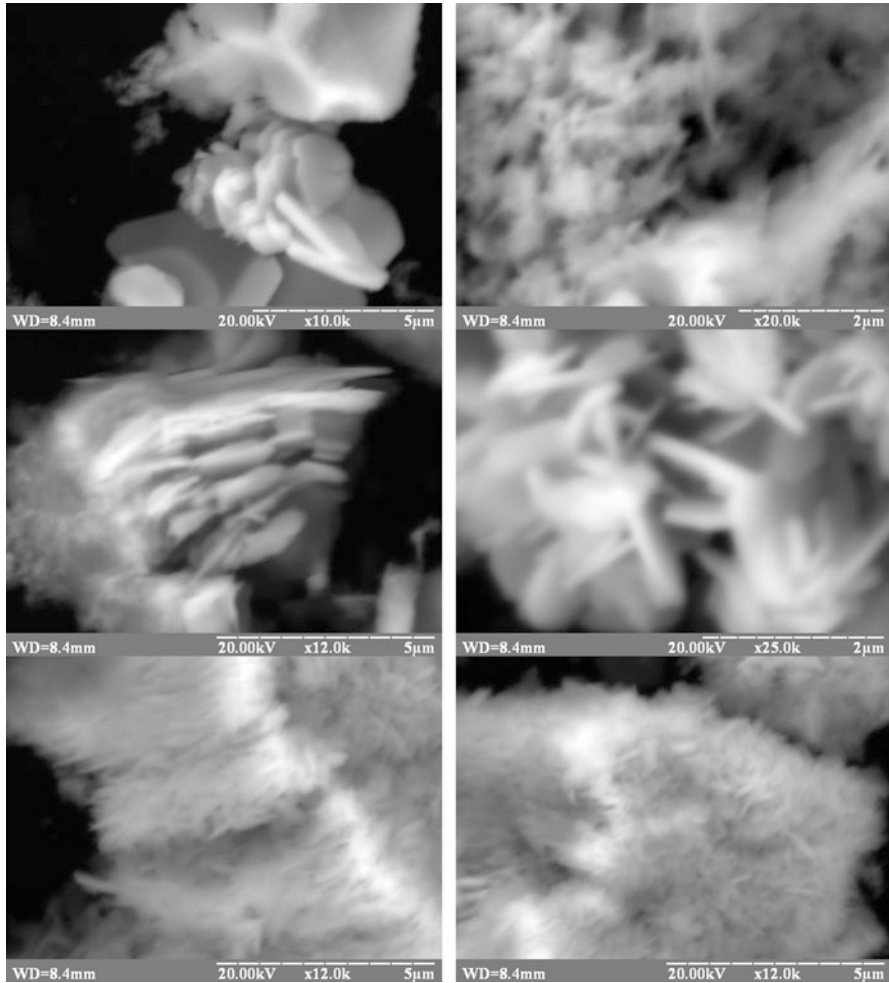


**Fig. 65.1** SEM image of graphene-like 2H-MoS<sub>2</sub> nanoparticles

It is known that the conduction mechanism in disordered semiconductor materials can be hopping conduction with variable hopping range. The temperature dependence of resistance in this case is described by equation [19]:

$$\rho(T) = \rho_0 \exp \left[ \left( \frac{T_0}{T} \right)^{1/n} \right] \quad (65.1)$$

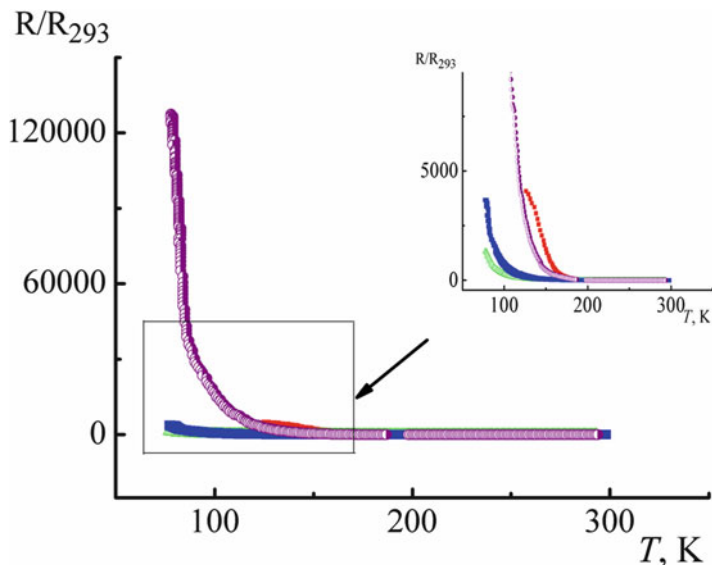


**Fig. 65.2** The temperature dependence of the resistance  $R/R_{293K}(T)$  for all samples: ■ –sample #1, ○ –sample #2, ▲ –sample #3, ■ –sample #4

**Table 65.2** Parameters of electrical resistance of samples

Sample	$\rho_{77}$ , Ohm·m	$\rho_{293}$ , Ohm·m	$\rho_{77}/\rho_{293}$	$T_0$ , K
Sample #1	$>>3 \cdot 10^8$	$5,9 \cdot 10^4$		
Sample #2	$1,7 \cdot 10^8$	$2 \cdot 10^2$	$5,1 \cdot 10^5$	$1,3 \cdot 10^6$
Sample #3	$8 \cdot 10^3$	6	$1,3 \cdot 10^3$	$6,3 \cdot 10^5$
Sample #4	$6 \cdot 10^3$	1,7	$3,5 \cdot 10^3$	$8,3 \cdot 10^5$

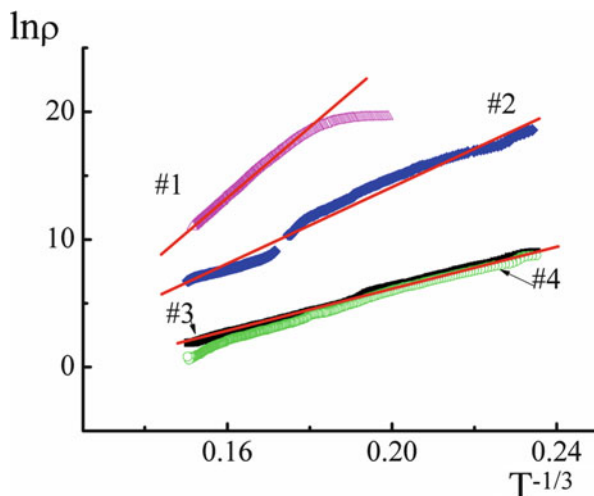
where

$$T_0 = \frac{\beta}{a_{loc}^d k_B N(E_F)}, \tag{65.2}$$

$n$  is a constant depending on dimension,  $a_{loc}$  is the localization radius of electron wave function,  $d$  is the movement dimension of the current carriers,  $n = 1 + d$ ,  $k_B$  is the Boltzmann constant, and  $N(E_F)$  is the density of states at the Fermi level. The experimental data are well described by formula (65.1) with  $d = 2$ .

Figure 65.3 shows the temperature dependence of the resistance logarithm for axes  $\ln[\rho(T)] = f(T^{-1/3})$  for 2H-MoS<sub>2</sub> samples in temperature range 80–300 K. As seen from Fig. 65.3, the samples with nanosized particles display a linear dependence of resistance in these axes, which indicates that they can be described by the theory of 2D hopping conductivity with variable hopping length. The physical sense of hopping conduction is electron tunneling between localized states accompanied by energy exchange with phonons. The variable hopping length means

**Fig. 65.3** The temperature dependence of the electrical resistance of samples, rebuilt in the coordinates  $\ln\rho = f(T^{-1/3})$  for (a) the micron powder sample #1, (b) sample #2, (c) sample #3, (d) sample #4



tunneling over long distances with small change in energy or over a small distance with a large change in energy. In other words, when the temperature becomes energetically favorable, the tunneling takes place over long distances.

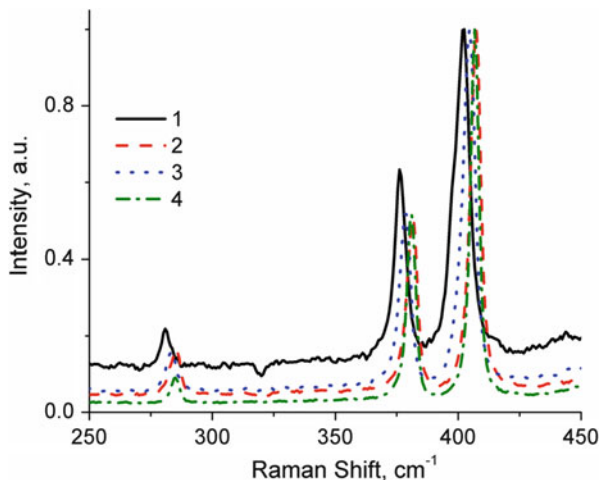
The increase of nanoparticle average sizes both for crystallographic directions [013] and [110] leads to the formation of 3D structure, and, as a result, the experimental dependences  $\rho(T)$  for the samples with micron-sized particles do not follow formula (65.2) for 2D hopping conductivity.

From dependences  $\ln\rho = f(T^{-1/3})$ , the parameters of  $T_0$  have been obtained (Table 65.2). As it is seen from formula (65.2), parameter  $T_0$  depends on the sample morphology, density of electronic states at Fermi level, and localization radius. The analysis of data from Table 65.2 shows that parameter  $T_0$  is almost independent of the number of layers, but it depends on the sizes of sample basal planes. For samples 3 and 4, the values of  $T_0$  are practically identical, which indicates that the values of localization radius  $a_{loc}$  and the density of states at the Fermi level for these samples are of the same order. With the decrease in nanoparticle sizes,  $T_0$  increases essentially, which could be connected basically with the decrease in the localization radius  $a_{loc}$  of electron wave function.

Raman spectroscopy was used for additional structural certification and study of vibrational and electronic properties of graphene-like 2H-MoS<sub>2</sub> NPs. For comparison, Fig. 65.4 presents the Raman spectra of graphene-like 2H-MoS<sub>2</sub> NPs (see Table 65.1) and 2H-MoS<sub>2</sub> micron powders, which were normalized and vertically offset for vividness. For micron 2H-MoS<sub>2</sub> powder, both modes are observed, the in-plane  $E_{12g}$  mode at 383 cm<sup>-1</sup> and out-of-plane mode  $A_{1g}$  at 409 cm<sup>-1</sup> (see Fig. 65.4, curve 1), which is in good agreement with the previous studies [20–26]. The closeness of the Raman spectra for micron powder and graphene-like 2H-MoS<sub>2</sub> NPs shows the homogeneity of the latter, which confirms the results of our previous X-ray and electron microscopic studies.



**Fig. 65.4** Raman spectra of graphene-like 2H-MoS<sub>2</sub> nanoparticles (curves 2–4) and micron particles of natural 2H-MoS<sub>2</sub> (curve 1), obtained at room temperature with excitation of Ar<sup>+</sup>-laser (488 nm). Numbers of curves correspond to the numbers of samples from Table 65.1



For micron 2H-MoS<sub>2</sub> powder, the spectral position of these modes was found to shift to 376 cm<sup>-1</sup> and 402 cm<sup>-1</sup>, respectively. A number of low-intensity bands in the spectral range 240–300 cm<sup>-1</sup> (curve 1, Fig. 65.4) were found. These bands are shifted to 283 cm<sup>-1</sup> (curve 3, Fig. 65.4) and 285 cm<sup>-1</sup> (curves 2 and 4, Fig. 65.4) depending on the average sizes of graphene-like 2H-MoS<sub>2</sub> nanoparticles. In this way, we have found that the shifts in the Raman spectra of graphene-like 2H-MoS<sub>2</sub> nanoparticles depend on nanoparticle size in crystallographic direction [110], i.e., the shifts are due not only to the number of S–Mo–S nanolayers but also to the nanoparticle sizes.

In general, the results of Raman studies indicate significant impact of anisotropy of grapheme-like 2H-MoS<sub>2</sub> NP sizes, in particular, in the direction [110] under constant number of S–Mo–S nanolayers, on the formation of the structure-sensitive optical properties and, accordingly, the characteristics of the semiconductor as a whole.

## 65.4 Conclusions

It has been found that the compacted samples of graphene-like 2H-MoS<sub>2</sub> nanoparticles display semiconductor type of conductivity (n-type) which correlates with nanoparticle sizes, in particular with size (17–53 nm) along the basal plane [100] at a constant number of nanoparticle S–Mo–S nanolayers ( $n = 6–8$ ). The mechanism of conductivity is supposed to be hopping conduction for 2D case.

The results of Raman studies indicate significant impact of anisotropy of 2H-MoS<sub>2</sub> NP sizes, namely, in the direction of [110], on the vibrational properties and accordingly the characteristics of semiconductor as a whole.

**Acknowledgments** The authors thank Akselrud L.G. (Lviv National University, Ukraine) for performing X-ray studies.

## References

1. Ferrari AC, Bonaccorso F, Fal'ko V, Novoselov KS, Roche S, Boggild P et al (2015) Science and technology roadmap for graphene, related two-dimensional crystals, and hybrid systems. *Nanoscale* 7:4598–4810
2. Gibney E (2015) The super materials that could trump grapheme. *Nature* 522:274–276
3. Chhowalla M, Liu Z, Zhang H (2015) Two-dimensional transition metal dichalcogenide (TMD) nanosheets. *Chem Soc Rev* 44:2584–2586
4. Kuc A, Heine T, Kis A (2015) Electronic properties of transition-metal dichalcogenides. *MRS Bull* 40:577–584
5. Fiori G, Bonaccorso F, Iannaccone G, Palacios T, Neumaier D, Seabaugh A et al (2014) Electronics based on two-dimensional materials. *Nat Nanotechnol* 9:768–779
6. Chhowalla M, Shin HS, Eda G, Li L-J, Loh K-P, Zhang H (2013) The chemistry of two-dimensional layered transition metal dichalcogenide nanosheets. *Nat Chem* 5:263–275
7. Tang Q, Zhou Z (2013) Graphene-analogous low-dimensional materials. *Prog Mater Sci* 58:1244–1315
8. Xu M, Liang T, Shi M, Chen H (2013) Graphene-like two-dimensional materials. *Chem Rev* 113:3766–3798
9. Song X, Hu J, Zeng H (2013) Two-dimensional semiconductors: recent progress and future perspectives. *J Mater Chem C* 1:2952–2969
10. Enyashin AN, Seifert G (2014) Electronic properties of MoS<sub>2</sub> monolayer and related structures. *Phys Chem Mat* 5:517–539
11. Ye M, Winslow D, Zhang D, Pandey R, Khin Y (2015) Recent advancement on the optical properties of two-dimensional molybdenum disulfide (MoS<sub>2</sub>) thin films. *Photonics* 2:288–307
12. Ahmad S, Mukherjee S (2014) A comparative study of electronic properties of bulk MoS<sub>2</sub> and its monolayer using DFT technique: application of mechanical strain on MoS<sub>2</sub> monolayer. *Graphene* 3:52–59
13. Kulikov LM, Konig NB (2008) Process for preparation of nanocrystalline powders of molybdenum dichalcogenides, Ukraine Patent 81588, January 10
14. Kulikov LM, Konig NB, Akselrud LG, Davidov VN, Kotko AV (2009) *Nanostruct Mater Sci* 3, 3
15. Akselrud LG, Grin Yu P, Pecharsky VK, Zavalij P Yu, Baumgartner BE(1992) A presented at second European powder diffraction conference. Enschede
16. Len T, Ovsienko I, Matzuy L, Prylutsky Y, Berkutov I, Andrievskii V et al (2015) Magnetoresistance and electrical resistivity of N-doped multi-walled carbon nanotubes at low temperatures. *Phys Status Solidi B* 252:1402–1409
17. Ovsienko I, Matzuy L, Len T, Zakharenko N, Babich N et al (2008) Magnetometric studies of catalyst refuges in nanocarbon materials. *Nanoscale Res Lett* 3:60–64
18. Len T, Matzui L, Ovsienko I, Prylutsky Y, Andrievskii V, Berkutov I et al (2011) Magnetoresistance nanocarbon materials based on carbon nanotubes. *Low Temp Phys* 37:1027–1032
19. Bonch-Bruevich VL (1990) *Physics of semiconductors*. Nauka Publ, Moscow
20. Lee C, Yan H, Brus L, Heinz T, Hone J, Ryu S (2010) Anomalous lattice vibrations of single- and few-layer MoS<sub>2</sub>. *ACS Nano* 4:2695–2700
21. Verbal J, Wieting T (1970) The observed degeneracy of mutually exclusive infrared- and Raman-active modes in MoS<sub>2</sub> is traced by means of group theory to the weak van der Waals interaction between layers. *Phys Rev Lett* 25:362–364
22. Frey G, Tenne R, Matthews M, Dresselhaus M, Dresselhaus G (1999) Raman and resonance Raman investigation of MoS<sub>2</sub> nanoparticles. *Phys Rev B* 60:2883–2892

23. Wieting T, Verble J (1971) Infrared and Raman studies of long-wavelength optical phonons in hexagonal MoS<sub>2</sub>. *Phys Rev B* 3:4286–4291
24. Ataca C, Topsakal M, Aktürk E, Ciraci S (2011) A comparative study of lattice dynamics of three- and two-dimensional MoS<sub>2</sub>. *J Phys Chem C* 115:16354–16361
25. Korn T, Heydrich S, Hirmer M, Schmutzler J, Schüller C (2011) Low-temperature photocarrier dynamics in monolayer MoS<sub>2</sub>. *Appl Phys Lett* 99:102109–1–10210-3
26. Li H, Zhang Q, Yap C, Tay C, Edwin T, Olivier A, Baillargeat D (2012) From bulk to monolayer MoS<sub>2</sub>: evolution of Raman scattering. *Adv Funct Mater* 22:1385–1390

# Chapter 66

## Dielectric Properties of Nanocarbon Polymer Composites with Binary Filler

M. S. Melnychenko, Yu. S. Perets, L. L. Aleksandrovykh, L. L. Vovchenko, O. A. Lazarenko, and Lyudmila Yu. Matzui

### 66.1 Introduction

In recent years, due to the extensive development of microelectronic devices, telecommunication systems, and cellular and satellite communications, which are working in radio frequencies, there was a problem of electromagnetic (EM) pollution. This pollution, also known as EMI [1] (electromagnetic interference), can lead to reducing in performance of electronic devices (noise, degradation, etc.) and to a negative impact on human health [2, 3]. So, the development of efficient protection against deleterious influence of radio frequency electromagnetic radiance (EMR) on electronic equipment as well as on human organism is seen to be a problem of special importance [4–6]. Total shielding effectiveness ( $SE_T$ ) is determined by absorption loss, reflection loss, and multiple reflections in the shield material, which are functions of its magnetic permeability and dielectric permittivity [7].  $SE_T$  can be improved by increasing the thickness of the screen [8], but often it is problematic. Fields of the application of shielding materials cause a number of requirements to them: they should be thin, flexible, corrosion and mechanical stress resistant, and not expensive in manufacturing. Traditionally metals and composites based on them are used as EMI shields. Such materials are simple, convenient, and cost-effective solution [9, 10]. However, metallic shields possess the essential shortcomings such as heavy weight and low corrosion resistance.

---

M.S. Melnychenko (✉) • Y.S. Perets • L.L. Aleksandrovykh • L.L. Vovchenko • O.A. Lazarenko  
Physics Faculty of Taras Shevchenko National University of Kyiv, Volodymyrska str. 64/13, Kyiv,  
Ukraine 01601  
e-mail: [mykola.melnichenko@gmail.com](mailto:mykola.melnichenko@gmail.com)

L.Y. Matzui  
Departments of Physics, Taras Shevchenko National University of Kyiv, Volodymyrska 64/13,  
01601, Kyiv, Ukraine

Different polymers have found a wide application in the manufacture of microwave absorbing materials, because of their flexibility, increased processability, good mechanical properties, and high resistance to impact of the environment. However, most polymers are completely transparent to electromagnetic radiation in the microwave frequency range. For this reason, the polymer-based microwave absorbing materials consist of a polymer matrix and electromagnetic wave absorbers [11, 12].

Polymer CMs with conductive filler are the new alternative candidate for electromagnetic interference (EMI) shielding, because of their unique properties, such as lightweight, low cost, good processability, and tunable conductivities over a wide range [13, 14]. However, there is a problem of requiring a large amount of filler. Theoretically, the critical concentration or percolation threshold  $\varphi_c$  for spherical, randomly dispersed filler (e.g., carbon black, metallic particles, and conducting polymer particles) is approximately 10–20 vol%, which is close to the percolation value of  $\varphi_c \sim 16$  vol% predicted by the classical percolation theory [15, 16]. Carbon nanotubes (CNTs), graphene, and graphite nanoplates (GNPs) have gained great attention worldwide owing to their high aspect ratio, excellent mechanical and electrical properties, as well as outstanding thermal performance [17, 18]. Unfortunately, their extreme agglomeration behavior during processing in host polymers generates the relatively high  $\varphi_c$ . The CMs with high  $\varphi_c$  always suffer from various drawbacks: high melt viscosities, low economic affordability, and inferior mechanical properties (esp. for ductility and toughness) [19, 20]. Therefore, decrease of  $\varphi_c$  efficiently has become a long-standing major topic during the fabrication of high-performance polymer CMs.

Dielectric properties and shielding effectiveness of CMs are widely studied in numerous works, but often they are investigated only in a limited frequency range. Particularly, in [21] the authors investigate the effect of different carbon-based nano- and microfillers on the electromagnetic performance of polymer composites in the frequency range from 8.2 to 18 GHz only. In another work [22] dielectric property of BaTiO<sub>3</sub>/polymer composites was investigated at frequencies from 100 Hz to 10 GHz. In work [23] authors performed the dielectric spectroscopy of short carbon fiber/silica composite in the frequency range from 8.2 to 12.4 GHz. In 2013 Y. Feng et al. published [24] results of the influence of BaTiO<sub>3</sub> nanowires on the dielectric properties under the frequencies  $10^{-2}$ – $10^7$  Hz. So, study of the dielectric properties of the CMs with conductive filler in a wide microwave range is still an actual task, which was one of the objectives of this work.

Recently, there is a new tendency to add a two or three types of conductive filler to a polymer matrix to improve the electric and thermal conductivities of binary composites [25–29]. For example, Tang's group found that the addition of multiwalled carbon nanotubes (MWCNTs) in carbon black (CB)/epoxy resin composites enhanced the electrical conductivity of composites, and the percolation threshold appeared when the ternary composite had 0.2 wt.% MWCNTs and 0.2 wt.% CB; however, the percolation threshold of CB/epoxy resin composites was 0.6 wt.%; in addition, the flexural stress and impact fracture toughness of the ternary composite with 0.2 wt.% MWCNT and 0.2 wt.% CB were higher than those of the

binary composite with 0.4 wt.% MWCNT or with 0.4 wt.% CB [25]. Yu's group prepared MWCNTs–graphite nanosheets (GNSs)/epoxy resin composites and found that with the same content of the fillers, the ternary composite had higher thermal conductivity than GNSs/epoxy composite [27].

These interesting results show that multicomponent composites have advantages in mechanical properties and electric and thermal conductivities. Also the possibility of the addition of magnetic nanoparticles to the composite with a conductive (particularly, nanocarbon) filler is actively studied. Thus, in work [30] electromagnetic properties were investigated in the frequency range of 12.4–18 GHz of the barium ferrite decorated with reduced graphene oxide ( $\text{BaFe}_{12}\text{O}_{19}/\text{RGO}$ ) nanocomposite. The presence of  $\text{BaFe}_{12}\text{O}_{19}$  nanoparticles in the nanocomposite enhances the space charge polarization, natural resonance, multiple scattering, and the effective anisotropy energy leading to a high electromagnetic interference shielding effectiveness of 32 dB ( $\sim 99.9\%$  attenuation) at a critical thickness of 3 mm. In [31] it had been shown that PS/TGO/ $\text{Fe}_3\text{O}_4$  composites exhibit obviously improved EMI shielding effectiveness in comparison with one of PS/TGO composite. The EMI shielding effectiveness of PS/TGO/ $\text{Fe}_3\text{O}_4$  composite is more than 30 dB in the frequency range of 9.8–12 GHz with 2.24% of graphene only.

The interesting alternative to using metallic filler is hybrid nanocarbon fillers, including expanded graphite–MWCNTs or GNPs/MWCNTs. In [32] authors describe dielectric behavior of expanded graphite (EG)–MWCNTs/cyanate ester (CE) composites. The ternary composites exhibit dielectric properties significantly different from the EG/CE and MWCNTs/CE binary composites, showing an obvious synergistic effect between EG and MWCNTs. The addition of EGs not only improves the dispersion of MWCNTs in the resin matrix but also helps to form conductive networks. However, the research mentioned above is carried out in the low frequency range (from  $10^2$  to  $10^6$  Hz), and we are interested in microwave range investigations. In work [33] authors investigated polypropylene/carbon nanotubes/exfoliated graphite nanoplatelets (PP/CNTs/xGNPs). An EMI SE of 36.5 dB at 1250 MHz was measured for the 80/10/10 wt % PP/CNTs/xGNPs composite; its sound transmission loss was more than 5 dB higher than that for pure PP at low frequencies (520–640 Hz). In [34] the synergistic effect of combining different carbon fillers on composite SE was also observed, but measurements were done at separate frequencies: 30, 100, 200, 300, 400, 500, 600, 700, 800, and 1000 MHz.

The main idea of the present paper is to identify the synergistic effect of using the combination of nanocarbon fillers with different structure and morphology on the electrodynamic properties and shielding effectiveness of polymer–carbon composite materials in wide frequency range. The dielectric properties and shielding effectiveness of CMs with ordinary nanocarbon filler (MWCNTs or GNPs) and binary filler (GNPs + MWCNTs) were investigated in a frequency range from 1 to 50 GHz.

**Table 66.1** Main physical properties of epoxy L285

Density (at 25 °C)	1.18 ÷ 1.23 g/cm <sup>3</sup>
Viscosity (at 25°C)	600 ÷ 900 mPa·s
Epoxy equivalent	165–170
Epoxy number	0.59 ÷ 0.65

**Table 66.2** Main physical properties of hardener H285

Density (at 25°C)	0.94 ÷ 0.97 g/cm <sup>3</sup>
Viscosity (at 25°C)	50 ÷ 100 mPa·s
Amine Number	480 ÷ 550 mg KOH/g

## 66.2 Materials and Experimental Details

In order to establish the effect of concentration and type of filler on the dielectric and shielding properties of nanocarbon polymer composites, the samples of epoxy (L285)/nanocarbon (MWCNTs, GNPs, MWCNTs + GNPs) have been prepared.

Epoxy resin L285 (Lange+Ritter GmbH, Germany) has been used as a polymer matrix. In the initial state, this polymer has two components: liquid epoxy resin and appropriate hardener H285. Main physical properties of epoxy L285 and hardener H285 are presented in Tables 66.1 and 66.2.

The following substances were used as fillers in the investigated composites:

- MWCNTs (Cheap Tubes Inc.), which were obtained by catalytic chemical vapor deposition (purity ~90%). Dimensions of these MWCNTs are the following: outer diameter  $d = 10 \div 30$  nm and length  $l = 10 \div 30$   $\mu$ m.
- GNPs, which were obtained from ultrasonic dispersion (USD) of expanded graphite (EG). To produce GNPs as liquid media for USD of EG, we used distilled water. USD process lasted for 30 hours in the ultrasonic bath BAKU 9050 with power 50 W and frequency 40 kHz. After that, dispersed GNPs are dried at room temperature until complete evaporation of water.
- Binary fillers, which consist of MWCNTs and GNPs with different relative concentrations.

SEM images of fillers that we used in this work are presented in Fig. 66.1.

CMs with epoxy polymer matrix and nanocarbon fillers were prepared by the following schemes.

For the first step, epoxy L285 was mixed with acetone to reduce viscosity. Then we add nanocarbon filler in appropriate mass ratio (depending on required concentration) stirring constantly. The next step is USD in ultrasonic bath during 30 min for GNPs and 60 min for MWCNTs. Finally, the resulting mixture was poured into molds for consolidation.

The samples of epoxy L285–GNPs (0.5, 1, 2 wt.%) and epoxy L285–MWCNTs (0.5, 1.5, 2, 3 wt.%) were prepared by this scheme.

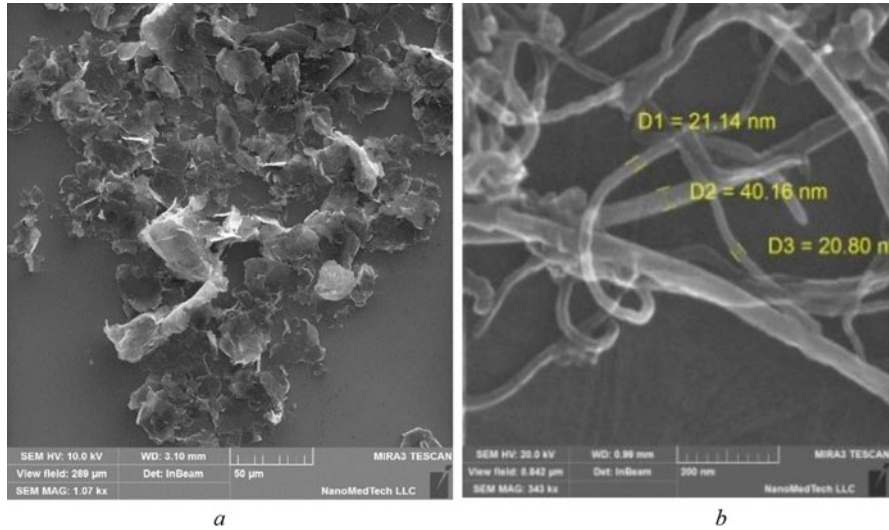


**Fig. 66.1** – SEM images of fillers: GNPs (a), MWCNTs (b)

Polymer CMs with hybrid fillers were prepared by the following scheme. First, MWCNTs were added into the pre-diluted epoxy, followed by the ultrasonic dispersing of this solution during 1 h. Then, GNPs were added to this system and the obtained mixture was dispersed for 30 min. Finally the resulting mixture was poured into molds for consolidation.

According to the scheme mentioned above, we received samples of CMs with hybrid (GNPs + MWCNTs) fillers with different relative concentrations of components (0.5 wt.% GNPs and 0.05, 0.15, 0.5, 0.75 wt.% MWCNTs).

The values of conductivity  $\sigma$  and percolation threshold  $\varphi_c$  of developed CMs were obtained under investigation of concentration dependences of dc conductivity [35].

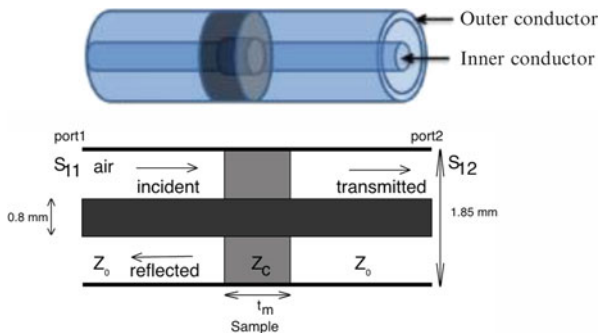
It should be mentioned that in our series of samples the concentrations of the filler in the CMs with GNPs are less than the critical concentration (percolation threshold) ( $\varphi_{c\text{ GNPs}} = 3.8\text{ wt.}\%$ ; see in Table 66.3) and therefore all investigated samples of CMs with GNPs are described by the system of conductive isolated particles in the dielectric matrix. Otherwise, in CMs with CNTs, the concentration of filler is higher than percolation threshold ( $\varphi_{c\text{ MWCNTs}} 0.25\text{ wt.}\%$ ), and in these samples the formation of the conductive chains is observed. The interval of the filler concentration in CMs with binary fillers is  $1\text{ wt.}\% \leq \varphi_c \leq 1.25\text{ wt.}\%$ . Accordingly, CMs with binary filler with  $\varphi/\varphi_c = 0.42, 0.5, 0.77$  can be described as a system of isolated conductive particles in dielectric matrix and CMs with  $\varphi/\varphi_c = 0.96$  as a system with conductive chains.



**Table 66.3** Conductive characteristics of studied CMs

Type of filler	c, wt.%	$\sigma$ , $\text{Omh}^{-1}$	$\varphi/\varphi_c$
GNPs $\varphi_c = 3.8 \text{ wt.}\%$	0.5	$1.06 \cdot 10^{-9}$	0.13
	1	$1.46 \cdot 10^{-8}$	0.263
	2	$1.49 \cdot 10^{-7}$	0.526
CNTs $\varphi_c = 0.25 \text{ wt.}\%$	0.5	$4.9 \cdot 10^{-6}$	2
	1.5	$2.5 \cdot 10^{-5}$	6
	2	$3.47 \cdot 10^{-5}$	8
	3	$3.7 \cdot 10^{-5}$	12
GNPs + CNTs $\varphi_c = 1.3 \text{ wt.}\%$	0.5 + 0.05	$3.16 \cdot 10^{-8}$	0.423
	0.5 + 0.15	$6.54 \cdot 10^{-8}$	0.5
	0.5 + 0.5	$3.97 \cdot 10^{-7}$	0.77
	0.5 + 0.75	$2.86 \cdot 10^{-5}$	0.96

**Fig. 66.2** The measurement scheme of dielectric spectra. Coaxial line and sample



## 66.3 Experimental Details

### 66.3.1 Measurements

The complex permittivity ( $\epsilon'$ ,  $\epsilon''$ ) spectra were measured by a vector network analyzer (Keysight Network Analyzer N5227A) using a coaxial transmission–reflection method in the frequency range of 1–50 GHz. Samples for the investigations were prepared in the toroid shape. The toroids tightly fit into the coaxial measurement cell. The cell (Fig. 66.2) has 0.803 mm inner diameter and 1.85 outer diameter. Full two-port calibration was initially performed on the test setup in order to remove errors due to the directivity, source match, load match, isolation, and frequency response in both the forward and reverse measurements. The complex permittivity ( $\epsilon_r$ ) is determined from the scattering parameters using the Nicolson models.

### 66.3.2 Microwave Shielding Properties

Interaction between EMR and CMs is determined by the attenuation of EMR on its propagation path through the waveguide with the CMs sample. EMR absorption ( $A$ )

and reflection ( $R$ ) indexes are related themselves and with EMR transmission ( $Tr$ ) index by power balance equation [36]:

$$1 = R + A + Tr \quad (66.1)$$

$R = |E_R/E_I|^2$ ,  $Tr = |E_{Tr}/E_I|^2$ ,  $E_R$ ,  $E_T$ ,  $E_I$  are the values of electric field of reflected, transmitted, and incident waves, respectively.

And, accordingly, reflection loss ( $RL$ ) and shielding effectiveness ( $SE_T$ ) (in dB) are determined as

$$RL = 10 \log R \quad (66.2)$$

and

$$SE_T = 10 \log Tr \quad (66.3)$$

The power balance equation for frequency dependences of the shielding effectiveness parameters registered in regime of metal-backed plate transforms to the form  $R + A = -1$ . In regime of matching loading, the equation is  $1 = R + A + Tr$ .

## 66.4 Results and Discussion

### 66.4.1 Dielectric Properties

In order to evaluate the influence of nanocarbon filler concentration on the dielectric constants of the epoxy-based composites filled with GNPs, MWCNTs, as well as GNPs/MWCNTs, the frequency dependences of real and imaginary parts of permittivity were studied over a broad frequency range (1–50 GHz).

The frequency dependences of real ( $\epsilon'$ ) and imaginary ( $\epsilon''$ ) parts of permittivity have been presented in Figs. 66.3, 66.4, and 66.5 for GNPs/L285, MWCNTs/L285, and MWCNTs/GNPs/L285, respectively, for different contents of the fillers. It is clear that both real ( $\epsilon'$ ) and imaginary ( $\epsilon''$ ) parts of the complex permittivity increased with increasing the filler content, in the frequency range of 1–50 GHz, but decreased slowly with increasing frequency for composites with low filler concentration (<1 wt.%). However, the absolute value of  $\epsilon'$ ,  $\epsilon''$  increases with increasing concentration of filler regardless of the type of filler. With increasing concentration of filler in CMs, regardless of the type of filler, there is a maximum on spectrum  $\epsilon''$ , which coincides with relaxation  $\epsilon$ .

Figure 66.6a, b presents the dependences of the dielectric constants ( $\epsilon'$ ,  $\epsilon''$ ) from filler content at 20 GHz. The synergistic effect is revealed in the dielectric constants for composites with binary fillers in comparison with the composites with single fillers:  $\epsilon'$  in CMs with binary filler is greater than in CMs with same

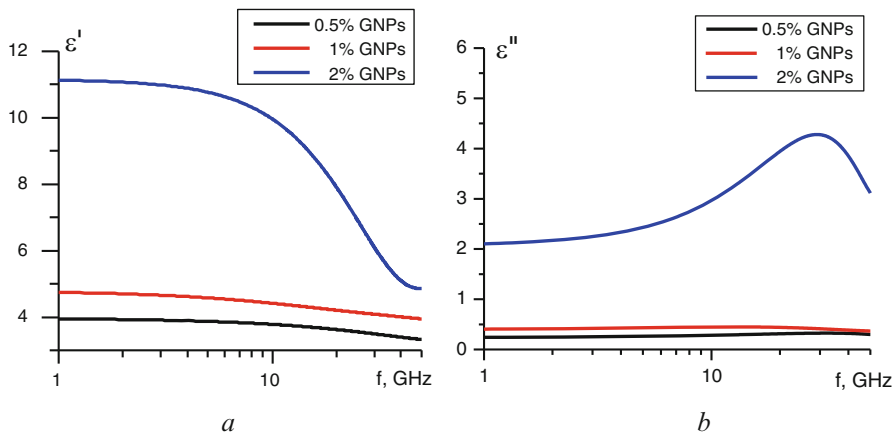


**Fig. 66.3** Spectra of the real  $\epsilon'$  (a) and imaginary  $\epsilon''$  (b) parts of the complex dielectric permeability of the CMs L285/GNPs

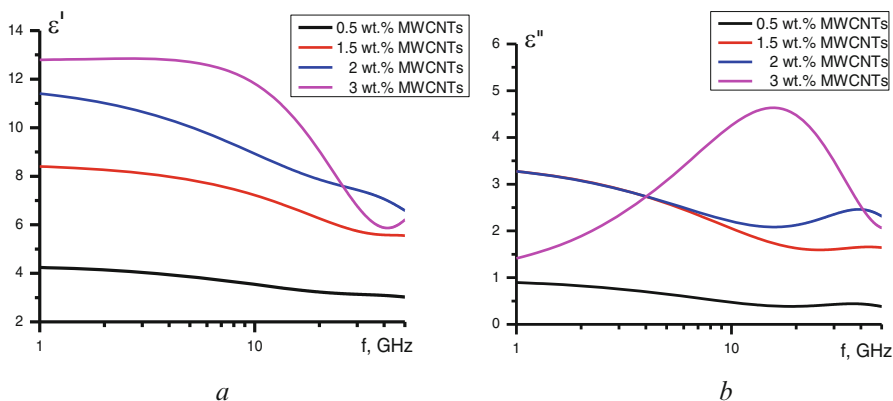


**Fig. 66.4** Spectra of the real  $\epsilon'$  (a) and imaginary  $\epsilon''$  (b) parts of the complex dielectric permeability of the CMs L285/MWCNTs

concentration of single filler. In composites with low filler content,  $\epsilon''$  shows intermediate values between the values  $\epsilon''$  in CMs with a binary filler and CMs with the same concentration of MWCNTs or GNPs. However, when concentration of hybrid filler approaches  $\varphi_c$  (0.5 wt.% GNPs + 0.75 wt.% MWCNTs),  $\epsilon''$  becomes higher than  $\epsilon''$  in CMs with the appropriate concentration of single filler.

It is known that dielectric loss mechanisms of the CMs with conductive particle are mainly caused by deflection of dipole and interfacial polarization [37]. The  $\epsilon'$  of composites depends on the configuration and internal fraction structure, which is proportional to the quantity of charge stored on the surface when the composites expose to electric field. The increase of the concentration of GNPs in polymer matrix

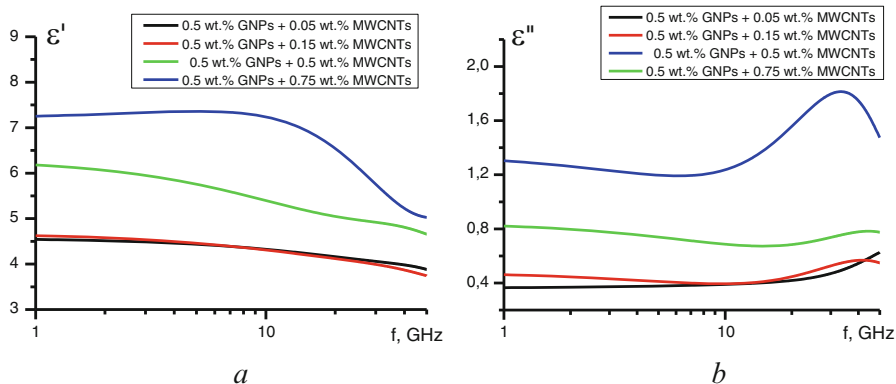


**Fig. 66.5** Spectra of the real  $\epsilon'$  (a) and imaginary  $\epsilon''$  (b) parts of the complex dielectric permeability of the CMs L285/CNTs/GNPs

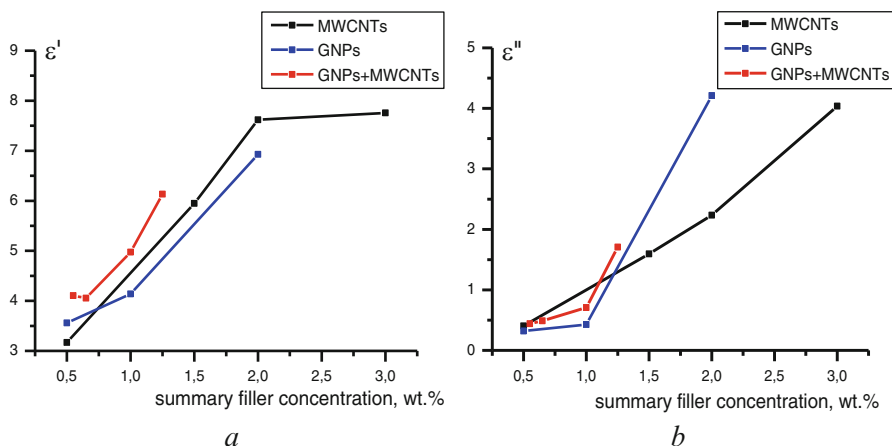


**Fig. 66.6** Concentration dependencies of the real (a) and imaginary (b) parts of the complex dielectric permeability of the CMs L285/MWCNTs/GNPs

leads to the formation of more interfaces in CMs, which certainly increased the  $\epsilon'$  of such CMs.

On the other hand, the main factor affecting the  $\epsilon''$  is the interfacial polarization when a sample is filled with low content of GNPs/MWCNTs. When the concentration of binary filler is near the percolation threshold, the conductive chains are formed in this composite, and the conductivity sharply increased which also can affect the values of the  $\epsilon''$  of such composites. The higher the electrical conductivity, the higher values of  $\epsilon''$  are observed, as it is seen in Fig. 66.6b. Thus, it is reasonable that the higher complex permittivity (both the  $\epsilon'$  and  $\epsilon''$ ) can be obtained when the composites filled with higher content of GNPs/MWCNTs.

### 66.4.2 The Influence of the Type and Concentration of Nanocarbon Filler on Shielding Characteristics of Nanocarbon–Epoxy Composites

The EMI shielding effectiveness ( $SE_T$ ) of a material is defined as the ratio between the incoming power and outgoing power of an electromagnetic wave. In general, SE is expressed in decibels (dB). In this study, the EMI shielding effectiveness of polymer (L285) composites with different nanocarbon fillers was investigated in broadband region (1–50 GHz), and synergistic effect in shielding properties in CMs with hybrid filler according to CMs with ordinary fillers was found.

EMI shielding effectiveness was calculated as follows (4), which are described in [38, 40]:

$$SE_T = -20 \log \left| \frac{1}{4n} \right| \cdot \left[ (1+n)^2 \cdot e^{\gamma \cdot l} - (1-n)^2 \cdot e^{\gamma \cdot l} \right] \quad (66.4)$$

Here  $n$  is the complex refractive index,  $\gamma = \alpha + i\beta$  is the electromagnetic wave propagation constant, and  $l$  is the thickness:

$$\alpha = \frac{2\pi}{\lambda} \cdot \sqrt{\varepsilon'} \cdot \sqrt{(0.5) \cdot \left( \sqrt{(1 + tg^2\delta)} - 1 \right)},$$

$$\beta = \frac{2\pi}{\lambda} \cdot \sqrt{\varepsilon'} \cdot \sqrt{(0.5) \cdot \left( \sqrt{(1 + tg^2\delta)} + 1 \right)}$$

Figure 66.7 shows the  $SE_T$  spectra of composites with different contents of GNPs/MWCNTs with the thickness of 1 mm in broadband frequencies (1–50 GHz). As it can be seen from figures,  $SE_T$  weakly depends on frequency, and the exclusion is CMs with high concentration of nanocarbon fillers. Thus, the transmission decreases with increasing concentration of filler.

Figure 66.8 shows the dependence  $SE_T$  values on the concentration of filler (in the case of binary filler, summary concentration) at a frequency 20 GHz. The synergistic effect in shielding effectiveness is clearly observed for the composites with concentrations near the percolation threshold (1 and 1.25 wt.%). Figure 66.8b presented concentration dependence  $SE_T$  in units  $\varphi/\varphi_c$ , i.e., in conventional units filler concentration to the critical concentration of the CMs with the appropriate type of filler.

One can conclude that good shielding properties of investigated MWCNTs–Larit285 CMs are primarily connected with low value of  $\varphi_c$  in these composites. Otherwise, the composites with GNPs demonstrate high value of  $SE_T$  at concentrations lower than  $\varphi_{c \text{ GNPs}}$  for these CMs. In other words in these composites high value of  $SE_T$  is achieved mainly due to good dispersion of GNPs in a polymer matrix and high level of interfaces. This allows assuming that synergistic effect on shielding effectiveness in CMs with binary filler appears due to different contributions of

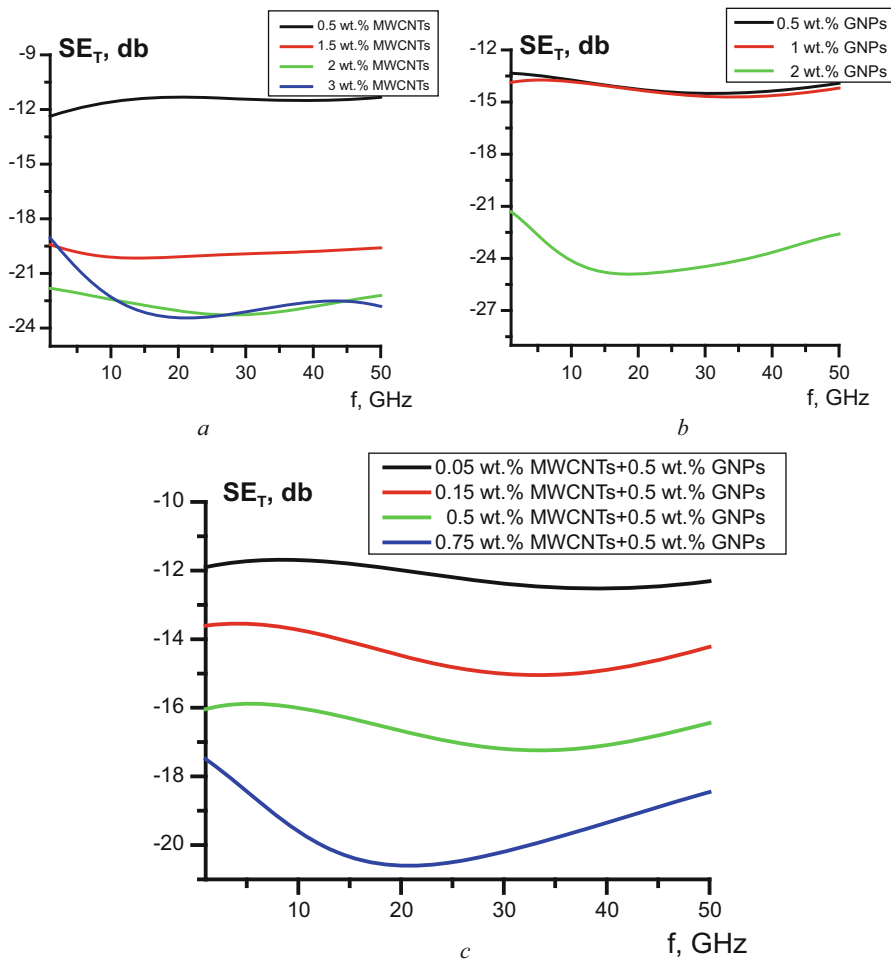


**Fig. 66.7** Spectra of  $SE_T$  for different types of nanocarbon fillers: (a) CNTs, (b) GNPs, (c) binary filler (CNTs + GNPs)

each individual filler. GNPs particles are well dispersed in polymer matrix that provide the formation of high interfaces which certainly increase the  $\epsilon'$ . MWCNTs form the conductive networks under low concentration. The addition of GNPs to a polymer containing MWCNTs not only improves the dispersion of MWCNTs in the polymer matrix but also creates the additional bridges connecting MWCNTs, making it easier to form a full conductive network in composites and increase the electrical conductivity and consequently shielding effectiveness.

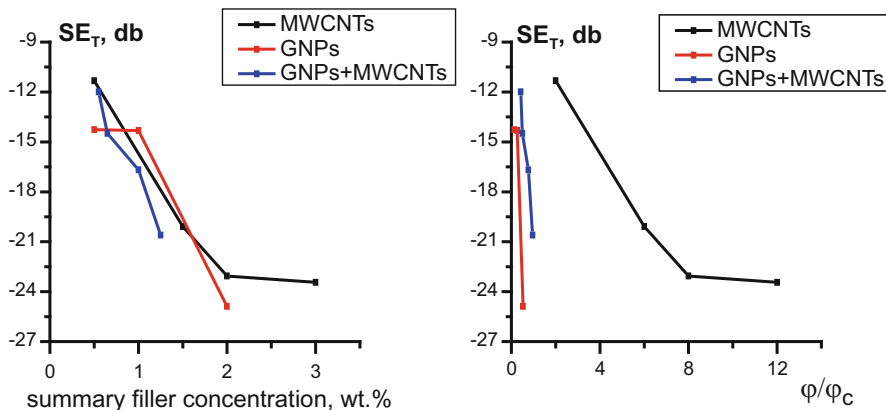


Fig. 66.8 Concentration dependencies of  $SE_T$  for different types of nanocarbon fillers at 20 GHz

### 66.4.3 Wave-Absorbing Properties

The wave-absorbing ability of CMs was also investigated. In the theory, the incident microwave in regime of metal-backed plate was divided into two parts (5), the reflected microwave and the absorbed one:

$$\begin{aligned}
 P_{in} &= P_R + P_A \\
 RL &= 10 \log P_R/P_{in} \\
 A &= 10 \log P_A/P_{in}
 \end{aligned}
 \tag{66.5}$$

where  $P_{in}$  is the power of the incident wave,  $P_R$  is the power of the reflected wave,  $P_A$  is the power of the absorbed wave, and  $RL$  and  $A$  are the reflection and the absorption losses, respectively, measured in decibels (dB). Here the microwave absorbing efficiency can be evaluated from  $RL$ . The larger the absolute value of  $RL$ , the stronger will be the wave-absorbing ability.

It is known that when the electromagnetic wave propagates through the medium, the reflectivity is affected by many factors, and not only by sample thickness. It also depends on permittivity, permeability, and electromagnetic wave frequency. In order to investigate the possibility to widen the range of strong absorption and increase the absorbing peak value for the composites with low concentration of nanocarbon filler, we simulated  $RL$  (dB) by applying the transmission line theory.  $RL$  of EMR under normal wave incidence at the surface of a single-layer material backed by a perfect conductor can be defined as [41]

$$RL = 20 \log \left| \frac{Z_{in} - Z_0}{Z_{in} + Z_0} \right|
 \tag{66.6}$$

where  $Z_0 = \sqrt{\mu_0/\varepsilon_0}$  is the characteristic impedance of free space and  $Z_{in} = \sqrt{\mu_0\mu/\varepsilon_0\varepsilon} (\tanh(i \cdot 2\pi f \sqrt{\mu_0\mu\varepsilon_0\varepsilon}d))$  is the input impedance at the interface of free space and material.

*RL* has been simulated for the MWCNTs/polymer nanocomposites (NCs) with different concentrations of filler and different sample thicknesses using experimental data for  $\varepsilon'$  and  $\varepsilon''$ . In our simulations we neglected the contribution of magnetic loss and permeability of composites into microwave absorption. We manually set  $\mu' = 1$  and  $\mu'' = 0$ . As shown in [41], the value of the magnetic tangent loss is very small for MWCNTs/epoxy NCs, and the dielectric loss tangent is much larger than the magnetic loss tangent for NCs with different MWCNT contents. Thus, we supposed that the main contribution in the microwave absorption should be made by the dielectric loss.

Theoretical spectra of *RL* for CMs (thickness  $d = 1$  mm) vs filler concentration are presented for all types of investigated fillers (Fig. 66.9). It is shown that in CMs *RL* peak value grows with increasing of filler concentration. The greatest *RL* value is  $-59.2$  dB (near 99.9% of absorption) for CM with 3 wt.% CNT at 29.5 GHz. Also Fig. 66.9 shows the increase in frequency bandwidth at high level of *RL* (for analysis we use  $RL < -10$  dB). The best result was observed in sample with 2 wt.% GNPs, where  $RL < -10$  dB from 20 GHz to end of investigated frequency range (50 GHz). These are amazing results, for example, in [41] natural rubber-based composites with carbon–silica hybrid fillers showed just near 3 GHz bandwidth ( $RL < -10$  dB) and *RL* peak value near  $-19$ dB at 1 GHz in natural rubber/CB composite; in another work [42] the highest result of reflection loss peak is near  $-12$ bd for 1.5 wt.% GNSs/0.5 wt.% MWCNTs with the thickness of 3.5 mm and bandwidth less then 2 GHz where  $RL < -10$ dB.

However, interesting results are observed in the CMs with binary filler. If the summary filler concentration is no more than 1 wt.% (0.5 wt.% MWCNT + 0.5 wt.% GNPs), peak *RL* value is more than in samples filled with GNPs and smaller than in samples filled with carbon nanotubes at relevant concentrations (Fig. 66.10a). However, in the sample with total concentration of binary filler 1.25 wt.% (0.75 wt.% MWCNTs + 0.5 wt.% GNPs), value of *RL* extremely grows higher than in CMs with both types of fillers with the same concentrations. This allows speaking about the presence of synergistic effect on absorbing properties in the CMs with binary nanocarbon fillers (GNPs + MWCNTs) compared to CMs with single fillers (GNPs or MWCNTs). Synergistic effect and a sharp improvement absorbing properties in the CMs with binary nanocarbon filler correlated to converge the percolation threshold, which in these composites is at a concentration 1.3 wt.% (0.8 wt.% MWCNTs + 0.5 wt.% GNPs) [35].



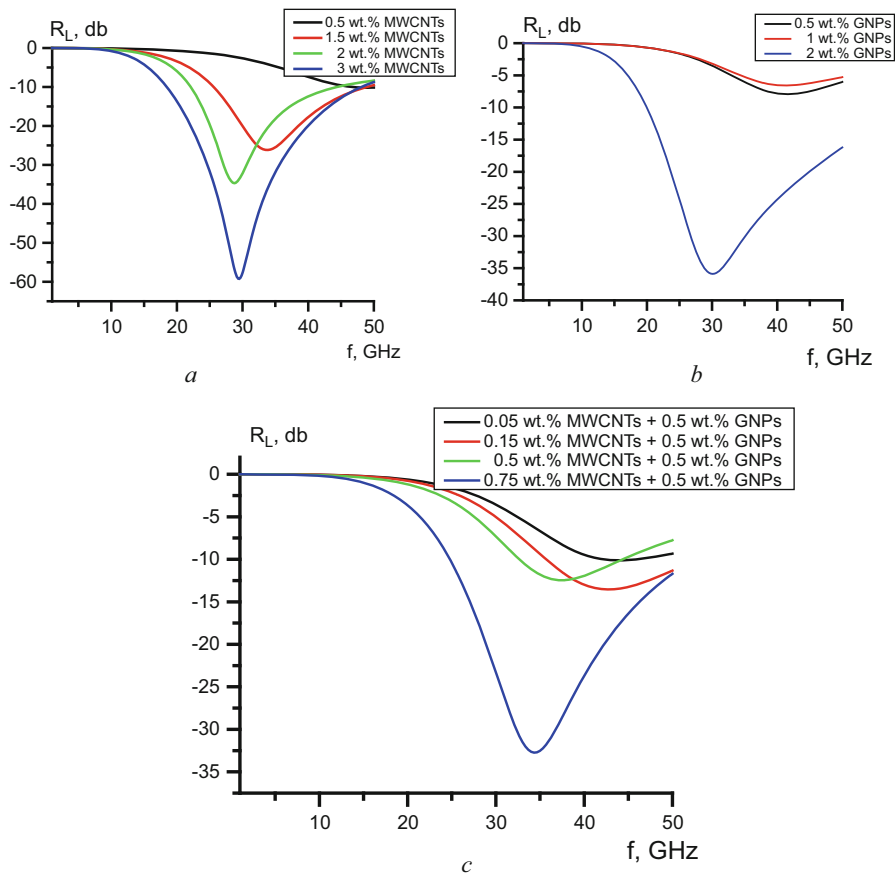


**Fig. 66.9** Frequency dependencies of  $RL$  in CMs with different filler concentrations: (a) CNT, (b) GNP, (c) binary filler

## 66.5 Conclusions

The electromagnetic and microwave absorbing properties of nanocarbon–epoxy Laritte 285 composites filled with GNPs and MWCNTs, as well as ternary CMs filled with GNPs and MWCNTs simultaneously, were studied as a function of frequency and fillers' weight content. It was shown that the values of  $\varepsilon'$ ,  $\varepsilon''$  increase with filler content increase for all investigated composites.

It was revealed that under transition from CMs with single (MWCNTs, GNPs) to CMs with binary filler (MWCNTs + GNPs) composites, the synergistic effect in behavior of real part of dielectric permittivity in the whole range of frequency and concentration took place. Meanwhile the synergistic effect in behavior of imaginary part of dielectric permittivity was observed only when the concentration of fillers in

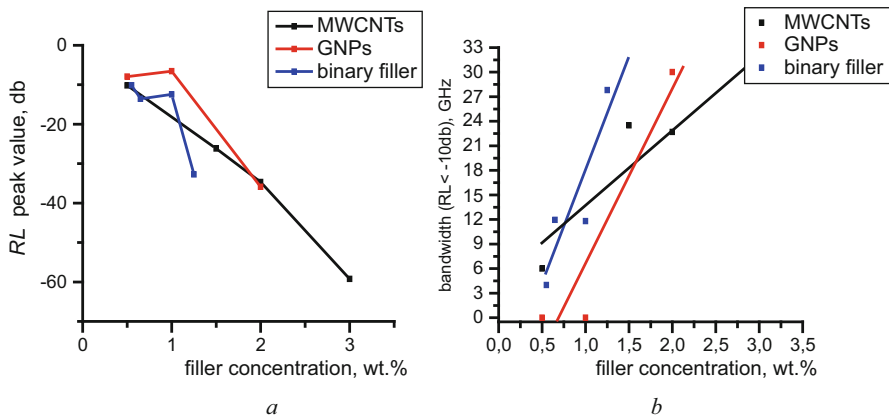


**Fig. 66.10** Concentration dependencies of *RL* peak value (a) and bandwidth at  $RL < -10\text{dB}$  (b)

composite with binary filler was larger than critical. Studies of microwave absorbing properties have shown that minimum reflection ( $\sim 33$  dB) and bandwidth at  $-10$  dB for composite with 0.5 wt.% GNPs and 0.75 wt.% MWCNTs in epoxy Laritte 285 were achieved at 28 GHz (thicknesses 1 mm) that is 1.5 and 3.5 times higher than bandwidth at  $-10$  dB for polymer–epoxy composites with 1.25 wt% MWCNTs and 1.25 wt% GNPs, respectively. So, the obtained results demonstrate that it is possible to adjust the properties of the composites, including the dielectric permittivity, shielding effectiveness, and microwave absorbing by a proper combination of nanocarbon fillers with different structure and morphology due to the synergistic effect of using binary fillers.

## References

1. Chung DDL (2000) Materials for electromagnetic interference shielding. *J Mater Eng Perform* 9:350–354
2. Qin F, Brosseau C (2012) A review and analysis of microwave absorption in polymer composites filled with carbonaceous particles. *J Appl Phys* 111:061301
3. Schmitt G et al (1991) Implantable Cardioverter defibrillator: possible hazards of electromagnetic interference. *Pacing Clin Electrophysiol* 14(6):982–984
4. Das NC et al (2001) Electromagnetic interference shielding effectiveness of ethylene vinyl acetate based conductive composites containing carbon fillers. *J Appl Polym Sci* 80(10):1601–1608
5. Wang Y, Xinli J (2005) Intrinsically conducting polymers for electromagnetic interference shielding. *Polym Adv Technol* 16(4):344–351
6. Shunichi S, Yaomi K, Kei U (1999) Conductive papers containing metallized polyester fibers for electromagnetic interference shielding. *J Porous Mater* 6(3):185–190
7. Geetha S et al (2009) EMI shielding: methods and materials—a review. *J Appl Polym Sci* 112:2073–2086

8. Yu ML et al (2016) Conductive and shielding properties of MWCNTs/polymer Nanocomposites with aligned filler distribution. *Fundamental and Applied Nano-Electromagnetics* Springer Netherlands:251–271
9. Xie N et al (2009) The influence of nano-Fe on the electromagnetic shielding properties of nano-Fe/carbon fiber/LDPE composites. *E-Polymers* 9.1:1127–1140
10. Pant RP et al (2002) Investigations on ferrofluid-conducting polymer composite and its application. *J Magn Magn Mater* 252:16–19
11. Yoshimori M, Morihiko M (1997) Two-layer wave absorber composed of soft-magnetic and ferroelectric substances. *IEEE Trans Magn* 33(5):3427–3429
12. Qiu Tai, et al. Microwave absorption properties of the carbonyl iron/EPDM radar absorbing materials. *Journal of Wuhan University of Technology-Mater. Sci. Ed.*, 2007, 22.2: 266-270.
13. Vovchenko L et al (2012) Shielding coatings based on carbon–polymer composites. *Surf Coat Technol* 211:196–199
14. Meenakshi V et al (2015) Barium ferrite decorated reduced graphene oxide nanocomposite for effective electromagnetic interference shielding. *Phys Chem Chem Phys* 17(3):1610–1618
15. Scher Harvey, Zallen Richard. Critical density in percolation processes. *J Chem Phys*, 1970, 53.9: 3759.
16. Hao T, Xinfang C, Luo Y (1996) Electrical and dynamic mechanical behavior of carbon black filled polymer composites. *Eur Polym J* 32(8):963–966
17. Coleman Jonathan N., Khan Umar, Gun'ko Yurii K. Mechanical reinforcement of polymers using carbon nanotubes advanced materials, 2006, 18.6: 689-706.
18. Wei C et al (2011) Improving thermal conductivity while retaining high electrical resistivity of epoxy composites by incorporating silica-coated multi-walled carbon nanotubes. *Carbon* 49(2):495–500
19. Andreas G, Gaurav K, Pötschke P (2009) Selective localization and migration of Multiwalled carbon nanotubes in blends of polycarbonate and poly (styrene-acrylonitrile). *Macromol Rapid Commun* 30(6):423–429
20. Grady BP (2010) Recent developments concerning the dispersion of carbon nanotubes in polymers. *Macromol Rapid Commun* 31(3):247–257
21. Bellis D, Giovanni, et al. (2011) Electromagnetic properties of composites containing graphite nanoplatelets at radio frequency. *Carbon* 49(13):4291–4300
22. Popielarz R et al (2001) Dielectric properties of polymer/ferroelectric ceramic composites from 100 Hz to 10 GHz. *Macromolecules* 34(17):5910–5915
23. Cao M-S et al (2010) The effects of temperature and frequency on the dielectric properties, electromagnetic interference shielding and microwave-absorption of short carbon fiber/silica composites. *Carbon* 48(3):788–796
24. Feng Y et al (2015) Enhanced dielectric properties of PVDF-HFP/BaTiO 3-nanowire composites induced by interfacial polarization and wire-shape. *J Mater Chem C* 3(6):1250–1260
25. Ma P-C et al (2009) Enhanced electrical conductivity of nanocomposites containing hybrid fillers of carbon nanotubes and carbon black. *ACS Appl Mater Interfaces* 1(5):1090–1096
26. Tong W et al (2010) The synergy of a three filler combination in the conductivity of epoxy composites. *Mater Lett* 64(21):2376–2379
27. Yu A et al (2008) Enhanced thermal conductivity in a hybrid graphite nanoplatelet–carbon nanotube filler for epoxy composites. *Adv Mater* 20(24):4740–4744
28. Yao S et al (2008) Modeling of the electrical percolation of mixed carbon fillers in polymer-based composites. *Macromolecules* 42(1):459–463
29. Melnichenko Mykola, et al. Electrodynamical properties of the nanocarbon/polymer composites with aligned by magnetic field secondary non-conductive component. In: *SPIE Microtechnologies*. International Society for Optics and Photonics, 2015. p. 951918-951918-11.
30. Meenakshi V et al (2015) Barium ferrite decorated reduced graphene oxide nanocomposite for effective electromagnetic interference shielding. *Phys Chem Chem Phys* 17(3):1610–1618
31. Yu C et al (2015) Enhanced electromagnetic interference shielding efficiency of polystyrene/graphene composites with magnetic Fe<sub>3</sub>O<sub>4</sub> nanoparticles. *Carbon* 82:67–76

32. Xinhua Z et al (2012) The origin of the electric and dielectric behavior of expanded graphite–carbon nanotube/cyanate ester composites with very high dielectric constant and low dielectric loss. *Carbon* 50(14):4995–5007
33. Myung-Sub K et al (2013) Synergistic effects of carbon nanotubes and exfoliated graphite nanoplatelets for electromagnetic interference shielding and soundproofing. *J Appl Polym Sci* 130(6):3947–3951
34. Krueger QJ, King JA (2003) Synergistic effects of carbon fillers on shielding effectiveness in conductive nylon 6, 6-and polycarbonate-based resins. *Adv Polym Technol* 22(2):96–111
35. Perets Yu. S., et al. The electrical and thermal properties of hybrid composites based on graphite nanoplatelets with multiwall carbon nanotubes. (in press)
36. Al-Saleh MH (2009) Sundararaj Uttandaraman. Electromagnetic interference shielding mechanisms of CNT/polymer composites. *Carbon* 47(7):1738–1746
37. Yuchang Q et al (2010) Epoxy-silicone filled with multi-walled carbon nanotubes and carbonyl iron particles as a microwave absorber. *Carbon* 48(14):4074–4080
38. Jinsoo J, Lee CY (2000) High frequency electromagnetic interference shielding response of mixtures and multilayer films based on conducting polymers. *J Appl Phys* 88(1):513–518
39. Zunfeng L et al (2007) Reflection and absorption contributions to the electromagnetic interference shielding of single-walled carbon nanotube/polyurethane composites. *Carbon* 45(4):821–827
40. Zunfeng L et al (2007) Microwave absorption of single-walled carbon nanotubes/soluble cross-linked polyurethane composites. *J Phys Chem C* 111(37):13696–13700
41. Al-Ghamdi AA et al (2016) Natural rubber based composites comprising different types of carbon-silica hybrid fillers. Comparative study on their electric, dielectric and microwave properties, and possible applications. *Mater Sci Appl* 7(06):295
42. Fang R et al (2015) Cyanate ester filled with graphene nanosheets and multi-walled carbon nanotubes as a microwave absorber. *J Polym Res* 22(5):1–7

# Index

## A

Absorption, 31, 32, 36–37, 56, 72, 73, 132, 140, 141, 249–260, 294, 300, 317, 320, 347, 350, 351, 417–418, 435, 485, 490, 499, 580, 587, 590, 603, 604, 607, 608, 611, 665, 688, 762, 817, 822, 824, 837, 855, 866, 867  
Abu Sal, B., 661–672  
Adamik, M., 694  
AK12M2MgN alloy, 508, 509, 511, 513–518, 520  
Akselrud, L., 802  
Aleksandrovych, L.L., 855–869  
Aniline derivatives, 837–838  
Annealing, 307, 308, 348–352, 376, 409, 410, 447, 449, 457–466, 482–484, 489, 490, 555, 801, 802, 846–848  
Antimicrobial properties, 642, 656–657  
Apatite, 631–633  
Asahi, R., 603  
Avramenko, T.G., 799–811

## B

Bairachniy, B., 557–570  
Bakonyi, I., 558  
Balega, A.V., 585–593  
Barbash, V.A., 497–504  
Barna, P.B., 694  
Bazela, W., 445–455  
Belyavina, N.N., 799–811  
Berger, L., 157  
Bertaut, E.F., 454  
Biexciton, 132, 133, 142, 143

Bildukevich, A., 675–684  
Bimetallic core-shell objects, 841  
Binding energy, 132–143, 148, 347, 413, 830  
Bis(acetylacetonato)dichlorotin, 53, 55  
Bobák, A., 63–76  
Bobitski, Y.V., 3–16, 231–245  
Bondarenko, N.V., 395–403  
Borovoy, N.A., 771–786  
Borysova, K.V., 631–636  
Boshko, O.I., 799–811  
Bououdina, M., 305–321  
Brazhnyk, I.V., 837–842  
Bromine resistivity, 773, 775–781  
Brynza, M., 661–672  
Bulavinets, T., 231–245  
Burlaka, A., 813–825  
Busch, D.H., 64  
Büttiker, M., 722

## C

Calvez, L., 479–490  
Cancer nanotechnology, 315  
Carbon, 30, 32, 116, 118, 121, 125, 126, 175, 187–189, 249–251, 319, 332, 395–403, 457, 554, 565, 570, 612, 615, 617, 619, 695, 702, 721, 729, 730, 735, 737, 739, 746, 747, 750, 758, 779, 784  
Catalyst, 305, 321, 355, 356, 360–363, 499, 507, 521, 522, 527, 528, 547, 557, 631, 758, 825, 838, 840  
Catalytic activity, 306, 361, 362, 507, 509, 514, 521, 522, 527–529, 557, 574  
Cation distribution, 311, 312, 315

- Ceramics, 19, 20, 309, 327, 457, 458, 479–490, 623–626, 628, 636  
 Ceramics based onto ZrO<sub>2</sub>, 459, 464–466  
 Chaix, C., 533–544  
 Chalyy, D., 479–490  
 Charge transfer, 120, 126, 175–185, 188, 204, 771–786, 842  
 Charmas, B., 729–741  
 Char/nanosilica composite, 729–731, 733, 737, 739, 741  
 Chemical composition, 305, 312, 315, 412–413, 498, 508, 510, 672, 688, 691, 707, 752, 847  
 Chemical heat treatment, 500, 502  
 Cherevko, V., 207–226  
 Chrzanowska, A., 469–475  
 Chumachenko, V.A., 585–593  
 Coagulation, 149, 705, 706, 744  
 Cobalt oxides, 517, 519, 522  
 Composite, 22, 295, 298, 299, 356, 357, 359–363, 423, 425, 427, 508, 544, 547, 611, 615–617, 619, 621, 641, 643, 664, 665, 667, 669–671, 676, 681, 683, 684, 706–708, 710, 711, 713, 729, 731, 736, 737, 739, 741, 759, 800, 802–807, 840, 846, 855–869  
 Copper oxide, 347–352  
 Costa-Kramer, J.L., 721  
 Coulomb and exchange interaction, 132, 139, 142, 143  
 Cuerno, R., 406  
 Cu/(Ni-Cu), 557–559, 565–567, 570  
 Current density, 97, 98, 104–106, 108, 157, 175, 184, 185, 342, 510, 513–520, 522, 525, 528–529, 558–559, 823  
 Current transient, 564
- D**  
 Dashevskiy, M.M., 799–811  
 Davydov, A.S., 188  
 Dawid, A., 29–42, 249–260  
 Decurtins, S., 64, 72  
 Demchenko, V., 641–657  
 Demchishin, A.V., 693  
 Density functional theory method, 65, 604  
 Depine, R.A., 417  
 Derhachov, M., 661–672  
 Derkachov, G., 275–281  
 Diffusion, 31, 36, 39, 47, 48, 96, 98, 99, 105, 107–111, 257, 275, 276, 302, 336, 368, 369, 374, 375, 406, 433, 438, 440, 540, 550, 562, 564, 575, 597, 611–615, 617–621, 643, 694, 700, 701, 805, 824  
 Diphenylamine (DPA), 838–840, 842  
 Discrete energy levels, 3, 4, 9, 13, 15, 16  
 Dmytrenko, O.P., 757–769  
 Dontsova, T., 705–718  
 Dopants, 315, 512, 520, 525  
 Doxorubicin, 814  
 Dozov, I., 469–475  
 Drickamer, H.G., 66, 67  
 Dridi, F., 537  
 Dul, M., 445–455  
 Dyakonov, V., 445–455  
 Dzyadevych, S.V., 573–583  
 Dzyazko, Y., 675–684
- E**  
 Electrochromism phenomenon, 837, 838  
 Electrodeposition, 558, 563, 799  
 Electronic structure, 65, 66, 125, 608, 690, 771, 777, 784  
 Electron irradiation, 759–763, 765–769  
 Electron microscopy, 499, 549, 554, 625, 688, 691, 697, 802, 847, 851  
 Electron spin resonance (ESR) spectra, 816–821, 823, 824  
 Electropolymerization, 841, 842  
 Estimations of dimensions, 202  
 Exploitation properties, 489  
 External field, 69, 71, 175–178, 180, 183–185, 187–204, 823
- F**  
 Fano, U., 428  
 Farre, C., 533–544  
 Feedback, 4, 94–99, 103–107, 300, 381  
 Fermi-Dirac distribution, 177  
 Ferrite, 19, 20, 310, 312, 313, 315–321, 618, 824  
 Filevska, L.M., 53–60  
 Fine crystalline graphite, 772, 782  
 Fitio, V.M., 3–16, 231–245  
 Fourier transformation, 699  
 Free volume, 479–490, 790, 794  
 Frolova, L.A., 19–27  
 Fuel cells, 557, 623–628, 631  
 Functional properties, 479–490, 522, 557, 563, 681, 837, 842
- G**  
 Gab, A.I., 687–691  
 Gab, I.I., 457–466  
 Galivets, Y.D., 19–27

- Gburski, Z., 29–42, 45–50, 249–260, 595–600, 789–796
- Getman, E.I., 631–636
- Gimzewski, J.K., 721
- Glasses, 30, 132, 133, 140, 141, 208, 209, 265, 268–270, 347, 348, 351, 434, 458–461, 463–466, 479–490, 497, 511, 525, 536, 570, 604
- Glucose/nanosilica composite, 730, 732, 733, 738
- Glushko, E.Y., 263–273
- Głowa, Ł., 335–344, 347–352
- Graphene, 249, 250, 320, 383–392, 727, 729, 739, 772, 789–796, 856
- Graphite intercalated compound (GIC), 771, 773–775, 778, 782, 784, 785
- Grebenyuk, A., 603–608
- Grinevych, V.S., 53–60
- Gudyma, Iu., 63–76
- Guglya, A., 693–702
- Gun'ko, V.M., 729–741
- Gurgol, J., 355–363
- H**
- Hadzaman, I., 479–490
- Hall, W.H., 448
- Hatala, I., 335–344
- Hauser, A., 64
- Holze, R., 661–672
- Honcharov, V., 355–363
- Hryn, V.O., 293–302
- Hydrogen, 20, 56, 139, 284, 318, 355, 356, 360, 362, 363, 437, 438, 441, 442, 502, 510, 577, 625, 687–690, 694, 695, 701, 702, 737, 739
- Hydrolysis, 284, 308, 499–503, 513, 579, 580, 586, 588, 604, 636
- I**
- Iakushev, D.A., 417–429
- Ibrayeva, A., 79–89
- Ihara, T., 604
- Ingram, A., 479–490
- Injected electron, 182–184, 190–192
- Inorganic graphene-like nanoparticles, 845, 847
- Intergranular pores, 694
- Interphase boundary, 427, 701
- Interpolyelectrolyte complexes (IPEC), 642–652, 654, 655, 657
- Interpolyelectrolyte–metal complexes (IMC), 642–657
- Ion-beam assisted deposition, 694
- Irie, H., 603
- Iron
- $\alpha$ -phase, 552, 556
  - oxide, 554, 706, 752, 813, 814, 816, 818–820, 822–825
- Isai, V.M., 383–392
- Ivanenko, K.O., 799–811
- Ivanusa, A., 479–490
- J**
- Jaffrezic-Renault, N., 533–544
- Jakubczyk, D., 275–281
- Janusz, W., 435, 729–741
- John Kennedy, L., 305–321
- Judith Vijaya, J., 305–321
- K**
- Kaczor, M., 335–344, 347–352
- Kaladkevich, Y., 327–332
- Kalchenko, A., 693–702
- Kalinichenko, D.V., 283–291
- Kaniukov, E., 79–89
- Karakurkchi, A.V., 507–529
- Kasap, B.O., 573–583
- Kavelin, V.V., 457–466
- Kharchenko, D.O., 365–381
- Kharchenko, V.O., 365–381
- Kinetics, dispersion, 457–466
- Kizilova, N., 207–226
- Klym, H., 479–490
- Kobzar, Y.L., 283–291
- Kolwas, K., 275–281
- König, E., 64, 66
- Konig-Ettel, N.B., 845–852
- Kornienko, L., 675–684
- Korol, A.M., 383–392
- Korostil, A.M., 93–111
- Kostiv, Y., 479–490
- Kostyuk, B.D., 457–466
- Kotsiuba, Y., 231–245
- Koudriavtsev, A.B., 68
- Kovalchuk, V.O., 497–504
- Kovzun, I.G., 743–754
- Kozlovskiy, A., 79–89
- Kozyrev, A., 327–332
- Kravchenko, V.N., 283–291
- Krit, A.N., 283–291
- Krupa, M.M., 93–111
- Kucherenko, I.S., 533–544, 573–583
- Kulikov, L.M., 845–852
- Kulish, M.P., 757–769
- Kurç, B.A., 573–583
- Kuryliuk, A.N., 283–291

Kushevskaya, N.F., 547–556  
 Kushnerov, O.I., 19–27  
 Kutsevol, N.V., 585–593

## L

Lagarde, F., 533–544  
 Landauer, R., 721, 722, 727  
 Lazarenko, O.A., 855–869  
 Len, T.A., 771–786, 845–852  
 Leucosapphire, 458, 459, 461–466  
 Limiting current, 561–563, 570  
 Linnik, O., 603–608  
 Litvynchuk, S.I., 383–392  
 Lobanov, V., 603–608  
 Longa, L., 471  
 Lorman, V.L., 469–475  
 Luchenok, A., 327–332  
 Lukin, S., 813–825  
 Luzanov, A.V., 115–127  
 Lyubchenko, E., 693–702

## M

Madeja, K., 64, 66  
 Magnetic characteristics, 26, 547–556, 713–717  
 Magnetic dynamics, 93–111  
 Magnetic nanocomplex, 813–825  
 Magnetic nanostructures, 93–96, 107–111  
 Magnetic properties, 20, 25, 27, 208, 311, 312, 314–315, 445, 455, 554, 557, 706, 707, 813–825, 857  
 Magnetization, 24–26, 68, 94–104, 106–108, 111, 157–160, 162, 314, 315, 716, 717, 816, 817  
 Magnetometry, 21, 816, 823  
 Maizelis, A., 557–570  
 Makarchuk, O., 705–718  
 Maksymov, A., 63–76  
 Malyshev, V.V., 547–556, 687–691  
 Mamchur, O.O., 573–583  
 Manganese oxide (MnO), 451, 507, 509, 512, 516–517, 520, 523, 524  
 Marchenko, S.V., 573–583  
 Marchenko, Y., 693–702  
 Matzui, L.Y., 771–786, 845–852  
 Matzui, V.I., 845–852  
 Mazui, L.Y., 855–869  
 Measurements of conductance, 721–728  
 Mechanochemical activation, 731, 801, 804, 814–815, 822  
 Mediator, 569  
 Medvid, N.V., 383–392

Melnichenko, M.M., 799–811  
 Melnychenko, M.S., 855–869  
 Memmer, R., 469–475  
 Metal, 20, 53, 64, 94, 145, 293, 306, 327, 355–363, 376, 383, 395, 405, 417, 431, 457, 480, 507, 557–570, 575, 585, 603, 612, 624, 636, 641, 661, 688, 693, 721, 729, 803, 827, 838, 845, 855  
 Metal oxide system, 145, 431, 528, 558  
 Methanol oxidation, 568–570  
 Meyer, R.B., 470  
 Microhardness, 329–332, 366, 409, 560, 566, 567, 570, 616, 618, 759, 762–763, 768, 799–811  
 Mixed oxides, 508, 514, 517, 518, 520–522, 524, 525, 528, 529  
 Moiseienko, V., 661–672  
 Molecular mechanics method, 396  
 Moller, R., 721  
 Molybdenum disulfide, 845–852  
 Movchan, B.A., 693  
 Multilayer coating, 557, 558, 560, 564–566, 570  
 Multi-walled carbon nanotube (MWCNT), 307, 757–769, 856–859, 861, 862, 865, 867, 868  
 Myronchuk, V., 675–684

## N

Nadtoka, O.M., 585–593  
 Nahirnyj, T.S., 827–835  
 Naidich, Y.V., 457–466  
 Nakonechna, O.I., 799–811  
 Nanocellulose, 497–504  
 Nanocluster, 115, 116, 118, 120, 121, 123, 124, 126–127, 145–156, 367, 395–403, 577, 662  
 Nanocomposite, 293–302, 356, 497, 533–544, 547–556, 611–621, 641–657, 661–672, 688, 707, 712–713, 715, 729, 757–759, 761, 765–768, 799–811, 839, 842, 845, 857, 867  
 Nanocrystalline structures, 694, 701, 702  
 Nanofilm, 457–466, 846  
 Nano-oscillations, 94, 159, 160, 162  
 Nanoparticles (NPs), 19–27, 76, 145–149, 151–156, 207, 208, 210–212, 226, 275–281, 293, 295, 299, 302, 312, 314, 395, 432, 450, 454, 455, 482, 534, 573, 577, 642, 675–676, 678, 711, 716, 717, 729, 731, 736, 746, 747, 837–842, 845–852



- Nanopores, 488–490, 625–628, 701, 702, 736, 739, 741
- Nanopowders, 21, 146, 156, 447, 448, 687–691
- Nanosilica, 729–731, 734, 735, 741
- Nano-sized layers, 564
- Nanosized tin dioxide, 53, 60
- Nanostructure, 80, 89, 93–111, 116, 146, 147, 293–294, 395, 405, 410, 431–442, 534, 721–728, 750, 789, 814, 822, 847
- Naumenko, A.P., 585–593, 845–852
- Naumenko, S.N., 283–291
- Naumova, D.D., 771–786
- Nawrocki, W., 721–728
- Nedolya, A.V., 395–403
- Nickel oxyhydroxide (NiOOH), 559, 569
- Nikipelova, O.M., 743–754
- Nitrogen doped titania, 603–608
- Nosach, L.V., 729–741
- Nosal-Wiercińska, A., 431–442
- Numerical solution, 3–16, 147, 165, 213–214
- Nychyporenko, O.S., 757–769
- O**
- Oliinyk, V.O., 743–754
- Optical properties, 116, 140, 263–264, 306, 314, 317, 321, 336, 405, 406, 490, 641, 845–852
- Optical spectra, 838, 841, 842
- Orel, V., 813–825
- Organosolv pulping, 503
- Ostash, O.P., 623–628
- Ostolska, I., 431–442
- Ovsiienko, I.V., 771–786, 845–852
- Oxidative polymerization, 838, 841
- Oxide, 20, 22, 53, 57, 79, 145, 287–289, 293, 307, 363, 431, 435, 457–466, 479–490, 507, 508, 511–522, 524–526, 528, 529, 557–570, 624, 632, 633, 642, 688–691, 729
- Oxygen parameter, 310
- P**
- Pajak, G., 471
- Pakhlov, E.M., 729–741
- Palladium (Pd), 146, 457–466, 507
- Panko, A.V., 743–754
- Paprotskaya, E.A., 547–556, 687–691
- Penney, W.G., 125
- Perekos, A., 705–718
- Perets, Y.S., 855–869
- Peter, L., 558
- Petrovska, H., 231–245
- Phase composition, 21, 22, 56, 328–330, 332, 510, 524, 528–529, 548, 549, 553, 633, 662, 688–690, 709, 710, 774
- Photocatalytic properties, 321, 603
- Photoluminescence, 759, 765–769
- Photovoltage, 284–288, 290
- Photovoltaic (PV) cells, 337, 347
- Piliponskiy, I.I., 573–583
- Pinchuk-Rugal, T.M., 757–769
- Planar and columnar growth of film, 340, 344
- Plasma electrolytic oxidation, 508, 510, 516, 517, 520, 522, 525, 528
- Platinum (Pt), 94, 107, 108, 357, 457–466, 507, 521, 522, 528, 536, 538, 560, 562, 631, 730, 838
- Podhurska, V.Y., 623–628
- Podlaha, E.J., 558
- Podolyan, A.A., 283–291
- Pokutnyi, S.I., 131–143
- Polarization cycles, 842
- Polyligand electrolyte, 558, 559, 561–566
- Polymer coatings, 283–291, 838
- Polypeptide, 175–185
- Polyvinylchloride (PVC), 757–769
- Popovych, D.I., 145–156
- Porod, G., 649
- Positron annihilation, 488
- Potential barrier (PB), 13, 131, 134, 149, 397–401, 771
- Potera, P., 347–352
- Prikhna, T., 327–332
- Printable electronics, 759
- Prokopenko, O.V., 157–171
- Prokopenko, V.A., 743–754
- Prokopov, O.I., 771–786
- Protein molecule, 175–184
- Prylutskiy, Y.I., 757–769
- Q**
- Quantum chemical calculations, 604
- Quantum dot (QD), 131–143
- Quartz glass, 458–461, 463–466
- R**
- Raczyńska, V., 45–50, 789–796
- Raczyński, P., 45–50, 595–600, 789–796
- Radio frequency, 813–825, 855
- Raimondi, G., 533–544
- Raman spectroscopy, 671, 838, 851
- Rare earth elements (REEs) silicates, 445, 631, 632, 636

- Raymand, D., 147  
 Resistivity, 97, 225, 366, 380, 511, 512,  
 514–515, 517, 519, 523, 524, 535, 773,  
 775–781, 784–786, 823  
 Revo, S.L., 799–811  
 Riabov, S., 641–657  
 Romakh, V.V., 3–16  
 Romanov, A., 813–825  
 Rozhdestvenska, L., 675–684  
 Ruthradevi, T., 318  
 Rybalchenko, N., 641–657  
 Rykhalskyi, O., 813–825
- S**  
 Sagan, P., 335–344  
 Sakhnenko, N.D., 507–529  
 Savin, S.M., 53–60  
 Savka, S.S., 145–156  
 Savkina, R.K., 405–415  
 Sawlowicz, Z., 355–363  
 Scanning electron microscope (SEM), 80–83,  
 85, 87–89, 338, 339, 356, 357, 359,  
 408, 409, 458, 459, 499, 500, 510, 549,  
 560, 625, 664, 671, 677–679, 688, 695,  
 698–700, 707, 712–714, 730, 733, 736,  
 744, 750, 751, 753, 758, 759, 801, 802,  
 804, 838, 847–849, 858, 859  
 Seki, S., 67  
 Serednytski, A.S., 145–156  
 Shakhnin, D.B., 547–556  
 Shevchenko, A., 813–825  
 Shlapatska, V.V., 757–769  
 Shmeleva, L.V., 175–185  
 Shniruk, O.M., 497–504  
 Shopa, Y., 275–281  
 Shpotyuk, O., 479–490  
 Shtompel', V., 641–657  
 Shumskaya, A., 79–89  
 Shut, M.I., 757–769  
 Silicate apatite, 631, 632  
 Silicon, 133, 143, 208, 265, 270, 283, 285–288,  
 336, 337, 339, 343, 344, 511, 512, 514,  
 516, 517, 520, 576, 631, 632, 695, 698,  
 721, 743  
 Skubiszewska-Zi'eba, J., 729–741  
 Skwarek, E., 729–741  
 Slavin, A.N., 160, 161  
 Slichter, C.P., 66, 67  
 Slonczewski, J.C., 157  
 Smirnov, A.B., 405–415  
 Smirnova, O., 603–608  
 Smirnova, T.N., 293–302  
 Smyntyna, V.A., 53–60  
 Socha, R., 355–363  
 Solar cell, 283–291, 336, 337, 343  
 Solar silicon crystals, 336, 337  
 Soldatkin, A.P., 533–544, 573–583  
 Soldatkin, O.O., 533–544, 573–583  
 Solopikhina, E., 693–702  
 Sorai, M., 67  
 Spatially separated electron and holes, 132,  
 133  
 Spin currents, 93–97, 99–111  
 Spinel structure, 310, 313, 315, 321, 486  
 Spin Hall effect (SHE), 94–100, 103–110, 513,  
 518  
 Stationary Schrödinger equation, 3–16  
 Steblenko, L.P., 283–291  
 Stepanyuk, A.N., 263–273  
 Stetsko, A.E., 611–621  
 Stetsyuk, T.V., 457–466  
 Stöber, W., 663  
 Storage, 29, 63, 249, 305, 320, 487, 542, 543,  
 662, 694, 695, 701, 702  
 Streda, P., 721  
 Structural characteristics, 408, 801  
 Structural defects, 671, 672  
 Structure, 3–5, 13–15, 20, 24, 27, 32, 36, 54,  
 55, 60, 65, 66, 69, 81, 97, 104, 109,  
 121, 125, 146, 148, 149, 154–160, 175,  
 179–181, 184, 190, 195, 232, 257, 260,  
 263, 264, 266, 268, 270–273, 287, 290,  
 291, 293–302, 305–321, 327, 336, 337,  
 339, 340, 344, 378, 379, 387, 391, 392,  
 406, 409–410, 413, 414, 432, 436, 442,  
 446, 449, 469, 489, 500, 510, 525, 574,  
 585–593, 615, 627, 631, 641–657, 662,  
 677–680, 695, 696, 698–701, 713, 739,  
 774, 799–811, 814, 828, 830  
 Substrate, 146, 264, 295, 301, 337–340, 343,  
 348, 367, 368, 373, 376, 380–381, 421,  
 458, 462–466, 508, 509, 514, 515, 538,  
 541, 542, 559, 566, 575, 576, 579,  
 580, 582, 677–680, 682, 683, 693–695,  
 698–700, 841, 846  
 Sudnik, L., 327–332  
 Sulymenko, O.R., 157–171  
 Suprun, A.D., 175–185, 187–204  
 Surface, 26, 36, 59, 67, 80, 131, 146, 208, 232,  
 255, 266, 283, 294, 306, 327, 336, 348,  
 355–363, 405–415, 417–429, 431, 457,  
 497, 508, 536, 547, 557, 574, 595, 605,  
 611, 625, 633, 643, 663, 675, 688, 694,  
 706, 730, 746, 757, 790, 800, 814, 827,  
 840, 846, 862

- Synthesis, 19–27, 89, 145, 284, 295, 305–321, 328, 356, 525, 534, 547, 575, 586, 631–636, 641, 663, 676, 687, 710, 759, 773, 814, 837
- Synthesis temperature, 549, 550, 552–554, 556
- Szytuła, A., 445–455
- T**
- Tarasov, Y.V., 417–429
- Tatarchuk, T., 305–321
- Tchervinka, K.A., 827–835
- Temperature, 3, 21, 30–31, 46, 54, 64, 86, 145, 158, 175–185, 208, 250, 275, 285, 306, 327, 337, 348, 356, 365, 396–397, 407, 431, 446, 457, 469, 480, 499, 507, 536, 548, 557, 574, 595, 604, 614, 623, 631, 642, 662, 678, 687, 693, 721, 730, 743, 758, 772, 790, 799, 822, 828, 846
- Tetrahedral interstices, 400
- Textural characteristics, 730–732, 736, 739
- Thermogravimetry, 54–58, 60, 731, 734, 736
- Thermomechanical properties, 644–651
- Thermopower, 773, 775, 776, 781–782, 785, 786
- Thin films, 53, 54, 146, 232, 336–338, 343, 347, 348, 350, 356–358, 365, 603–608, 693–702, 833, 834
- Thornton, J.A., 693
- Tiberkevich, V.S., 160, 161
- Tkachuk, V., 327–332
- Tkach, V.M., 757–769
- Transmission spectra, 347–352, 482, 484–486, 664
- Tsyganovich, O.A., 743–754
- Tungsten, 687–689, 726
- U**
- Ukrainetz, A., 675–684
- Ultrasound treatment, 20, 498–500
- Usatenko, O.V., 417–429
- V**
- Vacuum, 54, 110, 137, 160, 328, 338, 341, 418, 419, 421, 427, 457–466, 481, 489, 490, 676, 693, 700, 730, 758, 799, 847
- Van der Pauw, L., 625
- van Duin, A.C.T., 147
- Vasylyv, B.D., 623–628
- Vasylyuk, S.V., 187–204
- Ved, M.V., 507–529
- Virt, I., 335–344
- Vlasov, V., 693–702
- Voronin, E.F., 729–741
- Voronzova, L.A., 283–291
- Vovchenko, L.L., 855–869
- VT1-0 alloy, 509, 510, 523, 524, 526, 528
- Vyshnevskaya, Y.P., 837–842
- W**
- Water adsorption, 733
- Wave functions, 3–5, 7, 8, 14–16, 121, 123, 132, 137–141, 176, 190, 385, 850, 851
- Wheat straw, 498, 503
- Williamson, G.K., 448
- Wiśniewska, M., 431–442
- Wis, G., 335–344, 347–352
- Wood, R.W., 418, 428
- Woźniak, M., 275–281
- X**
- X-rays, 284, 287, 289, 408, 554, 643, 647–649, 651–652, 688, 802, 805, 847
- Y**
- Yakimchuk, D., 79–89
- Yaremchuk, I.Y., 3–16
- Yaschenko, O.V., 497–504
- Yashchenko, L.N., 283–291
- Yashchuk, V.N., 187–204
- Yavorskyi, R., 335–344
- Yezhov, P.V., 293–302
- Young's modulus, 759, 762, 768, 832, 833
- Z**
- Zazhigalov, V., 355–363
- Zdorovets, M., 79–89
- Zinc oxide (ZnO), 145–156, 211, 335–344, 512, 603
- Zloi, O.S., 771–786
- Zmievska, Y., 675–684